UNCLASSIFIED

AD NUMBER

AD811355

NEW LIMITATION CHANGE

TO

Approved for public release, distribution unlimited

FROM

Distribution authorized to U.S. Gov't. agencies and their contractors; Administrative/Operational Use; Dec 1966. Other requests shall be referred to Air Force Avionics Laboratory, Attn: AVPT, Wright-Patterson AFB, OH 45433.

AUTHORITY

AFWAL ltr, 25 Mar 1988

THIS PAGE IS UNCLASSIFIED

811355

AFAL-TR-66-391
VOLUME I

811355

TECHNIQUES FOR AIRBORNE RADOME DESIGN

VOLUME ONE

DR. THOMAS E. TICE
EDITOR-IN-CHIEF

THE McGRAW-HILL BOOK COMPANY, INCORPORATED
TECHNICAL WRITING SERVICE

TECHNICAL REPORT AFAL-TR-66-391, VOLUME I

DECEMBER 1966



This document is subject to special export controls and each transmittal to foreign governments or foreign nationals may be made only with prior approval of AFAL (AVPT), Wright-Patterson AFB, Ohio 45433.

AIR FORCE AVIONICS LABORATORY
RESEARCH AND TECHNOLOGY DIVISION
AIR FORCE SYSTEMS COMMAND
WRIGHT-PATTERSON AIR FORCE BASE, OHIO

NOTICES

When Government drawings, specifications, or other data are used for any purpose other than in connection with a definitely related Government procurement operation, the United States Government thereby incurs no responsibility nor any obligation whatsoever; and the fact that the Government may have formulated, furnished, or in any way supplied the said drawings, specifications, or other data, is not to be regarded by implication or otherwise as in any manner licensing the holder or any other person or corporation, or conveying any rights or permission to manufacture, use, or sell any patented invention that may in any way be related thereto.

This report supersedes WADC-TR-57-67, Volume I, Techniques for Airborne Radome Design, September 1957, which is redesignated and otherwise reprinted essentially without change.

Copies of this report should not be returned to the Research and Technology Division unless return is required by security considerations, contractual obligations, or notice on a specific document.

March 1957 - 600/2 - 556

PAGES NOT FILMED ARE BLANK

TECHNIQUES FOR AIRBORNE RADOME DESIGN

VOLUME ONE

DR. THOMAS E. TICE
EDITOR-IN-CHIEF

THE McGRAW-HILL BOOK COMPANY, INCORPORATED
TECHNICAL WRITING SERVICE

This document is subject to special export controls and each transmittal to foreign governments or foreign nationals may be made only with prior approval of AFAL (AVPT), Wright-Patterson AFB, Ohio 45433.

FOREWORD

This report was prepared by the Technical Writing Service of the McGraw-Hill Book Company, Incorporated, 330 West 42 Street, New York 36, New York, on Air Force Contract Number AF-33(616)-3279, under Task Number 41536 of Project Number 4158, "Radome Techniques and Components." The work was administered under the direction of the Electronic Components Laboratory, Directorate of Research, Wright Air Development Center, with Lieutenant William F. Croswell and Lieutenant Richard Quinn as the task engineers.

Included among those who cooperated in the preparation of the report were:

Thomas E. Tice ---------- Editor-in-Chief
Antenna Laboratory
Department of Electrical Engineering
Ohio State University

William F. Croswell ---------- Consulting Editor
Ohio State University

Alan F. Kay ---------- Consulting Editor
Technical Research Group

Keith Henney ---------- Consulting Editor
Technical Writing Service
McGraw-Hill Book Company

Robert E. Webster ---------- Assistant Editor
Ohio State University

Harry Baum ---------- Project Manager
Technical Writing Service
McGraw-Hill Book Company

AUTHORS

Fred Behrens ---------- Chapter 1
Wright Air Development Center

Jack H. Richmond ---------- Chapter 2
Ohio State University

E. O. Hartig ---------- Chapters 3 and 12
Goodyear Aircraft Corporation

W. E. L. Boyce ---------- Chapters 3 and 12
General Dynamics Corporation
(formerly with Goodyear Aircraft Corporation)

H. A. Schetne ---------- Chapter 4
Hughes Aircraft Company

Samuel S. Oleesky ---------- Chapter 5
Zenith Plastics Company

Robert W. Matlock ---------- Chapter 6
Zenith Plastics Company

George P. Peterson ---------- Chapter 7
Wright Air Development Center

Norman E. Wahl ---------- Chapter 8
Cornell Aeronautical Laboratory, Inc.

Edward B. McMillan ---------- Chapter 8
McMillan Laboratory, Inc.

Harold T. Smyth ---------- Chapter 9
Rutgers University

Allen S. Dunbar ---------- Chapter 10
Dalmo-Victor Company

Melvin J. Kofoid ---------- Chapter 11
Boeing Airplane Company

Samuel Wolin ---------- Chapter 13
U. S. Naval Air Development Center

TECHNICAL REVIEWERS

The editors were assisted by the following people who reviewed portions of the manuscript.

Lieutenant Irwin M. Lachman
Wright Air Development Center

John K. Burkley
Goodyear Aircraft Corporation

William H. Peak
Ohio State University

R. C. Tomashot
Wright Air Development Center

Saul Levinson
Technical Research Group

R. T. Schwartz
Wright Air Development Center

M. H. Norwalk
Corning Glass Works
(formerly with Wright Air Development Center)

Appreciation is also extended to Robert J. Henry of the McGraw-Hill Book Company who copy edited the report and to Miss Ann Lucas, Project Assistant, McGraw-Hill Book Company, who did much to coordinate the preparation of the illustrations and manuscript.

Mr. Behrens, author of Chapter 1, acknowledges the help given by the major aircraft companies of the United States and the service agencies under whose sponsorship they worked. Particular thanks are extended to John Keto, F. L. Holloway, Morris A. Hill, R. E. Long, A. R. John of the Wright Air Development Center; E. B. McMillan of the McMillan Laboratory; Joseph Ambrogi of the Naval Air Development Center; and Mrs. Irma Galane of the Navy Bureau of Aeronautics for

data contributed; as well as to the personnel of the United States Air Force Institute of Technology at Wright Air Development Center for their assistance in library research.

Mr. Schetne, author of chapter 4, expresses his appreciation to Mrs. Marjorie Delzell who, as technical editor for Hughes Aircraft Company, contributed greatly to the organization, writing, and preparation of illustrations for the chapter, and to many other people at Hughes Aircraft Company, particularly F. T. Hata and W. A. Snyder, for their technical assistance.

Mr. Oleesky, author of chapter 5, extends his thanks to C. E. Peach and D. H. McClure for accomplishing the computations, and to Dr. Arnold Marks for supervising curve plotting.

Mr. Dunbar, author of chapter 10, acknowledges the considerable assistance of Mrs. Sue Perry in the typing of the manuscript.

ABSTRACT

This report was written to provide a summary of the current status of the knowledge of radome design. It is intended to provide scientists and engineers working on radomes with a concise reference containing most of the information they will need. Topics covered include electrical theory, design, and measurements; organic and inorganic materials fabrication; rain erosion; and the effects of temperature, stress and aerodynamic factors. A comprehensive bibliography is included.

The publication of this report does not constitute approval by the Air Force of the findings or conclusions contained herein. It is published only for the exchange and stimulation of ideas.

Joseph A. Dombrowski

JOSEPH A. DOMBROWSKI
Lt Colonel, USAF
Chief, Electronic Warfare
Division

PREFACE

Before continuing to the text, the reader should know why this handbook has been published, and the reasoning behind the scope and technical level of the material contained herein.

The interest in the field of radomes has undergone a broad expansion in the last several years. Along with this expansion of interest, a large number of groups studying the radome problem have arisen in industrial and research organizations in many parts of the country. It was soon realized by members of these groups and by Government organizations, that the individual radome engineer was relatively isolated. This was due to insufficient regular meetings with his colleagues, and the lack of full dissemination of written reports pertaining to his field. The interest in the ONR Radome Symposium in Washington, D. C., in June 1953, clearly displayed that the coordination of Radome Research and Development being conducted throughout the country was badly needed and desired.

In early 1955, a decision was made by the Air Force and the Navy to remedy this situation. First, a system of regular, yearly Symposia was set up. These Symposia enable the full and free dissemination of technical information on radomes, by the presentation of papers, personal contacts, and the publication of proceedings. Second, to fulfill the need for a contemporary reference on radomes, the existing "Radome Engineering Handbook," AMC Manual 80-4 was reviewed, and the program to publish a modern one started by the award of a contract to the McGraw-Hill Book Company.

This Handbook has been written expecting that the majority of the scientists and engineers working on radomes are academically trained physicists, mathematicians, and electrical engineers. This decision was not meant to de-emphasize the fine contributions made by workers in the fields of materials, structures, and aerodynamics, but meant to insure that the handbook will be of maximum benefit to the majority of workers on radomes. Therefore, throughout the handbook, it is assumed that the reader has a degree in electrical engineering, physics or mathematics, with some knowledge of plane wave theory. As a result, the sections on materials, rain erosion, structures, and environment, are written to be informative and educational with the understanding that each subject would require a complete text in itself.

This Handbook should give the new engineer a well grounded background in the field of radomes, and give the experienced engineer a complete reference to rely upon.

The only purpose of this report, and its reason for existence, is service to the Government and to the radome industry. Only by receiving comment, both favorable and unfavorable, from the reader will we be able to find out how well this has been done. Criticism is earnestly solicited and should be addressed to the issuing agency.

W. H. CROSWELL

TABLE OF CONTENTS

Paragraph — Page

CHAPTER 1

ORIGIN AND HISTORICAL DEVELOPMENT OF RADOMES

1-1. Introduction. 3
1-2. Relations to VHF Radar. 3
1-3. Origin of Radome Problem. 3
1-4. Early Experimental Uses of Radomes 4
1-5. First Crash Program in Microwave Radar 5
1-6. Trend Away from Plywood Radomes 5
1-7. Other Early Radome Applications 6
1-8. Centers of Military Radome Development During and After World War II. 6
1-9. Origin of the Term "Radome" 6
1-10. "Dumbo" Pathfinder Crash Program 6
1-11. Origin of the Radome Electrical Design Problem 6
1-12. Switch to Polystyrene Fiber 7
1-13. Beginnings of Radome Research 7
1-14. AAF Interests in Expanded Hardboard 7
1-15. "Bombing Through the Overcast" Operations 7
1-16. Earliest Efforts at Streamlining Radomes. 7
1-17. Double-Wall Radomes 7
1-18. Development of the Three-Layer "A" Sandwich 8
1-19. Adoption of Sandwich Radomes 9
1-20. The Semistreamlined Blister Radome 9
1-21. Polystyrene Fiber K-Band Radomes 9
1-22. The Honeycomb Sandwich 10
1-23. Knitted-Sock Laminated Radomes 10
1-24. Earliest Efforts at Unified Antenna-Radome Design 10
1-25. Unification of Airframe and Radar-Radome Design. 10
1-26. Nacelle Lining Absorbers 10
1-27. Recognition of the Role of Phase Delay in Radomes 11
1-28. The "B" Sandwich. 11
1-29. Onset of the Rain Erosion Problem 11
1-30. Termination of Radiation Laboratory Activities. 12
1-31. Beginnings of Long Range, Post-War Radome Research 12
1-32. Adoption of the Neoprene Protective Coating. 12
1-33. Research on Laminating Resins 13
1-34. RDB Subpanel on Radomes. 13
1-35. Radome Engineering Manual 13
1-36. "A" Sandwich Foamed-in-Place Radomes. 13
1-37. Radome Design Criteria Development 14
1-38. Early Radome Error Prediction Work 15
1-39. Working Group on Small Supersonic Radomes 16
1-40. The Princeton Study 16
1-41. Gunfire Control and Missile Guidance Radome Design 16
1-42. The USAF Bomarc Radome 16
1-43. Investigation of Near Fields in Boresight Radome Design . . . 17
1-44. Supersonic Rain Erosion Investigation 17
1-45. The ONR Radome Symposium. 17
1-46. Radome Error Prediction 17
1-47. Error Correction by Empirical Means. 18

TABLE OF CONTENTS (cont)

Paragraph		Page
1-48.	Development of Ceramics for Radomes	18
1-49.	Loaded Core Sandwiches	18
1-50.	Radome Anti-Icing and De-Icing	18
1-51.	Large AEW Search Radomes	19
1-52.	Artificial Dielectric Research	19
1-53.	Recent Trends in Faired Radome Design	20
1-54.	Ohio State University Radome Symposia	20
REFERENCES		21

CHAPTER 2

ELECTROMAGNETIC FIELD AND OPTIC THEORY

INDEX OF SYMBOLS		24
SECTION A.	THEORETICAL DESIGN OF THE HOMOGENEOUS FLAT SHEET	27
2-1.	Interface Reflection Coefficients	27
	Lossy Materials	30
2-2.	The Homogeneous Flat Sheet	31
	Effect on Phase	32
2-3.	The Thin Homogeneous Flat Sheet	33
2-4.	The Half-Wave Homogeneous Flat Sheet	35
SECTION B.	THEORETICAL DESIGN OF FLAT SANDWICHES	38
2-5.	Coefficients for Multilayer Panels	38
	Formulas	38
	Matrix Formulation	40
2-6.	The "A" Sandwich.	41
2-7.	The "B" Sandwich.	47
2-8.	The "C" Sandwich.	47
SECTION C.	TOLERANCES IN THICKNESS AND DIELECTRIC CONSTANTS	48
2-9.	Parameters Affecting Permissible Tolerances	48
2-10.	Effect of High Dielectric Constant	48
2-11.	Calculation of Permissible Tolerances	49
SECTION D.	POLARIZATION	50
2-12.	Effect of Polarization	50
2-13.	Transmission Coefficients for Elliptical Polarization.	51
2-14.	Transmission Coefficients Using Axial Ratios	51
SECTION E.	MAGNETIC RADOME MATERIALS.	54
2-15.	Practical Difficulties	54
2-16.	Elimination of Refractive Shift	54
2-17.	Obtaining High Transmission Coefficient	54
2-18.	Insertion Phase Variation Versus Angle of Incidence	55

TABLE OF CONTENTS (cont)

Paragraph		Page
SECTION F.	ANISOTROPIC MATERIALS AND CONSTRUCTIONS	55
2-19.	Effect on Dielectric Constant	55
2-20.	Effect on Polarization	56
2-21.	Interface Reflection Coefficients	56
2-22.	Methods of Obtaining Anisotropy	58
2-23.	Analysis of Inhomogeneous Dielectrics	58
2-24.	Use of Metal Slats, Sheets, and Wire Grids	59
SECTION G.	THE RADOME SHAPE	60
2-25.	The Hemisphere	60
2-26.	The Spheroid	61
2-27.	The Ogive	62
2-28.	The Log Spiral	62
2-29.	The Cone	64
SECTION H.	THE FOCUSING EFFECT OF STREAMLINED RADOMES	66
2-30.	Refraction by Plane Sheets	66
2-31.	Focusing Effect of Radomes	67
SECTION I.	DIFFRACTION BY RADOMES	70
2-32.	Exact Formulations	71
2-33.	Diffraction by Dielectric Bodies of Simple Shape	74
2-34.	Lloyd's Mirror Effect	76
2-35.	Antenna-Radome Interaction	77
2-36.	Trapped Waves	77
SECTION J.	STREAMLINED LENS-RADOMES	77
2-37.	The Luneberg Lens	78
2-38.	Streamlined Lens	78
2-39.	Design Approach	78
2-40.	Manufacture of Lens	79
2-41.	Lens Feeding	80
SECTION K.	RADOMES FOR MILLIMETER WAVELENGTHS	80
2-42.	Difficulties at Millimeter Wavelengths	80
2-43.	Disadvantages of Higher-Order Half-Wave Walls	81
2-44.	Techniques Used in Infrared Systems	83
2-45.	Wall Constructions for Millimeter Wavelengths	84
REFERENCES		88

TABLE OF CONTENTS (cont)

Paragraph		Page
	CHAPTER 3	
	SEARCH RADOME DESIGN	
	INDEX OF SYMBOLS	94
	SECTION A. SEARCH RADAR ANTENNAS	97
3-1.	Patterns	97
3-2.	Illumination	97
	SECTION B. ELECTRICAL REQUIREMENTS	99
3-3.	Introduction	99
3-4.	Range Reduction Due to Radome	99
3-5.	Magnetron Frequency Pulling	100
3-6.	Interference and Pattern Distortion	101
	SECTION C. RADOME SHAPE	104
3-7.	Design Criteria	104
3-8.	General Requirements	104
3-9.	Electrical Requirements	105
3-10.	Weight Factor	106
	SECTION D. INCIDENCE ANGLE STUDY	110
3-11.	Preliminary Considerations	110
3-12.	Analytical Determination of Incidence Angles	111
	Transmission	113
3-13.	Graphical Determination of Incidence Angles	114
	SECTION E. WALL THICKNESS	118
3-14.	Optimum Data Presentation	118
3-15.	Case I: Thin Wall, Uniform Thickness	120
3-16.	Case II: Half-Wave Wall, Uniform Thickness	121
3-17.	Case III: Half-Wave Wall, Non-Uniform Thickness	121
3-18.	Insertion Phase Effects	122
3-19.	Case IV: Sandwich Wall, Uniform Thickness	123
3-20.	Case V: Sandwich Wall, Non-Uniform Thickness	123
	SECTION F. INTEGRATED ANTENNA-RADOME DESIGN	126
	REFERENCES	126
	CHAPTER 4	
	GUIDANCE AND FIRE CONTROL SYSTEM RADOME DESIGN	
	SECTION A. INTRODUCTION	129
4-1.	Radome Design Factors	129
4-2.	Electrical Requirements and Objectives	130
4-3.	Mechanical and Aerodynamic Restrictions	131
4-4.	Objectives of Chapter	131

Paragraph		Page
SECTION B.	FIRE CONTROL RADAR SYSTEMS	131
4-5.	Introduction	131
4-6.	Time Sequential Lobe Comparison Systems	132
	Conical Scan	132
	Sequential Lobing	133
4-7.	Simultaneous Lobe Comparison Systems (Monopulse)	133
	Phase Comparison	136
	Amplitude Comparison	136
	Phase-Amplitude	136
	Monopulse System Errors	136
4-8.	Comparison of Monopulse with Time Sequential Systems	136
SECTION C.	GUIDANCE SYSTEMS	140
4-9.	General Types	140
4-10.	Self-Contained Guidance Systems	141
	Homing Missiles	142
	Direct Pursuit Trajectory	142
	Constant-Bearing Trajectory	144
	Proportional Navigation	144
4-11.	Remote Guidance or Direction Systems	145
4-12.	Beamriders and Command Control	145
SECTION D.	SOURCES OF POINTING ERRORS	147
4-13.	Sequential Lobe Comparison	147
4-14.	Simultaneous Lobe Comparison	147
4-15.	Radome Errors	148
4-16.	Refraction	148
	Magnitude	148
	Compensation	149
4-17.	The Cavity Effect (Antenna-Radome Interaction)	149
	Magnitude	149
	Compensation	149
4-18.	Variation of Transmission Coefficients	149
	Magnitude	150
4-19.	The Phantom Feed	150
4-20.	Interference by Reflection	150
	Magnitude	150
	Compensation	151
4-21.	Trapped Waves	151
	Magnitude	151
	Compensation	151
4-22.	Depolarization	151
4-23.	Polarization Phenomena	152
4-24.	Antenna Depolarization	153
4-25.	Target Depolarization	154
4-26.	Measurement of Radar Cross Section	154
4-27.	Equipment for Cross Section Measurements	155
	Results of Radar Cross Section Measurements	156
4-28.	Cross Section and Scattering Relationships	156
	Radar Cross Section (General Case)	156
	Radar Cross Section (Restricted Case)	165
	Application of the Theory to Experiment	165

TABLE OF CONTENTS (cont)

Paragraph		Page
4-29.	Radome Depolarization	167
	Experimental Measurements	167
	Analysis of Experimental Measurements	169
	Rate of Change of Polarization Efficiency with Respect to r_t	177
	Consideration of the Polarization Efficiency	177
SECTION E.	EFFECT OF RADOME ERRORS ON FIRE CONTROL AND GUIDANCE SYSTEMS	178
4-30.	Effect of Radome Errors on Fire Control Systems	179
4-31.	Effect of Radome Errors on Missile Guidance	181
4-32.	Falcon Navigation	181
4-33.	Appearance of Radome Error in Falcon Transfer Function	182
4-34.	Radome Error and Missile Stability	183
	Positive Radome Error Limit	184
	Negative Radome Error Limit	185
4-35.	Radome Error and Navigation Constant	186
4-36.	Radome Error and Response to Noise	186
4-37.	Secondary Factors in Radome Error Analysis	186
4-38.	Nonlinear Radome Error Analysis	187
SECTION F.	PREDICTION OF RADOME ERRORS	187
4-39.	Radome Size and General Approaches	187
4-40.	Geometrical Optics (Ray Tracing)	189
4-41.	Modifications of Geometrical Optics	192
4-42.	The M′ Method	192
4-43.	Antenna Modification Method	193
4-44.	External-Equivalent-Aperture Method	194
4-45.	Error Prediction Based Directly on Maxwell's Equations: Radome Scattering Technique	194
	Derivation of the Basic Integral Equation	195
	Techniques of Solving the Integral Equation	195
	a. Grid Method	195
	b. Stationary Phase Approximation	196
	c. Lumped Field Methods	196
4-46.	Spherical Mode Transformation Technique	197
4-47.	Radome Boresight Errors in Monopulse Systems	199
4-48.	Derivation of Boresight Error Formula for Phase-Comparison Monopulse	199
4-49.	Experimental Data Required for Calculation of the In-Plane Error	201
4-50.	Determination of In-Plane Error for Amplitude-Comparison Monopulse	203
4-51.	Derivation of In-Plane Error Formula for Amplitude-Comparison Monopulse	204
4-52.	Practical Design Procedure for Monopulse Systems	204
SECTION G.	CORRECTION OF RADOME ERRORS	205
4-53.	General Methods of Approach	205
4-54.	Tapers and Lenses	206

TABLE OF CONTENTS (cont)

Paragraph		Page
4-55.	Correction of Electrical Non-Uniformity in Radome Walls	207
	Phase 1: Effect of Known Discontinuities	207
	a. Azimuth or Offset Run	207
	b. Roll Run	207
	c. Fixed Polarization Roll Run	209
	Phase 2: Location of Unknown Inhomogeneities	210
	Phase 3: Correction	212
4-56.	Dielectric Rings	214
	Experimental Technique	214
	Applications of the Technique	217
	Scattering by a Thin Dielectric Ring	218
SECTION H.	NEAR-FIELD MEASUREMENTS	221
4-57.	Near-Field Measurement Methods	221
4-58.	An Analysis of the Radiated Field of a Small Radome	221
	Test Setup	221
	Determination of Near-Field and Far-Field Zones	222
	No-Dome Measurements of the Near Field	224
	Near-Field Measurements with Radome Mounted	226
	Effect of Compensating Devices on Near-Field Distribution	227
REFERENCES		231

CHAPTER 5

BROADBAND RADOME DESIGN

INDEX OF SYMBOLS		236
5-1.	Bandwidth Requirements	237
5-2.	Solid Wall Radome	238
5-3.	Sandwiches ("A", "B", and "C")	238
5-4.	Multilayer Sandwiches	239
5-5.	Conclusions	239
REFERENCES		240

CHAPTER 6

RADOME STRUCTURAL AND ENVIRONMENTAL DESIGN AND TESTING

INDEX OF SYMBOLS		278
SECTION A.	STRUCTURAL DESIGN CRITERIA	281
6-1.	Introduction	281
6-2.	Aerodynamic Loads	281
6-3.	Inertia Loads	282
6-4.	Internal Pressure	283
6-5.	Blast Pressure	283
6-6.	Ambient Loads in Adjacent Structures	283

TABLE OF CONTENTS (cont)

Paragraph		Page
6-7.	Thermal Shock	284
	Stagnation Temperature	285
	Recovery Factor	286
	Equilibrium Temperature	287
	Transient Skin Temperature	287
6-8.	Thermal Stress	295
6-9.	Thermal Buckling	295
6-10.	Impact	296
SECTION B.	FACTORS AFFECTING THE STRENGTH OF RADOMES	297
6-11.	Introduction	297
6-12.	Shape	297
6-13.	Loading	297
6-14.	Materials	297
6-15.	Wall Construction — General	297
6-16.	Wall Construction — Honeycomb	298
	Core Shear Strength	298
	Face Thickness	298
	Strength and Flexibility of Bond	298
	Thickness of Core	298
	Gaps in Core Joints	299
6-17.	Wall Construction — Foamed-in-Place Core	299
6-18.	Wall Construction — Prefabricated Foam	299
6-19.	Wall Construction — Fluted Core	299
6-20.	Wall Construction — Waffle Core	300
SECTION C.	STRESS METHODS	300
6-21.	Introduction	300
6-22.	Area Theory of Stress Analysis	300
6-23.	Instability Buckling of Spherical Areas Under Lateral Pressure	301
	Solid Wall	301
	Sandwich Wall	301
6-24.	Instability Buckling of Cylindrical Areas Carrying Axial Load	302
	Solid Wall	302
	Sandwich Wall	302
6-25.	Instability Buckling of Cylindrical Areas Carrying Shear Loads	303
	Solid Wall	303
	Sandwich Wall	305
6-26.	Instability Buckling of a Cylindrical Area with External Pressure	305
	Solid Wall	305
	Sandwich Wall	305
6-27.	Instability Buckling of Flat Areas Under Edge Compression	308
	Solid Wall	308
	Sandwich Wall	308
6-28.	Instability Buckling of Flat Areas in Shear	309
	Solid Wall	309
	Sandwich Wall	309
6-29.	Flat Areas Under Lateral Pressure	309
6-30.	Stress Created by Thermal Shock	309
6-31.	Thermal Stress	313
6-32.	Impact	314
6-33.	Fatigue	315

TABLE OF CONTENTS (cont)

Paragraph		Page
6-34.	Stress Rupture	316
6-35.	Creep	316
SECTION D.	ENVIRONMENTAL DESIGN CRITERIA	316
6-36.	Icing Control — General	316
6-37.	Icing Control — Rubber Boot	317
	Advantages	317
	Disadvantages	317
6-38.	Icing Control — Anti-Icing Fluid	317
	Advantages	318
	Disadvantages	318
6-39.	Icing Control — Hot-Air System	318
	Advantages	318
	Disadvantages	318
6-40.	Icing Control — Internal Heating	318
	Advantages	319
	Disadvantages	319
6-41.	Precipitation Static	319
6-42.	Lightning	319
6-43.	Moisture	319
6-44.	Nuclear Radiation	321
SECTION E.	STATIC TESTING	321
6-45.	Fixtures for Static Testing	321
6-46.	Methods of Load Application	322
	Weights	322
	Hydraulic Jacks	322
	Air Pressure	322
	Water Pressure	323
6-47.	Static Tests at Elevated Temperature	323
6-48.	Instrumentation	325
	Stress	325
	Deflection	325
	Pressure	325
	Temperature	325
SECTION F.	ENVIRONMENTAL TESTING	326
6-49.	Thermal Shock	326
6-50.	Impact	327
6-51.	Shock, Vibration, Elevated Temperature, Low Temperature	327
	Shock	327
	Vibration	327
	Elevated Temperature	327
	Low Temperature	327
REFERENCES		327

TABLE OF CONTENTS (cont)

Paragraph		Page
	CHAPTER 7	
	SUBSONIC AND SUPERSONIC RAIN EROSION PROBLEMS	
	INDEX OF SYMBOLS	330
	SECTION A. INTRODUCTION	331
7-1.	Rain Erosion Problems	331
7-2.	Approaches to the Solution	331
	SECTION B. SUBSONIC RAIN EROSION	332
7-3.	Test Equipment and Procedures	332
7-4.	Erosion Criterion	332
7-5.	Test Conditions	334
7-6.	Variables Influencing Subsonic Rain Erosion	334
7-7.	Rain Erosion Properties of Coatings and Plastic Materials	335
	Effect of Temperature on Erosion	337
	Effect of Support on Erosion	338
	Epoxy Resins	339
	Polyurethane	339
7-8.	Subsonic Rain Erosion Properties of Ceramics and Glass	340
7-9.	Subsonic Flight Test Programs	340
	Flight Tests	341
	Test Results	343
	SECTION C. DEVELOPMENT OF A THERMALLY REFLECTIVE, ANTISTATIC HEAT RESISTANCE RAIN EROSION COATING	344
7-10.	Goodyear Tire and Rubber Company Program	344
7-11.	Gates Engineering Company Program	344
	SECTION D. MECHANISM OF RAIN EROSION	345
7-12.	General Subsonic Investigation	345
7-13.	Cavitation Effect on Initiation of Rain Erosion	346
7-14.	Mechanism of Supersonic Rain Erosion	347
	Captured Projectile Tests	347
7-15.	Effect of Shock Wave on Supersonic Rain Erosion	348
	SECTION E. SUPERSONIC RAIN EROSION	351
7-16.	Test Methods	351
7-17.	20-mm Ballistics Test Method	352
	Base and Transfer Hole	352
	Fuse	352
	Separation Charge	353
	Parachute and Specimen Adapter	353
	Velocity Measurement	353
	Test and Results	353
	Effect of Cone Angle	354
	Effect of Velocity	354
	57-Millimeter Tests	354
	Rainfall Intensity	355

TABLE OF CONTENTS (cont)

Paragraph		Page
7-18.	Rocket Sled Test Method	355
	Sled Details	356
	Test Runs	356
	Test Results	357
7-19.	Army Ordnance 57-Millimeter Program	357
	Test Details	357
	Test Results	358
7-20.	Missile Radome Flight Test Program	359
	Test Details	359
	Test Flights	359
SECTION F.	GENERAL SUMMARY	360
7-21.	Subsonic Rain Erosion	360
7-22.	Supersonic Rain Erosion	360
REFERENCES		361

CHAPTER 8

ORGANIC MATERIALS AND RADOME CONSTRUCTION

SECTION A.	INTRODUCTION	365
8-1.	Design Problem	365
8-2.	Radome Materials Development	365
	Polyfiber Radomes	365
	Reinforced Plastic Radomes	366
8-3.	Types of Radome Construction	366
SECTION B.	MATERIALS FOR RADOME CONSTRUCTION	366
8-4.	Classification of Plastics	366
8-5.	Laminates	367
8-6.	Glass Fibers	367
8-7.	Phenolic Resins	367
8-8.	Melamine Resins	368
8-9.	Silicones	369
8-10.	Polyester Resins	370
8-11.	Epoxy Resins	372
8-12.	Catalysts for Polyesters	373
8-13.	Reinforcements for Plastics	374
8-14.	Sizing for Glass Fabrics	375
8-15.	Adhesives for Radome Bonding	376
SECTION C.	SOLID RADOME CONSTRUCTION	378
8-16.	Normal Temperature (-60 to 225° F)	378
8-17.	High Temperature (225 to 500° F)	378
SECTION D.	SANDWICH RADOME CONSTRUCTION	378
8-18.	Types of Core Materials	378
8-19.	Honeycomb Core	378
8-20.	Fluted Core	380
8-21.	Foam Core	380

TABLE OF CONTENTS (cont)

Paragraph		Page
SECTION E.	PROPERTIES OF ORGANIC RADOME MATERIALS	381
8-22.	Electrical Properties	381
8-23.	Mechanical Properties	387
SECTION F.	FABRICATION METHODS FOR PLASTIC RADOMES	391
8-24.	Methods of Fabricating Radomes	391
8-25.	Bag Molding	392
	Preparation of Resin, Fabric, Bearing Blocks, and Inserts	392
	Lay-up of Fabric in Mold	393
	Elimination of Air	393
	Cure of Outer Skin Layers	394
	Incorporation of Bearing Block Inserts	394
	Core Construction	394
	Trimming	394
	Permissible Repairs	394
	Post-Curing	395
	Finishing	395
8-26.	Matched Tool Molding	396
	Foamed-in-Place Cores	396
	Preform Molding	399
	Marco Vacuum Injection	399
	Compression, Pressure Injection, and Transfer Molding	400
8-27.	Lathe Turning	400
8-28.	Tooling	401
8-29.	Methods of Obtaining Tolerances	404
8-30.	Inspection Methods	406
SECTION G.	METHODS OF ATTACHMENT	407
SECTION H.	FINISHES FOR RADOMES	408
GLOSSARY		409
REFERENCES		411

CHAPTER 9

INORGANIC MATERIALS AND RADOME CONSTRUCTION

SECTION A.	INTRODUCTION	419
9-1.	Scope	419
9-2.	Classification	419
SECTION B.	DENSE FIRED BODIES	419
9-3.	Definition and Characteristics	419
9-4.	Steatite	420
	The Rutgers Program	420
	Slip Casting	420
	Slip Control	420
	Batch Preparation	420
	Casting	421
	Bisque Firing	422
	Final Firing	422

TABLE OF CONTENTS (cont)

Paragraph		Page
9-5.	Alumina	422
	Machining	422
9-6.	Other Forming Methods	423
9-7.	Other Materials	423
9-8.	Beryllia	423
9-9.	Magnesia	423
9-10.	Spinel	424
9-11.	Forsterite	424
9-12.	Zircon	424
9-13.	Cordierite	424
9-14.	Lithium Aluminum Silicates	424
SECTION C.	POROUS BODIES	424
9-15.	Approaches to Fabrication	424
9-16.	Foaming Process	424
	Forming	425
	Firing	425
	Glazing	425
9-17.	Wollastonite Bodies from Xonotlite	425
9-18.	Dielectric Properties of Porous Ceramics	426
SECTION D.	GLASSES	426
9-19.	Possible Advantages of Glasses	426
9-20.	Glass Properties	426
9-21.	New Glasses	426
SECTION E.	GLASS-BONDED MICA AND FUSION-CAST CERAMIC MATERIALS	427
9-22.	Glass-Bonded Mica	427
9-23.	Fusion-Cast Ceramic Materials	427
SECTION G.	PHYSICAL PROPERTIES OF CERAMIC MATERIALS	427
9-24.	Introduction	427
9-25.	Mechanical Properties	428
	Strength	428
9-26.	Resistance to Impact	429
9-27.	Resistance to Thermal Shock	429
	Thermal Conductivity	429
9-29.	Elastic Constants	430
9-30.	Hardness	430
9-30.	Refractoriness	431
SECTION H.	ELECTRICAL PROPERTIES OF CERAMICS	431
9-31.	Effect of Composition	431
9-32.	Dielectric Losses	431
9-33.	Temperature Effects	432
9-34.	Losses Versus Structure	433
GLOSSARY		434
REFERENCES		435

TABLE OF CONTENTS (cont)

Paragraph — Page

CHAPTER 10

AIRBORNE RADAR INSTALLATION TOPICS

INDEX OF SYMBOLS 438

SECTION A. INTRODUCTION 439

SECTION B. STABILIZATION AND MOUNTING PROBLEMS 439

10-1. Pressurization 439
10-2. Stabilization 439
Platform Stabilization 440
Line-of-Sight Stabilization 440
Roll Stabilization 441
Pitch Stabilization 441
Yaw Stabilization 441
10-3. Swept Volume 441
Clearance 443
10-4. Stabilization for Various Types of Antennas 443

SECTION C. PATTERN DISTORTION BY AIRCRAFT STRUCTURE . . 445

10-5. Vision Requirements 445
10-6. Placement of Radome and Nacelle 445
10-7. Interference Effects 445
Synthesis of Edge Diffraction Patterns — Analysis Based on Physical Optics 447
Synthesis of Surface-Reflection Interference Patterns . . . 449
10-8. Nacelle Clearance 455
10-9. Allowable Pattern Distortion 455

SECTION D. PATTERN DISTORTION BY AIRCRAFT ENVIRONMENT; EFFECTS OF SHOCK FRONT AND TURBULENCE . . . 455

10-10. Introduction 455
The Shock Front 456
The Boundary Layer 456
The Air Prism 456
The Wake 456
10-11. Transmission Through the Shock Front 456
10-12. Turbulence in the Boundary Layer 458
10-13. Turbulence in the Air Prism 458
10-14. The Wake 458

GLOSSARY 459

REFERENCES 460

TABLE OF CONTENTS (cont)

Paragraph		Page
	CHAPTER 11	
	RADOME WALL MEASUREMENTS AND EVALUATIONS	
	INDEX OF SYMBOLS	462
	SECTION A. INTRODUCTION	463
11-1.	Need for Measurements	463
11-2.	Quantities to be Measured	464
	Measurements on Sandwich Walls with Lightweight Cores	464
	Measurements on Combinations of Solid Sheets	464
	Measurements on Single-Layer Walls	464
	SECTION B. FACILITIES FOR MEASUREMENT	465
11-3.	Insertion Phase Difference Measurements	465
	Choice of Method	465
	Interferometer Methods — Basic Manually Balanced Instrument	466
	Interferometer Methods — Automatically Balanced Instrument	466
	Single-Horn Complex-Reflection Measurement Method	470
	Single-Horn Minimum-Reflection Method	471
11-4.	Reflection Measurements	472
11-5.	Physical Thickness Measurements	472
	Mechanical Gages	472
	An Electromechanical Gage	473
	An Electrical Gage	473
11-6.	Dielectric Constant Evaluation	474
11-7.	Dissipation Factor Evaluation	475
11-8.	Measurements Under Special Environment	475
	SECTION C. MEASURED DATA AND ITS UTILIZATION	476
11-9.	Choice of Test Frequency	476
11-10.	Selection of Test Stations	476
11-11.	Value of Parallel Recording of Electrical and Physical Thicknesses	477
11-12.	Establishment of Wall Thickness Tolerances	477
11-13.	Evaluation of Radomes for High-Temperature Operation	477
11-14.	Effect of Loss on Phase Shift	478
11-15.	Dielectric Constant of Laminate Walls	478
11-16.	Importance of the Effect of Moisture on Electrical Wall Thickness	478
11-17.	Simplification in Inspection Tests	478
11-18.	Interpretation of Requirements	479
	REFERENCES	479

Paragraph — Page

CHAPTER 12

MEASUREMENT OF THE ELECTRICAL CHARACTERISTICS OF DIELECTRIC MATERIALS AND RADOMES

INDEX OF SYMBOLS 482

SECTION A. REVIEW OF WAVEGUIDE PRINCIPLES 483

12-1. Complex Permittivity and Permeability 483
12-2. General Analysis of Guided Waves 484
12-3. Summary on Guided Waves 484

SECTION B. IMPEDANCE MEASUREMENTS USING A TRANSMISSION LINE 486

12-4. Fundamental Relations 486
12-5. Impedance Measurement Using Slotted Line 487
12-6. Resonance Method of Impedance Measurement 487

SECTION C. SHORTED-LINE METHOD FOR OBTAINING DIELECTRIC PROPERTIES 488

12-7. Simplified Procedure for Unity Permeability 488
Short-Circuit Method 488
Open-Circuit Method 490
Combined Open- and Short-Circuit Method 490
12-8. Simplification for Medium-Loss Materials Having Unity Permeability 490
12-9. Corrections for Loss in the Waveguide Wall 491
12-10. Measurements on Magnetic Materials 492
12-11. Typical Equipment for Dielectric Measurements 493
Shorted-Line Method 493
Resonant Cavity Method 494
Surface-Wave Dielectrometer 494
12-12. Sources of Error 495
Impure Signal Source 495
Improper Isolation of the R-F Generator 495
Probe Loading 495
Sample Fit and Homogeneity 495
Higher Order Modes 495
Wall Losses 495

SECTION D. THE MEASUREMENT OF RADOME TRANSMISSION, REFLECTION, AND PATTERN DISTORTION 496

12-13. Radome Design Objectives 496
12-14. The Measurement of Radome Transmission 496
12-15. The Measurement of Radome Reflection 498
12-16. The Measurement of Radome Pattern Distortion 499

SECTION E. THE MEASUREMENT OF BORESIGHT ERRORS 502

12-17. Errors Caused by Radomes 502
12-18. Boresight Measurement Equipment for Conical Scan Antennas . . 503
12-19. Automatic Boresight Measurement Equipment 504
12-20. Boresight Measurements on Monopulse Systems 505

Paragraph		Page
SECTION F.	PHASE AND AMPLITUDE MEASUREMENTS IN THE NEAR FIELD	507
12-21.	Equipment for Near-Zone Measurements	507
12-22.	Discussion of Calibrated Phase Shifters	509
	Slotted Line Phase Shifter	509
	Phase Shifter Employing a Movable Piston	509
	Rotary Phase Shifter	510
12-23.	Automatic Near-Field Measurement Equipment	510
12-24.	Near-Field Measurements Using the Scattering Method	512
	Linear Conducting Scatterer	512
	Modulated Scatterer	513
	Comparison of Methods	514
REFERENCES		515

CHAPTER 13

PRACTICAL COMPUTATIONAL DESIGN PROCEDURES

INDEX OF SYMBOLS		518
SECTION A.	REFLECTION AND TRANSMISSION OF ELECTROMAGNETIC WAVES AT ARBITRARY INCIDENCE ANGLES BY LOSSY PLANE DIELECTRIC PANELS	519
13-1.	Available Data	519
13-2.	Data Calculation and Presentation	519
13-3.	Accuracy	520
13-4.	Graphical Calculation	520
13-5.	Graphs of Transmission and Reflection Coefficients	520
13-6.	Wall Dimension Tolerances	521
SECTION B.	CALCULATION OF THE FAR-FIELD RADIATION PATTERN FOR AN ANTENNA-RADOME SYSTEM	521
13-7.	A Ray-Tracing Method	521
13-8.	Other Ray-Tracing Techniques	522
REFERENCES		523

BIBLIOGRAPHY

SECTION A.	ELECTRICAL THEORY, DESIGN, AND MEASUREMENTS	579
1.	The Homogeneous Flat Sheet	579
2.	The Thin Sheet	580
3.	The Half-Wave Sheet	580
4.	The "A" Sandwich	582
5.	The "B" Sandwich	583
6.	The "C" Sandwich	583
7.	Tolerances in Thickness and Dielectric Constant	584
8.	Polarization	585
9.	Magnetic Radome Materials	586
10.	Anisotropic Materials and Construction	586

TABLE OF CONTENTS (cont)

Paragraph		Page
11.	The Radome Shape	587
12.	The Focusing Effect of Streamlined Radomes	587
13.	Diffraction by Radomes	588
14.	Luneberg Lens and Streamlined Lens Radomes	589
15.	Radomes for Millimeter Wavelengths	591
16.	Broadband Radome Design	591
17.	Guidance and Fire Control Radome Design	591
18.	Search Radome Design	594
19.	Measurements	594
20.	Diffraction by Aircraft Structure and Environment	597
SECTION B.	ORGANIC MATERIALS FABRICATION	598
SECTION C.	INORGANIC MATERIALS FABRICATION	601
SECTION D.	RAIN EROSION	602
SECTION E.	EFFECT OF TEMPERATURE, STRESS, AND AERODYNAMIC FACTORS	603
SECTION F.	MISCELLANEOUS	608

LIST OF ILLUSTRATIONS

Figure — Page

CHAPTER 1

1-1. Douglas B-18A, of the Type Used in Earliest Airborne Microwave Radar Flights 4

1-2. Northrop P-61 "Black Widow" Night Fighter with Nose Radome . . 5

1-3. Semistreamlined Radome on the Navy's Grumman F6F-3N 8

1-4. "Eagle" Vane Antenna and Radome Installation for the AN/APQ-7 Radar 8

1-5. Aircraft-Early-Warning Radome Installation on the Navy's Grumman AF-2W 9

1-6. Typical Semistreamlined Blister Radome on the Air Force B-29 . . 9

1-7. North American B-45 with Chin Radome, Exemplifying the Trend to Flush-Fairing of the Radome into the Airplane Loft-Lines . . . 11

1-8. Example of Early Foamed-in-Place Radome for the Nose Installation of an AN/APS-10 Radar on the C-54 14

1-9. Northrop F-89 with Nose Fire Control Radome of the Foamed-in-Place Type 14

1-10. North American F-86D with Thermally Anti-Icing Nose Radome for Fire Control Radar 15

1-11. McDonnell F3H Navy Fighter with Nose Type Fire Control Radome Shaped for Transonic Speeds 16

1-12. Aircraft-Early-Warning Radomes on an Air Force RC-121 19

1-13. Boeing B-52 Heavy Bomber with Nose and Chin Radomes Flushed-Faired into the Fuselage 20

1-14. Convair F-102A Fighter, With Nose Fire Control Radome and Instrumentation Boom 21

CHAPTER 2

2-1. Plane-Wave Reflection and Transmission at a Dielectric Interface with Perpendicular Polarization 28

2-2. Plane-Wave Reflection and Transmission at a Dielectric Interface with Parallel Polarization. 30

2-3. Interface Reflection Coefficients for Perpendicular and Parallel Polarization 30

LIST OF ILLUSTRATIONS (cont)

Figure		Page
2-4.	Angle of Refraction of Plane Wave Crossing A Dielectric Interface	30
2-5.	Transmission and Reflection by a Plane Dielectric Sheet for Perpendicular Polarization	32
2-6.	Transmission Coefficients of Lossless, Thin, Flat Sheets for Perpendicular Polarization	34
2-7.	Insertion Phase Delay of Lossless, Thin, Flat Sheets	34
2-8.	Design Thickness for First-Order, Half-Wave, Homogeneous Flat Sheet	36
2-9.	Transmission Coefficients of Lossless, First-Order, Half-Wave, Homogeneous Flat Sheet	37
2-10.	Insertion Phase Delay of Lossless, First-Order, Half-Wave, Homogenous Flat Sheet	38
2-11.	Plane Wave Crossing Two Interfaces	39
2-12.	Transmission Through Two Panels	39
2-13.	A Multilayer Panel	40
2-14.	Incident and Reflected Waves at an Interface	40
2-15.	Incident and Reflected Waves Referred to Two Planes in a Homogeneous Medium	40
2-16.	"A" Sandwich as Analyzed in Terms of its Interface and Position Matrices	41
2-17.	Symmetrical "A" or "B" Sandwich	41
2-18.	Transmission and Phase Delay Contours for "A" Sandwich with 0.024 0.024 Skin Thickness (Perpendicular Polarization) ($\Psi_\perp = \Delta_\perp$)	43
2-19.	Transmission and Phase Delay Contours for "A" Sandwich with 0.024 Skin Thickness (Parallel Polarization) ($\Psi_\parallel = \Delta_\parallel$)	44
2-20.	Transmission and Phase Delay Contours for "A" Sandwich with 0.055 Skin Thickness (Perpendicular Polarization) ($\Psi_\perp = \Delta_\perp$)	45
2-21.	Transmission and Phase Delay Contours for "A" Sandwich with 0.055 Skin Thickness (Parallel Polarization) ($\Psi_\parallel = \Delta_\parallel$)	46
2-22.	Symmetrical "C" Sandwich	48
2-23.	Power Transmission Coefficients of Lossless Homogeneous Plane Sheets for Normal Incidence (Transmission Exceeds 97 Percent in Shaded Regions)	49
2-24.	Coordinates for an Elliptically Polarized Wave Incident on a Dielectric Sheet	50

LIST OF ILLUSTRATIONS (cont)

Figure		Page
2-25.	Linearly Polarized Wave and its Parallel and Perpendicular Components	51
2-26.	Alternating Thin Flat Sheets	57
2-27.	Two-Layer Capacitor and Equivalent Homogenous Capacitor	58
2-28.	Two-Layer Capacitor and Equivalent Homogenous Capacitor	58
2-29.	Anisotropic Capacitor and Equivalent Isotropic Capacitor	58
2-30.	Dielectric Sheet Loaded with Wire Grids	59
2-31.	Radomes of Various Shapes, with Fineness Ratio 2.5	61
2-32.	Radome with Conical Section For Fairing into Missile Body	61
2-33.	Spheroidal Radome with Conical Fairing Section	62
2-34.	Angle of Incidence (θ) Versus Look Angle (ψ) for Spheroidal Radomes of Various Axial Ratios	63
2-35.	Ogive Radome with Conical Fairing	63
2-36.	Angle of Incidence (θ) Versus Look Angle (ψ) for Ogives of Various Calibers (c)	64
2-37.	Log Spiral Radome with Conical Fairing	64
2-38.	Conical Radome with Ogive Fairing	65
2-39.	Incidence Angle (θ) Versus Look Angle (ψ) for Conical Radomes of Various Vertex Angles (β)	65
2-40.	Refraction in a Plane Dielectric Sheet	66
2-41.	Refractive Shift Produced by First-Order, Homogeneous, Half-Wave Sheet for an Angle of Incidence of 70°	67
2-42.	Maximum Refractive Shift Which Can Be Produced by First-Order, Homogeneous, Half-Wave Sheet	67
2-43.	Dielectric Constant Which Produces Maximum Refractive Shift in Homogeneous, Half-Wave Sheet	68
2-44.	Refraction in a Conical Radome	68
2-45.	Calculated Near-Field Amplitude with Uniform Collimated Beam Passing Through Conical Radome	68
2-46.	Horn Antenna with Wedge-Shaped Radome	69
2-47.	Measured Near-Field H-Plane Amplitude of Horn Antenna With and Without Wedge-Shaped Radome	70
2-48.	Measured Near-Field H-Plane Phase of Horn Antenna With and Without Wedge-Shaped Radome	70

Figure		Page
2-49.	Reference Surfaces S and S′ Which Might Be Used in Radome Calculations	71
2-50.	Coordinate System for Radome Calculations	72
2-51.	Antenna with Large, Flat, Dielectric Sheet	74
2-52.	Antenna with Wedge-Shaped Radome	75
2-53.	Measured and Calculated H-Plane Patterns of Antenna with Wedge-Shaped Radome	75
2-54.	Parallel-Ray Model of Transmission Through a Radome	75
2-55.	Measured and Calculated H-Plane Far-Field Patterns of Antenna with Wedge-Shaped Radome, Using Parallel-Ray Theory	75
2-56.	Parallel-Ray Transmission Through Radome Showing Refraction	75
2-57.	Calculated Fields of Antenna with Wedge-Shaped Radome, Using Parallel-Ray Theory and Refraction	76
2-58.	Measured H-Plane Energy Flow Map for Horn Antenna at 9400 Megacycles	76
2-59.	Calculations for Wedge-Shaped Radome, Using Energy Flow Map and Refraction Theory	76
2-60.	Lloyd's Mirror Effect on a Radome	76
2-61.	Luneberg Lens and Ray Map	78
2-62.	Spheroidal Lens-Radome	79
2-63.	Power Transmission Coefficient for a Lossless Plane Dielectric Sheet	82
2-64.	Insertion Phase Delay Through a Lossless Plane Dielectric Sheet	83
2-65.	Transmission Coefficient of a Lossless Plane Sheet at Wavelength λ_0	86
2-66.	Transmission Coefficient of a Lossless Plane Sheet at Wavelength λ_0'	86
2-67.	Average Transmission Coefficient of a Lossless Plane Sheet for Wavelengths λ_0 and λ_0'	87

CHAPTER 3

3-1.	Cosecant-Squared Antenna and Pattern Configuration: (a) Antenna Front View; (b) Antenna Side View; (c) Pattern, Horizontal Cut; (d) Pattern, Vertical Cut	98
3-2.	Geometry for Uniform Ground Illumination	98
3-3.	Pattern Distortion Due to Reflections: Near-Field Reflection	102

LIST OF ILLUSTRATIONS (cont)

Figure		Page
3-4.	Pattern Distortion Due to Reflections: Far-Field Pattern Interference	102
3-5.	AN/APS-25 Antenna Patterns	103
3-6.	Hemispherical Radome	104
3-7.	30^0 Conical Radome	105
3-8.	Constant Transmission and Insertion Phase Contours (Single Sheet, Perpendicular Polarization)	106
3-9.	Constant Transmission and Insertion Phase Contours (Single Sheet, Parallel Polarization)	107
3-10.	Contours of Constant Power Transmission and Insertion Phase Delay for "A" Sandwich Panels as a Function of Normalized Core Thickness and Incidence Angle: Perpendicular Polarization	108
3-11.	Contours of Constant Power Transmission and Insertion Phase Delay for "A" Sandwich Panels as a Function of Normalized Core Thickness and Incidence Angle: Parallel Polarization	109
3-12.	Radome Geometry, Analytic Case	111
3-13.	Vector Relationships at Radome Surface	113
3-14.	Incidence Angle Projections	114
3-15.	Elevation and Oblique Planes of Antenna: (a) Edge View of Elevation Planes; (b) Edge View of Oblique Planes	114
3-16.	Radome Loft Lines, Vertical Cutting Planes: (a) Edge View of Vertical Cutting Planes; (b) Vertical Cutting Plane Contours	115
3-17.	Projected Incidence Angles: (a) True View of Vertical Antenna Cutting Planes; (b) True View of Oblique Cutting Plane Contours	116
3-18.	Relative Polarization and Incidence Angle Components Chart	117
3-19.	Transmission Coefficient Versus Incidence Angle Curves	119
3-20.	Curves of Insertion Phase Versus Incidence Angle	120
3-21.	Contours of Constant Power Transmission and Insertion Phase Delay for "A" Sandwich Panels as a Function of Normalized Thickness and Incidence Angle: Perpendicular Polarization	124
3-22.	Contours of Constant Power Transmission and Insertion Phase Delay for "A" Sandwich Panels as a Function of Normalized Thickness and Incidence Angle: Parallel Polarization	125
	CHAPTER 4	
4-1.	Conical Scan Radar System	132
4-2.	Sequential Lobing Radar System	133

LIST OF ILLUSTRATIONS (cont)

Figure		Page
4-3.	Three-Channel Monopulse Radar System	134
4-4.	Typical Sum Radiation Pattern of Monopulse Antenna	134
4-5.	Typical Difference Radiation Pattern of Monopulse Antenna	135
4-6.	R-F Voltage at Error Terminal of Antenna	135
4-7.	D-C Error Voltage at Servo Input	136
4-8.	Typical Fire Control Antenna Beam — Conical Scan	138
4-9.	Typical Fire Control Antenna Beam — Phase Comparison Monopulse	139
4-10.	Typical Fire Control Antenna Beam — Amplitude Comparison Monopulse	139
4-11.	Plan Views of Representative Guided Missiles which Require Radomes	141
4-12.	Air-to-Air Application of Self-Contained (Homing) Missiles. Other Applications: Air-to-Surface, Surface-to-Air, Surface-to-Surface (Terminal Guidance)	143
4-13.	Example of Trajectories Resulting from a Direct Pursuit Course	144
4-14.	Trajectory Resulting from Constant-Bearing Navigation	144
4-15.	Beamriding Missile; Applications: Air-to-Surface, Air-to-Air, Surface-to-Air, Surface-to-Surface (Short Range)	146
4-16.	Command-Control Missile; Applications: Surface-to-Air, Air-to-Surface, Surface-to-Surface	147
4-17.	Ray Geometry for Concentric Circles	148
4-18.	Image of Antenna in Radome or Fuselage	150
4-19.	Geometry of Antenna and Image	151
4-20.	Geometry of Antenna and Source	152
4-21.	Antenna Deviation as a Function of the Direction of Polarization of the Incident Wave	153
4-22.	Elevation and Aspect Angles of the Target	154
4-23.	Test Setup for Radar Cross Section Measurements	155
4-24.	Radar Cross Section Measurements of Various Aircraft at Constant Polarization	157
4-25.	B-17 Radar Cross Sections at Various Polarizations (Flight Pattern No. 1)	158
4-26.	B-47 Radar Cross Sections at Various Polarizations	161

Figure		Page
4-27.	Interceptor-Type Radome Error Curves with Linear Incident Polarization; Receiving Polarization 6-db, Right-Hand Elliptical	168
4-28.	Interceptor-Type Radome Error Curves with Elliptical Incident Polarization, Major Axis Horizontal; Receiving Polarization 6-db, Right-Hand Elliptical, Major Axis Horizontal	169
4-29.	Error Curves of Ellipsoidal Missile Radome with Various Incident Polarizations (Left-Hand Circular Receiving Polarization)	170
4-30.	Error Curves of Ogival Missile Radome with Various Incident Polarizations (Left-Hand Circular Receiving Polarization)	172
4-31.	Coordinate System for Analysis of Linearly Polarized Wave Incident on a Radome	174
4-32.	Plane of E Vector -- Linearly Polarized Incident Wave, Before Transmission Through a Radome	175
4-33.	Plane of E Vector — Linearly Polarized Incident Wave, After Transmission Through a Radome	175
4-34.	View of Radome from Exterior	176
4-35.	Relative Power Received by an Elliptically Polarized Antenna	178
4-36.	Definition of Radome Angles for Analysis of Error Effect on Fire Control Systems	179
4-37.	Coefficients of Miss Equation	181
4-38.	Radome Error Angular Relationship in Two-Dimensional (simplified) Case	182
4-39.	Radome Error Angular Relationship in Three-Dimensional Case	182
4-40.	Two-Dimensional Falcon Guidance System	183
4-41.	Two-Dimensional Guidance System with Radome Error	183
4-42.	Equivalent Servo Diagram with Radome Error	183
4-43.	Complete Falcon Guidance System with Total Radome Error	184
4-44.	Ratio of Exact to Approximate Positive $k\lambda_0$ Stability Limit for $\tau_1 = \tau_2$	185
4-45.	Ratio of Exact to Approximate Negative $k\lambda_0$ Stability Limit for $\tau_1 = \tau_2$	185
4-46.	Increase in Miss Due to Positive In-Plane Error Slope when Guidance System is Excited by Scintillation	186
4-47.	Comparative Importance of Radome in (a) Small and (b) Large Radome-Antenna Systems	188

Figure		Page
4-48.	Cylindrical Radome	189
4-49.	Cross Section of Radome Perpendicular to Elements of a Cylinder	189
4-50.	Approximate Beam Deviation for Concentric Circles	190
5-51.	Approximate Beam Shift for a Radome n Half-Waves Thick	191
4-52.	Error Vector	191
4-53.	Radome Layout for M' Error Prediction Method	192
4-54.	Radome Layout for Equivalent-External-Aperture Prediction Technique	194
4-55.	Two-Dimensional View of Phase-Comparison Monopulse System	199
4-56.	Illumination of Each Aperture in Two-Dimensional Phase-Comparison System	200
4-57.	Coordinate System for Circulation of the In-Plane Error	201
4-58.	Geometry of General Ray Used in Obtaining Experimental Data	202
4-59.	Common Ray Bundle for Both Phase Fronts of Amplitude-Comparison Monopulse with Nutating Feed	203
4-60.	Shift of Crossover Point Caused by In-Plane Error	204
4-61.	Radome Error Curves Showing Corrective Effect of a Taper Combined with Dielectric Rings	208
4-62.	Coordinate System of Automatic Error Measuring Facility	209
4-63.	Coordinate System of Interceptor	209
4-64.	Radome with Two Dielectric Patches Added to Surface	209
4-65.	Error Deviation Along Path 0-to-1	210
4-66.	Error Deviation Along Path 2-to-3	211
4-67.	Vector Method of Location of Known Non-Uniformity	213
4-68.	Location of Unknown Electrical Non-Uniformity on Test Radome by Vector Method	214
4-69.	Comparative Vertical Error Curves of Test Radome, Before and After Correction of Asymmetry	215
4-70.	Effect of Dielectric Ring on In-Plane Error Curve	216
4-71.	Fabrication of Dielectric Rings	216

Figure		Page
4-72.	In-Plane Error Curves of Test Radome Showing Effect of Ideal Combination of Corrective Rings	217
4-73.	Small Hemispherical Radome In-Plane Error Curves With and Without Rings	217
4-74.	Interceptor Radome In-Plane Error Curves With and Without Rings	218
4-75.	Coordinates and Ring Geometry of Approximation Technique	219
4-76.	Half-Wave Dipole Antenna Coaxial With Ring	220
4-77.	Typical Patterns of One Set of Rings Studied	220
4-78.	Near-Field Measuring Apparatus	222
4-79.	Radome and Antenna Mount of Near-Field Measuring Apparatus.	222
4-80.	Cross Section of Transmitter	223
4-81.	Coordinate System and Carriage Motion	223
4-82.	Power Pattern for Determination of Near-Field and Far-Field Regions	224
4-83.	No-Dome Constant Phase Contour Map in Y-Z Plane of Antenna Near-Field (X = 0)	225
4-84.	No-Dome Constant Phase Contour Map in X-Z Plane of Antenna Near-Field (Y = 0)	226
4-85.	No-Dome Power Contour Map in Y-Z Plane of Antenna Near-Field (X = 0)	227
4-86.	No-Dome Power Contour Map in X-Z Plane of Antenna Near-Field (Y = 0)	228
4-87.	Actual Far-Field H-Plane Power Pattern	229
4-88.	Near-Field Distribution of Antenna (No-Dome) at Point of Maximum Perturbation	230
4-89.	Near-Field Distribution of Antenna and Radome at Point of Maximum Perturbation (X = 0)	230
4-90.	Near-Field Distribution of Antenna and Radome With Compensating Rings at Point of Maximum Perturbation (Y = 0)	231
4-91.	Near-Field Distribution of Antenna and Radome With Compensating Rings and Nose Cone at Point of Maximum Perturbation (X = 0)	231

LIST OF ILLUSTRATIONS (cont)

Figure		Page
	CHAPTER 5	
5-1.	Nose Radome for Reconnaissance Airplane; a through f Are Sets of Horns, as Shown in (b).	238
	Curves of Power Transmission as a Function of Frequency Versus Incidence Angle, for a Solid Wall (ϵ = 4.0, tan δ = 0.014)	
	Wall Thickness (in.)	
5-2.	0.012.	241
5-3.	0.024.	242
5-4.	0.036.	243
5-5.	0.048.	244
5-6.	0.060.	245
5-7.	0.075.	246
5-8.	0.100.	247
5-9.	0.200.	248
5-10.	0.300.	249
	Curves of Power Transmission as a Function of Incidence Angle Versus Frequency for a Solid Wall (ϵ = 4.0, tan δ = 0.014)	
	Wall Thickness (in.)	
5-11.	0.012.	250
5-12.	0.024.	251
5-13.	0.036.	252
5-14.	0.048.	253
5-15.	0.060.	254
5-16.	0.075.	255
5-17.	0.100.	256
5-18.	0.200.	257
5-19.	0.300.	258

Figure			Page
	Curves of Power Transmission Efficiency as a Function of Incidence Angle Versus Frequency, for "A" Sandwich (ϵ_s = 4.0, tan δ_s = 0.014, ϵ_c = 1.2, tan δ_c = 0.004)		
	Skin Thickness (in.)	Core Thickness (in.)	
5-20.	0.024	0.250.	259
5-21.	0.024	0.300.	260
5-22.	0.024	0.350.	261
5-23.	0.024	0.400.	262
5-24.	0.036	0.250.	263
5-25.	0.036	0.300.	264
5-26.	0.036	0.350.	265
5-27.	0.036	0.400.	266
5-28.	0.048	0.250.	267
5-29.	0.048	0.300.	268
5-30.	0.048	0.350.	269
5-31.	0.048	0.400.	270
5-32.	Power Reflection from Normal Incidence "A" Sandwich (Skin Thickness 0.020 in., ϵ_s = 4.2, tan δ_s = 0.014; ϵ_c = 1.2, tan δ_c = 0.00492)		271
5-33.	Power Reflection from Normal Incidence "B" Sandwich (Skin Thickness 0.020 in., ϵ'_s = 4.2, tan δ_s = 0.014; ϵ'_c = 17.64, tan δ_c = 0.03)		271
5-34.	Power Reflection from Normal Incidence "B" Sandwich (Skin Thickness 0.100 in., ϵ'_s = 4.2, tan δ_s = 0.014; ϵ'_c = 17.64, tan δ_c = 0.0225)		272
5-35.	Power Reflection from Normal Incidence "B" Sandwich (Skin Thickness 0.200 in., ϵ'_s = 4.2, tan δ_s = 0.014; ϵ'_c = 17.64, tan δ_c = 0.0225)		272
5-36.	Transmission of 11-Layer Wall Radome with Skins 0.010 in. Thick and Cores 0.072 in. Thick		273
5-37.	Transmission of 11-Layer Sandwich Versus Frequency (Angle of Incidence 50°, Perpendicular Polarization)		275
5-38.	Effect of Core Thickness on Transmission of 11-Layer Sandwich (Angle of Incidence 50°, Perpendicular Polarization) . . .		275

Figure		Page
	CHAPTER 6	
6-1.	Pressure Distribution over Surface of a Subsonic Radome.	282
6-2.	Pressure Distribution Over Surface of a Conic Radome	282
6-3.	Aerodynamic Loading for a Conic Radome	282
6-4.	Unsymmetrical Air Loading on a Conic Radome	282
6-5.	Boundary Layer Velocity Gradient	285
6-6.	Specific Heat of Air	288
6-7.	Thermal Conductivity of Air	289
6-8.	Viscosity of Air.	290
6-9.	Temperature Recovery Factor Versus Velocity for Several Cone Angles	290
6-10.	Boundary Layer Temperature Versus Velocity (Neglecting Radiation).	291
6-11.	Radome Skin Temperature Versus Time for Different Values of Boundary Layer Heat Transfer Coefficient (h)	292
6-12.	Radome Skin Temperature Versus Time for Different Values of Thermal Conductivity (k)	293
6-13.	Radome Skin Temperature Versus Time for Different Values of Specific Heat (c)	294
6-14.	Radome Skin Temperature Versus Time for Different Values of Distance (x)	295
6-15.	Stress on Bond Adjacent to Gap	299
6-16.	Fluted Core and Lost Wax Core	300
6-17.	Flat Sandwich Parameters	301
6-18.	Cylindrical Sandwich Parameters.	303
6-19.	Critical Shear Stress Coefficients for Simply-Supported Curved Panels Having Circumferential Length Greater than Axial Length.	303
6-20.	Critical Shear Stress Coefficients for Simply-Supported Curved Panels Having Axial Length Greater than Circumferential Length	304
6-21.	Estimated Theoretical Critical Shear Coefficients for Curved Panels with Clamped Edges and Having Circumferential Length Greater than Axial Length	304

Figure		Page
6-22.	Estimated Theoretical Shear Stress Coefficients for Curved Panels with Clamped Edges and Having Axial Length Greater than Circumferential Length	305
6-23.	Buckling Coefficients for Cylinders of Isotropic Sandwich Construction in Torsion	306
6-24.	Buckling Coefficients for Cylinders of Isotropic Sandwich Construction in Torsion	307
6-25.	Buckling Coefficients of Infinitely Long Cylinders of Isotropic Construction in Torsion	308
6-26.	Nondimensional Stress Versus Nondimensional Time — Surface of a Plate	310
6-27.	Nondimensional Maximum Surface Stress Versus Nondimensional Heat Transfer	311
6-28.	Stress at Center of Plate	312
6-29.	Lightning Strikes on a Small Radome	319
6-30.	Dry Property Retention Versus Days of Exposure to 100 Percent Relative Humidity	320
6-31.	Loading Produced on a Large Radome by a Weight of Water	323
6-32.	Loading Produced on a Large Radome by Using Water to Transmit Pressure	324
6-33.	Thermocouple Attached to Metal Skin	326
6-34.	Thermocouple Attached to Plastic Skin	326
6-35.	Thermocouple Attached to Plastic Skin	326
	CHAPTER 7	
7-1.	Details of Test Blade	333
7-2.	Rain Erosion Cell at Cornell Aeronautical Laboratory	334
7-3.	Interior of Cornell Test Pit, Gear Box, Test Blade, and Method of Mounting Specimens	334
7-4.	Test Specimen Details	334
7-5.	Correlation of Drop Size Data on Polymethylmethacrylate	336
7-6.	Rain Erosion Test at 500 Miles Per Hour and 1-Inch Per Hour Rainfall	337
7-7.	Configuration of Slotted Laminates for Erosion Tests	338
7-8.	Placement of Specimens on Right and Left Wings of F9F Airplane	342
7-9.	Damage Depth Versus Impact Velocity — 2S Aluminum Specimens, Mercury Drops	348

Figure		Page
7-10.	Damage Depth Versus Impact Velocity — Lead Specimen, Mercury Drops.	348
7-11.	Damage Depth Versus Impact Velocity — Copper Specimens, Mercury Drops	349
7-12.	Damage Diameter Versus Impact Velocity — Lead Specimens, Mercury Drops	349
7-13.	Damage Diameter Versus Impact Velocity — 2S Aluminum Specimens, Mercury Drops.	349
7-14.	Damage Diameter Versus Impact Velocity — Copper Specimens, Mercury Drops	350
7-15.	Relation Between "C" of Equation (7-2) and Impact Velocity — 2S Aluminum and Lead, Mercury Drops	350
7-16.	Relation Between "C" and Impact Velocity, Based on Product of Damage Depth and Damage Diameter	351
7-17.	"C" Versus Velocity, for Water Drops 2 Millimeters in Diameter and Mercury Drops 1.93 Millimeters in Diameter	351
7-18.	Specimen Adapter, Scale 1:1	353
7-19.	Test Specimen Configurations	353
7-20.	Included Cone Angle Versus Distance Through Equivalent 1-Inch Per Hour Rainfall for Penetration.	354
7-21.	Mach Number Versus Distance Traveled Through Equivalent 1-Inch Per Hour Rainfall for Erosion Through 80 Percent of First Layer.	355
7-22.	57-Millimeter Rain Erosion Test Specimen	355
7-23.	Cross Section of Shell and Plastic Ogive	358

CHAPTER 8

8-1	Sketch of Honeycomb Core Structure	379
8-2.	Dielectric Constant Versus Temperature, Various Laminates.	386
8-3.	Loss Tangent Versus Temperature, Various Laminates.	386
8-4.	Electrical Properties of Joints	387
8-5.	Machine Impregnation of Fabric.	392
8-6.	Fluted Core Chin Radome.	394
8-7.	Pressure-Cast Aluminum Split Mold	395

LIST OF ILLUSTRATIONS (cont)

Figure		Page
8-8.	Laying-up Honeycomb Core.	396
8-9.	Sandwich Radome Ready for Trimming	396
8-10.	AN/APS-20E Radome After Preliminary Trim and Inspection	397
8-11.	Spraying Erosion Coating	397
8-12.	Making a Chopped Fiber Preform.	400
8-13.	Mixing Polyurethane Foam.	400
8-14.	Pouring Foam Into Matched-Die Mold	401
8-15.	Lay-Up of Fabric, Missile Radome	401
8-16.	Bagging Lay-Up, Missile Radome	402
8-17.	Wiping, Missile Radome.	402
8-18.	Lathe Grinding, Missile Radome	402
8-19.	Lay-Up of Radome with Glass Fabric and Epoxy Resin.	403
8-20.	Spraying Metal on Mold Pattern	403
8-21.	Templating Pressure-Cast Aluminum Die	404
8-22.	Diamond Wheel Grinding.	404
8-23.	Wide Temperature Range Dielectric Constant Interferometer	405
8-24.	Controlling Honeycomb Core Thickness.	406
8-25.	Multiple Thickness Gage Check	406
8-26.	Microwave Thickness Gage.	406
8-27.	AN/APS-20E on CL-28 Mock-Up at Cambridge Research Center Test Range	406
8-28.	Sketches of Typical Glass-Reinforced Laminate Sandwich Radome Constructions, Showing Various Methods of Attachment.	408
	CHAPTER 9	
9-1.	Section Drawing of Mold.	421
	CHAPTER 10	
10-1.	Two Arrangements for Platform Stabilization.	440
10-2.	Two Mounting Arrangements for Line-of-Sight Stabilization.	441
10-3.	Increase in Radome Size for Roll-Stabilized Antenna	441

LIST OF ILLUSTRATIONS (cont)

Figure		Page
10-4.	Axially-Symmetric Roll-Stabilized Sector Scanner Requiring No Increase in Radome Size	441
10-5.	Clearance of Antenna in Radome	442
10-6.	Beam Tilt Caused by Roll	444
10-7.	Axis Correction for Aircraft Attitude	444
10-8.	Placement of Radome in Aircraft	446
10-9.	Interference Effects Due to (A) Diffraction and (B) Reflection	447
10-10.	Edge Diffraction	447
10-11.	Cornu Spiral	449
10-12.	Intensity Distribution in Straight-Edge Diffraction Pattern	449
10-13.	Diffraction of Shaped-Beam Antenna in Nacelle	450
10-14.	Effect of Diffraction on Shaped Beam	450
10-15.	Simplified Diagram of Airplane	451
10-16.	Geometry for Calculation of Interference Patterns with Antenna Pointing Broadside	451
10-17.	Antenna Imaged in Reflecting Surface	452
10-18.	Depression of the Beam Versus Azimuth Angle	453
10-19.	Depression of the Beam Versus Roll Angle	453
10-20.	Distortion of Pattern by Reflection from Fuselage	454
10-21.	Distortion of Pattern by Reflection from Wing	455
10-22.	Section of Airfoil in Supersonic Flight	456

CHAPTER 11

11-1.	Basic Microwave Interferometer Arrangement	466
11-2.	Interferometer Arrangement in which Phase is Measured Independently of Amplitude	467
11-3.	Voltage Vector Relationships in Magic T of Interferometer Which Measures Phase Independently of Amplitude	467
11-4.	Elements of Semiautomatic Apparatus For Measuring and Correcting the Electrical Thickness of Radome Walls	468
11-5.	Apparatus for Measurement of Complex-Reflection Coefficient	470

Figure		Page
11-6.	Circuit Arrangement for the Measurement of Reflection Amplitude.	471
11-7.	Mechanical Micrometer for Measuring the Physical Thickness of Radome Walls	472
11-8.	Arrangement of Improved Mechanical Micrometer for Radome Walls.	473
11-9.	Circuit of Electrical Gage for Measuring the Physical Thickness of Radome Walls	474
	CHAPTER 12	
12-1.	Coaxial Waveguide Notation	485
12-2.	Rectangular Waveguide Notation	485
12-3.	Circular Waveguide Notation	485
12-4.	Transmission Line Notation	486
12-5.	Notation for Impedance Measurements.	486
12-6.	Resonance Method	487
12-7.	Shorted-Line Method	488
12-8.	Notation for Short-Circuit Method	488
12-9.	Notation for Open-Circuit Method	490
12-10.	Typical Equipment for Dielectric Measurements Using Slotted-Line Method.	494
12-11.	Typical Equipment for Dielectric Measurements Using Resonance Method	494
12-12.	Microwave Dielectrometer.	494
12-13.	Apparatus for Radome Transmission Tests	497
12-14.	Reflection Measurements by the Slotted-Line Method	499
12-15.	Reflectometer Method for Radome Reflection Tests	500
12-16.	Typical Pattern Measurement Equipment	500
12-17.	Antenna Test Mount	501
12-18.	Typical Boresight Measurement Equipment for a Conical Scanning Antenna	504
12-19.	Automatic Boresight Measurement Equipment	505

Figure		Page
12-20.	Functional Diagram of a Four-Horn Phase-Comparison System.	506
12-21.	Boresight Test Equipment for Use with a Monopulse Antenna	507
12-22.	Equipment for Near-Field Phase and Amplitude Measurements	508
12-23.	X-Band Pickup Probe	509
12-24.	Slotted-Line Phase Shifter.	509
12-25.	Movable Piston Phase Shifter.	510
12-26.	Rotary Phase Shifter	511
12-27.	Coherent Phase Discriminator	512
12-28.	Automatic Equipment for Near-Field Measurements	513
12-29.	Abbreviated Block Diagram of Scattering Method	514

CHAPTER 13

Curves of Transmission, Reflection, and Phase Delay for Perpendicular and Parallel Polarizations Incident on Solid Homogeneous Panels

	ϵ	Type of Curve	
13-1.	1.2	$T_\perp^2$. . .	526
13-2.	1.2	$T_\parallel^2$. . .	527
13-3.	1.2	$\Lambda_\perp$. . .	528
13-4.	1.2	$\Lambda_\parallel$. . .	529
13-5.	1.2	$R_\perp'$. . .	530
13-6.	1.2	$R_\parallel'$. . .	531
13-7.	2.0	$T_\perp^2$. .	532
13-8.	2.0	$T_\parallel^2$. . .	533
13-9.	2.0	$\Lambda_\perp$. . .	534
13-10.	2.0	$\Lambda_\parallel$. . .	535
13-11.	2.0	$R_\perp'$. . .	536
13-12.	2.0	$R_\parallel'$. . .	537
13-13.	4.0	$T_\perp^2$. . .	538

Figure	ϵ	Type of Curve	Page
13-14.	4.0	$T_{\parallel}^2$	539
13-15.	4.0	$\Lambda_{\perp}$	540
13-16.	4.0	$\Lambda_{\parallel}$	541
13-17.	4.0	$R_{\perp}'$	542
13-18.	4.0	$R_{\parallel}'$	543

Curves of Power Transmission Coefficients and Relative Phase Delays For Typical "A" Sandwiches ($\epsilon_s = 3.7$, $\epsilon_c = 1.4$, $\tan \delta_s = 0.014$, $\tan \delta_c = 0.005$, f = 5280 mc)

	ds (in.)	Type of Curve	
13-19.	0.030	$T_{\perp}^2$	544
13-20.	0.030	$T_{\parallel}^2$	545
13-21.	0.030	$\lvert T_{\perp}' - T_{\parallel}' \rvert$	546
13-22.	0.040	$T_{\perp}^2$	547
13-23.	0.040	$T_{\parallel}^2$	548
13-24.	0.040	$\lvert T_{\perp}' - T_{\parallel}' \rvert$	549
13-25.	0.050	$T_{\perp}^2$	550
13-26.	0.050	$T_{\parallel}^2$	551
13-27.	0.050	$\lvert T_{\perp}' - T_{\parallel}' \rvert$	552
13-28.	0.030	Constant $T_{\perp}^2$	553
13-29.	0.030	Constant $T_{\parallel}^2$	554
13-30.	0.040	Constant $T_{\perp}^2$	555
13-31.	0.040	Constant $T_{\parallel}^2$	556
13-32.	0.050	Constant $T_{\perp}^2$	557
13-33.	0.050	Constant $T_{\parallel}^2$	558

Curves of Insertion Phase Delay For "A" Sandwiches ($\epsilon_s = 4.0$, $\epsilon_c = 1.25$, $\tan \delta_c = 0.005$, $\tan \delta_s = 0.015$)

	ds/λ	Type of Curve	
13-34.	0.030	$\Lambda_{\perp}$	559

Figure	ds/λ	Type of Curve	Page
13-35.	0.030	$\Lambda_{\parallel}$	560
13-36.	0.060	$\Lambda_{\perp}$	561
13-37.	0.060	$\Lambda_{\parallel}$	562

Curves of Power Transmission Coefficients and Insertion Phase Delay for Typical "C" Sandwiches ($\epsilon_s = 4.0$, $\epsilon_c = 1.25$, $\tan\delta_s = 0.014$, $\tan\delta_c = 0.005$)

	ds/λ	Type of Curve	
13-38.	0.030	$T_{\perp}^2$	563
13-39.	0.030	$T_{\parallel}^2$	564
13-40.	0.030	$\Lambda_{\perp}$	565
13-41.	0.030	$\Lambda_{\parallel}$	566

13-42. Contours of Constant Power Transmission (T^2_{RCP}) and Insertion Phase Delays ($\Phi_{RCP} = \Lambda$), Homogeneous Panels; Transmitted Preserved Incident Component for Right-Circularly Polarized Incident Waves ($\epsilon_r = 4.1$, $\tan\delta = 0.014$). . . . 567

13-43. Contours of Constant Power Transmission (T^2_{LCP}) and Phase Delay (Φ^1_{LCP}) for Homogeneous Panels; Transmitted Depolarized Component for Right-Circularly Polarized Incident Waves ($\epsilon_r = 4.1$, $\tan\delta = 0.014$) 568

13-44. Contours of Constant Power Transmission (T^2_{RCP}) and Insertion Phase Delays ($\Phi_{RCP} = \Lambda$) for "A" Sandwich Panels; Transmitted Preserved Incident Component for Right-Circularly Polarized Incident Waves ($\epsilon_s = 4.2$, $\tan\delta_s = 0.015$, $\epsilon_c = 1.2$, $\tan\delta_c = 0.005$, $d_s/\lambda_0 = 0.0238$) 569

13-45. Contours of Constant Power Transmission (T^2_{LCP}) and Phase Delays (Φ^1_{LCP}) for "A" Sandwich Panels; Transmitted Depolarized Component for Right-Circularly Polarized Incident Waves ($\epsilon_s = 4.2$, $\tan\delta_s = 0.015$, $\epsilon_c = 1.2$, $\tan\delta_c = 0.005$, $d_s/\lambda_0 = 0.0238$) 570

13-46. Contours of Constant Power Transmission (T^2_{RCP}) and Insertion Phase Delays ($\Phi_{RCP} = \Lambda$) for "C" Sandwich Panels Composed of Two "A" Sandwiches in Tandem with $\epsilon_s = 4.2$, $\tan\delta_s = 0.015$, $\epsilon_c = 1.2$, $\tan\delta_c = 0.005$, $d_s/\lambda_0 = 0.0238$; Transmitted Preserved Incident Component for Right-Circularly Polarized Incident Waves. . 571

13-47. Contours of Constant Power Transmission (T^2_{LCP}) and Phase Delays (Φ^1_{LCP}) for "C" Sandwich Panels Composed of Two "A" Sandwiches in Tandem with $\epsilon_s = 4.2$, $\tan\delta_s = 0.015$, $\epsilon_c = 1.2$, $\tan\delta_c = 0.005$, $d_s/\lambda_0 = 0.0238$; Transmitted Depolarized Component for Right-Circularly Polarized Incident Waves 572

LIST OF ILLUSTRATIONS (cont)

Figure		Page
13-48.	Core Tolerance Curves for an "A" Sandwich, 9375 Mc, Perpendicular and Parallel Polarizations (ϵ_s = 3.7, ϵ_c = 1.4, tan δ_s = 0.014, tan δ_c = 0.005, d_s = 0.04 Inch)	573
13-49.	Skin Tolerance Curve for an "A" Sandwich, 9375 Mc, Parallel Polarization (ϵ_s = 3.7, ϵ_c = 1.4, tan δ_s = 0.014, tan δ_c = 0.005, d_c = 0.04 Inch)	573
13-50.	Skin Tolerance Curve for an "A" Sandwich, 9375 Mc, Perpendicular Polarization (ϵ_s = 3.7, ϵ_c = 1.4, tan δ_s = 0.014, tan δ_c = 0.005, d_s = 0.04 Inch)	574
13-51.	Core Dielectric Tolerance Curve for an "A" Sandwich, 9375 Mc, Perpendicular Polarization (ϵ_s = 3.7, ϵ_c = 1.4, tan δ_s = 0.000, tan δ_c = 0.000, d_s = 0.04 Inch)	574
13-52.	Skin Dielectric Tolerance Curves for an "A" Sandwich, 9375 Mc, Perpendicular and Parallel Polarization (ϵ_s = 3.7, ϵ_c = 1.4, tan δ_s = 0.000, tan δ_c = 0.000, d_s = 0.04 Inch)	575
13-53.	Equivalent Antenna System of a Paraboloidal Antenna and Its Radome	576
13-54.	Antenna-Radome Radiating System	576
13-55.	Array of Equispaced Radiators	577

LIST OF TABLES

Table		Page
2-I.	Thickness of λ/10 Sheets.	33
2-II.	Lens-radome Weight and Transmission Loss	80
2-III.	Feed Aperture Diameter Versus Lens Radius	80
4-I.	Major Source of Errors in Simultaneous Lobe	137
4-II.	Current Missiles With Electronic Guidance	140
4-III.	B-17 Radar Cross Section Measurements for Flight Pattern 2 .	156
4-IV.	Examples of Unit Vector T_1 for Various Polarizations. . . .	164
4-V.	Dependence of Cross Section on Antenna Configuration. . . .	166
4-VI.	Comparison of M' and Geometrical Optics Ray Tracing Methods for Central Ray with Typical Large Radome	193
7-I.	Effects of Temperature on Erosion	337
7-II.	Rain Erosion Properties of Materials Tested at 500 MPH Through 1/2-Inch Simulated Rainfall	341
8-I.	Comparison of Cotton and Glass Reinforcements	374
8-II.	Woven Glass Fabrics for Reinforced Laminates	375
8-III.	Properties of Polyurethane Foams	380
8-IV.	Dielectric Properties of Low Density Materials	381
8-V.	Dielectric Properties of Full Density Materials	383
8-VI.	Typical Mechanical Properties of Parallel Laminated (1/8-Inch Thick), Longitudinal, Low-pressure Laminated, Glass Fabric Base Plastic Material	388
8-VII.	Ultimate Flexural Strength (12 Plies of 181 Style Glass Cloth Laminates with Various Finishes — Parallel Laminated — Tested in Longitudinal Direction)	390
8-VIII.	Average Ultimate Flexural Strength, Modulus of Elasticity, and Loss in Weight (Heat Resistant Laminates of 181 Glass Cloth Tested at Temperature After 0.5 Hour at Temperature). .	390
8-IX.	Properties of Silicone Resin DC-2106 and Glass Cloth Laminate (Estimated Resin Content 40 Per Cent)	390
8-X.	Usual Methods of Fabricating Types of Radomes	391

LIST OF TABLES (Cont)

Table		Page
9-I.	Formulations Successfully Used in Casting Steatite Radomes	421
9-II.	Ceramic Mechanical Strength Values	428
9-III.	Ceramic Coefficients of Thermal Expansion	430
9-IV.	Ceramic Thermal Conductivities	430
9-V.	Young's Modulus for Ceramics	431
9-VI.	Ceramic Knoop Hardness Values	431
9-VII.	Ceramic Safe Operating Temperatures	431
9-VIII.	Densities of Ceramics	431
9-IX.	Dielectric Properties of Ceramic Materials	432
10-I.	Critical Angle for Total Reflection From Shock Front for Various Mach Numbers	457
10-II.	Refraction at the Shock Wave for Mach 3.2	458

Chapter 1

ORIGIN AND HISTORICAL DEVELOPMENT OF RADOMES

by

Fred H. Behrens

Wright Air Development Center
Wright-Patterson Air Force Base
Dayton, Ohio

Chapter 1

ORIGIN AND HISTORICAL DEVELOPMENT OF RADOMES

1-1. Introduction

In any treatise on a technical subject of this type, especially where it is intended for new men in the field as well as for the experienced, it is appropriate to outline some of the historical developments that brought the field to its present state. In this chapter, an effort is made not only to trace the significant stages of radome development, but to tie them in along the way with the corresponding developments in radar, particularly during World War II. By this means, the logical time scale of events will be seen, starting at the point where microwave radar, with its need for radomes, first came under serious consideration.

1-2. Relations to VHF Radar

Airborne radars of the premicrowave period were of the VHF type and operated with externally-mounted Yagi, or other dipole-array radiators requiring no radomes. These antennas served well in the early installations on the relatively slow-speed aircraft of that day. It was early realized, however, that the available antenna gains and resolution capabilities of practical airborne dipole-array antennas were so limited at the frequencies used (VHF), that an early shift to the use of microwave frequencies was indicated. Because of the unavailability of signal generators capable of producing microwave-pulsed signals of the required power, this shift to the microwaves was delayed.

1-3. Origin of Radome Problem

A low-powered, Sperry-built klystron equipment, believed to be the first experimental airborne microwave radar system, was test flown by the Army Air Forces in a B-18 aircraft in the late fall of 1940.[1] This aircraft was flown out of Moffett Field on the West Coast of the United States. Several successful experimental radar runs were made against the large hangar buildings at Moffett Field and against tankers in San Francisco Bay, as radar targets. By today's standards, the radar range obtained on these targets was very small, but these first runs clearly indicated the potentialities of microwave radar. No radome was used on these flights, since the equipment was merely suspended in the bomb bay of the B-18 and operated on an experimental basis through its open bomb bay doors. These early radar flight tests are significant to radome development historically because they not only served as the beginning of airborne microwave radar use, but also pointed out the need for radomes to streamline and protect the radar antenna.

The introduction of the microwave magnetron into the United States by the Tizard mission[2] from the United Kingdom in August of 1940 touched off the tremendous development in this country of microwave radar, destined to mean much in the defeat of the Axis powers in World War II. The magnetron provided the initial solution to the generation of pulsed microwave energy in sufficient power levels to be practicable for military radar purposes.

To exploit its potentialities, immediate arrangements were made by the National Defense Research Council (NDRC) of the Office of Scientific Research and Development to undertake the further radar research and development work necessary to bring microwave radar into being.[2, 3] The Radiation Laboratory was organized at the Massachusetts Institute of Technology under

NDRC sponsorship, where active research began on 10 November 1940. This laboratory, working in cooperation with laboratories in the United Kingdom, industrial and university laboratories of the United States as well as Military Service laboratories throughout the land, was destined to make an incalculable contribution to the war effort of the allied powers.

Exploitation of the new microwave magnetron tube, with its many potentialities in the radar field, then began without delay. Major efforts to develop the new microwave radar took place at the Radiation Laboratory and in industrial and government laboratories, resulting in a number of different experimental radar equipments being brought out for experimental flight testing and ultimate usage almost simultaneously. These will be touched on briefly in the paragraphs to follow.

1-4. Early Experimental Uses of Radomes

What is believed to be the first use of radomes in actual flight was a test demonstration for the AAF of an experimental version of Western Electric SCR-519 airborne radar.[4] It was operated from a B-18A airplane, in the early spring of 1941. See Figure 1-1. These flights were operated out of Mitchell Field, N.Y., flying against Ambrose Lightship, off Long Island, as a radar test target. A number of successful flights were achieved, in which the radar's ability to locate bombing targets and to guide bombing runs was compared directly with the performance of the famous Norden optical bombsight. The results obtained on these flights indicated that the radar could be developed into a powerful tool for military bombing operations. These first runs out of Mitchell Field further demonstrated the practicality of using radomes for streamlining and protecting the radar antenna. The radome used on these early flights was a hemispherical, thin-wall nose radome of plexiglas-like material, built in the experimental shops at Wright Field. It was given a frosting treatment to make it opaque for security purposes.

The above operation was carried out cooperatively by project engineers of the Signal Corps Aircraft Radio Laboratory at Wright Field and of the Bell Telephone Laboratory at Whippany, N. J.

The first experimental airborne microwave AI (Aircraft Intercept) radar equipment, developed and assembled by the Radiation Laboratory, was put into operation on the roof top of the laboratory in Cambridge on 4 January 1941.[2] The first successful flight test of this equipment was conducted in a B-18 airplane and is believed to have been flown out of Bedford Airport on 10 March 1941. This flight resulted in what is believed to be the first detection of airplanes with an airborne microwave radar. Ranges up to approximately five miles were obtained on this first AI flight. Still better results quickly followed. Although no definite statement has been found on the type of radome used in this specific flight, there is a general indication that the earliest airborne radar flights by Radiation Laboratory (MIT) used hemispherical plywood radomes. Since these radomes were all operating at microwave frequencies in the S-Band (3 kilomegacycles) and were only approximately one-quarter inch in thickness, it is clear that they were operating as thin-wall radomes, and hence did not yet require careful electrical design.

Two experimental Navy airborne radome installations at this time are also notable. The first is an experimental installation of an "ASD" Radar with 18-inch parabolic dish antenna installed on a PB-1 carrier-based bomber late

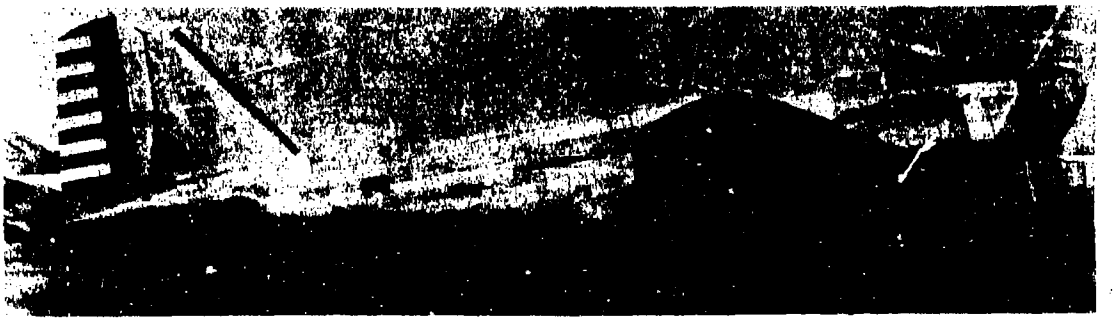


Figure 1-1. Douglas B-18A, of the Type Used in Earliest Airborne Microwave Radar Flights (Official Air Force photo)

in 1941.[2] The other is an "ASC" radar installation in the Navy PBM airplane in January 1942.[5] Details of the radomes of these two installations are lacking.

Other early flight tests, using a plexiglas-type radome similar to that used in the Long Island flights, were conducted out of McDill Field, Fla., in January, February, and March of 1942. These flights again used an experimental version of the SCR-519 radar, but with a new bombing computer. Some 100 bombs were dropped on test targets off Tarpon Springs.[4]

1-5. First Crash Program in Microwave Radar

The first crash development program for microwave radar equipment to be used in actual military operations by the AAF was the construction, by Radiation Laboratory, of 15 S-Band (3 kilomegacycles) AI radar equipments, which were installed in the earliest experimental models of the Army Air Force P-61 "Black Widow" night fighter in mid-1941. Two additional installations of this AI radar were also made about the same time in A-20 attack bombers, one of which was detailed in September 1941 to Bell Telephone Laboratory, where its radar equipment served as the predecessor of the future SCR-520 and SCR-720 AI radars.[2] The SCR-720 was destined to become standard for production installations in the P-61 in 1943. See Figure 1-2.

Thin-walled plywood radomes were applied to Navy PT boats during this same period. For the most part, they were built by the United State Plywood Corporation. These radomes served as the prototypes for a whole series of similar aircraft radomes that were to follow soon after.

1-6. Trend Away from Plywood Radomes

Plywood radomes were used extensively at this time for fixed radar installations on laboratory roof tops. Such radomes ranged in diameter up to 10 feet or more. Most of these were built by the United States Plywood Corporation. In-service electrical performance deficiencies with the plywood material were soon encountered, however, particularly where experimental laboratory propagation measurements were being made through radomes. These studies quickly demonstrated plywood's undesirable moisture absorption tendencies. Moisture-content variations with changes in weather were found to produce severe variations in electrical energy transmission through the radome walls. Efforts at rectifying these moisture difficulties took several forms. One approach, giving limited benefits, was to apply a thin overlay of resin-impregnated glass fabric to the outer surfaces of these plywood radomes to serve as a moisture barrier. (This was done in 1942, and is believed to be the first use of glass fabric in radome construction.) A second approach was to build radomes of a new polystyrene foam, using a solvent spray process. This latter approach produced radomes of good electrical performance but rather poor resistance to heavy physical stresses. The Blue Hills Observatory (near Boston) successfully used polystyrene foam radomes of this vintage for a number of years. A third approach to avoiding the moisture difficulties of plywood was to mold the radome of phenolic-resin impregnated cotton fabric (canvas). Elliptical radomes of this type were used in the wing nacelles of some of the early Navy installations of AIA X-Band (10 kilomegacycles) Aircraft Interception radars.[6]

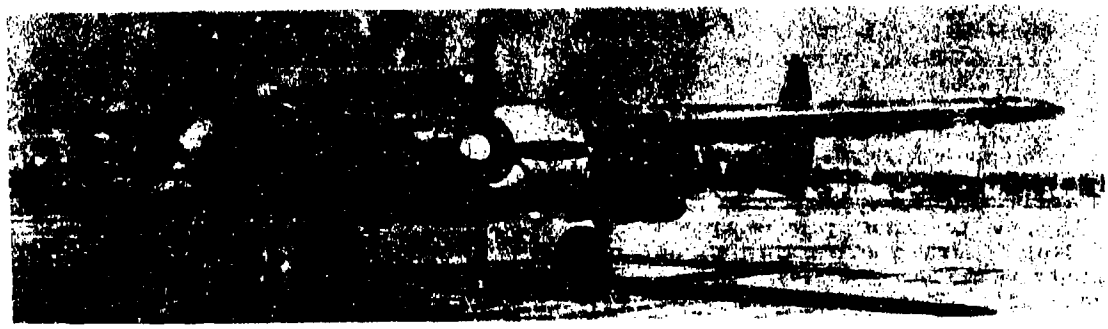


Figure 1-2. Northrop P-61 "Black Widow" Night Fighter with Nose Radome (Official Air Force photo)

1-7. Other Early Radome Applications

Another series of B-18 aircraft experimental flights was flown out of Langley Field, Va., in March 1942, using Radiation Laboratory's DMS-1 and DMS-10 radar systems (3 kilomegacycles). These experimental radars ultimately served as the prototypes for the Navy's successful and widely used ASG air-to-surface type radars.[2] Details of the specific radomes used are lacking, but since these were flights of Radiation Laboratory equipment, they were probably of plywood.

The equipping of Navy blimps, early in 1942, for antisubmarine warfare initiated what is probably the first use of microwave radar on lighter-than-air ships. They were of cylindrical plywood construction, by Vidal, and were of the simple, thin-wall type operating in the S-Band (3 kilomegacycles). No important electrical design problems were recorded, probably due to the fact that the radome walls were only about 4 percent of the wave length in thickness. The only recognized design problems of this series of radomes appear to have been physical rather than electrical in nature.[6]

The first operational Navy installation in airplanes was that of the ASG S-Band radar in the PB4Y-1 airplane about mid-1942 or early 1943. The radome used in this installation was the predecessor to the still active CW30/AP radome.[6]

1-8. Centers of Military Radome Development During and After World War II

During the early period of radome development, extending from 1942 to 1944, military interests in radomes were centered in three principle locations:

1. Radiation Laboratory, (Massachusetts Institute of Technology) Division 14, Group 54, represented by Mr. E. B. McMillan

2. Signal Corps Aircraft Radio Laboratory (Wright Field), represented by Major A. R. John

3. Naval Air Materiel Center (Bureau of Aeronautics), represented by Commander V. H. Soucek

Radiation Laboratory representation by Mr. McMillan continued until the close of that Laboratory in the Spring of 1946. Captains R. E. Long (1944) and Fred H. Behrens successively continued the representation of the Army Air Forces in the old Systems Engineering Laboratory at Wright Field. The Naval Air Materiel Center's representation was covered successively thereafter by Lt. Comdr. S. T. Harris, Lt. Comdr. A. J. Stanziano, Mr. E. J. Schlieben, and Mr. Joseph Ambrogi. Later, when the need arose for large ground radar installations with radome protection, a radome group was formed at the USAF Rome Air Development Center, which was represented continously from the beginning of its activity to the present day by Mr. C. S. Beal.

1-9. Origin of the Term "Radome"

It is of interest that the term "radome" has come to be used to denote all types of radar antenna dome covers. The term has its origin in a War Production Board meeting early in 1942. It is a contraction of the words radar dome, and was suggested first by Major A. R. John of the Signal Corps' Aircraft Radiation Laboratory (Wright Field).[6]

1-10. "Dumbo" Pathfinder Crash Program

The first experimental flight tests of the new X-Band (10 kilomegacycles) radars over Northern Ireland, beginning in March 1942, led to the first crash installation program of these radars in the noses of the "Dumbos" (B-24 "Liberators") by the Army Air Forces in late 1942.[7] These were the "pathfinders" for the Eighth Air Force, whose exploits over Europe during World War II are well-known. (The term "pathfinder" here refers to the use of a single radar-equipped bomber to lead a whole formation of non-radar-equipped bombers for "Bombing Through the Overcast.")

The radomes initially used on these "Dumbo" pathfinders were of two principal types. Some were of the earlier urea-bonded plywood construction, whereas most of the remainder were of glass cloth laminated construction. All radomes in these airplanes were of hemispherical type with fixed mountings.

1-11. Origin of the Radome Electrical Design Problem

The pathfinder program was scarcely under way before it came near foundering from severe radome wall reflection reaction. Severe magnetron frequency pulling nearly put the equipment out of operation. Even careful adjusting of the scanner axis to near coincidence with the radome axis did not entirely correct this difficulty. It was evident that the importance of minimizing reflections through keeping the radome walls thin, with respect to a wavelength, had not yet been fully appreciated. The neces-

sity for a rational basis and procedure for electrical design was clearly demonstrated.[6]

1-12 Switch to Polystyrene Fiber

The first correction of the reflection-pulling difficulty partially side-stepped the electrical design issue with the use of low dielectric constant materials. With only 3 weeks left before scheduled pathfinder use in major operations, a quick switch was made to a new, relatively untried, polystyrene fiber material developed by the Dow Chemical Corporation. A shrink-molding process was worked out cooperatively among representatives of the Radiation Laboratory, Dow Chemical Corporation, and the Virginia Lincoln Company, fabricators of the new radomes. This hurried switch to the new "polyfiber" construction was accomplished on schedule and, surprisingly, with a great deal of success. This polyfiber construction was relatively weak structurally, but it had a toughness property that served it in good stead in the operations over Europe, where it was able to resist tearing and shattering from antiaircraft flak penetration under conditions where other constructions failed.[6]

In the meantime, another shrink-molded polystyrene material called "plax" was being developed for the AIA radar by the Naval Aircraft Factory. Radomes of this material were to have been made up of laminations of stretched "plax" sheets. A unique material development resulted, but its rather high dielectric constant retarded its extensive use at this early stage in radome development.[6]

1-13. Beginnings of Radome Research

The difficulties of the pathfinder radome installations, in late 1942, provided a major impetus to the full recognition of the electrical problems of radome design and to the need for development of a rational and generalized theory of design for the future. The Radiation Laboratory organized a substantial Radome Development Group (Group 54 in Division 14) for a major component development. The half-wave wall design, as a means of curtailing radome reflections, was an early contribution. The many advances in radome technology that resulted from this group's efforts over the next few years still stand as a monument to the soundness of its pioneering work.[6] This group's principal works were initially published in a series of 26 Radiation Laboratory Bulletins, Series 483, dating from December 1943 to March 1946.

1-14. AAF Interests in Expanded Hardboard

Looking forward in early 1943 to a greatly increased use of airborne radar, the Army Air Forces sponsored the development of forming and application techniques for use of a new tough, rigid, low density, low refractive index, cellular, resin-impregnated rubber material called "SS expanded hardboard."[6,8] This material was developed by the United States Rubber Company, and was fabricated by drawing the hardboard over a male mandrel. A number of different SS hardboard radomes were designed with half-wave walls by the Army Air Forces for operation in X-Band (10 kmc) bomber radar installations. In addition, some thin-wall S-Band radomes were designed for use in cargo airplanes. These SS-expanded hardboard radomes served usefully for some time. Cold weather operation, however, so embrittled the material that ejected shell cases, falling rearward from the bomber's forward gun turrets, inflicted severe impact failures and brought about the ultimate discontinuance of this material in radome manufacture. It also was found to be attacked by solvents used around aircraft.[8] This, too, contributed to its replacement.

1-15. "Bombing Through the Overcast" Operations

In mid-1943, the second major AAF radome crash program at Wright Field went into effect. This program called for the equipping of a considerable number of B-17 bombers with retractable radomes of the hemispherical type. These installations were made for the new AN/APQ-13 and AN/APS-15 X-Band radars intended for the AAF's "Bombing Through the Overcast" campaign.[7] The radomes used were largely of glass-fabric laminated construction, as fabricated by the Virginia Lincoln Corporation using resins manufactured by Columbia (Pittsburgh Plate Glass Company) and the Bakelite Corporation. Other versions of these radomes were fabricated by Crosley Marine Company, Swedlow Plastics Company, and the United States Rubber Company. These other versions included some of polystyrene fiber construction.

1-16. Earliest Efforts at Streamlining Radomes

The wing-pod radome on the Navy's F6F-3N fighter airplane, Figure 1-3, represents one of the early attempts (1943) to streamline radomes. This wing-pod radome was made slightly elliptical in a design by Grumman Aircraft Engineering Corporation. It housed an AIA radar antenna.

1-17. Double-Wall Radomes

The so-called double-wall construction, consisting of two concentric thin-wall radome skins air-spaced from one another by approxi-

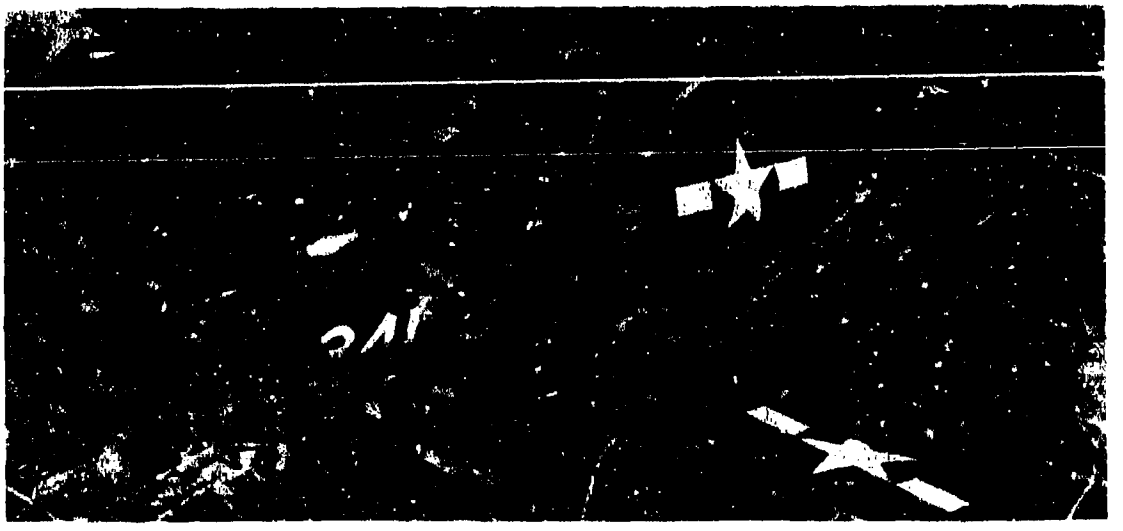


Figure 1–3. Semistreamlined Radome on the Navy's Grumman F4F–3N (By permission of Grumman Aircraft Engineering Corp.)

mately one-quarter wavelength, was tried for a time, at the suggestion of the Radiation Laboratory. The use of two air-spaced thin walls provided a means of neutralizing the excessive reflections common to single thin-wall radomes without the weight compromise of using the half-wave wall. A number of cylindrical radomes of this type were built for use in Navy blimps.[6] Similarly, a trial model of this construction was built by the AAF for use in the B-24 bomber. [8] A semistreamlined version of this construction was used in 1942 on the PBM patrol seaplane, with the ASG radar. These air-spaced sandwich radomes were not widely used, however, because of mechanical difficulties. Nevertheless, they served a most useful purpose in that they sparked the development of the three-layer "A" sandwich, which was to replace it. The double-wall construction found another use (1944) on the AN/APQ-7 "Eagle" radar vane-type antenna (see Figure 1-4), where the open spaces between the rib-spaced double walls were used as hot-air, ducts for thermal anti-icing purposes.

1-18. Development of the Three-Layer "A" Sandwich

Radiation Laboratory, in 1943 and 1944, developed the electrical design for the "A" sandwich, three-layered radome, as it is generally known today.[6] The "A" sandwich construction utilized strong but dense skins of glass-fabric laminates, spaced and bonded to a low density cellular material used as core. This construction not only provided the reflection neutralization sought in the double-wall construction that proceeded it, but also provided a strong, lightweight structure ideal for aircraft application. The high strength/weight ratio of this construction was the prime incentive behind the general adoption of sandwich construction for radomes by early 1944. The first aircraft radome sandwiches used polystyrene fiber material as cores with laminated glass-fabric skins. By early 1944, hemispherical "A" sandwich radomes had been installed by Radiation Laboratory on Navy PT boats. These were adhesive-bonded, cellular acrylonitrile (Hycar), expanded hard rubber cored sandwiches. It was soon found that this Hycar rubber core material tended to inhibit the curing of the laminating resins used in the

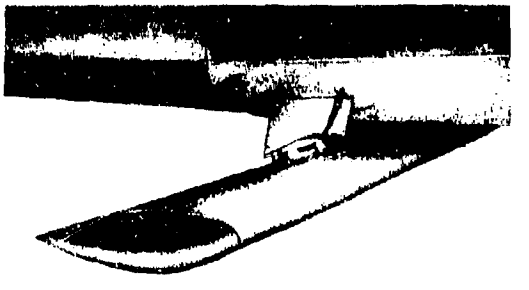


Figure 1–4. "Eagle" Vane Antenna and Radome Installation for the AN/APQ–7 Radar (Official Air Force photo)



Figure 1-5. Aircraft-Early-Warning Radome Installation on the Navy's Grumman AF-2W (By permission of Grumman Aircraft Engineering Corp.)

glass fabric skins. This undesirable property contributed to a difficult and time-consuming fabrication process. With the development in 1944 by Radiation Laboratory of a catalyst coating treatment for the cellular Hycar core material, a single-cycle, wet-lay-up process for sandwich construction was evolved. This improvement considerably accelerated the use of Hycar sandwich radomes throughout the remainder of World War II.[6] This success was tempered somewhat by an undesirable tendency of expanded Hycar to collapse occasionally under molding pressures, with resultant high rejection rates in production.[8] (It is interesting to note that British research simultaneously produced another sandwich radome construction using sheet methylmethacrylate skins with a foam core of the same substance.)[6]

1-19. Adoption of Sandwich Radomes

The general acceptance of sandwich construction for military aircraft radomes was chiefly pioneered in 1943-1944 by a development competition, sponsored by the Bureau of Aeronautics, for a large radome for the TBM torpedo bomber, which was being equipped with the AN/APS-20 aircraft-early-warning radar. This competition pitted the Naval Aircraft Factory's rib-reinforced, single-wall radome design against an "A" sandwich design developed at Radiation Laboratory. The weight-saving, flight-stability, and rigidity advantages found in the sandwich version of this radome firmly established the "A" sandwich construction as standard for a considerable period of time.[6] A model of this radome on the Navy AF-2W, in 1950, is illustrated in Figure 1-5.

1-20. The Semistreamlined Blister Radome

By late 1944, strong pressure was applied to reduce the aerodynamic drag penalty of radomes through streamlining. With electrical design aid from the Radiation Laboratory, both AAF and Navy brought out new designs for semistreamlined blister radomes for fixed mounting on existing aircraft, replacing the old hemispherical fixed and retractable radomes. These efforts were highly successful and established the trend toward flush-faired radome lofting. The AAF semistreamlined blister radome for the AN/APQ-13 radar on the B-29 airplane[8] illustrated in Figure 1-6 is a good example.

1-21. Polystyrene Fiber K-Band Radomes

What is believed to be the earliest K-Band (24 kilomegacycles) half-wave wall radomes of



Figure 1-6. Typical Semistreamlined Blister Radome on the Air Force B-29 (Official Air Force photo)

polystyrene fiber construction were developed at Radiation Laboratory in 1944.[6] Shortly thereafter a few similar radomes were designed and built by the AAF for use on its B-17 and B-29 aircraft for experimental K-Band radar insaltlations.[8] At K-Band frequencies, thickness tolerances were found quite critical. This led to the development by Radiation Laboratory of what is believed to be the first K-Band interferometer for use in sensing electrical thickness variations.

1-22. The Honeycomb Sandwich

With the development at Wright Field in 1944 of a resin-impregnated, glass-fabric based, honeycomb sandwich construction for airframe components, the use of honeycomb-cored "A" sandwich radomes was successfully tried.[6,8] (See Figures 8-1 and 8-8 of Chapter 8, "Organic Materials and Radome Construction.") Despite some rather considerable advantages over its Hycar rival, this construction did not achieve general popularity for radome use until after the end of World War II.

1-23. Knitted-Sock Laminated Radomes

In early 1945 the first use of laminated radomes of glass yarn, knitted into contour-formed socks, was introduced to provide a rapidly producible, pressurized, thin-wall radome for the AN/APS-4 X-Band Radar.[6,8] These radomes, developed jointly by Bell Telephone Laboratories, Radiation Laboratory, and Andover Kent, were installed on a small cigar-shaped radar unit carried outboard on the bomb racks of fighter aircraft. Although the knitted-sock construction avoided the need for hand lay-up of lapped-gore laminations, it produced a construction that was much weaker structurally than the woven-glass fabric laminate radomes. Undoubtedly, the stretching of knitted socks of this type over molding mandrels brought about some uneven distribution of the glass material in the radome walls, but these difficulties were not found serious for the radars of this early vintage. (This use of contour-knitted socks is an interesting predecessor to the contour-woven, glass-fabric laminate radome construction currently being considered for guided missile applications.)

1-24. Earliest Efforts at Unified Antenna-Radome Design

The first important departure from the generally round paraboloid reflector-and-feed type antenna with associated round blister radome came early in 1945. Considerations of still further aerodynamic drag reduction on the B-29 bomber sparked the development of a new scanner-radome configuration.[6,8] Radiation Laboratory, collaborating with the Boeing Airplane Company, developed a broad but shallow snow-shovel-like scanner and an associated broad flat turtle-shell-like sandwich radome to replace the original round AN/APQ-13 radar scanner and semistreamlined radome. The flat radome operated at unusually high angles of incidence for those days. Its development required much effort and care in both design and fabrication (see Chapter 3, "Search Radome Design"), but served usefully to expedite aircraft and radar development thinking toward the fully faired-in radome designs yet to come. This early action, aimed at the coordinated design of scanner and radome as a unit, represents one of the first recognitions of the intimate relationships that should exist between antenna and radome developments.

1-25. Unification of Airframe and Radar-Radome Design

The development of the jet bombers initiated the first major AAF efforts to integrate radar and radome installations into the initial design planning of Military aircraft, rather than to continue facing the compromising problem of adding radar to finished airplanes after primary design has been made firm. A delegation of radar system engineers, antenna engineers, and radome engineers from Bell Telephone Laboratory, Radiation Laboratory, and Wright Field was organized in the spring of 1945 to present the case to the aircraft prime countractors.[8] Integration of radar and airplane planning was accomplished in the cases of the North American XB-45, the Convair XB-46, the Boeing XB-47 and the Glenn L. Martin XB-48. With this accomplished at the preliminary mock-up stages, a major step forward was gained toward maximum joint effectiveness of radar and airplane. Much cleaner airplane lines, (see Figure 1-7) and correspondingly better airplane performance resulted. Furthermore, these actions initiated the current Air Force policy of turning over to its prime contractors the responsibility for radome hardware development and design. This policy replaced the earlier policy of developing radomes in the military service laboratories and having them produced independently as Government-Furnished Aircraft Equipment (GFAE). This policy change was necessitated by recognition of the excessive coordination difficulties that would accompany this integration, if the former GFAE policy were to be continued.

1-26. Nacelle Lining Absorbers

Microwave absorber screens came into general aircraft use for radar scanner-nacelle lining



Figure 1-7. North American B-45 With Chin Radome Exemplifying the Trend to Flush-Fairing of the Radome into the Airplane Loft-Lines (Official Air Force photo)

more or less coincidentally with the integration of antennas and radomes into airplane designs. Absorber liners in aircraft were first used in certain areas of the radome to mask off regions contributing to undesired ground-clutter pick-up and to avoid undesired fuselage reflection interference.[6] Use of such absorbers was soon extended to the complete lining of the metal areas of the antenna nacelle to eliminate interference from the bulkhead and other structural members.[8] The old Harp materials, designated MX 410/AP (X-Band, 10 kmc) and MX 355/AP (S-Band, 3 kmc), were used most frequently for these purposes.

1-27. Recognition of the Role of Phase Delay in Radomes

The role of insertion phase delay in radome design was early recognized by Radiation Laboratory in its design of the BUPX radar beacon antenna housing in 1944. The antenna was embedded in a streamlined block of hard rubber foam. Internal phase-equalization was accomplished by boring holes in the foam in judiciously chosen sizes and locations. The foam structure, after boring, was then covered with a thin, glass-fabric laminate skin to gain service durability. This design was extensively used for a number of years.[6] Radiation Laboratory, in publishing its research in 1945 on polarization effects at grazing incidence, not only satisfactorily explained many of the then recognized difficulties in radome design, but also anticipated many of the polarization problems destined to beset the supersonic streamlined radomes of today.

1-28. The "B" Sandwich

McMillan, Redheffer, and Leaderman continued polarization research during and after the Radiation Laboratory closed, and published, in 1948, their theories of the "B" sandwich (reversed-order, three-layer) radomes.[6] The "B" sandwich, having its high dielectric constant materials sandwiched between outer matching layers of lower dielectric constant materials, offers some distinct electrical design advantages (see Chapters 2, 5, 8, 9, and 13).

1-29. Onset of the Rain Erosion Problem

In mid-1945 the B-29 bombers operating out of the Marianna Islands against Japan uncovered a new and major radome problem.[11] Frequently, upon return from missions, the leading edge radome of the AN/APQ-7 (Eagle) vane-scanner (see Figure 1-4) had completely disintegrated. In many cases, only the mounting rims and a few remnants of the core-spacing ribs remained. The cause of this damage was not immediately apparent, since many of the damaged radomes had not been exposed to any known collision, flak, hail, or other damaging exposure. For a time it was thought to have been caused by loose grit, kicked up off the runways during takeoffs and landings. Investigation showed that frequent encounters with rain enroute were common to these operations. It remained for the Radiation Laboratory and the National Advisory Committee for Aeronautics, (NACA), working simultaneously, to establish conclusive evidence that the damage was due to rain erosion. Radiation Laboratory used an experimental whirling arm and water spray set-up to test small square sample panels of radome materials in a manner which was a prototype of the later whirling arm test facilities at Cornell Aeonautical Laboratory and elsewhere. The NACA laboratories at Cleveland demonstrated the cause of rain erosion by simulating flights through artificial rain in a wind tunnel. Thus began the still active search for rain erosion resistant radome materials. (See Chapter 7, "Subsonic and Supersonic Rain Erosion.")

1-30. Termination of Radiation Laboratory Activities

The Radiation Laboratory, after a major contribution to the radar and radome fields, stopped its operations in early 1946.[2] Its closing did not come, however, before an important portion of its achievements had been documented into permanent book form. The 28-volume shelf of radar books, generally referred to as the Radiation Laboratory Series," was prepared and released for publication through the McGraw-Hill Book Company. Volume 26, "Radar Scanners and Radomes, edited by Cady, Korelitz, and Turner, covers much of the Radiation Laboratory's radome development work. Other work related to radomes is contained in Volume 11, Techniques of Microwave Measurements, edited by Montgomery. Following the close of the Radiation Laboratory, the radome development work formerly active there was assumed by the military radome development groups of the Army Air Forces and Navy at Wright Field and Johnsville, Pa., respectively.

1-31. Beginnings of Long Range, Post-War Radome Research

In the fall of 1946 the Army Air Forces radome activity at Wright Field initiated a long range radome research and development contract program.[8] It was aimed at providing better materials and processes with which to build the radomes of the future. The contract was with the Goodyear Aircraft Corporation at Akron, Ohio. The scope of this early contract covered such subjects as rain erosion investigation, improved laminating techniques, improvement of the electrical properties of laminating resins, and development of better core materials and fabrication processes.

The Goodyear Aircraft Corporation's rain erosion studies were largely empirical in nature.[8] A whirling-arm rain erosion test machine was built, and rain erosion testing operations begun, in January of 1947. The peripheral speeds at which the test samples were carried through water sprays were initially 120 miles per hour, but were increased to 250 miles per hour in March of 1947 to reduce the amount of test time. These test operations quickly showed that all reinforced plastic radome materials then current were inadequate for operation under rainy weather flight conditions. These adverse findings initiated a comprehensive effort to develope rain erosion resistance in laminated materials, which at that time were all porous and opaque. From this effort there soon developed the concept of the void-free laminate. In March of 1947 it was found that a void-free laminate exhibited at least eight times the rain erosion resistance of a conventional voidy laminate. By May of 1947 methods had been evolved to produce void-free laminates, in a reasonably repeatable manner, so that by February of 1948, a tentative specification was released to industry to expedite its adoption.

Investigation of rain erosion was begun shortly thereafter at the Cornell Aeronautical Laboratory,[8] where another whirling arm machine was put into operation at about the beginning of 1948. This machine operated initially at a peripheral speed of 250 miles per hour, which was later increased to 500 miles per hour. The purpose of this second erosion study program was to investigate methods of testing for rain erosion and to look into the mechanism of erosion itself. This facility later became the center for most USAF subsonic speed rain erosion investigations.

A series of flight tests was conducted at Wright Field in the Spring of 1949 using an F-80 airplane as the test vehicle to correlate laboratory rain erosion test data with actual flight service experience. Numerous flights were made, at speeds approximating 400 miles per hour, through rain. The plastic laminated nose cap for the radio compass and the plastic laminated vertical fin-tip housing for the VHF command radio-link antenna were used as test samples. Dramatic demonstrations of the structural damage inflictable by rain erosion were obtained,[8] and from these demonstrations a good test correlation resulted, both for bare laminates and for the neoprene-coated laminates discussed next.[9]

1-32. Adoption of the Neoprene Protective Coating

In October of 1948 the Goodyear testing program demonstrated that a neoprene brushing cement coating, developed by the Gates Engineering Company of New Castle, Delaware, greatly improved the erosion resistance of radome laminates.[8] It was found that void-free laminates coated with approximately 10 mils of this material yielded life expectancies nearly 100 times those of bare laminates. Unfortunately, however, it was found that the initial version of this material exhibited a severe electrical energy absorption characteristic. Even a 10-mil thick coating reduced X-Band Radar transmission through a radar panel by as much as 40 percent.

Through the cooperation of the Gates Engineering Company, a new loading substance was substituted for the original carbon loading. This

change in loading did not alter the erosion resistance, but it decidedly improved the electrical properties. This early neoprene protective coating was of the heat-curing type, preceding the air-curing type which later became the standard coating. Another similar material designated 23-56 neoprene coating, was later placed on the market by The Goodyear Tire and Rubber Company.

1-33. Research on Laminating Resins

Goodyear, under its contract, also attempted for a time to modify existing laminating resins with the object of lowering their dielectric constants and loss factors.[8] While some success was achieved, it was found that the gains achievable through further work on the resins alone did not appear to be promising enough to warrant further effort. It became clear that if any substantial improvements in this direction were to be made, the greatest effort should be applied to lowering the dielectric constants and loss factors of the reinforcing fibers used in the laminating fabric. This led to a later effort to develop low-dielectric-constant glass fibers, designed specifically for radomes. Such a fiber was developed and produced in experimental quantities by Glass Fibers, Incorporated, but and unexpected finishing difficulty deterred its general adoption.

1-34. RDB Subpanel on Radomes

Shortly after the post-war research and development program began to settle down, following the dislocations caused by the end of the war, the Research and Development Board in Washington organized, under its Committee on Electronics, a Panel on Radiating Systems, charged with general responsibility for antenna and radome development.[8] The chairman, recognizing the important role of radomes in antenna development, established the Subpanel on Radomes in the fall of 1946. In a reorganization in 1951, the Panel on Antennas and Propagation was formed, replacing the Panel on Radiating Systems. The Subpanel on Radomes was again reconstituted and formally chartered under the new panel. The radome subpanel was charged with review of the several military services' requirements and their respective supporting research and development programs to define any gaps needing filling and to avoid all unnecessary and undesirable duplication of effort among the services. This subpanel was active until February 1954. Besides performing its assigned functions continuously through this period, it did much to foster the appreciation of radome development problems and to advance radome research through the sponsoring of technical sessions at a number of professional conventions, at which formal technical papers were presented. The subpanel further served a most useful function by bringing together the principle radome investigators and fostering their active cooperation.

1-35. Radome Engineering Manual

In recognition of the general need for a reference manual on radome design, the Army Air Forces and the Navy Bureau of Aeronautics cooperated in preparing and publishing an early Radome Engineering Manual issued in October of 1948. It was designated both as Navaer 16-45-502 and as AMC Manual 80-4. This manual,[5] however, covered only the problems of search-radome design. By this time, the complex problems of designing radar gunfire control radomes and radomes for missile guidance, as well as further problems associated with the design of radomes for use on wide frequency bands, were being recognized. At the time of the printing of this first Radome Engineering Manual, the proved design techniques for these latter applications were still to fragmentary to be reduced to handbook form.

1-36. "A" Sandwich Foamed-in-Place Radomes

The desirability of foaming the core of sandwich radomes in place between premolded skins, in lieu of laying-up hand-tailored gores of prefoamed core material, was recognized as early as 1945. Using plastic resin cores foamed-in-place, the Navy produced for the F7F airplane what were probably the first usable foamed-in-place sandwich radomes.[10] Processing difficulties with brittleness and non-uniformities deterred the general adoption of the process at that time. Army Air Force efforts during this period, to expand Hycar rubber cores in place were not promising.

The early AAF radome development contract with Goodyear also was charged with furthering development of the "A" sandwich by foaming-in-place.[8] After a series of only partially successful efforts at developing usable foam-in-place materials and processes along the lines of the earlier work, the alkyd isocyanate foams, based upon German experiments with toluene diisocyanate foaming agents, were successfully developed. The first successful experimental alkyd isocyanate foamed radome produced with this process was a 14-inch hemispherical "A" sandwich radome built by Goodyear for an Emerson radar fire control system intended for tail installation in the AAF's medium jet bombers. This radome was built in July of 1948. Larger experimental radomes of the C-54 nose

configuration were successfully foamed in December 1948. (See Figure 1-8.) A development report covering the process was issued in December 1949, supplemented by successive improvement reports in October 1950 and March 1952. Tentative specifications for the foam-in-place process and material were released in September 1949. A foam-in-place demonstration conference was held at the Goodyear plant on 10 November 1950 for the purpose of introducing the process into the radome industry generally. The first AF production use of the process was on the F-89 nose radome (see Figure 1-9) beginning in 1949. A subsequent development of a similar foam process and material, but for higher temperature (400° F) applications, was carried out under another Air Force contract effort by the Cornell Aeronautical Laboratory at Buffalo, N. Y., and released through a report dated March 1954. A great deal of follow-up characterization and improvement effort on these foams was executed by the Naval Air Development Center. The Lockheed Aircraft Company developed a similar foam and associated process which has since enjoyed widespread adoption and use.

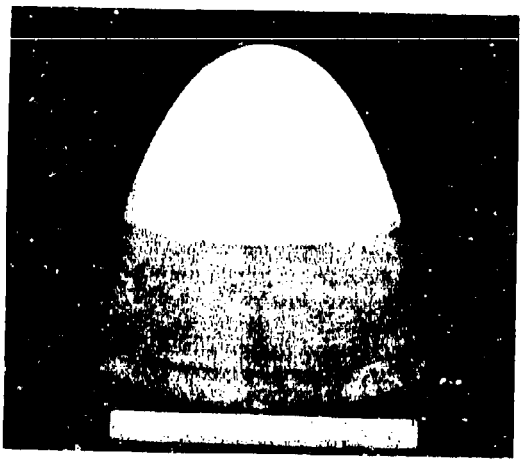


Figure 1-8. Example of Early Foamed-in-Place Radome for the Nose Installation of an AN/APS-10 Radar on the C-54 (By permission of Goodyear Aircraft)

1-37. Radome Design Criteria Development

During the period from 1949 to 1954, a considerable amount of general radome theoretical research and engineering design criteria de-

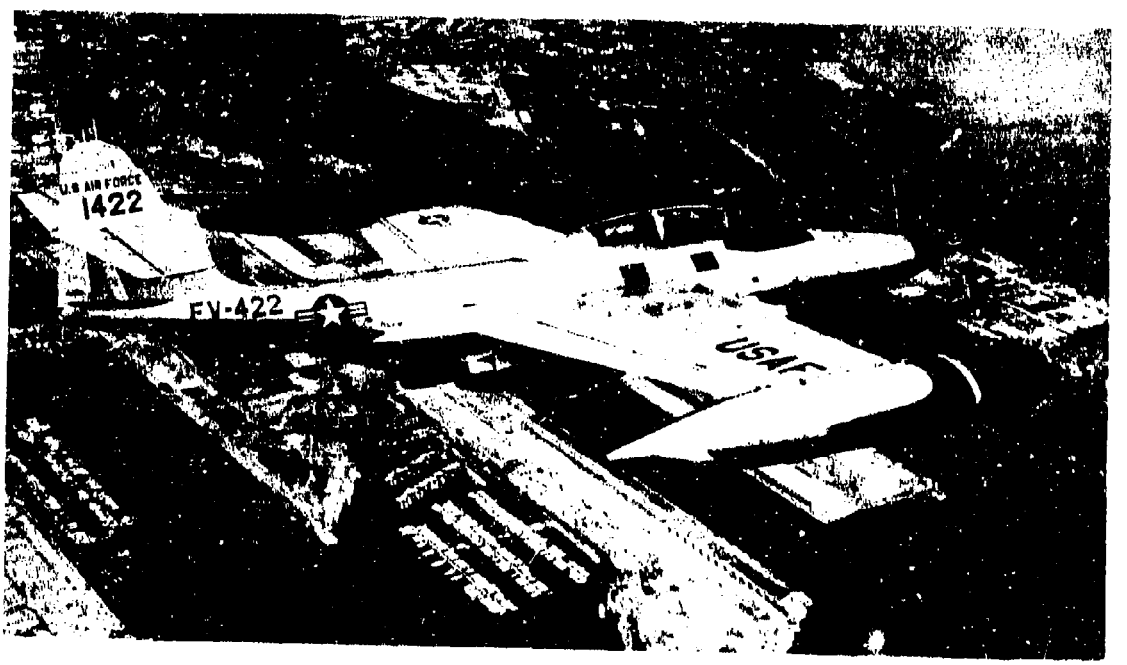


Figure 1-9. Northrop F-89 With Nose Fire Control Radome of the Foamed-in-Place Type (Official Air Force photo)

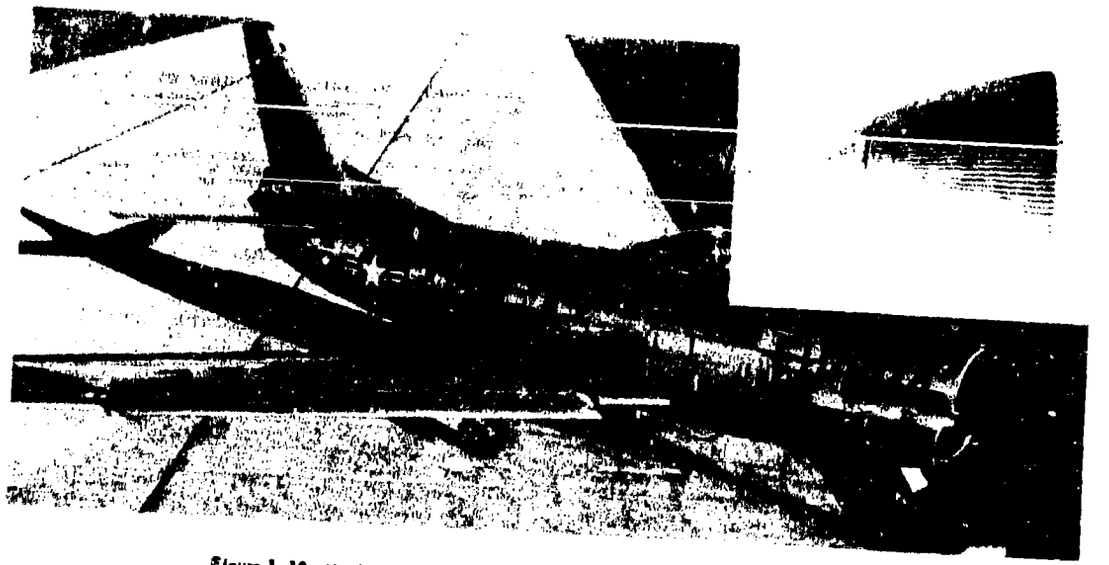


Figure 1-10. North American F-86D With Thermally Anti-Icing Nose Radome for Fire Control Radar (Official Air Force photo)

velopment was being carried out by both the Air Force and the Navy laboratories.[8,10] The AF activity was primarily through contract while the Navy carried out a large bulk of its effort at the Naval Air Development Center, with a smaller percentage executed through outside contracts. The Navy's work resulted in a series of valuable design criteria reference reports covering such engineering data as Tables of Fresnel Coefficients for the radome design equations and the computation and plotting of a large series of design curves for radome walls, considering losses. The Air Force contract activities in this period produced similar data for the double-sandwich radome through reports issued both by the Goodyear Aircraft Company in July 1951 and by the Douglas Aircraft Corporation in 1953. Other work was carried out on the double-sandwich radome by North American Aviation, as evidenced by their development of a fluted-core, double-sandwich radome for the F-86D airplane. (See Figure 1-10.) The outer core of the double sandwich was made of custom molded flutes, to provide for thermal anti-icing of the radome for all-weather operations with gunfire control radars. This radome dates from early 1950.

1-38. Early Radome Error Prediction Work

During the period between 1950 and 1954, the Naval Air Development Center devised its initial method of radar error prediction for use in the design of radar gunfire control radomes requiring close tolerances on allowable bending error. These methods were devised for application to conical-scan gunfire control radar systems. Based upon geometrical optics, these methods gave a first-order approximation of the expected radome error. In support of the NADC approach to boresighting error prediction, NADC developed, in 1950, what is believed to be the first manually operated radome boresight error test equipment.[10] This equipment was later arranged to provide a continuous automatic recording of error versus radome scan-angle.

Other efforts in this same direction were carried out for the Air Force by the McMillan Laboratories,[6] which also contributed techniques for the prediction and compensation of radome error. Each of these methods yields only approximate designs and requires supplemental experimental adjustments to produce satisfactory error-corrected radomes.

About 1952, the Ohio State University Research Foundation began work on an Air Force sponsored contract for research into the microwave optics of radomes.[8] Many useful results have come from this work. Perhaps most important among them is the development of techniques and equipment for studying the near field energy distribution of radar antennas using tiny parasitically excited scatterers modulated from a high impedance source through exceedingly high resistance leads which do not appreciably disturb the field being measured. Another important

outcome of this work is the development of techniques for far-field pattern prediction, as perturbed by radome structures in the near field, using a two-step process. This two-step prediction process is the basis upon which most of the succeeding efforts of radome error prediction are founded.

1-39. Working Group on Small Supersonic Radomes

By early 1951 considerable concern had built up in weapons systems development management circles over supersonic missile radome problems. Much concern was evident, both in regard to the inadequacies of electrical design procedures with which to correct radome imposed directional error, and with respect to the recognized inadequacies of radome materials from the thermal stability point of view. A special working group on small supersonic radomes was organized in early 1951 to investigate this situation and to recommend remedial action to the RDB Panel on Guidance and Control.[8] Specific recommendations were called for, pertaining to the AF Falcon Project and to the Navy's Sparrow I and Sparrow II Projects. This working group met briefly, prepared a report summarizing the situation, with appropriate recommendations, and then disbanded. It is interesting to note that in spite of the improvements made since that time, most of the serious radome problems recognized at that time, and set down in the report, are still paramount in the minds of radome designers.

1-40. The Princeton Study

In 1951, the Office of Naval Research, recognizing the need for a substantial effort on a broad front in the area of radome development for the supersonic guided missile, initiated, through the Princeton University research staff, a study to prepare a complete analysis of the supersonic guided missile radome problem and to make specific recommendations for supporting the research necessary to break the problem down to practical elements to which effective development work could be applied. The Princeton staff prepared an excellent and comprehensive report, which was presented to the Military Services in March 1952.[8,10] It contained a number of specific recommendations applicable to the several related interests of aircraft design, radar system design, aerodynamic shaping, and radome design. The greater portions of at least the radome recommendations later became the subjects of development contracts.

1-41. Gunfire Control and Missile Guidance Radome Design

Following the commencement of boresighting studies in 1949 and 1950, a number of error-corrected radome designs were prepared with some success. One of the first was the McDonnell Aircraft Company's design in late 1951 of the ogival radome for the Navy's F3H (see Figure 1-11), used subsequently for the USAF F-101A aircraft. This was based upon a geometrical optics design approach, somewhat similar to the NADC method. Other successful designs were prepared by McMillan Laboratory and Goodyear Aircraft Corporation for the Navy Sparrow II missile.[6]

1-42. The USAF Bomarc Radome[11]

Between 1951 and 1955, the Boeing Airplane Company developed what is probably the most precise supersonic streamlined guidance radome produced thus far. It is a half-wave thick, solid laminate radome in and ogival shape with a fineness ratio approximately 3.5:1, and is designed for use with a radar antenna aperature 19 wavelengths in diameter. This is a uniform-thickness radome wall designed for optimum performance at the highest angles of incidence encountered. Despite the fact that no correcting tapers were introduced into its wall design, it was found, when fabricated with the required degree of uniformity in materials and dimensions, to produce an exceptionally smooth error characteristic. Its ability to produce such a low error characteristic without taper correction is attributed to the large aperture through which



Figure 1-11. McDonnell F3H Navy Fighter With Nose Type Fire Control Radome Shaped for Transonic Speeds (By permission of McDonnell Aircraft)

the radar operates, and to the thoroughness of its high-incidence solid-wall design. The Bomarc radome faced, and is still facing, the necessity for attaining a precision in material uniformity and dimensional tolerance control which assumes almost fantastic proportions when viewed against current laminating standards. It was not until a novel post-fabrication adjustment of the radome by means of a localized insertion phase delay measurement and correction patching technique, that it became practical to produce these radomes with the desired precision (see Chapter 4, "Guidance and Fire Control System Radome Design"). To support the development of this radome, a number of special test and fabrication equipments were developed (see Chapter 11, "Radome Wall Measurements and Evaluations"). Precision, automatic recording, boresight error testing equipment[11] was developed and placed in operation in 1952. This was followed in 1953 by the placement in operation of fabrication and machining facilities for manufacturing precision, but as yet unadjusted, blank radomes. In 1955 came a precision microwave interferometer system[11] for measuring and recording, to high degrees of precision, variations in the radome wall insertion phase delay. This interferometer subsequently was supplemented by an automatic correcting machine,[11] which adds rectangular patches of dielectric tape material to the inner wall surface of the radome wherever the interferometer indicated the electrical thickness to be less then the desired value. It was found that, when adjusted to a given degree by this method, the boresighting error measured on the radome was assured to be within directional error tolerances. Through the use of automatic equipment, this procedure, complex as it is, still proved practical, and very well may be heralding a new trend in radome process control.

1-43. Investigation of Near Fields in Boresight Radome Design

In accordance with one of the recommendations of the Princeton Study Group in 1952, specific studies of the role of insertion phase delay in guidance and fire control radome designs were undertaken by both the Navy and the Air Force Radome Groups. Initially, most of the studies of phasing effects were conducted with manually operated equipment, but in 1954 both the Ohio State University Research Foundation and the Goodyear Aircraft Corporation Developed automatic test equipment[8] for measuring and recording the phase-front patterns of radar antennas, as perturbed by the radome. This equipment was of considerable aid in error investigation research.

1-44 Supersonic Rain Erosion Investigation

By the spring of 1953 the rain erosion problem again had become persistent. With the coming of supersonic flight, the rate of erosion for even neoprene-protected radomes had become critical. An urgent search for better means of protection and/or better basic radome materials had become mandatory. Under the sponsorship of Wright Air Development Center, the Convair Division of the General Dynamics Corporation at San Diego built and placed in operation a 20-millimeter ballistics test equipment and firing range for testing radome materials at speeds up to approximately Mach 2. This test facility and the program associated with it soon demonstrated that the usefulness of the neoprene coating was greatly impaired at these high speeds and that the usual plastic laminated radome materials were of only marginal usefulness. It was found, however, that adequate streamlining of the radome's shape, to incline the exposed surface at a shallow grazing angle to the droplet trajectories, markedly increased performance. (See Chapter 7 on Rain erosion problems for further details.)

1-45. The ONR Radome Symposium

It was apparent by early 1953 that a need existed for a general exchange on radome technology to stimulate development progress. In June of 1953, the Office of Naval Research sponsored a symposium on guided missile radomes at Washington.[10] This symposium gave a great deal of impetus to radome development efforts throughout both government and industry. The benefits derived from this meeting, particularly from the written proceedings issuing from it, proved conclusively the need for and the value of such meetings. These conclusions led to the initiation of the USAF sponsored Ohio State University Radome Symposium, discussed later in paragraph 1-54.

1-46. Radome Error Prediction

In 1954 and 1955 two USAF sponsored research and development contracts on boresighting error prediction were initiated for the monopulse and conical scan cases[8] at the Glenn L. Martin Company and Dalmo-Victor Corporation, respectively. These two programs are based upon the theory that it should be possible to calculate the error characteristics of a radome through use of modern high-speed electronic computers, if suitable near-field antenna aperture data can be measured and appropriate mathematical equations derived. Both programs are in the computation stage at this writing and hence cannot be assessed.

1-47. Error Correction by Empirical Means

Work on the USAF Falcon radome [8] by the Hughes Aircraft Corporation in 1955 demonstrated that if an initially uniform and symmetrical radome blank is first produced, its measured error characteristic can be corrected to tolerable performance limits by a systematic insertion of dielectric obstacles at carefully chosen stations on the inside surface of the radome. (See the material in Chapter 4 on Error guidance radomes for details.) This method provides an important means for designing and correcting radomes experimentally, regardless of the outcome of efforts at theoretical prediction of error. These obstacles also have been found useful for increasing the broadbanding characteristics of the radome.[11] (Early experimental work on the use of obstacle correction devices is also understood to have been done by both Goodyear Aircraft Corporation and Raytheon Manufacturing Company, but not reduced to a published systematic correction procedure for general use.)

1-48. Development of Ceramics for Radomes

Realizing that guided missiles would need radomes capable of operating at temperatures beyond the capabilities of plastic materials then available, the Air Force[8] and Navy,[10] in 1948, initiated work toward the development of ceramic materials and constructions. The Navy's work with Virginia Polytechnic Institute, was predominately on low density ceramic foams intended to be used ultimately as sandwich radome core material. The Air Force's work with the Stupakoff Ceramic Company concentrated both on low donsity core material and high-strength materials to be used ultimately as sandwich skins. Neither effort succeeded in producing immediately usable ceramic sandwich constructions. The Navy continued its efforts with VPI through the next several years. This resulted in adding a great deal more to the store of general knowledge of low density ceramic materials, but still no fully practical and usable construction resulted. Upon receipt of the recommendations contained in the Princeton study, the Bureau of Aeronautics, Navy Department,[10] initiated another development contract with Rutgers University for the development of solid-wall ceramic radomes and appropriate machining processes from which precision ceramic radomes could be produced. This latter program covered processes and materials for applying steatite ceramics to radomes. Slip-cast radomes are produced, which, in processing into precision finished radomes, are first dried, then bisque fired, and machined to finished contour and dimension. While further development is necessary to carry such constructions into general production use, the future prospects are very encouraging. A subsequent USAF program[8] on sandwich construction was initiated at the Ceramics Department of Engineering at the Ohio State University Experiment Station in June 1954. Although this program has succeeded in producing small radome-like shapes of ceramic "A"-sandwich construction, its product is far from practical at this time (1956).

1-49. Loaded Core Sandwiches

In recognition of the electrical advantages of the solid-wall, single-layer radome design, but seeking a lighter weight construction, the Boeing Airplane Company in 1952[8] investigated the possibilities of loading the lightweight foam core material of an "A" sandwich to match the dielectric properties of the structural skin of the sandwich. This ideally would produce a radome having the strength/weight ratio properties of "A"-sandwich construction, but having the electrical properties of the simpler solid-wall construction. Boeing reported on their findings in January 1953, and is understood to have filed a patent thereon. The McMillan Laboratories also devised a similar concept of loaded sandwich construction about 1953, and they, too, are understood to have applied for a patent. The difficulties with these early attempts at loading were that uniformity of dielectric constant throughout the body was below desirable limits and dielectric losses were rather high. Practical constructions did not become readily available for experimental use. The Air Force later sponsored some contract efforts to improve the uniformity and loss characteristics, through work at the Emerson & Cumming Company and the Goodyear Aircraft Corporation. It is understood that related work is under way at Lockheed Aircraft Corporation. Final results are not yet available for assessment of their ultimate practical value.

1-50. Radome Anti-Icing and De-Icing

Icing of radomes has long been a recognized problem, since accumulation of ice on the surface definitely upsets the otherwise carefully worked out electrical designs and results in severe pattern distortions, reflections, and losses. The undesirable effects of icing first came to attention in the case of shipborne radomes. Some early work on radome de-icing methods was carried out at Radiation Laboratory in late 1943 and reported in early 1944.[6] The degree to which icing is truly an important problem to airborne radomes is still somewhat obscure, not because of any doubts of its effects, but rather because of doubt that the full-time

compromises which attend provisions for its removal are warranted by the relatively few occasions of its encounter.

A number of different de-icing systems have been introduced into the radome field.[9] (See Chapter 6, on structural design.) The mechanical removal of ice with a rubber de-icing boot using pulsating air pressure to break up ice formations has been used with some success for lower frequency radars. A number of freezing-point depressant fluid type de-icing systems have been tried from time to time with moderate success. These systems generally utilize ethyleneglycol as the freezing-point depressant and removal agent. The ethyleneglycol is applied by spraying the radome surface during flight as necessary. The Northrop Aircraft Corporation, working on the F-89 radome, is believed to have been the first to develop this type of system, though Lockheed's work on the F-94 came about the same time. A third anti-icing and/or de-icing system has been used with similar degrees of success. In this method the sandwich radome wall is built with air ducts incorporated into the sandwich core material, through which high-temperature air is circulated to prevent or remove ice formations. North American Aviation, Inc., is believed to have been responsible for the initial successful pioneering of this method of radome ice control on its F-86D airplane. Figure 1-10 illustrates the construction of this early North American anti-icing radome. The Douglas Aircraft Company soon thereafter worked out a similar system, in which a fluted core construction, prepared by the lost wax process, considerably simplified the fabrication of the thermally de-iced radome. In this system, the core of the sandwich radome is made up of extruded wax strips wrapped with resin-impregnated glass-fabric tape, which is laid up in parallel array as core material and overlaid with a wet lay-up of the skin laminate. Upon curing of the laminating resin, the wax is melted out of the core, leaving continuous ducts for passing heated air through the core. (See Chapter 8, "Organic Materials and Radome Constructions.")

1-51. Large AEW Search Radomes

What is undoubtedly one of the largest airborne radomes thus far produced was built by the Lockheed Aircraft Corporation in 1953 for the Navy WV-2 aircraft[10] and for the similar USAF RC-121 aircraft.[8] This large radome is for AEW (Aircraft-Early-Warning) radar, and is intended for Continental Air Defense, to extend the coverage of the ground radar fence being installed around the perimeter of the North American continent. Two large 3-kilomegacycle blister radomes are installed on this Lockheed "Super Constellation," shown in Figure 1-12. The largest radome, on the belly of the aircraft, measures approximately 25 feet in length by 18 feet in width. The large radome hump on the top of the aircraft is that covering the height finder radar antenna. Other 10-kilomegacycle navigational radar equipment is installed in a smaller nose radome.

1-52. Artificial Dielectric Research

As a follow-up of another recommendation contained in the Princeton report of 1952, two research programs on artificial dielectrics were initiated by the Navy,[10] and a third by the USAF,[8] to seek an effective radome wall dielectric constant of unity. The Bjorksten Research Laboratory was the Navy contractor for investigating the embedding of metallic grids in the radome wall as a means of increasing the phase velocity through the wall. This was an attempt to neutralize the normal phase retarda-

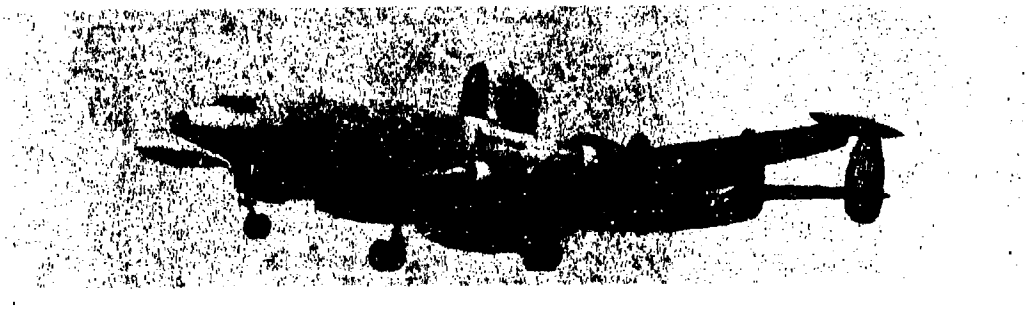


Figure 1-12. Aircraft-Early-Warning Radomes on an Air Force RC-121
(By permission of Lockheed Aircraft)

tion introduced by the dielectric constant of the material. The Bjorksten studies (1953-1954) demonstrated definite improvements for one of the two principal relative polarizations, but only limited gains for the orthogonal relative polarization. Nevertheless, the gains made were deemed sufficient to warrant further effort. A current follow-up contract initiated by the USAF in early 1956 with the Stanford Research Institute shows promise in approaching the solution to the remaining difficulties with the orthogonal polarization characteristic. The second related research project was a Navy sponsored Westinghouse study (1953-1954), in which efforts were made to neutralize the normal dielectric constant of the radome material by embedding oriented metallic dipoles in the form of tiny wire helices. This effort did not prove practical for general use, since tolerances on placement and orientation of the helix dipoles in three-dimensional array proved too difficult. The third effort, made by the USAF, was carried out through a contract (1953-1955) with the Laboratory for Insulation Research at Massachusetts Institute of Technology. This was a search for ferrite-type materials whose product of dielectric permittivity and magnetic permeability could be made equal to that of free space, and thereby make the propagation constant equal to that of space. This effort did not succeed in finding practical materials, since all those exhibiting desired values of the real part of the permittivity and permeability constant still exhibited too much absorption loss, and hence did not adequately produce the desired effect. This approach may warrant effort at a later period when ferrites have been developed further. These approaches, had they proved practical, would have subordinated the radome refraction effect by equating the propagation constant of radome wall to that of surrounding space, and would have permitted the designer to grade thickness to control reflections independently.

1-53. Recent Trends in Faired Radome Design

The trend, begun in 1945, to integrate the radome into the airframe design has continued ever since. Nearly all radomes in present day aircraft are faired-in flush with the aircraft skin, as illustrated in Figure 1-13. Further, a strong trend toward adding instrumentation booms and other accessories to the radome tip,[11] as illustrated in Figure 1-14, has complicated the radome problem in recent years.

1-54. Ohio State University Radome Symposia

After a 2-year gap following the ONR Radome Symposium in 1953, the USAF Wright Air Development Center undertook sponsorship of another radome symposium in June of 1955 with the Ohio State University Research Foundation as host.[8] The enthusiastic response to this symposium again clearly indicated the growing interest in the radome field, and the need for a continued interchange of technical information on radome development. As a result, a decision was reached to continue the program on a yearly basis, as long as the need remains. A second radome symposium was held at Ohio State

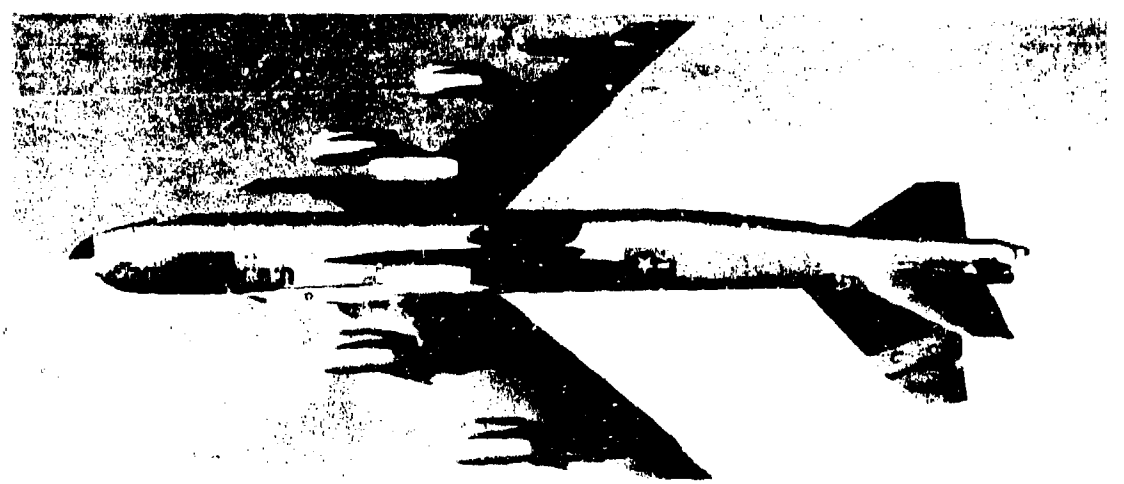


Figure 1-13. Boeing B-52 Heavy Bomber With Nose and Chin Radomes Flush-Faired into the Fuselage (Official Air Force photo)

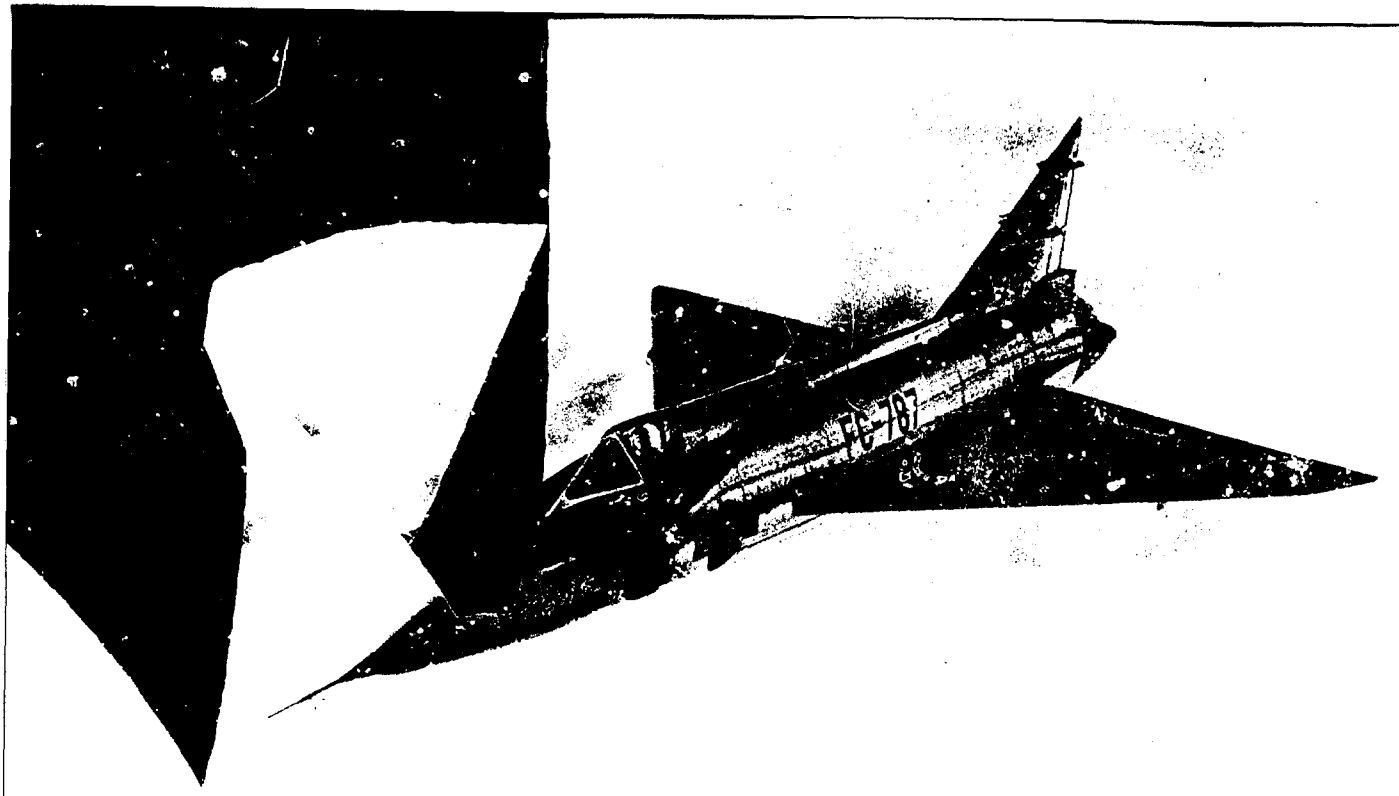


Figure 1–14. Convair F-102A Fighter, With Nose Fire Control Radome and Instrumentation Boom (Official Air Force photo)

University in June 1956. The reader is referred to the proceedings of these symposia to fill in the remainder of the historical development of the contemporary radome field

REFERENCES

1. Keto, J. Recollections of early radar history, 1956.
2. Baxter, J. P., III. Scientists Against Time. Little Brown and Co., Boston, 1952.
3. Eggleston, W. Scientists at War. Hunter Rose Co., Ltd., Canada 1950.
4. Holloway, F. L. Recollections of early radar history, 1956.
5. Radome Engineering Manual. AMC Manual 80-4, 1956.
6. McMillan, E. B. Personal notes on early radome history, 1956.
7. John, A. R. Recollections of early radome history, 1956.
8. WADC Radome Branch files, 1944-1956.
9. Behrens, F. H. The use of a Neoprene Cement Coating for the Protection of Laminated Aircraft Parts from Damage Due to Rain Erosion. Memorandum report MCREE 49-12, Wright Air Development Center, 1 Mar 1949.
10. Ambrogi, J. Personal notes on radome history, 1956.
11. Kofoid, M. J. Personal notes on radome history, 1956.

Best Available Copy

Chapter 2

ELECTROMAGNETIC FIELD AND OPTIC THEORY

by

Jack H. Richmond

Antenna Laboratory
Department Of Electrical Engineering
The Ohio State University
Columbus, Ohio

INDEX OF SYMBOLS

Notation. The following notation is employed in this chapter. Vector quantities are underlined, as $\underline{E}$. Complex quantities are dotted, as $\dot{T}$. Phase angles of complex quantities are primed, as T'. An asterisk indicates the conjugate quantity, as $E_\perp^*$. The conjugate of Ae^{jb}, for example, is Ae^{-jb} if A and b represent real numbers. A symbol neither dotted nor underlined indicates the absolute magnitude of the quantity. The subscript $_\perp$ indicates perpendicular polarization. The subscript $_\parallel$ indicates parallel polarization.

A	Aperture area, without radome
A	Aperture area, with radome
a	Distance from gimbal point to radome vertex
a	Semi-major axis of ellipse
b	Semi-minor axis of ellipse
C	Distance from base of radome to gimbal point
c	Caliber of ogive
d	Thickness
d_e	Electrical thickness (measured in wavelengths)
d_s	Skin thickness
d	As subscript, indicates "depolarized"
$\underline{E}$	Electric field intensity
$\underline{E}^i$	Incident field
$\underline{E}^s$	Scattered field
$\underline{E}^t$	Total field
$e^{j\omega t}$	Time variation factor
F	Fineness ratio
i	As subscript, indicates "incident"
$\underline{J}^s$	Current flowing in free space
J_1	First-order Bessel function
$\underline{H}$	Magnetic field intensity
ρ	Density (watts/area), without radome
ρ'	Density (watts/area), with radome
p_i	Distance from coordinate origin, along axis of propagation of incident wave
R	Radius of curvature of ogive
$\dot{R}_\perp$	Ratio of reflected and incident electric field intensities at dielectric surface
$R_\perp^2$	Power reflection coefficient
$R_\parallel^2$	Power reflection coefficient
R_B	Radius at base of radome
r	Axial ratio of polarization ellipse of incident wave
$r_\perp$	Reflection coefficient
$r_\parallel$	Reflection coefficient
$T_\perp$	Factor reducing amplitude of plane wave passing through plane sheet

INDEX OF SYMBOLS (cont)

$T_\perp^2$	Power transmission coefficient
$T_\parallel$	Factor reducing amplitude of plane wave passing through plane sheet
$T_\parallel^2$	Power transmission coefficient
t	Time
$t_\perp$	Interface transmission coefficient
$\tan \alpha$	Slope of conical section of conical radome fairing
β	Propagation constant of dielectric material
β_0	Free-space propagation constant
γ	Propagation constant
$\Delta_\perp$	Insertion phase delay
Δd	Amount by which sheet is uniformly too thick
$\Delta \epsilon_r$	Permissible tolerance (in dielectric constant)
δ_e	Electric loss tangent
δ_m	Magnetic loss tangent
ϵ	Dielectric constant
ϵ_c	Core rolative dielectric constant
ϵ_0	Dielectric constant of free space
ϵ_r	Relative dielectric constant
ϵ_s	Relative skin dielectric constant
ϵ_x	Dielectric constant of medium in x-polarized field
ϵ_y	Dielectric constant of mediuin in y-polarized field
ϵ_z	Dielectric constant of medium in z-polarized field
θ	Angle of incidence
θ_B	Brewster angle
θ_0	Angle of incidence at which perfect transmission will be obtained through a lossless sheet
θ_r	Angle of refraction
κ	Radius of curvature of rays
λ	Wavelength in dielectric material
λ_0	Wavelength in free space
μ	Permeability
μ_0	Permeability of free space
μ_r	Relative permeability
ξ	Polarizing angle between plane of incidence and major axis of polarization ellipse
σ	Conductivity of medium
ϕ	Far-field angle measured from antenna axis
ψ	Look angle
ω	Angular frequency

Chapter 2

ELECTROMAGNETIC FIELD AND OPTIC THEORY

SECTION A. THEORETICAL DESIGN OF THE HOMOGENEOUS FLAT SHEET

Many questions that arise in the design of radomes can be answered by reference to the theory of reflection and transmission of plane electromagnetic waves by infinite sheets of dielectric material. Indeed, plane-wave plane-sheet data are often employed in radome analysis to avoid the complexity of methods which apply more rigorously to curved radome shapes. To introduce radome terminology and some of the fundamental concepts, the equations for reflection at a dielectric interface will be derived. These equations will be followed by a brief analysis of transmission through plane homogeneous sheets and sandwiches, as well as of the effects of manufacturing tolerances in thickness and dielectric constant.

2-1. Interface Reflection Coefficients

Consider a plane wave impinging on the surface of an infinite dielectric medium, as indicated in Figure 2-1. Let the axis of propagation of the incident wave lie in the yz-plane and intersect the surface at an angle θ, measured from the surface normal. This angle is called the angle of incidence. All the space to the right of the xy-plane is filled with a dielectric material whose electrical properties are specified by its dielectric constant ϵ, permeability μ, and electric and magnetic loss tangents $\tan \delta_e$ and $\tan \delta_m$. For the present it is assumed that the material is lossless ($\tan \delta_e = 0$ and $\tan \delta_m = 0$). The region to the left of the xy-plane is free space that is lossless and has parameters ϵ_0 and μ_0.

The electric and magnetic field intensities $\underline{E}$ and $\underline{H}$ are vector quantities, having not only magnitudes (E and H) but also directions. In Figure 2-1 the incident electric field intensity, $\underline{E}_i$, is shown oriented in the x-direction. The orientation of the electric field intensity vector is described by the "polarization" of the field. It will be assumed that the direction of $\underline{E}_i$ does not vary with time; in other words, the incident wave is "linearly polarized." At any instant of time, the directions of the field intensity vectors of a plane wave have the following properties.

a. $\underline{E}$, $\underline{H}$ and the line of propagation are mutually perpendicular. Therefore, a plane wave is called a TEM wave (transverse electric magnetic).

b. $\underline{H}$ lies 90° clockwise from $\underline{E}$ from the viewpoint of an observer looking along the axis of propagation at the departing wave.

The field intensity vectors in Figure 2-1 are oriented in adherence to these rules.

The "plane of incidence" of the wave striking the dielectric interface is defined by the axis of propagation and the normal to the surface. Thus, in Figure 2-1, the plane of incidence is the yz-plane. Since $\underline{E}_i$ is perpendicular to the plane of incidence, the incident wave illustrated in Figure 2-1 is said to have "perpendicular polarization."

It is assumed that the incident wave is of a single frequency f, and that, therefore, the electric and magnetic field intensities vary sinusoidally at each point in space. A plane wave traveling through a lossless medium has uni-

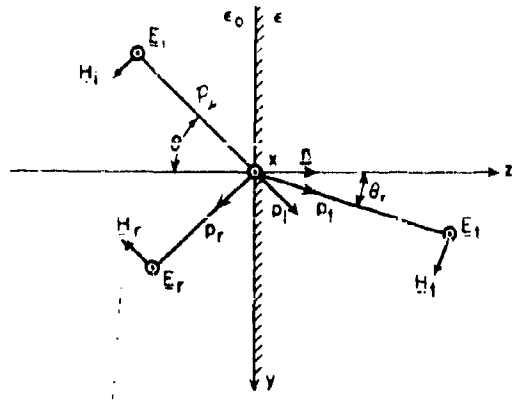


Figure 2-1. Plane-Wave Reflection and Transmission at a Dielectric Interface with Perpendicular Polarization

form amplitude at all points. Its phase is retarded by 360° for each wavelength the observer moves along the axis of propagation. The planes of constant phase are perpendicular to the axis of propagation. These statements are expressed more precisely by the following equation:

$$E_i = \cos(\omega t - \beta_0 p_i) \qquad (2\text{-}1)$$

where ω is $2\pi f$, the angular frequency;

t is time;

β_0 is $2\pi/\lambda_0$, the free-space propagation constant;

λ_0 is the wavelength in free space; and

p_i is distance from the coordinate origin, measured along the axis of propagation of the incident wave.

To facilitate mathematical derivations, Equation (2-1) is generally written as

$$E_i = e^{j(\omega t - \beta_0 p_i)} \qquad (2\text{-}2)$$

where j is $\sqrt{-1}$. In using this exponential form, it is understood that the value of E_i is given by the real part of the expression. With this understanding, Equations (2-1) and (2-2) agree. For brevity, the time-variation factor, $e^{j\omega t}$, will be omitted in what follows, as is customary.

From Figure 2-1,

$$p_i = z\cos\theta + y\sin\theta \qquad (2\text{-}3)$$

so that Equation (2-2) becomes

$$E_i = e^{-j\beta_0(z\cos\theta + y\sin\theta)} \qquad (2\text{-}4)$$

The magnetic field intensity is given by

$$H_i = \sqrt{\frac{\epsilon_0}{\mu_0}}\, E_i \qquad (2\text{-}5)$$

The corresponding expressions for the reflected wave shown in Figure 2-1 are

$$E_r = r_\perp e^{-j\beta_0 p_r} = r_\perp e^{-j\beta_0(-z\cos\theta + y\sin\theta)} \qquad (2\text{-}6)$$

and

$$H_r = \sqrt{\frac{\epsilon_0}{\mu_0}}\, E_r \qquad (2\text{-}7)$$

where $r_\perp$ is the interface reflection coefficient. From Equations (2-4) and (2-6) the interface reflection coefficient is defined by

$$r_\perp = \frac{E_r}{E_i} \qquad (2\text{-}8)$$

evaluated at the interface. Similarly, for the transmitted wave,

$$E_t = t_\perp e^{-j\beta p_t} = t_\perp e^{-j\beta(z\cos\theta_r + y\sin\theta_r)} \qquad (2\text{-}9)$$

and

$$H_t = \sqrt{\frac{\epsilon}{\mu}}\, E_t \qquad (2\text{-}10)$$

where θ_r is the angle of refraction;

$\beta = 2\pi/\lambda = \omega\sqrt{\mu\epsilon}$, the propagation constant of the dielectric material;

$\lambda = \dfrac{\lambda_0}{\sqrt{\epsilon_r}}$, the wavelength in the dielectric material;

$\epsilon_r = \epsilon/\epsilon_0$, the relative dielectric constant of the medium; and

$t_\perp$ is the interface transmission coefficient.

Thus

$$t_\perp = \frac{E_t}{E_i} \qquad (2\text{-}11)$$

evaluated at the dielectric interface.

It will be assumed that the dielectric material is nonmagnetic ($\mu = \mu_0$), which is essentially true of most dielectric materials. Magnetic materials are considered in Section E.

The reflection and transmission coefficients and the angle of refraction can now be determined by application of two boundary conditions:

a. The components of $\underline{E}$ tangential to the surface are continuous across the boundary.

b. The components of $\underline{H}$ tangential to the surface are continuous across the boundary.

The field in the free-space region in Figure 2-1 is composed of an incident wave plus a reflected wave, i.e.,

$$\underline{E} = \underline{E}_i + \underline{E}_r \tag{2-12}$$

Because $\underline{E}_i$ and $\underline{E}_r$ are parallel (Figure 2-1),

$$E = E_i + E_r \tag{2-13}$$

From Equations (2-4), (2-6) and (2-13), at the interface

$$E = (1 + r_\perp) e^{-j\beta_0 y \sin \theta} \tag{2-14}$$

The field in the dielectric-filled region in Figure 2-1 consists of just the transmitted wave, and at the surface it is, from Equation (2-9),

$$E_t = t_\perp e^{-j\beta y \sin \theta_r} \tag{2-15}$$

Equations (2-14) and (2-15) give the components of electric field intensity which are tangential to the dielectric interface on both sides of the boundary. The first boundary condition requires that these be equal:

$$(1 + r_\perp) e^{-j\beta_0 y \sin \theta} = t_\perp e^{-j\beta y \sin \theta_r} \tag{2-16}$$

Therefore,

$$\sin \theta_r = \frac{\sin \theta}{\sqrt{\epsilon_r}} \tag{2-17}$$

and

$$1 + r_\perp = t_\perp \tag{2-18}$$

Equation (2-17) is known as Snell's law. Equation (2-18) can also be derived from energy considerations, since the time-average power transmitted through a unit area of the dielectric surface must be the difference between the power incident on the area and the power reflected from the area.

The components of $\underline{H}_i$, $\underline{H}_r$, and $\underline{H}_t$ tangential to the interface are, from figure 2-1,

$$H_{iy} = H_i \cos \theta \tag{2-19}$$

$$H_{ry} = - H_r \cos \theta \tag{2-20}$$

$$H_{ty} = H_t \cos \theta_r \tag{2-21}$$

Application of the second boundary condition yields:

$$(1 - r_\perp) \sqrt{\epsilon_0} \cos \theta = t_\perp \sqrt{\epsilon} \cos \theta_r \tag{2-22}$$

From Equations (2-18) and (2-22) the desired expression for the reflection coefficient is obtained:

$$r_\perp = \frac{\cos \theta - \sqrt{\epsilon_r - \sin^2 \theta}}{\cos \theta + \sqrt{\epsilon_r - \sin^2 \theta}} \tag{2-23}$$

Figure 2-2 illustrates a dielectric interface with an incident wave polarized parallel to the plane of incidence. Since in this case the incident and reflected magnetic field intensities are parallel to each other and to the surface, it is convenient to define the reflection coefficient as

$$r_\parallel = \frac{H_r}{H_i} \tag{2-24}$$

evaluated at $z = 0$. Applying the boundary conditions as before, it is found that

$$r_\parallel = \frac{\epsilon_r \cos \theta - \sqrt{\epsilon_r - \sin^2 \theta}}{\epsilon_r \cos \theta + \sqrt{\epsilon_r - \sin^2 \theta}} \tag{2-25}$$

Equations (2-17) and (2-18) are also found to apply for parallel polarization, so that the angle of refraction is independent of polarization.

At normal incidence ($\theta = 0$), there is no distinction between parallel and perpendicular polarization and $r_\parallel$ and $r_\perp$ become equal in magnitude. They differ in sign at normal incidence only because $r_\perp$ was defined by Equation (2-8) as the ratio of reflected and incident electric field intensities, whereas $r_\parallel$ was defined by Equation (2-24) as the ratio of reflected and incident magnetic field intensities. At grazing incidence ($\theta = 90^\circ$), total reflection occurs for either polarization. At all other angles of incidence, $r_\parallel$ is smaller in magnitude than $r_\perp$.

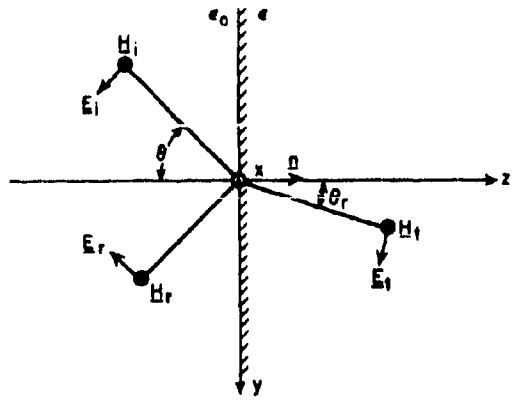


Figure 2-2. Plane-Wave Reflection and Transmission at a Dielectric Interface with Parallel Polarization

Tables of $r_{||}$, $r_{\perp}$, and θ_r for various dielectric constants and angles of incidence are given in References 1 and 2.

Figure 2-3 illustrates the interface reflection coefficients for various angles of incidence for a relative dielectric constant of 4. It will be noted that $r_{||}$ is zero at one angle of incidence. This is called the Brewster angle θ_B, and is given by

$$\tan \theta_B = \sqrt{\epsilon_r} \qquad (2\text{-}26)$$

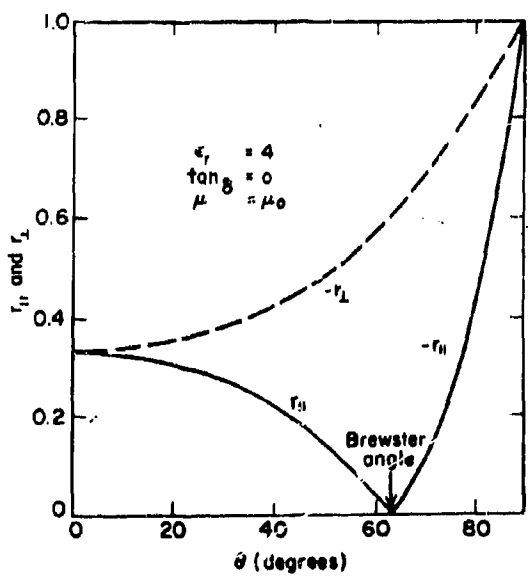


Figure 2-3. Interface Reflection Coefficients for Perpendicular and Parallel Polarization (From Reference 3 by Permission of McGraw-Hill Book Company, Inc.)

Figure 2-4 shows the angle of refraction as a function of angle of incidence for a relative dielectric constant of 4.

Lossy Materials. Thus far, only lossless dielectric materials have been considered. In lossy material the amplitude of a plane wave decreases exponentially with distance. The transmitted wave can be expressed as

$$E_t = t_{\perp} e^{az+by} \qquad (2\text{-}27)$$

The incident and reflected waves in the air region are again given by Equations (2-4) through (2-7). By applying the boundary condition on tangential $\underline{E}$, it is found that

$$t_{\perp} = 1 + r_{\perp} \qquad (2\text{-}28)$$

and

$$b = -j\beta_0 \sin \theta \qquad (2\text{-}29)$$

Now E_t must satisfy the wave equation, which can be written as follows if rectangular coordinates are used:

$$\nabla^2 \underline{E} = \gamma^2 \underline{E} \qquad (2\text{-}30)$$

where

$$\gamma = \sqrt{j\omega\mu(\sigma + j\omega\epsilon)} \qquad (2\text{-}31)$$

is the propagation constant and

$$\sigma = \omega\epsilon \tan \delta \qquad (2\text{-}32)$$

is the conductivity of the medium.

From Equations (2-27), (2-29), (2-30), (2-31), and (2-32),

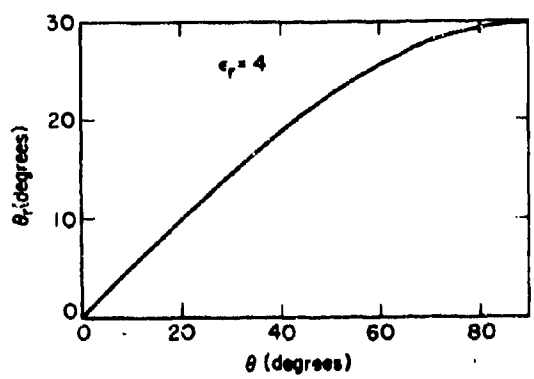


Figure 2-4. Angle of Refraction of Plane Wave Crossing a Dielectric Interface

$$a = -j\beta_0 \sqrt{\epsilon_r (1-j \tan \delta) - \sin^2 \theta} \quad (2\text{-}33)$$

Applying Maxwell's equation

$$\nabla \times \underline{E} = -j\omega\mu \underline{H} \quad (2\text{-}34)$$

it is found, from Equations (2-27) and (2-34) that the tangential component of the magnetic field intensity in the transmitted wave is

$$H_{ty} = \frac{jat_\perp e^{az+by}}{\omega\mu} \quad (2\text{-}35)$$

Finally, the reflection coefficient is determined by application of the boundary condition on tangential $\underline{H}$.

$$\dot{r}_\perp = \frac{\cos\theta - \sqrt{\epsilon_r (1-j \tan \delta) - \sin^2\theta}}{\cos\theta + \sqrt{\epsilon_r (1-j \tan \delta) - \sin^2\theta}} \quad (2\text{-}36)$$

For parallel polarization, the transmitted field is

$$H_t = t_\parallel e^{az+by} \quad (2\text{-}37)$$

where a and b are given by Equations (2-29) and (2-33) as before. The tangential component of transmitted electric field intensity is found from Equation (2-37) and

$$\nabla \times \underline{H} = (\sigma + j\omega\epsilon) \underline{E} \quad (2\text{-}38)$$

to be

$$E_{ty} = \frac{-at_\parallel e^{az+by}}{\sigma + j\omega\epsilon} \quad (2\text{-}39)$$

Thus, it is found that

$$\dot{r}_\parallel = \frac{\left\{ \epsilon_r (1 - j \tan \delta) \cos\theta - \sqrt{\epsilon_r (1 - j \tan \delta) - \sin^2 \theta} \right\}}{\left\{ \epsilon_r (1 - \tan \delta) \cos\theta + \sqrt{\epsilon_r (1 - j \tan \delta) - \sin^2 \theta} \right\}} \quad (2\text{-}40)$$

The reflection coefficients for lossy media are complex quantities, indicated by dots placed above the symbols, as in Equations (2-36) and (2-40). When the reflection coefficients are complex, this signifies that the incident and reflected waves are no longer in phase (or 180° out of phase) at the interface as they were in the lossless case.

It will be noted that the expressions for the reflection coefficients for lossy media differ from those for the lossless case only in that ϵ_r has been replaced with $\epsilon_r(1 - j \tan \delta)$.

For low-loss material, the interface reflection coefficients have practically the same absolute magnitudes as those for lossless material of the same dielectric constant. The phase of the reflected wave can, however, differ appreciably from what it is for a lossless medium.[3,4] Also, $r_\parallel$ does not quite vanish at the Brewster angle as it did in the lossless case. For low-loss material, it can be shown from Equations (2-29) and (2-33) that the angle of refraction is still given by Snell's law, given in Equation (2-17).

2-2. The Homogeneous Flat Sheet

Transmission and reflection by a plane dielectric sheet (also called a slab or a panel) can now be analyzed in terms of the interface reflection coefficients. The boundary conditions at the two parallel plane surfaces of a sheet can be satisfied if incident, reflected, and transmitted plane waves are assumed as in Figure 2-5. These waves are expressed by

$$E_i = e^{-j\beta_0 (z \cos\theta + y \sin\theta)} \quad \text{(in region I)} \quad (2\text{-}41)$$

$$E_r = \dot{R}_\perp e^{-j\beta_0 (-z \cos\theta + y \sin\theta)} \quad \text{(in region I)} \quad (2\text{-}42)$$

$$E_{2t} = \dot{T}_2 e^{-j\beta (z \cos\theta_r + y \sin\theta_r)} \quad \text{(in region II)} \quad (2\text{-}43)$$

$$E_{2r} = \dot{R}_2 e^{-j\beta (-z \cos\theta_r + y \sin\theta_r)} \quad \text{(in region II)} \quad (2\text{-}44)$$

$$E_t = \dot{T}_\perp e^{-j\beta_0 (z \cos\theta + y \sin\theta)} \quad \text{(in region III)} \quad (2\text{-}45)$$

The two plane waves in the dielectric sheet may be considered to be the resultant of multiple reflections at the two surfaces. By applying the boundary conditions at each surface, it is found that for a lossless sheet the complex reflection and transmission coefficients are

$$\dot{R}_\perp = \frac{r_\perp \left[1 - \exp\left(-2j\beta_0 d \sqrt{\epsilon_r - \sin^2\theta}\right) \right]}{1 - r_\perp^{*2} \exp\left(-2j\beta_0 d \sqrt{\epsilon_r - \sin^2\theta}\right)} \quad (2\text{-}46)$$

and

$$\dot{T}_\perp = \frac{(1-\dot{r}_\perp^2)\exp\left[-j\beta_0 d\left(\cos\theta - \sqrt{\epsilon_r - \sin^2\theta}\right)\right]}{1-\dot{r}_\perp^2 \exp\left(-2j\beta_0 d \sqrt{\epsilon_r - \sin^2\theta}\right)} \qquad (2\text{-}47)$$

where exp(x) is used to denote e^x.

The reflection and transmission coefficients for parallel polarization are obtained from Equations (2-46) and (2-47) merely by replacing the symbol $\perp$ with $\parallel$. The equations for lossy sheets are obtained from Equations (2-46) and (2-47) by replacing ϵ_r with $\epsilon_r(1-j\tan\delta)$ and by using the value of $\dot{r}_\perp$ or $\dot{r}_\parallel$ from Equation (2-36) or Equation (2-40).

It will be noted that $\dot{R}_\perp$ is the ratio of reflected and incident electric field intensities at the dielectric surface. $\dot{R}_\parallel$ is the ratio of reflected and incident magnetic field intensities at the surface. That is,

$$\dot{R}_\perp = \frac{E_r}{E_i}, \text{ at } z = 0 \qquad (2\text{-}48)$$

and

$$\dot{R}_\parallel = \frac{H_r}{H_i}, \text{ at } z = 0 \qquad (2\text{-}49)$$

Thus, $\dot{R}_\perp$ and $\dot{R}_\parallel$ have the same significance for dielectric sheets as $\dot{r}_\perp$ and $\dot{r}_\parallel$ have for dielectric media of infinite thickness; indeed, from Equation (2-46) it can be shown that $\dot{R}_\perp$ and $\dot{R}_\parallel$ became equal to $\dot{r}_\perp$ and $\dot{r}_\parallel$, respectively, as the thickness d becomes infinite, no matter how small the loss tangent may be.

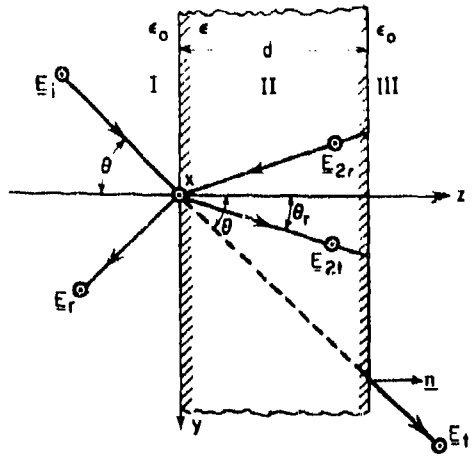


Figure 2-5. Transmission and Reflection By a Plane Dielectric Sheet for Perpendicular Polarization

The transmission coefficient $\dot{T}_\perp$ is defined as the ratio of the electric field intensity at any point in region III (Figure 2-5) in the presence of the sheet (with perpendicular polarization) to the electric field intensity at the same point in the absence of the sheet. Similarly, $\dot{T}_\parallel$ is the ratio of the magnetic field intensity transmitted through the sheet (with parallel polarization) to the magnetic field intensity which would exist at the same point if the sheet were removed. (However, since the incident and transmitted waves are traveling in the same medium and have the same axis of propagation, $E_t/E_i = H_t/H_i$ for either polarization.) Thus, the amplitude of a plane wave passing through a plane sheet is reduced by a factor $T_\perp$ or $T_\parallel$ due to reflection and absorption by the sheet.*

The power density in the wave passing through the sheet is reduced by a factor $T_\perp^2$ or $T_\parallel^2$, and these are called the "power transmission coefficients." Likewise, $R_\perp^2$ and $R_\parallel^2$ are the "power reflection coefficients."

Effect on Phase. In radome design it is necessary to know not only the power loss produced by a sheet but also the effect of the sheet on the phase of the transmitted wave. The phase of a plane wave transmitted through a plane sheet is advanced by an angle $T_\perp'$ or $T_\parallel'$ relative to the phase which the field would have at the same point in space if the sheet were removed. The insertion phase delay $\Delta_\perp$ or $\Delta_\parallel$ is, therefore,

$$\Delta_\perp = -T_\perp' \qquad (2\text{-}50)$$

or

$$\Delta_\parallel = -T_\parallel' \qquad (2\text{-}51)$$

The transmission coefficients are often defined in a different manner. The coefficients employed by various authors have the same absolute magnitude as that in Equation (2-47). However, the phase angles differ from that given by Equation (2-47) and are not equal to the insertion phase. A transmission coefficient essentially the same as that in Equation (2-47) is used in Reference 5, where it is called the "complex insertion transmission coefficient." This is quite appropriate and will serve to dis-

*The magnitude of a complex quantity is indicated by omission of the dot over the symbol.

tinguish this transmission coefficient from the "normal transmission coefficient" $\hat{T}$. According to the "normal convention" the phase of the wave emerging from the panel of Figure 2-5 is referred to the intersection of the z axis with the right face of the panel. The connection between $\hat{T}$ and T is expressed as

$$\hat{T} = Te^{-j\beta_0 d \cos\theta} \qquad (2\text{-}52)$$

$T_\perp$ and $T_\parallel$ become equal at normal incidence, and zero at grazing incidence. For any given sheet and given angle of incidence, the transmission coefficient for parallel polarization is equal to or greater than that for perpendicular polarization. (It was mentioned previously that $r_\parallel \leq r_\perp$.) For lossless sheets perfect transmission is obtained for parallel polarization at the Brewster angle.

Typical graphs of the transmission coefficients and insertion phase delay are given in Chapter 13. Graphs and tables of transmission coefficients, reflection coefficients, and insertion phase are given in References 6 through 16. Transmission through flat sheets is discussed in detail in References 3 and 17.

2-3. The Thin Homogeneous Flat Sheet

The electrical properties which are considered desirable in a flat sheet for radome construction include:

a. High transmission (T = 1);

b. Low reflection (R = 0);

c. Transmission independent of polarization ($T_\perp = T_\parallel$);

d. Insertion phase shift independent of polarization ($T'_\perp = T'_\parallel$);

e. Minimum refraction (Section H).

Furthermore, it is desired that the properties listed above be retained over a given range of frequencies, angles of incidence, and tolerances in thickness and dielectric constant. While these properties are always desirable, their relative importance is not the same for all radomes.

In principle, all of these properties can be obtained to any desired degree by using a sheet whose "electrical thickness" is sufficiently small. The electrical thickness d_e, or thickness measured in wavelengths, is given by*

$$d_e = \frac{d}{\lambda} = \frac{d\sqrt{\epsilon_r}}{\lambda_0} \qquad (2\text{-}53)$$

Thus, the electrical thickness depends on the physical thickness, the frequency, and the dielectric constant. Sheets which have an electrical thickness less than 0.1 have desirable properties, especially at low angles of incidence. Table 2-1 lists the thickness of $\lambda/10$ sheets for various frequencies.

Table 2-1. Thickness of $\lambda/10$ Sheets

f(mc)	thickness (inches) $\epsilon_r = 2$	$\epsilon_r = 4$
100	8.34	5.9
1,000	0.834	0.59
10,000	0.0834	0.059
50,000	0.0167	0.0118

It will be noted that the electrically thin sheet becomes excessively thin physically at the higher frequencies. Although satisfactory thin-wall radomes have been designed for 10,000 megacycles, it is doubtful that this structure can be utilized at significantly higher frequencies where strength is required.

For parallel polarization, the transmission coefficient of the thin sheet increases as the angle of incidence is increased, and reaches a maximum near the Brewster angle. However, the transmission coefficient for perpendicular polarization decreases and the difference in insertion phase shift for the two polarizations increases. It is found that good performance at high angles of incidence may require an electrical thickness of 0.01 or less. Some of these points are illustrated in Figures 2-6 and 2-7 which show the transmission coefficient and insertion phase delay for perpendicular polarization for sheets of electrical thickness 0.01 and 0.02.

*In the literature, the term "electrical thickness" is frequently used to refer to the quantity $d/\lambda_0\sqrt{\epsilon_r - \sin^2\theta}$. For normal incidence, this is the same as Equation (2-53).

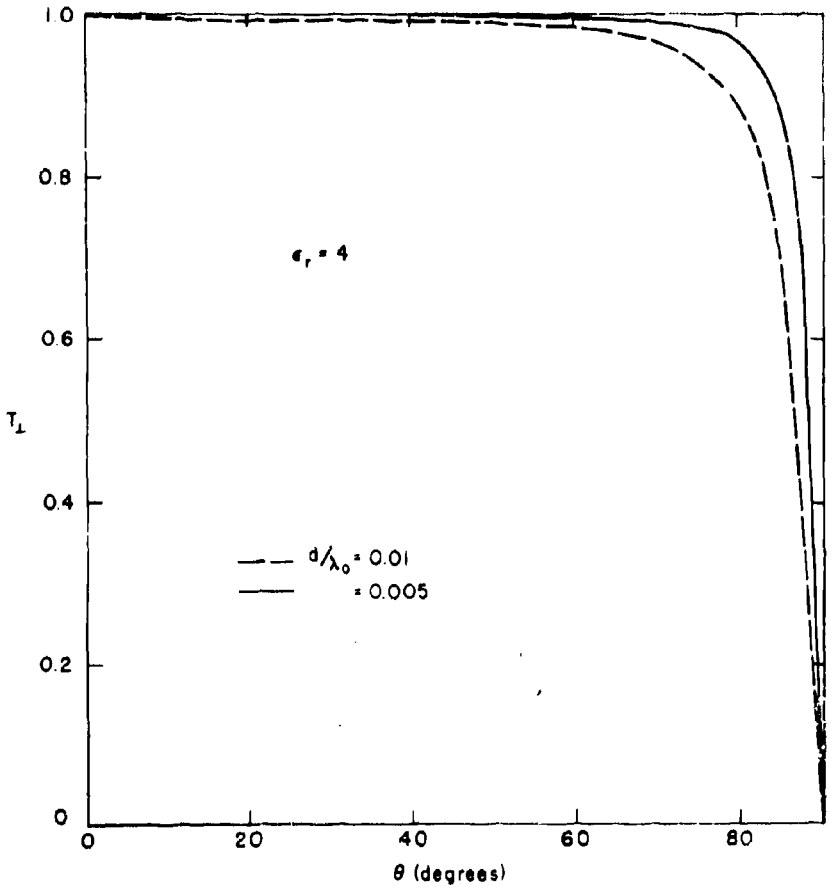


Figure 2–6. Transmission Coefficients of Lossless, Thin, Flat Sheets for Perpendicular Polarization

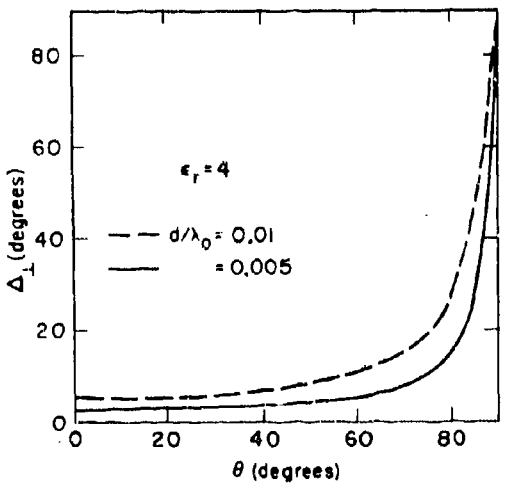


Figure 2–7. Insertion Phase Delay of Lossless, Thin, Flat Sheets

From Equation (2-47) the power transmission coefficient of a thin lossless sheet for perpendicular polarization is approximately

$$T_\perp^2 \approx 1 - \left[\frac{\pi d\,(\epsilon_r - 1)}{\lambda_0 \cos\theta}\right]^2 \qquad (2\text{-}54)$$

The difference in insertion phase shift for the two polarizations is approximately[4]

$$T_\parallel' - T_\perp' \approx \frac{\pi d\,(\epsilon_r - 1)^2}{\lambda_0\,\epsilon_r \cos\theta} \sin^2\theta \qquad (2\text{-}55)$$

When the thin wall is feasible, it offers the following advantages over other types.

a. Light weight.

b. Tolerances in thickness and dielectric constant are not critical providing the variations in

electrical thickness are not comparable to the design electrical thickness of the sheet. (See Figure 2-6 for example.)

c. High transmission is obtained even with relatively lossy materials.

d. The thin sheet is broadband since its performance is good at all frequencies below the design frequency.

e. The insertion phase shift is small and is relatively insensitive to change of polarization or angle of incidence.

f. Refraction is small (Section H).

The properties of thin sheets are discussed in Chapters 3 and 5 and in several references listed in the bibliography.

2-4. The Half-Wave Homogeneous Flat Sheet

From Equation (2-47), perfect transmission will be obtained through a lossless sheet at a given angle of incidence, θ_0 if the thickness is

$$d = \frac{n\lambda_0}{2\sqrt{\epsilon_r - \sin^2\theta_0}} \qquad (2\text{-}56)$$

where n is any positive integer. A sheet whose thickness is given by Equation (2-56) is referred to as a half-wave sheet of order n. The thin sheet can be considered as an approximation to a half-wave sheet of order zero. Both $T_\perp$ and $T_\parallel$ are unity for the half-wave lossless sheet at the design angle of incidence. Moreover, the insertion phase is the same for perpendicular and parallel polarization at the design angle of incidence, as is evident from Equation (2-47). Figure 2-8 shows the thickness of half-wave sheets of various dielectric constants versus the design angle of incidence. Figure 2-9 gives the transmission coefficients of a half-wave sheet which was designed for perfect transmission at 75° incidence. It will be noted that for parallel polarization the transmission is also perfect at the Brewster angle, and that everywhere $T_\parallel$ is equal to or greater than $T_\perp$. The insertion phase shift is plotted in Figure 2-10 for the same half-wave sheet, and it will be noted that the phase shift becomes independent of polarization at 75° incidence.

No choice of thickness will yield perfect transmission through a lossy sheet, but, if the loss tangent is small, maximum transmission is obtained at approximately the same thicknesses specified by Equation (2-56). The use of a lossy material in constructing a half-wave sheet will cause the maximum transmission coefficient to be somewhat less than unity. If the sheet is designed for normal incidence and if the loss tangent is small, the power transmission coefficient for normal incidence is approximately[3]

$$T^2 \approx 1 - \frac{n\pi(\epsilon_r + 1)\tan\delta}{2\sqrt{\epsilon_r}} \qquad (2\text{-}57)$$

For frequencies between 5 and 25 kilomegacycles (kmc), the thickness of the half-wave sheet of dielectric constant 4.0 ranges from approximately 0.6 to 0.12 inch. Therefore, half-wave walls are generally very rigid structures for the central band of microwave frequencies; in fact, their excellent structural strength and rigidity make them a suitable choice for many supersonic missile and aircraft applications. Another desirable feature of half-wave walls is their relative simplicity in terms of their electrical behavior. This is true primarily because the expression for the transmission coefficient of the half-wave wall is much less complex than that of a sandwich. While design computations for beam distortion can be cumbersome for a half-wave wall, the same computations for a sandwich are more so by a large factor.*

Although the half-wave sheet has excellent properties at the design angle of incidence, at other angles the transmission coefficients decrease and the insertion phase shifts, for the two polarizations become unequal. This problem is investigated in Reference 5, which discusses the choice of dielectric constant and the design angle θ_0 required to obtain the following electrical properties over a given range of incidence angles in the neighborhood of θ_0:

a. Minimum reflection $R_\perp$;

b. Insertion phase shift $T'_\perp$ or $T'_\parallel$ as nearly independent of angle of incidence as possible; and

c. Minimum differential phase shift $|T'_\perp - T'_\parallel|$.

It is shown[5] that the worst dielectric constant for achieving the above properties varies from 3 to 5 (depending on which criterion is used) for a normal incidence design, down to 1 or 2 for grazing incidence design. Thus, by any of the above criteria, the more desirable behavior is obtained by choosing ϵ_r near unity or ϵ_r very large, and, as the case may be, either the closer to unity or the larger, the better. For a

*This paragraph contributed by W. E. L. Boyce and E. O. Hartig, Goodyear Aircraft Corp.

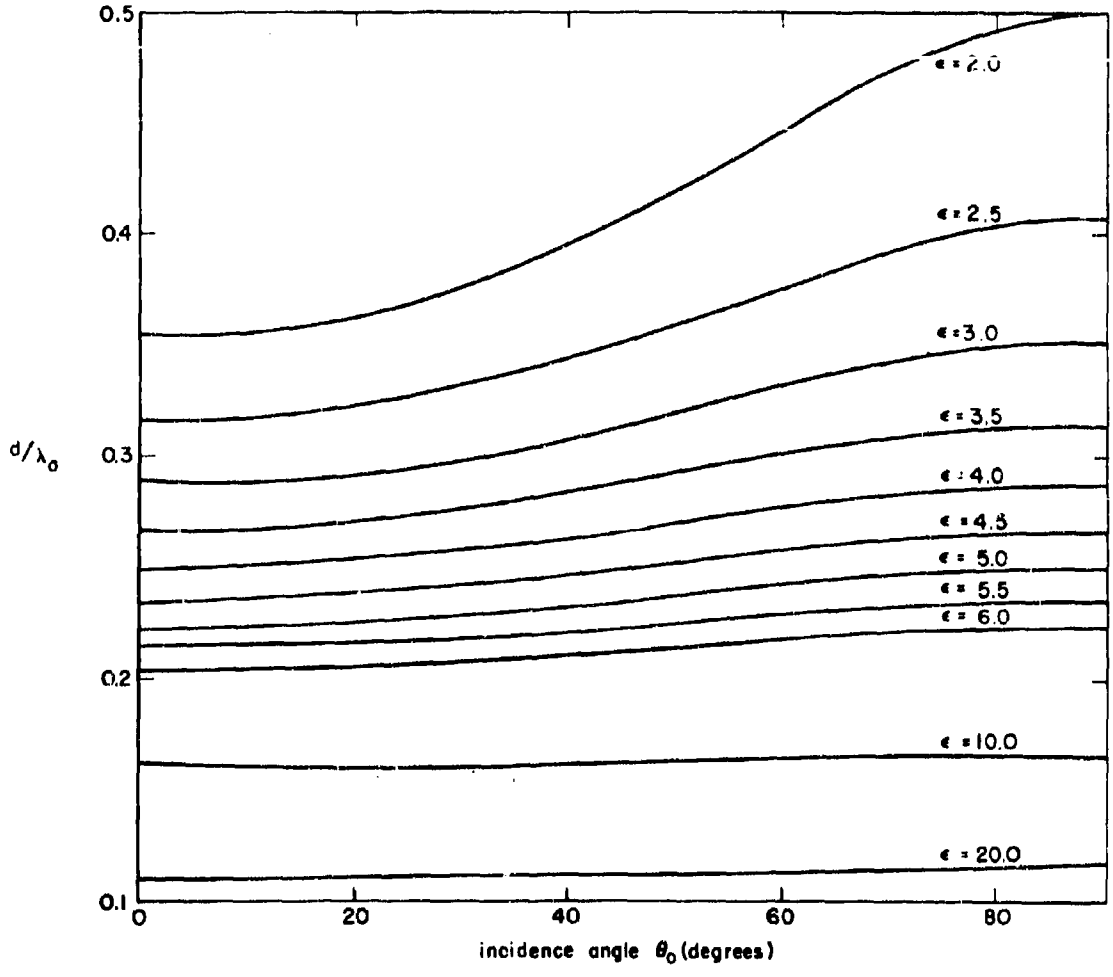


Figure 2-8. Design Thickness for First-Order, Half-Wave, Homogeneous Flat Sheet (From Reference 18 by permission of McMillan Laboratory, Inc.)

radome designed for high incidence angles the "good" range of ϵ_r is quite small, vanishing entirely as grazing incidence is approached. For large ϵ_r, tolerances play a dominant role. (See Section C.) Slight changes in dielectric constant or thickness may induce tremendous changes in the electrical properties. As the tolerances (in dielectric constant, thickness, loss tangent, and frequency) decrease, the optimum ϵ_r increases and the electrical properties improve. In the extreme of zero tolerances the optimum dielectric constant becomes infinite and perfect electrical behavior is indicated.

In practice the theoretical advantages of a low dielectric constant are difficult to realize, with the exceptions of broadband performance and larger permissible tolerances. Materials having a dielectric constant less than 1.5 are generally unsatisfactory for solid wall radome construction because of low strength or poor thermal resistance. Even artificial dielectrics, which can combine good mechanical and thermal properties with a very low dielectric constant, have not yielded a substantial improvement in the performance of high-incidence radomes.[17] Materials having a dielectric constant as high as 10 are available with low loss tangent and other properties suitable for radome construction. It is interesting to compare the properties of solid sheets of dielectric constant 2, 4, 6, and 9 for a given design angle (say 80°) and loss

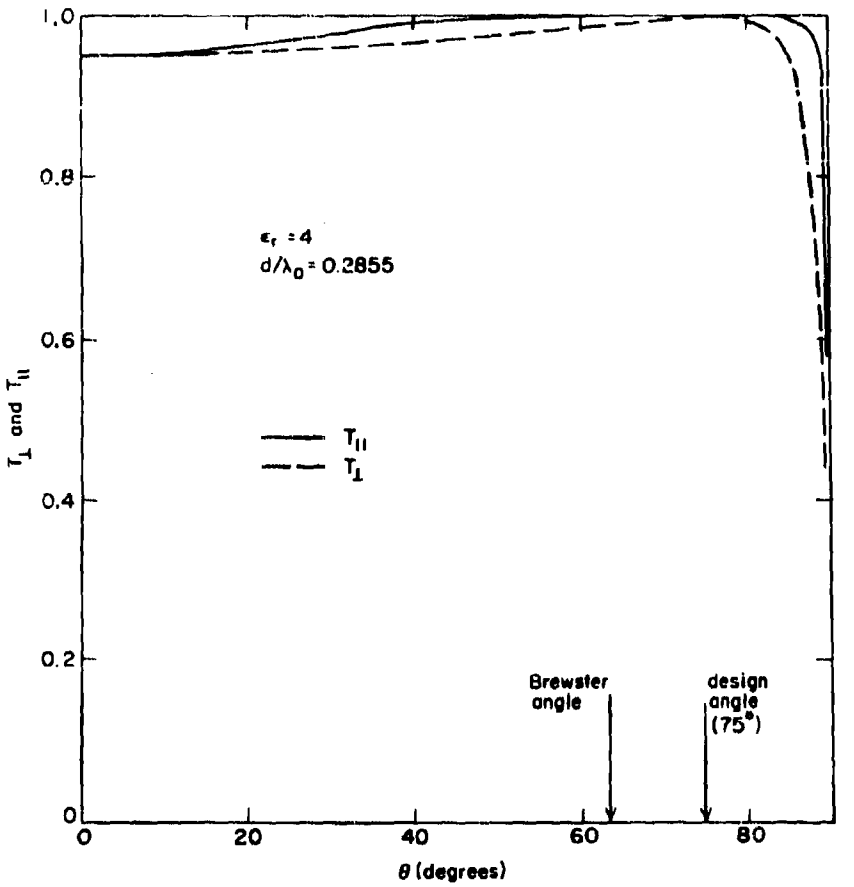


Figure 2–9. Transmission Coefficients of Lossless, First–Order, Half–Wave, Homogeneous Flat Sheet

tangent (say 0.01) plotted versus angle of incidence, as in Reference 10. No improvement is obtained in the differential phase shift nor in the power transmission coefficients by use of a high dielectric constant up to 9. In fact, at 80° incidence $T_\perp^2$ gets worse at the higher dielectric constants; however, the insertion phase shift for parallel or perpendicular polarization varies less rapidly with incidence angle as the dielectric constant is increased.

Graphs of transmission coefficients and insertion phase delay of homogeneous flat sheets are given in Chapter 13. Graphs and tables of transmission coefficients, reflection coefficients and insertion phase are given in References 6 through 16. The properties of half-wave sheets are discussed in Chapter 3 and in several references listed in the bibliography. Additional material on the subject will be found in Sections C, H, and K of this chapter.

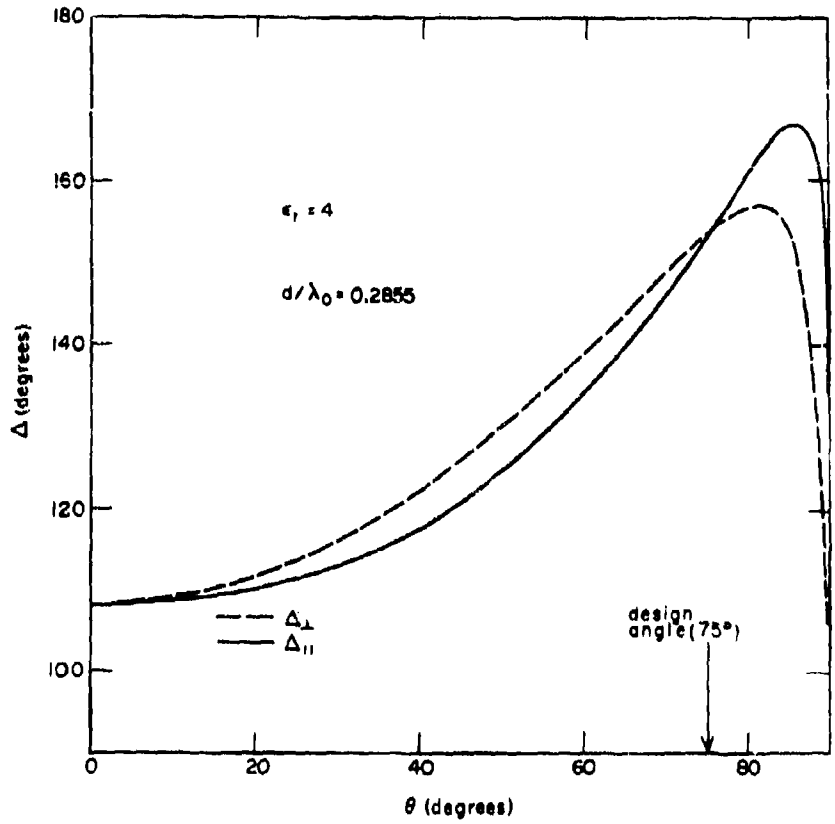


Figure 2-10. Insertion Phase Delay of Lossless, First-Order, Half-Wave, Homogeneous Flat Sheet

SECTION B. THEORETICAL DESIGN OF FLAT SANDWICHES

2-5. Coefficients for Multilayer Panels*

Formulas. If we wish to calculate the transmission and reflection coefficients for two or more plane homogeneous panels in tandem, a reiteration of the procedure followed to derive Equations (2-46) and (2-47) may be used. Consider a plane wave in medium 1 (Figure 2-11) incident on a flat sheet of material 2 and thence into medium 3 which extends to infinity. With the understanding that all coefficients may refer either to $\perp$ or $\parallel$ polarizations, we may write general expressions similar to Equations (2-46) and (2-47):

$$\dot{R}_{13} = \dot{r}_{12} + \frac{\dot{t}_{12}\,\dot{t}_{21}\,\dot{r}_{23}\,e^{2\gamma_2 d_2}}{1 - \dot{r}_{21}\,\dot{r}_{23}\,e^{2\gamma_2 d_2}} \qquad (2\text{-}58)$$

$$\dot{R}_{31} = \dot{r}_{32} + \frac{\dot{t}_{32}\,\dot{t}_{23}\,\dot{r}_{21}\,e^{2\gamma_2 d_2}}{1 - \dot{r}_{21}\,\dot{r}_{23}\,e^{2\gamma_2 d_2}} \qquad (2\text{-}59)$$

and

$$\hat{T}_{13} = \frac{\dot{t}_{12}\,\dot{t}_{23}\,e^{\gamma_2 d_2}}{1 - \dot{r}_{21}\,\dot{r}_{23}\,e^{2\gamma_2 d_2}} \qquad (2\text{-}60)$$

*Contributed by Robert E. Webster, The Ohio State University, Columbus, Ohio.

where $\dot{R}_{13}$ = total reflection coefficient of incident wave;

$\dot{R}_{31}$ = reflection coefficient of a wave incident on the panel from medium 3, with angle of incidence θ_3;

$\hat{T}_{13}$ = total transmission coefficient for the panel (from the left side of the 1-2 interface to the right side of the 2-3 interface) with phase reference taken according to the "normal convention," Equation (2-52).

and

$$\gamma_2 = -j\beta_0 \sqrt{\epsilon_2 (1 - j \tan \delta_2) - \sin^2 \theta_2} \quad (2\text{-}61)$$

The dielectric constants of medium 2 and medium 3 relative to that of medium 1 are denoted ϵ_2 and ϵ_3. The angles of propagation in regions 1, 2, and 3 are denoted by θ, θ_2, and θ_3, and are related by

$$\sin \theta_2 = \frac{\sin \theta}{\sqrt{\epsilon_2}} \quad (2\text{-}62)$$

and

$$\sin \theta_3 = \frac{\sin \theta}{\sqrt{\epsilon_3}} \quad (2\text{-}63)$$

The interface reflection coefficient $\dot{r}_{12}$ is given by Equations (2-36) and (2-40) for perpendicular and parallel polarization, after replacing δ by δ_2 and ϵ_r by ϵ_2 in these equations. Furthermore, $\dot{r}_{21} = -\dot{r}_{12}$ and $\dot{r}_{32} = -\dot{r}_{23}$. For perpendicular polarization,

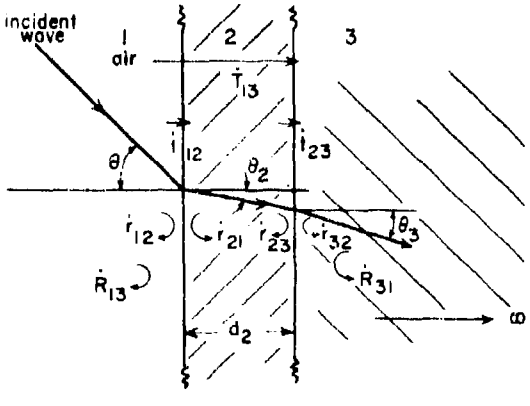


Figure 2-11. Plane Wave Crossing Two Interfaces

$$\dot{r}_{23} = \frac{\left\{ \sqrt{\epsilon_2 (1 - j \tan \delta_2) - \sin^2 \theta} - \sqrt{\epsilon_3 (1 - j \tan \delta_3) - \sin^2 \theta} \right\}}{\left\{ \sqrt{\epsilon_2 (1 - j \tan \delta_2) - \sin^2 \theta} + \sqrt{\epsilon_3 (1 - j \tan \delta_3) - \sin^2 \theta} \right\}} \quad (2\text{-}64)$$

and, for parallel polarization,

$$\dot{r}_{23} = \frac{\left\{ \epsilon_3 (1 - j \tan \delta_3) \sqrt{\epsilon_2 (1 - j \tan \delta_2) - \sin^2 \theta} - \epsilon_2 (1 - j \tan \delta_2) \sqrt{\epsilon_3 (1 - j \tan \delta_3) - \sin^2 \theta} \right\}}{\left\{ \epsilon_3 (1 - j \tan \delta_3) \sqrt{\epsilon_2 (1 - j \tan \delta_2) - \sin^2 \theta} + \epsilon_2 (1 - j \tan \delta_2) \sqrt{\epsilon_3 (1 - j \tan \delta_3) - \sin^2 \theta} \right\}} \quad (2\text{-}65)$$

The interface transmission coefficients are given by $t_{12} = 1 + r_{12}$, $t_{21} = 1 - r_{12}$, $t_{23} = 1 + r_{23}$ and $t_{32} = 1 - r_{23}$. If medium 3 were identical to medium 1, Equations (2-58) and (2-60) would reduce (with the exception of the insertion-phase factor $e^{j\beta_0 d \cos \theta}$ to Equations (2-46) and (2-47), the coefficients for a single-layer panel.

Now suppose medium 3 to be replaced by a region of free space followed by another panel which in turn is followed by an infinite half-space, as in Figure 2-12. A total transmission coefficient $\hat{T}_{15}$ of the same form as Equation (2-60) may be written as

$$\hat{T}_{15} = \frac{\hat{T}_{13} \hat{T}_{35} e^{-\gamma_3 d_3}}{1 - \dot{R}_{31} \dot{R}_{35} e^{-2\gamma_3 d_3}} \quad (2\text{-}66)$$

Where the interface coefficients have been replaced by the corresponding coefficients appropriate to the two panels of materials 2 and 4. Letting $d_3 \to 0$, we obtain the transmission coefficient for a two-layer panel from Equation (2-66):

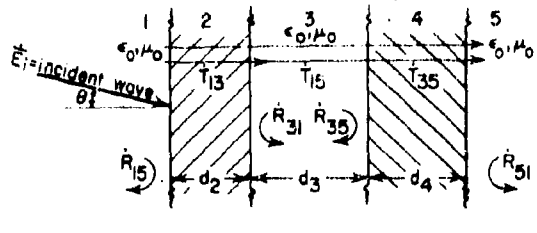


Figure 2-12. Transmission Through Two Panels

$$\hat{T}_{15}\Big]_{d_3 = 0} = \frac{\hat{T}_{13}\,\hat{T}_{35}}{1 - \dot{R}_{31}\,\dot{R}_{35}} \qquad (2\text{-}67)$$

Expressions for $\dot{R}_{15}$ and $\dot{R}_{51}$ maybe obtained similarly, and their form is that of Equations (2-58) and (2-59). Having evaluated $\hat{T}_{15}$, $\dot{R}_{15}$, and $\dot{R}_{51}$, we may add another layer in the same manner; and so on, for as many layers as desired. The calculation for the n^{th} layer requires a knowledge of the coefficients obtained after addition of the $(n-1)^{th}$ panel ($\hat{T}_{1n} = \hat{T}_{n1}$, $\dot{R}_{1n}$, and $\dot{R}_{n1}$) and calculations of the new coefficients $\hat{T}_{(n-1)(n+1)}$, $\dot{R}_{(n-1)(n+1)}$, and $\dot{R}_{(n+1)(n-1)}$ for the additional panel. The n subscripts refer to the layer numbers (see Figure 2-13), 1n meaning from the left side of the first layer to the right side of the (n-1), n interface (first subscript < second subscript); but n1 meaning from the right side of the (n— 1), n interface to the left side of the first layer (first subscript > second subscript). All coefficients are calculated, of course, with assumed free space on either side of the layer (or layers) in question. The expressions for the total transmission and reflection coefficients, after addition of the n^{th} layer, become

$$\hat{T}_{1(n+1)} = \frac{\hat{T}_{1n}\,\hat{T}_{(n-1)(n+1)}}{1 - \dot{R}_{n1}\,\dot{R}_{(n-1)(n+1)}} = \hat{T}_{(n+1)1} \qquad (2\text{-}68)$$

$$\dot{R}_{1(n+1)} = \dot{R}_{1n} + \frac{\hat{T}_{1n}^{\,2}\,\dot{R}_{(n-1)(n+1)}}{1 - \dot{R}_{n1}\,\dot{R}_{(n-1)(n+1)}} \qquad (2\text{-}69)$$

$$\dot{R}_{(n+1)1} = \dot{R}_{(n+1)(n-1)} + \frac{\hat{T}^2_{(n+1)(n-1)}\,\dot{R}_{n1}}{1 - \dot{R}_{n1}\,\dot{R}_{(n-1)(n+1)}} \qquad (2\text{-}70)$$

Matrix Formulation. The reiteration procedures described by Equations (2-68), (2-69), and (2-70) can be set up as a series of matrix multiplications. The formulation for any number of tandem panels is then systematic and compact. The formulation given here will use scattering matrices as described by Speer and Sisson.[80]

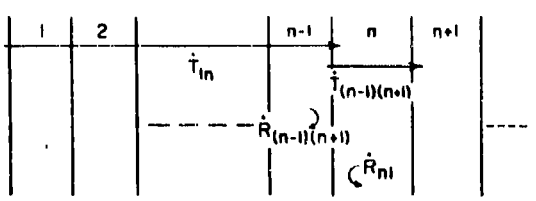


Figure 2-13. A Multilayer Panel

Consider an interface between two semi-infinite media, as in Figure 2-14. Assume plane waves traveling toward and away from the interface in both media, and denote these as A, D, B, C. By application of the boundary conditions it can be shown that the linear relation between the waves is given by

$$\begin{bmatrix} C \\ D \end{bmatrix} = \begin{bmatrix} \dfrac{1}{1 - \dot{r}_{12}} & \dfrac{-\dot{r}_{12}}{1 - \dot{r}_{12}} \\ \dfrac{-\dot{r}_{12}}{1 - \dot{r}_{12}} & \dfrac{1}{1 - \dot{r}_{12}} \end{bmatrix} \begin{bmatrix} A \\ B \end{bmatrix} \qquad (2\text{-}71)$$

Next consider waves in a homogeneous medium, referred to two parallel imaginary planes separated a distance d, as in Figure 2-15. The two sets of waves are then related linearly as

$$\begin{bmatrix} C \\ D \end{bmatrix} = \begin{bmatrix} e^{\gamma_n d} & 0 \\ 0 & e^{-\gamma_n d} \end{bmatrix} \begin{bmatrix} A \\ B \end{bmatrix} \qquad (2\text{-}72)$$

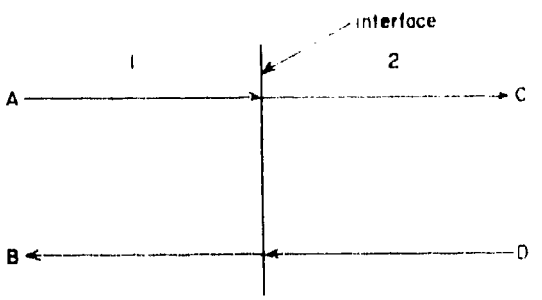


Figure 2-14. Incident and Reflected Waves at an Interface

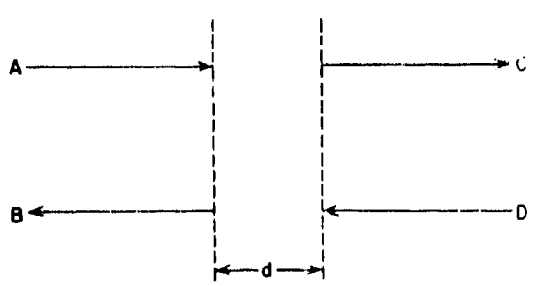


Figure 2-15. Incident and Reflected Waves Referred to Two Planes in a Homogeneous Medium

Equations (2-71) and (2-72) thus define an interface matrix and a position matrix. Now assume a multilayer sandwich panel, for example, the four-layer structure of Figure 2-16, which contains five interfaces and four panel thicknesses to be traversed. The interfaces are numbered 1, 3, 5, 7, and 9, and the thicknesses are 2, 4, 6, 8. With each interface and thickness we associate matrices M_1, M_2, . . . M_9, defined by Equations (2-71)(2-72),and write

$$\begin{bmatrix} G \\ H \end{bmatrix} = M_0 \begin{bmatrix} E \\ F \end{bmatrix} \qquad (2\text{-}73)$$

where

$$M_0 = \begin{bmatrix} \dot{m}_{11} & \dot{m}_{12} \\ \dot{m}_{21} & \dot{m}_{22} \end{bmatrix} = M_9 M_8 M_7 M_6 M_5 M_4 M_3 M_2 M_1 \qquad (2\text{-}74)$$

Then if H = 0 and E = 1, G = $\hat{T}$ and F = $\hat{R}$, for a wave incident on the left side of the sandwich. Equation (2-73) thus yields transmission and reflection coefficients for the four-layer panel. This matrix formulation is simple, systematic, and easy to program and check on a high-speed computer.

2-6. The "A" Sandwich*

The "A" Sandwich consists of two "skins" spaced by a "core" as in Figure 2-17, the core having a lower dielectric constant than the skins. The "A" sandwich was developed to obtain an increased strength-to-weight ratio as compared with the solid half-wave wall. In many cases where a thin wall is not sufficient structurally, and where a half-wave wall is too heavy, an "A" sandwich is used. The most widely used sandwich for search radomes is the "A" sandwich. The skins usually consist of high dielectric constant, high strength, relatively heavy materials. Low density foam materials or glass fiber honeycomb are used as a core material to obtain a low dielectric constant and light weight.

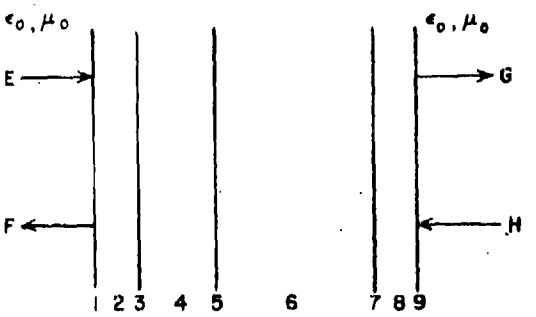


Figure 2-16. "A" Sandwich as Analyzed in Terms of its Interface and Position Matrices

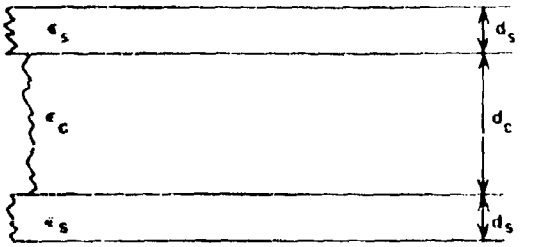


Figure 2-17. Symmetrical "A" or "B" Sandwich

The design of an "A" sandwich often proceeds as follows:

a. A skin material is chosen on the basis of its mechanical and thermal properties, as well as its dielectric constant and loss tangent.

b. The skin thickness is chosen in such a way as to provide sufficient strength without excessive weight.

c. The angles of incidence to be encountered in the radome are found from a knowledge of the radome shape and the location of the gimbal point, using formulas such as are given in Section G.

d. Sandwich transmission and phase delay curves (or contours such as shown in Figures 2-18, 2-19, 2-20, and 2-21) are used to select a core thickness which will provide good electrical performance over the given range of incidence angles for parallel and perpendicular polarization.

A Lossless "A" sandwich will give 100 percent transmission at design angle of incidence θ_0 if the core thickness d_c is given by:[27]

$$d_c = \frac{\lambda_0}{2\pi\sqrt{\epsilon_c - \sin^2\theta_0}} \left[n\pi - \tan^{-1} \frac{-r_s (1 - r_{sc}^2) \sin 2\phi_s}{-\left[r_{sc} (1 + r_s^2) + r_s (1 + r_{sc}^2) \cos 2\phi_s \right]} \right] \qquad (2\text{-}75)$$

*This section includes contributions from W. E. L. Boyce and E. O. Hartig of Goodyear Aircraft Corporation, and W. F. Croswell of Ohio State University (formerly Wright Air Development Center).

where

$$2\psi_s = \frac{4\pi d_s}{\lambda_0} \sqrt{\epsilon_s - \sin^2 \theta_0} \qquad (2\text{-}76)$$

The interface reflection coefficient r_s is given by Equations (2-23) and (2-25) for perpendicular and parallel polarization (replace ϵ_r by ϵ_s). Also, r_{sc} is given by Equations (2-64) and (2-65) (replace subscripts 2 and 3 by s and c).

Unlike the half-wave solid sheet, an "A" sandwich designed for maximum transmission at a particular angle of incidence for perpendicular polarization will not have maximum transmission for parallel polarization at the same angle. Furthermore, the "A" sandwich does not have the same insertion phase shift for the two polarizations at the angle of incidence for which its transmission coefficient is maximum, as does the solid sheet.

At first sight, it might seem reasonable to choose the core thickness which will provide maximum transmission at the highest angle of incidence to be encountered, using Equation (2-75) for perpendicular polarization. It is apparent in Figure 2-18, however, that such a design may result in poor transmission at lower angles of incidence. Thus, if Equation (2-75) is used to select the core thickness, care must be taken in choosing the design angle of incidence θ_0, and the design should be checked by computing the transmission which will be obtained for both polarizations over the required range of incidence angles.

Good transmission can be obtained by tapering the core thickness in accordance with the angle of incidence which will be encountered at each point on the radome wall. As seen in Figure 2-18 for perpendicular polarization, high transmission throughout the incidence angle range can be obtained in this manner.

However, comparison of Figures 2-18 and 2-19 shows that no matter what core thickness taper is used either $T_\perp$ or $T_\parallel$ will decrease rapidly at angles above the Brewster angle. As a result, the "A" sandwich is most useful at incidence angles below 74 to 80°. In fact, one of the principal disadvantages of the "A" sandwich is the sensitivity of its electrical characteristics to changes in polarization, particularly at high incidence angles. The transmission coefficient may vary from near 100 percent for perpendicular polarization down to 50 percent for parallel polarization.

It appears that excellent properties could be obtained by tapering both the core thickness and the core dielectric constant in accordance with the angle of incidence at each point of the radome wall. By this means it should be possible to obtain maximum transmission and constant insertion phase delay at each point. The dielectric constant could be tapered by varying the density of the foam material used as the core.

For radome designs where the variation of insertion phase delay is important, contour graphs such as Figure 2-18 are particularly useful. This graph shows that the constant insertion phase delay curves are nearly orthogonal to the constant transmission curves. This means that for sandwich radomes with fairly thin skins, a core taper for constant insertion phase shift will be inconsistent with the requirements for high transmission. However, Figures 2-20 and 2-21 show that up to 70° incidence a very low phase variation can be obtained by the use of thick skins and an increase of the dielectric constant of the skin. Since the thickness of the skin can be held to very close tolerances, the sandwich represented by these figures could be practical.

The previous discussion has been limited to the consideration of symmetrical "A" sandwiches. Now consider an "A" sandwich having skins of unequal thickness. In this case it is not possible to obtain perfect transmission for perpendicular polarization if the two skin dielectric constants are the same.[19] As a result, the use of this particular construction has been limited. Since the unsymmetrical "A" sandwich would be useful where it is desired to strengthen the outside skin to resist rain erosion, more analysis of this construction should be made. Under certain conditions, perfect transmission can be obtained in a lossless nonsymmetrical "A" sandwich if the skins differ both in thickness and dielectric constant.

A sandwich which has been introduced recently uses a foam core which is loaded with metallic particles to make the core dielectric constant equal to that of the skin. This construction combines the electrical properties of the solid half-wave wall with the physical properties of the sandwich.[78]

The lossless "A" sandwich can be designed for perfect transmission at two angles of incidence, but this requires thick skins.[13, 19] To explain how this is possible, assume that the core material is air and that each skin is a half-wave sheet with design angle θ_0; the sandwich will then give perfect transmission at angle of incidence θ_0, no matter what the core thickness is. At other angles of incidence some

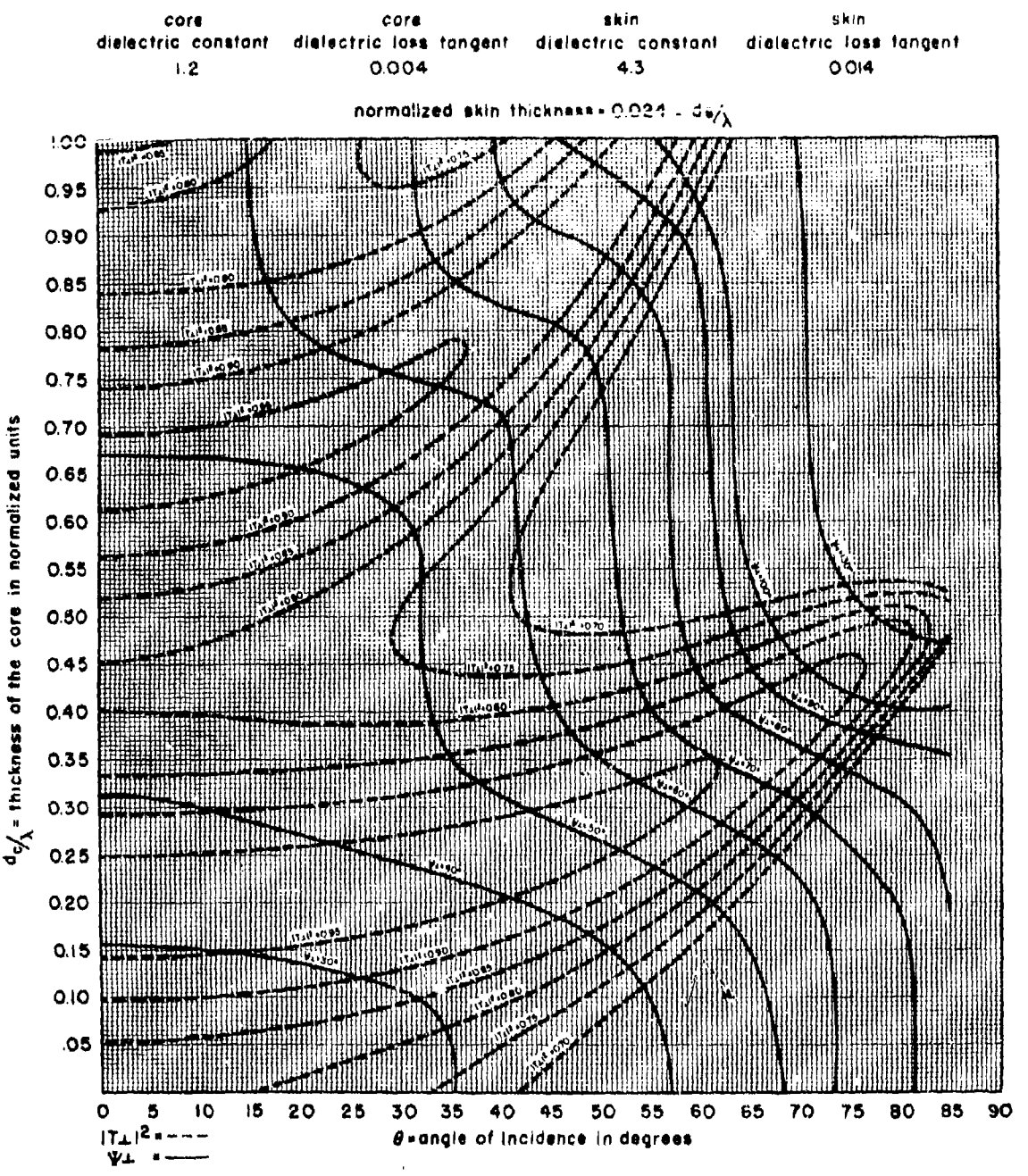


Figure 2-18. Transmission and Phase Delay Contours for "A" Sandwich With 0.024 Skin Thickness (Perpendicular Polarization) ($\psi_\perp = \Delta_\perp$)

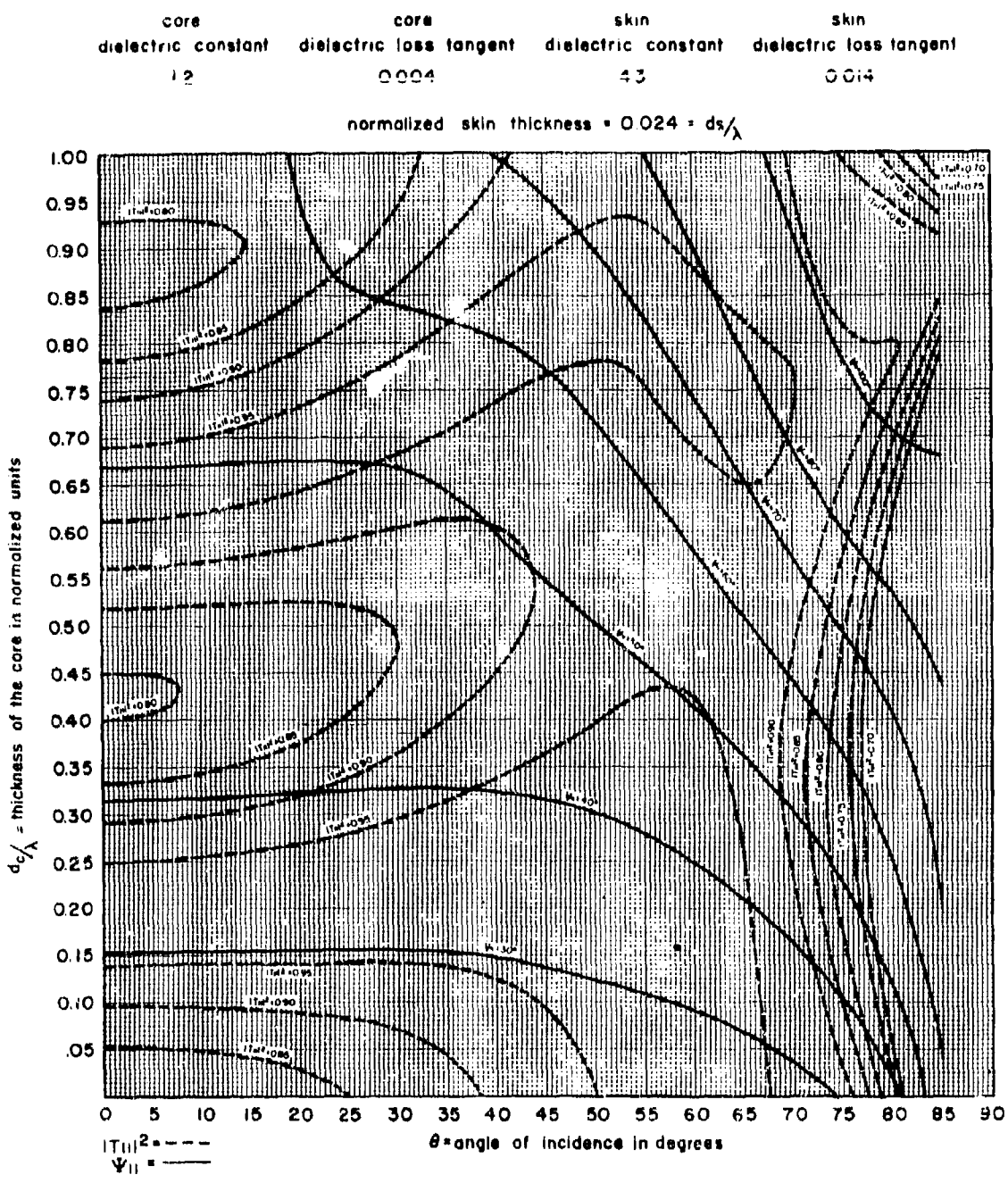


Figure 2-19. Transmission and Phase Delay Contours for "A" Sandwich with 0.024 Skin Thickness (Parallel Polarization) (Ψ_{II} - Δ_{II})

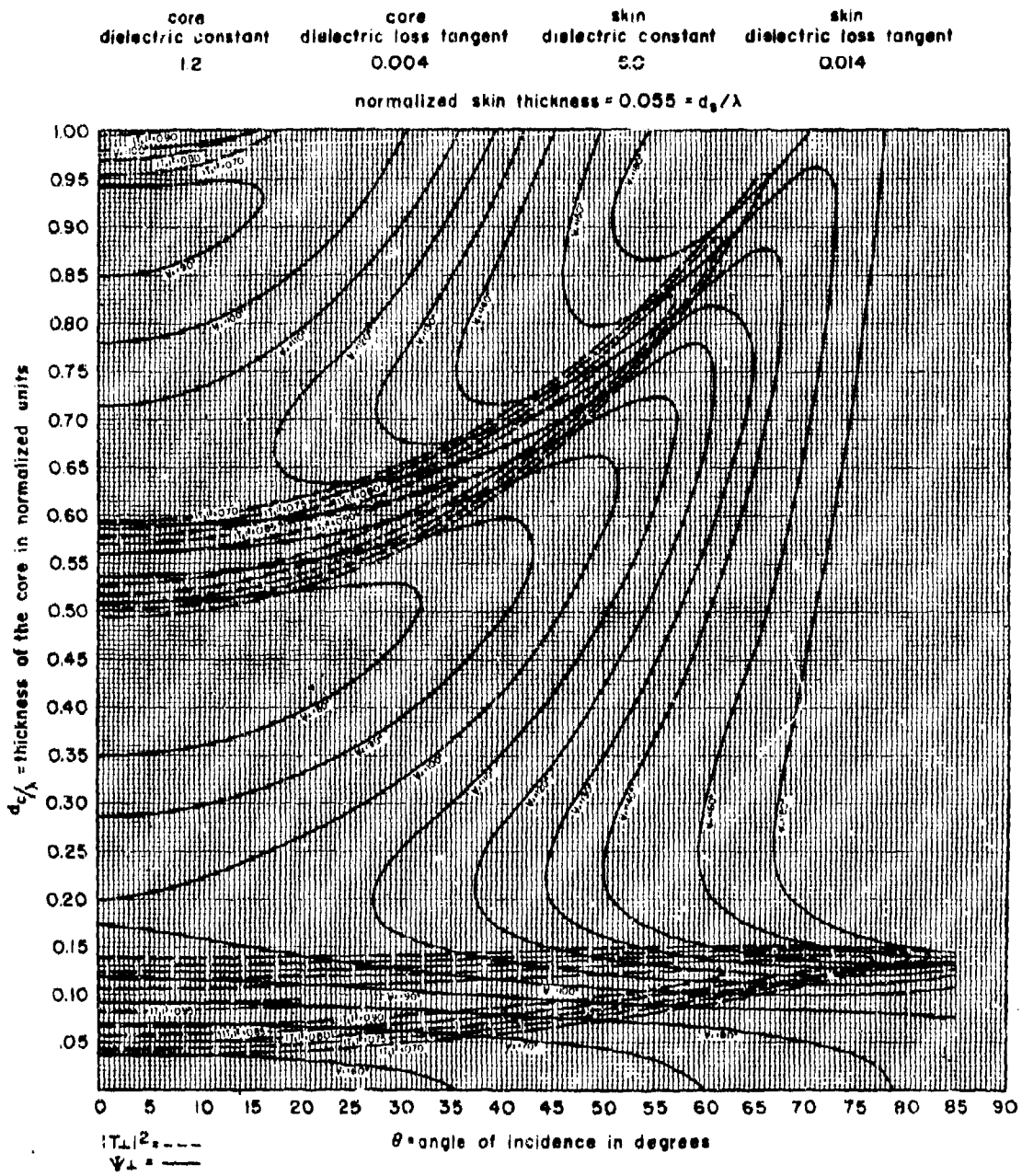


Figure 2-20. Transmission and Phase Delay Contours for "A" Sandwich with 0.055 Skin Thickness (Perpendicular Polarization) ($\Psi_\perp = \Lambda_\perp$)

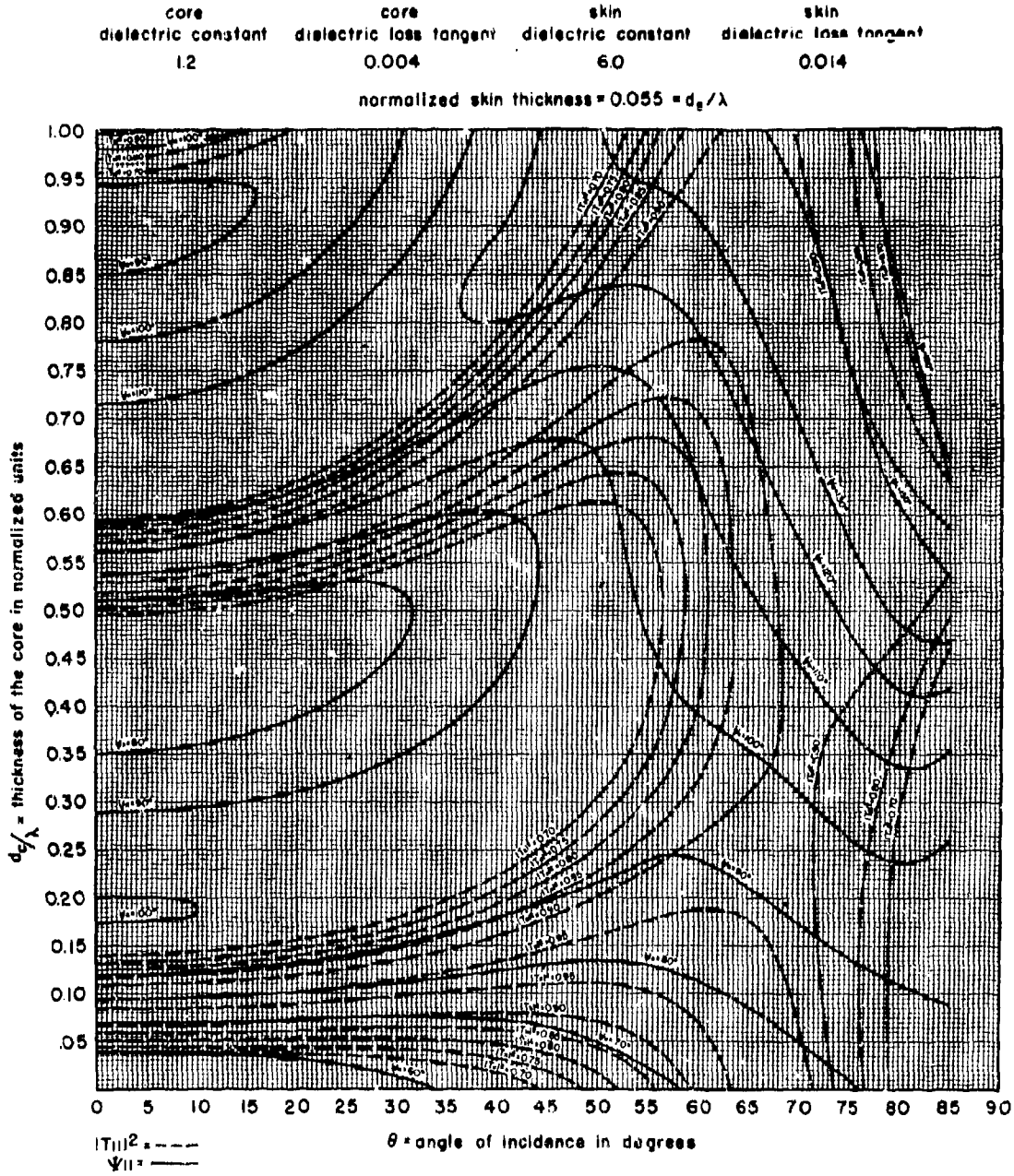


Figure 2-21. Transmission and Phase Delay Contours for "A" Sandwich with 0.055 Skin Thickness (Parallel Polarization) ($\Psi_{||} = \Delta_{||}$)

reflection will occur at each skin, but the core thickness can be chosen to make these reflections cancel at another angle of incidence θ_1. Perfect transmission will thus be obtained at angles θ_0 and θ_1. If the above design were carried out for perpendicular polarization, perfect transmission would be obtained for parallel polarization at angles θ_0 and θ_B (the Brewster angle). An "A" sandwich of this type might be particularly useful at very short wavelengths where its weight would not be excessive and its thickness would be an advantage rather than a disadvantage. If the air core is replaced with a spacer of low dielectric constant, perfect transmission can still be obtained at one angle θ_1 by proper choice of core thickness, but some loss of transmission would be expected at angles θ_0 and θ_B.

Additional data on "A" sandwiches are given in Chapters 3, 5 and 13. Tables of transmission and reflection coefficients and phase shift are given in reference 20. Graphs of these data for "A" sandwiches are given in references 7, 13, 14, and 21 through 26. Additional information on "A" sandwiches is given in several references listed in the bibliography.

2-7. The "B" Sandwich

Whereas the "A" sandwich has skins of higher dielectric constant than that of the core, the "B" sandwich has skins of lower dielectric constant than that of the core. The "B" sandwich is often designed with skins of thickness given by

$$d_s = \frac{\lambda_0}{4\sqrt{\epsilon_s - \sin^2\theta}} \qquad (2\text{-}77)$$

and with a skin dielectric constant given by

$$\epsilon_s = \sqrt{\epsilon_c} \qquad (2\text{-}78)$$

where ϵ_s is the relative dielectric constant of the skin. Under these conditions, regardless of the core thickness, equal transmission is obtained for both parallel and perpendicular polarization and the insertion phase shift is the same for either polarization, at the design angle of incidence.[18] This design does not provide maximum transmission. It is possible to design a "B" sandwich for maximum transmission for a given polarization at a given angle of incidence without specifying the core thickness, but such a design does not provide equal transmission or equal insertion phase shift for the two polarizations. The weight of the "B" sandwich is likely to be greater than that of the "A" sandwich in most cases. However, the "B" sandwich may have good transmission over a wider range of incidence angles.

The lossless "B" sandwich can be designed for perfect transmission at two angles of incidence.[19] To achieve this, the skin dielectric constant is specified by

$$\epsilon_s = \sqrt{\epsilon_c - \sin^2\theta}\cos\theta + \sin^2\theta$$

($\perp$ polarization) (2-79)

or

$$\epsilon_s^4(\epsilon_c - \sin^2\theta)\cos^2\theta = \epsilon_c^2(\epsilon_s - \sin^2\theta)$$

($\parallel$ polarization) (2-80)

The skin thickness is then chosen by use of Equation (2-58). This will result in perfect transmission at the angle of incidence used in Equations (2-78) and (2-79) or (2-80). If desired, the core thickness can then be selected to give perfect transmission at another angle.

The "B" sandwich is an extension of the idea of quarter-wave reflectionless coatings used on optical lenses and on infrared radomes (irdomes).[18] On the other hand, if the core thickness of the "B" sandwich is reduced to zero, the "B" sandwich reduces to a half-wave wall; thus, since the core is often very thin (perhaps even vanishing in certain regions of the radome), it seems natural to think of the "B" sandwich as a generalization of the half-wave wall. Whether the "B" sandwich is designed for maximum transmission or for equal treatment of the two polarizations, the core thickness is a free variable which can be used to introduce a taper into the radome wall to control the insertion phase, for example.[18]

The "B" sandwich is also discussed in several references listed in the bibliography.

2-8. The "C" Sandwich

The "A" and "B" sandwiches provide greater flexibility in radome design than the solid sheet construction. Additional flexibility is offered by the "C" sandwich (or double sandwich), which consists of five dielectric layers, as shown in Figure 2-22. A symmetrical "C" sandwich can be considered as two identical "A" sandwiches with zero spacing between them. Maximum transmission can be obtained with a lossless symmetrical "C" sandwich by two methods:

a. Design each of the two component "A" sandwiches for maximum transmission (or zero reflection); or

b. If the reflection coefficients of the two component sandwiches are not zero, make their individual reflections cancel.

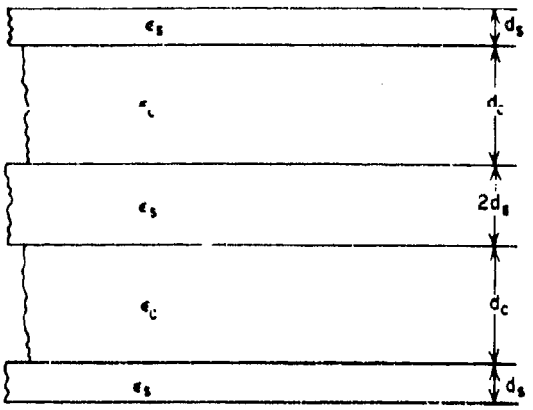


Figure 2-22. Symmetrical "C" Sandwich

By satisfying condition (a) at one angle of incidence and condition (b) at another, the lossless "C" sandwich can be designed to have perfect transmission at two angles of incidence.

The "C" sandwich is light in weight and is strong. The thicker construction required for the "C" sandwich (it is twice as thick as the corresponding "A" sandwich) gives much greater mechanical strength and rigidity — a factor which becomes very important in radome design for frequencies above X-band. The other factor that makes the "C" sandwich advantageous is that it can be designed for high transmission up to greater angles of incidence than is possible with the "A" sandwich. However, very close tolerances must be held on the skin thicknesses to take advantage of the high incidence angle transmission.[27]

Graphs of transmission and reflection for "C" sandwiches are given in Reference 27 and in Chapters 5 and 13. "C" sandwiches are discussed in several references listed in the bibliography. The transmission and reflection coefficients of the "C" sandwich can be readily obtained from those of the corresponding "A" sandwiches. The equations for this purpose are listed in Reference 20.

SECTION C. TOLERANCES IN THICKNESS AND DIELECTRIC CONSTANTS*

2-9. Parameters Affecting Permissible Tolerances

The cost of producing a radome depends to a considerable extent on the tolerances which are specified for the thickness and dielectric constant of the radome wall. Moreover, of course, the electrical performance of the radome depends largely on the accuracy achieved in constructing it according to specifications. Manufacturing tolerances are one of the chief limitations in the performance obtainable from radomes at the present time.

It can be stated in general that the permissible tolerances in wall thickness decrease as

a. The wavelength decreases

b. The dielectric constant increases

c. The angle of incidence increases.

Since thickness and dielectric constant tolerances are larger for parallel than for perpendicular polarization, design is often made on the basis of the latter.

2-10. Effect of High Dielectric Constant

A lossless half-wave wall of sufficiently high dielectric constant and precise thickness can give arbitrarily low reflection in any range of incidence angles. This is suggested in Figure 2-8, which shows the design thickness of half-wave sheets versus the design angle of incidence, for several choices of dielectric constant. If a high dielectric constant is used, the thickness required for perfect transmission becomes almost independent of the design angle of incidence. This is illustrated in Figure 2-63, where it will be noted that for a thickness of 0.283 wavelength the power transmission coefficient of a sheet having a dielectric constant of 4 remains above 0.93 for all angles of incidence up to 80°. A sheet of dielectric constant 8 and thickness 0.186 wavelength will provide a power transmission constant greater than 0.97 for angles up to 80°. (Sheets of extremely small dielectric constant also can give arbitrarily low reflection in any range of incidence angles.)

*Much of the material in this section is taken from: Norman N. Wiederhorn and Alan F. Kay, Radome Design Criteria for Precision Guidance Radar, Final Report, Contract AF33(038)-12283, McMillan Laboratory, Inc., Ipswich, Mass., 1 June 1954. (Confidential), (AD-49 423).

This situation is unfortunately modified critically by tolerances. The dielectric constant that may be optimally employed is limited by the tolerance in dielectric constant, thickness, frequency, and loss tangent. As these tolerances go down, the optimum dielectric constant goes up and the corresponding reflections go down. With the continued development of precision manufacturing techniques and quality control, higher dielectric constants could be employed, with ever improved electrical results.

This problem is illustrated for normal incidence in Figure 2-23, which shows the power transmission coefficient versus thickness for homogeneous sheets of dielectric constants 2, 4, and 8. Starting at the half-wave thickness in each case, a much larger change in thickness can be tolerated in sheets of low dielectric constant before the transmission falls below 0.97. The thickness variation permissible for transmission exceeding 0.97 is 0.12, 0.04, and 0.02 wavelength, for sheets of dielectric constant 2, 4, and 8 respectively.

2-11. Calculation of Permissible Tolerances

Manufacturing tolerances in wall thickness and dielectric constant are likely to occur as variations randomly distributed over the wall. However, they may occur in the following ways:

a. The wall is everywhere too thick or too thin by a fixed amount

b. The wall is uniformly tapered in thickness

c. The dielectric constant is everywhere too high or too low by a fixed amount

d. The dielectric constant varies linearly along the length of the wall.

The tolerances which are permissible depend on the manner in which the variations occur. The least harmful errors are those in which the thickness (or dielectric constant) has many rapid fluctuations along the length of the wall, such that the average value over any area of, say, one square wavelength of the surface is equal to the exact value specified. Long tapering errors are likely to introduce much more beam tilting and pattern distortion than randomly distributed tolerances.

To determine the fabrication tolerances necessary to maintain a given tolerance in transmission coefficient, consider the case in which the sheet is uniformly too thick by an amount Δd

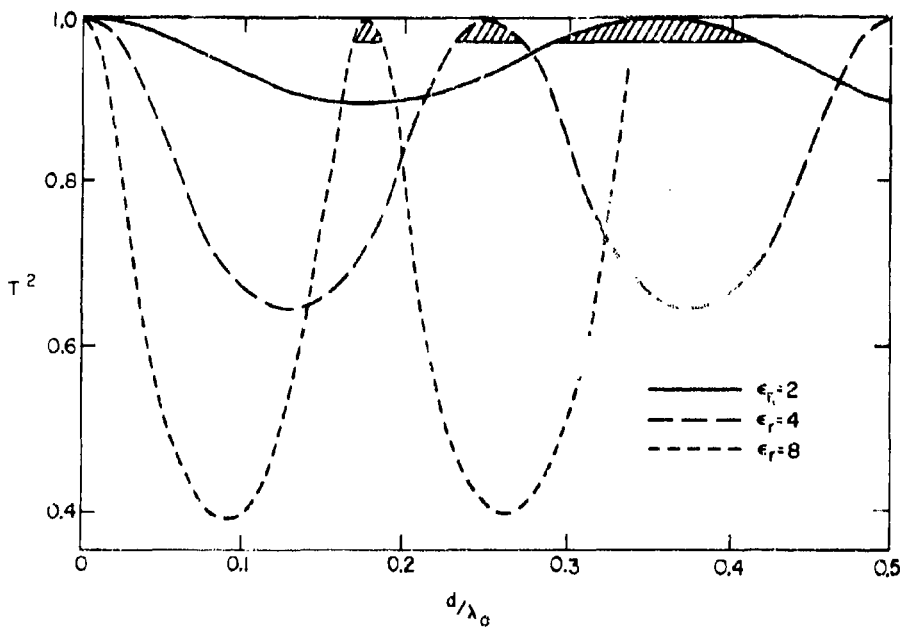


Figure 2-23. Power Transmission Coefficients of Lossless Homogeneous Plane Sheets for Normal Incidence (Transmission Exceeds 97 Percent in Shaded Regions)

and the dielectric constant is uniformly too high by an amount $\Delta\epsilon_r$. According to Equation (2-47), if the electrical thickness of a lossless homogeneous sheet differs slightly from that of a half-wave sheet of order n, the loss in power transmission will be

$$\Delta T_\perp^2 = \frac{\pi^2 (\epsilon_r - 1)^2}{\cos^2\theta}\left[\frac{\Delta d}{\lambda_0} + \frac{n\,\Delta\epsilon_r}{4\left(\sqrt{\epsilon_r - \sin^2\theta}\right)^3}\right]^2 \qquad (2\text{-}81)$$

If the transmission tolerance is equally distributed between tolerances in thickness and dielectric constant, and if a loss in power transmission of $\Delta T_\perp^2$ is permissible, the tolerances are

$$\Delta d = \frac{\lambda_0 \sqrt{\Delta T_\perp^2}\cos\theta}{2\pi(\epsilon_r - 1)} \qquad (2\text{-}82)$$

and

$$\Delta\epsilon_r = 2\,\frac{\left(\sqrt{\epsilon_r - \sin^2\theta}\right)^3 \sqrt{\Delta T_\perp^2}\cos\theta}{n\pi(\epsilon_r - 1)} \qquad (2\text{-}83)$$

From Equations (2-82) and (2-83), it will be seen that the permissible tolerances are comparatively large for low dielectric constants and low angles of incidence, but they become very small for high dielectric constants and high angles of incidence. Also, the tolerances are more severe in a high-order, half-wave sheet than in a lower order sheet. From Equation (2-81), it will be seen that if the dielectric constant is too high, it can be compensated by a reduction in thickness.

The thin sheet can be considered as a half-wave sheet of order zero. Now, the half-wave sheet of order zero has a design thickness of zero, as shown in Equation (2-56); thus, the thickness of the thin sheet is analogous to the thickness tolerance in the n^{th}-order half-wave sheet. With this in mind, Equation (2-81) is applicable to the thin sheet, and it is noted that Equation (2-81) agrees with Equation (2-54). Thickness and dielectric constant tolerances are quite unimportant in the thin sheet unless they produce changes in electrical thickness which are comparable to the design value of electrical thickness. This is illustrated in Figures 2-6 and 2-7 in which it is noted that a 100 percent increase in thickness of the thin sheet produced no serious change in electrical characteristics.

In sandwiches it is necessary to consider thickness tolerances in both the skin and the core, as well as dielectric constant tolerances in both the skin and the core. It is found that for the "A" sandwich good transmission can be obtained through high angles of incidence only if the skins are very thin and the core thickness is held to a close tolerance.[3,13] In the "C" sandwich, very close tolerances must be held on the skin thicknesses to obtain good transmission at high angles of incidence.[27]

The problems of tolerances are considered in several references listed in the bibliography.

SECTION D. POLARIZATION*

2-12. Effect of Polarization

Up to this point the characteristics of flat sheets have been considered only for incident plane waves having parallel or perpendicular polarization. In these two cases the transmitted and reflected waves have the same polarization as the incident wave. (This follows from the results obtained in Section A.) Generally, however, the wave incident at a given point on a radome wall has neither parallel nor perpendicular polarization; instead, the incident wave may be elliptically polarized as shown in figure 2-24, or it may be linearly polarized with its electric field intensity vector making an angle

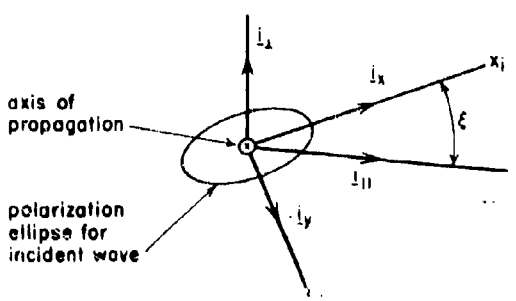


Figure 2-24. Coordinates For an Elliptically Polarized Wave Incident on a Dielectric Sheet

*Much of the material in this section, through Equation (2-96), is contained in Reference 28: Robert E. Webster, Elliptical polarizations and radome errors, Report 663-3, Contract AF 33(616)-3277, Antenna Laboratory, Ohio State University, 15 November 1956.

ξ with the plane of incidence, as in Figure 2-25. In these cases, the polarization of the transmitted wave will generally differ from that of the incident wave. This depolarization effect is undesirable since it may represent a loss of useful power and it contributes to the directional errors introduced by the radome.

2-13. Transmission Coefficients for Elliptical Polarization.

Transmission through an isotropic plane sheet or sandwich with an incident wave of arbitrary polarization can be expressed in terms of the transmission coefficients for parallel and perpendicular polarization. To do this, it is convenient to define two unit vectors $\underline{i}_{\parallel}$ and $\underline{i}_{\perp}$ which are perpendicular to each other and to the axis of propagation, as shown in Figures 2-24 and 2-25. Let $\underline{i}_{\parallel}$ and $\underline{i}_{\perp}$ be parallel and perpendicular to the plane of incidence, respectively. Then the transmitted wave can be expressed in terms of its components having parallel and perpendicular polarization, as follows:

$$\dot{\underline{E}}_t = \dot{E}_{t\perp}\,\underline{i}_{\perp} + \dot{E}_{t\parallel}\,\underline{i}_{\parallel} \qquad (2\text{-}84)$$

If $E_{i\parallel}$ and $E_{i\perp}$ denote the components of the incident wave having parallel and perpendicular polarization, the transmitted wave is also given by:

$$\dot{\underline{E}}_t = \dot{T}_{\perp}\,\dot{E}_{i\perp}\,\underline{i}_{\perp} + \dot{T}_{\parallel}\,\dot{E}_{i\parallel}\,\underline{i}_{\parallel} \qquad (2\text{-}85)$$

Frequently it is of interest to express the transmitted wave as the sum of a component $\dot{T}_i\dot{\underline{E}}_i$ having the same polarization as the incident wave, and a component $\dot{T}_d\,\dot{\underline{E}}_d$ having the orthogonal polarization, as follows:

$$\dot{\underline{E}}_t = \dot{T}_i\,\dot{\underline{E}}_i + \dot{T}_d\,\dot{\underline{E}}_d \qquad (2\text{-}86)$$

where

$$\dot{\underline{E}}_i = \dot{E}_{i\perp}\,\underline{i}_{\perp} + \dot{E}_{i\parallel}\,\underline{i}_{\parallel} \qquad (2\text{-}87)$$

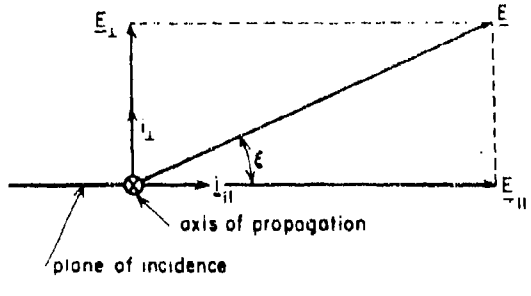


Figure 2-25. Linearly Polarized Wave and Its Parallel and Perpendicular Components

and

$$\dot{\underline{E}}_d = (\dot{E}_{i\parallel}^{*}\;\underline{i}_{\perp} - \dot{E}_{i\perp}^{*}\;\underline{i}_{\parallel})\,e^{j\phi} \qquad (2\text{-}88)$$

The subscripts i and d are intended to indicate the words "incident" and "depolarized," respectively.

The value of ϕ will depend on the choice of phase reference, and will be left arbitrary for the present. The expression for $\dot{\underline{E}}_d$ given by Equation (2-88) fulfills the following requirements:

a. It assures that the polarization of $\dot{\underline{E}}_d$ is orthogonal to that of $\dot{\underline{E}}_i$. (For example, right circular and left circular polarizations are orthogonal; vertical and horizontal linear polarizations are orthogonal.)

b. It makes the power density of the wave $\dot{\underline{E}}_d$ equal to that of the incident wave $\dot{\underline{E}}_i$. This normalizes $\dot{T}_d$ in the proper manner.

Equations (2-86) through (2-88) can be solved for the transmission coefficients, yielding

$$\dot{T}_i = \frac{\dot{T}_{\perp}\,E_{i\perp}^{\,2} + \dot{T}_{\parallel}\,E_{i\parallel}^{\,2}}{E_{i\perp}^{\,2} + E_{i\parallel}^{\,2}} \qquad (2\text{-}89)$$

and

$$\dot{T}_d = (\dot{T}_{\perp} - \dot{T}_{\parallel})\,\frac{\dot{E}_{i\perp}\dot{E}_{i\parallel}\,e^{-j\phi}}{E_{i\parallel}^{\,2} + E_{i\perp}^{\,2}} \qquad (2\text{-}90)$$

2-14. Transmission Coefficients Using Axial Ratios.

Equations (2-89) and (2-90) are compact and useful, but to use them one must insert the values of $\dot{E}_{i\perp}$ and $\dot{E}_{i\parallel}$ for the particular problem. In many cases the incident wave is more conveniently described by:

a. The axial ratio r (ratio of minor axis to major axis) of its polarization ellipse; and

b. The polarizing angle ξ between the plane of incidence and the major axis of the polarization ellipse. (See Figure 2-24.)

Expressions for $\dot{T}_i$ and $\dot{T}_d$ will now be derived in terms of r and ξ. The x_i- and y_i-axes and unit vectors $\underline{i}_x$ and $\underline{i}_y$ will be chosen to coincide with the major and minor axes of the incident polarization ellipse, so that the incident wave can be written:

$$\dot{\underline{E}}_i = (\underline{i}_x - jr\underline{i}_y)\,\dot{E}_{ix} \qquad (2\text{-}91)$$

The parallel and perpendicular components of the incident wave are, from Equation (2-91) and Figure 2-24,

$$\dot{E}_{i\parallel} = (\cos\zeta - jr\sin\zeta)\,\dot{E}_{ix} \qquad (2\text{-}92)$$

and

$$\dot{E}_{i\perp} = (\sin\zeta + jr\cos\zeta)\,\dot{E}_{ix} \qquad (2\text{-}93)$$

From Equations (2-85), (2-92), and (2-93), the transmitted wave is given by

$$\dot{\underline{E}}_t = \left[\dot{T}_{\parallel}(\cos\zeta - jr\sin\zeta)\,\underline{i}_{\parallel} + \dot{T}_{\perp}(\sin\zeta + jr\cos\zeta)\,\underline{i}_{\perp}\right]\dot{E}_{ix} \qquad (2\text{-}94)$$

The transmitted wave can also be written as in Equation (2-86) as follows:

$$\dot{\underline{E}}_t = \left[T_i(\underline{i}_x - jr\underline{i}_y) + \dot{T}_d(r\underline{i}_x + j\underline{i}_y)\right]\dot{E}_{ix} \qquad (2\text{-}95)$$

From Equations (2-94) and (2-95), the desired expressions for the transmission coefficients are

$$\dot{T}_i = \frac{(r^2\sin^2\zeta + \cos^2\zeta)\,\dot{T}_{\parallel} + (\sin^2\zeta + r^2\cos^2\zeta)\,\dot{T}_{\perp}}{1 + r^2} \qquad (2\text{-}96)$$

and

$$\dot{T}_d = (\dot{T}_{\perp} - \dot{T}_{\parallel})\left[\frac{1}{2}j\sin 2\zeta - \frac{r\cos 2\zeta}{1 + r^2}\right] \qquad (2\text{-}97)$$

In view of Equation (2-85), the quantities $\dot{T}_{\parallel}$ and $\dot{T}_{\perp}$ appearing in Equations (2-96) and (2-97) must be the "insert transmission coefficients" defined by Equation (2-47) (or corresponding equations in the case of sandwiches). From Equations (2-91) and (2-95), the transmitted wave component having the same polarization as the incident wave will, at each point in space, have field intensities equal to $\dot{T}_i$ times those which would exist at the same point if the dielectric sheet were removed. The phase angle of $\dot{T}_i$ is equal to the insertion phase advance angle for the wave component whose polarization has been unchanged in traversing the sheet. Also, from Equations (2-91) and (2-95), the phase angle of $\dot{T}_d$ equals the phase advance of the cross-polarized transmitted component relative to the phase the incident wave would have at the same point in the absence of the dielectric sheet. (The phase reference for $\dot{T}_d$ is the major axis of the incident polarization ellipse.)

From Equation (2-97), no depolarization will occur if

a. The incident wave has perpendicular polarization ($\zeta = 90^\circ$, $r = 0$);

b. The incident wave has parallel polarization ($\zeta = 0^\circ$, $r = 0$); or

c. $\dot{T}_{\perp} = \dot{T}_{\parallel}$.

If the incident wave is linearly polarized ($r = 0$) at angle ζ as indicated in Figure 2-14, Equations (2-96) and (2-97) show that

$$\dot{T}_i = \dot{T}_{\parallel}\cos^2\zeta + \dot{T}_{\perp}\sin^2\zeta \qquad (2\text{-}98)$$

and

$$\dot{T}_d = \frac{1}{2}j(\dot{T}_{\perp} - \dot{T}_{\parallel})\sin 2\zeta \qquad (2\text{-}99)$$

By IRE standards, the $\underline{E}$ vector of a right-circularly polarized wave rotates clockwise from the viewpoint of an observer looking along the axis of propagation at the departing wave; thus, if the incident wave is right-circularly polarized ($r = 1$), Equations (2-96) and (2-97) show that

$$\dot{T}_i = \frac{1}{2}(\dot{T}_{\parallel} + \dot{T}_{\perp}) \qquad (2\text{-}100)$$

and

$$\dot{T}_d = \frac{1}{2}(\dot{T}_{\parallel} - \dot{T}_{\perp})\,e^{-j2\zeta} \qquad (2\text{-}101)$$

An incident wave whose $\underline{E}$ vector rotates counterclockwise can be represented conveniently by assigning a negative numerical value to the axial ratio. For example, Equation (2-91) will represent a left-circularly polarized wave if r is given the value -1. Graphs of transmission coefficients for circular polarization are given in References 12 and 29.

In general, the transmitted wave component which is of interest will have a polarization (axial ratio r_1 and polarizing angle ζ_1) that may differ from that of the incident wave (r, ζ). In this event, it is convenient to express the wave transmitted through the plane sheet as a component $\dot{A}$ having polarization (r_1, ζ_1), plus an orthogonal component $\dot{B}$, as follows:

$$\dot{E}_t = \left[\dot{A}(\underline{i}'_x - jr_1\underline{i}'_y) + \dot{B}(r_1\underline{i}'_x + j\underline{i}'_y)\right]\dot{E}_{ix} \qquad (2\text{-}102)$$

where $\underline{i}'_x$ and $\underline{i}'_y$ are unit vectors parallel to the major and minor axes of the polarization ellipse of the transmitted component $\dot{A}$. The incident wave given by Equation (2-91) can also be expressed in terms of a component $\dot{A}_0$ having polarization r_1, ζ_1 and an orthogonal component $\dot{B}_0$ as follows:

$$\underline{\dot{E}}_t = \left[\dot{A}_0 (\underline{i}'_x - j r_1 \underline{i}'_y) + \dot{B}_0 (r_1 \underline{i}'_x + j \underline{i}'_y)\right] \dot{E}_{1x} \quad (2\text{-}103)$$

An expression for $\dot{A}_0$ can be obtained from Equations (2-91) and (2-103) and $\dot{A}$ can be obtained from Equations (2-94) and (2-102). In this manner the insert transmission coefficient for the component r_1, ξ_1 is found to be:

$$\dot{T}_1 = \frac{\dot{A}}{\dot{A}_0} = \frac{1}{2}\left[\dot{T}_{\parallel} + \dot{T}_{\perp} + (\dot{T}_{\parallel} - \dot{T}_{\perp}) \right. \quad (2\text{-}104)$$

$$\left. \frac{j(1-rr_1)\cos(\xi_1 + \xi) + (r-r_1)\sin(\xi_1 + \xi)}{j(1+rr_1)\cos(\xi_1 - \xi) - (r+r_1)\sin(\xi_1 - \xi)} \right]$$

$\dot{T}_1$ gives the amplitude and phase of the transmitted component r_1, ξ_1 relative to its amplitude and phase at the same point in the absence of the dielectric sheet. Thus, $\dot{T}_1$ may assume magnitudes greater than unity if the dielectric sheet has the proper depolarization properties.

It is desirable to define a similar transmission coefficient which is normalized to unit maximum magnitude. This can be accomplished by using as a reference the wave transmitted through a hypothetical sheet having the following properties:

1. nonreflecting,
2. lossless,
3. no insertion phase shift for component r_1, ξ_1,
4. completely transforms from polarization r, ξ to polarization r_1, ξ_1.

If the incident wave is given by Equation (2-91) or (2-103), the wave transmitted through such a sheet is expressed by

$$\underline{\dot{E}}_t = \sqrt{\frac{1+r^2}{1+r_1^2}} (\underline{i}'_x - j r_1 \underline{i}'_y) E_{1x} e^{jA'_0} \quad (2\text{-}105)$$

where A'_0 is the phase angle of $\dot{A}_0$ and is given by

$$A'_0 = \tan^{-1}\left[\frac{r + r_1}{1 + rr_1} \tan(\xi_1 - \xi)\right] \quad (2\text{-}106)$$

Thus, the normalized transmission coefficient is

$$\dot{T}_2 = \dot{A} \sqrt{\frac{1+r_1^2}{1+r^2}}\, e^{-jA'_0} \quad (2\text{-}107)$$

or

$$\dot{T}_2 = \frac{\left\{\begin{array}{l}(\dot{T}_{\parallel} + \dot{T}_{\perp})\left[j(1+rr_1)\cos(\xi_1 - \xi) - \right. \\ \left.(r + r_1)\sin(\xi_1 - \xi)\right] + \\ (\dot{T}_{\parallel} - \dot{T}_{\perp})\left[j(1-rr_1)\cos(\xi_1 + \xi) + \right. \\ \left.(r - r_1)\sin(\xi_1 + \xi)\right]\end{array}\right\} e^{-jA'_0}}{2j\sqrt{(1+r_1^2)(1+r^2)}} \quad (2\text{-}108)$$

These two transmission coefficients $\dot{T}_1$ and $\dot{T}_2$ have the same phase angles (equal to the insertion phase advance) but different magnitudes. While $\dot{T}_1$ uses the incident wave as a reference, $\dot{T}_2$ compares the wave transmitted through a sheet to that transmitted through a perfect polarization transformer. As would be expected, $\dot{T}_1$ and $\dot{T}_2$ both reduce to the same expression as is given by Equation (2-96) for $\dot{T}_1$ if $r_1 = r$ and $\xi_1 = \xi$.

As an example of the use of Equation (2-104), suppose the incident wave has 6 db elliptical polarization (that is, the field along the major axis is 6 db stronger than that along the minor axis) with clockwise rotation, and with the major axis parallel to the plane of incidence. Then $r = 0.5$ and $\xi = 0$. Now suppose that it is desired to determine the amplitude and phase of the right-circularly polarized component of the transmitted wave. Then $r_1 = 1$ and Equation (2-104) shows that

$$\dot{T}_1 = \frac{2\dot{T}_{\parallel} + \dot{T}_{\perp}}{3} \quad (2\text{-}109)$$

From Equation (2-108), the normalized transmission coefficient for this example is

$$\dot{T}_2 = \frac{2\dot{T}_{\parallel} + \dot{T}_{\perp}}{\sqrt{10}} \quad (2\text{-}110)$$

Additional formulas for polarization analysis and discussions of the relationships between polarization and radome errors are given in several references listed in the bibliography.

SECTION E. MAGNETIC RADOME MATERIALS

2-15. Practical Difficulties

Up to this point, the plane-wave transmission properties have been considered only for plane sheets constructed of nonmagnetic dielectric materials; that is, the permeability μ of the dielectric sheets was assumed equal to that of free space μ_0. Some dielectrics have a permeability appreciably different from that of free space, even at radar frequencies. Unfortunately, the ferrites appear to be too lossy in their present state of development for radome use.[30] However, the relative permeability of a dielectric can be made considerably less than unity by loading with metallic particles. A dielectric material can be made magnetic by embedding in it an array of conducting loops of the proper diameter. Similar effects are obtained if a thin metal sheet, perforated with an array of holes, is embedded in the dielectric sheet.[31] Generally the electric or magnetic loss tangent tan δ_e or tan δ_m becomes excessively large when a medium is loaded with metallic objects to produce a large change in dielectric constant or permeability. As an added complication, a metallic loading which reduces the permeability is likely to increase the dielectric constant in such a way as to make it difficult to achieve a propagation constant equal to that of free space.

2-16. Elimination of Refractive Shift

Snell's law for magnetic materials states that a plane wave incident at angle θ on a plane dielectric surface will be refracted at an angle θ_r, given by

$$\sin \theta_r = \frac{\sin \theta}{\sqrt{\mu_r \epsilon_r}} \tag{2-111}$$

where $\mu_r = \mu/\mu_0$ is the relative permeability; and $\epsilon_r = \epsilon/\epsilon_0$ is the relative dielectric constant.

To reduce the pattern distortion and the angular errors introduced by a radome, it is desirable to minimize the refractive shift experienced by a ray as it passes through the radome wall (see Section H). This can be accomplished in a nonmagnetic half-wave sheet only by use of a very low or very high dielectric constant. If a magnetic material is used, however, refraction is eliminated merely by choosing

$$\mu_r \epsilon_r = 1 \tag{2-112}$$

If Equation (2-112) is satisfied, the propagation constant in the sheet will be equal to that of free space, neglecting losses in the material.

2-17. Obtaining High Transmission Coefficient

Alternatively, magnetic materials could be used to obtain a high transmission coefficient. If a low-loss material is used, maximum transmission will be obtained if the sheet is designed to be nonreflecting. This might be accomplished by minimizing the interface reflection coefficients. For lossless magnetic dielectrics, Equations (2-23) and (2-25) become

$$r_\perp = \frac{\mu_r \cos\theta - \sqrt{\mu_r \epsilon_r - \sin^2\theta}}{\mu_r \cos\theta + \sqrt{\mu_r \epsilon_r - \sin^2\theta}} \tag{2-113}$$

and

$$r_\parallel = \frac{\epsilon_r \cos\theta - \sqrt{\mu_r \epsilon_r - \sin^2\theta}}{\epsilon_r \cos\theta + \sqrt{\mu_r \epsilon_r - \sin^2\theta}} \tag{2-114}$$

Equations (2-113) and (2-114) will apply to lossy materials if ϵ_r is replaced with $\epsilon_r(1-j \tan \delta_e)$ and μ_r is replaced with $\mu_r(1-j \tan \delta_m)$.

In nonmagnetic media the angle of zero interface reflection (Brewster angle) occurs only for parallel polarization; by using magnetic materials, however, the Brewster effect can be obtained for both polarizations. From Equations (2-113) and (2-114), zero reflection will be obtained at normal incidence if

$$\mu_r = \epsilon_r \tag{2-115}$$

If the permeability is chosen to satisfy Equation (2-115), this will match the impedance of the sheet to that of free space for normal incidence.

Lossless nonrefracting media ($\mu_r \epsilon_r = 1$) are considered in Reference 32.* For such media, Equations (2-113) and (2-114) become

$$r_\perp = -r_\parallel = \frac{\mu_r - 1}{\mu_r + 1} \tag{2-116}$$

Thus, the interface reflection coefficient becomes independent of polarization and angle of incidence. Now, reflection will be eliminated for all angles and for all polarizations if μ_r is

*The material in the remainder of this section is from Reference 32 by Charles K. Schramm, Jr., "Propagation Constant and the Radome," Technical Report 53-297, Wright Air Development Center, Ohio, August 1953, (AD-21 967).

1; see Equations (2-116). This shows that the ideal radome material (as far as the electrical properties are concerned) is air, since for air $\mu_r = \epsilon_r = 1$. We might let $\mu_r \epsilon_r$ be unity (to eliminate refraction), and see how far μ_r and ϵ_r can vary from unit before the electrical properties of the radome wall become poor.

From Equation (2-47), the transmission coefficient of a lossless homogeneous sheet is

$$T^2 = \frac{1 - 2r^2 + r^4}{1 - 2r^2 \cos\left(2\beta_0 d \sqrt{\mu_r \epsilon_r - \sin^2\theta}\right) + r^4} \quad (2\text{-}117)$$

Therefore, the thickness of a half-wave homogeneous sheet of order n is

$$d = \frac{n\lambda_0}{2\sqrt{\mu_r \epsilon_r - \sin^2\theta}} \quad (2\text{-}118)$$

At its design angle of incidence, the lossless half-wave magnetic sheet has perfect transmission for both polarizations, and the insertion phase shift is the same for both polarizations.

For a given angle of incidence, the transmission coefficient is minimum when the thickness is just one-half of the value given by Equation (2-118). In this situation, the sheet might be called a "quarter-wave sheet." At the angles of incidence for which the sheet is a quarter-wave sheet, the transmission coefficient is

$$T_{min} = \frac{1 - r^2}{1 + r^2} \quad (2\text{-}119)$$

and, for the nonrefracting case,

$$T_{min} = T_{min} = \frac{2\mu_r}{1 + \mu_r^2} \quad (2\text{-}120)$$

Now, it can be shown, from Equation (2-120), that the power transmission for a lossless nonrefracting sheet will exceed 80 percent for all angles of incidence if ϵ_r is less than 1.62 (or μ_r is greater than 0.618).

2-18. Insertion Phase Variation Versus Angle of Incidence

A very useful property of the half-wave nonrefracting sheet is the very small insertion phase variation versus angle of incidence. For example, if the dielectric constant is 2, the phase varies by only $\pm 7^\circ$ for incidence angles from 0 to 90°. Furthermore, since $r_\perp$ and $r_\parallel$ are equal (except for the minus sign), $T_\parallel$ and $T_\perp$ are also equal for all angles of incidence if the sheet is made of lossless material with $\mu_r \epsilon_r = 1$. As was shown in Section D, a sheet of this type will produce no depolarization.

Magnetic radome materials are considered in several references listed in the bibliography.

SECTION F. ANISOTROPIC MATERIALS AND CONSTRUCTIONS

The electrical properties of some materials depend on the relative orientation of the material in the electromagnetic field. This is true of many crystalline materials and of ferrites, electron beams, and ionized gas in the presence of a steady magnetic field. This anisotropic effect can be produced artificially by loading an ordinary dielectric material with a lattice of parallel metal dipoles. A great variety of other artificial anisotropic constructions have also been studied.

The properties of a homogeneous sheet of ordinary dielectric often seem to be inadequate for radome uses. The use of sandwiches widens the range of characteristics which the radome designer can obtain. Still greater flexibility is obtainable through the use of magnetic or anisotropic materials.

2-19. Effect on Dielectric Constant

In an anisotropic medium, the effective dielectric constant depends on the orientation of the electric field intensity vector. To an x-polarized field, the medium would appear to have a dielectric constant ϵ_x; to a y-polarized field the effective dielectric constant would be ϵ_y; and to a z-polarized field it would be ϵ_z. If the coordinate axes are chosen to coincide with the preferred axes (or "principal axes")* of the medium, the parameters ϵ_x, ϵ_y, and ϵ_z are sufficient to describe completely the dielectric properties of the material. The dielectric constant can then be represented as follows:

*These are related to the crystal axes in crystalline media, and to the dipole axis in media loaded with dipoles.

$$\epsilon = \begin{pmatrix} \epsilon_x & 0 & 0 \\ 0 & \epsilon_y & 0 \\ 0 & 0 & \epsilon_z \end{pmatrix} \qquad (2\text{-}121)$$

Maxwell's equation

$$\nabla \times \underline{H} = - j\omega\epsilon \underline{E} \qquad (2\text{-}122)$$

becomes, for anisotropic media, the following set of three equations:

$$(\nabla \times \underline{H})_x = - j\omega\epsilon_x E_x \qquad (2\text{-}123)$$

$$(\nabla \times \underline{H}_y \qquad j\omega\epsilon_y E_y \qquad (2\text{-}124)$$

and

$$(\nabla \times \underline{H})_z = - j\omega\epsilon_z E_z \qquad (2\text{-}125)$$

If the medium also possesses magnetic anisotropy, the permeability will have three principal values, and it can be represented in a manner similar to Equation (2-121). Then Maxwell's equation

$$\nabla \times \underline{E} = j\omega\mu \underline{H} \qquad (2\text{-}126)$$

can be written as a set of three equations similar to Equations (2-123), (2-124), and (2-125).

2-20. Effect on Polarization

Anisotropic media that have their own preferred axes may introduce undesirable depolarization when such materials are used in radome constructions. It has been pointed out that an isotropic flat sheet produces no depolarization when the incident plane wave has parallel or perpendicular polarization; however, with parallel or perpendicular incident polarization an anisotropic sheet will, in general, excite both parallel and perpendicular polarization components in the transmitted wave (unless two of the principal axes of the medium are in the plane of incidence). Thus, even at normal incidence depolarization may occur unless the incident field vectors are parallel with the principal axes of the medium.

This phenomenon has been put to practical use (Reference 33) in a polarizing panel consisting of an anisotropic dielectric with ϵ_y greater than ϵ_x. (The xy-plane is the surface of the panel, as shown in Figure 2-5). At intervals along the y-axis there are embedded in the panel metal slats whose planes are parallel to the xz-plane. For normal incidence, a y-polarized incident wave is not affected by the thin metal slats, its propagation constant in the panel being determined by ϵ_y and ω. An x-polarized incident wave, however, will propagate through the panel via a waveguide mode with a propagation constant determined by ϵ_x, ω, and the spacing of the slats. Because of this and because ϵ_y is greater than ϵ_x, the curve of propagation constant versus frequency for x-polarization is very nearly parallel to that for y-polarization over a broad band of frequencies. By properly choosing the panel thickness, a differential phase shift of 90° can be obtained for x-and y-polarized components of the incident wave. If a wave linearly polarized at an angle of 45° with respect to the y-axis is incident normally upon the panel, a circularly polarized wave will be transmitted through the panel. These techniques and modifications of them suggest interesting applications to radome construction.

If the incident wave has parallel or perpendicular polarization, there is one type of anisotropic flat sheet which will not depolarize, regardless of the plane of incidence. Assuming the xy-plane is parallel to the surfaces of the sheet, the parameters of this special medium are related by[34]

$$\epsilon_x = \epsilon_y \qquad (2\text{-}127)$$

and

$$\mu_x = \mu_y \qquad (2\text{-}128)$$

A medium which satisfies Equations (2-127) and (2-128) is called a uniaxial medium because it has only one preferred axis, the z-axis. An example would be a flat sandwich constructed of a number of thin, flat isotropic sheets of alternating dielectric constant, as shown in Figure 2-26. Such a sandwich behaves approximately as an equivalent homogeneous sheet having an effective dielectric constant along the z-axis which differs from its effective dielectric constant along the x- or y-axes.

2-21. Interface Reflection Coefficients

The transmission coefficients for solid sheets and sandwiches are derived for the uniaxial case in Reference 34. To illustrate the relationships involved, the interface reflection coefficients for this case will now be developed. For perpendicular polarization, using the coordinates and directions of propagation shown in Figures 2-1, Equations (2-123) through (2-126) become:

$$j\omega\mu_z H_z = - \frac{\partial E_x}{\partial y} \qquad (2\text{-}129)$$

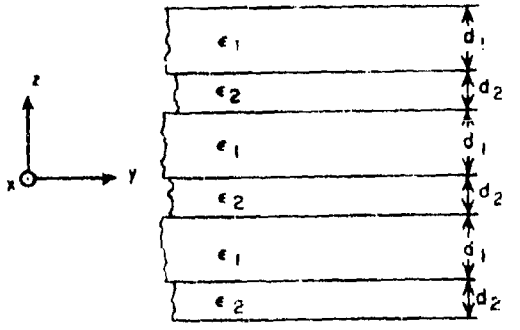


Figure 2-26. Alternating Thin Flat Sheets

$$j\omega\mu_x H_y = \frac{\partial E_x}{\partial z} \tag{2-130}$$

$$j\omega\epsilon_x E_x = \frac{\partial H_y}{\partial z} - \frac{\partial H_z}{\partial y} \tag{2-131}$$

Incident, reflected and transmitted waves will be assumed as follows:

$$E_i = e^{-j\beta_0 (z \cos\theta + y \sin\theta)} \tag{2-132}$$

$$E_r = r_\perp e^{-j\beta_0 (-z \cos\theta + y \sin\theta)} \tag{2-133}$$

$$E_t = t_\perp e^{-j (h_3 z + h_1 y)} \tag{2-134}$$

where h_1 and h_3 denote the propagation constants along the y- and z-axes, respectively, in the anisotropic medium. Now, from Equations (2-129) through (2-134),

$$H_{ty} = -\frac{h_3 E_t}{\omega\mu_x} \tag{2-135}$$

$$H_{tz} = \frac{h_1 E_t}{\omega\mu_z} \tag{2-136}$$

$$h_1^2 \mu_x + h_3^2 \mu_z = \omega^2 \epsilon_x \mu_x \mu_z \tag{2-137}$$

Application of the boundary condition on the tangential component of electric field intensity yields Snell's law for this situation:

$$\sin\theta_r = \frac{\sin\theta}{\sqrt{\frac{\mu_x \epsilon_x}{\mu_0 \epsilon_0} + \left(1 - \frac{\mu_x}{\mu_z}\right)\sin^2\theta}} \tag{2-138}$$

and

$$1 + r_\perp = t_\perp \tag{2-139}$$

Finally, application of the boundary condition on tangential H yields the interface reflection coefficient for the uniaxial anisotropic case:

$$r_\perp = \frac{\sqrt{\frac{\epsilon_0}{\mu_0}}\cos\theta - \frac{h_3}{\omega\mu_x}}{\sqrt{\frac{\epsilon_0}{\mu_0}}\cos\theta + \frac{h_3}{\omega\mu_x}} \tag{2-140}$$

where

$$h_3 = \omega\sqrt{\mu_x\left(\epsilon_x - \frac{\mu_0 \epsilon_0 \sin^2\theta}{\mu_z}\right)} \tag{2-141}$$

Similarly, for parallel polarization it is found that

$$\sin\theta_r = \frac{\sin\theta}{\sqrt{\frac{\epsilon_x \mu_x}{\epsilon_0 \mu_0} + \left(1 - \frac{\epsilon_x}{\epsilon_z}\right)\sin^2\theta}} \tag{2-142}$$

$$1 + r_\parallel = t_\parallel \tag{2-143}$$

$$r_\parallel = \frac{\sqrt{\frac{\mu_0}{\epsilon_0}}\cos\theta - \frac{h_3}{\omega\epsilon_x}}{\sqrt{\frac{\mu_0}{\epsilon_0}}\cos\theta + \frac{h_3}{\omega\epsilon_x}} \tag{2-144}$$

and

$$h_3 = \omega\sqrt{\epsilon_x\left(\mu_x - \frac{\mu_0 \epsilon_0 \sin^2\theta}{\epsilon_z}\right)} \tag{2-145}$$

It will be noted, from Equations (2-138) and (2-142), that, unlike the isotropic case, the angle of refraction for perpendicular polarization differs from that for parallel polarization; also, from Equations (2-135), (2-136), and (2-138), that the magnetic field intensity has a component parallel with the direction of propagation for

perpendicular polarization. With parallel polarization, the electric field intensity has a component parallel with the direction of propagation; therefore, these two cases are often called H-mode and E-mode waves, respectively. More generally, an E-mode is a solution of Maxwell's equations for which one of the H-components vanishes, whereas one of the E-components vanishes in an H-mode field. It is shown in Reference 35 that every homogeneous anisotropic substance can propagate E-modes and H-modes.

Furthermore, the fields in such a medium can always be expressed as the sum of an E- and an H-mode.

2-22. Methods of Obtaining Anisotropy

The effects of anisotropy can be obtained artificially by the use of inhomogeneous construction; for example, the honeycomb material often used as a core for sandwiches is slightly anisotropic. Honeycomb material is usually used, however, for its mechanical strength, light weight, and low dielectric constant rather than for its anisotropy. The effective dielectric constants of honeycomb material along its three principal axes have been derived in Reference 36. The dielectric constants were determined by calculating the capacitance of a parallel-plate capacitor filled with a block of the honeycomb material. The dielectric constants are related to the capacitances obtained for three different orientations of the honeycomb material in the capacitor.

2-23. Analysis of Inhomogeneous Dielectrics

Honeycomb and many other inhomogeneous dielectrics can be analyzed using the equivalent dielectric constants for a capacitor containing two dielectrics, as shown in Figures 2-27 and 2-28. It is also useful to know the equivalent dielectric constant of a capacitor filled with a homogeneous anisotropic material whose principal axes are not parallel with the natural axes of the capacitor (Figure 2-29).

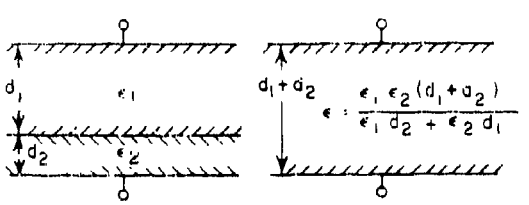


Figure 2-27. Two-Layer Capacitor and Equivalent Homogeneous Capacitor

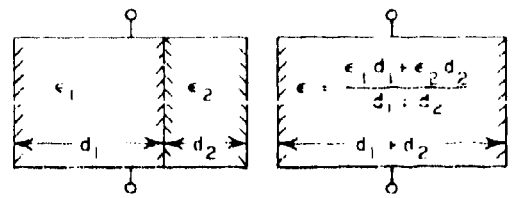


Figure 2-28. Two-Layer Capacitor and Equivalent Homogeneous Capacitor

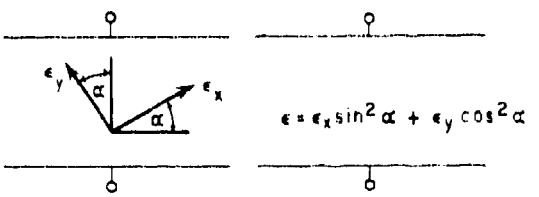


Figure 2-29. Anisotropic Capacitor and Equivalent Isotropic Capacitor

Thus, if the artificial dielectric medium is composed of a three-dimensional array of identical structures or "cells", one of these cells can usually be subdivided into a number of capacitors of the types shown in Figures 2-27, 2-28, and 2-29. The three principal dielectric constants of the medium are then determined by finding the total capacitance of the network of series and parallel capacitors. It is shown in Reference 36 that this simple method is valid in finding an anisotropic medium which is equivalent to the sandwich formed of extremely thin flat sheets as in Figure 2-26. At low frequencies, where the sandwich is equivalent to an anisotropic medium, the properties of the medium become independent of the direction of propagation and depend only on the orientation of the electric field intensity vector. When $\underline{E}$ is parallel to the dielectric surfaces, the effective dielectric constant is, from Figure 2-28,

$$\epsilon_x = \epsilon_y = \frac{\epsilon_1 d_1 + \epsilon_2 d_2}{d_1 + d_2} \qquad (2\text{-}146)$$

When $\underline{E}$ is normal to the dielectric surfaces, the effective dielectric constant is, from Figure 2-27,

$$\epsilon_z = \frac{\epsilon_1 \epsilon_2 (d_1 + d_2)}{\epsilon_1 d_2 + \epsilon_2 d_1} \qquad (2\text{-}147)$$

The reflection coefficients for an infinitely thick stack of such alternating thin flat sheets

would be the same as those given in Equations (2-140) and (2-144) for sufficiently low frequencies.

Broadband sandwiches have been constructed of thin layers, as shown in Figure 2-20. Using Equations (2-146) and (2-147), it is suggested in Reference 37 that the broadband characteristics of such sandwiches result merely from the low value of average dielectric constant obtained by using foam cores and by using skins which are much thinner than the cores.

The equivalent anisotropic sheet given by Equations (2-146) and (2-147) has the same thickness as the isotropic multilayer sandwich which it replaces, and is nonmagnetic if the original sandwich is nonmagnetic. It is shown in Reference 38 that the sandwich can also be replaced with an equivalent isotropic homogeneous sheet. For perpendicular polarization, the alternating sandwich is equivalent to a nonmagnetic homogeneous sheet of the same thickness and appropriate dielectric constant. For parallel polarization, it is equivalent to a homogeneous sheet with smaller thickness and with permeability less than unity. The degree with which the equivalent anisotropic homogeneous medium resembles the actual artificial dielectric depends on the frequency, the angle of incidence, and the lattice spacing.[36] If the lattice spacing in the artificial dielectric is greater than one-half of a free-space wavelength, there may be some angles of incidence for which the medium will act as a grating. The grating effect may produce strong reflections, and sets an upper limit on the frequency, angle of incidence, and spacing at which the equivalent homogeneous medium resembles the artificial dielectric.

It should be pointed out that not all artificial dielectrics are anisotropic. For example, a dielectric loaded with metal or dielectric spheres will be isotropic if the spacing between spheres is the same along the x-, y-, and z-axes. A dielectric loaded with dipoles is also isotropic if equal numbers of dipoles are oriented along the x-, y-, and z-axes. Artificial isotropic constructions have been used to obtain low dielectric constants without sacrifice of strength.

2-24. Use of Metal Slats, Sheets, and Wire Grids

Many forms of dielectric loading have been investigated in an effort to find a radome material having transmission properties superior to ordinary dielectrics. Flat panels constructed of parallel metal slats with no dielectric filler (similar to a venetian blind) were found[39] to have excellent transmission for linear polarization if the incident electric field intensity vector made an angle of at least 75° with the surface of each individual slat. Radomes were also constructed in the shape of a 40° cone, consisting of a thin outer dielectric skin supported with an array of parallel aluminum ribs. These radomes showed some promise, but were found to produce excessive boresight errors.

A thin metal sheet perforated with an array of dielectric-filled holes has been considered for radome construction.[31,40] Metal slats, perforated metal sheets, and grids of wires can subdivide the radome wall into waveguide channels which are capable of supporting one or more waveguide modes, and which may prevent the ordinary refracted wave from existing in the medium.[41] Certain of the waveguide modes can be matched to the incident wave more effectively than the ordinary refracted wave over a range of angles of incidence. In particular, conditions conductive to both zero reflection and zero phase shift can be achieved simultaneously with the H_{10} mode of ordinary rectangular waveguide at perpendicular polarization. Flat panels utilizing this principle have been constructed by embedding grids of fine wires which are parallel to the E vector and to the surfaces of the dielectric sheet, as shown in Figure 2-30. With this construction, the normal phase velocity and normal wave impedance can be closely matched to those of the incident wave over a wide range of incidence angles, for perpendicular polarization.[41] The properties of metal-loaded dielectric sheets have been investigated with the aid of the theory of filters, transmission lines, and waveguides.[41,42,43]

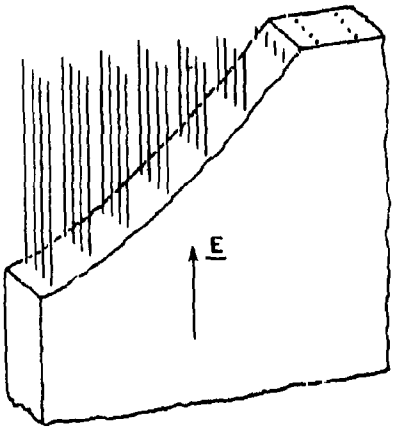


Figure 2-30. Dielectric Sheet Loaded With Wire Grids (From Reference 41 by permission of Bjorksten Research Laboratories Inc.)

Wire grid loading has been used to obtain a low reflection coefficient over a broad band of frequencies.[42]

Many of these artificial radome constructions are anisotropic. For example, a wire grid loading might allow incident waves of one polarization to travel through the dielectric sheet as though the wires were not even present, whereas they might force other waves to travel via a waveguide mode.

Anisotropic constructions are discussed in several references listed in the bibliography.

SECTION G. THE RADOME SHAPE*

Both electrical and aerodynamical considerations help govern the shape selected for a radome. The electrical design is simplified and the electrical performance improved by a smooth shape with large radius of curvature. High angles of incidence can be avoided by use of such a radome. On the other hand, at very low angles of incidence, trouble may be experienced from reflected waves which travel directly back into the antenna. The radome shape that will minimize wind resistance depends strongly on the location of the radome on the aircraft or missile. A highly streamlined shape with a fairly sharp vertex is desirable for nose radomes. Missile radomes are often figures of revolution. Shapes having simple mathematical formulas are often used, with modification near the base of the radome to fair it into the missile body. Formulas for a few of these shapes are given in this section. Radomes of four different shapes are shown in Figure 2-31 with no fairing.

If streamlining is necessary, any particular detailed shape (cone, ogive, etc.) does not appear to be superior to any other with respect to the electrical performance. (Some shapes, such as the cone, are more easily handled numerically than others.) The fineness ratio and the vertex angle (or radius of curvature at the vertex) are found to be of more significance in determining the radome boresight error. For large fineness ratios, the range of incidence angles is greater, phase front distortion tends to be greater, and the boresight error slopes tend to be greater.

In this section the following data will be given for the hemisphere, cone, log spiral, ogive, and ellipse:

a. The equation of the surface;

b. The angle of incidence of the central ray of the antenna versus look angle; and

c. The coordinate, for the point where the central ray intersects the wall, versus look angle.

All of the coordinates are for the inside surface of the radome, and the gimbal point is taken as the coordinate origin. This is not necessary but is desirable in the hemisphere and log spiral to take advantage of the angle of incidence properties.

If conical fairing is used, the conical section will start at the base of the radome and continue to the point where its slope (tan) is the same as that of the curved section. From that point on, the radome shape is that of the basic curve. The coordinate for the point at which the conical section fairs into the curved section is also given, and is denoted z_1.

As indicated in Figure 2-32, R_B is the radius at the base of the radome, and C is the distance from the base of the radome to the gimbal point. The distance from the gimbal point to the radome vertex will be denoted by the letter a.

For any radome shape, the fineness ratio F is

$$F = \frac{C + a}{2R_B} \qquad (2\text{-}148)$$

and, if conical fairing is used, the coordinate for the point at which the conical section intersects the basic curve is

$$r_1 = R_B - (C + z_1) \tan \alpha \qquad (2\text{-}149)$$

2-25. The Hemisphere

All points on the surface of a hemispherical radome are equidistant from the origin. If the antenna gimbal point is located at the origin, the central ray of the antenna will strike the radome wall with normal incidence for all look angles. This is desirable, since at normal incidence the

*Much of the material in this section is taken from: Norman M. Wiederhorn, and Alan F. Kay, "Radome Design Criteria for Precision Guidance Radar," Final Report, Contract AF 33(030) -12283, McMillan Laboratory, Ipswich, Mass., 1 June 1954, (Confidential), (AD-49 428).

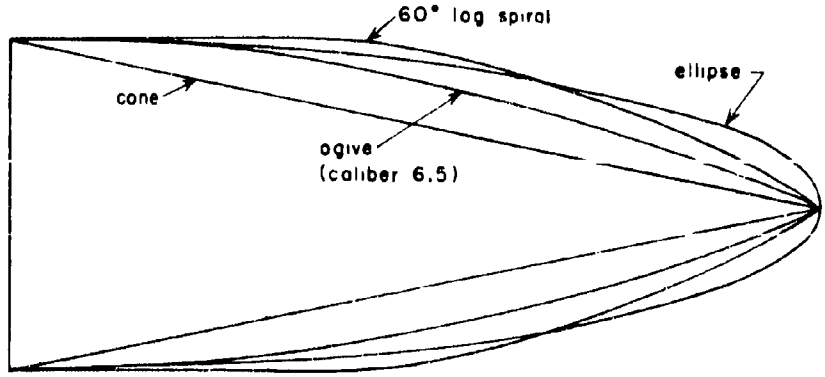


Figure 2-31. Radomes of Various Shapes, with Fineness Ratio 2.5

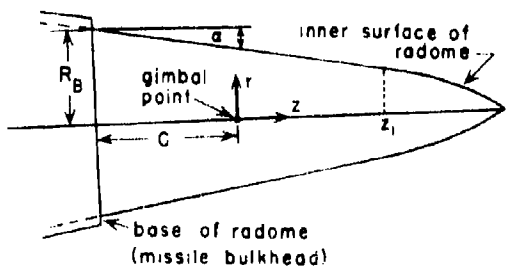


Figure 2-32. Radome with Conical Section for Fairing into Missile Body

transmission coefficients for parallel and perpendicular polarization are equal. Another desirable feature of this shape is that the range of angles of incidence that must be considered is small. However, because the angles of incidence are very small or zero, any waves reflected from the radome will travel directly back to the antenna.

Because of its symmetry, the hemisphere should produce no radome error except that due to tolerances and polarization considerations, and in fact hemispheres generally have very low crossover error rates. In conical scan systems, when the antenna is in any two opposite positions, the two surfaces of intersection of the beam and the radome wall are mirror images; therefore, if the wall is uniform, the only radome error must be due to dissymmetry in the antenna, in particular, polarization dissymmetry. The principal disadvantage of this shape is that it is not streamlined in itself. Hemispherical radomes, however, may still be utilized with streamlined missiles or airplanes without seriously impairing the aerodynamic performance, provided the radome forms the nose of a body which tapers to a diameter 5 or 10 times the radome diameter.

The equation which describes the surface of a hemispherical radome of radius a is

$$r = \sqrt{a^2 - z^2} \qquad (2\text{-}150)$$

The angle of incidence is zero for all look angles if the gimbal point is at the center of the sphere. The coordinate for the point at which the central ray of the antenna intersects the radome wall is given as a function of look angle ψ by

$$z = a \cos \psi \qquad (2\text{-}151)$$

The coordinate at which the fairing cone intersects the sphere is

$$z_1 = a \sin \alpha \qquad (2\text{-}152)$$

2-26. The Spheroid

A spheroid is the surface obtained by revolving an ellipse about one of its axes. An oblate spheroid is obtained by revolving an ellipse about its minor axis. A prolate spheroid (resembling a football) is produced when the major axis is used as an axis of revolution. Only the prolate spheroid will be considered here. The exact shape depends on the length of the semi-major axis (denoted by a) and the semi-minor axis (b), as shown in Figure 2-33. The equation for the spheroidal surface is

$$r = b \sqrt{1 - \frac{z^2}{a^2}} \qquad (2\text{-}153)$$

The angle of incidence on the radome wall is given by

$$\tan \theta = \frac{a^2 - b^2}{b^2 \cot \psi + a^2 \tan \psi} \qquad (2\text{-}154)$$

The "axial ratio" of an ellipse is defined as the ratio of the major axis to the minor axis, and is denoted by A:

$$A = \frac{a}{b} \tag{2-155}$$

Figure 2-34 shows the angle of incidence as a function of look angle for spheroidal radomes of various axial ratios.

The maximum angle of incidence is given by

$$\tan \theta = \frac{a^2 - b^2}{2ab} \tag{2-156}$$

and it occurs when the look angle is given by

$$\tan \psi = \frac{b}{a} \tag{2-157}$$

The coordinate for the point at which the central ray of the antenna intersects the radome wall is

$$z = \frac{ab}{\sqrt{b^2 + a^2 \tan^2 \psi}} \tag{2-158}$$

The fairing cone and the spheroid intersect at

$$z_i = \frac{a^2 \sin \alpha}{\sqrt{a^2 \sin^2 \alpha + b^2 \cos^2 \alpha}} \tag{2-159}$$

2-27. The Ogive

The ogive is a figure of revolution obtained by rotating an arc of a circle about an axis in the plane of the arc, as depicted in Figure 2-35. The surface of the ogive is given by

$$r = \sqrt{R^2 - z^2} + b - R \tag{2-160}$$

where R is the radius of the parent circle and b is the base radius of the ogive as in Figure 2-35. The angle of incidence on the ogive is given by

$$\sin \theta = \frac{R - b}{R} \cos \psi \tag{2-161}$$

The central ray of the antenna intersects the radome at

$$z = \left[(b - r) \sin \psi + \sqrt{(R - b)^2 \sin^2 \psi + b (2R - b)} \right] \cos \psi \tag{2-162}$$

The fairing cone and ogive intersect at

$$z_i = R \sin \alpha \tag{2-163}$$

The caliber c of an ogive is defined as the ratio of the radius of the parent circle to the base diameter of the ogive:

$$c = \frac{R}{2b} \tag{2-164}$$

Figure 2-36 gives the angle of incidence as a function of look angle for ogives of various calibers.

The distance from the origin to the radome vertex is

$$a = \sqrt{b (2r - b)} \tag{2-165}$$

2-28. The Log Spiral

The equation of the log spiral is

$$z^2 + r^2 = a^2 e^{-2 \tan \beta \tan^{-1}\left(\frac{r}{z}\right)} \tag{2-166}$$

where a is the distance between the gimbal point and the vertex of the log spiral radome, as in Figure 2-37. The expression for the log spiral is simpler in polar coordinates:

$$\rho = a e^{-\phi \tan \beta} \tag{2-167}$$

The central ray of the antenna has a constant angle of incidence on the log spiral radome, given by

$$\theta = \beta \tag{2-168}$$

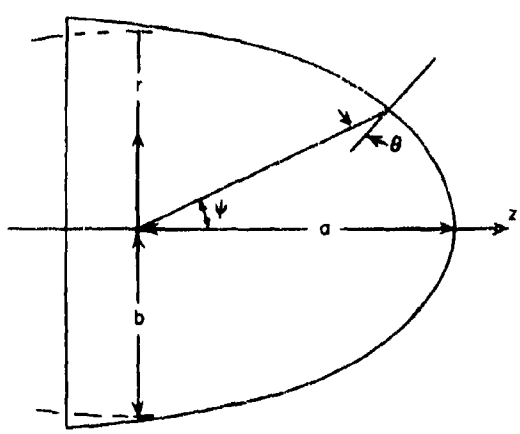


Figure 2-33. Spheroidal Radome with Conical Fairing Section

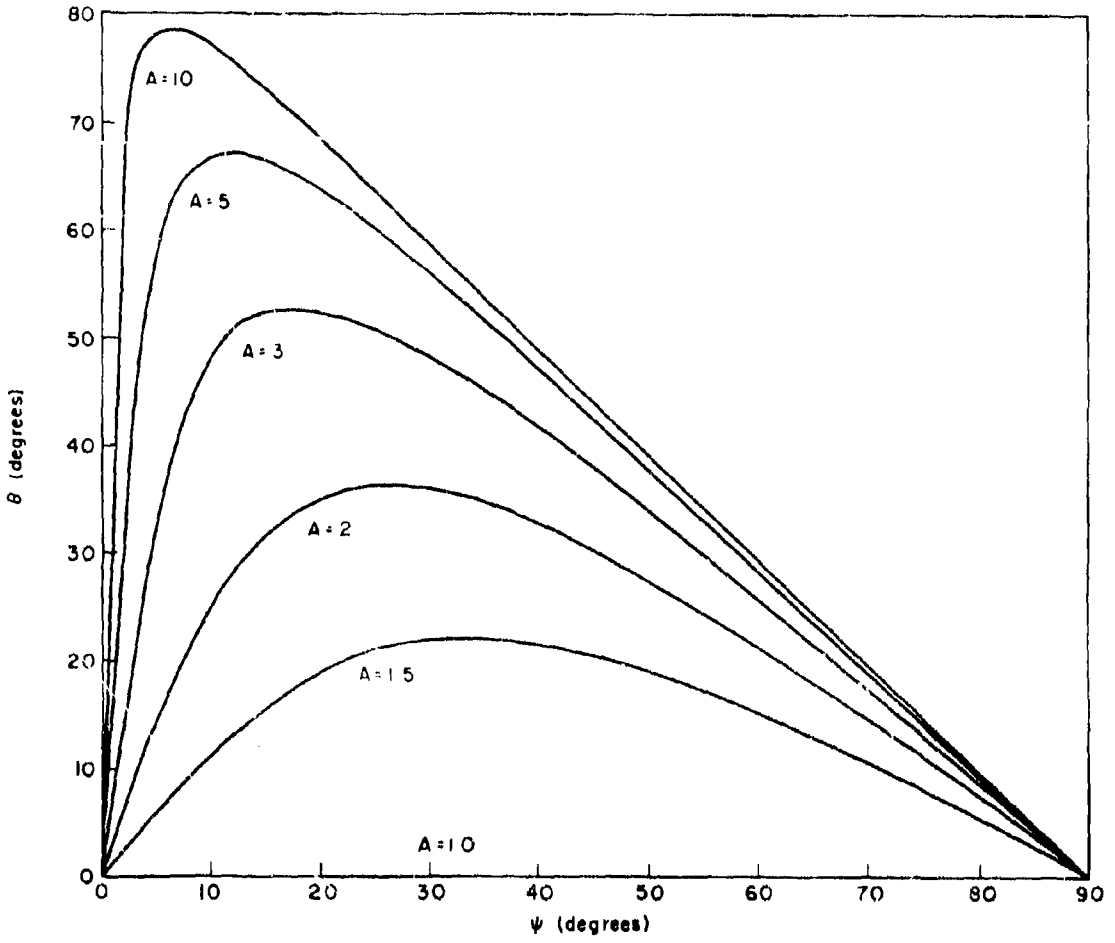


Figure 2-34. Angle of Incidence (θ) Versus Look Angle (ψ) For Spheroidal Radomes of Various Axial Ratios

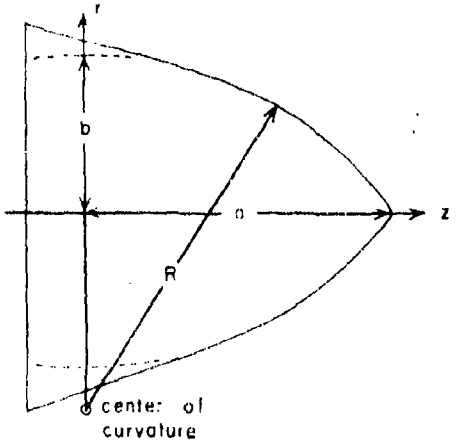


Figure 2-35. Ogive Radome with Conical Fairing

The hemispherical radome is a special case of the log spiral, since, when the angle of incidence is set equal to zero, Equations (2-166) and (2-167) become the equations of a circle of radius a.

Log spirals are designated by the value of the angle β. A "50° log spiral" is a curve specified by Equations (2-166) or (2-167) with β having the value of 50°. The r-coordinate of the log spiral is a maximum when ψ is equal to $\frac{1}{2}\pi - \beta$. The corresponding value of z is

$$z = a \sin \beta \, e^{-(\frac{1}{2}\pi - \beta)\tan \beta} \qquad (2\text{-}169)$$

The fairing will thus extend at least to this value of z. For log spirals having a large incidence angle, the fairing will extend over a large portion of the radome length.

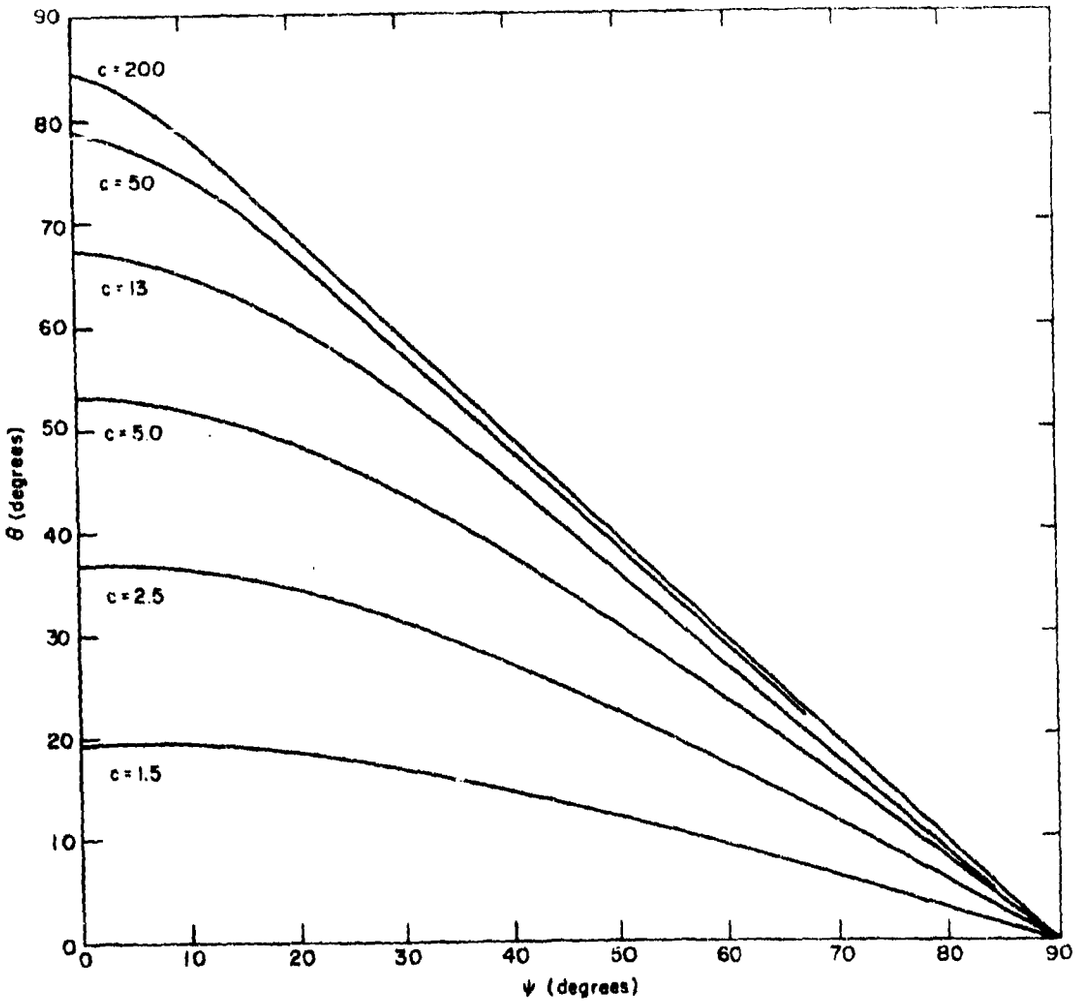


Figure 2-36. Angle of Incidence (θ) Versus Look Angle (ψ) for Ogives of Various Calibers (c)

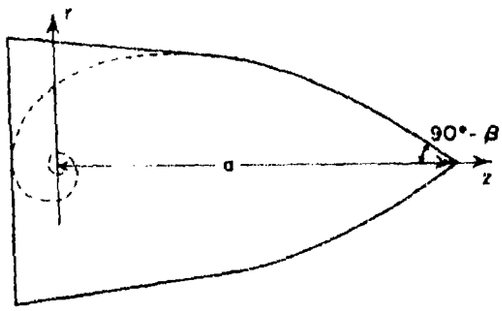


Figure 2-37. Log Spiral Radome with Conical Fairing

The central ray from the antenna intersects the radome at

$$z = a\, e^{-\psi \tan \beta} \cos \psi \qquad (2\text{-}170)$$

The conical fairing joins the log spiral at

$$z_1 = ae^{-\left(\frac{1}{2}\right)\pi - \alpha - \beta)\tan \beta} \sin (\alpha + \beta) \qquad (2\text{-}171)$$

In these equations where the angles α, β, and ψ appear in the exponent, they must be expressed in radians rather than degrees.

2-29. The Cone

The equation for a cone is

$$r = (a - x) \tan \frac{1}{2}\beta \qquad (2\text{-}172)$$

where a is the distance between the gimbal point and the vertex of the cone, as shown in Figure 2-38, and β is the total vertex angle of the cone. The angle of incidence of the central ray of the antenna on the cone is

$$\theta = 90 - \frac{1}{2}\beta - \psi \text{ degrees} \qquad (2\text{-}173)$$

Figure 2-39 shows the angle of incidence obtained with various conical radomes as a function of look angle.

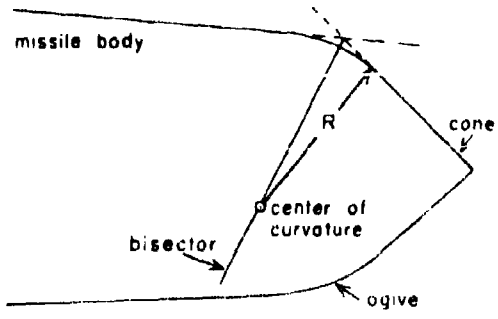


Figure 2-38. Conical Radome with Ogive Fairing

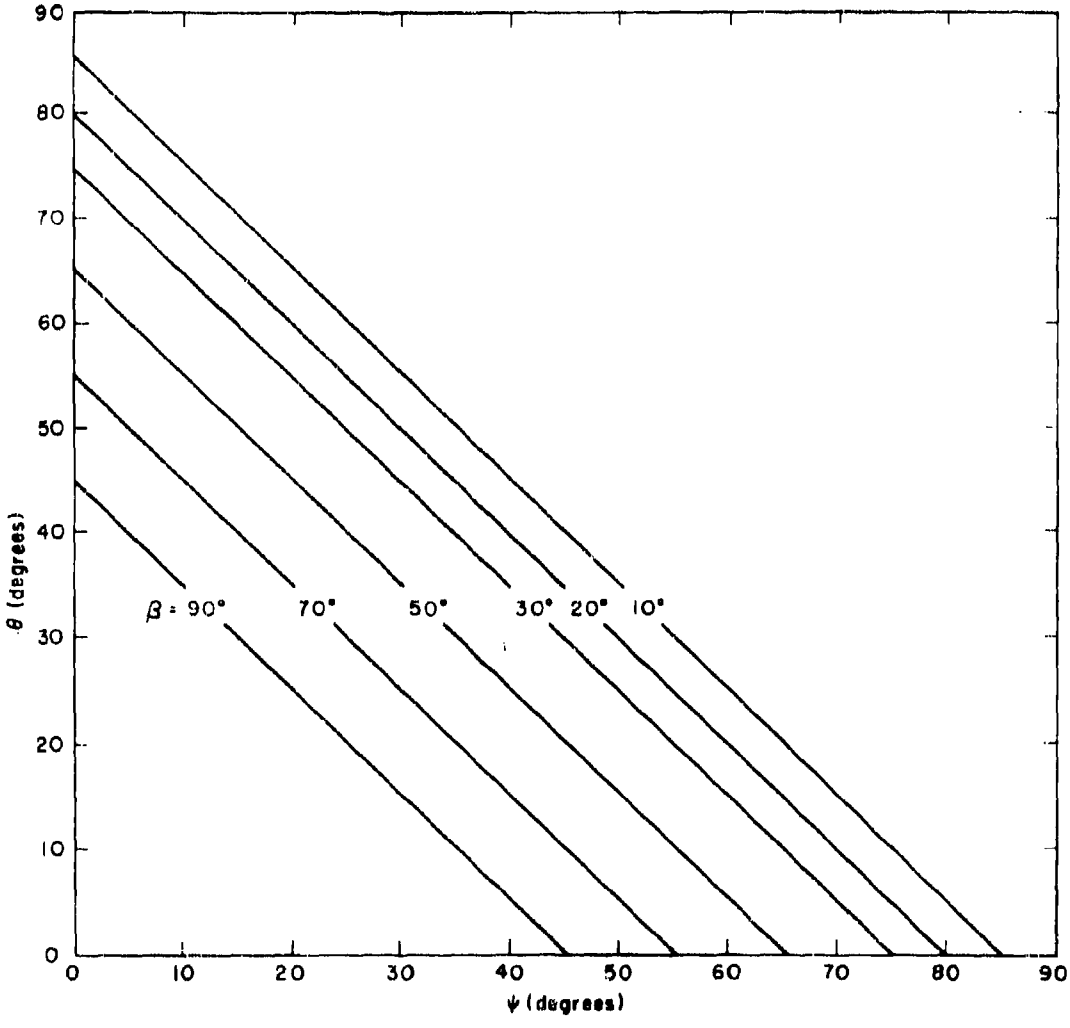


Figure 2-39. Incidence Angle (θ) Versus Look Angle (ψ) for Conical Radomes of Various Vertex Angles (β)

It is desirable to fair the radome into the missile body without any abrupt change in slope. An ogive fairing section will serve this purpose for the conical radome if the center of curvature of the ogive is located on the line which bisects the angle formed by the extensions of the conical radome and the missile body (see Figure 2-38). The coordinates of the center of curvature of the ogive are

$$z_0 = -C - R \sin \alpha \qquad (2\text{-}174)$$

and

$$r_0 = R_B - R \cos \alpha \qquad (2\text{-}175)$$

where R is the radius of curvature of the ogive. The numerical value to be used for R is governed largely by aerodynamical considerations. If R is extremely small, there will be an abrupt change in slope of the missile contour. If R is very large, the conical section of the radome will vanish and the entire radome will have the ogive shape.

The cone and ogive intersect at

$$z_1 = z_0 + R \sin \tfrac{1}{2} \beta \qquad (2\text{-}176)$$

and

$$r_1 = r_0 + R \cos \tfrac{1}{2} \beta \qquad (2\text{-}177)$$

Procedures for calculating the angle of incidence for any radome shape are given in Chapter 3. Additional information on radome shapes will be found in Chapter 3 and in several references listed in the bibliography.

SECTION H. THE FOCUSING EFFECT OF STREAMLINED RADOMES*

2-30. Refraction by Plane Sheets

A plane wave incident at angle θ on the surface of a plane dielectric sheet is refracted, and travels at angle θ_r within the dielectric medium. From Snell's law for nonmagnetic media,

$$\sin \theta_r = \frac{\sin \theta}{\sqrt{\epsilon_r}} \qquad (2\text{-}178)$$

Upon emerging from the far side on the dielectric sheet, each ray of the plane wave is again refracted so that it propagates along an axis parallel with its original line of travel, as in Figure 2-40. Thus, refraction shifts each ray a distance b perpendicular to its axis of propagation. For a plane homogeneous sheet of thickness d,

$$b = \frac{d}{\cos \theta_r} \sin (\theta - \theta_r) \qquad (2\text{-}179)$$

For a symmetrical sandwich having skin and core thicknesses d_s and d_c, and skin and core relative dielectric constants ϵ_s and ϵ_c

$$b = \left[2d_s + d_c - \left(\frac{2\, d_s}{\sqrt{\epsilon_s - \sin^2 \theta}} + \frac{d_c}{\sqrt{\epsilon_c - \sin^2 \theta}} \right) \cos \theta \right] \sin \theta \qquad (2\text{-}180)$$

Equation (2-180) can also be expressed in the same form as Equation (2-179) if d is replaced with $(2d_s + d_c)$ and θ_r is replaced with θ'_r where[17]

$$\tan \theta'_r = \left(\frac{2\, d_s}{\sqrt{\epsilon_s - \sin^2 \theta}} + \frac{d_c}{\sqrt{\epsilon_c - \sin^2 \theta}} \right) \frac{\sin \theta}{2d_s + d_c} \qquad (2\text{-}181)$$

It will be shown that refractive shift contributes to the antenna pattern distortion and direc-

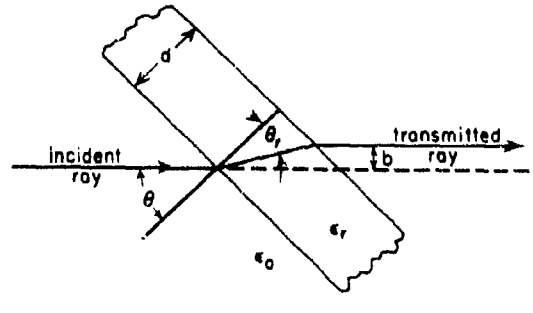


Figure 2-40. Refraction in a Plane Dielectric Sheet

*The material in this section is taken from: Jack H. Richmond, "The Focusing Effect of Radomes," Report 655-3, Contract AF33(616)-3212, Antenna Laboratory, The Ohio State University, 1 June 1956.

tional errors introduced by a radome. As pointed out in Section E, refraction can be reduced by use of magnetic radome materials if the permeability is less than that of free space, and is eliminated entirely if $\mu_r \epsilon_r = 1$. However, to obtain high transmission over a range of angles of incidence, the dielectric constant of such a nonrefracting material must be low (less than 1.6 for 80 percent power transmission), and the magnetic and dielectric loss tangents of the material must be low. These properties are not easily combined with mechanical strength.

For nonmagnetic materials, it is apparent from Equations (2-178) and (2-179) that the refractive shift cannot exceed

$$b_{max} = d \sin \theta \qquad (2\text{-}182)$$

(this maximum is approached if ϵ_r is very large), and that it is minimized by use of a thin sheet of low dielectric constant; thus, the electrically thin sheet (Section A) has the most desirable refractive properties.

No refractive shift occurs at normal incidence. To minimize refraction a radome shape approaching that of a hemisphere with large radius is desirable.

From Equations (2-179) and (2-56), for the half-wave homogeneous sheet of order n, the refractive shift (at the design angle of incidence θ_0), measured in wavelengths, is

$$\frac{b}{\lambda_0} = \frac{n \sin (\theta_0 - \theta_r}{2 \sqrt{\epsilon_r} \cos^2 \theta_r} \qquad (2\text{-}183)$$

Consequently, the refractive shift is proportional to the order of the half-wave sheet, so that the lowest usable order is desirable. It can be shown, from Equation (2-183), that the refractive shift in a half-wave sheet vanishes as the relative dielectric constant approaches unity or infinity. For arbitrary fixed values of n, λ_0, and θ_0, the refractive shift at the design angle in a half-wave sheet has maximum value

$$\frac{b_{max}}{\lambda_0} = \frac{n \tan \theta_0}{8} \qquad (2\text{-}184)$$

and it reaches this maximum value when the dielectric constant is

$$\epsilon_r = 1 + 3 \cos^2 \theta_0 \qquad (2\text{-}185)$$

Figure 2-41 shows the refractive shift produced by a first-order, half-wave sheet for an angle of incidence of 70° as a function of the dielectric constant of the sheet. It is seen that the refractive shift is maximum when the dielectric constant is 1.35, and that it can be made as small as desired by using a sufficiently small or sufficiently large dielectric constant. Figure 2-42 shows the maximum refractive shift which can be produced by a first-order, half-wave sheet as a function of the angle of incidence. Grazing incidence, of course, must be avoided if the refractive shift is to be kept small. Figure 2-43 shows the dielectric constant that produces maximum refractive shift in a half-wave sheet at various angles of incidence. To avoid refraction effects, it is desirable to use a dielectric constant much larger or much smaller than the value given in Figure 2-44 for the design angle of incidence.

2-31. Focusing Effect of Radomes

Refraction can produce a focusing effect which causes the effective aperture area of an antenna

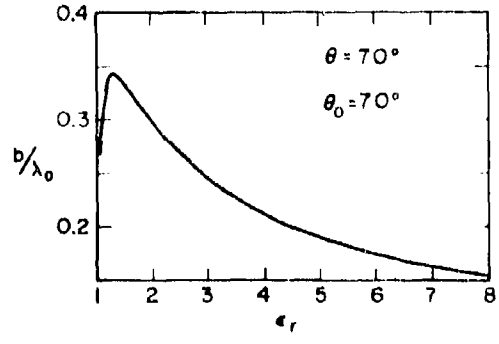


Figure 2-41. Refractive Shift Produced by First-Order, Homogeneous, Half-Wave Sheet for an Angle of Incidence of 70°

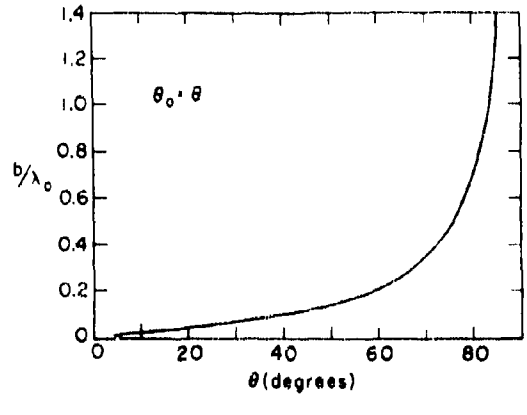


Figure 2-42. Maximum Refractive Shift Which Can Be Produced by First-Order, Homogeneous, Half-Wave Sheet

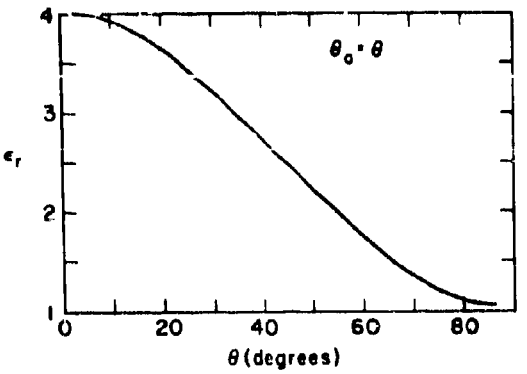


Figure 2-43. Dielectric Constant which Produces Maximum Refractive Shift in Homogeneous, Half-Wave Sheet

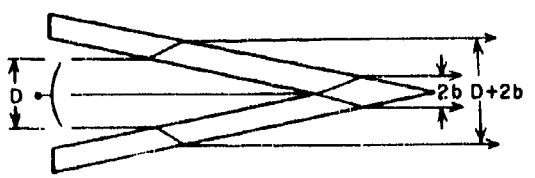


Figure 2-44. Refraction in a Conical Radome

to be greater with radome than it is without the radome.[17] For example, consider a paraboloidal antenna transmitting through a conical radome, as in Figure 2-44, with the antenna axis coinciding with the radome axis. Suppose the antenna transmits a well-collimated beam of diameter D without radome. With the radome in place, refraction will increase the beam diameter to D + 2b, and will introduce a shadow zone of radius b at the radome vertex. The ratio of the aperture area A' with radome to the aperture area without radome is

$$\frac{A'}{A} = 1 + \frac{4b}{D} \qquad (2\text{-}186)$$

Here we are considering the antenna aperture to be a section of an imaginary plane which passes through the radome vertex and is perpendicular to the radome axis.

It seems reasonable to assume that the total transmitted power with radome will be the same as without radome, if we consider only the refraction caused by the radome and ignore for the moment other effects such as reflection, absorption, and depolarization. Usually the klystron or magnetron is isolated from the antenna sufficiently to prevent appreciable changes in its frequency or power output when the radome is introduced, especially if the radome reflects very little power back toward the antenna. To keep the total radiated power unchanged when the radome is introduced, the power density in the aperture must decrease when the radome is put in position, since the aperture area increases. For example, if the aperture illumination is uniform in the absence of the radome, the power density ρ' (watts/area) with radome is given in terms of the power density ρ without the radome by

$$\rho' = \frac{(r - b)}{r}\rho, \text{ for } b < r < \frac{1}{2}D + b \qquad (2\text{-}187)$$

Equation (2-187) is an optical approximation obtained by considering the power passing through each small unit of aperture area with and without radome. In Equation (2-187), r is the radial distance from the radome vertex to any point on the aperture plane. The field distribution obtained from Equation (2-187) is shown in Figure 2-45.

The relative far-field pattern of a uniformly illuminated aperture of diameter D is[44]

$$E(\phi) = \frac{J_1\left(\frac{1}{2}\beta D \sin\phi\right)}{\sin\phi} \qquad (2\text{-}188)$$

where ϕ is the far-field angle measured from the antenna axis, and J_1 is the first-order Bessel function. If the antenna diameter D is much larger than the refractive shift b, the effects of the vertex shadow zone and the intensity taper, Equation (2-187), will be small, and the major effect will be the increase in

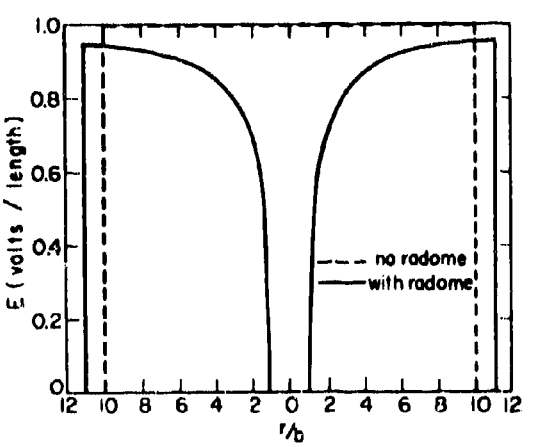


Figure 2-45. Calculated Near-Field Amplitude with Uniform Collimated Beam Passing Through Conical Radome

aperture diameter from D to D + 2b. The antenna pattern with radome is then approximately

$$E(\phi) \propto \frac{J_1\left[\frac{1}{2}\beta\,(D + 2b)\sin\phi\right]}{\sin\phi} \qquad (2\text{-}189)$$

Since the beam width between half-power points for a large, uniformly illuminated, circular aperture of diameter D is[44]

$$\text{B. W.} \approx \frac{58\lambda_0}{D} \text{ degrees} \qquad (2\text{-}190)$$

the decrease in beam width produced by focusing effect is

$$\Delta\ \text{B. W.} \approx 58\lambda_0 \frac{2b}{D\,(D + 2b)} \text{ degrees} \qquad (2\text{-}191)$$

If the vertex shadow zone and the intensity taper are considered, the decrease in beam width will be somewhat greater than that given by Equation (2-191)

The far-field radiation intensity on the antenna axis is thus increased by the focusing effect if the total radiated power is unchanged by the radome and if only the refraction is considered. When the antenna is used as a receiver, the focusing effect will also increase the power delivered to its terminals (when the distant source is on axis) by increasing the effective aperture area.

The focusing effect also occurs in rounded radomes such as the hemisphere, although in this case no well-defined shadow zone is produced.

If the antenna axis does not coincide with the radome axis, the vertex shadow zone will no longer be located at the center of the aperture, and the refractive shift will differ for rays passing through the radome at different points. This is true because the refractive shift is a function of the angle of incidence.

The importance of the vertex shadow zone produced by refraction is roughly proportional to the ratio of the aperture area that is lost in the shadow zone to the total aperture area; thus, the pattern distortion and radome error associated with the shadow zone may be expected to be less serious when using a large antenna than when using a small antenna.[45]

The focusing effect has also been observed with wedge-shaped radomes constructed of two flat sheets that come together to form a sharp edge. The shadow zone in this case produces much more pattern distortion than in the case of the conical radome. This is true because the shadow zone in the case of the wedge is a long rectangular strip of width 2b, whereas in the case of the conical radome it is a circle of diameter 2b. The percentage of antenna aperture area which is obscured by the shadow zone is much greater for the wedge than for the conical radome. A decreased beam width has been observed with wedge radomes as well as with radomes which are figures of revolution.

The boresight error produced by the shadow zone at the vertex of a sharp-nosed radome is studied in Reference 46. From a simplified and approximate analysis, it was estimated that in practical radomes "refraction displacement can be generally ignored."

To verify the existence of the vertex shadow zone, the fields have been measured near the radome shown in Figure 2-46 with the horn transmitting. The radome consisted of two flat sheets forming a 30° wedge, as shown. Amplitude and phase measurements were made along the y-axis which passes through the radome vertex perpendicular to the radome axis. The antenna axis coincided with the radome axis. The measurements with and without radome are shown in Figures 2-47 and 2-48. (The far-field diffraction associated with refraction in this radome is indicated by comparing Figures 2-53 and 2-55.) Figure 2-47 shows the vertex shadow zone quite strikingly. The measurements also show the effects of the rather low transmission coefficient of the plane sheets which comprised the radome, as well as the interference between the direct transmitted rays and rays reflected from the plane sheets. In Figure 2-48 it is noted that the phase is strongly retarded in the vertex shadow zone. Measurements on several sharp-nosed missile radomes have shown the same general appearance as that in Figures 2-47 and 2-48.

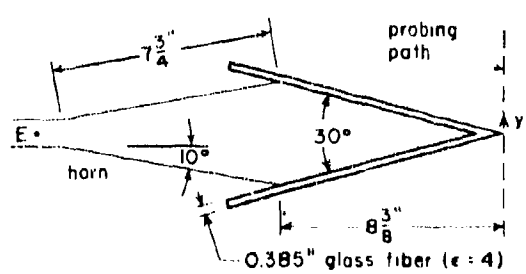


Figure 2-46. Horn Antenna With Wedge-Shaped Radome

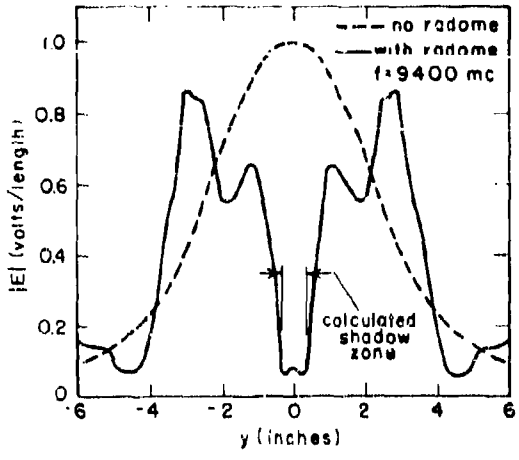


Figure 2-47. Measured Near-Field H-Plane Amplitude of Horn Antenna with and without Wedge-Shaped Radome

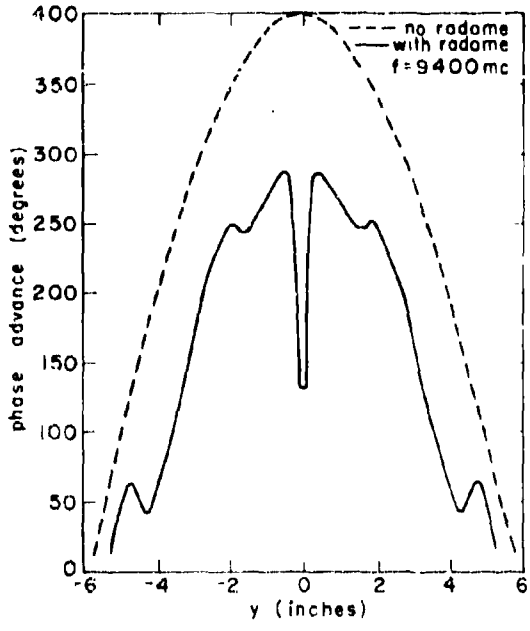


Figure 2-48. Measured Near-Field H-Plane Phase of Horn Antenna with and without Wedge-Shaped Radome

Additional discussion of the focusing effect and refraction will be found in several references listed in the bibliography.

SECTION I. DIFFRACTION BY RADOMES

The effects of a radome on an electromagnetic wave include refraction, reflection, attenuation, and change of phase. The far-field pattern of an antenna is altered by the presence of a radome. The distortion may include beam shift, change in beam width, and change in total radiated power. The radome phenomena which contribute to the pattern distortion include focusing effect (see Section H), Lloyd's mirror effect, wave trapping, depolarization, and radome-antenna interaction. The total effect is denoted by the word "diffraction." It has been shown[46] that the total field distortion produced by a radome is the algebraic sum of the perturbations contributed by all the distortion-producing phenomena acting separately, provided the individual perturbations are sufficiently small; thus, in dealing with a well-designed radome, its various effects can be evaluated separately, before adding them up to determine the net result. When the individual effects are relatively large, however, the total distortion may include interaction effects among the various primary sources of distortion.

Several approaches to the analysis of diffraction by obstacles are described in Chapter 10 and in References 47 and 48. A method for calculating diffraction by radomes is given in Chapter 13.

A useful device for measuring radome diffraction is a wave-front plotter such as one used at Cambridge Air Force Research Center. A number of phase contour maps obtained with this instrument are included in Reference 49 to demonstrate vividly the Lloyd's mirror effect.

Similar phase contour maps can also be obtained by use of a water ripple analogue.[50,51] The antenna is simulated by a directive source of water ripples. The radome is simulated by an obstacle of the same shape as the radome cross section, submerged a distance under the water depending on the dielectric constant to be simulated. Photographs are then taken by allowing the ripples to focus light on a sheet of film. Diffraction of the water ripples is found to resemble closely the electromagnetic diffraction. This technique has been used to investigate conventional missile radomes[52] as well as streamlined versions of the Luneberg lens.[53] It is especially convenient in obtaining information on the effects of changes in such parameters as frequency, dielectric constant, and antenna-radome spacing.

2-32. Exact Formulations

The exact solution has been obtained for the fields of an infinitesimal dipole of arbitrary location and orientation inside a spherical radome.[54,55] This problem was solved by applying the boundary conditions at the inner and outer surfaces of the radome. The solution is expressed as an infinite series involving spherical Bessel functions and associated Legendre functions. The tables of these functions are being extended to permit numerical calculations for a number of spherical radomes.

The fields set up by a plane wave incident normally on an infinitely long, hollow, dielectric cylinder of circular cross section and uniform wall thickness are solved rigorously as a boundary value problem in Reference 56. The number of radome shapes which can be analyzed by the boundary-value method is, however, severely limited.

The fields of an antenna with radome can be expressed in terms of their values on some reference surface S which lies outside the radome. Let $\underline{E}$ and $\underline{H}$ be the electric and magnetic field intensities of the antenna transmitting through the radome. Choose a surface S which completely separates the space containing the antenna and radome from the space where it is desired to compute the fields. (See Figure 2-49, for example.) If the region on the source-free side of S is free space, the field at any point P in this region is given by[60]

$$\underline{E}(P) = \frac{-\nabla \times \underline{F}}{\epsilon_0} - \frac{j}{\omega \epsilon_0 \mu_0} \nabla \times \nabla \times \underline{A} \qquad (2\text{-}192)$$

where

$$A(P) = \frac{\mu_0}{4\pi} \int_S (\underline{n} \times \underline{H}) \frac{e^{-j\beta_0 r}}{r} ds \qquad (2\text{-}193)$$

and

$$\underline{F}(P) = \frac{\epsilon_0}{4\pi} \int_S (\underline{E} \times \underline{n}) \frac{e^{-j\beta_0 r}}{r} ds \qquad (2\text{-}194)$$

Here $\underline{n}$ is a unit normal which points toward the source-free region, and r is the distance from the element of area ds to the point P. The differentiation indicated in Equation (2-192) is with respect to the coordinates of point P.

The problem is simplified if S is chosen to be an infinite plane, in which case

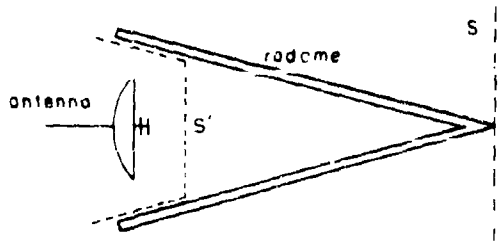


Figure 2-49. Reference Surfaces S and S' Which Might be Used In Radome Calculations

$$\underline{E}(P) = -\frac{2}{\epsilon_0} \nabla \times \underline{F} \qquad (2\text{-}195)$$

$$= \frac{-2j}{\omega \epsilon_0 \mu_0} \nabla \times \nabla \times \underline{A} \qquad (2\text{-}196)$$

Additional simplification can be accomplished as follows, if it is required to calculate only the far fields of the antenna with radome.

Let S be the xy-plane, and let spherical coordinates r_0, θ, and ϕ specify the location of point P, as in Figure 2-50. The distant radiation field will have θ- and ϕ-polarized components given, from Equations (2-194) and (2-195), by[79]

$$E_\theta = \frac{j\beta_0 e^{-j\beta_0 r_0}}{2\pi r_0} \int_S (E_x \cos\phi + E_y \sin\phi) \, e^{j\beta_0 (x \cos\phi + y \sin\phi) \sin\theta} \, dx \, dy \qquad (2\text{-}197)$$

and

$$E_\phi = \frac{j\beta_0 e^{-j\beta_0 r_0}}{2\pi r_0} \cos\theta \int_S (-E_x \sin\phi + E_y \cos\phi) \, e^{j\beta_0 (x \cos\phi + y \sin\phi) \sin\theta} \, dx \, dy \qquad (2\text{-}198)$$

where E_x and E_y are the x- and y-polarized components of the field on S.

In using Equations (2-197) and (2-198), it is necessary first to determine the fields E_x and E_y existing on S when the antenna is transmitting through the radome. Approximate methods such as ray-tracing and plane-wave, plane-sheet theory are often employed for this purpose. These may give satisfactory calculations if the

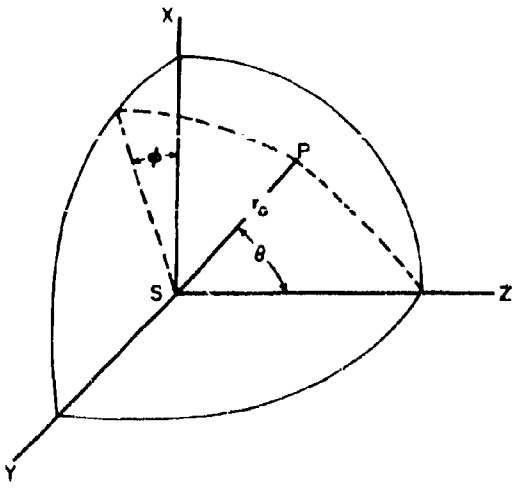


Figure 2-50. Coordinate System for Radome Calculations

antenna has a well collimated beam and if the radome has no regions of high curvature. The task of describing transmission through the radome of the complicated Fresnel-zone fields can be traded for the simpler problem of analyzing the transmission of a plane wave through the radome.[61, 62] Let S' be any surface which completely encloses the antenna and passes between the antenna and the radome, as in Figure 2-49, for example. Let $\underline{E}_1$ and $\underline{H}_1$ represent the fields existing on S' when the antenna is transmitting without radome. These fields can be obtained by measurements even if the radome has not yet been constructed. Now consider the antenna as a receiving antenna, cover it with the radome, and let $\underline{E}_2$ and $\underline{H}_2$ be the fields existing on S' when a plane wave is incident from a distant source. To determine $\underline{E}_2$ and $\underline{H}_2$ it is necessary to analyze the transmission of the plane wave through the radome, including any reflections from the antenna. (If the radome is available, these fields might be obtained by direct measurements, of course.) If the antenna terminals are located in a waveguide or transmission line which supports only a single mode, impedances Z_g (looking toward the generator) and Z_l (looking toward the load) can be defined. Let I denote the current flowing through the terminals when the antenna is transmitting without radome. Then the voltage V induced at the antenna terminals by the incident plane wave is [61, 62]

$$V = \frac{-Z_g}{(Z_g + Z_l)\, I} \int_{S'} (\underline{n} \times \underline{H}_2 \cdot \underline{E}_1 - \underline{E}_2 \times \underline{n} \cdot \underline{H}_1)\, ds \qquad (2\text{-}199)$$

The unit vector $\underline{n}$ is normal to surface S'. The far-field pattern of the antenna with radome can be obtained by calculating the voltage V with Equation (2-199) for plane waves incident from several different directions. This formulation of the radome analysis problem has been tested successfully on simplified "radomes" consisting of finite plane sheets. It was found that reflections from the antenna can often be neglected in determining $\underline{E}_2$ and $\underline{H}_2$ without excessive loss of accuracy.

The radome analysis problem can be set up in another form by defining the following fields:

a. $\underline{E}_1$, $\underline{H}_1$ is the field existing when the antenna is transmitting without radome,

b. $\underline{E}$, $\underline{H}$ is the field existing when the antenna is transmitting with radome, and

c. $\underline{E}_S$, $\underline{H}_S$ is the "scattered field" of the radome, such that

$$\underline{E} = \underline{E}_1 + \underline{E}_S \qquad (2\text{-}200)$$

The field equations for the scattered field are obtained by writing Maxwell's curl equations for the total and incident fields and subtracting, yielding: [58]

$$\nabla \times \underline{E}_S = -j\omega\mu_0 \underline{H}_S \qquad (2\text{-}201)$$

and

$$\nabla \times \underline{H}_S = j\omega\epsilon_0 \underline{E}_S + j\omega(\epsilon - \epsilon_0)\underline{E} \qquad (2\text{-}202)$$

Equation (2-202) can be written

$$\nabla \times \underline{H}_S = \underline{J}_S + j\omega\epsilon_0 \underline{E}_S \qquad (2\text{-}203)$$

$$\underline{J}_S = j\omega(\epsilon - \epsilon_0)\underline{E} \qquad (2\text{-}204)$$

$$= \begin{cases} j\omega(\epsilon_1 - \epsilon_0)\underline{E} & \text{in region v} \quad (2\text{-}205) \\ 0 & \text{outside v} \quad (2\text{-}206) \end{cases}$$

where ϵ_1 is the dielectric constant of the radome material, and v is the region of space occupied by the radome. Thus, the scattered field can be thought of as the field generated by current $\underline{J}_S$ flowing in free space. This current is the sole source of scattered radiation. The scattered field at any point P outside region v is given by

$$\underline{H}_S = \frac{1}{\mu_0} \nabla \times \underline{A}_S \qquad (2\text{-}207)$$

and

$$\underline{E}_S = \frac{\nabla \times \nabla \times \underline{A}_S}{j\omega \epsilon_0 \mu_0} \qquad (2\text{-}208)$$

where

$$\underline{A}_S = \frac{\mu_0}{4\pi} \int_v \underline{J}_S \frac{e^{-j\beta_0 r}}{r} dv \qquad (2\text{-}209)$$

where r is the distance between the element of volume dv and point P. The differentiation indicated in Equations (2-207) and (2-208) is with respect to the coordinates of point P.

When magnetic radome materials are used, a magnetic polarization current $\underline{K}_S$ also contributes to the scattered field, where[57]

$$\underline{K}_S = j\omega(\mu - \mu_0)\underline{H} \qquad (2\text{-}210)$$

If the electric or magnetic loss tangent of the radome material is not zero, the polarization currents are modified by letting ϵ_1 or μ_1 become complex, as mentioned in Sections A and E of this Chapter.

If it is required to find the scattered field only at points a great distance from the radome, simplified expressions can be obtained from Equations (2-208) and (2-209). Let J_x, J_y, and J_z be the rectangular components of the polarization current $\underline{J}_S$. Then the distant scattered field has θ- and ϕ-polarized components given by[79]

$$E_{S\theta} = \frac{j\omega\mu_0 e^{-j\beta_0 r_0}}{4\pi r_0} \int_v (-J_x \cos\theta\cos\phi - J_y \cos\theta \sin\phi + J_z \sin\theta)$$

$$e^{j\beta_0 (x \sin\theta\cos\phi + y\sin\theta\sin\phi + z\cos\theta)} \, dx\,dy\,dz$$

$$E_{S\phi} = \frac{j\omega\mu_0 e^{-j\beta_0 r_0}}{4\pi r_0} \int_v (J_x \sin\phi - J_y \cos\phi) \qquad (2\text{-}212)$$

$$e^{j\beta_0 (x \sin\theta\cos\phi + y\sin\theta\sin\phi + z\cos\theta)} \, dx\,dy\,dz$$

where r_0, θ, and ϕ are the spherical coordinates of point P at which the scattered field is being observed.

Once the scattered field $\underline{E}_S$ has been computed, it must be added to the incident field $\underline{E}_1$ to determine the pattern of the antenna with radome; see Equation (2-200). Generally the far-field amplitude pattern of the antenna without radome is available, but in using the polarization-current method it is also necessary to know the far-field phase pattern, since phasor addition is implied in Equation (2-200).

The chief difficulty encountered in using the polarization-current method is that the field $\underline{E}$ in the dielectric radome material is unknown. If the antenna has a well-collimated beam and if the radome has no regions of high curvature, plane-wave, plane-sheet theory might be used to approximate $\underline{E}$ with sufficient accuracy. Again, however, the information contained in the Lorentz reciprocity theorem can be employed to trade this problem for the simpler one of determining the fields induced in the radome material by a plane wave incident on its outer surface. The data required to compute the voltage V_S induced at the antenna terminals by the polarization currents in the radome are:[79]

a. The total electric field intensity $\underline{E}^t$ induced in the radome by an incident plane wave, including any reflections from the antenna; and

b. The electric field intensity $\underline{E}_1$ existing when the antenna is transmitting without radome.

As before, the polarization current $\underline{J}_S$ given by Equation (2-204) (with $\underline{E}$ replaced by $\underline{E}^t$) is the source of the scattered field. Again, let Z_g be the impedance at the antenna terminals looking toward the generator, Z_l the impedance at the terminals looking toward the load, and I the current flowing through the terminals when the antenna is transmitting without radome. The voltage induced at the terminals by radome scattering is[79]

$$V_S = \frac{-Z_g}{(Z_g + Z_l) I} \int_v \underline{E}_1 \cdot \underline{J}_S \, dv \qquad (2\text{-}213)$$

The integration is carried out through the volume v occupied by the radome.

If V_1 denotes the voltage induced at the antenna terminals by the plane wave without radome, the total voltage V_t induced by the plane wave with radome is

$$V_t = V_1 + V_S \qquad (2\text{-}214)$$

The far-field pattern of the antenna with radome is determined by computing V_t for plane waves incident from several different directions. V_1 is the far-field pattern of the antenna without radome, and is often available from measurements. Since V_1 and V_S are complex quantities, phasor addition is implied in Equation (2-214).

2-33. Diffraction by Dielectric Bodies of Simple Shape

To explain the phenomena of transmission through radomes, studies, in addition to those already mentioned, have been made of several idealized dielectric bodies. The boresight error produced by large flat sheets is studied in Reference 63. Antenna pattern distortion by large flat sheets is considered in References 61 and 62, with the following result.

Consider an antenna with a plane dielectric sheet (as in Figure 2-51). If interaction between the sheet and the antenna is negligible, it can be shown, from Equation (2-206) that the far-field pattern $E'(\phi)$ with dielectric sheet is related to the pattern $E(\phi)$ without dielectric sheet by

$$E'(\phi) = T(\phi)\, E(\phi) \qquad (2\text{-}215)$$

where $T(\phi)$ is the plane-wave plane-sheet transmission coefficient for angle of incidence ϕ and for the polarization appropriate to the particular antenna considered. No assumption was made regarding the distance between the antenna and the dielectric sheet; thus, Equation (2-215) is applicable to the measurement of plane-wave, plane-sheet transmission coefficients in systems where the sheet is in the Fresnel zone of one antenna but in the far zone of the other antenna.

Plane-wave diffraction by a thin, plane, semi-infinite dielectric sheet is derived in Reference 64. The far-field distortion produced by a finite plane dielectric sheet placed near the aperture of an antenna is considered in References 61 and 62. Diffraction of surface waves by a semi-infinite dielectric sheet is investigated in Reference 65. The boresight error produced by a solid dielectric wedge is considered in References 59 and 66.

The beam shift was calculated by determining the approximate insertion phase variation along the wedge from plane-wave, plane-sheet theory. The thin, solid wedge is also investigated in Reference 63. An approximate expression for the beam tilt produced by a wedge is obtained by considering the multiple reflections within the wedge. It is found that the beam shift produced by the wedge is a function of the thickness of the wedge at the point where the beam enters it. It is also dependent on the plane of polarization of the incident wave.

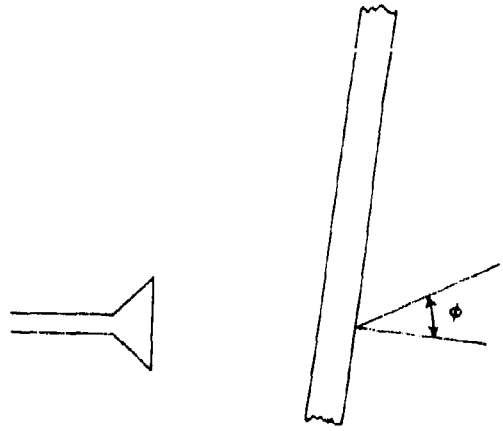


Figure 2-51. Antenna With Large, Flat, Dielectric Sheet

The hollow dielectric wedge formed of two plane sheets has been studied in a number of reports.[59] The boresight error of the wedge-shaped radome is considered in Reference 66 and 67. The beam-shift calculations are based on the calculated insertion phase shift produced by the sheets. Generally the angles of incidence for the two sheets are different, and as a result phase front distortion is produced by the difference in insertion phase shift for the two sheets.

In References 45 and 68, the field distortion produced by wedge-shaped radomes is shown by phase and amplitude measurements. It is shown that in the Fresnel region the field distortion can be reproduced by a pair of equivalent Huygen's sources located near the vertex of the wedge.

In reference 69 the field distortion by the wedge-shaped radome of Figure 2-52 is investigated. The measured far-field patterns with and without radome are shown in Figure 2-53. At a slightly lower frequency where the transmission coefficient is maximum, the measured pattern was almost the same as in Figure 2-53, indicating that the pattern distortion is not associated with reflection in this case. Figure 2-53 also shows the calculated pattern obtained by integration of the measured near-fields shown in Figures 2-47 and 2-48. Attempts were also made to calculate the far-field pattern without

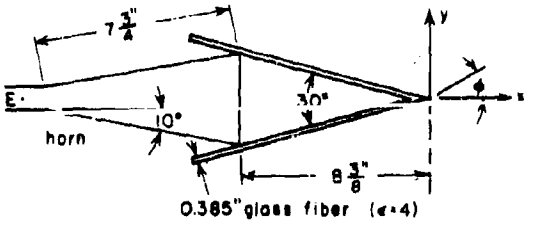


Figure 2-52. Antenna With Wedge-Shaped Radome (From Reference 69 by permission of Ohio State University)

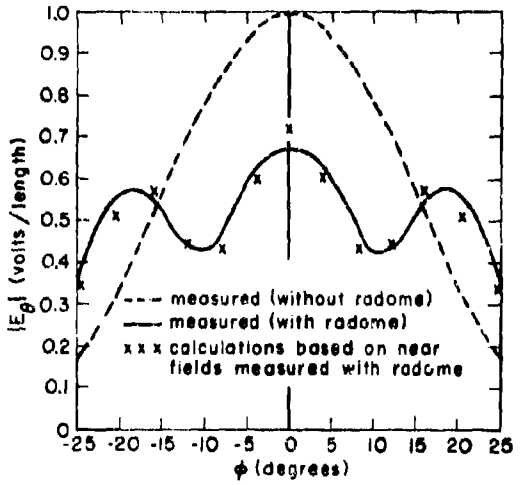


Figure 2-53. Measured and Calculated H-Plane Patterns of Antenna With Wedge-Shaped Radome (By permission of Ohio State University)

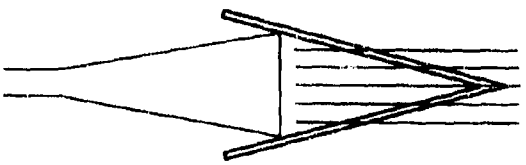


Figure 2-54. Parallel-Ray Model of Transmission Through a Radome (From Reference 69 by permission of Ohio State University)

the aid of these measured near fields. The simplest approximation to the wedge radome problem is suggested in Figure 2-54, in which parallel rays are pictured as traveling from the antenna through the radome. Here the only effect of the radome is to change the amplitude and phase of each ray according to the plane-wave, plane-sheet transmission coefficient for the appropriate angle of incidence. While this simple model may serve quite well in some situations, it yielded unsatisfactory calculations in this case, as shown in Figure 2-55. Much better results were obtained by taking into account the refractive shift of each ray as it passes through the radome (Figure 2-56), as shown in Figure 2-57. Since a small, broad-beam antenna was being used, it was believed that a further increase in accuracy could be obtained by taking into account the ray curvature. This was done by using the measured ray map shown in Figure 2-58. The resulting calculations, including the effects of the transmission coefficient, refraction, and ray curvature, are shown in Figure 2-59.

The chief remaining sources of error in the calculations are believed to be:

a. The use of plane-wave, plane-sheet theory to describe transmission through the radome, especially near its vertex;

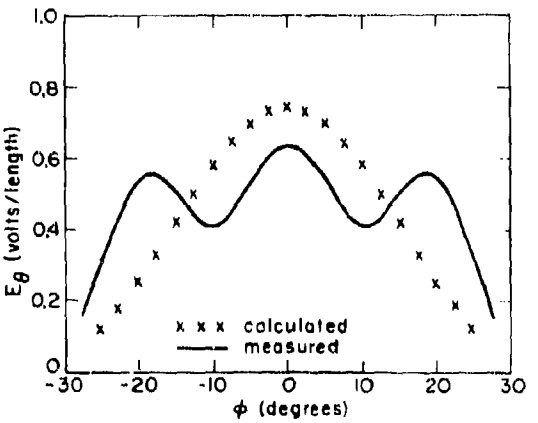


Figure 2-55. Measured and Calculated H-Plane Far-Field Patterns of Antenna with Wedge-Shaped Radome, Using Parallel-Ray Theory (By permission of Ohio State University)

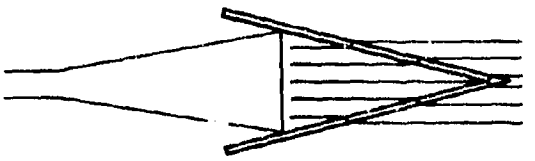


Figure 2-56. Parallel-Ray Transmission Through Radome Showing Refraction (From Reference 69 by permission of Ohio State University)

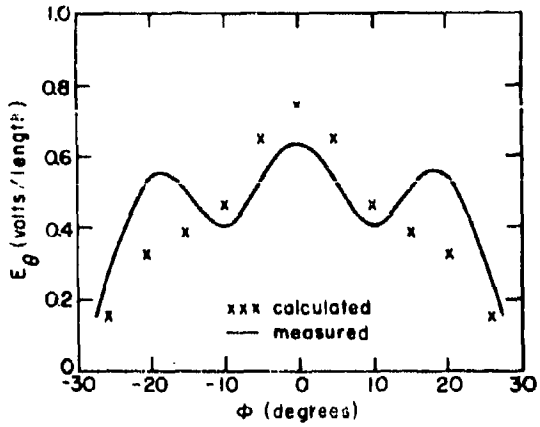


Figure 2–57. Calculated Fields of Antenna with Wedge-Shaped Radome, Using Parallel–Ray Theory and Refraction (From Reference 69 by permission of Ohio State University)

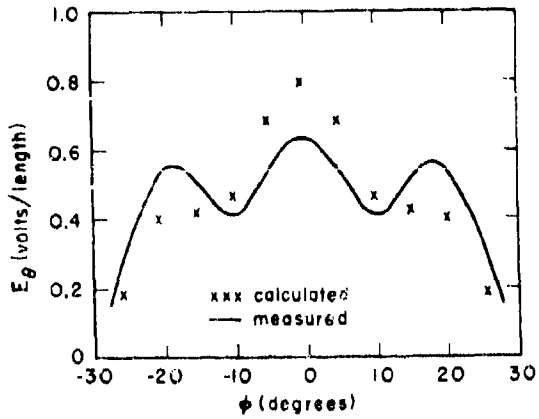


Figure 2–59. Calculations for Wedge Shaped Radome, Using Energy Flow Map and Refraction Theory (From Reference 69 by permission of Ohio State University)

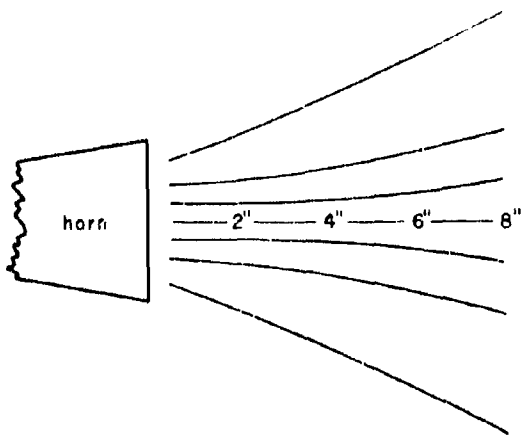


Figure 2–58. Measured H–Plane Energy Flow Map for Horn Antenna at 9400 megacycles (From Reference 69 by permission of Ohio State University)

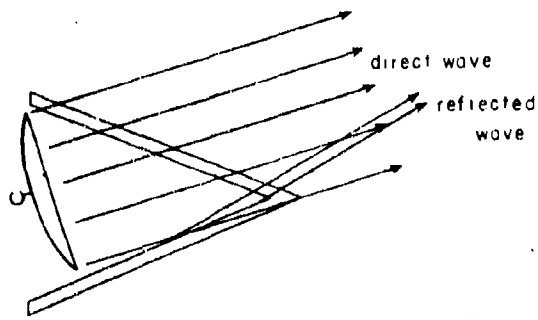


Figure 2–60. Lloyd's Mirror Effect on a Radome

b. The use of optical ray theory to project the fields from one reference surface to another; and

c. The use of approximations in numerical evaluation of the double integral appearing in the far-field pattern expression.

The wedge radome results just described are for perpendicular polarization. At parallel polarization much less pattern distortion was produced. The chief effect of the radome in this case was to reduce the beam width, as discussed in Section H.

2-34. Lloyd's Mirror Effect[59]

Waves reflected from the radome walls may arrive in phase with the main beam at one distant point, and out of phase at some other point. The interference between the direct and reflected waves, illustrated in Figure 2-60, is refered to as the Lloyd's mirror effect.

The reflected wave carries less power than the main beam, since the reflection coefficient of radome walls is small. The reflected beam is likely to be broader than the main beam.

Although the reflected beam is not aimed in the same direction as the main beam, some overlapping of the two beams may occur, especially at certain look angles. When the antenna axis coincides with the radome axis, the reflected waves may produce nothing more than side lobes. At look angles large enough so that the beam clears the radome vertex, the reflected beam is aimed in such a direction that it is not likely to overlap the main beam. At intermediate look angles, the Lloyd's mirror effect will be maximum. At such angles, the main and reflected beams are aimed in nearly the same direction. Furthermore, at such look angles the angle of incidence may be quite high on a portion of the radome, and this may result in a rather high reflection coefficient. The Lloyd's mirror effect is, of course, minimized if the reflection coefficient is kept small. It is also minimized by keeping the effective reflecting area small compared with the antenna aperture area.

Reflection is responsible for much of the near-field distortion shown in Figure 2-47 and 2-48. This was deduced by comparing these figures with measurements obtained with one sheet of the wedge-shaped radome removed. In the far-field patterns obtained with the same radome, side lobes are observed as a result of this reflection. In Figure 2-53, these side lobes were displaced too far from the main beam to show up.

The boresight error produced by the Lloyd's mirror effect is analyzed in References 49 and 59.

2-35. Antenna-Radome Interaction[59]

In blunt-nosed radomes some energy reflected from the radome can travel back to the antenna, and contribute to diffraction after reflection from the antenna. The radome error produced by this phenomenon tends to be sensitive to small changes in position of the antenna gimbal point. Such interaction has been observed with blunt radomes and with flat sheets near normal incidence. This effect is minor in high-incidence radomes where the reflected waves do not tend to travel back toward the antenna.

2-36. Trapped Waves[59]

A sheet of dielectric may serve as a waveguide for the propagation of energy in a direction parallel to the surface of the sheet.[70] Such "trapped waves" can propagate along a solid sheet or sandwich, no matter how thick or thin it may be. The fields associated with a trapped wave extend outside the dielectric sheet, but decrease exponentially in amplitude with distance from the dielectric. A trapped wave loses no energy to radiation in regions where the sheet is flat, but does radiate in regions of high curvature. Trapped waves are most likely to be excited if the clearance between the antenna and the radome wall is small and if the angle of incidence is large. The energy taken out of the primary beam in this manner will travel along in the radome wall until at some point near the vertex the increasing curvature will allow it to reradiate. The effect on the far-field pattern and the boresight shift depends on the amount of power carried by the trapped wave and the pattern in which it is reradiated. The reradiation pattern depends on the radome shape. Trapped waves are likely to have minor effect in radomes having adequate clearance between antenna and radome.

Trapped waves are studied in several references listed in the bibliography.

SECTION J. STREAMLINED LENS-RADOMES*

The conventional antenna used with a radome is a paraboloidal dish and feed. The feed serves as a source of spherical waves and the dish focuses or collimates this energy into locally plane waves which travel out into space. Electrically, the radome serves no useful purpose and is designed to produce minimum effect on the fields. A focusing element of another type occasionally used instead of the dish is a dielectric lens. Because the lens action of radomes has frequently been observed, it seems natural to ask if it is not possible to combine the function of the dielectric housing (the radome), and the antenna focusing element into a single unit, a "lens-radome."

In a certain sense, lens-radomes have been used. Any time a dielectric lens is used in a flush-mounted application or without a radome, the focusing and housing functions are being performed by a single component. Such appli-

*This section is a condensation of: Alan F. Kay, "Streamlined Lens-Radomes," (Technical Research Group, New York, N. Y.), W.A.D.C.-O.S.U. Radome Symposium, June 1956.

cations, however, are not the ones in which radomes have difficult problems; for one thing, until recently, lens-radomes have not been streamlined. Their exterior surfaces have been flat, almost flat, or at most, spherical.

2-37. The Luneberg Lens

An example of the latter is the Luneberg lens (Figure 2-61). The Luneberg lens is a spherically symmetric lens whose relative dielectric constant varies from a maximum of 2 at the center to unity on the outer surface following the law

$$\epsilon_r = 2 - \left(\frac{r}{a}\right)^2 \qquad (2\text{-}216)$$

where a is the radius. On the basis of geometrical optics, a point source placed on the surface of the Luneberg lens is focused into a plane collimated beam. Because of the spherical symmetry, the beam will scan throughout all space without distortion if the source traverses the surface of the lens appropriately.

Lunebergs have been built and tested at many laboratories and have been found to operate well in the microwave range up to frequencies above X-band. A proof that geometrical and physical optics are quite accurate for the Luneberg lens has been obtained by H. Jasik,[11] who gives an exact solution of radiation from both a dipole and an omnidirectional source on the surface of a Luneberg lens. Jasik compared this solution with the physical optics solution and found no practical difference for the main lobe and the first side lobes for a lens as small as 2 1/2 wavelengths in diameter. Unlike conventional radomes, a Luneberg lens has a slowly varying dielectric constant. There are no discontinuities and the maximum dielectric constant is relatively small.

2-38. Streamlined Lens

The Luneberg lens, however, is not streamlined. It would be desirable to develop an axially symmetric lens-radome with fineness ratio as high as 3 to 1, capable of scanning to $\pm 45^{\circ}$, for applications where there are weight, strength, thermal, and erosion problems, as well as electrical transmission and boresighting requirements.

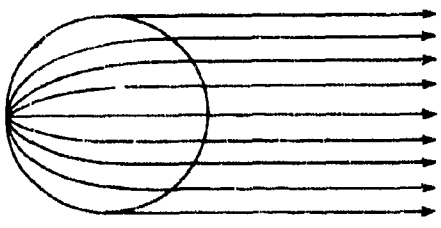


Figure 2-61. Luneberg Lens and Ray Map

Certain theoretical considerations, as well as the weight of experience, show that only the Luneberg lens and certain modifications of it that are also spherically symmetrical can achieve perfect focusing for a range of scan angles. Therefore, only designs which focus approximately throughout a scanning range will be considered. A two-dimensional analysis in the plane of the feed offset is sufficient to show that most design approaches are unsatisfactory. A number of design procedures have been considered. A particular type of dielectric constant variation was considered first, then some criterion of focusing and scanning was employed such as two- or three-point correction or the Abbe sine condition, and then the ray paths were determined. These analytical attempts were abandoned for one or more of the following reasons: inadequate streamlining, computational complexity, inadequate scanning range, or impractical values of dielectric constant.

2-39. Design Approach

The approach which proved most successful is the reverse of the analysis procedure. It begins by choosing a field of curves which, if they were rays, would mean good focusing and scanning properties. Then a dielectric constant variation is "synthesized" in such a way that the rays associated with it are the chosen curves. The desirable focusing and scanning properties are thereby realized.

For example, suppose we would like the outer surface of the lens-radome to be aspheroid with semi-major axis a, and axial ratio A as in Figure 2-62. The fineness ratio can be chosen as large as desired. Now we want a family of rays which focus and imply some scanning ability. We choose a family of ellipses, for a number of reasons:

1. They focus; that is, they all start from the axial feed point and emerge at the outer surface of the lens parallel to the axis.

2. They satisfy the Abbe sine condition. This condition implies that when the feed point is moved off the axis for a short distance the beam will scan and the lens will continue to focus those rays in the plane shown, as well as the rays leaving the source and entering the lens in all directions in space.

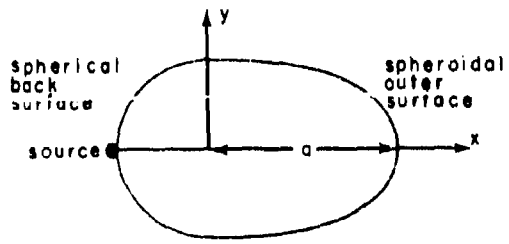


Figure 2-62. Spheroidal Lens-Radome

3. When A is unity, this design reduces to the ordinary Luneberg lens.

Now how do we determine a dielectric constant variation which actually makes the elliptical curves into rays? In a design by analysis one would know the dielectric constant and desire to find the ray paths. Here we have the ray paths and desire to determine the dielectric constant. We first find the orthogonal trajectories of the rays; these are the wave fronts. This can be done numerically or by the simple graphical means of starting at a point on the outer lens surface and, with the aid of triangles, tracing by eye a curve which intersects each successive ray at right angles. The graphical method has proved quick, simple, and accurate for this problem.

Next, the dielectric constant is found, as follows. Let s denote arc length along a particular wave front. We take a pair of dividers with a fixed small spacing Δs, and lay off a series of equidistant points, say 1, 2, ..., j, on the wave front, the first point being at the outer surface. Then the relative dielectric constant ϵ_j at point j is found from Equation (2-217)

$$\ln \epsilon_j = \ln \epsilon_0 + (\kappa_0 + \kappa_j + 2\sum_{i=1}^{j-1} \kappa_i)\Delta s \qquad (2\text{-}217)$$

where κ_i is the radius of curvature of the rays, and κ_i is obtained by interpolation from the values of curvature of the rays near point i. Equation (2-217) is obtained by integrating Equation (14), on page 112 of Reference 44 and applying the trapezoidal rule. ϵ_0 is the dielectric constant on the outer surface and is arbitrary. In this way, we determine ϵ on each wave front and repeating for all the wave fronts we have ϵ at a set of points covering the whole lens. By interpolation we determine contours of constant dielectric constant, the "isofracts." This method was tested with the Luneberg lens, and it gave the correct result with an accuracy in $\sqrt{\epsilon}$ of ± 0.005 or better.

This method has been used to design a spheroidal lens having an axial ratio A of 2, as well as an ogival lens having an overall fineness ratio of about 2:1 and a surface dielectric constant of 1.04. If the surface dielectric constant is chosen greater than unity, then refraction will take place at the boundary; this must be accounted for in the equations for the rays. While the method still applies in principal, difficulty is experienced near the nose. In view of the requirements of focusing, the Abbe sine condition, and a large fineness ratio, if we ask for a surface dielectric constant of 1.4 or greater, then the thickness, through which a dielectric constant appreciably greater than unity prevails, turns out to be so thin that it seems just as satisfactory and much simpler to work with an $\epsilon_0 = 1$ design to begin with and then add a thin, high dielectric constant layer to the outer surface. The error introduced thereby may be partially compensated later.

2-40. Manufacture of Lens

Let us turn now to some practical considerations. How would one make such a lens? To answer this question we examine the technology developed for the Luneberg lens; for example, one suitable for X-band or lower frequencies. It has been found satisfactory to approximate the dielectric constant gradient by 10 homogeneous concentric spherical shells. The loss tangent must be less than 0.01, but dimensional tolerances are half the thickness of the layer and are no problem at all. Luneberg lenses are now available commercially from at least three places. Methods of manufacture differ: the layers may be machined or molded in matched dies, they may be made of polyfoam of various densities, perhaps loaded with conducting particles, or of a ceramic foam; or they may be artificial dielectric.

All these techniques apply equally well to the streamlined lens-radomes. As an illustration of cost, it is estimated that a single experimental model of either the blunt or streamlined shape, held to tolerances, and made by machining, would cost $7,000. If matched dies were used, the cost would be much higher, especially since the layers are not spherical.

Two practical problems are transmission loss and weight. Table 2-II shows the estimated maximum transverse diameter in wavelengths for a streamlined lens-radome for a 3-db and a 1-db maximum transmission loss for three typical materials. Table 2-II also gives the weight of the lens-radome for two diameters and the same materials.

It appears that loaded materials are likely to be far too lossy but that unloaded materials may be too heavy; or, alternatively, a small lens-radome should have no loss or weight problem, but a large lens-radome would probably require an unusually low-loss, lightweight foam to be feasible.

2-41. Lens Feeding

Feeding the lens is another problem. Table 2-III shows the maximum feed aperture diameter versus the lens radius, based on physical optics and the Raleigh criterion.

The Abbe sine condition does not guarantee a large amount of scanning. How do these lenses behave off axis? Can they scan to 45°? To answer these questions, ripple tank model studies have been made. Although the scanning range appears to be at least ±30°, this study is still in progress and definite conclusions cannot be stated at this time (June 1956). Additional discussion of lenses and lens-radomes will be found in the references listed in the bibliography.

Table 2-II. Lens-Radome Weight and Transmission Loss

Material	Maximum diameter, wavelengths		Weight, lbs.	
	for 3-db loss	for 1-db loss	diameter 5 inches	diameter 30 inches
1. Polystyrene foam	444	148	0.89	193
2. Loaded polyfoam	6.3	2.1	0.22	48
3. Ceramic foam	133	44	0.71	154

Table 2-III. Feed Aperture Diameter Versus Lens Radius

Lens Radius in Wavelengths	Maximum Feed Diameter in Wavelengths	
	λ/8 Criterion	λ/16 Criterion
3	0.58	0.33
4.8	0.84	0.48
6	1.0	0.58
10	1.45	0.87
18	2.16	1.34
30	3.0	1.92
50	4.1	2.68

SECTION K. RADOMES FOR MILLIMETER WAVELENGTHS*

2-42. Difficulties At Millimeter Wavelengths

A number of difficulties arise in designing a radome for use at millimeter wavelengths. At wavelengths from 1 to 10 mm (frequencies from 30 to 300 kmc), the electrically thin radome would be only a few thousandths of an inch thick. Even the first-order half-wave homogeneous sheet or sandwich becomes too thin and weak at millimeter wavelengths. Sufficient strength might be obtained with a first-order half-wave wall by pressurization. This technique has been proposed for thin-wall missile radomes at X-band.[72]

As the wavelength decreases, the permissible tolerance Δd in wall thickness decreases, as given (for the half-wave sheet) by Equation (2-82):

*The material in this section is taken from: Jack H. Richmond and David C. Stickler, "Radomes for Millimeter Wavelengths," Report 655-4, Contract AF 33(616)-3212, Antenna Laboratory, The Ohio State University, August 1956.

$$\Delta d = \frac{\lambda_0 \sqrt{\Delta T_\perp^2 \cos \theta}}{2\pi(\epsilon_r - 1)} \qquad (2\text{-}218)$$

Thus, at a wavelength of 5 millimeters the thickness tolerance is only one-sixth as large as at 3 centimeters, for a given permissible loss in power, given angle of incidence, and dielectric constant.

At the higher frequencies where first-order half-wave walls become too thin, one might consider the use of second-order (full-wavelength) or higher order walls. For a given dielectric constant and design angle of incidence, the higher order homogeneous flat sheets have several disadvantages in comparison with the first-order half-wave sheet, including the following.

a. The permissible tolerance $\Delta\epsilon_r$ in dielectric constant decreases as the order n increases, as given by Equation (2-83):

$$\Delta\epsilon_r = \frac{2\sqrt{\Delta T_\perp^2}\,(\epsilon_r - \sin^2\theta)^{3/2}\cos\theta}{n\pi(\epsilon_r - 1)} \qquad (2\text{-}219)$$

b. The loss in transmission at the design angle of incidence increases almost in direct proportion with n; for example, if the sheet is designed for normal incidence, the loss in power transmission due to dielectric losses is, by Equation (2-57):

$$\Delta T^2 \approx \frac{\epsilon_r + 1}{2\sqrt{\epsilon_r}} n\pi \tan\delta \qquad (2\text{-}220)$$

Thus, in constructing the higher order half-wave sheets it becomes more important to use low-loss radome materials.

c. The refractive shift b is proportional to n, as given by Equation (2-183):

$$\frac{b}{\lambda_0} = \frac{n \sin(\theta_0 - \theta_r)}{2\sqrt{\epsilon_r}\cos^2\theta_r} \qquad (2\text{-}221)$$

The refractive shift is never greater than the thickness of the radome wall itself. The refractive shift will therefore probably be no greater in a millimeter radome than in any other radome; however, the diameter of the vertex shadow zone (Section H) may amount to several wavelengths at the higher frequencies. In this case, the far-field diffraction pattern associated with the shadow zone may become quite directive, thus introducing pattern distortion and system errors.

d. The performance over a given range of angles of incidence deteriorates as n increases.

e. The performance over a given range of frequencies deteriorates as n increases.

2-43. Disadvantages of Higher-Order Half-Wave Walls

The decreased performance over a range of angles of incidence can be illustrated by reference to Figure 2-63. Assuming a lossless radome material with a dielectric constant of 4, suppose it is desired to choose a wall thickness to make $T_\perp^2$ as constant as possible for all angles of incidence from 0 to 80°. From Figure 2-63, this requires a thickness of 0.302 free-space wavelengths for the (modified) first-order sheet or 0.592 wavelengths for a second-order sheet. The power transmission coefficients obtained in the two cases are about 0.83 and 0.67, respectively.

As another example, suppose we wish to choose a wall thickness to maximize the minimum $T_\perp^2$ over the range of angles of incidence from 0 to 80°. From Figure 2-63, this requires a thickness of 0.283 or 0.565 wavelengths for a first- or second-order sheet, respectively. The minimum power transmission coefficients obtained in the two cases are 0.937 and 0.760, respectively.

Or, consider the problem of minimizing the variation in insertion phase shift for angles of incidence between 0 and 85°. From Figure 2-64, this requires a thickness of about 0.23 or 0.53 wavelengths. The variation in insertion phase delay is 0.18 or 1.18 radians, respectively.

In this particular case ($\epsilon_r = 4$, $\tan\delta = 0$, perpendicular polarization, homogeneous flat sheet), if the thickness is chosen to maximize the minimum transmission, to minimize the variation in transmission, or to minimize the variation in phase shift, the second-order sheet provides much poorer results than the first-order. The third-order sheet is even worse.

Now, we may wish to use a compromise design which, for the given range of angles of incidence, will sacrifice performance on each of the individual design criteria in hopes of obtaining better overall characteristics. The compromise thickness must be somewhere between 0.230 and 0.302 wavelengths for the half-wave sheet, or between 0.530 and 0.592 wave-

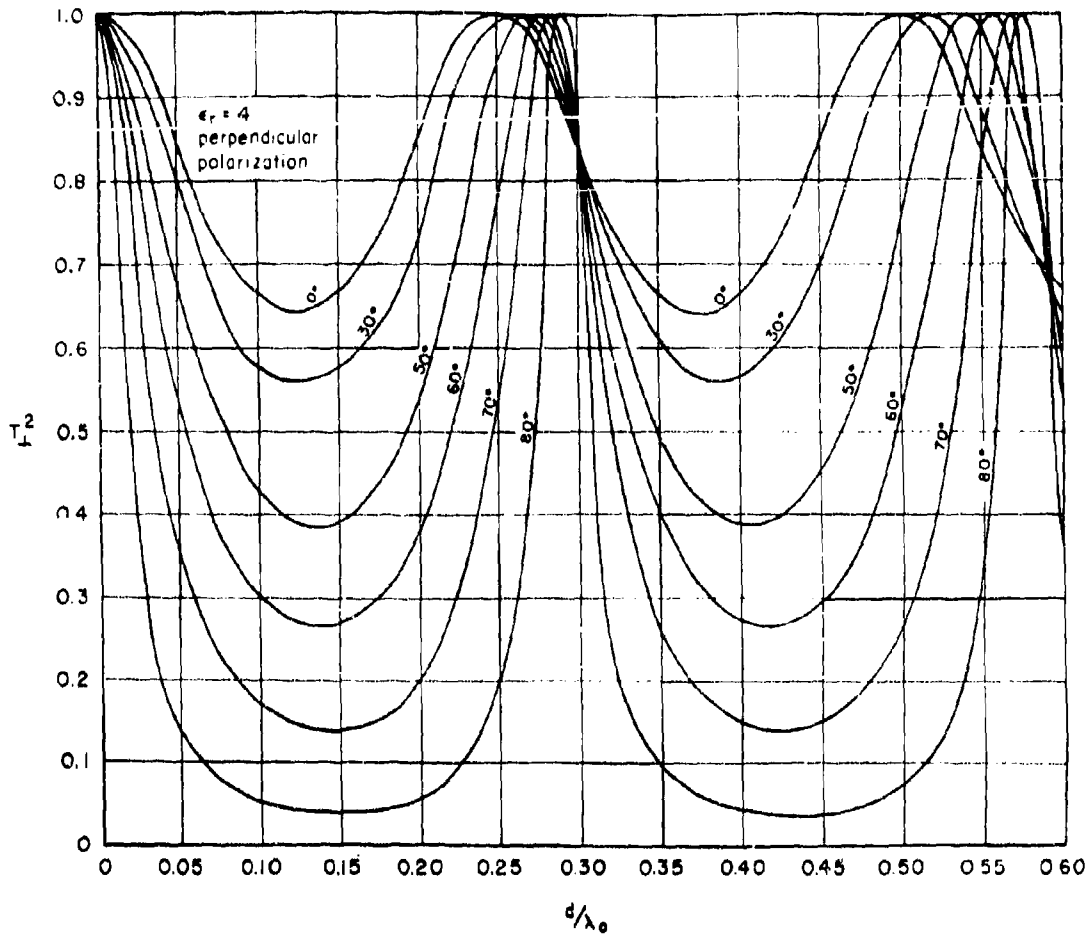


Figure 2-63. Power Transmission Coefficient for a Lossless Plane Dielectric Sheet (From Reference 6 by permission of U. S. Naval Air Development Center, Johnsville, Pennsylvania)

lengths for the full-wave sheet. It is apparent, after a closer study of Figures 2-63 and 2-64, that a compromise full-wave sheet will be substantially poorer than a compromise half-wave sheet. The same conclusions are reached by studying curves for homogeneous sheets of other dielectric constants.

It was stated that the bandwidth over which good performance is obtained decreases as the order of the half-wave homogeneous flat sheet is increased. This can be illustrated by referring again to Figure 2-63. Assume a lossless material with dielectric constant of 4. If the design angle of incidence is zero degrees, the thicknesses of first- and second-order sheets, measured in free-space wavelength at the design frequency, will be

$$\frac{d_1}{\lambda_0} = 0.25 \qquad (2\text{-}222)$$

and

$$\frac{d_2}{\lambda_0} = 0.50 \qquad (2\text{-}223)$$

respectively. At the design frequency and angle of incidence, perfect transmission is obtained in both sheets. Now, consider the performance at a somewhat lower frequency where the free-space wavelength is, say,

$$\lambda_0' = 1.2\lambda_0 \qquad (2\text{-}224)$$

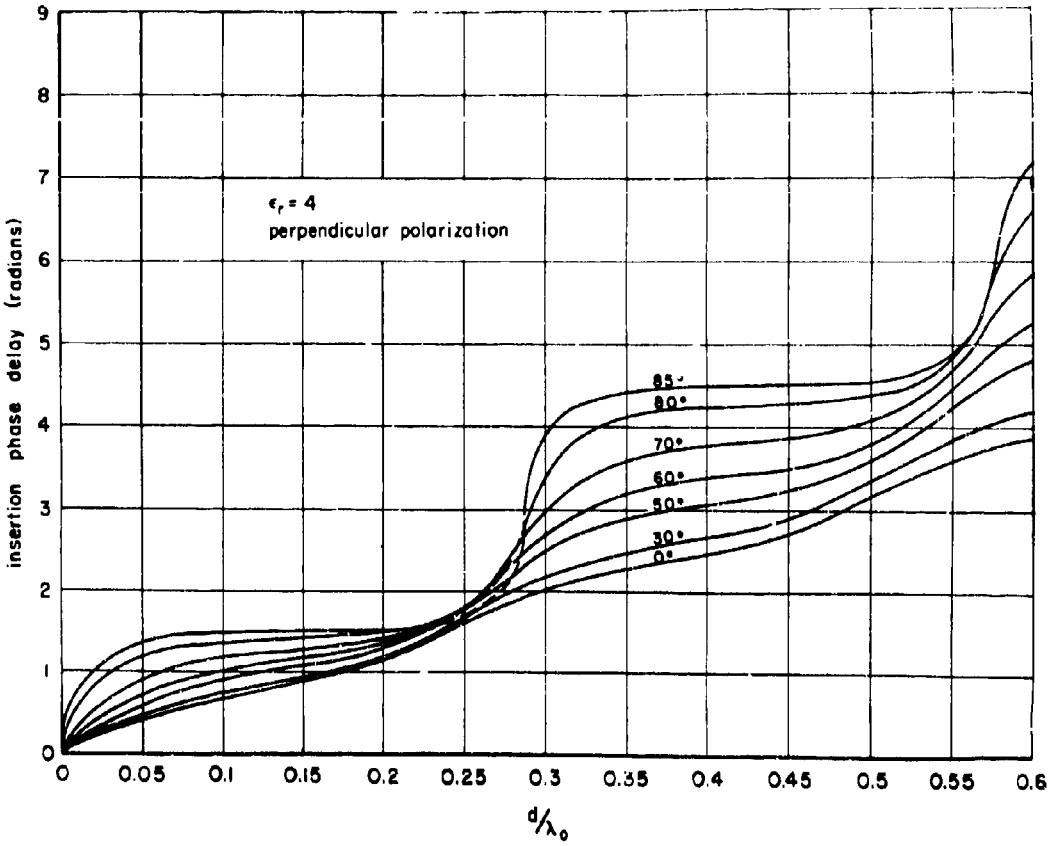


Figure 2-64. Insertion Phase Delay Through a Lossless Plane Dielectric Sheet (From Reference 6 by permission of U. S. Naval Air Development Center, Johnsville, Pennsylvania)

The thicknesses, in terms of the free-space wavelength, become

$$\frac{d_1}{\lambda_0'} = 0.206 \qquad (2\text{-}225)$$

and

$$\frac{d_2}{\lambda_0'} = 0.416 \qquad (2\text{-}226)$$

From Figure 2-63, at the new frequency the power transmission coefficients of the first- and second-order sheets drop to 0.888 and 0.700, respectively; thus, the higher order sheets are more narrow banded.

It appears that all the pertinent electrical properties of the homogeneous half-wave flat sheet become worse as the order is increased. When a higher order sheet must be used to obtain sufficient strength, poorer radome performance must be expected unless, for example, the fineness ratio of the radome is reduced or the antenna beam width is decreased. No easy solution to this problem is known.

2-44. Techniques Used In Infrared Systems

We might inquire how this problem is overcome in the "irdome" (radome for infrared systems). At a wavelength of 2 microns (1 millimeter = 1,000 microns), an irdome wall thickness of 0.5 centimeters with a dielectric constant of 2 yields a half-wave wall of order 7,070 for normal incidence. As the angle of incidence is raised, the order rapidly decreases, becoming 7,000 at 11.5°, and 5,000 at grazing incidence, Equation (2-56). The same effect is produced by a change in frequency.

For example, at normal incidence the order is changed from 7,070 to 7,000 by changing the free-space wavelength from 2 microns to 2.02 microns; thus, the transmission coefficient varies rapidly through alternate maxima and minima as the frequency or angle of incidence is varied.

A variation in thickness of this irdome of only 0.001 inch will change its order by 36, assuming normal incidence. A dielectric constant increase to 2.01 will increase the order by 18. Obviously, if the irdome were to be used with an infrared system employing a single wavelength, it would introduce severe beam tilt, depolarization, and reflection. The permissible tolerances in wall thickness, shape, dielectric constant, and frequency would be fantastically small. These difficulties are avoided by using a band of frequencies, with wavelengths extending from, say, 1 to 5 microns. Although the irdome may have poor transmission for some of the frequency components, it will have good transmission for others. The average transmission coefficients over the range of frequencies may be quite high if low-loss materials are used, the dielectric constant is low, and thin skins of lower dielectric constant are used to reduce reflection.[73,74,75] Furthermore, the average transmission coefficient may be nearly constant over a range of incidence angles.

Depolarization loses much of its significance in the infrared system, since the generators and detectors are usually unpolarized (randomly polarized). Insertion phase shift loses much of its importance since the infrared radiation is incoherent (randomly phased). These considerations also apply to optical systems, such as the human eye, with, for example, a glass window pane serving as a "radome."

In view of the difficulties encountered in designing a millimeter radome, especially at the shorter millimeter wavelengths, it may be advantageous to adapt some of these infrared techniques to the millimeter wavelengths. For example, consider a lossless, homogeneous sheet, one-half inch thick, to be used at a wavelength of 2.54 millimeters: then, d/λ_0 is 5, and the transmission coefficient is as shown in Figure 2-65, assuming a dielectric constant of 4. Figure 2-66 also shows the transmission coefficient for the same sheet at a slightly different wavelength, λ_0', where d/λ_0' is 5.14.

The transmission coefficient at each of these wavelengths varies excessively versus angle of incidence. Suppose, however, a radar system were designed to employ both wavelengths simultaneously, and to respond to the average of the power levels received at the two wavelengths; the effective transmission coefficient T_{av}^2 would then be the average of the values T_1^2 and $T_1'^2$ at the two wavelengths. That is,

$$T_{ave}^2 = \frac{1}{2}(T_1^2 + T_1'^2) \qquad (2\text{-}227)$$

This average transmission coefficient, shown in Figure 2-67, is much less dependent on angle of incidence than the original transmission coefficients. Of course, to take best advantage of this effect λ_0 and λ_0' must be properly chosen, as described in Reference 76. Additional improvement could be obtained by using a lower dielectric constant, by adding thin low-reflecting skins to the sheet, and by using more than two frequencies (or by using a band of frequencies).

2-45. Wall Constructions for Millimeter Wavelengths

An "A" sandwich with half-wave skins and with a very low core dielectric constant has been suggested for use at very short wavelengths, such as K_a-band.[13,19] As explained in Section B, this type of sandwich can be designed for perfect transmission (assuming lossless materials and air core) at two angles of incidence. At millimeter wavelengths this construction would not be excessively heavy, and its extra thickness (compared with the ordinary thin-skin "A" sandwich) would be an advantage.

In reference 38 it is suggested that a dielectric sheet having a continuously varying dielectric constant might be designed for extreme broadband performance. The dielectric constant would be low at the surface and would gradually rise to a maximum at the center of the sheet. It would seem that if practical sheets of this type were developed they might show promise for use at millimeter wavelengths.

C sandwiches have been used at K_u-band for their good electrical properties and mechanical strength.[27] Certain multiple sandwich constructions have been found to be extremely broadband, therefore; it would seem that they might also prove useful for millimeter radomes.

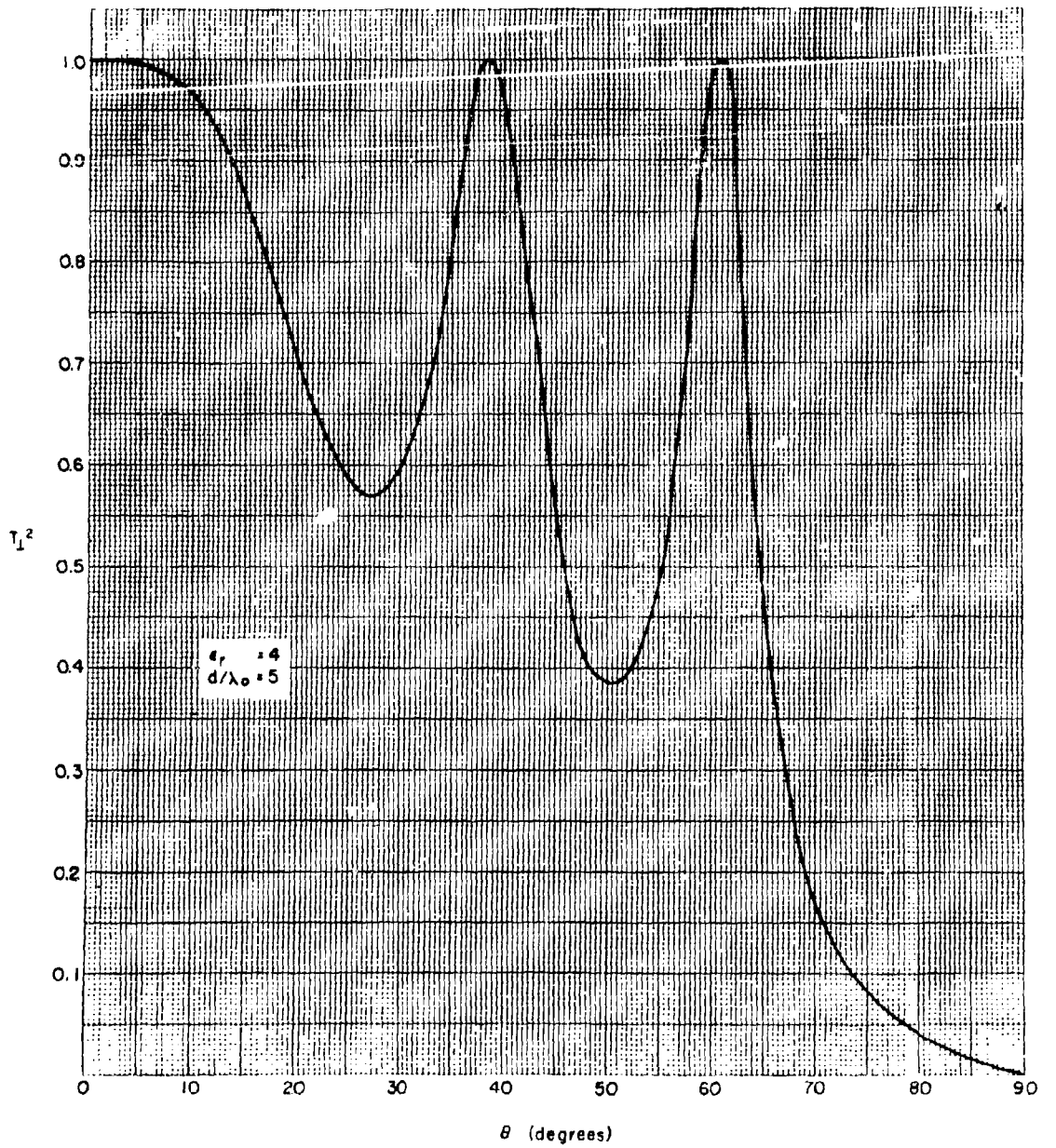


Figure 2–65. Transmission Coefficient of a Lossless Plane Sheet at Wavelength λ_0

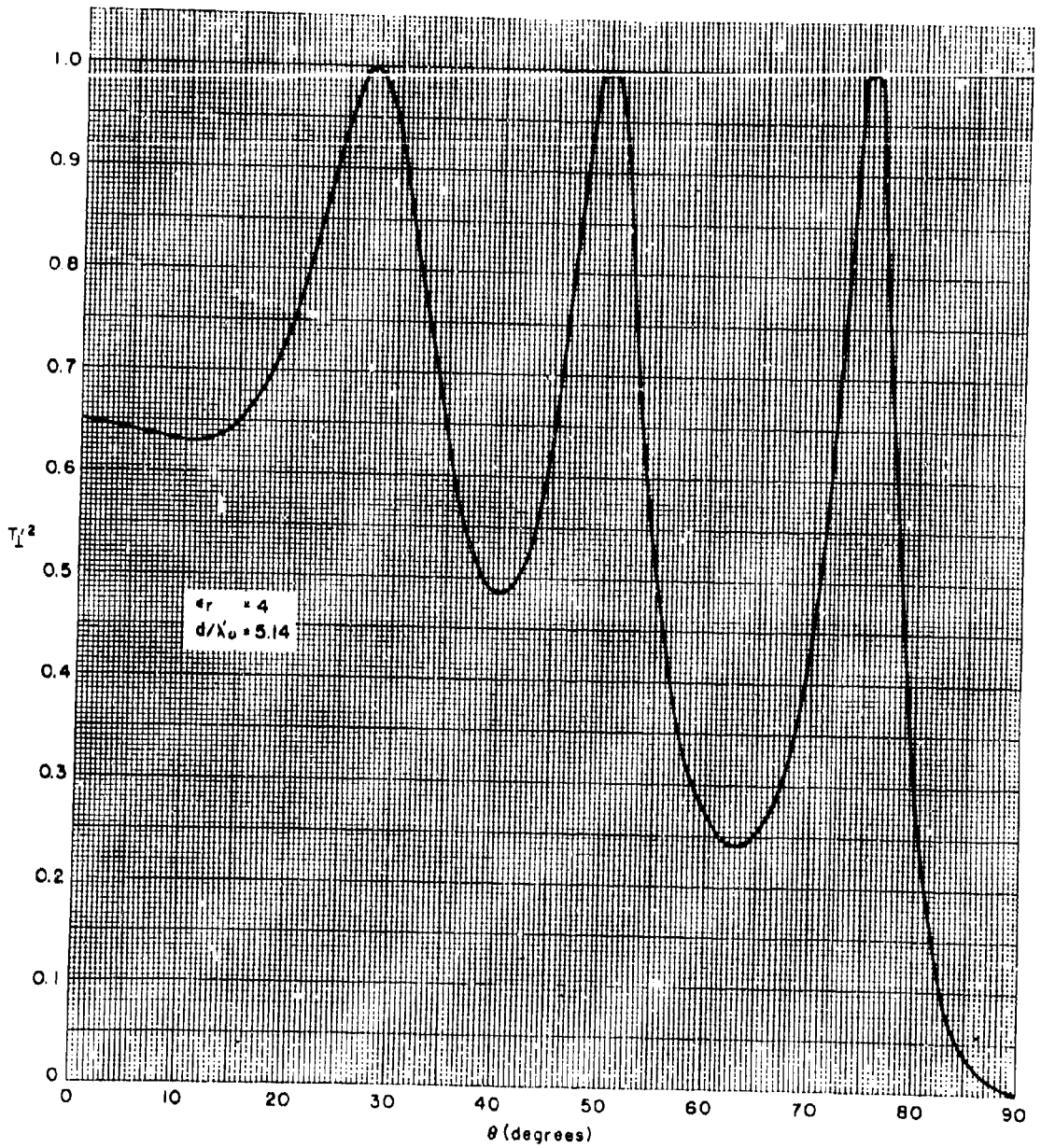


Figure 2–66. Transmission Coefficient of a Lossless Plane Sheet at Wavelength λ_0'

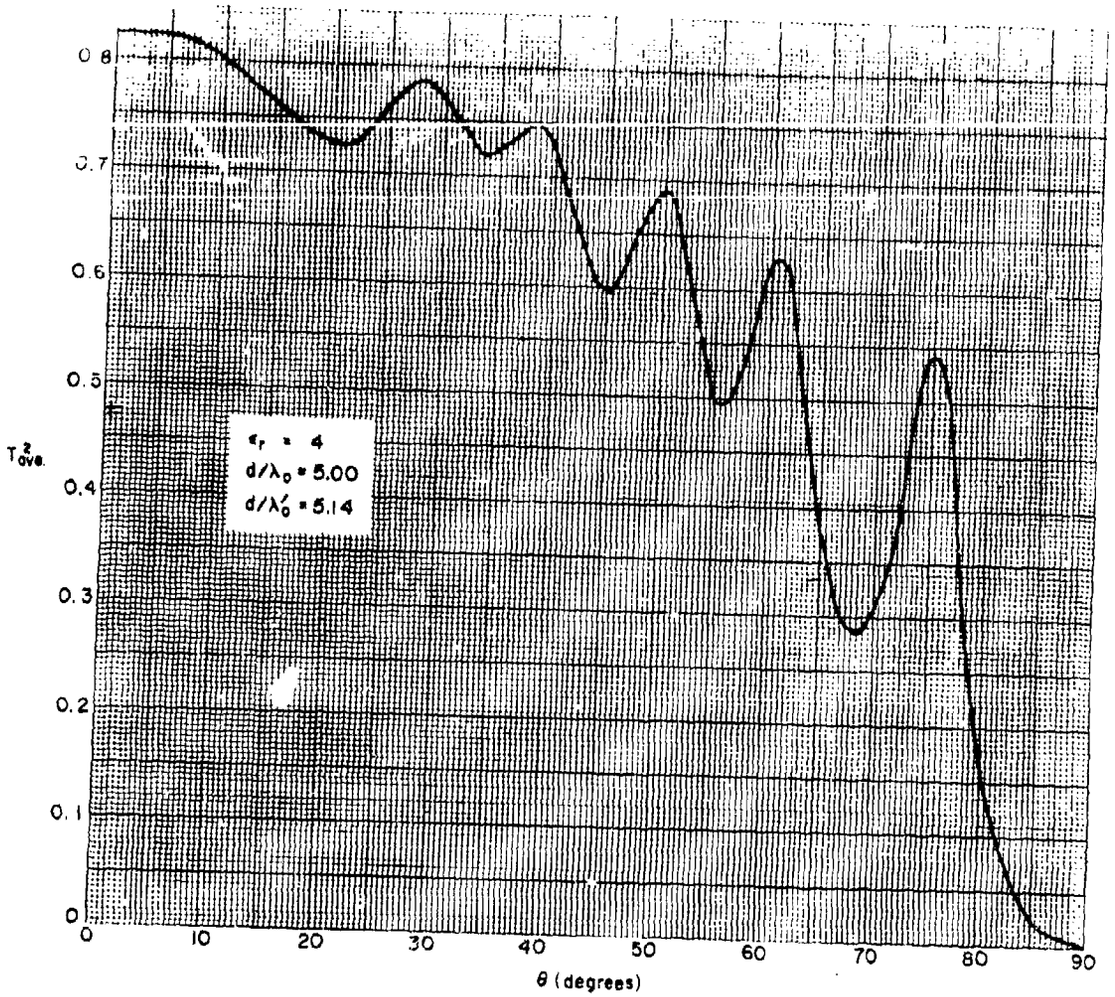


Figure 2–67. Average Transmission Coefficient of a Lossless Plane Sheet for Wavelengths λ_0 And λ_0'

REFERENCES

1. Wolin, S. Tables of Fresnel's Coefficients, Snell's Law and Other Radome Design Quantities. Report NADC-EL-5104, U. S. Naval Air Development Center, Johnsville, Pennsylvania, 22 January 1952.

2. Wolin, S. Supplementary Tables of Fresnel's Coefficients, Snell's Law, and Other Radome Design Quantities. Report NADC-EL-53189, U. S. Naval Air Development Center, Johnsville, Pennsylvania, 9 July 1954. (AD-37 153)

3. Cady, W. M., Karelitz, M. B., and Turner, L. A. Radar Scanners and Radomes. (Massachusetts Institute of Technology, Radiation Laboratory Vol. 26), McGraw-Hill Book Company, New York, 1948.

4. Kotik, J. Some Remarks on Thin Dielectric Walls. Report No. 12283-8M, Contract AF 33(038)-12283, McMillan Laboratory, Ipswich, Massachusetts, 15 March 1953. (Confidential)

5. Kay, A. F. The Electrical Design of the Homogeneous Radome Wall. Report 12283-8K, Contract AF 33(038)-12283, McMillan Laboratory, Ipswich, Massachusetts, 15 February 1953. (Confidential)

6. DiToro, J. A. Graphs of Transmission and Phase Data of Plane Dielectric Sheets for Radome Design. Report NADC-EL-5313, U. S. Naval Air Development Center, Johnsville, Pennsylvania, 1 July 1953. (AD-45 316)

7. DiToro, J. A. Supplementary Graphs of Transmission and Phase Delay of Plane Dielectric Sheets and Sandwich Constructions for Radome Design. Report NADC-EL-5313, U. S. Naval Air Development Center, Johnsville, Pennsylvania, 16 June 1954. (AD-45 543)

8. Wolin, S. Tables of Transmission and Reflection Coefficients of Lossy, Homogeneous Dielectric Sheets. Report NADC-EL-52195, Vol. 1, U. S. Naval Air Development Center, Johnsville, Pennsylvania, 11 February 1954. (AD-36 518)

9. Wolin, S. Tables of Transmission and Reflection Coefficients of Lossy, Homogeneous Dielectric Sheets. Report NADC-EL-52195, Vol. 2, U. S. Naval Air Development Center, Johnsville, Pennsylvania, 7 October 1954.

10. Kofoid, M. J. Calculated Electrical Transmission Characteristics of Half-Wavelength Thick Solid Plane Sheets. Document No. D-13622, Boeing Airplane Company, Seattle, Washington, 24 October 1952. Revised 12 March 1954. (AD-42 401)

11. Lengyel, B. A., Langenberg, D. N., and Henschke, R. A. Transmission Through Half-Wave Sheets. Technical memo. No. 327, Hughes Aircraft Company, Culver City, California, 1 November 1953. (AD-22 010)

12. Webster, R. E., and Moore, D. P. Transmission Coefficients of Elliptically Polarized Waves Incident on Homogeneous Isotropic Panels. Report 663-5, Contract AF 33(616)-3277, Antenna Laboratory, The Ohio State University Research Foundation, 31 December 1956. (Confidential)

13. Everhart, E. M. Radome Wall Reflections at Variable Angles of Incidence. Report 483-20, Radiation Laboratory, Massachusetts Institute of Technology, 4 January 1946.

14. Radome Engineering Manual. AMC Manual No. 80-4, NAVAER 16-45-502. Published by direction of The Chief of the Bureau of Aeronautics and The Commanding General of The Air Material Command, 1 October 1946.

15. Weedon, M. G. B., and Stott, A. L. Calculations on the Transmission of Electromagnetic Waves Through Plane Dielectric Sheets. Technical note No. G. W. 282, Royal Aircraft Establishment, Great Britain, November 1953. (Confidential) (AD-25 779)

16. Luoma, E. J. Phase Retardation Design Curves for Solid Lossless Dielectric Panels. Technical Report 56-116. Wright Air Development Center, Wright-Patterson Air Force Base, Ohio, February 1956. (AD 110514)

17. Wolin, S. Theory of Lossy High-Incidence Radomes. Report NADC-EL-5116, U. S. Naval Air Development Center, Johnsville, Pennsylvania, 15 January 1952.

18. Wiederhorn, N. M., and Kay, A. F. Radome Design Criteria for Precision Guidance Radar. Final Report, Contract AF 33(038)-12283, McMillan Laboratory, Ipswich, Massachusetts, 1 June 1954. (Confidential) (AD-49 428)

19. Snow, C. J. Report on Applications of the Impedance Concept to Radome Wall Design. Report NADC-EL-52136, U. S. Naval Air Development Center, Johnsville, Pennsylvania, 6 April 1953.

20. Wolin, S. Tables of Transmission and Reflection Coefficients of Lossy, Symmetrical Dielectric Radome Sandwiches. Report NADC-EL-52188, U. S. Naval Air Development Center, Johnsville, Pennsylvania, 22 October 1953.

21. Bowlby, C. W. Calculated Electrical Transmission Characteristics of Symmetrical Sandwich Flat Sheets. Document D-13643, Boeing Airplane Company, Seattle, Washington, 30 October 1952.

22. Wolin, S. Electrical Design of Lossy High-Incidence Radomes. Report ADC EL-123-50, U. S. Naval Air Development Center, Johnsville, Pennsylvania, 11 July 1950.

23. Everhart, E. M. X-Band Sandwiches at Variable Angles of Incidence. Report 483-8, Radiation Laboratory, Massachusetts Institute of Technology, 19 December 1944.

24. Redheffer, R. M. Transmission and Reflection of Parallel Plane Sheets. Report 483-12, Radiation Laboratory, Massachusetts Institute of Technology, 26 January 1945.

25. Dowker, Y. Transmission of Lossy Sandwiches. Report 483-22, Radiation Laboratory, Massachusetts Institute of Technology, 23 January 1946.

26. Croswell, W. F. Constant Phase Retardation Characteristics of an "A" Sandwich Radome. Report TR 56-32, Wright Air Development Center, Ohio, December 1955. (Confidential) (AD-95 556)

27. Hartig, E. O., and Horton, M. C. The Theory of the Lossless Double Symmetrical Sandwich Radome. Report GER-2731, Contract W33-038ac-14153, Goodyear Aircraft Corporation, Akron, Ohio, 2 July 1951.

28. Webster, R. E. Elliptical Polarizations and Radome Errors. Report 683-3, Contract AF 33(616)-3277, Antenna Laboratory, The Ohio State University Research Foundation, 15 November 1956.

29. Boyce, W. E. L. The Angular Error Characteristics of a Radome as a Function of the Polarization of the Field Incident on the Radome. (Goodyear Aircraft Corporation, Akron, Ohio) Proceedings of the O.S.U.-W.A.D.C. Radome Symposium, Vol. 2, June 1955, pp. 205-230. (Confidential) (AD-86 660)

30. Von Hippel, A. R., Westphal, W. B., and Miles, P. A. Dielectric Analysis of Ferrites and Their Appraisal as Radome Materials. W.A.D.C. Technical report 55-149, Contract AF 33(616)-2191, Massachusetts Institute of Technology, February 1955. (AD-76 793)

31. Worthington, H. R., Jr. Investigation of Babinet Principle for Possible Radome Application. Report NADC-EL-5372, U. S. Naval Air Development Center, Johnsville, Pennsylvania, 8 May 1953. (Confidential)

32. Schramm, C. K., Jr. Propagation Constant and the Radome. W.A.D.C. Technical report 53-297, Wright Air Development Center, August 1953. (AD-21 967)

33. Kirschbaum, H. S. A Polarizing, Reinforced, Broad-Band Anisotropic Panel. (Antenna Laboratory, The Ohio State University) O.S.U.-W.A.D.C. Radome Symposium, June 1956, Vol. I. (AD-97 150).

34. Cutler, S., and Kotik, J. The Propagation of Electromagnetic Waves Through Anisotropic Multilayers. Contract AF 19(604)-1307, Technical Research Group, New York, 30 January 1956. (AD-87 092)

35. Friedman, B. Modes in Anisotropic Structures. Report 3, Contract AF 19(604)-1015, Technical Research Group, New York, January 1955.

36. Kotik, J. Propagation Through Dielectric Honeycomb Material. Contract AF 33(616)-2973, Technical Research Group, New York, July 1955. (AD-67 674)

37. Kotik, J. The Dielectric Tensor of Alternating-Layer Material with Application to Honeycomb and Broadband Radomes. (Technical Research Group, New York) O.S.U.-W.A.D.C. Radome Symposium, June 1956, Vol I. (AD-97 150).

38. Refheffer, R. M., Sampson, J. H., Janus, N. N., and Webber, A. H. A Study of Broadbanding Techniques. Final report, Contract AF 33(600)-29749, McMillan Laboratory, Ipswich, Massachusetts, 31 January 1956. (Confidential) (AD-90 649)

39. Paiss, M. H. Investigation of Metal-Ribbed Radomes. Report NADC-EL-53153, U. S. Naval Air Development Center, Johnsville, Pennsylvania, 27 April 1953.

40. Worthington, H. R., Jr. Investigations of the Microwave Transmitting Properties of Metal Screens. Report NADC-EL-53188, U. S. Naval Air Development Center, Johnsville, Pennsylvania, 26 January 1954. (Confidential)

41. Worthington, H. R., Jr. Improvement of Radome Performance by Means of Metal Grids. (Bjorksten Research Laboratories, Inc., Madison, Wisconsin) Proceedings of the O.S.U.-W.A.D.C. Radome Symposium, Vol. 2, June 1955, pp. 106-116. (Confidential) (AD-86 660)

42. Jones, E. M. T., Cohn, S. B., and Robinson, L. A. Wide-Band Radomes Matched by Reactive Walls. (Stanford Research Institute, Menlo Park, California) Proceedings of the O.S.U.-W.A.D.C. Radome Symposium, Vol. 1, June 1955, pp. 52-67.

43. Lippmann, B. A., and Oppenheim, A. Loaded Dielectrics. Contract Nonr-1230(00), Technical Research Group, New York, 30 April 1954.

44. Silver, S. (editor). Microwave Antenna Theory and Design. McGraw-Hill Co., Inc., New York, 1949.

45. Sledge, O. D., and Hata, F. T. Investigation of Electromagnetic Field Distortions Caused by Dielectric Sheets, Wedges, and Radomes Placed Near an Antenna. NBS Report 10-E-251, National Bureau of Standards, Corona, California, 31 August 1953. (Confidential)

46. Kay, A. F. Simple Mathematical Models of Radomes. Report 12283-8-0, Contract AF 33(038)-12283, McMillan Laboratory, Ipswich, Massachusetts, 23 September 1953. (Confidential) (AD-31 771)

47. Mason, S. J., and Redheffer, R. M. Diffraction. Report 12283-4, Contract AF 33(038)-12283, McMillan Laboratory, Ipswich, Massachusetts, 17 February 1951.

48. Woonton, G. A. The Effect of an Obstacle in the Fresnel Field on the Distant Field of a Linear Radiator. (McGill University, Montreal, Canada) Journal of Applied Physics, Vol. 21, No. 6, June 1950, pp. 577-580.

49. Kay, A. F., and Barrar, R. B. Lloyd's Mirror Effect in Radome Error. Contract Nonr-124700, McMillan Laboratory, Ipswich, Massachusetts, 18 March 1954. (Confidential) (AD-50 473)

50. Rix, N. D. The Ripple Tank as a Device for Studying Wave Propagation. Jour. Acous. Soc. America, Vol. 21, 464A, 1949.

51. Walbridge, N. L., Smith, H. M., and Woodward, L. A. Water Ripple Analogue of Electromagnetic Wave Propagation. Report 2, Contract Nonr-597-(01), University of Vermont, January 1955. (AD-57 875)

52. Walbridge, N. L., Woodward, L. A., and Smith, H. M., Jr. The Ripple Tank Analogue as an Aid in Radome Design. (University of Vermont) Proceedings of the O.S.U.-W.A.D.C. Radome Symposium, Vol. 1, June 1955., pp. 106-116.

53. Kay, A. F. Streamlined Lens Radome. (Technical Research Group) (New York) O.S.U.-W.A.D.C. Radome Symposium, June 1956, Vol. I. (AD-97 150)

54. Tice, T., and Adney, J. Transmission Through a Dielectric Spherical Shell. Report 531-3, Contract AF 33(616)-277, Antenna Laboratory, The Ohio State University, Columbus, Ohio, 1 August 1953.

55. Tai, C. T., and Barnett, R. I. Characteristics of Large Spherical Radomes. (Antenna Laboratory, The Ohio State University) Proceedings of the O.S.U.-W.A.D.C. Radome Symposium, Vol. 1, June 1955, pp. 77-93.

56. Barrar, R. B. The Diffraction of an Electromagnetic Plane Wave by a Curved Wall. Report 12283-8L, Contract AF 33(038)-12283, McMillan Laboratory, Ipswich, Massachusetts, 16 March 1953. (Confidential)

57. Cohen, M. H. Application of the Reaction Concept to Scattering Problems. I.R.E. Transactions, Vol. AP-3, No. 4, October 1955.

58. Rhodes, D. R. On the Theory of Scattering by Dielectric Bodies. Report 475-1, Contract AF 18(600)-19, Antenna Laboratory, The Ohio State University, Columbus, Ohio, 1 July 1953.

59. The Radome Problem in Guided Missiles. Final report, Contract N6 ONR-27023 (Sponsored by Office of Naval Research) Princeton University, Princeton, New Jersey, 1 March 1952. (Secret)

60. Bronwell, A. B., and Beam, R. E. Theory and Application of Microwaves. 1st edition, McGraw-Hill Book Co., Inc., New York, 1947, pp. 451-453.

61. Richmond, J. H. Antenna Pattern Distortion by Dielectric Sheets. (Antenna Laboratory, The Ohio State University) Proceedings of the O.S.U.-W.A.D.C. Radome Symposium, Vol. 1, June 1955, pp. 94-105.

62. Richmond, J. H. Antenna Pattern Distortion by Dielectric Sheets. (Antenna Laboratory, The Ohio State University) I.R.E. Transactions, Vol AP-4, No. 2, April 1956, pp. 139-142.

63. Wiederhorn, N. M., and Kay, A. F. The Displacement of Radar Beams by Dielectric Sheets and Wedges. Report 12283-8P, Contract AF 33(038)-12283, McMillan Laboratory, Ipswich, Massachusetts, 5 April 1954. (Confidential)

64. Kay, A. F., and Kotik, J. The Propagation of Plane and Surface TE Waves in Semi-Infinite, Thin Dielectric Panels. Symposium on Microwave Optics, McGill University, Montreal, Canada, Vol. 1, June 1953.

65. Angulo, C. M. Diffraction of Surface Waves by a Semi-Infinite Dielectric Slab. Report AF 1391/1 Contract AF 19(604)-1391, Brown University, Providence, Rhode Island, August 1955. (AD-78 552)

66. Horton, M. C., Boyce, W. E. L., and Hartig, E. O. Optical Theory for Microwave Transmission Through Dielectric Wall Structures. Report No. GER-5530, Goodyear Aircraft Corporation, Akron, Ohio, 4 August 1953. (AD-42 719)

67. Kay, A. F. The Two-Step Antenna Model of Radome Boresight Errors. Contract Nonr-124700, McMillan Laboratory, Ipswich, Massachusetts, 10 March 1954. (Confidential) (AD-27 077)

68. Hata, F. T. Investigation of Electromagnetic Field Distortion Caused by Dielectric Sheets, Wedges, and Radomes Placed Near an Antenna. (National Bureau of Standards) Office of Naval Research, Washington, D.C., Symposium on Guided Missile Radomes, June 1953, pp. 104-116. (Confidential)

69. Baechle, J. R., Richmond, J. H., and Stickler, D. C. Antenna Pattern Distortion by a Wedge-Shaped Radome. Report 655-2, Contract AF 33(616)-3212, Antenna Laboratory, The Ohio State University, Columbus, Ohio, 1 March 1956. (Confidential)

70. Ramo, S., and Whinnery, J. R. Fields and Waves in Modern Radio. John Wiley and Sons, New York, 1944, pp. 349-353.

71. Jasik, H. The Electromagnetic Theory of the Luneberg Lens. Report TR-54-121, Air Force Cambridge Research Center, November 1954. (AD-61 510)

72. Wachendorf, F. Investigation on the Properties of Radomes. Report 423, Contract AF 33(038)-10836, Perkin-Elmer Corporation, Norwalk, Connecticut, 31 December 1955. (Secret)

73. Snow, O. J. The Development of Irdomes. Report ADC EL-19-51, U. S. Naval Air Development Center, Johnsville, Pennsylvania, 24 January 1951. (Confidential)

74. Snow, O. J. The Development of Irdomes. Report NADC EL-5107, U. S. Naval Air Development Center, Johnsville, Pennsylvania, 11 October 1951. (Confidential)

75. Jenness, J. R., Jr. The Development of Irdomes. Report NADC-EL-5453, U. S. Naval Air Development Center, Johnsville, Pennsylvania, 23 June 1954. (Confidential)

76. Richmond, J. H., and Stickler, D. C. Radomes for Millimeter Wavelengths. Report 655-4, Contract AF 33(616)-3212, Antenna Laboratory, The Ohio State University, Columbus, Ohio, 1 September 1956.

77. Klotzbaugh, G. A., Flarherty, J. M., and Hughes, R. H. A Study of Artificial Dielectrics with Unity Dielectric Constants. Report GR-177, Contract Nonr-863(00), Westinghouse Electric Corporation, East Pittsburgh, Pennsylvania, 2 April 1954. (Confidential) (AD-41 732)

78. McMillan, E. B. The Half-Wave (Loaded Core) Sandwich. (McMillan Laboratory, Inc.) O.S.U.-W.A.D.C. Radome Symposium, Vol. 1, 1955, pp. 132-136.

79. Richmond, J. H. (Unpublished work), Antenna Laboratory, The Ohio State University, Columbus, Ohio.

80. Speer, W. Matrix Method of Radome Transmission Computation. Memorandum Report No. EG-MR-3, Douglas Aircraft Company, El Segundo, California, 4 January 1951. (ATI 178476)

Chapter 3

SEARCH RADOME DESIGN

by

W. E. L. Boyce

Convair Division
General Dynamics Corporation
San Diego, California

(formerly Aerophysics Laboratories
Goodyear Aircraft Corporation
Litchfield Park, Arizona)

and

E. O. Hartig

Aerophysics Laboratories
Goodyear Aircraft Corporation
Litchfield Park, Arizona

INDEX OF SYMBOLS

a	Extremity of antenna aperture
b	Extremity of antenna aperture
c	Constant of the ogive
d	Constant of the ogive
d	Diameter of the circular aperture
d	Normal sheet thickness
d	Thickness of radome
d/λ	Normalized wall thickness
d_c/λ	Normalized core thickness
d_s/λ	Constant normalized skin thickness
$\underline{E}$	Electric field vector
$\underline{e}$	Polarization vector in HV plane
G	Gain of antenna
$\underline{H}$	Magnetic field vector
h	Elevation of aircraft
$\underline{i}_x$	Unit vector parallel to x-axis
$\underline{i}_y$	Unit vector parallel to y-axis
$\underline{i}_z$	Unit vector parallel to z-axis
$\underline{i}_{\parallel}$	Vector located along intersection of incidence plane and plane HV
$\underline{n}$	Outward-directed unit normal vector to surface at (x, y, z), direction defined by gradient of surface function F (x, y, z)
P	Antenna pattern
$\underline{P}_a$	Power density received at a fixed position in the antenna beam without a radome present
$\underline{P}_b$	Power density received at same point as $\underline{P}_a$, but when radome is properly installed above antenna
P_h	Power density along ground for aircraft at elevation h
P_m	Minimum detectable power level into the receiver
P_r	Received power in the presence of a radome
P_{r0}	Power at the receiver
P_0	Total transmitted power
$\underline{\rho}$	Unit vector of direction of propagation of radiated field
R	Constant of the ogive
R	Slant range to point on ground under consideration
R_e	Mean radius of the earth
R_g	True ground range
R_m	Maximum range in the presence of the radome
R_{m0}	Maximum range at which target having cross section of σ can be detected
R_0	Chord subtended by angle α at radius R_e

INDEX OF SYMBOLS (cont)

r	Radius at axial station point z
S	Surface area of radome
T_0	Effective complex transmission coefficient
T^2	Power transmission coefficient of the radome
$\dot{T}_\perp, \dot{T}_\parallel$	Complex transmission coefficients of a linearly polarized wave
W	Weight of radome
W_A	Weight of sandwich radome (pounds)
W_S	Weight of solid-wall glass fiber radome (pounds)
x_i	Radome surface coordinate
y_i	Radome surface coordinate
z	Axial station point
z	Radome surface coordinate
α	Angle between $i_\parallel$ and V-axis
α	Angle between z_i- and z-axes
α	Antenna orientation angle
α	Half-power beam width (in degrees) of the main beam (central-maximum)
Δ	Insertion phase
ΔS	Surface of radome
ϵ_c	Core dielectric constant
ϵ_r	Relative dielectric constant of solid wall
ϵ_s	Skin dielectric constant
θ	Angle measured from the horizontal plane to R
θ	Depression angle
θ	Incidence angle
θ	Incremental element of radome of surface ΔS having position coordinates x, y, and z
θ_B	Brewster's angle
θ_H, θ_V	Angles between $\underline{p}$ and the projections of $\underline{n}$ of each of the planes VP and HP
λ	Free-space wavelength of transmitted signal
ξ	Angle which the polarization vector makes with the incidence plane
ρ	Density of radome wall
ρ_c	Density of alkyd-isocyanate foam
ρ_s	Density of glass fiber laminate
σ	Effective scattering cross section of the target
Φ	Electrical thickness in radians at an arbitrary angle θ
ϕ	Angle between $\underline{e}$ and $\underline{i}_{x_i}$
ϕ	Angle relating polarization vector $\underline{e}$ in HV plane to V-axis

Chapter 3

SEARCH RADOME DESIGN

SECTION A. SEARCH RADAR ANTENNAS

The term "search radar" is a generic term applicable to a whole family of radars whose principal function is ground or aerial surveillance of one form or another. The associated antennas are usually of the primary-feed-plus-reflector variety where the shape of the reflector has been determined on the basis of the pattern coverage required. Although it would be possible to illuminate simultaneously the whole ground area or spatial volume of interest with a broad-beamed antenna, the mode of operation of most search radars requires that azimuthal information be obtained by noting the direction in which the antenna is beamed. Range information is usually obtained by transmitting pulses of r-f energy and detecting the travel time to and from various targets. Thus most search antennas are designed to have a relatively narrow beam in the azimuthal plane with broader coverage in the vertical plane.

3-1. Patterns

Search antenna patterns are usually obtained by using an antenna feed and reflector system which is similar in principle to an automobile headlight; that is, a primary feed source (such as an open-ended wave guide) is the light bulb of the analogy, and is located at the focal point of a paraboloid of revolution that in turn is represented by the reflector. Hence, the energy emanating from the primary source is collimated into an axially symmetric pencil-like beam. Actually the collimation of a pencil beam is never perfect, since the energy, whether it be visible light or microwaves, propagates as waves and not rays; however, if the wavelength of the radiation is very small compared to the diameter of the parabolic reflector, the ray analogy is generally adequate. By calculating the Fraunhofer diffraction pattern for a circular aperture,[1] it can be shown that the half-power beam width α, in degrees, of the main beam (central-maximum) can be related to the diameter of the circular aperture d and to the wavelength λ by

$$\alpha = \frac{70\lambda}{d} \qquad (3\text{-}1)$$

where λ and d are measured in the same units.

The asymmetrical type of pattern normally required for search radars can be obtained by using a parabolic reflector whose aperture dimension in the azimuthal plane is large in comparison to its dimension in the vertical plane.

However, it is customary to perturb the contour of the antenna in the vertical plane to permit uniform illumination of the ground as a function of range. Views of Figure 3-1 (a and b) represent a plan view and a cross sectional view, respectively, of a search antenna. Figure 3-1 (c and d) represent polar coordinate plots of the idealized angular variation of radiated power density from the antenna as measured in the azimuthal and vertical planes, respectively. These plots of radiated power are commonly referred to as antenna patterns.

3-2. Illumination

The requirement of uniform ground illumination somewhat complicates the design of search radar antennas.[2] For the case of a flat earth and for

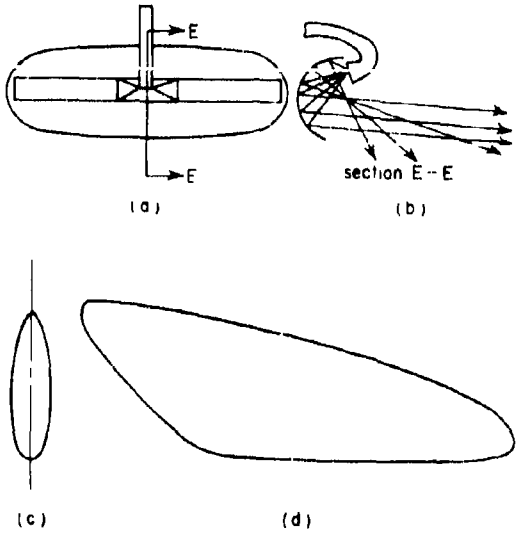


Figure 3-1. Cosecant-Squared Antenna And Pattern Configuration: (a) Antenna Front View; (b) Antenna Side View; (c) Pattern, Horizontal Cut; (d) Pattern, Vertical Cut

uniform illumination the antenna pattern P will be of the form

$$P = \frac{P_h h^2 \csc^2 \theta}{R^2} \qquad (3\text{-}2)$$

where P_h is the power density along the ground when the aircraft is at an elevation h; R is the slant range to the point on the ground under consideration; and θ is the angle measured from the horizontal plane to R, as shown in Figure 3-2. Of course Equation (3-2) represents the idealized case which would require an infinite power density in the direction of the horizon. In actual practice there is a finite range of coverage over which uniform illumination is required. It is customary to depress the main beam component of the search antenna so that the direction of maximum intensity within the beam may be between 2^o and 10^o below the horizontal, depending on the altitude of the aircraft and the maximum desired range of illumination. With the aid of the geometry of Figure 3-2 it can be shown that the true ground range R_g is related to the depression angle θ, the elevation h, and the mean radius of the earth R_e by

$$R_g = R_e \alpha \qquad (3\text{-}3)$$

where

$$\alpha = \cos^{-1}\left(1 - \frac{R_0^2}{2R_e^2}\right) \qquad (3\text{-}4)$$

and where

$$R_0 = \frac{h \cos\theta \sin(\theta - \alpha)}{\cos^2\alpha - \cos^2\theta} \qquad (3\text{-}5)$$

Now R_0 is simply the chord subtended by the angle α at the radius R_e, and since α is in general very small it is obvious that

$$R_0 \simeq R_g \qquad (3\text{-}6)$$

With the aid of Equation (3-5) for the case of small α, the ground range R_g to a first approximation is therefore given by

$$R_g \simeq h \operatorname{ctn} \theta \qquad (3\text{-}7)$$

It should be carefully noted that while the approximation of Equation (3-7) is quite convenient, its use is limited to angles which lie below the horizon. Thus

$$\theta > \tan^{-1}\sqrt{\frac{2h}{R_e} + \frac{h^2}{R_e^2}} \qquad (3\text{-}8)$$

Usually the pattern of an airborne search radar is determined on the basis of providing uniform

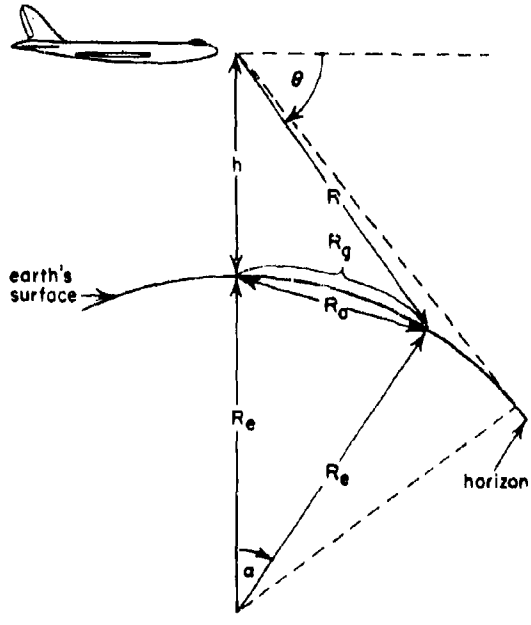


Figure 3-2. Geometry for Uniform Ground Illumination

illumination on the ground over a given range interval for various altitudes. Thus, with the aid of Equation (3-7), an immediate determination of the angular range over which the pattern must satisfy a $\csc^2 \theta$ power distribution may be made.

The $\csc^2 \theta$ pattern just discussed essentially illustrates the basic requirement of most airborne bombing or navigational search radars — uniform ground illumination; however, the peculiar functional requirements of any particular search radar may necessitate an antenna having a special pattern. Therefore, it is often necessary for the radome designer to have all the details of the antenna design prior to beginning the radome design. In most cases the design of the radome and the antenna should be undertaken concurrently with the two designs coordinated to eliminate incompatible requirements.

SECTION B. ELECTRICAL REQUIREMENTS

3-3. Introduction

Theoretically, the influence of a radome on the structure of a radiated field can be determined by solving Maxwell's electromagnetic field equations with the appropriate boundary and initial conditions. Even if this were practical, which in general it is not, it would still be necessary to have available a detailed quantitative description of the radar system before the overall effects of the radome on the performance of the radar could be determined.

The great variety of search radars in existance today precludes a detailed discussion of all the peculiar radome problems that may exist, and the following discussion has been limited, accordingly, to a few of the more important ones which are common to conventional airborne, ground-mapping radars.

In Chapter 2 an analysis was made of plane, linearly polarized electro-magnetic waves traversing idealized isotropic, homogeneous plane sheets of infinite extent. The absorption, reflection, and transmission coefficients of the sheets were related to various parameters such as frequency, polarization, permittivity, permeability, dielectric and magnetic loss, normal thickness of sheet, and the incidence angle. As was the case for the dielectric sheets, the effect of the radome on the r-f field can be related in terms of its complex transmission and reflection characteristics to the same set of parameters; but in addition, the geometry of the radome shape, its structure, and its physical orientation with respect to the radiating system and other surrounding objects in space must also be known. One other major point of difference between the idealized case and the radome is that the idealized case was based on plane linearly polarized waves traversing the sheets, whereas a radome interacts with a field which at best can only be approximated by a plane wave. Because of the complexity of the interaction between the radome and the r-f field, it is difficult to relate specific radome parameters to the many indirect effects the radome has on the performance of the radar system; it is therefore desirable to examine the effects first and then consider the causes.

3-4. Range Reduction Due to Radome

Range reduction is probably the most common performance degradation caused by the radome, although it is seldom the most serious. This reduction can result from the absorption of power by the radome or from the redistribution of power in the radiated field, or from both. Usually, the latter cause has the most noticeable effect, since in general most radome wall materials currently in use are relatively lossless. The redistribution of energy in the field may result from phase perturbations produced by the radome, from a high radome wall reflection coefficient, or from both. Generally the phase shifts across the beam are never great enough to produce more than a few degrees deflection and, except where beams having sharp maximums are involved, beam deflection can usually be considered secondary in terms of range reduction. The principal cause is usually a large coefficient of reflection, which is evidenced by the radome transmission properties.

In addition it should be mentioned that while phase perturbations produced by the radome are not usually a problem in conventional noncoherent search radars, there is a family of coherent radars that utilize phase and rate of change of phase (frequency) information. This latter group is composed of various doppler navigation and moving target indicator (MTI) radars. Since all are characterized by their utilization of phase and frequency information, any phase shift produced by the radome may be a source of error. In general, however, phase shifts produced by the radome are not a problem if the radome behaves isotropically.

It is only when the phase shift is a function of direction that it becomes a problem. Due to the great variety of coherent radars, it is impossible to design for them as a class; however, when the particular requirements are known it is usually possible to design a radome having the required phase properties by utilizing design techniques similar to those employed for radomes where beam bending is a major problem. Those techniques are discussed in Chapter 4.

It is common practice to measure the transmission characteristics of a radome in terms of the reduction in power density produced by the radome at various points within the antenna beam as a function at the relative orientation of the radome and antenna. To determine the relation between range and radome transmissivity let

$$T^2 = \frac{\underline{P}_b}{\underline{P}_a} \tag{3-9}$$

where T^2 is the power transmission coefficient of the radome as determined by two measurements: (1) the power density $\underline{P}_a$, received at a fixed position in the antenna beam without a radome present; and (2) the power density $\underline{P}_b$, received at the same point when the radome is properly installed about the antenna. It should be noted that T^2 is a function of the direction coordinates with respect to the antenna beam, and also of the orientation of the coordinates of the radome with respect to the antenna. The well-known radar range equations in the absence of a radome defines the power P_{r0} at the receiver as

$$P_{r0} = \left(\frac{P_0\, G}{4\pi R^2}\right)\left(\frac{\sigma}{4\pi R^2}\right)\left(\frac{G\lambda^2}{4\pi}\right) = \frac{P_0 G^2 \lambda^2 \sigma}{(4\pi)^3 R^4} \tag{3-10}$$

where the first quantity in parentheses is the magnitude of the power density at the target which, together with the second quantity in parentheses, is the magnitude of the reflected power density in the vicinity of the receiver. The third quantity in parentheses is simply the cross sectional area of the receiving antenna. Here P_0 is the total transmitted power, G is the gain of the antenna (the same antenna is used for both transmitting and receiving; by reciprocity,[3] the gain G is the same for both the transmitting and receiving functions) R is the one-way range to the target, σ is the effective scattering cross section of the target, and λ is the free-space wavelength of the transmitted signal. Now if the minimum detectable power level into the receiver is designated as P_m, then the maximum range R_{m0} at which a target having a cross section σ can be detected is given by

$$R_{m0} = \sqrt[4]{\left(\frac{P_0}{P_m}\right)\frac{G^2 \lambda^2 \sigma}{(4\pi)^3}} \tag{3-11}$$

With the radome present, the power will be reduced by a factor T^2 as it passes through the radome wall for both the outgoing and incoming waves. This modifies Equation (3-10) so that the received power in the presence of a radome, P_r, is given by

$$P_r = T^4 P_{r0} \tag{3-12}$$

Hence for the same minimum detectable power P_m the maximum range in the presence of the radome, R_m, is given by

$$R_m = T R_{m0} \tag{3-13}$$

It is apparent that the maximum range at which a particular target can be detected is directly proportional to the square root of the power transmission coefficient of the radome and to the fourth root of the total power, P_0, being radiated; thus much of the effort spent in developing high-power microwave oscillators can be negated by a radome with poor transmission properties.

3-5. Magnetron Frequency Pulling

Another effect attributable to the radome is so-called "pulling" of the magnetron. The magnetron, like any oscillator, has a resonant frequency which is a function of a set of physical parameters normally referred to as boundary conditions, and, as might be expected, the radome is one of the parameters. Furthermore, the effect of the radome on the magnetron frequency is dependent on the relative positions of the radome and the antenna. Thus, as the radar antenna is sweeping in the azimuth or elevation direction, the r-f frequency may vary over a perceptible range.

To appreciate fully the effect of magnetron "pulling" on system performance requires some knowledge of radar display techniques. One method that is used to present an instantaneous ground map is the Plan Position Indicator (PPI) display.[4] In the PPI display the ground map is painted on the face of a cathode-ray tube, using a polar coordinate system. The electron beam is deflected radially from near the center of the tube out to the periphery with the time base of the sweep being proportional to range. During the sweep, which is synchronized with the pulse repetition frequency (PRF) of the

radar, the intensity of the electron beam is modulated as a function of the amplitude of the returning radar signal. In addition, the angular orientation of the radial sweep about the center of the tube is related directly to the azimuthal position of the antenna. As the antenna sweeps in azimuth, a picture of the ground is simultaneously painted on the cathod-ray tube.

The radar signal must be amplified to provide the signal strength required to modulate the accelerating voltage of the electron beam. Since it is inconvenient to do this at the transmitted frequency, the information signal is transferred to a carrier at an intermediate carrier frequency (i-f) and then amplified and demodulated. The intermediate carrier frequency is obtained by mixing the returning radar signal with a c-w (continuous-wave) signal of slightly higher or lower frequency, called the local oscillator (LO). By summing the LO signal and the returning radar signal, the i-f carrier is obtained at the difference frequency. If the local oscillator is tuned to a fixed frequency, any change in the magnetron frequency due to reflections will produce a corresponding change in the i-f carrier. If the bandwidth of the i-f amplifier is less than the bandwidth of the frequency variations produced by the radome, some of the return signal information will be lost. This effect may become noticeable in the PPI display by the absence of known targets.

Variation of the magnetron frequency, caused by radome reflection or otherwise, may be compensated by variation of the LO frequency with automatic frequency control (AFC). An AFC is an electronic servomechanism that tunes the local oscillator in such a way that the proper difference frequency between it and the magnetron is maintained. The speed of the tuning can usually be made great enough to follow any pulling of the magnetron that may occur during the scanning cycle. However, the response of the AFC is not instantaneous and extreme situations may arise in which the magnitude or phase of the reflection changes so rapidly that the AFC cannot compensate. Also, compensation cannot be achieved if the magnetron frequency pulling is so great that the electronic tuning range of the LO is exceeded. These limitations on the use of AFC serve to emphasize the necessity of minimizing reflections from the radome.

The phenomenon of pulling can be related directly to the phase and amplitude of the standing wave in the line being fed by the magnetron.[5] To minimize it, direct reflections from the radome back into the antenna should be minimized. Radomes presenting large areas normal to the beam of the antenna (so-called "normal-incidence radomes") will in general produce more pulling then streamlined radomes where the reflected energy is not directed back into the antenna. In some cases of very streamlined or pointed radomes, the reflection coefficient of the walls is large enough to produce secondary and tertiary reflections that reach the antenna and produce pulling.

Since the degree of pulling produced by any radome-radar combination is a function of the pulling characteristics of the magnetron as well as the shape, orientation, and transmission characteristics of the radome, there is no standard maximum allowable VSWR which the radome may produce. Each radar system presents an individual problem. However, the development of ferrite load isolators during the last few years has greatly alleviated this problem.[6] By utilizing the nonreciprocal properties of ferrites it has become possible to match the oscillator to a line whose impedance is very nearly independent of the radome.

3-6. Interference and Pattern Distortion

Another common cause of target obliteration is interference within the antenna beam as a result of reflections. Although these reflections are more frequently from the surrounding nacelle structure than from the radome, a knowledge of their effects is a prerequisite to an intelligent choice of radome location and type of installation.

A detailed discussion of the antenna nacelle design and its ramifications is presented in Chapter 10. Figures 3-3 and 3-4 depict the essentials of the interference problem. In Figure 3-3 the mechanism of reflection is shown in terms of idealized rays. Actually the field structure in the vicinity of the radome and the aircraft is quite complicated. However, the ray analogy is reasonably satisfactory at the higher microwave frequencies, where the dimension of the radome and aircraft are an order of magnitude, or more, greater than the wavelength of the r-f field. But it is this complexity of the field that allows for the divergence of the main beam rays and the resulting interference pattern sketched in Figure 3-4.

Significant beam distortion may also result if a portion of the antenna beam is intercepted by internal structural members such as ribs or attachment rings. This latter phenomenon is sometimes referred to as edge diffraction, but actually the basic antenna pattern is nothing more than a specialized diffraction pattern and the introduction of an obstacle simply changes

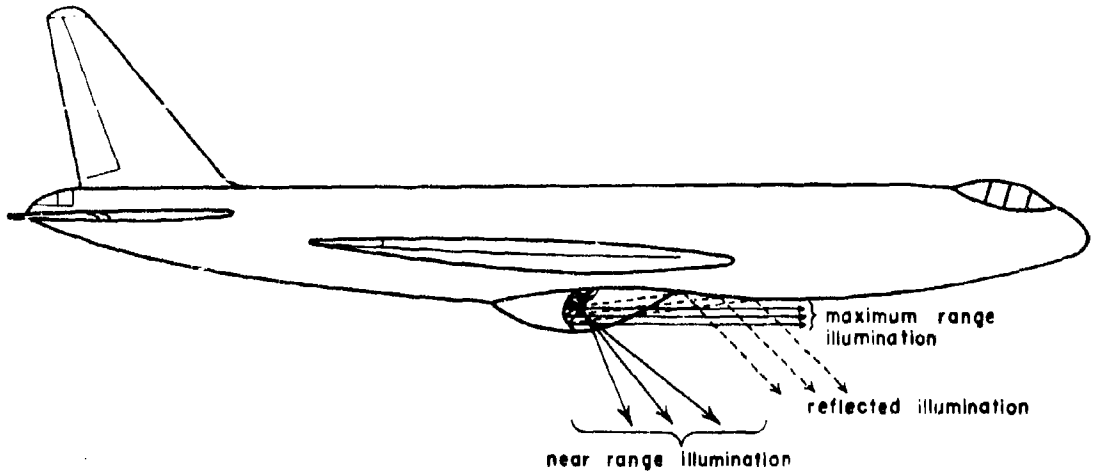


Figure 3-3. Pattern Distortion Due to Reflections: Near-Field Reflection

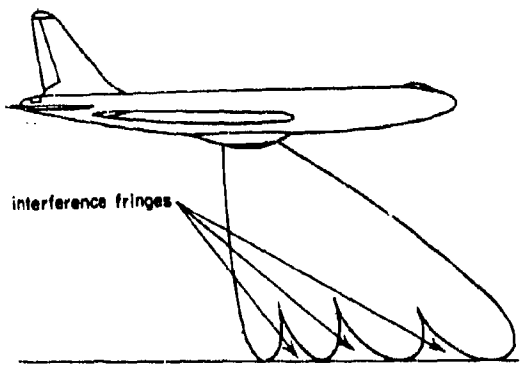


Figure 3-4. Pattern Distortion Due to Reflections: Far-Field Pattern Interference

the pattern. Most of the beam distortion problems arising from reflections and obstacles in the beam can be avoided by the proper choice of antenna location and installation; furthermore, unwanted reflections can be minimized by covering the reflecting surfaces with absorbing material.[7] However, it is rather futile to attempt to remove interfering obstacles from the path of the main beam by covering them with absorbing material. The absorbing material will appreciably reduce the scattered field from an object, but it does not prevent diffraction effects from occurring in the region behind the obstacle.

As was noted in the discussion of interference and diffraction, some of the radome's degrading effects on radar performance can be related directly to changes in the antenna beam. For this reason, numerous radome specifications are written in terms of allowable changes in the antenna pattern. Figure 3-5 shows the antenna pattern contours for an AN/APS-25 antenna with and without the radome. These cases are representative of the pattern distortions produced by a reasonably good radome. Most of the differences in the three patterns occur in the side lobes, although there is a reduction of power in the main lobe for the case where the antenna is oriented at 40° in elevation and 55° in azimuth with respect to the radome.

The AN/APS-25 antenna is a 24-inch paraboloid which produces a pencil beam. The pattern cuts shown in Figure 3-5 were taken in a plane containing the axis of revolution of the paraboloid (the axis of symmetry of the beam, not to be confused with the axis of mechanical revolution of the antenna) and parallel to the electric field vector $\underline{E}$. Such cuts are commonly referred to as E-plane cuts or patterns. Pattern cuts taken in the axial plane perpendicular to the E-plane are called H-plane patterns, since they normally are parallel to the magnetic field vector $\underline{H}$.

As might be suspected, one of the major problems in determining radome distortion of the field pattern is due to the difficulty of measuring the pattern for all possible relative orientations of the antenna with respect to the radome. When the antenna beam and the radome are axially symmetric and the field is plane polarized, an adequate description of pattern distortion can be obtained as a function of the offset angle between the two symmetry axes, and as a function of the angle that the electric field vector makes with the plane formed by the same axes. But for the more usual case where the radome or the antenna, or both, are asymmetrical, the

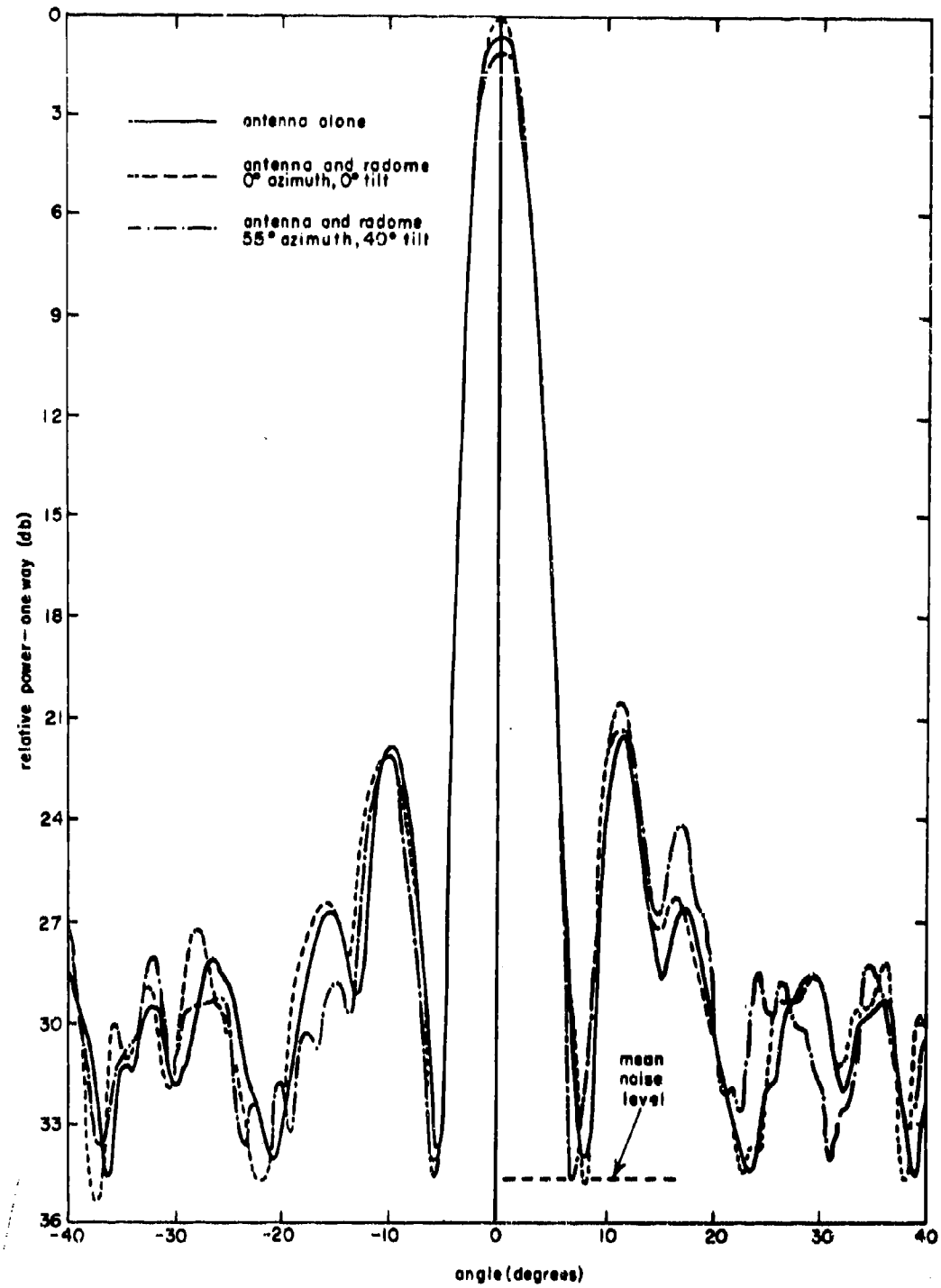


Figure 3-5. AN/APS-25 Antenna Patterns

problem of determining the method of testing can be as sizable as the design problem itself.

Some of these problems are dealt with in Chapter 12; however, most testing procedures have to be developed in terms of the particular system under consideration. One important feature to be remembered when contemplating antenna pattern distortion measurements is the desirability of determining the effects of the radome in the presence of the surrounding bulkhead and nacelle structure.

SECTION C. RADOME SHAPE

3-7. Design Criteria

In the design of ground-based and shipborne radomes, the shape is normally chosen on the basis of optimum electrical performance. In the case of airborne radomes, it is generally optimized aerodynamically. As a result, many of today's aircraft radomes bear a strong resemblance to an icicle, both in terms of outward appearance and in terms of their optical and electrical properties. In fact, the optical distortion, which may be observed when looking through a right circular cone of glass from the base toward the apex, is in essence the type of distortion that has to be corrected in the design of extremely high-fineness ratio radomes. Since shape is such an important factor in radome design, it has been found convenient to classify radomes electrically on that basis; thus radomes are frequently referred to as being either "normal-incidence" radomes or "streamline" radomes. The former are identified by the fact that all or most of the area illuminated is approximately normal to the beam, and therefore their transmission properties are similar to those exhibited by plane dielectric sheets when traversed by plane waves normal to the surface. Streamline radomes, as the name implies, have large fineness ratios (the ratio of length to base diameter), usually 3:1 or greater.

If permitted to express a preference in regard to size and shape, an individual responsible solely for the electrical characteristics of a radome would normally choose a spherical radome with a radius of curvature as large as could be conveniently tolerated and with the antenna gimbal point (the point of intersection of the gimbal axes) located at the center of the sphere. Rarely is it possible to surround the antenna with a spherical radome; hence, the next best step is to make spherical as much of the radome surface as can be permitted. One of the simpler radome configurations is composed of a hemisphere and right circular cylinder, as shown in Figure 3-6. The reasons for choosing a large spherical radome are rather obvious. First, if the antenna is gimbaled about a point, or even two axes which are separated only slightly, the effect of the radome can be made entirely symmetrical; that is, there is no preferred direction, assuming the radome wall is electrically uniform. Second, if the radius of the spherical section is an order of magnitude or more greater than the wavelength, the incidence is nearly normal over the whole illuminated surface area. In view of the transmission properties discussed in Chapter 2 for sheets traversed by plane waves at or near normal incidence. It is reasonable to expect power transmission in the vicinity of 95 to 98 percent for relatively low-loss dielectric wall constructions. Although spherical or hemispherical radomes afford the simplest solution to many electrical design problems, normal incidence characteristics can be undesirable if the radar system is particularly sensitive to direct reflections from the radome. As mentioned previously, proper design of the radar system to include "load isolators" in combination with proper radome wall design can eliminate this cause of system malfunctioning. Unfortunately the use of a spherical radome which is much, much larger than the antenna aperture is seldom feasible in airborne systems.

3-8. General Requirements

Streamlined radomes usually represent a compromise between electrical and aerodynamic design considerations. However, by carefully evaluating the required radome performance characteristics, it is generally possible to achieve a design configuration compatible with most of the requirements. It is difficult to out-

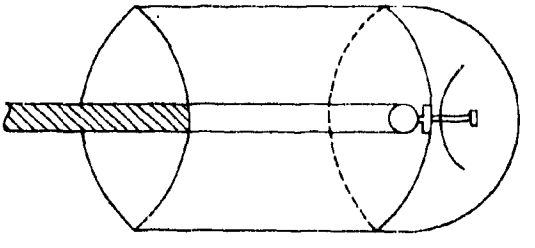


Figure 3-6. Hemispherical Radome

line a specific approach to all such problems, but there are two basic steps that should be considered as prerequisites to beginning the actual design.

First, the various radome requirements should be weighted in terms of their relative importance. Although this sounds relatively simple, it is frequently the most difficult design task. As an example, consider the design of an aerial search and fire control radome which is to be mounted on the nose of an aircraft whose function is intercepting supersonic bombers. If the aircraft requires a streamlined radome to be supersonic, the accuracy requirement of the search and fire control radar and its surrounding radome would probably be secondary to the streamlining requirement. Actually, an acceptable compromise must be found which will satisfy both aerodynamic and electrical requirements, and thus enable the weapons system to perform its mission.

After all the requirements are properly weighted, the next design step is the concurrent choice of radome shape and wall construction. It is important to note that they are not independent. To illustrate this point, consider the problems attendant to the choice of the shape and wall construction for the search and fire control interceptor radome just discussed. Let it be assumed that to satisfy the velocity requirement of the aircraft a cone having an included angle at the apex of 30° is recommended. As shown in Figure 3-7 for the case where the antenna looks out the apex, all the incidence angles will be 75° on the basis of ray geometry. As the antenna is directed away from the position shown, the incidence angles increase on one side of the radome and decrease on the side toward which the antenna is turning. Depending on the relative sizes of the antenna and the radome, the range of incidence angles will vary from above 75° down to normal incidence when the antenna is rotated 75°. The radome design thus presents a difficult problem in terms of either the search or the fire control requirements of the enclosed radar. The search function would normally place stringent requirements on radome transmission, and the fire control operation would require that radome beam refraction be minimized or eliminated. Furthermore, on an aircraft of the interceptor variety, the weight of the radome would be of prime importance. The problem is therefore to find a type of radome wall which will satisfy the electrical requirements, allow for a 30° conical shape, and be light in weight.

3-9. Electrical Requirements

In terms of the electrical requirements, a prudent choice might be a solid wall, approxi-

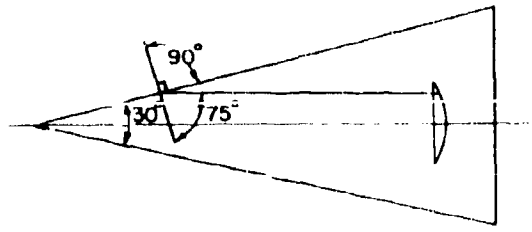


Figure 3-7. 30° Conical Radome

mately a half-wavelength thick. Examples of solid-wall electrical characteristics are given in Figures 3-8 and 3-9. The curves shown are calculated from equations developed in Chapter 2 for the transmission of plane linearly polarized waves through plane homogeneous, lossless, isotropic dielectric sheets of infinite extent. In Figures 3-8 and 3-9 the normal sheet thickness d, normalized in terms of free-space wavelength λ, is plotted versus the incidence angle θ, in degrees, for the case where the conductivity is zero, the relative permeability is unity, the relative dielectric constant is 4, and for the plane of polarization perpendicular (Figure 3-8) and parallel (Figure 3-9) to the incidence plane. The dashed lines are plots of d/λ versus θ for constant percentage values of transmitted power; the solid lines are for constant values of insertion phase. The term "insertion phase" refers to the phase retardation of the wave traversing the dielectric sheet relative to what it would have been at a point beyond the sheet if the sheet had not been present. An examination of the phase and transmission characteristics of Figures 3-8 and 3-9 reveals that for all values of θ less than 90° there is a value of d/λ for which it is theoretically possible to obtain 100 percent transmission (lossless case). Furthermore, the insertion phase is the same for both polarizations when the transmission is 100 percent. Thus it might be possible — a little sophistry may be required — to design an electrically satisfactory radome by properly choosing the radome wall thickness on the basis of a thorough investigation of incidence angles and polarization. However, a solid-wall radome is not particularly desirable in terms of its strength-to-weight ratio. A better choice in this respect would be the conventional "A" sandwich construction described in Chapter 2. The curves shown in Figures 3-10 and 3-11 are similar to those shown for the case of a single wall in Figures 3-8 and 3-9 except that they are plotted in terms of normalized core thickness, d_c/λ, versus θ, for constant normalized skin thickness d_s/λ of 0.024, a core dielectric constant ϵ_c of 1.2, and a skin dielectric constant ϵ_c of 4.3 (both relative).

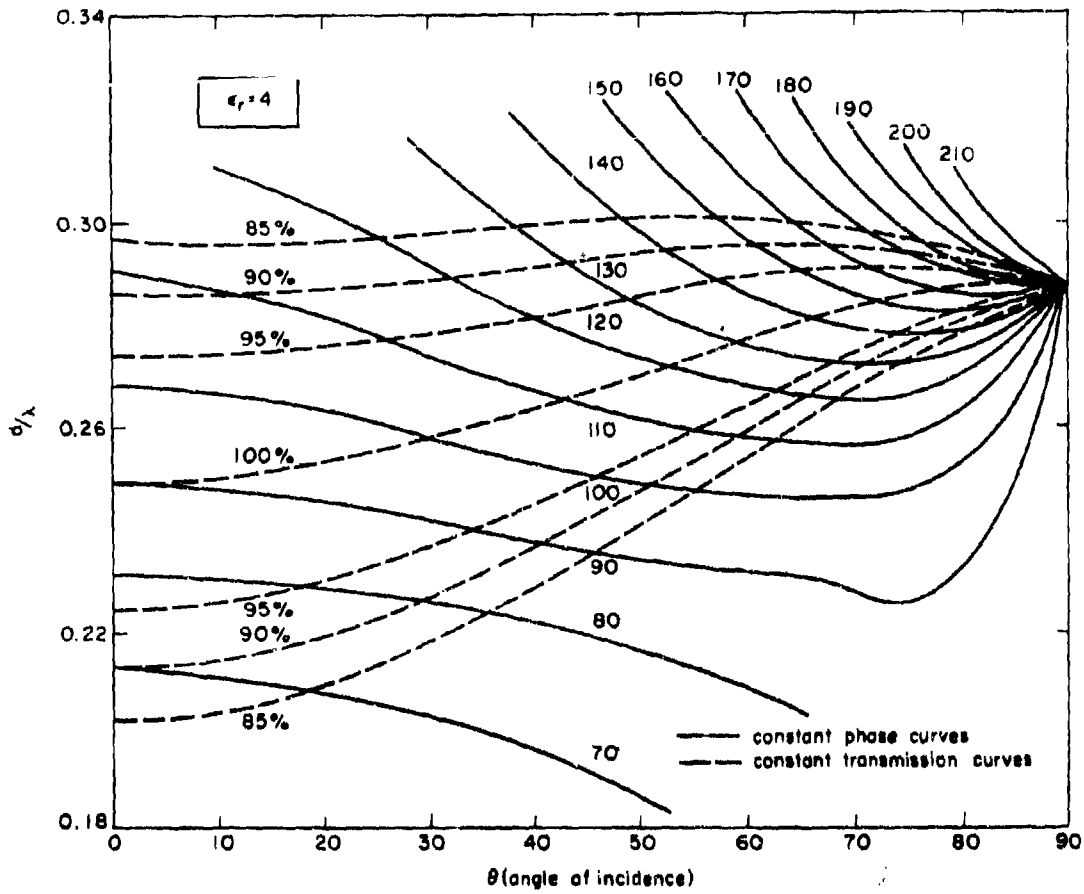


Figure 3-8. Constant Transmission and Insertion Phase Contours (Single Sheet, Perpendicular Polarization)

From Figures 3-10 and 3-11 it can be determined that in the vicinity of θ equal to 75° a value of d_c/λ does not exist which will provide 100 percent transmission for both polarizations. Also the insertion phase is a function of polarization for all values of d_c/λ when θ is greater than zero. Thus, for high-incidence-angle radomes, the choice of an "A" sandwich construction is not entirely, if at all, compatible with requirements for good transmission and low boresight errors (beam-refraction errors). But bad as the "A" sandwich electrical characteristics may be at extremely high incidence angles (below 60° the transmission and phase properties are very good), an appreciable saving in weight can be achieved by its use.

3-10. Weight Factor

If the surface area of the radome is denoted by S, its thickness by d, and the density of the wall by ρ, then the weight, W, can be approximated by

$$W = S\rho d \qquad (3\text{-}14)$$

Now the density ρ_s, of glass fiber laminate having a relative dielectric constant of 4.3 is approximately 100 pounds per cubic foot and the density ρ_c of alkyd-isocyanate foam having a dielectric constant of 1.2 is about 20 pounds per cubic foot. On the basis of Figures 3-8 and 3-9, it is reasonable to choose a normalized wall thickness where d/λ equals 0.285 to achieve good transmission out to incidence angles of 75° or more. Therefore the weight W_s, in pounds of the solid-wall glass fiber radome, with the aid of Equation (3-14), will be

$$W_s = 28.5\lambda S \qquad (3\text{-}15)$$

where the product λS is in cubic feet. Referring to Figures 3-10 and 3-11, there are several choices of core thickness, d_c/λ, that satisfy the requirements used in obtaining Equation

(3-15). However, to simplify the matter, let the choice of d_c/λ be premised on the additional, but arbitrary, restriction that the polarization is more nearly perpendicular to the incidence plane than parallel; a value of d_c/λ equal to 0.460 would therefore appear to be a realistic choice. Since the curves are based upon a parametric value of d_s/λ equal to 0.024, the weight in pounds of the sandwich radome is approximated by

$$W_A = 14.2 \lambda S \qquad (3\text{-}16)$$

For a conical radome having a length of 6 feet and an included angle of 30^0, the surface area would be about 31 square feet. For a wavelength

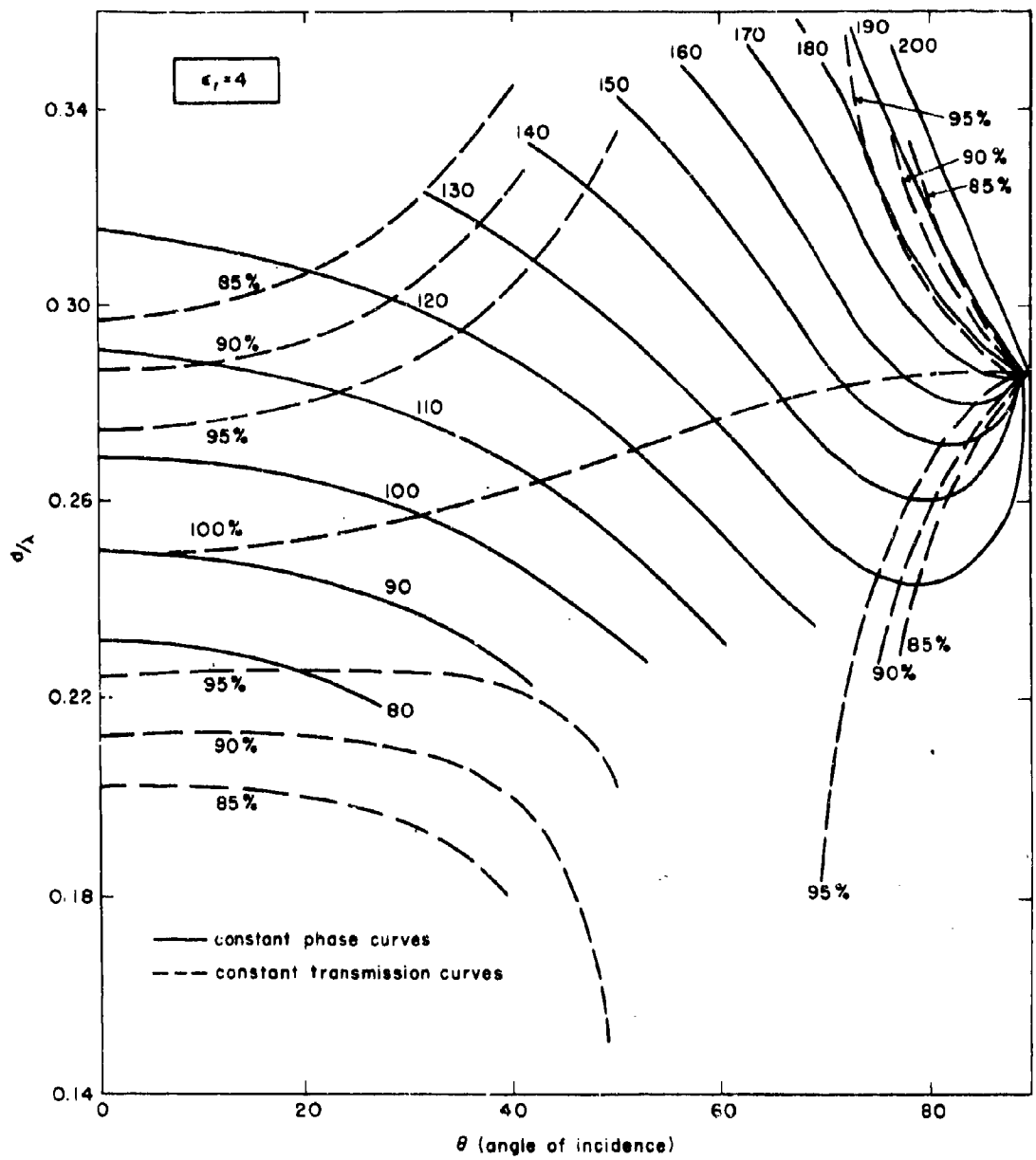


Figure 3-9. Constant Transmission and Insertion Phase Contours (Single Sheet, Parallel Polarization)

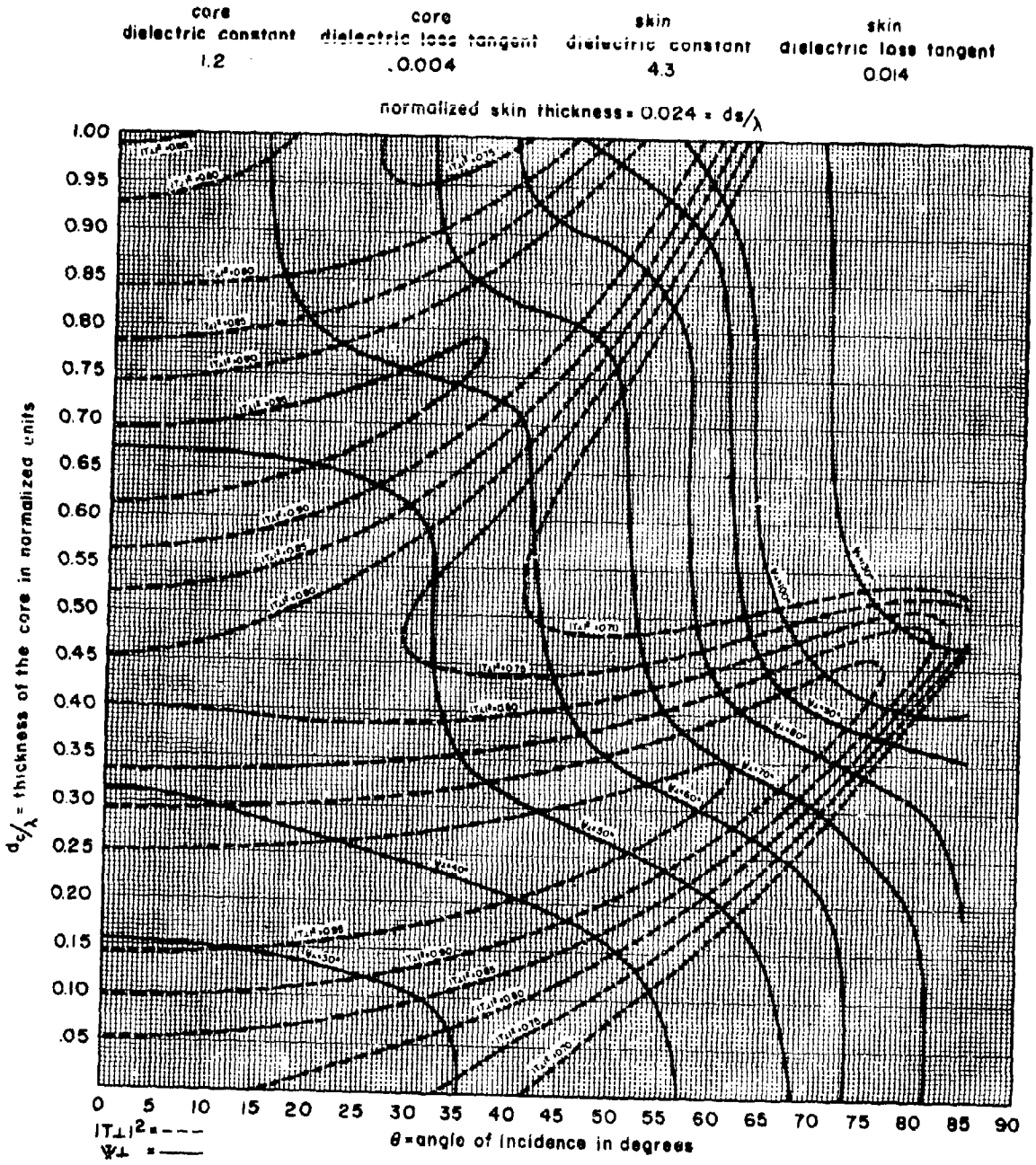


Figure 3-10. Contours of Constant Power Transmission and Insertion Phase Delay for "A" Sandwich Panels as a Function of Normalized Core Thickness and Incidence Angle: Perpendicular Polarization

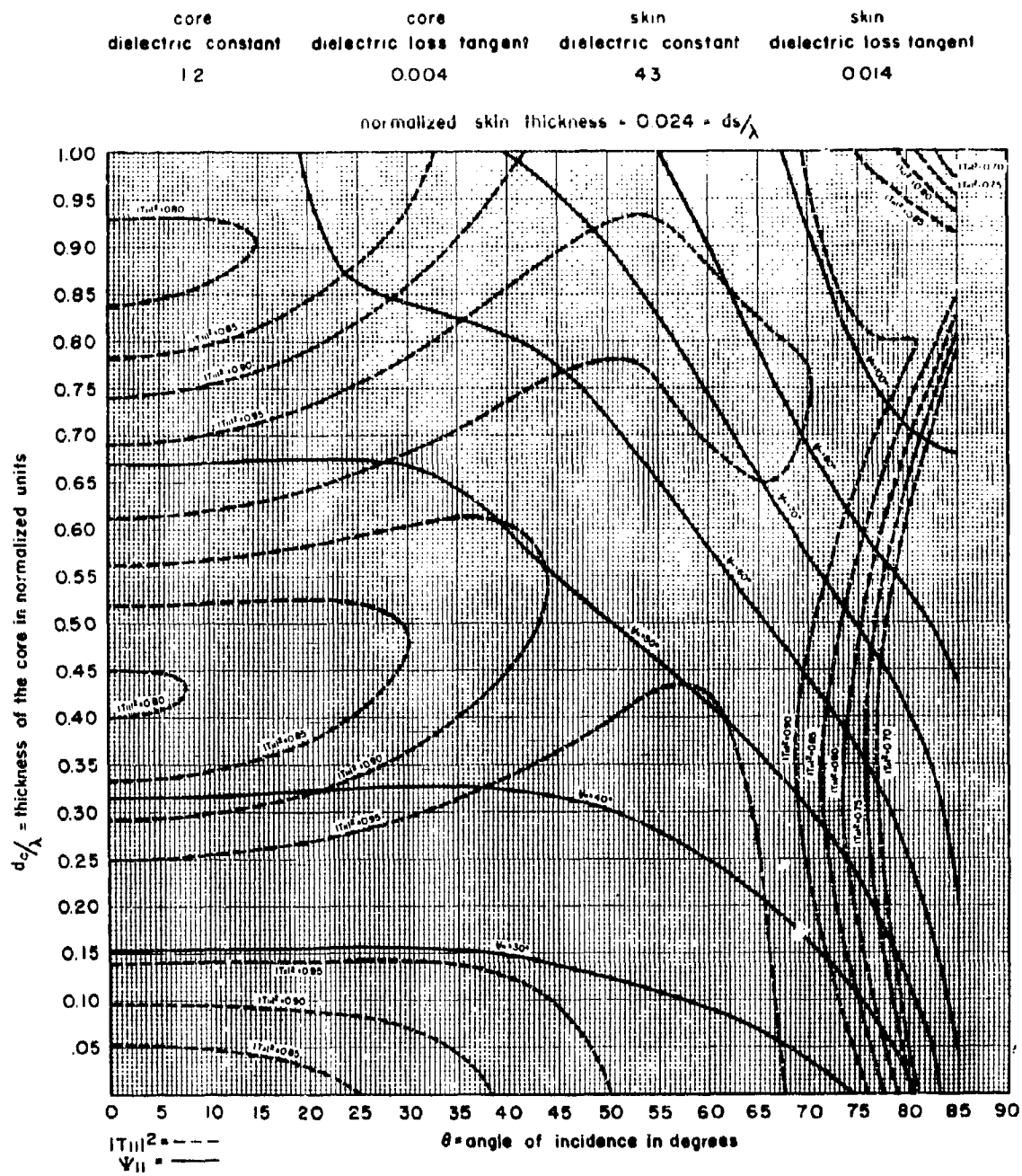


Figure 3-11. Contours of Constant Power Transmission and Insertion Phase Delay for "A" Sandwich Panels as a Function of Normalized Core Thickness and Incidence Angle: Parallel Polarization

of 0.1 foot, the weight of the solid radome would be approximately 88 pounds, or about 44 pounds heavier than the "A" sandwich radome.

It would seem reasonable to investigate the possibility of using an "A" sandwich wall and to determine whether the attendant reduction in weight would be sufficient to offset the performance penalty resulting from the change in shape required to make the radome electrically satisfactory. The radome shape which was originally chosen solely on the basis of aircraft aerodynamic requirements should also be considered as a function of the wall construction.

It should be mentioned that although the previous example was chosen principally for the purpose of illustrating the need for concurrence in radome shape and wall structure design, it is also representative of the type of problem encountered in radome design.

One other facet governing the choice of radome shape is the ease with which the chosen shape lends itself to analysis. In the following sections of this chapter the problems associated with making theoretical determinations of the effects of the radome are discussed. After considering these problems, it becomes quite apparent that radome geometry, if properly chosen, can greatly simplify the analysis problem. In particular, it is especially helpful if both the radome and the antenna are figures of revolution. Furthermore, it is also helpful if the shape of the radome is that of a conic section. However, the aspect of convenience in the choice of shape should not be considered fundamental to the design problem.

SECTION D. INCIDENCE ANGLE STUDY

3-11. Preliminary Considerations

Once the radome shape and wall construction have been tentatively chosen, the next design step is to undertake a preliminary evaluation of radome performance. To accomplish this it is necessary to have available design data, either experimental or theoretical, on the amplitude transmission properties (and phase also, if beam distortion is of interest) of the wall structure being considered. If the wall structure is conventional, utilizing low-loss materials, then curves such as those shown in Figures 3-8 through 3-11 will usually suffice. If the wall structure is not isotropic or homogeneous, then experimental curves of power transmission and insertion phase should be obtained as a function of sheet thickness, frequency, incidence angle, and polarization for plane sheet samples illuminated with a plane wave front. (In making experimental measurements of the complex transmission coefficient of plane sheets, care must be exercised to insure that the wave front is sufficiently plane and the sheet is sufficiently large to minimize diffraction effects.) If theoretical curves are used which are based on lossless dielectric material, an allowance must be made for losses. For half-wave or "A" sandwich radomes with wall materials having loss tangents of 0.02 or less and where the maximum incidence angles are less than 50°, the reduction in power transmitted will be about 5 percent or less. (See Figures 2-9 and 2-18 through 2-21.)

It should be carefully noted that the usefulness of the theoretical and experimental data on the transmission of plane waves through plane sheets depends entirely on the approximation that the radius of curvature of the radome wall is large compared to the wavelength of the incident field. When this is true, it is reasonable to assume that each small area on the radome being illuminated is essentially a plane sheet. Thus by relating the various incremental areas on the radome surface to the parameters of polarization, frequency, and incidence angle it is possible to choose a local wall thickness that will optimize the transmission properties for the particular area being considered. In many cases, however, an average uniform wall thickness can be chosen that will satisfy the design requirements over the whole radome surface for all antenna orientations.

Although simple in principle, the determination of the incidence angles and the orientation of the polarization vector as a function of the relative position of the antenna with respect to the radome becomes quite complicated in detail due to antenna-radome geometry. Occasionally when the antenna beam is well collimated and the aperture is small in comparison with the diameter of the radome, it is sufficient to consider the central ray as being representative of the bundle of parallel rays. Thus each incremental area of radome surface has only a single incidence angle associated with it. More frequently, it is necessary to consider the beam both in terms of its finite cross sectional area and its divergent properties. The latter consideration is particularly important in incidence angle studies involving antennas having broad beams in at least one plane. The cosecant-squared pattern used for uniform ground illumination is

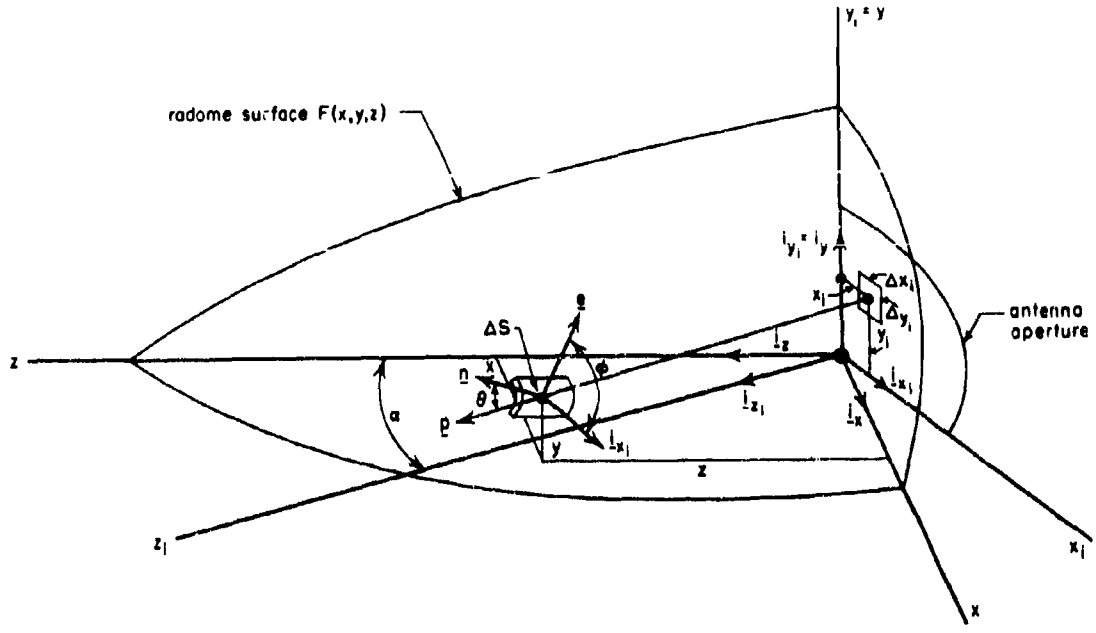


Figure 3.12. Radome Geometry, Analytic Case

a good example of an antenna pattern that requires consideration of the beam's divergent nature.

It is convenient to divide radomes into two classes for purposes of making incidence angle studies. One classification refers to all radomes that can be studied by analytical means; the other, which unfortunately includes most radomes, refers to those requiring graphical methods of attack. For convenience the former may be designated as analytic and the latter as non-analytic radomes. Actually the incidence angle study of any radome problem could probably be handled either analytically or graphically; however, when the radome is a figure of revolution, and particularly when its contour is a conic section, analytical methods of computing incidence angles are quite convenient. For the more general case where the radome contour is described in terms of loft lines (curves formed by the intersection between a family of parallel, arbitrarily spaced planes and the surface of a geometrical figure of interest), graphical methods are usually more convenient. It might be noted that although the lofting contours may not be given exactly in terms of analytic functions, they can, through curve-fitting techniques[8] be represented analytically. Thus it is occasionally worthwhile to obtain an approximate analytic representation to a lofted radome, particularly if it is easily represented in terms of simple functions.

3-12. Analytical Determination of Incidence Angles

As an example of the procedure to be followed in making an analytical determination of incidence angles, consider the radome depicted by Figure 3-12. Let the surface be represented by

$$F(x, y, z) = 0 \tag{3-17}$$

and let the origin of the x-, y-, z-coordinate frame be coincident with the origin of the x_l-, y_l-, z_l-frame. Furthermore it will be assumed that the antenna is a circle whose axis of symmetry is the z_l-axis and whose aperture is in the plane x_l-y_l, that the direction of propagation of the radiated field is defined by the unit vector $\underline{p}$, and that

$$\underline{p} = \underline{i}_{z_l} \tag{3-18}$$

where i_{z_l} is a unit vector parallel to the z_l-axis. In other words it is assumed that the antenna aperture is large and produces a well-collimated beam circular in cross section and propagating in a direction normal to the aperture. If the radiation from the aperture is assumed to be divergent as in the case of a shaped beam antenna, more recondite methods of analysis must be used.*

* See Section 8.14, p. 464, of Reference 3.

Since the radome is assumed to be a figure of revolution, the coordinates of a point on its surface satisfy the relation

$$z = z\left(\sqrt{x^2 + y^2}\right) = z(r) \qquad (3\text{-}19)$$

where r is the normal distance from a point on the surface to the z-axis, and

$$F(x, y, z) = z - z\left(\sqrt{x^2 + y^2}\right) = 0 \qquad (3\text{-}20)$$

For example, if the radome surface is conical

$$z = m\sqrt{x^2 + y^2} + b = mr + b \qquad (3\text{-}21)$$

$$F(x, y, z) = z - m\sqrt{x^2 + y^2} + b = 0 \qquad (3\text{-}22)$$

Because of the symmetry of the radome and the antenna, there is no preferred plane in which to rotate the antenna with respect to the radome. The orientation of the polarization of the field is normally constant with respect to one of the antenna gimbal axes; therefore, if only one axis of antenna rotation is assumed, it is necessary and sufficient to investigate the behavior of the radome as a function of both antenna rotation and polarization.

Let the single axis of antenna rotation be the y_i axis. Hence

$$y_i = y \qquad (3\text{-}23)$$

and

$$\underline{p} = \underline{i}_x \sin\alpha + \underline{i}_z \cos\alpha \qquad (3\text{-}24)$$

where $\underline{i}_x$ and $\underline{i}_y$ are unit vectors parallel, respectively, to the x- and y-axes, and α is the angle between the z_i- and z-axes.

Now the incidence angle θ, on an incremental element of radome of surface ΔS having position coordinates x, y, and z, is defined by

$$\theta = \cos^{-1}(\underline{n} \cdot \underline{p}) \qquad (3\text{-}25)$$

where $\underline{n}$ is the outward directed unit normal vector to the surface at (x, y, z). The unit vector $\underline{n}$ has its direction defined by the gradient of the surface function F (x, y, z), which is given by Equation (3-20). Hence

$$\underline{n} = \frac{\nabla F(x, y, z)}{|\nabla F|} \qquad (3\text{-}26)$$

If Equation (3-26) is expanded in terms of its rectangular components, then by substitution the expression for θ may be written as

$$\theta = \cos^{-1}\frac{-\frac{\partial z}{\partial x}\sin\alpha + \cos\alpha}{\left[\left(\frac{\partial z}{\partial x}\right)^2 + \left(\frac{\partial z}{\partial y}\right)^2 + 1\right]^{-1/2}} \qquad (3\text{-}27)$$

Thus by solving the right side of Equation (3-27) it is possible to determine the incidence angle at a specific point (x, y, z) on the surface as a function of the angular position α of the antenna. However, Equation (3-27) does not restrict the incidence angles to only those that actually occur when the point of interest is being illuminated by the antenna. This latter restriction can be obtained for the case of a nondivergent beam by solving both x and y explicitly in terms of x_i and y_i and substituting the resultant expressions for x and y into Equation (3-27).

To recapitulate, in Equation (3-27), the incidence angle θ is expressed as a function of the coordinates of a point on the radome surface (x, y) and the antenna orientation angle α. The z-dependence was eliminated by Equation (3-20), which merely requires that the point lie on the radome surface. Now we wish to express θ as a function of the antenna aperture coordinates (x_i, y_i) and the orientation angle α. From the geometry of Figure 3-12

$$x = z\tan\alpha + x_i \sec\alpha \qquad (3\text{-}28)$$

and

$$y = y_i \qquad (3\text{-}29)$$

The specific radome shape, as defined by Equation (3-20), is substituted for z in Equation (3-28). The resulting equation for x and Equation (3-29) for y are substituted into Equation (3-27). In this manner, the incidence angle may be expressed as

$$\theta = \theta(\alpha, x_i, y_i) \qquad (3\text{-}30)$$

By tabulating θ for all values of x_i and y_i as limited by the boundary of the antenna, the incidence angles may be determined for all values of α of interest. Again it should be emphasized that the above comments are limited by the restrictive assumptions stated in connection with Equation (3-18).

An alternate method for arriving at Equation (3-30) proceeds as follows: From Equation (3-20)

$$F(x, y, z) = z - z\left(\sqrt{x^2 + y^2}\right) = 0 \qquad (3\text{-}31)$$

From Figure 3-12,

$$x = x(x_i, z_i, \alpha) = x_i \cos\alpha + z_i \sin\alpha \qquad (3\text{-}32)$$

$$y = y_i \qquad (3\text{-}33)$$

$$z = z(x_i, z_i, \alpha) = -x_i \sin\alpha + z_i \cos\alpha \qquad (3\text{-}34)$$

Substituting Equations (3-32), (3-33), and (3-34) into Equation (3-20) yields

$$F_i(x_i, y_i, z_i, \alpha) = 0 \qquad (3\text{-}35)$$

which defines the radome shape in the antenna coordinates (x_i, y_i, z_i). As in Equation (3-26),

$$\underline{n} = \frac{\nabla F_i}{|\nabla F_i|} \qquad (3\text{-}36)$$

Then

$$\cos\theta = \underline{n} \cdot \underline{p} \qquad (3\text{-}37)$$

which is a function of x_i, y_i, z_i, and α, but the z_i-dependence is eliminated by using Equation (3-35). The result is Equation (3-30).

Since any general form of elliptical polarization can be represented by two linear components orthogonal in space, it will be sufficient to demonstrate the procedure in terms of a single linear component polarization normal to the propagation vector $\underline{p}$. If $\underline{e}$ is defined by

$$\underline{e} = \underline{i}_{x_i} \cos\theta + \underline{i}_{y_i} \sin\phi \qquad (3\text{-}38)$$

where $\underline{i}_{x_i}$ and $\underline{i}_{y_i}$ are unit vectors parallel, respectively, to the X_i and Y_i axes, and ϕ is the angle between $\underline{e}$ and $\underline{i}_{x_i}$, it is then possible to simulate with a single axis of antenna rotation all the relative radome and antenna positions that would be obtained using two axes of rotation with fixed polarization.

Transmission. If it is desired to determine the transmission through an incremental area, ΔS, it is necessary to know the angle ξ the polarization vector makes with the incidence plane as well as the incidence angle θ. The incidence plane is defined as the plane containing the vectors $\underline{n}$ and $\underline{p}$. Let $\underline{i}_\parallel$ and $\underline{i}_\perp$ be unit vectors (both perpendicular to $\underline{p}$) parallel and perpendicular respectively to the incidence plane, as shown in Figure 3-13. Also refer to Figures 2-1, 2-2, and 2-24 of Chapter 2. Thus

$$\underline{i}_\perp = \frac{\underline{p} \times \underline{n}}{\sin\theta} \qquad (3\text{-}39)$$

and

$$\underline{i}_\parallel = \underline{p} \times \underline{i}_\perp \qquad (3\text{-}40)$$

As discussed in Equation (2-84) of Chapter 2, the transmitted electric field may be resolved into its parallel and perpendicular components as

$$\dot{E}_t = \dot{E}_t \, \underline{i}_\perp + \dot{E}_{t_\parallel} \, \underline{i}_\parallel \qquad (3\text{-}41)$$

$$= \dot{T}_\perp \, \dot{E}_i \, \underline{i}_\perp + \dot{T}_\parallel \, \dot{E}_{i_\parallel} \, \underline{i}_\parallel \qquad (3\text{-}42)$$

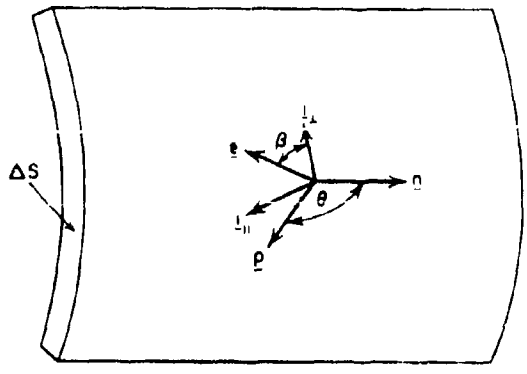


Figure 3-13. Vector Relationships at Radome Surface

For the case of an incident wave linearly polarized at an angle ξ with respect to the incidence plane, the effective complex transmission coefficient is given by Equation (2-91) of Chapter 2 as

$$\dot{T}_0 = \dot{T}_\parallel \cos^2\xi + \dot{T}_\perp \sin^2\xi \qquad (3\text{-}43)$$

A good approximation to the over-all transmission properties of the radome can be obtained by simply summing the product $|\dot{T}_0 \, \dot{E}_i|$ over x_i and y_i for all values of α and dividing by the sum of $|\dot{E}_i|$. Hence, if T^2 is the approximate power transmission, then

$$T^2(a)\, T^2(\alpha) \approx \frac{\int_{-a}^{a}\int_{-b}^{b} \left| \dot{T}_0(\alpha, x_i, y_i)\, \dot{E}_i(x_i y_i) \right| dx_i\, dy_i}{\int_{-a}^{a}\int_{-b}^{b} \left| \dot{E}_i(x_i, y_i) \right| dx_i\, dy_i} \qquad (3\text{-}44)$$

where a and b are the extremities of the antenna aperture. It should be emphasized that the expression given for $T^2(\alpha)$ in Equation (3-44) is only a first approximation to radome transmission efficiency, and as such is not intended for use in problems where beam distortion is being calculated. Methods of predicting the latter phenomena are discussed in detail in Chapter 4.

The analytical methods that have been presented, although relatively simple in principle, are not always so in practice. For instance, if the contour of the radome is an ogive where

$$F(x, y, z) = (z - c)^2 + (r - d)^2 - R^2 = 0 \qquad (3\text{-}45)$$

then

$$z = \sqrt{R^2 - \left(\sqrt{x^2 + y^2} - d\right)^2} + c \qquad (3\text{-}46)$$

where $r = \sqrt{x^2 + y^2}$ is the radius at the axial station point z, and where c, d, and R are constants of the ogive. Equations for other shapes are given in Section G of Chapter 2.

If the right side of Equation (3-46) is substitutued into Equation (3-28), the resultant expression is a quartic equation in x. Although it is possible to determine which of the four roots of x are the proper ones to use in an analytical calculation of the incidence angles, the complexity of such a calculation argues in favor of utilizing simpler and more direct graphical methods. This is particularly true in problems where neither the radome nor the antenna has axial symmetry.

3-13. Graphical Determination of Incidence Angles

The simplicity of most graphical methods of analysis is dependent upon being able to relate conveniently the incidence angle to its projection on two perpendicular planes. In Figure 3-14 the direction of propagation of a ray is denoted by the vector $\underline{p}$, and the incidence angle θ is, by definition, the angle between the normal to the surface $\underline{n}$ and the propagation direction $\underline{p}$. Now two perpendicular planes have been joined along the vector $\underline{p}$. These are designated planes VP and HP, and the angles between $\underline{p}$ and the projections of $\underline{n}$ on each of the planes are designated as θ_V and θ_H, respectively. In addition, the polarization vector $\underline{e}$ in the plane HV is related to the V axis by the angle ϕ. Also shown is the vector $\underline{i}_{\parallel}$, which is located along the intersection of the incidence plane and plane HV. From the geometry of Figure 3-14

$$\tan^2\theta = \tan^2\theta_V + \tan^2\theta_H \qquad (3\text{-}47)$$

If α is the angle between $\underline{i}_{\parallel}$ and the V axis, then

$$\tan\theta_H = \tan\theta \sin\alpha \qquad (3\text{-}48)$$

and

$$\tan\theta_V = \tan\theta \cos\alpha \qquad (3\text{-}49)$$

or

$$\tan\alpha = \frac{\tan\theta_H}{\tan\theta_V} \qquad (3\text{-}50)$$

The planes HP and VP are representative of two families of planes that may be related to the antenna. Since many search radar antennas are gimbaled in azimuth about a vertical axis, it is convenient to subdivide the antenna aperture with a number of equally spaced parallel planes that are perpendicular to the antenna aperture and parallel to the vertical azimuth axis. In (a) of Figure 3-15 an edge view of such a family of planes is shown where the planes are designated as AA, BB, etc. An edge view of the other family of planes is shown in (b) of Figure 3-15.

The latter family has planes designated as aa, bb, etc., and these planes have been chosen on the basis of a ray diagram of the antenna. Thus, all the directions of propagation of rays emanating from the antenna aperture are represented by the lines of intersection of the two families of planes. Thus, the plane VP of Figure 3-14 corresponds to any one of the planes E'E' through EE, and the plane HP corresponds to any one of the planes aa through gg. Thus, in view of Equations (3-48) through (3-50), it should be possible to determine the incidence

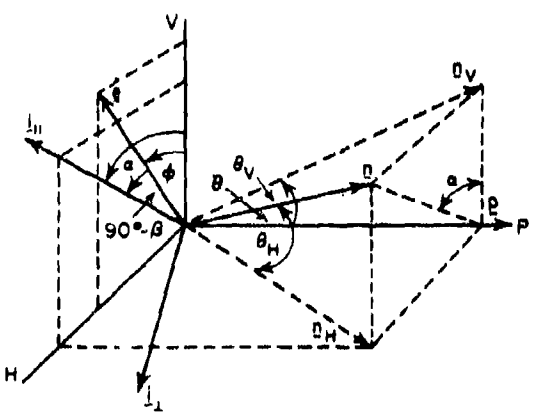


Figure 3-14. Incidence Angle Projections

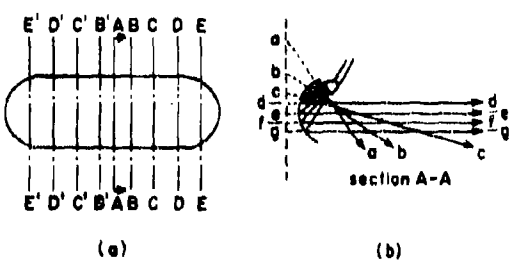


Figure 3-15. Elevation and Oblique Planes of Antenna: (a) Edge View of Elevation Planes; (b) Edge View of Oblique Planes

angle θ and the relative orientation of the polarization vector, with respect to the incidence plane, by graphically determining θ_H and θ_V.

The angles θ_H and θ_V may be determined with aid of radome loft lines similar to those shown in the sketches of Figure 3-16. Two views of the vertical radome and antenna cutting planes are shown in Figure 3-16. For the case of aircraft radomes the loft lines produced by the vertical cutting planes are usually referred to as buttock lines, and the loft lines resulting from horizontal cutting planes are called water lines. Both are usually available on drawings of aircraft radomes; however, to avoid confusion, only the buttock lines are shown in Figure 3-16. The edge view of the cutting planes is shown in (a), and (b) represents the buttock lines of intersection made by the radome cutting planes 0 through 8 and the representative antenna cutting planes E'E', AA, and EE. The latter are shown obliquely in (b) of Figure 3-16; hence, to determine the projection angle θ_V, true views of these planes must be obtained by combining true measurements of length in horizontal planes as measured from (a) with true lengths in vertical planes as measured in (b).

To obtain the true views, horizontal cutting planes are constructed which pass through the antenna aperture and through the points on the radome where the buttock lines of the radome intersect the vertical antenna cutting plane of interest, for example, plane AA. Assuming that the vertical position of the antenna within the radome is known, it is possible to determine where the horizontal cutting planes intersect the antenna aperture by constructing the cutting planes as horizontal lines on a view such as (b) of Figure 3-16. For the construction of a true view of a vertical antenna cutting plane, the horizontal lines are then chosen so as to pass through the points where the vertical antenna cutting plane intersects the buttock lines. Once the points on the aperture intersected by the horizontal cutting planes have been established, the true view of the intersection of a vertical antenna cutting plane with the radome surface is constructed by projecting lines perpendicular to the edge view of the antenna aperture at each of

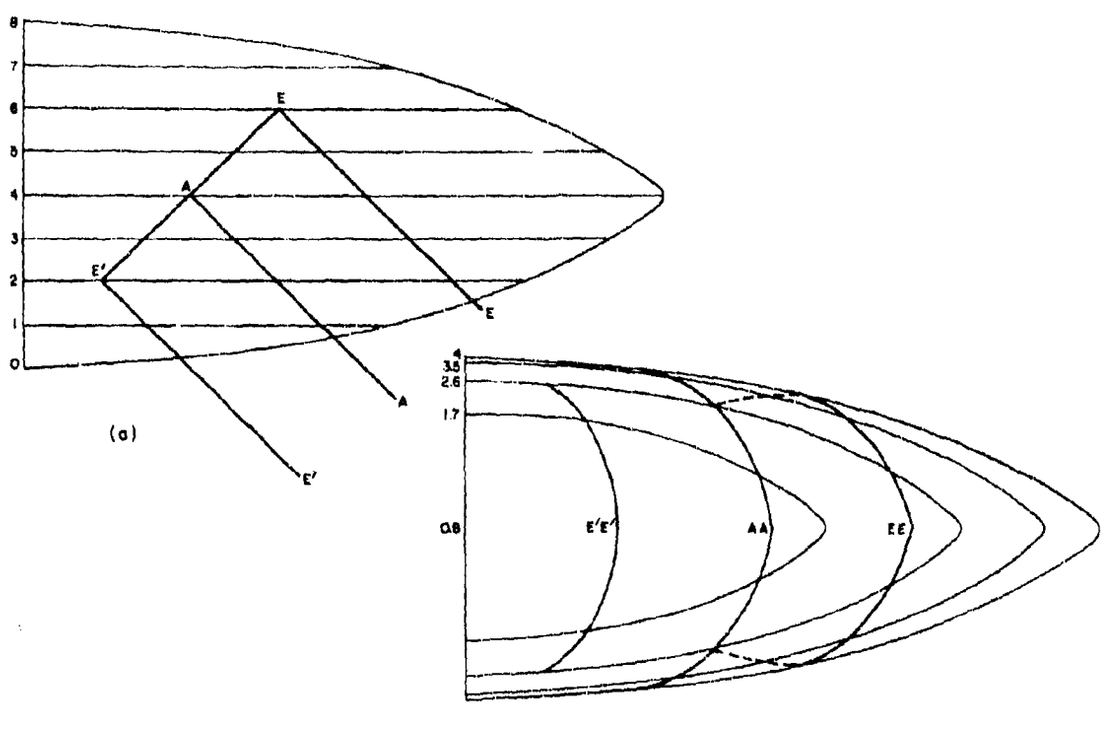


Figure 3-16. Radome Loft Lines, Vertical Cutting Planes: (a) Edge View of Vertical Cutting Planes; (b) Vertical Cutting Plane Contours

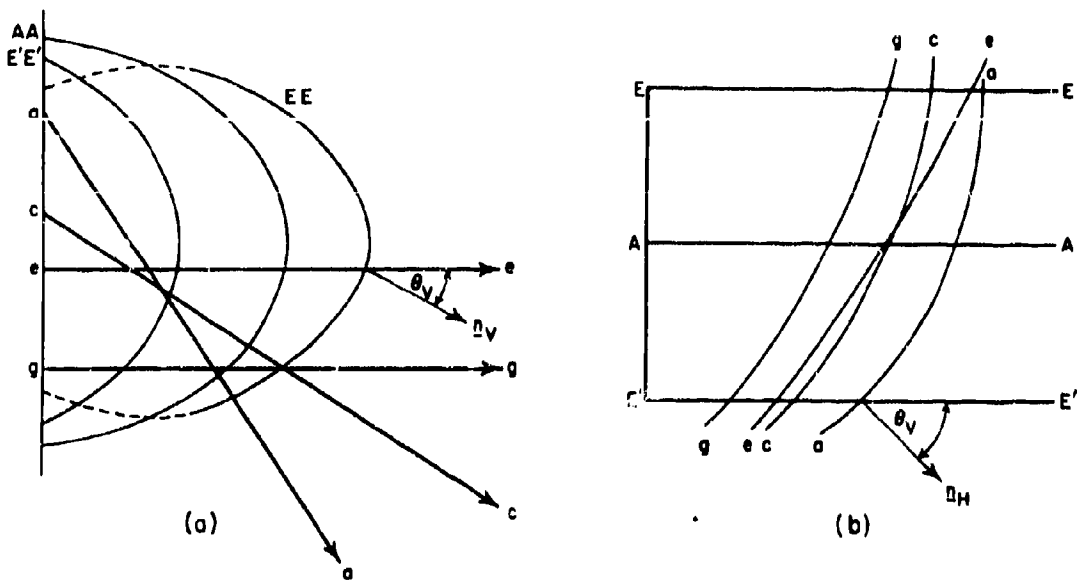


Figure 3-17. Projected Incidence Angles: (a) True View of Vertical Antenna Cutting Planes; (b) True View of Oblique Cutting Plane Contours

the points at which the aperture is intersected by the horizontal cutting planes. For this purpose a view of the antenna such as that shown in (b) of Figure 3-15 is used, where the dashed line is arbitrarily chosen as the effective aperture. The same aperture is shown again in (a) of Figure 3-17 as the solid line from which the oblique antenna cutting planes aa, cc, etc., are emanating. Now each line perpendicular to the aperture corresponds to the line of intersection between the vertical cutting plane of interest and a horizontal cutting plane that intersects a particular buttock line. Hence all the lines lie in the vertical cutting plane and each line intersects a particular buttock line. Thus by locating the points of intersection of each line with its respective buttock line, the locus of points of the curve of intersection between the radome surface and the vertical cutting plane is obtained. The points at which the lines intersect the radome are found by measuring the distance from antenna aperture to the radome surface. Since each line is in a horizontal plane, and each line intersects a particular buttock line on the surface, the distances are obtainable directly from a view such as that shown in (a) of Figure 3-16. In that figure, these distances are measured from the aperture to the respective buttock line along the line which represents an edge view of the particular vertical antenna cutting plane under consideration; thus, if plane AA is being developed into a true view, measurements of length would be made from line E'AE along line AA to its intersection with lines 4, 3, 2, 1, and 0. In (a) of Figure 3-37 true views of planes E'E', AA, and EE are shown superimposed on an edge view of the antenna and its associated ray diagram. The construction used in their development is not shown because of the complexity of lines which would result; however, the construction lines along which the distances are measured would be perpendicular to the solid line from which the rays originate.

Once the true views, as shown in (a) of Figure 3-17, are developed and superimposed on the antenna ray diagram, the vertical projection angles θ_V may be obtained directly by erecting normals to the contours E'E', AA, and EE at the points of intersection with the planes aa through gg.

To determine the angles θ_H, true views of the oblique antenna cutting planes aa through gg are obtained directly from a view such as (a) of Figure 3-17 by measuring true lengths along aa, cc, etc., from a fixed reference point out to the point of intersection with the contours E'E', AA, etc. Then by constructing a view such as (b) of Figure 3-17 where planes E'E', AA, etc. are shown as an edge view, the true lengths from the reference line are measured from line E'A... along lines E'E', AA, etc. Thus by connecting the locus of points for aa, cc, etc., true views of the curves of intersection between the radome and the planes aa, cc, etc., are obtained. Note that when measuring distances along aa, cc, etc., in (a) of Figure 3-17 to their respective intersections with E'E', AA, etc.,

it is not necessary that the reference point lie on the antenna aperture. All that is required is that for any one plane, such as aa, the same point be used to reference measurements out to E'E', AA, etc. After the contours aa, cc, etc., are obtained it is a simple matter to construct normals to them at the points of intersection with the planes AA, etc., as shown in (b) of Figure 3-17.

When θ_V and θ_H have been found by these graphical methods, the true incidence angle θ may then be obtained with the aid of Equation (3-47), and the angle α which the incidence plane makes with the vertical plane VP may be found with the aid of Equation (3-50). Thus if the angle ψ which the polarization vector ξ makes with the vertical plane VP is known, it is possible to resolve the polarization vector ξ into components which are parallel and perpendicular to the incidence plane. The transmission of these components can then be easily treated and the resultant wave can be reconstructed as it emerges from the radome wall.

As an aid in the computation of θ and α, Figure 3-18 has been prepared. Values for θ and α can

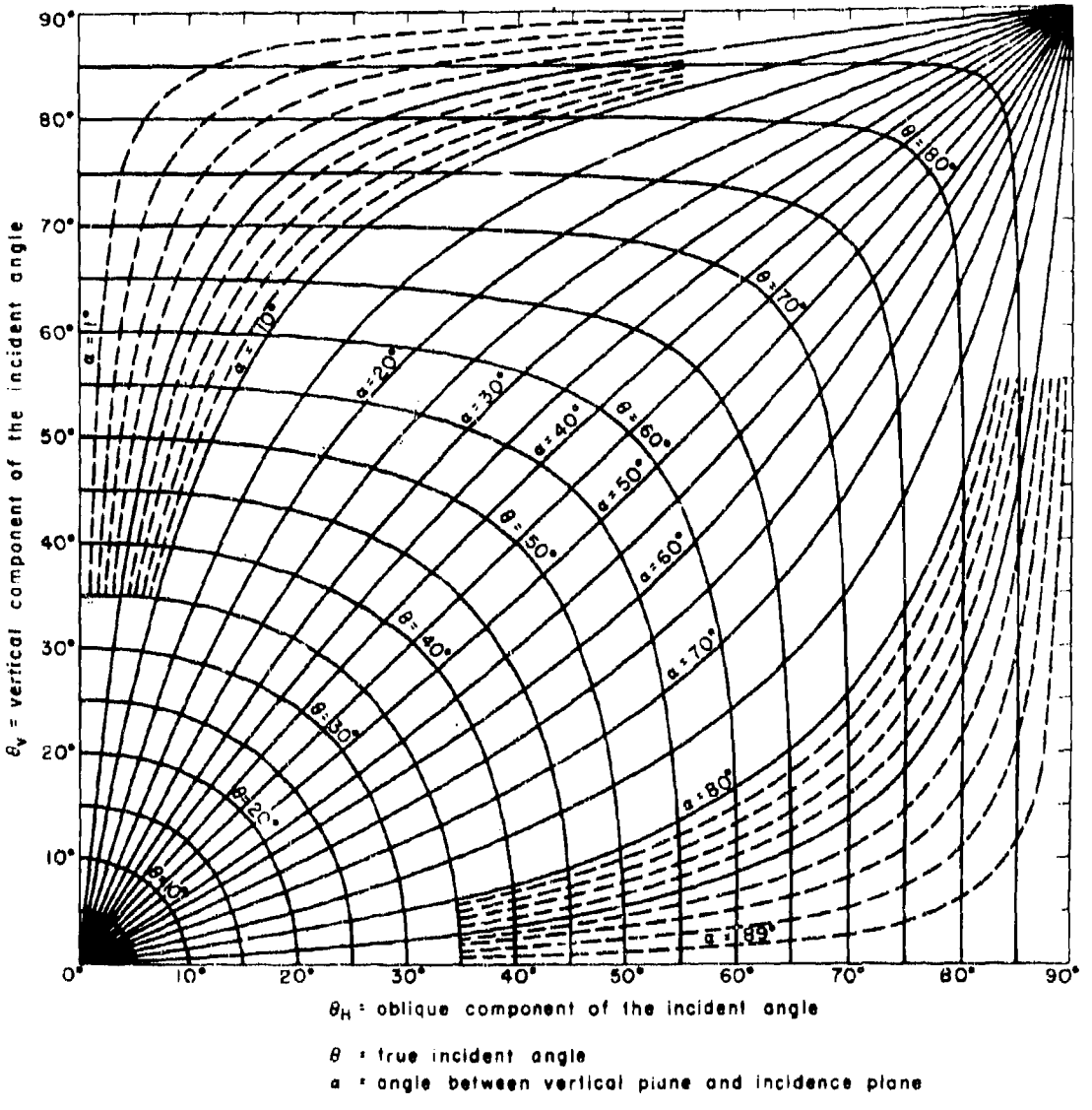


Figure 3-18. Relative Polarization and Incidence Angle Components Chart

be obtained from it directly if θ_H and θ_V are known.

It might be noted that usually it is sufficient to make an incidence angle study at only the critical positions of the antenna, which normally can be determined in advance. Hence the average incidence angle study for a nonstreamlined radome may require investigation of only one or two relative positions of the antenna with respect to the radome. However, where high performance requirements exist, it is usually necessary to consider all possible antenna-radome orientations.

SECTION E. WALL THICKNESS

3-14. Optimum Data Presentation

The final step in the design procedure is the determination of the thickness of the radome wall. For normal-incidence radomes it is usually sufficient to choose a wall of uniform thickness. For more complicated design problems where beam bending and high incidence angles are considerations, it is frequently necessary to vary the thickness of the wall over the surface of the radome. Since the ultimate design criterion is high transmission with a minimum of beam distortion, the ideal wall design would be one that provides 100 percent transmission and constant insertion phase for all incidence angles and all polarizations at all frequencies; thus, it is convenient to examine the electrical behavior of various wall constructions as a function of incidence angle, polarization, and frequency. Curves that present such information were given in Figures 3-8 through 3-11 for a solid wall having a relative dielectric constant ϵ_r of 4.0 and for an "A" sandwich wall having a normalized skin thickness to wavelength ratio d_s/λ of 0.024, a relative skin dielectric constant ϵ_s of 4.3, and a relative core dielectric constant ϵ_c of 1.2.

Curves of this general type, where normalized wall thickness is plotted as a function of incidence angle for constant values of transmission and insertion phase, are particularly useful in wall thickness design problems involving variable-thickness walls. In the case of sandwich walls, either the skins or the core, or both, could be varied in thickness; however, from the standpoint of fabricating a foamed-in-place "A" sandwich radome* it is most convenient to vary the core thickness, keeping the thickness of the skins constant.

Another method of presenting theoretical data for design problems involving uniquely polarized antenna systems is presented in Figure 3-19.

The transmission coefficient T_0, is plotted as a function of incidence angle θ for various values of normalized wall thickness d/λ. The curves of Figure 3-19 were calculated for the case of a circularly polarized, homogeneous plane wave of wavelength λ traversing a homogeneous, isotropic, lossless plane sheet having a relative dielectric constant of 4.0, unity relative permeability, and a normal thickness d. The transmission coefficient T_0 is the voltage amplitude of the transmitted circularly polarized wave which has the same sense of rotation as the incident wave. In terms of the complex transmission coefficents $\dot{T}_\perp$ and $\dot{T}_\parallel$ of a linearly polarized wave

$$T_0 = 1/2 \left| \dot{T}_\perp + \dot{T}_\parallel \right| \qquad (3\text{-}51)$$

Data of the form shown in Figure 3-19 are useful in determining what the transmission characteristics would be for a constant thickness wall over the range of incidence angles of interest. It is also quite convenient to have transmission and phase information for the specific polarization that is being considered; however, it is seldom feasible to calculate a whole family of special phase and transmission coefficients just for a single radome design problem.

For design problems where bandwidth and dielectric constant variations are considerations, still another method of presenting data is shown in the curves of Figure 3-20. In this figure the insertion phase Δ has been plotted as a function of the incidence angle θ for the cases of parallel and perpendicular polarization of a linearly polarized wave traversing solid, lossless dielectric sheets having relative dielectric constants ϵ_r of 1.02, 1.50 and 4.00.* The thickness of each sheet was chosen so that ϕ is equal to π when θ equals 50° (half-wave wall at 50°). This last family of curves is useful in illustrating the effect of changes in dielectric constant on insertion phase; in fact, one very important aspect of radome design is made obvious, that is, a low-dielectric-constant wall reduces the variation of insertion phase with polarization. The fact that insertion phase

* Reference foamed-in-place construction in paragraph 8-26.

* See Equation (2-53) in Chapter 2.

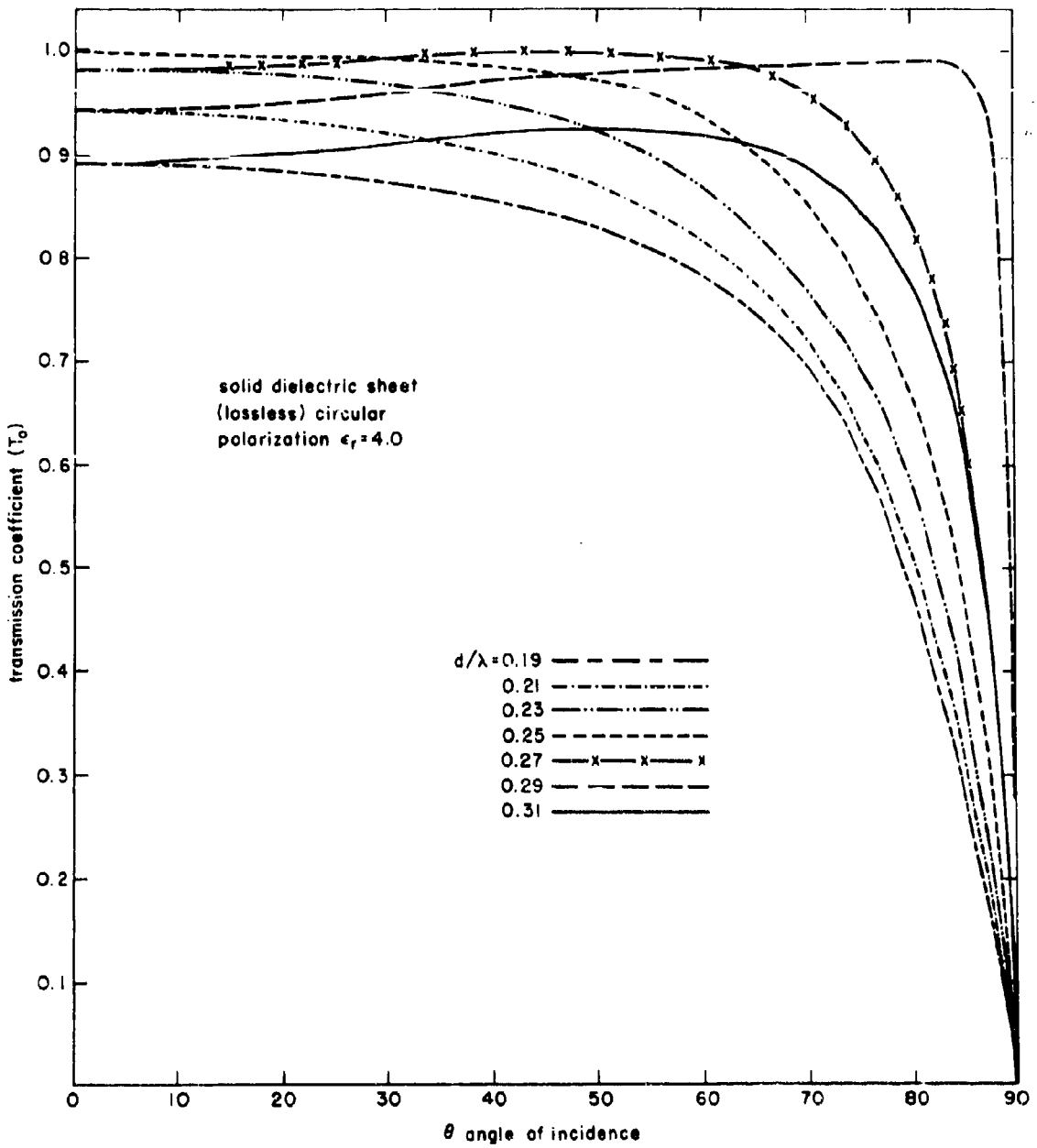


Figure 3-19. Transmission Coefficient Versus Incidence Angle Curves

is a function of polarization is quite important in the design of radomes having stringent requirements on beam refraction errors. Usually in such designs the major problem is one of designing a compromise wall structure that satisfies the restrictions on beam deflections for both polarizations. When both polarizations behave in nearly the same fashion, the design requirements for the two cases are more compatible.

Sometimes experimental data on the phase and transmission coefficients of sample test panels are required. This is particularly true for unique wall constructions that exhibit inhomogeneous or anisotropic properties. In general,

if honeycomb cores are being used in high-incidence-angle applications, it is usually advisable to make up test samples of the wall structures being considered. By conducting free space transmission tests the data can be presented in a fashion similar to that employed in the curves of Figures 3-19 and 3-20.

3-15. Case I: Thin Wall, Uniform Thickness

From Equation (2-47) of Chapter 2, it may be shown that

$$T^2 = \frac{(1 - r^2)^2}{(1 - r^2)^2 + 4\, r^2 \sin^2 \phi} \tag{3-52}$$

where

$$\phi = \frac{2\pi d}{\lambda_0} \sqrt{\epsilon_r - \sin^2 \theta} \tag{3-53}$$

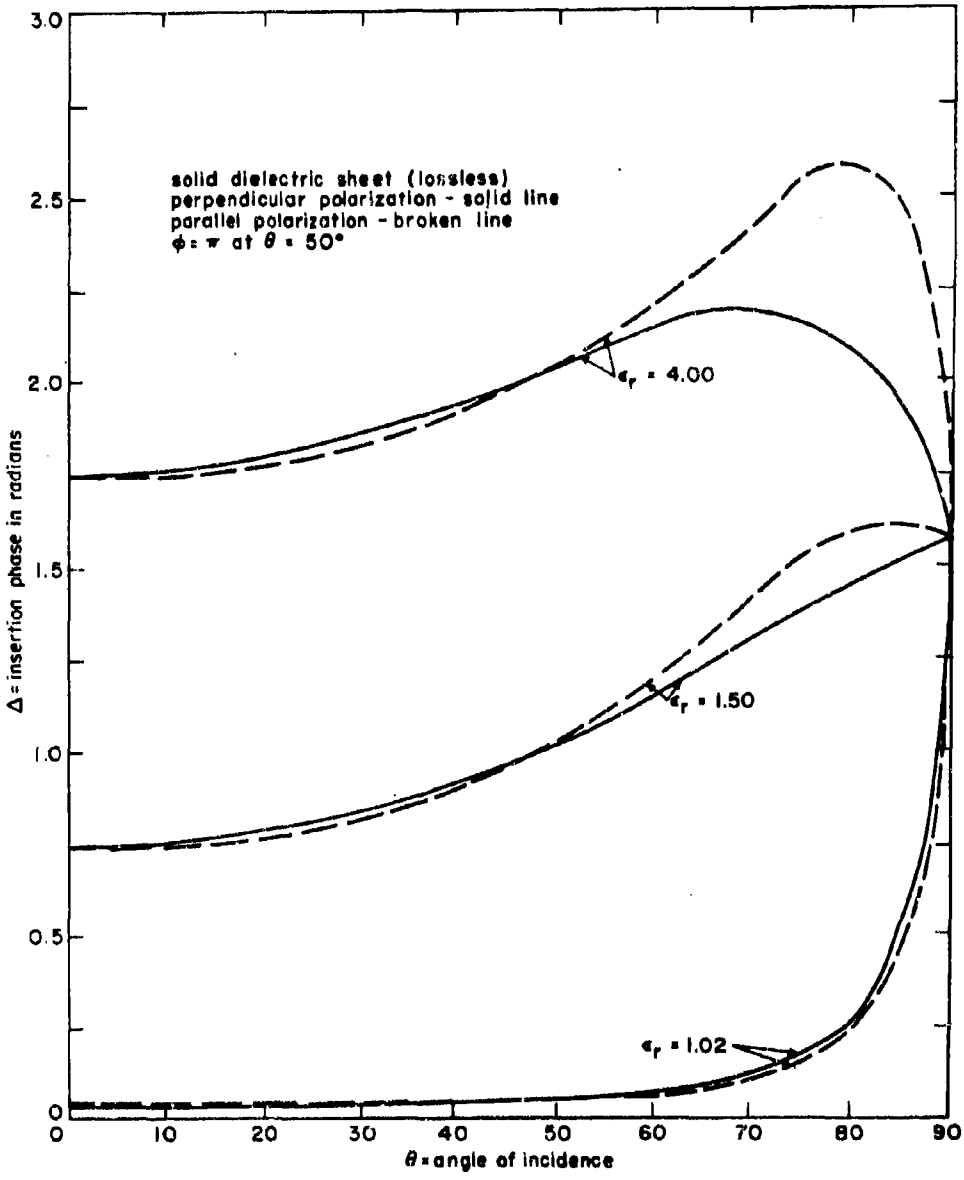


Figure 3-20. Curves of Insertion Phase Versus Incidence Angle

ϕ = electrical thickness in radians at an arbitrary angle θ.

For the case of a thin wall, such that

$$\phi \approx \sin \phi \tag{3-54}$$

Equation (3-52) may be solved for d to yield

$$d^2 \approx \frac{(1 - T^2)}{T^2} \left[\frac{(1 - r^2)^2 \lambda_0^2}{16 r^2 \pi^2 (\epsilon_r - \sin^2 \theta)} \right] \tag{3-55}$$

When the required power transmission is known, the maximum allowable thickness can be calculated for any incidence angle and polarization. In general, for the case of perpendicular polarization, as the incidence angle increases the allowable maximum wall thickness must be decreased; however, for the case of parallel polarization, the presence of Brewster's angle, θ_B, permits 100 percent transmission for a lossless sheet of any thickness d when the incidence angle θ equals θ_B where

$$\theta_B = \tan \sqrt{\epsilon_r} \tag{3-56}$$

In Equation (3-56), as before, ϵ_r is the dielectric constant of the sheet relative to the surrounding medium.

3-16. Case II: Half-Wave Wall, Uniform Thickness

In many transmission design problems, where the range of incidence angles is small and the transmission requirements are not too stringent, it is possible to choose a single wall thickness on the basis of the criterion that the proper thickness is the one that will maximize the minimum value of transmission coefficient at any incidence angle in the range of angles of interest. In terms of the reflection coefficient, the optimum wall thickness is the one that minimizes the maximum reflection coefficient that occurs at any angle of incidence in the range of interest. As an example of the application of the criterion, consider the case of a radome having a range of incidence angles varying from 15 to 65° for perpendicular polarization. For polarization parallel to the incidence plane, the same approximate maximum value of reflection coefficient is obtained, but only at incidence angles near 15°. At the large incidence angles the reflections have been reduced because of Brewster's angle. In using curves for the lossless case, it is well to remember that the effect of loss, although small in lossless dielectrics at near normal incidence, becomes increasingly important as the incidence angle is increased (see Chapter 2).

3-17. Case III: Half-Wave Wall, Non-Uniform Thickness

Although uniform-thickness walls are satisfactory for the majority of search radomes, sometimes the restrictions on electrical performance make it desirable to vary the wall thickness of the radome as a function of position on the radome surface. The simplest case to consider is the one where the radome is a figure of revolution. If the antenna is roll stabilized, variations in wall thickness are restricted to the axial direction. When the enclosed antenna is not roll stabilized, it may be helpful to vary the wall thickness circumferentially. In this case, the need for variation in the circumferential direction stems from the fact that when the antenna axes are fixed with respect to the radome the polarization usually remains the same with respect to horizontal and vertical reference planes within the radome.

As noted earlier, the first-order theoretical contours of zero reflection are the same for both polarizations (see Figures 3-8 and 3-9). Therefore, it might be expected that at each point on the radome the thickness could be adjusted to provide a theoretical 100 percent transmission for both polarizations; actually, such a procedure could be followed if the antenna beam were a single ray. However, the cross sectional area of the beam generally is of the same order of magnitude as the radome surface area; hence any point on the surface of the radome is illuminated for more than one position of the antenna with respect to the radome. In general, therefore, there will be a whole family of incidence angles associated with each surface point. To determine the proper thickness at a point, the incidence angles associated with the point must be weighted relative to each other. One method that can be used when the antenna is a paraboloid of revolution is to base the design thickness on the incidence angle made by the central ray of the antenna. Such a choice presupposes that the range of incidence angles is centered about the angle made by the central ray. Also, it assumes that the power density of the radiated field is greatest in the direction of the central ray.

When the enclosed antenna is a cylindrical section of a paraboloid of the type commonly used for uniform ground illumination, the wall thickness may be determined on the basis of optimizing the transmission for the range of incidence angles existing when only the rays in the central or symmetry plane of the antenna are considered. However, for a shaped beam or cosecant-squared antenna there is no simple criterion of weighting, such as choosing the

center ray as being representative. Fortunately, in most practical problems the range of incidence angles associated with a particular point on the radome surface is small enough so that a single thickness can be determined that satisfies all of the incidence angles.

In cases where the geometry of the radome yields to analytical methods, the radome wall thickness d, which satisfies the criterion of optimum transmission, can be expressed in terms of the radome surface coordinates x, y, and z. Consider, for example, the case of an axially symmetric radome whose geometry is similar to that shown in Figure 3-12. In Section D of this chapter it was shown that the incidence angle θ could be related to the antenna offset angle α, and a particular antenna ray denoted by x_i and y_i, as in Equation (3-30).

Thus, by choosing the ray of maximum interest, such as the central ray where x_i and y_i equal zero, the angle θ may be expressed as

$$\theta = \theta(\alpha) \tag{3-57}$$

But with the aid of Equations (3-19), (3-28), and (3-29), α may be solved for explicitly as a function of z. Hence, if Equation (3-53) is solved for d when Φ equals π, then

$$d = \frac{\lambda}{2\left\{\epsilon_r - \sin^2\left[\theta(z)\right]\right\}^{-1/2}} \tag{3-58}$$

One problem which arises frequently in the calculation of radome wall thickness is whether the inner or outer surface of the radome wall should be used in calculating incidence angles. Usually the outer surface of the radome is specified; however, in calculating incidence angles by the methods outlined in Section D, small errors can arise due to the finite thickness and the curvature of the wall. In general, the errors caused by calculating the inner surface incidence angles in terms of the outer surface are small in comparison with errors that result from such assumptions as the treatment of incremental elements on the radome surface and on the wave front of the antenna as being planar.

So far only the problem of choosing a wall thickness for optimum transmission has been considered, and therefore many of the problems, such as the dependence of insertion phase and transmission on polarization, have been tacitly avoided. When it is necessary to consider insertion phase effects the difficulty of determining the correct wall thickness is greatly enhanced. Since beam refraction design problems are treated in considerable detail in Chapter 4, it will suffice now to consider only some of the qualitative aspects of the problem.

3-16. Insertion Phase Effects

Insertion phase becomes an important consideration in problems where beam distortion and refraction are critical. The effect of insertion phase on the antenna beam is in general quite complicated. If, however, a uniform variation of phase is produced across the beam as it traverses the radome wall, the antenna beam will be refracted in a manner very similar to that of light refracted by a prism – with one significant difference. In the case of the prism, the uniform variation in insertion phase across the beam results from the uniform thickness taper of the prism, whereas for the radome the variation in phase is due to the variation in the angles of incidence across the radome surface being illuminated. If the curvature of the radome is small, the effects of insertion phase are minimized. It was pointed out previously that a spherical radome, large with respect to the antenna, simplified radome design. The choice of the sphere was obvious from symmetry considerations, but the requirement for the sphere to be large with respect to the antenna was based on minimizing the variations in incidence angle. It should be noted that, when the insertion phase Δ is expressed as a power series of position x within a beam originally symmetrical with respect to x, then

$$\Delta = \Delta_0 + \sum_{j=1}^{\infty} \Delta_j x^j \tag{3-59}$$

Now, the even terms of the series produce symmetrical beam distortion effects, such as widening of the main beam and changes in the side lobe levels. The odd terms result in asymmetrical effects, such as beam bending.

One method of minimizing insertion phase effects is to vary the wall thickness, as a function of incidence angle, so as to maintain constant insertion phase over the whole wave front. This requirement differs from those outlined for transmission design in that it is necessary to consider the phase effect at a point on the surface relative to other illuminated points for all positions of the antenna that illuminate the point of interest. Thus, in addition to knowing all the incidence angles and polarizations associated with a single point, as in the case of transmission design, it is also necessary to know the insertion phase at one point relative to the phase at all other points being illuminated at the same time. The problem is therefore one of making

the design thickness, which is required at a single point for one position of the antenna, compatible with the requirements for the other positions of the antenna, except that the thickness at any point is also a function of the thickness at the surrounding points. Since the solution to the insertion phase problem (that is, the proper design thickness at any arbitrary point) requires a knowledge of the insertion phase produced by surrounding points, about the only design procedure is one of synthesis by analysis, or as it is more commonly referred to, "cut and try."

In many search radome problems requirements on beam distortion are limited to a small range of antenna offset angles. When such is the case it is usually feasible to design for uniform insertion phase in the area illuminated when the antenna occupies the central or some other properly weighted position within the range of interest. Then the design thickness of adjacent areas can be matched to the central area so as to maintain a uniform phase front as the antenna is moved angularly away from the central position. The same procedure may be extended to the whole radome surface; however, unless the geometry is relatively simple, the experimental methods of design discussed in Chapter 4 are to be preferred.

3-19. Case IV: Sandwich Wall, Uniform Thickness

The same design techniques as those discussed for the uniform-thickness solid wall may be used for "A" sandwich walls. As was the case for the solid wall, curves of constant transmission and insertion phase similar to those of Figures 3-10 and 3-11 are very helpful in determining the proper design thickness. One major difference between the solid-wall design and the sandwich wall design techniques may be noted by comparing the curves of Figures 3-8 and 3-9 with those of Figures 3-10 and 3-11. For the sandwich construction, the zero percentage reflection contours are not identical for the two polarizations, whereas the contours are identical for the lossless solid wall. Moreover, at high incidence angles (60° or greater), sandwich wall construction is a poor transmitter of parallel polarization; hence, in very streamlined radomes where parallel polarization is encountered, the use of sandwich walls is to be avoided. For incidence angles below 60° symmetrical sandwich constructions, can be designed to provide excellent transmission over a broad band of frequencies.* For the "A" sandwich, the transmission is very much a function of the thickness of the skins. Figures 3-21 and 3-22 are constant transmission and insertion phase contours similar to those of Figures 3-10 and 3-11, except that the normalized skin thickness ratio d_s/λ equals 0.055 instead of 0.024. It should be noted that, as the thickness of the skins is reduced (as shown in Figures 3-10 and 3-11), the range of core thicknesses and the range of incidence angles for which good transmission can be obtained is increased, except that for parallel polarization at incidence angles above 60° the transmission continues to drop off rapidly.

Occasionally in the design of sandwich radomes having honeycomb cores or other cores held in place by foreign adhesive materials, it is necessary to consider the effect of the adhesive. Normally the electrical effect of the adhesive is accounted for by considering the effective thickness of the skin to be the total thickness of skin plus adhesive, since in general the dielectric constant of the adhesive is less than or equal to the dielectric of the skins. If the dielectric constant of the adhesive is very much greater than that of the skins, the adhesive layers should be treated as layers in a multiple sandwich.* The same procedure may be used for rain erosion coatings.

3-20. Case V: Sandwich Wall, Non-Uniform Thickness

The problem of designing nonuniform sandwich walls is most meaningful in terms of "A" sandwich walls having a variable thickness core. As was the case for the solid wall radome, tapering the wall thickness permits uniform transmission as a function of antenna position even though the incidence angles change. In the case of a sandwich radome a different wall thickness taper is required for perpendicular polarization than is required for parallel polarization. Furthermore, a tapered wall affords only a small improvement over a uniform thickness wall when the polarization is parallel to the incidence plane (see Figures 3-11 and 3-22). Only when the polarization remains perpendicular to the incidence plane can a significant improvement in transmission be achieved by tapering the wall; when this is done, the method is essentially the same as that employed for tapering a solid wall radome.

The real advantages in using tapered core "A" sandwich walls accrue when it is necessary to maintain uniform insertion phase across the

* See pp 306-338 of Reference 9 for a detailed treatment of sandwich walls.

*See Chapter 2 for methods of computing transmission through complex sandwich structures.

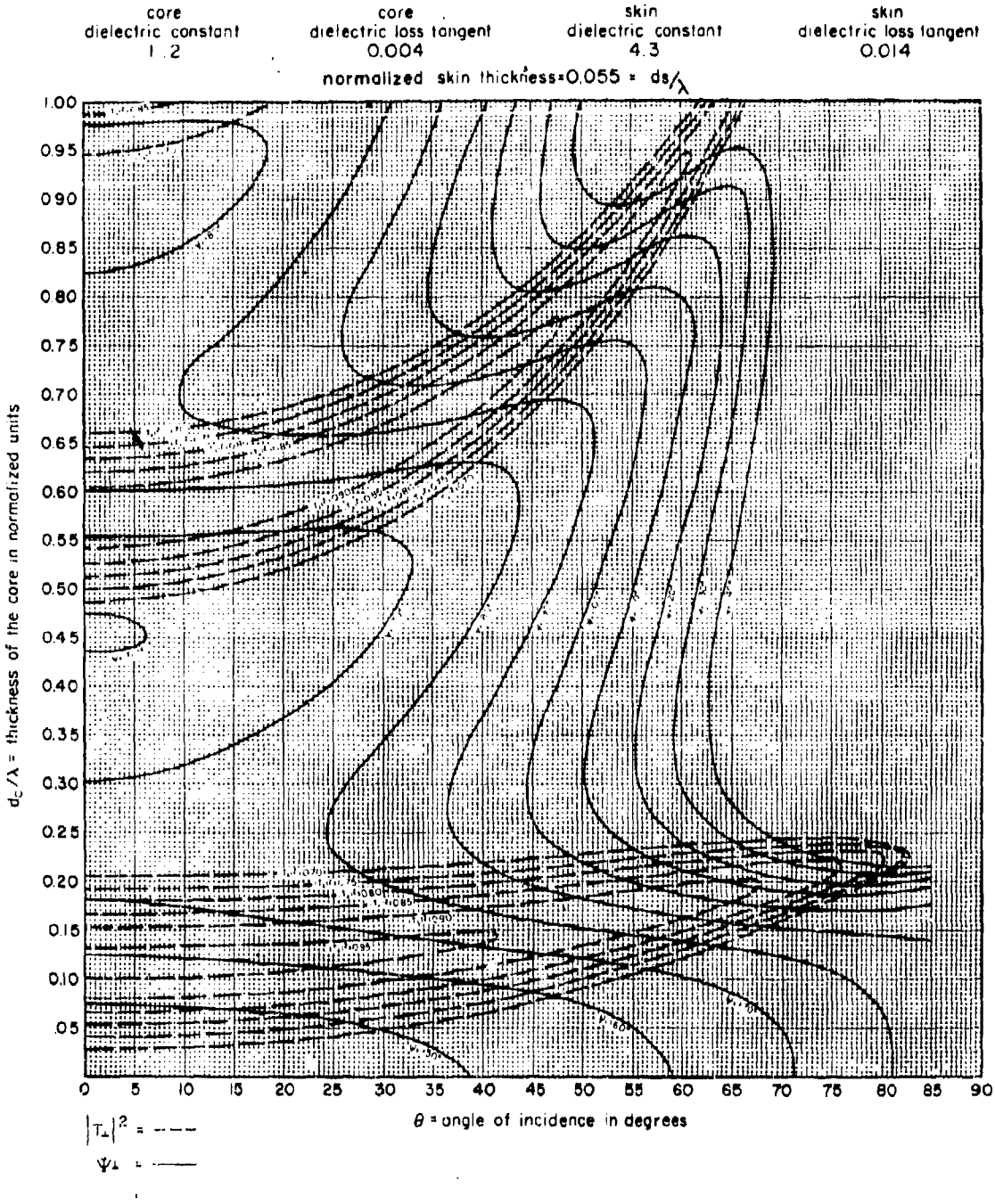


Figure 3-21. Contours of Constant Power Transmission and Insertion Phase Delay for "A" Sandwich Panels as a Function of Normalized Thickness and Incidence Angle: Perpendicular Polarization

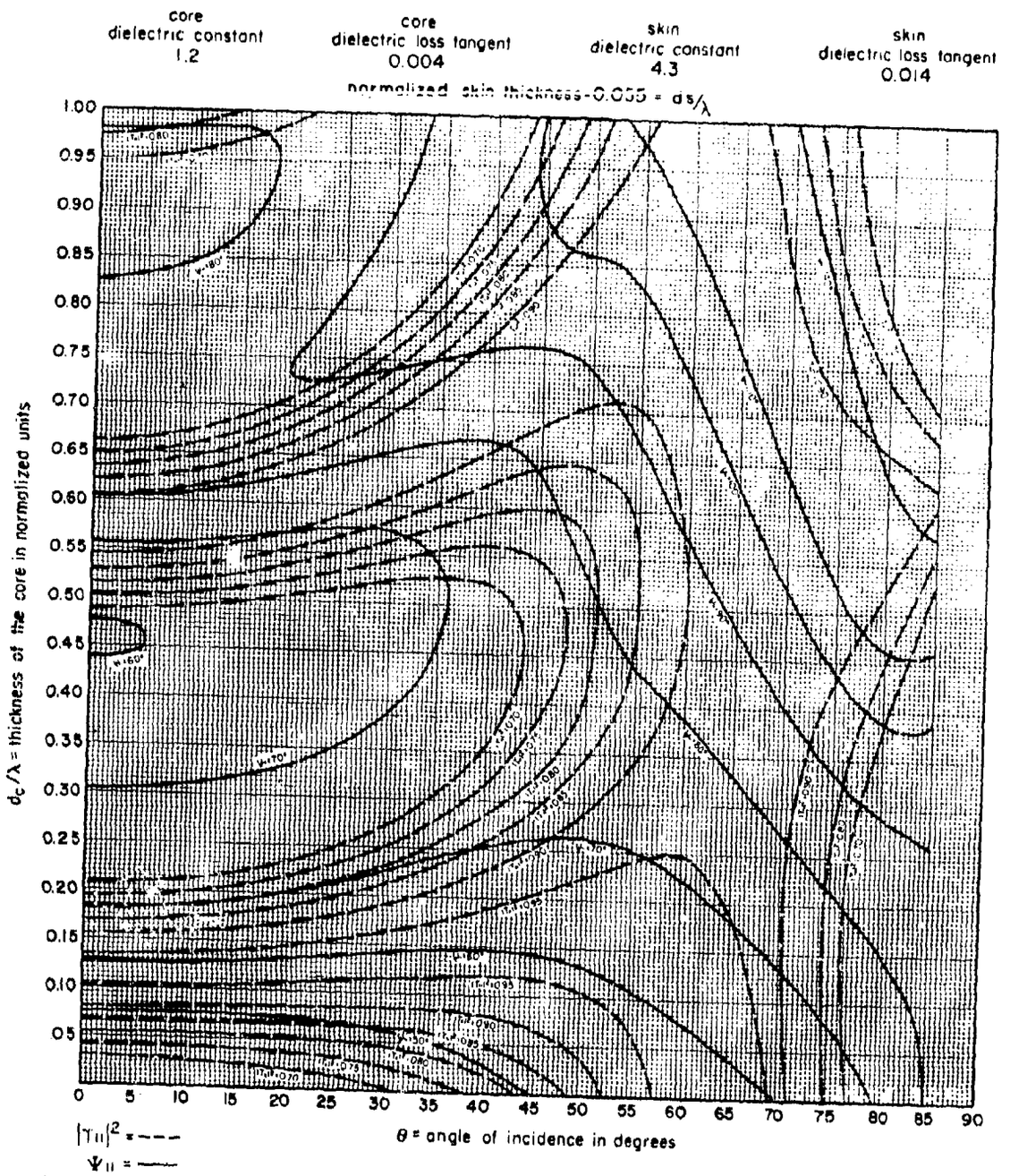


Figure 3-22. Contours of Constant Power Transmission and Insertion Phase Delay for "A" Sandwich Panels as a Function of Normalized Thickness and Incidence Angle: Parallel Polarization

antenna wave front, or when it is desired to reduce the rate of change* of beam refraction as a function of antenna position. For these problems it is possible to vary the core thickness over a considerable range without adversely affecting the transmission characteristics, particularly when the radome skins are relatively thin, as they are for the case shown in Figures 3-21 and 3-22.

SECTION F. INTEGRATED ANTENNA-RADOME DESIGN

There is much to be said in favor of integrating the design of radomes and antennas, at least to the extent that antenna and radome designers are familiar with each other's problems. For example, when the designer of the antenna is requested to provide a shaped beam for a specific function, he should have data on where the antenna will be mounted in the aircraft, the shape of radome the aerodynamicist will allow, and shape desired by the radome designer. In turn the radome designer should be familiar with the functional requirements of the radar and the relationship of such requirements to the radome design specifications. A mutual understanding of the antenna and radome problems will eliminate most of the incompatible aspects of the respective design problems.

Even if antenna and radome problems are semi-independent, the near field of the antenna is common to both, and it is in terms of providing detailed information on the near field that the antenna designer can make a direct contribution to simplifying radome design. Actually, by considering the near-field structure of the antenna, the design of the antenna can be simplified as well. The design of precision radomes is already very much dependent on an accurate knowledge of the near field and much specialized test equipment* has been developed to measure it. Thus, by utilizing the same procedures of relating the far field to the near field that are used for improving radome design, not only can antenna design techniques be improved, but the design of the radome will be aided directly by having immediately available all the information of interest on the antenna.

*See Chapter 4 for a discussion of error rates.

* See Chapter 12.

REFERENCES

1. Jenkins, F. A., and White, H. E. Fundamentals of Physical Optics. McGraw-Hill Book Co., Inc., New York, 1937, pp. 121-122.
2. Silver, Samuel, and James, H. M. Microwave Antenna Theory and Design. McGraw-Hill Book Co., Inc., New York, 1949, pp. 497-508. (Vol. 12, Radiation Laboratory Series.)
3. Stratton, J. A. Electromagnetic Theory. McGraw-Hill Book Co., Inc., New York, 1941, p. 479.
4. Soller, Theodore, Starr, M. A., and Valley, G. E., Jr. Cathode Ray Tube Displays. McGraw-Hill Book Co., Inc., New York, 1948, p. 19. (Vol 22, Radiation Laboratory Series.)
5. Reintjes, F. J., and Coate, G. T. Principles of Radar. McGraw-Hill Book Co., Inc., New York, 1952, p. 799.
6. Fox, A. G., Miller, S. E., and Weiss, M. T. Behavior and Application of Ferrites in the Microwave Region. The Bell System Technical Journal, Vol. XXXIV, No. 1 (January 1955), p. 93.
7. King, D. D. Measurements at Centimeter Wavelength. Van Nostrand Co., Inc., New York, 1952, p. 266.
8. Hoel, P. G. Introduction to Mathematical Statistics. John Wiley and Sons, Inc., New York, 1954, p. 126.
9. Cady, W. M., Karelitz, M. B., and Turner, L. A. Radar Scanners and Radomes. McGraw-Hill Book Co., Inc., New York, 1948, p. 247. (Vol. 26, Radiation Laboratory Series.)

Chapter 4

GUIDANCE AND FIRE CONTROL SYSTEM RADOME DESIGN

by

H. A. Schetne

Research Laboratories
Hughes Aircraft Company
San Diego, California

Chapter 4

GUIDANCE AND FIRE CONTROL SYSTEM RADOME DESIGN

SECTION A. INTRODUCTION

4-1. Radome Design Factors

Radomes used on high-speed aircraft* must withstand the aerodynamic rigors of supersonic flight and must produce a minimal effect on the radiation pattern of the guidance system. These requirements force a dual role on the radome: it is a structural part of the aircraft and an integrated component of the radar system. In the design of such radomes, compromises must be made which involve electromagnetics, aerodynamics, thermodynamics, structures, and materials and processes. As will be brought out, the design of any radome is usually accomplished by reference to factors other than those which concern only the radome. Best results can be obtained if a group of technically trained personnel co-operate in the design, and if the radome is considered as an integral part of the radar system — not as an item which is thrown in after everything else is designed and frozen.

Of all the aircraft, high-speed missiles probably demand the most from the radome, and the requirements of these missiles illustrate the complexity of the problems involved in designing radomes for sonic and supersonic flight. Missiles reach maximum velocity in a very few seconds after firing. An effect of such a rapid increase in speed is the production of a thermal shock. Temperatures involved in such a shock can be in excess of 1,000° F. The ability of materials to withstand such heat varies. Some materials are capable of maintaining their physical characteristics when the temperature is increased gradually but do not do so when the temperature is increased rapidly. If moisture is present in the radome wall, its sudden conversion to steam may destroy the radome. During flight, the temperature inside the radome wall increases, and if the flight is long enough in time, an equilibrium temperature may be reached. A temperature gradient usually exists through the wall, and differential expansion of the material may result in the destruction of the radome. Frontal air pressures of 100 pounds per square inch or more can exist with negative pressures possible over certain portions of the radome when the aircraft is flying at certain angles of attack. Structurally, then, the missile radome (and to some extent, fire control radomes) must withstand thermal shock, differential expansion, and wide variations in aerodynamic loads. The radome must also be capable of withstanding erosion effects of rain, hail, and possibly dust. In some missiles, the electronic system demands that the radome be pressu !zed; in others, the guidance system is required to operate in a vacuum. Special treatment may also be required for the elimination of moisture passing through radome walls.

Radars used in guidance and fire control systems are very precise units. They must provide present-position and angular-rate data, describing the motion of the object observed to some computer which compares the radar output with a reference value. The difference comprises an error signal, which is appropriately employed to command the servo sys-

*In this chapter, missiles are classified as aircraft.

tem to reduce the error signal to zero. Specific electrical requirements vary from system to system. Detailed discussion will be given on the ways in which radome error affects altitude stability, missile control time constant, navigation constant, flight path instability, and response to target noise. Acceptable limits of radome error depend upon the details of the control system used, and the limits placed on the radome by different systems may differ for many reasons.

The majority of the missile systems under development at present use what is commonly known as proportional navigation. The basic piece of information about the target which is required is the rate at which the true line-of-sight to the target appears to be moving with respect to a fixed direction in space. This information is required because these navigation systems aim to bring the missile onto a collision course with the target; for a given target position and velocity and missile velocity, the instantaneous "collision course" for the missile is defined as the direction of motion which would have the straight-line constant-velocity projections of the missile and target paths intersecting at a later time. Such a collision course is characterized by the fact that the true line-of-sight from missile to target has a constant direction in space; hence, the rate of change of the true line-of-sight is a measurement of the deviation from the collision course. Rates of change of the pointing error with respect to the radome have serious effects on the navigation system. The actual maximum rates which can be tolerated are functions of the allowable miss distance and vary from missile to missile.

4-2. Electrical Requirements and Objectives

The primary electrical objective in the design of radomes to be used in fire control and guidance systems is the selection of materials, constructions, dimensions, and shapes that will reduce the effect of the radome on the antenna patterns. This objective usually is very difficult to accomplish. Loss, from both absorption and reflections, must be minimized. In an active seeker missile system, large reflections can introduce a mismatch in the antenna, which may result in power loss and frequency pulling, as well as in a change in the apparent line-of-sight to the target. Another electrical requirement imposed upon radomes, especially in systems in which the electromagnetic energy is elliptically polarized, is that the complex transmission coefficients for parallel and perpendicular radiation be equal. If these two coefficients are unequal, pointing errors may occur when the energy passes through the curved radome wall, and then the antenna pattern will be distorted. If the missile is to be used at low altitudes over either land or sea, the radome must not enhance the sidelobes of the radiation pattern. If the sidelobes are raised, the antenna may lock on a reflection from the ground or sea and completely ignore the target.

Antennas are not point sources and most radomes are not spheres. A closer approximation is to assume that parallel rays are radiated from the antenna, and it is correct to assume that the individual rays will experience varying amounts of attenuation, reflection, and diffraction due to the variation of incidence angles and the changing radius of curvature of the radome wall. As a result of passage through the radome wall, all rays are operated on differently and experience different amounts of attenuation and diffraction. If the wavefront of an electromagnetic wave incident on the radome is assumed to be plane, the emerging wavefront will be distorted, and the far-field patterns with and without the radome will be different.

Present consensus among designers is to design for minimum reflection, maximum transmission, minimum absorption, and minimum phase shift variations, and then to look to the overall system of which the radome is a part for ways to reduce the impairing effect of the radome. The system may be a gun laying system or a missile guidance system. These are inherently the same: the objective in both is the direction of a projectile to a target. In the gun laying system, the problem of directing the projectile is done once, and in the missile system, continuously. In both, however, data relating to the angular direction of the target and angular rate of change must be accurate.

In a conical scan system (fire control or missile), the radar seeks a null signal (unmodulated) and is on null when it is on target. A shift in the null means a pointing error (that is, a false target position), and a changing antenna heading means false information on change of target bearing. The pointing shift produced by the radome is usually broken into components perpendicular and parallel to a plane defined by the radome axis and the true line-of-sight to the target. These components are referred to in this chapter as the crosstalk error and the in-plane error, respectively. In gun laying systems, the magnitude of the pointing error, as well as its rate of change, can cause appreciable system error, aside from the possible effects on the stability of the system. The intelligence the radar gathers is angular information; a

given displacement of the target from the line-of-sight and along its flight path will cause a larger angular displacement of the antenna in seeking a new line-of-sight as range decreases, and as a consequence the system gain will increase. In practice the change in gain which can be tolerated is limited by airframe and component resonances. It is possible for a radome, in causing pointing shift as the range decreases, to produce a pointing error rate which will make the system unstable through its effect on gain.

Pointing error rate also affects system performance through its effect on the navigation constant λ (proportionality factor between missile rate of turn and rate of change of line-of-sight to target). The effective navigation constant, which results from the pointing error rate, is $\lambda' = \lambda(1 - k)/(1 - k\lambda)$, where k is the pointing error rate in degrees per degree. Positive pointing error, an increasing value of null shift in the same direction as antenna scan, causes an increase in navigation constant, which has the effect of commanding the missile to turn at a greater rate than it would ordinarily. Similarly, a negative error rate results in a smaller effective navigation constant than the true constant. Since the navigation constant is a parameter of the missile feedback control system, a change in the feedback control characteristics can establish the condition for instability of the control system. Depending on response times and phase relationships that exist among the various units, instability may be realized at one or more frequencies. Instability may be evidenced at aerodynamic frequencies and at low frequencies. In the first case, the effect will be missile attitude oscillation, and in the second, flight path instability evidenced by wide swings from the intended flight path.

4-3 Mechanical and Aerodynamic Restrictions

It cannot be assumed that a radome found satisfactory for use with one system will necessarily be satisfactory if used to house some other radar system. Important parameters in radome design are antenna size, antenna scan angles, radar frequency, type of polarization, and location of antenna within the radome. Good electrical radome shapes and constructions are not necessarily good aerodynamic or structural designs, and the criteria by which parameters should be emphasized or changed in the design compromise vary from application to application. For example, for many requirements, hemispherical shapes with walls made of material with low dielectric constant and a few thousandths of an inch thick are sufficient; however, this design is usually unacceptable aerodynamically or structurally for most current radar installations in aircraft. Thus, a compromise is necessary, but if an existing radome is being considered for use with a new radar, a complete design and test evaluation is in order. There is some evidence that blunting of the radome nose can be tolerated electrically without significantly changing the aerodynamic characteristic, but sometimes system performance can be improved only at the cost of aerodynamic efficiency. Radome design must be conducted through the cooperative efforts of the radar designer and the systems engineer operating as a team. Since all are handicapped by the lack of rigorous analytical tools for electrical, aerodynamic, structural, and environmental evaluation of a proposed design, adequate designs require considerable discretion on the part of the team. It cannot be stressed too strongly that the optimum radome design for any application will result from early consideration of the radome as an integral part of the radar system.

4-4. Objectives of Chapter

In the present chapter, airborne radomes which require pointing accuracy to any degree will be discussed. A brief description of fire control and missile guidance systems which require these types of radomes is provided to serve as a general basis for the detailed discussion. No attempt has been made to present complete analyses, since the primary interest is on radomes for these systems, not on the systems themselves. Following the descriptions of the systems, sources of pointing error are described, effects of these errors on the various systems are analyzed, and methods of prediction and of correction of radome pointing errors are outlined.

SECTION B. FIRE CONTROL RADAR SYSTEMS

4-5. Introduction

The purpose of an airborne fire control radar system is to supply to a computer (human or electronic) accurate range and pointing angle (directional) information concerning a target, for use in the firing of the plane's armament. While precise measurement of the range can be made by timing the radar echo, the pointing accuracy of a simple radar can be basically no

better than the beamwidth of the antenna. The antenna beamwidth is approximately λ/D (radians, where λ is the wavelength of the radiation and D is the antenna width, or, for a paraboloid, the diameter. As the beamwidth gets narrower, the pointing angle accuracy will improve. Since a beamwidth of several degrees is typical of airborne fire control radar antennas, additional features are required in the system to provide the desired pointing accuracy of a few milliradians, which is only one or two hundredths of the beamwidth. The basic method of obtaining the higher accuracy may be termed "lobe comparison," and the numerous variations of the method may be classified as "time sequential" and "simultaneous."

4-6. Time Sequential Lobe Comparison Systems

The time sequential classification includes conical scan and sequential lobing systems.

Conical Scan. In this system (Figure 4-1) the antenna beam axis is made to describe a cone in space by the rotation of an offset feed or a skewed reflector. Because of the motion of the beam, the target echo will, in general, vary in time and produce a modulation at the conical scan frequency of the received r-f signal. The amplitude of this modulation is proportional (for small errors) to the angular deviation of the target true line-of-sight from the antenna crossover axis, which (for no pointing error) is coincident with the axis of rotation. Error signals in both azimuth and elevation are obtained from the relation of the phase of the signal modulation to the position of the rotating antenna element. D-c voltages drive servos which position the antenna so that the target is on the crossover axis, for which condition the error signals are zero. The antenna thus tracks the target, and the desired pointing information is obtained from gyros on the antenna or from resolvers at the antenna gimbals.

The conical scan system usually incorporates a mechanically scanning paraboloidal antenna radiating a pencil beam. The antenna rotates continuously about the mechanical axis with the antenna set at an angle to this axis such that the center of the beam describes a cone in space. The included angle is usually less than the beamwidth. A target falling within the beam during revolution of scan will return an echo that is amplitude-modulated as the beam rotates. This modulated signal is used as an error signal for positioning the antenna. Zero modulation, or a "null" of the fundamental scan frequency, means that the antenna crossover axis is passing through the target. Since angular accuracy of less than several milliradians is required in some systems, it is desired that the pencil beam pattern remain undistorted during scan if the crossover points are to define a point and not an irregular volume. In general, however, the beam is distorted during the scan cycle. This distortion produces pointing errors by shifting the angular position of the minimum or null of the fundamental scan frequency. At the null the amplitude of the fundamental is reduced to a minimum, but in general the amplitudes of the harmonics are not reduced proportionately. This disproportionate reduction is particularly true of odd harmonics, which, at the null, may have magnitudes several

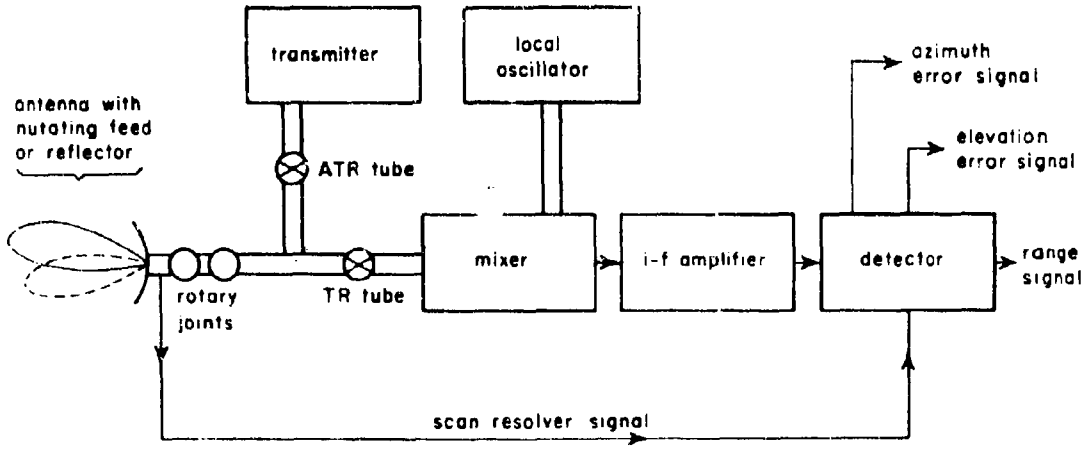


Figure 4-1. Conical Scan Radar System

times that of the fundamental. Thus, it is necessary that efficient filters be provided in the system to prevent pointing errors caused by harmonics.

Since error signals are required for only two perpendicular planes, the rotating part of the antenna need assume only four positions, and the continuous conical scan motion is for mechanical convenience only.

Sequential Lobing. A time sequential radar system which provides only four positions in rotation is the "sequential lobing" type (Figure 4-2). The sequential lobing antenna has four feed apertures. By means of waveguide switches, these four apertures may be used individually in sequence to provide without motion the same result as conical scan but at much higher scanning speeds than are possible mechanically. The construction of sequential lobe comparison systems inherently provides a further advantage over conical scan: all four apertures transmit simultaneously; only one receives at a time. In this way the peak of the transmitted beam is on the crossover axis, giving a larger target reflection than in the conical scan system, in which the beam peak is displaced from the crossover axis.

4-7. Simultaneous Lobe Comparison Systems (Monopulse)

In the simultaneous lobe comparison system complete target position information is obtained on each pulse of the radar set. For this reason the system is commonly called monopulse.

From the target echo the monopulse antenna derives signals which give the range of the target and its direction relative to the axis of the antenna. There are three waveguide terminals, one for the transmit and range signal reception, and one each for azimuth and elevation error signal reception (Figure 4-3). The r-f signals which appear at these three terminals are used to provide the d-c pointing error voltages. The signals picked up by the feed apertures are combined in such a manner that their sum and differences are obtained. Two types of radiation patterns result in each plane, a sum pattern (Figure 4-4) and a difference pattern (Figure 4-5). The sum signal is used for search operations and gives the range of the target. The sum pattern, obtained by the addition in phase of the echo signal received by the two apertures in one plane, is characterized by a main lobe of considerable directivity along the antenna axis. The difference pattern for any one plane is obtained from the difference between the echo signal as received by each of the apertures in that plane. From these signals the azimuth and elevation error signals are obtained by comparison of the difference signals with the sum signal in each plane to give the magnitude and direction of the pointing angle in that plane. The difference pattern has two main lobes and a null on axis. The main lobes are symmetrical and equal for a difference pattern plotted in power; however, the fields associated with the two lobes are 180 degrees out of phase, and the r-f voltage appearing at the antenna error channel terminals varies with angle as in Figure 4-6. (This description assumes perfect symmetry in the antenna.)

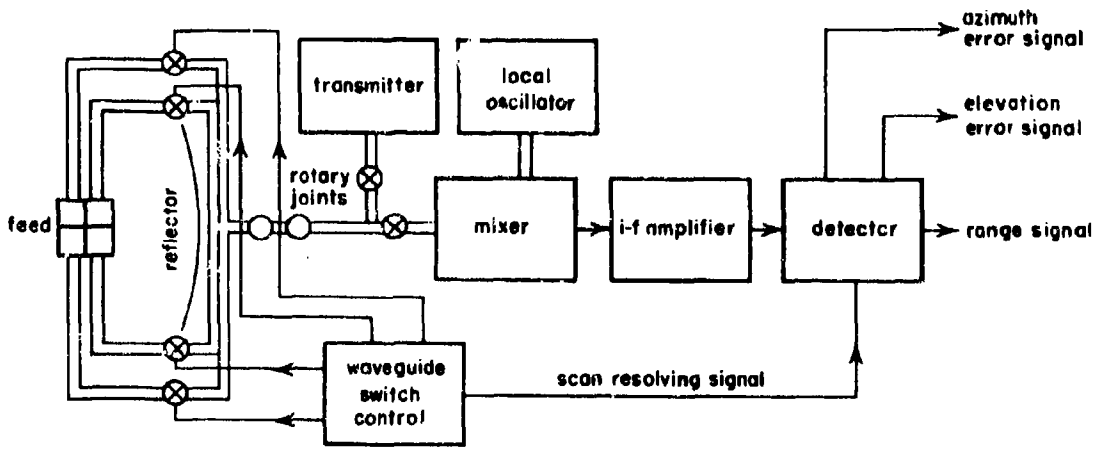


Figure 4-2. Sequential Lobing Radar System

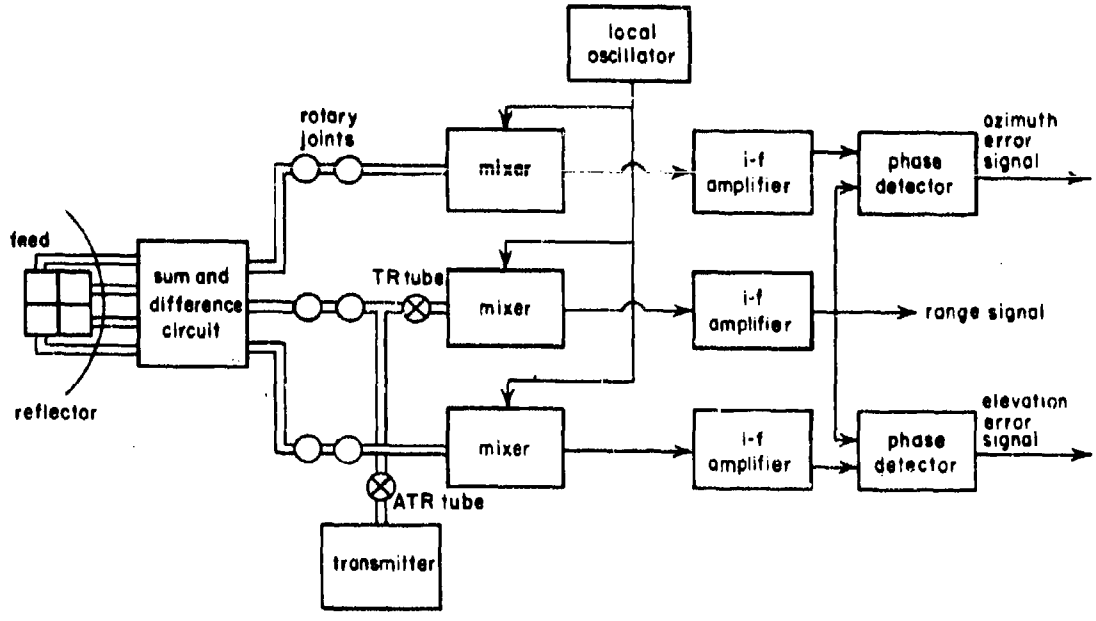


Figure 4–3. Three-Channel Monopulse Radar System

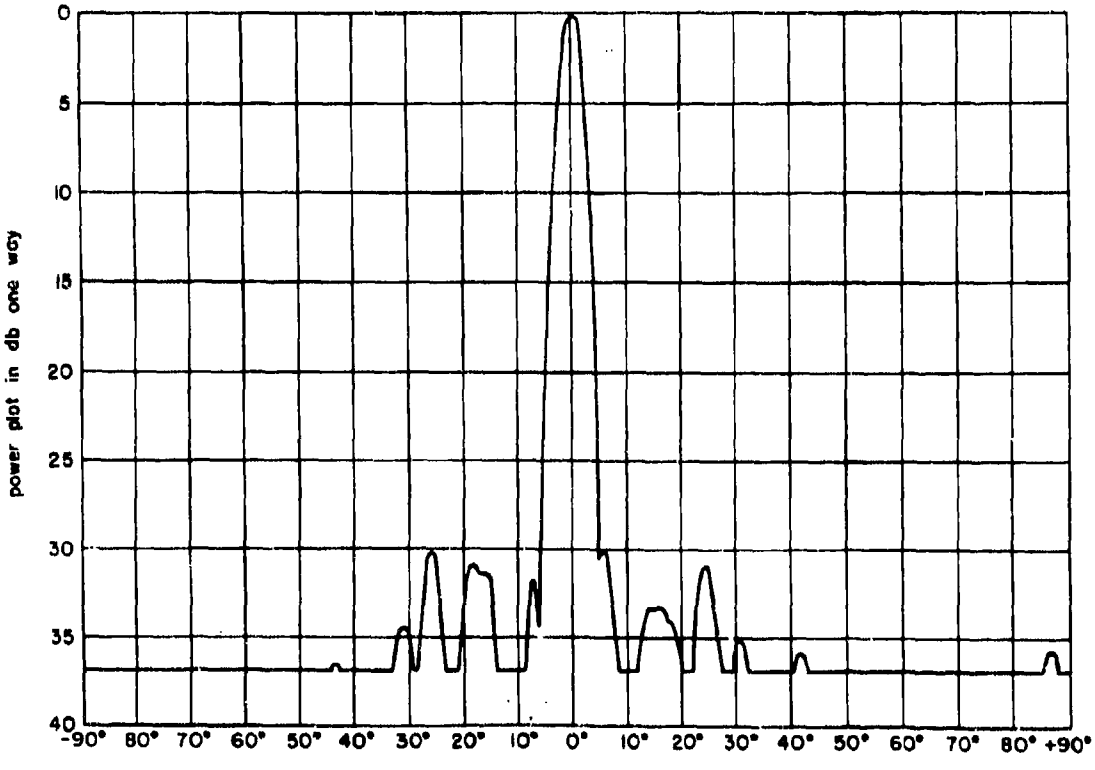


Figure 4–4. Typical Sum Radiation Pattern of Monopulse Antenna

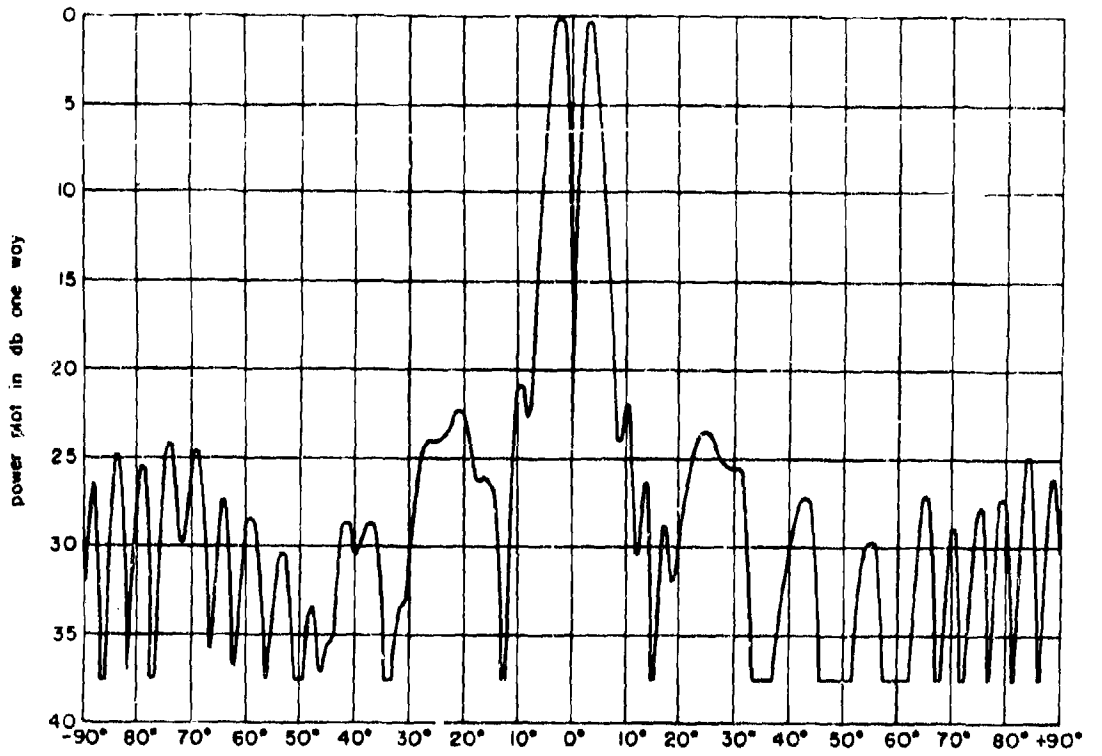


Figure 4–5. Typical Difference Radiation Pattern of Monopulse Antenna

The nonlinear response of the radar receiver with its automatic gain control modifies the error characteristic so that the final d-c error signal which controls the antenna pointing servos varies somewhat with pointing error, as shown in Figure 4-7. The pointing accuracy of the system is dependent on the steepness of the overall characteristic near zero. If the noise in the system has an amplitude as shown in Figure 4-7, small error signals will be masked by the noise, and the antenna will point erratically between the angle $+\beta$ and $-\beta$. A steeper characteristic decreases this error. The steepness of the overall characteristic is proportional to the slope of the antenna difference voltage characteristic, and it is desirable to design the antenna to maximize this slope. The error characteristic is an intrinsic feature of the antenna and depends on the aperture illumination.

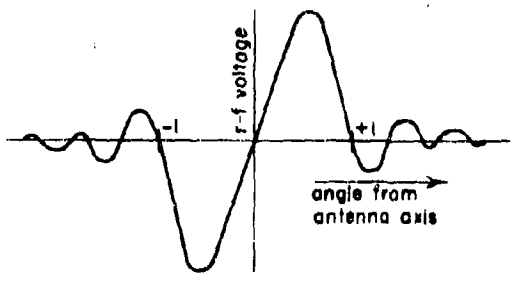


Figure 4–6. R–F Voltage At Error Terminal of Antenna

The relative level of the noise (Figure 4-7) depends on the signal-to-noise ratio, so that the signal-to-noise ratio in the final error signal output determines the pointing accuracy of the system. The overall signal-to-noise ratio is determined by the r-f signal at the mixer, and this signal depends on both the antenna-transmitting and the error-receiving characteristics. The received wave is a reflection of the transmitted wave, and is proportional to the gain of the antenna transmit channel. Thus, a true measure of the antenna error sensitivity must be a function not only of the slope of the antenna error voltage characteristic, but also of the antenna transmit channel gain.

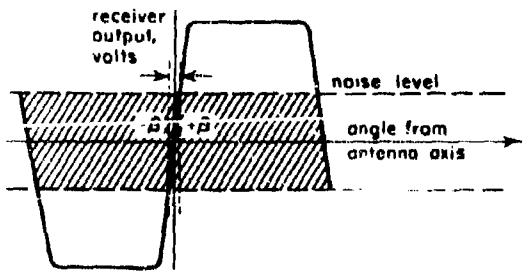


Figure 4-7. D-C Error Voltage At Servo Input

Monopulse systems are usually classified as phase comparison, amplitude comparison, or phase-amplitude comparison, depending on the characteristics of the antenna.

Phase Comparison. In the phase comparison type there are always two or more apertures in each plane that are fed independently. The target echoes picked up by the two apertures are equal in amplitude because the apertures are oriented together; but, when the target is not on the axis of the antenna, the echoes picked up by the apertures differ in phase, since one aperture of the antenna is closer to the target than the other.

Amplitude Comparison. In this monopulse system, at least two components of the feed aperture are alined in each plane and are generally smaller than those of the phase comparison type (since there is no need for size or geometric separation to pick up several phases of the incident wave). The target echo excites each aperture differently, and pointing information is derived from the resulting amplitude difference.

Phase-Amplitude. In this system, literally a combination of the other two types, error signals are obtained by phase comparison in one plane and by amplitude comparison in the other.

Monopulse System Errors. In any of the monopulse antenna systems, pointing errors can arise in two distinct ways. Phase or amplitude discrepancies in the received signals, which result from asymmetries in the feed structure or from radome refraction, give rise to pointing errors. A second contribution to the pointing error arises from the joint effects of the radome error and the asymmetries and of phase errors between the parallel receiver channels which are required in a monopulse system. Signal errors in phase or amplitude are always present to some degree, since the feed structure and the radome cannot be perfect. Similarly, phase discrepancies between receiver channels will generally be present. For satisfactory system performance, however, it is mandatory that both sources of pointing error be minimized. In fact, the design of i-f amplifiers with satisfactory phase characteristics over a large dynamic range constitutes one of the major problems in a monopulse system.

A constant phase distortion causes the antenna pointing angle to deviate a fixed distance as long as the frequency is constant; however, at a constant frequency variations will occur in the errors introduced by amplitude distortions in combination with phase errors between receiver channels. For example, for a phase comparison system, a relationship can be defined to show the effect on the pointing axis of the phase distortions. If the total width of the feed apertures in one plane is 2D, so that the effective separation of the centers of the two component apertures is D, the phase angle ζ is given by

$$\zeta = \frac{2\pi D \sin \theta}{\lambda} \qquad (4-1)$$

where θ is the antenna pointing angle. This relationship assumes that the apertures of the antenna have the same gain and receiving pattern and that the amplitudes of the received target echo are equal. Differences in electrical length ϕ between the connecting waveguides will create a pointing error which will cause the position of the antenna to shift to the angle $\theta \pm f(\phi)$. For a factor $(2\pi D/\lambda)$ on the order of 40, the error in θ is about 2 1/2 percent of ϕ. With an antenna of this size, a phase error of 10° would shift the pointing axis about 4 milliradians. This shift in itself is not detrimental (as long as the frequency is constant), since it merely defines a new pointing axis. The position of the new axis, however, varies with frequency, and it is the shift of the pointing axis with frequency which is important. The phase error between feeds may result from structural asymmetries in the feed, or it can result from radome effects as well. Since the phase errors caused by the radome vary as the antenna scans, a variable shift in pointing axis then results, even with a fixed frequency. The major sources of error for both phase and amplitude comparison monopulse systems are indicated in Table 4-1.

4-8. Comparison of Monopulse with Time Sequential Systems

Table 4-1. Major Sources of Errors in Simultaneous Lobe Comparison Systems

Phase Comparison Antenna	Amplitude Comparison Antenna
Primary Error	Primary Error
Phase errors in feed system	Amplitude errors in feed system
Secondary Error	Secondary Error
Amplitude errors in feed (in front of sum and difference circuit)	Phase errors in feed
Plus Phase Errors between receiver channels	Plus Phase errors between receiver channels

The essential characteristic of both the conical scan and sequential lobing systems is that they measure echoes received at different times. (See Figure 4-8.) The monopulse systems, on the other hand, derive all range and pointing information from each single pulse echo (Figures 4-9 and 4-10). The classification of fire control antennas as simultaneous lobe comparison or time sequential lobe comparison is made because a significant advantage of monopulse appears in this connection. Since time sequential lobing entails comparison of two echoes separated in time, changes in the reflective properties (scintillation) of the target or fluctuations in transmitted power can cause false error signals. For the same reason, the sequential system is vulnerable to certain types of jamming. The higher scan speed obtainable by sequential lobing with waveguide switches instead of mechanical motion reduces but does not eliminate these spurious error signals. The monopulse, deriving complete information from each pulse, is not susceptible to these effects.

An advantage monopulse enjoys over conical scan, although not necessarily over sequential lobing, is a greater overall angular sensitivity, because the target is tracked at the peak of the transmitted beam. In conical scan the target is tracked at the beam crossover, which is usually near the half-power point. The voltage sensitivity is essentially equal for both monopulse and conical scan antennas, but the overall angular sensitivity is less for the conical scan because of the weaker echo. The sequential lobing antenna can be designed to track the target at the peak of the transmitted beam and can avoid the power loss inherent in the conical scan. However, with a sequential lobing system, the r-f noise produced in the received signal by existing lobe switching tubes is a major disadvantage.

In a conical scan antenna, input impedance varies with rotation of the scanning mechanism. The changing load presented to the magnetron causes fluctuations both in frequency and in power. A unilateral device, such as a ferrite gyrator, is necessary to overcome this problem. The input impedance of a monopulse antenna remains essentially constant, since there are no moving elements except the rotary joints.

Mechanically, the monopulse antenna is somewhat more complex than the conical scan type, but there are no moving parts in the antenna proper. Since the antenna feed has no bearings or drive mechanisms, the monopulse system is less subject to mechanical breakdown. Pressurization may be easier. However, the additional rotary joints which are necessary if receiver components are not mounted on the antenna are an added complexity. Although monopulse antennas vary in weight from type to type, they compare favorably with the conical scan when the weight of the spin motor and resolver is considered.

In sequential lobe comparison and conical scan systems, the pointing error information appears as an amplitude modulation of the received signal. Only one channel, involving one rotary joint in each gimbal axis, one mixer, and one i-f amplifier, is necessary to carry this information. In a sense this single channel is time shared. The monopulse system, on the other hand, deriving complete pointing information from each pulse echo, cannot time-share one channel, but requires two or three. The multiplicity of receiver components and rotary joints adds weight and complexity and tends to decrease the electrical reliability. The additional rotary joints may be avoided by mounting some receiver components on the antenna, although this arrangement adds inertia to the antenna and requires the use of flexible cables. The

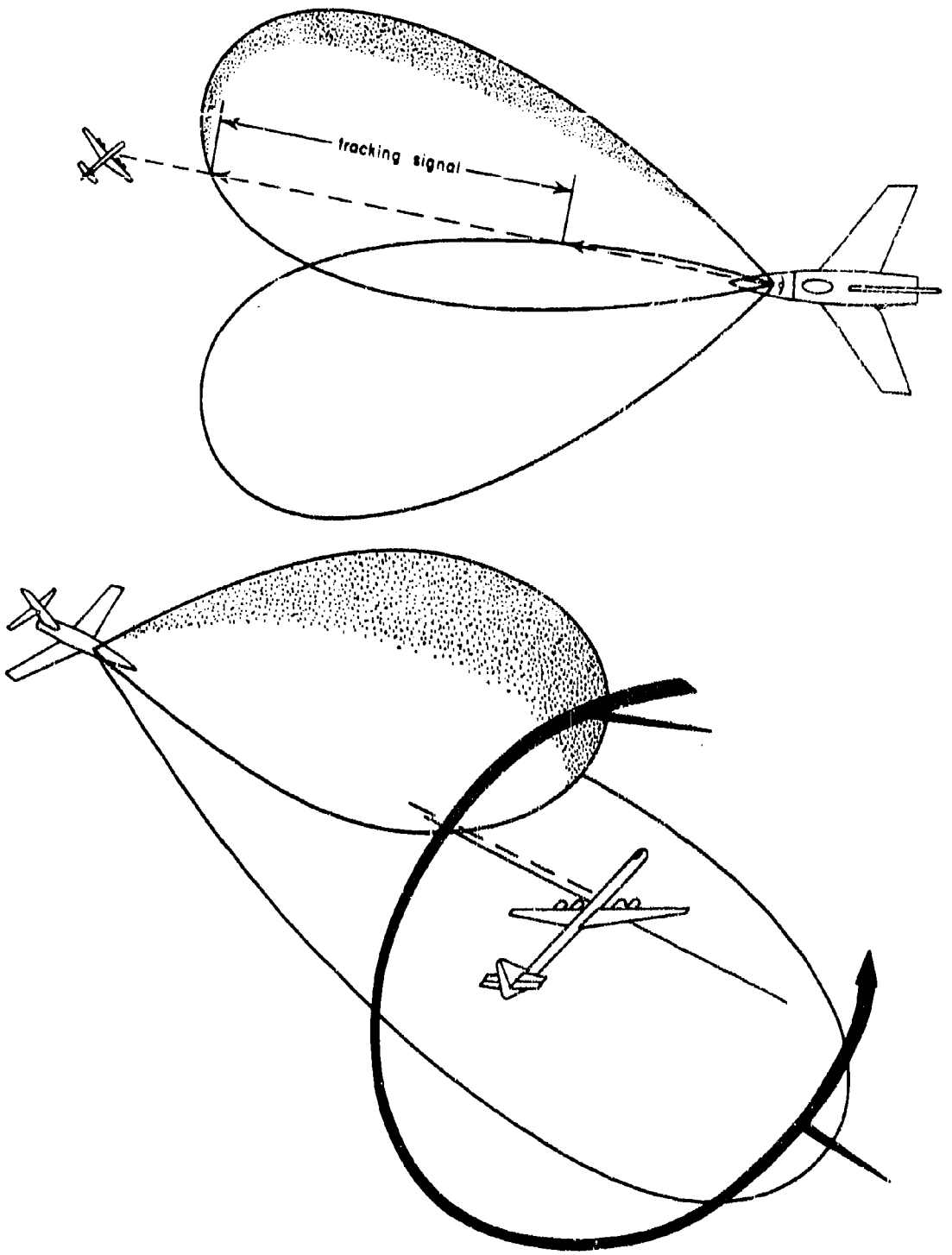


Figure 4–8. Typical Fire Control Antenna Beam – Conical Scan

decision whether to suffer the additional rotary joints or to avoid them by placing receiver components on the antenna is an involved one which must be reached for each particular application.

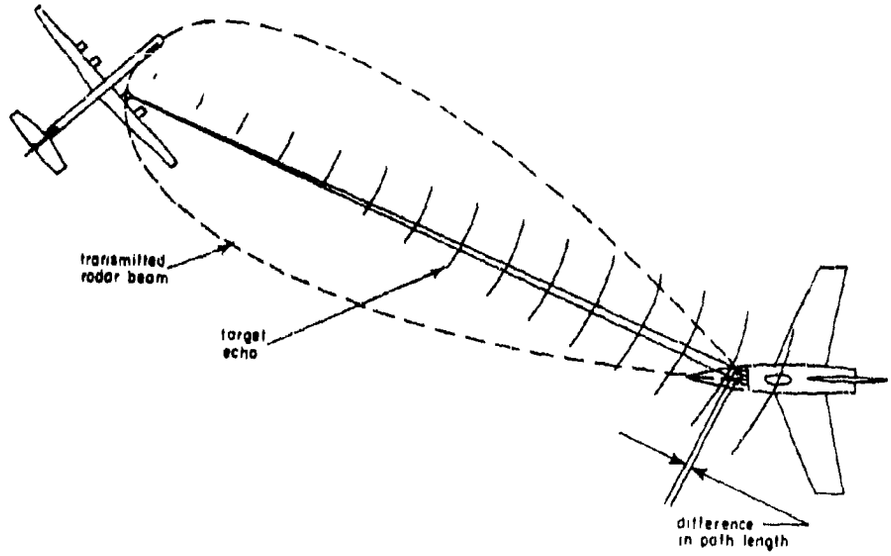


Figure 4–9. Typical Fire Control Antenna Beam – Phase Comparison Monopulse

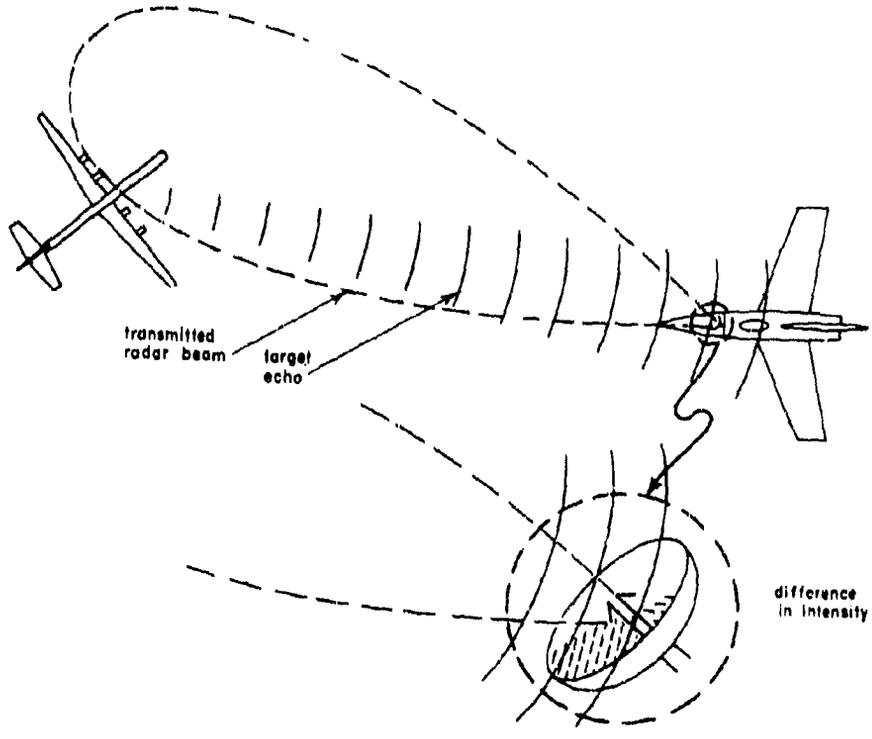


Figure 4–10. Typical Fire Control Antenna Beam – Amplitude Comparison Monopulse

SECTION C. GUIDANCE SYSTEMS

4-9. General Types

Missile guidance systems are usually defined in terms of the method by which a missile receives its information about the target. Missiles fall loosely into two categories, self-guided (or self-contained) and remotely guided or directed. Self-guided missiles are of two types: (1) those which receive instructions as to target position and trajectory prior to launch and carry out these instructions by responding to some form of continous navigation (long-range ballistics missiles) and (2) those which receive the target positional information directly during flight and home on that target (homing missiles). The remotely guided or directed category of missiles may receive some instructions before take off, but receive further instructions during the entire flight. Missiles which fall into this category include the "command-control" and the "beamriding" missiles. In actual practice missiles are often a combination of types of guidance; the midcourse guidance may be as a directed missile or as a beamriding missile, while the terminal phase may utilize self-guidance. Current guided missiles are listed for reference in Table 4-II, grouped according to tactical employment.

*Table 4-II. Current Missiles With Electronic Guidance**

Missile	Guidance	Company or Country
Air-to-Air		
*Falcon 1, 3	semiactive radar	Hughes
Falcon 2, 4	passive i-r	Hughes
Sidewinder	passive i-r	Philco
*Sparrow I	beamrider	Sperry
*Sparrow II	active radar	Sperry
*Sparrow III	semiactive c-w radar	Raytheon
*Velvet Glove	beamrider	Canada
Air-to-Surface		
Rascal	inertial and radar command	Bell
*Crossbow	passive radar	Radioplane
Surface-to-Air		
*Bomarc	command, midcourse; active radar, terminal guidance	Boeing
Nike	command	Douglas
*Talos	beamrider midcourse; semiactive radar, terminal guidance	Bendix
*Terrier	beamrider	Convair
*Tartar	semiactive c-w radar	Convair
*Hawk	semiactive c-w radar	Raytheon
Stooge	command	Great Britain
*Red Shoes	semiactive radar	Great Britain
Surface-to-Surface		
Corporal	beamrider; ballistic trajectory	Firestone
Regulus	command	Chance-Vought
*Matador	atran	Martin

*Missiles with guidance systems which require boresighting radomes are starred.

To the radome designer the homing missiles present the most serious problem. Since these missiles seek out and home on their targets, their antennas are carried as far forward as possible, so that the missile fuselage will not interfere with the guidance operations. A nose or leading edge position for the antenna places the radome in an extremely strategic spot. It must have low loss and high pointing accuracy, so that it will not introduce errors into the target positional information and cause the missile to go astray. It must also fulfill paradoxical aerodynamic considerations. A supersonic missile needs a pointed nose, but a pointed radome, solving the aerodynamic problem, creates additional electrical ones. A blunt radome eases the electrical problem and complicates the aerodynamic one. In addition to these problems, the homing missile radome must possess the physical properties necessary to withstand the high temperatures of supersonic flight. In the present state of the art, a compromise has to be made in which the three problems (physical, electrical, aerodynamic) are resolved for each application.

Some design is also required in radomes for command-control and beamriding missiles, although the problem is considerably less complicated than for the homing missile radomes. In a command-control missile, the antenna is usually in the tail or wings; in a true beamrider the antenna is in the rear. Since the radome is not a leading surface, it does not have to meet as stringent physical requirements, and temperature and material strength demands are usually lower. The radome shape is often not important; sometimes the antenna is merely a slot array covered with plastic. For command-control missile radomes, electrical requirements are not especially high. Commands may even be sent to the missile from the control radar in the form of coded information by a radio link, rather than by radar. But for beamriders, pointing accuracy of the radome must be high, since the missile must ride the center of the beam to hit the target. In addition, many beamriders utilize some type of homing system for terminal guidance, so that their radomes must meet the same stringent requirements as those of homing missiles. Plan views of several guided missiles which require radomes are shown in Figure 4-11.

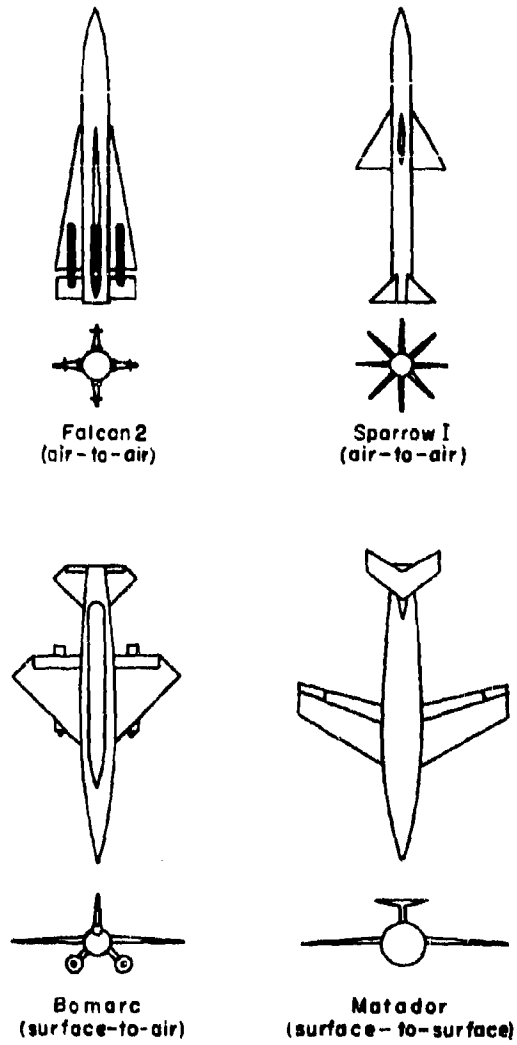


Figure 4-11. Plan Views of Representative Guided Missiles Which Require Radomes

4-10. Self-Contained Guidance Systems

There is a growing interest in long-range air-to-surface and surface-to-surface missiles. These missiles may be used when the target position is known before launch and is not likely to change during the missile flight time. They may have any of the several types of guidance systems but the emphasis is on a ballistics approach for the greater portion of the flight (for example, the North American Navaho, the Chrysler Redstone, and the Convair Atlas). Information about target position is first supplied to the launching station at which it is used to preset the desired trajectory into the missile. During flight the missile maintains the set trajectory by some form of continuous navigation, such as automatic celestial or inertial guidance. In these forms of navigation the missile knows the position of the target relative to the point of

departure and can determine its own current position from its velocity and direction in relation to some fixed point. In inertial guidance, the fixed points are the coordinates of the starting point with reference to a system of free gyroscopes and accelerometers. In celestial guidance, the points are the sun or the stars with reference to time.

Homing Missiles. Continuous navigation is of little use, however, when the target is likely to change position during flight, such as with a maneuvering aircraft, or when external target information is inaccurate. For these applications the homing missiles are best adapted. They can be used as air-to-air, air-to-surface, surface-to-air, and terminal guidance of surface-to-surface. These missiles are equipped with "seekers," some combination of receiving and computing mechanisms capable of determining a line-of-sight to a target and homing on it. Basically, the seeker may be one of three types. It may be active (Figure 4-12a), a system in which the missile carries both transmitter and receiver. Energy generated by the missile transmitter is reflected by the target, picked up, and acted upon by the missile receiver. It may be semiactive (Figure 4-12b), a system in which the missile carries only a receiver, and the target is illuminated by energy generated by the launching aircraft or by some other radar. The missile picks up and homes on the reflected signal. It may be passive (Figure 4-12c), a system in which the missile carries only a receiver; the signal on which it homes is generated by the target. No external source of illumination other than that from the target is necessary.

Both active and semiactive seeker systems utilize radar, but the passive seekers can be designed to home on r-f energy, infrared energy, sound energy, or, theoretically, any other type of energy. Since the radome by definition is associated only with radar missiles, the discussion of seeker missiles will assume that only r-f energy is involved. Examples of typical radar seekers include the Hughes Falcon 1 and 3 (semiactive), Radioplane's Crossbow (passive), the Convair Tartar (semiactive), and terminal guidance of the Bomarc.

Passive seekers have the strategic advantage of not announcing their presence to the target, since no form of external illumination is present to warn the target. Active and semiactive systems are used when larger amounts of power are required from the target, the semiactive seeker giving the largest power of all because the transmitter, if on the ground, can be of virtually unlimited size. The semiactive homing missile has the optimum combination of desirable factors for many applications: it is highly accurate and highly directional; it is lighter in weight and less complicated than the active seeker; it can find a target when the target is not radiating energy, a seeking characteristic which the passive missile does not have; and it is longer ranged than active seekers.

Direct Pursuit Trajectory. The homing missiles can fly several types of trajectories. The simplest and best known is the direct pursuit course in which the missile always aims directly at the target. The only information required about the target is its bearing, that is, the direction of the line-of-sight from missile to target. The missile then merely has to keep its velocity vector coincident with the line-of-sight.

A fixed, forward-looking seeker is employed, which detects any deviations between the missile axis and the line-of-sight and then sends corrective signals to the control surfaces. The equations for the ideal pursuit course may easily be derived in terms of the missile-target range R and the angle β between the line-of-sight and the target velocity vector. The following relations hold for a nonmaneuvering target.

$$R = V_t \cos \beta - V_m \tag{4-2}$$

$$\frac{d\dot{R}}{d\beta} = - V_t \sin \beta \tag{4-3}$$

in which V_t is target velocity and V_m missile velocity. As the missile-target range approaches zero, the angle between the line-of-sight and the target velocity vector also approaches zero, so that the missile always ends up in a tail chase. The terminal acceleration is given by

$$a_m = V_m \dot{\beta} = \begin{cases} 0 & \text{if } 1 < k < 2 \\ \dfrac{4V_m V_t \sin \beta_0}{R_0 (1+\cos \beta_0)^2} & \text{if } k = 2 \\ \infty & \text{if } k > 2 \end{cases} \tag{4-4}$$

where (R_0, β_0) and $k = V_m/V_t$ denote the initial conditions. The terminal acceleration called for becomes infinite for speed ratios greater than 2:1. In any case, the missile path is continuously curved; two examples of trajectories are shown in Figure 4-13.

Pure pursuit navigation requires the missile to follow a curved trajectory even against a straight-flying target, thereby using up a good

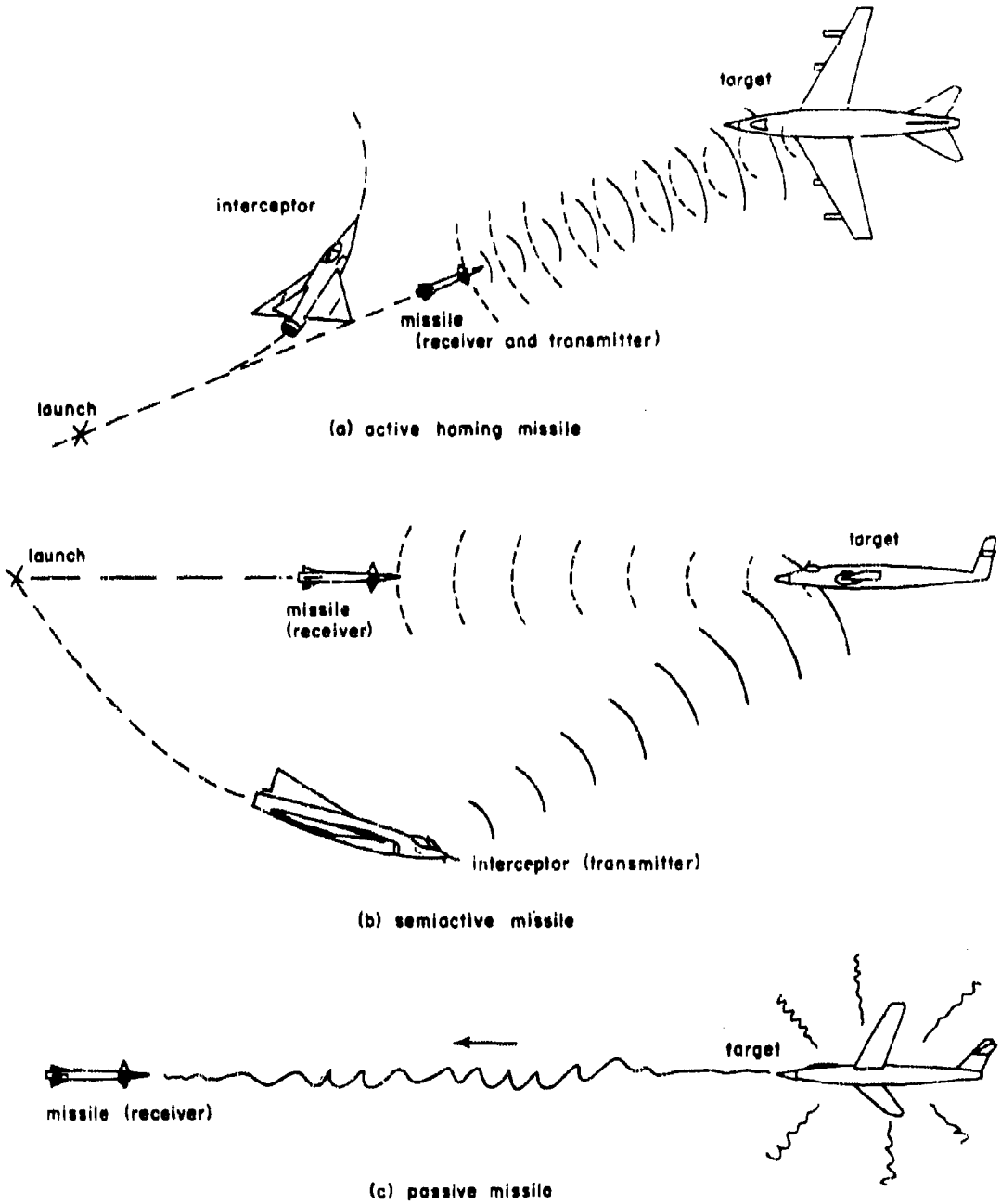


Figure 4–12. Air–To–Air Application of Self–Contained (Homing) Missiles. Other Applications: Air–To–Surface, Surface–To–Air, Surface–To–Surface (Terminal Guidance)

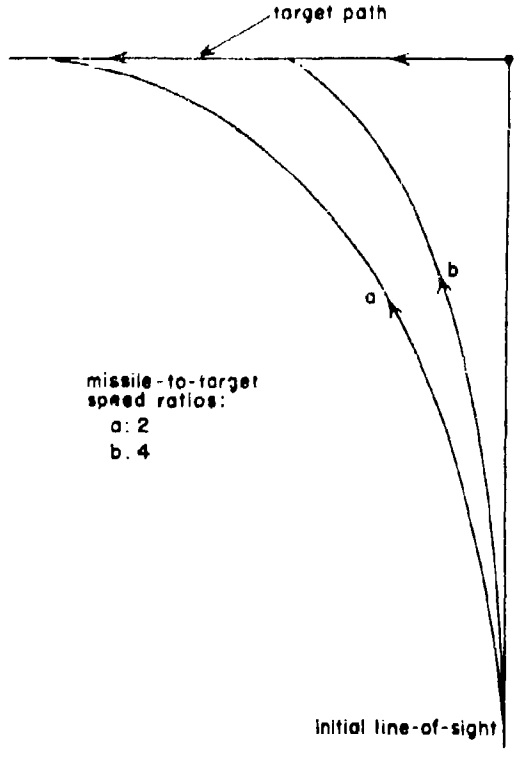


Figure 4-13. Example of Trajectories Resulting From A Direct Pursuit Course

part of its acceleration capability. In addition, since the missile must also be capable of correcting-out initial aiming errors, overcoming gravity and drifts, and following target maneuvers, a pursuit missile would have to be provided with very high maneuverability in order to be at all effective.

Constant-Bearing Trajectory. A more desirable trajectory is one in which the missile velocity leads the line-of-sight by just the right angle, so that for a nonmaneuvering target the missile flies a straight-line path to collision, as illustrated in Figure 4-14. The characteristic feature of this type of navigation is the constant bearing in space of the line-of-sight, achieved by the alinement of the relative missile-target velocity, with the line-of-sight (rather than the actual missile velocity, as in pursuit course navigation); in target coordinates, therefore, the missile will appear to be coming in straight at the target, though pointed off by the lead angle. It is not difficult to show that if the missile can keep the line-of-sight bearing constant, a collision will always occur even if the target should maneuver. Unfortunately, such constant-bearing navigation requires the missile to be able to detect and correct instantaneously any changes in the line-of-sight direction.

Proportional Navigation. A more practical scheme for an actual missile is so-called proportional navigation. As long as the missile remains on a collision course, as indicated by zero rotation of the line-of-sight, no steering commands are given; any rotation of the line-of-sight, indicating departure from a collision course, is detected by the missile, which then turns at a rate proportional to this rotation in such a direction as to reduce the line-of-sight rate and get back onto a constant-bearing course. Thus if γ and σ denote, respectively, the bearing angles of the missile velocity and of the line-of-sight, both measured relative to any fixed reference lines, then the missile steers so as to satisfy

$$\dot{\gamma} = K\dot{\sigma} \qquad (4\text{-}5)$$

where K is a constant, typically between 3 and 5. (A discussion of the effect of radome errors on this type of missile navigation is introduced in paragraph 4-31.)

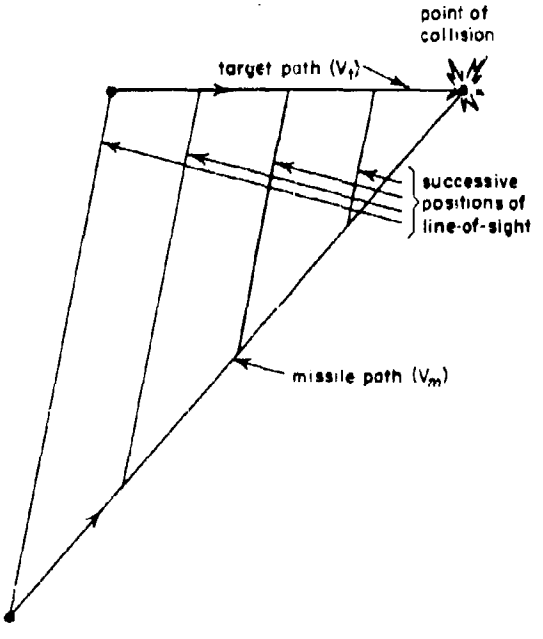


Figure 4-14. Trajectory Resulting From Constant – Bearing Navigation

4-11. Remote Guidance or Direction Systems

Remote guidance or direction systems are those in which information is continuously transmitted to a missile from an external station during the missile flight time. Command-control and beamriding missiles come under this type of guidance. They are used when information about the target can be more accurately estimated at some location other than the missile. United States missiles which utilize this type of guidance include the Sparrow I, the Terrier, and the Corporal (beamriders) and the Bomarc, the Nike, and the Regulus (command-control). (See Table 4-II.)

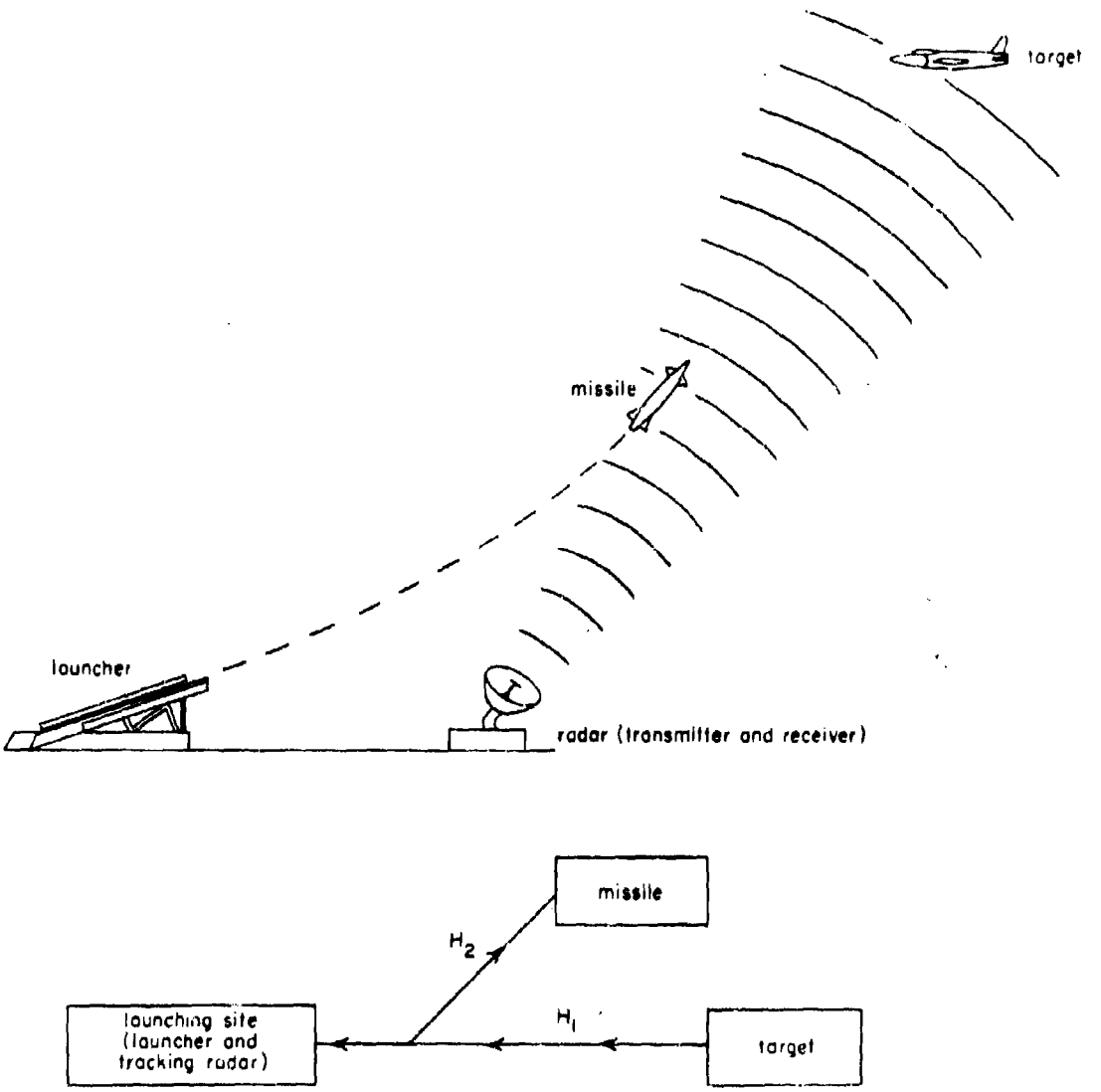
4-12. Beamriders and Command Control

The beamrider missile literally rides a radar beam to the target (Figure 4-15). The launcher (platform or aircraft) tracks the target and, through its radar tracking beam, lays down the direction to the target along which the missile must fly. To keep in the center of this beam, the missile must be able to determine (and correct) any deviation it may have from the center of the beam. A simple method is through the addition of a small nutation to the beam (conical scan). The signal received by a rearward-looking antenna on the missile will then be amplitude modulated whenever the missile gets off axis, the amount of modulation being roughly proportional to the position error. For a surface-to-air beamrider missile the launch point is fixed. The lower the missile-to-target speed ratio, the greater the missile acceleration required to stay in the beam. The maximum acceleration occurs at the end of the flight where the missile acceleration called for by tracking noise (beam wander) is also greatest. A more important disadvantage of beamrider missiles is the reduction in accuracy with an increase in launcher-to-target range. The width of the tracking beam increases as a function of range, so that at the target, where the least dispersion of the missile about the beam axis is most desired, the maximum dispersion occurs.

Because of this limitation additional techniques, such as a homing device, are required for accurate terminal guidance. To improve accuracy, as fine a pencil beam as possible should be used. This requirement, however, further aggravates the problem of beam entry and capture which is particularly acute for air-to-air missiles. These must be launched forward along the airplane axis while the tracking beam may be offset through an appreciable angle (except for near tail and near head-on attacks). A wider capture beam for initial guidance could be used, or the launching aircraft could fly a pursuit course initially until the missile starts to guide, and then could turn sharply to try to achieve a constant-bearing course in order to minimize missile acceleration required by line-of-sight rotation.

With beamriding missiles, the launcher tracks the target and launches the missile down the tracking beam; with the command-control missiles the launcher tracks both target and missile, and on the basis of these data transmits suitable commands to the missile to enable it to locate the target (Figure 4-16). The missile picks up signals only from the launcher, usually by means of a receiver located in the tail. In practice most command-control guidance systems require separate radar beams to track the target and missile. From their relative positions a computer at the launching station calculates the optimum path for the missile and sends it corresponding commands. This path will in general not be along the launcher-target beam; for a surface-to-air missile, for example, a desirable trajectory may be one which rises nearly vertically initially to get the missile out of the dense, high-drag lower atmosphere as rapidly as possible to conserve speed, and which goes over into a near-constant-bearing course during the terminal phase.

An advantage of command guidance is the greater electronic simplicity it offers over homing missiles. All the computing and tracking equipment is located at the launcher, and the missile has only to carry a receiver and a steering system. With the exception of the V-1 and V-2, all of the guided missiles (more than a dozen) developed during World War II, mostly by Germany, were of the command type. Only as miniaturization and component reliability have advanced has it become possible to utilize the more sophisticated systems of guidance which give guided missiles independence from their launching sites.



H_1 = target-bearing information

H_2 = information on missile position relative to tracking beam

Figure 4-15. Beamriding Missile; Applications: Air-to-Surface, Air-to-Air, Surface-to-Air, Surface-to-Surface (Short Range)

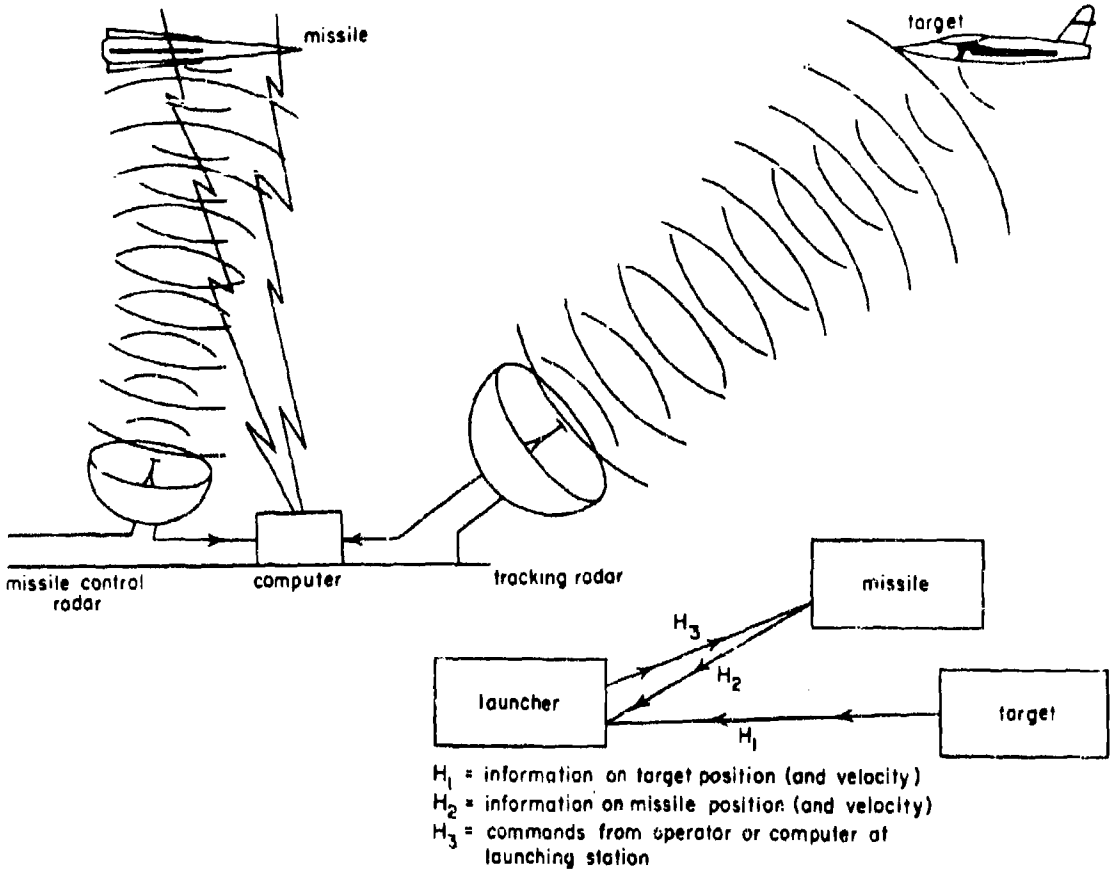


Figure 4-16. Command-Control Missile; Applications: Surface-to-Air, Air-to-Surface, Surface-to-Surface

SECTION D. SOURCES OF POINTING ERRORS

4-13. Sequential Lobe Comparison

In sequential lobe comparison radars, the antenna attempts to point in that direction for which the signals received by the radar are the same at all parts of the scan. Looked at in two-dimensional cross section, the scan reduces to an alternation between two antenna directions. The target appears to be at the point at which the patterns for the two directions cross. In actual practice, because the lobes in a scan cycle are not quite symmetrical, the positions of the crossover points vary as the antenna scans, so that the antenna points along an axis which is an average of the crossover points of the entire scan cycle. A variation in the antenna crossover axis produces a modulated r-f signal which has a modulation amplitude proportional (for small errors) to the angular deviation of the true line-of-sight to the target from the crossover axis. This modulated signal is the tracking signal, and when there is zero modulation or a null, the antenna is on target.

4-14. Simultaneous Lobe Comparison

In simultaneous lobe comparison radars, the antenna attempts to point along the peak of the transmitted beam. The different receiving apertures in the antenna receive slightly different signals (varying in phase or in amplitude or in both, depending on the type of system), which are

converted to tracking signals by the antenna circuits. Any effect which alters the locus of the crossover points (conical scan) or the phase or amplitude of the received r-f signals (monopulse) introduces a pointing error into the system. Those errors caused by the radome which produce such effects are called the radome pointing errors or radome boresight errors, or simply radome errors.

4-15. Radome Errors

In the discussion of the sources of radome errors, the chief sources are classified first, very simply. Estimates only of their relative importance are provided and the methods used are deliberately approximate. Results are to be taken as suggestive of the order of magnitude only, having the merit of giving definite, understandable numerical values. The suggested compensations are intended to indicate only general approaches. Specific correction techniques are described in Section G. It is assumed in the discussion that the radar is one-way; if the radar is send-receive, many of the error estimates should be doubled.

The effect of the radome on incident polarization is thought to be of sufficient importance to merit detailed discussion. Radome error differences due to changes in polarization (either received or transmitted or both) are quite significant. Experimentally, it is usually possible to measure the errors introduced by the changes in polarization without too much difficulty, a procedure which is not always true for other types of errors. And polarization errors are measurable with both large and small radomes. Other types of errors often disappear as the antenna-radome system increases in size. It is felt that reduction of the errors caused by polarization changes would often reduce the total radome error sufficiently to fall within specifications. If radome errors could be made the same for all types of polarization, they could probably be reduced to specifications in most designs.

4-16. Refraction

Because the radome surfaces are curved, an incident wave does not, in general, emerge parallel to itself. This situation is true even when the inner and outer surfaces of the radome are parallel. In these circumstances, the direction of an incoming wave is shifted towards the outer normal at the point of incidence, as it enters the wall, and away from the inner normal as it emerges from the wall.

If the radome is replaced by concentric circles, as in Figure 4-17, the direction of shift can be examined more closely with the aid of simple ray optics. At the point of incidence the outer normal N_1 is constructed, and at the point of emergence the inner normal N_2 is constructed. The angle at the center formed by the two normals is called c. With reference to Figure 4-17, $\theta_2 = (\theta_3 + c)$, since θ_2 is an exterior angle of the long triangle. In a medium in which the index of refraction n is greater than one, the angle of refraction increases more slowly than the angle of incidence. As the angle of refraction is increased from θ_3 to $(\theta_3 + c)$, the corresponding angle of incidence increases from θ_4 to a value larger than $(\theta_4 + c)$. Thus,

$$\theta_1 > \theta_4 + c \qquad (4\text{-}6)$$

This expression shows that the deviation is toward the normal.

Magnitude. In many situations the effect of beam refraction alone is sufficient to cover all the observed deviation. Simple optical ray tracing will often give an approximate magnitude of what the theoretical radome boresight error is for one particular design and polarization. However, this type of analysis does not account for all the various types of polarization which might be incident on the radome. From optical methods, the beam deviation for small radomes caused by refraction is on the order of 0.8° in reasonable cases. To obtain this estimate of magnitude, from Figure 4-17,

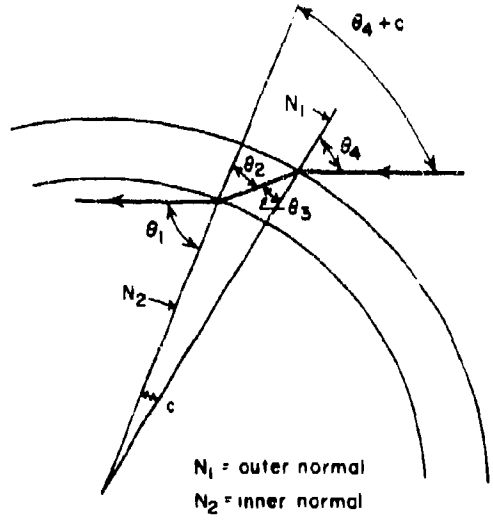


Figure 4-17. Ray Geometry For Concentric Circles

$$\sin \theta_1 = n \sin \theta_2 \qquad (4\text{-}7)$$

$$\theta_3 = \theta_2 - c \qquad (4\text{-}8)$$

$$\sin \theta_4 = n \sin \theta_3 \qquad (4\text{-}9)$$

where $n = \sqrt{\epsilon_2/\epsilon_1}$ = index of refraction.

The first expression gives θ_2, the second then gives θ_3, and the third gives θ_4, all in terms of θ_1. The deviation is

$$(\theta_4 + c) - \theta_1 \qquad (4\text{-}10)$$

and is known in terms of θ_1 and c. The value of c, which involves the radome thickness, is obtained by plane geometry. The calculation outlined is presented in full in Reference 1 with graphical representation and specialization to half-wave radomes. Independent computation from two of the curves yields the value 0.85° for an unfavorable but not untypical case.

Compensation. The effect of refraction can be partially corrected, sometimes, by the introduction of a taper in the radome wall thickness (see Section G) or in the thickness of the inner layer for sandwich radomes.

4-17. The Cavity Effect (Antenna — Radome Interaction)

Even when the antenna is matched, there is reradiation of received power. The area between antenna and radome can be considered to behave like a very low Q cavity. As the distance between the two changes, the cavity goes into and out of resonance, producing corresponding changes in the power received by the antenna. The effect is approximately periodic, in many situations, with the period equal to $\lambda/2$. Because the change in distance covering the range of maximum to minimum received power is only $\lambda/4$, it is quite possible for the power to be at a maximum for one lobe of a lobe-switching or conical-scan system and at a minimum for another. The crossover shifts position accordingly.[2]

The cavity effect can also be described from a viewpoint in which the radome is regarded as a tuner which increases or decreases the antenna mismatch, depending on its position.

Magnitude. The magnitude of the cavity effect can be calculated for small radomes from experimental data[2] with the use of the Barker-Lengyel equation for beam distortion.[3] That portion of their equation which expresses the differential lobe attenuation can be written

$$\Delta = \frac{\theta_0}{3}(a_2 - a_1) \qquad (4\text{-}11)$$

where Δ = radome error

a_1, a_2 = the fractional decrease in the maximum power at the opposite scan positions with radome mounted

$2\theta_0$ = half-power beamwidth of the undistorted patterns (crossover at half-power points).

This effect can be experimentally checked if position of the crossover points versus distance from antenna to radome is measured. The curvature of the radome gives a changing aspect, which superposes a trend on the expected periodic effect. When this trend is subtracted, a sinusoidal half-wave residual may result with an amplitude which gives the measure of the cavity effect. Correlation with the known "cavity" properties (that is, with experimental transmission versus distance) makes possible the checking of the calculation of the beam shift from differential lobe attenuation.

For large radomes, the curvature also changes the impedance of the radome, but experimental measurements on large pointed radomes indicate that the variation in voltage standing wave ratio (VSWR) with offset angle is very low.

Compensation. The radome error introduced by the cavity effect is directly proportional to the amplitude reflection coefficient of the radome.

4-18. Variation of Transmission Coefficients

Closely allied to the refraction and cavity effects is the error introduced by the variation of radome transmission with angle of incidence. One lobe of the scan is incident on the radome at one angle, the other lobe at another angle; and the attenuation of each is different. Computation of these attenuations must take due account of depolarization (see paragraphs 4-23 through 4-29). Because the important rays from an antenna do not all emanate from one point (not even from the point at infinity), the effect of different transmission coefficients at different incidences can be obviated by the use of a log spiral for the radome surface. This type of design only insures that a particular family of rays will see the same incidence angle.

The transmission coefficient should really be conceived of as an integration over a range of incidence angles, with due regard to the importance of the various rays being considered. Since the summation over the emerging rays must take account of phase, the average amplitude transmission depends also on the phase of the transmission. The effect of the transmission coefficients is really entangled with that of refraction. Since wavefronts and not separate rays are incident on the radome, the variation in phase shift along the wave front as it passes through the radome is the decisive factor in producing the error. A great many changes are introduced into the emergent wave at any one instant, and the result is a composite shift in the wave front. A beam deviation may be predicted for a given lobe of the scan even if the radome transmits 100 percent over the whole range of incidence angles.

Magnitude. For small antennas and radomes the effect of transmission coefficients on beam deviation can be on the order of 0.3°. The effect decreases with increase in antenna-radome size and decrease of fineness ratio.

4-19. The Phantom Feed

The radome wall is close to the feed, especially at certain parts of the scan. The wall produces a feeble image of the feed, and the source which the paraboloid (reflector) sees is probably a distributed source consisting of the feed together with this image. Compensation can be accomplished by keeping the reflection low (paragraph 4-20) and the spillover small.

4-20. Interference by Reflection

The entire antenna may be reflected in the radome wall, on a bulkhead, or in a fuselage (Figure 4-18). Antenna spillover (excess r-f energy from the feed which is not contained within the dish aperture) will often strike the bulkhead, portions of the fuselage, and the radome mounting rings which are back of the antenna. This energy is reradiated and may introduce false signals. The overall antenna pattern is the pattern of this composite system, which changes in the course of the scan as the amount of spillover varies. As the pattern changes, the crossover locus also changes.

Magnitude. Interference in the beam by reflection gives deviations of about 0.05° for a radome with 10 percent reflection and of about 0.3° for a bulkhead with 60 percent reflection. These magnitudes are for a 3-inch antenna; for larger antennas the effect is smaller.

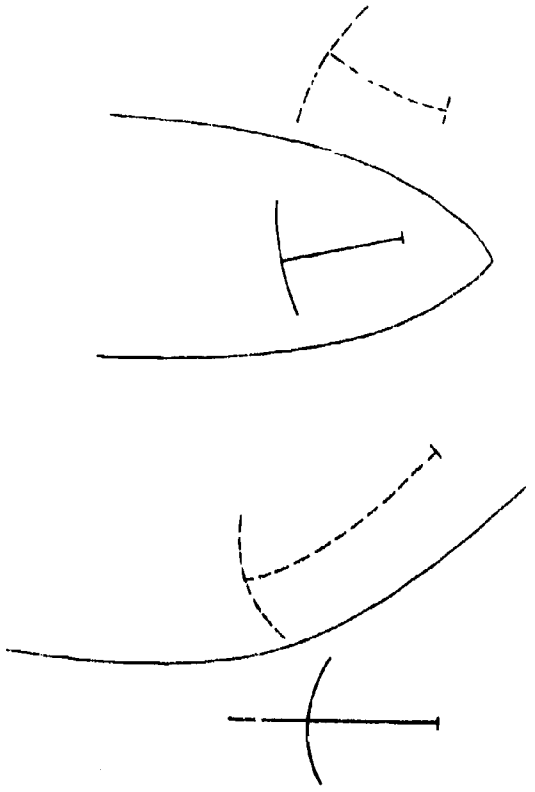


Figure 4-18. Image of Antenna in Radome or Fuselage

Estimates of the magnitude can be obtained through the use of the geometry of the antenna and its image (Figure 4-19). The amplitude pattern of the antenna is $A(\theta)$ and that of the image is $rA(-\theta)$, where r is the effective reflection coefficient. Each pattern is referred to the vertex and axis of its own antenna. The pattern of the composite system is

$$A_1(\theta) = A(\theta) + rA(2\phi - \theta)\, e^{-j\frac{2\pi d}{\lambda_0}} \qquad (4\text{-}12)$$

where d is the distance indicated in Figure 4-19.

The antenna is cocked through offset angles $+\alpha$ and $-\alpha$. The angle θ is then found at which the two powers, for $\pm\alpha$, are equal. For an unperturbed pattern, the crossover is a root θ of

$$|A(\theta + \alpha)|^2 = |A(\theta - \alpha)|^2 \qquad (4\text{-}13)$$

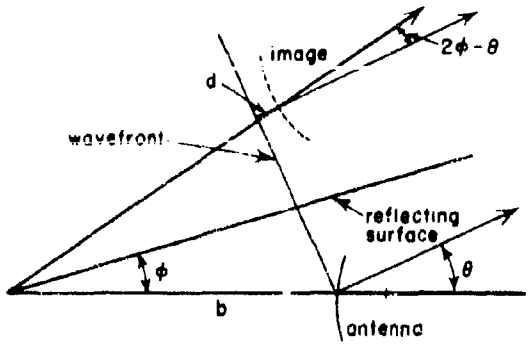


Figure 4-19. Geometry of Antenna and Image

If $A(\theta)$ is symmetrical, as is assumed, then $\theta = 0$ is a root, so that the value of the new crossover, for $A_1(\theta)$, is actually the value of the error which the image introduces. Hence, the error is the root θ, near $\theta = 0$, of

$$\left|A(\theta + \alpha) + rA(2\phi - \theta + \alpha)e^{-j\frac{2\pi d}{\lambda_0}}\right|^2 = \left|A(\theta - \alpha) + rA(2\phi - \theta - \alpha)e^{-j\frac{2\pi d}{\lambda_0}}\right|^2 \quad (4\text{-}14)$$

This root can be found by Newton's method:

$$\theta_1 = \theta_0 - \frac{f(\theta_0)}{f'(\theta)_0} \quad (4\text{-}15)$$

where zero is taken for θ_0 and the desired root for θ_1. A plot of this relationship for an antenna with uniform illumination will yield curves from which the estimate of order of magnitude can be made.

The behavior of the crossover point may profitably be studied as a large plane sheet is brought into the vicinity. The dependence of the crossover on sheet reflection coefficient as well as on its aspect can be studied. The cavity effect can be canceled by quarter-wave motion.

Compensation. Keep the reflection low.

4-21. Trapped Waves

It has been proved theoretically[4] that because the radome wall is not an infinite plane sheet, some of the radiation propagates along or inside the dielectric and is reradiated from an area near the rear or near the nose. The propagation is similar to that in a dielectric antenna, though the method of excitation is different. This guided radiation combines with that of the antenna to yield a perturbed pattern and, hence, a boresight error.

Magnitude. The error has been calculated to be on the order of 0.4° of beam deviation in typical cases for small radomes. For large radomes the effect of the error is always less.

All the trapped wave power is assumed to radiate from the nose as an isotropic source. The power in the trapped wave is estimated as 1 percent in the literature, but this estimate applies chiefly to a semi-infinite plane. The small radome may be presumed to trap a good deal more. In Figure 4-20 the antenna amplitude pattern is $A(\theta)$, as in the discussion of image reflection geometry, and the amplitude pattern of the antenna plus the trapped-wave source is $A(\theta) + r\, e^{-j2\pi d/\lambda_0}$. For the sake of simplicity the magnitude r is taken as being the same for offset angles $+\alpha$ and $-\alpha$. The same procedure as that used in the proof of the reflection effect indicates that the new crossover, and the value of the boresight error, is the root θ near $\theta = 0$ of

$$\left|A(\theta - \alpha) + ae^{-j\frac{2\pi d}{\lambda_0}}\right|^2 = \left|A(\theta + \alpha) + ae^{-j\frac{2\pi d}{\lambda_0}}\right|^2 \quad (4\text{-}16)$$

As before, the principal term may be obtained by Newton's method with $\theta = 0$ taken for the initial approximation.

Compensation. Absorbers near the base of the radome may help in some situations.

4-22. Depolarization

If a linearly polarized plane wave is incident on a plane sheet with the incident polarization neither in nor perpendicular to the plane of incidence, the transmitted wave is usually elliptically polarized. In practice, the plane wave will be incident on a doubly curved sheet, the radome. Generally, when an incident wave which is elliptically polarized passes through a radome, the character of that ellipticity is altered. This effect of the radome on incident polarization is called its depolarization effect. In addition to the depolarization caused by the radome, the transmitted (and received) wave may also be depolarized as a result of asymmetries in the antenna and by the configuration and location of the target. Studies of antenna

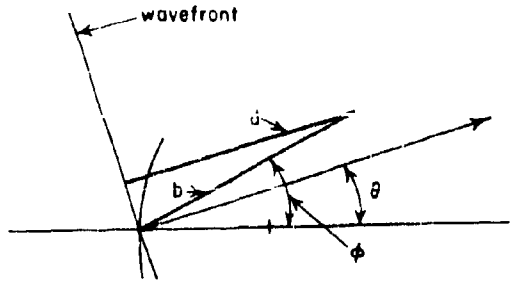


Figure 4-20. Geometry of Antenna and Source

gain and crossover position as a function of the ellipticity of incoming radiation and measurements of radome error curves with various states of polarization offer productive sources of information concerning this source of radome error.

4-23. Polarization Phenomena

In the analysis and design of radomes, one generally thinks in terms of transmission of plane electromagnetic waves through plane dielectric walls. The plane electromagnetic wave at the point of transmission through a wall can be resolved mathematically into two field components, one with the electric or E vector perpendicular to the plane of incidence and the other with the electric or E vector parallel to the plane of incidence. Each component of the resolved wave is transmitted through the wall and recombined to give once again a plane electromagnetic wave. While the wave is in air, the ratio of the minor to major axes of the ellipse of the E vector does not change in either magnitude or phase. However, when the wave traverses the dielectric wall, because the transmission coefficients of the wall are usually unequal for perpendicular and parallel polarizations, the axial ratio and orientation will change. The only conditions under which equal wall transmission coefficients, $\dot{T}_{||}$ and $\dot{T}_{\perp}$, are present, and therefore no change in ellipticity or orientation of the wave occurs, are a zero angle of incidence or a dielectric-wall thickness (lossless material) of one-half wavelength for the angle of incidence. (Mathematical proof of the second condition can be found in Volume 26 of the M.I.T. Radiation Laboratory Series.[5])

Because of the doubly curved nature of radomes and the continual variance of the antenna scan angle, the angle of incidence for the electromagnetic waves will not generally be optimum for all transmission points on the radome. With these physical conditions existing, there will always be a difference between $\dot{T}_{||}$ and $\dot{T}_{\perp}$. In addition, the difference in the transmission coefficients will vary from one transmission point on the radome to the next. Thus, if a linearly polarized plane wave is incident on a radome surface, the transmitted wave may be linearly polarized, elliptically polarized, or even circularly polarized, depending on the curvature of the surface and the electrical thickness of the wall. Incident waves of other polarizations usually result in transmitted waves which differ considerably from those obtained with a linearly polarized incident wave.

In addition to the changes in incident polarization which the radome may cause, asymmetries in the antenna, such as curvatures in the reflector or nonsymmetrical feeds, may change the polarization. A change in polarization of the emergent wave (caused either by antenna asymmetries during transmission or reception, by the radome, or by both) has the effect of varying the power of the target echoes received by the antenna. Since an error signal is essentially a comparison of the difference in amplitude of target echoes received at several scan positions, the variation in received power becomes an amplitude modulation which gives rise to an error signal. The degree of error caused by the radome or by the antenna is indicated by the magnitude of the modulation in power received with scan angle. If the incident wave is received in such a manner that there is no modulation in the power received, there will be no error. However, the wave usually does experience a change in polarization in traversing the radome wall and, correspondingly, there is modulation of the received power. The change depends on the portion of the radome traversed by the wave and on the polarization of the incident wave. And further, the variation of the power received depends on the polarization characteristics of the receiving antenna.

It has been assumed in the discussion that the characteristics of the incident wave, which is actually the energy reflected from the target, are known. In practice, this information is not generally known. A target illuminated by a plane electromagnetic wave of a given elliptical polarization produces a scattered field which may be analyzed in terms of two orthogonal polarization components. The strengths and phases of these components vary with the physical configuration and aspect angle of the target. One component is defined as having the polarization which is matched to the receiving antenna. The orthogonal component may be viewed as a depolarized component, and will

affect the error characteristics of the radome. The depolarization effects of the antenna, the target, and the radome are discussed separately in the following sections.

4-24. Antenna Depolarization

It has been experimentally determined that asymmetries in target-tracking antennas may introduce polarization changes and as a result cause pointing errors, even in the absence of a radome. Unpublished measurements made at Hughes Aircraft Company show that the electrical axes of conically scanning antennas shift as the direction of polarization of a linearly polarized incident wave is varied (see Figure 4-21). A theoretical discussion of pointing-error dependence on antenna polarization in a conical-scan system has been given by Silver.[6]

It should be emphasized that the three antennas utilized in the experimental investigation (Figure 4-21 results) were not laboratory or prototype models; they were standard aircraft radar antennas modified only to provide the various polarizations.

In any analyses, the antenna contribution to the total pointing error should be added to the radome-caused error. Investigators should be aware that antenna asymmetries can and do cause changes in polarization characteristics. Conclusions drawn from measured "radome-error" curves should be carefully weighed so that the radome is not assumed to be the sole source of the errors. Serious consideration should be given to the performance of the free (no-dome) antenna system. And it is recommended that, in the final design, the radome-

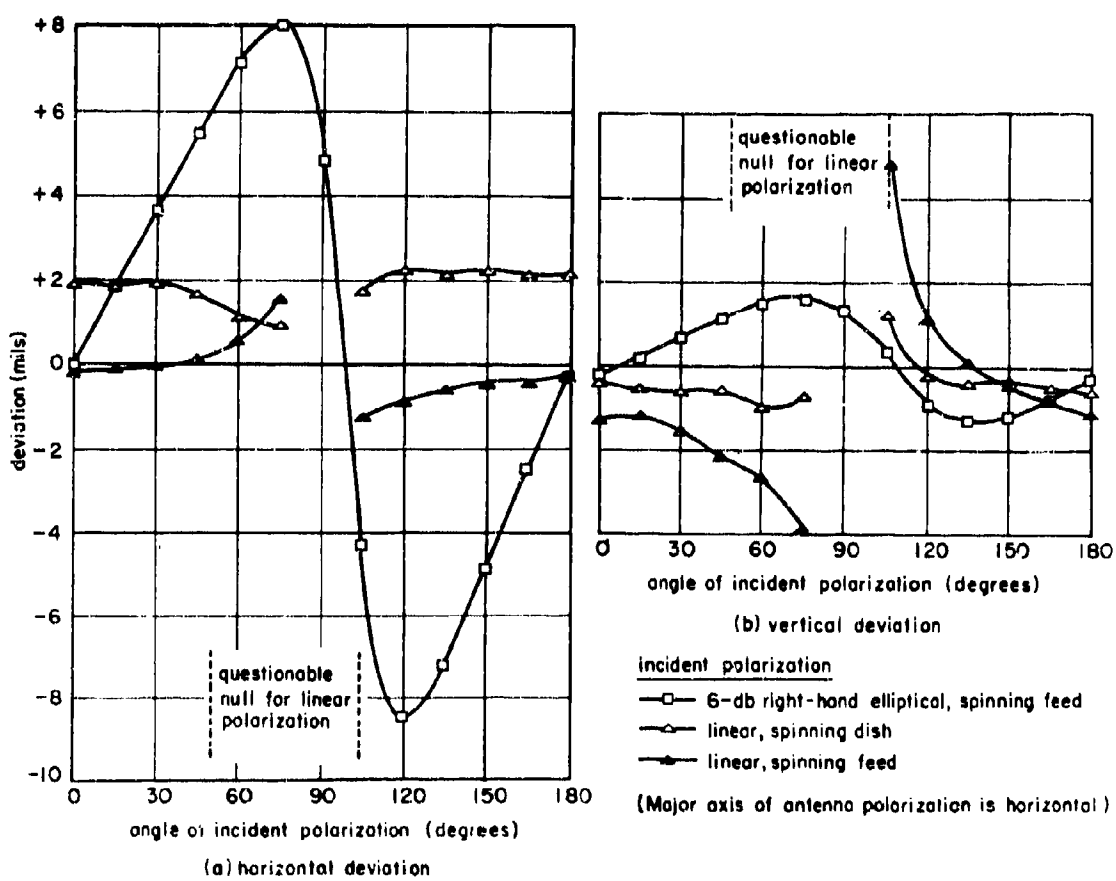


Figure 4-21. Antenna Deviation as a Function of the Direction of Polarization of the Incident Wave; the Angle of Incident Polarization is Zero When Both Antenna and Incident Polarization are Parallel

antenna system be considered as one integral unit.

4-25. Target Depolarization

As stated previously, the signal reflected from a target may be analyzed in terms of two orthogonal polarization components, with amplitudes and phases which vary with physical configuration and aspect angle of the target. The dominant portion of the signal is usually due to specular reflection; and the system is usually designed so that specular reflection produces a reflected polarization which is matched to the receiving antenna. The depolarized signal is usually several decibels weaker than the specularly reflected signal. The least depolarization from an aircraft target seems to occur if the radar beam strikes the target broadside; maximum depolarization occurs with a tail chase.[7] The depolarized components can be experimentally determined by means of measurements of the cross sections of the radar echo. A radar cross section is the physical area which must be associated with a scatterer (target) to account for the magnitude of the echo return under the assumption of isotropic scattering. In terms of the radar equation,

$$P_R = P_T \frac{G_T G_R \lambda^2 \sigma}{(4\pi)^3 R_T^2 R_R^2} \qquad (4\text{-}17)$$

where P_R = power received
P_T = power transmitted
G_T = transmitting antenna gain
G_R = receiving antenna gain
λ = wavelength
R_T = distance from transmitter to scatterer
R_R = distance from scatterer to receiver
σ = radar cross section of scatterer

Radar cross section is independent of P_R, P_T, G_R, G_T, R_R, R_T, and λ (at least for limited variations in λ), but it is highly dependent on the geometry associated with the transmitter, the scatterer, and the receiver. If the transmitter and receiver are at the same location, as is usually true, the number of possible geometrical configurations is reduced and the cross section becomes a function only of the particular aspects of the scatterer viewed; that is, this dependence can be completely described in terms of the elevation and aspect angle shown in Figure 4-22. In addition to this geometrical dependence, radar cross section will

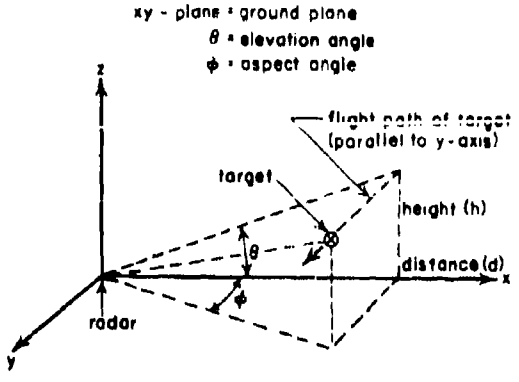


Figure 4-22. Elevation and Aspect Angles of the Target

in general depend upon the transmitting and receiving antenna polarizations.

4-26. Measurement of Radar Cross Section

The method of measuring radar cross section can best be explained in terms of the radar equation, Equation (4-17). If this equation is rearranged under the assumption that the transmitting and receiving antennas are at approximately the same point in space, the following equation is obtained:

$$\sigma = k \frac{P_R}{P_T} R^4 \qquad (4\text{-}18)$$

where $R = R_T = R_R$ = range to scatterer

$$k = (4\pi)^3 / \lambda^2 G_T G_R$$

If two targets illuminated consecutively by the same radar set are considered, then

$$\sigma_1 = k \frac{P_{R_1}}{P_{T_1}} R_1^4 \qquad (4\text{-}19)$$

$$\sigma_2 = k \frac{P_{R_2}}{P_{T_2}} R_2^4 \qquad (4\text{-}20)$$

where the subscripts identify the respective targets. Combining Equations (4-19) and (4-20) under the assumption of constant transmitter power ($P_{T_1} = P_{T_2}$) gives

$$\sigma_1 = \sigma_2 \left(\frac{P_{R_1}}{P_{R_2}}\right)\left(\frac{R_1}{R_2}\right)^4 \qquad (4\text{-}21)$$

From Equation (4-21) it becomes apparent that if σ_2 and R_2 are known from previous measurements, then for evaluation of σ_1 only the values of R_1 and $(P_{R_1})/(P_{R_2})$ are needed.

Absolute measurements of transmitted or received power are not necessary — only power ratios and ranges are needed. These parameters are utilized in the technique of cross section measurements to be described. In the description of the technique,[8] it is assumed that the flight line of the target aircraft is as shown in Figure 4-22, although other flight patterns may be used. The choice would depend on the type of equipment available and the ease of obtaining the required data.

4-27. Equipment for Cross Section Measurements

The equipment necessary to perform the tests consists of two radar sets, an optical tracker, a calibrated reference target, and appropriate data handling devices. Figure 4-23 shows the manner in which these elements are incorporated into the test setup. The radar set should be capable of tracking a target and also of providing range and angle data. Use of separate transmitting and receiving antennas, each provided with a means for changing the polarization, results in a setup for measuring the polarization of the energy scattered by the target. A camera alined with the radar beam and operated during the tests can detect the quality of the tracking, and poor sections of the data can be eliminated. A second radar set, operated at a different frequency, is also used. In conjunction with an automatic plotting board, this set is used to monitor the operation and to keep the aircraft flying in the proper flight patterns. The radar plot so obtained can be used to aid in the reduction and evaluation of the data. The reference target used can be a corner reflector with a relatively large cross section. This reflector can be calibrated in the laboratory and mounted on a long pole located near the radar test range.

The procedure for obtaining the necessary data involves the alinement and calibration of the various components of the equipment. The alinement requires the positioning of the transmitting antenna, the receiving antenna, and the camera so that all will point in the same direction. The items requiring calibration are the target range data, the corner reflector range,

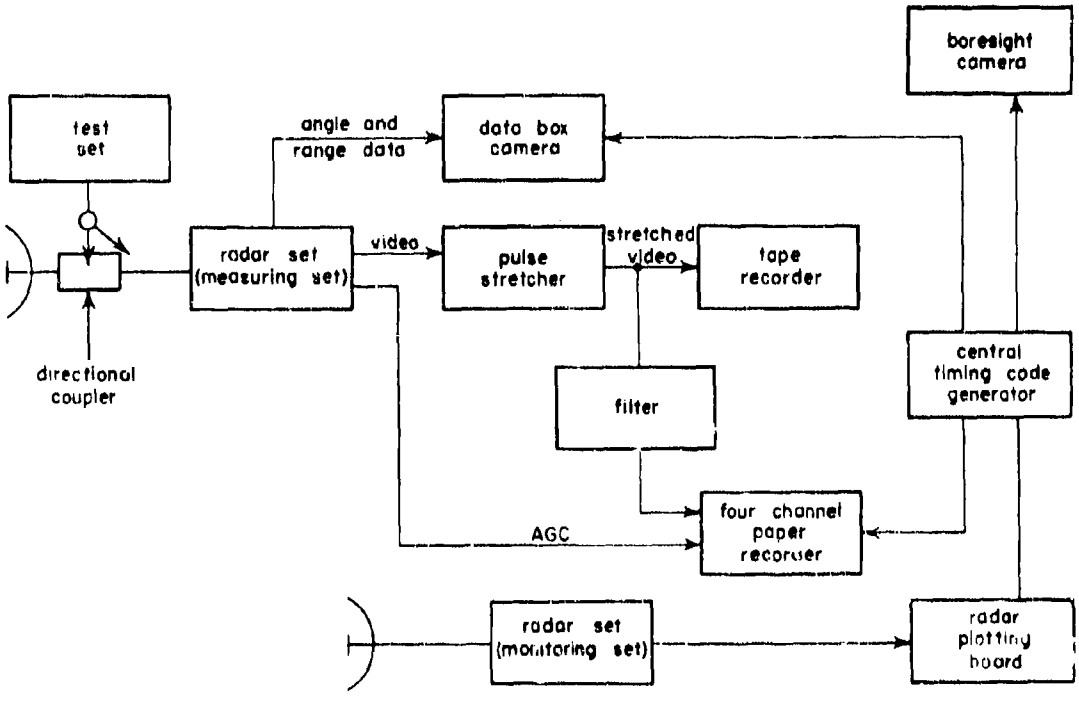


Figure 4-23. Test Setup for Radar Cross Section Measurements

the video data, the AGC data, and the corner reflector cross section. During each pass of the target aircraft, continuous recordings of the video data, the AGC data, the range data, and the angle data are made. The continuous video and AGC data are averaged over some interval of time (for example, 1-second intervals), and the cross sections are calculated by means of Equation (4-21).

Results of Radar Cross Section Measurements. The cross section measurement procedure described above was employed by Hughes Aircraft Company to obtain radar cross section data at X-band on B-17, B-47, B-45, B-29, F-80, and F-86 aircraft. The data for the latter four aircraft were obtained only for the condition in which both transmitting antenna and receiving antenna were vertically polarized. For the B-17 (a propeller-driven bomber) and the B-45 (a tactical jet bomber), data were obtained for this condition and also for conditions of other polarizations. The measurements taken at constant polarization are presented in Figure 4-24 and compared with similar measurements made by other organizations. Although complete details associated with the measurements can be found in published reports, the following information relating to the other studies is most pertinent: the Ohio State Antenna Laboratory,[9] model measurements (simulated 2600 megacycles) and vertical polarization; the Naval Research Laboratory,[10] X-band measurements on full-scale aircraft and horizontal polarization; McGill University,[11] model measurements (λ = 25 centimeters) and vertical polarization.

The cross-section data under various conditions of polarization are shown in Figure 4-25 for the B-17 aircraft. Each experimental value represents an average over $\pm 5^{\circ}$ in aspect angle. For these measurements the distance d (shown in Figure 4-22) and the height h were 5,000 feet and 2,000 feet, respectively. Measurements were also made at d = 0 and h = 3,000 feet, and are shown in Table 4-III. Each experimental value represents an average over 2 1/2 degrees in elevation angle.

The cross section data for the B-47 aircraft are shown in Figure 4-26 for three different flight patterns. Each experimental value on the graphs represents an average over $\pm 5^{\circ}$ in aspect angle.

4-28. Cross Section and Scattering Relationships

The electromagnetic scattering properties of any target can be completely described by a matrix. If this scattering matrix is known and if the transmitting and receiving polarizations are given, the relative radar echo from the target for these polarizations can be calculated.[12]

In this section the relationships between the scattering matrix and the cross section of an arbitrary target will be developed. Methods are outlined by which the radar cross section of this target can be evaluated for any polarization of the transmitting receiving antennas in terms of a finite number of known cross section values.[13]

Radar Cross Section (General Case). The configuration considered consists of a transmitter, a scatterer, and a receiver. The transmitter and receiver need not be at the same location, but in the theory developed it is assumed that the transmitter, scatterer, and receiver have a fixed spatial relationship. The relationship between radar cross section and the polarization of both transmitter and receiver has been investigated under this fixed geometry condition.

Table 4-III. B-17 Radar Cross Section Measurements for Flight Pattern No. 2

Elevation Angle (degrees)	Transmitter–Receiver Polarization (sq ft)				V = linear vertical H = linear horizontal R = circular, right-hand L = circular, left-hand
	V – V	H – H	L – R	L – L	
12 1/2	220	300	130	170	
7 1/2	400	185	180	200	

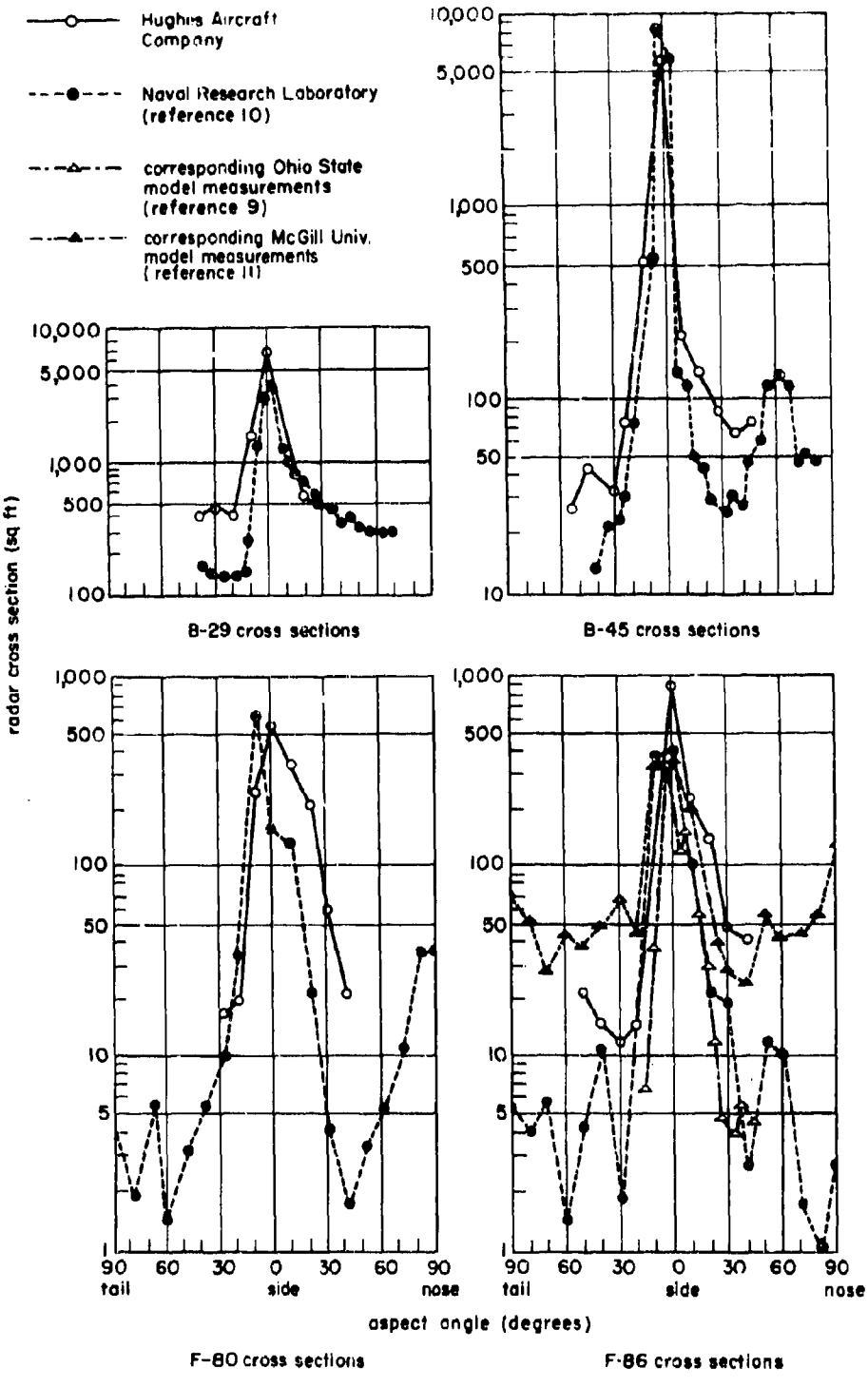


Figure 4-24. Radar Cross Section Measurements of Various Aircraft at Constant Polarization

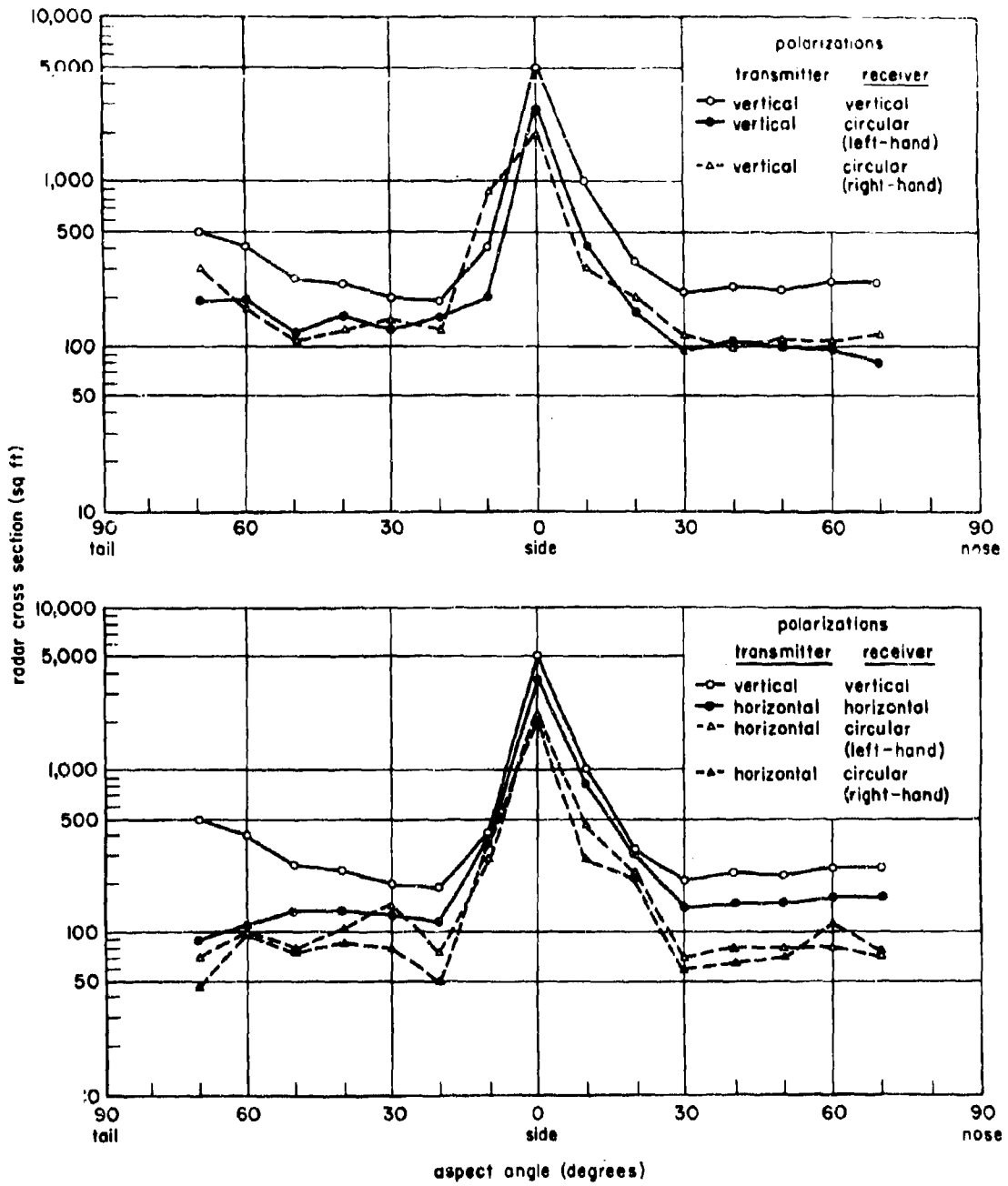


Figure 4-25. B-17 Radar Cross Sections At Various Polarizations (Flight Pattern No. 1)

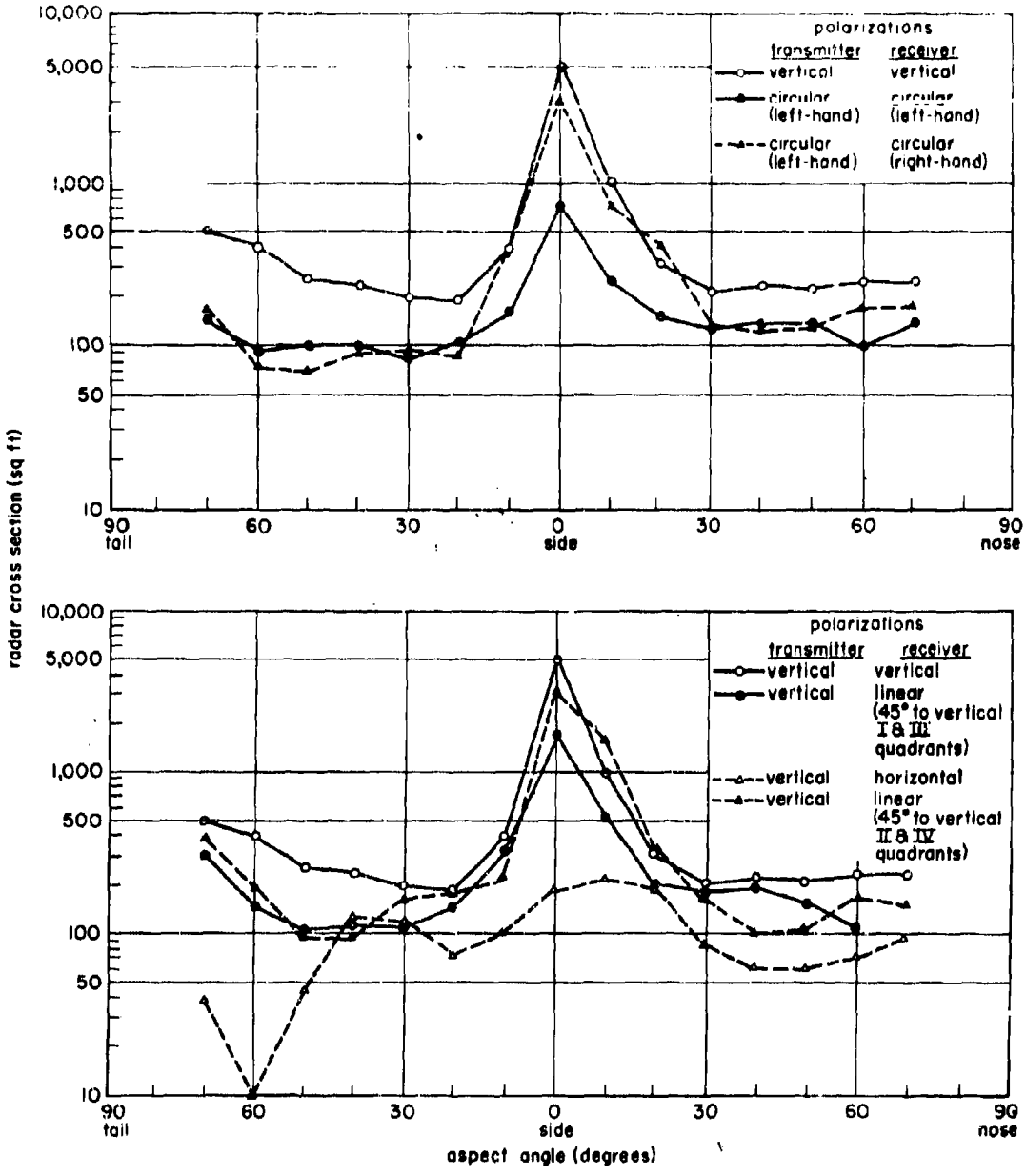


Figure 4-25. (Continued). B-17 Radar Cross Sections at Various Polarizations (Flight Pattern No 1)

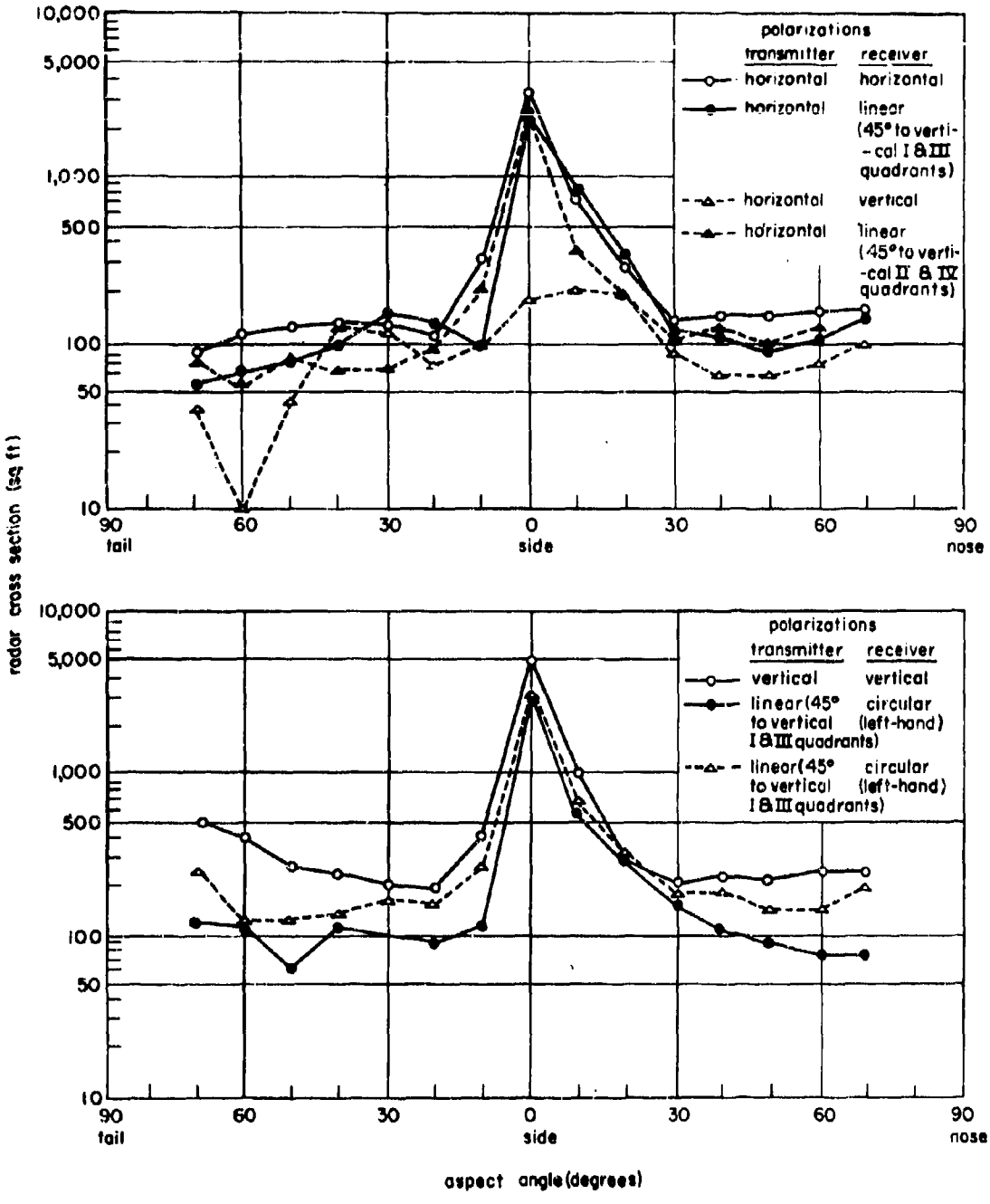


Figure 4–25. (Continued). B–17 Radar Cross Sections at Various Polarizations (Flight Pattern No 1)

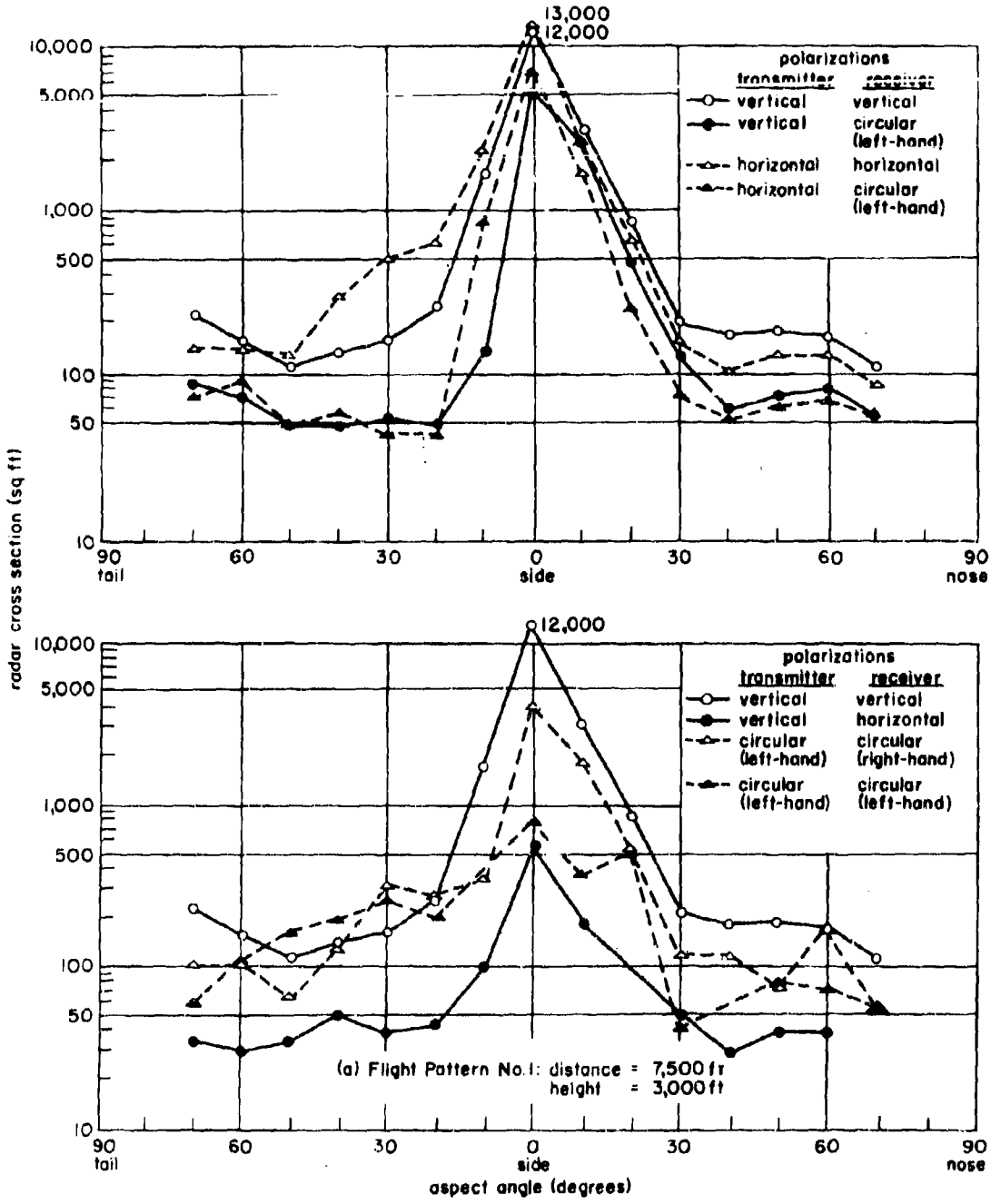


Figure 4-26. B-47 Radar Cross Sections at Various Polarizations

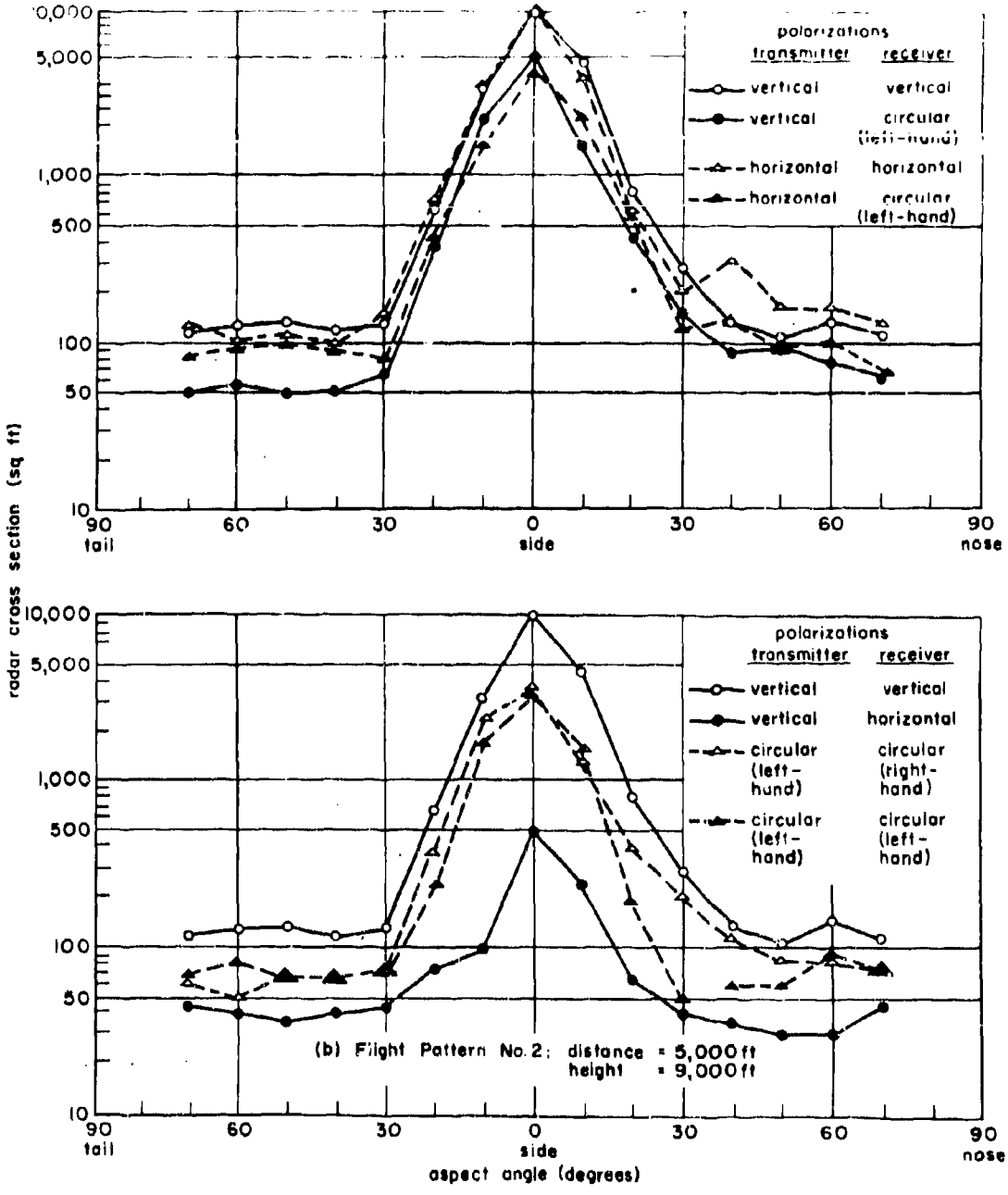


Figure 4-26. (Continued). B-47 Radar Cross Sections at Various Polarizations

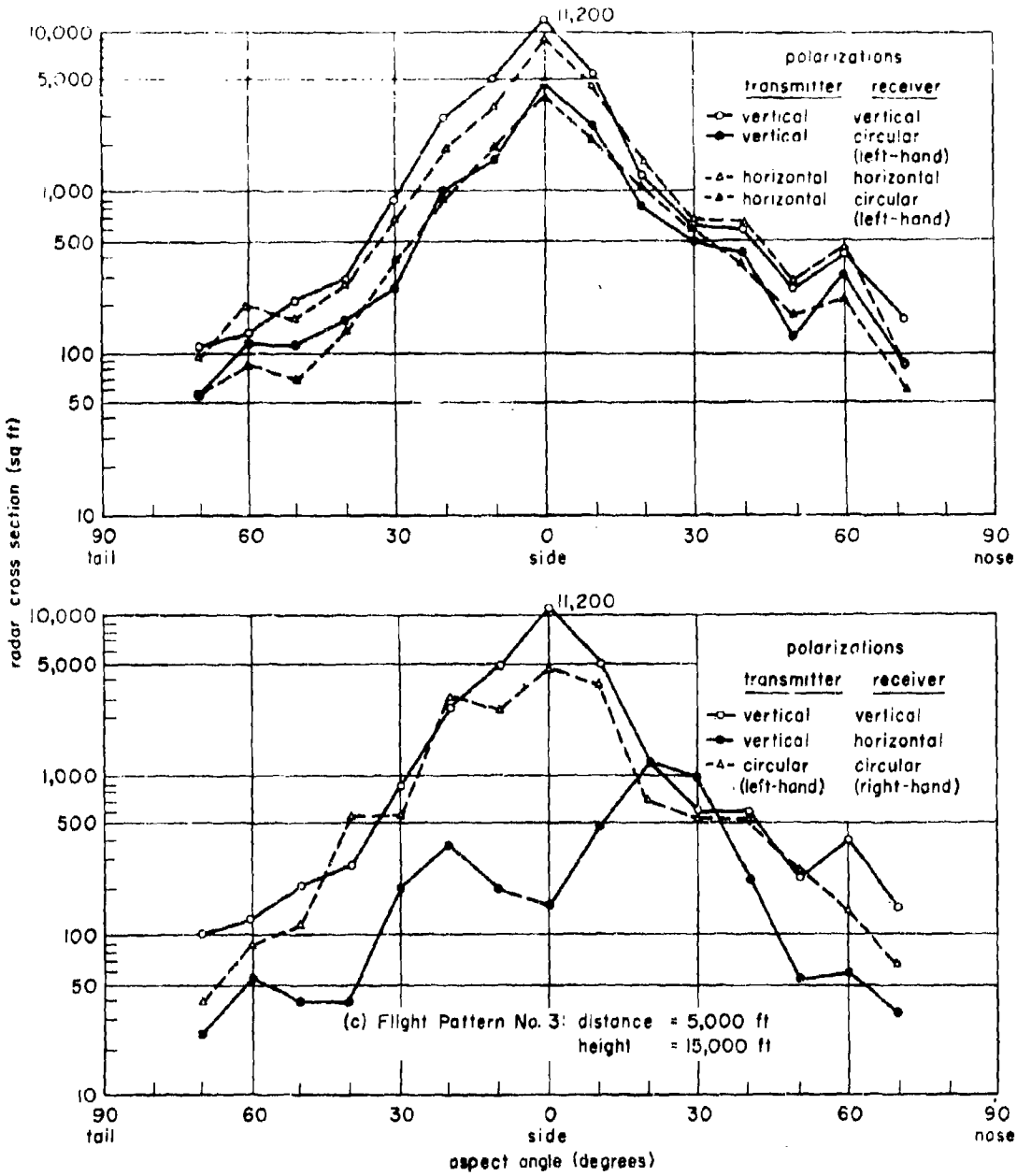


Figure 4–26. (Continued). B–47 Radar Cross Sections at Various Polarizations

Any transmitting antenna can be characterized by a vector $\underline{T}$ which is defined by the following expression [14]

$$\underline{E}^t = \frac{jZ_0 I}{2\lambda r} \underline{T} e^{jkr} \qquad (4\text{-}22)$$

where $\underline{E}^t$ = electric vector of transmitted wave

Z_0 = impedance of free space

I = antenna current

k = propagation constant

r = distance measured from the transmitter toward the scatterer

λ = wavelength

e = 2.71828. . .

A unit vector $\underline{T}_1$ can then be defined in terms of the vector $\underline{T}$ by

$$\underline{T}_1 = \frac{\underline{T}}{\sqrt{\underline{T}^+ \underline{T}}} \qquad (4\text{-}23)$$

where $\underline{T}^+$ is the adjoint of $\underline{T}$. This unit vector can be expressed as follows:

$$\underline{T}_1 = \begin{pmatrix} e^{j\alpha} \cos\phi \\ \sin\phi \end{pmatrix} \qquad (4\text{-}24)$$

where $\cos\phi$ = magnitude of horizontal component of the transmitter

$\sin\phi$ = magnitude of vertical component of the transmitter

α = phase difference between the components (phase angle of the transmitter)

A few examples of T_1 are given in Table 4-IV.

The scatterer can be characterized by a scattering matrix S such that

$$\underline{E}^r = S\underline{E}^t \frac{1}{r} \qquad (4\text{-}25)$$

where $\underline{E}^r$ = electric vector as scattered in the direction of the receiver

$\underline{E}^t$ = electric vector incident on scatterer

r = distance measured from scatterer toward receiver

For the case where the transmitter and receiver are at the same aspect with respect to the target, the scattering matrix can be expressed as

$$S = \begin{pmatrix} Ae^{j\gamma} & B \\ B & Ce^{j\delta} \end{pmatrix} e^{j\alpha} \qquad (4\text{-}26)$$

Table 4-IV. Examples of Unit Vector T_1 for Various Polarizations

Transmitter Polarization	Phase Difference Between Components	Magnitude of Horizontal Components ($\sin\phi$)	Magnitude of Vertical Components ($\sin\phi$)
Linear — vertical	...	0	1
Linear — horizontal	...	1	0
Linear — 45° to vertical, I and III quadrants	0	$1/\sqrt{2}$	$1/\sqrt{2}$
Linear — 45° to vertical, I and IV quadrants	π	$1/\sqrt{2}$	$1/\sqrt{2}$
Circular — left-hand	$\pi/2$	$1/\sqrt{2}$	$1/\sqrt{2}$
Circular — right-hand	$3\pi/2$	$1/\sqrt{2}$	$1/\sqrt{2}$

where $e^{j\alpha}$ has been factored out, making A, B, and C real. (The equality of the off-diagonal terms is a result of the application of the reciprocity relationship; otherwise, the matrix is perfectly general.)

The receiving antenna is characterized by a unit vector $\underline{R}_1$. (This vector is analogous to the unit vector $\underline{T}_1$; in fact, $\underline{R}_1$ and $\underline{T}_1$ are identical if the same antenna is used to transmit and receive.) The unit vector $\underline{R}_1$ can be expressed as

$$\underline{R}_1 = \begin{pmatrix} e^{j\beta} \cos \psi \\ \sin \psi \end{pmatrix} \tag{4-27}$$

where $\cos\psi$ = magnitude of horizontal component of the receiving antenna

$\sin\psi$ = magnitude of vertical component of the receiving antenna

β = phase difference between the components (phase angle of the receiving antenna)

The voltage at the receiver will be

$$V_r \propto \tilde{\underline{R}}_1 \underline{E}_r \tag{4-28}$$

or

$$V_r \propto \tilde{\underline{R}}_1 S \underline{T}_1 \tag{4-29}$$

where $\tilde{\underline{R}}_1$ = transpose of $\underline{R}_1$

The cross section can then be expressed as

$$\sigma \propto |V_r|^2 \tag{4-30}$$

or for a fixed geometry[15]

$$\sigma = K \left| \tilde{R}_1 S T_1 \right|^2 \tag{4-31}$$

where K = constant

The expression for cross section when expanded in terms of the notation introduced above becomes

$$\begin{aligned} \sigma = K \{ & A^2 f_1 + B^2 f_2 + C^2 f_3 + (AB \cos \gamma) f_4 + \\ & (AB \sin \gamma) f_5 + [AC \cos (\gamma - \delta)] f_6 + \\ & [AC \sin (\gamma - \delta)] f_7 + (BC \cos \delta) f_8 + \\ & (BC \sin \delta) f_9 \} \end{aligned} \tag{4-32}$$

where the f_i are functions of α, β, ϕ, and ψ, and their values are completely determined by the polarizations of the receiving and transmitting antennas. The theoretical cross sections, evaluated by means of Equation (4-32), for all possible combinations of the polarizations given in Table 4-IV are listed in Table 4-V. (The tabulated cross section expressions are still correct if the transmitter and receiver polarizations are interchanged.)

Radar Cross Section (Restricted Case). Equation (4-32) expresses the dependence of radar cross section on antenna configuration in its most general form. If the antenna polarizations are restricted to those for which the corresponding polarization ellipse has its principal axes oriented vertically and horizontally, then f_4, f_7, and f_8 are identically zero. Thus, in this restricted case, six coefficients are required to define the cross section, and Equation (4-32) becomes

$$\begin{aligned} \sigma = K \{ & A^2 f_1 + B^2 f_2 + C^2 f_3 + \\ & (AB \sin \gamma) f_5 + [AC \cos (\gamma - \delta)] f_6 + \\ & (BC \sin \delta) f_9 \} \end{aligned} \tag{4-33}$$

Application of the Theory to Experiment. In principle, cross-section measurements must be made for seven different antenna configurations, three to determine A, B, and C, and two for each angle measured directly for a target in flight, since A, B, and C occur squared or in cross products and vary over a range of values as the target pitches, yaws, or rolls. As a result, only average values of the coefficients of the f_i in Equation (4-32) can be measured and thus cross-section measurements must be made for nine different antenna configurations.[16] Once these coefficients have been determined, Equation (4-32) may be used to calculate the average cross section of the target for a completely arbitrary antenna configuration. It can be observed from Table 4-V that these coefficients are related to the cross sections tabulated there; typically,

Table 4-V. Dependence of Cross Section on Antenna Configuration

I = Linear — 45° to vertical, I and III quadrants

II = Linear — 45° to vertical, II and IV quadrants

Antenna Configuration		Theoretical Cross Section, Derived from Equation (4-32)
Transmitter Polarization	Receiver Polarization	
Vertical	Vertical	KC^2
Vertical	Horizontal	KB^2
Vertical	45° to Vertical (I and III)	$\frac{K}{2}(B^2 + C^2 + 2BC \cos \delta)$
Vertical	45° to vertical (II and IV)	$\frac{K}{2}(B^2 + C^2 - 2BC \cos \delta)$
Vertical	Circular, left-hand	$\frac{K}{2}(B^2 + C^2 + 2BC \sin \delta)$
Vertical	Circular, right-hand	$\frac{K}{2}(B^2 + C^2 - 2BC \sin \delta)$
Horizontal	Horizontal	KA^2
Horizontal	45° to vertical (I and III)	$\frac{K}{2}(A^2 + B^2 + 2AB \cos \gamma)$
Horizontal	45° to vertical (II and IV)	$\frac{K}{2}(A^2 + B^2 - 2AB \cos \gamma)$
Horizontal	Circular, left-hand	$\frac{K}{2}(A^2 + B^2 - 2AB \sin \gamma)$
Horizontal	Circular, right-hand	$\frac{K}{2}(A^2 + B^2 + 2AB \sin \gamma)$
45° to vertical (I and III)	45° to vertical (I and III)	$\frac{K}{4}[A^2 + 4B^2 + C^2 + 4AB \cos \gamma + 2AC \cos(\gamma - \delta) + 4BC \cos \delta]$
45° to vertical (I and III)	45° to vertical (II and IV)	$\frac{K}{4} A^2 + C^2 - 2AC \cos(\gamma - \delta)$
45° to vertical (I and III)	Circular, left-hand	$\frac{K}{4}[A^2 + 2B^2 + C^2 + 2AB \cos \gamma - 2AC \sin(\gamma - \delta) + 2BC \cos \delta - 2AB \sin \gamma + 2BC \sin \delta]$
45° to vertical (I and III)	Circular, right-hand	$\frac{K}{4}[A^2 + 2B^2 + C^2 + 2AB \cos \gamma + 2AC \sin(\gamma - \delta) + 2BC \cos \delta + 2AB \sin \gamma - 2BC \sin \delta]$

Table 4-V. Dependence of Cross Section on Antenna Configuration (cont)

Antenna Configuration		Theoretical Cross Section, Derived from Equation (4-32)
Transmitter Polarization	Receiver Polarization	
45° to vertical (II and IV)	45° to vertical (II and IV)	$\frac{K}{4}\left[A^2 + 4B^2 + C^2 - 4AB\cos\gamma + 2AC\cos(\gamma - \delta) - 4BC\cos\delta\right]$
45° to vertical (II and IV)	Circular, left-hand	$\frac{K}{4}\left[A^2 + 2B^2 + C^2 - 2AB\cos\gamma + 2AC\sin(\gamma - \delta) - 2BC\cos\delta - 2AB\sin\gamma + 2BC\sin\delta\right]$
45° to vertical (II and IV)	Circular, right-hand	$\frac{K}{4}\left[A^2 + 2B^2 + C^2 - 2AB\cos\gamma - 2AC\sin(\gamma - \delta) - 2BC\cos\delta + 2AB\sin\gamma - 2BC\sin\delta\right]$
Circular, left-hand	Circular, left-hand	$\frac{K}{4}\left[A^2 + 4B^2 + C^2 - 4AB\sin\gamma - 2AC\cos(\gamma - \delta) + 4BC\sin\delta\right]$
Circular, left-hand	Circular, right-hand	$\frac{K}{4}\left[A^2 + C^2 + 2AC\cos(\gamma - \delta)\right]$
Circular, right-hand	Circular, right-hand	$\frac{K}{4}\left[A^2 + 4B^2 + C^2 + 4AB\sin\gamma - 2AC\cos(\gamma - \delta) - 4BC\sin\delta\right]$

$$KA^2 = \sigma\,(H,H) = \sigma\,(x,y) \qquad (4\text{-}34)$$

$$KC^2 = \sigma\,(V,V) \qquad (4\text{-}35)$$

etc.

where σ (x, y) represents the cross section measured with transmitter polarization x and receiver polarization y. Thus, the nine coefficients in Equation (4-32) can be determined by measuring cross sections corresponding to suitable combinations of the antenna polarizations listed in Table 4-V.

For antenna configurations with polarizations in which the polarization ellipses are oriented vertically and horizontally, only four antenna polarizations need be considered: (1) Linear vertical, (2) Linear horizontal, (3) Circular left-hand, (4) Circular right-hand.

For these restricted configurations, a set of six independent antenna configurations would be sufficient.

4-29. Radome Depolarization

As the target moves or vibrates, the matched and depolarized components of the target echo signal scintillate in amplitude to produce a very complex reflection coefficient. From another point of view, the signal received by an antenna can be regarded as scintillating in polarization as well as in amplitude. Since the radome error changes with the polarization of the return signal, the scintillation in polarization will be converted by the radome into apparent scintillation in position. This scintillation in position results in scintillation noise in the receiver, which is added to ordinary amplitude and angular scintillation. The effects on the radome error of the different types of polarization of the target echo are described in the remainder of this section. Some general observations are drawn which may be of value in design work.

Experimental Measurements. Measurements of radome errors under various types of incident polarization (target echo polarization) have been made for both missile-type[17] and interceptor-type[18] radomes. Two series have been recorded for the interceptor-type radome, one using a 6-db right-hand, elliptically polarized receiving antenna, and the other using a circularly polarized antenna. Both missile-type radomes measured used right-hand, circularly polarized receiving antennas, but one radome was a 2.5:1 ellipsoidal radome and one was an ogive.

The interceptor-type radome employed approximates a cone in shape and is constructed of homogeneous material 0.320 inch thick, with a dielectric constant of 4. It is 30 inches in diameter and 52 inches long. Figures 4-27 and 4-28 show the error curves obtained with a 6-db. right-hand, elliptically polarized receiving antenna. The major axis of the incident wave was always aligned parallel to the major axis of the polarization of the antenna.

Figure 4-27 presents the errors obtained when the incident polarization was linearly polarized. The curves show that the errors reverse in sign when the incident polarization is rotated 90°. Tests conducted with a linearly polarized receiving antenna also show that, when the incident polarization is rotated 90°, the errors reverse in sign.

Figure 4-28 presents the error curves obtained when the major axis of the polarization of the receiving antenna was horizontal, Curves are given for incident waves of left-hand and right-hand circularly polarizations and for several elliptical polarizations. They show that the errors are lowest in in-plane at right-hand circular polarization and in crosstalk at 6-db right-hand elliptical polarization. Both in-plane and crosstalk errors are largest at left-hand circular polarization. Error curves measured with the major axis of the receiving antenna in a vertical position show the same trend as those of Figure 4-28, except that the in-plane error reversed in sign.

Error curves were measured for a circularly polarized receiving antenna with, first, a circularly polarized incident wave of the same sense, and, second, with a linearly polarized incident wave. The curves show that the first condition results in the lowest error and the second results in the worst error, both relative to all the results obtained under the other states of polarizations.

Both missile-type radomes measured employed a left-hand circularly polarized antenna as the receiving unit. The symmetry of the receiving antenna might be considered to offer some advantages over a linearly polarized antenna, regardless of the incident polarization.

The curves of Figure 4-29 are the measured error curves of a 2.5:1 ellipsoidal radome as a function of the illuminating polarization. Those in Figure 4-30 are similarly measured error curves for an ogival radome. Six polarizations were investigated with both radomes: (a) nearly left-hand circular (0.6 db of ellipticity); (b) 3-db left-hand elliptical; (c) 6-db left-hand elliptical; (d) 9-db left-hand elliptical; (e) 12-db left-hand elliptical; and (f) linear. For each particular polarization investigated, four measurements of radome error as a function of offset angle were made: in-plane and crosstalk error characteristics for the major axis of the incident polarization oriented perpendicular to the antenna offset plane; and in-plane and crosstalk error characteristics for the major axis oriented parallel to the offset plane.

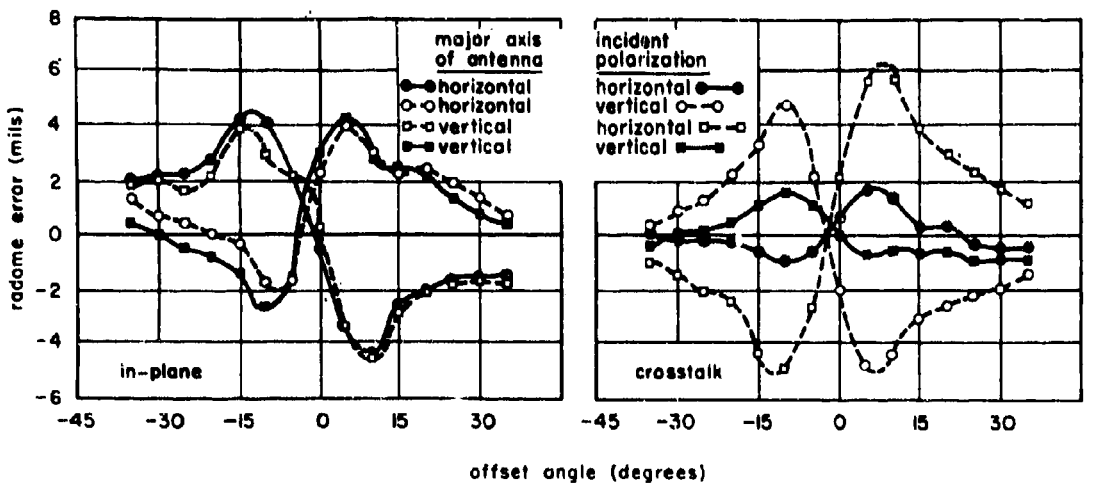


Figure 4-27. Interceptor-Type Radome Error Curves With Linear Incident Polarization; Receiving Polarization 6-db, Right-Hand Elliptical

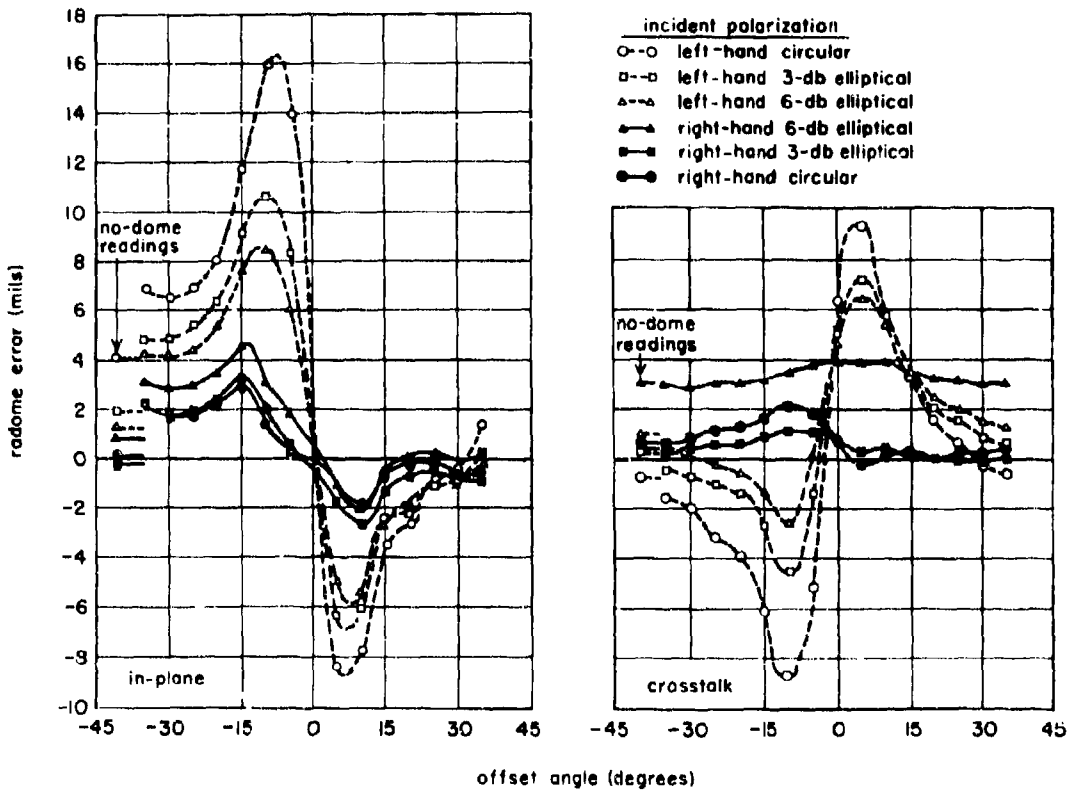


Figure 4-28. Interceptor-Type Radome Error Curves with Elliptical Incident Polarization; Major Axis Horizontal, Receiving Polarization 6-db, Right-Hand Elliptical, Major Axis Horizontal

Both sets of curves show that any significant change in the relative orientation of the elliptical axes with respect to the antenna offset plane produces sizable changes in both crosstalk and in-plane error characteristics. Of particular significance is the fact that, with both the ellipse and the ogive, the most desirable radome error characteristics were obtained when the incident polarization was nearly left-hand circularly polarized (antenna and incident polarizations matched).

Analysis of Experimental Measurements. That the radome modifies the polarization of a wave which traverses its walls has been studied and reported by many investigators (References 17 through 25). The major factor in the effect of the radome on incident polarizations is the amplitude and phase distortion resulting from varying angles of incidence and orientations of the electric vector. This dependence can be illustrated by the transmission coefficients for a plane wave incident on a plane homogeneous dielectric slab. As discussed in Chapter 2 and elsewhere in this book, the transmission coefficients $\dot{T}_{\parallel}$ and $\dot{T}_{\perp}$ are complex quantities and differ both in magnitude and phase. The range of variation with angle of incidence is quite sensitive to the electrical thickness of the slab (see graphs of tolerances in Chapter 13). Another discussion with numerical values is given in the M.I.T. Radiation Laboratory Series, Volume 26.[5]

The effect of these factors on polarization may be illustrated as follows: a plane wave is assumed to be incident on a radome, regarded as a streamlined surface of revolution. The wave is assumed to be linearly polarized, with the direction of propagation at an angle θ with respect to the radome axis. The x-axis is oriented to lie in the plane of incidence which passes through the z-axis, as shown in Figure 4-31. The axes in the plane of the E vector are designated ζ and η, where ζ is in the x-z plane.

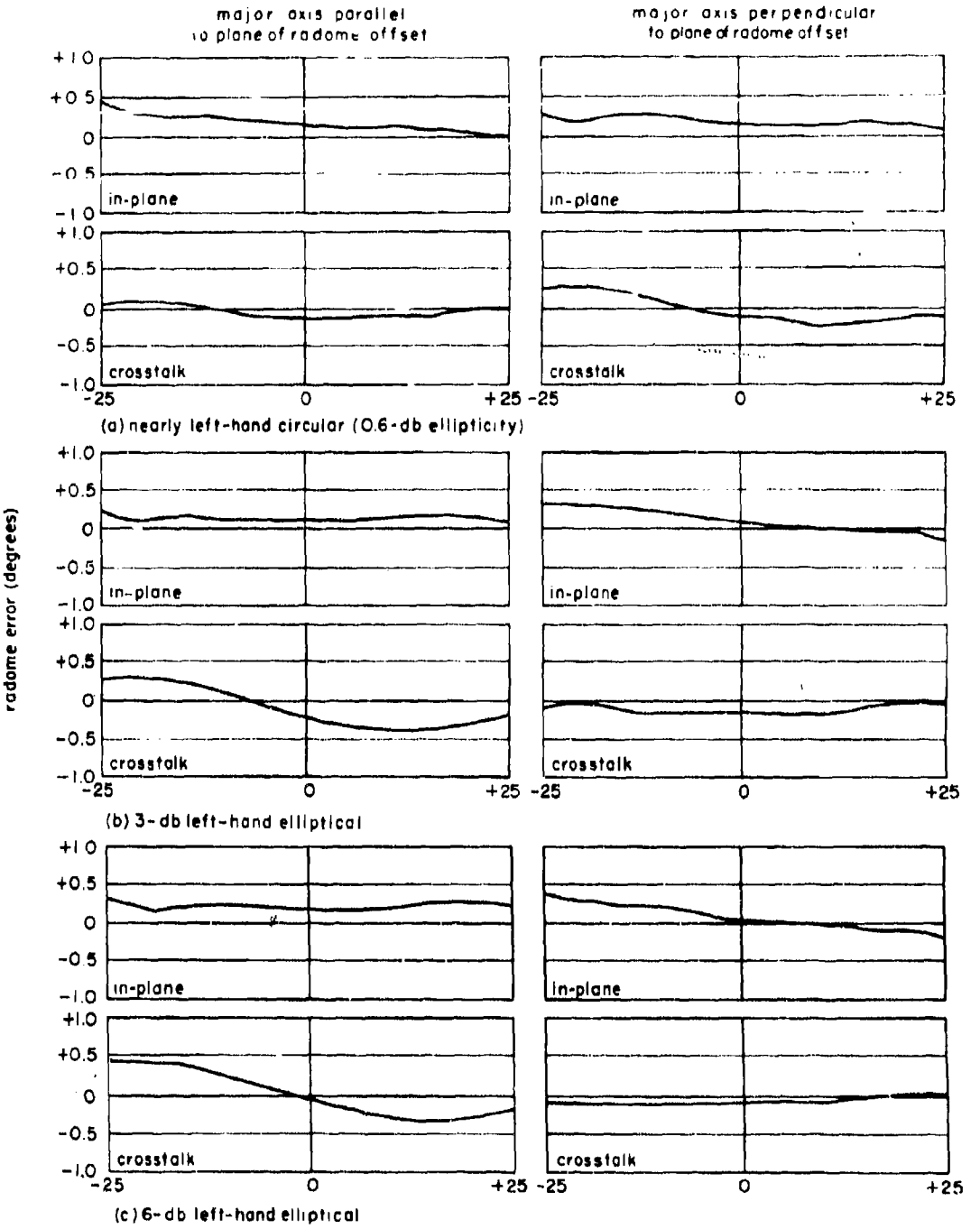


Figure 4–29. Error Curves of Ellipsoidal Missile Radome With Various Incident Polarizations (Left-Hand Circular Receiving Polarization)

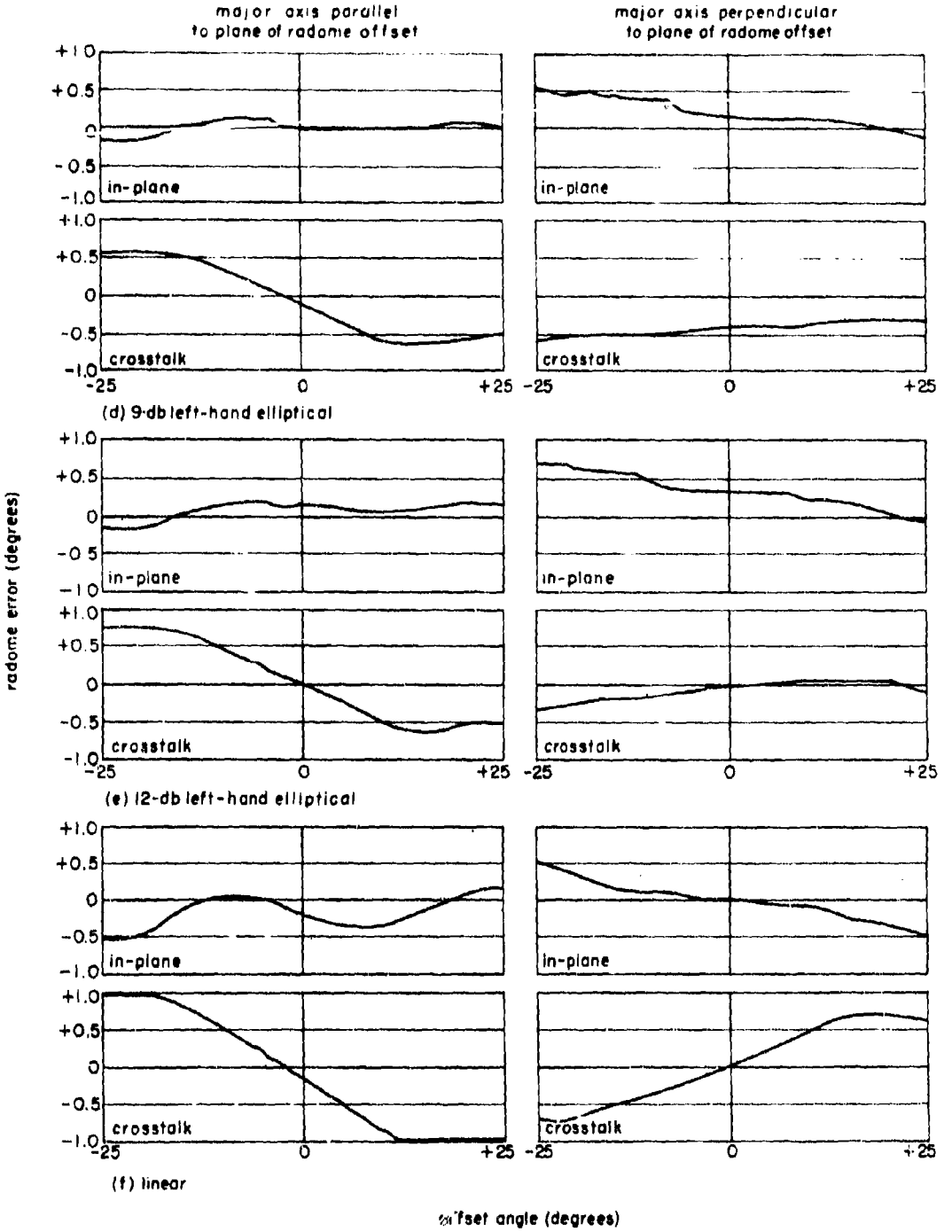


Figure 4–29 (Continued). Error Curves of Ellipsoidal Missile Radome With Various Incident Polarizations (Left-Hand Circular Receiving Polarization)

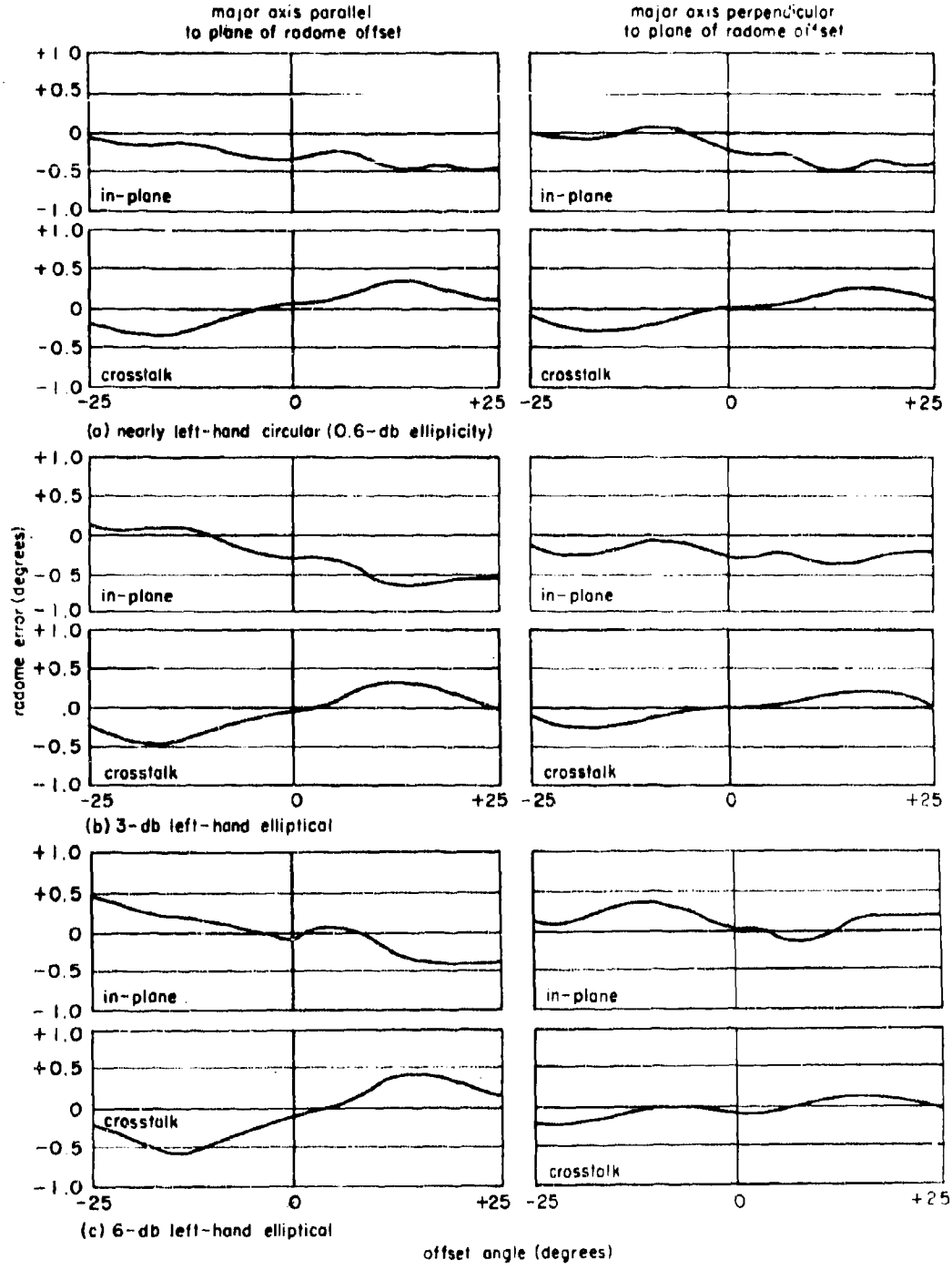


Figure 4-30. Error Curves of Ogival Missile Radome with Various Incident Polarizations (Left-Hand Circular Receiving Polarization)

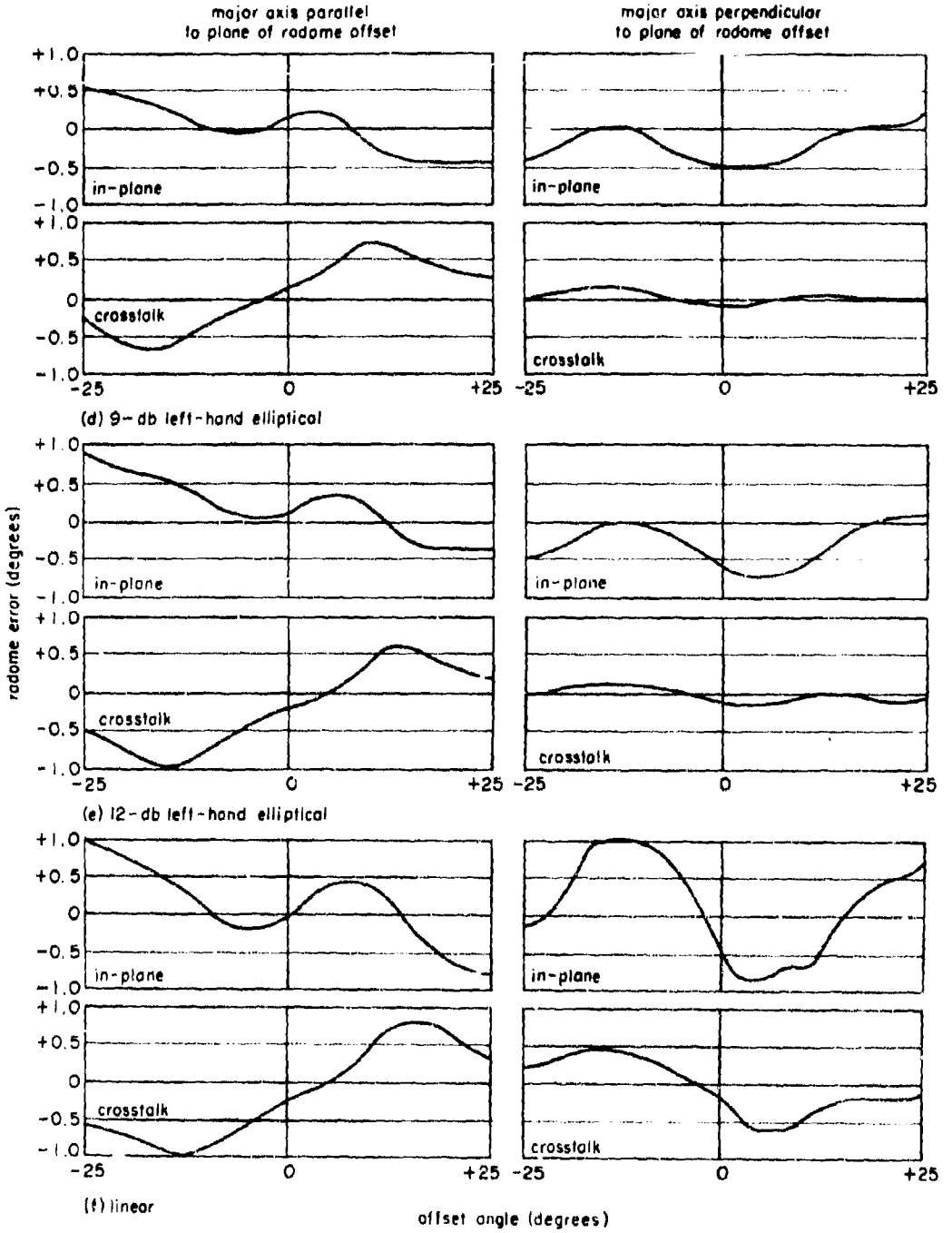


Figure 4-30 (Continued). Error Curves of Ogival Missile Radome With Various Incident Polarizations (Left-Hand Circular Receiving Polarization)

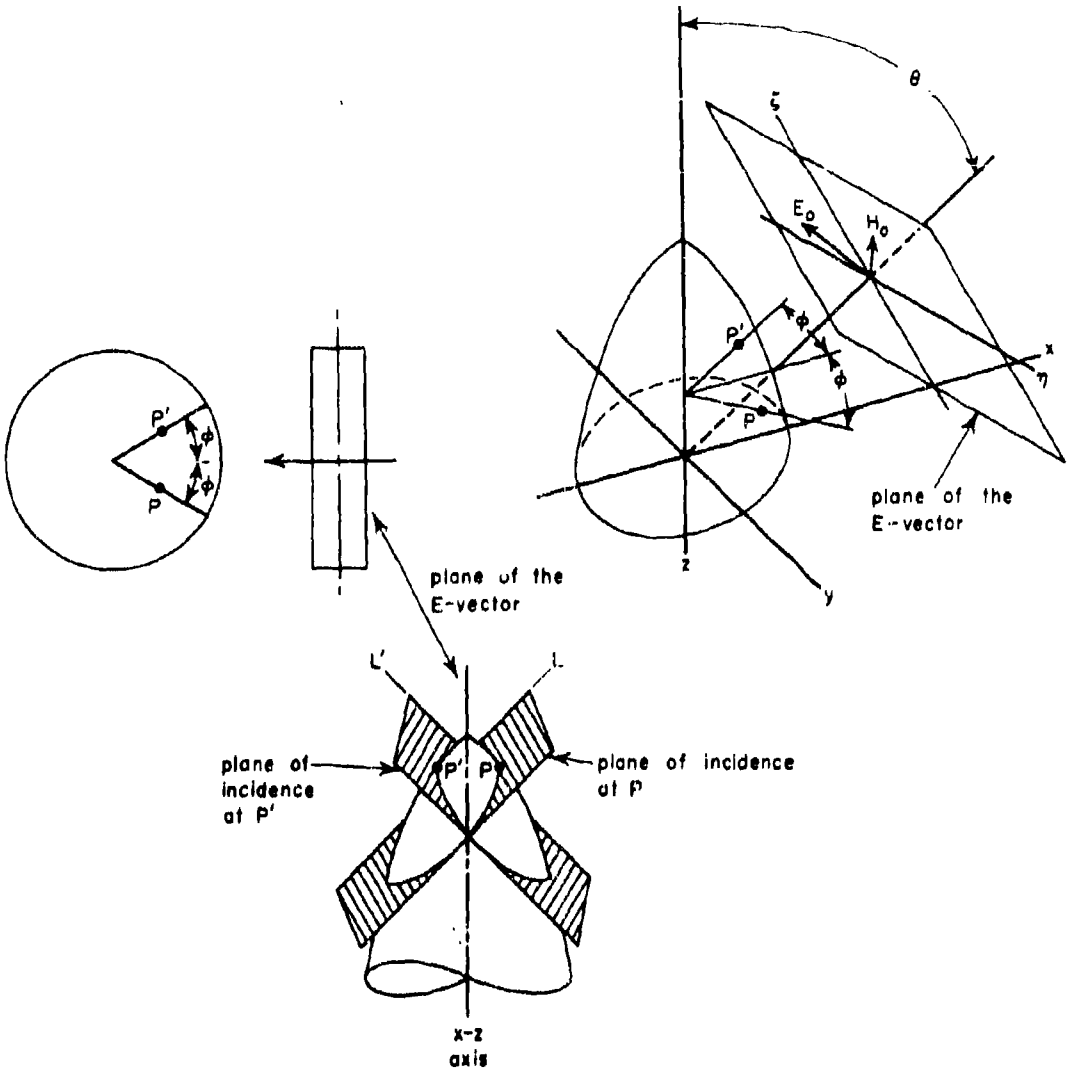


Figure 4-31. Coordinate System for Analysis of Linearly Polarized Wave Incident on a Radome

In general, the E vector has an arbitrary orientation with respect to the ζ axis. The antenna, in scanning, will necessarily observe the wave through some two points P and P' on the surface of the radome (Figure 4-31) located symmetrically with respect to the x-axis and determined by $\pm\phi$.

The problem of radome crosstalk, or deviations of radar line-of-sight from the plane $\phi = 0$, is inherently concerned with the nature of the fields seen by the antenna at P and P' and their effect upon the ability of the antenna to discern the direction of the incident wave with respect to ϕ. If the fields at P and P' are identical in every respect, then the receiving system will indicate that the target lies in the x-z plane. Any deviation from this identity will cause the antenna to orient itself in such a manner as to make the response identical at some other point Q and Q' and thus deviate from the true plane of offset.

For the effect of the radome on the fields at P and P' to be determined, the incident E vector must be resolved into components which are

parallel and perpendicular to the planes of incidence at these two points, as shown in Figure 4-32. The complex transmission coefficient of the radome wall is a different function of the angle of incidence for each of these components. In general, the components parallel to the plane incidence will undergo less phase retardation and reflection loss upon transmission than the vertical component. After transmission and recombination of the components, there is, in general, elliptical polarization in which the direction of rotation of the polarization ellipses of each component will be as shown in Figure 4-33. The directions of rotation or screw senses of the transmitted components at the two points P and P' are opposite because of the relative phase of the components at these points. The radome thus introduces several types of polarization changes into the incident linearly polarized wave. Similar analysis may be employed to show the effect for other incident polarizations.

The preceding analysis is based on transmission of the incident wave at one angle of incidence on the radome. Because of the geometry of the radome, the characteristics of the transmitted wave vary from one angle of incidence to the next. Therefore, the total effect of the radome on incident polarization can be obtained only by integration over the receiving area of the radome; that is, the area or section of the radome through which energy passes and contributes to the power absorbed by the receiving antenna. This concept can be enlarged, with reference to Figure 4-34, where the conical scan axis of the antenna is perpendicular to the paper and is pointed towards the reader. The path abcd represents the intersection between the center ray of the antenna and the outer contour of the radome. The nose of the radome is to the left and away from the paper towards the reader (represented by point 0). The incident wave travels in the direction the reader is looking and arrives normal to the plane of the paper. The plane FE, perpendicular to the paper, is a plane of incidence for the wave incident at point E, and β is the angle between this plane of incidence and the offset plane. Because of symmetry, the crosstalk error is proportional to the difference in power received when the antenna is at position a and when it is at position c. A similar proportion, however, does not apply for in-plane errors, because an antenna beam with its central ray passing through point b is not oriented with respect to the radome precisely the same as is an antenna beam with central ray passing through d.

An area centered about point b and another area centered about d must be considered, and it is seen that the area centered at b has associated with it angles β which are greater than the angles associated with the area centered at d. This difference in the location of the planes of incidence is sufficient to cause a difference in the character of the ellipses associated with the transmitted wave. And, as with crosstalk error, a change in the polarization ellipse of an incident wave results in in-plane error.

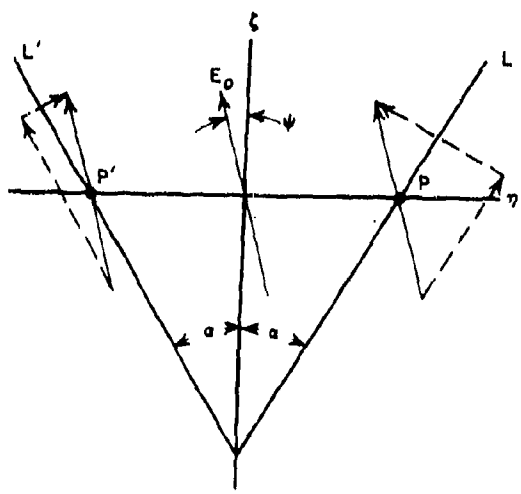


Figure 4-32. Plane of E Vector – Linearly Polarized Incident Wave, Before Transmission Through a Radome

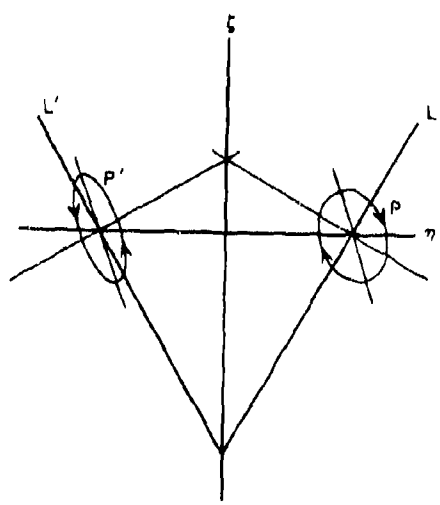


Figure 4-33. Plane of E Vector – Linearly Polarized Incident Wave, After Transmission Through a Radome

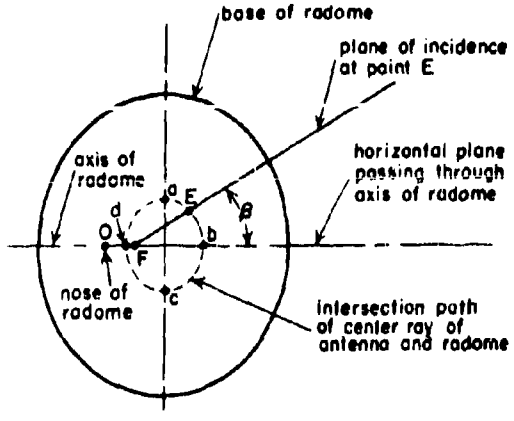


Figure 4-34. View of Radome From Exterior

Examination of the expression for polarization efficiency, Equation (4-36), sheds further light on the relationship between antenna pointing errors and changes in the ellipticity of the incident wave resulting from transmission through the radome wall.[26]

$$f = \frac{(1 \pm r_r r_t)^2 + (r_r \pm r_t)^2}{2(1 + r_r^2)(1 + r_t^2)} + \frac{(1 - r_r^2)(1 - r_t^2)\cos 2\delta}{2(1 + r_r^2)(1 + r_t^2)} \qquad (4\text{-}36)$$

where f = polarization efficiency, the ratio of the power received by an antenna of any polarization in any polarized field to the power received by a linearly polarized antenna polarized parallel to a linearly polarized field (with the power density of the fields remaining a constant)

r_r = axial ratio of the receiving antenna (minor-to-major axis with + denoting left-handed and - denoting right-handed senses)

r_t = axial ratio of the incident field

δ = angle between the major axis of the receiving antenna and the major axis of the incident field

\+ for the same senses of polarization

\- for opposite senses of polarization.

The effect on polarization effici cy of changes in the axes of the polarization ellipses is direct. For example, for circular polarization of the same sense for both receiving antenna and incident field, the polarization efficiency would be 1; since the polarization ellipse is actually a circle in circular polarization, each major axis equals each minor axis and their ratios are ±1. For linear -- linear polarization, f should also be 1 ($r = 0$, because the minor axis = 0). For a circular receiving antenna polarization and a linear incident polarization, the polarization efficiency would be 0.50. Elliptical polarizations become more complex because of the infinite number of possible ellipses. Polarization efficiencies range between 0 and 1, because the values of r fall into this range.

Equation (4-36) yields the order of magnitude of the relative power received at two opposite scan positions of the antenna. For final calculation of the order of magnitudes of the radome error, a formula derived by Barker and Lengyel can be employed.[3] In the derivation of the formula it is established that the far-field power pattern should be written as

$$P(\theta) = 1 - \frac{5}{8}\left(\frac{\theta}{\theta_0}\right)^2 + \frac{1}{8}\left(\frac{\theta}{\theta_0}\right)^4 \cdots \qquad (4\text{-}37)$$

where θ is the angle position and $2\theta_0$ is the half-power beamwidth. The slope of the pattern at half-power point is $(-3/4\ \theta_0)$, which is very nearly the slope of a pattern for a uniformly illuminated circular aperture. If a conically scanning antenna (crossover at half-power points), with only changes in maximum power as a function of scan angle is assumed, the error can be expressed as

$$\Delta = \frac{\theta_0}{3}(\alpha_2 - \alpha_1) \qquad (4\text{-}38)$$

where Δ is the radome error and the α's are the fractional decrease in the maximum power at the opposite scan positions when the radome is mounted. In the expressions derived by Barker and Lengyel, other terms appear which involve the changes in beamwidth and shifts in the angular position of the main beam. The contributions of these terms are considered to be negligible in the foregoing analysis.

Further examination of polarization efficiency through the use of Equation (4-36) can be used to indicate some trends which might be expected when radomes are tested under various conditions of polarizations. The assumption is made that radome errors are caused only by the variation (with conical scan) of the ellipticity of the waves transmitted through the

radome. Of course, this assumption is not valid when other effects dominate: these effects include error correcting obstacles, refraction, high loss in the radome walls, and diffraction created by the nose. The effect of depolarization of a radome (the changes in incident polarization caused by the radome) is to change r_t, the axial ratio of the incident field. The contributing factors to the pointing error of a conically scanning antenna are the rate of change of polarization efficiency with change in axial ratio of the incident field (df/dr_t) and the value of the polarization efficiency obtained at the states of polarization, that is, the values assigned to r_t and to r_r, the axial ratios of the incident field and the receiving antenna respectively.

Rate of Change of Polarization Efficiency with Respect to r_t. When the derivative (df/dr_t) is taken with an arbitrary sense of polarization assumed, the result is

$$\frac{df}{dr_t} = \frac{2r_r\,(1 - r_r^2)}{(1 + r_r^2)\,(1 + r_t^2)^2} - \frac{2\,(1 - r_r^2)\,r_t \cos 2\delta}{(1 + r_r^2)\,(1 + r_t^2)^2} \tag{4-39}$$

In this operation, it is assumed that δ, the angle between the major axis of the receiving antenna and the major axis of the incident field, remains constant. In general, this condition does not exist. However, since the variation in δ with respect to r_t is small, the condition is assumed for the analysis. When Equation (4-39) is set equal to zero and solved for r_t,

$$r_t = \frac{r_r^2 - 1}{2r_r} \cos 2\delta + \frac{1}{2r_r}\left[(1-r_r^2)^2 \cos^2 2\delta + 4r_r^2\right]^{1/2} \tag{4-40}$$

In general, when radome errors are measured, $\delta = 0$. Under this condition, Equation (4-40) becomes

$$r_r = r_t \tag{4-41}$$

If Equation (4-39) is differentiated with respect to r_t, the following expression is obtained.

$$\frac{d^2f}{dr_t^2} = \frac{4r_r\,r_t\,(r_t^2 - 3)}{(1 + r_r^2)\,(1 + r_t^2)^3} - \frac{2(\cos 2\delta)\,(1 - r_r^2)\,(1 - 3r_t^2)}{(1 + r_r^2)\,(1 + r_t^2)^3} \tag{4-42}$$

Equation (4-42), when set equal to zero, gives the worst condition for r_r and r_t when radome error slope is the only criterion. For example, if $\delta = 0$ and $r_r = 0$, $r_t = 0.577$; or, if $\delta = 0$ and $r_r = 1$, then $r_t = 0$.

If the condition given by Equation (4-41) were substituted into Equation (4-42),

$$\frac{d^2f}{dr_t^2} = -\frac{2}{(1 + r^2)^2} \tag{4-43}$$

where $r_t = r_r = r$. When $r = 1$ (which is circular polarization), d^2f/dr_t is minimum, a condition which is optimum for minimum error.

Consideration of the Polarization Efficiency. Figure 4-35 is a plot of Equation (4-36) with the assumption that $\delta = 0$. The curves for the three values of r_r show the relative amounts of power received for variations in r_t of the incident wave. Careful investigation shows that, for small pointing errors to be achieved at any given set of axial ratios, not only is the slope of the curves important but the relative values of the powers received must also be considered. For example, an r_t of 0 can be considered with interest, then confined to r_r's of 1 and 0.50 (Figure 4-35). The slopes of the operating points A and B are approximately the same: and if a radome changes the axial ratio of r_t by a finite amount which depends on the position of the conical scan cycle of the antenna, it might be suspected at first glance that the errors would be the same at the two axial ratios of 1 and 0.50. However, this condition does not exist, since the fractional change in the powers received at two opposite positions of the conical scan cycle must be considered. This fractional change is given in the derivation of the Barker-Lengyel formula, Equation (4-11). For a given axial ratio change in r_t due to the radome, operating point A will result in a larger fractional change in polarization efficiency than operating point B. Hence, radome errors should be lower at operating point B than at operating point A.

The analysis of the effect of the radome in changing the axial ratio of the incident wave

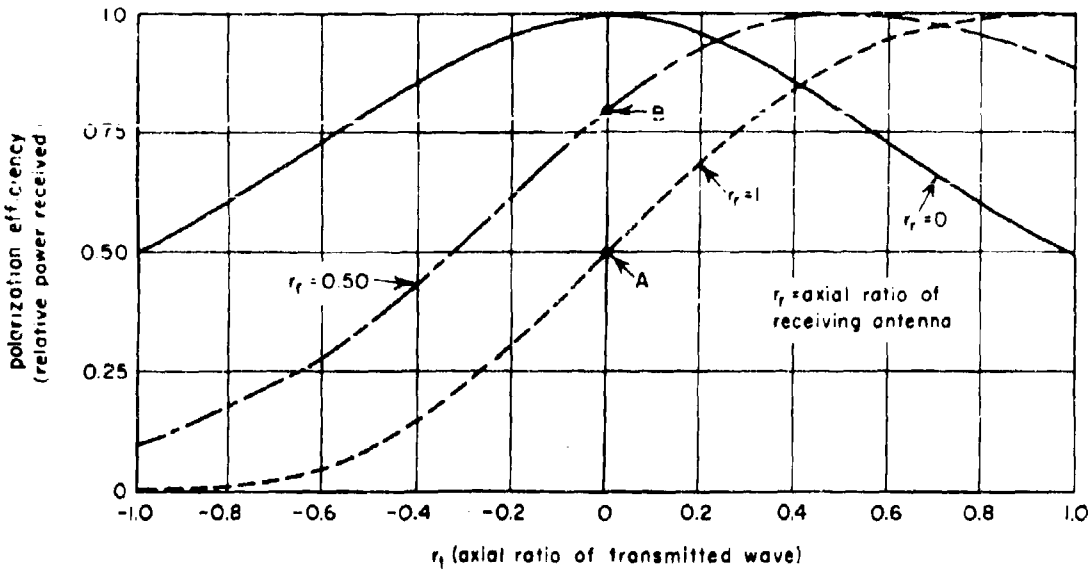


Figure 4-35. Relative Power Received by an Elliptically Polarized Antenna

appears correct when the predicted results are compared with the actual measured values of radome errors. The analytical prediction that the lowest errors should result when $r_t = r_r = 1$ (a circularly polarized receiving antenna with a circularly polarized incident wave of the same sense) is verified by experimental measurements such as those shown in Figures 4-27 through 4-30. The prediction that low errors result when $r_t = r_r$ and that larger errors are found to exist with a circularly polarized receiving antenna with a linearly polarized incident wave is also verified by the measurements of Figures 4-27, 4-28, 4-29 (f) and 4-30 (f). And the analytical result that operating point B of Figure 4-35 should produce lower errors than operating point A is verified by the curves of Figure 4-28. From the measurements of actual radome errors under the various states of polarization, it appears that polarization efficiencies above 0.80 will result in errors which are comparable to those taken at a polarization efficiency of 1. Minimum errors can be obtained if the polarization of the incident wave and the polarization of the receiving antenna are circularly polarized and are of the same sense.

This analysis then describes error behaviors as a function of the variations in polarization of a wave after transmission through a radome wall. The exact modification of the original incident-wave polarization produced by the radome wall was not given explicitly. The complex coefficient $\dot{T}_1$ defined in Chapter 2 is the same type of coefficient as the polarization efficiency f, and the expression for $\dot{T}_1$ has been used in an analysis which indicated that, for a given incident polarization, a "matched" receiving polarization is not always the correct one for minimum boresight error.[22]

SECTION E. EFFECT OF RADOME ERRORS ON FIRE CONTROL AND GUIDANCE SYSTEMS

It is fairly common knowledge in the radome design field today that fire control radome errors adversely affect the accuracy of missile and rocket firing, as well as the stability of the radar-autopilot-airplane loop. When the radome errors can be correlated with resulting fire control errors, the results can be used to specify the allowable errors in the interceptor's radome. These specifications are important in light of the compromise which must be made in the air-frame design between a low-error radome (high-drag "rounded" nose) and a large-error radome (low-drag "sharp" nose). Studies of sequential lobe comparison systems have found that the radome errors are most detrimental during the interceptor's rock-

et-firing mode of operation; the effect of errors in the interceptor's radome on the missile launching problem is not so significant. If the error limits imposed by the rocket-firing problem are met, the radar-autopilot-airplane loop will be stable for the expected airplane response times, and the missile will be launched with the necessary accuracy to place it on the proper initial course. A typical analysis of the interrelation of radome error and fire control error will be developed to show these results in greater detail.[26]

4-30. Effect of Radome Errors on Fire Control Systems

In the fire control system (conical scan) studied in the analysis, the coordinate system shown in Figure 4-36 was used. The angle between the line-of-sight to the target and the longitudinal axis of the aircraft is defined as σ. This angle can vary from 0° to the maximum offset angle of the radar (about 70°). The angle between the plane of the interceptor's wings and the plane through the longitudinal axis containing the line-of-sight is called ζ. It varies from 0 to 360° and lies between 0 and 90° when the target is above and to the right of the interceptor.

In general, the radome will bend the radar beam so that the apparent line-of-sight will not coincide with the true line-of-sight. In the analysis the in-plane error $\Delta\sigma$ equals the value of σ for the apparent line-of-sight minus the value of σ for the true line-of-sight, and the crosstalk error $\Delta\zeta$ equals the value of ζ for the apparent line-of-sight minus the value of ζ for the true line-of-sight.

Through the fire control equations associated with the lead-collision type of attack, the magnitude and the angular rates of change of the radome errors (for any arbitrary direction of the line-of-sight) can be related to the fire control "miss" caused by these radome errors. It is convenient to resolve the fire control "miss" into two components, M_{σ} and M_{ζ}.

The miss in yards in the plane in which σ is measured is the M_{σ} component. When the interceptor is on a proper firing course, the geometry is such that the target is heading for some point on the interceptor's longitudinal axis,* and consequently the target's longitudinal axis lies in the plane in which σ is measured. When the rocket passes in front of the target, M_{σ} is taken as positive. Therefore, M_{σ} is the miss along the target's fuselage in the special case of a direct beam attack.

The M_{ζ} component of the fire-control "miss" is the miss in yards perpendicular to the plane in which σ is measured; therefore, M_{ζ} is a miss perpendicular to the target's fuselage.

*Gravity drop and jump angles are second-order effects in this analysis and are therefore neglected.

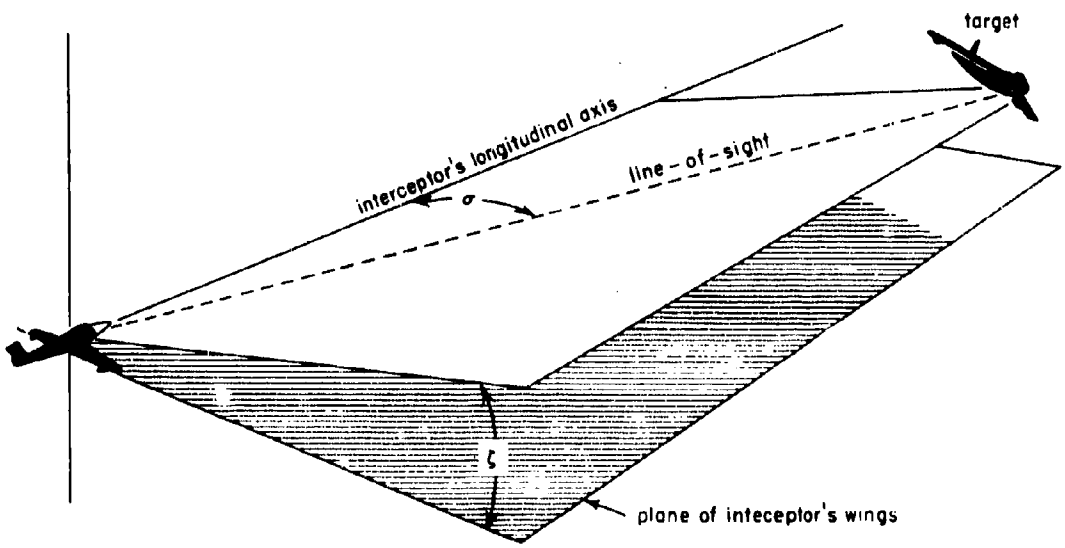


Figure 4-36. Definition of Radome Angles for Analysis of Error Effect on Fire Control Systems

This component is taken as positive in the direction of positive ζ; for example, a positive M_ζ corresponds to the rocket passing over the target when the target comes from the right and passing under the target when it comes from the left.

The following expressions have been derived for M_σ and M_ζ.

$$M_\sigma = - C_1 \Delta\sigma + C_2 \frac{\partial(\Delta\sigma)}{\partial\sigma} - C_3 \frac{\partial(\Delta\sigma)}{\partial\zeta} \qquad (4\text{-}44)$$

$$M_\zeta = - C_4 \frac{\partial(\Delta\zeta)}{\partial\sigma} + C_5 \frac{\partial(\Delta\zeta)}{\partial\zeta} \qquad (4\text{-}45)$$

where $C_1 = F\left[\cos\sigma + \sin^2\sigma \dfrac{F - \dfrac{F}{t_f}}{\dot{F}\cos\sigma - \dot{R}}\right]$

$C_2 = F \sin\sigma$

$C_3 = \phi R t_f$

$C_4 = F \sin^2\sigma$

$C_5 = \phi R t_f \sin\sigma$

F = rocket travel distance (in yards) relative to the interceptor

F = rocket speed relative to interceptor at time of impact

t_f = time-of-flight of rocket

R = range of target at time of firing

$\dot{R}$ = range rate of target at firing

ϕ = roll rate of interceptor at firing, taken as positive if right wing is going down.

Since the target is essentially a long rectangle, it is clear that M_ζ (the miss component perpendicular to the fuselage) should be kept smaller than M_σ. Both M_ζ and M_σ should be a small part of the total "miss" caused by all adverse effects combined. By means of published data the effect of any given values of M_σ and M_ζ on the probability of kill of rockets can be determined.[27] A reasonable design objective for an interceptor radome appears to be $|M_\zeta| < 1$ yard; $|M_\sigma| < 5$ yards. Values of M_ζ and M_σ which are compatible with the rocket firing problem have no significant effect on the missile launching problem.

Figure 4-37 shows the plots of the coefficients C_1, C_2, C_3, C_4, and C_5 in yards for a typical set of firing conditions:

F = 500 yards

$\dot{F} = a t_f = \dfrac{2}{t_f}\left(\dfrac{1}{2} a t_f^2\right) = \dfrac{2F}{t_f}$

t_f = 1.5 seconds

target speed = Mach 0.95

interceptor speed = Mach 1.9

altitude = 30,000 feet

$\dot{\phi}$ = 0.2 radian per second

The coefficients are plotted against σ. For the particular set of conditions, this angle at firing does not exceed 22°, but for other specific conditions it can assume somewhat larger values. (Consideration of the radome design problem must include the fact that when the true line-of-sight angle is σ degrees, the actual radiation from the antenna passes through areas of the radome at angles which are both greater and less than σ.) Also shown on the graphs of Figure 4-37 are folded scales which give β, the angle between the paths of the interceptor and target. For a tail attack, β is taken as 0°. The range of the target at the time of firing depends on β for any given target speed, interceptor speed, time of flight of the rocket, and distance traveled by the rocket. The target range is thus a double-valued function of σ, and there are two branches of C_3 and C_5. Since $\dot{R}$ is also double-valued, C_1 also has two branches.

It is interesting to note that in an electrically symmetric system (that is, a system with a circularly symmetric radome and circular polarization), $\Delta\zeta$, $\partial(\Delta\zeta)/\partial\zeta$, $\partial(\Delta\zeta)/\partial\sigma$, and $\partial(\Delta\sigma)/\partial\zeta$ all vanish, so that only $\Delta\sigma$ and $\partial(\Delta\sigma)/\partial\sigma$ are significant.

On the basis of these data, the order of magnitude of the tolerances which will eventually be set upon radome error can be estimated. When the effect of smoothing the angular data is taken into account, the derivatives turn out to be most conveniently specified in terms of a maximum allowable excursion of the radome errors in some interval. When the derivatives are so specified, the order of magnitude of the allowable radome tolerances, for the region σ less than 30° might be

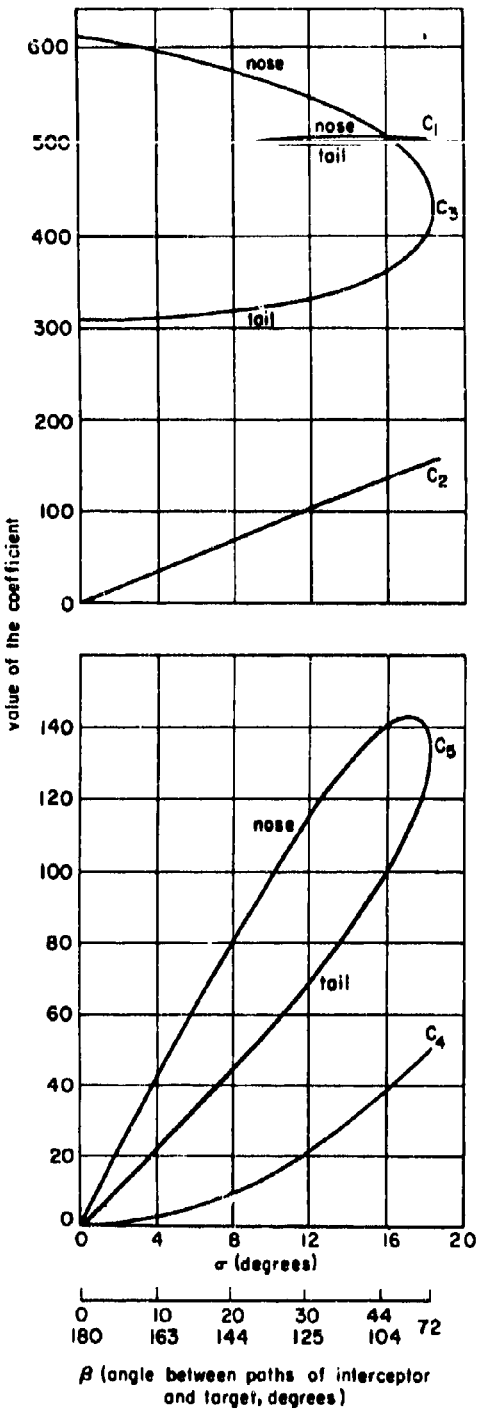


Figure 4-37. Coefficients of Miss Equation

$\Delta\sigma$ { less than 2 mils; may not vary more than 1 mil in any 4° interval of σ; may not vary more than 0.5 mil in any 10° interval of ζ

$\Delta\zeta$ { may not vary more than 0.5 mil in any 4° interval of σ; may not vary more than 0.7 mil in any 10° interval of ζ

4-31. Effect of Radome Errors on Missile Guidance

Of the various types of missiles the homing missiles have the most stringent radome requirements. High boresighting accuracy and low loss characteristics must be provided so that errors will not be introduced into target positional information. At the same time aerodynamic and material strength considerations must be fulfilled so that the missile can fly at supersonic speeds. As described in paragraph 4-10, there are three types of homing missiles: active seekers, semiactive seekers, and passive seekers. Since at the present state of the art semiactive seekers seem to offer the optimum combination of desirable factors, the discussion of the effect of radome error on missile guidance is concerned with this type of missile. Specific reference is made to the Hughes Falcon for the analysis.[28]

4-32. Falcon Navigation

The antenna of the Falcon missile consists of a conically scanning paraboloid mounted on the rotor of a precessed gyroscope. When the antenna and gyroscope are enclosed in a radome, the apparent line-of-sight does not coincide with the true line-of-sight. The angle η_r between the apparent and true lines-of-sight (Figures 4-38 and 4-39) is called the radome error angle, or simply the radome error. The components of this angle in and perpendicular to the plane of offset frequently are referred to as the in-plane error and the crosstalk error, respectively. As was noted in Section D, the radome error is not a property of the radome alone, but rather depends on the complex electromagnetic interactions of the complete radome-antenna missile body system.

If the radome and missile structure are carefully constructed and are axially symmetric, and if the receiving antenna and illuminating signal are circularly polarized, the radome error should have axial symmetry and thus

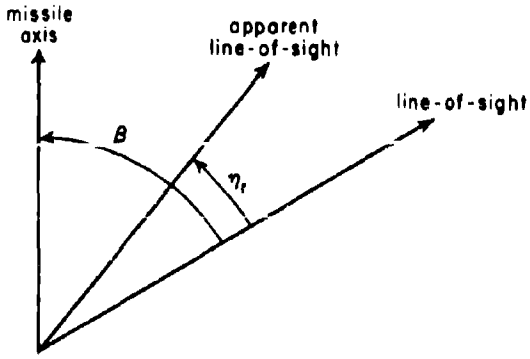


Figure 4-38. Radome Error Angular Relationship in Two Dimensional (Simplified) Case

should not be a function of roll attitude. If the polarization of either the transmitter or receiver is not circular, the radome error in general will not show axial symmetry.

The Falcon seeker is sensitive not to the absolute orientation of the line-of-sight in space, but rather to the rate at which this orientation is changing. Correspondingly, it is not primarily the radome error itself which affects navigation but rather the rate of change of the radome error with change in orientation of the line-of-sight relative to missile coordinates. Figure 4-38 indicates the angles of interest for the simplified nonrolling missile navigating in a plane, and the radome error derivative k is defined as

$$k = d\eta_r/d\beta \qquad (4\text{-}46)$$

The actual three-dimensional case is shown in Figure 4-39. The definitions of the angles β and η_r are the same as those in the simplified case but need not be coplanar. Four component derivatives analogous to the k of Equation (4-46) are required to characterize the radome error completely; it is convenient to define these derivatives with respect to the missile control coordinates. Since the angle η_r is small, it may be resolved into yaw and pitch components, η_{r1} and η_{r2}, respectively. An infinitesimal change in the line-of-sight can also be described by yaw and pitch components, $d\beta_1$ and $d\beta_2$, respectively. The four radome error derivatives are:

$$\begin{aligned} k_1 &= \partial\eta_{r1}/\partial\beta_1 \\ k_{12} &= \partial\eta_{r2}/\partial\beta_1 \\ k_2 &= \partial\eta_{r2}/\partial\beta_2 \\ k_{21} &= \partial\eta_{r1}/\partial\beta_2 \end{aligned} \qquad (4\text{-}47)$$

Derivatives k_{12} and k_{21} represent a cross-connection between the missile control channels, motion of the target in one of the missile coordinates causing an apparent motion in the other coordinate as well if these cross-derivatives have finite values.

4-33. Appearance of Radome Error in Falcon Transfer Function

The basic linearized proportional navigation guidance system of the Falcon missile, in the absence of radome error and under the idealization of a single-channel nonrolling missile navigating in a plane, is indicated by the servo diagram of Figure 4-40. A flipper deflection δ, proportional to the measure line-of-sight rotation rate $\dot{\sigma}$, gives rise to an angle of attack α and thus to a rotation rate $\dot{\gamma}$ of the missile velocity vector. This sequence in turn reacts on $\dot{\sigma}$ in accordance with the trajectory geometry equation. Other symbols used in Figure 4-40 are defined as follows:

p = d/dt (also represented by a dot)

Q = static value of α/δ

r = ratio of closing velocity to component of missile velocity along line-of-sight

T = time of flight remaining to collision

Z_m = missile control transfer function denominator (static value unity)

Z_0 = aerodynamic transfer function denominator, $(\rho^2/\omega_0^2 + 2\zeta_0\rho/\omega_0 + 1)$

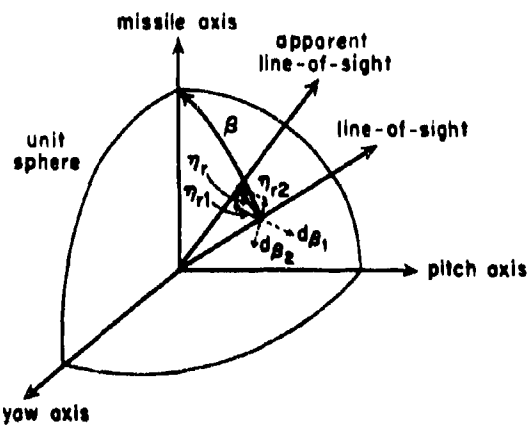


Figure 4-39. Radome Error Angular Relationship in Three Dimensional Case

ω_0 = natural weathercock frequency

ζ_0 = aerodynamic damping constant

λ_0 = navigation constant (static value $\dot{\gamma}/\dot{\sigma}$) in absence of radome error

τ_s = turning time constant

It can be seen from Figure 4-40 that the trajectory represents a feedback loop between the output and input of the missile transfer function. When the effects of radome error are considered, the servo diagram is modified. The apparent line-of-sight and the true line-of-sight now differ by the boresight error, as illustrated in Figure 4-38. To linearize the problem, the radome error derivative k, as defined by Equation (4-46), is assumed independent of the offset angle of the line-of-sight from the missile axis. The appropriate equations are

$$\dot{\sigma}_r = \dot{\sigma} + \dot{\eta}_r \qquad (4\text{-}48)$$

$$\dot{\eta}_r = k\dot{\beta} = k(\dot{\theta} - \dot{\sigma}) = k(\dot{\alpha} + \dot{\gamma} - \dot{\sigma}) \qquad (4\text{-}49)$$

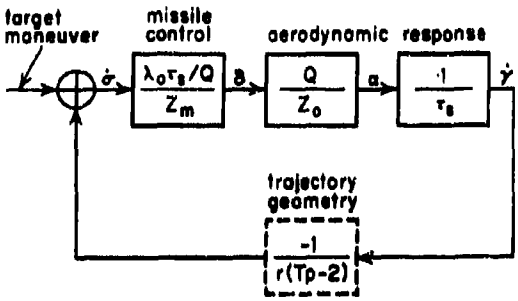


Figure 4-40. Two Dimensional Falcon Guidance System

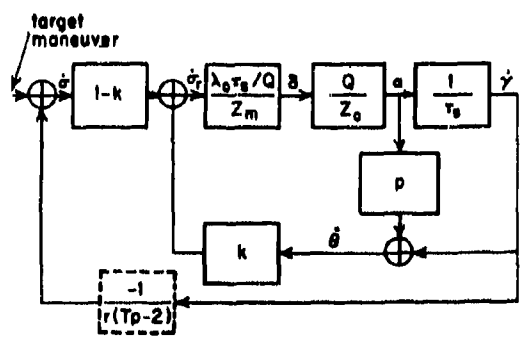


Figure 4-41. Two Dimensional Guidance System With Radome Error

where θ = rate of rotation of missile axis.

As is shown in the resulting servo diagram of Figure 4-41, the radome error introduces a second feedback loop between the output and input of the missile transfer function.

With all the coefficients in the inner loop considered constant, it is possible to replace this loop in the servo diagram by an equivalent straight-through transfer function, as indicated in Figure 4-42, where Z_s represents the operator $(\tau_s p + 1)$. Comparison with Figure 4-40 shows that the overall effect of the assumed radome error is to change the missile transfer function Y (including aerodynamics) from

$$Y_0 = \lambda_0 / Z_m Z_0 \qquad (4\text{-}50)$$

into

$$Y = \frac{(1 - k)\lambda_0}{Z_m Z_0 - k\lambda_0 Z_s} \qquad (4\text{-}51)$$

Since the static values of Z_m, Z_0, and Z_s are all unity, it is seen from Equation (4-51) that λ, the effective navigation constant, is given by

$$\lambda = \frac{1 - k}{1 - k\lambda_0}\lambda_0 \qquad (4\text{-}52)$$

If the analysis is extended to the actual three-dimensional case, Equations (4-48) and (4-49) become

$$\dot{\sigma}_{r1} = \dot{\sigma}_1 + \dot{\eta}_{r1} = \dot{\sigma}_1 + k_1\dot{\beta}_1 + k_{21}\dot{\beta}_2 \qquad (4\text{-}53)$$

$$\dot{\sigma}_{r2} = \dot{\sigma}_2 + \dot{\eta}_{r2} = \dot{\sigma}_2 + k_2\dot{\beta}_2 + k_{12}\dot{\beta}_1 \qquad (4\text{-}54)$$

where the subscripts 1 and 2 designate the two missile control channels in Figure 4-39. The resulting complete servo diagram is given in Figure 4-43 with Y_0 defined by Equation (4-50).

4-34. Radome Error and Missile Stability

A very serious effect that can arise from radome error is instability of the missile tra-

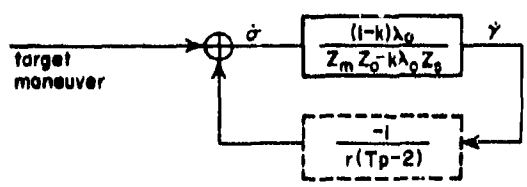


Figure 4-42. Equivalent Servo Diagram with Radome Error

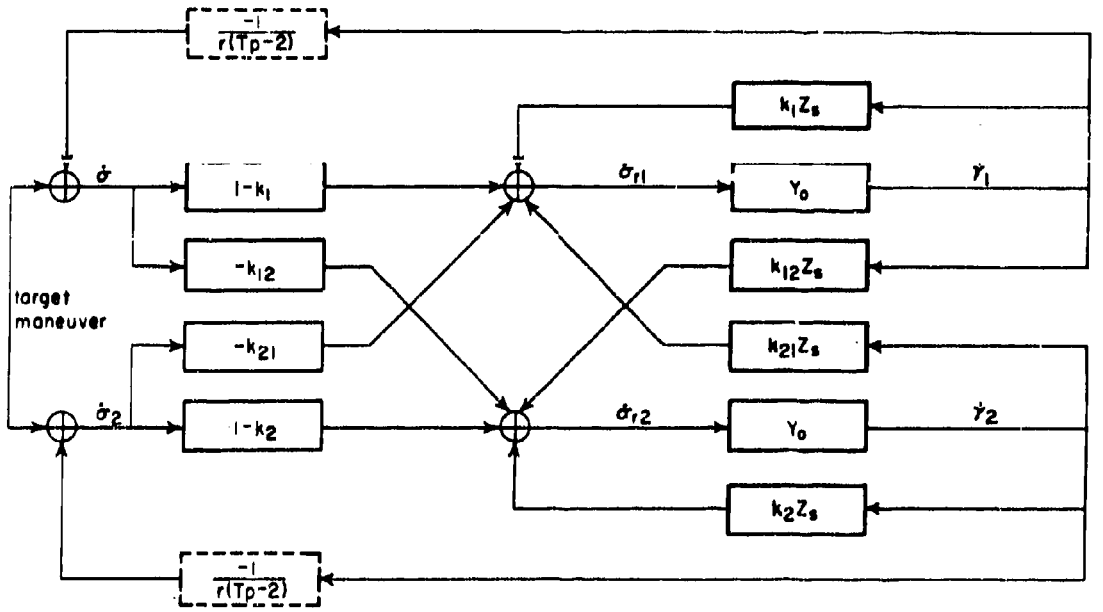


Figure 4-43. Complete Falcon Guidance System with Total Radome Error

jectory. An unstable missile trajectory does not approach a collision course but, instead, oscillates with increasing amplitude about such a course. This oscillation may build up to a point at which it overloads the control system, causing loss of control of the missile.

The two-dimensional case is considered first. The stability of the trajectory is investigated by neglecting the trajectory geometry feedback. If the remaining transfer function Y is unstable, the trajectory is classed as long-range unstable.

For Y to be stable, it is necessary that the static value λ be positive and that all the roots of the characteristic equation

$$Z_m Z_0 - k\lambda_0 Z_s = 0 \qquad (4\text{-}55)$$

have negative real parts. Since λ_0 is always greater than unity, the first condition applied to Equation (4-52) requires either that $k\lambda_0$ be less than unity or that k be greater than unity. Only the first alternative is found to be of practical significance. It is found that the transfer function Y becomes unstable if the parameter $k\lambda_0$ falls outside a critical range of values (the quantity $k\lambda_0$ is the d-c loop gain of the radome error feedback loop shown in Figure 4-41). Apart from the general requirement that $k\lambda_0$ be less than unity, the limits of this critical range depend upon the numerical constants of the system. If $k\lambda_0$ is neglected, with respect to unity, an approximate expression for the radome error stability limits is the following:

$$\left[1 - \tau_1\tau_2\omega^2 + j\omega(\tau_1 + \tau_2)\right]\left(1 - \frac{\omega^2}{\omega_0^2} + j2\zeta_0\omega/\omega_0\right) - j\omega k\lambda_0\tau_s \approx 0 \qquad (4\text{-}56)$$

where τ_1 and τ_2 represent roughly equal time lags. If the frequencies ω_0 and $(\tau_1\,\tau_2)^{-1/2}$ are well separated, as usually is the case, then the real part of Equation (4-56) is satisfied approximately at each of these two frequencies. Approximate stability limits for $k\lambda_0$ may be found, therefore, by a solution of the imaginary part of Equation (4-56) at these two frequencies, respectively.

Positive Radome Error Limit. If ω_0 is much larger than $\omega_1 = (\tau_1\,\tau_2)^{-1/2}$, then in the neighborhood of the latter frequency the radome stability limit is approximated by

$$k\lambda_0 = \frac{\tau_1 + \tau_2}{\tau_s} \qquad (4\text{-}57)$$

where the low frequency damping constant is set equal to zero. Curves indicating the accuracy of this approximate expression are given in Figure 4-44. It follows from Equation (4-57) and from the additional requirement that be positive that the long-range stability restrictions which apply to positive radome error derivatives are

(1) $k\lambda_0$ must be less than 1 when

$$\tau_s < \tau_1 + \tau_2 \qquad (4\text{-}58)$$

(2) $k\lambda_0$ must be less than $\frac{\tau_1 + \tau_2}{\tau_s}$ when

$$\tau_s > \tau_1 + \tau_2 \qquad (4\text{-}59)$$

The first limit is exact; the second is approximate. The first limit is applicable to the missile at low altitudes and the second, at high altitudes. When the first stability limit is exceeded, the instability is at zero frequency, and the missile turns steadily away from a collision course instead of toward one. When the second stability limit is exceeded, the missile trajectory oscillates with increasing amplitude at a low frequency whose period is determined primarily by the time constants τ_1 and τ_2.

The aerodynamic parameter τ_s is a function of air density and increases at higher altitudes. Correspondingly, the stability limit on positive radome error derivative becomes increasingly tight at higher altitudes.

Negative Radome Error Limit. Again, if ω_0 is much larger than $(\tau_1\ \tau_2)^{-1/2}$, then in the neighborhood of ω_0 the requirement that the high frequency damping constant ζ_0 remain positive yields, as the long-range stability restriction on negative radome error derivative,

$k\lambda_0$ must be greater than

$$\frac{-2\zeta_0\omega_0\tau_1\tau_2}{\tau_s} \qquad (4\text{-}60)$$

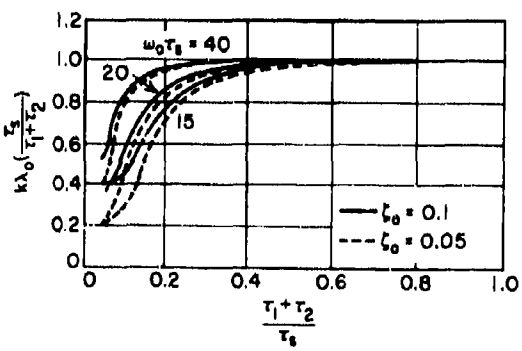


Figure 4-44. Ratio of Exact To Approximate Positive $k\lambda_0$ Stability Limit for $\tau_1 = \tau_2$

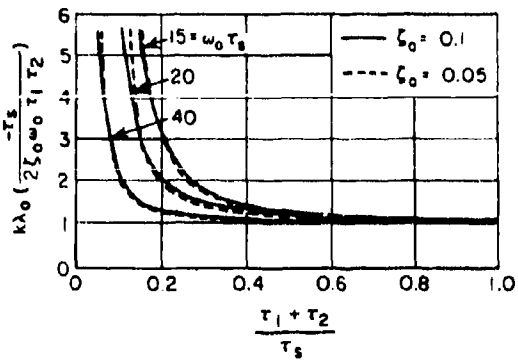


Figure 4-45. Ratio of Exact To Approximate Negative $k\lambda_0$ Stability Limit for $\tau_1 = \tau_2$

Curves indicating the accuracy of this approximate expression are presented in Figure 4-45.

If the radome error derivative becomes more negative than the above limit, the missile becomes unstable at approximately the weathercock frequency, and the weathercock oscillations increase with time instead of dying out.

The aerodynamic parameter ratio $\zeta_0\omega_0/\tau_s$ decreases rapidly with increasing altitude, and the stability limit on negative radome error derivative becomes exceedingly small (on the order of -0.01) at maximum altitude.

Analytical and simulator studies have shown that the trajectory feedback tends to increase the effects of positive radome error derivative and to decrease the effects of negative radome error derivative. The simulator studies have also shown that, if the positive radome error derivative is as large as two-thirds of the limiting value for long-range stability, the miss may be several times larger than with no radome error, even in the absence of noise. On the other hand, the negative radome error derivative can be equal to or slightly outside the long-range stability limit, and with no input noise the miss remains relatively small.

The foregoing stability analysis applies to each of the two missile control channels individually. The radome error cross-derivatives k_{1_2} and k_{2_1} also affect the stability of the actual three-dimensional trajectory, because of the small closed loop which they introduce into the overall system. Similar analysis, with some extensions, shows that the amount of cross-coupling which can be permitted depends upon the amount of direct radome error deriv-

ative which is present, and the true stability limit is a joint one involving k and $\sqrt{k_{1_2} k_{2_1}}$. If there is any cross-coupling present, a smaller amount of direct radome error derivative is required to cause instability. Larger amounts of cross-coupling can cause instability even if the direct radome error derivative is zero. It should be noted, however, that the effect of radome errors on guidance accuracy becomes pronounced long before the system becomes unstable. A typical curve of guidance miss due to scintillation noise as a function of positive in-plane error slope alone is shown in Figure 4-46.

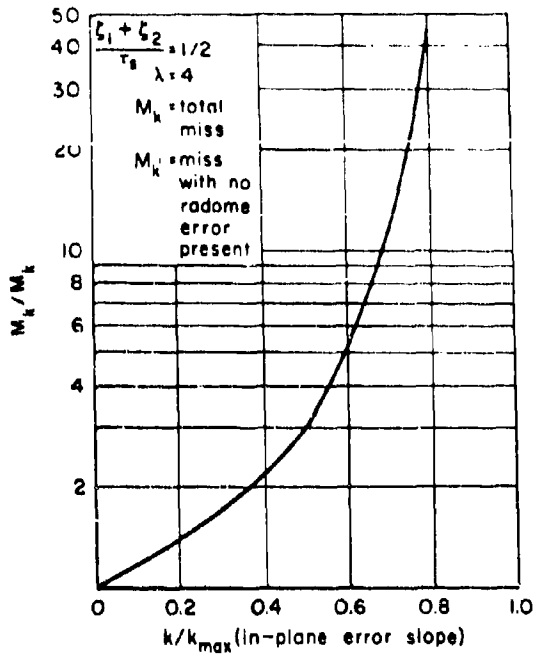


Figure 4-46. Increase in Miss Due to Positive In-Plane Error Slope When Guidance System is Excited by Scintillation

4-35. Radome Error and Navigation Constant

A quantity of fundamental importance in a proportional navigation system is the navigation constant λ, defined as the steady-state ratio of the rate of turn of the missile to the rate of rotation of the line-of-sight ($\dot{\gamma} = \lambda\dot{\sigma}$). This zero frequency gain of the missile transfer function Y is affected by radome error. Accordingly then, the navigation constant in the presence of radome error λ is related to the navigation constant in the absence of radome error λ_0 by

$$\lambda = \frac{1 - k}{1 - k\lambda_0} \lambda_0 \qquad (4\text{-}61)$$

As can be seen, the navigation constant becomes infinite when $k = 1/\lambda_0$. This condition corresponds to the instability at zero frequency mentioned previously. If the radome error derivative is negative, a maximum limit is set on the available λ; even if λ_0 is infinite, λ is equal only to $-(1 - k)/k$.

With most radomes, the radome error derivative, k, is a function of the antenna offset angle. As a result, the navigation constant of a missile varies throughout its flight and may depart significantly from the optimum or desired value. To maintain a reasonable probability of kill, this variation of navigation constant cannot be allowed to be excessively large — a restriction which constitutes one of the most important limitations on radome error for the tactical missile.

4-36. Radome Error and Response to Noise

It has been shown that a finite radome error derivative changes the transfer function relating the line-of-sight angle σ to the flight-path angle γ. Even when the radome error derivative is of insufficient magnitude to produce instability, it still may produce marked changes in the response of the missile to scintillation noise.

Simulator studies of missile trajectories have shown that with negative radome error derivatives as large as the stability limit, the rms miss due to scintillation noise is not significantly altered, even though the rms lateral acceleration is greatly increased. However, the limit on positive radome error derivative imposed by noise is much tighter than the limit imposed by missile instability. If the radome is not to cause excessive decrease in the probability of kill when considerable amplitude scintillation noise is present, the positive radome error derivative generally must be less than one-fifth the limit set by stability considerations.

4-37. Secondary Factors in Radome Error Analysis

The above discussion has introduced a brief analysis of some of the more important factors influencing radome error. There are several other factors which will not be discussed in detail but must be brought to the reader's attention.

In addition to two principal time lags, there are usually several other smaller time constants involved. Such time lags tend to reduce the missile response to noise. Because of the additional phase shift which they introduce, however, these small time lags might make the radome error stability limits even tighter.

Another influencing factor is the polarization of the incoming signal. This factor can affect the missile navigation in several ways, depending on what combination of signal polarization, receiving antenna polarization, and roll control is used. The effect of polarization on radome error is discussed in detail in paragraphs 4-23 through 4-29.

4-38. Nonlinear Radome Error Analysis

In the analyses which have been summarized in the preceding sections, it has been shown that a radome error derivative which falls outside a certain range of values leads to an unstable trajectory. These analyses dealt with a linearized version of the problem. All parameters were assumed to be constant, and the radome error derivative k was assumed to be independent of the offset angle β of the line-of-sight from the missile axis. It is possible to obtain useful results by considering k as a function of β, which is the case in the physical problem. Though at the present time such analysis is not conclusive or complete, nonlinear radome error analysis appears to promise some relaxing of the limit on positive radome error derivative. It seems possible that the positive radome error derivative limit can be relaxed over a limited range of angles.

SECTION F. PREDICTION OF RADOME ERRORS

4-39. Radome Size and General Approaches

For convenience of discussion in radome error prediction techniques, radomes are divided into two general groups: large radomes and small radomes. The large radome is characterized by an antenna aperture of more than 10 wavelengths in diameter, a circle of clearance between antenna and radome on the order of one or more wavelengths, and small wall curvatures compared with wavelength. All other radomes are considered to be small. The line of demarcation between the two general groups is rather nebulous, and, undoubtedly, radomes exist that could fall into either group. As far as prediction methods are concerned, it is advisable to classify these radomes as small.

Large radomes are associated with small boresight errors, usually no greater than a few mils in the nose area for a well-designed radome. Most large systems are designed to transmit fairly narrow beams which are highly directive, and it is usually assumed that the antenna does not see much of the radome area at any one look angle. For these reasons the angles of incidence at which the energy reaches the wall of a large radome do not vary appreciably, except in the nose area, and errors that might be introduced are low. The distance between antenna aperture and radome wall in the large systems acts as another error-minimizing factor: any radome is a scatterer (secondary radiation source) in the system, but the perturbations caused by a large radome in the transmitted field will be somewhat less than those of a small radome for two reasons: (1) The separation between radome and antenna aperture in a large system allows for a better defined field, and (2) the energy region adjacent to the antenna is very sensitive to any obstacles, but the farther away the radome is, the less of an obstacle it appears to be.

In large antenna-radome systems, the variation in boresight error in supposedly similar radomes, due for example to a lack of concentricity, is frequently of the same magnitude as the error itself. The variation makes difficult the correlation of theory and experiment in any error-prediction method. Most current prediction techniques are directed toward the calculation of boresight error curves by means of geometrical-optics methods or modifications of these methods. For large radomes simple ray tracing is frequently used and except in the nose area, often predicts errors with sufficient accuracy to recommend its use alone. Another technique that has been found very useful in large radome applications is based on an angular-magnification method and was originally applied to lens design. The technique makes possible rapid beam-shift calculations for a large section of the radome and requires only the use of a slide rule or desk calculator. For the parts of the large radome that have radii of curvature comparable to wavelength (chiefly the nose portion), phase-retardation methods must be employed.

Small radomes inherently have fairly large boresight errors for several reasons. The radii of the wall curvatures are the same order of magnitude as the wavelength in the small an-

tenna-radome systems, and the angles of incidence for any look angle will vary widely. The antenna may see the entire side of the radome at one look angle. The comparatively short distance from radome wall to antenna aperture makes the radome appear to be a large obstacle in the radiated field inside the radome. The various scattering effects (reflections, images, etc.) will introduce perturbations which make the field inside the radome extremely complex. Consequently, it is extremely difficult, if not impossible, to analyze exactly any changes in that field that may occur as the field traverses the radome wall. As was mentioned in Section D, radome errors generally increase in size as the antenna aperture decreases in diameter. Figure 4-47 shows the comparative positions of antenna aperture and radome for a typical small system (a) and for a typical large system (b). In the small system, an aperture of 5 inches diameter and a radome length of 10 inches are assumed. With a wavelength of, say, 1.3 inches, a maximum of only 7.7 wavelengths separate aperture from radome. In contrast, the large system has an assumed aperture diameter of 20 inches and a radome length of 72 inches. With the 1.3-inch wavelength there would be a maximum of about 55 wavelengths separating the two scatterers in the system. Furthermore, in a small radome-antenna system the small separation (antenna and side of radome) may be on the order of a small fraction of a wavelength, whereas for a large radome-antenna system the separation is a wavelength or so. The possible potential effect of the small radome on the field contained within it is appreciably greater than that of the large radome.

There are a number of approaches towards accurate prediction of boresight errors in the small radome-antenna systems; others are being developed. None of the several methods has as yet produced a completely general method of approach, primarily because the fields inside the small radome have not yet been accurately analyzed. Because of the complexity of the mathematics involved, the standard method of approach can only involve the determination of the fields by some approximation. A few of the prediction techniques for small radomes will be discussed briefly to illustrate the current approaches to the problem.

In general, the following statements can be made about prediction techniques:[29]

a. For the large radome, there are at least three approaches that yield accurate prediction of boresight error.

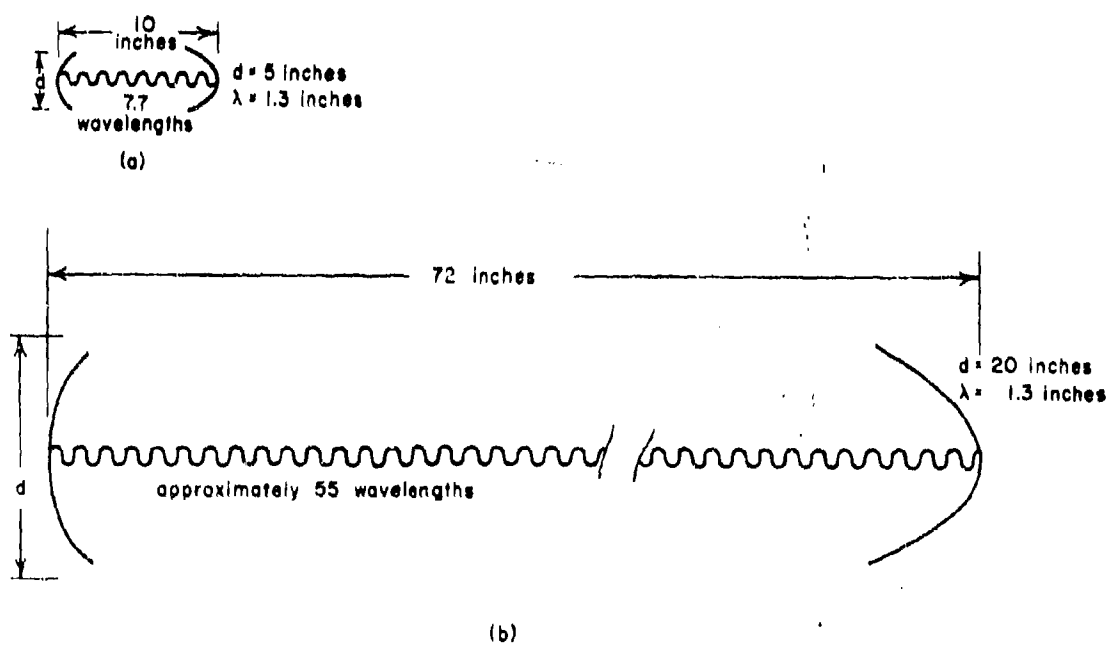


Figure 4-47. Comparative Importance of Radome in (a) Small and (b) Large Radome-Antenna Systems

b. For the small radome, no one method has consistently predicted boresight error accurately, although several methods have met with limited success.

4-40. Geometrical Optics (Ray Tracing)

The use of geometrical optics in the design of radomes has been practiced by every radome designer and manufacturer of radomes at one time or another. Though more sophisticated procedures are required for many types of radomes, ray-geometry and cylindrical-symmetry applications should not be overlooked. Many times these simplified methods are of sufficient accuracy to turn out the required radome. The techniques can be used for an approximate prediction of average beam shift caused by a radome[30] and are particularly useful with large radomes.

In the most simple methods of ray tracing, a central beam is assumed to originate as a plane wave from the antenna aperture. The ray is traced through the radome wall, and the deviation introduced by the radome is calculated. The analysis generally makes use of a geometrical model. Parallel surfaces can be shown to have a common normal at corresponding points and to have simply related radii of curvature. If arbitrary cylinders are replaced by their osculating circular cylinders, a simple formula can be obtained for the ray deviation introduced by curvature. An approximation for small curvature and one for a dielectric constant near unity can be made. It can also be shown that the beam deviation will increase with the dielectric constant for constant thickness but will increase and then decrease when the thickness is half-wave.

It is first assumed that the radome is part of a cylinder (not necessarily circular) and that

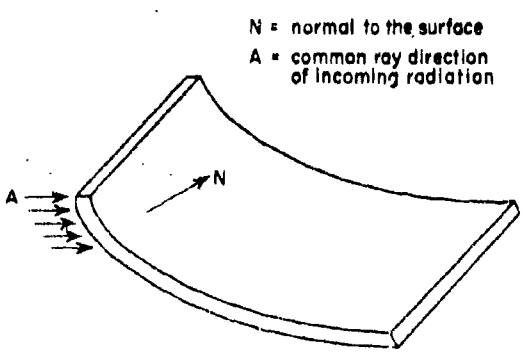


Figure 4-48. Cylindrical Radome

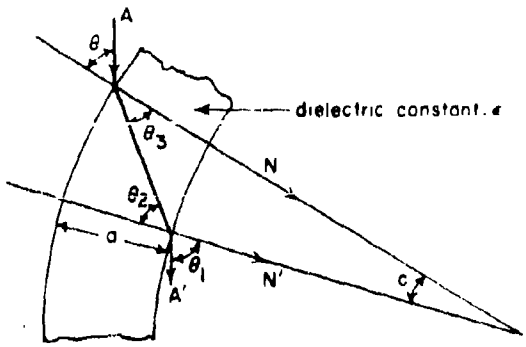


Figure 4-49. Cross Section of Radome Perpendicular To Elements of a Cylinder

rays represent the electromagnetic energy. The rays are parallel to one another and perpendicular to the elements of the cylindrical wall (Figure 4-48). Sufficient symmetry is assumed so that sideways deviation of the beam is neglected as far as ray geometry alone is concerned. The common ray direction is denoted by a unit vector A, and the normal to the surface by N. The vector A is fixed, while N changes from point to point on the surface. At a given point a plane can be passed through A and N intersecting the surface in two plane curves. Except for terms $0(a^2)$ in the thickness (a), the plane curves may be replaced by their circles of curvature. Figure 4-49 represents the situation obtained when circles are considered. The problem is reduced to two dimensions and all terms of $(a/r)^2$, where r is the radius of curvature, are neglected. By Snell's Law and with reference to Figure 4-49,

$$\frac{\sin \theta_1}{\sin \theta_2} = \frac{\sin \theta}{\sin \theta_3} = \sqrt{\epsilon} \qquad (4\text{-}62)$$

and the law of sines gives

$$\frac{\sin \theta_3}{r - a} = \frac{\sin \theta_2}{r} \qquad (4\text{-}63)$$

Equations (4-62) and (4-63) give

$$\sin \theta = 1 - \frac{a}{r} \sin \theta_1 \qquad (4\text{-}64)$$

showing that the relation of θ_1 to θ does not involve the dielectric constant ϵ.

Since $c = \theta_2 - \theta_3$, Equation (4-62) can be used to show that

$$\epsilon \sin c = \sin \theta_1 (\epsilon - \sin^2 \theta)^{1/2} - \sin \theta (\epsilon - \sin^2 \theta_1)^{1/2} \quad (4\text{-}65)$$

Now the beam deviation δ is

$$\delta = \theta_1 - (\theta + c) \quad (4\text{-}66)$$

By proper simplifying approximations when small curvatures are considered such that

$$a/r \tan^2 \theta << 1 \quad (4\text{-}67)$$

the deviation δ is obtained from Equations (4-64), (4-65), and (4-66):

$$\delta \cong \frac{a}{r} (\sin \theta) \left[\sec \theta - (\epsilon - \sin^2 \theta) \right]^{-1/2} \quad (4\text{-}68)$$

This relationship is plotted in Figure 4-50.

The curves of Figure 4-50 indicate that the beam deviation increases with the dielectric constant, other things being equal, and according to Equation (4-68), the limiting value is $(a/r) \tan \theta$. If a half-wave wall construction is used for a given angle of incidence,

$$a = (n\lambda/2) (\epsilon - \sin^2 \theta)^{-1/2} \quad (n = 1,2,3, \ldots) \quad (4\text{-}69)$$

As the dielectric constant increases, the wall thickness decreases, and it would appear that the beam shift would decrease too, so that

$$\delta \cong \left(\frac{n\lambda}{2r}\right) \sin \theta (\epsilon - \sin^2 \theta)^{-1/2} \left[\sec \theta - (\epsilon - \sin^2 \theta)^{-1/2} \right] \quad (4\text{-}70)$$

Equation (4-70) is zero for $\epsilon = 1$ and approaches zero for $\epsilon \to \infty$. Since the expression is positive, it must have one maximum, which is found to occur at

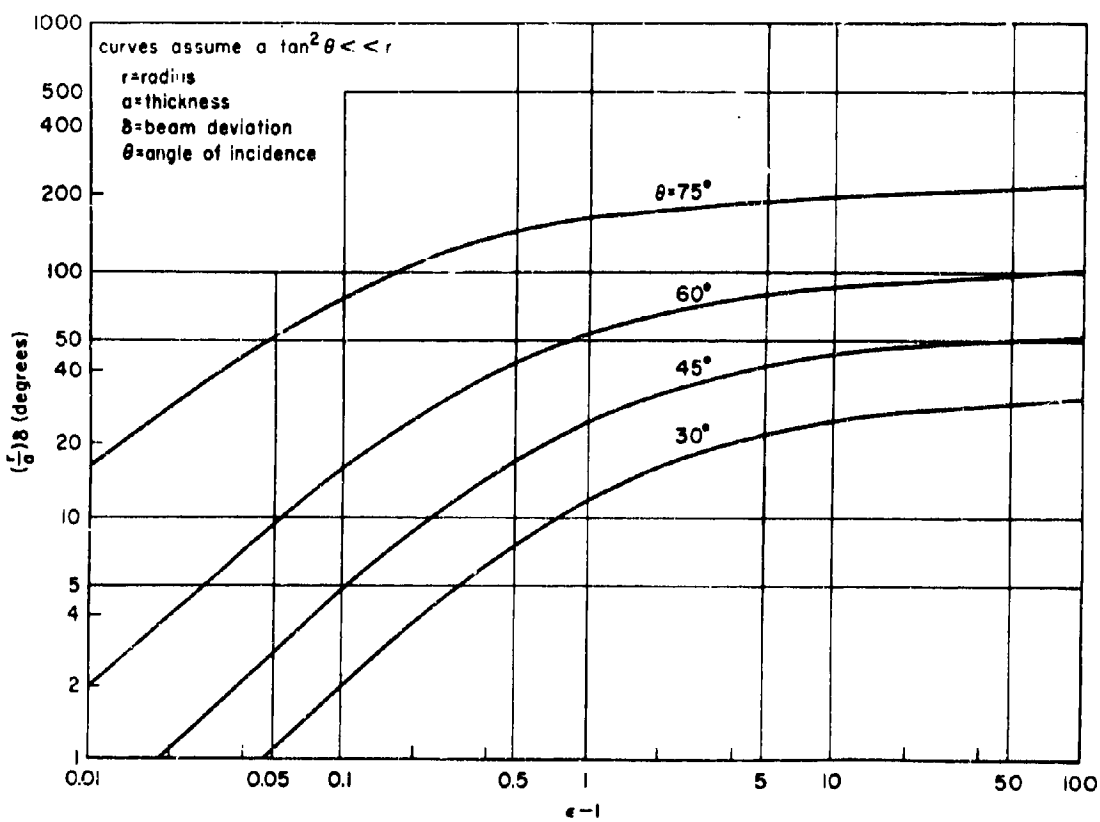


Figure 4-50. Approximate Beam Deviation for Concentric Circles

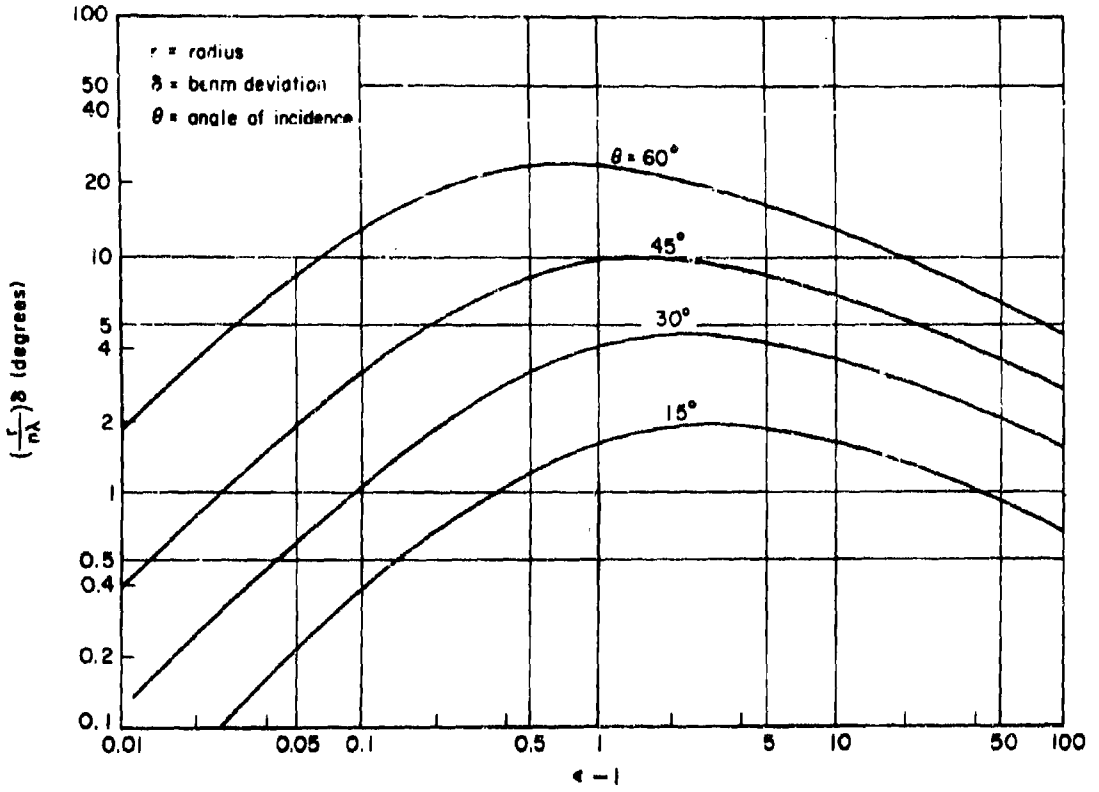


Figure 4-51. Approximate Beam Shift for a Radome n Half-Waves Thick

$$\epsilon = 4 - 3 \sin^2 \theta \qquad (4\text{-}71)$$

and to have the value

$$\delta_{max} = \frac{n\lambda}{8r} \tan \theta \sec \theta \qquad (4\text{-}72)$$

Thus, the reduction in thickness given by Equation (4-69) is sometimes sufficient to offset the increased beam shift predicted by Equation (4-68). It should also be noted that under the present considerations the worst possible ϵ for a solid half-wave wall occurs between 1 and 4. Graphical presentation is given in Figure 4-51.

The various rays must be combined after transmission to give a sort of "average deviation." For small deviations the angle is nearly equal to the component of the error vector A' - A, as shown in Figure 4-52. By Equation (4-68) it can be seen that the shift of each ray is toward the normal of the surface at the point of observation. The average shift should then be in a direction away from the radome apex, and this prediction is found to be true. The average beam deviation of radomes with several layers, as in sandwich radomes, can be predicted by repeated use of these relations.

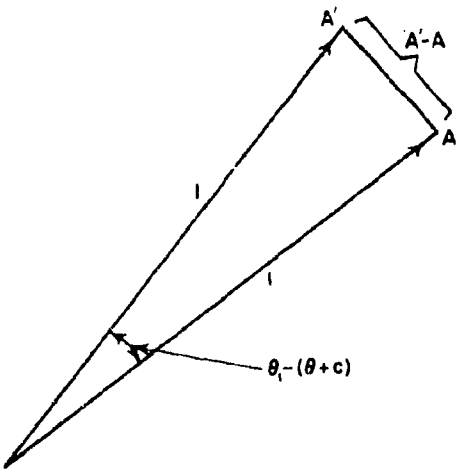


Figure 4-52. Error Vector

The chief recommendation for the use of cylindrical symmetry and ray geometry is the simplicity of the techniques. They do, however, have shortcomings: radomes encountered in practice are certainly not cylindrical, and the methods fail to account for crosstalk deviation. The latter failure is inherent in any scalar theory that is bound to predict zero crosstalk for every system that has as much symmetry as those in use. A definitive theory can be found only by the inclusion of polarization in the analysis.

4-41. Modifications of Geometrical Optics

The calculation of ray deviations through a radome may be regarded as a problem of determining the optical angular magnification of the radome. A prediction technique that follows this type of approach is the M' method. The in-plane error of a given radome can be calculated and is a zeroth approximation to the true error. From work done at the Dalmo-Victor Company the technique can be briefly outlined.[29]

4-42. The M' Method

The radome is considered as a lens of weak magnification and the angles of incidence are not assumed to be large. Layout of the radome for the M' method is shown in Figure 4-53. The in-plane error is calculated for each look angle, and an error curve is plotted from the data. For each look angle a family of general rays is drawn so that each ray is parallel with the axis of the reflector or antenna aperture. At the point at which each ray strikes the inner surface of the radome a tangential sphere is constructed with the same radius of curvature as the radome at that point. An optical axis is drawn parallel with the radome axis from the center of the sphere to its edge. The distance along the optical axis from the center of the tangential sphere to the intersection of the optical axis with the tangential sphere is termed U and is a parameter in the prediction equation. The distance U will be different for each ray at each look angle, since the tangential spheres will all have different centers.

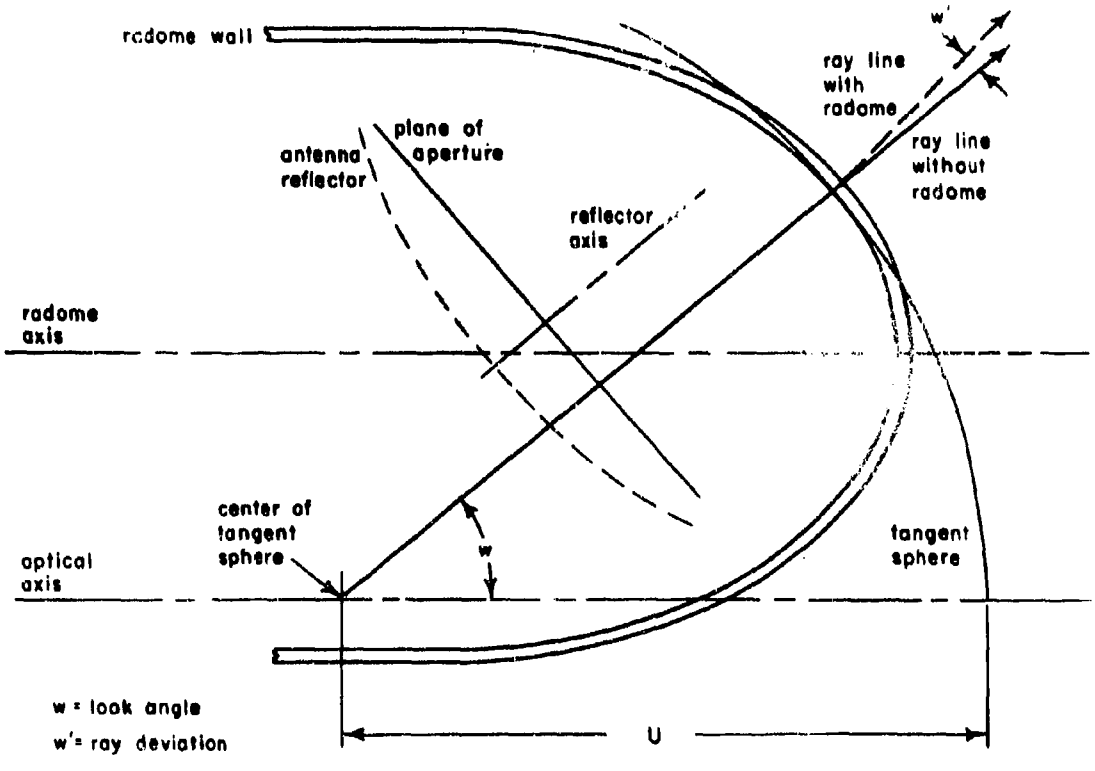


Figure 4–53. Radome Layout for M' Error Prediction Method

The ray deviation ($\Delta w'$) can be expressed as

$$\Delta w' = (M' - 1)w \qquad (4\text{-}73)$$

where

$$M' = \left(\frac{1}{1 - U D_e}\right)\left(\frac{1}{1 - \left(\frac{t}{n}\right)D_1}\right) \qquad (4\text{-}74)$$

$\Delta w'$ = ray deviation or in-plane error

w = look angle

U = distance along the optical axis between the point of intersection of each ray with its optical axis and the intersection of that optical axis with the tangential sphere for the ray

$$D_e = \frac{D_1}{1 - \left(\frac{t}{n}\right) D_1} + D_2$$

D_1 = dioptric power of outer surface of radome

D_2 = dioptric power of inner surface of radome

t = thickness of radome

n = index of refraction of radome

The results of a prediction by the M' method of the error introduced into a central ray by a typical large radome are compiled in Table 4-VI with comparative data obtained by a geometrical-optics ray tracing method. Both methods predict errors less than 1 mil; the measured in-plane error of the radome was also less than 1 mil for look angles greater than 10°.

*Table 4-VI. Comparison of M' and Geometrical Optics Ray Tracing Methods for Central Ray with Typical Large Radome**

Look Angle, w (degrees)	Predicted Beam Deviation Caused by Radome	
	M' Method (mil)	Geometric Optics (mil)
6.2041	0.0195	0.3022
10	0.0192	0.0833
25	0.0176	0.0429
35	0.0159	0.0281
45	0.0138	0.0184

*Measured in-plane error less than 1 mil for $w \geq 10°$.

The method is quite general and can be extended to cover any type of sandwich radome structure, but more accurate results will be obtained with large radomes than with small ones. Symmetry is assumed in the radome so that the method does not take crosstalk into account. In addition, since polarization is ignored, results are meaningful in magnitude only, not in sign.

4-43. Antenna Modification Method

When a small radome or the nose area of a large radome are to be studied, more refined methods of prediction are required than the optical methods described above. The variation in incidence angles for rays emerging from different parts of the antenna becomes appreciable; so does the change in phase and amplitude suffered by different rays as they traverse the radome. In view of these facts reasonably accurate information cannot be obtained on purely geometrical optics bases. A slightly refined ray-tracing technique appears to be a fairly good approach.[29]

A well collimated perfectly plane wave is assumed to emerge from the antenna with an amplitude variation that follows the theoretical taper of the antenna. Rays perpendicular to the antenna aperture are then traced to the radome surface, and the incidence and polarization angles are noted. Because of the polarization dependence of the transmission coefficients, the rays must be divided into parallel and perpendicular components. Flat panel data and local transmission coefficients are used next in the calculations of the phase and amplitude changes as the rays traverse the wall. After a number of rays originating across the face of the aperture are traced through the radome wall and the changes in amplitude and phase are noted, the radome is removed and the antenna aperture distribution is reconstructed to reflect the effects of the radome. The reconstructed or modified aperture distribution is integrated in the usual manner to yield the far-field patterns. This method is discussed in detail in Chapter 13.

The change in beam parameters in a parabolic beam approximation (that is, angular beamshift, fractional change in beam amplitude, and fractional change in half-power beamwidths) can be calculated by means of a comparison of the theoretical antenna patterns with the patterns obtained from the reconstructed distribution. For conical-scan [illegible] as the calculations must be carried out for the two extreme spin-scan positions for each look angle. The in-plane error or the change in

crossover point is obtained by use of the formula derived by the Princeton Group. The formula was improved by Barker and Lengyel[31] by matching the beam shape at the crossover point. In reduced form, the expression is

$$\Delta = \frac{\theta_0}{3}(\alpha_2 - \alpha_1) - \frac{\theta_0}{2}(\beta_2 - \beta_1) + \frac{1}{2}(\delta_1 + \delta_2) \qquad (4\text{-}75)$$

where $2\theta_0$ = half-power beamwidth

β = fractional increase in width of beam at half power

δ = shift of the maximum in radians (or degrees)

α = fractional change in power at a lobe maximum; subscripts 1 and 2 refer to opposite positions of the conical scan

4-44. External-Equivalent-Aperture Method

In the antenna-modification method the direction of energy travel through the radome was arbitrarily assumed. Furthermore no account was taken of reflections inside the radome — the modified aperture distribution was obtained from a single transmission coefficient, for each ray. Further refinements in ray-tracing techniques have been used which consider these and other problems of the near-field distribution. A procedure representative of those employed by several investigators[32,33] is as follows:

A phase and amplitude front is determined experimentally on a plane across the antenna aperture. This plane is subdivided into a convenient number of squares or other shapes. With each unit is associated a value of phase and amplitude. Rays are then traced whose initial amplitude and phase are those of the units from which they originate and whose direction is determined by the best normal to the phase at the rays' points or origin. At the radome wall, for each polarization, the rays are split up into transmitted and reflected rays, and each one of these is traced to an imaginary external plane (Figure 4-54). It will usually be necessary to consider higher order reflections, as well as the reflections from each surface of discontinuity. In the transfer of the rays through the walls, flat-panel, transmission coefficients are used. The total fields obtained by addition of all rays at the imaginary external plane are then used as on an equivalent aperture distribution. The far-field patterns are finally computed from this equivalent distribution in the conventional manner.

4-45. Error Prediction Based Directly on Maxwell's Equations: Radome Scattering Technique

Basically, the scattering technique[34] regards the radome as a source of perturbation or of scattered fields. The electromagnetic fields due to this source are measured (for each offset or scan angle) and combined by means of iteration with the corresponding fields due to the antenna without the presence of the radome. The boresight shift is determined by a comparison of the two field configurations. The electromagnetic formulation is of necessity

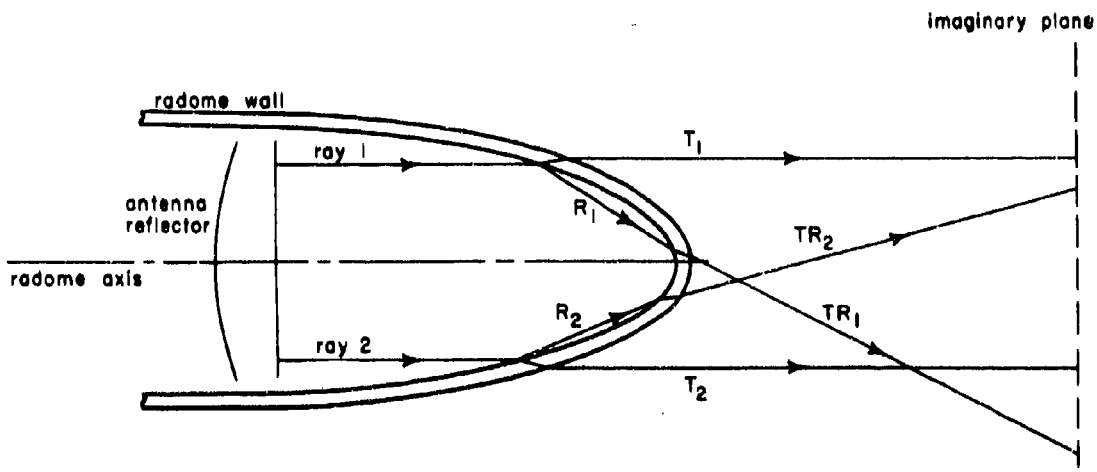


Figure 4-54. Radome Layout for Equivalent-External-Aperture Prediction Technique

fully three dimensional; none of the usual optic or plane-wave approximations is made, and flat-panel transmission and reflection coefficients are not employed. The same formulation is used in analyzing the scattering from dielectric rings in Scattering by a Thin Dielectric Ring under paragraph 4-56.

Derivation of the Basic Integral Equation. Maxwell's equations for electromagnetic fields in a dielectric of volume V and with a time variation of the form $e^{-j\omega t}$ are:

$$\bar{D} = \epsilon \bar{E} \qquad \underline{B} = \mu \underline{H}$$

$$\nabla \times \bar{E} - j\omega\mu \bar{H} = 0 \qquad \nabla \times \underline{H} + j\omega\epsilon \underline{E} = 0 \qquad (4\text{-}76)$$

$$\nabla \cdot \bar{E} = 0 \qquad \nabla \cdot \underline{H} = 0$$

where all symbols have their usual meanings. Similar equations hold in free space, if ϵ and μ are replaced by ϵ_0 and μ_0, respectively.

The electromagnetic fields in the problem are the same as those that would be generated if a distribution of virtual currents were present instead of a dielectric. To rephrase the problem in these terms the following notation is assumed:

S = surface bounding the volume V
J = virtual current distribution inside V

Here

$$\underline{J} = -j\omega\left(\frac{\epsilon\mu}{\mu_0} - \epsilon_0\right)\underline{E} \qquad (4\text{-}77)$$

The vector potential can then be written:

$$\underline{A}_p(P) = \mu_0 \int_V \underline{J}(Q)\,\frac{e^{j\beta_0 R}}{4\pi R}\,dV \qquad (4\text{-}78)$$

where P and Q represent field and source points, respectively, and

$$\beta_0 = \omega\sqrt{\mu_0 \epsilon_0} \qquad (4\text{-}79)$$

The subscript p refers to the perturbation (or scattered) fields; these can be calculated from the perturbation potentials.

When $\mu = \mu_0$, one finds the electric field from $\frac{j\nabla \times \nabla \times \underline{A}_p}{\omega\epsilon_0\mu_0}$, resulting in

$$\underline{E}_p(P) = (\epsilon_r - 1)\left[\beta_0^2 \int_V \underline{E}(Q)\,\frac{e^{j\beta_0 R}}{4\pi R}\,dV - \int_S \underline{n} \cdot \underline{E}(Q)\,\nabla\,\frac{e^{j\beta_0 R}}{4\pi R}\,dS\right] \qquad (4\text{-}80)$$

with $\epsilon_r = \epsilon/\epsilon_0$

$\underline{E}(Q)$ = total electric field

$\underline{n}$ = outward normal to S

Equation (4-80) is an integral equation relating the perturbation fields to the antenna fields and the physical properties of the radome. Since $\underline{E}(Q) = \underline{E}_p(Q) + \underline{E}_0(Q)$, the equation must be used for two separate calculations:

a. Determination of $\underline{E}(Q)$, that is, the effect of the presence of the radome on the field in the volume occupied by the radome itself.

b. Calculation of $\underline{E}_p(P)$, that is, the far-field effects of the perturbation sources.

For the second set of calculations, the following approximation is usually made: Some convenient origin 0 in or near V is assumed with $\underline{r} = \underline{m}\,r$ as the vector from 0 to P ($\underline{m}$ being a unit vector). If $\underline{g}$ denotes the vector from 0 to the point of integration Q, then

$$R = r - \underline{m} \cdot \underline{g} + 0\left(\frac{1}{r}\right) \qquad (4\text{-}81)$$

If only the first two terms are retained, Equation (4-80) reduces to

$$\underline{E}_p(P) \cong -(\epsilon_r^2 - \epsilon_0^2)\,\frac{e^{j\beta_0 r}}{4\pi R}\,\underline{m} \times \left[\left(\underline{m} \times \int_V \underline{E}(Q)\right)(e^{-j\beta_0 \underline{m} \cdot \underline{g}})\,dV\right] \quad \underline{E}(Q) = \underline{E}_g(Q) + \underline{E}_0(Q) \qquad (4\text{-}82)$$

Techniques of Solving the Integral Equation. It is clear that solutions to Equation (4-80) or to Equation (4-82) cannot be obtained in closed form. The starting data are the measured fields ($\underline{E}_0$) in numerical form. While it would be possible to fit these data in some polynomial approximation, the complicated geometry of most radomes prevents exact solutions. Numerical methods are therefore resorted to, and three methods have been considered:

a. The Grid Method. Suppose $\underline{F}_p(P)$ denotes an approximation to $\underline{E}_p(P)$; then $\underline{F}(P) = \underline{E}_0(P) + \underline{F}_p(P)$ is an approximation to $\underline{E}(P)$. It is possible to define an error term

$$\delta = \int_V \underline{R}(Q) \cdot \underline{R}^*(Q)\, dV \qquad (4\text{-}83)$$

where the R's are defined in such a manner that they vanish when $\underline{F}(P) = \underline{E}(P)$. The radome volume is now covered by a grid of N points sufficiently close together; the approximation $\underline{F}_p(P)$ is assumed as due to contribution from the N points:

$$\underline{F}_p(P) = \sum_{n=1}^{N} a_m \underline{E}_p(P) \qquad (4\text{-}84)$$

The error term then becomes

$$\delta = \sum_{m=1}^{N} \sum_{n=1}^{N} R_{mn}\, a_m\, a_n^* \qquad (4\text{-}85)$$

which is minimized by equating the $\partial\delta/\partial a_m$ and $\partial\delta/\partial a_n^*$ to zero for $n = 1 \ldots N$. This procedure gives N linear equations in the N complex a_n's; these equations are solved, the results are substituted into Equation (4-84), and $\underline{F}_p(P)$ is obtained.

b. Stationary Phase Approximation. The second method considered depends on the fact that the integrals in the integral equation have integrands involving the product of $(e^{j\beta_0 R})/4\pi R$ and the internal electric field. If the internal electric field behaves locally like a plane wave, it contains a factor $e^{j\beta x}$, where x is the coordinate in the direction of the wave. The two exponential factors are responsible for the change in phase as the point of integration moves about in the dielectric shell.

Consider a straight line drawn outward from the point of observation R = 0. Suppose for simplicity that x = 0 when R = 0. On this line the ratio R/x remains constant, and the exponential argument $j\beta_0 R + j\beta x$ increases linearly as R increases. However, on some lines, the factor of proportionality is zero, so that the phase remains constant. The lines are all those lying on a cone (which might be called the "cone of stationary phase") with an axis that is parallel to the direction of propagation of the interior electric field and to which elements are inclined at an angle equal to the complement of the critical angle for the dielectric. On one side of this cone the phase increases as R increases, and on the other side the phase decreases as R increases. The contributions to the integral from the region near the cone add together and reinforce each other. The contributions from the region well away from the cone have a tendency toward mutual cancellation.

The dielectric sheet is approximated locally by a flat sheet, which fits as closely as possible to the curve of intersection of the cone of stationary phase and the surface of the dielectric sheet. The integrals in the integral equation for that flat sheet are evaluated on the basis of the assumption that the electric field is essentially plane in the region of importance in the integral, since the cone of stationary phase occupies only a limited region near the point of observations. This process gives rise to what may be considered a flat-plate theory. However, it is not the usual sort of flat-plate theory. In the usual theory, the dielectric shell is approximated by a flat plate whose two sides are tangent to the shell in the local region of interest. The plate is held fixed in the determination of the field at all points of the local region. In the present theory, the orientation and thickness of the fitting flat plate change from point to point and depend on other properties of the shell than its thickness alone. These differences may be expected to give a more accurate theory than the usual flat-plate theory.

c. Lumped Fields Method. Another approach is to divide the radome into a number of circular disks on the order of a wavelength in diameter. The point is to "lump" the local behavior of the electric field in each disk in a way that can be handled and to use the basic integral equation to tie together the fields in the different disks. The electric field throughout each disk must first be expressed in terms of the field at the center. For these expressions it is assumed that the internal field in the disk is approximated by two plane waves whose directions of propagation may be set at will but may, in particular, be given the directions that the internal waves in a flat sheet would take when acted upon by the local electromagnetic field considered as a plane wave. If the direction of propagation is so set, a good deal of plane sheet theory can be applied to simplify calculations of the local fields.

Calculations of the total field at the center of each disk by integrations over each disk and summation over all the disks are then possible. The problem reduces to a set of linear equations in the unknown fields at the centers of the disks. A least squares and successive approximation theory can be used rather than direct solutions of these equations.

All three methods are considerably complex. The grid method, to provide sufficient accuracy, requires an excessively large number of points taken. The stationary phase method is hampered by the difficulty of fitting the sheets to the cones of stationary phase. The lumped-field technique looks the most promising of the three.

4-46. Spherical Mode Transformation Technique

The so called spherical mode transformation technique proposes the use of spherical mode series for the calculation of the antenna near field from free space near-field data measured over a spherical surface. Mathematics that derive the analytical expressions used in the technique are based on the work of Bailin and Silver,[36] but the application is unique. The calculated near field is used in a subsequent calculation of the power pattern of the far field, and the radome error is derived from the far-field pattern expressions. An important feature of the spherical mode method is that it handles offset and scan variations in a relatively simple manner. The same set of measured data can be used for each offset or scan angle, at least for a symmetrical antenna field. Another feature is that variations in offset can then be directly carried to the far field through the formulas. A brief outline of the technique follows.

It is well known that the coefficients of spherical mode series for the free space spherical components of E and H can be obtained if the values of tangential E are known on the surface of a sphere. The series and coefficients in the most general case have the forms indicated in the following Equations (4-86) to (4-95). When rotational symmetry of the antenna field with respect to some axis obtains, considerable simplification can be made.

$$E_r = \sum_n \sum_m \frac{1}{j\omega\epsilon} \frac{n(n+1)}{r} h_n^{(2)}(\beta r)\, P_n^m(\cos\theta) \begin{matrix} C_{mn}\cos \\ D_{nm}\sin \end{matrix} m\phi \qquad (4\text{-}86)$$

$$E_\theta = \sum_n \sum_m m h_n^{(2)}(\beta r) \frac{P_n^m(\cos\theta)}{\sin\theta} \begin{matrix} -A_{nm}\sin \\ B_{nm}\cos \end{matrix} m\phi + \sum_n \sum_m \frac{1}{j\omega\epsilon r} \frac{d}{dr} \left[r\, h_n^{(2)}(\beta r)\right] \frac{d}{d\theta}\left[P_n^m(\cos\theta)\right] \begin{matrix} C_{nm}\cos \\ D_{nm}\sin \end{matrix} m\phi \qquad (4\text{-}87)$$

$$E_\phi = \sum_n \sum_m -h_n^{(2)}(\beta r) \frac{d}{d\theta}\left[P_n^m(\cos\theta)\right] \begin{matrix} A_{nm}\cos \\ B_{nm}\sin \end{matrix} m\phi + \sum_n \sum_m \frac{m}{j\omega\epsilon r} \frac{d}{dr} \left[r\, h_n^{(2)}(\beta r)\right] \frac{P_n^m(\cos\theta)}{\sin\theta} \begin{matrix} -C_{nm}\sin \\ D_{nm}\cos \end{matrix} m\phi \qquad (4\text{-}88)$$

$$H_r = \sum_n \sum_m -\frac{1}{j\omega\mu} \frac{n(n+1)}{r^2} h_n^{(2)}(\beta r)\, P_n^m(\cos\theta) \begin{matrix} A_{nm}\cos \\ B_{nm}\sin \end{matrix} m\phi \qquad (4\text{-}89)$$

$$H_\theta = \sum_n \sum_m -\frac{1}{j\omega\mu r} \frac{d}{dr}\left[r\, h_n^{(2)}(\beta r)\right] \frac{d}{d\theta}\left[P_n^m(\cos\theta)\right] \begin{matrix} A_{nm}\cos \\ B_{nm}\sin \end{matrix} m\phi + \sum_n \sum_m m\, h_n^{(2)}(\beta r) \frac{P_n^m(\cos\theta)}{\sin\theta} \begin{matrix} D_{nm}\cos \\ -C_{nm}\sin \end{matrix} m\phi \qquad (4\text{-}90)$$

$$H_\phi = \sum_n \sum_m \frac{-m}{j\omega\mu r} \frac{d}{dr}\left[r\, h_n^{(2)}(\beta r)\right] \frac{P_n^m(\cos\theta)}{\sin\theta} \begin{matrix} -A_{nm}\sin \\ B_{nm}\cos \end{matrix} m\phi + \sum_n \sum_m -h_n^{(2)}(\beta r) \frac{d}{d\theta}\left[P_n^{(m)}(\cos\theta)\right] \begin{matrix} C_{nm}\cos \\ D_{nm}\sin \end{matrix} m\phi \qquad (4\text{-}91)$$

$$A_{nm} = -\frac{(2n+1)(n-m)!}{2n(n+1)(n+m)!} \frac{1}{\pi h_n^{(2)}(\beta a)} \int_0^{\pi} \int_0^{2\pi} \left[\frac{m}{\sin\theta} E_\theta\, P_n^m \sin m\phi + E_\phi \left(\frac{d}{d\theta} P_n^m\right) \cos m\phi\right] \sin\theta\, d\theta\, d\phi \qquad (4\text{-}92)$$

$$B_{nm} = \frac{(2n+1)(n-m)!}{2n(n+1)(n+m)!} \frac{1}{\pi h_n^{(2)}(\beta a)} \int_0^{\pi}\int_0^{2\pi} \left[\frac{m}{\sin\theta} E_\theta P_n^m \cos m\phi - E_\phi \left(\frac{d}{d\theta} P_n^m \right) \sin m\phi \right] \sin\theta \, d\theta \, d\phi \quad (4\text{-}93)$$

$$C_{nm} = \frac{(2n+1)(n-m)!}{2n(n+1)\ n+m)!} \frac{j\omega\epsilon a}{\pi \left[\frac{d}{dr} \left(r h_n^{(2)}(\beta r) \right) \right]_{r=a}} \int_0^{\pi}\int_0^{2\pi} \left[E\theta \left(\frac{d}{d\theta} P_n^m \right) \cos m\phi - \frac{m}{\sin\theta} E_\phi P_n^m \sin m\phi \right] \sin\theta \, d\theta \, d\phi \quad (4\text{-}94)$$

$$D_{nm} = \frac{(2n+1)(n-m)!}{2n(n+1)(n+m)!} \frac{j\omega\epsilon a}{\pi \left[\frac{d}{dr} \left(r h_n^{(2)}(\beta r) \right) \right]_{r=a}} \int_0^{\pi}\int_0^{2\pi} \left[E_\theta \left(\frac{d}{d\theta} P_n^m \right) \sin m\phi + \frac{m}{\sin\theta} E_\phi P_n^m \cos m\phi \right] \sin\theta \, d\theta \, d\phi \quad (4\text{-}95)$$

In these formulas r, θ, ϕ = spherical coordinates about the center of the data sphere.

a = radius of the sphere

$P_n^m(\cos\theta)$ = associated Legendre polynomial

$h_n^{(2)}(\beta r)$ = (outgoing) spherical Hankel function

These series converge at all points exterior to the sphere.

It is proposed to obtain these series from measurements of tangential E, in amplitude and phase, at a number of points on the surface of a mathematical sphere surrounding the radiating system and contained inside the given radome. The sphere is centered at the intersection of the gimbal axis with the antenna offset plane.

Although the measurements are taken with a fixed antenna offset, the variation in tangential E resulting from changes of the offset angle can be accounted for by a rotation of the data values through the given increment of angles. Near-field values at a point are therefore obtainable through a resumming of the mode series with only an appropriate change in the angular coordinates, the coefficients remaining the same. The mode series evaluations of the free space field components are used to obtain their values at points that lie on the inner surface of a given radome.

A formula of J. H. Richmond[37] is employed for calculations of the power function at a given far-zone observation point. The calculation involves the combination by means of Equation (4-96) of the previously found free space antenna field components at points lying on the inner radome surface with the field components arising at these points due to a plane wave impinging on the exterior of the radome from the point of observation and with the antenna absent.

$$V(\theta, \phi) = C_1 \int_S (\underline{n} \times \underline{H}_B \cdot \underline{E}_A - \underline{n} \times \underline{E}_B \cdot \underline{H}_A) \, dS \quad (4\text{-}96)$$

where V = the voltage induced by the antenna-radome system at the terminal of an antenna at the far-zone observation point

C_1 = an inconsequential constant of proportionality

S = inner radome surface

E_A, H_A = free space field vectors of the antenna

E_B, H_B = field vectors arising on S due to plane wave impinging on the outer radome surface from the direction of the observation point, as calculated with the antenna absent

From the far-field pattern expressions thus obtained, the radome error is derivable. The transmission of the field of the plane wave to the interior surface of the radome is a difficult problem. It is possible, however, that this calculation can be carried out with sufficient accuracy by the use of plane-wave, plane-sheet transmission coefficients in the standard manner.

In the spherical mode technique, the following assumptions and approximations are made:

a. The measurement of the free space tangential E components can be made without large perturbations of the antenna near field.

b. The field on the inner radome surface with the radome present is essentially the same as the free space field.

c. The field on the inner radome surface due to the impinging plane can be calculated with sufficient accuracy by some practical method, for example, by plane-wave, plane-sheet transmission coefficients.

4-47. Radome Boresight Errors in Monopulse Systems

A formula has been derived at the Glenn L. Martin Company[38] by which the boresight errors of monopulse systems can be determined and applied in the design of radomes. For any given monopulse system the theoretical boresight error curves of a radome can be calculated. The boresight error formula is derived first for a phase-comparison monopulse system (two-dimensional configuration), and the experimental data required for utilization of this formula in calculation of boresight error are outlined. The procedure is extended to include calculation of errors occurring in amplitude-comparison monopulse systems. Differences in derivation of the boresight error formula for the amplitude-comparison systems are noted. Two types of amplitude-comparison systems are discussed: those with scanning apertures and those with nutating feeds. The work was performed specifically for the simultaneous lobe-comparison systems, but very strong similarities were found to exist between the error criteria of amplitude-comparison monopulse systems and those of conical-scan systems.

4-48. Derivation of Boresight Error Formula for Phase-Comparison Monopulse

The phase-comparison monopulse system is considered to have two apertures, A and B (Figure 4-55). Each aperture can be considered as having its own pattern, but both patterns are identical and point in the same direction — normal to a line connecting the phase centers of the apertures. A difference in amplitude between the feeds of each aperture does not change the direction of the maximums or minimums of either the sum or the difference pattern. If an amplitude difference does exist, the difference pattern will not have an absolute null, and poorer system sensitivity will result.

It is necessary to know what effect a phase difference between the phase centers of the two apertures will produce on the direction of either the sum pattern or the null of the difference pattern. The illumination of the left aperture is designated A and that of the right aperture, B (Figure 4-56). Both illuminations have similar far-field patterns, which are normalized and designated F_0. At an angle of arrival at the apertures, θ, (measured from the antenna axis), the received voltage will be advanced by $\zeta/2$ at B and retarded by $\zeta/2$ at A, where ζ is

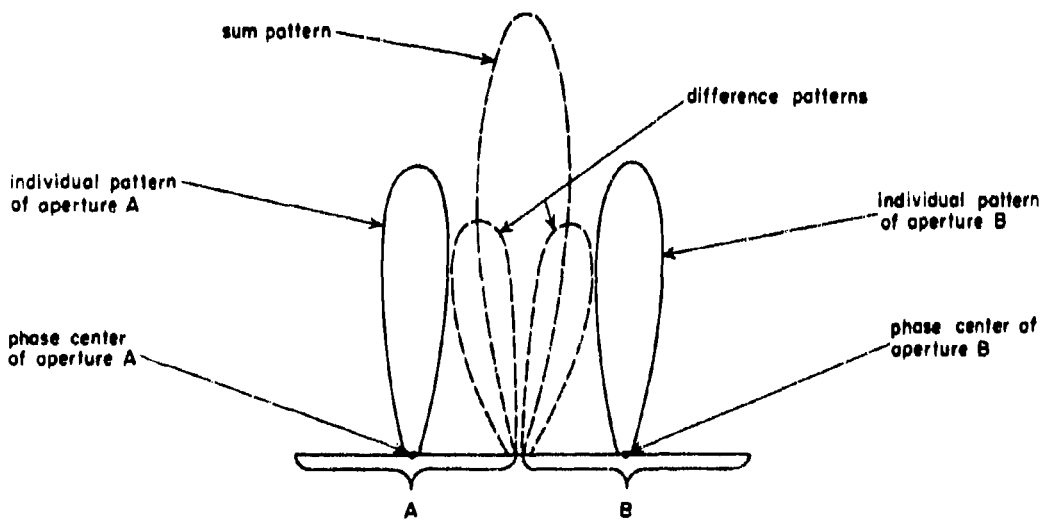


Figure 4-55. Two-Dimensional View of Phase-Comparison Monopulse System

the total phase difference between the apertures. The far field in the direction θ is given by

$$E = F_0 \exp\left[-j\frac{\zeta}{2}\right] + F_0 \exp\left[+j\frac{\zeta}{2}\right] \qquad (4\text{-}97)$$

where F_0 = the normalized far-field composite pattern caused by all the feed apertures

The normalized far-field is given by

$$E = F\cos\frac{\zeta}{2} \qquad (4\text{-}98)$$

where F = the normalized far-field pattern caused by each aperture

$$\zeta = \frac{2D}{\lambda}\sin\theta + \delta = \text{total phase difference between one aperture} \qquad (4\text{-}99)$$

where δ = the phase difference between the two apertures introduced by the circuits

If there is no phase difference in the circuits ($\delta = 0$), then $\zeta = 0$ on the crossover axis ($\theta = 0$) and, as can be seen from Equation (4-98), the maximum intensity would be the sum pattern. If $\delta = 180^0$, which would mean that the two channels are out of phase by π, then the intensity in the $\theta = 0$ or crossover direction is given by

$$E = F\cos\frac{\zeta}{2} = F\cos\frac{0^0 + 180^0}{2} = 0 \qquad (4\text{-}100)$$

This expression gives the null or crossover axis where θ is zero and where the two channels are out of phase by 180^0. If a radome is added to the antenna system, it may introduce a slight phase difference η into both channels. When both channel voltages are subtracted, the condition is obtained in which $\delta = \pi - \eta$. Then, from Equation (4-98)

$$E = F\cos\left(\frac{\pi D}{\lambda}\sin\theta + 90^0 - \frac{\eta}{2}\right) = 0 \qquad (4\text{-}101)$$

If Equation (4-101) is solved for any angle of arrival at the apertures (θ) with the conditions that $F \neq 0$ and the η is small, then for E to equal zero,

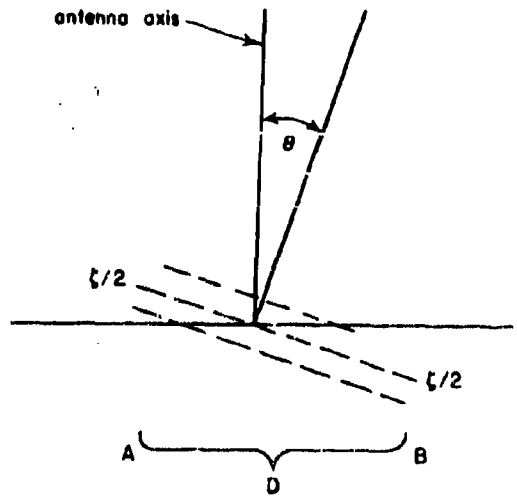


Figure 4-56. Illumination of Each Aperture in Two-Dimensional Phase Comparison System: D, Distance Between the Aperture Phase Centers; θ, Angle of Arrival at the Apertures; ζ, Total Phase Difference Between the Apertures

$$\frac{\pi D}{\lambda}\sin\theta + 90^0 - \frac{\eta}{2} = 90^0$$

$$\sin\theta = \frac{90^0 - 90^0 + \eta/2}{(\pi D)/\lambda} = \frac{\eta\lambda}{2\pi D}$$

$$\theta = \sin^{-1}\frac{\eta\lambda}{2\pi D} = \Delta\sigma \qquad (4\text{-}102)$$

Equation (4-102) defines the in-plane error introduced by the radome, since the arrival angle θ is equivalent to the rotation angle that the antenna would inscribe in lining up the virtual target direction with the antenna null direction.

The analysis of the boresight error criteria permits three conclusions:

a. The pattern rotates clockwise or counterclockwise as the phase difference caused by the radome, η, is negative or positive, respectively, and increases from zero to 4π.

b. The in-plane error direction can be compared with the null direction of an electrically scanned null lobe. If the phase difference, η, were controlled and electrically changed in the system, then the null could be caused to scan.

c. For a given phase difference, η, the in-plane error $\Delta\sigma$ can be reduced by increasing the diameter of the aperture. This relation can be seen by the in-plane error formula Equation (4-102) and conforms with the empirical

fact that large apertures and radomes give smaller boresight errors than small antennas with small radomes.

The in-plane error formula, Equation (4-102), looks very simple, but it becomes quite cumbersome when it is remembered that the phase difference must be known not only for each particular antenna pointing angle but also for a number of angles of arrival in the region of expected errors. For calculation of the exact location of the null position, the pattern of the null region must first be obtained, since the phase error introduced by the radome, η, is a function of the radome configuration. A first approximation of the in-plane error can be obtained by the determination of η in the original null direction. The location of all sources can therefore be neglected because the total phase lag at the apertures, ζ, would be zero and all distribution vectors have simply to be added. The η in the original null direction can be used in the formula as a first approximation of the in-plane error.

4-49. Experimental Data Required for Calculation of the In-plane Error

1. The radome is located in a coordinate system such as is illustrated in Figure 4-57. The equations of the outer and inner radome surfaces are given by $F'(X', Y')$ and $F''(X'', Y'')$, respectively. The offset point of the antenna is the origin of the coordinates X and Y. The offset positions are simulated by the rotation of the radome. The rotation angle is designated as β, and the radome coordinates are obtained by the transformation formulas:

$$X' = X \cos \beta + Y \sin \beta \qquad (4\text{-}103)$$

$$Y' = Y \cos \beta - X \sin \beta \qquad (4\text{-}104)$$

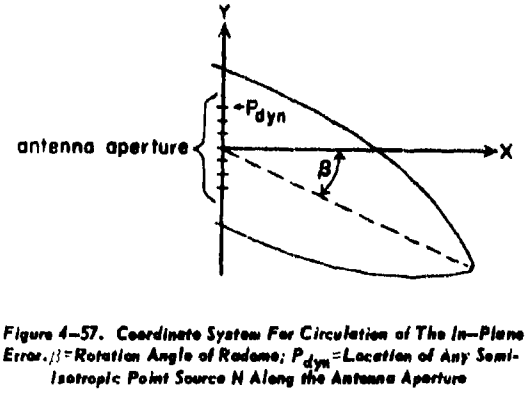


Figure 4-57. Coordinate System For Circulation of The In-Plane Error. β = Rotation Angle of Radome; P_{dyn} = Location of Any Semi-Isotropic Point Source N Along the Antenna Aperture

2. To make possible an examination of each ray, including the near-field rays, the geometry of a general ray is established in relationship to a radome, an antenna aperture, and an arbitrary near-field region (Figure 4-58). If the near field angle (α_s) with respect to the antenna axis is zero, the far-field method is applicable. (The far-field method investigates only parallel rays normal to the antenna aperture and holds only for an approximation of the pointing error.) If

$$0 \leq \left| \alpha_s \right| \leq \alpha_0 + \omega \qquad (4\text{-}105)$$

is utilized, the designation "near-field method" is used. Here α_0 = first null direction of antenna far-field pattern and

$$\omega = \cos^{-1} \frac{2l_x \cos \alpha_s}{2l_x + \lambda \cos \alpha_s} = \alpha_s \qquad (4\text{-}106)$$

3. The distance l_x between the antenna aperture and the near-field region of interest is assigned. It is most convenient to locate the near-field region of interest as close as possible to the apex of the radome. The distance l_x must be expressed in radians $2\pi l_x/\lambda$ for later use, and for convenience (l_x/λ) should be an integer.

4. The complex amplitude E_{dyn} (normalized) of each of the point sources at its location P_{dyn} along the antenna aperture is determined (Figure 4-58).

5. For the general ray, the mathematical expression for a straight line is set up:

$$Y = (X - X_1)(\tan \alpha_s / Y_1) \text{ with } P_{dyn}(0, Y_1) \qquad (4\text{-}107)$$

Variation of Y_1 gives N parallel rays for each particular near-field angle α_s.

6. A high-speed digital computer capable of handling a large amount of stored information is used to perform several operations:

a. Trace and perform the necessary operations on the N parallel rays for each near-field angle α_s.

b. Vary α_s in small steps between $(-\alpha_0 - \omega)$ and $(+\alpha_0 + \omega)$.

c. Determine, by the intersection of each N^{th} parallel ray with the radome surface, its point of incidence at the inner radome surface, its angle of incidence (iyns), and the effective thickness of the material according to the actual point of entrance and exit.

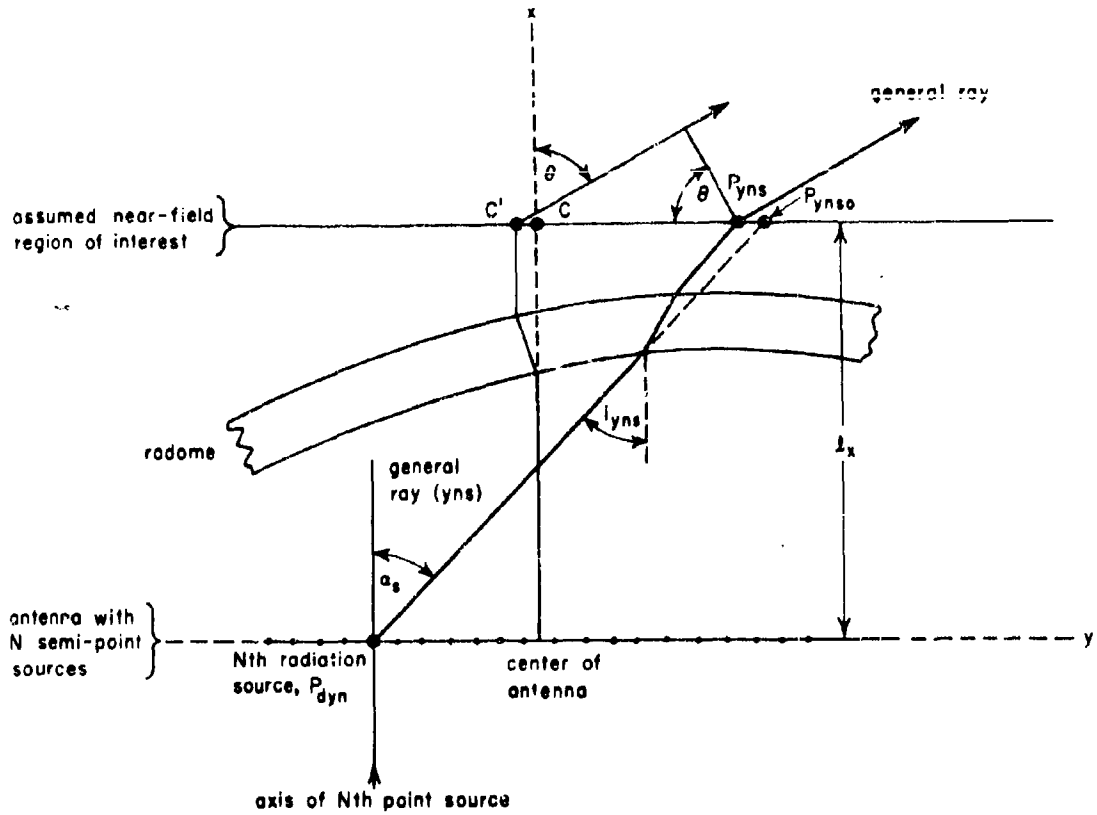


Figure 4-58. Geometry of General Ray Used in Obtaining Experimental Data: C=Phase Center of Antenna Without Radome (Original Phase Center); C'=Phase Center of Antenna With Radome (Phase Center of Near-Field Region; α_s=Near-Field Angle with Respect to the Antenna Axis; d_{yns}=Distance Between C' and P_{yns}; d_{ynso}=Distance Between C and Point P_{ynso} at which General Ray would Intersect Assumed Edge of Near-Field Region of Interest if no Radome were Present

d. Find the intersection point P_{yns} of the near-field region ($X = l_X$) and each ray from the radome exit points. (By transference the point P_{yns} becomes the radiation source of the near field and determines the distance d_{yns} to the phase center C' of the near-field region. The source rearrangement results in the focusing effect of the normalized patterns.)

e. Ascertain the amplitude transmission coefficient T_{yns} and the phase de. · Δ_{yns} for each ray, and calculate the gain factor, K, for each ray which results from the focusing effect by

$$\frac{E_{effect}}{E_{aperture}} = \frac{d_{yns}}{d_{ynso}} \qquad (4\text{-}108)$$

f. Determine the relative field E_{yns} at P_{yns} of each radiation source along the near-field region:

$$\bar{E}_{yns} = \bar{E}_{dyn} \left|T\right|_{yns} K \angle -\Delta_{yns} - \frac{2\pi l_x}{\lambda} \frac{1}{\cos \alpha_s} - 1 \qquad (4\text{-}109)$$

g. Determine the location of the phase centers on the near-field region. If interest is in the phase difference introduced by the radome, η, between the channel voltages of a phase-comparison system, use of the in-plane error criteria depends on the separate treatment of each aperture and on the use of the phase centers C and C'. The direction at which the phase angles of the two phase centers are equal is the true in-plane error direction. If, on the other hand, interest is in the difference voltage between the two channels, then use of only the phase center C' is sufficient.

h. Determine the relative field of the transferred semipoint source (P_{yns}) in the far-field direction θ with reference to the phase center

C, C_1, or C_2, according to the previous step, by means of the expression

$$\left(\bar{E}_{yns}\right)_\theta = \bar{E}_{yns}\angle\frac{2\pi d_{yns}}{\lambda}\sin\theta \qquad (4\text{-}110)$$

i. Determine the total relative field $\bar{E}_{T\theta}$ in the direction θ by a summation of all the field vectors:

$$\bar{E}_{T\theta} = \sum_1^N \sum_1^S \left(\bar{E}_{yns}\right)_\theta \qquad (4\text{-}111)$$

j. Compute $\bar{E}_{T\theta}$ for each applicable far-field angle.

7. The outlined procedure is repeated until the in-plane error is computed for each desired offset angle and the theoretical in-plane error curve (error versus the offset angle) is plotted.

4-50. Determination of In-Plane Error for Amplitude-Comparison Monopulse

The in-plane error calculation for an amplitude-comparison monopulse system with a scanning aperture is very similar to the procedure outlined for phase-comparison monopulse. The common aperture (reflector or other focusing element) faces in the apparent target direction. Only the resultant amplitudes in the θ region of expected in-plane error have to be computed. The chief differences from the procedure for the phase-comparison system are:

a. The amplitude and phase distribution across the entire aperture must be determined for each feed.

b. There is one phase center common to the phase fronts of the two feeds.

c. All vectors along the near-field aperture produced by one beam must be summed for determination of one resultant amplitude.

d. For various θ's in the region of the in-plane error about $\theta = 0$, the amplitudes must be plotted versus θ. The same procedure must then be repeated for the second beam. The position of the crossover point would determine the in-plane error.

The in-plane error computation procedure for amplitude-comparison monopulse systems with nutating feeds differs from that for phase-comparison systems also in a few basic points:

a. There are two apertures that are equivalent to two antenna positions. Two near-field distributions A' and B' must be found. These near-field distributions will include the common ray bundle for both phase fronts L_1 and L_2 (see Figure 4-59). From these distributions the two resultant fields in the directions α and $-\alpha$ must be computed.

b. Either of the procedures for beam A' or for beam B' is analogous to the procedure outlined for the phase-comparison monopulse system.

c. The region of far-field angles or angles of arrival for which the patterns must be calculated are $(\alpha \pm \Delta\sigma)$ where α is half the conical-scan angle and $\Delta\sigma$ is the expected pointing error. By means of the expression

$$\bar{E}_{T\theta} = \sum_1^N \sum_1^S \left(\bar{E}_{yns}\right)_\theta \left(A\angle\varphi\right)_\alpha \text{ and } \left(B\angle\zeta\right)_{-\alpha} \qquad (4\text{-}112)$$

two voltage vectors

$$(A\angle\varphi)_\alpha \quad \text{and} \quad (B\angle\zeta)_{-\alpha}$$

are obtained. The system sees only the amplitudes, and the null direction is given where the fields at apertures A and B are equal. Both fields must be plotted for all angles in the neighborhood of the apparent target direction,

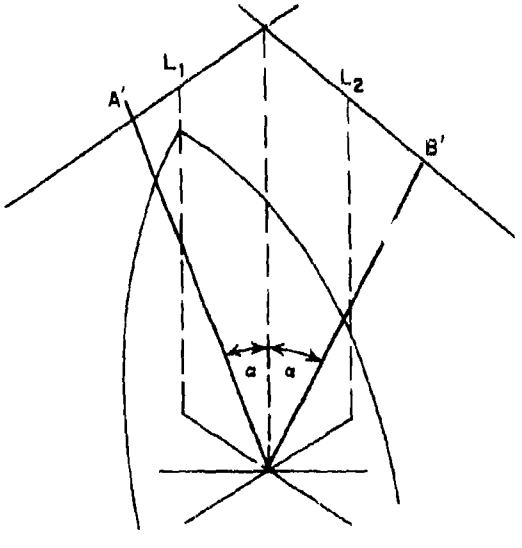


Figure 4-59. Common Ray Bundle for Both Phase Fronts of Amplitude-Comparison Monopulse with Nutating Feed: α, Squint Angle of the Antenna; A', Near-Field Distribution; B', Near-Field Distribution; L_1, Limits of Common Ray Bundle; L_2, Limits of Common Ray Bundle

and the position of the crossover locus determines the in-plane error. This procedure must be repeated for all offset positions of interest, and the true in-plane error curve is then given.

4-51. Derivation of In-Plane Error Formula for Amplitude-Comparison Monopulse

The derivation of the in-plane formula for the amplitude-comparison system is straightforward and made analogous to conical scan. If a constant amplitude and phase distribution across the antenna aperture is assumed (two feeds for monopulse), the far-field pattern is given by (sin x)/x where

$$x = \frac{\pi D}{\lambda} \sin \theta \qquad (4\text{-}113)$$

If the phase front is tilted by an angle α, (which is half the conical-scan angle), then the pattern is given by

$$\frac{\sin\left[\frac{\pi D}{\lambda} \sin (\theta + \alpha)\right]}{\frac{\pi D}{\lambda} \sin (\theta + \alpha)} \qquad (4\text{-}114)$$

The intensity in the direction α is given where $\theta = 0$, and if α is sufficiently small, it can be substituted in radians for sin α. Then

$$A_{1,2} = \frac{\sin \frac{\pi D}{\lambda} \alpha}{\frac{\pi D}{\lambda} \alpha} \qquad (4\text{-}115)$$

The amplitudes A_1 and A_2 in the direction α are equal for two equal antennas, since α is the crossover direction of two diverging patterns. If A_2 changes its value to ρA_2, where ρ is the deleterious effect caused by the radome,

$$\frac{A_2}{A_1} = \rho \leq 1 \qquad (4\text{-}116)$$

Then the two amplitudes in the direction α are

$$A_1 = \frac{\sin \frac{\pi D}{\lambda} \alpha}{\frac{\pi D}{\lambda} \alpha} \text{ and } \dot{A}_2 = \rho \frac{\sin \frac{\pi D}{\lambda} \alpha}{\frac{\pi D}{\lambda} \alpha} \qquad (4\text{-}117)$$

and the crossover point will shift by an amount determined by the boresight error $\Delta\sigma$ (Figure 4-60). The amplitudes in the new crossover direction are equal again; therefore,

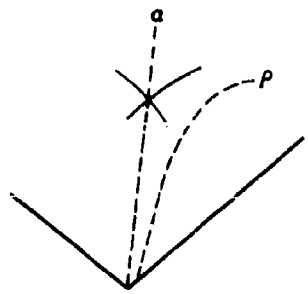


Figure 4-60. Shift of Crossover Point Caused By In-Plane Error: α, Crossover Direction of Two Diverging Patterns; ρ, Effect of Radome

$$\frac{\sin \frac{\pi D}{\lambda} (\alpha + \Delta\sigma)}{\frac{\pi D}{\lambda} (\alpha + \Delta\sigma)} = \rho \frac{\sin \frac{\pi D}{\lambda} (-\alpha + \Delta\sigma)}{\frac{\pi D}{\lambda} (-\alpha + \Delta\sigma)} \qquad (4\text{-}118)$$

Solving for $\Delta\sigma$ gives the expression for the approximate boresight error. It is only an approximation for several reasons:

a. The amplitude distribution across the antenna aperture will not be constant; therefore, the pattern is not given exactly by (sin x)/x.

b. The parameter, ρ, is not constant but is a function of the radome configuration at the various angles of arrival.

c. The distance $\pi D/\lambda$ between the centers of the two feeds in any one plane is not generally the same as the distance $\pi D/\lambda$ between the feeds in another plane.

4-52. Practical Design Procedure for Monopulse Systems

In the present state of radome design, there are three approaches that are more or less practical for the design of boresighting radomes for monopulse systems. (1) Empirical design procedures can be used with a series of tests, compensations, retests, and additional compensations until the desired error is achieved. (2) A second method utilizes both a high-speed computer and the procedure outlined earlier for computing the radome error; a series of error curves is run for various radome wall tapers

and skin inserts until the desired error is achieved. (3) The third method uses a graphical method for determination of the parameters necessary for a boresighting radome; it is based on the same theoretical background as that used in the second method but graphical techniques replace the computer. This third method has been used successfully by Martin in the design of radomes that meet strict boresight requirements.

With the graphical method for both types of monopulse systems, two large-scale drawings are used. On one drawing the inside surface of the radome is given with respect to a designated coordinate system. On the second drawing, which is made on transparent paper, the antenna aperture (for conical-scan systems and the analogous amplitude-comparison monopulse systems with scanning apertures) or both apertures (for amplitude comparison with nutating feed) are drawn with respect to the same coordinate system. The second drawing is placed over the radome drawing, and antenna rotation (gimbaling) is simulated by the rotation of the second drawing about the gimbal axis of the antenna. A ray analysis is made to determine the angles of incidence, the effective thickness, and the location of the near-field radiation source. In conjunction with the graphical study, a set of transmissional phase-delay curves versus thickness must be provided for determining the radome criteria according to the various angles of incidence. Since the radome error criteria are the same for the phase-comparison system, the amplitude-comparison system with scanning aperture, and the conical-scan system with nutating feed, the graphical design method is the same for all three systems.

For monopulse systems in which the phase distribution is constant, the parallel rays are drawn parallel to the direction the antenna is looking, and phase-delay curves are used in determination of the wall taper which gives a constant phase delay. The radome contours must then be modified so that a constant phase delay is given for all applicable offset positions. This compensation is sufficient only if the near-field contributions are neglected. If these contributions must be included in the compensation, the wall taper not only must satisfy the requirement for constant phase delay but also must give equal transmission coefficients between pairs of mirror-symmetrical rays.

For monopulse systems in which both phase and amplitude distributions are not constant, only the mirror-symmetrical pairs of rays are investigated. The taper introduced into the wall must satisfy the same conditions as those imposed by the near-field distributions.

SECTION G. CORRECTION OF RADOME ERRORS

In spite of some improved techniques in radome manufacture, quantity production of radomes that have uniform electrical wall thickness is still very difficult and very costly. Small radomes with electrically uniform walls are being produced in production quantities by the use of matched metal dies under pressure,* and it is hoped that in the future large radomes can also be made in production quantities by the same technique.

4-53. General Methods of Approach

At present the most generally accepted procedure for both large and small radomes is to make them to reasonable tolerances by such techniques as hand layups and vacuum bag molding and then to improve on the tolerances by some systematic procedure. Several experimental techniques are in use by which uniform electrical wall thickness can be achieved. After electrical uniformity is achieved, the radome pointing error can be reduced by the use of dielectric obstacles. Institutions such as Boeing Aircraft,[39] Convair,[40] and Hughes[41, 42] have all reported excellent results with various techniques. Although these techniques differ slightly in approach, in general the end goal is the correction of electrical non-uniformities. The technique to be described is drawn from procedures developed at Hughes Aircraft Company,[41] since the writer has greater familiarity with this method than with those of other institutions. This technique makes possible the correction of electrical non-uniformity through the systematic location of the unknown electrical discontinuities on a radome surface and subsequent compensation for these discontinuities by the addition or removal of dielectric at appropriate intervals. The inherent radome error can then be substantially reduced by the use of systematically placed dielectric patches.

Aerodynamically, radomes for high-speed aircraft must have pointed shapes. Such a contour inherently introduces large variations in

*The Hughes Falcon.

the incidence angles of electromagnetic energy. One means of reducing this inherent error is the reduction of the range of angles through which the antenna looks by the introduction of wall tapers into the shape of the radomes. Ideally, if the pointed shape is to be retained, the taper should be introduced on the inner surface of the radome; however, small tapers on the external surface will usually introduce very little change in the aerodynamics of the aircraft. Reduction of the range of incidence angles, or the range of angles through which the antenna looks, can also be effectively accomplished by the placement of lenses at appropriate positions inside the radome to refocus the emergent wave front. A third means of correcting for the inherent radome error of a pointed radome is the systematic placement of dielectric rings on the inner surface in such a way that they introduce errors that have the effect of cancelling the error.[42]

4-54. Tapers and Lenses

Tapers can be introduced into the shape of a radome by one of two methods: by a variation in the actual physical thickness of the wall while the dielectric constant is fixed or by a variation of the dielectric constant of the radome material while the physical thickness of the wall is held constant. At present, utilization of the second of these methods is difficult because proper control of the dielectric constant is a definite barrier. A report on the determination of proper tapers can be found in the works of Alan F. Kay.[43]

When the crosstalk error is of the same magnitude as the in-plane error, correction by tapers alone seems impossible. Tapering does not change the crosstalk error appreciably. However, partial correction of the theoretical divergent lens effect of a radome with uniform wall thickness (measured along the surface normal) is possible by a taper that increases in thickness toward the radome nose. Certainly, for radomes of a half-wave wall design, consideration of tapers as a correction technique is logical, for the thickness of a true half-wave wall varies with the angle of incidence, as is shown by the following equation:

$$d = \frac{\lambda}{2} \frac{1}{\sqrt{\epsilon_r - \sin^2 \theta}} \qquad (4\text{-}119)$$

where d = wall thickness

λ = free space wavelength

ϵ_r = dielectric constant of the wall

θ = angle of incidence the beam makes with the radome wall

A bounded plane wave will not change direction on passage through a sheet of homogeneous dielectric. If a radome wall is considered as a curved sheet, from a geometric optics point of view the normals to the inner and outer surfaces of the sheet are not parallel for a given ray when it enters and emerges from the sheet. For these rays the sheet will act as a prism and cause a refraction. If a change in the wall thickness is so introduced (by a taper, for example) as to make the normals to the inner and outer surfaces parallel, a ray passing through the wall at this point would not be deflected.

In reality, however, rays are an approximation, and what must be considered is the behaviour of all parts of the radiated beam. The best way to express the behavior of the beam is in terms of the insertion phase shift and the beam attenuation caused by the radome, rather than in terms of the emergent directions of various rays. For smooth variation of insertion phase shift it has been shown that the influence of the radome on the beam deflection, to a first approximation, is obtained by consideration of only the linear term in the variation of the phase shift across the beam. The emergent wave front is then considered as a plane surface of constant phase, and the normal to these emergent phase planes will have been deflected with respect to that of the incident wave.

An approximation for the beam deflection due to nonparallel wall boundaries can be found in the Princeton University Radome Study[44] in which the final result is

$$\delta = \frac{-\Delta\phi}{l} \qquad (4\text{-}120)$$

where $\Delta\phi$ = total phase shift

l = beamwidth

In conjunction with tapers the use of lenses for the correction of radome boresight errors immediately comes to mind, since the radome itself has some lens effect on the beam.

Because of the complexity due to the continuously varying look angle, a complete solution by a lens is almost impossible. Lenses have been constructed to correct radome errors at particular offset angles with good success but, at the present stage, the technique should be consideredas a means of correcting specific radomes rather than an overall means of correcting radome error. The amount of deflection is dependent on the total radome insertion phase shift across the beamwidth. In this manner a radome can be considered as producing a

smoothly varying linear beam deflection, and, to a certain degree of accuracy, a taper in the radome wall will in turn introduce a similar effect. Thus, a certain amount of correction can be introduced with the use of tapered walls. It certainly seems possible that a combination of tapers with other correction techniques would give good results, and for several specific radomes such a combination has proved to be true. For example, Figure 4-61 presents four sets of crosstalk and in-plane error curves of a pointed, missile-type radome; the curves were measured for (a) the radome alone, (b) the radome plus a taper, (c) radome plus dielectric rings,* and (d) radome plus both taper and rings. The taper alone cuts the total magnitude of the in-plane error curve about in half (from a range of +0.45 to -0.5° to a range of +0.25 to -0.35°). A combination of dielectric rings reduces both total magnitude and slope of the in-plane error. But taper and rings together result in a minimum error curve which, for the particular radome measured, is well within specifications.

4-55. Correction of Electrical Non-Uniformity in Radome Walls

The Hughes correction technique for large radomes[41] is broken into three distinct phases. In Phase 1 error curves are measured when known discontinuities in the form of single and multiple dielectric patches are added to the radome surface. From these curves data are obtained that show the effect on the error curve of both location and magnitude of discontinuity. In Phase 2 these data are used to map the electrical non-uniformities of a given radome. Phase 3 is the actual correction step of the technique; the electrical non-uniformities are reduced by the removal or addition of dielectric material at the appropriate locations. Data are recorded with the use of an automatic radome error measuring facility. Such a facility simulates the coordinate system of an interceptor, as is shown in Figures 4-62 and 4-63, which present the coordinate systems used both in an interceptor and in the facility. The angle between the line-of-sight to the target and the longitudinal axis of the interceptor is called the offset angle σ. The angle between the plane of the interceptor's wings and the plane through the longitudinal axis containing the line-of-sight is called the roll angle ζ. The angle between the apparent line-of-sight and the true line-of-sight is the radome error. The radome error may be resolved into two components, the horizontal error ($\Delta\sigma$) and the vertical error ($\Delta\sigma \sin\sigma$). The individual effects of a dielectric obstacle are called, respectively, the horizontal deviation or the vertical deviation. The two error components are plotted on a recorder.

Phase 1: Effect of Known Discontinuities. In the first step of the correction technique, horizontal and vertical components are measured for a radome to whose surface dielectric patches* of different diameters and thicknesses are added, first singly and then in multiple. For each position and thickness of the patch or patches, a set of error curves results. Any discontinuity placed on the radome surface should appear in both vertical and horizontal error curves; however, if a dielectric patch is located so that it moves on a horizontal path directly through the crossover of a conically scanning beam (transmitter of the automatic facility), there will be no vertical error deviation. To isolate the errors in the test radome, radome-only curves are subtracted from radome-plus-patch curves for corresponding runs. The resulting curves are termed the "effect" curves.

Three types of runs are made to measure the radome errors that occur.

a. Azimuth or Offset Run. The roll angle ζ is held fixed while the offset angle σ is varied. To simulate the actual conditions in the interceptor, the supporting structure holds the antenna fixed in space while the radome revolves about the gimbal axis of the antenna. If the radome is absolutely uniform electrically, there will be no vertical deviation in the radome error, but there will be a horizontal deviation. This horizontal error will be symmetrical about the $\sigma = 0$ position. Although the curve is not truly sinusoidal, it has sinusoidal characteristics. The horizontal error usually is due to the shape of the radome and the resulting change in incidence angle as the offset angle is varied. Consequently, it is sometimes referred to as shape error. The shape error changes when the incident polarization is changed, that is, when ellipticity and direction of polarization change with respect to offset angle.

b. Roll Run. The offset angle σ is held fixed while the roll angle ζ is varied. In a roll run,

*See Experimental Technique under paragraph 4-56.

*The patches used at Hughes were laminated fiberglass circles with the dielectric constant the same as that of the test radome.

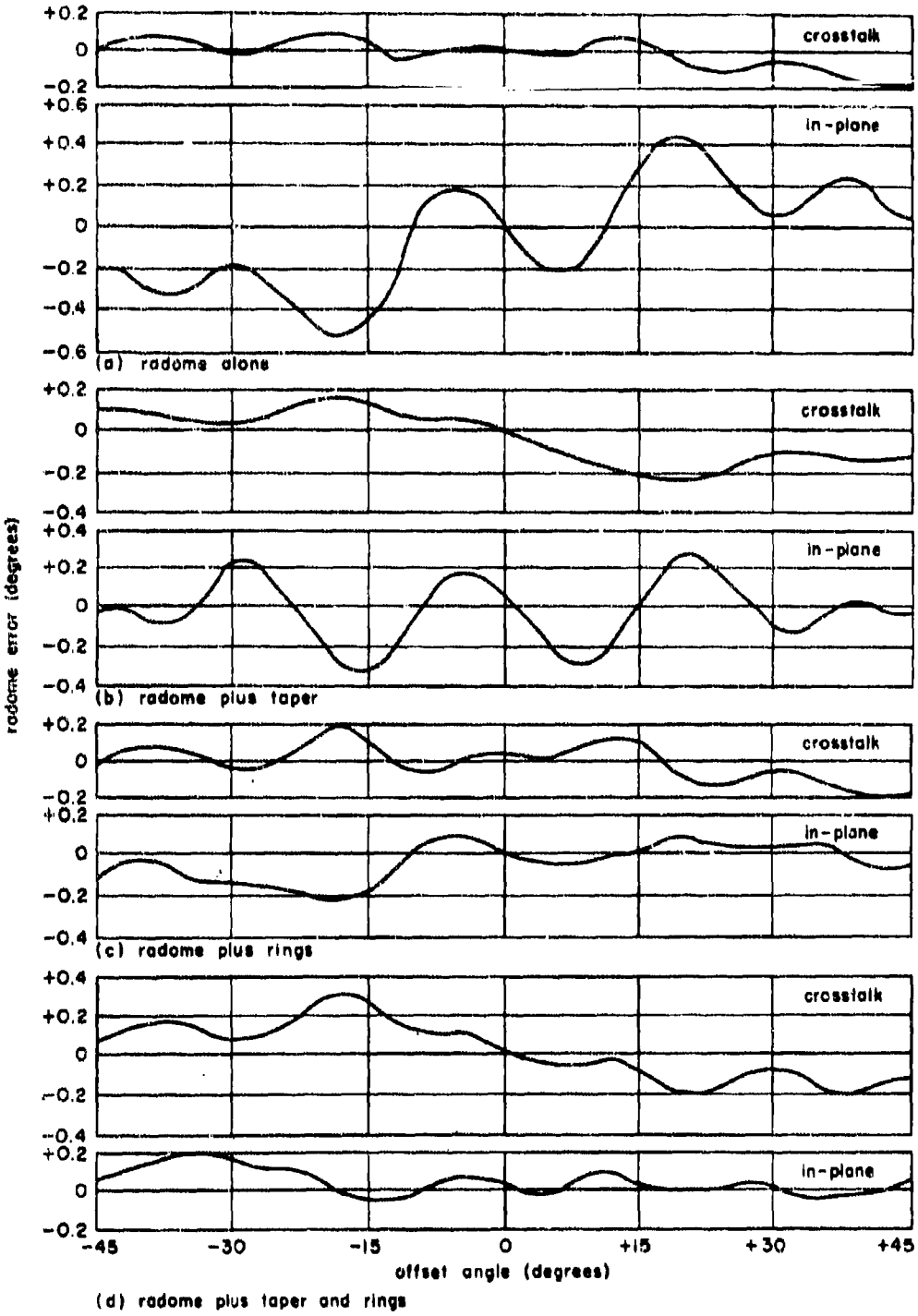


Figure 4-61. Radome Error Curves Showing Corrective Effect of A Taper Combined With Dielectric Rings

the supporting structure holds the radome at a fixed offset angle with respect to the antenna; simultaneously this structure rolls the radome about its own longitudinal axis and the antenna about its own axis. (In this type of run the direction of polarization with respect to the

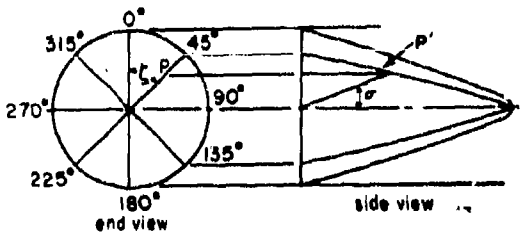


Figure 4-62. Coordinate System of Automatic Error Measuring Facility

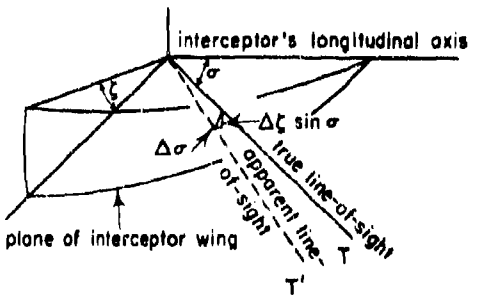


Figure 4-63. Coordinate System of Interceptor

offset angle is varied.) The transmitting antenna remains pointed towards the receiver, a four-horn null seeker. Each horn of the null seeker must roll about its own longitudinal axis in synchronism with the transmitting antenna to keep the polarization of the transmitter and receiver alined.

c. Fixed Polarization Roll Run. Only the roll angle ζ of the radome can be varied, while the roll angle of the antenna and null seeker horns remains fixed. The fixed polarization roll run is essentially a check on the electrical uniformity of the radome. A perfectly uniform radome should produce no error deviation as the radome is rolled.

The effect curves obtained from azimuth runs show that the deviation is always toward the thickest area, which is the dielectric patch. An increase in the diameter or thickness of the patch increases the magnitude of the deviation. Similar results can be shown with effect curves obtained from fixed-polarization roll runs. Again, the deviation is toward the thickest area with a magnitude approximately proportional to the volume of the patch.

After the effect of one patch on the radome error curves has been determined, two identical patches are placed on the test radome (Figure 4-64). The error deviations caused by these patches are also measured (Figures 4-65 and 4-66). Along path 0-to-1 (shown in Figure 4-64), patches A and B have the indivi-

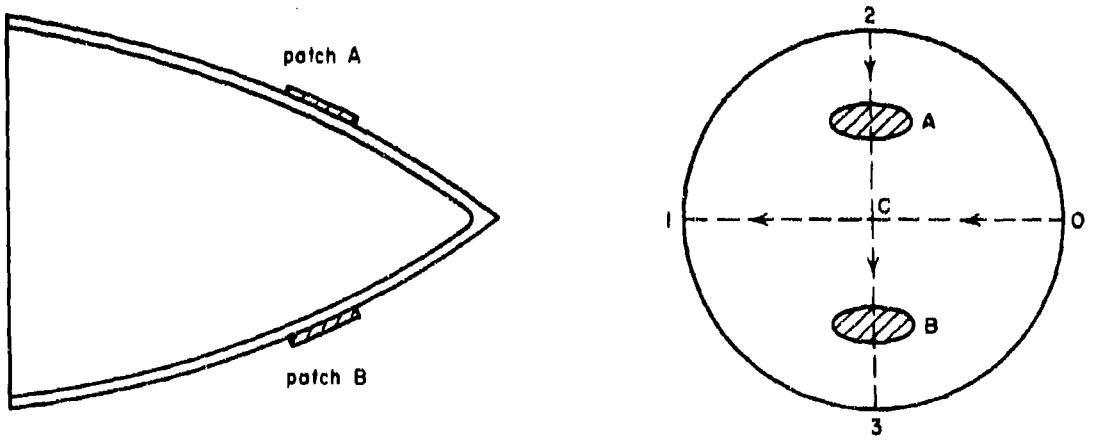


Figure 4-64. Radome With Two Dielectric Patches Added To Surface; 0-To-1 And 2-To-3 Indicate the Paths Traversed by the Antenna Axis (Conical-Scan Axis)

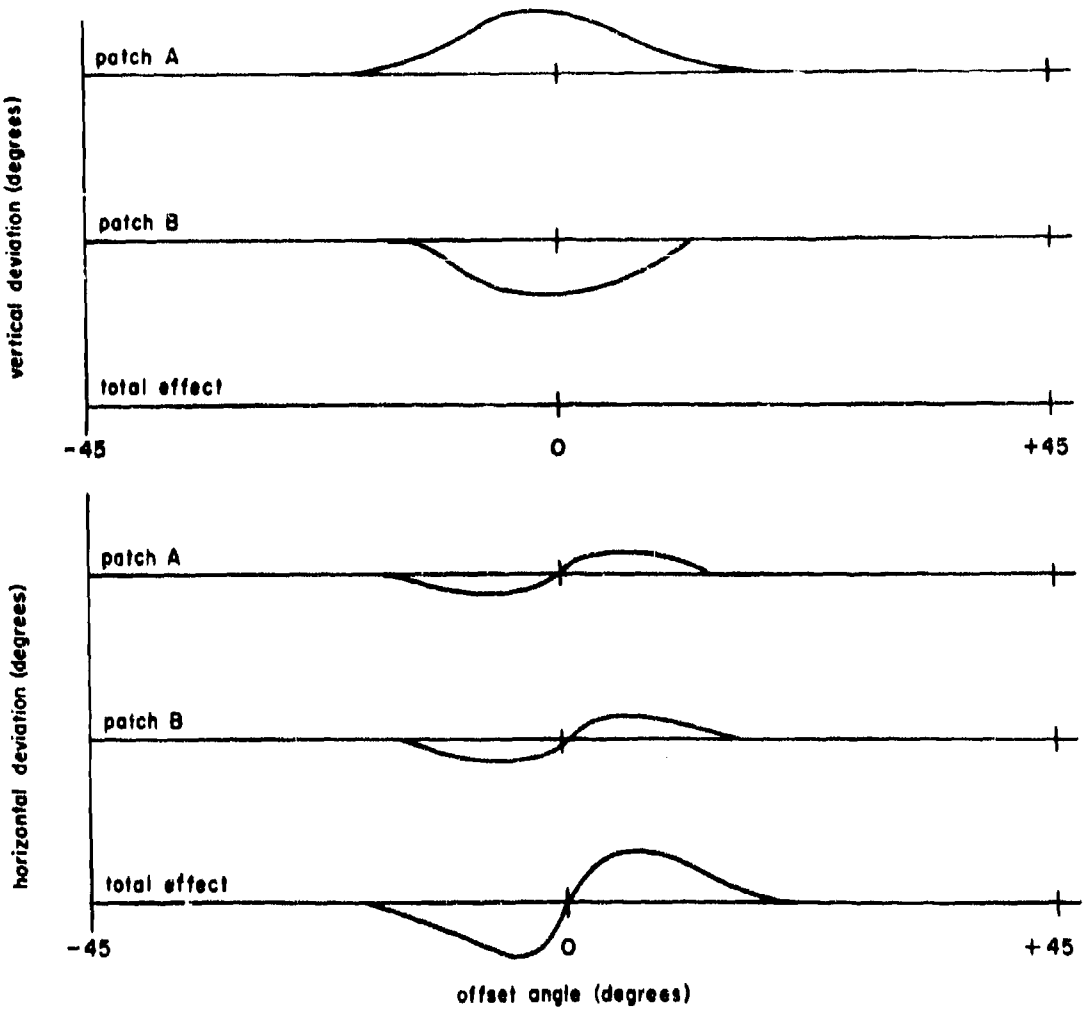


Figure 4-65. Error Deviation Along Path 0-To-1

dual effects shown in Figure 4-65. The total vertical deviation is zero because of the symmetrical location of the patches about the path traversed. The total horizontal deviation is doubled because each patch has a similar effect. For each patch the horizontal deviation is toward point C. Along path 2-to-3, patches A and B have the individual effects shown in Figure 4-66. The vertical deviation is zero because the path passes through the center of each patch. The horizontal deviation caused by each individual patch has a sinusoidal characteristic again. Each sinusoidal variation crosses the zero axis at a point corresponding to the σ position of the patch. The slope, magnitude, and length of each oscillation depend on the size, thickness, and location of each patch. In the example under consideration, the total horizontal deviation is a doubly oscillating curve.

In Figure 4-64, (a) could also represent, in cross section, a patch that completely encircles the radome. The vertical deviation of a ring could be expected to be negligible because each segment has a similar segment located symmetrically on the other side of the radome. The horizontal deviation would be expected to have more than one oscillation.

Phase 2: Location of Unknown Inhomogeneities. When the effects of known inhomogeneities over the radome surface have been established, the inherent variations in any given

radome can be located. These inhomogeneities include both the physical non-uniformities and the nonhomogeneities of the fabricating material. A single discontinuity can easily be located by making a series of roll and azimuth runs. The family of vertical deviation curves for azimuth runs determines the roll position of the discontinuity. After this location is determined, the horizontal deviation curves for roll runs are observed to locate the offset position of the discontinuity. This method of locating the discontinuity becomes very tedious and difficult if the discontinuity is extended over a large region or if there is more than a single discontinuity.

An alternative method of locating the discontinuity is to plot, in the form of vectors, the errors obtained from a series of fixed-polarization roll runs, preferably on a fan-shaped diagram. This transformation gives a serviceable coordinate system which simulates the actual radome surface unfolded. At convenient intervals on the fan-shaped diagram, a vector is plotted that is proportional to the error that occurs as the conical-scan axis of the transmitted beam passes through the corresponding point on the radome. The direction of the vector indicates the direction of the error at this point. Since it has been determined that the error is in the direction of the thick parts

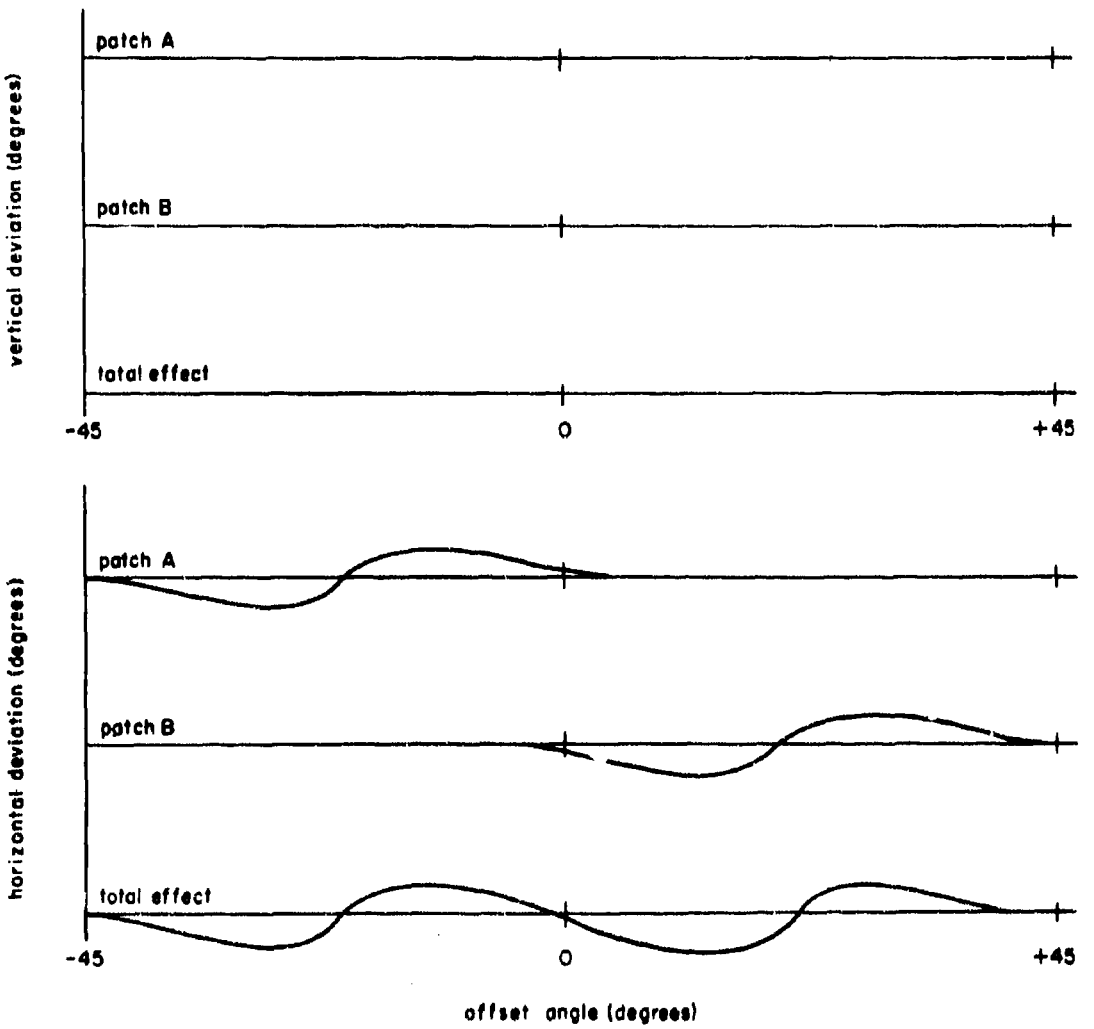


Figure 4-66. Error Deviation Along Path 2-To-3

of the radome, the system of vectors will point toward these thick parts.

For this method it is necessary to establish a reference thickness from which the relative thickness of the discontinuities can be determined. The reference thickness is arbitrary, but the average electrical thickness of the radome wall at one offset angle can be taken as the reference. This average thickness can be determined if the radome is rolled at an offset angle of zero degrees and the average values of the horizontal and vertical variations are taken. After this step is accomplished, a series of roll runs with various offset angles is made. The magnitudes of the error deviations are taken at appropriate intervals and plotted in the form of vectors on the fan-shaped diagram. In (a) of Figure 4-67, the curves represent the horizontal and vertical deviation for three roll runs. The information contained in the vertical effect curves of this figure are transferred to a fan-shaped diagram, shown in (b) of Figure 4-67. In this diagram the radial lines represent constant roll angle lines, and the circles with center at zero represent constant offset angle lines.

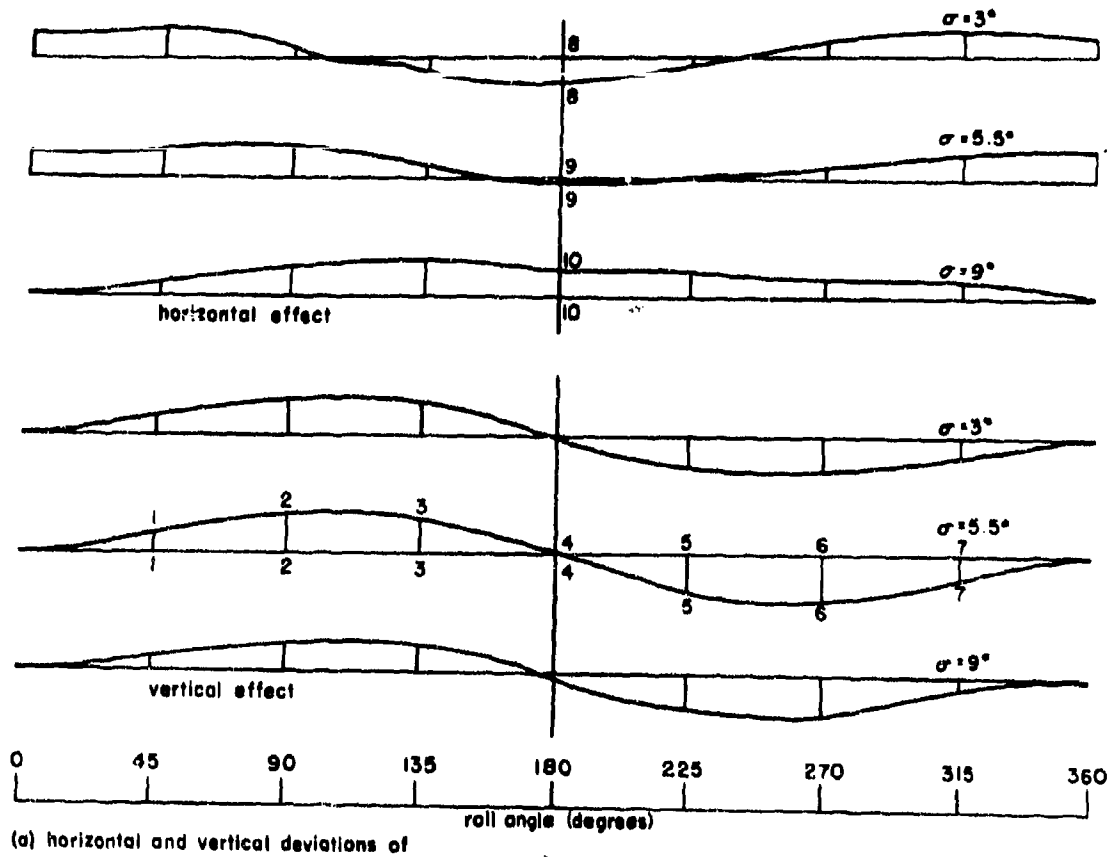
Vectors 1' to 7' are proportional to the vertical deviation at corresponding points on the vertical error curve. The point at which the vectors reverse in direction indicates the ζ position of the discontinuity. Vectors 8' to 10' are proportional to the horizontal deviation at corresponding points on the horizontal error curve. These vectors are plotted to determine the σ position of the discontinuity. The point at which vectors 8' to 10' reverse in direction represents the σ position of the discontinuity. The magnitude of the vectors is kept proportional to the magnitudes of deviation on the error curves. The direction of the vertical deviation vector should be tangential to the constant σ circles. The direction of the horizontal deviation vector should be radial. The thickness and the size of the discontinuities can be estimated by observing the magnitudes and the rate of change of the vectors. The distribution of the non-uniformities found by this method for one experimental radome is shown in Figure 4-68.

Phase 3: Correction. The third phase of the correction technique consists of the actual correction of the radome for uniformity and for inherent boresight error.

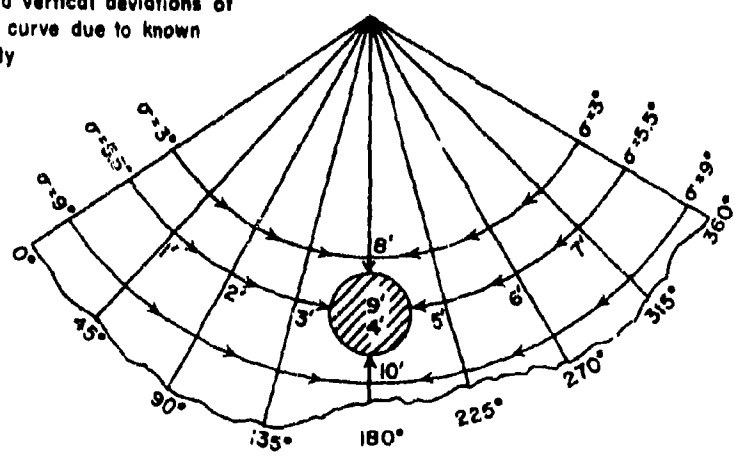
Once the non-uniformity distribution of a radome is plotted by the vector method of Phase 2, the physical location of the discontinuities on the radome surface can readily be found by their σ and ζ coordinates. Patches are then added or material is ground away, depending on whether the region is too thin or too thick. When the uniformity corrections are accomplished, there will be no vertical deviation in an azimuth run and no vertical or horizontal deviation in a fixed polarization roll run.

Most interceptors have radomes of such a contour that the incidence angles that the radar beam makes with the radome wall vary over a large range. This variation in incidence angle generally gives rise to substantial in-plane errors when azimuth runs are made. The in-plane errors usually have sinusoidal characteristics. If the radome is electrically uniform, the in-plane error curve is symmetrical about zero offset, and it is usually easy to reduce the magnitude by adding identical dielectric obstacles symmetrically around the radome at appropriate offset positions. With some experience one can determine this position with little difficulty. It is essential that the radome be corrected for uniformity before any attempt be made for in-plane correction. Symmetrical placement of identical patches applies when the polarization is held fixed with respect to offset angle. When direction of the polarization varies with the roll of the radome, as in conventional interceptor radomes, correction of the radome must include correction of the additional effects due to the polarization changes. For correction of these additional effects, the antenna may be fixed to a horizontal linear polarization and the in-plane errors corrected by placement of identical dielectric obstacles on the horizontal plane. This correction can be considered to correspond to patches A and B with an azimuth run being made from 2-to-3 (see Figure 4-64). The radome and the antenna are both rolled 90°, and the in-plane error is again corrected. The second correction corresponds to an azimuth run from 0-to-1 in Figure 4-64. The correcting patches placed along path 0-to-1 generally are not the same as those placed along path 2-to-3 (A and B in Figure 4-64). The patches are tapered toward each other so that no abrupt discontinuity occurs. By this method, the errors for the intermediate polarization are compensated in the test radome. Typical curves before and after correction in this manner are shown in Figure 4-69.

A second method of correction of the additional polarization effects consists of the radome and the antenna being rolled synchronously. The non-uniformity distribution diagram is plotted in a manner similar to the vector diagram in Phase 2 of the overall correction technique. This diagram differs from the pre-



(a) horizontal and vertical deviations of radome error curve due to known non-uniformity



(b) location of known non-uniformity by a plot of vectors

Figure 4-67. Vector Method of Location of Known Non-Uniformity

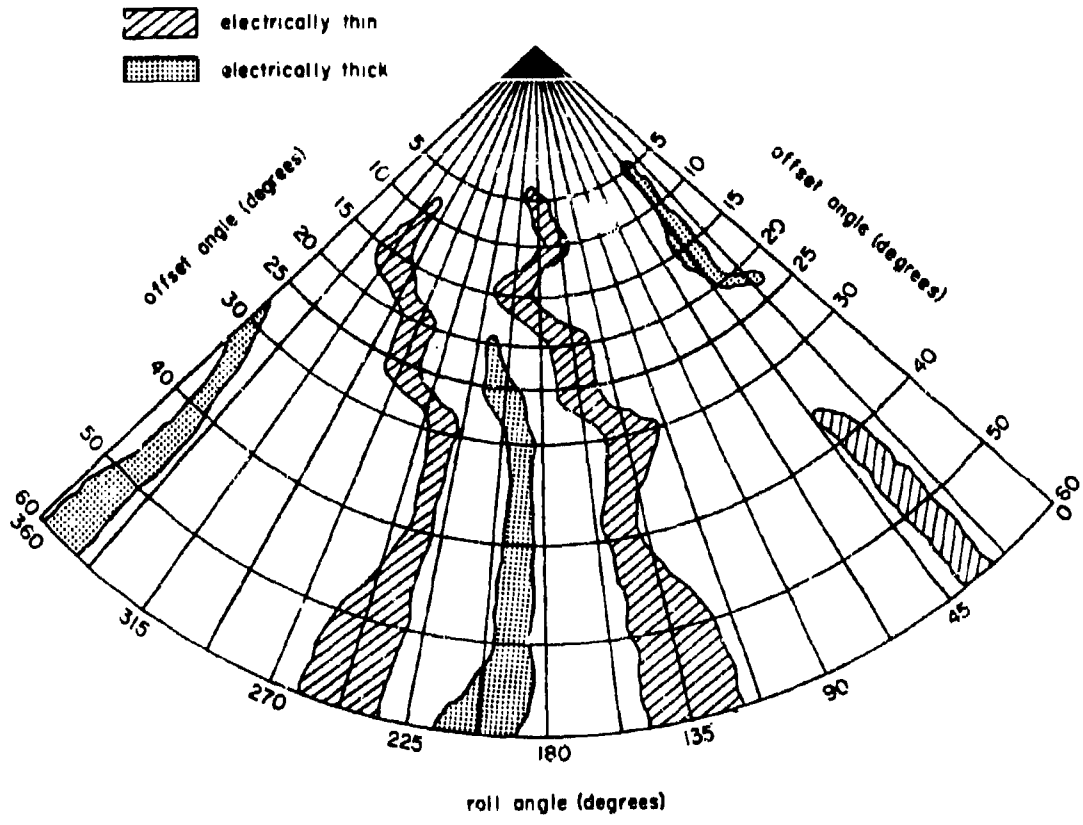


Figure 4-68. Location of Unknown Electrical Non-Uniformity on Test Radome by Vector Method

vious one in that the additional effects introduced by varying the polarization are included. The correction technique follows the same pattern as that for a fixed polarization. After this correction is made, another set of roll runs is made with a reference thickness again established at an arbitrary reference. There should be no variation in the curves themselves for each corresponding roll run, but the reference levels of the horizontal curves will be above or below the reference thickness. The shift in the level indicates whether a given location is thick or thin. (This method has not been experimentally verified at the time of writing.)

The correction technique has been used with dielectric patches on a typical interceptor system, and a substantial reduction in error slopes and magnitude was achieved. The results of this program can be used as a guide to the correction of small radomes (conventional missile radomes). It is thought, however, that the technique is more beneficial with large radomes. Errors of missile-type radomes have been more specifically corrected by the use of dielectric rings.

4-56. Dielectric Rings*

A systematic experimental technique has been established by means of which the inherent error in a given radome can be corrected. By this technique the residual error in the radome can be reduced. As presently used, the procedure consists of the placement of dielectric rings on the inner radome surface. The location of the rings and their thicknesses are determined mathematically through a minimizing procedure.

Experimental Technique. The major portion of the work on corrective dielectric rings has been done in connection with the development of

*This technique and associated explanatory literature are covered by a Department of Commerce secrecy order.

a streamlined radome for the Hughes GAR-1A Falcon missile.[42] The contour of this radome is essentially ogival and the base of the radome is just large enough to fit over a 5-inch reflector dish. Typically, a very flat crosstalk error curve is obtained with this type of radome so that the in-plane error curve is the major problem. The in-plane error curve has a number of oscillations which contain slopes as high as 0.08° per degree. When a corrective ring is inserted in the radome, a large change in the in-plane error curve will result. It can be observed from Figure 4-70 that this particular ring has the effect of reversing the nature of the error slope. Since this reversal is possible, it can be reasoned that an error curve can be made flat in certain regions so that at least the large error regions can be corrected. Therefore, to correct the in-plane error, an error must be introduced into the radome so that the two curves will cancel. Dielectric rings can be used to introduce such an error to minimize the net in-plane error. The rings used in development of the technique were made of the same material as the radome and formed to the same contour (Figure 4-71); however, other dielectric materials can be used to achieve the same results.

With the ring technique, the error curve of a radome alone is recorded. Then, one at a time, each ring is inserted inside the test radome and fastened temporarily at the point at which the configurations matched. For each ring inserted, an in-plane error curve of the radome-ring combination is recorded; the data

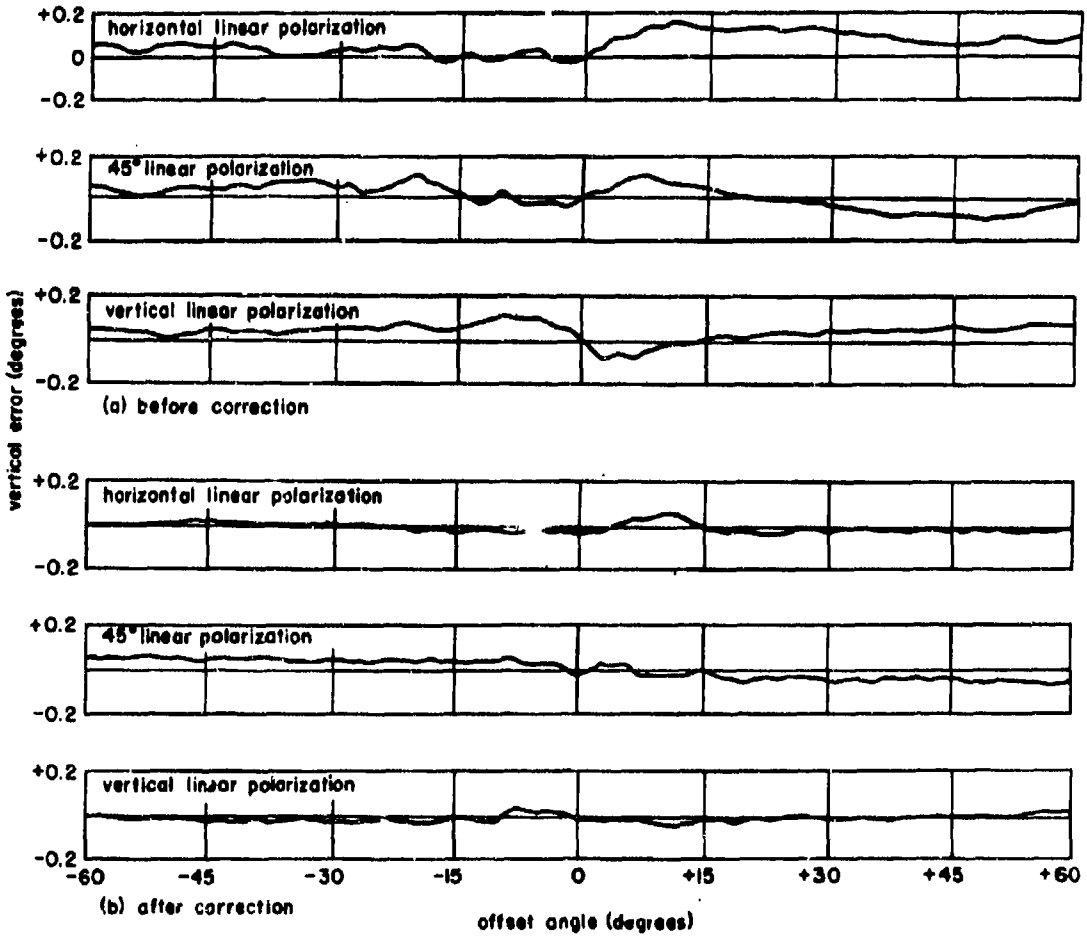


Figure 4-69. Comparative Vertical Error Curves of Test Radome, Before and After Correction of Asymmetry: (a) Before Correction; (b) After Correction

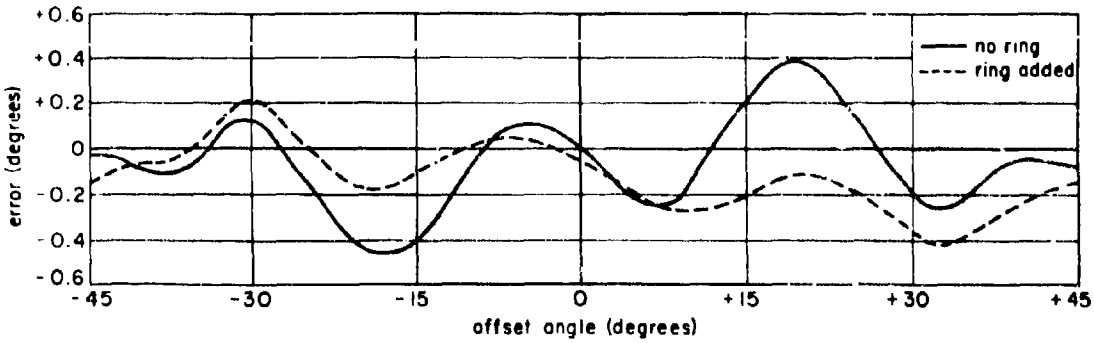


Figure 4–70. Effect of Dielectric Ring on In-Plane Error Curve



Figure 4–71. Fabrication of Dielectric Rings: Application of the Ring Correction Technique Is Facilitated if the Rings Have the Same Contour as the Radome to be Corrected. Shown Above are the Rough Radome (Left), Finished Radome (Center), and the Corresponding Rings (Right) Fabricated in Development of the Technique

points are taken from each curve and listed in tabular form. Ring effect curves are calculated from these tables by subtracting the radome error curve from each radome-plus-ring error curve. By this subtraction method an effect curve for each individual ring is obtained. (As a check on this method the rings were tested individually in free space; the same effect curves were obtained as were obtained by subtraction.) To correct the in-plane error of the radome, a combination of ring error curves is found which, when added, gives an error curve opposite from that of the radome. The rings corresponding to the desired error curves are placed in the radome, which is then tested. When a proper combination of rings has been chosen, it can be used on all radomes of the same configuration and materials with the results repeating for each radome, provided there are no additional errors in any radome

as a result of imperfections in fabrication. In the development of the technique, use of the best combination of corrective rings in the test radome reduced the total excursion of the in-plane error curve from approximately 0.7° to 0.3° error and the slope from a maximum of 0.08° per degree to 0.02° per degree or less (Figure 4-72).

Changes in the width and the thickness of the rings have an additive effect. The amount of in-plane error is proportional to the thickness and also to the width of the ring. For example, in the experimental approach, a 1/2-inch-wide ring was placed at the same position in the radome as two adjacent rings 1/4 inch wide. The wider ring gave an error curve identical with the sum of the error curves of the two 1/4-inch-wide rings. Since each individual ring produces an individual effect curve and since effect curves are additive, the radome designer is able to combine, by calculation, several ring error curves to evaluate rapidly the effect the combination will have on the radome without actually performing the measurement.

The additive effect of both the width and the thickness of the rings can be shown graphically. It is possible that, for the best error curve, a set of rings is needed in which each individual ring requires a different thickness. To solve this problem in a nonexperimental manner, a least-square method can be used to determine the best thickness for each ring. A set of rings is taken that gives good error curves and the least-square method is applied to find the optimum thickness. In this manner many needless experiments can be eliminated, and only those combinations need to be measured that have promise.

Applications of the Technique. The dielectric ring technique has given excellent results for a particular experimental radome design. Thus, the question arises, "Is the technique applicable to general radome design?" The method has been applied to two other radome configurations to show its versatility. Figure 4-73 is a comparison of the error of a small thin-skin hemispherical radome before and after ring correction for in-plane error. The slope has been reduced from 0.045° per degree to 0.025° per degree by the addition of rings.

The dielectric ring technique was also applied to a half-wave wall interceptor radome with a large dish and a fairly pointed nose. The error curves with and without rings are shown in Figure 4-74. Again there is a reduction, the radome slopes dropping from 0.05° per degree to 0.01° per degree.

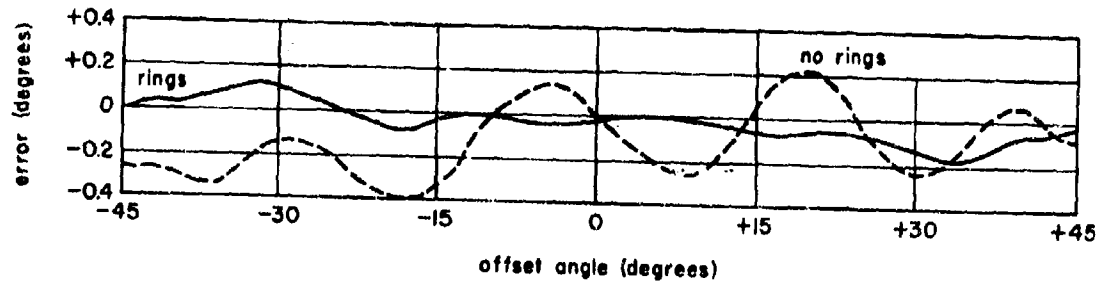


Figure 4-72. In-Plane Error Curves of Test Radome Showing Effect of Ideal Combination of Corrective Rings

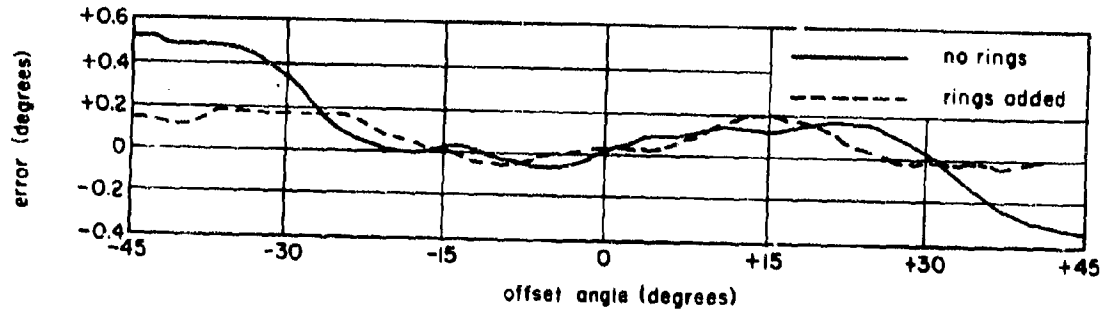


Figure 4-73. Small Hemispherical Radome In-Plane Error Curves With and Without Rings

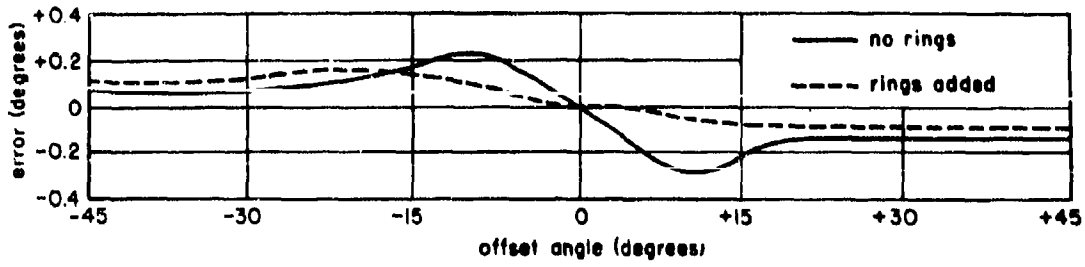


Figure 4-74. Interceptor Radome In-Plane Error Curves With and Without Rings

In addition to half-wave wall and thin-skin radomes, there is reason to believe that radomes of sandwich construction can also be corrected by the dielectric ring technique. Size does not limit the use of the technique, since large and small radomes of both missile and interceptor type have been satisfactorily corrected. Some experimental work has also been done on correction of in-plane error by the use of negative rings in the form of grooves. These grooves are cut in the inner surface of the radome wall and have the reverse effect of a ring placed in the same position.

As a result of these investigations, the radome designer has several choices of methods for compensating a radome. He can use dielectric patches, rings, grooves, or a combination of the dielectric obstacles. Since the ideal radome for production would have a smooth inner contour, a combination that could be molded into the radome is probably the best.

Scattering by a Thin Dielectric Ring. To give a fuller understanding of the effect of the dielectric rings as correcting devices, L. L. Philipson[45] has carried out an analysis of the scattering effect of a thin dielectric ring on an electromagnetic field. The ring inserts can be considered as introducing an out-of-phase perturbation that cancels the radome-caused perturbation of the free-space far-zone power pattern of the antenna. As observed experimentally, the ring perturbation is essentially independent of the presence of the radome, at least for thin dielectric rings and low-reflection radomes. Thus, for calculation of the effect of the ring as an error-correcting device, it is only necessary that the ring be considered in free space and illuminated by an electromagnetic field.

As noted in Equation (4-80), various investigators have utilized Maxwell's equations to show that the volume polarization currents, J of Equation (4-77), radiating in free space in the absence of the scatterer, may be regarded as the source of the field scattered by a dielectric body such as the radome of Section 4-45 or the rings of Section 4-56. Under the assumption that the presence of a ring does not appreciably affect the source, Barrar and Dolph[53] have utilized an integral equation formulation as follows:

$$\underline{H}(P) = \underline{H}_i(P) - \gamma \int_V \underline{F}(P,P_1)\, dV_1 \qquad (4\text{-}121)$$

where $\underline{H}$ = magnetic vector of the total field

$\underline{H}_i$ = magnetic vector of the incident field

P = point of observation

P_1 = point of integration in the obstacle volume

V = volume of the scatterer (in this analysis, the ring)

γ = constant, depending on the difference of the squares of the propagation constants in V and in free space.

The vector function $\underline{F}$ is given by

$$\underline{F}(P,P_1) = \nabla_1 \left(\frac{e^{jk_0R}}{R}\right) \times \underline{E}(P_1) \qquad (4\text{-}122)$$

where the Green's function $\psi = (e^{jk_0R})/R$ involves the distance R between P and P_1. The electric vector of the total field is $\underline{E}$. A further relation between $\underline{E}$ and $\underline{H}$ is Maxwell's equation

$$\underline{E}(P) = \frac{j\omega\mu_0}{k^2} \nabla \times \underline{H}(P) \qquad (4\text{-}123)$$

The scatter is taken to be a thin cylindrical dielectric ring. As indicated in Figure 4-75 the system employed has cylindrical coordinates r, θ, z about the center 0 of a ring with an inner radius a, thickness h, and height $2l$. The method

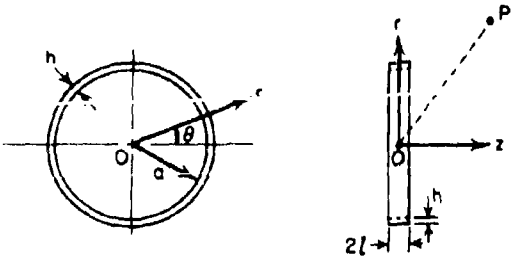


Figure 4-75. Coordinates and Ring Geometry of Approximation Technique: h, Thickness of Ring; 2l, Height of Ring; a, Inner Radius of Ring; r, θ, a, Coordinates; P, Point of Observation

of analysis makes use of a perturbation technique used by J. B. Keller,[54] which leads from the integral equation to a formal expansion for the vectors of the total field in powers of the radial thickness of the ring.

The $\underline{H}$ series can be written in the form

$$\underline{H}(P) = \underline{H}_i(P) + \sum_{n=1}^{\infty} h^n \underline{H}_n(P) \qquad (4\text{-}124)$$

for all P not lying on the inner ring surface or at the sources. The $\underline{E}$ series is analogous. In these formal series it is assumed that the total field reduces to the incident field when the thickness of the ring $h \to 0$.

If the perturbation series is substituted into the integral equation and Equation (4-123) is used, an iteration formula for the vectors $\underline{H}_n$ is obtained. The higher order vectors are difficult to calculate, but the coefficient of the linear term in the series is not. It is possible to write the following equation

$$\underline{H}_1(P) = -\jmath a \int_0^{2\pi} \int_{-l}^{l} (\nabla_1 \psi \times \underline{E}_i(P_1))\, dz_1 d\theta_1 \qquad (4\text{-}125)$$

where only $\underline{E}_i$, the incident electric vector, is required. $\underline{H}_1$ is then calculated by an explicit vector integration.

Experimental work done at Hughes Aircraft Company[55] indicates that for sufficiently small dielectric volumes the scattering effect is linear with respect to changes in volume. For a thin ring the volume is essentially proportional to its thickness; thus, it is practical to consider only the terms through the first power of h in the perturbation series. Moreover, it can be rigorously established that the first order terms in the formal series are asymptotically equal to the total vector for $h \to 0$.

$$\underline{H}(P) = \underline{H}_i(P) + h\,\underline{H}_1(P) + 0(h^2) \qquad (4\text{-}126)$$

provided that, as assumed, the total vectors become equal to the incident vectors as $h \to 0$. For sufficiently thin rings, $\underline{H}_i + h\underline{H}_1$ gives an approximation for $\underline{H}$. As this representation is asymptotic, questions of error bounds and their dependence on various parameters are involved and are best settled by observations on the agreement of measured values with values obtained from the formulas.

When an approximation for the magnetic vector $\underline{H}$ is obtained, a corresponding approximate formula for the far-zone power pattern function is found. If σ is the distance of the far-zone point of observation from the center of the ring, the power pattern function is obtained from Equation (4-127):

$$P = \lim_{\sigma \to \infty} K\left[\left|\sigma e^{-jk_0\sigma} H^{(r)}\right|^2 + \left|\sigma e^{-jk_0\sigma} H^{(\theta)}\right|^2 + \left|\sigma e^{-jk_0\sigma} H^{(z)}\right|^2\right] \qquad (4\text{-}127)$$

where $H^{(r)}$, $H^{(\theta)}$, $H^{(z)}$ are cylindrical components of $\underline{H}$. If the evaluation of $\underline{H}$ is used, P can be written in the form

$$P = P_1 + hP_p + 0(h^2) \qquad (4\text{-}128)$$

where P_1 is the far-zone pattern function of the incident field, without the ring, and P_p is the "first order perturbation" power pattern function.

Measurement and calculations of P, Equation (4-128), were carried out for the condition in which the incident field was generated by a half-wavelength dipole which had the same axis as the ring. Figure 4-76 depicts the geometry of the test situation, ϕ being the angle between the point of observation and the axis. Due to symmetry, calculations and measurements for $0 \le \phi \le 90^\circ$ lying in any plane through the Z-axis are sufficient. Since the radiated power of the dipole is small near the axis, only a range $30^\circ \le \phi \le 90^\circ$ was actually considered. For the calculations and measurements, a wavelength of 1.29 inches and a dielectric constant of 6:3 were used. The inner-ring radius (a) was kept constant at 3 inches and the height ($2l$) at 0.5 inch. The thicknesses of the rings (h) were successive doubles of 0.0125 inch. Typical patterns for one

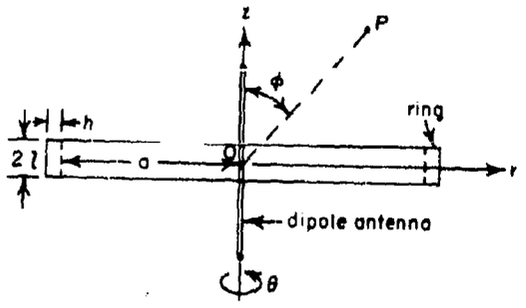


Figure 4-76. Half-Wave Dipole Antenna Coaxial With Ring: a, Inner Ring Radius; 2 l, Height of Ring; h, Thickness of Ring; P, Point of Observation

set of rings studied are represented in Figure 4-77. For these curves the thicknesses of the rings were 0.025 and 0.050 inch. In Figure 4-77 are depicted the theoretical free space dipole pattern, the measured free space dipole pattern, the perturbed pattern as predicted by analysis, and the measured perturbed pattern.

The curves presented are indicative of the good overall agreement that was obtained for rings with a thickness of less than about 0.1 inch. As the thickness of the rings increased, the approximation technique, which is based on an asymptotic expansion of the field in powers of the thickness, became less and less applicable. As indicated previously, establishment of the ranges of the various ring parameters, such as the thickness, which permit a preassigned accuracy of the proposed technique, must await further investigation.

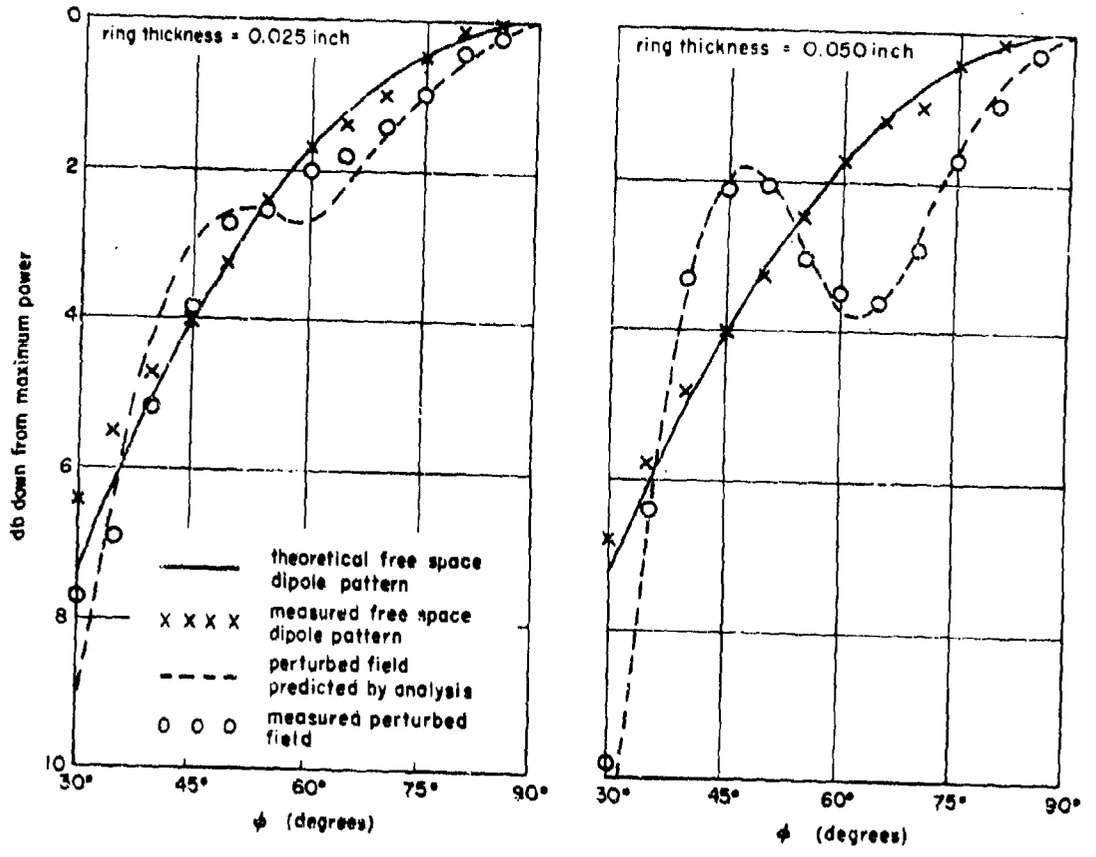


Figure 4-77. Typical Patterns of One Set of Rings Studied

SECTION H. NEAR-FIELD MEASUREMENTS

As was mentioned in the introduction, the size of a radome is of considerable importance in the development and application of accurate prediction methods. Physical optics methods can be used with fair accuracy in the prediction of errors in large radomes, but these methods and their modifications are of little practical use with small radomes. The small physical dimensions increase the severity of the scattering effect of the radome in the antenna-radome system so that the fields contained within the small radome become extremely complex. Similar factors disturb the fields within the large radome but to a considerably less extent. The fields contained by both large and small radomes are part of the near-field or Fresnel region, and before precise analytical methods for predicting radome errors can be completely developed and proved, a full understanding of the near-field radiation of antenna-radome systems appears necessary.

Briefly, the near field includes the fields closest to the antenna aperture and extends an arbitrary distance, $2D^2/\lambda$,* where D is the diameter of the antenna aperture. The outer fields beyond $2D^2/\lambda$ are the far-field or Fraunhofer region. In the far field the measurable field components are transverse; that is, the E and H vectors are at right angles to the direction of propagation. The shape of the field pattern is independent of the radius at which it is taken, because for most purposes the energy can be safely assumed to have been formed into a beam or plane wave by the time it reaches the far field. In the near field, the radial field may be appreciable and the shape of the field pattern is in general a function of the radius.[56] No clear picture has yet been formulated of the fields which exist within the near field, and no simplifying approximations can even be made for the region in the immediate neighborhood of the aperture (the so-called near-zone region).[57] Because of the size of the small radome, most of the fields contained within it will fall into this complex near-zone region. A detailed study of the integrals for this region and for the entire near field is beyond the purpose of the present discussion. It is sufficient to emphasize the importance of the near field in the development of precise analytical methods, particularly for small radomes.

*Some investigators have found that D^2/λ is sufficient to enclose the fields of greatest interest.

4-57. Near-field Measurement Methods

Before the effect of the radome as a scatterer in the antenna-radome system can be analyzed, the near field of the antenna alone needs to be known. Many studies have been and are being worked on, such as those at the Ohio State University Antenna Laboratory,[58,59,60] at McGill University,[61] and at Hughes Aircraft Company.[62,63] The two current methods of studying the near fields of antennas are based on direct measurements of the distribution across different planes of the near field by means of receiving probes or reflecting (scattering) probes. Amplitude and phase data are recorded and plotted at increasing distances from the antenna aperture and for various offset angles to give a picture of the progressive diffusion of the field. (A third method[63] has been suggested which differs from the two conventional plotters in its use of two field-sampling probes instead of one. A phase reference taken from the field itself replaces a fixed reference signal taken directly from the source.) These methods can also be used for measurements of the near field of the entire antenna-radome system, but studies of the radome effect are hampered by lack of sufficiently accurate data on the antenna's near field.

Various near-field measuring techniques are discussed in Chapters 2, 11, and 12.

4-58. An Analysis of the Radiated Field of a Small Radome

A study which deals directly with the antenna-radome problem is now being conducted at the Hughes Aircraft Company. Some of the findings and thoughts which such a study has brought forth will be presented. The equipment used is merely a guide as to what can be used, for there are many other fine measuring setups throughout the country.

Test Setup. The transmitter was a conical scanning antenna which had a reflector aperture of 4.9 inches, and the radome had the Hughes N-65A configuration. A slot-fed quarter-wavelength dipole connected to a small missile coaxial feed line was used as the receiving probe. Measurements were made at 9135 megacycles, and horizontal linear polarization was used for both transmitter and probe. Figure 4-78 is a photograph of the test setup, with a closeup of the antenna and radome mount shown in Figure 4-79.

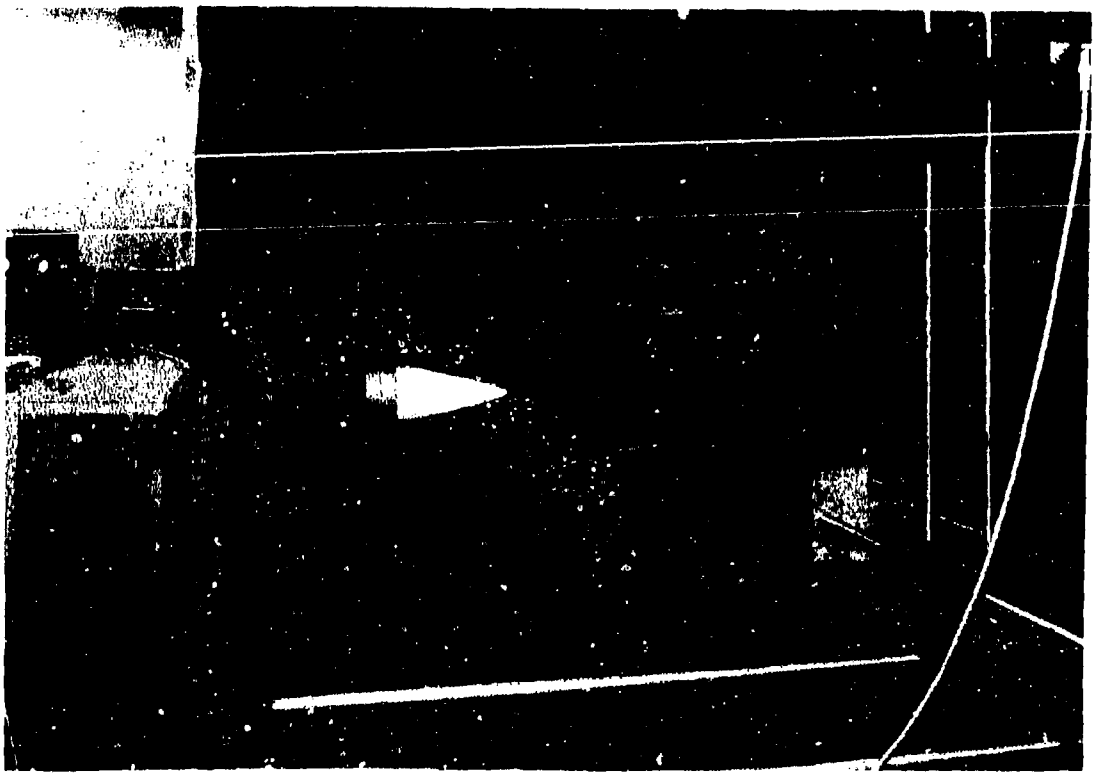


Figure 4-78. Near-field Measuring Apparatus

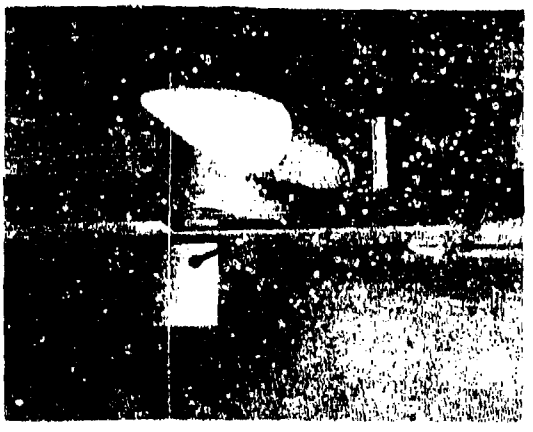


Figure 4-79. Radome and Antenna Mount of Near-field Measuring Apparatus

The radome was mounted on a portion of a missile body so that the radome axis was coincident with the missile body axis at all times. The axes of the reflector and feed also remained fixed in relation to each other. The radome and missile body could be rotated in offset relative to the reflector, either vertically or horizontally, on a gimbal located behind the base of the reflector on the reflector axis (Figure 4-80). Measurements discussed were all made with the radome offset vertically. The receiving dipole was mounted on a carriage to permit motion along three mutually perpendicular axes which are the coordinates used in the measurements: the Z-axis is parallel to the axis of the reflector with the X-axis horizontal and the Y-axis vertical (Figure 4-81).

Determination of Near-field and Far-field Zones. Far-field scans were taken 29.7 inches from the outer perimeter of the reflector. This distance was considered sufficient for far-field measurements for a 5-inch reflector since, according to Silver[64] and others, the minimum distance at which far-field patterns should be measured lies between D^2/λ and $2D^2/\lambda$, where D is the diameter of the reflector. To verify that the 29.7-inch distance was adequate for the far field, the relative power along the reflector axis was measured for zero offset with the radome mounted (Figure 4-82). Amplitude varies

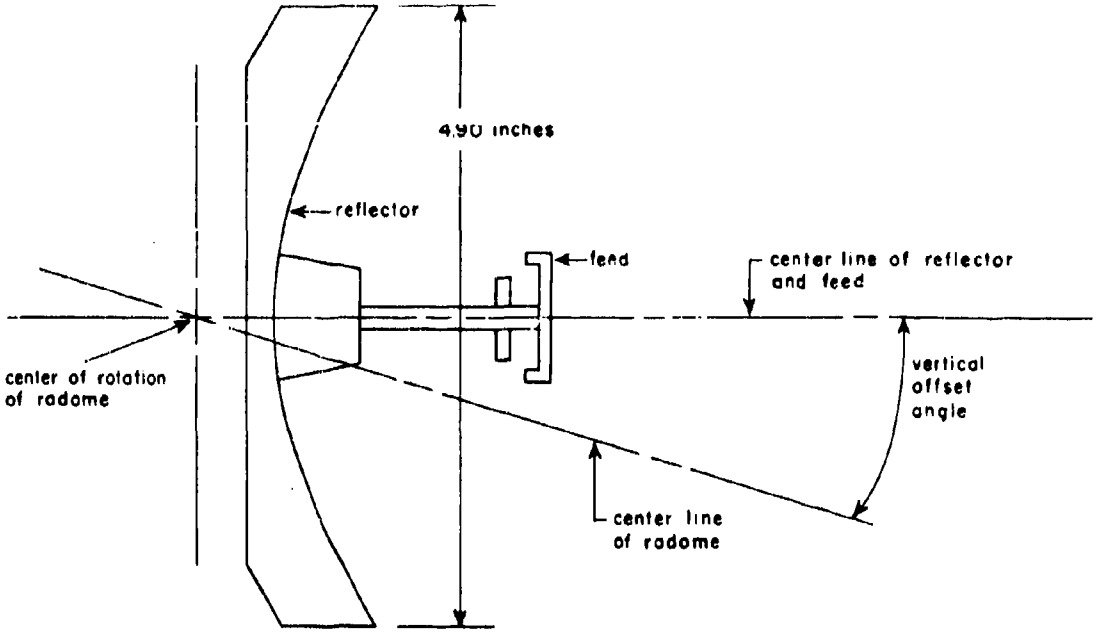


Figure 4–80. Cross Section of Transmitter

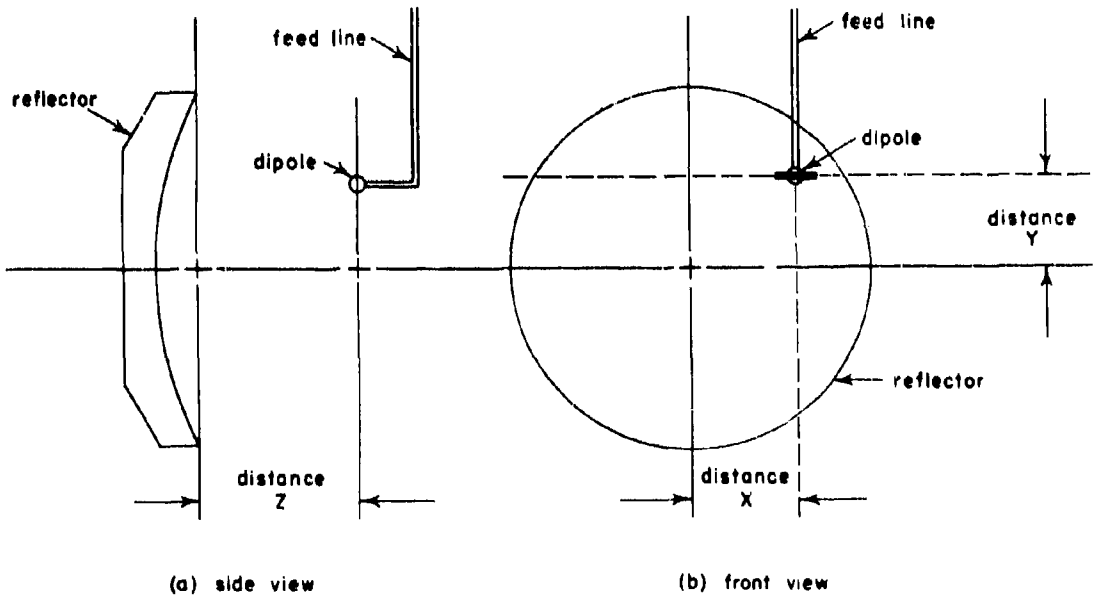


Figure 4–81. Coordinate System and Carriage Motion

inversely as the square of the range; in the far field a $1/Z^2$ variation of power intensity is therefore to be expected. The curve indicating the expected power drop is indicated by the broken line curve in Figure 4-82. Beginning near 18 inches the measured curve approximates the $1/Z^2$ curve but some variations still are apparent. The 18-inch distance is approximately D^2/λ, so that the distance of 29.7 inches is quite adequate for far-field measurements for the

situation in these tests. Figure 4-82 also indicates that the maximum perturbation of the field which could be measured occurred at a distance about 10.5 inches from the antenna aperture along the Z-axis. This distance distinguishes the region in which the near-field measurements were taken. Scans were taken along the X-axis and along the Y-axis.

No-Dome Measurements of the Near Field. Measurements were first made of the amplitude and phase of the near field (no radome). Values of the field were measured at discrete distances from the antenna aperture along the Z-axis in both the Y-Z plane and the X-Z plane. The scans were made in 0.4-inch steps along the two perpendicular axes. Grid patterns were plotted from the measured values, and phase and power contour maps were drawn. In general, the highest amplitude measured in each set was normalized to unity. The grid pattern amplitude measurements and corresponding power contour maps in each plane are plotted in decibels. The value at each point denotes the amplitude level in decibels below the value at the reference point. For the phase measurements the most advanced phase measured in each set was normalized to zero degrees. Figures 4-83 and 4-84 represent the contour maps of the relative phase measurements for the Y-Z plane and the X-Z plane, respectively. The contour maps of the relative amplitude measurements in the two planes are presented in Figures 4-85 and 4-86. The grid patterns are not shown but are available in the literature.[55]

The main value of the grid maps lies in their use in the analysis of the diffraction due to various obstacles which might be in the near field of the antenna. The contour maps present a pictorial view of the near field. They show both a rapid decrease in amplitude as the distance from the reflector axis increases and also the essential planarity of the phase front in the vicinity of the reflector axis. Another interesting observation from the contour maps, especially from Figure 4-84, is the spherical shape of the last two or three phase fronts 10 to 11 inches from the reflector. The shape of these phase fronts indicates that there is a virtual source behind the reflector. Qualitatively, this observation agrees with unpublished results found independently by other investigators at Hughes.

On the Y-Z plane (H plane) amplitude contour map of Figure 4-85, polar radial lines are drawn at the far-field amplitude null and peak angular positions of the sidelobes. The actual far-field H-plane power pattern is shown in Figure 4-87. This pattern was taken with an elliptically polarized pickup horn with a 6-decibel axial ratio. Measurements taken of the cross-polarized component of the field indicated that this component was negligible with respect to the horizontal component, so that, for any practical interpretation of the far-field pattern of Figure 4-87, the pickup horn may be regarded as linearly polarized. It should be noted that the null and peak positions of the sidelobes indicated by the broken lines on Figure 4-87 correspond in angular position to the radial lines drawn on Figure 4-85. Apparently, the sidelobe structure of the far field actually manifests itself very close to the reflector in the region which is considered as the near field. This property of the near field is significant in a number of respects, among which is the fact that the near-field sidelobe structure may reveal the manner in which the field illumination of such obstacles as rods affects the far-field main beam structure. The

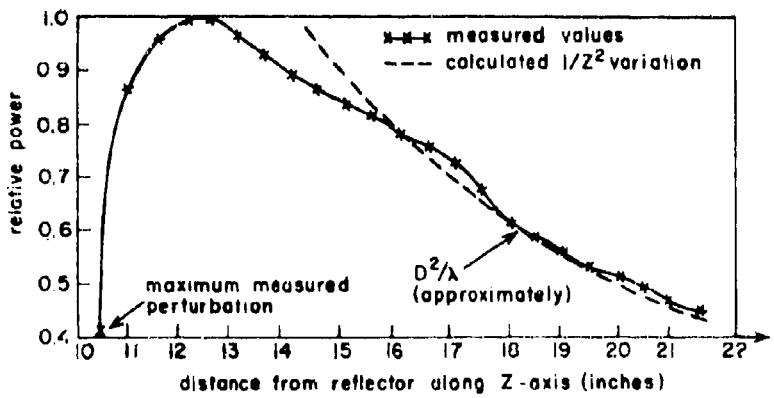


Figure 4-82. Power Pattern for Determination of Near-field and Far-field Regions

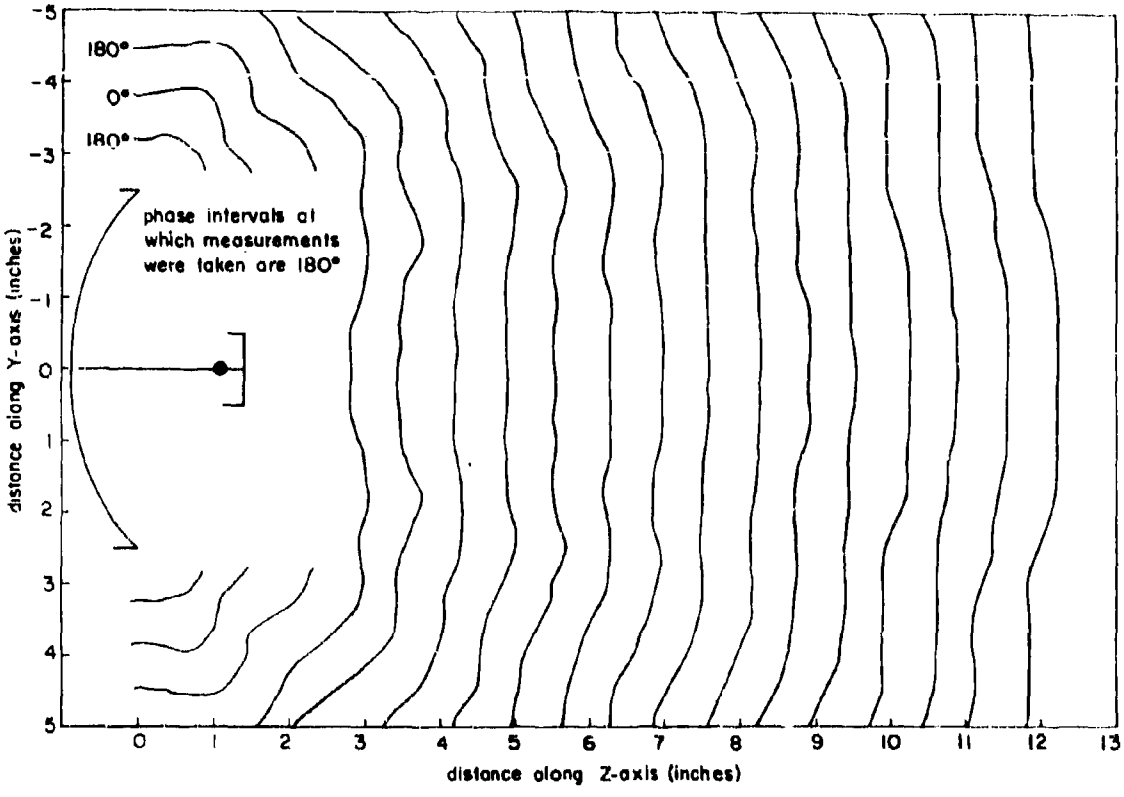


Figure 4-83. No-Dome Constant Phase Contour Map in Y-Z Plane of Antenna Near-field (X = 0)

effect of such obstacles is noticeable in radome error versus offset angle curves of the obstacles.

Relative phase and power graphs (Figure 4-88) were plotted on an increased scale for each plane at the distance from the antenna aperture (Z = 10.45 inches) at which maximum perturbation of the near field had been noticed. Within the limits of error involved in making the measurements,* the sets of graphs for each plane are essentially the same. A similar comparison can be made between the phase contours of the two planes (Figure 4-83 for the Y-Z plane and Figure 4-84 for the X-Z plane) and the power contours (Figures 4-85 and 4-86). The similarity indicates a considerable degree of cylindrical symmetry of the horizontally polarized field. Furthermore, some measurements of the cross-polarized component of the field have shown that this component is essentially negligible in amplitude. This observation is also true of the radial E-field component. (To check the validity of this observation further, some supplementary measurements were taken of the horizontally polarized component of the field when a circularly polarized feed was used at the reflector. The circular feed and reflector radiated circular polarization along the entire Z-axis. The measurements were taken in the same position as those of Figure 4-88, and the measured patterns in each plane were found to be the same as those of Figure 4-88.)

The apparent cylindrical symmetry of the field can be very useful from both analytical and experimental points of view in that it may simplify many of the calculations and measurements necessary in the solution of various diffraction problems. It also appears that the radome errors of various polarizations may be additive in some simple manner to yield the radome error of a

*Interference in the near field caused by the measuring probes and supporting equipment is one of the major problems facing investigators. Most current prediction techniques require empirical data of high accuracy, but it is difficult to obtain these data, since effect of the equipment on the field has not yet been accurately determined.

resultant polarization. The degree to which cylindrical symmetry and polarization separation can be assumed to exist, in consideration of the problem of predicting error to a sufficient accuracy, is being investigated further.

Near-field Measurements with Radome Mounted. With the radome mounted over the antenna, three sets of measurements were made along the X-axis and along the Y-axis relative to the point on the Z-axis at which maximum perturbation had been noticed in the no-dome measurements. It was desired to see what effect the radome would have on the field at this point (Z = 10.45 inches). The measurements were taken with the radome vertically offset at three angles: 0° offset (radome axis and reflector axis coincident), -5° offset, and -20° offset. The measurements at the different offset angles in the Y-axis direction are compared in Figure 4-89 and should be compared also with the no-dome measurements taken along the same line (Figure 4-88). The measurements in the X-axis direction were again essentially the same as those shown in Figure 4-89.

For the radome-mounted measurements at all offset angles there was a large and very definite phase retardation and amplitude reduction in the region near the nose. It can be seen that as the radome is offset the phase retardation and amplitude reduction accompany the position of the nose. As a matter of fact, the minima occur on the line of the radome axis. The broken vertical line in Figure 4-89 denotes the intersection of the radome axis with the line of measurements at an offset angle of -5°. In the curves measured with the radome offset at -20°, no sharp minima are noticeable, since the nose of the radome is out of the range of the line of measurements. What is important, however, is that the phase and amplitude curves at this offset angle compare very favorably with the no-dome curves of Figure 4-88. Even such small differences in amplitude and phase as exist between the -20° offset curves and the no-dome curves, however, are known to give rise to appreciable boresight errors, but it is apparent that the comparatively very large perturbations of the field caused by the radome nose are of primary significance.

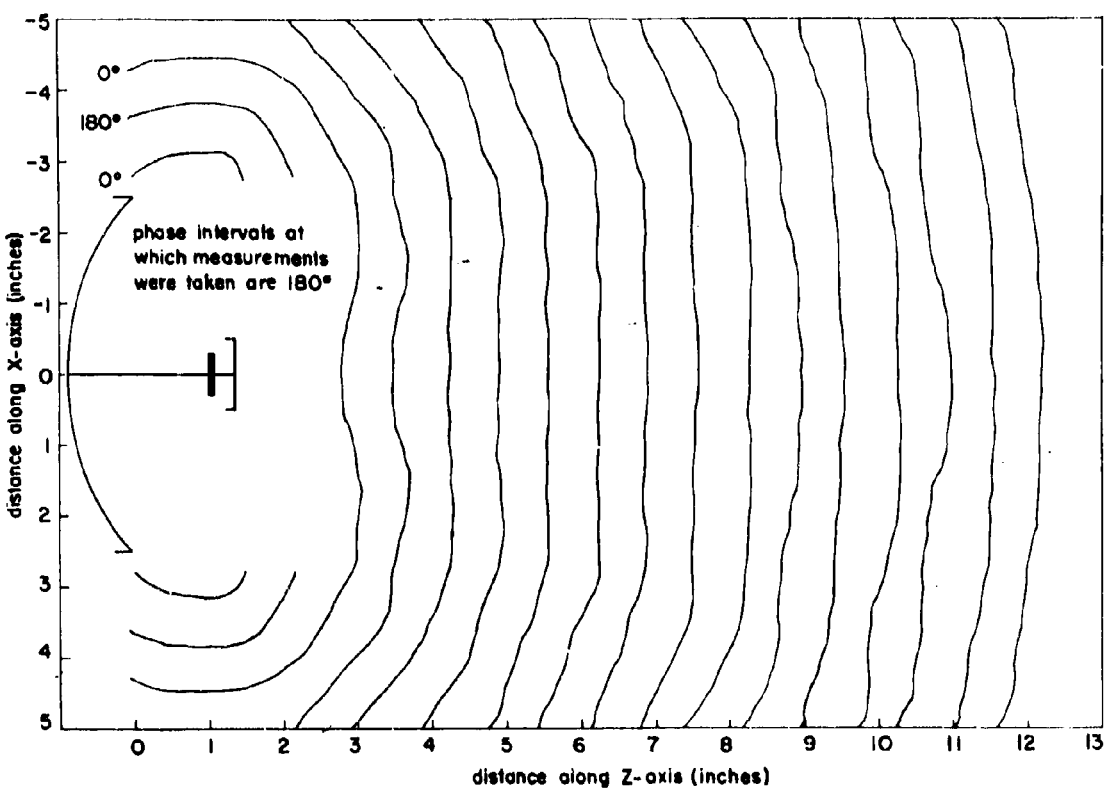


Figure 4-84. No-Dome Constant Phase Contour Map in X-Z Plane of Antenna Near-field (Y = 0)

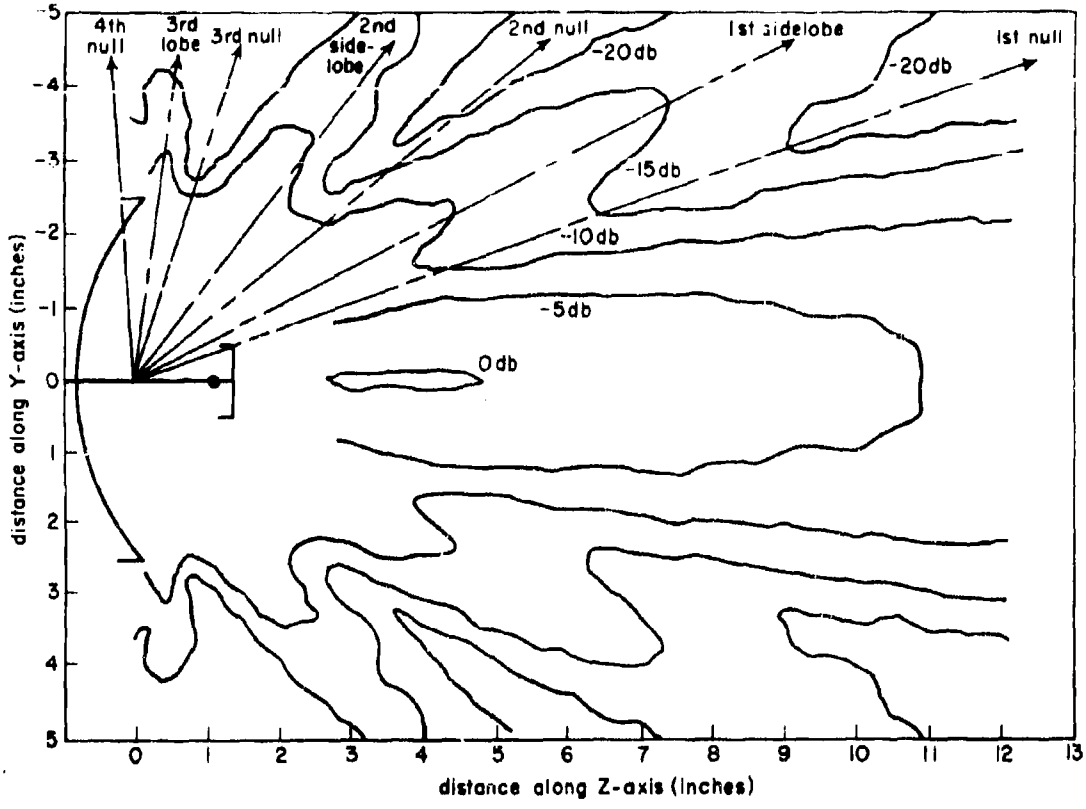


Figure 4-85. No-Dome Power Contour Map in Y-Z Plane of Antenna Near-field (X = 0)

Effect of Compensating Devices on Near-field Distribution. An additional series of measurements was made to see what effect compensating devices had on near-field distribution. Thin dielectric rings and a nose cone were used since these devices have been successful in compensating radome errors (see paragraph 4-56). Preliminary to near-field measurements, error curves were taken of the antenna and radome alone and of the antenna and radome in various combinations with rings and nose cone. Crosstalk errors were found to be negligible for the polarization used (linear and perpendicular to the offset plane), but steep in-plane errors were noticeable. The compensating rings reversed the sign of the errors and reduced the total magnitude when the polarization was perpendicular to the plane of offset; when the polarization was parallel to the plane of offset, no reversal of sign occurred but the total magnitude of the errors was again reduced. The change in the error curves which appeared when the compensating rings were inserted into the radome has been found to depend on the ring configuration only (for thin rings); in other words, this change in error could be effected on any set of obstacles merely by the addition of the same ring configuration to the obstacles.[55]

Measurements similar to those plotted in Figures 4-88 and 4-89 were made of the near-field distribution of the antenna and radome with compensating rings and with rings and a nose cone. As before, scans were taken along the Y- and X-axes at the point of maximum perturbation on the Z-axis. The radome was offset at the same angles as used for the no-dome antenna and the antenna-radome measurements. Results are plotted in Figures 4-90 and 4-91 for the Y-scans. It can be seen that the perturbation of the field due to the rings is insignificant in comparison with the effect of the radome itself. The nulls caused by the radome nose are not so sharp as they are on the curves in Figure 4-89 and are shifted towards the -Y direction.

An analytical technique which has predicted small perturbations of the far field of a half-wave dipole due to a compensating ring has been developed by L. L. Philipson (see paragraph

4-56 and Reference 65). It is hoped that this technique can be applied successfully to predict near-field perturbations such as those shown in Figures 4-90 and 4-91. Further, an analytical technique is being developed which may accurately use known perturbations due to small obstacles, such as the rings, in predicting resultant radome errors.[55] Of particular significance is the fact that both these investigations and other near-field analyses have shown that the perturbation field of compensating rings may be subtracted, linearly, from the perturbation field of the radome and rings combination to yield the radome perturbation field alone.

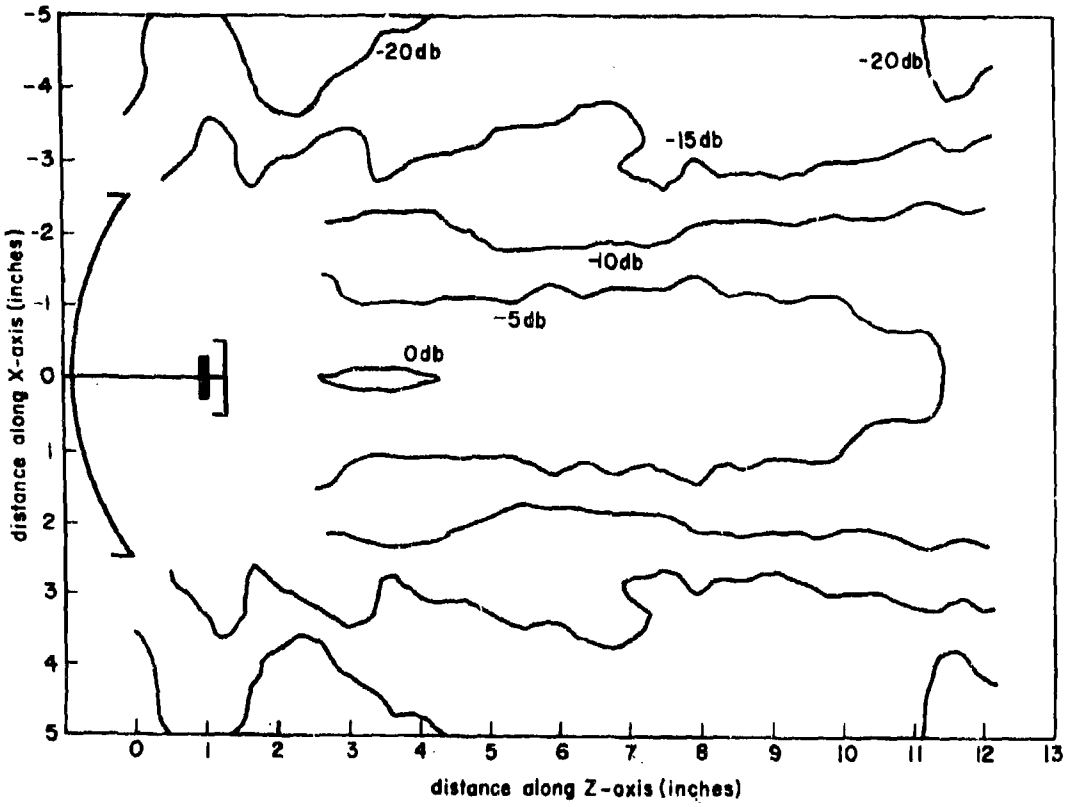


Figure 4-86. No-Dome Power Contour Map in X-Z Plane of Antenna Near-field (Y = 0)

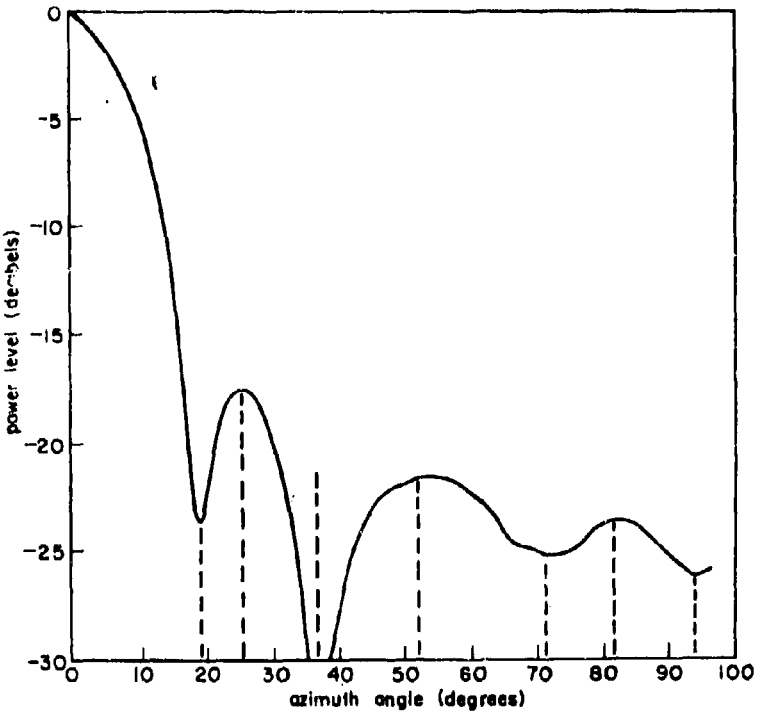


Figure 4–87. Actual Far–field H–plane Power Pattern

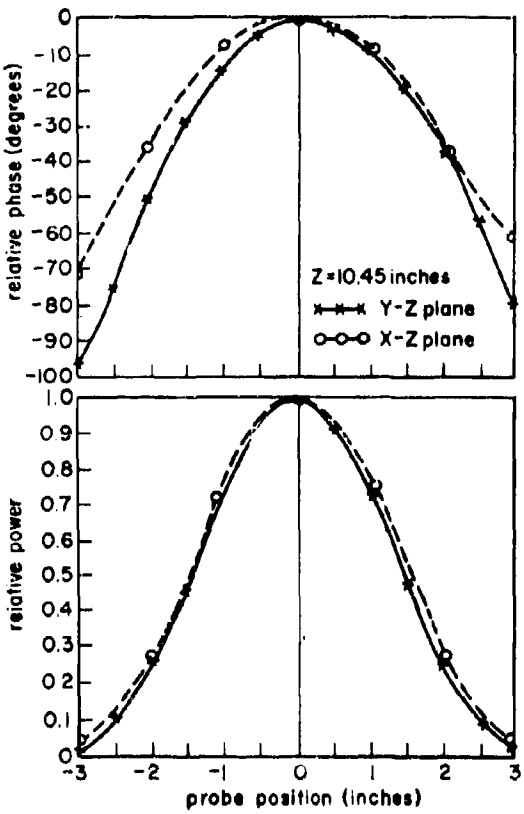


Figure 4-88. Near-field Distribution of Antenna (No-dome) at Point of Maximum Perturbation

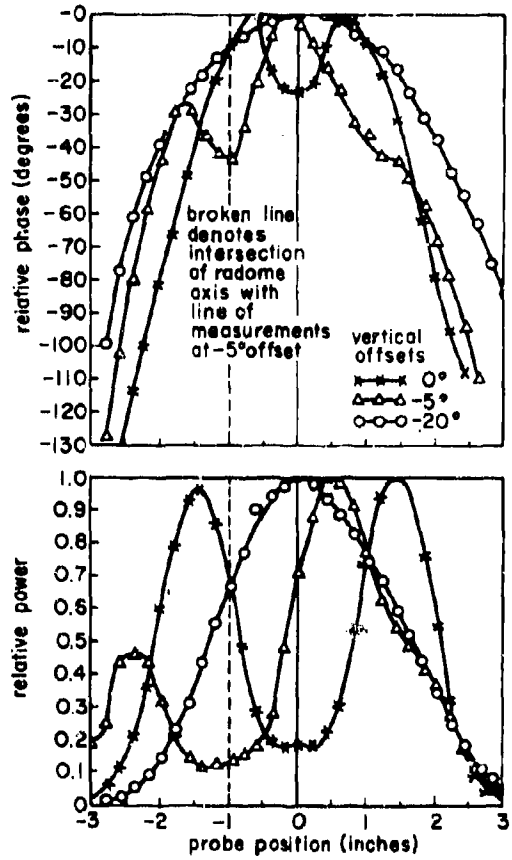


Figure 4-89. Near-field Distribution of Antenna and Radome at point of Maximum Perturbation (X = 0)

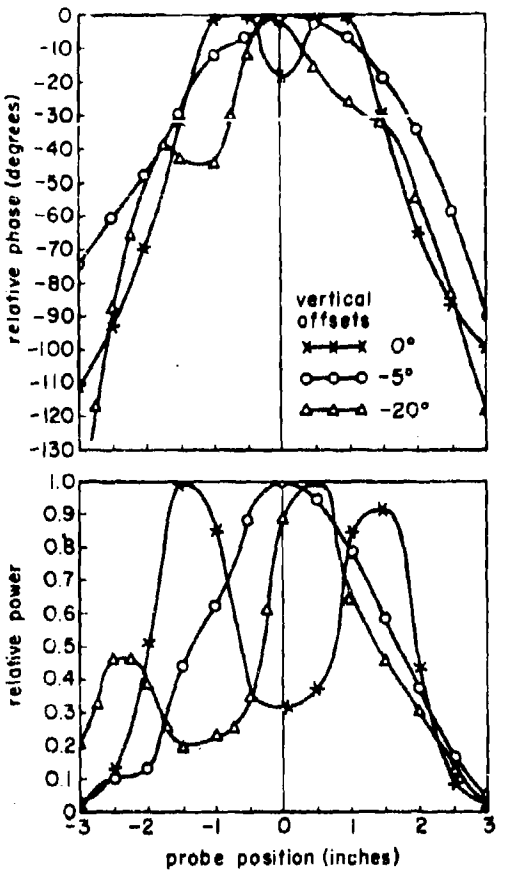


Figure 4-90. Near-field Distribution of Antenna and Radome with Compensating Rings at Point of Maximum Perturbation (Y = 0)

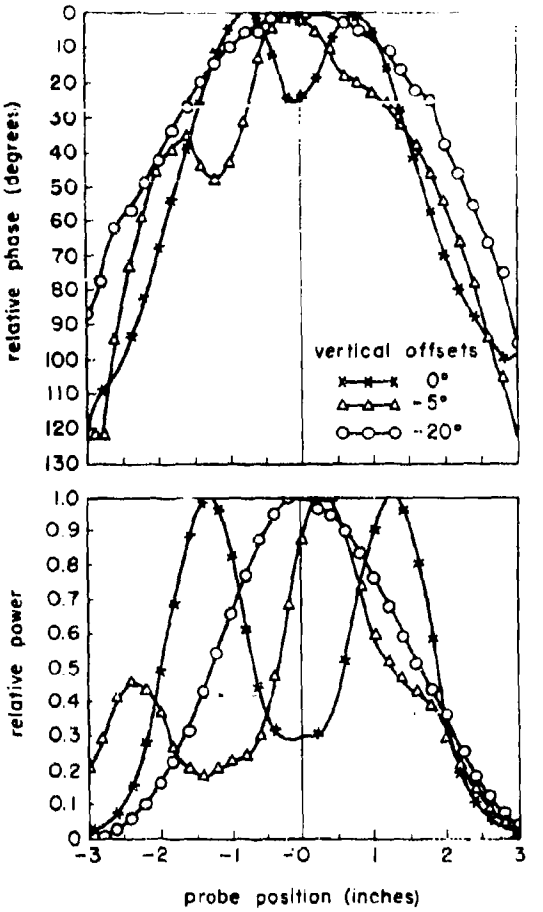


Figure 4-91. Near-field Distribution of Antenna and Radome with Compensating Rings and Nose Cone at Point of Maximum Perturbation (X = 0)

REFERENCES

1. McMillan, E. B., and Redheffer, R. M. A Study of Radome and Radar Antenna Installation Design Criteria. Technical Report No. AF33(038)-12283-6, McMillan Laboratory, Inc., 21 August 1951.

2. Redheffer, R. M. The Interaction of Microwave Antennas with Dielectric Sheets. Report 438-18, Radiation Laboratory, Massachusetts Institute of Technology, 1 March 1946.

3. Barker, C. B., and Lengyel, B. A. The Effect of Beam Distortion in Conical Scanning. Technical Memorandum No. 404, Research Laboratories, Hughes Aircraft Company, April 1955.

4. An Analysis of the Sources of Radome Error. Appendix B, The Radome Problem in Guided Missiles. Final Report of the Princeton University Radome Study, 1 March 1952, p. B42.

5. Cady, W. M., Karelitz, M. B., and Turner, L. A. Radar Scanners and Radomes. (Massachusetts Institute of Technology, Radiation Laboratory Series. Vol. 26) McGraw-Hill Book Company, New York, 1948.

6. Silver, S. Polarization Errors in Semi-Active Systems. Appendix H, The Radome Problem in Guided Missiles, Final Report of the Princeton University Radome Study, 1 March 1952.

Microwave Antenna Theory and Design. (Radiation Laboratory Series, Vol. 12) McGraw-Hill Book Co., Section 12.3.

7. Muchmore, R. R., and Weiss, L. Radar Echo Scintillation from P-80 and A-20 Airplanes. Technical Memorandum No. 212, Guided Missile Laboratory, Hughes Aircraft Company, 30 November 1948.

8. Wanlass, S. D., Tanielian, G., and Jacob, D. M. X-Band Radar Cross-Section Measurements. Technical Memorandum No. 371, Guided Missile Laboratory, Hughes Aircraft Company, 1 August 1954.

9. Echo Measurements of the F-86 Aircraft at 2600 Mc. Data Set No. 7, 10 May 1952.

Echo Measurements of the F-80 Aircraft at 2600 Mc. Data Set No. 10, 15 August 1952, The Antenna Laboratory, Ohio State Research Foundation.

10. Ament, W. S., MacDonald, F. C., and Passerini, H. J. Quantitative Measurements of Radar Echoes from Aircraft, VI, Corrected F-86 Amplitude Distribution and Aspect Dependence. Letter No. C-3460-143A/52, Naval Research Laboratory, 15 December 1952.

Quantitative Measurements of Radar Echoes from Aircraft, VIII, B-45. Memorandum Report No. 116, Naval Research Laboratory, 28 January 1953.

Quantitative Measurements of Radar Echoes from Aircraft, XI, B-29. Memorandum Report No. 164, Naval Research Laboratory, 25 May 1953.

11. Hay, D. R. Radar Cross Sections of Aircraft. Eaton Electronics Research Laboratory, McGill University, 1 June 1952.

12. Sinclair, G. Modification of the Radar Range Equation for Arbitrary Targets and Arbitrary Polarization. Report 302-19, Contract W36-039sc33634, Antenna Laboratory, The Ohio State University. September 1948.

13. Kennaugh, E. M. Effects of Type of Polarization on Echo Characteristics. Report 389-2, Contract AF28(099)-90, Antenna Laboratory, The Ohio State University, 16 December 1949.

14. Sinclair, G. The Transmission and Reception of Elliptically Polarized Waves. Proceedings of the IRE; Vol. 37, February 1948, pp. 155-158.

15. Kennaugh, E. M. Effects of Type of Polarization on Echo Characteristics. Report 389-1, Contract AF 28(099)-90, Antenna Laboratory, The Ohio State University, 16 September 1949.

16. Kennaugh, E. M. Effects of Type of Polarization on Echo Characteristics. Report 389-9, Contract AF 28(099)-90, Antenna Laboratory, The Ohio State University, 16 June 1951.

17. Boyce, W. E. L. The Angular Error Characteristics of a Radome as a Function of the Polarization of the Field Incident on the Radome. Proceedings of the O.S.U.-W.A.D.C. Radome Symposium, Vol. II, June 1955.

18. Hata, F. T. Depolarization Effects on Radome Errors. Technical Memorandum No. 399, Research Laboratories, Hughes Aircraft Company, 30 June 1955.

19. Silver, S. Polarization Errors in Semi-Active Systems. Appendix H, The Radome Problem in Guided Missiles, Final Report of the Princeton University Radome Study, 1 March 1952.

20. Bailin, L. L., Golvin, B., and McEuen, A.H. Some Considerations of Radome Errors. Presented at the RDB Symposium on Antennas and Radomes, San Francisco, 1 August 1951.

21. Snow, O. J. Discussion of the Ellipticity Produced by Radomes and Its Effect on Crossover-Point Position for Conically Scanning Antennas. Report No. NADC-EL-5108, Naval Air Development Center, 13 November 1951.

22 Webster, R. E. Elliptical Polarization and Radome Errors. Report 663-3, Contract AF-33(616)-3277, Antenna Laboratory, The Ohio State University, 15 November 1956.

23. Webster, R. E., and Moore, D. P. Transmission Coefficients of Elliptically Polarized Waves Incident on Homogeneous Isotropic Panels. Report 663-5, Contract AF 33(616)-3277, Antenna Laboratory, The Ohio State University, 31 December 1956.

24. Webster, R. E., and Moore, D. P. Transmission Coefficients of Circularly Polarized Waves Incident on "A" and "C" Sandwich Panels. Report 663-6, Contract AF 33(616)-3277, Antenna Laboratory, The Ohio State University, 31 December 1956.

25. Kotik, J. The Variation of Tracking Error with Dish Illumination Polarization in 1-way and 2-way Conical Scanning Systems. McMillan Laboratory Report No. 1293, Contract NONR-1247(00), November 1954.

26. Fire Control Errors Caused by Radome Errors. The Integrated Electronic and Control System — Project MX-1179, Study Report of 1 March 1952, Part IV-1, Research and Development Laboratories, Hughes Aircraft Company.

27. Berman, B. The Attack of a Rocket Bearing Interceptor on a Passive B-29 Type Bomber. Technical Memorandum No. 243, Fire Control System Laboratory, Hughes Aircraft Company, 10 November 1950.

28. Moreno, T., Mathews, W. E., and Greenbaum, M. The Effect of Radome Error on Falcon Navigation. Technical Memorandum No. 258, Guided Missile Laboratory, Hughes Aircraft Company, 15 October 1951.

29. Damonte, J. B., Hahn, G. M., and Gunter, R. C., Jr. Error Prediction Methods. Proceedings of the W.A.D.C.-O.S.U. Radome Symposium, Vol. III, June 1955, pp. 9-19.

30. Redheffer, R. M. Beam Alignment in Radomes — Part I. Technical Report No. AF33(038)-12283-6, McMillan Laboratory, Inc., 21 August 1951.

31. Barker, C. B., and Lengyel, B. A. The Effect of Beam Distortion in Conical Scanning. Technical Memorandum No. 404, Research Laboratories, Hughes Aircraft Company, April 1955.

32. Kay, Alan F. The Two-Step Antenna Model of Radome Boresight Errors. Contract No. NONR-1247(00), McMillan Laboratory, Inc., 10 March 1954.

33. Baechle, J. R., Richmond, J. H., and Stickler, D. C. Antenna Pattern Distortion by a Wedge-Shaped Radome. Report 655-2, Contract AF 33(616)-3212, Antenna Laboratory, The Ohio State University, March 1956.

34. Hahn, G. M., and Pinney, E. J. Three-Dimensional Error Prediction. Proceedings of the O.S.U.-W.A.D.C. Radome Symposium, June 1956.

35. Stratton, J. A. Electromagnetic Theory. McGraw-Hill Book Company, Inc., New York, 1941.

36. Bailin, L. L., and Silver, S. Exterior Electromagnetic Boundary Value Problems for Spheres and Cones. IRE Transactions on Antennas and Propagation, Vol. AP-4, No. 1, January 1956, pp. 5-16.

37. Richmond, J. H. Antenna Pattern Distortion by Dielectric Sheets. Proceedings of the O.S.U.-W.A.D.C. Radome Symposium, Vol. I, June 1955, Equation (6), p. 97.

38. Cox, W. G. A Design Procedure for Boresight Radomes for Monopulse Systems. Proceedings of the W.A.D.C.-O.S.U. Radome Symposium, Vol. II, June 1955, pp. 160-170.

39. Kofoid, M. J. A Procedure For Making Precision Half-Wave Solid Wall Radomes. Proceedings of the O.S.U.-W.A.D.C. Radome Symposium, Vol. II, June 1955, pp. 232-237.

40. Cope, D., and Donhaiser, J. A Radome and Its Correction to a Boresight Dome on a Production Basis. Proceedings of the O.S.U.-W.A.D.C. Radome Symposium, June 1956.

41. Tsuda, George, and Jenkins, Vaughn. Pointing Error Correction on Interceptor-Type Radomes as Performed on the Hughes Automatic Pointing Error Measuring Facility. Technical Memorandum No. 428, Hughes Aircraft Company, 1 March 1956.

42. Schetne, H. A. The Use of Dielectric Rings in Reducing Radome Error. Technical Memorandum No. 403, Hughes Aircraft Company, 15 June 1955.

43. Lee, Alan F. Beam Alignment in Radomes - Part II. Section D — Tapered Radomes. Technical Report No. AF33(038)-12283-7, McMillan Laboratory, Inc., 14 March 1952.

44. The Radome Problem in Guided Missiles. Final Report of the Princeton University Radome Study, Contract No. N6 ONR-27023, 1 March 1952.

45. Philipson, L. L., and Adler, D. E. On Scattering by a Thin Dielectric Ring. Proceedings of the O.S.U.-W.A.D.C. Radome Symposium, June 1956.

46. Hart, R. W. and Montroll, E. W. On the Scattering of Plane Waves by Soft Obstacles. I. Spherical Obstacles. Jour. Appl. Phys., Vol. 22, April 1951, pp. 376-386.

47. Montroll, E.W., and Hart, R. W. Scattering of Plane Waves by Soft Obstacles. II. Scattering by Cylinders, Spheroids, and Disks. Jour. Appl. Phys., Vol. 22, October 1951, pp, 1278-1289.

48. Montroll, E. W., and Greenberg, J. M. Scattering of Plane Waves by Soft Obstacles. III. Scattering by Obstacles With Spherical and Circular Cylindrical Symmetry. Phys. Rev., Vol. 86, June 15, 1952, pp. 889-897.

49. Rhodes, D. R. On the Theory of Scattering by Dielectric Bodies. Report 475-1, Antenna Laboratory, The Ohio State University, July 1, 1953.

50. Rhodes, D. R. An Investigation of Pulsed Radar Systems for Model Measurements. Report 475-6, Antenna Laboratory, The Ohio State University, December 1, 1953.

51. Cohen, M. H. Electromagnetic Scattering by Dielectric Bodies. Report 475-14, Antenna Laboratory, The Ohio State University, 30 June 1954. Also presented at URSI-IRE Meeting, Washington, D. C., May 1954.

52. Galindo, V., and Hata, F. T. A Study of the Radiation Field of the GAR-3 Falcon Missile System. Technical Memorandum No. 436, Research Laboratories, Hughes Aircraft Co., March 1956.

53. Barrar, R. B., and Dolph, C. L. On a Three Dimensional Transmission Problem of Electromagnetic Theory. Journal of Rational Mechanics and Analysis, Vol. 3, No. 6, November 1954.

54. Keller, J. B. Reflection and Transmission of Electromagnetic Waves by Thin Curved Shells. Research Report No. 172-5, Mathematical Research Group, Washington Square College, New York University.

55. Galindo, V. and Adler, D. E. Experimental Studies on Dependence of Boresight Error on Various Obstacle Parameters. Technical Memorandum No. 431, Research Laboratories, Hughes Aircraft Company, 17 January 1956.

56. Kraus, J. D. Antennas. McGraw-Hill Book Co., Inc., New York, 1950, p. 6.

57. Silver, S. Microwave Antenna Theory and Design. (Massachusetts Institute of Technology, Radiation Laboratory Series, Vol. 12) McGraw-Hill Book Company, New York, 1949, pp. 170 ff.

58. Richmond, J. H., and Tice, T. E. Probes for Microwave Near-Field Measurements. IRE Transactions on Microwave Theory and Techniques, Vol. MTT-3, No. 3, April 1955, pp. 32-34.

59. Richmond, J. H. Measurement of Time-Quadrature Components of Microwave Signals. IRE Transactions on Microwave Theory and Techniques, Vol. MTT-3, No. 3, April 1955, pp. 13-15.

60. Richmond, J. H. A Modulated Scattering Technique for Measurement of Field Distributions. IRE Transactions on Microwave Theory and Techniques, Vol. PGMTT-3, No. 4, July 1955, pp. 13-15.

61. Borts, R. B., and Woonton, G. A. The Effect of the Directivity of the Probe upon the Measurement of Aperture Fields. Technical Report 21, Eaton Electronics Research Laboratory, McGill University, July 1952.

62. Hata, F. T. Investigation of Electromagnetic Field Distortions Caused by Dielectric Sheets, Wedges, and Radomes Placed near an Antenna. Proceedings of the Symposium on Guided Missile Radomes, Washington, D. C., June 1953, pp. 104-116.

63. Ajioka, J. S. A Microwave Phase Contour Plotter. Proceedings of the IRE, Vol. 43, No. 9, September 1955, pp. 1088-1090.

64. Ehrlich, M. J., Silver, S., and Held, G. Studies of the Diffraction of Electromagnetic Waves by Circular Apertures and Complementary Obstacles: The Near-Zone Field. Jour. Appl. Phys., Vol. 26, No. 3, March 1955, pp. 336-345.

65. Philipson, L. L. An Analytical Study of Scattering by Thin Dielectric Rings. Technical Memorandum No. 416, Research Laboratories, Hughes Aircraft Co., 3 January 1956.

Chapter 5

BROADBAND RADOME DESIGN

by

Samuel S. Oleesky

Micronics Division
Zenith Plastics Company
Gardena, California

INDEX OF SYMBOLS

d_c	Core thickness
ECM	Electronic countermeasures
R^2	Power reflection coefficient
T^2	Power transmission coefficient
$\tan \delta$	Loss tangent
$\tan \delta_c$	Loss tangent, core
$\tan \delta_s$	Loss tangent, skin
ϵ	Dielectric constant
ϵ_c	Dielectric constant, core
ϵ_s	Dielectric constant, skin
θ	Angle of incidence

Chapter 5

BROADBAND RADOME DESIGN

5-1. Bandwidth Requirements

In the design of search, navigation, and gun-laying radar housings, normal conditions require that good performance be provided by the radome over a relatively narrow band of frequencies, usually centered about a nominal operating frequency.

For example, a typical armament system may include a radar set operating at 9.2 kilomegacycles with an upper range of 9.5 and a lower range of 8.9 kilomegacycles. Operating band width, then, is about 6.5 percent for the radome involved.

If the performance requirements of the system are not too stringent, conventional approaches to the design problem will usually yield a radome that meets specification requirements. Depending upon size and structural limitations, a thin-wall, half-wave, or "A" sandwich will satisfy the needs of the system.

Performance of such configurations is shown extensively in curves published by Naval Air Material Center[1] and at the Naval Air Development Center at Johnsville, Pa.[2] The former are based upon lossless materials, but have been adequate for simple shapes and low angles of incidence generally encountered in Type I general-purpose radomes. (See Chapters 2, 3, 4 and 13.)

In contrast with the narrow-band applications discussed above, an electronic countermeasures (ECM) specification calls for satisfactory system performance over the band from 1 to 40 kilomegacycles. In terms of radome requirements for such a system, the designer's chief problem is to cover the 10:1 band from about 4 kilomegacycles up to 40 kilomegacycles, since a radome construction that will work satisfactorily in this band will probably also work satisfactorily from 4 kilomegacycles down. Other ECM systems have less stringent requirements, perhaps a 6:1 frequency band or less. A typical boresight radome requires a bandwidth of about ±500 megacycles.

The purpose of ECM Ferret equipment is to determine various properties of an enemy radar or communications system. These may include frequency, location, and pulse characteristics, such as pulse repetition frequency, pulse width, etc. Having established these properties of an enemy radar, the system may be required to set jamming equipment and to release chaff. Such ECM equipment includes various types of antennas designed to receive radiation over wide ranges of frequencies and almost all angles of incidence and polarizations.

One of the many types of ECM Ferret antenna systems is illustrated in (a) of Figure 5-1. This could be a nose radome installation on a reconnaissance airplane. The letters a, b, c, d, e, and f represent sets of receiving horns, shown in (b) of Figure 5-1, which cover the frequency spectrum under investigation. In this case, the horns may also be mounted in the belly or in the wingtips of the aircraft.

If a source of electromagnetic energy is radiating from point t, the signal received by b will be greater than that received by c. By comparing the intensity in b and c, the system gives a good approximation to the bearing of the hostile signal.

To the radome designer, the most important desired factor in the radome performance with

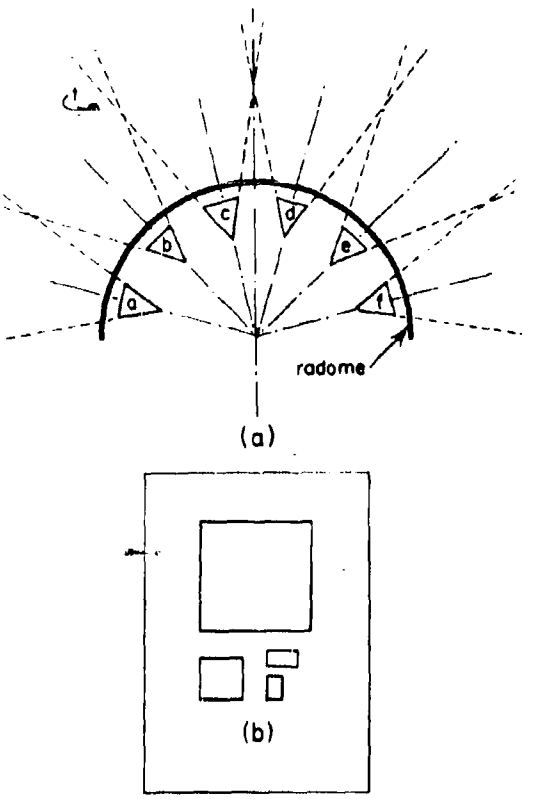


Figure 5-1. Nose Radome for Reconnaissance Airplane; a Through f are Sets of Horns, as Shown in (b)

such a system is absolute uniformity of transmission efficiency as a function of incidence angle and frequency. Variations in transmission of power to any components of the receiving system amount to distortions of the electromagnetic field which would, in effect, give false target-bearing information.

5-2. Solid-Wall Radome

Except for systems with extremely broad bandwidth requirements, the simplest electrical solution to the radome problem is the thin-wall configuration. By general acceptance, this construction is defined as a homogeneous wall whose thickness is of the order of one twentieth wavelength (18°) or less in the dielectric.

At X-band frequencies the physical thickness and strength of such a radome are such that it is doubtful that the thin wall can be used for airborne applications. Figures 5-2 through 5-10 illustrate the performance of several thin-wall configurations at various frequencies. It will be seen that increasing frequency usually reduces the efficiency of power transmission for a given wall thickness.

The family of curves in Figure 5-2 is a simple illustration of thin-wall performance. At a thickness of 0.012 inch, the reflection coefficient of the wall increases continuously from the lowest to the highest frequency shown, with a resultant drop in transmission efficiency. The same trend exists in Figures 5-3 and 5-4. Beginning with Figure 5-5, however, where curves for an 0.048-inch wall are shown, it will be seen that the performance does not continue to drop with increasing frequency. As wall thickness increases, the characteristics of half-wave performance begin to appear. These are progressively apparent in Figures 5-6 and 5-7. In Figure 5-8, for instance, efficiency of almost 90 percent is attained at normal incidence for 35 kilomegacycles.

Figures 5-11 through 5-19 are, in essence, crossplots of the first set, relating efficiency to frequency. These curves have been illustrated to 13 kilomegacycles, but further data, if required, may be selected from Figures 5-2 through 5-10.

5-3. Sandwiches ("A," "B," and "C")

Response curves for "A" sandwiches will be seen in Figures 5-20 through 5-31. Again in these curves, the sensitivity to change in frequency and/or incidence angle is apparent. Serious degradation of performance is evident at angles from 60° upward. The curves presented herein are plotted from tabulated data. Information required for any specific problem should be checked by computation using standard procedures.

The "C" sandwich is a five-layer wall, consisting essentially o' two contiguous "A" sandwiches. Its frequency sensitivity is somewhat less than that of the "A" sandwich, so that it is effective where reasonably increased bandwidth is required.

The McMillan report[3] prefers to treat radome walls from the standpoint of reflected power. In discussing the relative merits of various wall configurations with respect to broad-banding, Webber's chapter of the report[3] says essentially that the "A" sandwich has slightly lower reflections throughout a broad frequency range than the half-wave wall. Figure 5-32 represents the reflected power from three such sandwiches at normal incidence. It shows that the reflection is less than 10 per-

cent up to about 16 kilomegacycles for a 0.200-inch core. As the core thickness increases, the broadness of range below 10 percent reflection is considerably reduced. Other illustrations show that at a 60° incidence angle, the range has been reduced from the 1- to 16- kilomegacycle shown in Figure 5-32 to only 1- to 4-kilomegacycle for reflections under 10 percent.

The three-layer conventional "B" sandwich consists of two skins and a core of dielectric media, with the core having a higher dielectric constant than the skins, usually equal to or greater than the square of the dielectric constant of the skins. Reflections were computed for sandwiches with three cores of different dielectric constants and loss tangents.

In Figure 5-33, the skins are too thin for an electrically efficient "B" sandwich in the X- or K-band range, but the design improves the bandwidth between 65 and 75 kilomegacycles. One may see from Figure 5-34 that the thicker "B" sandwich has less than 10 percent reflection in the 13- to 20-kilomegacycle range and less than 15 percent in the 12- to 24-kilomegacycle range. Figure 5-35 shows that the use of a still thicker skin provides a method of broadening bandwidth at still lower frequencies. Here, the reflection is under 15 percent from about 6 to 13 kilomegacycles. By proper selection of parameters, the 3-layer "B" sandwich may be made to increase bandwidth at any discrete frequency in the range, but like the "A" sandwich, it can only do this to a limited extent. As the skins of the "A" sandwich approach a quarter wavelength in thickness, it becomes considerably less broadbanded than the "B" sandwich. Consequently, the latter proves to be better suited than the former to the construction of mechanically adequate radomes for the higher frequencies.

5-4. Multilayer Sandwiches

As of the date of publication of this handbook, much work is being done toward the development of radome configurations that will provide the necessary uniformity of transmission efficiency over the ranges of frequency and incidence angle required. For the particular ECM system shown in (a) of Figure 5-1, a multilayer* construction appears to be the most promising solution suggested to date. This design, and the methods involved, will be discussed in the following paragraphs. However, as noted previously, all ECM and broadband requirements are not as stringent as the system of (a) of Figure 5-1, and in such cases other wall designs may provide a satisfactory solution.

Methods of computing the transmission of multiple-layer dielectric walls are discussed in Sections B and F of Chapter 2 and in Chapter 13.

Illustrative response curves are given in Figure 5-36 for the frequency range 5 to 30 kilomegacycles. The designation "11-1072 Sandwich" is an identification that represents an 11-layer wall whose skins are 0.010 inch (10 mils) thick and whose cores are 0.072 inch thick. The six skins are laminated glass-resin alternating with five lightweight, equal-thickness cores.

A typical calculated response curve over a wider range of frequencies is shown in Figure 5-37. Variations in skin or core parameters will shift the curves, but the general shapes will not be changed appreciably.

Figure 5-38 illustrates a typical example of the effects of changing core thickness in an 11-layer sandwich. Here a portion of the same curve as that shown in Figure 5-37 is represented by the dotted curve labeled "median core."

As of the date of publication, other approaches to the determination of optimum wall configuration are being studied. One approach, for example, involves the investigation of quarter-wave matching transformer theory, with Tchebyschev distribution of skin and/or core thicknesses.

A serious consideration is the question of maximum practicable wall thickness. Unless the individual skins and cores are held to relatively small dimensions, the ultimate configuration can become cumbersome and heavy. This must be carefully examined in aircraft design, where weight is usually a prime factor.

5-5. Conclusions

For the designer of ECM radomes, then, there are a number of practical solutions. The one selected will be dictated by several governing considerations. First of these is the frequency range in which the radome is expected to perform. In the spectrum below about 3 kilomegacycles almost any reasonable wall will give acceptable response. A solid wall approximately 20 electrical degrees or

*The multilayer design was developed by Micronics, Inc., of Gardena, California, and patent applications have been made.

less in thickness will give good power transmission with low reflection (under 10 percent). An "A," "B," or "C" sandwich will also be efficient if parameters are selected with care.

In the frequency ranges above S-band, the bandwidth required will indicate the probable choice of wall. The term broadband is, after all, only relative. With frequency spread of 1.2 to 1, for instance, acceptable walls may be designed in the same configurations as mentioned in the preceding paragraph. For 2 to 1, 3 to 1, and even 5 to 1, there may be specific combinations that will meet the requirements of the particular system without going into multiple sandwiches.

From present indications, however, when the broadband requirements approach the order of 10, 20, 30, or 40 to 1, the practical solution is the multiple sandwich.

For complete design information, the reader is referred to the work of McMillan and Redheffer and to reports submitted by Micronics Division, Zenith Plastics Company, under WADC Contract AF33(616)-3497. The conclusions in the McMillan final report[3] indicate that:

Feasible "A" sandwiches can be designed for continuous spectrum performance at 0^{o}-40^{o} incidence up to K_u or at 0^{o}-60^{o} up to C band.

Better electrical performance can be obtained up to K_u with the "C", 7-layer sandwiches or higher order multilayer sandwiches, (to the extent that we know the latter) but at that point mechanical usefulness becomes limited.

At the higher frequencies the 3-layer "B" sandwich is mechanically adequate and can be designed to give greater bandwidth in a single band, for example, 16,500 ±3,500 megacycles.

The present state of the art, as published, does not appear to disclose inductive, capacitive, or magnetic loaded walls which will provide a continuous low reflection spectrum to 75 kilomegacycles.

Here again, the conclusions are based upon the definition of bandwidth as far as broadband radomes are concerned. The example of 16,500 ±3,500 megacycles is a little greater than 1.5 to 1, and conventional walls are acceptable in that range. For many ECM applications, other configurations must be examined.

REFERENCES

1. Notes on Electrical Design of Radomes, Radome Div., U.S. N.A.M.C. Philadelphia, Pa., May 1946 (based in part on RadLab 483 series of reports).

2. Wolin, S. Electrical Design of Lossy Radomes. U.S. N.A.D.C. Report No. ADC-EL-123-50, 11 July 1950.

3. A Study of Broadbanding Techniques, McMillan Lab., Inc., Report on WADC contract AF33(600)-28749.

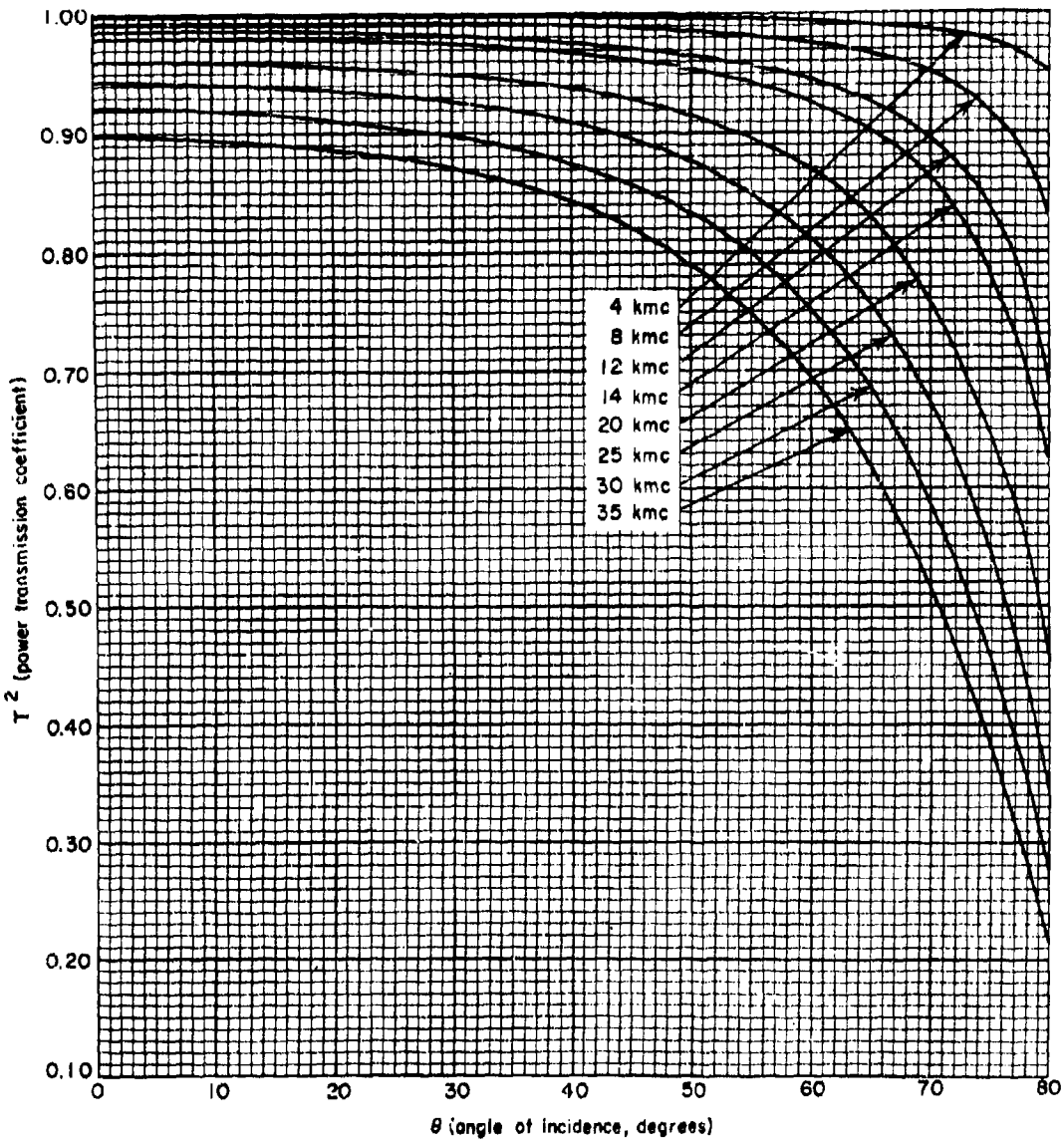


Figure 5-2. Effect of Frequency on Transmission Efficiency, Solid-Wall Radome, Wall Thickness 0.012 in. (ϵ = 4, Tan δ = 0.014, Perpendicular Polarization)

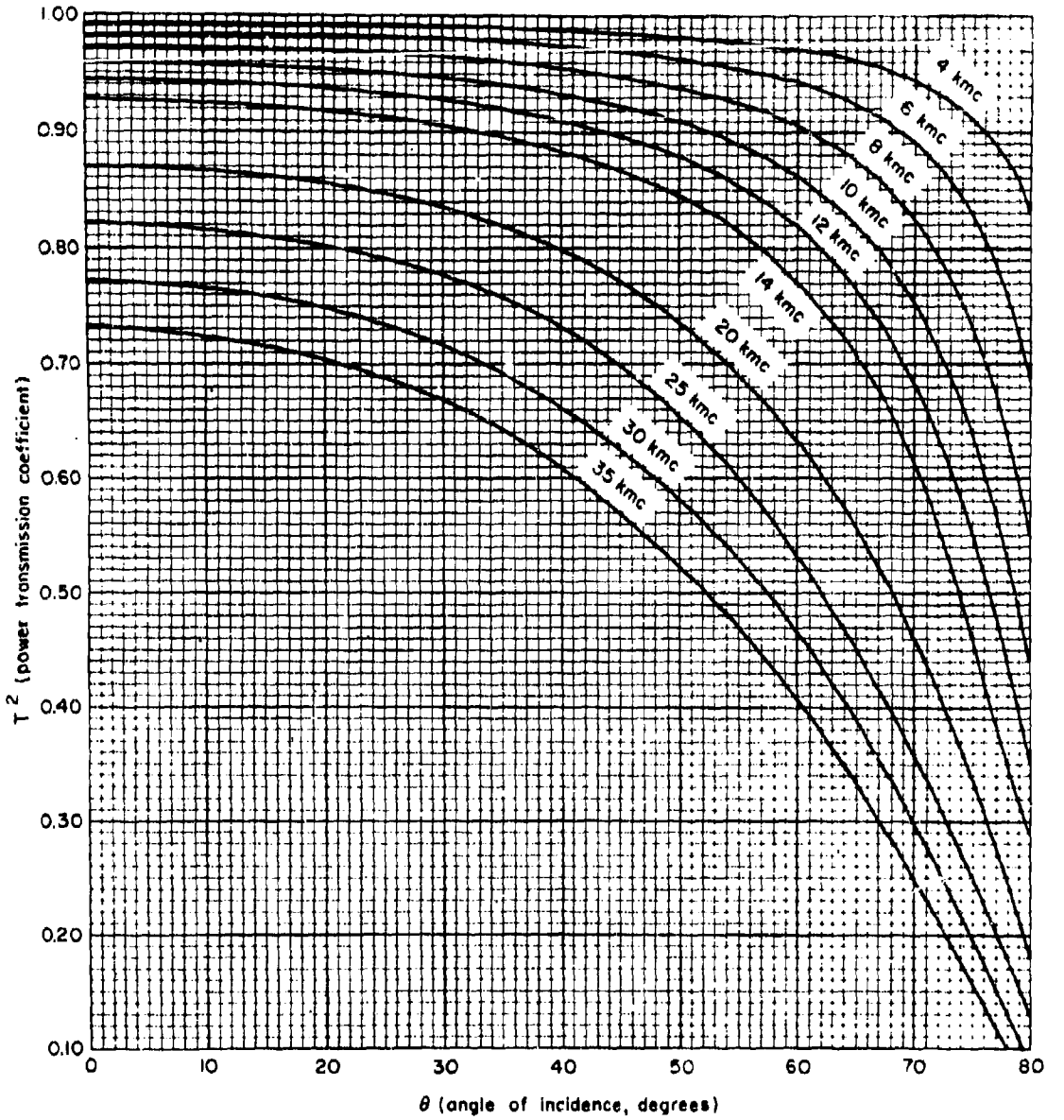


Figure 5-3. Effect of Frequency on Transmission Efficiency, Solid-Wall Radome, Wall Thickness 0.024 in. ($\epsilon = 4$, Tan $\delta = 0.014$, Perpendicular Polarization)

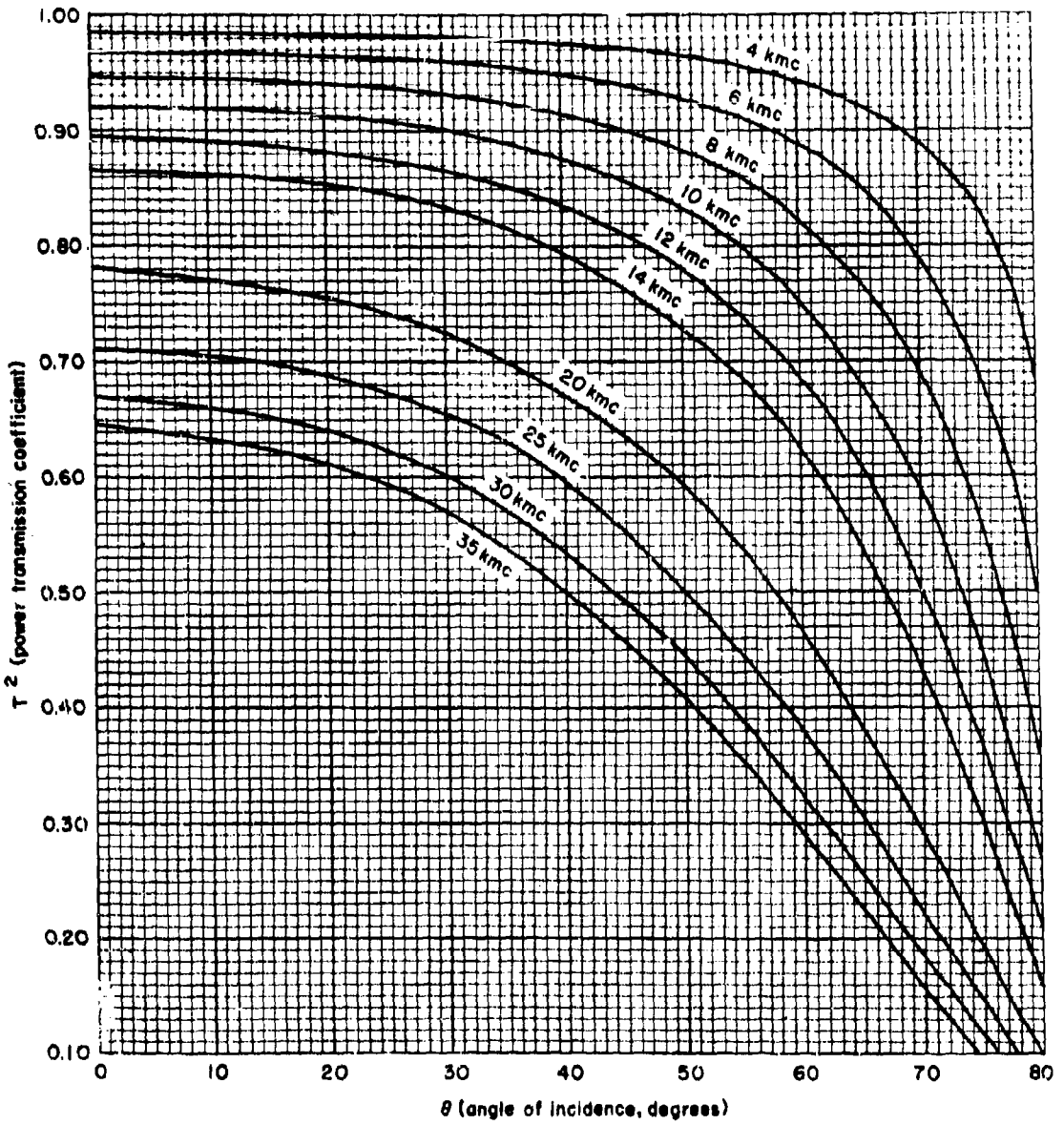


Figure 5-4. Effect of Frequency on Transmission Efficiency, Solid-Wall Radome, Wall Thickness 0.036 in. ($\epsilon = 4$, Tan $\delta = 0.014$, Perpendicular Polarization)

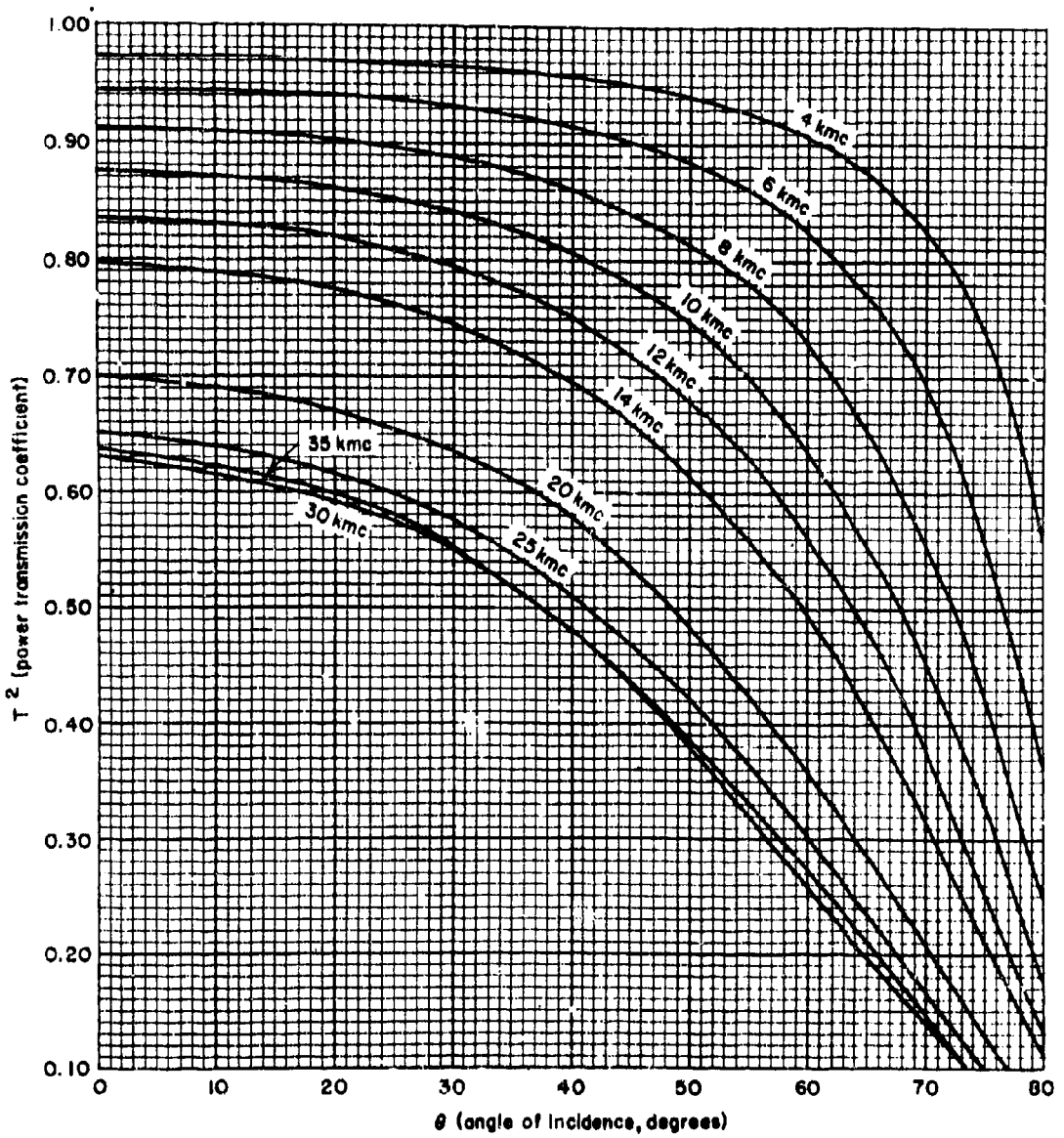


Figure 5–5. Effect of Frequency on Transmission Efficiency, Solid–Wall Radome, Wall Thickness 0.048 in. ($\epsilon = 4$, Tan $\delta = 0.014$, Perpendicular Polarization)

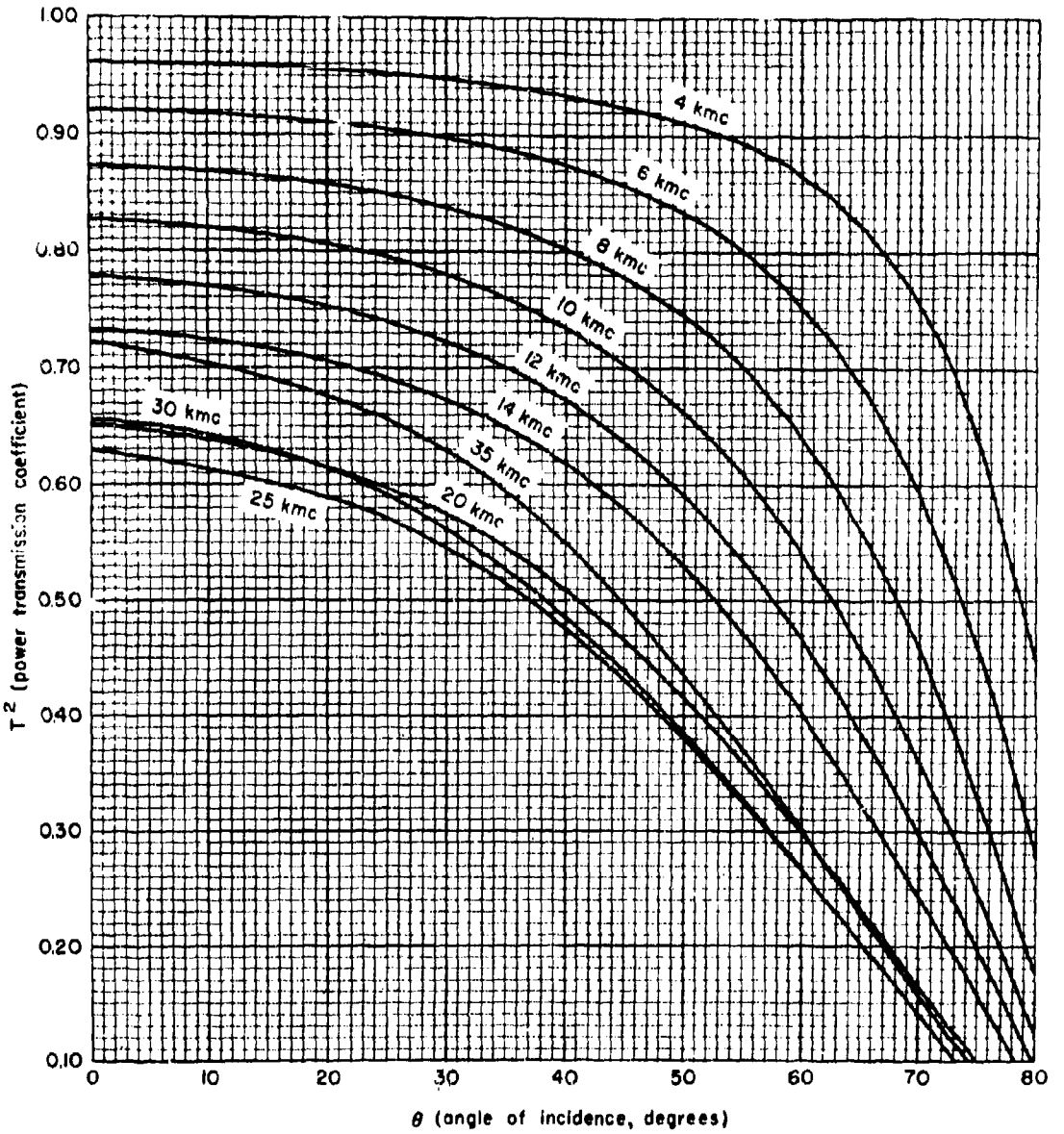


Figure 5–6. Effect of Frequency on Transmission Efficiency, Solid-Wall Radome, Wall Thickness 0.060 In. ($\epsilon = 4$, Tan $\delta = 0.014$, Perpendicular Polarization)

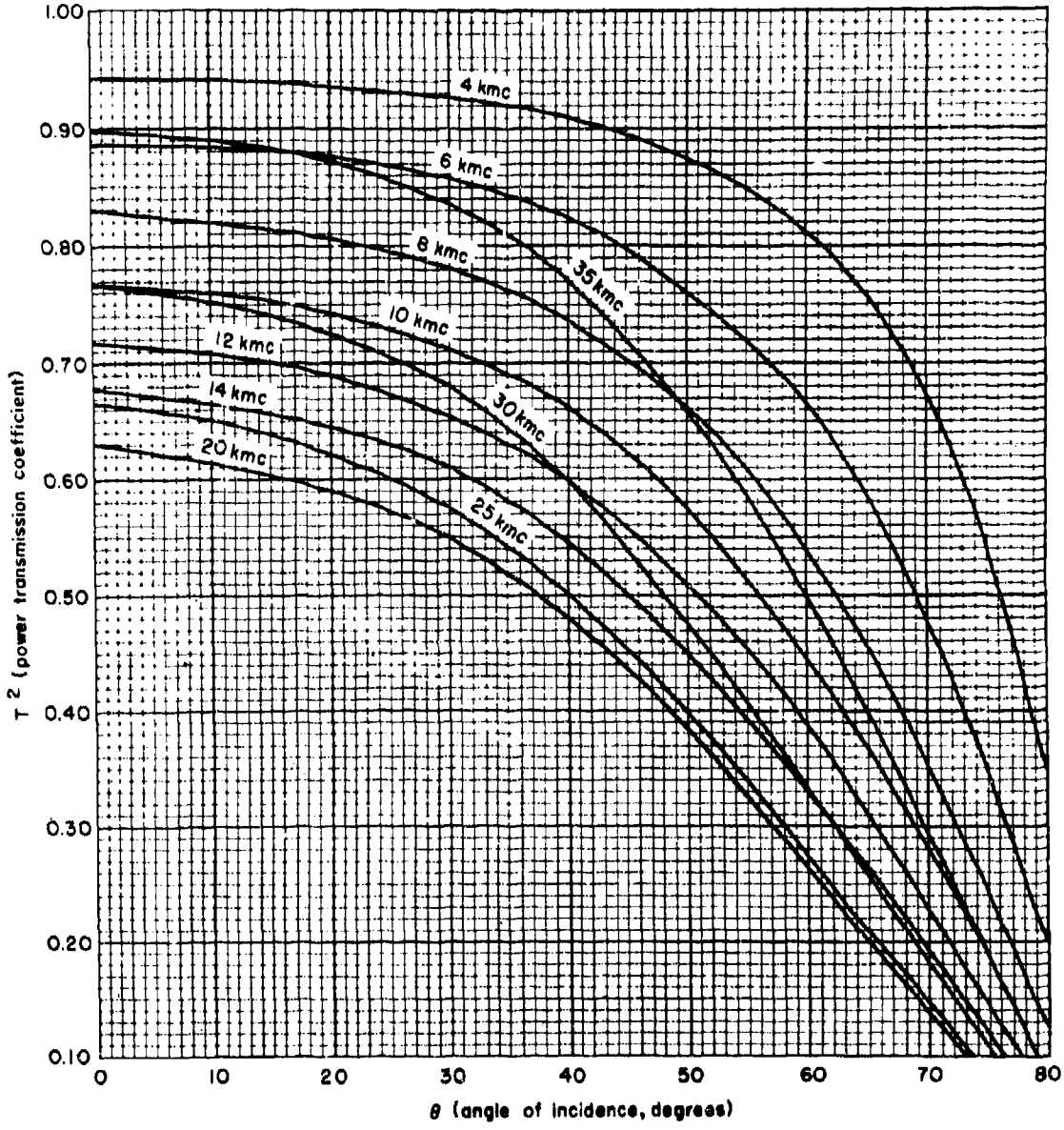


Figure 5-7. Effect of Frequency on Transmission Efficiency, Solid-Wall Radome, Wall Thickness 0.075 in. ($\epsilon = 4$, Tan $\delta = 0.014$, Perpendicular Polarization)

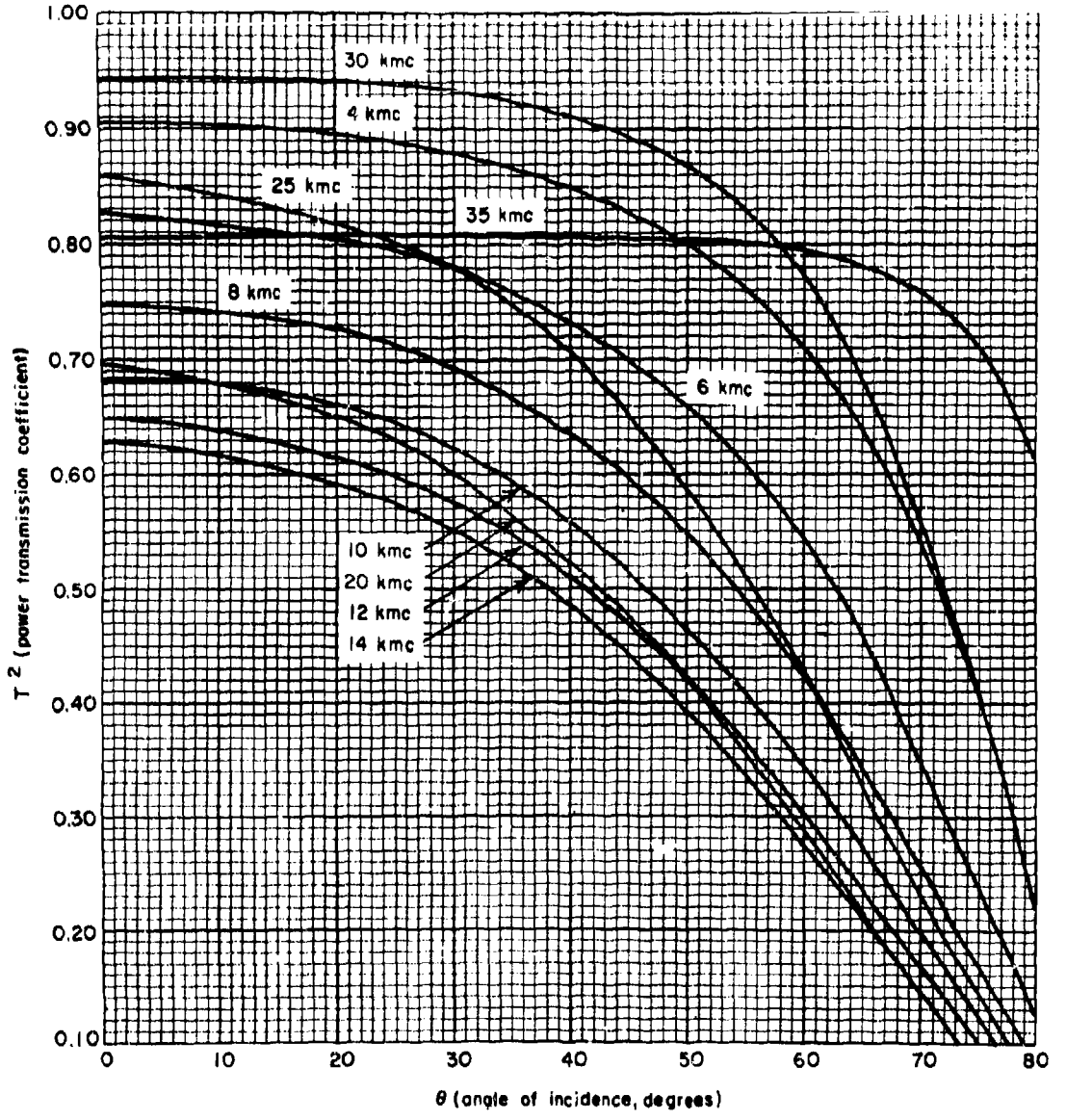


Figure 5–8. Effect of Frequency on Transmission Efficiency, Solid-Wall Radome, Wall Thickness 0.100 In. ($\epsilon = 4$, Tan $\delta = 0.014$, Perpendicular Polarization)

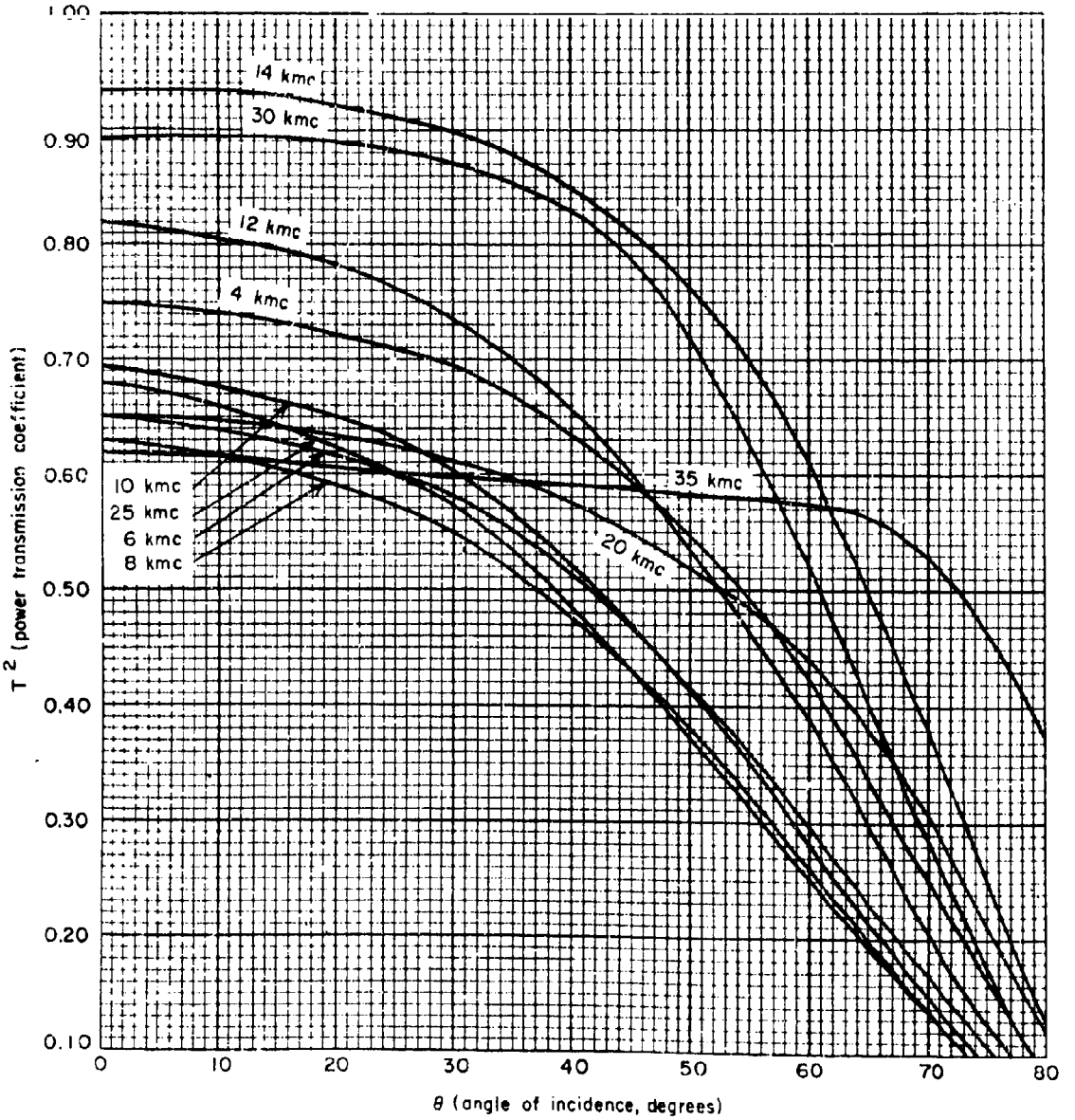


Figure 5–9. Effect of Frequency on Transmission Efficiency, Solid–Wall Radome, Wall Thickness 0.200 In. (ϵ = 4, Tan δ = 0.014, Perpendicular Polarization)

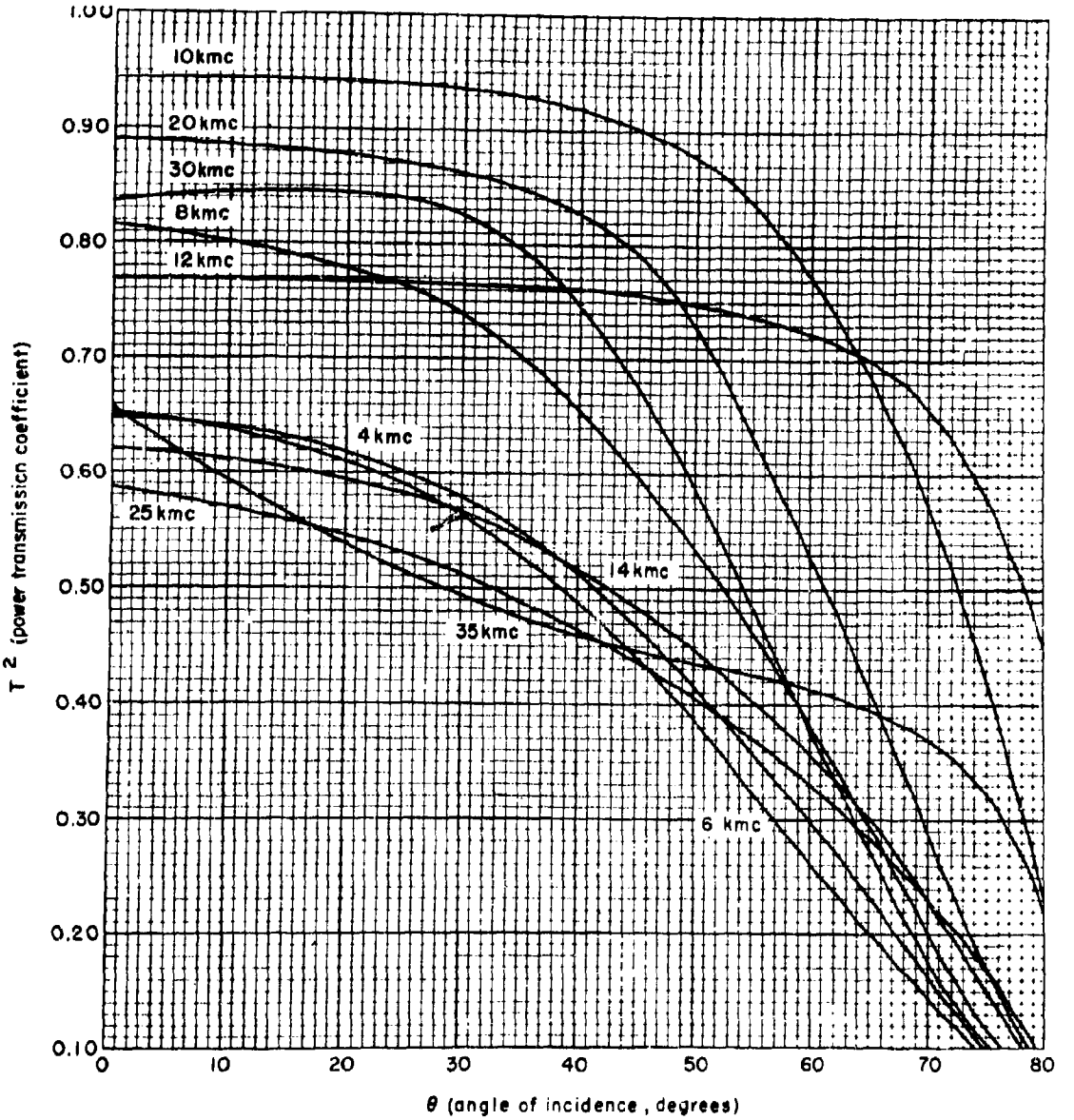


Figure 5–10. Effect of Frequency on Transmission Efficiency, Solid–Wall Radome, Wall Thickness 0.300 in. ($\epsilon = 4$, Tan $\delta = 0.014$, Perpendicular Polarization)

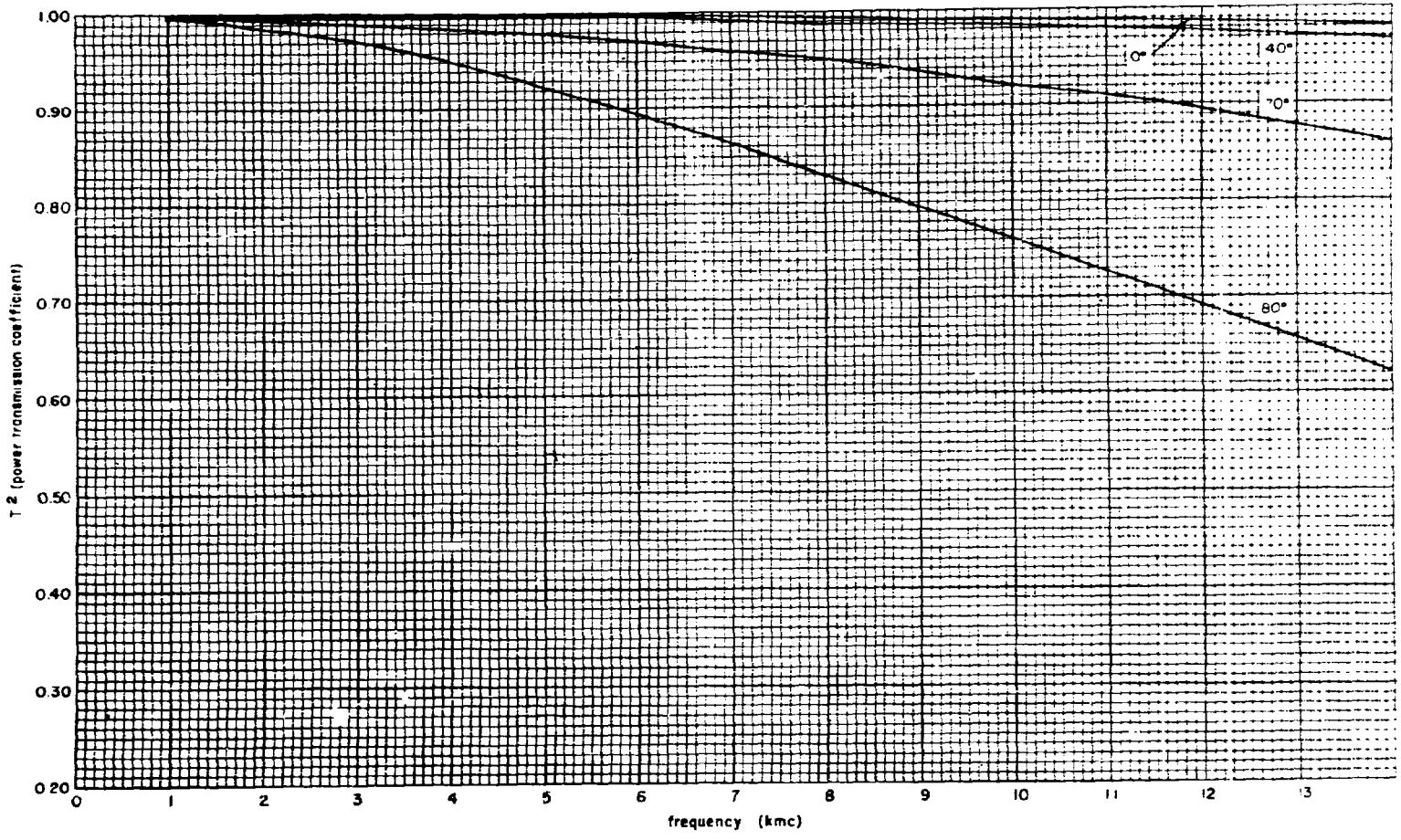


Figure 5–11. Solid–Wall Radome Transmission Efficiency, Wall Thickness 0.012 In. (ϵ = 4, Tan δ = 0.014, Perpendicular Polarization)

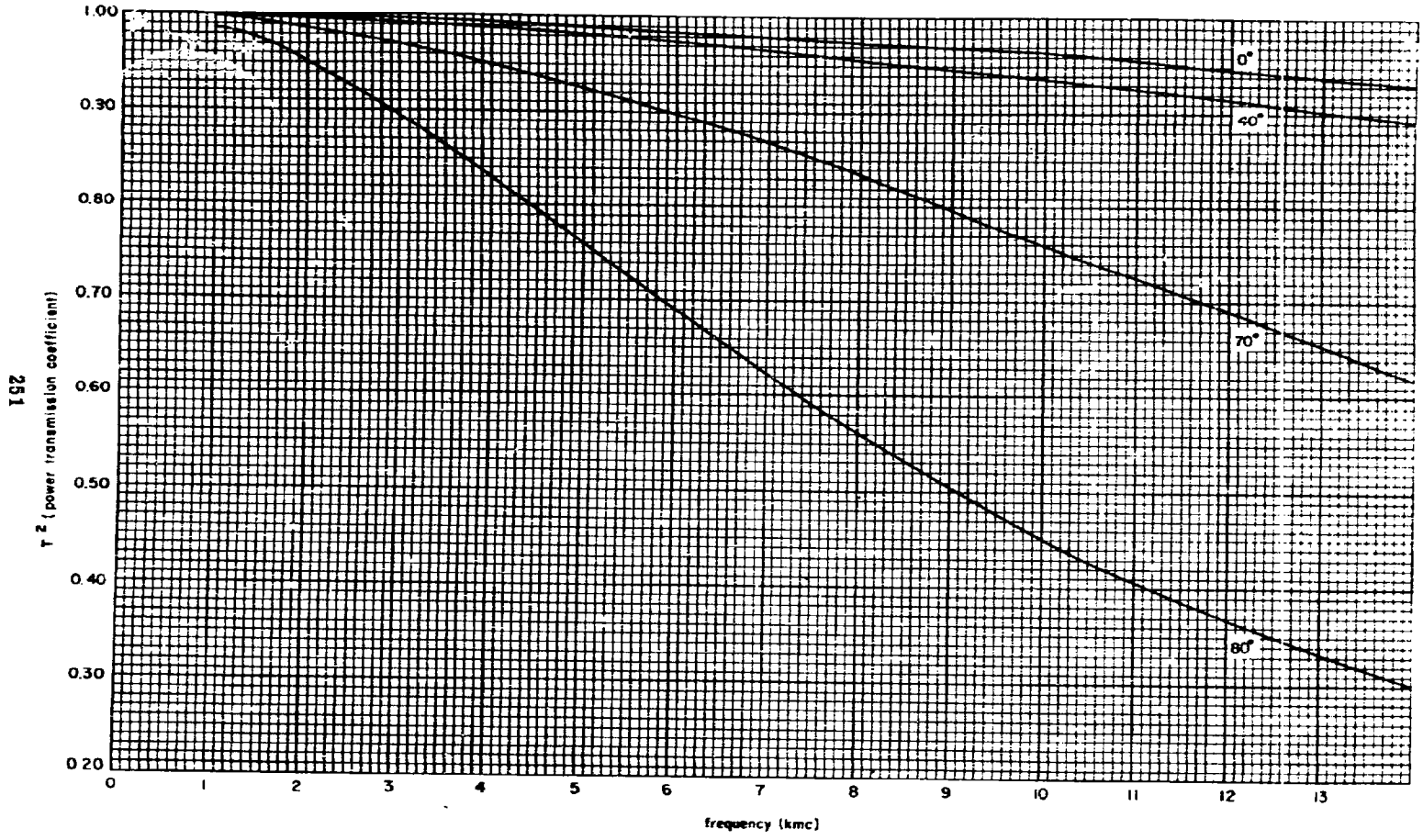


Figure 5–12. Solid–Wall Radome Transmission Efficiency, Wall Thickness 0.024 In. ($\epsilon = 4$, Tan $\delta = 0.014$, Perpendicular Polarization)

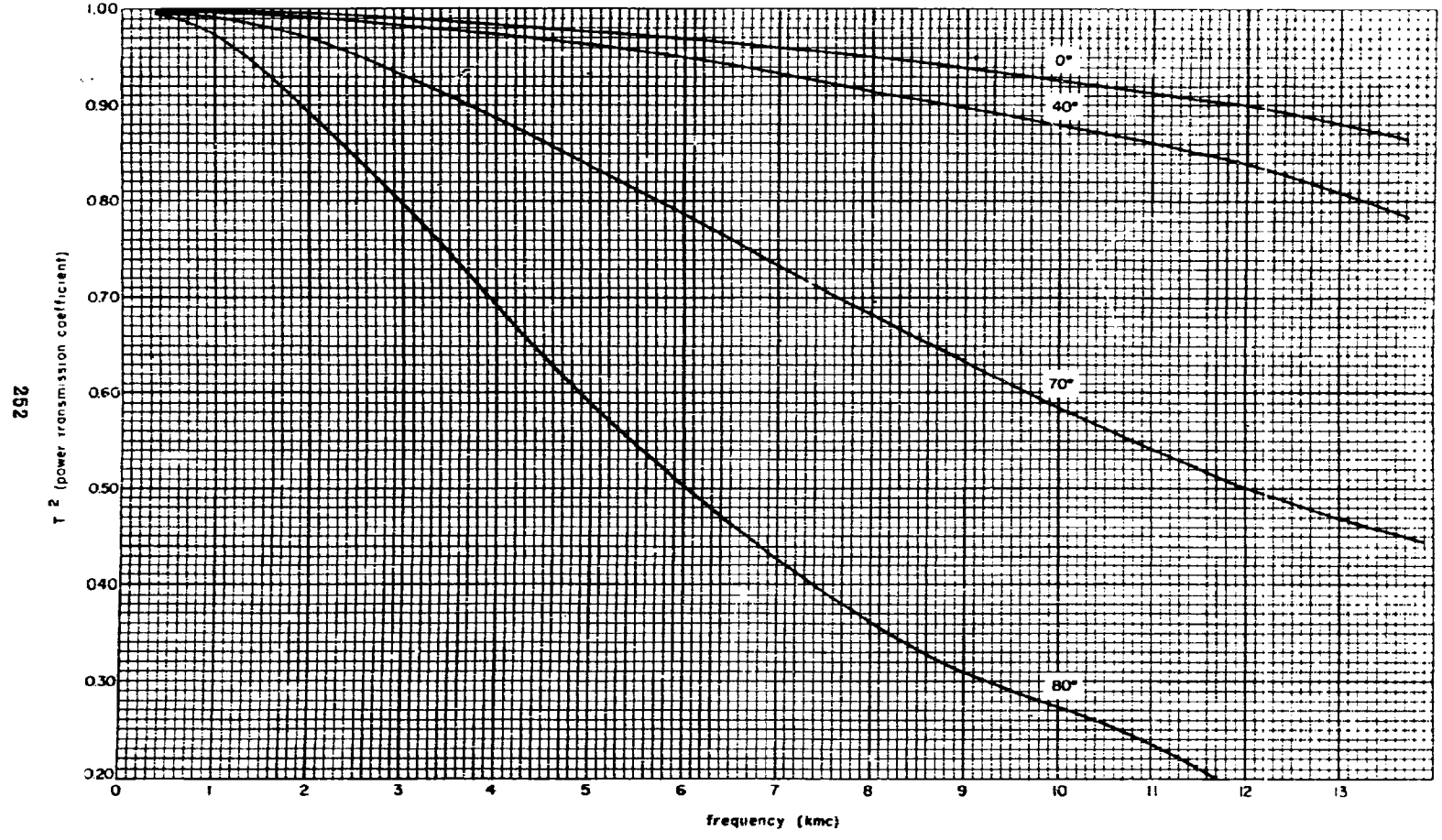


Figure 5–13. Solid–Wall Radome Transmission Efficiency, Wall Thickness 0.036 In. ($\epsilon = 4$, Tan $\delta = 0.014$, Perpendicular Polarization)

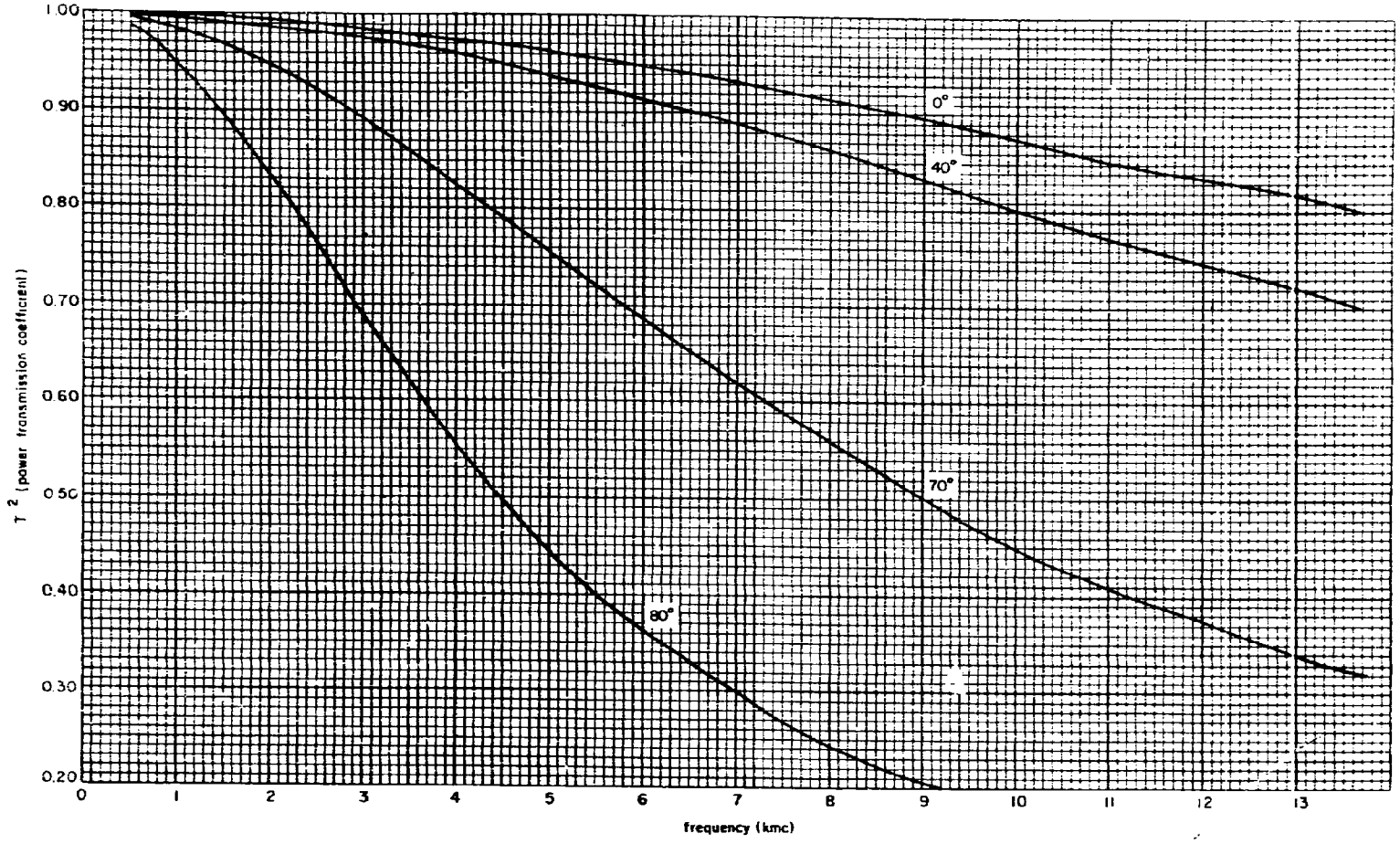


Figure 5–14. Solid–Wall Radome Transmission Efficiency, Wall Thickness 0.048 in. ($\varepsilon = 4$, Tan $\delta = 0.014$, Perpendicular Polarization)

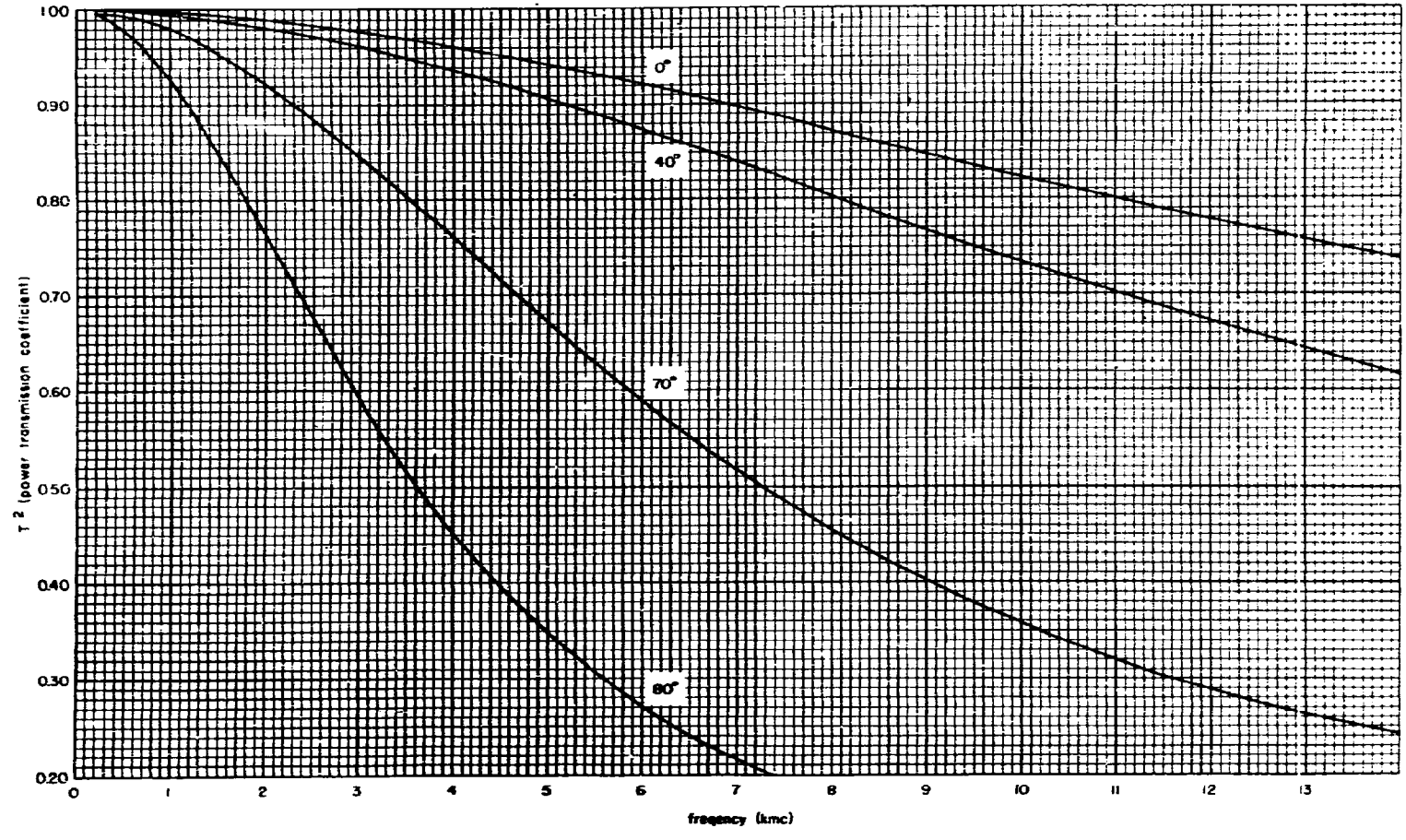


Figure 5–15. Solid–Wall Radome Transmission Efficiency, Wall Thickness 0.060 In. ($\epsilon = 4$, Tan $\delta = 0.014$, Perpendicular Polarization)

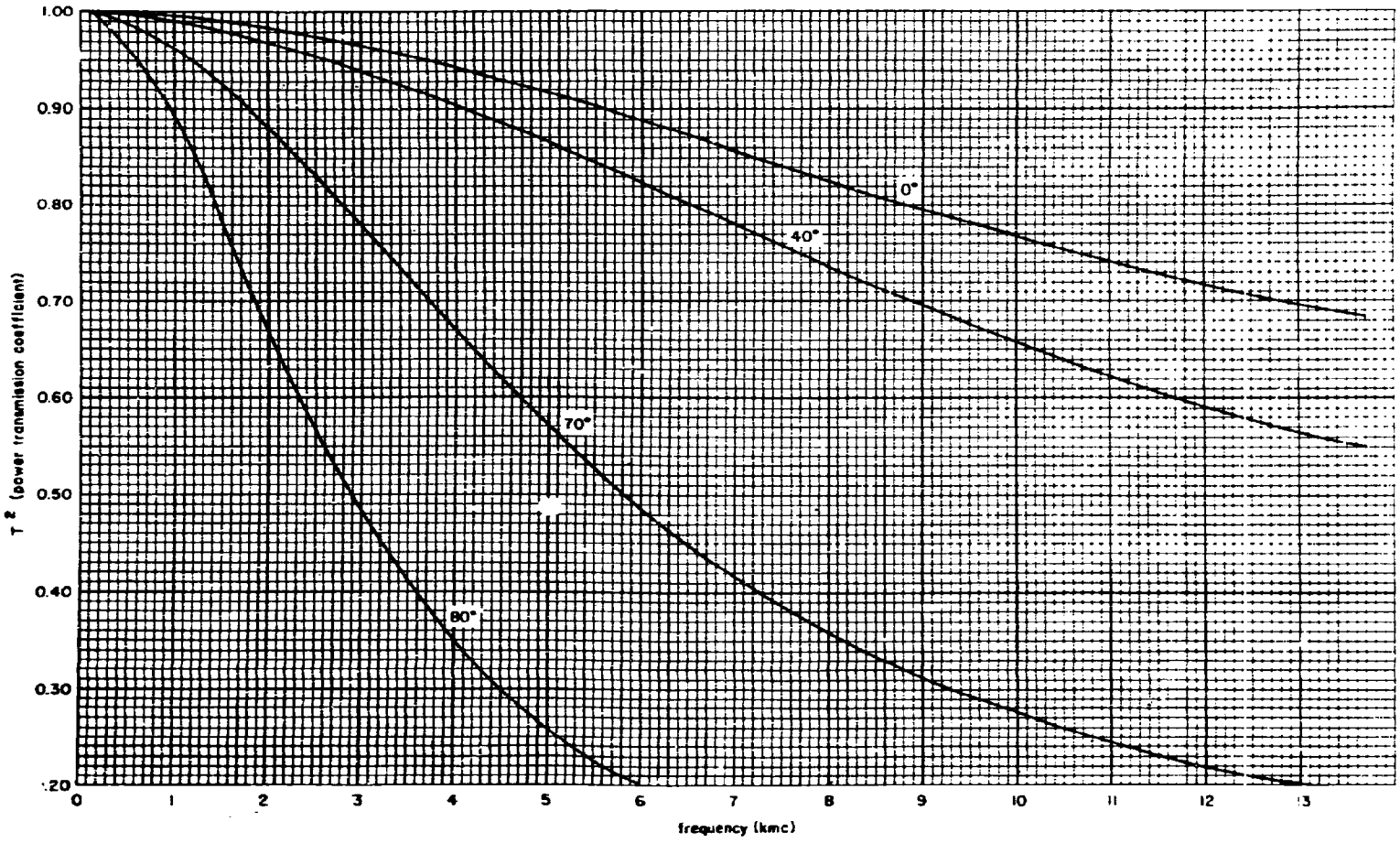


Figure 5–16. Solid–Wall Radome Transmission Efficiency, Wall Thickness 0.075 In. ($\epsilon = 4$, Tan $\delta = 0.014$, Perpendicular Polarization)

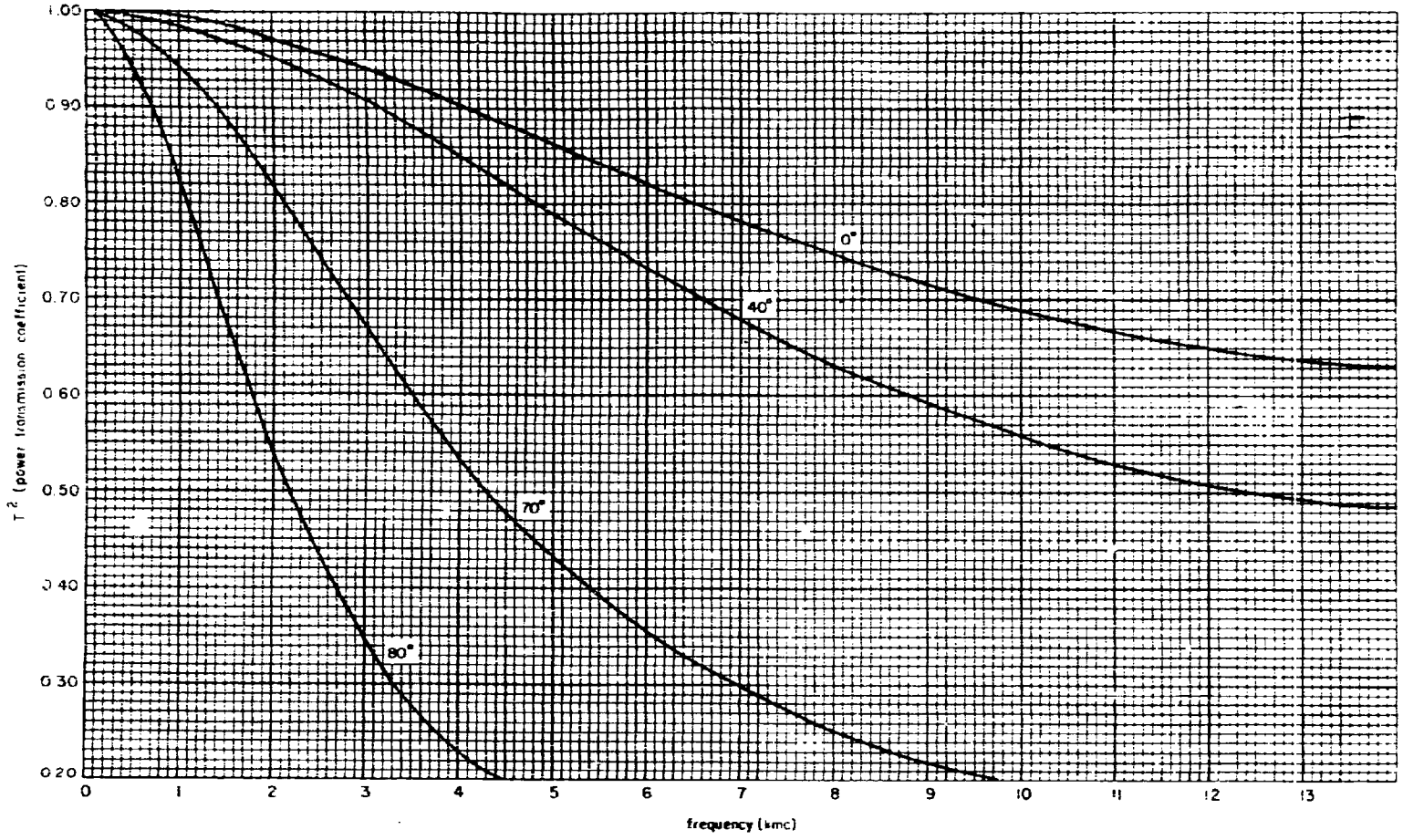


Figure 5–17. Solid–Wall Radome Transmission Efficiency, Wall Thickness 0.100 In. ($\epsilon = 4$, Tan $\delta = 0.014$, Perpendicular Polarization)

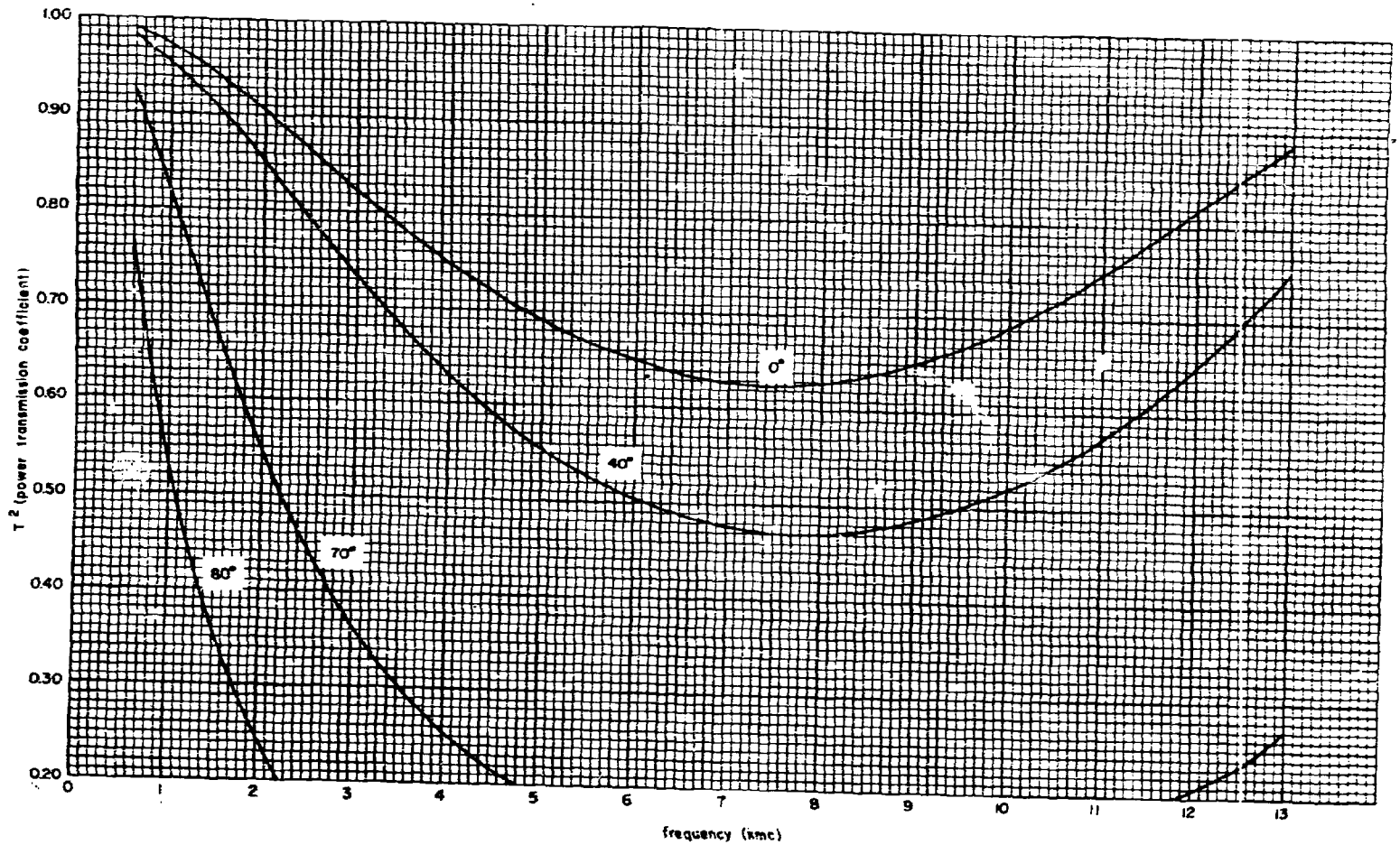


Figure 5-18. Solid-Wall Radome Transmission Efficiency, Wall Thickness 0.200 In. (ϵ = 4, Tan δ = 0.014, Perpendicular Polarization)

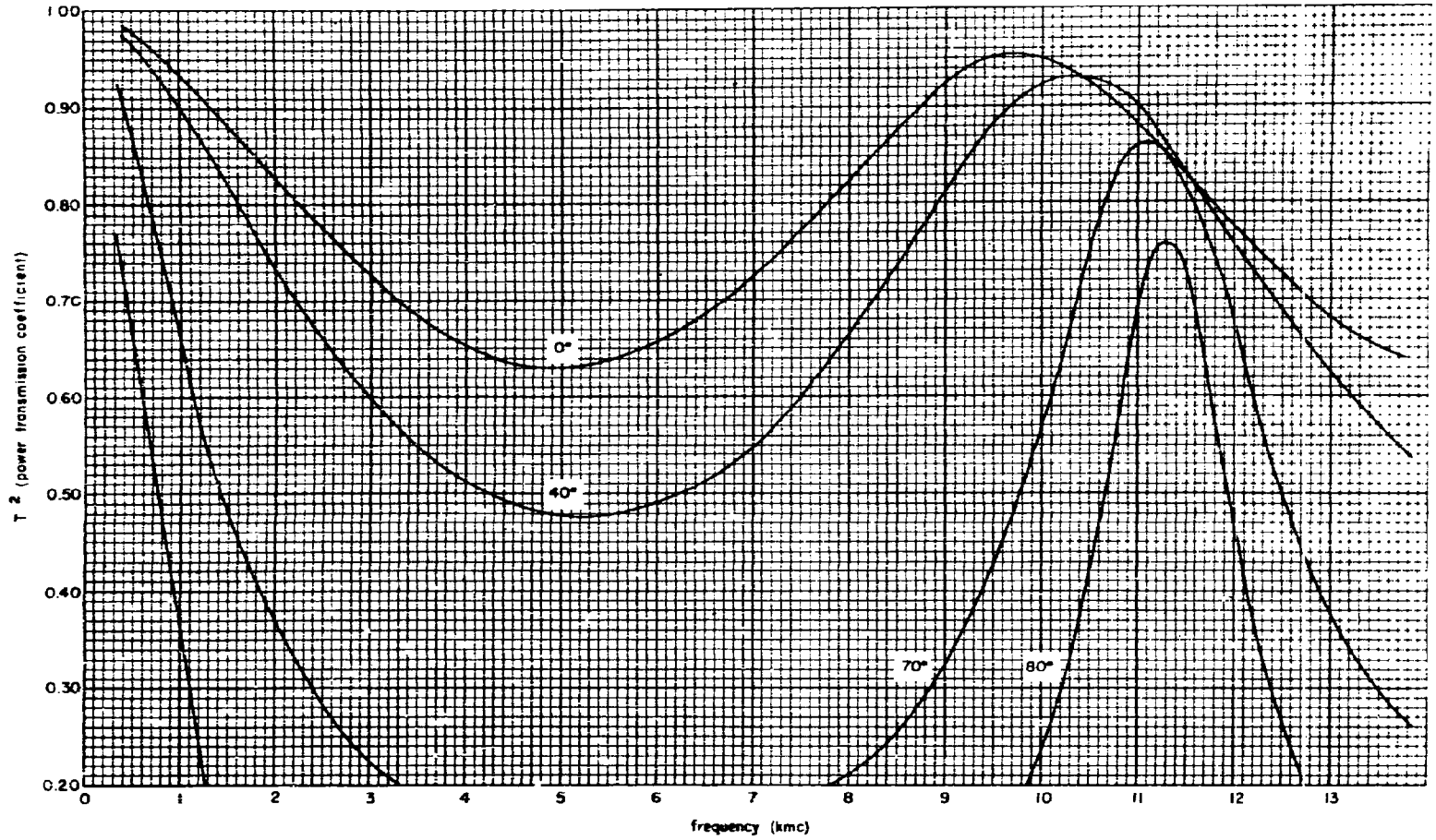


Figure 5–19. Solid–Wall Radome Transmission Efficiency, Wall Thickness 0.300 In. ($\epsilon = 4$, Tan $\delta = 0.014$, Perpendicular Polarization)

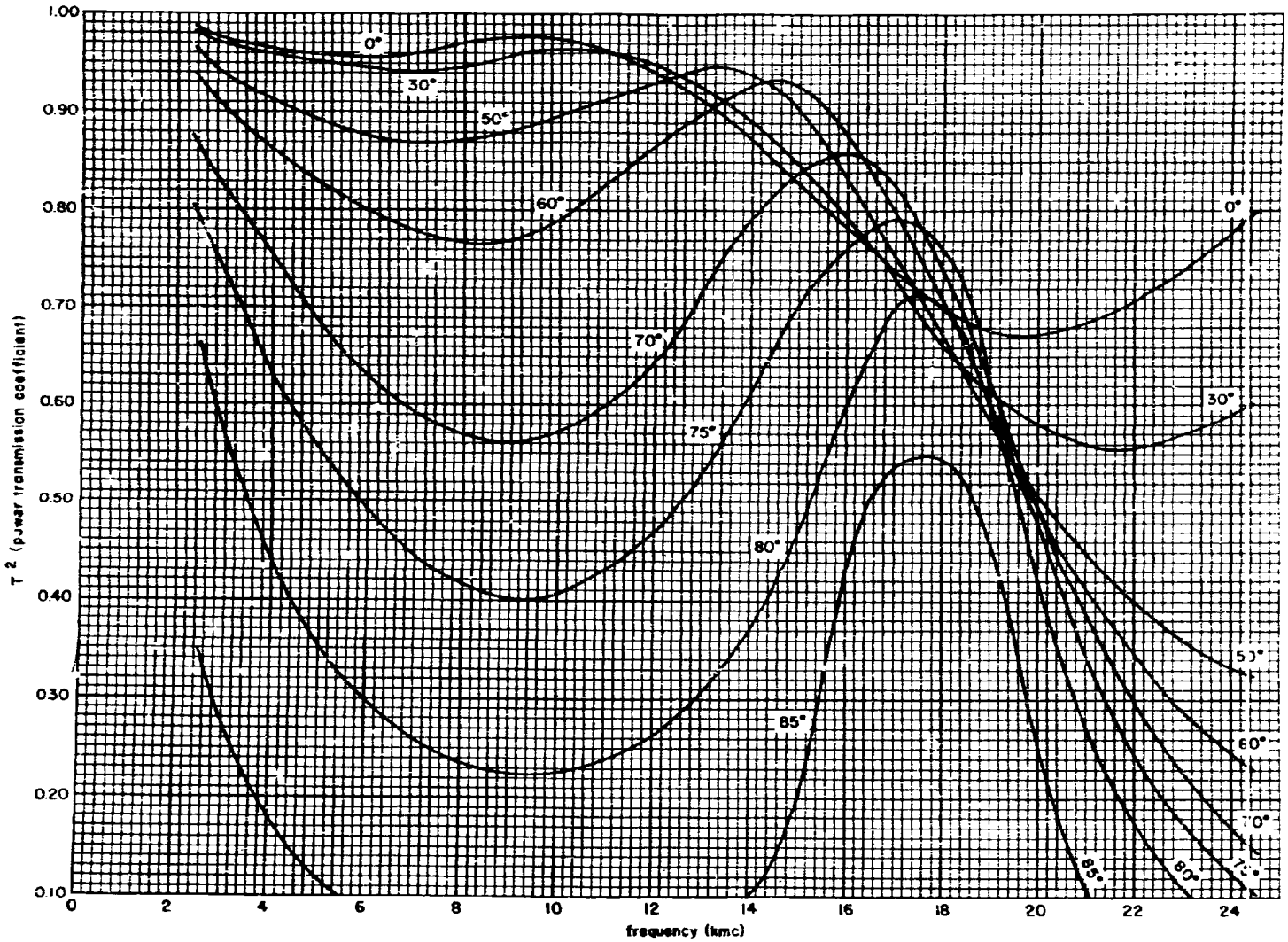


Figure 5–20. Single Sandwich Radome Transmission Efficiency, Skin Thickness 0.02± In., Core Thickness 0.250 In. (ϵ_s=4, ϵ_c=1.2, Tan δ_s=0.014, Tan δ_c=0.004, Perpendicular Polarization)

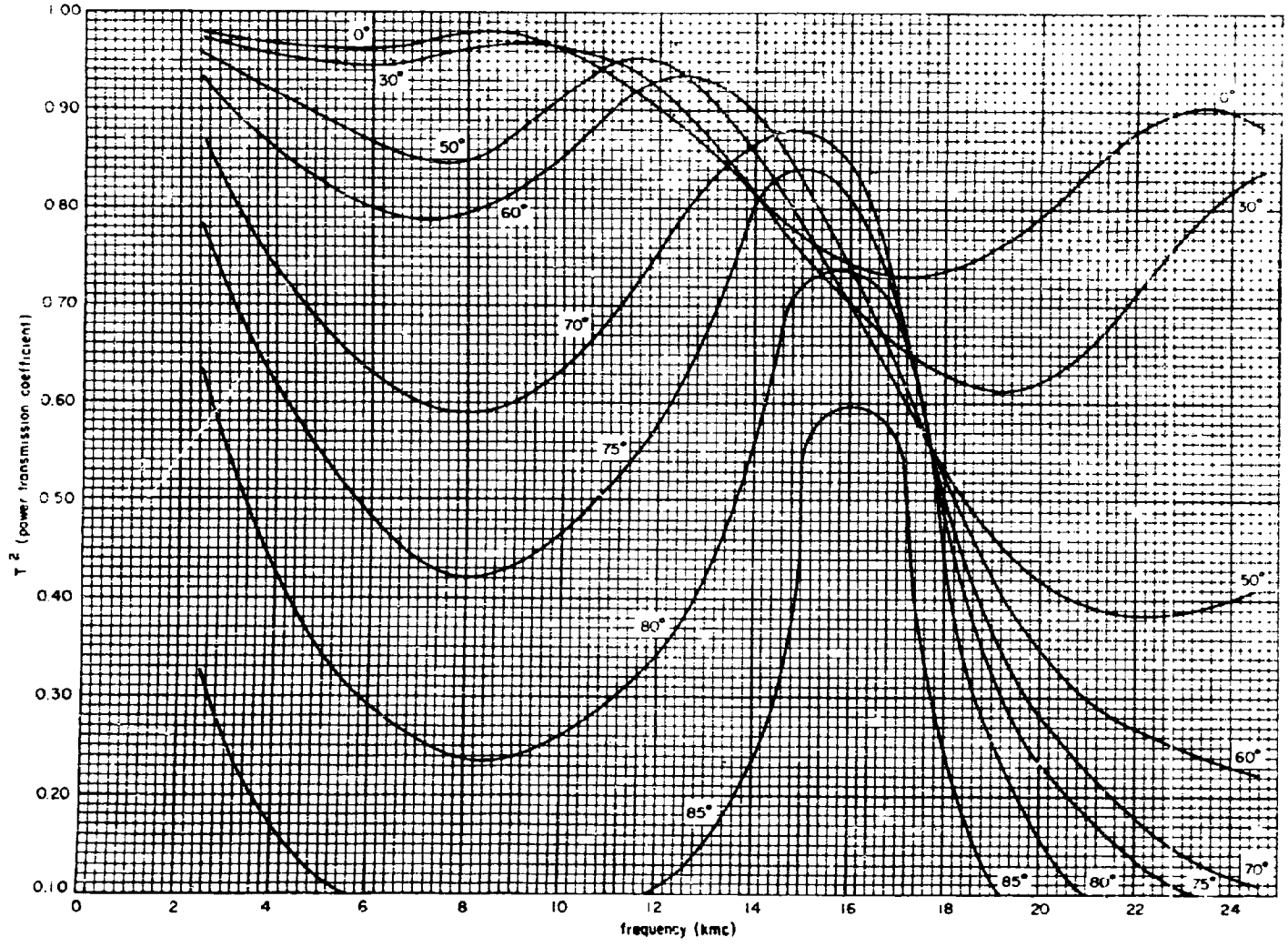


Figure 5-21. Single Sandwich Radome Transmission Efficiency, Skin Thickness 0.024 In., Core Thickness 0.300 In. (ϵ =4, ϵ_c=1.2, Tan δ_s=0.014, Tan δ_c=0.004, Perpendicular Polarization)

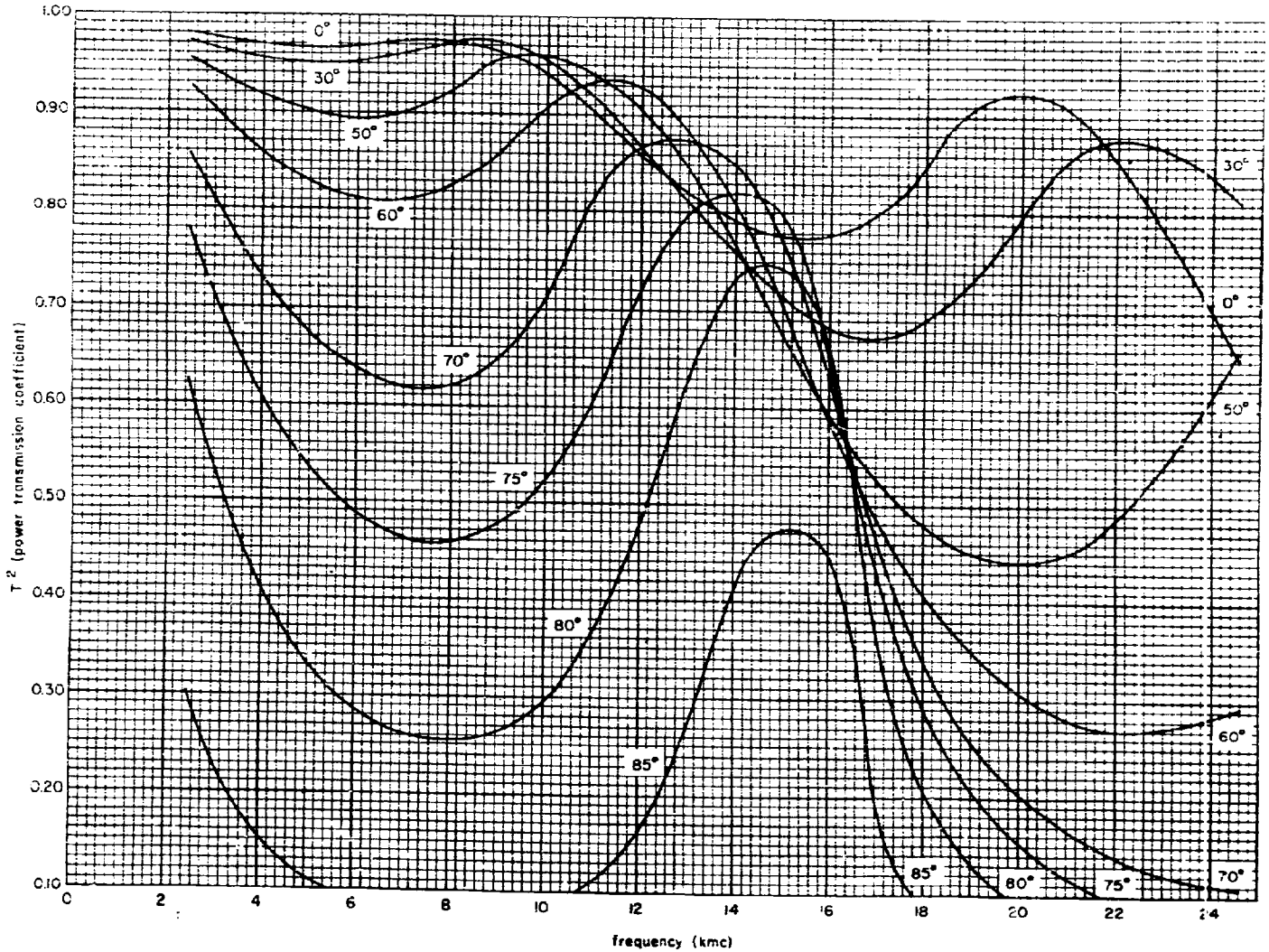


Figure 5–22. Single Sandwich Radome Transmission Efficiency, Skin Thickness 0.024 In., Core Thickness 0.350 In. (ϵ_s=4, ϵ_c=1.2, Tan δ_s=0.014, Tan δ_c=0.004, Perpendicular Polarization)

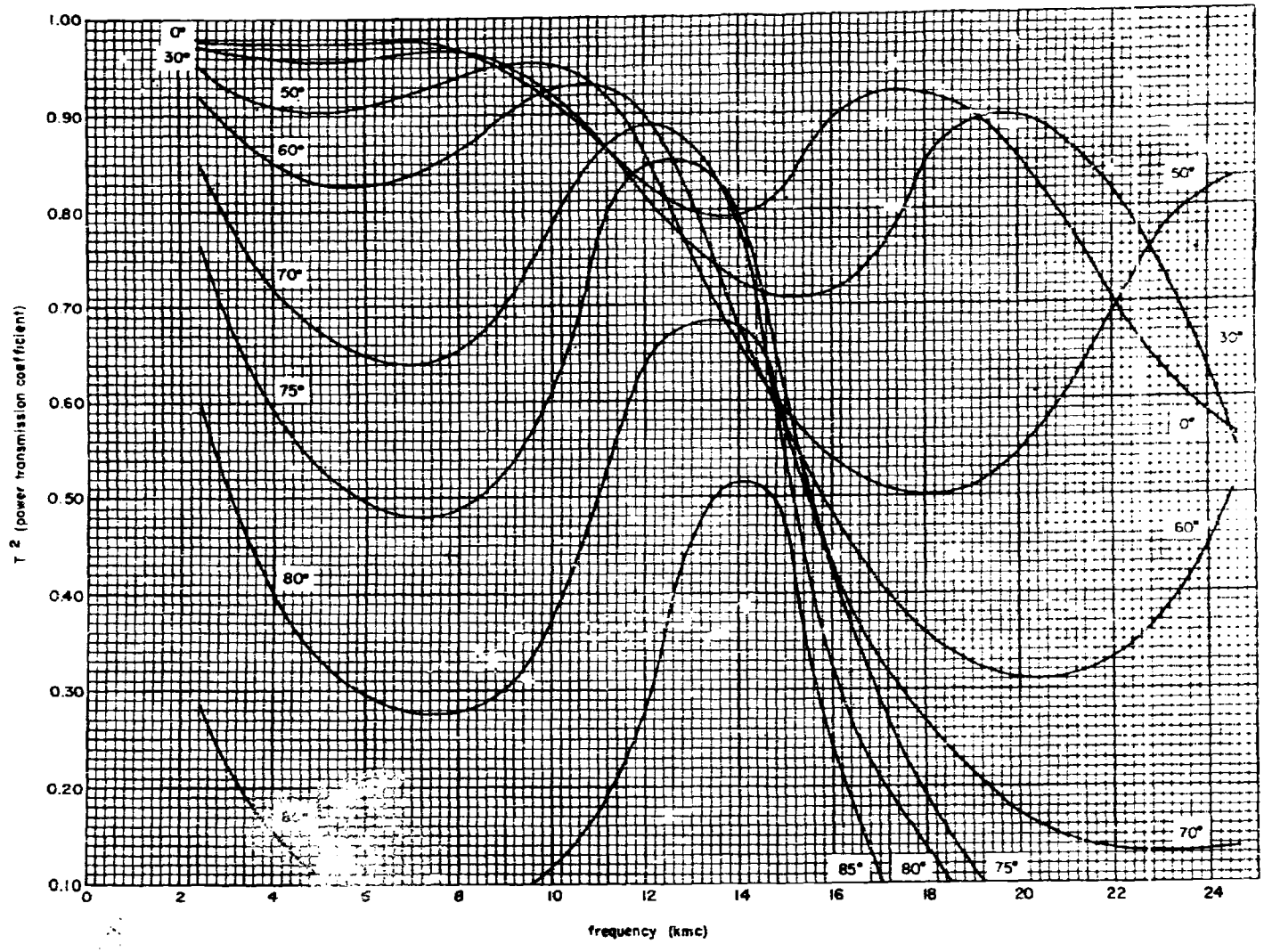


Figure 5–23. Single Sandwich Radome Transmission Efficiency, Skin Thickness 0.024 In., Core Thickness 0.400 In. (ϵ_s=4, ϵ_c=1.2, Tan δ_s=0.014, Tan δ_c=0.004, Perpendicular Polarization)

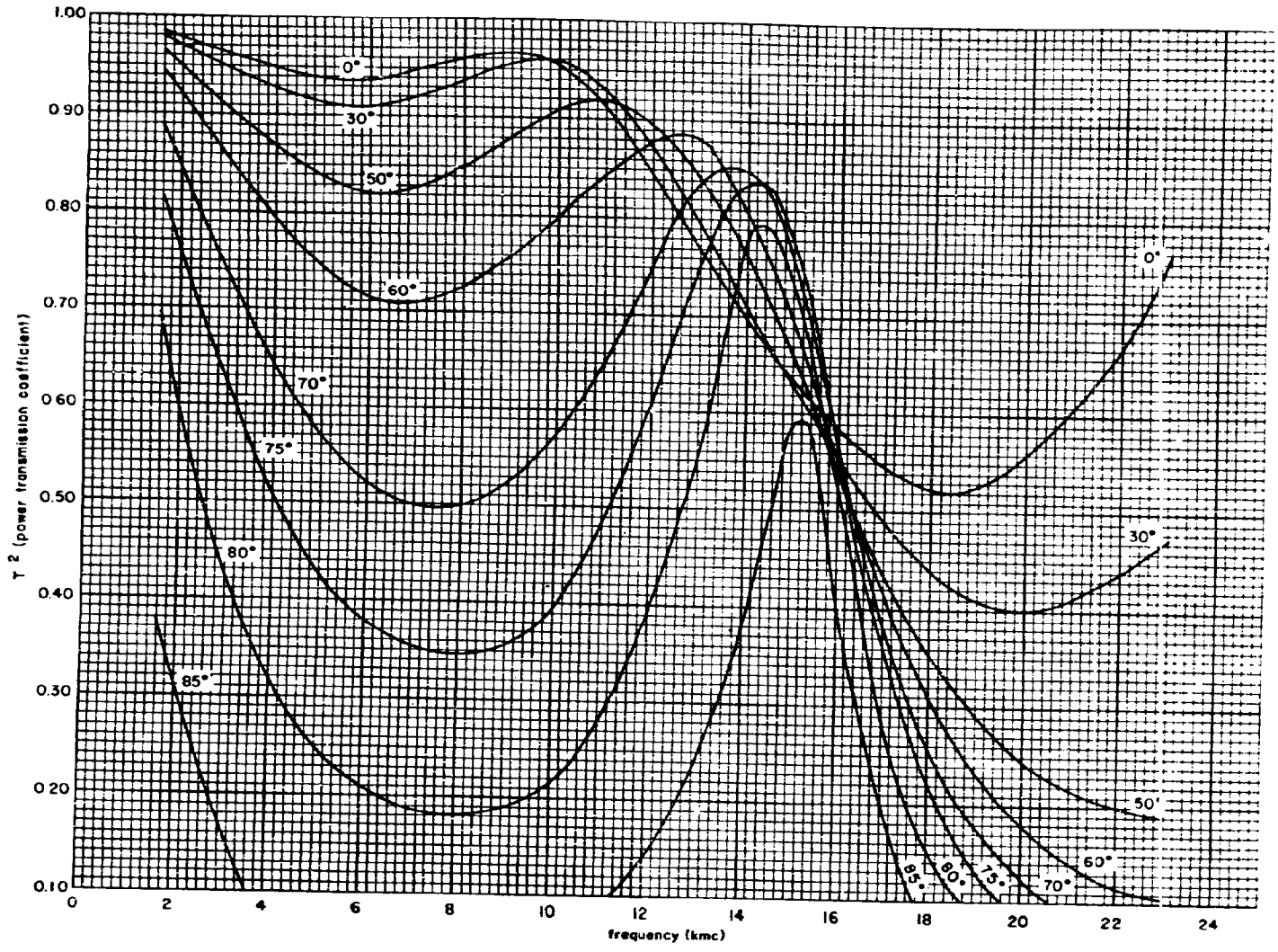


Figure 5–24. Single Sandwich Radome Transmission Efficiency, Skin Thickness 0.036 In., Core Thickness 0.250 In. (ϵ_s=4, ϵ_c=1.2, Tan δ_s=0.014, Tan δ_c=0.004, Perpendicular Polarization)

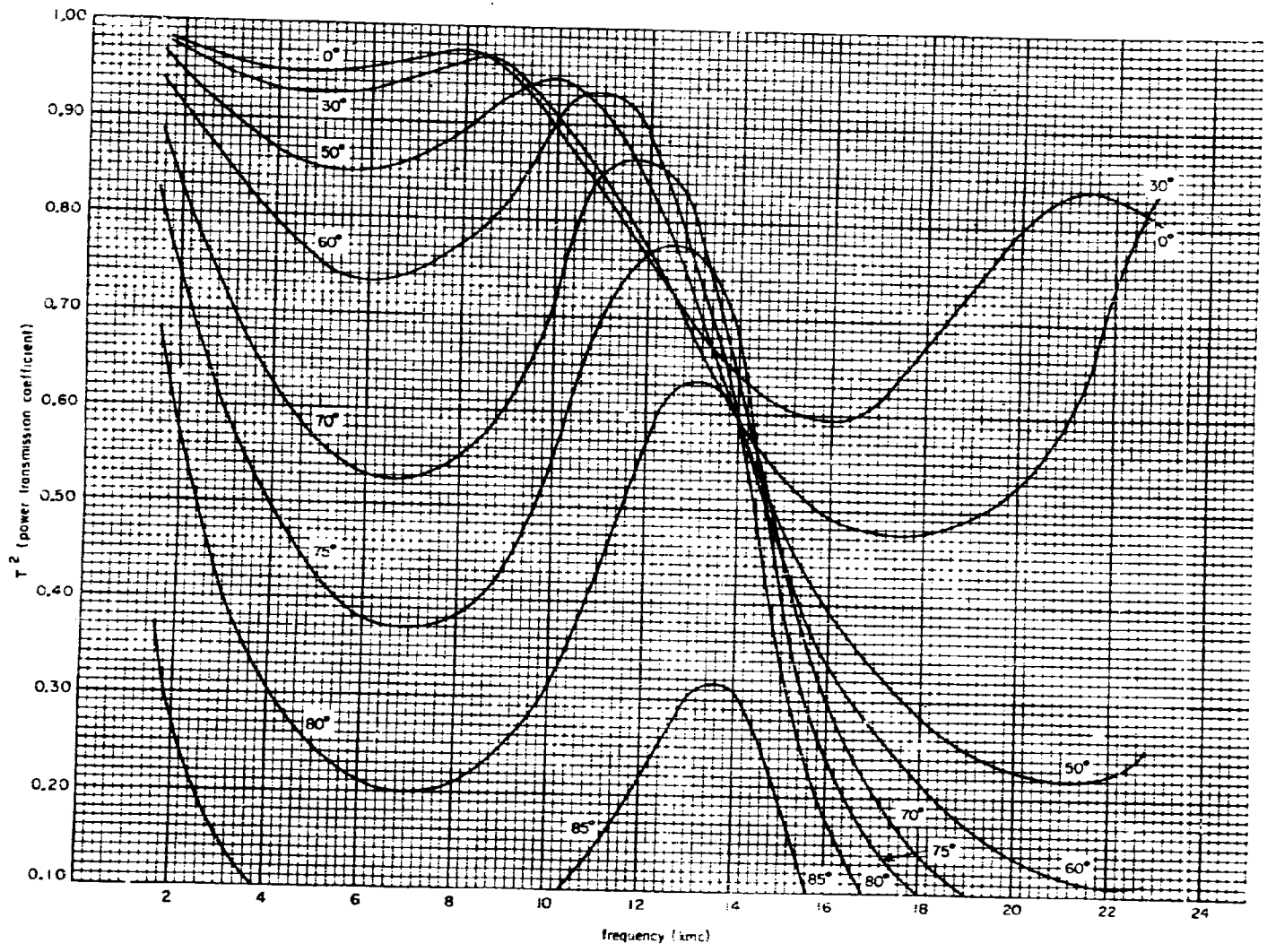


Figure 5–25. Single Sandwich Radome Transmission Efficiency, Skin Thickness 0.036 in., Core Thickness 0.300 In. (ϵ_s=4, ϵ_c=1.2, Tan δ_s=0.014, Tan δ_c=0.004, Perpendicular Polarization)

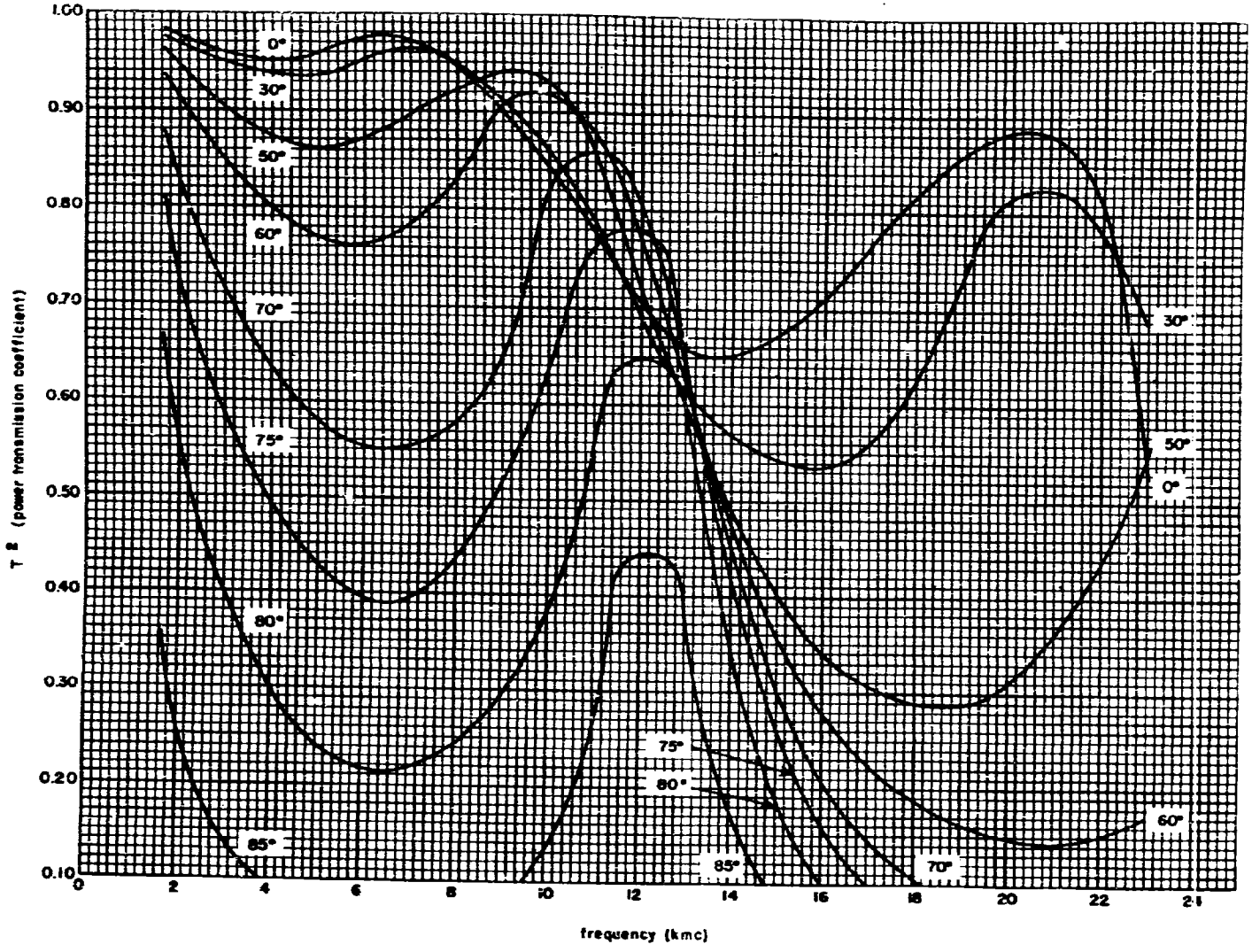


Figure 5-26. Single Sandwich Radome Transmission Efficiency, Skin Thickness 0.036 In., Core Thickness 0.350 In. (ϵ_s=4, ϵ_c=1.2, Tan δ_s=0.014, Tan δ_c=0.004, Perpendicular Polarization)

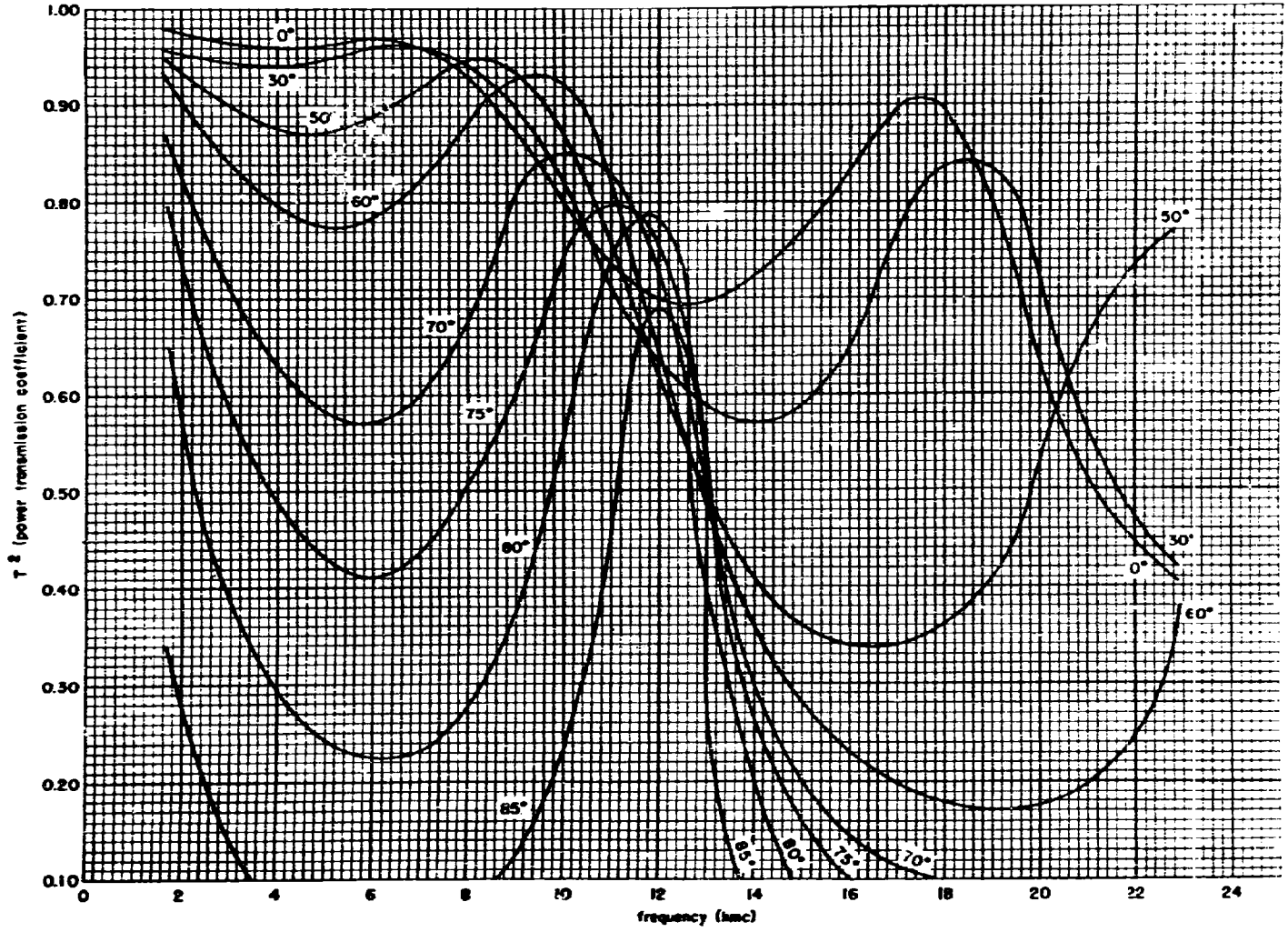


Figure 5–27. Single Sandwich Radome Transmission Efficiency, Skin Thickness 0.036 in., Core Thickness 0.400 in. (ϵ_s=4, ϵ_c=1.2, Tan δ_s=0.014, Tan δ_c=0.004, Perpendicular Polarization)

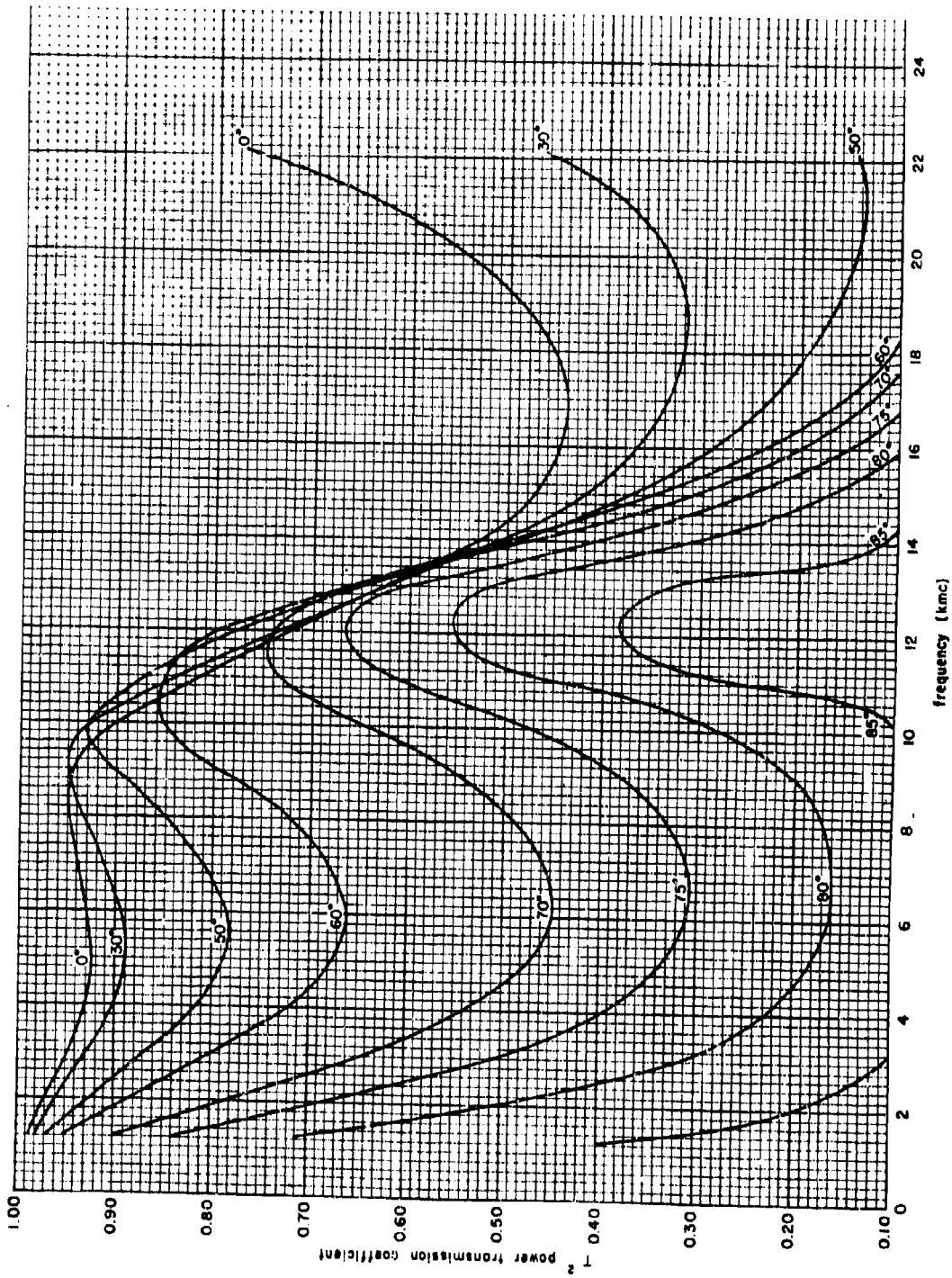


Figure 5-28. Single Sandwich Radome Transmission Efficiency, Skin Thickness 0.048 In., Core Thickness 0.250 In. (ϵ_s=4, ϵ_c=1.2, Tan δ_s=0.014, Tan δ_c=0.004, Perpendicular Polarization)

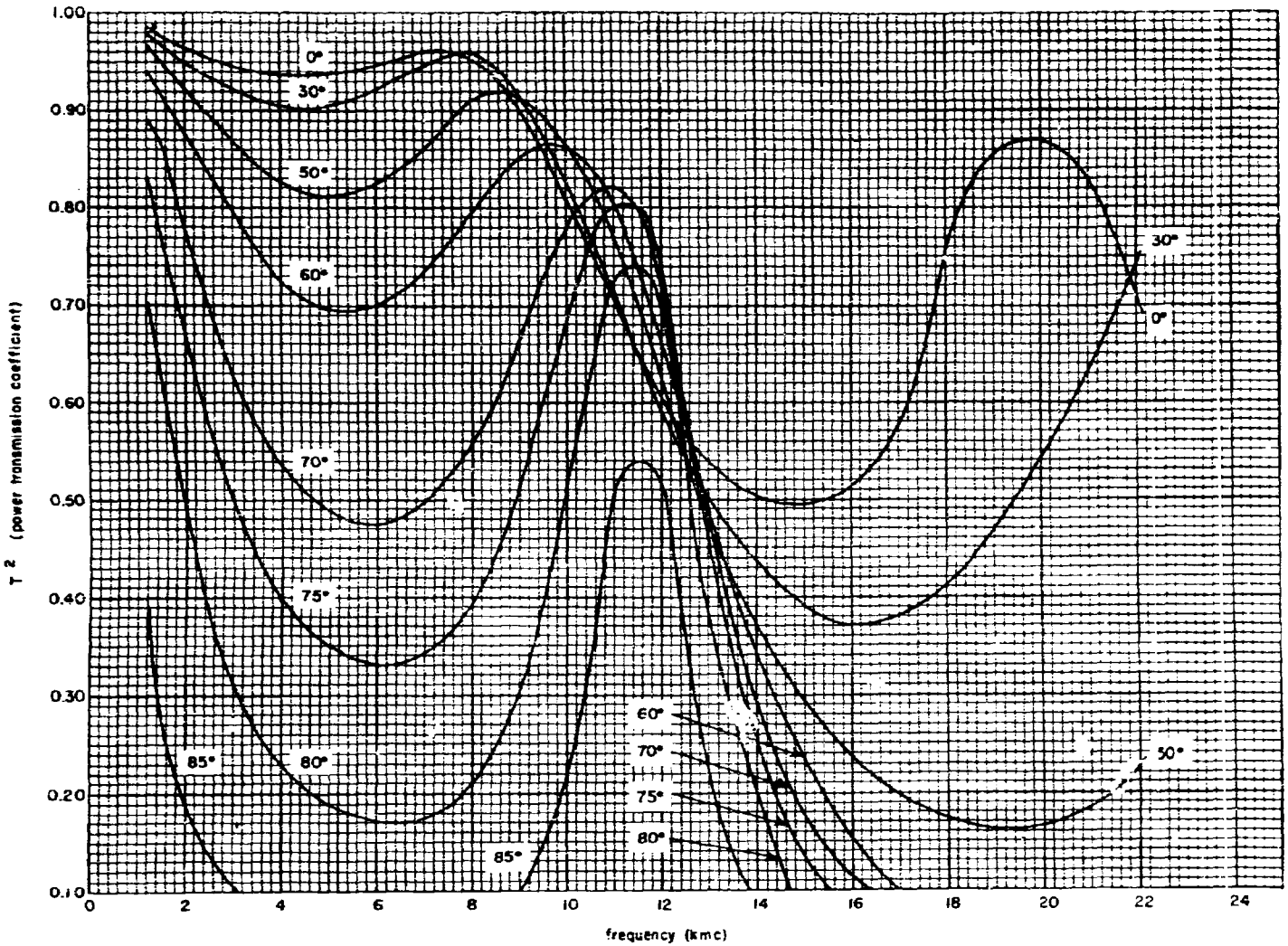


Figure 5–29. Single Sandwich Radome Transmission Efficiency, Skin Thickness 0.048 In., Core Thickness 0.300 In. (ϵ_s=4, ϵ_c=1.2, Tan δ_s=0.014, Tan δ_c=0.004, Perpendicular Polarization)

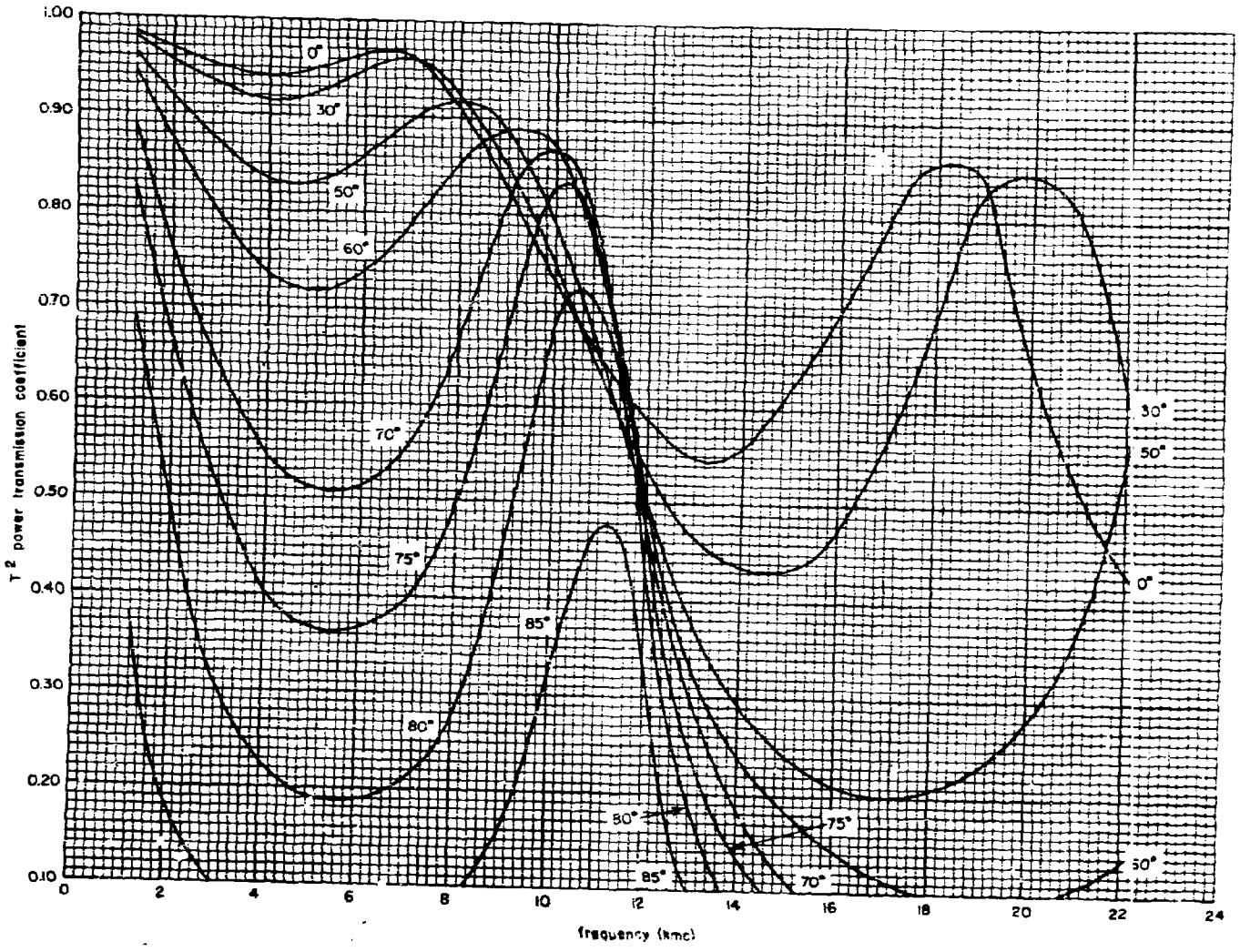


Figure 5–30. Single Sandwich Radome Transmission Efficiency, Skin Thickness 0.048 In., Core Thickness 0.350 In. (ϵ_s=4 ϵ_c=1.2, Tan δ_s=0.014, Tan δ_c=0.004, Perpendicular Polarization)

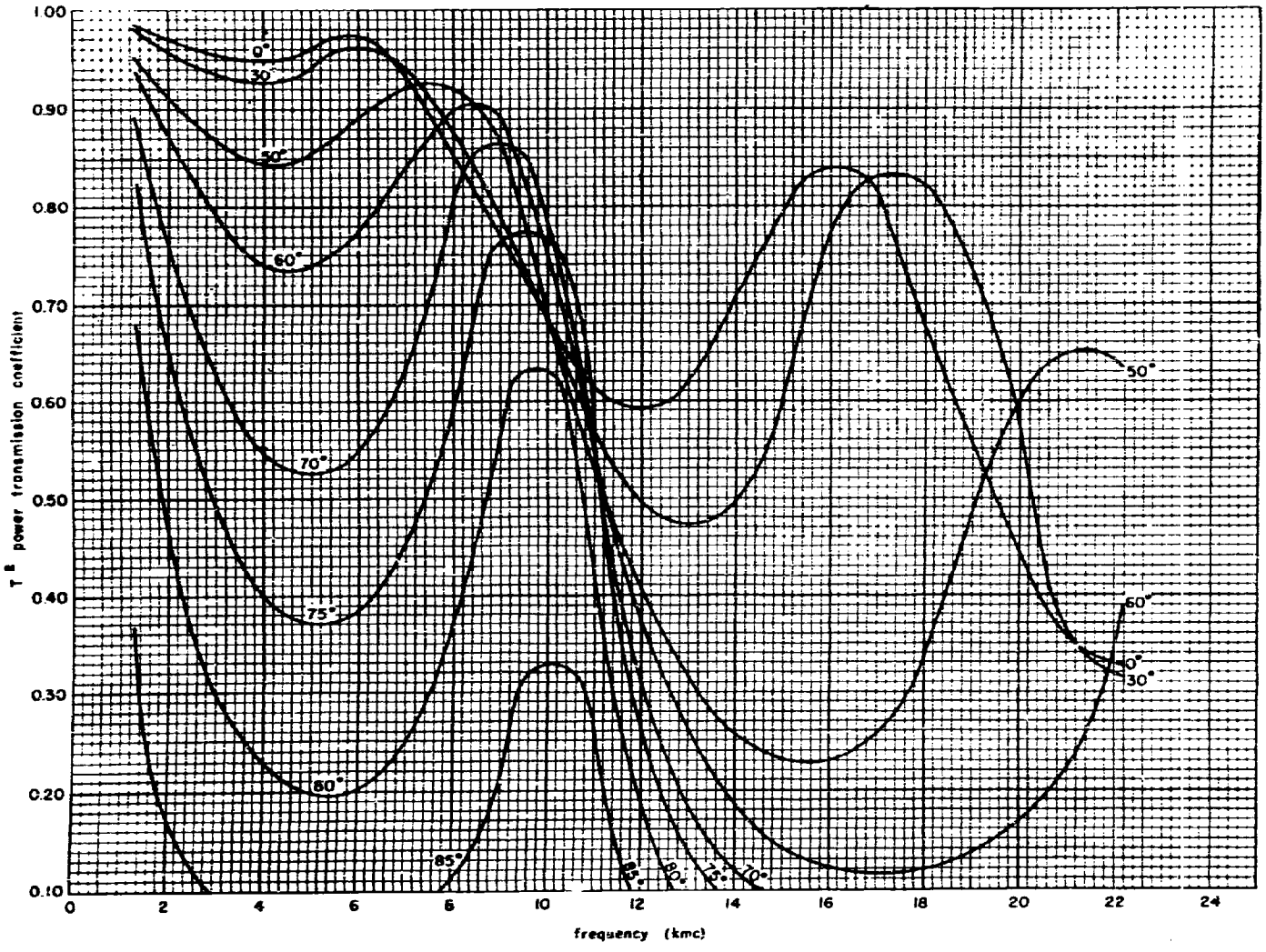


Figure 5–31. Single Sandwich Radome Transmission Efficiency, Skin Thickness 0.048 In., Core Thickness 0.400 In.
(ϵ_s=4, ϵ_c=1.2, Tan δ_s=0.014, Tan δ_c=0.004, Perpendicular Polarization)

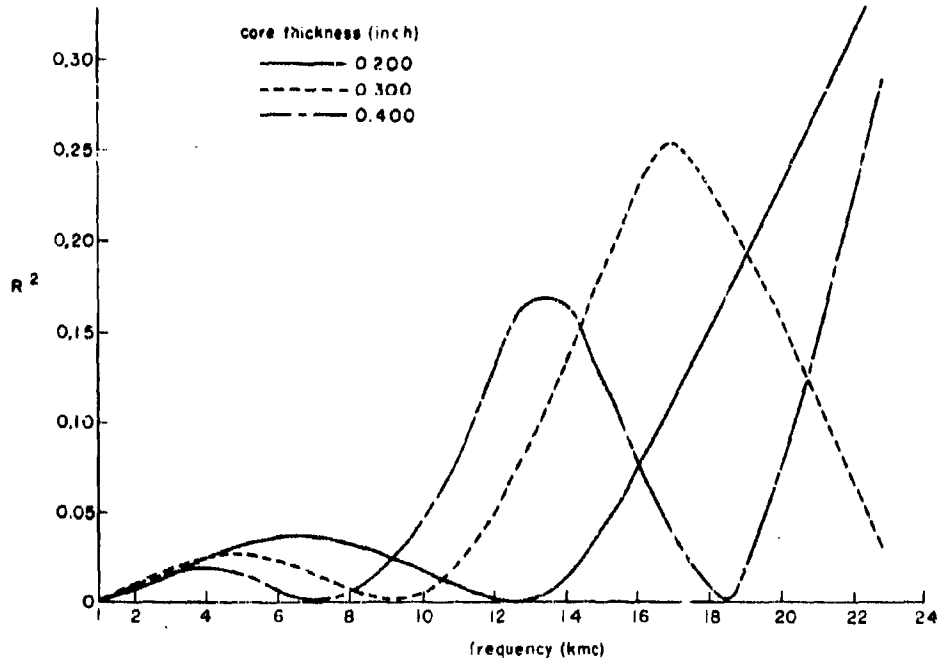


Figure 5-32. Power Reflection from Normal Incidence "A" Sandwich (Skin Thickness 0.020 In., ϵ_s=4.2, Tan δ_s=0.014, ϵ_c=1.2, Tan δ_c=0.00492)

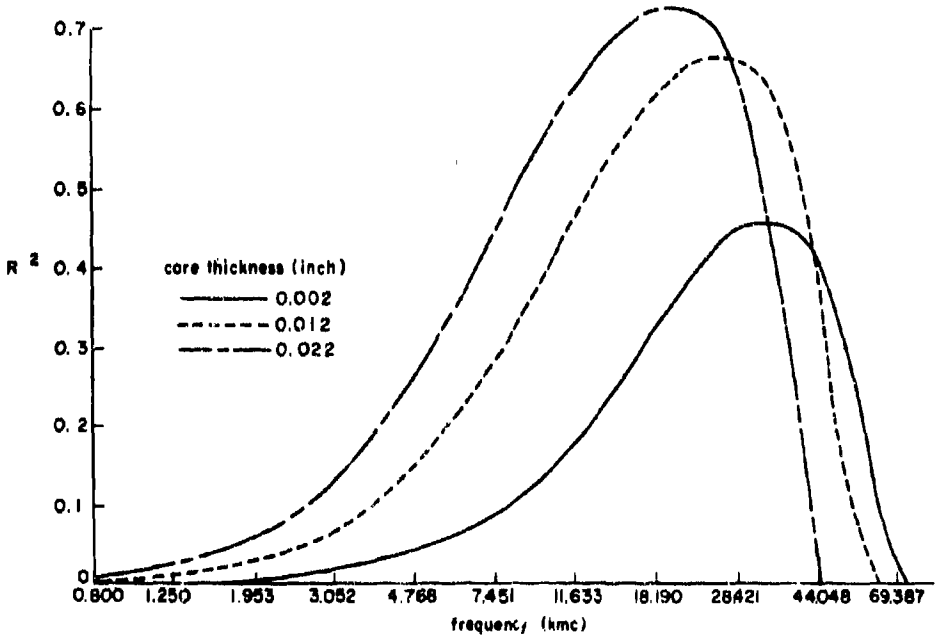


Figure 5-33. Power Reflection from Normal Incidence "B" Sandwich (Skin Thickness 0.020 In., ϵ_s'=4.2, Tan δ_s=0.014, ϵ_c'=17.64, Tan δ_c=0.03)

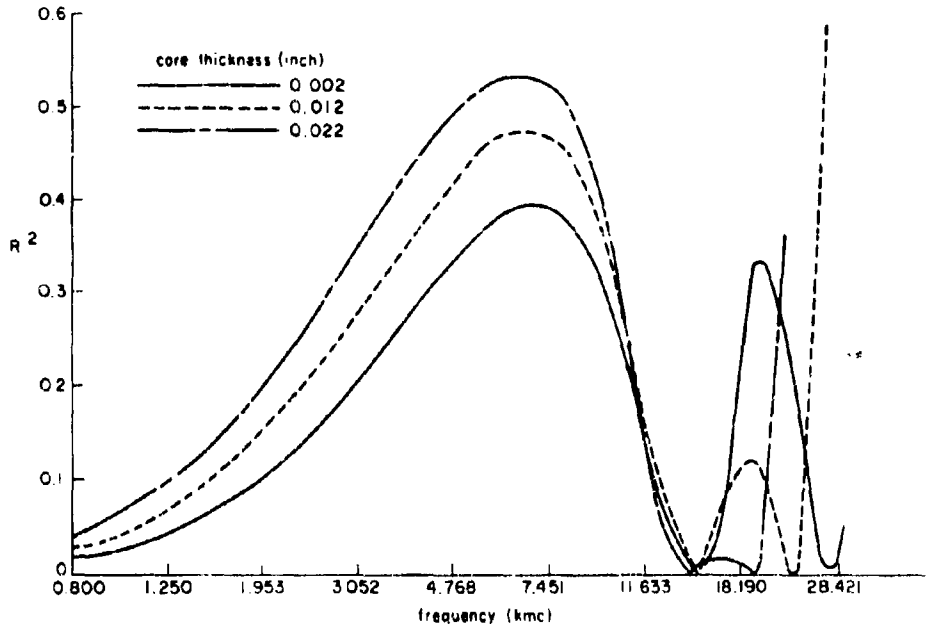


Figure 5–34. Power Reflection from Normal Incidence B Sandwich (Skin Thickness 0.100 in., $\epsilon_s' = 4.2$, Tan $\delta_s = 0.014$; $\epsilon_c' = 17.64$, Tan $\delta_c = 0.0225$)

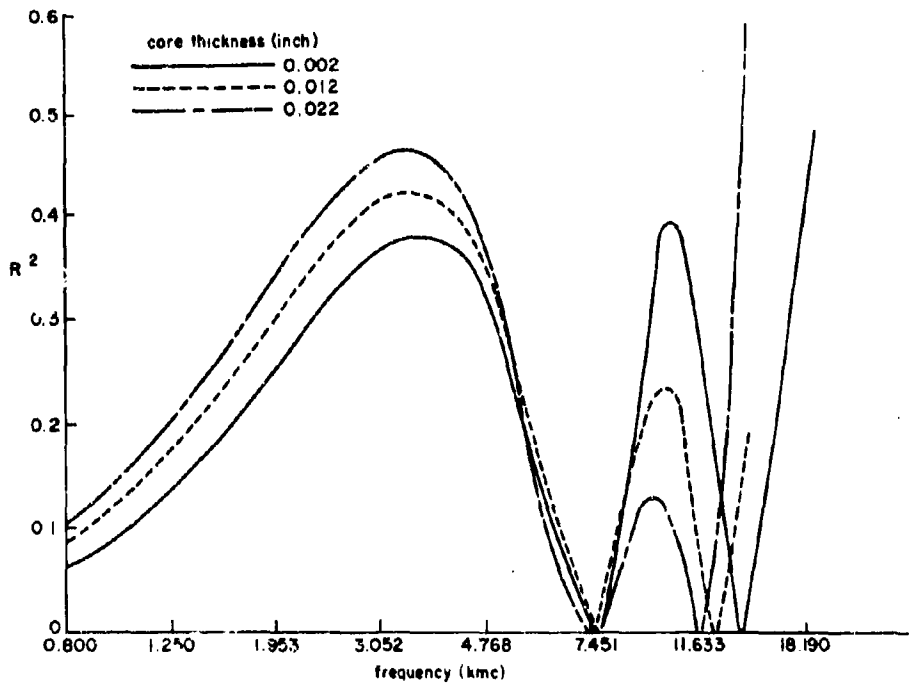


Figure 5–35. Power Reflection from Normal Incidence B Sandwich (Skin Thickness 0.200 in., $\epsilon_s' = 4.2$, Tan $\delta_s = 0.014$; $\epsilon_c' = 17.64$, Tan $\delta_c = 0.015$)

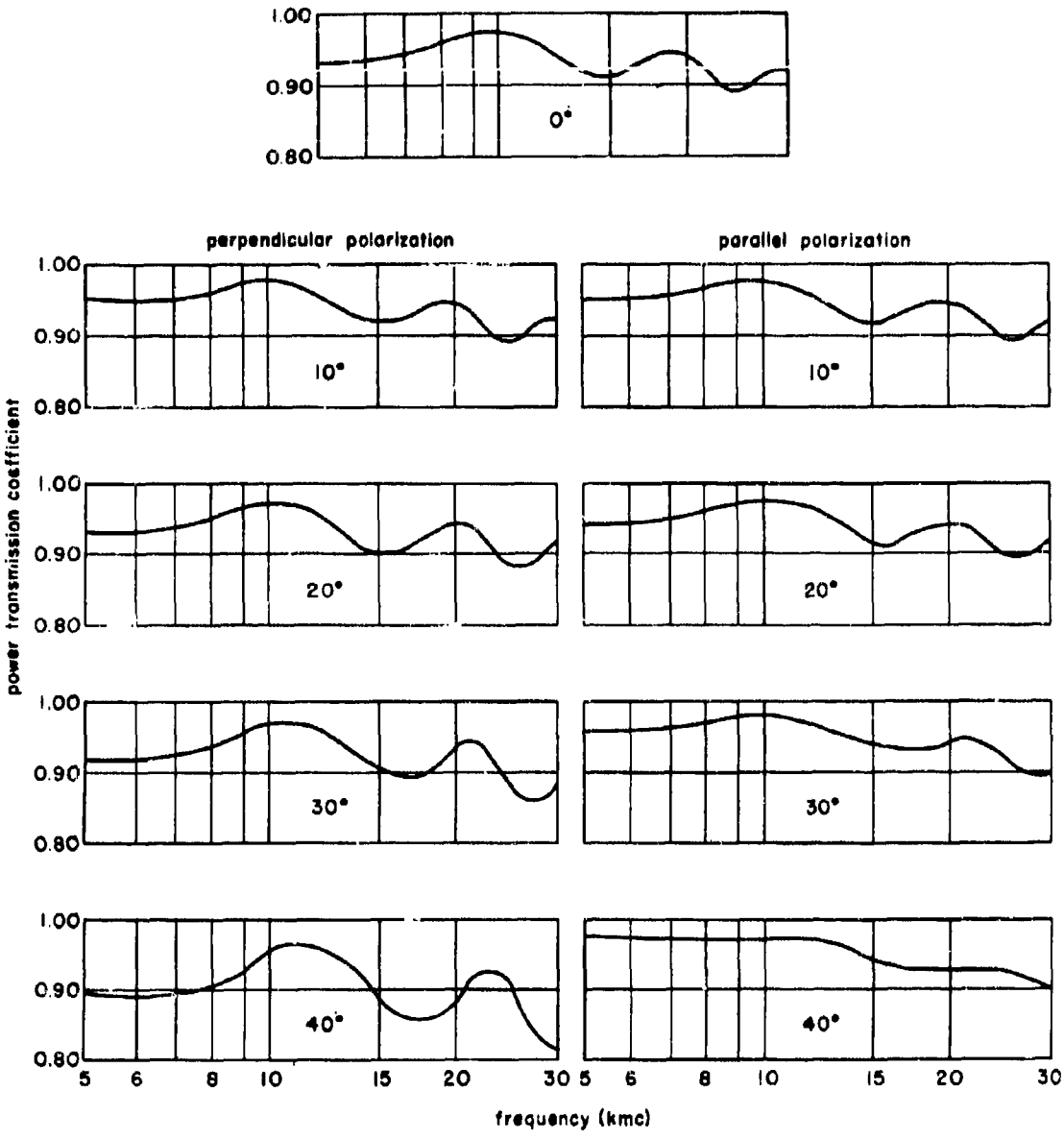


Figure 5–36. Transmission of 11–Layer Wall Radome with Skins 0.010 In. Thick and Cores 0.072 In. Thick

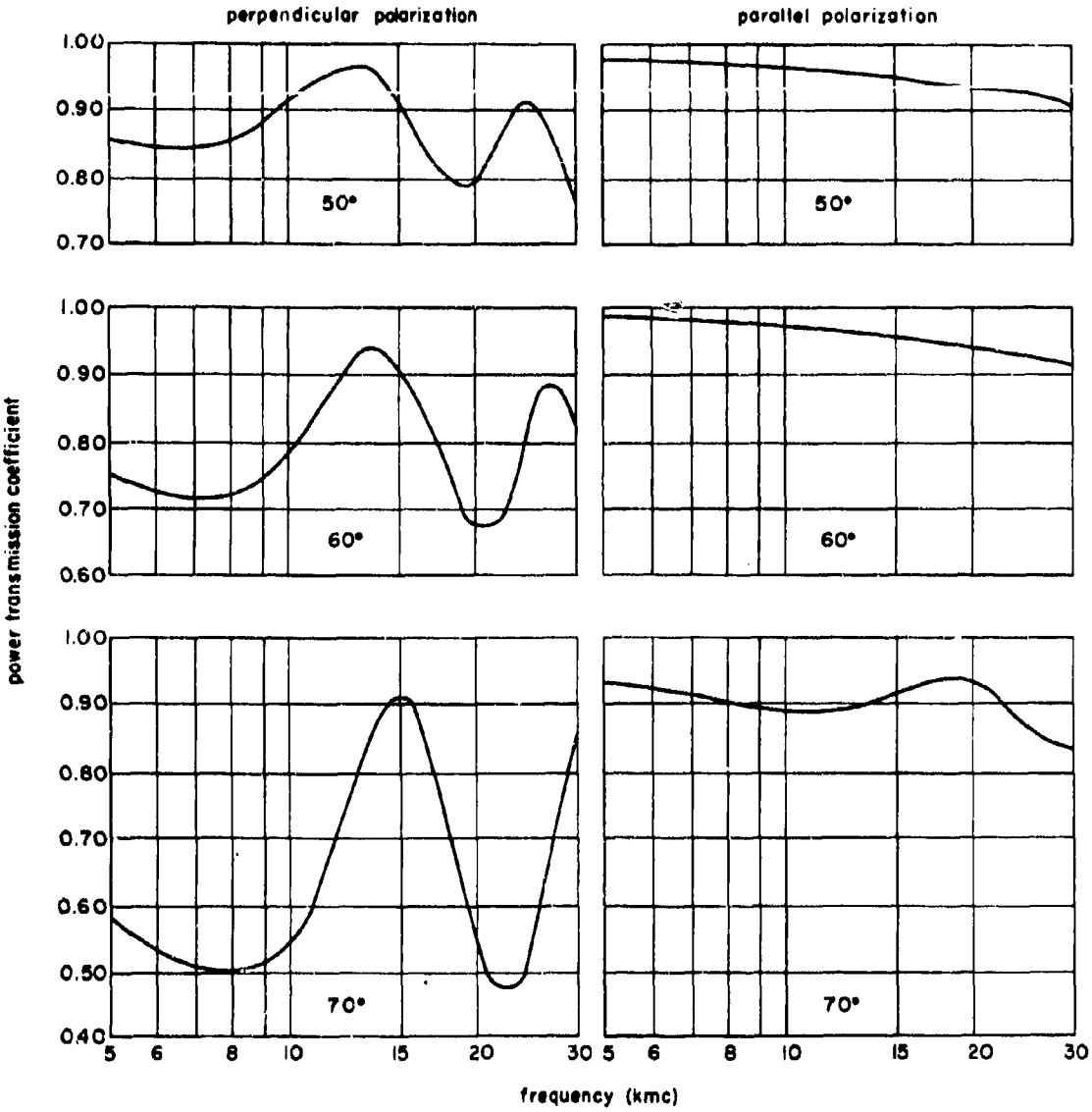


Figure 5-36 (continued). Transmission of 11-Layer Wall Radome with Skins 0.010 in. Thick and Cores 0.072 in. Thick

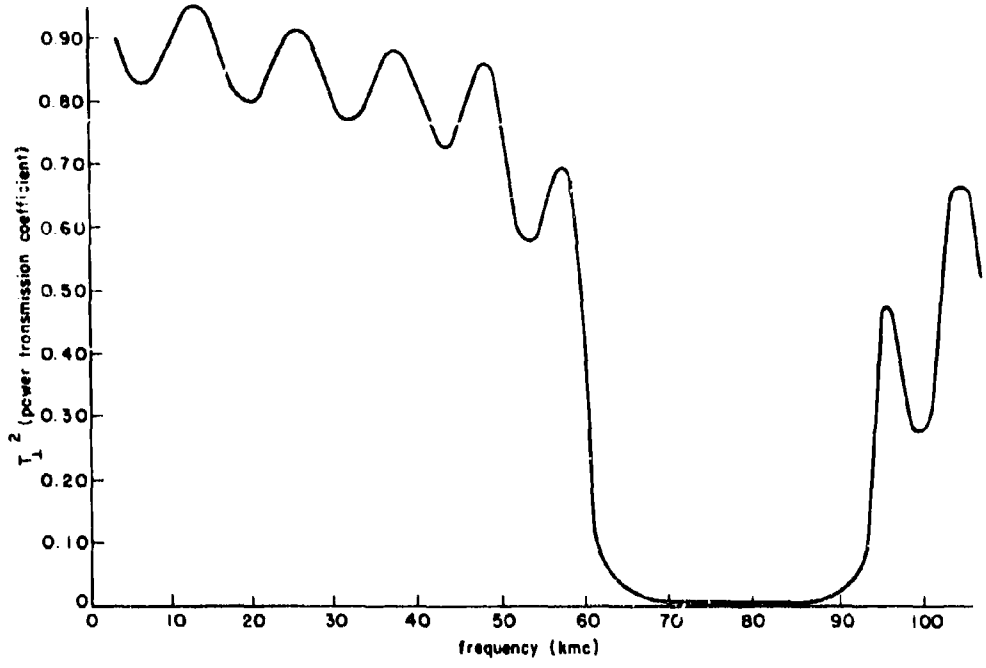


Figure 5–37. Transmission of 11–Layer Sandwich Versus Frequency (Angle of Incidence 50°, Perpendicular Polarization)

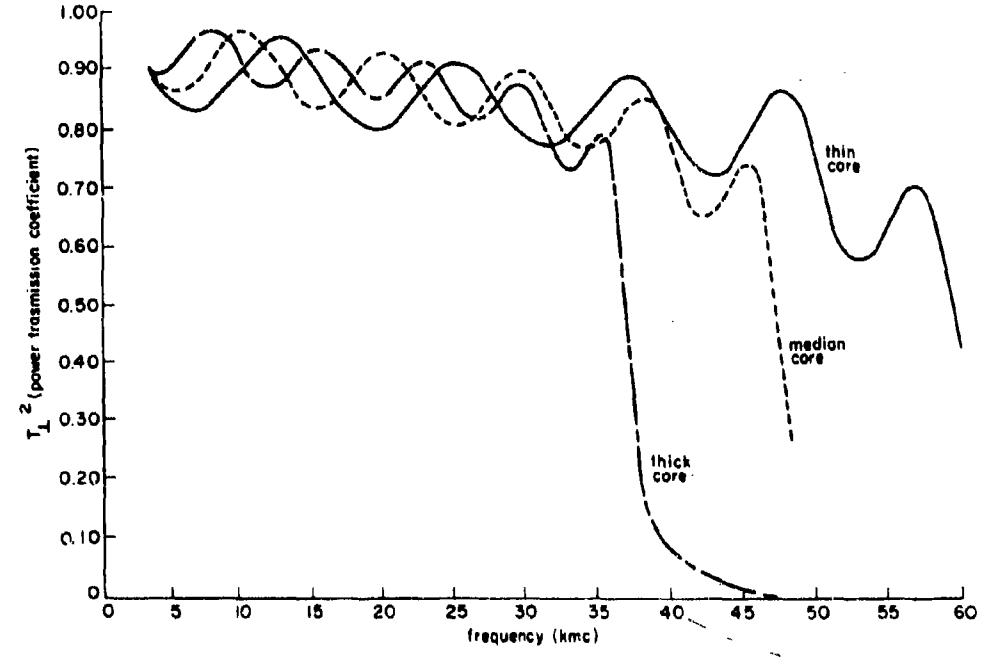


Figure 5–38. Effect of Core Thickness on Transmission of 11–Layer Sandwich (Angle of Incidence 50°, Perpendicular Polarization)

Chapter 6

RADOME STRUCTURAL AND ENVIRONMENTAL DESIGN AND TESTING

by

Robert W. Matlock

Micronics Division
Zenith Plastics Company
Gardena, California

INDEX OF SYMBOLS

A	Area, square inches
a	Acceleration, feet per second per second
a	Half thickness, feet
a	Outer radius of sphere, inches
a	Radius of outside face
b	Inner radius of sphere, inches
b	Radius of inside face
C	Specific heat, Btu per pound, ^{O}F
c_p	Specific heat in Btu per slug, ^{O}F
$\frac{c_p \mu}{k}$	Prandtl number
dy	Element of thickness
E	Young's Modulus, pounds per square inch
e	Base of natural logarithms
E_f	Modulus of elasticity of the face material
E_k	Kinetic energy, foot pounds
F	Force, pounds
F_R	Young's Modulus, radome, pounds per square inch
F_S	Young's Modulus, structure pounds per square inch
f_R	Stress in radome, pounds per square inch
f_S	Stress in structure, pounds per square inch
G_c	Shear modulus
$G_{r\theta}$	Shear modulus in $r\theta$ plane
g	Gravity
g	Acceleration of gravity, feet per second per second
h	Heat transfer coefficient
h	Sandwich shear thickness, inches
I	Moment of inertia of the wall per inch of length of the cylinder
J	Mechanical equivalent of heat (778 foot-pounds per Btu)
k	Thermal conductivity, Btu per square foot-second - ^{O}F per foot
L	Length, inches
L	Load due to acceleration, pounds
M	Mach number
m	mass, slugs
P	Load, pounds
P	Pressure, pounds per square inch
P_{CR}	Calculated buckling pressure, pounds per square inch
P'_{CR}	Corrected buckling pressure, pounds per square inch
Q	Quantity of heat, Btu
q	Dynamic pressure, pounds per square foot
r	Average radius
r	Distance from the center, inches
r	Radius of the sphere, inch
r	Recovery factor

INDEX OF SYMBOLS (cont)

r_t	Recovery factor for turbulent flow	x	Distance normal to surface, feet
r_p	Recovery factor for laminar flow	y	Distance from center to element, inches
S-N curves	Stress to number of cycles to failure	α	Coefficient of thermal expansion, dimensionless
T	Temperature, ^{o}F	β	Nondimensional heat transfer parameter
T	Temperature rise at element, ^{o}F	Δp	Indicates increase in pressure above ambient pressure
T'	Temperature of body, ^{o}Rankine	ΔT	Change in temperature, ^{o}F
T_b	Boundary layer temperature, ^{o}F	δ	Constant, 1.63
T_i	Temperature of the inner surface	δ_S	Elongation due to stress, inches
T_o	Change of temperature of the surrounding medium	δ_T	Elongation due to temperature change, inches
T_s	Stagnation temperature, ^{o}F	θ	Nondimensional time parameter
Tx	Temperature in skin at depth x, ^{o}F	μ	Absolute viscosity of air, slug per foot-second
T'_s	Stagnation temperature, ^{o}Rankine	μ	Poisson's ratio
T_1	Ambient temperature, ^{o}F	μ_f	Poisson's ratio for the face material
T'_1	Ambient temperature, ^{o}Rankine	ρ	Density of material, pounds per cubic foot
t	Thickness, inches	ρ_m	Density of radome wall material
t	Thickness of panel	σ	Stress, pounds per square inch
t	Time, seconds	σ_{CR}	Critical buckling stress
t_e	Solid wall thickness, equivalent	σ_R	Stress in radial direction, pounds per square inch
V	Airspeed, miles per hour	σ_T	Stress in tangential direction, pounds per square inch
v	Airspeed, feet per second		
v	Velocity, feet per second		
W	Weight of item, pounds		

Chapter 6

RADOME STRUCTURAL AND ENVIRONMENTAL DESIGN AND TESTING

SECTION A. STRUCTURAL DESIGN CRITERIA

6-1. Introduction

Many radomes installed on aircraft must be considered as primary structures whose failure would endanger or cause loss of the aircraft. These radomes may be of various configurations, may carry cabin pressure or airframe loads, or may perform other vital functions. The loads or conditions that affect the strength of the radome are discussed on the following pages.

6-2. Aerodynamic Loads

Aerodynamic loads are usually the most critical of those imposed on a radome. The loading may be a function of several conditions, the most important being airspeed, aircraft attitude, radome shape, and the location of the radome on the aircraft.

The determination of the air pressure and its distribution over the surface of the radome is the responsibility of the aerodynamics engineer. The knowledge required and the methods employed are beyond the scope of this work. However, certain fundamentals may be presented.

Figure 6-1 shows an example of a typical pressure distribution over the surface of an elliptical radome on the nose of a fuselage. The stagnation point is the theoretical location of the dividing point of the airstream. At this point the air velocity with respect to the aircraft is assumed to be reduced to zero, thereby converting its dynamic energy to static pressure. This pressure may be calculated from the relation.

$$q = \frac{V^2}{391} \qquad (6\text{-}1)$$

where q = dynamic pressure, pounds per square foot

V = airspeed, miles per hour

The pressure at other points on the surface of the radome is usually expressed in terms of the relation $\Delta p/q$, where Δp indicates the increase in pressure above the ambient pressure. The value of $\Delta p/q$ may be presented either as a scale drawing, as indicated by Figure 6-1A, or by curves, as indicated in Figure 6-1B. Note that at the stagnation point the stagnation pressure has a value of $\Delta p/q = 1.0$.

The radome shown in Figure 6-1 is of a shape satisfactory for subsonic aircraft. At higher speeds the radome tends to be more streamlined. The conic radome shown in Figure 6-2 is an example of a configuration for very high speed flight. The typical aerodynamic loading is shown in Figure 6-3.

If there is lack of symmetry caused by a yaw or pitch attitude of the aircraft, or by a gust, the radome will pass through the airstream at an angle. This will produce unsymmetrical pressures on the radome, which in turn will create a bending moment and shear load. Such a condition of unsymmetrical air loading is shown in Figure 6-4.

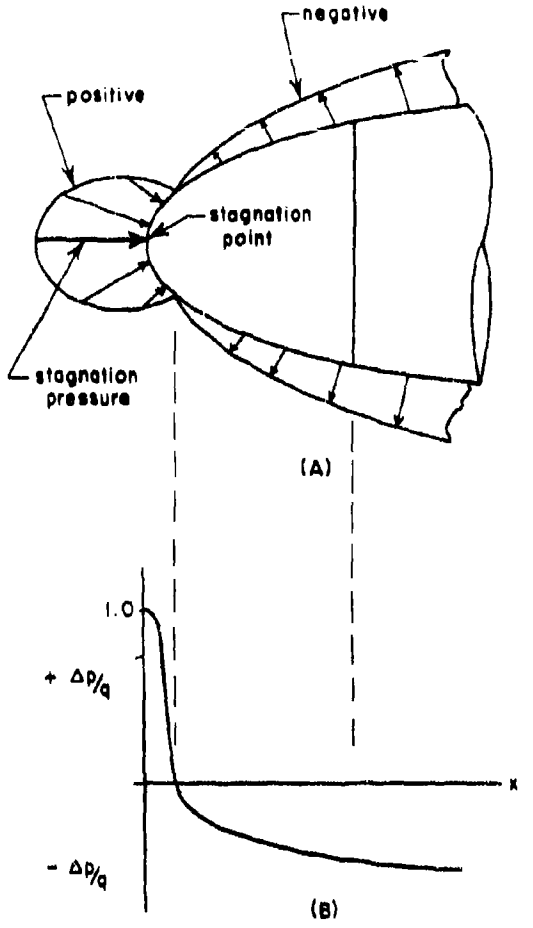


Figure 6-1. Pressure Distribution Over Surface of a Subconic Radome

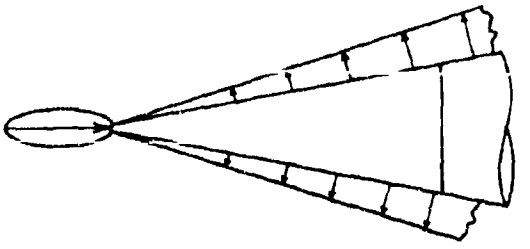


Figure 6-2. Pressure Distribution Over Surface of a Conic Radome

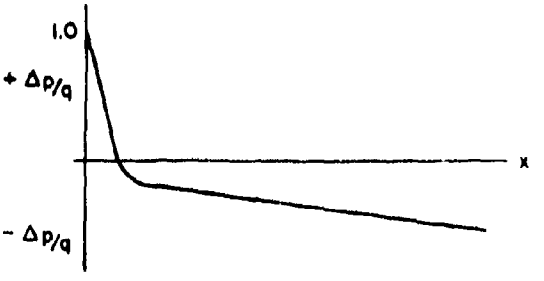


Figure 6-3. Aerodynamic Loading For a Conic Radome

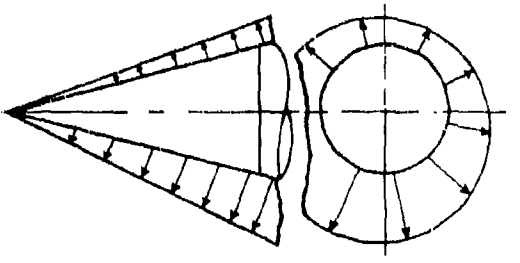


Figure 6-4. Unsymmetrical Air Loading On a Conic Radome

6-3. Inertia Loads

Inertia loads are caused by sudden changes in the direction of motion of the aircraft. Such accelerations may be engendered by acrobatic maneuvers, by landing, braking, or by encountering a gust. Inertia loads may also be created by rotational accelerations of the aircraft about any one of its axes, by vibration, or from many other causes.

Inertia loads are measured in terms of gravity, or "g". If an airplane essays a 3g maneuver, every item of weight will be tripled. A radome or antenna that normally weighs 100 pounds will weigh the equivalent of 300 pounds.

Because the loads produced by aerodynamic forces are generally very large in comparison to the inertia loads of the radome, the latter may generally be neglected. Exceptions to this general statement may be the cases where a large and heavy boom is carried in the nose of the radome, where antennas or other items of heavy equipment may be supported directly by the wall of the radome or where the radome is constructed of a very dense material such as a ceramic. In these cases the inertia load due to translational acceleration may be calculated as follows:

$$L = \frac{Wa}{g} \qquad (6\text{-}2)$$

where L = load due to acceleration, pounds

W = weight of item, pounds

a = acceleration, feet per second per second

g = acceleration of gravity, feet per second per second

Radome deflections caused by inertial loads may be critical where close clearance exists between the radome wall and antenna dish. In this case, radome and dish deflections should be analyzed to insure clearance under maximum accelerations. Excessive radome deflection is undesirable electrically in any case and may be a serious problem with high fineness ratio configurations that require low beam deflection errors.

6-4. Internal Pressure

The location of a radome on the aircraft is usually determined by electrical considerations. It may therefore be found in areas where internal pressure must be carried. In some instances internal pressure is required for proper operation of attendant antennas. In both of these cases the pressure will not only be known, but will be controlled within very close limits. The known loads on the radome will thus allow an accurate basis for the calculation of stress in the radome and in its attachment to the aircraft structure.

It is more usual for a radome to be installed in an unpressurized area. Here the designer and stress engineer might assume that the internal pressure is ambient. This could be a very dangerous assumption, particularly if the radome has a shape that makes it inappropriate or weak as a pressure vessel.

It has been found that pressure variations of some magnitude may be created in radome cavities by the opening of a door, the lowering of a flap, or some other circumstance that may alter the character of the air flow. If the radome shape or wall construction is such that small positive or negative loads can produce critical stresses, than conservative assumptions of internal pressure must be made.

A hemispherical or cylindrical shape is obviously excellent for carrying internal pressure if the material has good tensile strength. If the internal pressure is negative the radome will be critical for instability buckling. The critical pressure for such a case is difficult to predict accurately. Particularly if the shape is something other than spherical or cylindrical, very high bending moments may be developed with very low differential pressures.

6-5. Blast Pressure

The term "blast pressure" is applied to pressure waves from explosions. The pressure created is similar to that produced by aerodynamic loading but is of short duration, generally sever, and almost always asymmetric in application. Blast pressures themselves vary considerably in duration, depending on the source, and differ in their structural effect on the radome.

A pressure wave induced by the explosion of a very heavy charge may have a duration of several seconds. This interval of time is large enough to consider the pressure produced as a static loading. The blast pressure in this case may be considered to act in conjunction with other static loads applicable to the condition.

A pressure wave of very short duration, even though of high intensity, is not likely to produce a general instability failure of a radome. The inertia of the radome wall itself will largely resist any loading of short duration. If the blast pressure is repeated at high frequency, as from a machine gun, it is possible that a resonance may be set up that could result in failure of the radome. This is a transient condition almost impossible to analyze.

The greatest danger from high-frequency blast is general disintegration of the random wall. This is particularly likely for sandwich walls with light cores.

6-6. Ambient Loads in Adjacent Structures

The electrical requirements of radomes usually require their placement on extremities of the airplane, such as the nose or tail of the fuselage, the tips of the wing or fin, or suspended as an appendage to some other portion of the aircraft. In all of these locations the structural loads are comparatively slight. The very common type of radome installation, consisting of a hemispherical shaped enclosure attached to the belly of the aircraft, is a case, however, where the radome may be fitted to a heavily loaded structure. Here again, the shape is such that very little load can be transmitted into the radome itself. In all of these cases the stress analysis of the radome can usually proceed under the assumption that the mounting structure is rigid and undistorted,

and that no structural loads are transmitted into the radome.

As aircraft speeds increase there is increasing necessity to employ more shallow radome shapes, or to make them flush with the aircraft contour. When these radomes are located at some distance from the extremities, the surrounding structure may be highly stressed. If the radome be solidly attached to the surrounding members, it is inevitable that it will, assume some of their load. The stresses thus created must be considered in the design with all the care of the primary or direct loads. In fact, a radome of this type may be taken as an article of primary structure since any sudden failure would result in a sudden shifting of load to adjacent material and could cause failure of the primary structure.

The amount of stress assumed by the radome in parallel structures of the type described will be proportional to the rigidity of the two materials. Since rigidity is a function of Young's Modulus, the relation is:

$$f_R = f_S \frac{E_R}{E_S} \qquad (6\text{-}3)$$

where f_R = stress in radome, pounds per square inch

f_S = stress in structure, pounds per square inch

E_R = Young's Modulus, radome, pounds per square inch

E_S = Young's Modulus, structure, pounds per square inch

As an example of the severity of the loads that can be imposed, a stress of 10,000 pounds per square inch will be imposed on a glass-reinforced plastic radome if it is attached to an aluminum structure carrying a stress of 40,000 pounds per square inch. In this case Young's Modulus of the plastic was assumed to be 2.5 million and that of the aluminum to be 10 million.

In addition to the direct axial loads, tension, and compression, the radome may be forced to pick up all of the shear flow in its local area. In this case the load may not be proportional to rigidity.

6-7. Thermal Shock

Thermal shock is the term applied to the condition in which large temperature gradients are induced in a structure. These gradients produce differential expansion which, in turn, produces stresses in the material. These are termed thermal stresses. Some of the factors that influence the amount of stress that may be created in the wall of a radome by thermal shock are listed and described below.

a. Temperature distribution. The rate of flow heat is a function of the applied temperature with respect to the temperature of the part under consideration.

b. Heat transfer coefficient. The rate of flow of heat between the surrounding medium and the part is also a function of the heat transfer coefficient. The heat transfer coefficient is defined as the amount of heat that can be transferred in unit time between the surrounding medium and a unit area of the part for each unit of temperature difference.

c. Thermal conductivity. The rate of heat transfer into the part and the thermal gradients within the part are largely controlled by the thermal conductivity of the material, or materials if the part is a sandwich structure.

d. Thickness of the part. The thickness of the part affects the temperature gradients within the part, and therefore the thermal stresses that are developed.

e. Emissivity. The loss of heat due to radiation is a function of the emissivity of the material.

f. Time of exposure. The duration of exposure determines the degree of heat penetration and, with other factors, determines the temperature gradients and stresses in the material.

The combined effect of these many factors is frequently complex and not always analytically determinable. If a material had an infinitely high thermal conductivity, so that it could instantly assume a uniform temperature consistent with any change of temperature of the surrounding medium, then there could be no thermal stress generated in the part. (This is not true for a sandwich using two materials having different coefficients of thermal expansion.) This might lead to the general conclusion that a high thermal conductivity is always helpful in eliminating failure from thermal stress. This assumption, however, is entirely incorrect for the case of a material with a low tensile

strength when subjected to a very high temperature for a short period of time. With low thermal conductivity only the outermost fibers become heated and, when expanded, require only low internal tensile stresses for equilibrium. If the material had high thermal conductivity, a greater amount of the outside fibers would become heated, and would require higher internal tensile stresses for equilibrium. An excellent discussion of the phenomena of heat transfer and thermal stresses is given in Reference 1.

Thermal shock may be imposed on an aircraft structure from many sources, e.g., the engines or other propulsion units, devices to assist in takeoff, or proximity to an explosion of great intensity. The most usual case, however, will be that of the aircraft traveling for short periods of time at velocities sufficient to generate a great amount of heat through friction with the atmosphere. The temperature rise associated with this type of heating is termed "aerodynamic heating".

The determination of the thermal effect due to engines or propulsion units is too broad a subject to be considered here. The multitude of variables in power plant installations with respect to radomes precludes any possibility of adequate discussion. In addition, the design criteria related to the thermal effects of high-intensity explosions cannot be discussed for several reasons. Therefore, only the design criteria for aerodynamic heating will be considered.

The source of the heat that produces the temperature rise in the aircraft surfaces is the kinetic energy available in the relative windstream. At the stagnation point on the nose or leading edge entering the windstream, where the windstream velocity is reduced to zero, the entire kinetic energy is assumed to be converted into heat energy. Along the sides of the surface, skin friction produces a boundary layer effect, which results in a theoretical velocity of zero at the surface. As the airstream adjacent to the surface is moving at airstream velocity, it is apparent that a shearing action must take place between the adjacent layers of air as shown in Figure 6-5. Due to the viscosity of the air, a friction force is generated, which produces a temperature rise. The air, heated by these two phenomena transfers heat to the relatively cool surfaces of the aircraft until the temperature rises enough to cause loss of heat from the body, due to conduction and radiation, to just offset the input of heat. At this temperature, thermal equilibrium exists.

The temperature due to aerodynamic heating and the temperature gradients in the wall of solid-wall radomes may be calculated from the following equations.

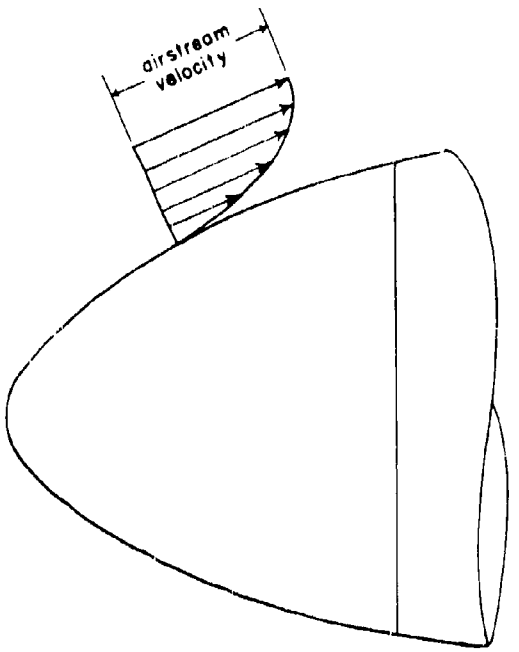


Figure 6-5. Boundary Layer Velocity Gradient

Stagnation Temperature. The stagnation temperature is the temperature reached by the air brought to a complete rest at the nose or leading edge of a surface entering the windstream. The temperature of the air may be calculated from the following equation[2]

$$T_S = 1/2 \frac{v^2}{Jc_p} + T_1 \qquad (6\text{-}4)$$

where T_S = stagnation temperature, °F

T_1 = ambient temperature, °F

v = airspeed, feet per second

J = mechanical equivalent of heat (778 foot-pounds per Btu)

c_p = specific heat in Btu per slug, °F (one slug = 1 geepound = 32.174 pounds)

The specific heat of air is not a constant but varies with temperature. The value of c_p may be taken from Figure 6-6, calculated from Equation (6-5)

$$c_p = 8.055 \times 10^{-7} T^2 + 7.60 \times 10^{-5} T + 7.717 \quad (6\text{-}5)$$

where c_p = specific heat, Btu per slug, °F

T = temperature in °F.

The stagnation temperature may also be calculated from an equation presented by N.J. Hoff[3], which assumes that c_p is independent of temperature.

$$T_s' = T_1' \left(1 + \frac{M^2}{5} \right) \quad (6\text{-}6)$$

where T_s' = stagnation temperature, °Rankine (Degrees Rankine is °F plus 460.)

T_1' = ambient temperature, °Rankine

M = Mach number

Recovery Factor. The temperature rise of the boundary layer of air around an object in the airstream is generated by friction. The layer of air adjacent to the surface is assumed to have zero velocity. Subsequent layers away from the surface are moving at increasing speeds until free airstream velocity is reached. The difference in velocity of the layers of air with respect to each other produces friction among the molecules, and a corresponding rise in temperature. The ratio of the temperature rise due to friction as compared to the temperature rise due to compression is called the recovery factor. The recovery factor may be expressed mathematically by

$$r = \frac{T_b - T_1}{T_s - T_1} \quad (6\text{-}7)$$

where r = recovery factor

T_b = boundary layer temperature, °F

T_1 = ambient air temperature, °F

T_s = stagnation temperature, °F

The recovery factor may be calculated to a degree of accuracy suitable for most practical applications from the following equation which was derived for a flat sheet parallel to the windstream.

$$r_\rho = \left(\frac{c_p \mu}{k} \right)^{1/2} \quad (6\text{-}8)$$

$$r_t = \left(\frac{c_p \mu}{k} \right)^{1/3} \quad (6\text{-}9)$$

where r_ρ = recovery factor for laminar flow

r_t = recovery factor for turbulent flow

c_p = specific heat of air in Btu per slug, °F

μ = absolute viscosity of air, slug per foot-second

k = thermal conductivity of air, Btu per square foot-second-°F per foot

$\frac{c_p \mu}{k}$ is usually referred to as the Prandtl number. for c_p, k, and μ may be taken from Figures 6-6, (Values 6-7, 6-8, and Equation (6-5).)

The recovery factor for various cone angles and airstream velocities[2] is shown in Figure 6-9. The axis of the cone coincides with the direction of motion. In addition to the variation with cone angle and velocity, the recovery factor is influenced by the station along the cone, since the thickness of the boundary layer increases with distance from the nose. As the thickness of the boundary layer increases, less heat is transmitted. The attitude of the cone would also affect the temperature because of its effect on turbulence, but it is doubtful that this effect can be evaluated at this time.

Boundary layer temperatures for various velocities and altitudes, and for laminar and turbulent flow, are shown in Figure 6-10. The data presented are intended to be indicative, not precise. It is doubtful that precise calculations of temperature along the sides of a radome can be made at the present time.

Equilibrium Temperature. With increased time of exposure, the temperature of a surface will gradually approach the temperature of the boundary layer. Most of the difference between the two temperatures will be due to heat lost through radiation. At lower speeds and lower temperatures, the difference will be less than at higher speeds and higher temperatures.

The radiation loss of a black body is:

$$Q = 0.481\left(\frac{T'}{1000}\right)^4 \text{ Btu per sq. ft. - sec.} \quad (6\text{-}10)$$

where Q = quantity of heat, Btu per square foot-second

T' = Temperature of body, ^{0}Rankine

Since the temperature loss from radiation is proportional to the fourth power of the absolute temperature, it is only at high Mach numbers and corresponding high temperatures that radiation losses are appreciably high.

Another source of heat loss is conduction into other portions of the airframe, such as the structural members, the fuel, and other items making up the mass of the structure.

Transient Skin Temperatures. An exact determination of the time-temperature history of the thermal gradients in a radome wall under conditions of thermal shock is difficult. Reference 2 presents both a simplified method and a more exact method for use with solid-wall radomes. The equation for the simplified method is given here for convenience.

$$T_x \approx T_b - (T_b - T_1)\left(1 - \frac{h'e^{\frac{-\delta x}{2a\sqrt{t}}}}{\frac{\delta}{2a\sqrt{t}} + h'}\right) \quad (6\text{-}11)$$

where T_x = temperature in skin at depth x, ^{0}F

T_b = Boundary layer temperature, ^{0}F

T_1 = ambient temperature, ^{0}F

h' = h/k

h = heat transfer coefficient, Btu per square foot-of-second

k = thermal conductivity ^{0}F air

δ = constant, 1.63

e = base of natural logrithms, 2.71828

x = distance normal to surface, feet

a = diffusivity, $\left(\frac{k}{\rho_m C}\right)^{1/2}$

k = Thermal conductivity of radome wall material.

ρ_m = Density of radome wall material.

C = specific heat of radome wall material.

t = time, seconds

Typical, approximate, computed curves of temperature versus time are given in Figures, 6-11 through 6-14 as a function of h, k, C, and x.

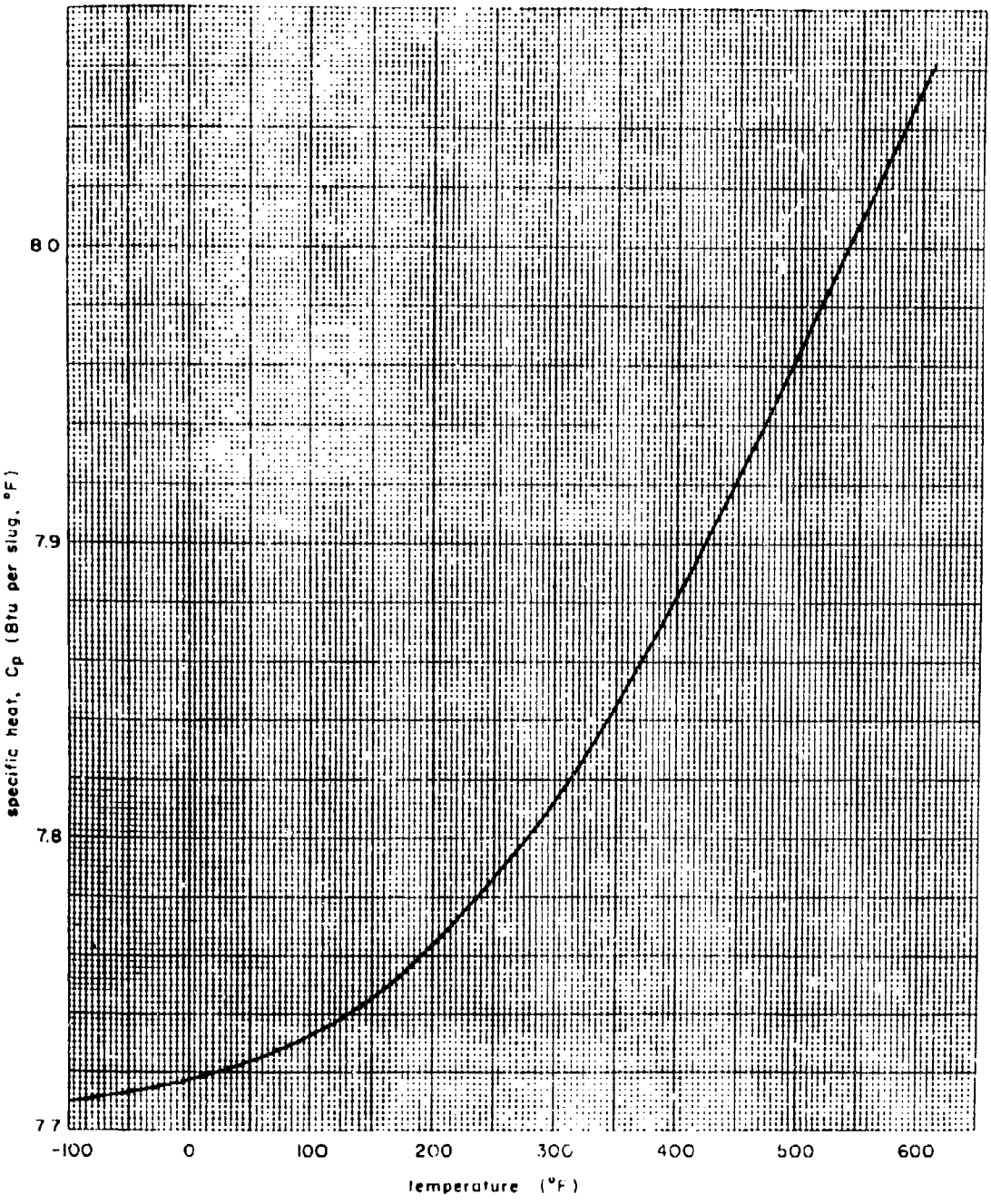


Figure 6-6. Specific Heat of Air

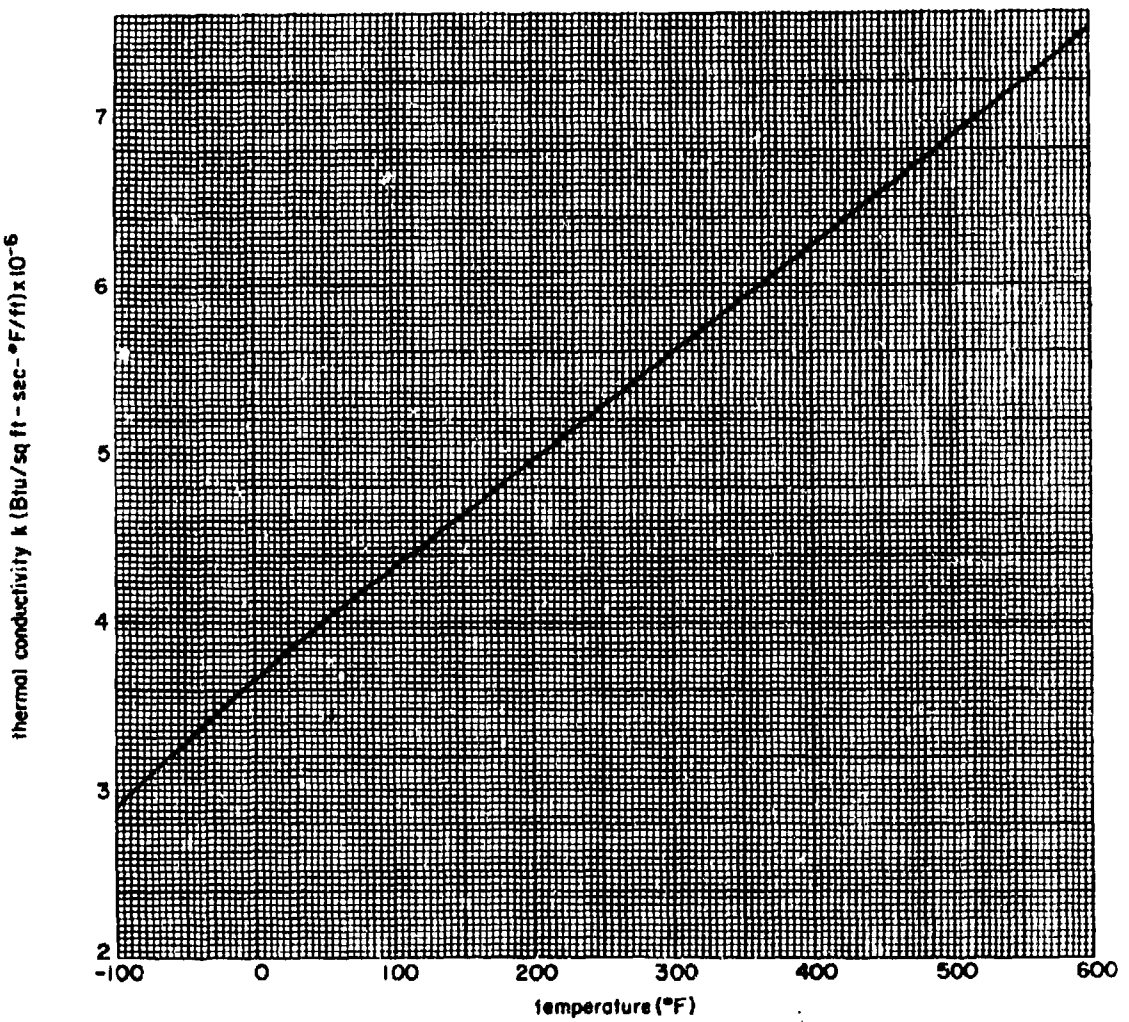


Figure 6-7. Thermal Conductivity of Air

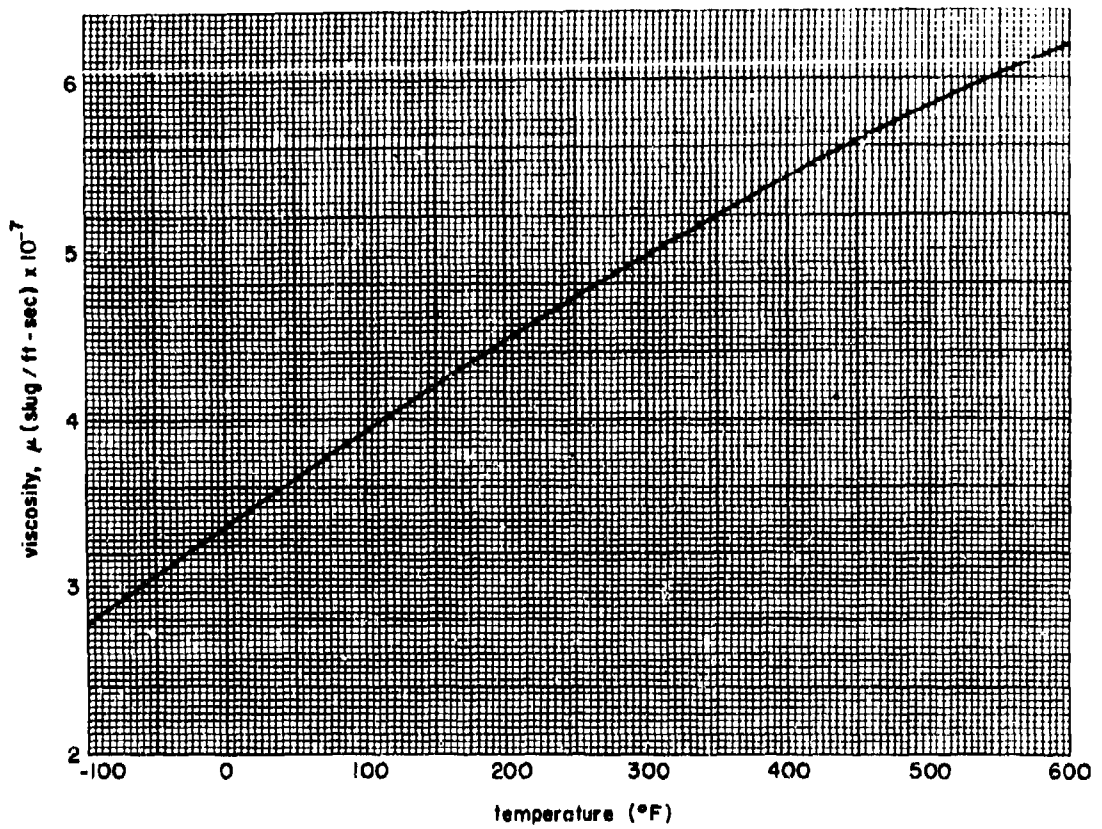


Figure 6–8. Viscosity of Air

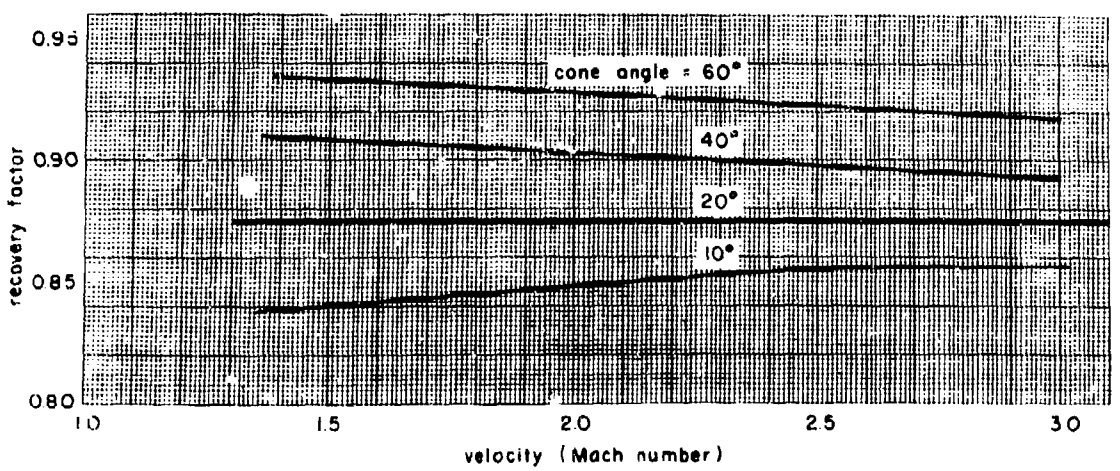


Figure 6–9. Temperature Recovery Factor Versus Velocity for Several Cone Angles

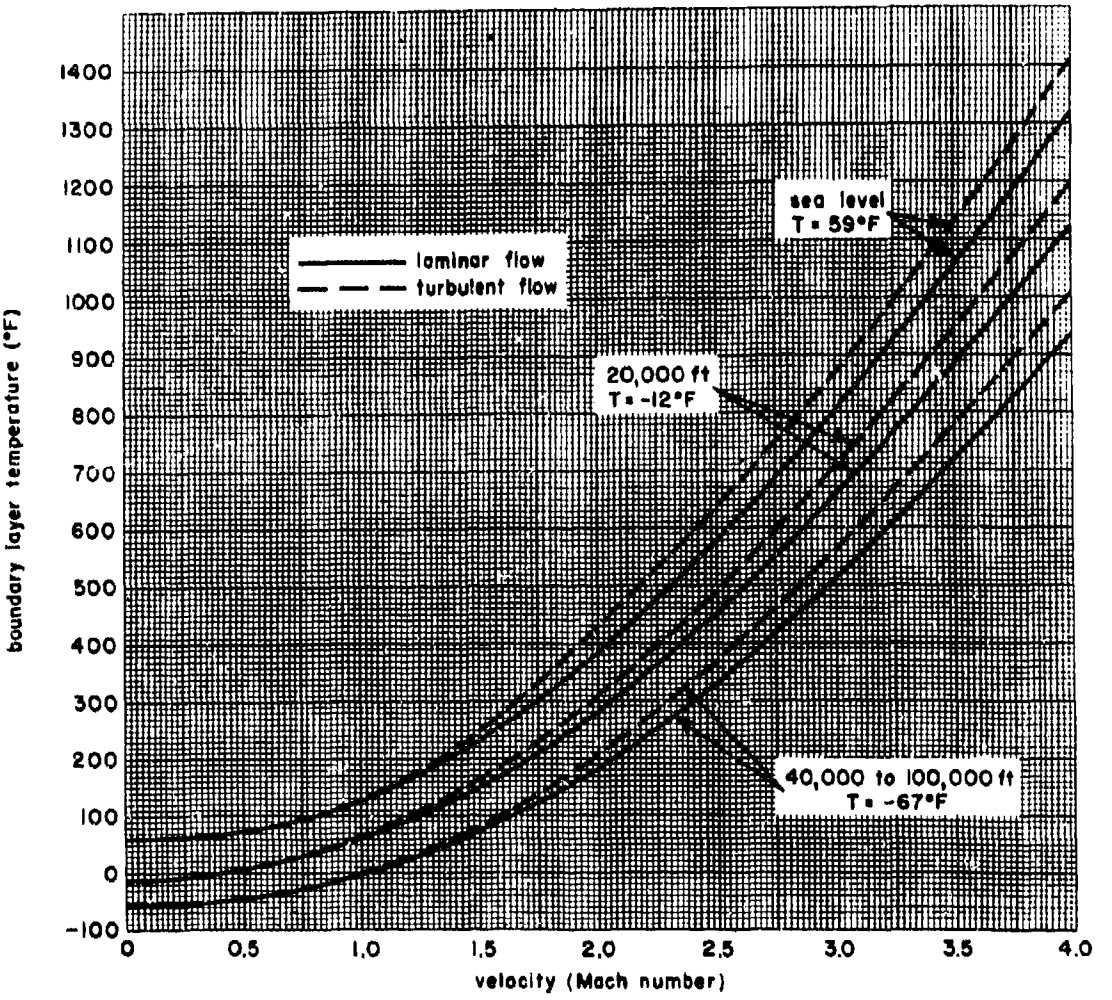


Figure 6-10. Boundary Layer Temperature Versus Velocity (Neglecting Radiation)

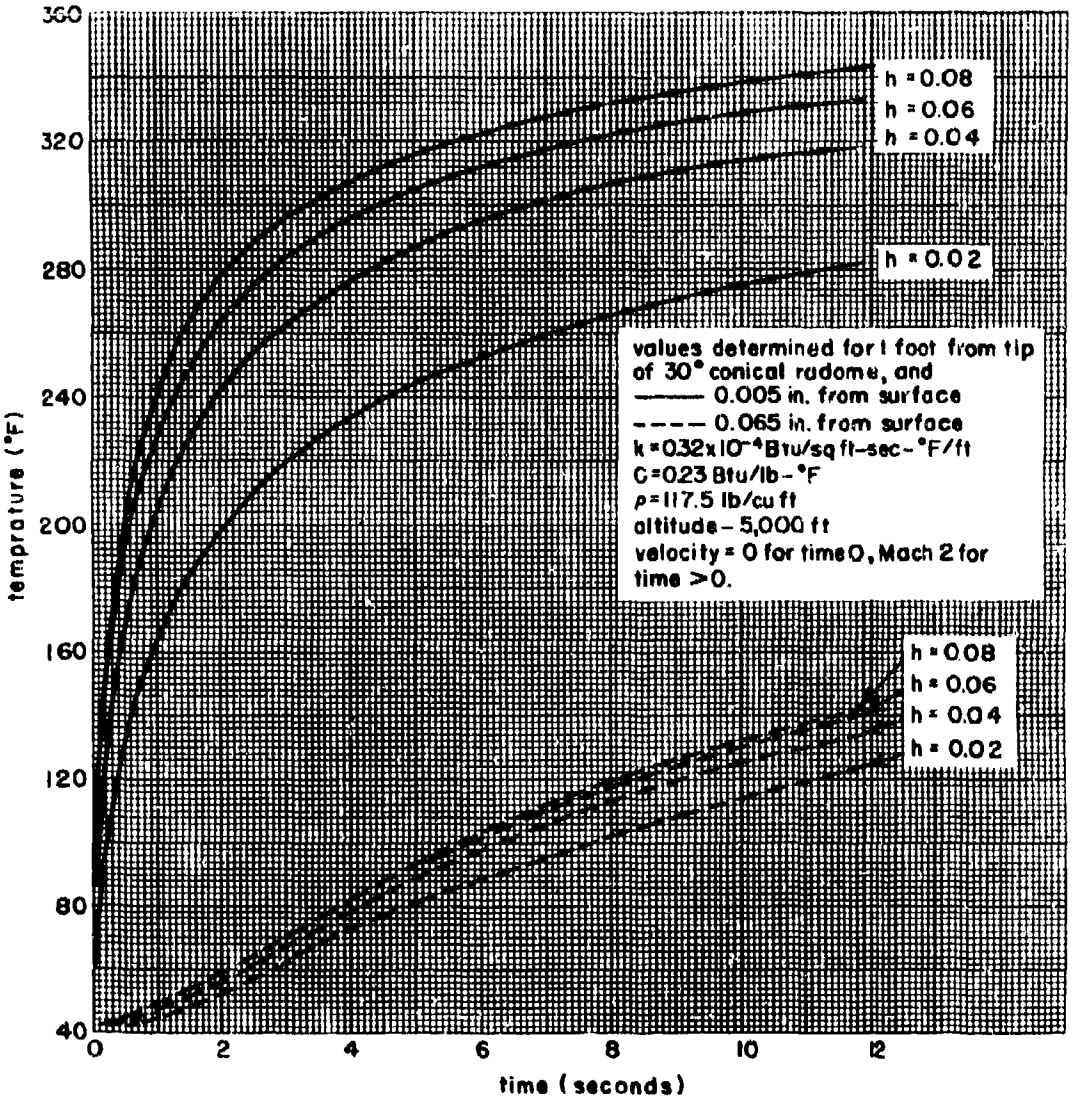


Figure 6-11. Radome Skin Temperature Versus Time for Different Values of Boundary Layer Heat Transfer Coefficient (h)

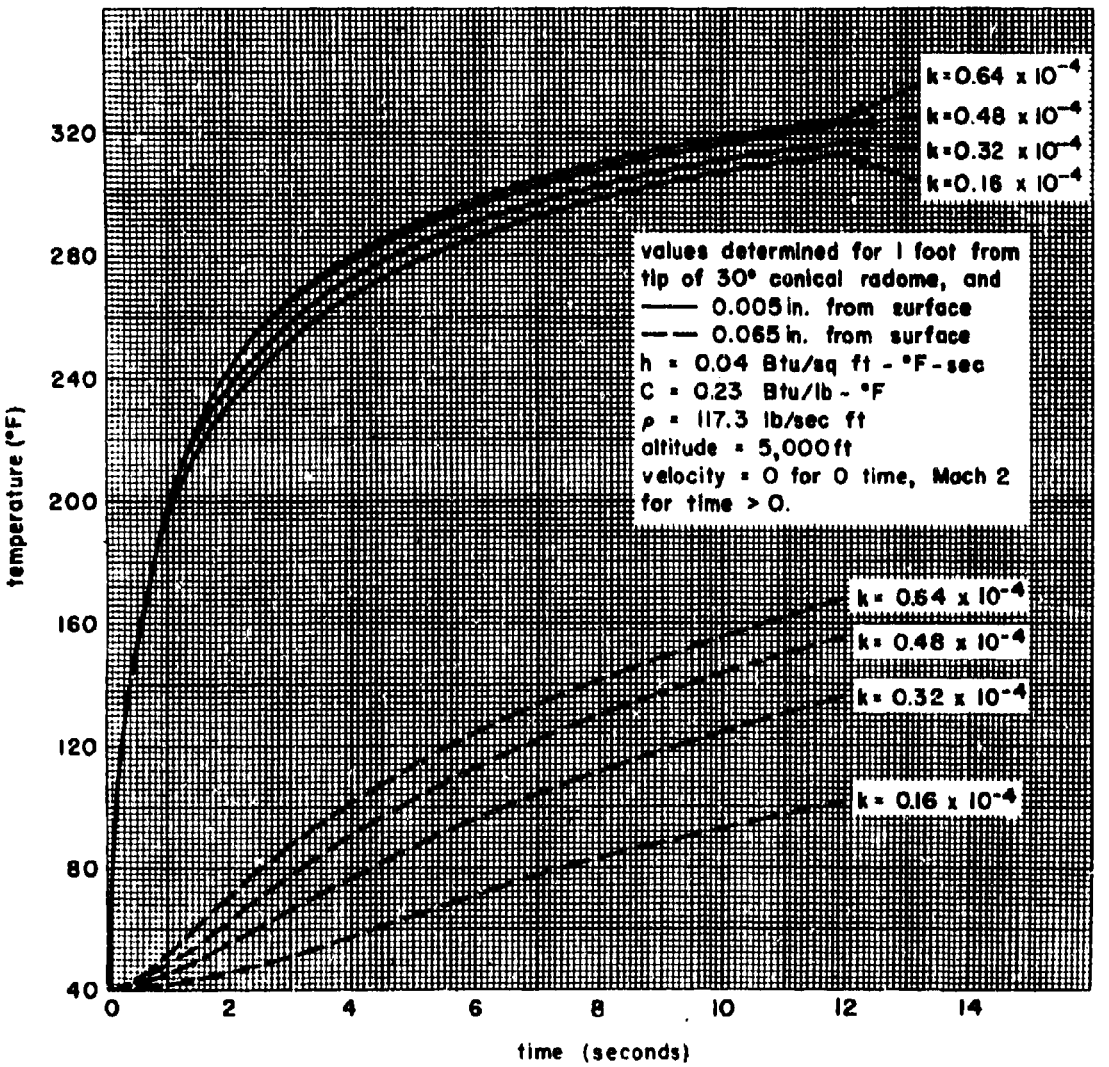


Figure 6–12. Radome Skin Temperature Versus Time for Different Values of Thermal Conductivity (k)

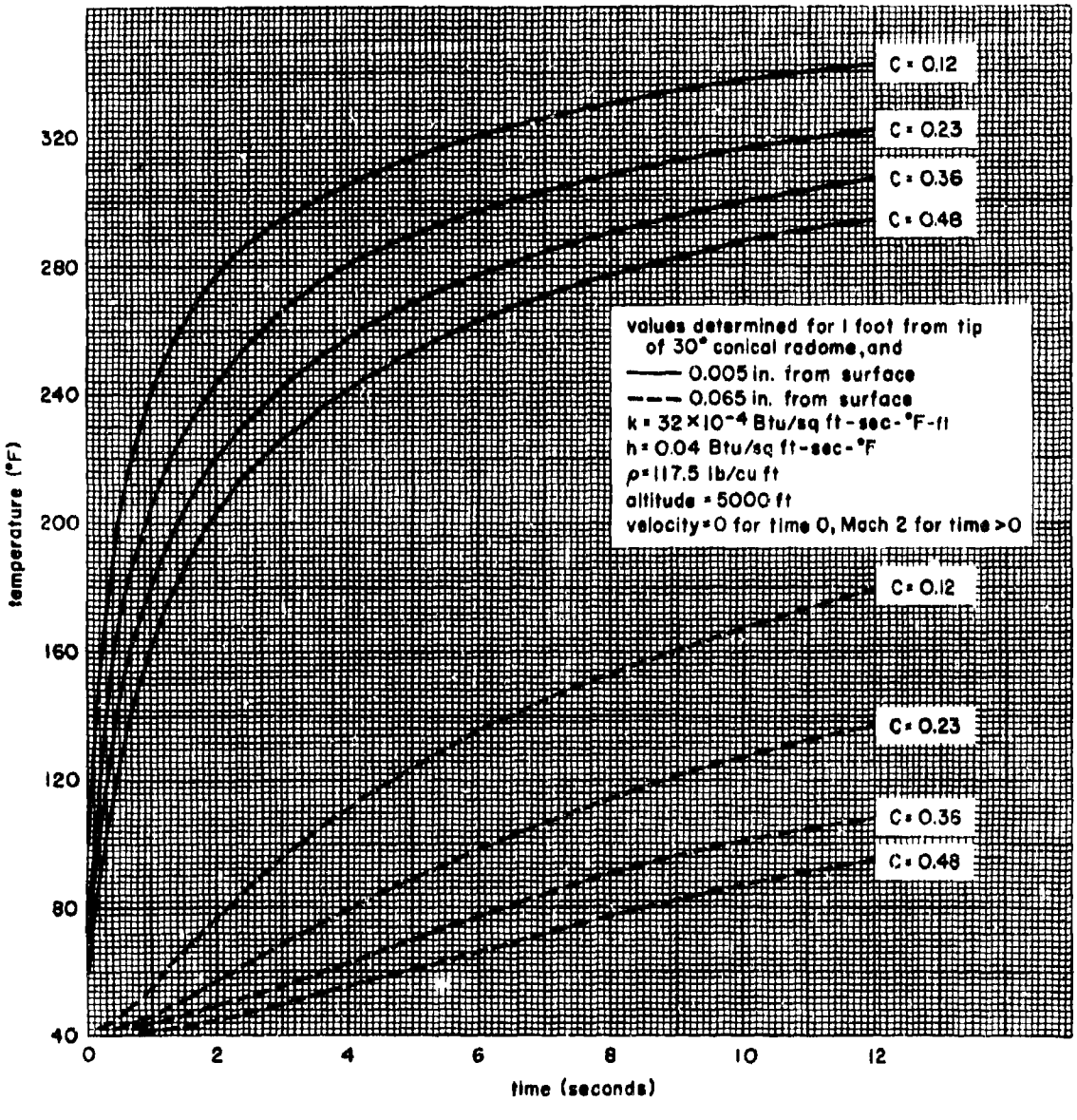


Figure 6–13. Radome Skin Temperature Versus Time for Different Values of Specific Heat (c)

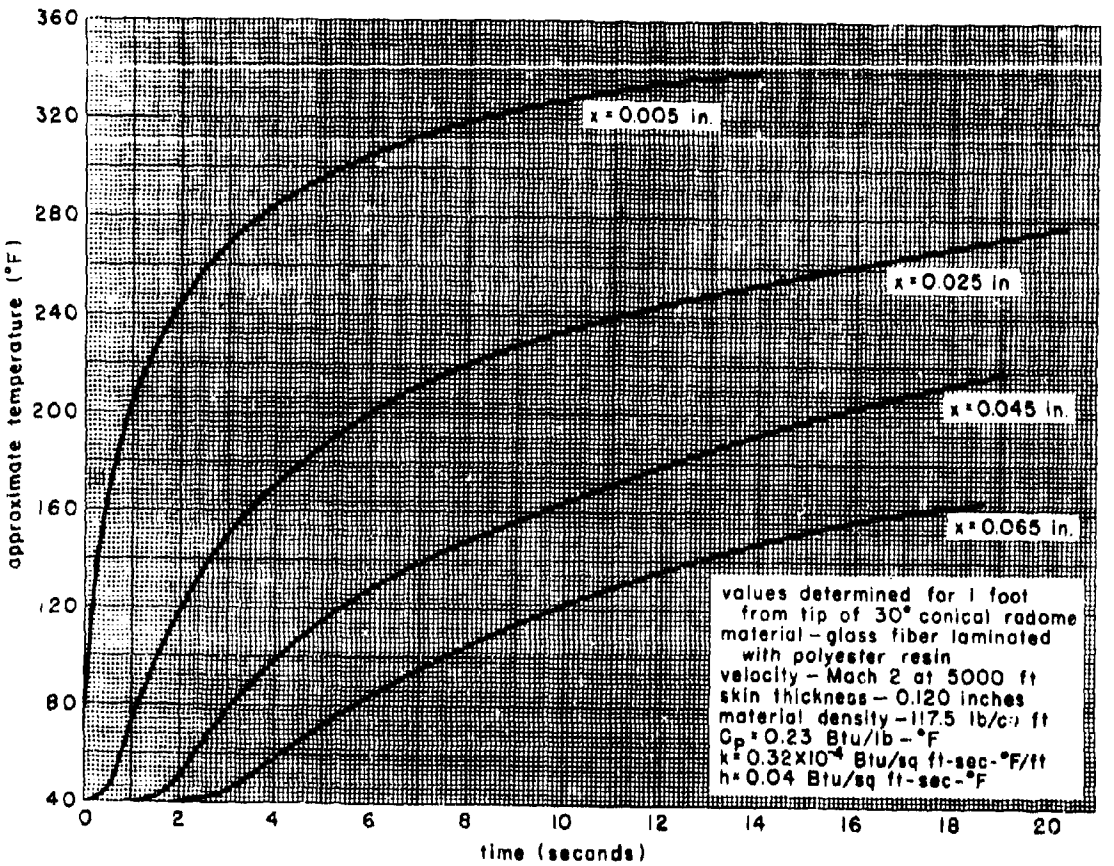


Figure 6–14. Radome Skin Temperature Versus Time for Different Values of Distance (x)

6-8. Thermal Stress

As discussed in paragraph 6-7, thermal shock produces stress because of the thermal gradients within the walls of the material. As the temperatures within a homogeneous material equalize, the thermal stress disappears.

On the other hand, in structures composed of materials with different coefficients of thermal expansion, thermal stresses will still exist, under isothermal conditions as a result of the original temperature change. An example of this is the stress induced when dissimilar metals are restrained with respect to each other, and subjected to a change of temperature. Another example is the case of a radome using a sandwich construction.

Similarly, thermal stresses exist when the skins of a wing become heated and expand, while the interior of the wing remains relatively cool. In this case all of the factors exist in a manner identical to thermal shock, except that the time interval is much longer.

Some of the factors that affect the degree of thermal stress induced in a structure by temperature changes are: the relative temperatures, the coefficients of thermal expansion, Young's Modulus, and the areas of the two materials acting in mutual restraint.

6-9. Thermal Buckling

Thermal buckling is caused by thermal stress, whether it results from temperature differential or from the difference in elongation of dissimilar materials. The term "buckling" implies compression or shear stress. If parts of the aircraft structure are loaded in compression or shear, and if thermal stresses produce an initial bowing or bending, then the primary stresses may become critical, and result in premature failure of the part. It should be noted that the buckling of panels is

not the creation of stress, but rather the relief of stress. A homogeneous slab with unequal face temperatures will bow in a curve, which will completely relieve stress provided there is no restraint. The stress associated with the temperature differential, in a restrained part, may be calculated as the stress produced in forcing the bowed bar into its original straight shape.

If the part under consideration is an external surface, the smoothness or waviness requirements of the aircraft may be destroyed by thermal buckling. Buckled or warped panels, twisted frames, gaps, or protruding edges are obviously aerodynamically undesirable.

6-10. Impact

The problem of impact resistance of radomes has received little attention, and there are no common design criteria for this condition. A simple analysis of the problem may, however, be of some help.

Impact loads may be divided into four classes:

a. High velocity-low mass objects, such as the impact of hailstones in flight.

b. High velocity-high mass objects, such as the impact of large birds in flight.

c. Low velocity-high mass objects, such as striking a radome with a ladder or other object while handling or servicing.

d. Low velocity-low mass objects, such as small particles of gravel driven by a high wind or blast from another aircraft.

The Naval Air Development Center, Johnsville, Pa., recognizing the importance of impact resistance, developed a test method for sandwich construction, which consists of dropping a 2-inch-diameter steel ball a distance of 26 feet onto a 12-inch-square panel with simple edge support. Sandwich panels capable of resisting this test were designed and constructed. These panels were made with flexible resins and special core material (high-density honeycomb dipped in flexible resin). Test panels patterned after this construction demonstrated that this impact-resistant construction was somewhat superior to conventional sandwich constructions.

Although the panels described offered more resistance to impact than regular panels, it could not be said that they were hail resistant. The question of hail resistance must include the factors of hailstone size and aircraft velocity; and to the writers knowledge suitable criteria have not been defined for any aircraft.

The impact of "bird-sized" objects in flight can be expected to be accompanied with such a high level of energy that considerable damage may be done. The amount of damage that can be expected will depend on the mass of the object, velocity, angle of impact, and the strength and rigidity of the structure. Solid wall radomes are highly impact resistant due to the high strength and flexibility of reinforced plastic materials. Sandwich structures are extremely susceptible to damage due to their relatively weak core materials.

Sandwich structures may easily be delaminated by a single blow, from handling or by impact with an object while in flight. Although the delamination may be small, its effect on the strength of the part may be serious. The low peel strength of the brittle bonds employed do not tend to contain or limit areas of failure and delamination of unbonded areas will propagate rapidly when subjected to vibratory loads.

Impact damage from handling is unlikely in solid wall radomes of reinforced plastic, but is a serious problem with sandwich construction. Every effort should be made to protect the radome from damage and abuse. Frequent inspections should be made during its service life to insure early knowledge of failure.

Small impact loads can usually be sustained even by a fragile sandwich. Impacts of small rocks or gravel, or by a screwdriver, will not normally result in damage unless the skins are unusually thin. Rain erosion coating or rubber boots are of considerable aid in resisting this kind of damage.

The use of heavy wall constructions, boots, and flexible resins usually results in inferior strength-to-weight ratio and electrical characteristics. The gain in impact resistance by these methods is usually at the expense of poorer radome performance.

SECTION B. FACTORS AFFECTING THE STRENGTH OF RADOMES

6-11. Introduction

The stress analysis of radomes is basically no different than that of any other structure. The sequence of thought and solution to be followed is identical to the stress analysis of any other part of the aircraft. The steps normally followed are presented below:

a. Determine the loads or conditions that may cause or contribute to failure.

b. Visualize the various modes of failure that may take place.

c. Determine the stresses, or, if the part is critical for instability buckling, determine the loading applicable to the mode of failure.

d. Determine the allowable stress, or, if checking for instability, determine the allowable load applicable to the mode of failure under consideration.

Although the basic methods of stress analysis for radomes are like those for any other structure, the details of the analysis are much more difficult because they are complicated by many of the factors listed and discussed on the following pages.

6-12. Shape

The general geometry of radomes places them in the category of shells or unsymmetrical pressure vessels. This is a configuration category generally conceded to be one of the most difficult to analyze. The design problem is further complicated by the fact that most radomes do not have analytic shapes, such as spheres, cones, cylinders, or ellipsoids. In many cases the shape is largely determined by the structure to which the radome is attached or is forced to conform to unnatural contours by surrounding structure. These shapes usually are not mathematically defined, but are described by loft lines only.

6-13. Loading

The loading on radomes can be highly complex, consisting of aerodynamic loads, inertia loads, internal pressure, blast pressure, primary structure loads, thermal stresses, vibration, and impact. These loads may be applied separately, or together in many different combinations. Wings, fuselages, surfaces, and gear usually have well-defined and simple loading systems. A radome, on the other hand, is likely to have rapidly varying loads as a result of positive and negative pressures over its surface. The very first phase of the stress assessment may thus become impossibly complex and require simplifying assumptions before analysis can begin. If several loads are simultaneously applied, further simplifications must be made. It is apparent that a considerable amount of judgement must be used to prevent the simplifications from becoming either excessively conservative or dangerously unconservative.

6-14. Materials

Reinforced plastic materials used in radome construction are usually unfamiliar to the stress analyst. In place of the familiar steel and aluminum alloys, which have well documented physical properties with minimum guaranteed physical properties, the analyst is forced to deal with an unknown material having ill-defined and probably inconsistent physical properties and characteristics. Metals, the materials familiar to most designers, are blessed with isotropic, or near-isotropic properties. With but few exceptions, reinforced plastic materials are not isotropic, and may not even be orthotropic. This may become all the more confusing if the known direction of the fibers gets lost in the layup.

In metal design, the stress analyst is required to work with relatively few well-known materials. Reinforced plastics, on the other hand, may be fabricated from any one or a mixture of many types of cloth, using one of several resins, and with various catalysts, cures, pressures, and curing time, each factor being significant in the strength of the final laminate.

6-15. Wall Construction — General

The radome wall may be fabricated either as a solid wall, or as sandwich wall. Although solid wall radomes may be considered as conventional, little data is available for analytical approaches for shapes normally found in radomes. If the wall construction is a sandwich, the stress analysis is greatly complicated. Much of the data suitable for use with solid-wall radomes is useless or must be used with conservatism when applied to a sandwich structure. In radome construction, the faces of the sandwich are almost invariably made of reinforced plastic. The core material, on the other hand, may be glass-reinforced plastic honeycomb, foamed in place, prefabricated

expanded plastics, fluted core, or waffle core. Other core materials of sundry materials and characteristics may also be employed.

The core materials enumerated exhibit diverse properties, many of which have a decided effect on strength. It is deemed worthwhile to discuss these properties in detail, since knowledge of their characteristics is very necessary in the preparation of an accurate prediction of radome strength.

6-16. Wall Construction — Honeycomb

The most common core material is glass-cloth reinforced plastic honeycomb. This material may be considered relatively uniform, reproducible, and consistent in strength. Occasionally there may be found a small variation in weight, and like wood, a corresponding variation in strength. Honeycomb core material is produced in a variety of materials, cell sizes, and weights. Each type will vary somewhat in physical properties. Because of fabrication techniques, the material has a "with ribbon" direction and a "cross ribbon" direction. (See Figure 8-1 of Chapter 8.) The Physical Properties in the two directions are quite different.

Another factor inherent in manufacturing is the finite size of the blocks of honeycomb that can be laid into the sandwich. The resulting joints have a profound effect on the amount of core shear stress that the sandwich can carry. The edge bonding of the honeycomb blocks to insure shear continuity appears to be a logical solution, but production difficulties are so sever as to have made this method impractical. To minimize the effect of core joints, radome specifications call for the core material to be laid up in a random pattern. Unfortunately, this also is an impractical solution. It would be extremely difficult, if not impossible, to make the core layup in such a fashion as to comply with the intention of this requirement. Since it is common practice to fabricate radomes without shear continuity between the blocks of honeycomb core, it is well for the stress analyst to be fully aware of the condition, and to evaluate properly the structure as it will exist.

Fortunately, the principal purpose of the core material in a sandwich wall is to separate the faces and provide a large moment of inertia to prevent buckling. Due to the shape of most radomes, the majority of the shear load is carried in the face material. The core itself is required to carry local pressure loads until they can be distributed into the faces, and in some cases to carry concentrated loads.

Although the listed strengths of honeycomb core may appear to be quite high, the designer should be very much aware of the possible loss of strength due to core joints. Some of the variables affecting the efficiency of shear transfer across a joint are listed and discussed below.

Core Shear Strength. The stronger the core material, the higher the shear load that can be carried in the basic material. Since shear load is carried across unbonded joints by bending in the faces, it is apparent that the limiting amount of load is due to face strength. With face strength a constant, efficiency will decrease with increasing core shear strength. (Efficiency is defined as the ratio of the load that can be carried in shear across the joint, or gap, to the load that can be carried in the basic material.)

Face Thickness. Since shear load is principally transferred across unbonded core joints by face bending, it is apparent that face thickness is a very important factor in core joint efficiency. Since the moment of inertia of the face is proportional to the cube of the thickness and strength is proportional to the square of the thickness, it is seen that thin skins may present a dangerous weakness from the standpoint of core shear strength.

Strength and Flexibility of Bond. When the faces of the sandwich are required to transfer shear load across an unbonded core joint, the faces act in "free but guided" bending, as Figure 6-15 indicates, the bond adjacent to the gap is subjected to an extremely high concentration of stress. If the bond is extremely strong, then an appreciable percentage of the load can be transmitted across the joint. If the faces of the sandwich are strong and rigid, they will tend to reduce the peak stress, and distribute the load over more of the face bond.

Another factor that is of great importance is the brittleness of the bond. If the adhesive is flexible, it will allow some yielding, reducing the peak stress, and allowing a redistribution of load into more of the bond. On the other hand, if the bonding material is brittle, the entire face will delaminate at the first sign of failure. Because many of the resins used in radome fabrication are of the brittle type, this should be given careful consideration.

Thickness of Core. The greater the thickness of the core, the greater the load it can be expected to carry. Considering the thickness of the faces to be a constant, and therefore of constant strength, core joint shear efficiency will decrease with increasing core thickness.

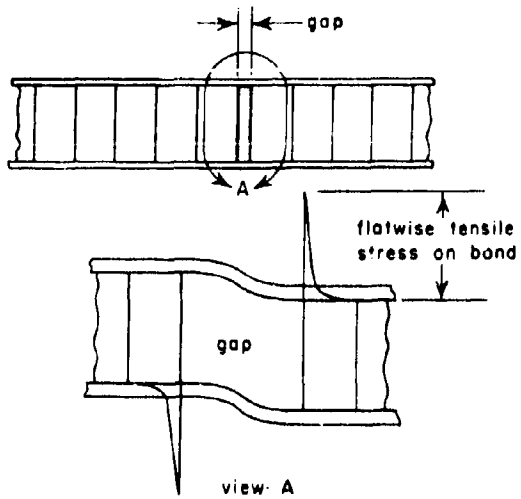


Figure 6-15. Stress on Bond Adjacent to Gap

Gaps in Core Joints. If the joints between blocks of honeycomb core material are separated a finite distance instead of being butted or interlocked, the effect is to further reduce the load carrying ability of the sandwich. If the faces are also loaded in compression, another critical factor is added.

6-17. Wall Construction — Foamed-in-Place Core

In fabricating a foamed-in-place sandwich, the skins are first molded and precured. The resin containing the foaming agents is then admitted between the two skins, which are contained in matched metal molds. As the foaming takes place, the material flows under considerable pressure, due to its viscosity, between the two skins. Since the foam clings and bonds to the two skins, the velocity of flow next to the skin is zero. This creates a condition of strain in the material next to the bond lines and usually results in a plane of weaker material next to the face of the sandwich. A close examination of a cross section of the foam will show the enlarged cell structure next to the skin. It is this plane of weakness that determines the strength of the core material in shear. In creating the core material of the sandwich by foaming in place, there may be a considerable variation in density between radomes. The nominal density of the foam may be controlled within wide limits, but an allowable variation of from 10 to 15 percent should be expected. This point is discussed because the strength of foam core varies almost directly with its density. Shear and compression values should be based on minimum densities expected rather than nominal values.

Foamed-in-place core materials do not pose the problem of core joints and reduced efficiency as does honeycomb. The shear strength, therefore, may actually be higher from the standpoint of useable strength, althoug.. the theoretical strength of the foam may be less. The reliability of bonds is excellent for foamed-in-place sandwiches. It may also be noted that foam density variations occur within the radome and tend to be a function of radome size and length. In general such variations may be as high as ±10 percent or more of nominal density.

6-18. Wall Construction — Prefabricated Foam

Prefabricated foam is made by foaming the material in open or closed molds and precuring without skins. The material is then cut to the proper thickness and size and laid up in the sandwich in the same manner that blocks of honeycomb are used. The use of the material in the form of prefabricated blocks again results in a discontinuous structure with core joints. In this case, however, it is not impossible to bond together the flat sides of the core blocks to facilitate shear continuity. Another advantage of prefabricated foam is the control that can be exerted on cell structure and weight. As cured blocks, the material may be visually examined, weighted, or otherwise tested and rejected if found unsatisfactory.

The disadvantages of prefabricated foam lie principally in the high cost of the core blocks, the added cost of layup in the sandwich, particularly if it is necessary to edge-bond the blocks or to countour the material. Another disadvantage is the necessity to make secondary bonds instead of the primary bonds formed by foaming in place.

6-19. Wall Construction — Fluted Core

"Fluted core", or "channeled core", is fabricated by either the lost wax method, or by molding in matched metal dies. The result is a core material of open ducts through which hot air can be forced for the purpose of anti-icing. See Figure 6-16. Because this type of construction is usually used for anti-icing radomes, which require very thin skins and thin and widely spaced webs for best hot air flow and conductivity, structural problems can be expected. The very thin faces are easily punctured and damaged, and the thin and widely spaced webs are easily crushed.

It is apparent from Figure 6-16 that a sandwich using fluted core will have shear continuity

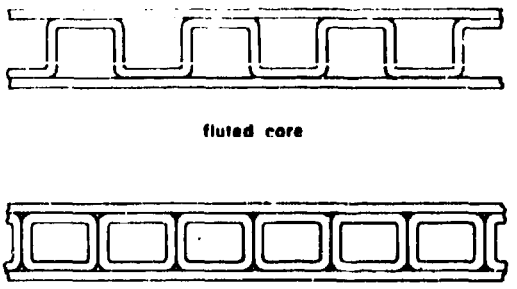


Figure 6-16. Fluted Core and Lost Wax Core

in only one direction. (Shear continuity denotes continuous shear-carrying material, or webs.) This is usually an unacceptable structural condition unless the application is such that the flutes can be aligned and unloaded over a short span. A common solution to this problem is to employ a double sandwich, with the flutes oriented at right angles, or to use a honeycomb core in the innermost sandwich. The structural efficiency of this type of construction is less than that of a single sandwich of honeycomb core.

6-20. Wall Construction — Waffle Core

Waffle core has the unique property of having no shear continuity in any direction. For this reason it has found little use in structures requiring high strength. The spacing of the waffle posts must inherently create the same effect as core gaps in honeycomb core, and due to the regularity of design, these core spaces will be continuous in two directions. One of the advantages of waffle core stems from the fact that it does lack shear continuity in two directions. Because of its flexibility, waffle core may be formed into compound curvatures without bridging. The term "bridging" is used to denote the anticlastic bending demonstrated by most materials. Anticlastic bending is literally secondary curvature of a bar at right angles to the direction of primary bending. This point can best be appreciated by the demonstration of bending a rubber eraser.

SECTION C. STRESS METHODS

6-21. Introduction

Stress methods for plates, spheres, and cylinders of isotropic materials are well known and can be used with some confidence. These methods are applicable to metal, which is an isotropic material, but are not completely suitable for the analysis of similar shapes of reinforced plastic, which is generally an orthotropic material. If the radome wall is of reinforced plastic sandwich construction, the process of stress analysis becomes even more complex. Sandwich structures are still a relatively new method of construction, and as such, have not received the degree of study and research expended on solid-wall configurations.

Admittedly there are little data and few proved equations applicable to the stress analysis of reinforced plastic structures, particularly sandwich structures; however, it is believed that a careful stress analysis, using the best tools available, can produce a structurally acceptable design. With this philosophy, the following methods are presented.

6-22. Area Theory of Stress Analysis

The simplest approach to the problem of stress analysis of a radome structure is to treat the radome as a series of disconnected strips or rings. These rings or strips then lend themselves to conventional methods of analysis. Although this method is easy and convenient, the results are frequently grossly inaccurate. The "strip" method ignores the support of adjacent rings or strips, which indeed is to ignore the shape of the radome, the principal factor in its ability to carry load.

A more logical approach to the problem is to recognize that most radome shapes consist of areas composed of spheres, cylinders, cones, or even flat areas. If the radome is viewed in terms of its various areas, and in conjunction, with the loading system it must carry, its modes of failure may be visualized in terms of the failure of whole areas, rather than individual strips. It has been found that this basic approach to the problem of radome stress analysis is very helpful, and that the results obtained are much closer to test results than what could be obtained by the strip method.

Structures generally considered capable of stress analysis by existing methods are cylinders, spheres, and flat plates. Since it is unlikely the radome shape will conform directly to any of these shapes, a certain amount of simplification will have to be performed. This will

consist, for example, of substituting an equivalent sphere for an ellipsoidal area, or assuming an equivalent cylinder for a conical area. It is in this matter that the stress analyst must apply his common sense and judgement to the problem.

In the process of simplification, the loads must also be considered. It will be the rare case if a critical area be chosen and the load on the area is not a complex system. In this case also, the stress analyst will need to make simplifying assumptions to apply some of the known methods of analysis.

The thoughtful study and analysis of most radome shapes can result in a general understanding of how the radome supports its loads, how the initial failure will take place, and how the critical area can be simulated by a structure capable of stress analysis. It is admitted that this approach is highly unscientific, but until accurate methods of stress analysis are developed and experimental data for verification obtained, no better method can be recommended.

6-23. Instability Buckling of Spherical Areas Under Lateral Pressure

Solid Wall. A spherical area of a radome, loaded by uniform external pressure, may be examined for instability buckling by the following expression[3]

$$p = \frac{2E t^2}{r^2 \sqrt{3(1-\mu^2)}} \qquad (6\text{-}12)$$

where p = pressure, pounds per square inch

E = Young's Modulus, pounds per square inch

r = radius of the sphere, inches

μ = Poisson's ratio

t = thickness, inches.

This equation is for an isotropic material, and to this extent the equation is unconservative. It must also be considered unconservative for other reasons. Additional work on this subject by Von Karman and Tsien[4] provides the following relation:

$$\sigma_{CR} = 0.18258\, E \frac{t}{r} \qquad (6\text{-}13)$$

where σ_{CR} = critical buckling stress

E = Young's Modulus

t = thickness, inches

r = radius, inches

Equation (6-12) by Timoshenko may be compared to the above equation by writing them in the same terms. In this form Equation (6-13) is

$$\sigma_{CR} = 0.60\, E \frac{t}{r} \qquad (6\text{-}14)$$

Because of manufacturing tolerances and other effects that can have a powerful influence on the critical load, the following equation is suggested for use:

$$\sigma_{CR} = 0.10\, E \frac{t}{r} \qquad (6\text{-}15)$$

Sandwich Wall. The basic equations presented for the solid-wall sphere may be applied to the sandwich wall by the use of an equivalent thickness. The equivalent thickness of a solid wall to a sandwich wall may be found from the following relation:

$$t_e = (6\, t\, h^2)^{1/3} \qquad (6\text{-}16)$$

where t_e = solid wall thickness, equivalent

t = sandwich face thickness, inches

h = sandwich shear thickness, inches (See Figure 6-17.)

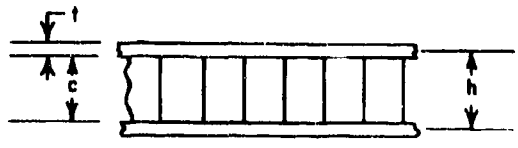


Figure 6-17. Flat Sandwich Parameters

The direct substitution will be unconservative because of the neglect of the reduced shear modulus of the core material. The following equation, (paragraph 3.15 of Reference 6), offers the following method of correction.

$$p'_{CR} = \frac{1}{\frac{1}{p_{CR}} + \frac{1}{U}} \qquad (6\text{-}17)$$

where p'_{CR} = corrected buckling pressure, pounds per square inch

p_{CR} = calculated buckling pressure, pounds per square inch

$U = G_c h$

G_c = shear modulus, core material

If the core material is orthotropic, the value of G_c used should be the average of the shear modulus in the two directions.

6-24. Instability Buckling of Cylindrical Areas Carrying Axial Load

Solid Wall. Considerable work has been done on this problem, and the equations presented below may be considered quite reliable if applicable. Note, however, that the equations are for complete, long cylinders under axial load and not for incomplete areas with unknown degrees of edge fixity. It is suggested, therefore, that this material be used with due caution and a considerable measure of conservatism. Reference 6 presents the following equation, which again was taken from other sources as noted in that reference.

$$\sigma_{CR} = \frac{E t}{\sqrt{3}\ \sqrt{1-\mu^2}\ r} \qquad (6\text{-}18)$$

where σ_{CR} = critical buckling stress

E = Young's Modulus, pounds per square inch

t = thickness, inches

r = radius, inches

μ = Poisson's ratio

Using Poisson's ratio as equal to 0.3, this equation becomes:

$$\sigma_{CR} = 0.606\ E\ \frac{t}{r} \qquad (6\text{-}19)$$

A very different equation is presented by Kempner in Reference 7, as follows:

$$\sigma_{CR} = 0.182\ E\ \frac{t}{r} \qquad (6\text{-}20)$$

Because of manufacturing errors and slight inconsistencies in shape and material, the following equation is recommended for use:

$$\sigma_{CR} = 0.10\ E\ \frac{t}{r} \qquad (6\text{-}21)$$

Sandwich Wall. Considerable work has been done on sandwich curved panels carrying axial load by the United States Forest Products Laboratory.[8] Using this material, Mr. W.C. Zophres has developed the following equation[9] (See Figure 6-18.)

$$\sigma_{CR} = \frac{0.4\ N\ E_f\ (c + 2t)}{r\ \sqrt{1-\mu^2}} \qquad (6\text{-}22)$$

where $N = 1 - 0.286\ S$

when $S \leq 0.513$ (sandwich strong in shear)

$$N = \frac{0.436}{S}$$

when $S \geq 0.513$ (sandwich weak in shear)

and $$S = \frac{c\,t\,E_f}{3(c + 2t)\ r\ G_c\ (1 - \mu^2)}$$

E_f = modulus of elasticity of the face material.

Note again that the shear modulus, G_c, is for an isotropic core material. If an orthotropic core material is being used, the value of G_c should be taken as the average of the values in the two directions, or the minimum of the two.

When this equation is carried to the limit of a solid thin-wall cylinder, it becomes, using Poisson's ratio as 0.3,

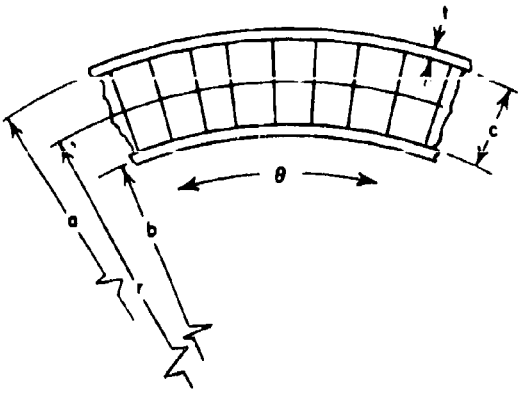


Figure 6-18. Cylindrical Sandwich Parameters

$$\sigma_{CR} = 0.242\,E \qquad (6\text{-}23)$$

Note that this coefficient is approximately twice as large as that recommended for solid-wall cylinders. This does not necessarily denote that the value is unconservative. The basic stiffness of the sandwich wall in comparison to manufacturing tolerances is probably higher than could be expected of a thin-wall cylinder.

6-25. Instability Buckling of Cylindrical Areas Carrying Shear Loads

Solid Wall. For solid-wall radomes the value of the critical shear stress may be determined by the use of Reference 10. This method is again based on thin-wall isotropic materials. The equations presented are in the following form. (See Figures 6-19 to 6-22.)

$$\sigma_{CR} = K_s \frac{\pi^2 D}{b^2 t} \qquad (6\text{-}24)$$

where $D = \dfrac{E t^3}{12(1-\mu^2)}$

t = thickness of panel

The value of K_s may be found from the tables of curves presented by Reference 10 for various ratios of axial length to curved length and for various conditions of edge support. (See Figures 6-19, 6-20, 6-21, and 6-22.)

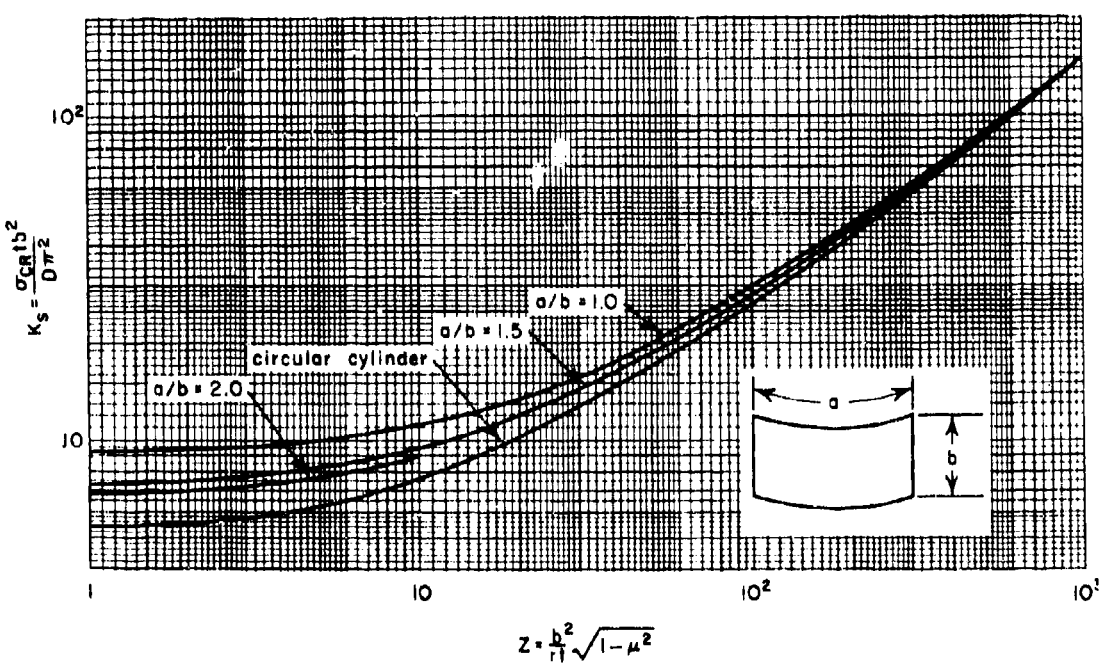


Figure 6-19. Critical Shear Stress Coefficients for Simply-Supported Curved Panels Having Circumferential Length Greater than Axial Length

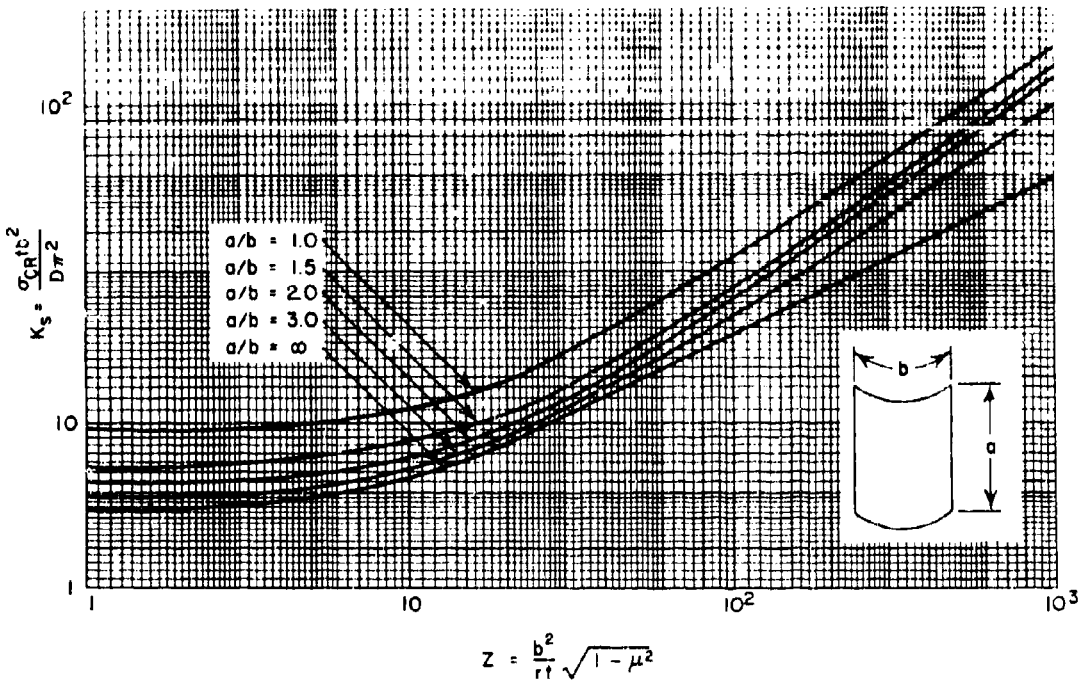


Figure 6–20. Critical Shear Stress Coefficients for Simply-Supported Curved Panels Having Axial Length Greater Than Circumferential Length

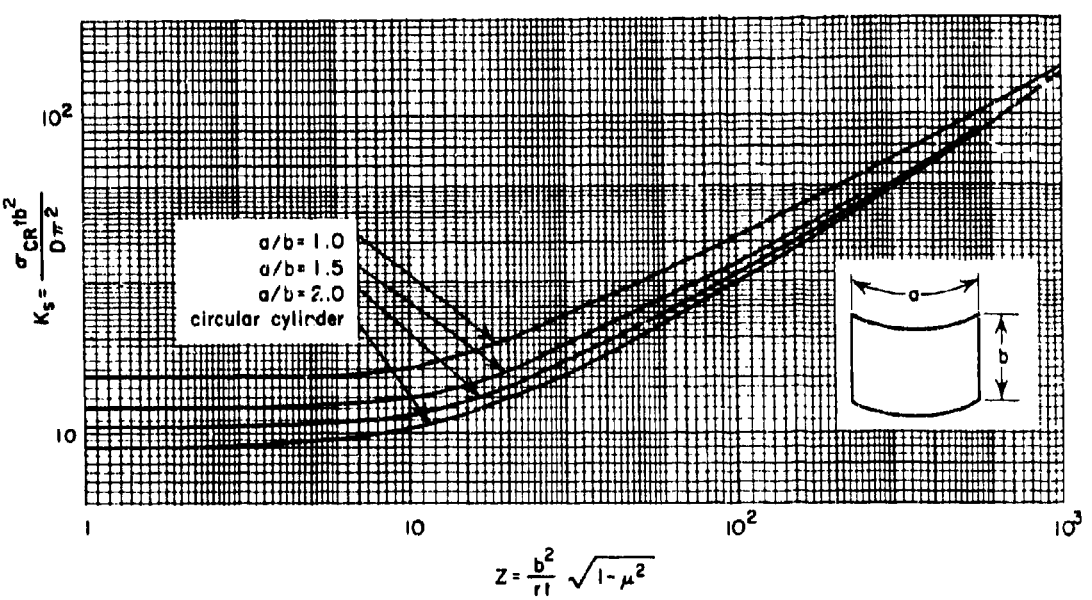


Figure 6–21. Estimated Theoretical Critical Shear Coefficients for Curved Panels with Clamped Edges and Having Circumferential Length Greater Than Axial Length

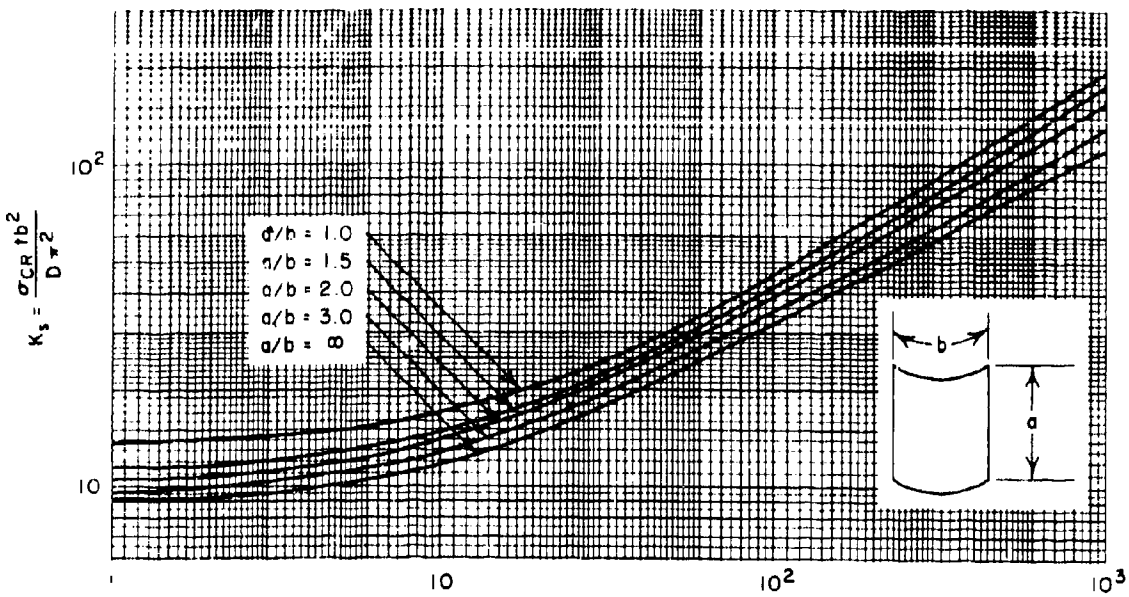


Figure 6-22. Estimated Theoretical Shear Stress Coefficients for Curved Panels with Clamped Edges and Having Axial Length Greater than Circumferential Length

Sandwich Wall. Considerable work has been accomplished by the United States Forest Products Laboratory on the subject of curved panels carrying shear load.[11] Note that these values are for isotropic sandwich cylinders in torsion. It is not known how to modify the equations presented to account for orthotropic materials, or how to interpret properly the effect of transverse shear as compared to torsional shear. It is believed, however, that these differences will be small compared to the overall inaccuracies that may exist in the radome stress analysis.

The data presented in Reference 11 has been revised by W. C. Zophres,[9] and may be presented in the form:

$$\sigma_{CR} = K_f \quad E_f \quad \frac{(c + 2t)}{r} \qquad (6\text{-}25)$$

The value of K_f may be taken from the curves, Figures 6-23, 6-24, and 6-25. In these curves,

f_1, f_2 = the thicknesses of the two faces of the sandwich (inches)

$J = b^2/hr$

μ' = shear modulus of rigidity of the core = G_c and

$$S = \frac{c f_1 f_2 E_f}{(f_1 + f_2)\ hr\mu'\ (1 - \mu_f^2)} \qquad (6\text{-}26)$$

where

b = length of cylinder (inches)

h = total thickness of sandwich (inches)

= $c + f_1 + f_2$

c = core thickness (inches)

r = mean radius of cylindrical shell (inches)

E_f = modulus of rigidity of face material (psi)

μ_f = Poisson's ratio for face material.

6-26. Instability Buckling of a Cylindrical Area with External Pressure

Solid Wall. The critical external pressure that will produce buckling in a thin cylinder is given by Timoshenko[3] as:

$$P_{CR} = \frac{3EI}{r^3 (1 - \mu^2)} \qquad (6\text{-}27)$$

where I is the moment of inertia of the wall per inch of length of the cylinder.

This equation is derived for an isotropic material, and a comparison of the theoretical equation to test data usually indicates a large degree of unconservatism may exist in the calculation.

Sandwich Wall. The United States Forest Products Laboratory has investigated the condition of instability buckling of sandwich cylinders under external pressure. This data is

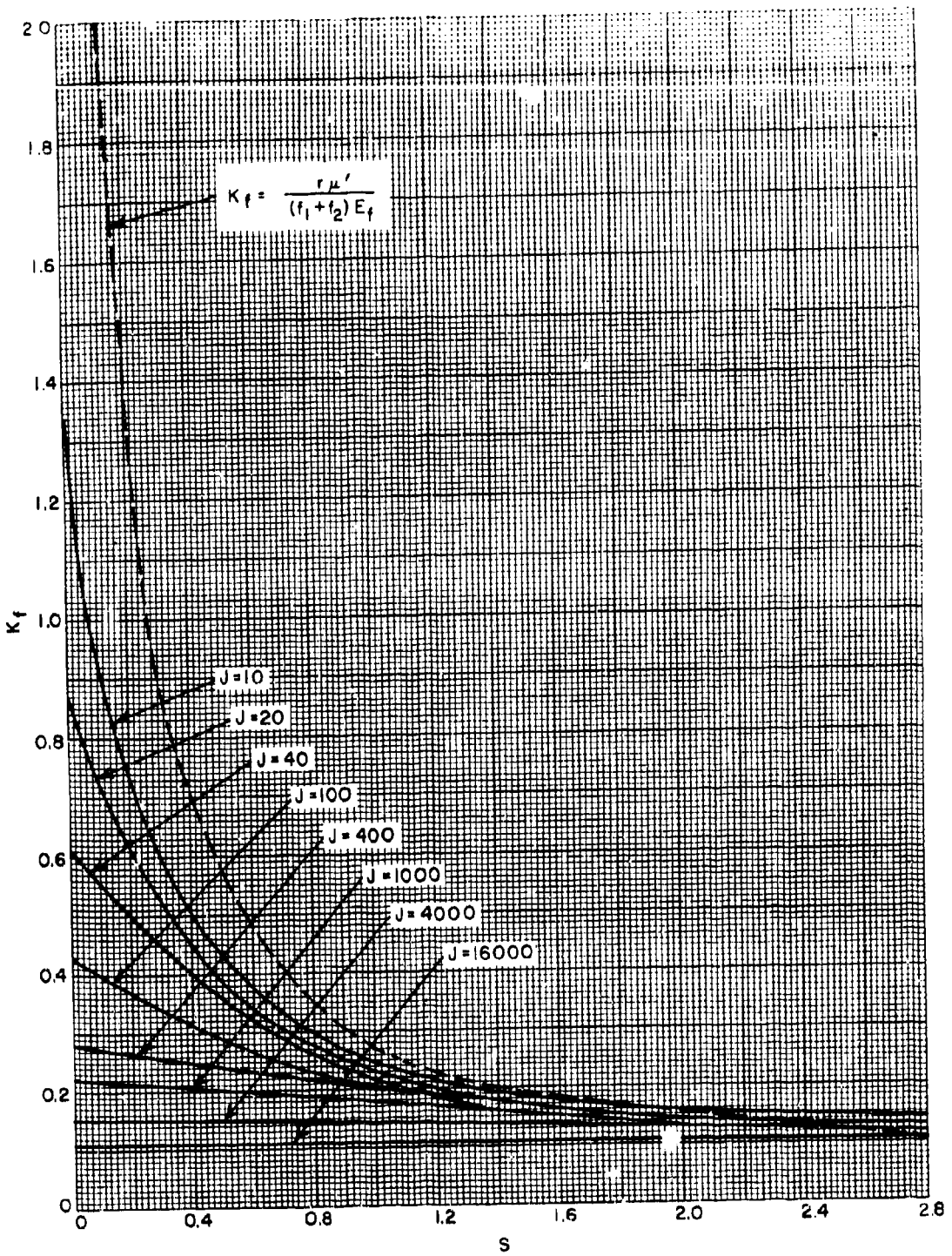


Figure 6-23. Buckling Coefficients for Cylinders of Isotropic Sandwich Construction In Torsion (c/h = 0.70)

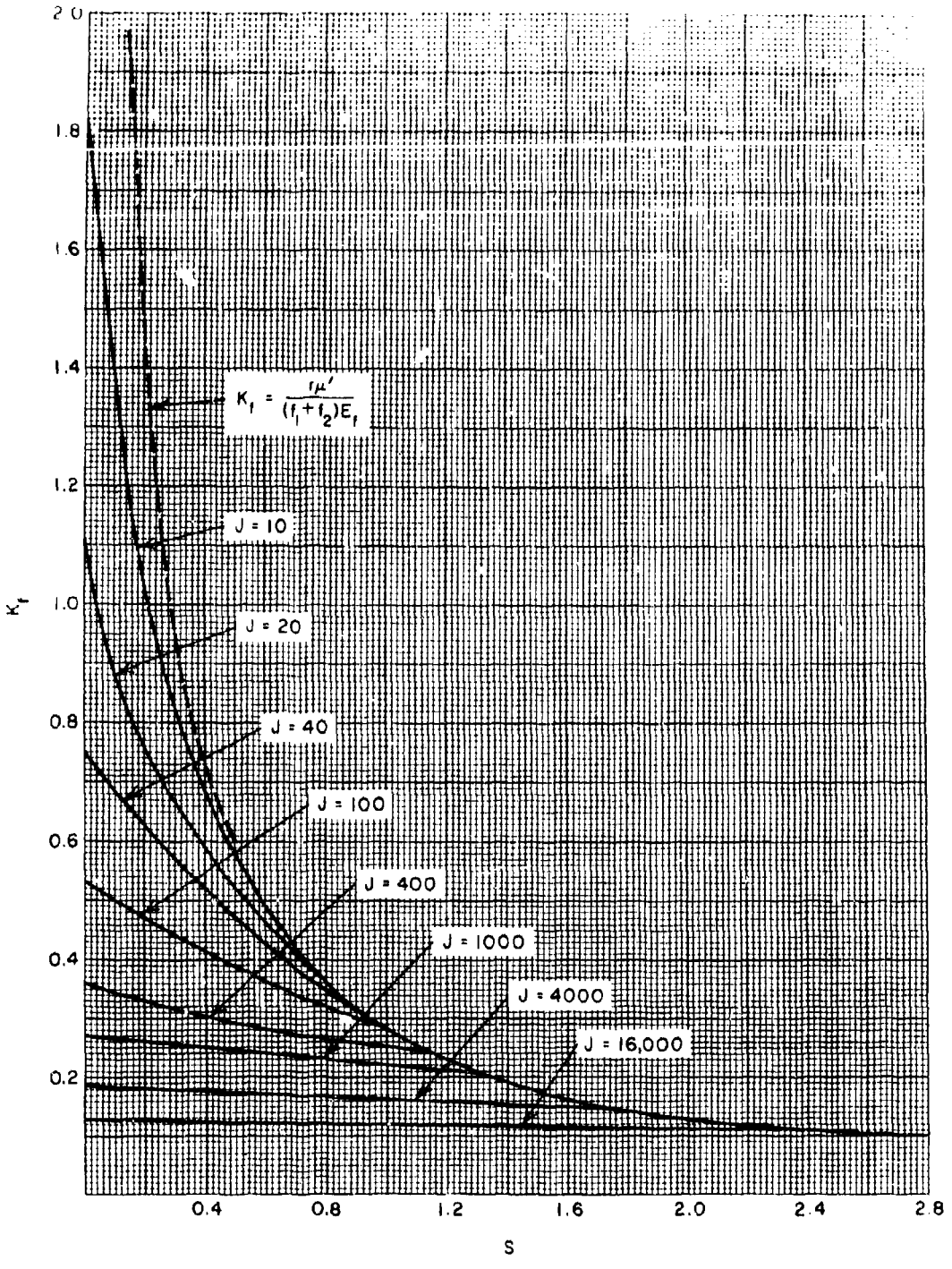


Figure 6-24. Buckling Coefficients for Cylinders of Isotropic Sandwich Construction in Torsion (c/h = 1.00)

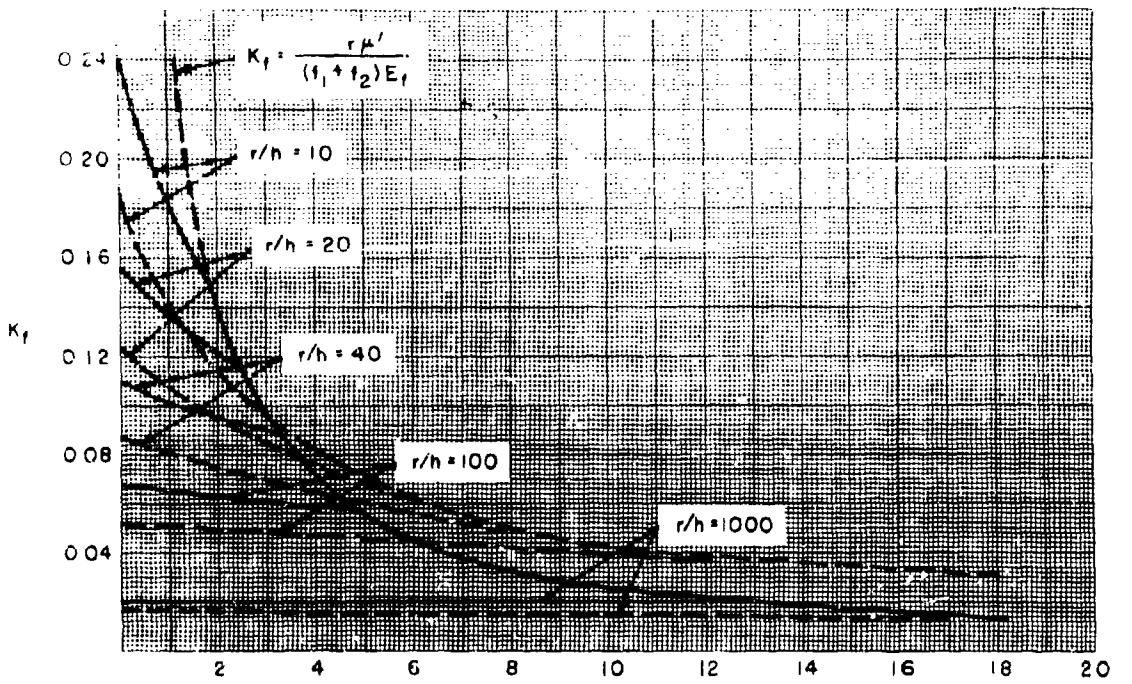


Figure 6-25. Buckling Coefficients of Infinitely Long Cylinders of Isotropic Construction in Torsion (c/h = 1.00)

presented in Reference 12, and has been rearranged by W. C. Zophres[9] in the following form for infinitely long cylinders:

$$p_{CR} = \frac{3E_f\, t(c + t)^2}{2\, r^3\, (1 - \mu_f^2)} \qquad (6\text{-}28)$$

$$\left\{ \frac{\left(1 + \frac{b}{a}\right)^3}{4\left(1 + \frac{b^2}{a^2}\right)\left[1 + \frac{2E_f t\,(c + t)}{G_{r\theta}\, ab\, (1 - \mu_f^2)}\right]} \right\}$$

where $G_{r\theta}$ = shear modulus in $r\theta$ plane, pounds per square inch

r = average radius, inches

a = radius of outside face, inches

b = radius of inside face, inches

μ_f = Poisson's ratio for the face material.

All other symbols are as previously defined. (See Figure 6-18.)

If G becomes infinity, and b/a equals 1, this expression becomes:

$$p = \frac{3E_f\, t(c + t)^2}{2r^3\, (1 - \mu^2)} \qquad (6\text{-}29)$$

If the value of I for a sandwich be substituted in this equation, the expression becomes that of Timoshenko for a solid wall.

$$I_{sand} = \frac{t(c + t)^2}{2} \qquad (6\text{-}30)$$

The preceding expressions are for an infinitely long cylinder. Forest Products Laboratory Report 1844-B[12] investigates the case of cylinders of finite length. The stability criterion, however, is minimized only for certain values of the elastic constants and parameters of the cylinder. Estimates of the effect of length may be obtained from Figures 6 to 8 of that report.

6-27. Instability Buckling of Flat Areas Under Edge Compression

Solid Wall. The instability buckling of solid-wall flat rectangular panels has been the subject of much investigation. Data contained in References 3 and 6 is suggested.

Sandwich Wall. Data for the investigation of flat rectangular sandwich panels is given in Reference 5 for both isotropic and orthotropic

construction, and for various conditions of edge support.

6-28. Instability Buckling of Flat Areas in Shear

Solid Wall. Data on instability buckling of flat areas in shear may be found in References 3, 6, and 13.

Sandwich Wall. Data for the investigation of the buckling of flat rectangular sandwich areas in shear may be found in Reference 5 for both orthotropic and isotropic construction.

6-29. Flat Areas Under Lateral Pressure.

Data for the deflection produced by lateral pressure on plates may be found in References 3 and 6. Data for sandwiches may be found in Reference 5. The deflections produced may be considered to be critical when existing in conjunction with compressive load in the faces. Methods of analysis for these conditions are not known.

Reference 14 presents data obtained on sandwich panels with simply supported loaded edges and free unloaded edges, loaded in compression with lateral pressure.

6-30. Stress Created by Thermal Shock

If a plate is submerged in a hot medium, the surfaces will begin an immediate expansion. Because a finite time is required for the inner material to become heated, the outer layers are restrained by the cooler, unexpanded, inner layers. A stress equilibrium is thus created in which the outer layers are in compression and the inner layers are in tension.

If the thermal conductivity of the material is low, the temperature of the surface will reach a given temperature more quickly than if the thermal conductivity is high. High conductivity would allow rapid flow of heat away from the surface layers and into the inner layers. In the case of low conductivity, the maximum surface stresses will be reached within a very short time after immersion, and then gradually reduce as the interior of the part becomes warm. The tensile stresses, conversely, initially will be low due to the large amount of material in the center remaining cool. As the heat is conducted inward, the percentage of cool material decreases with respect to the hot material and the tensile stresses continue to grow greater.

If the thermal conductivity of the material is high, the surface compressive stress will not reach the maximum that would be obtained for a material of lower conductivity. In this case, however, the rate of heating of the cross section will be much more rapid, bringing to temperature a much larger mass of material near the surface while the interior is still relatively cool. Because of the greater amount of material expanding at the surface, the tensile forces restraining the expansion must be much larger and exist in a smaller amount of material. That is, the tensile stress will be high. It can also be seen that the maximum value of tensile stress will not be reached as rapidly as will the maximum compressive stresses created on the surface.

Some of the factors that affect the amount of thermal stress developed as a result of thermal shock are: thermal conductivity, time, thickness of the plate, and the coefficient of heat transfer, which governs the amount of heat flow from the medium into the plate. Other factors are the temperature differential, the density of the material, and the specific heat, the latter being the two factors that determine the temperature change produced by a given quantity of heat. It is also evident that the coefficient of thermal expansion and Young's Modulus also influence the amount of stress created.

Reference 1 presents nondimensional coefficients and curves by which the stresses at the surface and center of plates with equal thermal conditions on each side may be determined. These nondimensional coefficients are as follows:

$$\theta = \frac{kt}{\rho a^2 c} \qquad (6\text{-}31)$$

$$\beta = \frac{ah}{k} \qquad (6\text{-}32)$$

where k = thermal conductivity, Btu per square foot-second-^{o}F per foot

t = time of exposure, seconds

ρ = density of material, pounds per cubic foot

a = half thickness, feet

c = specific heat, Btu per pound, ^{o}F

h = heat transfer coefficient, Btu per square foot-second-^{o}F per foot

Note that θ is a nondimensional time parameter, while β is a nondimensional heat transfer parameter.

By the use of the curves of Figure 6-26 the maximum surface stress may be calculated from the conditions of time, plate thickness, and the physical characteristics of the material. Figure 6-26 shows that as β increases, the maximum surface stress results, and that for a given β, the stress is influenced by θ.

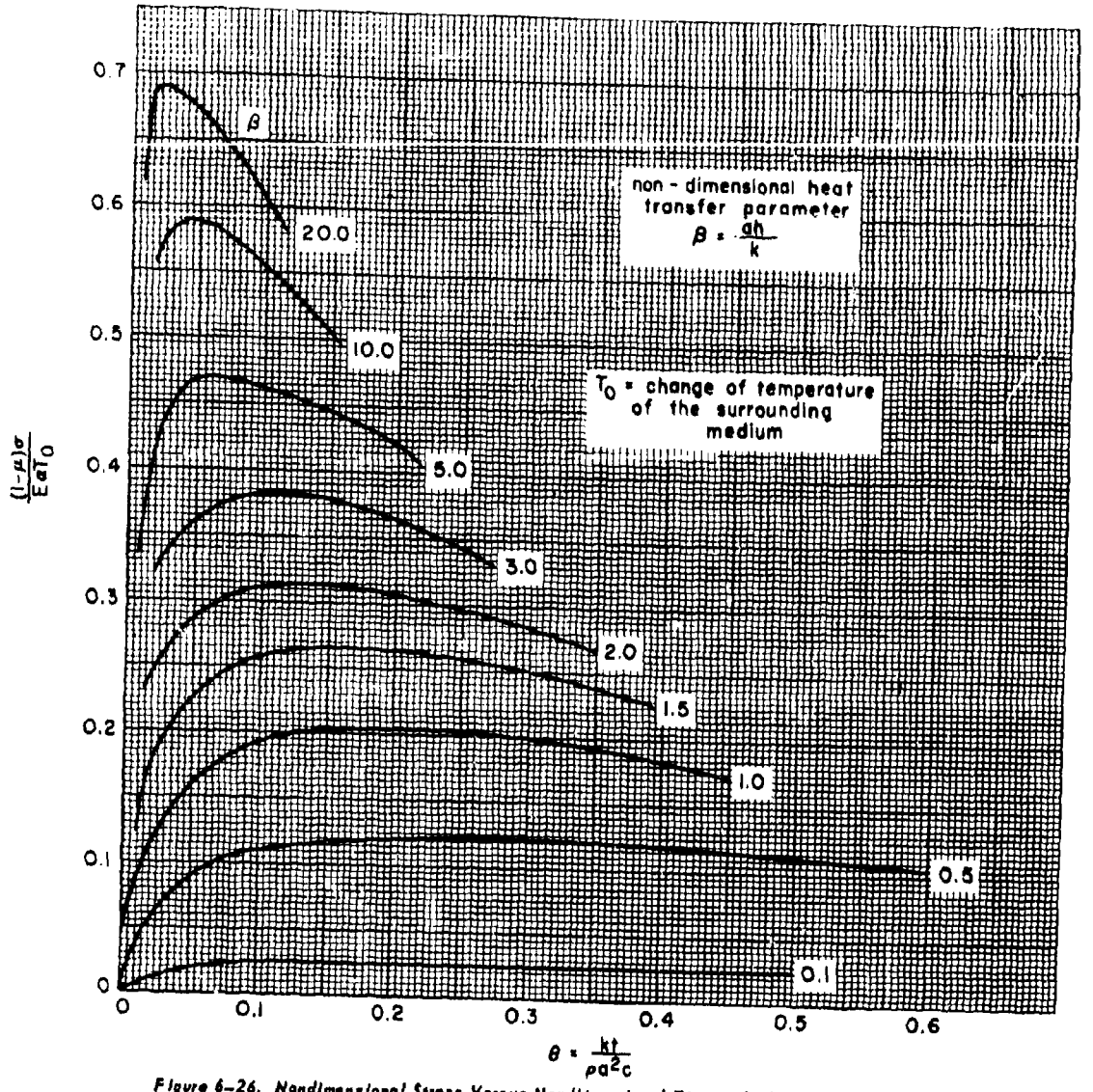


Figure 6-26. Nondimensional Stress Versus Nondimensional Time – Surface of a Plate

Figure 6-27 may be used to determine the maximum surface stress regardless of time. The maximum stress at the center of a plate may be calculated by use of the curves of Figure 6-28 for conditions of time, plate thickness, and characteristics of the material.

It is recognized that the case of a flat plate with equal thermal conditions on each side is not directly applicable to the case of a radome wall where a high temperature condition may exist on one side only. However, it is felt this data may be useful in that certain modifications and assumptions may enable analytical approximations. In the case just cited, no warpage or buckling will take place in the plate because of symmetry about a median plane. Under the condition of a temperature differential on the two faces, a constant temperature distribution will establish itself after a certain length of time. Under this condition, the plate will assume a buckled condition, but if unrestrained, there will be no stress in the plate. The act of buckling relieves the strains created by the thermal gradient. It can be seen, therefore, that the stresses induced by the steady-state thermal gradient are due only to the restraint imposed. It is logical to assume, therefore, that if the

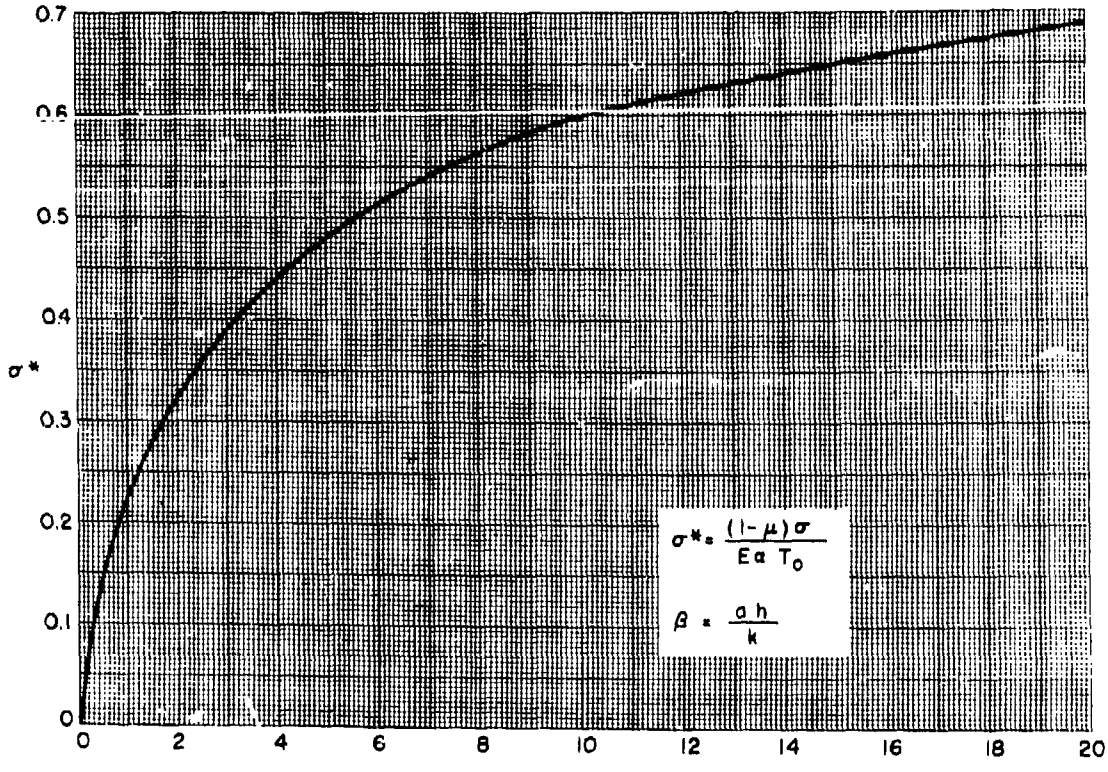


Figure 6-27. Nondimensional Maximum Surface Stress Versus Nondimensional Heat Transfer

plate were perfectly restrained the stresses would be equivalent to that of a plate of twice the thickness whose center plane temperature was that one of the faces.

Timoshenko[3] treats the case of a flat plate with a nonlinear temperature distribution, and presents the following general solution:

$$\sigma = \frac{\alpha TE}{(1-\mu)} + \frac{1}{2a\ (1-\mu)} \int_{-a}^{+a} \alpha\, TE\, dy + \frac{3y}{2a^3\,(1-\mu)} \int_{-a}^{+a} \alpha\, TE\, y\, dy \qquad (6\text{-}33)$$

where σ = stress, pounds per square inch
α = coefficient of thermal expansion, dimensionless
T = temperature rise at element, °F
E = Young's Modulus, pounds per square inch
μ = Poisson's ratio, dimensionless
a = half thickness, inches
dy = element of thickness, inches
y = distance from center to element, inches

This equation is for a flat plate. Other cases of discs, spheres, and rods are discussed. Unfortunately, however, none of these is directly applicable to radome shapes. The inter-relationship of shape, restraint, and nonisotropic materials has not, to the writer's knowledge, been solved. It may be reasoned, however, that if the radome shape is such as to cause considerable resistance to warping and buckling, the data presented for flat plates may be of some use in predicting stress levels.

Timoshenko also considers the case of the hollow sphere, which may be useful for certain types of hemispherical radomes. This data is presented as follows:

$$\sigma_R = \frac{2\alpha E}{(1-\mu)} \left[\frac{r^3 - a^3}{(b^3 - a^3)\, r^3} \int_a^b T r^2\, dr - \frac{1}{r^3} \int_a^b T r^2\, dr \right] \qquad (6\text{-}34)$$

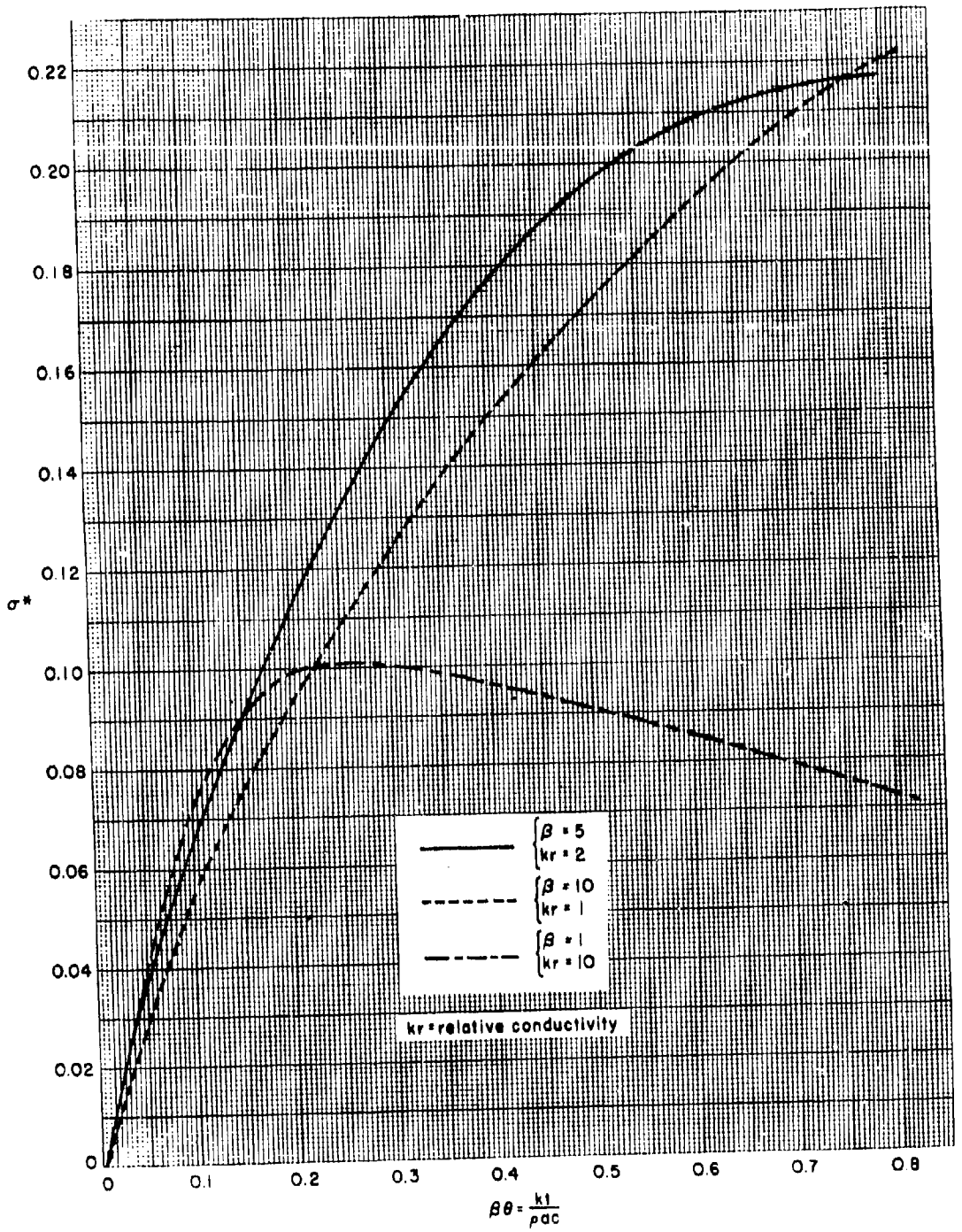


Figure 6–28. Stress At Center of Plate

$$\sigma_T = \frac{2\alpha E}{(1-\mu)}\left[\frac{2r^3 + a^3}{2(b^3 - a^3)r^3}\int_a^b Tr^2\,dr + \frac{1}{2r^3}\int_a^r T\,r^2\,dr - \frac{1}{2}T\right] \quad (6\text{-}35)$$

where σ_R = stress in radial direction, pounds per square inch

σ_T = stress in tangential direction, pounds per square inch

α, T, E, and μ, are as previously defined

and r = distance from the center, inches

a = outer radius of sphere, inches

b = inner radius of sphere, inches

If the time is such that a steady flow rate will be established, the following equation may be used to calculate the stress:

$$\sigma_R = \frac{\alpha E T_i}{(1-\mu)}\,\frac{ab}{b^3 - a^3}\left[a + b - \frac{1}{r}(b^2 + ab + b^2) + \frac{a^2 b^2}{r^3}\right] \quad (6\text{-}36)$$

$$\sigma_T = \frac{\alpha E T_i}{(1-\mu)}\,\frac{ab}{b^3 - a^3}\left[a + b - \frac{1}{2r}(b^2 + ab + b^2) - \frac{a^2 b^2}{2r^3}\right] \quad (6\text{-}37)$$

In this case T_i is taken as the temperature of the inner surface, while the temperature of the outer surface is assumed to be zero.

Because of the many variables that affect thermal stresses, it is recommended that the reader study the text of Reference 1 for an excellent discussion of the process of heat transfer and the creation of thermal stress.

6-31. Thermal Stress

If dissimilar materials having different coefficients of thermal expansion are combined in a structure in such a way that they must expand or contract together, then changes in temperature will create stress in the members. The factors that affect the stress developed are the relative coefficients of thermal expansion, the change of temperature, Young's Modulus, and the relative areas of the two materials effective in mutual restraint. The stresses resulting from such a combination can be calculated by simple considerations of the following equations for elongation due to temperature and to stress.

$$\delta_S = \frac{PL}{AE} \quad (6\text{-}38)$$

$$\delta_T = \alpha L \Delta T \quad (6\text{-}39)$$

where δ_S = elongation due to stress, inches

δ_T = elongation due to temperature change, inches

P = load, pounds

L = length, inches

A = area, square inches

E = Young's Modulus, pounds per square inch

α = coefficient of thermal expansion, dimensionless

ΔT = change in temperature, ^{o}F

If the nature of the installation is such that the member is completely constrained and if it is subjected to a change in temperature, the stress created will be as follows:

$$\sigma = E\alpha\Delta T \quad (6\text{-}40)$$

where symbols are as previously noted.

If the member is rigidly attached to the other structure, so that they must expand or contract together, the stress created will be:

$$\sigma = E \Delta T (\alpha_1 - \alpha_2) \qquad (6\text{-}41)$$

This equation is based on the assumption that the two structures undergo the same change in temperature and that the area of the main structure is very large in comparison to that of the member under consideration.

If two structures of different materials, having different coefficients of thermal expansion, different values of Young's Modulus, and somewhat equivalent areas are attached so they must expand and contract together, and are subjected to a temperature change from that at which they were originally installed, the following mutual load would be created in the two members:

$$P = (\alpha_1 - \alpha_2)\Delta T \frac{(A_1 E_1 A_2 E_2)}{(A_1 E_1 + A_2 E_2)} \qquad (6\text{-}42)$$

where symbols are as previously noted.

The stress created may be calculated by the familiar relation of P/A.

6-32. Impact

The term "impact" implies a striking or colliding force. This is necessarily a short-time loading condition and is usually associated with a small area of loading. Damage resulting from this condition therefore usually does not result in total failure, but local or superficial damage only. The exception to this may be the case of impact with a large or heavy object. The type of failure resulting from the impact of small objects will be by bearing or crushing of solid-wall radomes, or puncturing or separation of the skins if a sandwich wall is used. Crushing of the core of sandwich walls is also commonly found.

Impact is an energy phenomenon in which the force developed by the impact is related to the rigidity of the bodies, the masses, and the squares of the velocities of the two bodies before and after impact. If a small object at high speed is brought completely to rest, a considerable amount of energy may be released in a very local area. If the object is large, and at high velocity, a proportionate amount of energy will be released, but over a larger area. The first case will result in local failure, but the latter may result in complete disintegration of the structure.

Methods of analysis of impact loads on even the most simple structures are extremely complex. Therefore there is little point in attempting to present stress methods for complicated radome shapes and radome materials. For rough estimates and general conclusions of the effect of various impact loads, simple calculations may be made using the basic equations of energy and forces involved in the accelerations of bodies. These equations are as follows:

$$E_k = \frac{1}{2} mv^2 \qquad (6\text{-}43)$$

$$F = ma \qquad (6\text{-}44)$$

where E_k = kinetic energy, foot pounds

m = mass, slugs

v = velocity, feet per second

F = force, pounds

a = acceleration, feet per second per second

To make use of these equations, it is necessary to know or assume the mass of the striking object, the impingement angle, the change of velocity of the striking object, and the area over which the load will be spread. It will also be necessary to estimate or calculate the distance in which the change of velocity is brought about. This will be the total of the deflections of the two bodies as the impact load builds up to its maximum.

It is apparent that an analysis of this nature can only produce answers of a very general nature. It is recommended that experimental studies be made if more exact data is needed. It is known that Lockheed Aircraft Corporation has performed a number of experiments in which both actual birds and simulated hailstones have been hurled at panels representing radome wall configurations.

Some resistance to impact may be obtained from the design of the radome. In impact resistance, solid-wall radomes are much superior to sandwich-wall radomes with their thin skins, relatively weak core materials, and the tendency for separation between the faces and the core. Even the sandwich-wall radomes can be

improved, however, by the use of flexible resins and the heaviest possible faces and core materials. This unfortunately may compromise electrical performance.

6-33. Fatigue

Requirements for withstanding fatigue are unusual for radomes, since fatigue failures are associated with a large number of loading cycles. The exception will be the radome that is subjected to a vibratory loading condition from some external source.

Since many radomes are used for gun laying, one of the most usual sources of vibration will be from gun fire, the loads being the result of muzzle blast, or from the vibration and shock of the structure to which the guns and radome are mounted. Other sources of vibration may be created by propellers particularly if the radome is in or near the propeller plane, from the sonic blast of jet engines or rocket assist units, from aerodynamic shock waves, or from eddy currents in the air. It may also be possible that other mechanisms in or near the radome may be the source of vibrations.

The fatigue life of a radome will depend on the nature of the load, the number of cycles, the mean stress level of the radome in conjunction with the stress due to the vibrating load, and the nature of the radome wall configuration and material. Although there are no stress methods available for a rigorous analysis of the problem of predicting the radome fatigue life, the following discussion of the various factors mentioned above may be of some help.

Vibratory loading may be applied directly to the radome wall in the form of pressure waves, or it may be applied to the radome through the structure to which it is attached. In the first case the loading will probably be carried by the radome as a normal load, in much the same fashion as a pressure loading. If the vibratory loading is applied to the radome through the structure, the loading will depend on the nature of the vibrations in the structure itself. The airframe may be vibrating in the plane of the radome attachment, normal to it, or a combination of both.

The effects of shock waves, eddy currents, and propeller tip vibrations are usually unknown quantities, since every aircraft and installation presents new and different problems. A considerable amount of data on gun blast is available which will allow an estimate of the pressures involved.[15]

One of the most serious loading conditions that can be imposed on a radome is to expose it to sonic blast of a large jet engine. Because of the weak and brittle bonds usually associated with radome construction, and the constantly increasing power of engines, accompanied by very high noise levels, radomes are becoming increasingly critical from the standpoint of resistance to sonic vibrations.

In the case of both gun blast and sonic vibration, the magnitude of the condition can be determined with a fair degree of accuracy. It is suggested that, if the radome appears to be in the critical range, laboratory tests be conducted to simulate the radome and the loading, and thus determine the fatigue life.

The number of cycles of vibration to which the radome will be subjected may usually be determined from the type of the source. For example, if the vibration under consideration is produced by propellor tip effect, the number of blades, the average revolutions per minute of the propellers, and the service life desired of the airplane or radome will approximately determine the number of loads to which the part will be subjected.

Likewise, if the loading source is muzzle blast, the expected number of rounds to be fired can be estimated with a fair degree of accuracy.

The number of cycles of load is not as important a consideration as is the degree of stress. Data on materials show S-N (stress to number of cycles to failure) curves plotted on logarithmic scales, indicating that a small reduction in stress level will allow a marked increase in the number of cycles that can be resisted. Conversely, a small increase in the vibratory stress, or an increase in the mean stress level of the radome, while it is being subjected to the vibratory load, may greatly reduce the resistance to fatigue.

The material and construction of the radome are obviously important in considering the effect of fatigue. A solid-wall radome has the usual advantage of greater shear and bending stiffness for the same thickness, but far more important, it does not utilize the very weak core material and face bond which are inherent in sandwich walls. Hence, solid-wall construction should in general be more resistant to fatigue.

Although it is not possible to present a great amount of data on the fatigue strength of various radome materials, data presented in Reference 16 may be of interest and help. Forest Products Laboratory Report 1823-A shows that

a typical glass-reinforced polyester laminate will endure a 9,000 pounds per square inch alternating stress for 10 million cycles; Report 1559-C shows that a glass fiber reinforced honeycomb material exhibits a strength of 42 percent of static strength at 30,000 cycles; and Report 1559-J shows a fatigue strength of 30 percent of static at 30 million cycles for alkyd-isocyanate foam.

6-34. Stress Rupture

Stress rupture is a failure associated with a long sustained tensile load. Loads of this nature are usually the result of a direct air loading, or from body, wing, or empennage bending. The most likely case is that of a part subjected to a fairly high degree of stress from a direct air load. Another case might be that of a wing outer panel insulator section. In this case the stress level could again be fairly high for reinforced plastic material.

Reference 17 shows that a stress rupture failure may occur at 60 percent of static strength if the load is maintained for a total of 300 hours. Projecting this data to the expected life of the airframe and considering the effect of exposure, weathering, and elevated temperatures, which materially affect the creep strength of plastic materials, it is seen that some danger can exist from stress rupture. Particular attention should be accorded an application where the radome is to be subjected to a relatively high level of stress over a long length of time, or at intervals of sufficient frequency that a considerable amount of time can be accumulated.

Little is known of the effect of stress rupture on sandwich materials. In general, it can be concluded that if the loading is resisted principally by the faces, the values for laminates would apply. If the core material is loaded in shear or flatwise tension, it is felt there is considerable cause for concern, even though the sustained stress level be fairly low. In this case it will be the plastic bond itself that will be loaded, and some concern would be felt for the values of reduced allowable stress over that of the reinforced material. In these cases, tests should be conducted of the exact materials and construction to determine allowable stresses and any adverse factors that may exist.

6-35. Creep

The tendency of plastic materials to continue to deflect under a long-sustained load is well known. Paragraph 6-34, Stress Rupture, discussed the effect of long sustained tensile loads. The same effect is noticed if the material is loaded either in compression or shear.

The rate of creep of metals is very low, or negligible, except at elevated temperatures, where it may become a serious problem. Most of the plastic materials, however, demonstrate definite creep even at room temperatures. This characteristic may be expected to be much more severe at moderately high temperatures. There is little data available for design purposes for reinforced plastic materials, particularly for sandwich construction.

As in the case of stress rupture, attention should be given to applications where the stress level can be expected to be maintained at a fairly high level, and where high or moderately high temperatures can be expected to act in conjunction with the stress.

Most radomes are critical for instability type failures in which the stresses are relatively low. If the radome is resistant to buckling, then it may be operating at a relatively high stress level. A combination of this high stress and an elevated temperature will probably constitute the most likely case of instability failure due to creep buckling. Since these criteria apply most often to sandwich-wall radomes, it is suggested that particular attention be paid to this configuration, and that special consideration be devoted to sandwich walls where the core material may be highly loaded in shear.

SECTION D. ENVIRONMENTAL DESIGN CRITERIA

6-36. Icing Control — General

The formation of ice on the aircraft structure has long been a serious problem to the aircraft engineer. The spoiling of a carefully designed flight surface by an accumulation of ice results in a loss of lift, loss of control, or both. In addition, the weight resulting from the load of ice contributes to the difficulty of maintaining flight and control and creates further damage by forming on and breaking antennas.

Icing is caused by the entry of a cold aircraft into an area where moisture exists in the form of water droplets at above-freezing temperatures, or by the aircraft entering an area where the droplets are existing in the supercooled state. The obvious answer to the icing problem

is to avoid areas where icing may take place, but operational requirements sometimes preclude this possibility, even though means have been found to accurately locate and avoid these areas.

Since the advent of radar, another icing problem has been created. The formation of ice on radomes proscribes full efficiency and performance of the equipment, from both the standpoint of transmission and beam shift. The requirement for ice-free radomes creates the need to either prevent ice from forming, or to be able to remove it quickly once it has formed.

The search for methods of anti-icing has led to numerous proposals, and several solutions, none of which is completely satisfactory. None have gained universal acceptance.

Ice control may be divided into two classes or types, anti-icing and de-icing. Anti-icing methods attempt to prevent the formation of ice. De-icing techniques remove the ice once it is formed. It is apparent that all things being equal, the anti-icing method will be preferable from the standpoint of radar performance.

Of the many approaches to the problem of ice control on radomes, only four methods are considered here. Of these four, only three are known to have been successfully used on aircraft installations.

6-37. Icing Control — Rubber Boot

The use of rubber boots on the leading edges of wing and empennage surfaces is a tried and proved method of ice removal. It is not unexpected, therefore, to find this method in use on radomes for the same purpose.

The late acceptance of the expanding rubber boot was probably due to the fact that early radomes were almost invariably fabricated of sandwich construction. It was felt that the losses created by the electrical unbalance of the thick layer of rubber would be unacceptable, even in its retracted state, to say nothing of the complications imposed while the segments were in the act of expanding and contracting; also earlier boot materials were excessively lossy.

Advanced methods of electrical design have made the boot more compatible with the radome wall design. In addition, the electrical requirements of new designs are causing more and more radomes of solid wall construction to be produced. The solid-wall (half-wave) radome is much more compatible to the use of a boot than is the sandwich wall. For these reasons the boot can be expected to grow in favor, particularly for solid-wall radomes.

Some of the advantages and disadvantages of rubber boot installations for de-icing are listed and discussed below:

Advantages.

a. The expandible rubber boot is a proved and effective way of removing ice from the surface of the radome.

b. The boot serves as an excellent cover for protecting the radome from damage by flying rocks or other debris, and from handling. Unfortunately, however, the boot is ineffective in preventing damage from hail.

c. Since most aircraft are equipped with both a pressure and a vacuum system, and since flow rates are relatively low in operation, the cost in both dollars and weight is likely to be less for a boot installation than for any other type.

d. The boot serves as an excellent surface to prevent rain erosion. Since most radome installations require the use of a rain-erosion-resistant surface, the boot eliminates the necessity for the special coating. Since the boot is much thicker and more durable, frequent replacement of the rain-erosion material is avoided.

Disadvantages.

a. The boot has a deleterious effect on radar performance regardless of efforts to minimize its presence. The effect while in operation is practically impossible to predict.

b. The boot can be used only for de-icing; that is, it must allow a certain amount of ice to accumulate before removal can take place. The ice layer, even though it is thin, may be expected to have an adverse effect.

6-38. Icing Control — Anti-Icing Fluid

Anti-icing fluid has been used for a number of years for anti-icing measures on propellers and windshields. Note that in both cases the formation of ice to any appreciable extent cannot be tolerated.

As in the case of the rubber boot, this method of ice control was ignored for a considerable period of time in the search for methods of anti-icing radomes.

Advantages.

a. Because most aircraft are equipped with an anti-icing system, the added weight and complexity of the system itself is not great.

b. This system of preventing ice formation has been demonstrated to be effective through many years of service.

Disadvantages.

a. Adverse electrical effects are produced by the nozzles and fluid lines conducting the fluid to the nose of the radome, and possibly by the fluid itself.

b. The system can only be used to anti-ice as long as anti-icing fluid is available. When the fluid is used up, the system is inoperative.

c. If sufficient fluid is carried aboard for the worst conditions that may ever be encountered, the weight of the fluid may become an adverse factor.

d. Some doubt may exist as to the distribution of the fluid at various speeds and angles of attack of the aircraft. This may entail a considerable amount of wind tunnel or flight testing to insure proper operation of the system.

e. There is also some possibility that the nozzle may become iced over prior to its being actuated, thereby preventing fluid-spray action in flight.

6-39. Icing Control — Hot-Air System

The hot-air system for anti-icing the leading edges of wing and empennage surfaces has gradually been adopted by the majority of aircraft manufacturers, thus replacing the familiar rubber boots serving the same purpose. This point may be worth consideration in any comparison of the two systems for ice control of radomes. As in the case of the boot and the anti-icing fluid system, hot air is always available in the aircraft, although not always at the point in the aircraft where it is convenient for use. The fact that hot air was not adopted for anti-icing radomes at the outset of the search was because there was no known practical method of fabricating ducted core material for the manufacture of radomes, and also because early plastic resins would not stand the temperature necessary to transmit the required heat through the insulating skins. The development of the lost wax method of fabrication of the core material by Douglas Aircraft, and the successful molding of fluted core in matched metal dies by North American Aircraft, opened the way. In operation, both types of construction employ a circulation of hot air distributed and collected by the proper manifolding system.

Advantages.

a. The method has been demonstrated as satisfactory in service in prevention of ice formation on leading edges and surfaces, as well as radomes.

b. Very little, or minimum, upkeep and maintenance is required.

c. Generally speaking no sacrifices in electrical properties or performance may be anticipated.

Disadvantages.

a. To obtain good heat transfer through the wall, the skin must be very thin, thus making it subject to easy damage and costly repair. This has proved to be serious in some cases.

b. The method is applicable only to sandwich radomes. This is no disadvantage if a sandwich is desired for other reasons.

c. Repair methods are difficult, and cannot normally be completed in the field.

d. Due to the large quantities of heat required to maintain proper skin temperatures, a large airflow is needed.

e. Because the flutes have shear continuity in only one direction, it is almost always necessary to employ a double sandwich construction to provide sufficient physical strength. This significantly increases radome weight and cost.

f. The hot air reduces the physical properties of the reinforced plastic material, thus aggravating any stress problem.

6-40. Icing Control — Internal Heating

The method of heating the interior face of the radome, either from radiant heat or from heating the air in the entire cavity has been used only on very large ground radomes of the thin-wall, rubber, air-supported type, where radiant heat from infrared lamp banks was employed.

No known installation using this method has been employed for aircraft radomes. The thin walls required, and the amount of electrical energy consumed are not compatible with aircraft design requirements.

Advantages.

a. The complexity of the system is of the very lowest order.

Disadvantages.

a. The method can be practical only if the radome wall is of the thin solid-wall type. This is no disadvantage if the wall was selected to be this type for other reasons.

b. The radar equipment housed within the radome wall will have definite limitations of temperature to which it can be exposed. It may be difficult to prevent this equipment from becoming over heated.

c. Heat obtained from infrared bulbs is very expensive.

d. If the heat is obtained through heating the entire quantity of air in the cavity, the rate of heat transfer from the air to the radome wall will be very low unless some method for providing high turbulence or flow is provided.

6-41. Precipitation Static

Precipitation static is produced by the accumulation and discharge of high potential electricity. As the aircraft sweeps through the air it encounters charged particles which release their energy to the structure. When a sufficient potential has been attained, a discharge takes place. To prevent the discharge from interfering with the operation of electronic equipment, the aircraft will be equipped with static dischargers. These devices gradually discharge any accumulation of energy to the air at low potential.

On nonconductive surfaces, such as radomes, the charges collected cannot transfer to the aluminum structure of the aircraft without local discharges. These discharges adversely affect the performance of the radar system. For this reason, conductive coatings are sometimes applied to the radome. Such coatings are generally of elastomeric type and similar to that used for rain-erosion protection. The resistance of these materials is somewhat unstable, changing with age and weathering, and as a result they are not completely satisfactory.

6-42. Lightning

Many lightning strikes on aircraft radomes have been reported. Although intense heat may be generated and high local pressure waves created, the damage may not be as serious as might be expected. The danger apparently lies in the general weakness of the radome itself.

The photograph presented to show typical damage, Figure 6-29, shows that the damage is of a local nature, and that the blast pressure did not cause a general collapse of the radome. It follows, therefore, that if the radome has some margin of safety in strength, it may suffer local damage and still complete the flight without total failure. Since aircraft are designed for speeds far in excess of those at which they are normally operated, it is unlikely that a radome would be subjected to a lightning strike and a subsequent maximum dive speed in the same flight.

Lightning protection is generally not used on aircraft radomes. On some antenna covers discontinuous strips of metal or metal spray material are utilized to conduct the electrical charge into the airframe structure. A strip of metal attached to the airframe and the radome (or instrumentation boom) is effective in providing protection against lightning strikes.

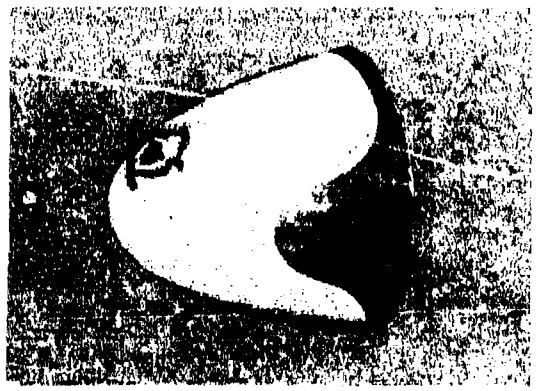


Figure 6-29. Lightning Strikes on a Small Radome

6-43. Moisture

A radome may be subjected to moisture either by direct exposure to water, or to exposure to the moisture in the air. Under conditions of high relative humidity and altitude cycling, the absorption of moisture from the air may be much greater than that which can be picked up even by immersion in water.

Moisture absorption will result in a decrease in electrical performance and a degradation of the physical properties of glass-reinforced

plastic materials usually used in radome construction. This is particularly true of the honeycomb core material which is essentially thin. Reinforcing materials other than glass fibers almost universally have much greater tendency to moisture absorption than do the glass fibers.

Moisture absorption of alkyd-isocyanate foam-core material is relatively low because of the unicellular construction of the bubbles. Experiments performed by Zenith Plastics show that foam-core radomes with holes drilled at frequent intervals through the inner face, will not absorb enough water in direct contact to noticeably affect radar transmission. These tests were performed by so drilling a radome and leaving it filled with water for a period of 24 hours. The water was then removed and the surface wiped dry. The electrical tests were performed immediately afterward.

The following table of physical properties of wet and dry, glass fiber, reinforced polyester resin laminates is presented to illustrate the loss of strength due to moisture absorption. These values were determined for laminates of 181 glass cloth with garan finish and polyester resin, and at zero degrees to the warp.

	Dry	Wet
Tensile Strength, pounds per square inch	43,000	40,000
Compressive Strength, pounds per square inch	43,000	34,000
Tensile Modulus, pounds per square inch	2.5×10^6	2.4×10^6
Compressive Modulus, pounds per square inch	3.4×10^6	3.1×10^6

Additional data is given in Chapter 8 and in Figure 6-30, which shows the percentage of strength retention of a polyester laminate for tension and compression stresses at 45° and 90° to the warp direction of the fibers. This data also shows the effect of time of exposure.

Recent advances in the field of finishes for the glass fibers have materially increased the resistance to moisture absorption and loss of

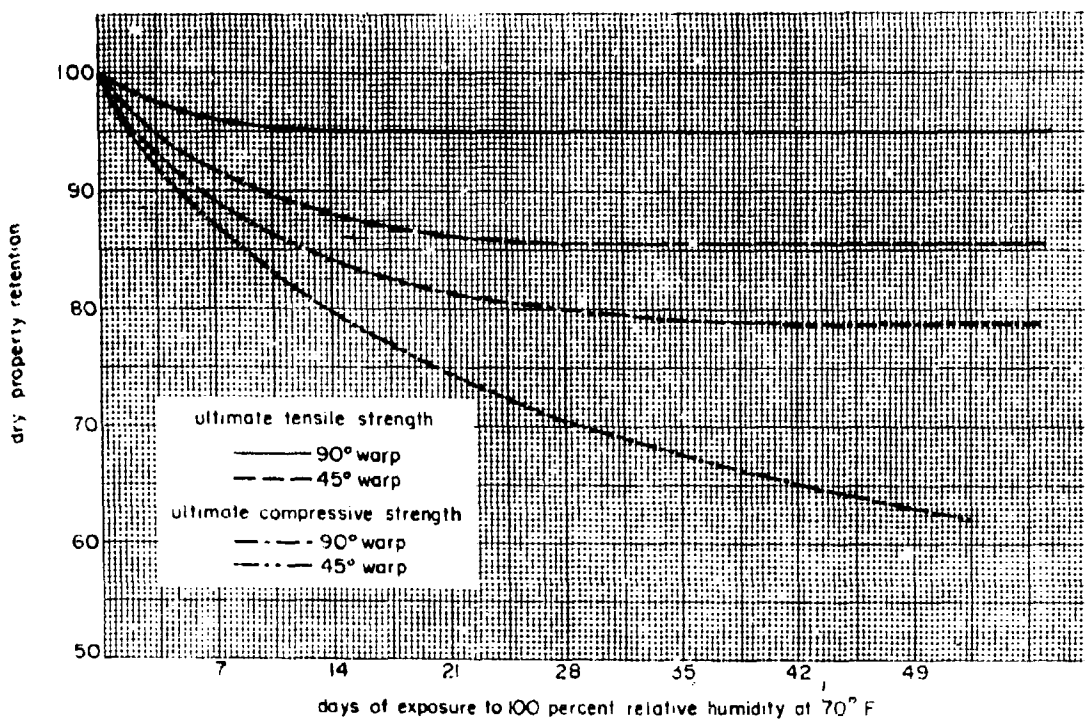


Figure 6-30. Dry Property Retention Versus Days of Exposure to 100 Percent Relative Humidity

strength. The data presented in Figure 6-30 and in the previous table was based on the use of the improved finishes.

The reduction in strength of glass cloth honeycomb core materials is expected to be in the order of 50 percent. This fact, along with the loss of electrical transmission, requires that core materials be protected from moisture absorption to the greatest degree possible.

As an aircraft climbs from a warm, moist sea level environment into the cold and rarified air of high altitudes, any moisture in the cells condenses into water and subsequently freezes. If the faces of the sandwich are porous, the pressure in the cells will be greatly reduced. As the aircraft returns to lower levels, more warm, moist air will flow into the cells. After repeated cycles of this nature, the cells may be found to contain large amounts of water, which will adversely affect both the electrical and physical properties of the radome.

Recent changes in specifications for sandwich construction have created requirements for sandwich faces of radomes to be "void-free." This process, originally developed by Goodyear Aircraft Corporation, is a fabrication technique for removal of entrapped air or residual volatiles from the wet layup before cure, resulting in a virtually nonporous laminate. Cycling tests of reinforced plastic laminate faces made by void-free techniques approved by this specification have shown adequate resistance to moisture absorption.

If a totally wet laminate is allowed to dry, its physical and electrical properties will return to normal. However, exposure of the glass cloth materials to moisture before impregnation with resin may result in permanent loss of strength.

6-44. Nuclear Radiation

There is little definitive data on the effect of nuclear radiation on reinforced plastic laminates. Degradation of polyester laminates after prolonged exposure to gamma radiation has been noted. The improvement in thermal properties of such plastics as polyethylene by radiation is due to molecular cross linking. Unfortunately polyester polymers cannot be further modified in such fashion.

Although little information is currently available on the effect of nuclear radiation on reinforced plastic materials, it is known that research on this subject is being prepared at this time. The investigators include Lockheed Aircraft Corporation, Convair, and perhaps others.

SECTION E. STATIC TESTING*

6-45. Fixtures for Static Testing

The external loads applied to a part must be balanced by the reacting loads from the structure to which the part is attached. It is important, therefore, that the fixtures on which the part is to be mounted for static testing simulate as closely as possible the actual structure that supports the part. If the structure cannot be duplicated for the static test fixture, then a careful study of the reacting forces should be made, and a static test fixture designed to duplicate the method of load transfer. This method will usually reflect the data gained from, and made a part of, the stress analysis of the structure involved.

In attempting to simulate the actual structure, it is usually considered sufficient to duplicate the rigidity. This unfortunately creates another problem. A structure that is comparable to another from the standpoint of rigidity will, in all probability, be comparable in strength. A great many embarrassing situations have developed as a result of this situation, caused by a failure of the supporting structure before the part under test has failed. To insure that the part being tested will fail before the fixture fails, it is common practice to design the static test fixture to have a margin of strength of several hundred percent over that of the part.

The difficulty lies in making a design compatible with both the requirements to duplicate

*The term "static testing" is applied to those tests where an actual part is subjected to loading systems similar or equivalent to those that it will encounter, or be expected to encounter, in service. Other tests, performed on samples to determine physical properties, for example, will be referred to as "mechanical tests," or "environmental tests."

as closely as possible the rigidity of the structure, and yet retain a sufficient margin of strength to insure a proper test of the ultimate strength of the part.

Another point that should be given careful attention is the matter of deflection. In addition to the data that will be gathered in regard to the strength of the part, it is usually of great importance to gather proper deflection data. A supporting structure that is very flexible may not only support the part improperly but also make it extremely difficult to gather good deflection data. This data will probably entail overall deflections, and deflections of one part with respect to another part or area.

The deflection readings that are to be taken should be determined before the design of the fixture is undertaken so that ample provisions may be made in the design for ease and accuracy of measurements.

6-46. Methods of Load Application

Weights. The simplest method of applying a static test load is by means of weights. For convenience, the weights are usually in the form of small bags filled with sand or lead shot. Weights range from 10 to 25 pounds. The bag itself is usually constructed of canvas.

Some of the other advantages of this method of loading are the uniform loading or pressure obtained, the ease of distribution of load, the ability to duplicate varying pressure or load, and the ability to add and remove load very slowly and precisely. In addition, there is very little expense involved in equipment and maintenance.

The disadvantages of the system are that loading must necessarily be slow, and that catastrophic (total) type failures are produced. It is not possible to remove the load suddenly to save the part being tested from total destruction. In some cases it may be absolutely necessary to prevent total failure of the part, in which case supports may be placed under the test specimen and gradually removed as the part deflects under increasing load.

It should be pointed out that there is some element of danger in applying large amounts of load by means of weights. A sudden and unexpected collapse of the part may precipitate an avalanche of weights on the test engineers.

Another disadvantage of using weights is the lack of uniform distribution of load if the height of the bags becomes appreciable. As the height increases, and the part deflects, it can be seen that bags tend to lean against each other, and distribute the load towards the supports, the areas that are not deflecting. This tendency will prevent the actual bending moments and shears from reaching the values calculated.

It is also apparent that the method is suitable only for loading fairly flat and horizontal surfaces, and that the direction of load must necessarily be downward. This seriously handicaps the versatility of the method.

Hydraulic Jacks. Hydraulic jacks are very commonly used as a method of applying static load. The load is easily measured and controlled, and sudden failure of the part does not necessarily mean that complete destruction of the part will take place. The load may be either suddenly applied or removed at will.

Load is applied to the part either directly through pads, or by a whiffletree arrangement with cables. In the case of the whiffletree and cable arrangement, the load can only be applied in tension, since cables are incapable of carrying compression. This may on occasion require a complicated arrangement of jacks and holes through the part itself to provide passage for a cable to apply load in the right direction. The development of high-strength, reliable adhesive systems has greatly aided in attaching pads to the structure to be tested.

Air Pressure. Air pressure is a very versatile tool in static testing. Loads may be applied either by ambient pressure created by vacuum, or by pressure contained by inflatable bags.

The use of several bags will allow excellent distribution of load. The loads are measurable to very close limits by means of simple manometer tubes, and can be applied rapidly or slowly as required. Total failure of the part will not result if the bag itself will restrain the pressure after a given amount of deflection has been provided for.

If high pressures are involved, failure of the part may release a very dangerous amount of energy. This is particularly true if the volume of air being used is large. If no bag is provided for restraint, a catastrophic failure may take place, both in the part and in the general vicinity of the test setup.

Considerable difficulty has been encountered in using vacuum pressure for loading from the standpoint of leakage. Since the maximum pressure that can be attained from this method is in the order of 14 pounds per square inch, it is usually necessary to provide a high degree of

vacuum. Since most vacuum sources are of the low flow type, small leaks can result in inability to develop the vacuum needed.

Another disadvantage of the vacuum system is the inability to continue the test to failure if the part turns out to be stronger than expected. For example, if 10 pounds per square inch vacuum is required for failure by calculation, then an overload of only approximately 40 percent can be applied before the test must be discontinued. The art of stress analysis is not sufficiently developed to avoid this situation, particularly on radomes of reinforced plastic material.

Water Pressure. Water may be used to provide tremendous pressures and loads, without the danger of air, due to its lack of compressibility. The load may be applied simply as a weight, as shown in Figure 6-31, or may be used simply as the medium to transmit pressure.

In the latter case, the pressure on the water may very conveniently be produced by the use of a standpipe to produce the proper head. It is also noted that water, or other liquid, has the unique property of creating a varying pressure, dependent on the depth. This factor can occasionally be used to great advantage. See Figure 6-32.

Water is normally slow to load and unload, and requires the use of bags to contain it. It does not lend itself to easy distribution and control.

6-47. Static Tests at Elevated Temperature

The increased velocity of aircraft creates elevated temperatures in its components. This has led to the necessity of testing radomes while the material is hot, or being heated. This latter case is for the condition of thermal shock. An examination of the physical properties of reinforced plastic materials will show that small increases in temperature above room temperature values will result in very appreciable degradation in the strength of the part.

Some attempts have been made to avoid testing structures at elevated temperature by the reduction of test data taken at room temperature. This method involves knowing the physical properties of the material at both room temperature and the elevated temperature. The failing load at elevated temperature is calculated by the use of this strength ratio.

If the part being tested is critical for one mode of failure only, this method may be suitable. Knowing the mode of failure, the values of the critical physical properties may be determined to calculate the amount of reduction required. If the mode of failure is not known, then the static test is required at elevated temperature, not only to determine the failing load but the mode of failure as well. The reason for this is that the various physical properties of reinforced plastic materials are not reduced by the same percentage. For example, compressive strength is reduced more by elevated temperatures than is tensile strength, and strength is reduced more than rigidity, as expressed by Young's Modulus. Thus, a part may fail by instability buckling at room temperature and by face compressive stress at elevated temperature.

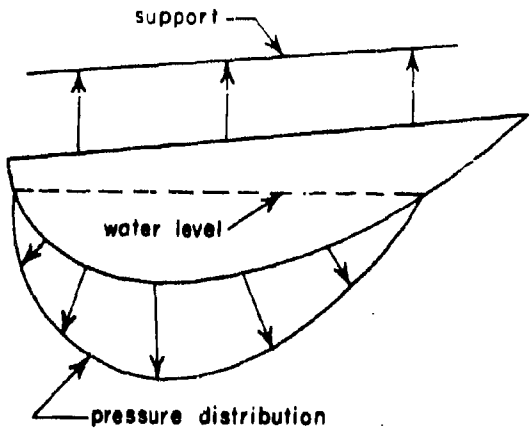


Figure 6-31. Loading Produced on a Large Radome by a Weight of Water

It is unfortunate that stress analysis of radome shapes and radome materials is not usually sufficiently precise to predict accurately even the mode of failure that may take place. For the reasons cited, it is strongly recommended that static tests be conducted at the temperature at which the part itself is expected to operate. If proof testing is desired, it may then be done at room temperature, with loads based on the failing load and mode of failure determined in the destruction test.

The most common method of static testing at elevated temperature is to place the entire assembly into a large oven and bring it to the proper temperature. Although this method appears to be very simple, it involves a great amount of problems not normally associated with testing.

The high temperatures provide unwanted tests of the fixtures and loading methods as well as

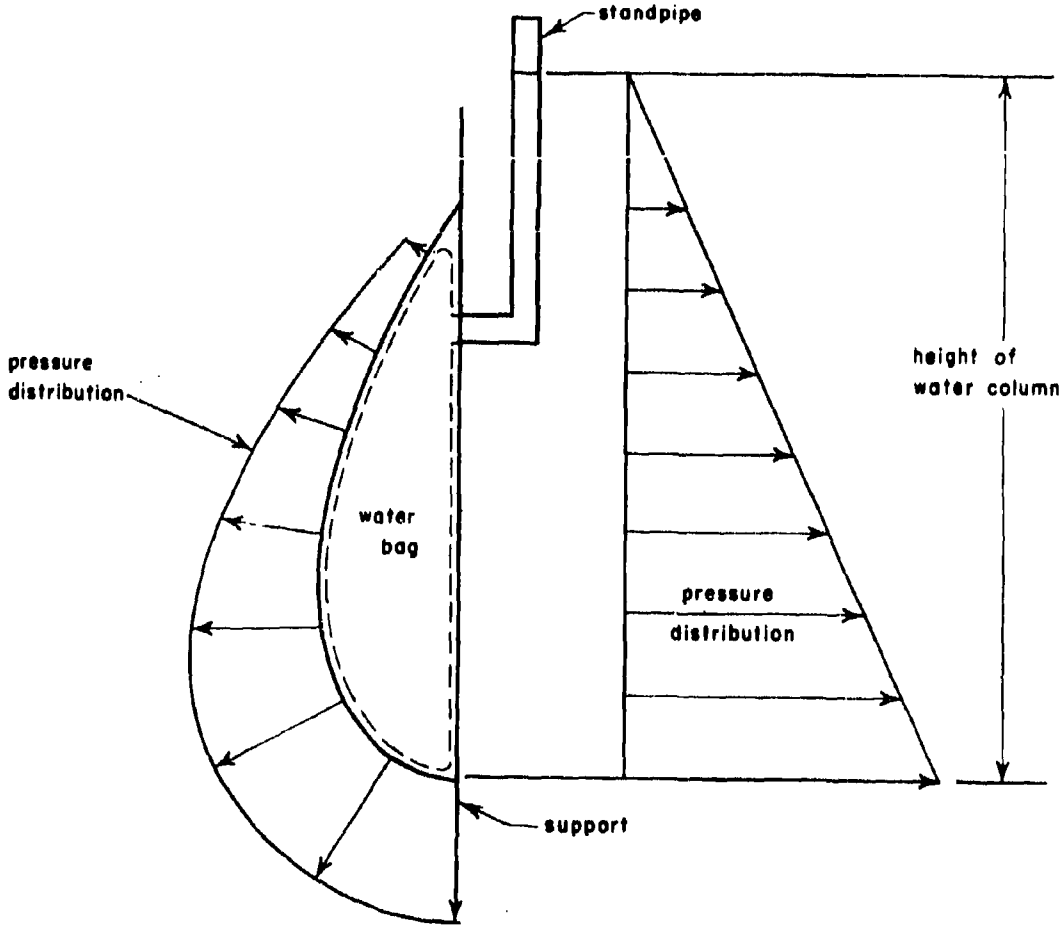


Figure 6-32. Loading Produced on a Large Radome by Using Water to Transmit Pressure

for the part itself. Deflections are usually more difficult to read or require more elaborate instrumentation. Close observation of the part while under load and while load changes are difficult. Windows in the test oven are a necessity, and field glasses or other optical instruments are helpful. High-temperature-resistant microphones installed on the part are useful for listening for sounds of failure, but it should be remembered that at the elevated temperatures, reinforced plastic materials tend to yield and fail without the loud noises usually associated with imminent failure. It has been found that a man can enter an oven at 260°F for short periods of time without harmful effects. The limit of endurance is not known, either as to degree of temperature, or to time the heat can be endured. It is apparent, however, that full and accurate examination of the part is not likely under these circumstances.

Other methods of applying heat while the part is being loaded are resistance heating blankets, and infrared lamps. Both of these methods will allow the test engineer close proximity to the part, and the use of lamps will allow good visibility as well. Although little experience is available on these methods, it is expected that the use of ovens for all temperature testing will be most satisfactory, and that the use of infrared lamps will provide the best method of creating temperature changes in the part while under load, or simply testing for thermal shock. Experience has shown that rapid changes in temperature cannot be produced in an oven unless

a high velocity of air flow can be attained over the part.

8-46. Instrumentation

The purpose of static testing is to determine if a part will carry a prescribed load without failure, or, in some cases, to determine the ultimate load the part can withstand before failure occurs. In addition to the load-carrying ability of the structure, the stress engineer may desire to know the stress distribution in various areas of the part and the deflection history that takes place as the part is loaded. He also may require temperature data if the part is being tested at elevated temperatures.

For the record, and for purposes of applying load, it will be necessary in many cases to measure pressure, either of a liquid or of a gas. The types of instrumentation required to measure the type of data noted above are very briefly discussed below.

Stress. Stress may be measured by electrical strain gages. These devices are applied to the part to be tested with an adhesive and receive the same strain under load as the area of the part to which they are attached. Since stress is in general proportional to strain, and the strain can be measured by the change in electrical resistance of the wires of the gage, stress can be measured. The gages may be aligned in any direction desired, and, by the use of three gages aligned at 0^{0}, 45^{0}, and 90^{0}, to each other, shear stress can be measured.

An accurate knowledge of the modulus of the material is vital to the successful use of strain gages. Conversion of strain gage data to stress data is entirely dependent on the use of stress-strain relationships. Reinforced plastic materials may be either isotropic, orthotropic, or neither, depending on the type of reinforcement used or the technique applied in the layup. In the orthotropic materials, the values of the physical properties are approximately equal in the 0^{0} and 90^{0} directions, but entirely different at 45^{0}, and varying in some nonlinear fashion between the two.

When several layers of cloth are used in the laminate, the random orientation of the various plies of cloth may produce an entirely different and unknown set of conditions.

For the reasons cited, the use of strain gages on reinforced plastic parts is more difficult than on other materials, particularly metals. It is advisable, therefore, if possible, to calibrate the strain gages on the actual part if known loads and closely known stresses can be produced. If this is not practical, and it seldom is, another approach is to remove specimens in the area of the strain gages, with the gages still attached, and conduct tests in the laboratory to determine either the validity of the reading or the correction which should be applied. Unfortunately great difficulties are encountered in using strain gages on parts being heated because of their sensitivity to temperature changes.

Deflection. Deflection data is usually measured by means of dial indicator gages. These instruments are accurate, easily read, and relatively inexpensive. They may be mounted in many ways and positions. These instruments are also available in materials that are not damaged by relatively high temperatures, thus allowing their use for elevated temperature testing.

If the deflection is expected to be large and accuracy is not of primary importance, ordinary machinists' scales may be attached to the part and read directly, or from a distance, by means of an optical instrument. Because of the deflection that will take place in the test fixture, care must be taken to provide a proper reference point against which the reading will be made.

Pressure. Pressure or vacuum may be read by the use of suitable gages or by the use of manometer tubes.

Since unit pressures dealt with an aircraft work are usually low, the pressures can usually best be measured by means of manometer tubes. These instruments are very simple, yet very accurate, and with little chance of malfunction without detection. The usual fluid used in the manometers is mercury, although water is often used to provide more accurate readings if the pressures are very low. If desired, other liquids of various densities are available to give a complete range of pressure excursions. It is sometimes convenient to position the manometer tube at an angle to the vertical to increase its sensitivity.

It is recommended that all low-pressure readings be taken by manometer tubes and the pressure gages be used when the pressures are outside the range that can be measured by manometers.

Temperature. Temperatures may be recorded by many means, ranging from an ordinary thermometer to the more complicated thermocouple and recording system. There is little to be said of methods of measuring static temperatures, since this is an old science. The problems con-

nected with temperature measurement are associated with the measurement of rapid changes of temperature, and the rate of change of temperature within an object, or of the surface of the object. Rapid changes of temperature can best be measured with a thermocouple and a rapid response recorder. The thermocouple and the wires should be as small as possible to reduce the heat absorbing mass.

Methods of measuring skin temperatures under transient conditions are relatively new, and no method has been universally adopted as standard. The suggestions shown here are the best known to the writer at this time. It is expected that rapid advances will be made in this art due to the great interest in thermal stress and thermal shock criteria.

For metal skins, the thermocouple may be attached as shown in Figure 6-33. For plastic materials, the use of the metal screw does not seem permissible. The variation, as shown in Figure 6-34 may give reliable data, assuming that the wedge is of the same material as the skin.

Because of finite diameters of thermocouples it is not considered practical to attempt to bury them in the laminate. The smaller the thermocouple head the more accurate this method could be. Most accurate results may be expected from the method shown in Figure 6-35. It is apparent, however, that the installation will require very precise work. Again it is felt that minimum sizes of thermocouple heads will contribute to the accuracy of readings, particularly those involving rapid temperature changes.

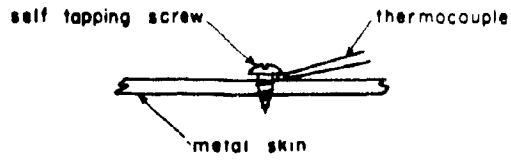


Figure 6-33. Thermocouple Attached to Metal Skin

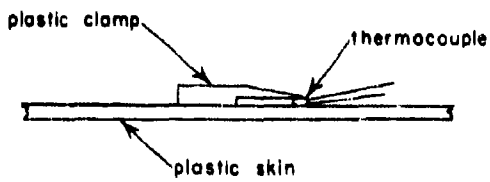


Figure 6-34. Thermocouple Attached to Plastic Skin

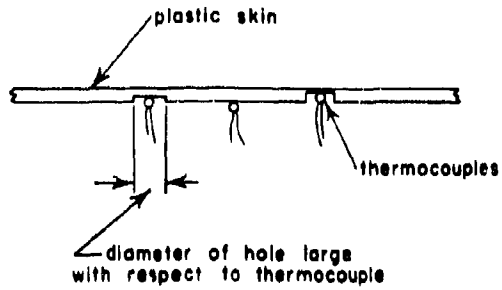


Figure 6-35. Thermocouple Attached to Plastic Skin

SECTION F. ENVIROMENTAL TESTING

Environmental conditions that are closely related to structural requirements are thermal effects, vibration, and shock. Methods of test for these conditions are outlined below.

6-49. Thermal Shock

In thermal shock, high thermal gradients are caused to exist in a part by sudden and severe changes of temperature. The thermal gradients create strains in the material due to differences in the rates of expansion.

Thermal shock is usually applied by rapidly changing the test specimen from one medium to another, by changing the temperature of the medium, or by exposing the part to a sudden application of heat from heat lamps or other source of radiant energy.

An example of the first type of test is one in which the part is stabilized at one temperature, say a cold box, and then removed and quickly placed in a hot oven. This type of test is unsatisfactory from several standpoints, mainly the lack of control over time and temperature.

The only advantage seems to be in the simplicity and low cost of the equipment. If the part were to be placed in a medium of high specific heat and conductivity, such as oil or water, very high rates of change may be induced. Again, however, control over rate and temperature is difficult, if not impossible.

Producing thermal stress by changing the temperature of the medium is much more subject to control than the previous method. Since a

considerable time lag would be involved in raising or lowering the temperature of the medium, the change can best be accomplished by utilizing a flowing material, with changes of temperature being produced by proper mixing of hot and cold. By the use of valves, close control over the rate of change of the medium may be attained.

Although either method outlined above can produce the required rate of change of the medium surrounding the part, the problem in most cases concerns producing a rate of change on the surface of the part. This may be a much more difficult problem since the conductivity of a gaseous medium may be much lower than that of the part, and the conductivity of a liquid medium may be much higher than that of the part. The use of radiant energy avoids the necessity of coping with thermal conductivity, but is concerned only with the intensity of the heat source and the distance to the part. Rates of change may be obtained by varying one or both of these factors, usually the distance being most convenient.

6-50. Impact

Impact testing of complete parts is not a usual condition for testing. Radomes are recognized as fragile structures, and if subjected to impact loads, may be expected to suffer damage. If specific requirements are called for in the design specification, then these conditions will form the basis for testing.

Impact tests are performed on small specimens in order to evaluate materials. Standard tests for this are defined in Government Specification LP-406.

6-51. Shock, Vibration, Elevated Temperature, Low Temperature

Shock. Shock tests are performed on complete parts as required by design specifications. These tests are usually performed by drop-testing on special test devices designed for this purpose. The purpose of the drop test is to produce the required acceleration on the part at the prescribed angle, or in the prescribed direction.

Vibration. Vibration tests are performed by the use of vibration tables for this purpose. The test provides the acceleration, the frequency, the amplitude, and the number of cycles as prescribed by the specification.

Elevated Temperature. Methods of testing at elevated temperatures are described in paragraph 6-47.

Low Temperature. Reinforced plastic materials are stronger at low temperatures than at high or room temperatures. For this reason it is usually not necessary to test at low temperature. As in most materials, brittleness and lack of impact resistance increase at low temperatures. Since these effects can be studied and evaluated on sample panels and specimens, it is not normally necessary to test full-scale parts to determine the effect.

REFERENCES

1. Manson, S. S. Behavior of Materials Under Conditions of Thermal Stress. NACA Report No. 1170.
2. U. S. Naval Air Development Center Report No. NADC-EL-5503, March 7, 1955. (Confidential)
3. Timoshenko and Goodier. Theory of Elasticity. 2d Edition, 1951.
4. Von Karman, Theodore, and Tsien, H. S. The Buckling of Spherical Shells by External Pressure. Journal of the Aero. Sciences, December 1939.
5. Sandwich Construction for Aircraft. ANC-23 Bulletin, Part II, 1955.
6. Roark, R. J. Formulas for Stress and Strain.
7. Kempner, J. Journal of the Aeronautical Sciences, May 1949.
8. March, H. W., and Kuenzi, E. W. Buckling of Cylinders of Sandwich Construction in Axial Compression. Forest Products Laboratory Report No. 1830, 1952.
9. Zophres, W. Buckling Criteria for Sandwich Shells. Proceedings of the OSU-WADC Radome Symposium, June 1956.
10. National Advisory Committee for Aeronautics, Report 1348.

11. March, H. W., and Kuenzi, E. W. Buckling of Sandwich Cylinders in Torsion. Forest Products Laboratory Report No. 1840, 1953.

12. Raville, M. E. Analysis of Long Cylinders of Sandwich Construction Under Uniform External Lateral Pressure. Forest Products Laboratory Report No. 1844, A and B, 1954.

13. Strength of Metal Aircraft Elements. ANC Document 5a, Aircraft Committee of the Munitions Board, 1949.

14. Investigation of Sandwich Constructions Under Lateral and Axial Loads. NACA Technical Note No. 3090.

15. Boller, K. H. Fatigue Tests of Glass-Fabric Base Laminates Subject to Axial Loading. U. S. Forest Products Laboratory Report No. 1823 and 1823-A, 1954.

16. U. S. Forest Products Laboratory Report No. 1599 C and 1599-J.

17. Boller, K. H. Stress-Rupture Tests of a Glass-Fabric Base Plastic Laminate. U. S. Forest Products Laboratory Report No. 1839, 1953.

Chapter 7

SUBSONIC AND SUPERSONIC RAIN EROSION PROBLEMS

by

G. P. Peterson

Materials Laboratory
Directorate of Research
Wright Air Development Center
Wright-Patterson Air Force Base, Ohio

INDEX OF SYMBOLS

C	Velocity of compressional wave in water (5,000 feet per second); proportionality constant
C'	Speed of the compressional wave
d	Drop diameter
S'_s	Shear strength of surface
S'_t	Tensile strength of surface
V_c	Velocity of impact
V_0	Vertical velocity of massive fast moving surface
α	Coefficient giving, on average, the fraction of the advance velocity of the fast moving surface which is impacted by the water molecules
ϵ'	Damage parameter
μ	Drop viscosity
ρ	Density of water; drop density
ρ'	Density of the striking surface

Chapter 7

SUBSONIC AND SUPERSONIC RAIN EROSION PROBLEMS

SECTION A. INTRODUCTION

7-1. Rain Erosion Problems

With the advent of higher speed subsonic aircraft and supersonic aircraft and missiles, many new engineering problems have been encountered. One of the most severe is the phenomenon of erosion of exterior plastic leading edges during high speed flights through rain.

Damage due to rain erosion was first reported in 1945 on a laminated plastic radar housing which was part of the "Eagle" vane antenna installation on the B-29 airplanes. The severity of rain erosion damage has increased with higher flight speeds and the extent of the erosion has increased with the more extensive use of plastics in aircraft. Erosion damage, while undoubtedly more severe on plastic parts, such as radomes, has also been detected on such metals as magnesium and aluminum.

The damage has been severe enough to cause complete structural failure of the radome, which could result in vastly reduced performance of the aircraft or even complete loss. The use of nonmetallic materials, such as glass-reinforced polyester resin laminates, for radomes is necessary from the electrical standpoint. It is also advantageous, where applicable, to use lightweight nonmetallic reinforced plastics in place of metals. The Air Force has investigated the rain erosion problem in an effort to obtain materials that will resist erosion for long periods of flight through rain.

7-2. Approaches to the Solution

Obviously the most satisfactory solution to the problem would be the development of a radome material which would be rain erosion resistant in itself. Typical polyester laminates, such as are currently being utilized, are definitely unsatisfactory, from the standpoint of rain erosion resistance, without some means of protection. This fact has led to the development of coating materials that would protect the plastic aircraft surfaces from erosion.

The most satisfactory coatings developed to date are of the neoprene type, presently utilized on aircraft plastic leading edges, for example, radomes. For the best combination of rain erosion and electrical properties, these coatings are applied in a 10-mil thick film.

A coordinated military specification, MIL-C-7439B, covering the requirements for rain erosion coatings, is presently being utilized for procurement of neoprene rain erosion coatings. The specification has been expanded to include an antistatic coating requirement; a coating has been obtained which conforms to the specification requirements. If these coatings are applied to structurally sound radomes, which provide good support, and if maintenance and inspection are satisfactory, the coatings provide adequate radome protection at subsonic speeds.

From the standpoint of resistance to rain erosion, relatively few "unsatisfactory reports" have been received, during the past several years, on approved rain-resistance coatings.

SECTION B. SUBSONIC RAIN EROSION

7-3. Test Equipment and Procedures

A subsonic rain erosion program conducted at Cornell Aeronautical Laboratory has as its purpose the evaluation of the rain erosion resistance properties of nonmetallic aircraft materials. The tests are carried out on apparatus consisting of a blade that rotates at speeds of 500 to 650 miles per hour in a horizontal plane through simulated rainfall. The presently utilized rotating arm apparatus was designed and constructed by Cornell in 1952.[1]

Previous tests on various plastics and coatings in the speed ranges of 250 to 500 miles per hour indicated that the rate of erosion increases greatly (roughly to the 8th or 10th power) as the speed is increased; therefore, to keep pace with the speeds of new aircraft, it was believed desirable to construct a piece of test equipment that would simulate transonic or perhaps supersonic velocities, and to study the phenomena of rain erosion at higher velocities. Preliminary studies on the development of a supersonic rotating arm test apparatus indicated that horsepower requirements for 1,000 miles per hour would be in the range of 400 to 500. Since it was economically unfeasible to purchase a motor of this power, it was decided that new test apparatus would be designed and built around a 100 horsepower, wound-rotor motor, which would be in the desired cost range.

Plans and drawings were made for a test cell, gear transmission, and a test blade to rotate at a top speed of 6,800 revolutions per minute (rpm). Figure 7-1 shows the detailed design of the blade. Figure 7-2 outlines the general layout of the cell. The pit containing the test blade and gear box is 10 feet below ground and is rubber covered. Figure 7-3 shows the interior of the pit, gear box, test blade, and specimens.

The equipment was revised to provide a continuously variable speed from 500 mph to 700 mph in the middle of the test specimen.

Tests were conducted to compare the relative erosion rates of the old and new test apparatus on elastomeric materials. Two sets of specimens were prepared. Bostik 1007 primer with Goodyear neoprene coating 23-56 was sprayed on glass laminate test specimens to obtain a total thickness of 10 mils.

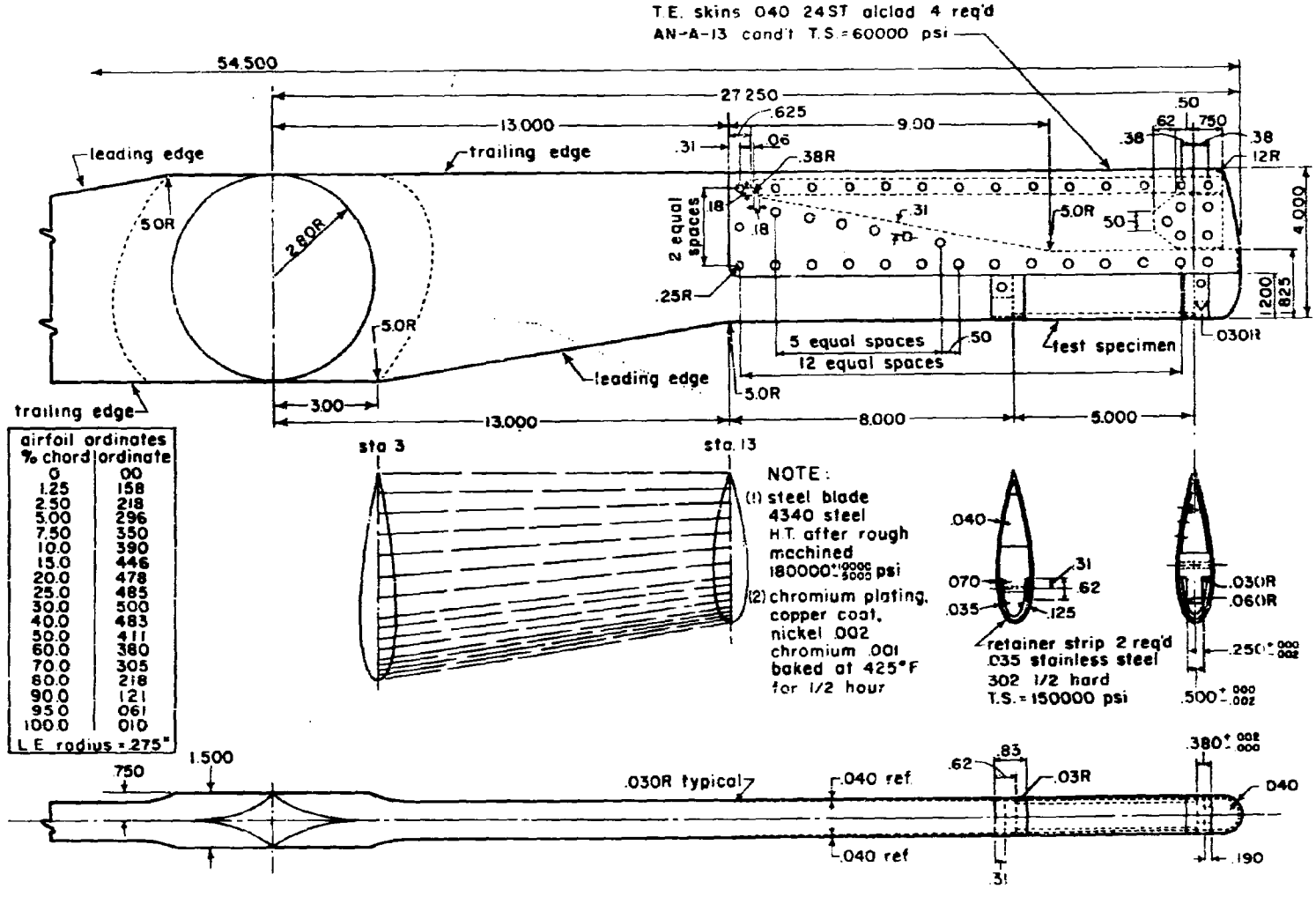
Specimens No. 402 were tested on the old apparatus and specimens No. 403 were tested on the new apparatus at a nominal speed of 500 miles per hour. The total times of exposure were 180 minutes for the old apparatus versus 120 minutes for new apparatus. This indicates an approximate factor of 1.5 in converting rain erosion time on the new apparatus to data obtained on the old apparatus.

The standard rain erosion test which is used to compare all materials is at 500 miles per hour though a 1-inch per hour simulated rainfall with a 1.9-millimeter droplet size. All subsonic rain erosion times cited in this chapter are for this standard test unless otherwise specified. Test specimens of airfoil shape, conforming to Figure 7-4, were attached to each end of the blade; these specimens of plastic or metal, were tested with or without coatings.[1]

This test apparatus does not reproduce exactly the amount of erosion experienced during the same time interval as one obtains under actual flight conditions; however, it has been shown to rate materials satisfactorily in their relative order of in-service durability, and this is the purpose of the equipment. It is probably at least three times more severe as a rain erosion test than actual flight tests. This is a factor that has not been clearly determined due to a lack of sufficient flight test data.

7-4. Erosion Criterion

Studies of rain erosion resistance have been determined for typical aircraft plastics. To pursue such study, a basic need was to recognize the extent of erosion. Early work, however, showed the inadequacy of weight loss as a possible method for determining the extent of erosion. Depth of penetration of erosion, as, for example, the number of plies eroded, was not useful in this work because the time for initiation of erosion was of especial interest. It was found that an early stage of erosion could be recognized when approximately 50 percent of the surface is covered with fine pits and the remaining 50 percent is unpitted. It is referred to as the 50 percent initiation point. It was observed that the pits appear to have a maximum size of approximately 0.01 to 0.02 inch across, and that, as erosion continues, pits of this size overlap. In the test runs there appeared to be no evidence of the initial formation of pits larger than this size. Recognition of this degree of erosion was sufficiently precise so that comparisons of velocity and time of erosion could be made. All specimens were eroded to this same degree.



airfoil ordinates	
% chord	ordinate
0	00
1.25	158
2.50	218
5.00	296
7.50	350
10.0	390
15.0	446
20.0	478
25.0	485
30.0	500
40.0	483
50.0	411
60.0	380
70.0	305
80.0	218
90.0	121
95.0	061
100.0	010

L.E. radius = .275"

Figure 7-1. Details of Test Blade

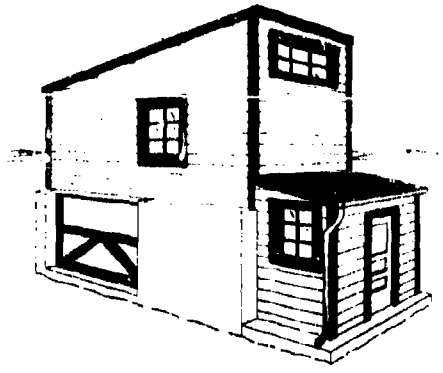


Figure 7-2. Rain Erosion Cell at Cornell Aeronautical Laboratory

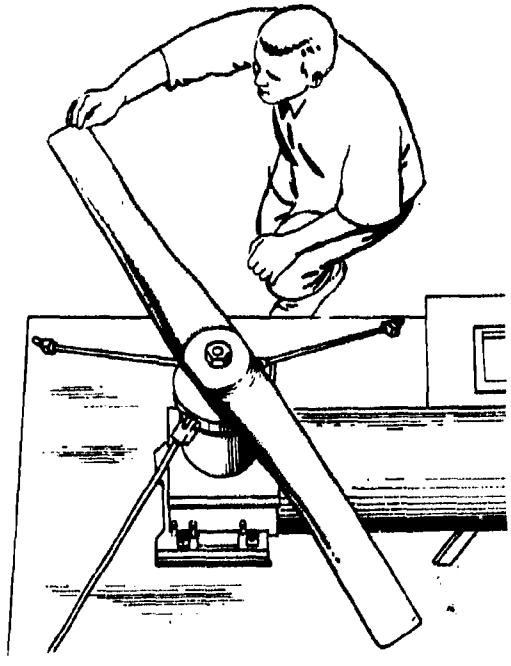
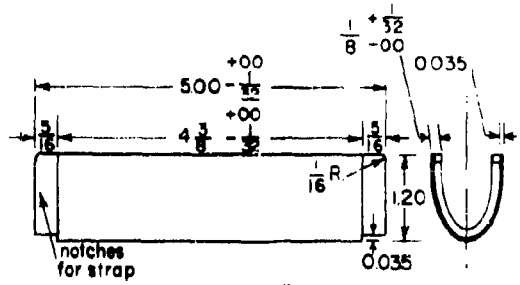


Figure 7-3. Interior of Cornell Test Pit, Gear Box, Test Blade, and Method of Mounting Specimens

7-5. Test Conditions

In performing a test, the specimen was eroded on the whirling arm testing machine until the 50 percent initiation point occurred somewhere along the leading edge. The actual location of this point was then determined by microscopic examination and the radius of the arm at this point was determined. From the radius and the



0.0025 airfoil — 4" chord

% chord	ordinates distance from l. e.	ordinate
.00	.00	.00
1.25	.05	158
2.50	.10	218
5.00	.20	296
7.50	.30	350
10.00	.40	390
15.00	.60	446
20.00	.80	478
25.00	1.00	485
30.00	1.20	500

outer dimensions of 1/8" specimen

Figure 7-4. Test Specimen Details

speed of rotation, the velocity of the specimen at the 50 percent initiation point was computed. From the velocity and the rainfall rate, the number of raindrop impacts per square inch were estimated. This latter estimation is based on the concentration of rain drops in the atmosphere and the volume swept through by the specimen. For a 1-inch per hour rainfall, in which the average drop size is 1.9 millimeters, the number of impacts per square inch is 5.09Vt where V is the velocity of the specimen in miles per hour and t is the time of exposure in minutes.

Use of 50 percent erosion point was restricted to polyester resins and polymethylmethacrylate, since it was found that other plastic and elastomeric coatings did not give reproducible results.

For elastomeric coatings, the time of failure is defined as the time to erode through the coating to the laminate or supporting material underneath. After the coating has eroded through, the plastic laminate underneath rapidly deteriorates and the coating no longer performs its protective function.

7-6. Variables Influencing Subsonic Rain Erosion

In addition to evaluating all promising materials for rain erosion resistance the work at Cornell

has also involved determining the effect of such variables as velocity of the specimen, temperature, droplet size, angle of attack, and rainfall rate.

Cornell has established that the angle between the surface and the path of the drop is a major factor in influencing amount of rain erosion damage. It has been determined that, at angles of 60° or less between the surface and the path of the drop, the erosion was considerably less than when the angle was greater than 60°. At angles of 15° or less, erosion is negligible, and the use of coatings for rain erosion protection at the speeds tested (200 to 600 miles per hour) is not necessary.

Tests at Cornell have also indicated that the time of exposure required to produce a given amount of erosion is inversely proportional to the eighth power of the velocity of the specimen in the speed range of 250 to 600 miles per hour.[1]

A study has been conducted of the influence of drop size and rainfall rate on the amount of erosion produced. The stress caused by the impact of a drop is proportional to approximately the 3.2 power of the diameter of the drop. The data supporting this relation was originally obtained using polymethylmethacrylate in 3-inches per hour rainfall in which the median drop size was 2.5 millimeters. In comparing with other data, it is to be noted that both drop size and rainfall rate are varied; and in the great majority of tests, these have been held at 1.9 millimeters and 1 inch per hour.

Rainfall rate and drop size normally vary together. Tests were made, however, in which rainfall rate was varied while the drop size was held constant. This was accomplished by using three, rather than one, of the nozzles designed for simulating 1-inch per hour rainfall. The results of the tests in variations of rainfall rate and drop size are organized in Figure 7-5. The line for 1.9 millimeters drops when 3-inch per hour rainfall is taken from a similar plot of data using the three 1-inch per hour rainfall nozzles. A plot of the logarithm of the total number of impacts per square inch to initiate erosion damage versus the reciprocal velocity (multiplied by a constant term which is the diameter to the 3/2 power), results in straight lines, as illustrated in Figure 7-5.

The line for 2.5-mm drops was obtained from calculations based on photographs of early specimens. It is to be noted that inclusion of the correction for drop size, $d^{3/2}$, brings the slope of the line for the larger drop to that of the line for the smaller drop.

It is also to be noted that with constant drop size, more impacts are required in 3-inch per hour rainfall than in 1-inch per hour rainfall to initiate erosion. This decrease in efficiency of a given size drop in producing erosion as rainfall rate increases is attributed to an interference phenomenon. On impact, the drop splashes back in the form of a fine spray moving ahead of the specimen. As the number of impacts per unit time increases, the density of this spray must increase. Thus, at very high rainfall rate, the drops must penetrate through a more dense spray, moving generally in the opposing direction, before reaching the surface. This interference between spray and drops is apparent in visual observation using stroboscopic light. The spray is considered to decrease the relative velocity of the drops at impact. Inasmuch as the amount of erosion is very sensitive to velocity changes, even a slight decrease in velocity would have a very noticeable effect.[1]

7-7. Rain Erosion Properties of Coatings, and Plastic Materials

Typical polyester resin reinforced plastic laminates have extremely poor rain erosion resistance in themselves. In the standard rain erosion test they will erode through a 1/8-inch laminate in 3 to 4 minutes. The problem of obtaining plastic materials which will resist erosion for long periods of flight through rain is still to be solved. Many approaches have been investigated to improve the glass reinforced laminate or its components. Studies have been disappointing. Although new epoxy resins have greatly increased the rain erosion resistance capabilities of plastics, the epoxys in themselves are still far from being a satisfactory solution, and the majority of the exterior plastic parts utilized in aircraft today are fabricated from polyester resins. Overlays and new techniques of fabrication have not been successful and offer little promise. Therefore, a great many coating materials have been investigated to determine the most satisfactory one for plastic protection.

To date, the neoprene type coatings have been the most satisfactory. Of the many neoprene coatings evaluated, only three meet the requirements of MIL-C-7439B for rain erosion coatings over plastic laminates. These are the Goodyear 23-56 Class I and Goodyear 23-57 Class II coatings, and the Gates H-79 Class I coating. When these materials are properly applied to a polyester glass cloth reinforced laminate specimen, a 10-mil coating may be expected to resist erosion at 500 miles per hour in 1-millimeter rainfall for approximately 80 minutes in the simulated rain erosion test. These coatings are

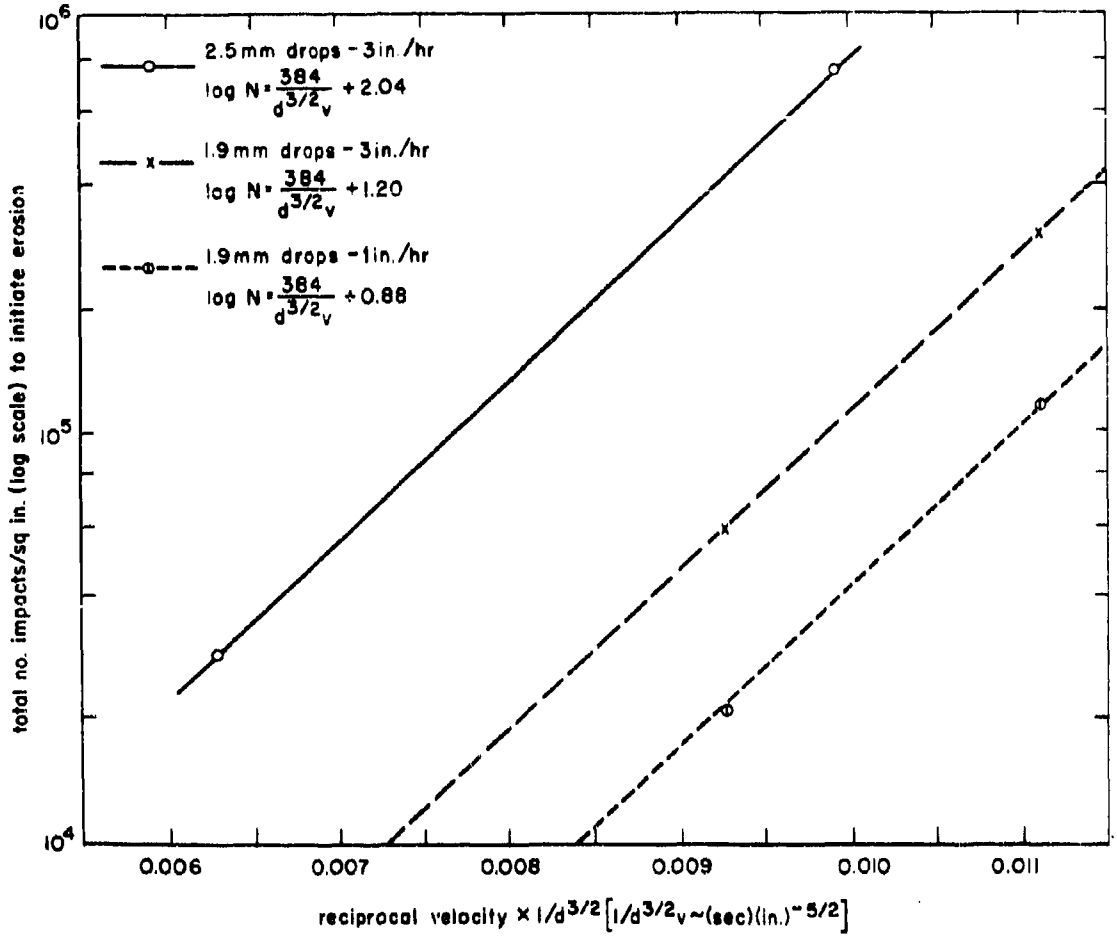


Figure 7-5. Correlation of Drop Size Data on Polymethylmethacrylate

all of the air drying type and can be applied by either brush or spray. When applied in a 10-mil thick film, they meet the electrical requirements for aircraft radomes. Thicker coatings possess much superior rain erosion resistance but seriously impair the electrical properties.

A study of the relation of the thickness of neoprene coatings to their rain erosion resistance was carried out (1) to determine whether the rate of erosion changes as the thickness of the coating is increased; and (2) to obtain a curve that could be used to predict the relative rain erosion resistance of various thicknesses of a typical neoprene coating, such as Goodyear 23-56.[2]

Twenty standard glass-reinforced laminates were primed with and then brush coated with Goodyear 23-56 neoprene so as to give coatings ranging from 1 to 33 mils thick. Tests were conducted on the coated specimens at a speed of 500 miles per hour and 1-inch per hour rainfall. The time to obtain the first hole in the neoprene coating was recorded, and these data were used to prepare the graph shown in Figure 7-6. The tests were stopped when erosion had progressed through the coating and one to two plies of the glass-reinforced laminate beneath.

The graph indicates that the rate of erosion is greater in the range of 1 to 8 mils than in the range from 8 to 33 mils. It can be generally stated that the time to erode through neoprene coatings of the Goodyear 23-56 type is a function of the coating thickness. The general equation shown by the dotted line, that is, time

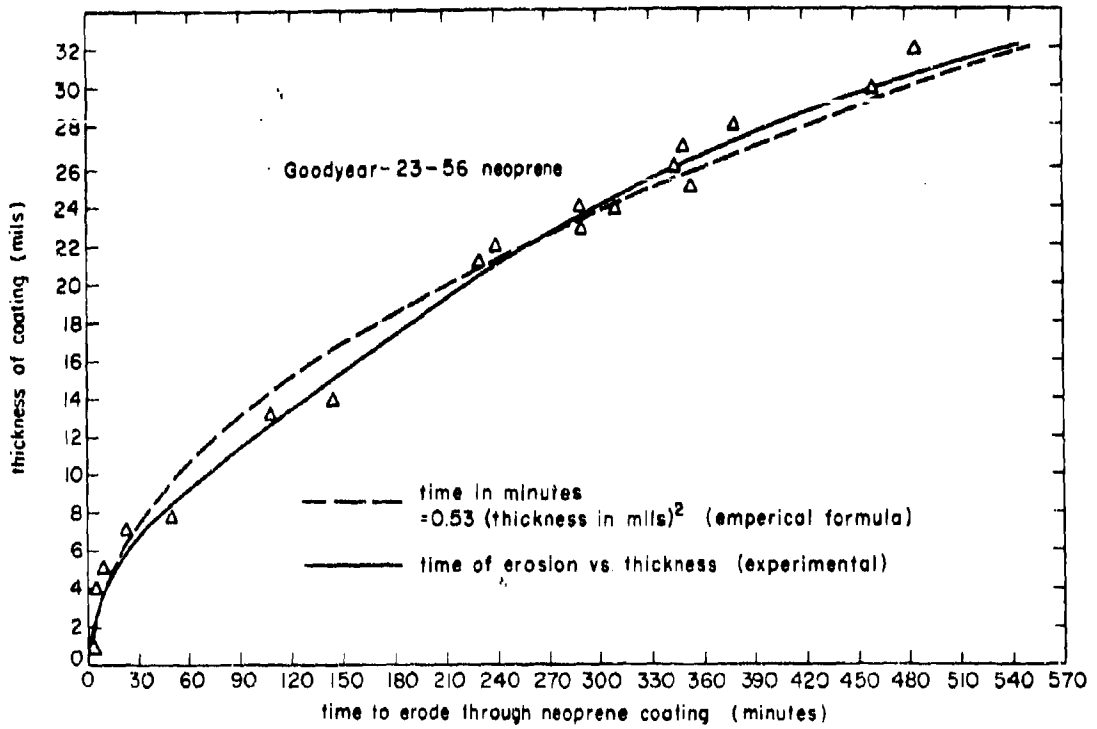


Figure 7-6. Rain Erosion Tests at 500 Miles Per Hour and 1-Inch Per Hour Rainfall

to erode through the coating in minutes = 0.53 times (thickness in mils)^2, can be used to predict how long a neoprene coating would last.

Effect of Temperature on Erosion. The approved neoprene coatings meet MIL-C-7439B temperature requirements of exposure at 200° F for 20 hours with no reduction in rain erosion resistance. However, as aircraft speeds have increased, the problem of increased heating, due to friction, was encountered; therefore, the approved neoprene rain erosion coatings were investigated after exposure to elevated temperatures.[1,3]

The effect of heat on the erosion resistance of neoprene coatings Gates N-79 and Goodyear 23-56 was determined under the following conditions:

1. 180° F for 72 hours
2. 225° F for 72 hours
3. 300° F for 20 hours

The results of these tests indicated that heating for periods up to 72 hours at 180° F does not materially affect the erosion resistance; heating for 72 hours at 225° F does affect the coating. In general, the presently approved coatings can be considered satisfactory after exposure to temperatures up to 200° F for periods in the range of 100 hours. As the temperature increases to 300° F, exposure for shorter periods renders these coatings unsatisfactory for rain erosion resistance. The results are indicated in Table 7-I.

Table 7-I. Effects of Temperature

Coating	Average Time to Erode Through 10-Mil Coating			
	Room temp air dry 100 hours	180° F for 72 hours	225° F for 72 hours	300° F for 20 Hours
Gates N-79	88 min	96 min	48 min	1.5 min
Goodyear 23-56	131	75	55	5

In all cases, as the temperature increased, the coating became darker. At 300° F, the film became black and very brittle. Failure was due primarily to loss of adhesion.

Based on these results, approved MIL-C-7439B coatings exposed to temperatures above 200° F for periods over 4 hours should be inspected frequently for signs of early degradation due to rain erosion.

Tests were also conducted on specimens coated with Gates N-79 and Goodyear 23-56 exposed to 400° F for 10 minutes. The specimens were tested for rain erosion resistance at 500 miles per hour and 1-inch per hour simulated rainfall. In testing, all specimens failed, primarily due to loss of adhesion of the neoprene coating to the glass laminate, which caused bubbling along the leading edge and tearing loose of the coating along the sides of the specimens. The results indicated that the Gates N-79 coating lasted for 30 minutes and the Goodyear 23-56 an appreciably longer time of 110 minutes, since the adhesion was superior for the Goodyear coating.

Further studies on the effect of heat treatment upon the rain erosion resistance of Gates and Goodyear neoprene coatings at temperatures between 300 and 400° F were carried out, under the conditions outlined below.

Material	Condition
Goodyear 23-56 Gates N-79	300° F for 10 minutes
Goodyear 23-56 Gates N-79	375° F for 10 minutes
Goodyear 23-56	400° F for 10 minutes

The specimens heat treated at 400° F failed, due to loss of adhesion after 20 to 40 minutes of testing.

The coatings on the specimens, heated at 300 and 375° F all failed in 30 minutes. Failure of all these heat treated specimens can be attributed mainly to loss of adhesion of neoprene coating to the glass fiber laminate.

In general, the neoprene coatings appeared tougher than normal when cured at 175° F for 4 hours, and then at 300, 375, and 400° F for 10 minutes. Based upon the results and observations of the specimens used, it is believed that if a satisfactory adhesion system can be obtained between the neoprene and the glass reinforced laminate, the Goodyear 23-56 and Gates N-79 coating should have satisfactory rain erosion resistance when exposed to an upper limit of 375° F for 10 minutes.

The approved neoprene coatings were also evaluated after exposure to temperatures of -65° F. This was done because natural rubber and neoprene show a greater tendency to undergo a process of crystallization when exposed to low temperature or high stress. Tests conducted on Goodyear 23-56 and Gates N-79 after exposure to -65° F for one-half hour indicated that there was no decrease in erosion resistance.

Effect of Support on Erosion. The protective value of the neoprene coatings is directly related to the support offered by the reinforced plastic material to which the coating is applied. Sandwich type airfoil specimens, similar in construction to F-86D aircraft, were evaluated.[4] The approved Goodyear 23-56 rain erosion coating was applied to slotted conventional laminates with thin outer sheets bonded to them which had thicknesses of 15 mils and 30 mils respectively (Figure 7-7).

Solid laminates, utilizing the same laminate material, were coated with Goodyear 23-56 and evaluated as a control. The 8-mil neoprene coating over the solid wall laminate failed in approximately 12 minutes. A neoprene coating of the same thickness lasted 6 minutes over the slotted laminate with the 0.030-inch shell and only 4 minutes over the slotted laminate with the 0.015-inch shell. After the rain eroded through the neoprene coating over the slotted areas, it eroded rapidly through the laminate. A check of the laminates used in these specimens indicated a low Barcol hardness of 45 and compressive strength of 25,000 pounds per square inch. The low compressive strength probably accounted for the failure of the laminate beneath the neoprene coating. Based on these results, the use of laminated parts with Barcol hardness below 55 should be critically examined before putting them into service on the exterior of an aircraft where they would be subjected to pos-

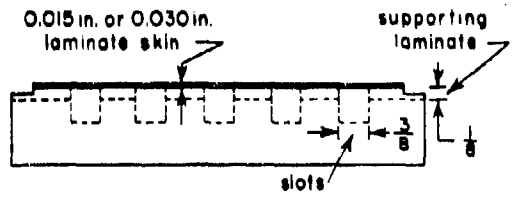


Figure 7-7. Configuration of Slotted Laminates for Erosion Tests

sible erosion by rain. Also, the use of thin outer layers of sandwich construction (15 mils and 30 mils) does not offer proper support for the neoprene coating under impact of rain drops at high speeds. A heavier shell would probably produce the desired support.

Epoxy Resins. Recent tests have indicated that currently available epoxy resins reinforced with glass cloth or glass filaments produce a stronger and more uniform supporting laminate than glass reinforced epoxy laminates previously tested. Scotchply 1002 and 1005 epoxy resins, and glass cloth and glass filament laminates were found to have appreciably greater rain erosion resistance than reinforced polyester laminates.[4]

Minnesota Mining and Manufacturing Company originally submitted the 1002 and 1005 epoxy resin with their Scotchply material (isotropic glass filaments). The test results indicated that the 1005 took 70 minutes to erode and the 1002 took 30 minutes to erode through a 1/8-inch laminate. The 70-minute erosion time for the 1005 epoxy resin has not been reproducible in later tests. A study was conducted on glass cloth versus parallel glass strands and also on Shell Chemical Company Epon 828 versus the 3M epoxy resins.

These tests resulted in the following conclusions.

a. Glass cloth reinforced epoxy laminates withstand erosion noticeably better than epoxy laminates with glass fibers. In these tests it required 70 minutes to erode completely through the 1/8-inch glass cloth reinforced 3M epoxy laminate, whereas it took only 40 minutes to erode through the laminate reinforced with glass fibers.

b. The 3M 1005-181 epoxy laminate was superior in rain erosion resistance to the Epon 828-181 epoxy laminate. The 1005-181 laminate eroded through in 70 minutes. The Epon 828-181 laminate eroded through in 32 minutes.

c. Glass cloth reinforced epoxy laminates have greater erosion resistance than similar polyester laminates. This can be attributed to the greater bond strength of the epoxy laminate, which prevents delamination under the impact of the rain.

Recent retests of the 3M epoxy 1002 and 1005 resins indicated that the time to erode through a 1/8-inch glass cloth laminate varies between 30 and 50 minutes; further evaluation is in progress.

Practically all rain erosion tests have been conducted on coatings applied to polyester resin laminates, since glass reinforced epoxy laminates have shown greater erosion resistance than similarly reinforced polyester laminates. It was considered desirable to evaluate and compare the erosion resistance of approved neoprene rain erosion coatings with the two types of laminates. The specimens that were evaluated utilized Goodyear 23-56 over Epon 828, 3M 1005 and polyester laminates fabricated with 181 glass cloth and Volan A finish. A 10-mil neoprene coating over the 3M epoxy laminates lasted approximately two hours at 500 miles per hour in 1-inch per hour rainfall before a hole eroded through the neoprene to the laminate. The Goodyear 23-56 over the Epon 828 laminate lasted about one and one-half hours for the same degree of erosion. The neoprene coating resisted rain erosion for a noticeably longer period over the epoxy laminates than over polyester laminates in the preliminary evaluation. Further evaluation of these epoxy resins for rain erosion resistant laminates is presently in progress, since, based on the work accomplished to date (1956), neoprene coated epoxy laminate radomes would have twice the service durability of currently used polyester glass radomes. Also, once the neoprene has been eroded through, the epoxy laminates themselves possess approximately 10 times the erosion resistance of the bare polyester laminates.

Polyurethane. The most promising new rain erosion resistant coating material evaluated has been the polyurethane type.[4] "Estane", a trade name for a clear polyurethane material developed by B.F. Goodrich Company, is transparent and has excellent low-temperature flexibility and a relatively high melting temperature. Based on tests conducted, the unprimed Estane coating in 5-mil thicknesses will resist erosion for 35 minutes, and 10-mil thick films will last 55 minutes.

A 23-mil thick film of Estane polyurethane coating over a polyester laminate specimen lasted four hours at 500 miles per hour and 1-inch per hour rainfall. This is slightly longer than a 23-mil Goodyear 23-56 neoprene coating would last under the same test conditions.

The Estane polyurethane material erodes in a different pattern from neoprene. Whereas neoprene pits and erodes uniformly all along the leading edge of test specimens, the rain impact on the polyurethane coating produced numerous small cuts or slits on the leading edge. These become longer and deeper as the test progressed; however, the majority of the leading edge showed virtually no erosion.

An 11-mil film of Estane, which had good adhesion to the polyester glass laminate, lasted for 80 minutes before heavy pitting and erosion through to the laminate occurred.

The University of Cincinnati is also conducting a program for the Bureau of Aeronautics on the development of a rain erosion resistant polyurethane coating. They have reported excellent rain erosion resistance.

7-8. Subsonic Rain Erosion Properties of Ceramics and Glass

Johns Hopkins University has been conducting a program for the Navy on the Terrier missile that has included some work on rain erosion. Primary emphasis has been placed on ceramics and pyrocerams as possible radome materials for missile applications.

A method of evaluation used by Johns Hopkins has been the polyethylene pellet gun. In this technique, synthetic "raindrops" of polyethylene, which has a density comparable to water, are fired from a gun. The polyethylene pellets strike the specimen and splatter. Using this method and polyethylene pellets of 2-millimeter diameter, single drop impacts have been obtained at supersonic speeds on a variety of materials. The most promising materials, as shown by these tests, have been ceramics, such as alumina and pyroceram.[5]

Subsonic rain erosion tests have been conducted at Cornell Aeronautical Laboratory, for the Applied Physics Laboratory of Johns Hopkins University on ceramics, glass, cerams, and glass bonded mica.

The materials evaluated were made of flat specimens that measured approximately 4 inches long, 1/2 inch wide and 1/4 inch thick. The samples were mounted in special metal adapters attached to each end of the whirling-arm test blade. The sides of the specimens were beveled to hold them in place.

The specimens were evaluated at 500 miles per hour and 1-inch per hour rainfall, and were tested until they were pitted moderately and eroded approximately the same amount.

Based on the results of these tests, the following conclusions were reached relating to the rain erosion resistance of these materials.

a. The ceramics and cerams are far more resistant to rain erosion than the glasses tested. In particular, Corning Glass cerams 843 GV, 607BUZ (#8606), 607AVE (#8605), and American Lava Alsimag 570 of alumina have good rain erosion resistance at 500 miles per hour. The test samples lasted in the range of 5 to 8 hours before they were pitted moderately.

b. Corning Glass 1710 has greater rain erosion resistance than Corning glasses 7740, 7910, or 7070. The 1710 glass (alumina silicate type) specimens lasted in the range of 35 to 45 minutes at 500 miles per hour. All tempered glass was found to be superior to annealed glass.

c. In general, the rain erosion resistance of the bonded mica was rather low. Supramica 555, a glass-reinforced synthetic mica, has greater erosion resistance than Mycalex 410 and 410X which are reinforced natural micas. The Mycalex materials with the molded finish were slightly better than the materials with the ground finish. Supramica with the molded finish lasted 5 minutes, whereas the specimens with the ground finish lasted only 2 minutes before the surfaces were pitted moderately.

In summation, the ceramics and cerams tested at speeds of 500 miles per hour have excellent rain erosion properties. However, the present possibility of their use for subsonic aircraft radomes is considered limited, due to difficulties in forming them, expecially in large sizes. Furthermore, failure of these materials is usually a complete cracking which can come with extreme suddenness, rather than as a gradual deterioration. This complete type of failure is extremely different from the gradual erosion noted in the neoprene coatings and, since the entire radome would be destroyed, could conceivably result in loss of the aircraft and pilot[5] unless designs for their application are so modified as to avoid such possibilities.

Table 7-II presents an overall summation of the rain erosion properties of plastic materials, coatings, and promising ceramics evaluated to date. For more complete data see the various reports listed in the references.

7-9. Subsonic Flight Test Programs

Studies conducted by Cornell on laboratory test equipment have been of great value to the Air Force on evaluation of materials. However, there has been a great need for actual flight testing of various materials to obtain a comparison in erosion rates and also to substantiate the laboratory test equipment data.

Due to the difficulty of obtaining the use of an all-weather aircraft for these tests, no data could be obtained. However, during a slack period in the flight test program of an F9F airplane on bailment to Cornell Aeronautical Laboratory arrangements were made to use this airplane

Table 7-I. Known Erosion Properties of Materials Tested at 500 Miles per Hour Through 1/2-inch Simulated Rainfall

General Material Description	Time to Initiate Pitting	Time to Erode Through
Methyl methacrylate	1 min	--
1/8-inch Epoxy Laminate	2-3 min	30-50 min
1/8-inch Polyester Laminate	30 sec	5 min
1/8-inch Phenolic Laminate	15 sec	3 min
*10-mil Kel-F Coating	--	5-9 min
*10-mil Teflon Coating	--	60 sec
*10-mil Lactoprene Coating	--	15-25 min
*10-mil Neoprene Coating	--	50-70 min
*10-mil Silicone Coating	--	10 min
*10-mil Polyurethane Coating	--	50 min
*10-mil Gates White Neoprene	--	50-70 min
*10-mil Hypalon Coating	--	10-20 min
**Alumina (AlSiMag 576)	--	300-420 min
**Pyroceram	--	300-480 min
**Mycalex	--	5 min
**Glass (1710)	--	35-45 min

*Coating Placed over Typical Polyester Laminate

**Moderate Pitting

for actual rain erosion flight tests for a limited time.[2]

Specimens of various coatings were applied directly to the 24ST metal leading edge as well as on glass-reinforced laminates that were bonded to the leading edge. These laminates were 0.090-inch thick. Figure 7-8 shows the specimens applied, and lists the materials used. All specimens were 7 inches long and extended back from the leading edge approximately 4 inches. The neoprene and other elastomeric coatings were close to 10 mils thick. The paint coatings averaged 2 mils in total thickness for the zinc chromate primer and finish coat. Each material was applied in duplicate, that is, one on each wing.

Flight Tests. A total of 16 minutes flight through rain was obtained in two increments of 5 minutes each and two increments of 3 minutes each. The first flight in rain was for 5 minutes in a moderate to light rain, at an indicated airspeed of 475 miles per hour, at 2,500 feet altitude. Examination of the specimens after this flight showed that standard lacquer and enamel paint coatings applied over zinc chromate primer (Specimens No. 9 and 11) had generally eroded off most of the leading edge. Specimen No. 8 of vinyl type paint coatings showed some pitting and flaking off of small areas. Specimen No. 1 of uncoated, void-free, glass-reinforced laminates showed slight pitting of the resin surface.

The second flight in rain was also of 5 minutes duration, but the rain was fairly light. The speed



Key to Position of Specimens

Coated and Uncoated Plastic Specimens

#1 Uncoated, void-free, glass-reinforced laminate 6 plies 181-36 cloth; Selectron 5003
#2 Coated, glass-reinforced laminate primer — Bostic 1007; topcoat — Goodyear 23-56
#3 Coated, glass-reinforced laminate primer — Gates N-15; topcoat — Gates N-79
#4 Coated, glass-reinforced laminate primer — Gates N-15; topcoat — Gates N-79; antistatic — Gates N-51
#5 Coated, glass-reinforced laminate primer — none; topcoat — 3M 843 +5 percent Al
#6 Coated, glass-reinforced laminate primer — Pro Seal 581; topcoat — Pro-Seal 582
#7 Uncoated
Lucite — 0.060 inch

Coatings on Aluminum Leading Edge

#8 Sherwin Williams — Navy vinyl system primer — E42YP7; topcoat — F55AP2
#9 Glidden — Standard system zinc chromate — Primer MIL P6889; enamel — topcoat — MIL E7729
#10 Minnesota Mining & Mfg. Co. primer — zinc chromate; topcoat — 3B 843 +5 percent Al
#11 Glidden — Standard system chromate — primer — MIL P6889; lacquer — topcoat — MIL L7178
#12 Goodyear — Neoprene system primary — Bostic 1007; topcoat — Goodyear 23-56
#13 Gates — Neoprene system primer — Gates N-15; topcoat — Gates N-79

Figure 7-8. Placement of Specimens on Right and Left Wings of F9F Airplane

was 475 miles per hour, at 500 feet altitude. Specimen No. 1 of uncoated, void-free, glass-reinforced laminate had eroded through the surface resin to the first ply. Specimen No. 7 of methyl methacrylate sheet showed slight erosion by a frosty appearance. The vinyl coatings (Specimen No. 8) were practically eroded off the leading edge.

The third flight of 3 minutes was through an extremely light rain at 475 miles per hour at 6,000 feet. Examination of the specimens showed no apparent increase in erosion over the previous flight.

The fourth flight was through a heavy thunderstorm at a speed of 460 miles per hour, at 3,000 feet, for 3 minutes. This gave a total flight time of 16 minutes. The uncoated, void-free, glass-reinforced laminate showed considerable erosion through one or more plies (Specimen No. 1). Methyl methacrylate Specimen No. 7 showed some pitting of the surface and fine cracks. The specimen of 3M-843 elastomeric coating with 5 percent aluminum pigment on glass laminate, Specimen No. 5, and the 24ST aluminum leading edge, Specimen No. 10, showed considerable amount of erosion after 16 minutes flight. The neoprene coatings, such as Goodyear 23-56, Gates N-79, N-15 antistatic, and Pro-Seal 582, showed no signs of erosion after 16 minutes of flight through rain at speeds in the range of 500 miles per hour.

Based upon the flight tests reviewed above, the relative rain erosion resistance of various materials tested can be listed in the following order:

1. Neoprene coatings, such as Goodyear 23-56, Gates N-79, Gates N-51, and Pro-Seal 582
2. 3M-843 elastomeric coating
3. Methyl methacrylate sheet
4. Void free laminates
5. Vinyl coatings
6. Paint or lacquer coatings.

A program has also been conducted at Wright-Patterson Air Force Base. The program was initiated in February 1952, to obtain flight test data on the ability of the approved neoprene rain erosion coatings to protect adequately exterior plastic leading edges. It was anticipated that the flight tests would also indicate a correlation between the rotating-arm laboratory test data and actual in-service test life. Rain erosion data has therefore been accumulated on various fighter aircraft which have been stationed at Wright-Patterson Air Force Base.

Fighter aircraft were selected as the logical vehicles because there are more of these available and they can achieve the desired high speed flights in rain. All aircraft exterior plastic leading edges were required to be coated with approved neoprene coating. This meant that the aircraft would need no modification at all for these tests.

Various F-94A, F-94B, F-94C, F-89C, and F-89D aircraft were involved in this program. The velocity at which these aircraft flew through rain was 375 knots (432 mph). The time in rain, degree of rain, and velocity were recorded by the pilot personnel, and inspection of the radomes was made after each flight by personnel from Materials Laboratory, WADC.

Times in rain at this speed were accumulated in the range of 80 to 145 minutes with no erosion damage on F-94 aircraft.

An F-94A aircraft was flown for a total time of 2 hours, accumulated over three flights, at speeds varying from 320 to 375 knots (368 to 432 mph) before the coating eroded and peeled. The peeled coating was examined and found to be 5 mils thick maximum. The rain intensity varied from light rain for 35 minutes to heavy rain for 35 minutes. Another F-94 aircraft was flown at 375 knots for a total time of 200 minutes, accumulated over four flights, before the coating peeled. This was in light to moderate rain.

These were the only two cases where erosion on this flight test program was obtained using the approved neoprene coating. In no case was the radome damaged to any extent other than a slight hole or roughening of the surface. It is also stressed that there was no previous history on these radomes available which would allow an accurate estimate of the total life of the coating to be made.

At this point it was observed that most of the data were being accumulated on F-94A and F-94B aircraft. These aircraft utilize a radome which is interchangeable. It was decided, therefore, to limit the program to F-94A and B aircraft. A test radome was obtained and coated and utilized in all flight tests regardless of the aircraft being flown. The change is accomplished in a short period of time, and transfer was made, when the weather conditions were appropriate, to whatever F-94A or B aircraft was in operating condition.

The initial material applied to this radome and evaluated was the Goodyear 23-57 antistatic coating system. Three flights were made in rain, varying from light to moderate intensity, at a velocity of 350 knots (402 mph). The total time accumulated in rain was 56 minutes before the coating bubbled and peeled considerably. There was no damage to the radome. The thickness of the coating was measured and found to be 5 mils, which is only half the specified thickness.

This radome was then recoated with the approved Gates N-79 neoprene coating. Three flights were made in rain, varying from light to very heavy, at a velocity of 350 knots. The total time accumulated in rain was 110 minutes before the radome was damaged. The coating was still in good shape; however, because of a damage area consisting of a small hole, it was necessary to obtain a new radome.

This program is still in progress (1956) and it is hoped that sufficient time will be obtained to complete it.

Test Results. Points that can be obtained from the data accumulated to date are:

a. It is essential that great care be taken in applying the coating to insure that sufficient primer is applied. The failures in most cases were due to loss of adhesion.

b. It is essential that 10-mil coatings be applied for maximum rain erosion protection consistent with satisfactory electrical performance. Several radome coatings examined after failure had considerably less than the required coating thickness.

c. The Cornell Laboratory test is more severe than actual flight tests. It is considered that satisfactorily applied coatings will not suffer rain erosion damage in flights at 375 knots before at least three hours in moderate rainfall.

SECTION C. DEVELOPMENT OF A THERMALLY REFLECTIVE, ANTISTATIC HEAT RESISTANCE RAIN EROSION COATING

The neoprene coatings presently being utilized on exterior plastic leading edges are satisfactory up to temperatures of 200° F, but rapidly lose their efficiency as the temperature increases. At 350° F or over, an extended exposure will deteriorate the coating's efficiency completely. It was anticipated that the constantly increasing speed of military aircraft and missiles will cause the outer surfaces of the planes to be at high temperatures, due to skin friction. Also, the practice of passing hot gases through specially constructed radomes to prevent ice formation on their outer surfaces may lead to subjection of the protective rain erosion coatings to elevated temperatures.[6,7]

7-10. Goodyear Tire and Rubber Company Program

A contract was made with the Goodyear Tire and Rubber Company to develop a rain-erosion resistant material which would withstand temperatures of 500° F for an appreciable period and would also be electrically satisfactory.

All available coating materials were investigated and it was found that there are very few which will withstand 500° F for 30 minutes. Goodyear found that silicone rubber, Teflon, and properly compounded acrylic copolymers, such as Lactoprene E. V., and Acrylon rubbers are the only available materials which would pass this test.

The Teflon and Kel-F material evaluated are unsatisfactory in rain erosion resistance, and the silicone rubbers, while they appear promising, have never been completely evaluated, due to their extremely poor adhesion to other materials. The Kel-F materials are relatively hard and inelastic, and, although good adhesion to the plastic laminate specimen has been obtained, they erode rapidly in times of less than 10 minutes at 500 miles per hour through 1-inch per hour of simulated rainfall.

The Lactoprene coatings were concentrated upon, since they were considered to be the most promising materials after exposure to 500° F. To date, while they show excellent heat resistance, they have not come close to reaching the excellent erosion resistance of neoprenes when neoprenes are tested with no exposure to elevated temperatures. A major problem is that of obtaining adequate adhesion. This aspect of the problem has not been completely solved. The material itself is also basically not as resilient and flexible as the approved neoprene.

The best of the Lactoprene coatings developed to date have lasted only 10 to 15 minutes after exposure to 500° F for 1/2 hour. These coatings have lasted as long as 30 minutes in rain erosion resistance with no exposure to elevated temperatures.

The work at Goodyear has been completed with no further improvement of the rain erosion resistance of the Lactoprene type coatings. Presently Cornell Aeronautical Laboratory is conducting a complete evaluation of the rain erosion properties of the Goodyear R-12 x 4-239, which is the most successful Lactoprene developed by Goodyear.

The one-half hour at 500° F requirement for heat resistant rain erosion coatings was an arbitrary choice, and coating materials which have possibilities for application at temperatures lower than 500° F were evaluated. Hypalon coatings, which are chlorosulfonated polyethylene elastomers manufactured by the DuPont Company fit in this catagory.

Several Hypalon coatings with no heat exposure, were evaluated at 500 miles per hour in 1-inch per hour rainfall; these were Gates XP-104, DuPont epoxy Hypalon A-2205A, and Goodyear R14L-23-495. None of these materials had promising rain erosion properties. Erosion was initiated after a few minutes exposure and progressed rapidly after initiation of damage. In general, the Hypalons tested, while flexible, do not possess much resiliency.

7-11. Gates Engineering Company Program

Gates Engineering Company is presently under Air Force contract, working on the development of a white, thermally reflective rain erosion coating. The target properties for the coating are that it will be as satisfactory as the approved neoprenes in all properties and will, in addition, possess an average 85-percent thermal reflectivity in the range of 0.4 to 2 microns. Two other items included in this work, once the coating has been developed or concurrent with the above item are: (1) antistatic white which will possess surface resistivity properties of 0.5-15 megohms/square inch; and (2) better heat resistant properties than the approved neoprenes (at least 100 hours at 400° F). In summation, the overall program calls for development of a thermally reflective, antistatic, heat resistant rain erosion coating.

Initial work has been the development of a plain white, thermally reflective coating. Initial physical property, peel, and reflectivity tests are conducted by Gates and the most promising materials are forwarded to Cornell for rain erosion evaluation. Based on satisfactory data being obtained, electrical transmission and surface resistivity tests would then be conducted.

The materials evaluated by Cornell to date have been white pigmented neoprene, Hypalon, polyacrylic rubber, and combinations of these materials applied over various primers and tie cements. All tests were conducted at the standard condition of 500 miles per hour and 1-inch per hour rainfall on the rain erosion tester at Cornell.

The most satisfactory white erosion coating evaluated to date has been K-223-A, which lasted 70 minutes before a hole eroded through the 11-mil film to the laminate. This system is a white neoprene topcoat utilizing Gates fillers, tiecoats, and primer.

This type of material almost meets all the minimum target requirements. Thermal reflectivity evaluations will be conducted, as well as further rain erosion and electrical property evaluations.

By the use of ionizable agents in conjunction with white neoprene coatings, it is anticipated that the antistatic requirements can be met. This work is in progress; it is hoped that the coatings will be developed in the near future.

SECTION D. MECHANISM OF RAIN EROSION

7-12. General Subsonic Investigation

The purpose of the work being conducted by the National Bureau of Standards under Air Force contract is to develop an understanding of the actual mechanism of rain erosion. Such an understanding would then aid in the development of more satisfactory rain-erosion resistant plastic materials for subsonic and supersonic speeds. The initial part of the work was largely concentrated on subsonic speed investigations.

The destructive force causing rain erosion results from the collision of the solid surface with the waterdrop at high impact velocities. The waterdrop acts as though it were a hard sphere, but unlike a sphere of hard material it undergoes an outward radial flow of very high velocity as a result of the collision.

An equation for the magnitude of the pressure, P, developed in collision of waterdrops against solid surfaces is:

$$P = \frac{a}{z}\left[\frac{C\rho V_0}{1 + \frac{aC\rho}{aC'\rho'}}\right] \qquad (7\text{-}1)$$

where

a = coefficient which gives, on the average, the fraction of the advance velocity of the fast moving surface which is impacted by the water molecules;

C = velocity of the compressional wave in water (5,000 feet per second);

ρ = density of water;

V_0 = vertical velocity of massive fast moving surface;

C' = speed of the compressional wave;

ρ' = density of the striking surface.

The impact pressure between a flat surface and jet of water struck from the side has been determined, using a piezoelectric gauge. The pressure developed when a flat solid surface strikes a cylindrical water surface should be between that developed when it strikes a flat water surface and that resulting from striking a spherical water surface. For a velocity of 35 meters per second, the piezoelectric pressure recorded was 310 kilograms per square centimeter. Using Doctor Engel's equation above, a pressure of 245 kilograms per square centimeter was predicted, assuming a to be about 0.09. Assuming a flat water surface a pressure of 490 kilograms per square centimeter, was predicted. Therefore substantiation of the assumptions for Equation (7-1) and of Doctor Engel's equation itself was obtained. The pressure estimated for neoprene rubber rain erosion coatings at V_0 = 600 miles per hour and z as assumed unity is 20,000 pounds per square inch. This suggests that the success of neoprene in reducing rain erosion on the leading edge of aircraft is not wholly explained by diminution of the pressure on the surface. Other factors, such as extent of elongation at break or attenuation on passing through the material have a definite bearing.

Another important factor is the radial flow of a waterdrop when it impinges on a solid surface. This flow has been mapped chemically by use of a very small crystal fragment of sodium dichromate inserted into the bottom surface of the droplet just before it left the dropping pipette. The droplet, when impinged on filter paper that was wet with acidified starch and potassium iodide solutions, gave a print of the wash of the drop. The waterdrops are actually deformed very slightly before they enter into radial flow. This drop deformation is a vital factor in the erosion process, and tends to tear rubber and elastomeric coatings free from the laminate, especially when impact occurs over a surface depression. Radial flow of a water sphere when a surface is moving at a relative velocity of 600 miles per hour is about 1,400 miles per hour at the instant of impact.

Erosion is thought to occur first at weak spots on the surface of the specimen being tested. First damage sites are either points where pressure multiplication takes place or where weak spots are located in the material. Microscopic pits act as pressure multiplying centers that can multiply the pressure by a factor of 4 or 5 or even more. A comparison has been made between the erosion process of brittle materials of low tensile strength, such as methyl methacrylate, and metal materials which have high tensile strength.[10] This was done by use of firing projectiles of steel spheres and deforming lead pellets from a .22 caliber gun. Radial cracking of the methyl methacrylate was noted for the impacts of steel spheres but not the deforming lead pellets. The impact sites on Lucite were compared, using the deforming lead pellets and water impacts obtained with the rotary arm tested at Cornell. It was determined that the mechanics of damage were identical, the only difference being of degree.

Metals which have high tensile strength also erode and fail, due to the impact of water droplets. This failure cannot be attributed to impact pressures alone. Pits on the surface of the metals act as pressure raisers of sufficient magnitude to cause erosion damage. Polished metal surfaces are more erosion resistant to water impact stress then unpolished surfaces. Even the polished surfaces, however, erode eventually, indicating that surfaces, no matter how highly polished, develop pits which then serve as pressure raisers.

Tests indicate that there are two possible types of materials which are rain erosion resistant. These are soft, very resilient substances, such as neoprene, and very hard materials such as glass and ceramics. A very resilient rubber may be depressed repeatedly by waterdrop impacts without cracking. An extremely hard substance does not crack because it does not undergo any depression at all under water impacts.

Rubber type materials however, have definite resilience. In the event that the rubber is loaded at an extremely high rate, it acts as a hard material, since it does not have a chance to recover. Very hard materials have definite application at very high speeds. This is borne out by the supersonic rain erosion test data where ceramic materials far surpass neoprene coatings in supersonic rain erosion resistance.

7-13. Cavitation Effect on Initiation of Rain Erosion

Cavitation was investigated to determine if it occurs at the impact of a drop on a solid surface. This study has special application to hard surfaces which do not depress under water blows. It was considered that cavitation might be a source for the first surface roughening which leads to pit formation and then to pressure raising possibilities.[4,6]

A 42-foot tube was used, so that droplets could be dropped onto a glass impact plane. Fastax cameras took photographs of the collisions, and an attempt was made to discern if a pressure reduction occurred in the center of the radial wash in its last stages of flow after impact. This would cause the pressure to fall below the vapor pressure of water, and cavitation might then occur in the center of the wash.

Evidence was obtained which indicates that cavitation does occur but further tests are needed to substantiate the fact and to determine its influence in the erosion process.

Schleiren photography was utilized to study the impacts of water droplets. Water saturated with argon gas was used so that bubble formation would be different from that of plain water and so one could definitely identify the small white spots noted as bubbles. Bubbles were noted in these tests, indicating the possible existence of cavitation.

The terminal velocity of the waterdrop used in all these tests was 26.9 feet per second. It is highly possible that cavitation would be more evident if droplet velocities of 880 feet per second (600 miles per hour) were investigated. This phase of the work has not been initiated as yet because of the unsuitability of equipment to accelerate droplets to these speeds.

The recent work on mechanism of rain erosion has been concentrated on the supersonic area.[11, 12, 13, 14]

7-14. Mechanism of Supersonic Rain Erosion

An investigation was initiated to determine the possibility of utilizing impacts of drops of high density materials at low velocity to simulate damage produced by waterdrops at high velocities. The problem was to determine the velocity that the heavy metal drops must have to produce the same amount of damage that would be produced by waterdrops at some specified higher velocity.

This work has been done by National Bureau of Standards and supported by Convair.

The equation developed for predicting damage resulting from a liquid drop impacting a surface is:

$$\epsilon' = C \frac{d^3 \rho^2 V_c^3}{\mu} \left(\frac{1}{S'_s} + \frac{1}{S'_t} \right) \qquad (7\text{-}2)$$

where

C = proportionality constant;

ϵ' = damage parameter;

d = drop diameter;

ρ = drop density;

V_c = velocity of impact;

μ = drop viscosity;

S'_s = shear strength of surface; and

S'_t = tensile strength of surface

Captured Projectile Tests. Tests were conducted at Convair utilizing the rotating arm for velocities of impact less than 900 feet per second while tests at higher velocities, up to 2,600 feet per second, were conducted using the "captured projectile" test apparatus.

The captured projectile test method involves the use of a smooth bore, 20-millimeter cannon, which has adapted to it, 100 feet of heavy wall tubing of similar bore diameter. The first 20 feet of tubing, after leaving the gun barrel, is perforated with a pattern of diametrically opposed holes to permit the escape of propulsive gases and to allow introduction of liquid drops in the path of the projectile. After passing through the perforated section, the projectile enters the closed tube, which is "plugged" near the discharge end. Air in the tube is compressed, decelerating the projectile to zero forward velocity, at which time the pressure buildup is sufficient to eject the plug, to release the pressure, and thereby to cause the test specimen to remain captured in the tube. Liquid drop size is accurately controlled and metered. Velocity is measured by means of an electronic timer. The drop size was determined by the size of the hole and shape of the exit surface of a removable dripper insert, as well as by the head of the high-density liquid in the container. Each particular dripper insert was calibrated by catching a known number of drops on a watch glass of oil which had previously been weighed. This allowed a check of liquid head versus drop diameter. By reweighing, the drop diameter average is ascertained. Droplets of mercury, ranging in size from 0.7 to 2.9 millimeters, were used successfully as the high-density liquid.

Tests were conducted using 1.0-, 1.5-, 1.98-, and 2.85-millimeter mercury drops on lead annealed at 400° F and furnace cooled; using 1.0-, 1.5-, 1.98-millimeter drops on 2S aluminum annealed at 800° F and furnace cooled; and using 1.0- and 1.5-millimeter drops on electrolytically pure copper annealed at 1,100° F and furnace cooled.

Figures 7-9, 7-10, and 7-11 are plots of damage depths versus velocity, and Figures 7-12, 7-13, and 7-14 show a comparison of damage diameter versus velocity. These curves indicate a difference in slope between aluminum and the lead and copper materials. Inspection of the damage marks indicated that the surface damage diameter is larger than any other damage diameter. The aluminum, however, at velocities greater than 800 feet per second, has a "ballooning" action where most of the damage occurs below the surface.

Values of C were calculated, as in Equation (7-2), using the surface damage area as equal to ϵ' and then, in an effort to make C more nearly constant, various combinations of surface damage diameter (d_c), damage depth (d_e), and damage volume (V_d), were used as damage parameters. Of all damage parameters used, $\epsilon' = d_c\, d_e$ has proven the most satisfactory. Figures 7-15 and 7-16 illustrate the use of damage diameter and of $d_c\, d_e$ for the damage parameters. There is no theoretical basis for this — it is based strictly on experimental data.

Similar tests using waterdrops approximately 2 millimeters in diameter were conducted to determine if "C" stayed within the same general range of 1×10^{-9} to 9×10^{-9}. This was established, and is shown by Figure 7-17.

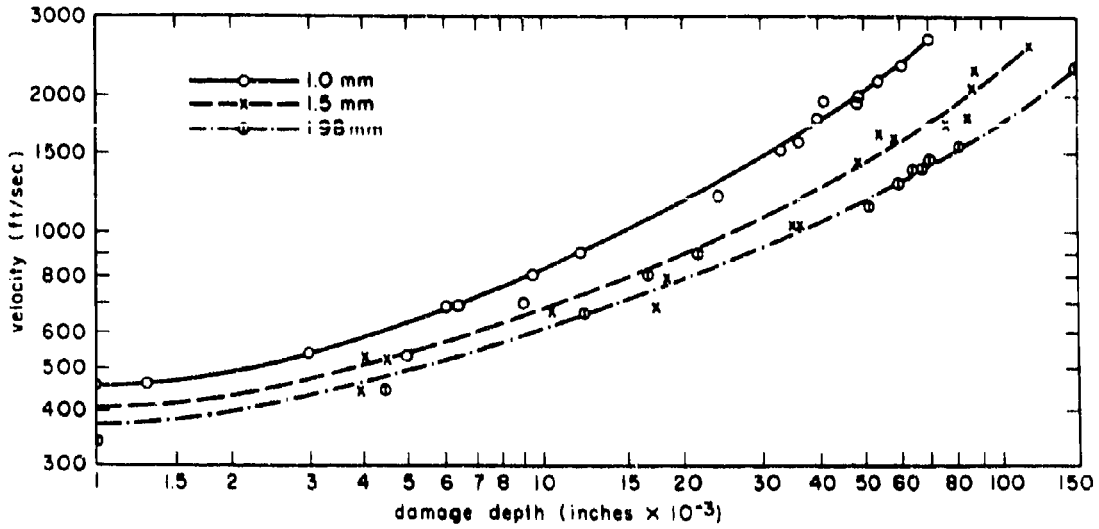


Figure 7-9. Damage Depth Versus Impact Velocity – 2S Aluminum Specimens, Mercury Drops

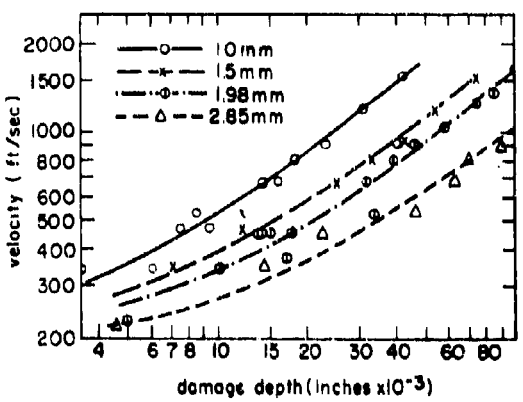


Figure 7-10. Damage Depth Versus Impact Velocity – Lead Specimen, Mercury Drops

Doctor Engel's equation was developed with the restriction that it applied to drops 2 millimeters in diameter or larger. This is substantiated but it is considered to be of value even for smaller drops.

7-15. Effect of Shock Wave on Supersonic Rain Erosion

There has been some thought that objects traveling at supersonic speeds would not be subject to rain erosion damage because the shock wave would cause a breakup of the water droplets before impact could occur.[15] A study was conducted on this aspect by National Bureau of Standards. If the leading edge is a sharp point, the shock wave is attached to it; if the leading edge is blunt, the shock wave is detached and is separated from the leading surface of the object by a zone in which air is moving ahead of the object.

The width of the zone by which the detached shock wave is separated from the object depends on the radius of curvature of the object and the velocity at which it is moving. The width of a zone of separation behind the detached shock wave that precedes a sphere 2 feet in diameter moving at 1.7 Mach is 0.276 feet. If the shock wave preceding this sphere should move into the space occupied by a relatively stationary waterdrop, the time that would elapse from the instant the shock passed the waterdrop until the waterdrop was struck by the 2-foot sphere would be 144 microseconds. This is the time during which atomization would have to occur to be of significance to the erosion problem of objects of this size moving at Mach 1.7 velocity. For objects less than 2 feet in diameter, the time would be even less.

Shock tube apparatus at the Naval Ordnance Laboratory was utilized to conduct tests on the effect of a supersonic stream of air on a stationary droplet. High speed photography was utilized to analyze the effect at time intervals starting at 10 microseconds until the waterdrop broke up. Pictures and data were obtained at Mach 1.3, 1.5, and 1.7. The results of this

program have clearly indicated that, at these speeds, the waterdrop definitely does break up, due to the influence of the shock wave. However, the time for breakup is much too great, and the solid object would impact the drop before any breakup could occur. This has been substantiated by Falcon flight tests and rocket sled tests on full scale radomes at Mach 2.6 and 2.0, respectively. It is planned to continue this investigation at higher Mach numbers, using new apparatus.

Similar conclusions were reached by Seidl of Boeing Airplane Company using high-speed photographs of the effects of the bow-wave of 60-caliber and 20-mm gun projectiles upon simulated rain drops.[19]

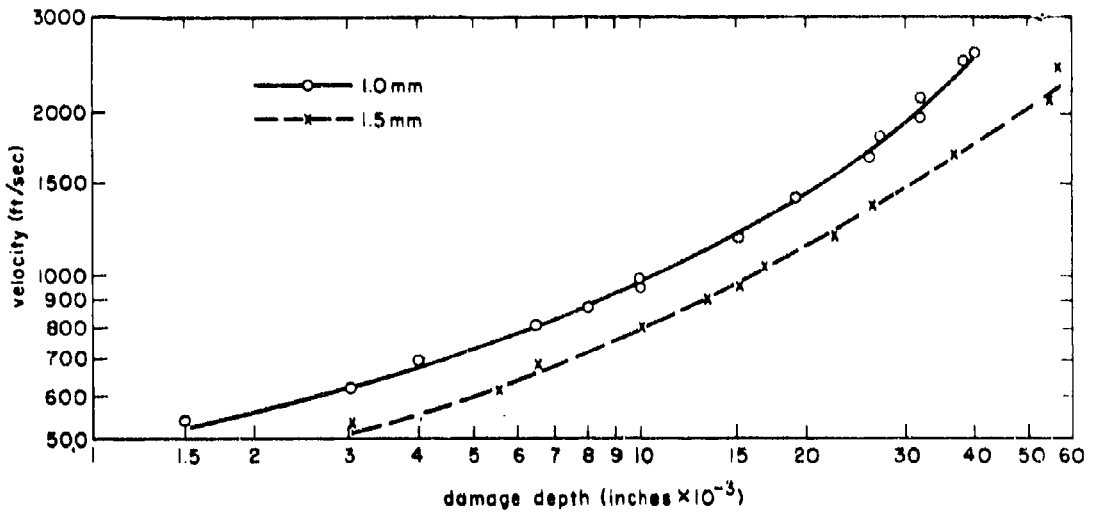


Figure 7-11. Damage Depth Versus Impact Velocity — Copper Specimens, Mercury Drops

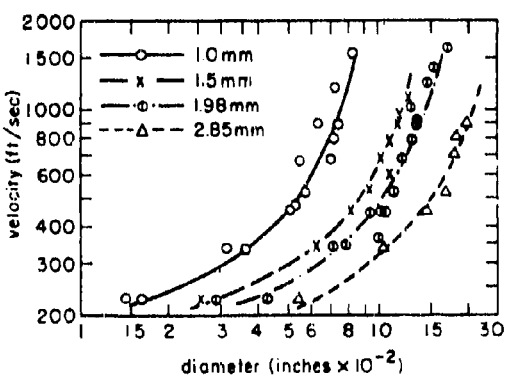


Figure 7-12. Damage Diameter Versus Impact Velocity — Lead Specimens, Mercury Drops

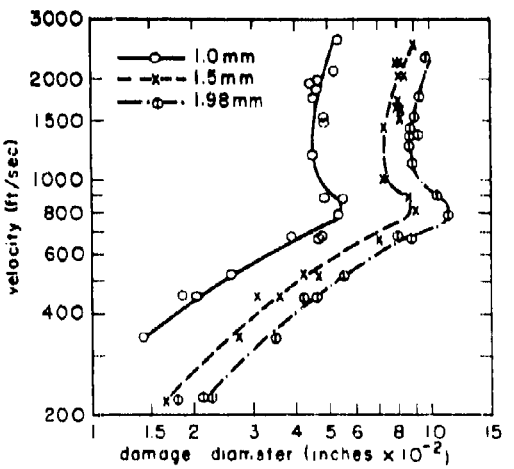


Figure 7-13. Damage Diameter Versus Impact Velocity — 2S Aluminum Specimens, Mercury Drops

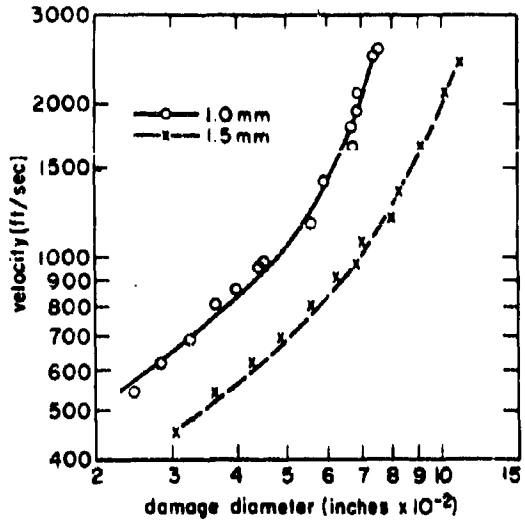


Figure 7-14. Damage Diameter Versus Impact Velocity — Copper Specimens, Mercury Drops

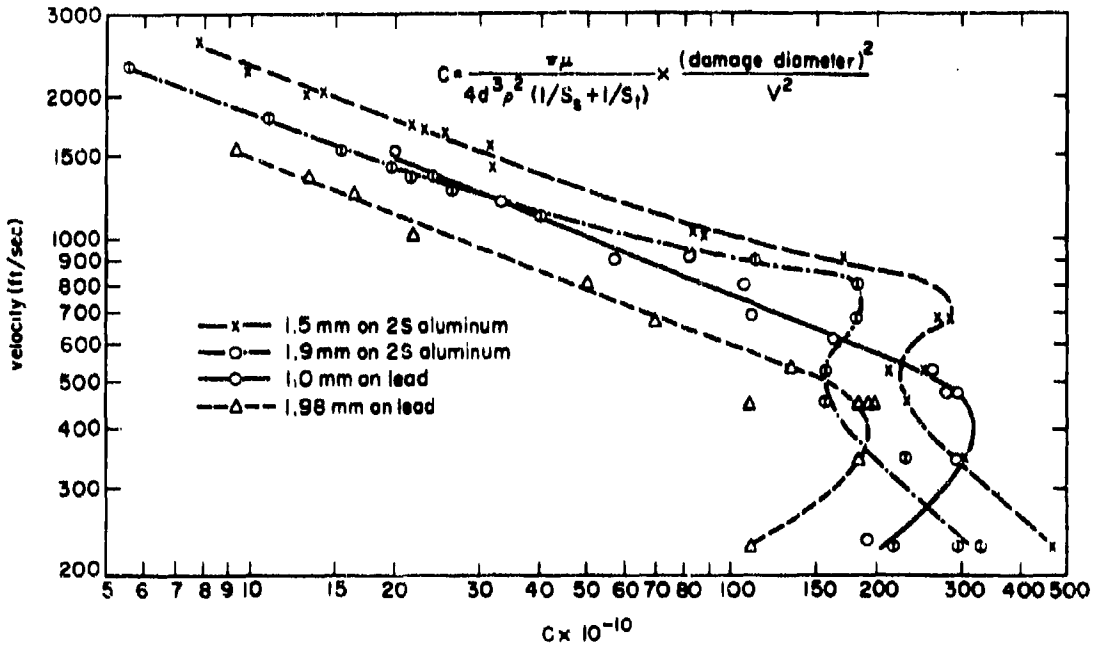


Figure 7-15. Relation Between "C" of Equation (7-2) and Impact Velocity — 2S Aluminum and Lead, Mercury Drops

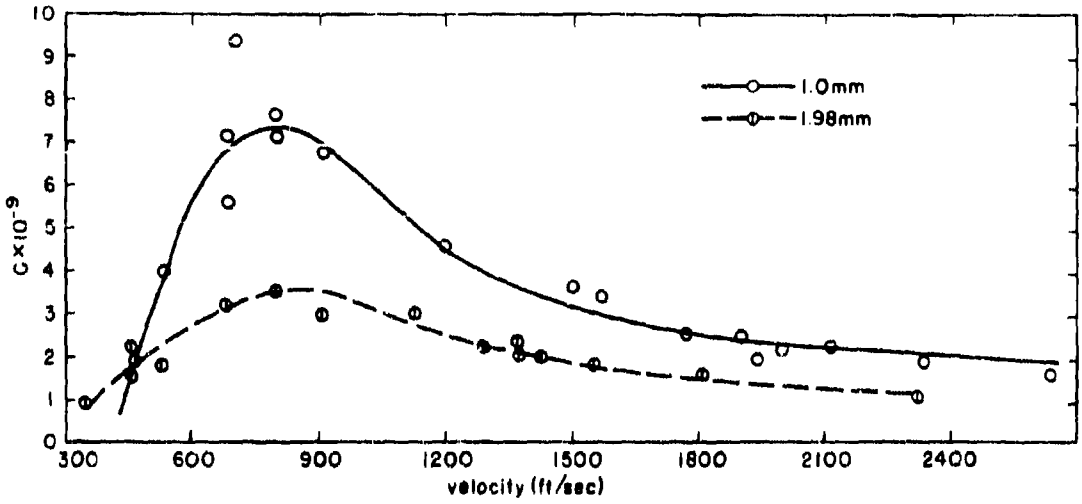


Figure 7-16. Relation Between "C" and Impact Velocity, Based on Product of Damage Depth and Damage Diameter

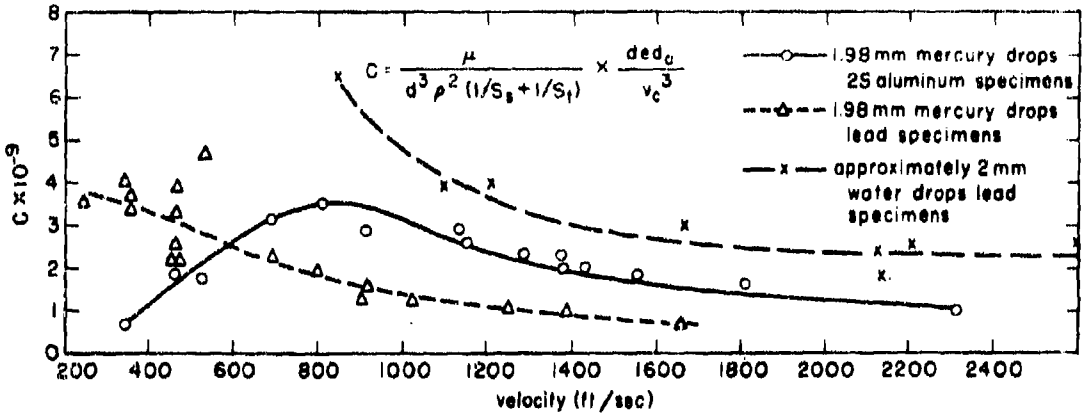


Figure 7-17. "C" Versus Velocity, for Waterdrops 2 Millimeters in Diameter and Mercury Drops 1.98 Millimeters in Diameter

SECTION E. SUPERSONIC RAIN EROSION

7-16. Test Methods

Convair was issued an Air Force contract to develop a rain erosion test method which would evaluate plastic materials at supersonic speeds.[16]

The three basic methods explored were (1) a ballistic method employing a projectile as a supersonic test vehicle; (2) a water droplet acceleration method; and (3) captive flight testing, utilizing a rocket sled and research track.

Of the three methods of investigation, the ballistics type was the most completely developed. With the installation of simulated rainfall, actual rain erosion tests were started, using a recoverable modified 20-millimeter projectile. Five major problems were involved.

These were (1) external ballistics of the projectile, (2) timing fuse to effect separation, (3) separation charge, (4) specimen recovery parachutes, and (5) rainfall simulation.

Due to the high cost of operation, the rocket sled phase of the investigation was discontinued for materials evaluation, but is feasible and is continuing for final proof testing of critical full-scale models. The water droplet acceleration method, which is the most desirable due to controlled test conditions and ease of operation in the laboratory, and the ballistics test method were therefore investigated in detail by Convair.

The water acceleration study dealt with the acceleration of water droplets up to Mach 2 and the inpingement of these droplets on a stationary plastic specimen. Attempts to accelerate droplets to Mach 2 by aerodynamic drag were unsuccessful, since a breakup into fine mist occurred instantaneously as the edge of the droplet touched the Mach 2 airstream. The droplet was entirely disintegrated before it could penetrate the airstream. Attempts were made to inject the liquid at a velocity equal to the air velocity so that this breakup would not occur. A Bausch diesel fuel injector was adjusted to eject liquid under pressure through air orifices into a nearly complete vacuum to break up the stream into 2-millimeter droplets. Various atmospheres, from 0.20 to 0.40 inch of mercury absolute, were utilized and the shadowgraphs indicated some breakup of the water stream but no droplets were discernible. The aerodynamic drag of a 2-millimeter droplet size was too great, and water droplets of this size were impossible to obtain; the water droplet acceleration method for obtaining supersonic rain erosion data was therefore discontinued.[7] This left the bulk of the work on supersonic rain erosion to the ballistics test method, which was noticeably more successful. Most of the data has been obtained utilizing a 20-millimeter cannon firing a plastic nose at speeds up to Mach 2.6 through controlled simulated rainfall of 1.9-millimeter droplet size. The range utilized was a 500-foot path at the United States Navy's Camp Elliot Annex.

7-17. 20-mm Ballistics Test Method

The Camp Elliot ballistic range is equipped with an engine-driven centrifugal pump capable of supplying 6,000 gallons per hour at a head of 90 feet, delivers water from a portable 200-gallon water tank to the midpoint of the 500-foot exposure range pipe system. This system, supported on steel posts, includes 50 equally spaced No. 1/4 U-8050 Vee Jet spray nozzles elevated 45° above horizontal and flow-adjusted by means of individual stopcocks. Since the spray from each nozzle covers slightly more than 100 feet parallel to the pipe, continuous exposure is accomplished, except for a short gap at the midpoint of the range. The cannon is mounted to fire through an area where the average droplet diameter is 1.9 millimeters and the rain intensity is approximately 2 inches per hour. Results from each firing closely correspond to flight through 1,000 feet of 1.0-inch per hour rainfall.[13]

The specimen is carried by a 20-millimeter TP M99 round modified to contain a fuse and compartment for the parachute and separation charge. Upon firing the shell, the tracer is ignited. It burns for a predetermined time interval sufficient to carry the projectile through the rain path and over the drop area. At this point the tracer or fuse, having burned through to a separation charge, causes the latter to ignite and expel the nose specimen which floats to the ground on a small parachute.

Base and Transfer Hole. Fuse material near the metal wall of the fuse hole tends to chill and burn less readily. With a 59° (drill bit angle) fuse hole base, the fuse frequently stops burning before the black powder in the transfer hole is ignited, causing separation failure. To minimize this difficulty the base of the fuse hole is made flat, the transfer hole diameter is increased, and the transfer hole length is held to a minimum. The maximum transfer hole diameter is a function of the ability of the fuse material to resist being blown through the transfer hole by propelling pressures in the cannon. With a 19/64-inch fuse diameter and operation at Mach 2, the optimum transfer hole diameter for tracer fuses is approximately 0.09 inch. Close tolerances between the specimen adapter and the projectile case prevent accidental opening of the parachute compartment during loading operations.

Fuse. The major problem of the ballistics method was to obtain a reliable fuse. On bench tests and low speed tests nearly all types of fuses tested worked successfully. At high speed, however, only a few worked, and none seemed very reliable. The 20-millimeter igniter and tracer pellets held the most promise, although the percentage of separations was just slightly better than 50 percent. The tracer material was hard to ignite and the igniter material did not seem hot enough to ignite the separation charge; therefore, several mixtures were tried. The most reliable fuse consisted of four parts of tracer and one part of igniter material. The fuse consisted of approximately 0.25 grams of the 4/1 tracer-igniter mix and

one pellet of igniter. The pellet of igniter was placed on top of the mix and pressed at 60,000 pounds per square inch. This fuse approached 100 percent reliability.

Separation Charge. The separation charge consists of 0.25 grams of black powder meal and 0.85 grams of DuPont fffg grade powder. The powder meal is tamped into the transfer hole to assure ignition. By this method, separation has occurred every time the fuse has ignited.

Five disks of Velumoid gasket material are fastened together to serve as a wad to hold the separation charge in place. This wad also serves as a piston to push the parachute and specimen out of the projectile while preventing the burning powder from igniting the parachute. The parachute is wrapped in a metal foil liner to protect the chute from burns. This also reduces the load on the parachute by delaying opening.

Parachute and Specimen Adapter. The canopy type parachute designed by Convair and made by the Prevost F. Smith Parachute Co. is being used. The canopies are made of 2-ounce, cross-ribbed nylon parachute cloth, and have eight 100-pound test shroud lines, each composed of four 3-cord nylon treads. This parachute with a 4.5-gram specimen, has a terminal velocity less than 10 feet per second. This type of parachute has been fired 4 or 5 times before replacement was necessary. The type of specimen adapter now being used is shown in Figure 7-18.

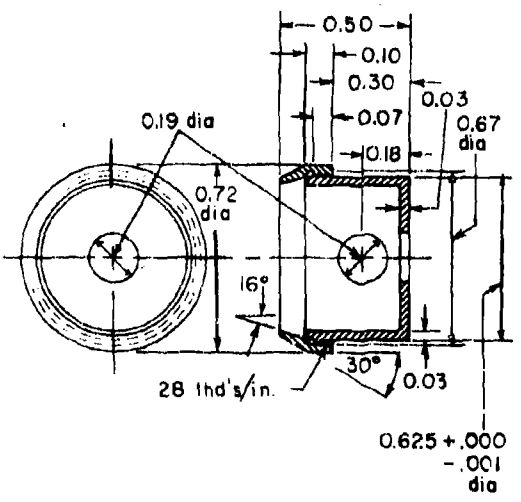


Figure 7-18. Specimen Adapter, Scale 4:1

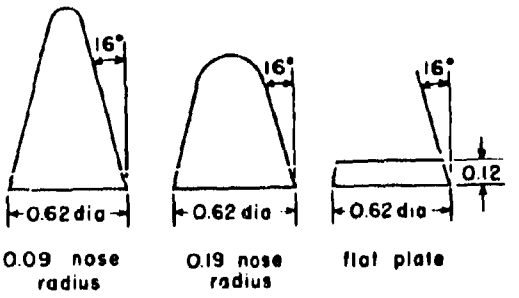


Figure 7-19. Test Specimen Configurations

Velocity Measurement. The velocity of the specimens was carefully checked and found to be 2,260 feet per second from 10 to 30 feet in front of the gun. At 480 to 500 feet in front of the gun the velocity was found to be 1,870 feet per second. The speed was measured by a Berkely time interval counter. The targets were set 20 feet apart. The projectile started the timer by shorting two sheets of metal foil at the first target and stopped the timer by shorting two sheets of metal foil which made up the second target. The elapsed time was used to determine the average speed.[13]

Test and Results. The standard test used for evaluating plastic materials has been at Mach 2 over a 500-foot path of simulated rainfall. The rainfall droplet size is held to 1.9 millimeters. Materials are rated by distance traveled through 1-inch per hour rainfall, at Mach 2. It has been determined by Convair that 2-inch per hour rainfall for 500 feet will result in approximately the same number of impacts as 1-inch per hour for 1,000 feet. Therefore, all results specified will be in terms of distance traveled in 1-inch per hour simulated rainfall with a 1.9-millimeter droplet size at Mach 2. This can also be related to time, since it takes approximately 1/4 second to traverse 500 feet at Mach 2.

The standard 20-millimeter specimen has a 0.19-inch nose radius, as indicated by Figure 7-19. Flat plate specimen and 0.09-inch ceramic specimen configurations are also illustrated.

Test results obtained to date indicate that the approved neoprene coatings, which were the most satisfactory at subsonic speeds, do not provide sufficient rain erosion protection for reinforced plastics at supersonic speeds. They last for 2,000 feet through a 1-inch per hour rainfall at Mach 2 before they are eroded and completely torn off. Typical polyester rein-

forced plastics last for 1,000 feet in 1-inch per hour rainfall with no protective coating. Bare epoxy type specimens, such as Epon 1001, will last for 3,000 to 4,000 feet before severe damage occurs, and even then the damage is not as severe as caused to the bare polyester after just one firing. This is a further substantiation of the data being obtained on polyester versus epoxy resin reinforced plastics at subsonic speeds by Cornell.[13]

The most erosion resistant material evaluated thus far has been a ceramic made by the Raytheon Corporation. The 97 percent Al_2O_3 (alumina) specimen was a 30° cone with a 0.09-inch radius. In 37,500 feet of travel at Mach 2 in a 1-inch per hour rainfall, the specimen has exhibited no erosion. This also substantiates the Cornell work, where ceramics and cerams have been outstanding.

Based on the poor supersonic rain erosion properties of the plastic materials themselves, variations in configuration were attempted. This consisted of short, pointed, metal-tipped conical specimens utilizing approved neoprene coatings along the sides of the specimen. A 30° cone (included angle) with Goodyear 23-56 along the sides had the coating penetrated in 43,500 to 66,000 feet of travel. These figures are for the coating system applied to 24ST aluminum specimens. With a polyester laminate base material and metal cap, the maximum distance obtained in 30° specimens was 18,000 feet. At this time the coating was deeply abraded but not penetrated. Failure of the laminate at the parachute attachment prohibited further testing.[14]

Effect of Cone Angle. One of the studies undertaken was to determine the effect of changing the cone angle with respect to the erosion rate. In changing from a 30° cone to a 60° cone, the erosion rate was approximately doubled. This can be seen in Figure 7-20. For a 30° 24ST aluminum cone with a Goodyear 23-56 coating, the specimen traveled through an equivalent distance through 1-inch per hour rainfall of from 43,500 to 66,000 feet before the coating was penetrated. For the 60° cone with similar coating, the distance was reduced from 24,000 to 27,000 feet before penetration of the coating. The 90° cone traveled from 12,000 to 15,000 feet before penetration.[14]

Effect of Velocity. A similar study was undertaken to determine the erosion rate at various specimen velocities. Flat plate disks, 1/8-inch thick, of Epon 1001 reinforced laminate were used as test specimens. To erode through 80 percent of the first layer of glass fiber it was

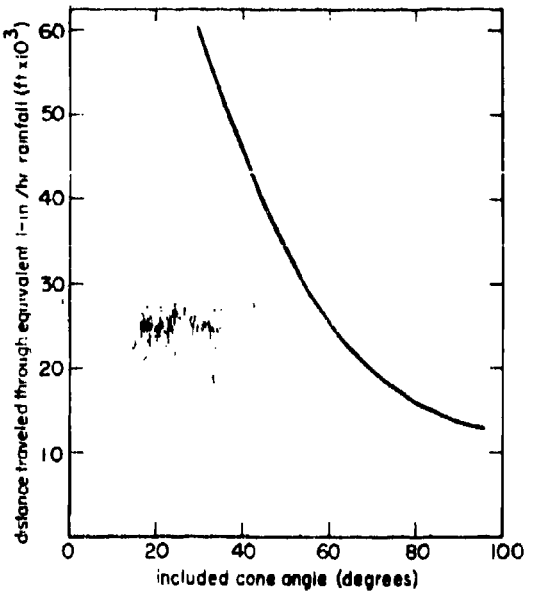


Figure 7-20. Included Cone Angle Versus Distance Through Equivalent 1-inch Per Hour Rainfall for Penetration

necessary for the specimens to travel through over 1,500 feet at 2,800 feet per second (Mach 2.5), 6,000 feet at 2,240 feet per second (Mach 2), and 12,000 feet at 1,700 feet per second (Mach 1.5). It appears that in increasing the speed by 1/2 Mach number the erosion rate was approximately doubled. Figure 7-21 is a curve of these results.

57-Millimeter Tests. One of the most severe drawbacks to the 20-millimeter test procedure is the small size of the test specimens. This has caused difficulty in fabricating and coating the specimens properly and also in evaluating the rain erosion damage incurred in the test firings.

Therefore, a 57-millimeter cannon has been obtained and installed at the Camp Elliot test range. The recovery method is basically the same. Stronger parachutes have been designed and evaluated. Preliminary firings have been conducted and recovery techniques and fusing problems solved.

This cannon is presently ready for use. A program will be initiated immediately to evaluate typical plastic materials such as polyester, phenolic, epoxy resin-glass laminates. These will be evaluated with and without coatings and with and without metal caps. A standard 57-millimeter test specimen has been designed; it

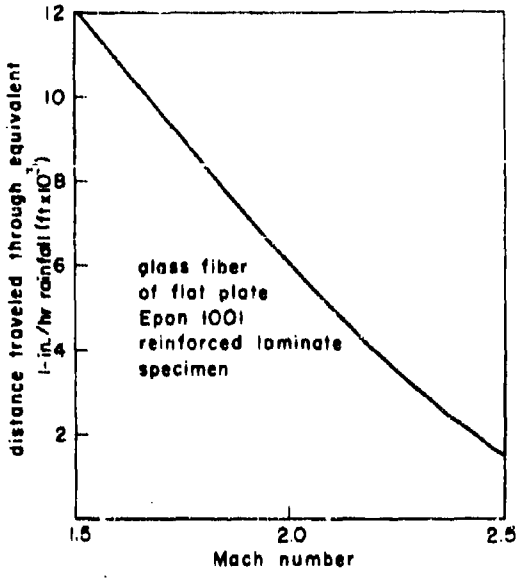


Figure 7-21. Mach Number Versus Distance Traveled Through Equivalent 1-inch Per Hour Rainfall for Erosion Through 80 Percent of First Layer

is illustrated in Figure 7-22. Ceramic and ceram 57-millimeter specimens will be fabricated, and will be evaluated at supersonic speeds. These will include all available ceramics and new ceramic materials developed for superior rain erosion resistance properties.

The rain erosion test range has been improved and expanded to 1,500 feet, which will supply 6-inch per hour rainfall. This will make one firing through this range equivalent to 9,000 feet of travel through 1-inch per hour rainfall or the equivalent of 4 1/2 seconds of exposure at Mach 2 through a 1-inch per hour rainfall. The rainfall issues from spray nozzles mounted 15 feet above ground level and directly over the projectile path. The width of the spray will be enough to prevent the wind from shifting the entire spray out of the trajectory of the projectile. Supply water will be pumped from a water main in Murphy Canyon to the storage tanks at the range. This will alleviate the water shortage problem prevalent in the 500-foot facility.

Rainfall Intensity. An important aspect of high-speed rain erosion studies is the simulation of the parameters of the actual rainfall. The most important parameter is the rain intensity, which is simulated by using the parameter water content per unit volume in place of inches per hour rainfall. The rain intensity is defined in greater detail by specifying size and percentage distribution of various drop diameters. In conducting the water content survey, two separate analyses are required, drop size distribution and total water content. Waterdrops are captured in a pan of oil and the total drop number per unit area is determined. The oil pan utilizes 1/8 inch of motor oil and over 1/8 inch of silicone oil. Actual-size pictures indicate the drop count and size determination by use of a comparator. Checks can be made by catching 5 to 10 drops in a small dish of oil, which are estimated for size visually and then accurately weighed in an analytical balance. The resultant average diameter has checked out extremely closely for both methods.[14]

The total amount of free water per cubic volume is determined by means of a collection bottle attached to the end of a rotating arm. The arm is rotated by an electric motor which also actuates a revolution counter. The apparatus is set up in the rain area and is rotated for approximately one minute. The collection bottle is removed and weighed. Then, knowing the area traversed by the sampling container, the number of revolutions, the frontal or capture area of the sampler, and the net weight of water, it is possible to determine the volumetric water content. From this information the number of drop impacts can be determined along with the drop sizes.

7-18. Rocket Sled Test Method

The use of a rocket sled at Convair to propel a full-scale radome through simulated rainfall was planned to evaluate radomes and radome

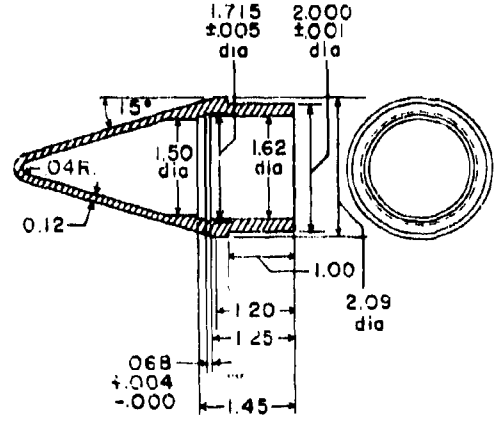


Figure 7-22. 57-Millimeter Rain Erosion Test Specimen

materials. The object is to determine that the results obtained by the ballistic method on small-scale projectiles are applicable to full-scale flight, and to accumulate supersonic rain erosion data on the full-scale radome.[14]

Sled Details. The Northrop Aircraft Company built a rocket sled to carry a full-scale Bomarc and a multiple arrangement of Falcon radomes at speeds of Mach 2 through simulated rainfall. This test vehicle was designed to operate on the 10,000 foot Edwards Air Force Base high-speed experimental track. A sprinkler system was installed to supply a simulated rainfall between 3,800 feet and 5,000 feet along the track. The rainfall rate at the radome center line was 4.3 inches per hour; all drops were 1.9 millimeter in diameter.

The completed rocket sled was designed to attain the maximum velocity of Mach 2.0, using V4 rockets (solid propellant) with a rated thrust of 11,000 pounds each. A pusher sled mounting five identical rockets was available for initial acceleration. The rocket sled weight was 1,191 pounds without the rockets, but with the instrumentation and the Bomarc radome.

The first firing of the sled carrying the Bomarc radome attained a maximum velocity of 1,022 feet per second through the rainfall and was a successful checkout run.

The second run, at a speed of Mach 1.2, resulted in the sled flying off the track at station 4200 at a velocity of 1,490 feet per second, due to failure of the slippers, which were made of 75ST aluminum.

Convair designed and fabricated the second rocket sled and pusher combination. The sled was designed for light-weight (300 pounds) presentation of minimum drag area, and minimum horizontal plate area at track level.

A group of twelve rockets of 11,000-pound thrust, which burn for only 2.2 seconds, are necessary for the acceleration of the Bomarc radome to Mach 2.0. Each rocket contains 142 pounds of solid propellant. Seven of the rockets are on the sled and five are on a pusher sled. The pusher sled accelerates the test unit to a speed of more than 620 miles per hour on the first 950 feet of track. The rockets on the sled are fired automatically at this point and the sled accelerates away from the pusher with a force of 25 G.

The firing device for the sled is a bronze screen between the track, which, when cut by two knives mounted on the sled, shoots a 600-volt current into the igniters on the bottles. The four slippers are made of steel, lined with stainless steel inserts which ride on top and underneath the rail flange. They are red hot during the runs, and reach temperatures of 1,500° F. The inserts usually last four runs. Telemetering equipment is built into 37 inches of the sled frame, which is made up of three curbed and welded 5 1/2-inch diameter steel tubes, with a wall thickness of about 3/16 inch. Accelerometers are used to measure vertical, lateral, and longitudinal acceleration throughout the run. The Bendix accelerometers send the information to a recording center.

Sled speed is measured by a magnet on the frame passing over coils located at intervals along the track. Recording oscillographs measure the speed of the sled by registering time intervals between 50-foot lengths of track to within 0.0001 second.

A standard water trough at the end of the rack (water brake) is used to decelerate the sled. A water scoop is built below the sled frame. The frame is curved back over the twin rear slippers, channeling water up out of the trough, turning it through 160°, then discharging it out both sides at the rear. The sled is thus stopped by momentum transfer. The water trough is 2,000 feet long and the track slopes down to permit the scoop to enter the water gradually.

Test Runs. Three successful runs were conducted utilizing this sled carrying the Bomarc radome through the simulated rainfall. They were at average speeds of Mach 1.25, 1.35, and 1.67 through the 1,200-foot simulated rainfall path. The Bomarc radome had a metal nose cap with an epoxide Epon 1001 plug in the center of the nose and was uncoated along the sides. After the Mach 1.67 run, severe delamination was noted, and on the front portion of the radome just to the rear of the metal cap the epoxide plug had become seriously delaminated. The sides of the radome, while exhibiting evidence of droplet impacts, were not seriously eroded.

A successful Mach 2 rocket sled run was made on 25 April 1956, at Edwards Air Force Base, carrying a full-scale Bomarc radome. The sled achieved a velocity of Mach 2.023 (1,560 miles per hour) which is a world's speed record for recoverable sleds. Up to this time, the maximum recoverable sled velocities which had been attained were 1,280 miles per hour.

The sled was fired through the 1,200 feet of simulated rainfall on the 10,000-foot high-speed experimental track. The water range had a

water content of 0.25 gram per cubic foot, which is analagous to a natural rainfall rate of 8 inches per hour with a 1.9 millimeter droplet size. This rainfall path is equivalent to 16,800 feet of 1-inch per hour rainfall.

Twelve rockets developing a thrust of 132,000 pounds were utilized to accelerate the 800-pound sled to Mach 2. A 2,000-foot brake, which starts at station 8000, was used to decelerate the sled, which came to a halt 200 feet from the end of the track.

The Bomarc radome is made with Vibrin 135 heat-resistant polyester resin, and is approximately 0.3 inch thick. A metal cap which can hold a small plug was located on the nose end of the radome. The plug was an Epon 1001 resin-glass cylindrical plug that had been exposed to the three previous checkout runs at Mach 1.25, 1.35, and 1.67 through simulated rainfall. The entire Bomarc radome, from the metal cap back, was coated with MIL-C-7439B approved Goodyear 23-56 rain erosion coating system.

Test Results. Severe rain erosion damage resulted after this one-second run through the simulated rainfall. The coating was peeled back and the laminate delaminated through four to five plies at least one foot back on the radome from the metal cap. The metal cap also showed indentions from the impact of the rain drops, and the Epon 1001 plug was seriously eroded.

The sides of the radome back from the eroded area were not eroded through the coating, although the droplet impact marks could easily be seen.

It is planned to fire this radome at least twice more to ascertain whether damage will occur to the sides of the radome on extended exposure to rain at Mach 2. A metal cap will be fabricated to replace the eroded portion of the radome which will be cut off.

The results obtained to date indicate that the Bomarc radome, after a 1-second exposure to 8-inches per hour rainfall, will suffer severe rain erosion damage with the use of the present metal cap and radome design. This indicates a possible problem area for the present Bomarc radome configuration on flights through rain.

Immediately after completion of the Bomarc testing the Falcon program will be initiated. Hughes, Convair and Edwards Air Force Base are presently coordinating on the design of the Falcon radome and specimen adapter for these tests.

7-19. Army Ordnance 57-Millimeter Program

A program at Edgewood Arsenal under Army Ordnance supervision was sponsored by the Air Force to obtain further data on the phenomena of rain erosion at supersonic speeds through rainfall.[17]

Test Details. Shells with a solid plastic nose section, as shown in figure 7-23, were fired vertically at initial velocities of Mach 2.0 and 2.75 through natural rainfall. The shells, due to a weighted base, return to earth tail first and are buried in the ground with relatively no damage to the plastic nose section. After recovery, the materials are examined for erosion damage.

The plastics were fabricated by Cornell Aeronautical Laboratory and have a 1/4-inch radius. Specimens were molded of glass-reinforced polyester resin, reinforced heat resistant resins, and a reinforced alkyd molding compound. Part of the specimens were dip coated with approved neoprene rain erosion coatings meeting the requirements of MIL-C-7439B. Heat resistant lactoprene type coatings developed by Goodyear Tire and Rubber Company were also evaluated.

The 57-millimeter gun at Edgewood Arsenal was standardized by firing a series of projectiles, using aluminum ogive noses of the approximate weight and design as the test specimens. A potter's type counter chronograph was used to time the projectiles and, by experiment, the amount of propellant required to obtain the desired velocities was determined. Approximately 26 ounces of M-1 propellant are needed to reach a muzzle velocity of Mach 2.0 and 38 ounces for Mach 2.75. Based on computations, the velocity of the specimens fired at an initial value of Mach 2.0 drops off to 1.2 at 6,500 feet. Similarly, the velocity drops from an initial Mach 2.75 to 1.82.

The charged shell and projectile are loaded into a 57-millimeter gun designed especially for these tests and fired nearly vertically (85 to 90^{0} depending upon wind direction and velocity). The projectile rises 25,000 feet and requires approximately 80 seconds for a complete trajectory at Mach 2.0 and 93 to 95 seconds at Mach 2.75. The projectile falls tail first at close to 1,100 feet per second and ordinarily strikes the earth in a 1,200-foot square field marked in squares, about 400 feet from the gun station. Men in three towers spot the impact by sight and sound and then record the 100-foot square regions in which the projectiles can be located.

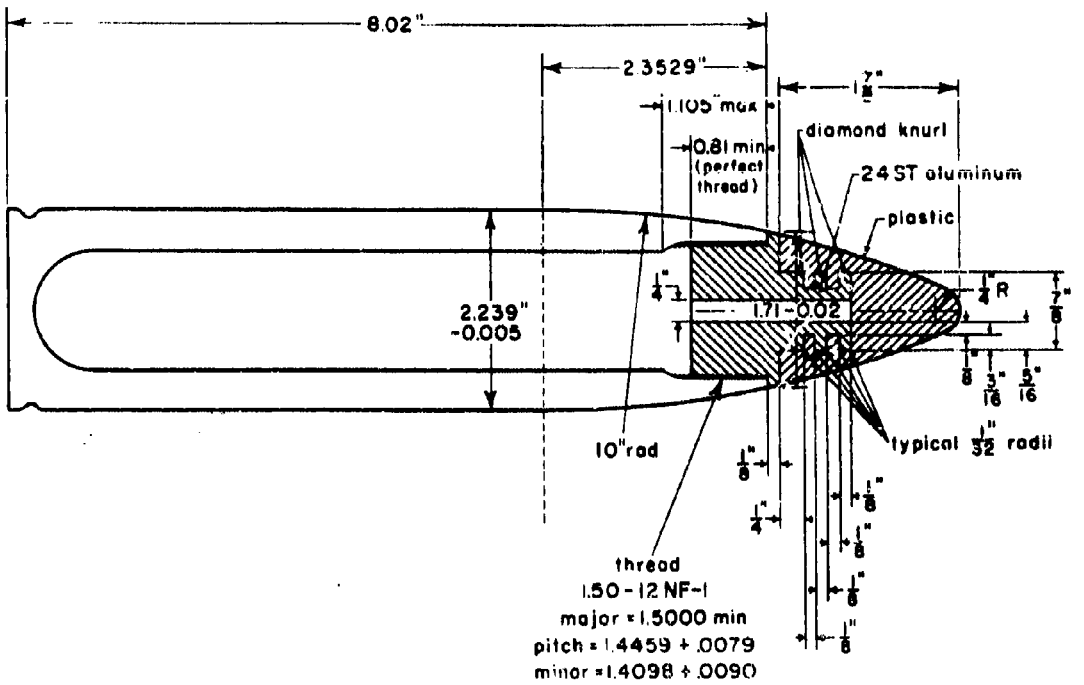


Figure 7-23. Cross Section of Shell and Plastic Ogive

The amount of rainfall during the test is measured by volume and then converted to inches per hour. An 8-inch diameter glass funnel is held for 1 minute in the vicinity of the gun during each firing. The water flows into a graduated cylinder and the volume figure is converted into inches per hour.

A standard rain gage is also used when the tests last for extended periods. This is in addition to the volumetric method. This gage consists of an 8-inch diameter metal funnel which necks down to a tube approximately 3 inches in diameter, and about 2 feet long. A rule is inserted into the tube after a specified period and the water depth read off a calibrated scale.

For this program, the height of the rain is assumed to extend to the top of the clouds. The altitude of the clouds is computed by the Friendship International Airport at Baltimore with a quadrant which measures the angle to the top of a beam of light. The cloud height determines the length of the rain course and is used to determine average velocities and time of flight through rain.

The U. S. Department of Commerce pamphlet called "Climatological Data" gives a day-by-day account of the amount of precipitation at a number of locations in the Edgewood Arsenal vicinity. During the summer months of 1953, rain occurred approximately 6 days per month with an average of 0.5 inch for each day. In the winter months, rain also occurred 6 days per month but with an average of 0.6 inch per day. One of the major inadequacies of this type of test is that the program is dependent upon natural rainfall; also, the rain conditions are never uniform over an area and naturally vary from day to day. However, extremely useful data have been obtained from this program, which basically substantiates the Convair supersonic rain erosion test results obtained by a controlled uniform simulated rainfall.

Test Results. Bare and coated reinforced polyester plastic specimens fabricated from 181 Volan A glass cloth, with Selectron 5003 resin, were evaluated against 181 Volan A glass cloth with heat resistant Vibrin X-1068 resins. The approved neoprene coatings (Goodyear 23-56 and Gates N-79) were utilized. Also, 181 Volan A fabric, impregnated with Vibrin 135 and coated with Goodyear 23-56, and Goodyear Lactoprene R-12x4-239 materials were evaluated. Plaskon 440A reinforced alkyd molding compound was also evaluated.

The results obtained indicated that:

a. The coated and uncoated glass reinforced plastic laminates erode in rain at Mach 2.0 and 2.75 after just one firing for rain exposures of 2 and 1.5 seconds, respectively.

b. The uncoated Selectron 5003 laminate specimens have slightly better rain erosion resistance at the supersonic velocities of Mach 2.0 and Mach 2.75 than the uncoated, heat-cured Vibrin X-1068 laminate specimens. The erosion of both laminates is greater at Mach 2.75 than 2.0.

c. The rain erosion resistance of neoprene coatings of Goodyear 23-56 and Gates N-79 are very much alike at supersonic speeds.

d. In these tests, the rain erosion of 10-mil coatings of Goodyear 23-56 and Gates N-79 neoprene is negligible after 2 seconds at Mach 2.0 in light rainfall. After 4 seconds, however, the coatings show increased pitting on the nose.

e. When the velocity is increased to Mach 2.75 in 0.1-inch per hour rainfall the 10-mil neoprene coatings fail almost completely after 1 1/2 seconds. The air-dried Goodyear 23-56 coating was covered with small erosion pits on the sides of the ogive after exposure to rain at Mach 2.7.

f. Goodyear 23-56 and Gates N-79, applied over the Vibrin X-1068 laminate specimens and baked for 10 minutes at 375° F, eroded at a slightly greater rate at supersonic speeds than the same coatings over Selectron 5003 laminates that have not been baked.

g. Thicker coatings of approved neoprene resist erosion better at supersonic speeds than 10-mil coatings. The 10-mil coatings pitted heavily or eroded off the glass laminate specimens after 1 1/2 seconds, whereas the 20- and 30-mil coatings showed only moderate pitting after 2 1/2 seconds at Mach 2.75. These tests were conducted through an average rainfall of 0.15-inch per hour and through a 6,500-foot rain course.

h. The Goodyear Lactoprene coating R-12 x 4-239 eroded much faster than the Goodyear 23-56 and Gates N-79 neoprene coatings. The Lactoprene was pitted and the coating eroded through the nose at Mach 2, whereas the 10-mil coating neoprene materials showed only slight traces of erosion at this velocity. At Mach 2.75 both Lactoprene and neoprene eroded badly.

These results correlate closely with the Convair, supersonic rain erosion data and also with conclusions reached in the subsonic investigation at Cornell.

This program is still in progress. Further data should be available in the near future.

7-20. Missile Radome Flight Test Program

This program was initiated by the Hughes Aircraft Company to investigate the effect of rain on missiles on supersonic flights through rainfall, utilizing full-scale radomes.[18]

Test Details. The test vehicle utilized on this program was developed by the Lockheed Aircraft Corporation. It is capable of recovering the radome intact and allows for refiring if necessary.

The testing was originally done at Holloman Air Development Center, but was transferred to Eglin Air Force Base, where the bulk of the rain erosion testing was accomplished, because it rains more often in Florida. Range facilities at Eglin are satisfactory.

The flight time of the missile is adjusted for a trajectory which will land the nose section in an area where it can be recovered easily. After the necessary flight time has been obtained (usually 11 seconds), a second motor is blown off and the missile tumbles for 3 seconds, at which time the parachute canister is blown off and the chute opens. The parachute spikes are ejected after another 3 seconds and the missile is floated to the ground, where the spikes impinge. The spikes are in the rear of the missile and the nose section lands face up.

The maximum speed capability of this test procedure is at present Mach 2.9 with a one-stage vehicle using a Deacon rocket motor.

The rain intensity at the time of firing is measured by using tipping-bucket rain gages located along the flight path. These are used at the Eglin test site and are connected to a recorder at the launch site so that rainfall data throughout the flight path will be continuously available. These data are used in determining the time for initiating the firing, the time in rain for each firing, and the average rainfall encountered in flight.

All test results were obtained on ground-launched test missiles launched at a 25° angle into a rainstorm.

Test Flights. The first flight was made in July 1954; the radome evaluated was hemispherical in shape constructed of 0.030-inch thick phenolic

(CTL-91LD) laminate backed with a thermosetting tool plastic. It was launched into a very heavy rain of approximately 1.5 inches per hour. The radome was eroded through and stripped from the backing; about one-third of the tool plastic was also eroded. The average velocity of the test missile for the 12-second flight was Mach 1.6 and the maximum speed attained was Mach 2.6.

A plastic radome was fabricated, utilizing a Diall 795B diallyl phthalate molding compound filled with Orlon fibers and loaded with titanium dioxide. It had a metal tip and was half coated with Gates N-79 approved neoprene coating. The other half was uncoated. The radome was ogival in shape and had a wall thickness of approximately 1/4 inch (half wave length). It was fired into an 0.1-inch per hour rainfall and successfully recovered. It attained a maximum velocity of Mach 2.6. This radome successfully withstood flight in rain, and there was little damage to the plastic, although the coated half peeled considerably. The metal cap, ogival in shape, utilized in this radome construction is the same type as that used on the metal-capped, conical-shaped specimens, which proved the most rain erosion resistant type evaluated in the ballistics test.

Subsequent tests utilizing this method have evaluated the Diall molding compounds with and without metal caps. When fired into light rainfall, these radomes are not seriously damaged even with the metal tips for the short time duration of approximately 10 seconds which is involved. Mycalex type material, which has been evaluated at subsonic speed and found to be unsatisfactory, was also seriously eroded in the supersonic flight test program. Complete data on these tests are not available at the present time but should be available in the near future.

SECTION F. GENERAL SUMMARY

Paragraphs 7-21 and 7-22 summarize the present approach to subsonic and supersonic rain problems.

7-21. Subsonic Rain Erosion

1. The approved coatings being applied to aircraft exterior plastic parts are relatively satisfactory in service at subsonic speeds. They provide adequate protection when properly applied in proper thickness to a structurally sound radome. New coating materials with promise, such as polyurethanes, will continue to be evaluated as possible equivalent or superior coating systems.

2. The use of rain erosion coatings over epoxy type laminates may provide increased rain erosion exposure capabilities, since epoxys have exhibited rain erosion properties much superior to polyesters. The support properties of the laminate must be adequate to insure proper coating performance.

3. The neoprene coatings have unsatisfactory thermal reflection properties. A white rain erosion coating is being developed and results are anticipated in the near future.

7-22. Supersonic Rain Erosion

1. The supersonic rain erosion problem is much more acute then the subsonic. The Convair ballistics test results have been corroborated by the rocket sled tests on full-scale radomes. The use of metal-tipped radomes with a small included angle, and of ceramic with conical shapes, have been the most successful means developed to date of obtaining more satisfactory rain erosion properties. Materials and configurations currently used on subsonic aircraft are unsatisfactory at speeds of Mach 2 and higher. It is considered that a solution to the problem will be a combination of improved materials and design techniques.

2. The present supersonic test apparatus is accumulating vitally needed data. However, this test is of short time duration, and extensive recovery and refiring is necessary to accumulate even short time exposures. A program has recently been initiated at Cornell Aeronautical Laboratory to determine the feasibility of utilizing a supersonic rotating arm for evaluation of radome materials for extended time periods at supersonic speeds. The availability of such apparatus and the accumulation of more supersonic rain erosion test data on all available materials are necessary to provide a basis for future work by the Air Force on the development of supersonic rain erosion resistant materials.

REFERENCES

1. WADC TR 52-20. A Study of the Rain Erosion of Plastics and Metals. September 1952.

2. WADC TR 53-185. Part II, A Study of the Rain Erosion of Plastics and Metals. May 1955.

3. WADC TR 53-185. A Study of the Rain Erosion of Plastics and Metals. February 1954.

4. WADC TR 53-185. Part III, A Study of the Rain Erosion of Plastics and Metals.

5. Robinson, Ralph O., Jr., and Robertson, A. L. Interim Report on APL/JHU Terrier Radome Materials Test Program. October 24, 1955.

6. WADC TR 53-511. Part I, Development of a Heat-Resistant, Rain Erosion-Resistant Coating. November 1954.

7. WADC TR 53-511. Part II, Development of a Heat-Resistant, Rain Erosion-Resistant Coating.

8. WADC TR 53-192. Part I, Impact Pressure in Solid-Liquid Sphere Collisions. July 1953.

9. WADC TR 53-192. Part II, A Critical Review of Erosion by Water Drop Impact. August 1953.

10. WADC TR 53-192. Part III, Mechanism Studies on Plastics and Metals. December 1953.

11. WADC TR 53-192. Part VI, Dimensional Analysis of Rain Erosion Damage. July 1955. (Classified)

12. WADC TR 53-192. Part VII, Mechanism Studies on 2S and 3S Aluminum. (Classified)

13. WADC TR 53-173. Part II, A Study of Rain Erosion Testing Methods for Supersonic Speeds. May 1955. (Classified)

14. WADC TR 53-173. Part III, A Study of Rain Erosion Testing Methods for Supersonic Speeds. (Classified)

15. WADC TR 53-192. Part VIII, On the Breakup of a Waterdrop in the Zone Behind a Detached Shock Wave. August 1955.

16. WADC TR 53-173. A Study of Rain Erosion Testing Methods for Supersonic Speeds. November 1953. (Classified)

17. WADC TR 55-195. A Study of Rain Erosion of Aircraft Materials at Supersonic Velocities. August 1956. (Classified)

18. Armi, E. L., and Smith, E. F. Supersonic Rain-Erosion Tests of Falcon Radomes. Hughes Aircraft Co. Report No. 4W 11-377, April 1955. (Classified)

19. Seidl, F. G. P. Photographs of Some Effects on Raindrops of Shockwaves Produced by 60-caliber and 20-mm Projectiles. Boeing Airplane Co., Proceedings of 1956 WADC-OSU Radome Symopsium, Volume I.

Chapter 8

ORGANIC MATERIALS AND RADOME CONSTRUCTIONS

by

Norman E. Wahl

Cornell Aeronautical Laboratory, Inc.
Buffalo, New York

and

Edward B. McMillan

McMillan Laboratory, Inc.
Ipswich, Massachusetts

Chapter 8

ORGANIC MATERIALS AND RADOME CONSTRUCTIONS

SECTION A. INTRODUCTION

Radomes for aircraft have presented many difficult problems, both to the designer and materials engineers, due to the limitations of size, weight, electrical properties, and the great range of operating conditions encountered.

8-1. Design Problem

The type of materials used in the fabrication of these rigid structural housings has been dictated by such factors as moisture absorption, mechanical strength, and electrical properties under extremes of temperatures ranging from -60 to 500° F. It is important to realize that airborne radar antenna housings are the result of a compromise among the radar, structures, materials, and production engineers, for there is no magic material that will completely satisfy the requirements of each design group.

The problem of designing a radome that is satisfactory from an aerodynamic, electrical, structural, and production standpoint has occupied the best research and development talent for the last decade.

8-2. Radome Materials Development

During World War II, the first radomes were made from wood veneers impregnated and bonded together with phenolic resins to form ogive-shaped housings of plywood. This wood, with thin glue lines, had a low dielectric constant. It was soon found that, due to the high water absorption on exposure to rain, the dielectric constant increased to such a degree that they were unsatisfactory. This difficulty was partially overcome by impregnating the veneer with the phenolic resin which was also used for bonding. This resulted in radomes that were satisfactory in that the water absorbed was reduced, but the dielectric constant was materially higher. Since the radome walls could not be made thinner, the radomes had rather high reflections.

Polyfiber Radomes. A great amount of research work was carried out during this period investigating various organic materials with low dielectric constants that could be fabricated into shapes that were structurally satisfactory for airborne radomes.

Late in 1942 Dow Chemical Company developed a process for extruding very fine polystyrene fibers. These fibers were available in mats which could be compression molded with fairly low pressures and temperatures into a dense structural, low dielectric, material. This material was called Polyfiber. Laboratory tests at M.I.T. and production development work indicated that satisfactory radomes could be made from this material. Since this material could be molded under low-pressure conditions and had good electrical properties, Dow Chemical Company went into large-scale production to meet the requirements of the services for radomes. Manufacturing methods were improved, and a large number of these Polyfiber radomes were produced.[1]

The optimum range of density was found to be between 50 and 56 pounds per cubic foot. This density gave a dielectric constant in the range of 2.1 to 2.5. At lower densities the fibers

would not bond together properly, while at higher densities the radome housings were brittle with higher dielectric constants.

In about 1944, the Bakelite Corporation developed a solventless method for making a similar polystyrene fiber. Both of these materials were used in radome fabrication.

The Polyfiber radomes had extremely low water absorption; however, their heat resistance was low, and some cases were reported of thermal collapse of nose-type radomes when exposed to the sun. In addition, these Polyfiber radomes, though structurally satisfactory at normal temperatures, were found to be rather brittle at low temperatures, and were also readily attacked by aromatic aviation fuels.

Reinforced Plastic Radomes. The search for inorganic materials with satisfactory electrical properties was continued. Most of these materials were plastic in nature, and in general they were not satisfactory because of their low mechanical strengths, which necessitated relatively thick-walled radomes with very high reflections.

It was about this time that woven glass cloth was used to strengthen the relatively weak thermosetting plastic materials. This was the forerunner of the currently used glass-reinforced plastic radomes. Late in 1943, the use of various types of reinforcement for increasing the mechanical properties of the relatively weak plastic materials gained considerable interest.

8-3. Types of Radome Construction

In Chapters 2, 3, 4, and 5 various types of radome wall construction are described, primarily from an electrical point of view. These include:

1. Solid homogeneous wall
 a. Thin
 b. Half-wave
2. Sandwiches
 a. "A" Sandwich
 (1) Foam core
 (2) Honeycomb core
 (3) Fluted core
 b. "B" Sandwich
 c. Multiple wall or multiple sandwich.

In many cases where the thin wall is not sufficient structurally and where a half-wave wall is too heavy, a sandwich is used to advantage. The relatively thin double or multiple skins are stabilized against buckling by a low density core which results in a light weight, mechanically strong and stiff structure. The foam-core type "A" sandwich probably possesses the optimum strength-to-weight ratio. Tooling for the honeycomb core is less expensive, but here thickness cannot be maintained as precisely. Fluted core sandwiches provide channels in which hot air is circulated for anti-icing.

The solid type "B" sandwich is similar in structural properties to the solid half-wave wall except that it has a thin, solid core at the mechanical neutral axis. The core has a relatively high dielectric constant.

The multiple sandwich has a multiplicity of skins separated by low density cores. It may be considered as two or more "A" sandwiches with zero spacing between them.

SECTION B. MATERIALS FOR RADOME CONSTRUCTION

8-4. Classification of Plastics

When considering organic materials for airborne radome construction, necessity forces one into the use of plastics or elastomers. The elastomers, except for foamed core materials, are quickly ruled out because of their low modulus of elasticity, which makes them structurally undesirable.

The more rigid plastic materials can be classified into two general types, thermoplastic or thermosetting.

The thermoplastic or heat-softened materials, such as methylmethacrylate or polystrene as mentioned previously, soon lost favor for airborne radomes, due to their extreme brittleness at temperatures of -20° F and loss of shape and strength at temperatures of 180° F.

Thermosetting resins, including (1) phenolics, (2) melamines, (3) silicones, (4) polyesters, and (5) epoxies, have been used for radomes at various times. Each type offers a particular advantage and disadvantage and requires a

specific range of temperatures and pressures, as well as catalysts to cure or harden them.

The physical state of these uncured resins will vary from a low viscosity liquid to a solid. The solid resins generally have a higher molecular weight than the liquid resins. The solid resins can be made usable for radome fabrication by heating them above the melting point or dissolving them in a solvent or monomer. When this reduced resin is used, the solvent evaporates and the monomer enters into combination or copolymerizes with the solid portion of the resin upon hardening or curing.

While it would be possible to cast small radomes from these thermosetting resins, they would not have satisfactory mechanical properties if the walls were thin enough to meet the electrical requirements. In general these radomes cast from the thermosetting resins would be brittle and would tend to break or crack upon impact; however, they would not distort and lose shape upon exposure to 180° F, as would the radomes made from thermoplastic materials such as the Polyfiber previously mentioned.

8-5. Laminates

Previous research has established the fact that the physical properties, such as tensile, flexural, and impact strength, can be improved by the addition of reinforcing fibers, such as yarns or woven cloth, to the resinous materials.

The combinations of resins with layers or laminae of fibers, yarns, or cloth are generally known as plastic laminates. The earliest commercially made examples were combinations of paper, linen, or cotton cloth impregnated with phenolic resins. It was soon found that the use of these cellulose materials in a laminate was undesirable for most radome applications, since the moisture absorption was relatively high, which resulted in unsatisfactory dielectric constants and loss tangents. In addition, the cotton or linen reinforcements impregnated with these early phenolic varnishes required from 1,000 to 10,000 pounds per square inch pressure for molding. This pressure made the molding of very large radomes impractical. These factors forced the design engineers to investigate other reinforcing materials.

8-6. Glass Fibers

About 1943 glass fibers became commercially available in the form of yarns, strands, mats, and woven fabrics. Investigators soon found that, due to the particular characteristics of glass, the use of these forms of fibers as a reinforcement for resins increased the tensile, compressive, flexural, and impact strengths to a greater extent than organic fibers. In addition, the water absorption of this glass-reinforced laminate was usually less than 1 percent.

Studies indicated that the glass fibers reinforced the resins in much the same manner as steel rods reinforce concrete. The glass filaments could be placed in several directions to give a relatively isotropic material, or they could be placed in one direction to give very high strengths in one direction.

The use of woven glass cloth laminated with a thermosetting resin has become an established material for aircraft radome construction.

The thermosetting resins commonly used with glass fiber reinforcement for airborne radomes can be classified according to the pressure required for molding.

The use of high pressures for glass-reinforced structural laminates has been restricted by the size of the radome and the fact that high molding pressure tends to crush the woven glass fibers. The contact, or low pressure molding resins, such as alkyd styrene or alkyd triallylcyanurate copolymers, diallylphthalate and epoxies, require from 0 to 15 pounds per square inch molding pressure. These resins are 100 percent reactive, and polymerize by an addition reaction giving off no water or other volatile material. They can be polymerized at room temperatures with no heat, but are generally cured at temperatures ranging from 120 to 225° F.

The low or medium pressure molding resins, used with glass fiber reinforcement such as the phenolics, melamines, and silicones, are usually solids that are made liquid by the addition of a solvent such as toluol, alcohol, or water; they produce the best structural laminates with pressures ranging from 15 to 200 pounds per square inch. These resins all yield volatile byproducts upon polymerization and generally require temperatures above 300° F for hardening.

8-7. Phenolic Resins

Phenolic resins are prepared by the reaction of many different phenols, aldehydes, or ketones, and catalysts. The almost infinite number of possible combinations allows for the preparation of many different phenolic resins with various properties.

In general, when phenol and formaldehyde are combined in the presence of an acid catalyst, they form resins which are soluble in naphtha or aromatic solvents. These resins are usually used in paints and varnishes. With an alkaline catalyst, however, these materials produce a resin which becomes insoluble and infusible when a two-stage chemical reaction is carried out. This type of reaction is used in the process for making laminating resins.

In preparing phenolic resins for laminating, equal molecular proportions of phenol and formaldehyde are run into the reaction vessel and some alkaline catalyst such as ammonia or caustic soda is added. Heat is used to start the reaction, while an agitator stirs the mixture. The heat is not needed after the reaction is started, since an exothermic reaction takes place. The water which forms as a result of the chemical reaction is removed with a vacuum pump. When the reaction of the chemicals has been completed, the resin has the consistency of cold molasses or is a solid. This phenolic resin, which may be hardened or polymerized further by heat and pressure, is called a resol. It is also known as a stage A resin, which, when heated further, passes into stage B, which is hard and infusible.

The reaction between the phenol and the formaldehyde with either an acid or a base catalyst is called a condensation reaction. This condensation reaction is one in which molecules join together, or polymerize, to produce a large molecular structure and, as a byproduct of the process, a small amount of water, vapor, ammonia, or other volatile substance is given off. Polymerization is a reaction in which a number of molecules unite to form larger molecular structures of the same composition.

Phenolic resins for laminating are generally used in the form of a varnish or a water solution. The varnish is produced by dissolving the highly viscous or solid resin in alcohol. This varnish, or the water solution of resin, is applied to the glass fabric by coating machines.

In one method, the glass cloth is passed through a bath of phenolic varnish and then between a pair of squeeze rolls or under a doctor blade, either of which can be adjusted to control the percentage of resin remaining in the glass cloth. A second method uses a system of roll-coaters to control the amount of resin impregnated into the glass cloth.

After impregnation, the cloth is passed through a drying oven, which serves two purposes: to drive off the residual solvent in the liquid resin, and to advance the cure of the resin. At this stage, the resin still requires further cure but provides a non-tacky surface on the glass cloth.

All of these steps require continuous control and sampling, since the process is very critical and overheating will cause the phenolic resin to set up hard. The rolls of coated reinforcement are stored in cool rooms having a low moisture content until they are ready for laminating.

In general, most glass reinforced phenolic laminating materials require 200 to 500 pounds per square inch molding pressure to obtain the optimum properties of the laminated structure. Within the last few years, however, several so-called low pressure phenolic molding resins have been developed, such as Bakelite 11946 and 17085 and Cincinnati Testing Laboratory CTL-91 LD, which can be molded with 15 pounds per square inch molding pressure and cured at 325° F for approximately 1/2 hour.

The phenolic glass reinforced materials used in radome applications have been generally restricted to these newer resins because of the low pressures required for molding and the ability of these laminates to maintain most of their strength for extended periods at temperatures up to 500° F.

8-8. Melamine Resins

To produce melamine formaldehyde resins, calcium carbide is heated in air, from which it absorbs nitrogen to form calcium cyanamide. The calcium cyanamide is then reacted to form dicyandiamide, of which melamine is the trimer.* Melamine is then reacted with formaldehyde, using an alkaline catalyst, such as sodium hydroxide. The reaction between the melamine and formaldehyde is stopped while the resin is still in the intermediate stage and is still water soluble. The melamine formaldehyde resin is a clear substance, dissolved in water or ethyl alcohol.

This water or alcohol solution, usually containing about 50 percent of melamine resin, is used to impregnate glass mats, glass cloth, or asbestos in the same type of squeeze rolls used for preparing phenolic laminates. After the

*A compound having the same percentage composition as another but three times its molecular weight.

glass cloth or other melamine impregnated material is run through the squeeze rolls, the water or alcohol is driven off by running the material through a drying oven. The drying must be carried out carefully or the melamine resin will advance in cure and be too stiff for laminating.

Although melamine-formaldehyde has proved extremely useful because of its superior electrical properties, high heat resistance, surface hardness, general inertness, and resistance to organic solvents and acids, it has not been actively used for large radome applications because molding pressures of above 250 pounds per square inch are generally required. Melmac 402, produced by American Cyanamid Company, has been successfully used in producing small ogive-shaped radomes in matched metal molds, using mats as a filler, with as little as 100 pounds per square inch molding pressure.

The greatest use of these resins in the last five years has been in the combination of a melamine laminating resin with glass fiber for panel boards and other electrical items. This glass-mat, melamine combination provides very high impact strength as well as fire, heat, and arc resistance.

Many other potential combinations of fillers and melamine resins are under development for specialized applications in which the basic properties of heat resistance, good electrical characteristics, low water absorption and general inertness are of importance.

8-9. Silicones

Silicone is a general term used to describe a group of inorganic-organic polymers which may be liquid, rigid resin or rubber-like in nature. They are prepared from silica. Silica sand is converted to silicon tetrachloride by burning with coke and chlorine. By a direct catalytic process, one, two or three of the chlorine atoms of the silicon are replaced with organic radicals derived from petroleum. In this method of joining the organic and inorganic materials, an intermediate called organochlorsilane is produced. The remaining steps involve the separation of the desired organochlorsilanes followed by hydrolysis to remove the chlorine. A molecule having an inorganic nucleus, with organic radicals taking up the remaining valences on the silicon atom, is produced. This can be polymerized to form a resin or elastomer.

Depending upon the type of organic radical used, its arrangement, the number of organic radicals introduced, and the processing, the final product may be a resin, nondrying oil, or a rubber-like material.

The silicone resins have good resistance to temperatures as high as 600° F, a high degree of resistance to moisture, inertness to many chemicals, and good electrical qualities.

The early silicone resins developed were thermoplastic, brittle materials which had to be dissolved in toluol or xyol to form an impregnating varnish. The early work on laminating resins was directed toward making materials that could be molded at low pressure.

The development of low-pressure laminates using glass fabrics bonded with polymerizable silicone resins was investigated intensively by Dow Corning Corporation. This research program resulted in silicone resins that could be used with low pressure laminating techniques for the production of molded parts having curved surfaces or large areas. Equally important were the properties of strength at elevated temperatures, toughness, durability, water resistance, and electrical insulating properties. Because of the excellent heat stability of silicone polymers, it was inevitable that the silicone resins be investigated for the preparation of heat resistant laminates by low-pressure techniques. Research sponsored by Wright Air Development Center found that Dow Corning 2106 silicone resin was suited for the production of laminates at pressures of 30 pounds per square inch or less, and in general silicone resins may be considered satisfactory for use in low-pressure lamination. Low-pressure, silicone-glass laminates can be prepared from all glass fabrics or mats.

Studies have been made on the effect of cleaning or sizing glass fabric to prepare it for coating with silicone resin solution. Although much remains to be learned about the methods of cleaning and sizing the glass cloth for silicone resins, the results at the present time show that heat cleaning is the most satisfactory method. Some data indicate that there is no advantage in using sizings over the heat-cleaned cloth.

The properties of silicone resins that make them well adapted to low-pressure lamination are the high initial viscosity at laminating temperature and a gel time that can be controlled by the use of catalyst. Amine catalysts and others have been especially developed for use with silicone heat-setting resins. The amount of catalyst employed will depend upon the laminating pressure. For low-pressure lamination, the amount of catalyst is 0.5 to 1.0 percent of triethanolamine.

Low-pressure laminating generally requires the use of high flow resins. Because the bubbles and voids in the laminate must be removed by the flow of the resin rather than by pressure, it is necessary to use an excess of resin over that normally used in low-pressure molding. For structural laminates, however, it is also desirable that the resin flow be held to a minimum. Laminates with a silicone resin content of approximately 30 percent give the best properties at high temperatures. A 40 percent pickup of resin has been found most satisfactory on the impregnated cloth, so that a squeeze-out may be obtained.

Heat-cleaned glass fabric is impregnated with a catalyzed solution of silicone resin in toluol. After the fabric is impregnated it may be allowed to air dry for 1/2 hour. The cloth may be immediately precured for 5 minutes at 230° F, but the air-dry reduces the tackiness considerably. The laminating stock is soft and tacky when removed from the oven after the toluol is driven off; it may be shaped and straightened at this point. On cooling, the glass impregnated with silicone is stiff. Advantage may be taken of the flexibility of the stock when warm to preform and stretch it to various shapes before molding. This can be done by warming the stock to approximately 175° F and stretching it over a cold mold.

When proper flow and gel time are obtained, silicone laminating stocks may be laminated in a manner similar to the other conventional low-pressure resins. It is best to allow the laminating buildup to heat up to the laminating temperature of approximately 350° F under contact pressure before closing the mold and applying pressure. The pressure on the mold should then be increased gradually until 30 pounds per square inch is reached.

For lamination in a positive mold or in a bag mold it is satisfactory to place the layup in the mold and to close the mold immediately, maintaining the desired pressure during the curing cycle.

The time of cure is dependent upon the thickness of the laminate and the silicone resin. For Dow Corning resin 2106, a 15 minute cure is recommended for 1/8-inch laminates; a 30 minute cure is recommended for 1/4- or 1/2-inch laminates. Laminates thicker than 1/2 inch, up to 2 inches, should be cured for 1 hour. Laminates made in a bag, vacuum, or metal mold should be cured for 1/2 hour. All laminates should be cooled to below 212° F before removal of pressure.

To obtain the best high-temperature properties, it is necessary to give the silicone laminates an additional cure in an oven after they are removed from the mold. The following schedule is recommended for Dow 2104 resin: 16 hours at 194° F, 1 hour at 257° F, 1 hour at 302° F, 1 hour at 347° F, 1 hour at 419° F, and from 80 to 150 hours at 482° F. At no time during the after cure should laminates be allowed to cool off. No difficulty with distortion of complex-shaped radomes has been noted when using this schedule. The physical properties of silicone laminates are particularly satisfactory after long aging periods at 500° F. Results have indicated that the limit of endurance of DC-2106 resin laminates exposed to high temperatures is approximately 700° F.

A high-impact silicone molding compound has been prepared containing chopped glass fibers and inert filler. It has a bulk factor of 10 as shipped, and after preforming at 500 to 1,000 pounds per square inch, its bulk factor is 3. Pressure of 500 pounds per square inch is required for molding; however, small radomes molded in matched metal molds have shown astounding strength and resistance to heat degradation at temperatures as high as 700° F for 1 hour.

Molding temperatures are 350 to 400° F and time is 200 minutes for simple pieces. Small moldings can be removed from the mold hot. An after-bake of 8 to 16 hours at 195° F and 2 hours each at 260, 300, 350, and 400° F is necessary to develop optimum properties. In a mechanically controlled oven the after-bake can be accomplished by starting at 195° F and increasing temperature 15° per hour until 400° F is reached, followed by 2 hours at 400° F.

8-10. Polyester Resins

The alkyd styrene copolymers, or as they are generally called "polyesters," are quite easily polymerized. Their ability to form infusible, insoluble, thermosetting resins by addition rather than condensation makes them especially interesting for low-pressure molding. In contrast to the phenolic resins, no water or volatile materials are formed which have to be eliminated by breathing and the use of high molding pressure. This characteristic has been the salient feature in promoting the use of polyester resins with glass reinforcement for large airborne radomes.

The reaction product of polybasic acids (those acids with more than one functional carboxyl group) and polyhedric alcohols (alcohols with more than one hydroxyl group) are chemically

called esters. Those that form resinous bodies are generally designated as alkyd resins. When a dihydric alcohol and dibasic acid are esterfied, a linear, long-chained molecule is obtained with no residual carboxyl or hydroxyl groups to allow further crosslinking. The reaction of adipic acid and ethylene glycol produces this type of resin. These unsaturated alkyd resins will not crosslink with a monomer, such as styrene, and consequently are usually thermoplastic, or can be easily softened by heat. If these resins are exposed to low temperature, they tend to remain relatively flexible. These types of unsaturated resins are not generally used for laminating.

When alcohols having more than two hydroxyl groups are reacted with dibasic acids such as adipic, or an unsaturated dibasic acid, a thermosetting resin is formed which is hard and infusible.

Resins from unsaturated acids that have reactive double bonds are called unsaturated alkyds, which have the facility of crosslinking with monomers such as styrene, vinyl acetate, methyl methacrylate, or triallylcyanurate.

When glycols and unsaturated dibasic acids, such as maleic or fumaric acid, are reacted, an unsaturated alkyd is formed which is usually a high viscosity liquid. For laminating purposes, a monomer such as styrene or triallylcyanurate is added to the alkyd. When this resin and monomer combination or copolymer is cured by the addition of a peroxide catalyst, the linear unsaturated polyester chains are crosslinked by the reactive monomer forming a solid, infusible material. These resins can be polymerized at temperatures as low as 80° F in 3 to 4 hours.

Another group of unsaturated esters having low molecular weights are diallyl-phthalate, and diallyl-diglycol carbonate. These resins are very thin, water-like liquids which can be polymerized alone or copolymerized with more viscous alkyd resins.

The allyl resins are based upon the polymers and copolymers formed by either allyl alcohol or its derivatives. To form the simple esters of allyl alcohol, it is combined with the acid in the presence of dehydrating or acidic-type catalysts such as sulfuric or phosphoric acid. Generally, the water formed is removed by simple or azeotropic distillation.

Diallyl phthalate may be produced from phthalic anhydride and allyl alcohol using p-toluenesulfonic acid as catalyst or by ester exchange with dimethyl phthalate in the presence of sodium.

The polymerization of a typical allyl ester, diallyl phthalate, gives a linear or slightly branched unsaturated chain. After about 25 percent monomer conversion, a gel formation occurs resulting from the formation of a crosslinked polymer. Mixtures of unsaturated esters, such as diethylene maleate and diallyl phthalate, result in copolymers. As the ester is heated in the presence of a peroxide, the viscosity increases gradually until the gel point is reached. Initially the gel is highly elastic, but as the heating continues it becomes harder and tougher, finally forming a thermoset resin. Using diallyl phthalate with 2 percent of benzoyl peroxide, conversion to the prepolymer occurs in 2 hours at 180° F.

Diallyl esters polymerize readily with peroxide catalysts, but polymerize very slowly upon exposure to heat or light. This is advantageous since little or no inhibitor is required for storage. The catalyst becomes in integral part of the polymer chain.

Two factors have influenced the use of allyl resin. One is the use of a two-stage polymerization. The use of prepolymer reduces cure time and flow during the curing of a glass-reinforced laminate. The other factor is this: by undergoing additional polymerization, the problem of water reaction, ammonia vapors, or generation of other byproducts is eliminated in the formation of glass laminates. This permits the allyls to be used with very low molding or laminating pressures. It also leads to radomes with improved electrical properties. Some resins, such as phenolics, form water during their cure, and this complicates the processing. The absorption of some of this water in the laminate also tends to increase the electrical losses and dielectric constant. The major problem left to the radome manufacturers using pregelled allyl resins for thermoset laminates is that of eliminating the air bubbles.

Most of the allyl resins will gel at low temperatures, but require a minimum temperature of 200° F for complete polymerization.

Although the properties of the finished laminate depend on the particular allyl resin used, all the allyl resins or copolymers may be handled with basically similar techniques.

The first commercially produced unsaturated polyester resins appeared in this country about 1942, and were originally used, in lieu of acrylic plastics, for casting bomb-bay noses. The

first to be used in this work, and for reinforced laminates, was Allymer CR39, produced by Pittsburgh Plate Glass Company. This resin is said to be a condensation product of allyl acid carbonate ($CH_2 : CH \cdot CH_2 \cdot O:COOH$) and a glycol. However, these early allyl resins required curing temperatures above 225° F and curing times from 72 to 96 hours, which caused them to lose favor, compared with the more rapid and lower temperature cures of the styrene alkyd copolymers. This difficulty, however, has been overcome to a great extent, and the allyl resins have again gained favor for use in preimpregnated glass cloth.

The potential use of these polyesters as low-pressure laminating resins with glass fiber reinforcement has been under study for the last 12 years, and they have become recognized as the most appropriate materials for radome structures, due to the excellent strength to weight ratio, as well as chemical and moisture resistance.

8-11. Epoxy Resins

The first epoxy resins were produced commercially approximately a decade ago. Within the last 3 years they have been used on a large scale with glass cloth for radome fabrication. Chemically, the principal epoxy resins used for laminating are the condensation products of epichlorohydrin and bisphenol. The epoxy resins are polymerized by the use of metals, alkalies, organic bases, and acid anhydrides. The hardeners currently in favor for radome fabrication are amines, such as triethylene tetramine or metaphenylene diamine. An extensive research program has been conducted on high-strength epoxy laminates by Shell Chemical Company for Wright Air Development Center.[2]

In this work it was found the use of CL (metaphenylene diamine) curing agent with Epon 828 results in considerably better heat resistance and strength properties than is generally obtained with other amines, or anhydrides.

One of the disadvantages in the use of epoxy resins is the fact that most of the hardeners used are amines which are irritating to the eyes, and, being strongly basic, can produce chemical burns where they come in direct contact with the skin. Prolonged exposure to the epoxy resins and hardeners may cause dermatitis in hypersensitive individuals.

An approach to the problem of dermatitis or toxicity is the use of a polyamide resin which is not considered toxic. The amide groups react with the epoxides to give a three-dimensional or crosslinked polymer that is tough and strong. The use of 35 to 50 parts of polyamide, such as Versamide, with 65 to 50 parts of an epoxy resin, results in a satisfactory laminating resin that will harden at room temperature in 3 to 4 hours or can be cured in 15 minutes at temperatures of 150-200° F.

The liquid epoxy resins — for example, Epon 828 — used for laminating with glass fiber reinforcement such as cloth or mat, require 12 to 15 percent of CL hardener as compared to the 1.0 percent of peroxide catalyst used with the polyesters.

Glass cloth epoxy laminates have very high interlaminar bond strengths which give very high shear and compressive strengths as compared to polyester laminates. Compressive strengths as high as 60,000 pounds per square inch have been obtained.

Glass cloth laminates can now be prepared that have ultimate flexural strengths as high as 75,000 pounds per square inch, dropping to 57,000 pounds per square inch at 300° F. At temperatures of 350° F, epoxy laminates lose most of their strength. After boiling in acetone, the flexural strength may be as high as 62,000 pounds per square inch, and after 3 hours in boiling water may be as high as 72,000 pounds per square inch. They have retained their physical characteristics almost intact after 90 days immersion in 30 percent sulphuric acid, 60 percent hydrochloric acid, glacial acetic acid, 50 percent sodium hydroxide, ethylene dichloride, jet fuel, aromatic gasoline, or any of a number of other chemicals.[2]

Another program in the development of epoxy resins is Scotchply, a product of Minnesota Mining and Manufacturing Company. This material consists of glass filaments impregnated with a stable epoxy resin. The plastic is reinforced with linearly alined glass filaments. The individual sheets of filaments are plied together within the laminate in an arrangement to give either an isotropic or directional strength pattern to the structure. In each sheet, the glass filaments coated with the resin and curing agent are uniformly dispersed and the glass filaments are alined straight and parallel, without crimp, slack, or twist. Weaving of the glass filament reinforcement is thus eliminated and a more efficient structural laminate is produced that can be more easily formed to the radome shape, since the glass filaments will conform to the complex contours. This type of reinforcement, impregnated with epoxy resin, is approximately 60 percent glass and 40 percent plastic resin.

The low density and high strength of the epoxy-coated filament results in a product with a high strength-weight ratio. When used in fabricating radomes, Scotchply offers a method of obtaining strength in any desired area because of the flexibility provided by tailored orientation.

8-12. Catalysts for Polyesters

Most styrene alkyd polyester resins will polymerize by setting at room temperature or upon exposure to sunlight. It is generally necessary to add an inhibitor, such as hydroquinone or tertiary butyl catechol, to prolong the storage life. The use of an organic peroxide tends to reduce the effect of the inhibitor, as well as to increase the rate of polymerization of polyesters.

Benzoyl peroxide, obtained commercially as small granules or as a paste, is used as a general purpose catalyst for promoting the polymerization of unsaturated polyester resins. As a paste with tricresyl phosphate or as a suspension in styrene monomer, it is readily soluble in polyester resins. In general it is the best and most widely used organic peroxide, particularly for laminating applications. With most polyesters, 1 percent of benzoyl peroxide is usually used, which causes the polyester to cure at temperatures as low as 180° F in 5 to 10 minutes. If left at room temperature after catalyzing with 1 percent benzoyl peroxide, the poylester will gel in about 8 hours, but the polyester will not become completely cured.

In spite of its general usefulness, benzoyl peroxide does not fulfill the requirements of a catalyst for curing polyester resins at room temperature. A considerable amount of work has been conducted on room temperature cures of polyester resins when used with large radomes. Benzoyl peroxide alone is not satisfactory for this application, but accelerators are available which, when used with benzoyl peroxide make room temperature cures possible. These accelerators can be obtained commercially under various trade names, but in general they are based upon such chemicals as triethanolamine or dimethyl aniline. Approximately 0.01 percent of dimethyl aniline with 0.5 percent of benzoyl perioxde will result in hardening of most polyesters in 4 hours at room temperature. The pot life of polyester resins with this accelerator and catalyst system, however, is usually about 30 minutes.

One of the peroxides that is used alone in the case of room temperature hardening polyesters is of 0.5 to 1.0 percent of 60 percent methyl-ethyl ketone peroxide in dimethyl phthalate. The pot life of polyester resins with this percentage of catalyst is approximately 1 2 hour. The effect of using catalysts other than benzoyl peroxide depends on the activity temperature of the catalyst. Some catalysts, such as methyl-ethyl ketone peroxide, methyl is obutyl ketone peroxide, or hydroxy-heptyl peroxide, become active at relatively low temperatures, these may be used for room temperature laminating. For efficient and complete curing at room temperature, the addition of a few tenths of 1 percent of a promotor is frequently required in addition to the catalyst. A promotor usually makes the catalyst more active, and is usually a compound such as cobalt or manganese naphthenate. Promotors also increase the rate of hardening when higher temperature reacting catalysts such as benzoyl peroxide are used.

A number of organic peroxides covering a wide range of catalytic properties can be obtained commercially for use with polyester resins. In general the percentage of catalyst used ranges from 0.5 to 2.0 weight percent based upon the resin. If no satisfactory resin-catalyst combination can be found, there is a selection of various other peroxides available for use with promotors. In laminating radomes, the size and shape of the radome limits the amount of heat which can be tolerated, due to the "exotherm" developed. As a result, blends of catalysts are usually used to control this exotherm. A mixture composed of two organic peroxides, benzoyl and methyl-ethyl ketone peroxide has been found advantageous in cases where a large part has to be cured with little external heat.

Some work usually has to be carried out on the development of the proper resin-catalyst combination to develop a curing cycle of a specified time and temperature for each particular part which is to be fabricated.

The selection of a catalyst for each particular condition depends upon the following factors: (1) the reactivity of the polyester resin used, (2) the curing temperature that can be employed, and (3) the approximate gelation time of the particular glass reinforced laminate layup. If a large radome is being fabricated, this gelation period might be of 4 to 6 hours duration in order to allow for layup of the laminated radome. There is no catalyst formulation available at present which will satisfy all requirements of curing temperature or gelation time for all general applications. It is possible however, to obtain a satisfactory combination by utilizing available catalysts.

The two main sources of organic peroxides are Lucidol Corporation, Buffalo, New York and Cadet Chemical Division of McKesson and Robbins, New York City.

8-13. Reinforcements for Plastics

The use of reinforcement is not new in the plastics field. Since about 1910, reinforcement of high-pressure phenolic resins has been a common practice.

In general, cellulose materials in the form of paper, linen, or cotton cloth, as well as asbestos in the form of chopped fiber, felts, or papers, were used to obtain increased physical properties such as impact and flexural strengths. These types of reinforcement, particularly those containing cotton fibers, tended to have relatively high moisture absorption.

In the late 1930's, glass fibers and woven glass cloth became available, but attempts to use them as a woven reinforcement for high-pressure phenolic resins were generally unsatisfactory, due to the fact that the glass fibers became crushed during molding, so that the outstanding physical properties of the glass fibers were ruined.

When the polyester resins that could be molded with little pressure became available late in 1942, the use of glass fibers in the form of mat and woven glass cloth resulted in a new material with excellent strengths and light weight. Today, however, due to intensive research in the development of low-pressure molding phenolic resins, they can be used with glass cloth and molded at pressures as low as 15 pounds per square inch. Table 8-I compares the properties of a phenolic resin reinforced with woven glass and with woven cotton.

Other types of synthetic fibers, such as nylon, Orlon, Fortisan, rayon, Dacron, and Dynel, have been intensively studied for use as a reinforcement for polyester and epoxy resins, but none produces laminates that are as satisfactory in physical properties as are glass-reinforced laminates.

Fortisan rayon is the only fiber that produces laminates approaching the strength of glass-reinforced plastics. However, the modulus of elasticity of Fortisan rayon laminates is generally lower than glass, and it has not gained favor as a competitive reinforcement.

Nylon, Dacron, and Dynel are sometimes used for surfacing glass-reinforced laminates for special applications to improve abrasive, chemical, or electrical properties.

The glass fibers used in reinforcement for plastic laminates are produced from lime-alumina-borosilicate glass. These fibers are made from small glass marbles in a platinum furnace using platinum spinerets. The fibers are in the form of continuous filaments which are collected into bundles or strands which are

Table 8-I. Comparison of Cotton and Glass Reinforcements

Reinforcement Resin	Cotton 35% Phenolic 65%	Glass Cloth 38% Phenolic 62%
Flexural Strength (psi)		
1/8-in. panel, flatwise	18,000	48,500
1/8-in. panel, edgewise	17,500	62,300
Tensile Strength (psi)	9,000	40,000
Impact Strength (ft-lb/in. notch)		
Flatwise	4.0	29.0
Edgewise	2.5	12.5
Bonding Strength (psi)	600	900
Water Absorption (24 hrs %)		
1/8-in. panel	1.25	0.45
Insulation Resistance, Wet (megohms)		
(megohms)	2.5	60
ASTM Arc Resistance, sec.	10	190

then thrown into yarns for weaving. The mats and rovings are made from strands and can be used for reinforcement after the sizing has been removed.

Fibers of four different diameters are commercially available, as follows:

Strand Count	No. of Filaments Per Strand	Filament Diameter (Inches)
900	102	0.00021
450	204	0.00021
225	204	0.00028
150	204	0.00034

All these glass fiber strands consist of bundles of parallel filaments. Such groups of filaments play an important part in the reinforcing of the laminate because they enable stresses to be passed quickly and easily from filament to filament through the low-strenght laminating resin.

Generally, the coarser the fiber, the cheaper it is to produce. Woven fabric is produced in 150-, 225-, and 450 count yarns. Fabrics with 150-count yarns are not often used in structural laminates. It has not been shown that the use of this 150-count yarn represents the upper limit to the diameter of fiber in fabrics which are used for structural applications.

A great number of woven glass fabrics are made commercially for plastics reinforcement. In general, they vary in thickness, weight, and type of weave. All woven fabrics that are used in radome construction meet the requirements of MIL-P-8013.[3] Characteristics of these fabrics are given in Table 8-II.

8-14. Sizing for Glass Fabrics

A considerable amount of research and development has been conducted not only in the formulation of resins, but also on the use of finishes for the glass reinforcement used in the form of woven fabrics, yarn, and mat.

In general, the fabrics are woven from continuous filaments or staple fibers that are sized. This size, usually consisting of a mixture of starch and vegetable oil, is necessary to hold the fibers together and to lubricate the yarn and prevent abrasion during weaving.

In the early days of preparing glass-reinforced laminate structures, it was found that the size prevented full utilization of the strength of the glass fibers. The resin did not bond well to the glass because of the oily size; consequently, low flexural strengths were obtained. Early in 1943, woven glass fabric was used in which this size had been removed by exposing the cloth to temperatures of approximately 600° F. This heat treatment caramelized the size and gave the glass a light tan color. The next improvement in the preparation of woven glass consisted of running the heat-treated cloth through a chemical solution of methylacrylate chromic complex salt. This treatment improved the physical properties of the laminates. However, late in 1945, it was found that laminates exposed to weathering conditions of high humidity or immersion in water lost as much as 50 percent of their mechanical strength. The large loss in flexural strength of glass-fiber polyester laminates caused by water can be traced to the inadequate nature of the bond between the resin and glass filaments. This was thought to be caused by moisture penetrating between the resin and glass

Table 8-II. Woven Glass Fabrics for Reinforced Laminates

Fabric Number	Average Thickness (inches)	Average Wgt/Sq Yd (ounces)	Type Weave	Yarn		Threads per Inch	
				warp	fill	warp	fill
112	0.003	2.09	Plain	450	450	40	39
116	0.004	3.16	"	450	450	60	58
128	0.007	6.00	"	225	225	42	32
162	0.015	12.20	"	225	225	28	16
164	0.015	12.60	"	225	225	20	18
120	0.004	3.16	4-Harness Satin	450	450	60	58
181	0.0085	8.90	8-Harness Satin	225	225	57	54
182	0.013	12.40	8-Harness Satin	225	225	60	56
183	0.018	16.75	8-Harness Satin	225	225	54	48
184	0.027	25.90	8-Harness Satin	225	225	42	36
143	0.009	8.90	Crowfoot Satin	225	450	48	30

fiber interface. Since 1945, a number of research programs on glass fabric treatment have been carried out by both industry and Wright Air Development Center.[4] The Owens Corning Glass Company evolved a finish, designated "Volan A," which gave laminates good wet strength retention. This finish is also based on methylacrylate chromic chloride.[5] An outstanding finish, designated B.J.Y., base upon vinylchlorosilane, has been developed by Bjorksten Laboratories, but because of the formation of hydrochloride acid, commerical processing techniques have not been worked out, and this finish has not been used on a very large scale.[6]

In an attempt to eliminate the use of acidic or acid-producing chemicals in glass treating plants, a silicone polymer has been worked out which contains vinyl groups on each silicon atom. This resin is free of chlorine and is a neutral polymer that can be used in a toluol solution. This resin size, marketed as Linde treatment GS-1, can be applied to heat-treated glass cloth from a hydrocarbon solution producing a finish on the glass having properties similar to those obtained by sizing with vinyltrichlorosilane. The result of this treatment is to cover the glass filaments with a nearly continuous sheath of silicone. This coating not only covers the glass fibers but is firmly attached, either by some type of strong surface force or actual chemical reaction with the glass. This silicone treatment prevents wetting of the glass by water, and is not seriously affected by breaks or fissures. In addition, the vinyl groups attached to each silicon atom in this sheath are available for double bond polymerization with suitable unsaturated resins.

The amount of size on the glass can be controlled simply by adjustment of the concentration of the solution. Investigations at Linde have shown that below about 0.2 percent of size on the glass filaments, the wet strength retention begins to fall off. Wet strength retention does not seem to be affected by greater amounts of this size, but a definite decrease in dry strength becomes apparent above 0.5 percent size.

To avoid processing which involves the use of hydrocarbon solvents, Linde Silicone Division has recently developed a new vinyl silicone emulsion that can be applied to the fabric in a water solution. These silicone treatments are designated as A-172 for polyesters, and A-1100 for phenolic and epoxy resins. The applicable specification for the finish of glass fabric is MIL-F-9118. Another new treatment is called Garan finish.[7] This finish improves the wet strength of glass laminates and is available commercially.

Preliminary data indicate that with most polyester resins, laminates will maintain 90 percent or more of their physical properties after 30 days immersion in water with these Garan, Bjorksten, and Linde sizing treatments.

Personnel at the Naval Ordnance Laboratory in Washington have worked with silane finishes and have developed on outstanding finish designated NOL-24.[8] This finish, or size, not only reduces the loss in strength of polyester laminates due to water immersion, but vastly improves the physical properties of phenolic and epoxy resin laminates. The theory of why this finished improves the flexural strength and modulus of glass-reinforced phenolic or exopy laminates is based upon the fact that the finishes react chemically with the surface of glass fibers and the resin, thus bridging the discontinuity at their interface. This chemical bond between the glass and the resin causes the system to work as a unit, utilizing to a greater degree the high strength of the fibers.

The current status of finishes intended primarily for woven glass fabrics may be summarized as follows: Volan and Garan are used to the greatest extent, since they are approved under MIL-F-9118,[9] and are readily available commercially; the other finishes, such as Linde A-172 and A-1100, NOL-24 and Bjorksten, have to be ordered specially from various fabric weavers.

8-15. Adhesives for Radome Bonding

This paragraph treats the use of adhesives for bonding various plastic or metal attachments to reinforced plastic radomes. This involves the reduction of plastic-to-plastic, plastic-to-metal, or metal-to-metal bonding. The use of adhesives in bonding sandwiches will be discussed under the section on sandwiches.

Adhesives employed for bonding aircraft components are usually classified into two groups, cold setting and hot setting. Both types require enough pressure applied to the bonding areas to insure contact. Usually 15 pounds per square inch is the minimum desired pressure, with 200 pounds per square inch the maximum.

The adhesives used in bonding radome assemblies together in structural applications are synthetic in nature, and are based upon polyester, melamine, phenolic, resorcinol, furane, and epoxy resins. After considerable

research, these adhesives have proved the most satisfactory, since they cannot be softened by solvents or a normal amount of heat after cure.

Before an adhesive is selected for a bonding application, the following factors must be taken into consideration: (1) the working properties of the adhesive; (2) methods of preparing the bonding surfaces; (3) the pot life; (4) the method of application, and amount and duration of bonding pressure and temperature; (5) the ultimate strength of the adhesive bond at temperatures ranging from 80 to 400° F; as well as (6) the degree to which the adhesive or the adhesive-bonded joint can resist moisture, solvents, and stresses that tend to deteriorate the strength of the joint in service.

All structural bonding operations are similar, in general, these steps are followed: (1) Preparation of surfaces to be bonded; (2) Application of adhesive to faying surfaces; (3) Curing of the bond; (4) Quality control test of the bond.

In any bonding process the most critical factor in obtaining a strong, satisfactory joint is the preparation of the surfaces to be bonded. In all cases the bonded areas must be clean and free of grease or other contamination. With reinforced plastics, this is usually accomplished by sanding the plastic surface or by peeling off one ply of the glass reinforcement. An extensive amount of research has been devoted to the preparation of metals before bonding.[10] Usually the metal is degreased by the use of a hydrocarbon solvent and then treated with an alkali cleaner.

Cold-setting adhesives, such as the polyesters, furanes, resorcinols, and epoxies, are usually liquids that have to be accelerated or catalyzed with a second component. These adhesives correspond to Types II, III, or IV of MIL-A-8331.[11]

After addition of the catalyst, the pot life ranges from 10 to 90 minutes. During this time the surfaces of the bonded part must be coated by brush or spray and the parts assembled and held under pressure at room temperature. In general, the pressure must be kept on the assembly for 1 to 8 hours to allow the adhesive to set. Most cold-setting adhesives require from 24 to 96 hours at room temperature to obtain their optimum physical properties.

Certain types of modified phenolics or melamine resins, are used as liquids, films, or in the solid form as powders. These adhesives meet specifications for Types I, II, VI, and VII of MIL-A-8331. In the form of liquids, they are brushed or sprayed on the surfaces to be bonded; films or powders are laid between the faying surfaces before closing the assembly. For these hot-setting adhesives, the temperatures required for curing or setting range from 285 to 325° F. (at the glue line) for 15 minutes to 1/2 hour. The pressure required is usually about 50 pounds per square inch. The pressure can be removed as soon as the assembly is brought back to room temperature. Adhesives cured in this manner have obtained their full strength and can be used immediately.

The pressure and temperature may be produced by any of several conventional methods: heated platen in an air or hydraulic press; dead weight loading; vacuum bags in heated ovens or autoclaves; spring-loaded fixtures, such as a screw clamp or toggle clamp; or any other method that will give a dry heat source in combination with uniform pressure loading. To assure proper temperature at the glue line a thermocouple lead should be enclosed in the joint, at least in the preliminary setup.

The generally accepted method of testing the quality of an adhesive joint is to subject the bond to a tensile shear load.[11] This is done by cutting 1-inch strips of the overlapped joint and pulling the units apart on a tensile testing machine. The length of the strips should be approximately 9 inches, with a 1/2 inch overlap. The overlap area should be calculated to the nearest thousandth inch and then the unit pulled at the rate complying with MIL-A-8331. After the failure is recorded, the shear strength is calculated. It is general practice to test a certain percentage of the production units to determine the quality of the bond. In some cases, however, a test specimen is made for each production unit and accompanies it through the various operations. At the end of the operations, the test specimen is evaluated.

Due to aerodynamic heating which occurs on high speed aircraft, there is a need for adhesives to withstand higher temperatures. Such adhesives are needed for joining metals and glass-reinforced plastics to themselves and to each other.

All adhesives commercially available are organic and are therefore subject to definite temperature limitations. In load-carrying application, the upper limit at present is approximately 350° F; above this temperature the strength of most adhesives falls off rapidly.

Investigations on the development of high temperature adhesives are described in References 12 and 13.

The biggest disadvantage of adhesive bonding is the fact that there has been no satisfactory method of determining by test whether or not the bonded assemblies are structurally efficient. Inspection methods have been under intensive study for a number of years.[14]

SECTION C. SOLID RADOME CONSTRUCTION

8-16. Normal Temperature (-60 to 225° F)

For the most part solid radomes for operation at temperatures ranging from -60 to 225° F are constructed of glass-reinforced laminates ranging from 0.020 to 0.500 inch thick.

Airborne radomes are usually constructed of woven glass cloths (116, 120, 181 or combinations of these) impregnated with styrene alkyd copolymers, diallyl phthalate, or epoxy resins.

8-17. High Temperature (225 to 500° F)

Solid radomes for high temperature use are made of the same types of woven glass reinforcement (such as 116, 120 or 181), but the resins are usually restricted to silicones, phenolics, and the triallylcyanurate copolymers. The woven cloth used is covered by MIL-F-9084.[15] The finishes used on the woven glass cloth are covered by MIL-F-9118.[9]

The silicone resins that are currently used are Dow Corning's 2106 and General Electric's 81369.[16] The silicone resin requirements are outlined in MIL-R-25506.[17] The low pressure silicone laminates are covered in MIL-P-25518.[18]

The most heat resistant phenolic developed to date is Cincinnati Testing Laboratory's CTL-91LD.[19] The CTL-91LD, phenolic glass-reinforced laminate meets the requirements of MIL-P-25515.[20] Of the triallylcyanurate copolymers, three are available commerically that are used for radome fabricating. They are Naugatuck Chemical Company's Vibrin 135; American Cyanamid's 4232; and Pittsburgh Plate Glass Company's 5000-468-53.[21] The specification covering the requirements of these heat resistant polyester resins is MIL-R-25042.[22] Laminates made from these three types of resins and 181 cloth have been extensively evaluated for physical properties at room and elevated temperatures.[23,24,25] The requirements for the completed laminate are covered in MIL-P-25395.[26]

The greatest difficulty in the use of these three types of resins in the fabrication of solid-wall radomes has been to develop methods of post-curing the laminates so as to eliminate the formation of bubbles or blisters between the glass laminate, which causes delamination of the plies of glass reinforcement.[21,24]

The triallylcyanurate resin laminates also tend to crack upon exposure to 500° F. Studies indicate that an asbestos overlay sheet tends to eliminate this difficulty.[21]

SECTION D. SANDWICH RADOME CONSTRUCTION*

Sandwich construction consists of two or more thin skins stabilized against buckling with a lightweight core material.

8-18. Types of Core Materials

The organic materials commonly used in sandwich radomes consist of glass fiber-reinforced plastic skins made with glass cloth of such weaves as 112, 116, 120, 181, impregnated with polyester, epoxy, phenolic, or silicone resins. These laminate skins meet the requirements of the applicable laminate specifications.[3] The core used is usually of one of the following types: (1) Honeycomb core, (2) Fluted core, (3) Foam core.

8-19. Honeycomb Core

In general, the honeycomb and fluted core can be considered as one type of core material, since they are usually made from glass fabric impregnated with a minimum amount of resin and vary only in their geometry. The greatest difference between them, perhaps, lies in their method of manufacture and use.

*From the view of materials and fabrication techniques, the multiple sandwich can usually be considered as two or more identical, single sandwiches with zero spacing between them. Therefore, only the methods of fabricating a single sandwich will be discussed.

Glass fabric honeycomb core materials are made with hexagonal shaped cells of several sizes. They are usually made from 112 cloth in which the cell nodes are bonded together with thin layers of organic resin. The cell sizes usually used are 3/16, 1/4, and 3/8 inch with densities ranging from 2.5 to 9 pounds per cubic foot.

Honeycomb cores are of two types. The cheaper of the two types is fabricated by a process in which adhesive is applied in alternately spaced and interspersed strips to the upper surfaces of the stacked sheets from which the honeycomb is to be made. These strips or nodes form the bonding points of the honeycomb cell upon curing of the adhesive. The flat sheet is then cut in the required thickness and the honeycomb expanded by pulling on each end of the flat sheet. In the second type, mandrels are used for cell formation.[27] For double curvature work the unexpanded core is dipped in resin that has been diluted, stretched over the appropriate contour, and allowed to cure in position. It is also possible to machine sections from the unexpanded blocks of honeycomb, so that when the sections are expanded curvatures are again obtained.

The precision type of honeycomb core is supplied in the expanded condition. See Figure 8-1. It is possible, by warming sheets of the resin-impregnated honeycomb, to post-form sections to a fair double curvature. Machined double curvatures are possible; in order to provide support for the cell walls, the core may be temporarily embedded in a matrix of fusible alloy or wax. Contoured honeycomb sections cut to fabricators' shapes are commercially available.

There are generally two deficiencies to be overcome in the use of honeycombs in sandwich radomes. The first is the difficulty of obtaining accuracy in the core thickness; the second is the trouble experienced in obtaining the optimum bond between the honeycomb and the surface skins at all times. In the expansion type of honeycomb, the blocks of core are cut into slices by power-operated guillotines. Contoured thicknesses of the preformed core are cut from this block with a bandsaw, leaving the cut edges of the sheet with a somewhat stringy frayed edge of glass fiber.

Glass-reinforced honeycombs display pronounced directional shear properties, but, this

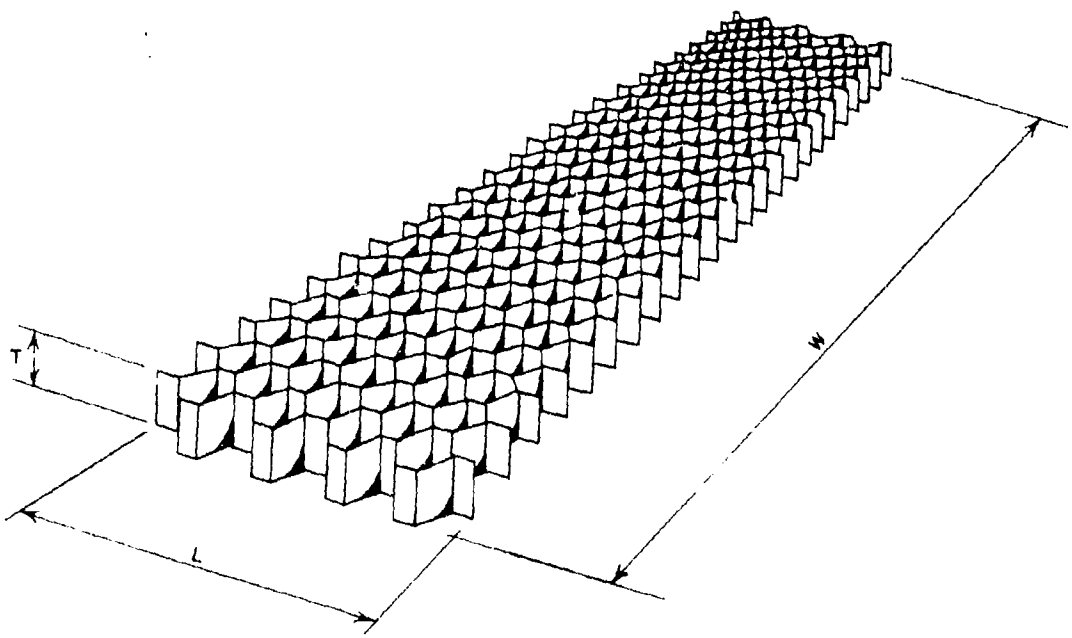


Figure 8-1. Sketch of Honeycomb Core Structure (T is the thickness, or depth; L is the width, also called the ribbon direction or longitudinal direction; W is the length, sometimes termed the transverse direction or direction perpendicular to the ribbons)

is usually overcome by orienting the core so the major loads are carried in the longitudinal or ribbon direction shown in Figure 8-1.

The National Advisory Committee for Aeronautics and the Forest Products Laboratory have carried out an extensive study of the physical properties of honeycomb cores and plastic sandwiches prepared from them. Analysis of compressive, shear, and creep properties are outlined in their reports (see References 26 through 39). Data on methods of inspecting bonds and methods of repair of sandwich constructions are also outlined in Forest Products Laboratory reports (References 14, 40, 41).

The specification covering honeycomb core is MIL-C-8073.[42] The specification covering sandwich construction is MIL-S-9041.

8-20. Fluted Core.

Another type of core material has been developed by several aircraft companies for deiceable airborne radomes. This is known as a fluted core. A description of its manufacture will be found in paragraph 8-25 under "Core Construction."

8-21. Foam Core

In view of the general use of foam cores a treatment of the foaming-in-place process has been included in paragraph 8-26 under "Foamed-in-Place Cores."

The specification covering polyurethane foamed-in-place core materials is MIL-C-8087,[43] and the requirements of sandwich construction of glass-reinforced laminate skins and alkyd isocyanate foamed-in-place cores are covered in MIL-S-25392.[44]

Because of the temperatures encountered in flight on high-speed aircraft and missiles, the need of temperature-resistant foams for sandwiches became evident early in 1952. As considerable success had been achieved in the research on resins for heat-resistant, glass-reinforced laminate skins, the next logical step in the preparation of heat-resistant sandwiches was to evolve a thermally stable foamed-in-place core material.

Wright Air Development Center sponsored several investigations to develop formulations, materials, techniques of foaming, and equipment for the production of a heat-resistant, foamed-in-place, low-density, dielectric core material for radomes. Such radomes are to meet the following requirements: (1) they will be subjected to short-time operation at temperatures of approximately 500° F; (2) the foamed-in-place core dielectric must lend itself to use in sandwich radome designs; (3) the sandwich skins, between which the foam is to be expanded and to which it must bond automatically during foaming, is to be of low-pressure, glass-fabric reinforced laminates which may be spaced uniformly or in controlled graduation of spacing ranging from 0.25 to 0.50 inch; (4) radomes will range in size from approximately 6 inches in diameter by 12 inches long to approximately 20 inches in diameter by 60 inches long; (5) radome skin thicknesses will range from approximately 0.010 to 0.040 inch; (6) sandwich molding thickness must be controllable to ±0.005 inch.

Based upon this research, two heat-resistant, foamed-in-place core materials have been developed. In the first program polyurethane foams prepared from tolylene diisocyanate and unsaturated alkyd-triallylcyanurate copolymeric materials have retained 50 percent of their room temperature strength when tested at 400° F, after 1/2 hour at 400° F.[45] Some of the properties of this foamed-in-place core material are given in Table 8-III.

Table 8-III. Properties of Polyurethane Foams

	75° F	400° F
Compressive Strength (Flatwise)	270 psi	150 psi
Shear Strength	85 psi	40 psi
Shear Modulus	7,300 psi	3,400 psi
Tensile Strength (Flatwise)	100 psi	70 psi
Dielectric Constant 8.5 Kmc	1.16 ± 0.01	1.23 ± 0.01 (392° F)
Loss Tangent 8.5 Kmc	0.0034 ± 0.0002	0.0024 ± 0.0002 (392° F)

In the second program, methods for producing foamed-in-place sandwich structures from silicone resins have been developed.[46] This process consists of expanding a dry powdered silicone resin containing a blowing agent, catalyst, and inert filler. The powder mixture melts and expands readily. Core density can be conveniently controlled by adjustments in the temperature used for expanding the powdered resin.

Foamed-in-place sandwiches can be consistently reproduced with a density variation of approximately ±1 pound per cubic foot. Foams have been made with densities ranging from 11 to 24 pounds per cubic foot. At room temperature the compressive strength of these foams varied from 80 to 400 pounds per square inch, depending on the density. Compressive strength after one-half hour exposure to 500° F ranged from 20 to 100 pounds per square inch. For instance, a panel having a density of 18 pounds per cubic foot had a room temperature compressive strength of 200 pounds per square inch. After 200 hours at 500° F, its compressive strength was 70 pounds per square inch.

SECTION E. PROPERTIES OF ORGANIC RADOME MATERIALS

8-22. Electrical Properties

Compositional and environmental changes and factors influence the microwave behaviour of radome and other dielectric materials, as evidenced by directional errors and range reduction. The former is the summation of such microwave optical phenomena as refraction, phase front shape, and polarization distortions; the latter is a result of power loss through absorptive dissipation and reflection.

The dielectric constant of a material is a determinant of its refraction, reflection, and electrical thickness. The material's loss tangent is a coefficient proportional to its energy absorptive characteristic, and affects in varying degrees polarization distortions, reflection, and range reduction.

Dielectric constant and loss tangent values of materials of interest are periodically published by A. R. Von Hippel for a wide range of frequencies and temperatures.[47]

Dielectric constant and loss tangent values of particular interest to radome designers are reported by Lt. Richard H. Forbes and Byron Noe in the following WADC Technical Reports:

1. "Microwave Electrical Characteristics of Radome Materials at 8.5 Kilomegocycles Per Second," Technical Report No. 54-273, April 1954.

2. Supplement 1, June 1956.

For the convenience of the reader the dielectric measurements from a number of sources of properties of typical and proposed radome materials have been compiled in Table 8-IV, "Dielectric Properties of Low Density Materials," and Table 8-V, "Dielectric Properties of Full Density Materials."

Table 8-IV. Dielectric Properties of Low Density Materials

Class	Name	Description	sp.gr (gm/cc)	Temp (° C)	Freq (mc)	Dielectric Constant (Dry)	Loss Tangent (Dry)	By
Honeycomb or Similar	Glass fiber 0.0065" wall, 1/4" open cell:		0.06					
	a) E vector ⊥ double cell walls			25	8,500	1.10		WADC
	b) E vector ∥ double cell walls			25	8,500	1.15		WADC
	c) E vector ⊥ sample			25	8,500	1.20		WADC
	McMillan Isotropic Core	40% Al	0.10	25	9,300	4.03	0.0146	McM

Table 8–IV. Dielectric Properties of Low Density Materials (cont)

Class	Name	Description	sp. gr (gm/cc)	Temp (° C)	Freq (mc)	Dielectric Constant (Dry)	Loss Tangent (Dry)	By
Mineral	Emerson and Cuming sodium silicate		0.38	25	8,500	1.65	0.005	WADC
	Foamglass		0.71	25	9,300	1.14	0.025	NADC
	Ohio State University fire bloated ceramic		0.88	25	8,500	7.4	0.009	WADC
	Owens-Illinois integrated Wollastonite		0.28	250	8,500	1.41	0.0010	WADC
	same converted at 1,700° F		0.30	250	8,500	1.44	0.0009	WADC
	Pittsburgh-Corning Foamed Silica		0.16	25	8,500	1.15	0.002	WADC
	Virginia Polytechnic (90%)		0.53	25	9,370	1.7	0.005	NADC
			1.24	25	9,370	2.54	0.005	NADC
	VPI-B77 calcium aluminate			room	9,370	1.52	0.001	NADC
				316	9,370	1.55	0.001	NADC
	VPI-90% alumina		1.45	25	9,370	8.55	0.001	NADC
	VPI-Steatite		1.29	25	9,370	6.0	0.001	NADC
Resin	McMillan Polyurethane	13% Al	0.23	25	9,300	2.4		McM
		22% Al	0.23	25	9,300	4.5		McM
		30% Al	0.10	25	9,300	3.6	0.008	McM
	Silicone XR544		0.17	25	8,600	1.18		WADC
			0.38	25	8,600	1.45		WADC
			0.26	25	8,600	1.31	0.0015	WADC
			0.26	250	8,600	1.43	0.0017	WADC
Resin	Lockfoam	10% Al	0.273	25	8,500	3.16	0.050	WADC
Resin	Lockfoam		0.126	25	8,500	1.16	0.004	WADC
Resin	Goodyear Alkyd-Isocyanate		0.160	25	9,160	1.2	0.004	Goodyear

Data sources: McM: Von Hippel; NADC: Naval Air Development Center; WADC: Wright Air Development Center

The reader not familiar in detail with the principles of microwave optics is cautioned that the electrical behavior of a radome is not independent of thickness. The effect of thickness is reduced when the dielectric constant is very low or certain arrangements of the layers of the radome wall are made.[48, 49, 50] For acceptable boresight accuracy it may prove preferable to use high dielectric constants. Efforts have been made to improve transmission properties with magnetic materials.[51, 52]

In a radome, dielectric materials are disposed in definite thicknesses, gradients, and shapes. From the viewpoint of microwave optics mechanical thickness is important as it directly combines with dielectric constant to give electrical thickness as the product. This latter property affects phase front shape, polarization distortion, and reflection.

Usual mechanical sources of variation in electrical thickness include flight erosion, de-

Table 8-V. Dielectric Properties of Full Density Materials

Class; Name	Description	Sp gr (gm/cc)	Temp (° C)	Freq (mc)	Dielectric Constant (Dry)	Dielectric Constant (Soaked)	Loss Tangent (Dry)	Loss Tangent (Soaked)	By
Ceramics:									
Alsimag 576-L5A	Cordierite	3.4	room	10,000	8.5		0.0023		AML
Alumina	90% A10	ca. 3.6	room	9,375	8.5		0.001		MIT
Alumina	Sapphire	ca. 3.6	25	1.0	8.25		0.001		MIT
			500	1.0	8.25		0.001		MIT
Alumina, Coors AI-200	96%	3.61	25	10,000	8.79		0.0015		MIT
			500	10,000	9.03		0.0021		MIT
Boron-silicon-nitride			0	5,000	5.0		0.04		MIT
			70	5,000	4.8		0.04		MIT
McMillan 2-6	m.p. 2,500° C	ca. 1.7	25	10,000	9.65		0.0003		MIT
Rutgers composition	Alumina	3.67	room	8,600	8.6		0.002		Rutgers
Steatite 228	Cordierite	ca. 3.4	25	10,000	5.95		0.0019		MIT
		ca. 3.4	500	10,000	6.1		0.0035		MIT
Zircon, VPI	$ZrSiO_4$	ca. 3.7	room	9,375	8.6		0.001		VPI
Zircon	$ZrSiO_4$	ca. 3.7	0	5,000	6.7		0.005		MIT
Zircon	$ZrSiO_4$	ca. 3.7	800	5,000	7.0		0.005		MIT
Epoxy Laminates:									
Epon 828 (28.0)	ECC-181	1.93	-73	34,700	4.3	4.67W	0.0045	0.013W	McM
			+260	34,700	5.4		0.0075		McM
			23	8,500	4.64	4.67	0.013	0.013	WADC
			-73	16,100	4.7		0.0035		McM
			+260	16,100	5.5		0.0115		McM
Epon 828 (33.0)	Borosilicate 181 Volan A fabric		25	8,500	3.46	0.012			WADC
Glasses:									
Corning 0120	Potash-soda-lead	3.05	25	1.0	6.6		0.011		MIT
1710	Alumino silicate	2.53	25	1.0	6.3		0.023		MIT
7070	Potash-Lithia-Borosilicate	2.13	25	10,000	4.00		0.0021		MIT
			100	10,000	4.00		0.0021		MIT

Table 8-V. Dielectric Properties of Full Density Materials (cont)

Class; Name	Description	Sp gr (gm/cc)	Temp (° C)	Freq (mc)	Dielectric Constant (Dry)	Dielectric Constant (Soaked)	Loss Tangent (Dry)	Loss Tangent (Soaked)	By
Glasses: (Cont)									
Corning 7740	Borosilicate	2.23	25	10,000	4.52		0.0085		MIT
7900	96% Silica	2.18	20	10,000	3.82		0.0009		MIT
			100	10,000	3.82		0.0013		MIT
7911	96% Silica	2.18	25	10,000	3.82		0.0006		MIT
Mica:									
Bureau of Mines	Synthetic mica		room		5.6		0.002		NADC
			316		5.7		0.007		McM
Mycalex No. 400	Mica, glass		25	10,000	7.12		0.0033		MIT
Mycalex No. 400	Mica, glass		80	10,000	7.32		0.0057		MIT
Supramica No. 500	Glass-synthetic fluor-phlogopite		25	9,375	7.0				McM
			372	9,375	7.48				McM
Supramica No. 555	Mica, glass	4.13	25	8,500	9.32		0.007		WADC
Neoprene:									
Antistatic Coating Goodyear R-14-123-252			23	8,500	13.31		0.031		WADC
Erosion Coating Goodyear 1801-C			23	8,500	2.99		0.35		WADC
Phenolic Laminate:									
CTL-91LD (28.3)	ECC 181-114	1.87	70	16,100	5.25		0.006		McM
			260	16,100	6.00		0.011		McM
Polyester Laminates:									
Laminac 4323 (25)	ECC 181-114	1.68	-73.3	34,730	3.9		0.003		McM
			260	34,730	4.5		0.007		McM
			-73.3	16,100	4.4		0.012		McM
			260	16,100	4.7		0.015		McM
Paraplex P-43 (37.3)	ECC-181	1.78	23	8,500	4.20S	4.27W	0.011S	0.011W	WADC
Paraplex P-43	Fiberglass Mat	1.75	23	8,500	4.21S	4.15W	0.023S	0.016W	WADC
Selectron 5003 (40.5)	ECC-181		23	8,500	4.21S	4.22W	0.0115S	0.012W	WADC

Table 8-V. *Dielectric Properties of Full Density Materials (cont)*

Class; Name	Description	Sp gr (gm/cc)	Temp (° C)	Freq (mc)	Dielectric Constant (Dry)	Dielectric Constant (Soaked)	Loss Tangent (Dry)	Loss Tangent (Soaked)	By
Selectron 5065		1.77	37	9,370	4.64		0.040		McM
(36.2)	ECC-181	1.99	70	9,370	4.79				McM
Sunform A-1									
(40.1)	ECC-181	1.8	23	8,500	4.27	4.29	0.017	0.016	WADC
Stypol 16B (45.5)	ECC-181	1.75	23	8,500	4.11S	4.31W	0.018S	0.030W	WADC
Stypol 25 (40.9)	ECC-181	1.79	23	8,500	4.24S	4.26W	0.021S	0.021W	WADC
Vibrin 135 (32.0)	ECC-181 Volan	2.15	24	9,600	4.16	4.39	0.006	0.008	McM
Vibrin 135 (38.7)	Borosilicate 181		260	9,600	4.51				McM
	Volan A fabric		25	8,500	3.50		0.015		WADC
Pyroceram:									
Corning	No. 8606	3.18	24	9,375	5.4		0.003		McM
	No. 8606	3.18	426	9,375	5.8		0.003		McM
Quartz:									
MIT Sample	Fused		1200	5,000	3.85		0.002		MIT
Silicone Laminate:									
30% DC2106	ECC-181		20	8.6	4.35		0.0058		MIT
250 Final cure	Heat cleaned		300	8.6	4.31		0.0063		MIT
Teflon Laminate:									
DuPont Sample	ECC-112		23	8.5	2.97S	3.00W	0.0046S	0.006W	WADC

Notes: Condition S - 50% RH
Condition W - wiped dry after 24 hours in H_2O at room temperature (35.5) means resin content 3.5%.

Data sources: AML: American Lava; McM: McMillan; MIT: Von Hippel; NADC: Naval Air Development Center
WADC: Wright Air Development Center; VPI: Virginia Polytechnic Institute.

viation from dimensional and smoothness specifications, surface films of water or other fluids, and encrustations of ice, frost, fungus, dirt, and salt. Temperature fluctuations produce mechanical thickness variations which may be accentuated in electrical thickness effect by dielectric constant and loss tangent changes.

Environmental changes, for example of temperature and humidity, usually but not always produce reversible changes in dielectric constant and loss tangent. Process variations in the manufacture of dielectrics or the radomes themselves are sources of permanent deviations from the desired dielectric properties. Common process factors include variation in the ratio of raw material ingredients, such as styrene and polyester; changes in composition of a laminate resulting from catalysts, pigments, trapped air, or moisture; impurities; proportioning of resin and glass fiber; and the degree of post-cure.

The reader who is a chemist or chemical physicist is directed to Reference 53 for the molecular theory of dielectrics and a treatment of dielectric constant as a function of temperature. The electrical engineer is referred to Chapter 2, "Electromagnetic Field and Optic Theory," in this book, and to Reference 54.

Data measured and compiled by G. R. Blair on the change of dielectric properties with temperature for several laminates is shown in Figures 8-2 and 8-3. (See also Reference 55.) In Reference 56 E. B. McMillan discusses the influence of dielectric changes with temperature rise on the electrical design of missile radomes. The chemist and the fabricator will find reason

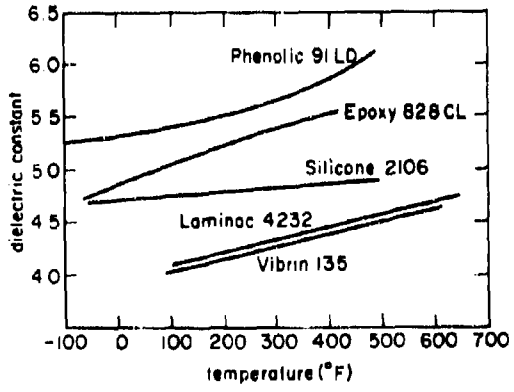


Figure 8-2. Dielectric Constant Versus Temperature, Various Laminates (By permission of McMillan Laboratory, Inc.)

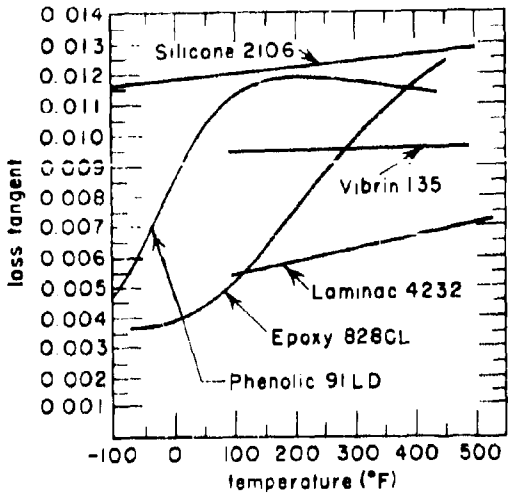


Figure 8-3. Loss Tangent Versus Temperature, Various Laminates (By permission of McMillan Laboratory, Inc.)

to provide materials having the least change of dielectric constant and loss tangent with temperature.

When an isotropic dielectric is specified or implied the chemist must guard against an orientation of the dielectric during fabrication process steps such as might result from foam core striations and parallel alignment of oriented fabrics. A calculated orientation is introduced when wires, grids, and plates are made a part of the radome wall, as has been done experimentally.[57,58]

Electrical resistivity varies with materials, often with their temperature, and at the surface is influenced by moisture. Relative movement with respect to dry or ionized air may produce, or in the latter case reduce, electrical charge accumulation at the surface. Interface ionization has been thought to produce a limited degree of radio interference and localized microwave dielectric property changes.

The electrical designer endeavors to avoid dielectric discontinuities, but the fabricator and the installer may need joints for practical reasons. The pattern distortion of a joint prepared in a laboratory experiment may be seen in Figure 8-4. When the plastic foam of the sandwich core was loaded with aluminum powder until all elements of the radome wall were nearly electrically homogeneous, the shape of the radiation pattern was substantially restored. It can be seen that the use of metal powders may in certain instances be necessary and is not harmful per se; however, there must be

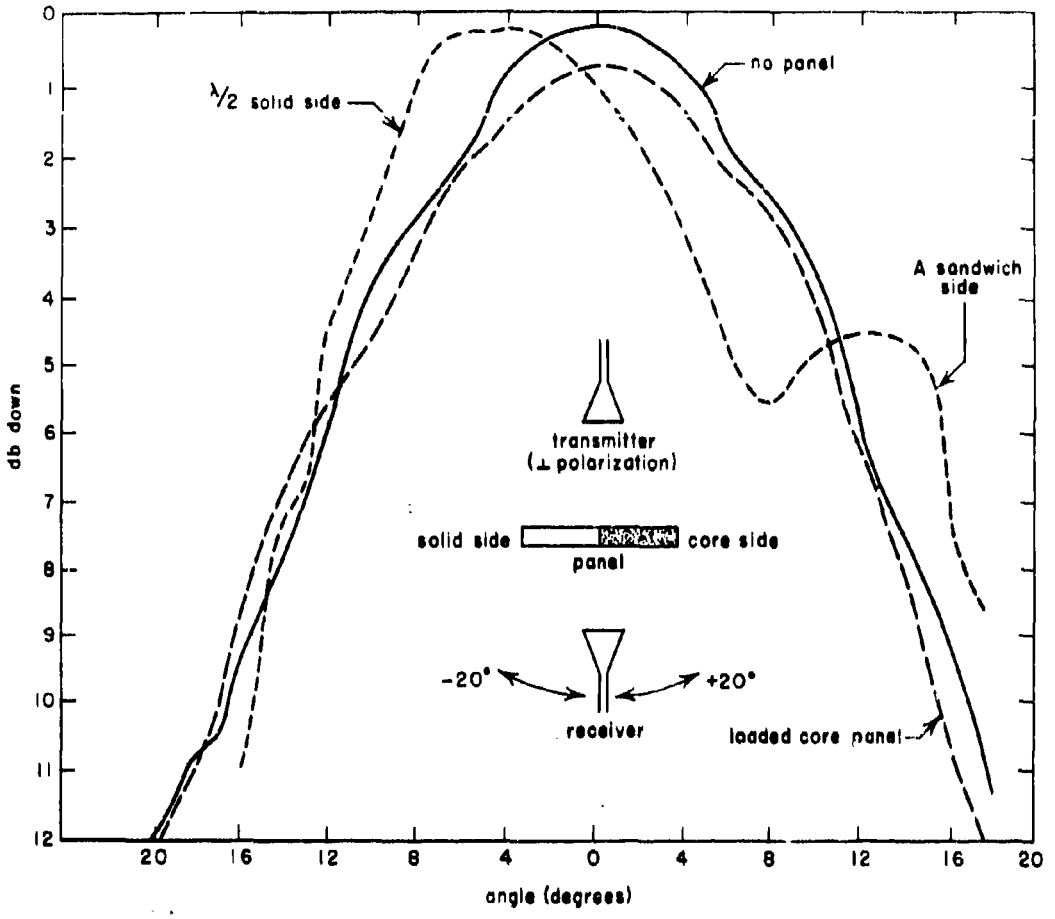


Figure 8-4. Electrical Properties of Joints (By permission of E. B. McMillan)

careful electrical design thought, as well as conformity with military specifications where applicable.

In connection with a radome installation or as a covering for certain radome areas or supports, a dielectric sheet of high loss and low reflection may be needed. In addition to MX410/AP materials, gradient foams or hair mats, thin wave-trapping flexible laminates, and dentate nonreflecting systems have been available.

8-23. Mechanical Properties

The basic mechanical properties, such as tension, compression, and flexural strengths, of glass-reinforced laminates differ from similar properties of other structural materials in that the resultant laminate is anistropic; that is, the various physical properties vary in different directions in the plane of the sheet. In most woven fabrics used in the reinforcement of structural plastics, the yarns are woven at right angles, designated as warp and fill directions. Generally, in structural laminates, the plies of woven glass cloth are laid up so all the plies of the laminate are parallel to the warp, or so that alternate plies are parallel and perpendicular to the warp. Fabrics having an essentially square or balanced weave (those with the same yarns in equal amount in the warp and fill directions) give laminates with approximately equal strength in directions at right angles to each other. Physical properties of laminates made with balanced weave fabric generally result in equal strengths in the longitudinal direction (warp) and in the transverse direction (fill). Most data on strength properties are reported in two directions, the longitudinal and the trans-

verse. Fabrics with unbalanced weave or unidirectional fabrics such as 143, are usually plied in a parallel fashion in most laminates.

Table 8-VI outlines the minimum strength values of polyester laminate panels that are required under MIL-P-8013A on low-pressure, structural, glass-reinforced plastics.[3] These values, while representative of the mechanical properties obtained on flat panels of typical polyesters and various weaves of fabric, should not be used for design. Even with one specific fabric, many factors such as type of resin, fabric finish, shape, fabrication and molding procedures influence the mechanical properties of the final laminate.

Strength properties of glass-reinforced laminates have been found to vary considerably, depending upon the processing of the laminates. Differences of 25 percent may be found in physical properties.

It is common for different rolls of supposedly identical glass fabric to yield very different strengths when all other conditions were thought to be equivalent. In fact variations in strength have sometimes been found within a given roll of cloth. One cause for this difficulty can be traced to the application of the finish. If the heat-desized glass cloth has traces of alkali on its fibers, the properties of the finishing treatment are adversely affected. The sized glass cloth also can deteriorate if adequate control of the temperature in heat cleaning is not maintained. For example, woven glass cloth that has been heated up to 675° F will lose 30 percent or more of its original strength.

All these variables tend to discourage the designer of structural, reinforced-plastic radomes, since it is difficult to arrive at dependable design values. As with other structural materials, the ultimate strength of glass fiber laminates is reduced by cycles of repeated or reversed loads.

The application of stresses as low as 75 percent of the instant ultimate stress will result in failure if the time of application is sufficiently long. The variation of time to failure with the amount of applied stress is not well defined.

Table 8-VI. Typical Mechanical Properties of Parallel Laminated (1/8-Inch Thick), Longitudinal, Low-Pressure Laminated, Glass Fabric Base Plastic Material

Fabric No. or Weave	Ultimate Tensile Strength (psi)		Compressive Strength (psi)		Flexural Strength (psi)		Flexural Modulus of Elasticity (Initial) (psi 10^6)	
	Dry	Wet	Dry	Wet	Dry	Wet	Dry	Wet
112	40,000	38,000	33,000	30,000	50,000	45,000	2.6	2.5
116	40,000	38,000	30,000	27,000	45,000	39,000	2.6	2.5
128	40,000	38,000	23,000	21,000	45,000	39,000	2.6	2.5
162	40,000	38,000	16,000	14,000	33,000	29,000	2.2	2.1
164	40,000	38,000	16,000	14,000	33,000	29,000	2.2	2.1
120	40,000	38,000	33,000	30,000	50,000	45,000	2.6	2.5
181	40,000	38,000	35,000	30,000	50,000	45,000	2.7	2.5
182	43,000	40,000	32,000	29,000	45,000	40,000	2.6	2.5
183	43,000	40,000	30,000	27,000	45,000	40,000	2.6	2.5
184	43,000	40,000	26,000	23,000	45,000	40,000	2.6	2.5
143	80,000	75,000	48,000	43,000	90,000	78,000	4.7	4.5
Mat	20,000	18,000	20,000	18,000	25,000	20,000	1.4	1.2

Mechanical properties of polyester laminates are commonly obtained on sheets 1/8 to 1/4 inch thick. Tests have shown, however, that tensile, compressive, and flexural properties are significantly lower for very thin sheets, particularly below about 1/16 inch thick. Some solid wall radomes are in this range and the designer must take this effect into account.

The use of 181-weave glass cloth, commonly employed in the manufacture of aircraft parts, is fairly standard for testing and evaluating various laminating resins. Most data on the strength of reinforced laminates made with this fabric and various resins have been published. For the last six years, 181 cloth has been used in the manufacture of radomes and other structural aircraft parts. It has the following advantages. It has good drapability for compound curves. It is relatively thin (0.0085 inch) so that it may be used to advantage in thin or thick laminates. It is nearly equal in strength in both the warp and fill directions; there are 57 warp yarns and 54 fill yarns per inch. Fill yarns are parallel to the length of the roll and warp yarns are perpendicular to the length of the roll. In comparison with other weaves it has high strength in relation to its thickness and weight.

It is also recognized that the finish on the glass cloth plays a significant role in the ultimate mechanical properties of woven-glass reinforced laminates. In general, Volan A and Garan has been approved under MIL-F-9118, and a great deal of data on 181-Volan with polyester resin has been accummulated.

With phenolics and epoxies 181 NOL finish has shown considerable merit, but this finish has not been finally approved under MIL-F-9118. Table 8-VII, extracted from an article by Silver and Erickson[71] of NOL on the influence of finish on the mechanical properties of 181 glass-reinforced laminates with P-43 (a polyester resin), Epon 828 (an epoxy resin), and BV-17085 (a phenolic resin), is presented to illustrate this point. A considerable amount of research and data on plastic laminates has been reported by Forest Products Laboratory and Wright Air Development Center(see Reference 59 through 69).

Under sponsorship of Wright Air Development Center, Bureau of Aeronautics, and the Civil Aeronautics Administration, Forest Products Laboratory has developed methods of theoretical analysis of plastic laminates and sandwich constructions to aid the design of structural aircraft parts. In addition, Forest Products Laboratory, in cooperation with members of the armed services and members of aircraft companies on the ANC-17 Panel, has issued the ANC-17 Bulletin "Plastics for Aircraft."[70] This bulletin has all the latest approved data on properties and criteria for use in designing reinforced plastic structures for aircraft, and is recommended for any design data.

As would be expected, the physical properties of glass-reinforced laminates vary with temperature. Some data are available on the influence of temperatures as low as -70° F which indicate that mechanical properties of glass-fabric reinforced laminates generally improve as the temperature becomes lower.[72, 73, 74] The increase in strength varies both with the type of resin and the property involved.

Polyester resins for low pressure laminating conforming to Specification MIL-R-7575 (Reference 75) possess a wide range of strengths at temperatures as low as 200° F. Woven glass laminates made with polyester resins, in general, lose most of their strength when exposed to temperatures over 200° F. Relatively few polyester resins will give laminates that maintain 50 percent of their strength at temperatures as high as 300° F.

A considerable amount of research has been conducted on heat-resistant laminates fabricated from glass cloth and silicone, triallylcyanurate, and phenolic resins.[16, 19, 24] Table 8-VIII, compiled from data extracted from a Wright Air Development Center Technical Report by J. Wier and D. Pons,[25] indicates the strength that woven glass cloth laminates can maintain at temperatures up to 700° F after 1/2 hour exposure at the temperature of test. Table 8-IX gives properties of glass cloth laminates with silicone resin DC-2106.

The outer skins of a sandwich radome usually determine its elastic and strength properties; the center lamination, or core, serves to separate the facings and to restrain them from becoming elastically unstable. The facings are therefore usually made of strong, rigid materials having a high modulus of elasticity and the cores of light materials having only sufficient elastic and strength properties to accomplish their purpose. Most radomes of sandwich construction can be analyzed as a three-ply laminate in which the mechanical properties of the core are very different from those of the facings. In the determination of the mean elastic and strength properties of such a construction, the interaction between the core and the facings is considered, as well as their respective mechanical properties. The materials of the core and the facings will be considered to

Table 8-VII. Ultimate Flexural Strength (12 Plies of 181 Style Glass Cloth Laminates with Various Finishes – Parallel Laminated – Tested in Longitudinal Direction)66

Finish	Polyester Paraplex P-43			Epoxy Epon 828			Phenolic BV-17085		
	Dry	Wet	% Resin	Dry	Wet	% Resin	Dry	Wet	% Resin
181-112	47,800	31,700	30.2	73,000	53,000	30.6	52,000	30,000	29.8
181-136	75,100	65,900	32.7	73,100	63,300	32.7	55,000	27,800	29.4
181-Volan	86,600	66,900	28.1	89,000	79,600	31.0	76,600	75,500	29.2
181-Garan	89,200	71,800	32.2	74,400	65,600	31.4	44,600	47,200	29.4
181-NOL	94,200	65,100	29.1	98,300	91,000	26.5	98,500	99,600	29.3

Table 8-VIII. Average Ultimate Flexural Strength, Modulus of Elasticity, and Loss in Weight (Heat Resistant Laminates of 181 Glass Cloth Tested at Temperature After 0.5 Hour at Temperature)[25]

Temperature (° F)	Silicone DC-2104			Phenolic CTL-91-LD			Triallylcyanurate Laminac 4232		
	Flexural (psi)	Modulus (× 10^6)	% Loss*	Flexural (psi)	Modulus (× 10^6)	% Loss*	Flexural (psi)	Modulus (× 10^6)	% Loss*
80	25,000	2.3	-	62,500	4.2	-	39,800	3.0	-
300	13,100	1.8	0.1	59,700	3.8	-	42,300	2.8	3.2
400	10,400	1.9	0.2	58,500	3.9	1.9	42,400	2.8	3.2
500	9,000	1.8	0.2	51,000	3.6	1.8	32,400	2.6	3.6
600	8,600	1.8	0.2	45,700	3.6	2.8	22,800	2.3	9.9
700	7,500	1.6	0.5	32,100	3.3	6.5	10,100	1.6	26.4

*Loss in weight based upon resin

Table 8-IX. Properties of Silicone Resin DC-2106 and Glass Cloth Laminate (Estimated Resin Content 40 Percent)

	Room Temperature	500° F after 1/2-hour exposure
Tensile Strength (psi)	53,900	31,100
Compression Strength (psi)	23,800	6,280*
Flexural Strength (psi)	41,000	15,500
Flexural Modulus (psi × 10^6)	2.6	2.1
Specific Gravity: 1.93		
Water Absorption (percent in 24 hours): 0.10		

* At 375° F

be orthotropic and oriented so that the natural axes of all three plies are parallel to each other, thus forming an orthotropic laminate. In the design of sandwich radomes, material for the facings is chosen that will be acceptable both from an electrical and structural standpoint.

For design data and test methods on sandwich fabricated with glass-reinforced laminate faces, the AIA Reports, MIL-STD-401 (References 76, 77, 78) and ANC-23 Bulletin on sandwich constructions for aircraft are recommended.

N.A.C.A. and Forest Products Laboratory have also issued a number of reports on design analysis and various physical properties (References 35, 36, 37, 92, 93).

A great deal of research and development work on honeycomb or foamed-in-place core sandwiches with woven glass skins for specific applications, which has not been reported in the literature, has been carried out by various organizations.

Some data on high temperature sandwiches have been reported in Wright Air Development Center Technical Report 54-249.[45]

SECTION F. FABRICATION METHODS FOR PLASTIC RADOMES

8-24. Methods of Fabricating Radomes

MIL-R-7705A (ASG) of 12 January 1955 outlines the procedure to be followed by the fabricator in obtaining approval of his materials process specification. Related Federal and Military Specifications are listed. Usual methods of fabricating various types of radomes are given in Table 8-X.

Table 8-X. Usual Methods of Fabricating Types of Radomes

Radome Type	Method	Materials
Solid		
thin	bag	GF* or nylon laminate
half-wave	bag or matched die	GF with heat-resistant resin
type B	bag, matched die, lathe-turned	GF with heat-resistant resin and pigments
"A" Sandwich		
foam-in-place	matched die	GF laminate polyurethane foam core
honeycomb	bag	GF laminate, GF phenolic-core cell walls
pre-formed core	bag or press	GF laminate, foam core
Multiple "A"		
heat de-iced	bag	GF laminate, fluted GF core
broadband	matched die or bag	foam or honeycomb core
Half-Wave Sandwich	bag or matched die	GF laminate, loaded foam with or without honeycomb partitions

* GF: glass fiber cloth

8-25. Bag Molding

A typical vacuum bag molding process has as the principal steps: (1) preparation of resin, fabric, bearing blocks, and inserts; (2) lay-up of the fabric in a prepared female mold or on a male mold; (3) elimination of air; (4) cure of the outer skin layers; (5) incorporation of bearing block inserts; (6) preparation and incorporation of core (in sandwich construction); (7) lay-up of inner skin layers; (8) second cure; (9) permissible repairs; (10) trimming; (11) post-cure when required; (12) finishing; and (13) identification.

Preparation of Resin, Fabric, Bearing Blocks, and Inserts.

In preparing the resin, the amount and type of catalyst recommended by the supplier is thoroughly dispersed with a mechanical agitator, avoiding the incorporation of excess air. Unless it is to be refrigerated, only enough is prepared to meet 8 hours requirements.

The glass fabric, cut to approximate size, is immersed in a tank of catalyzed resin and soaked until thoroughly saturated, as indicated by uniform color. It is then removed and the excess resin squeezed out until the fabric contains 95 ± 5 parts of resin for every 100 parts of fabric by weight. It is stored on a revolving roll or stretched on flat aluminum cauls or a cellophane-covered bench, and covered, in each case, with cellophane until time of use. Then, as each piece of fabric is removed for lay-up it is checked to remove resin "pools." Figure 8-5 shows the machine impregnation of fabric before cutting.

In general, bearing blocks are laid up in the form of belt sections around the circumference of the radome. After premolding they are machined to the correct dimensions.

To meet the requirements of MIL-P-8013, laminate voids must be eliminated to the extent presently obtainable with good commercial workmanship. In solid-radomes this limits the thickness that can be laid-up in any one molding operation to about 1/8 inch.

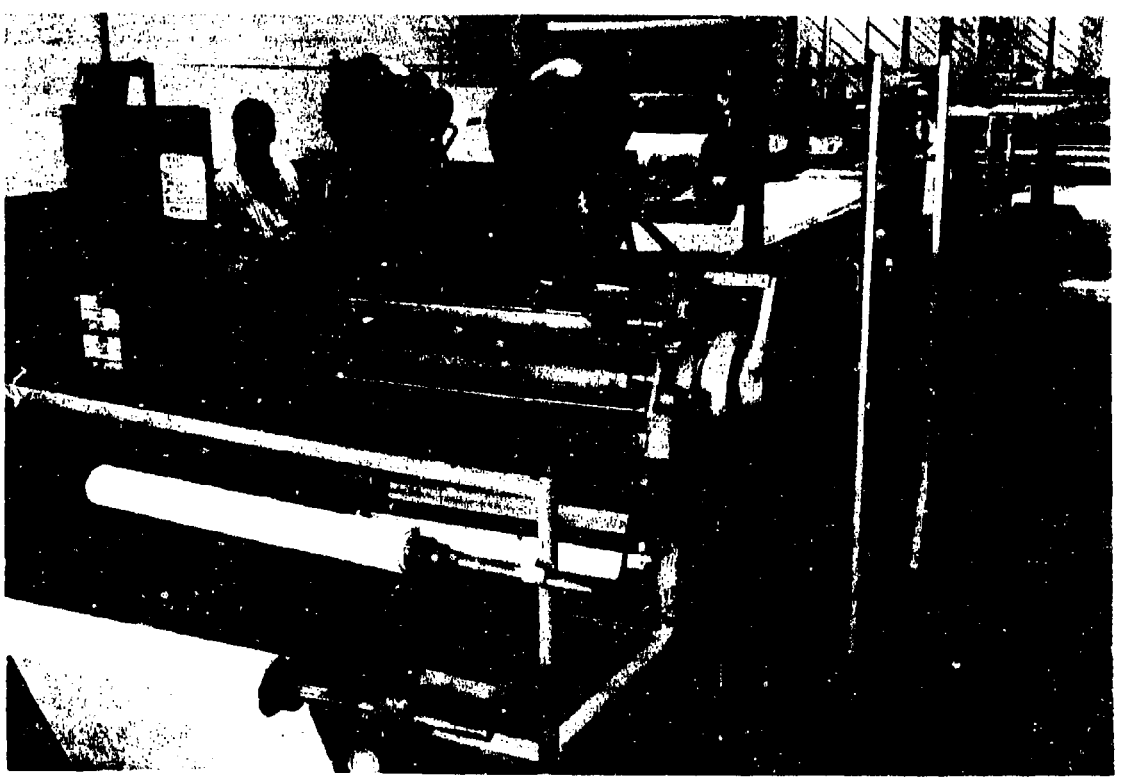


Figure 8-5. Machine Impregnation of Fabric (By permission of North American Aviation, Inc.)

Lay-up of Fabric in Mold. Generally, the woven glass cloth, after tailoring, is laid upon the surface of the male mold or in the female portion of the mold after coating with a parting agent. Most parting agents used are waxes such as carnuba, lacquers based upon cellulose acetate or vinyls, or silicone oils or greases. They are usually applied by brushing or spraying.

In the lay-up of the skin layers each piece of fabric is worked tightly to the mold, templated, and cut to avoid wrinkles. In some cases pieces must be butt-jointed. Otherwise a joint 3/4-inch wide ±1/4-inch is used, the number kept to a minimum, and the joints staggered to avoid an excess of crossing over other joints.

The following faults in molding technique have been noted. In one radome, lap joints in the glass cloth of the skins were allowed, and considerable freedom as to their number and location was permitted. This procedure produced electrically unsatisfactory radomes. For this case the joints should have been butt joints; their number should have been reduced to the minimum by means of careful lay-up and tailoring. All butt joints should have been spaced or staggered to avoid planes of weakness. The lay-up technique has to be carefully planned and laid out for each radome. The widest fabric should be employed and more use should be made of deformable fabric constructions, such as satin-weave, or special woven or sewn-fabric lay-ups that match the contour of the radome. Once the lay-up design is complete, it should be specified in detail and inspection should insure that it is adhered to during fabrication.

In another radome, fabricated by bag molding, the vacuum bag was badly fitted; this resulted in creases or depressions in the surface of the laminate. The effect of surface wrinkles, creases, butt and lap joints, and high and low resin content on properties of laminates has been investigated by Forest Products Laboratory.[79] This report indicates that all these factors are generally detrimental to the various physical properties of the laminates and should be kept to a minimum.

Elimination of Air. Some of the methods of eliminating air to obtain a void-free condition comprise: (1) vacuum wiping; (2) prewiping; (3) gelation of resin in fabric impregnation; (4) use of a perforated caul. For vacuum wiping the proper number of plies are placed in the female cavity, excess resin and air are stroked out, and the laminate is covered with a transparent layer of polyvinyl alcohol film, around the edges of which runs a porous vent-fabric leading to vacuum lines. Then, with contoured wiping tools, excess resin and air are wiped from the center of the laminate to the vents until no air bubbles or fibers are visible to the eye. It is an essential part of the technique that there is a continuous liquid seal of resin between the covering cellophane and the laminate. The layers of glass cloth have a natural springiness, but, provided the seal is intact, no air will enter. If a pinhole is made in the cellophane, or if a strand of glass fiber extends across the seal, air will enter the laminate very rapidly, and it cannot normally be swept out again because the excess resin has been previously removed. The number of plies of glass cloth should be carefully controlled so that the amount of resin squeezeout or runoff is such that the percentage of resin in the final laminate is 38 ±2 percent.

In the prewiping process, the air is worked out prior to lay-up in the mold, while the layers of impregnated cloth are stretched out on a hard, smooth surface. Wiping can be dispensed with if pre-impregnated fabric, prepared in such a way that the resin is brought to a semi-gel state under conditions which eliminate entrapped air, is used.

A perforated molding caul is usually a fiber glass laminate about 1/32 inch thick or a 1/16 to 1/8 inch thick contoured flexible rubber sheet. The perforations are 3/32 to 1/8 inch vent holes on 1 1/2 to 2 inch centers. Both sides of the caul are coated with a polyvinyl alcohol solution. The caul is placed to cover the laminate. A layer of coarse fabric is placed over the caul for venting of air. Over this is placed cellophane and then a rubber bag. Vacuum is drawn and held up to 30 minutes to eliminate air prior to curing.

In most solid radomes, it is desirable to have transparent, void-free laminates. This type of laminate is produced by sweeping out all the air bubbles with an excess of resin, keeping the number of lap or butt joints to a minimum, and curing the resin at a relatively low temperature so the refractive indices of the polymerized resin will be very close to that of the glass cloth. If a high temperature in the range of 225 to 250° F and a high rate of cure are used, the refractive index becomes higher and the resultant laminate will be opaque and slightly white in color.

If heat is applied at too high a rate, bubbles appear throughout the laminate. Some believe that these voids are due to expansion of air dissolved in the resin; more probably they are

bubbles caused by vaporization of the free styrene in the polester resin, possibly with some oxygen bubbles caused by catalyst decomposition. It has been observed that even after gelation at low temperature, when the laminate is rigid enough for removal from the mold, further heating at 200° F still produces voids.

There is no reliable data available that shows any significant difference in the strength of the transparent and opaque laminates. However the transparent laminates appear to be desirable for quality control, since a quick visual inspection will show any defects in the radome.

Cure of Outer Skin Layers. Curing of the laminate is conducted by the temperature-time cycles recommended for the resin. An ascending temperature cycle is employed, and is timed in a manner to avoid vaporization. After cure, the bag is removed and the skin is carefully inspected for defects.

Incorporation of Bearing Block Inserts. Before incorporation of the bearing blocks or layup of a core of additional skin layers, the inner surface is first sanded and then treated with a very light coat of resin. The dimensioned bearing blocks and inserts are then put in place. If a preconstructed core is to be used, it is inserted at this time. Otherwise, the inner skin layers are added and processed in the same way as the outer layers.

Core Construction. The following is a technique for incorporation of a honeycomb core: the flat or preformed sections of impregnated honeycomb are transferred to the partially constructed radome in the mold and crowded in tightly to form locking joints. If the radome has reverse curves and the core is not preformed, flat core sections are pressed against the curvature and the assembly is cured in place locally.

Another type of core material, developed for de-iceable airborne radomes, is a fluted core. The flutes usually consist of thin, U-shaped channels of 112 or 120 glass cloth impregnated with resin and cured.

In the process developed and used by the Douglas Aircraft Company, glass fabric impregnated with resin is wrapped over rectangular-shaped wax mandrels, which are then carefully laid together so as to form a core structure of the required thickness. After the skins and core have been bonded together and cured at low temperature, the finished radome is gently heated so that the wax can be melted out. The method has great utility for de-iceable radomes, since the cavities left by the wax



Figure 8-6. Fluted Core Chin Radome (By permission of Bruswick-Balke-Collender)

form the necessary air channels. There is some doubt as to whether sufficient support is given to the face skins by the larger size of corrugation, and the rain erosion resistance has been shown to be very poor. A slight disadvantage of the Douglas system is that the wax mandrels must be melted down and reshaped for each radome. There is no specification on this type of core material, and no published reports on the process or strength of the resultant sandwich. Figure 8-6 shows a fluted core chin radome.

Greater pressure may be needed to laminate fabric socks or to overcome the resistance to curvature of thick sections of honeycomb.

If pressure molding with a mating inner die or an inner pressure bag is to be used, the steps up to this point are essentially the same. The cure cycle for press-molded parts will depend upon the mold construction, mold material, and part construction. References 80 through 83 are suggested for additional information on molding processes.

Trimming. After completion of all molding operations, the radome may be trimmed, using the flanges of the mandrel or a suitable trim fixture as a guide. Prior to finishing, the completed radome is inspected for defects.

Permissible Repairs. Allowable or repairable defects are described by MIL-P-8013 and MIL-P-9400. Blisters are repaired by puncturing, injecting resin, applying pressure until

cured, and then are lightly sanded. Areas lacking resin are given an additional coat of resin. Excessive thickness buildups are removed by grinding provided the reinforcing plies are not disturbed.

Post-Curing. For radomes to be used above 200° F, post-curing is usually necessary to remove constituents capable of vaporizing with resultant damage to the laminate. The post-curing time-temperature program, which can be obtained from the resin supplier, is planned for an ascending scale of temperatures in the shortest time that will not cause blistering or crazing. The product usually darkens under these conditions, but this is of no importance.

Finishing. If application of an erosion-resistant finish is called for, this is the next step. With care being taken not to expose the fabric, the glaze of the surface film of resin is removed with light sanding. After removal of sanding dust, any erosion resistant coating conforming to MIL-C-7439 may be applied.

After inspection of the finished part, radomes which have been accepted are labeled in accordance with the purchaser's prints or other applicable specifications. Crating is normally regulated by specification.

Figures 8-7 through 8-10 illustrate some of the steps in the vacuum bag molding of a chin position radome for the installation of the AN/APS-20E search Radar under the Royal Canadian Air Force Maritime Reconnaissance, Canadair, Limited, CL-28 version of the Bristol "Britannia." Figure 8-7 shows the two mirror image mold halves, at the time of manufacture the largest aluminum pressure castings yet made. Electrical strip heaters provided on the back of each half are wired to a programming console of timers and relays. The castings were impregnated from the back face with an anaerobic silicone resin, while the front face was treated with Garalease 915. Other suitable parting agents available included Vegin AC, Dow-Corning DC-4 and DC-7 and L3X425 Micostrip.

In Figure 8-8, (the outer skin having been cured, sanded, coated with uncured resin mix, and the bearing block molding, installed) 1 1/4 inches thick, 1/4-inch cell, uncured, resin-dipped Hexcel honeycomb core is being fitted tightly into place. The construction provides for the retraction of the nosewheel through doors in the aft end of the radome.

In Figure 8-9 the mold halves have been alined optically and assembled, and the completed honeycomb sandwiches spliced longitudinally without electrical discontinuity. The edges, bearing blocks, inserts, and nosewheel door frame areas will be given their final trim in the mold, but first the radome will be removed,



Figure 8-7. Pressure-Cast Aluminum Split Mold (By permission of McMillan Industrial Corp.)

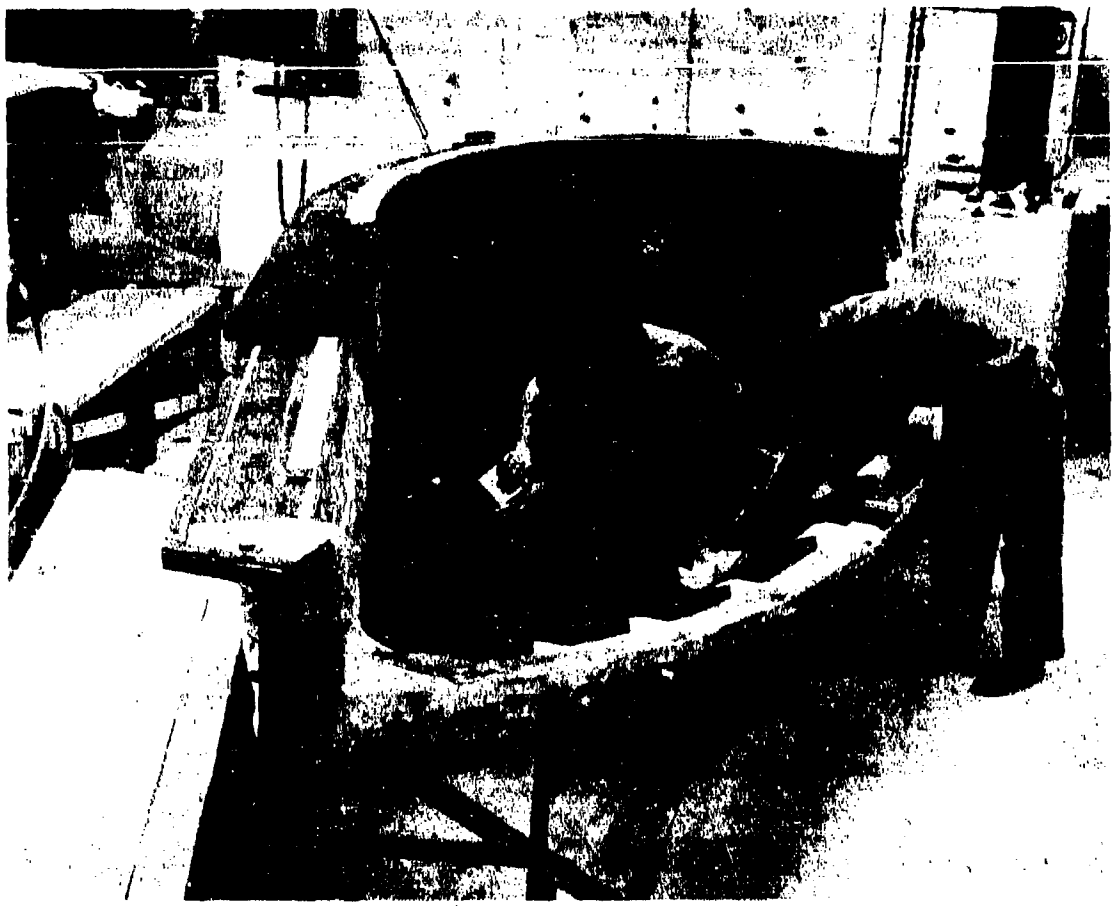


Figure 8–8. Laying–Up Honeycomb Core (By permission of McMillan Industrial Corp.)

inspected, and rough-trimmed. In Figure 8-10 it is seen temporarily out of the mold for rough trimming.

Figure 8-11 illustrates spray application of a rain erosion protective coating.

8-26. Matched Tool Molding

Matched tool molding processes are generally employed for radomes based upon (1) foamed-in-place cores; (2) sharply curved thick honeycomb; (3) preformed mats; or (4) molding compounds.

Foamed-in-place Cores. The use of a foam core for sandwich radomes intrigued early workers, since it offered possibilities of reducing the amount of labor involved in laying-up the honeycomb core, as well as improving



Figure 8–9. Sandwich Radome Ready for Trimming (By permission of McMillan Industrial Corp.)

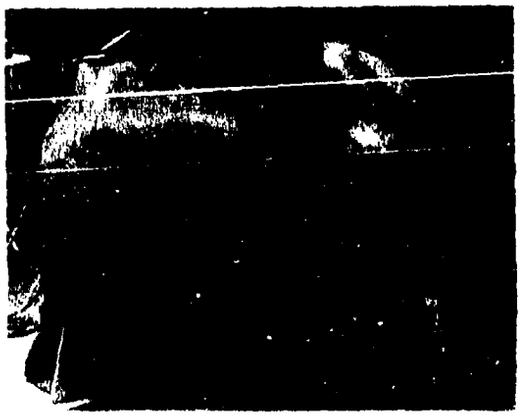


Figure 8–10. AN/APS–20E Radome After Preliminary Trim and Inspection (By permission of McMillan Industrial Corp.)

the bond strength and reducing the electrical variations because greater uniformity in the sandwich construction could be achieved.

Early investigations consisted of trying to foam polyester resins with carbonates or other gas-producing chemicals. While these foams were a step in the right direction, they were generally unsatisfactory because they would not rise and fill the cavities of very large radomes, and were nonuniform and too dense to give satisfactory properties for most radome applications.

At the end of World War II, a Hycar rubber foam was produced commercially that had good uniformity, density, and electrical properties. This foam, however, could only be produced in blocks that had to be cut into desired thickness. The Hycar foam was somewhat thermoplastic and could be formed into compound curvatures. However, the use of a foamed-in-place core had more to offer, and after a considerable amount of research the first polyurethane core material to be extensively used was introduced in 1949.[84, 85, 86]

Polyurethane foams are based upon the reaction of an unsaturated alkyd resin with an isocyanate. These types of foam are the result of a reaction of the free hydroxyl (-OH) and carboxyl (-COOH) groups of the alkyd resin and the isocyanate to give a resin molecule of increased length and the liberation of carbondioxide gas. This reaction can be illustrated by the following general equation:

$$R\text{-}COOH + R'NCO \rightarrow RCONHR + CO_2$$

The chief advantage of the foamed-in-place core over honeycomb or other types of core is the ease of fabrication. The preparation of the foam involves no more equipment than a mixer and a temperature recording device; hence this part of the equipment is low cost. Intricately shaped structural sandwiches can be molded with ease. However, it must be realized that matched metal molds are required. Although these molds are not cheap, radomes fabricated by this method possess the following advantages: (1) Uniformity in construction: (2) Lower unit cost on large volume production; (3) Possibility of making tapered wall thicknesses with greater control over final wall thickness.

The greatest disadvantage in the use of foamed-in-place radome construction is the more costly tooling required. Usually, one set of metal or plastic tools is used to preform the inner and outer skins. After the skins are fabricated and inspected to determine their compliance with design thickness specifications, the sanded skins are placed on a set of matched metal tools, usually mounted in a hydraulic press or on some type of lifting device that will locate the male mandrel accurately with respect to the female cavity. The foaming mixture is prepared and then poured into the female portion of the mold containing the outer skin, and the mandrel containing the inner skin is lowered into place. Spacer blocks are used to maintain core thicknesses when the entire assembly is bolted together. Heavy molds are required to withstand the pressures developed during the foaming reaction. If the mold is tightly closed, the pressure can reach 100 pounds per square inch. After the foam has risen to fill the space between the skins, it is



Figure 8–11. Spraying Erosion Coating (By permission of Brunswick–Balke–Collender)

subjected to a cure cycle which develops its full physical properties.

With foamed-in-place radome construction, it is possible to take full advantage of any thickness variation that may be required by different angles of incidence over the wall area. Thus, a vertical tapered-wall construction can be built into each radome with no more effort than would be required for uniform wall thickness.

The materials for producing foams can be obtained as two component systems commercially from such companies as Nopco Chemical Company or American Latex Company, or the components can be purchased from the following:

Foaming Resin	Tolylene Diisocyanate
American Cyanimide Co.	E. I. DuPont Co.
Mobay Chemical Co.	National Aniline Co.
Pittsburg Plate Glass Co.	Mobay Chemical Co.

The foaming process that can be used with such resins as Selectron 5922 from Pittsburgh Plate Glass or Laminac 4231 from American Cyanamid, and tolylene diisocyanate from the above sources, is as follows.

1. A weighted amount of resin is poured into the mixer.

2. For every 100 parts of resin by weight, 85 parts by weight of tolylene diisocyanate is added slowly to the resin. If the tolylene diisocyanate, which has a viscosity in the same range as water, is added all at once to the alkyd resin, it floats on top of the resin, forming a distinct phase, and splashes out when the mixer is started. Therefore it is necessary to add the tolylene diisocyanate in about four or five portions at 3 to 4 minute intervals. The mixing of the tolylene diisocyanate and the alkyd resin into a homogeneous blend takes 20 to 25 minutes at 75° F.

3. The reaction between the foaming agent and the alkyd resin is very exothermic. It is necessary to keep the batch at a temperature of 75 to 85° F at all times by the addition of crushed dry ice. If the temperature is allowed to reach 95° F, the reaction will proceed so rapidly that the entire foaming reaction will be completed in a few minutes without any control.

4. After the tolylene diisocyanate has been completely blended into Selectron 5922 or Laminac 4231, 2 to 3 percent by weight of di-tert-butyl peroxide catalyst, based upon the resin, is added to the mixture.

5. As the reaction proceeds, the viscosity increases. After 35 minutes of total mixing time the viscosity of the mixture is taken at 3 to 5 minute intervals until a viscosity of approximately 1,500 poises at 80 to 85° F is reached. This viscosity is usually reached after 45 to 55 minutes of total mixing time. At this time 8 to 10 percent by weight (based upon the resin) of Aerosol-Acetone solution is added. This solution contains 10 percent of Aerosol OT in 90 percent of dry acetone.

6. Mixing is continued until a viscosity of the mix is reduced to approximately 500 poises. The foam is then poured into the mold. The mold is then closed and the foam cured for 1 hour at 150 to 160° F; for high temperature foams an additional cure of 2 hours at 300° F and 4 hours at 400° F is needed.

To obtain any desired density of foam core material, the following calculations can be used.

1. Determine volume of the cavity or wall thickness of the sandwich in which the foam is to be used.

2. Using the following relationship

$$D = \frac{W}{V} \qquad W = DV$$

where D = density, W = weight, and V = volume, the weight in pounds of foaming mixture required is calculated. This includes both resin and diisocyanate.

3. Calculation of correct amount of each component is then made by using the resin-diisocyanate ratio applicable to the resin employed. For Selectron 5922 and Laminac 4231, the ratio is 100 to 85. Thus for each 100 parts of resin, 85 parts by weight of diisocyanate is used.

For example, to obtain a 6 pounds per cubic foot density foam as described above, the following calculations were made.

1. Core for square test panel, size: 16 × 16 × 5/8 inches = 160 cubic inches = 0.0926 cubic foot.

2. $D = \frac{W}{V}$

$$6 = \frac{W}{0.0926}$$

W = 0.556 pound or 252.4 grams of material required

3. For Selectron 5922 and Laminac 4231 a ratio of 100 parts resin to 85 parts diisocyanate is used. The weights to be used are, therefore, resin — 136.4 grams and diisocyanate — 116.0 grams.

A general formula is given below for calculating quickly the necessary amount of resin and diisocyanate needed to obtain any desired density. Only the volume of the cavity of the sandwich need be known. From the equation W = V × D the total weight of material required can be found from

$$W = \frac{\text{Volume of core (cu. in.)}}{1728 \text{ (in. per cu. ft.)}} \times \text{Density (lbs. per cu. ft.)} \times 454 \text{ (g per lb.)} \quad (8\text{-}1)$$

or

$$W = \text{Volume of core} \times \text{Desnity} \times 0.263 \quad (8\text{-}2)$$

or

$$W = V \times D \times 0.263 \text{ total weight} \quad (8\text{-}3)$$

The resin-diisocyanate ratio is 100 to 85 or on a percentage basis.

100 g resin
85 g diisocynate

185 g

$$\text{Thus percentage of resin} = \frac{100}{185} \times 100 = 54.05$$

$$\text{Percentage of Diisocyanate} = \frac{85}{185} \times 100 = 45.95$$

Since Equation (8-3) gives the total weight required, the weight of resin in grams required therefore equals:

$$W = V \times D \times 0.263 \times 0.5405 = V \times D \times 0.1422 \quad (8\text{-}4)$$

Similarly, the required amount of diisocyanate is found from

$$W = V \times D \times 0.263 \times 0.4595 = W \times D \times 0.1208$$

Reference 87 describes a partially pre-expanded foam core structure that may be fabricated so that its final expansion pressure bonds it to skins in a matched-die mold system. A completely pre-expanded foam may be employed with the same bag molding process details as the conventional honeycomb core. It is, in fact, a conventional honeycomb core having each cell filled with an aluminum-powder loaded resin composition, partially or completely expanded as may be required. The entrapment of the loaded foam within discrete partitions provides a freedom from dielectric orientations, so that a sandwich made with this core, in place of the heavier solid half-wave or solid type B wall constructions, is suitable for use where severe polarization or boresight restrictions are necessary.

While there are numerous other methods and variations thereof for matched-die molding, it is only possible to treat at this time several of the principal ones, namely, preform molding; vacuum injection (Marco patent); and compression, pressure injection, and transfer molding.

Preform Molding. In the usual preform molding process, the male die is heated, the unimpregnated preform is dropped over it, and the resin mix poured onto the top of the preform. The press brings the male and female dies together, the movement becoming slower as the stops at the final matched position are approached so that preform air will have time to escape. When the resin has finally displaced the air, the resin appears as a flash.

Only moderate pressure is required to reach the stops if the preform weight is proper. If pressure is light it may be found later that air is trapped in the product or that there are resin-rich areas which may crack. If the pressure is above normal, resin-starved areas may be created due to excessive preform weight.[88] Gelling before the press is closed may prevent the resin from reaching the bottom of the preform. A wrinkled product may be due to a poorly fitting preform. The lower strength of a preform molding, compared with a fabric laminate, has limited its use to thick sections, as for the half-wave construction. Where specifications permit, a chopped fiber preform such as that shown in Figure 8-12 may be suitable.

Marco Vacuum Injection. Since a press is not needed, very large parts may be made by the Marco vacuum injection process. The matching dies are fitted together easily, as the bulk of the preform is kept low. The lower open edges of the two dies are immersed in a peripheral trough containing resin mix. A vacuum line at the highest point in the upper die sucks the resin

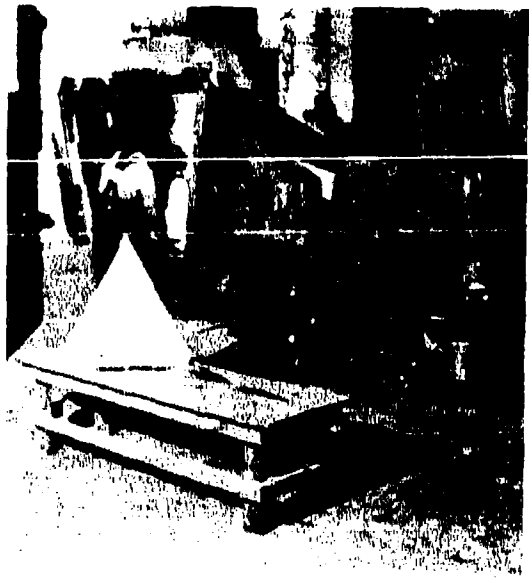


Figure 8-12. Making a Chopped Fiber Preform (By permission of Brunswick-Balke-Collender)

up through the mold cavity. With proper preform density, air removal is very good, but if lay-up of the preform is poor the relative distribution of glass and resin in the product is variable. When strength and uniformity requirements are high, the use of the process for airborne radomes is limited. References 81 and 82 contain additional information on preform and vacuum injection molding.

Knitted or woven fabric has been used. Both gravity-distributed and vacuum-injected resin distribution has been employed with knitted socks. The recent availability of seamless woven fabric socks has led to study of their use in pressure closed matched die systems with and without pre-impregnation. With proper product design the very stringent strength and dielectric uniformity requirements of missile and other supersonic radomes should be more readily met with seamless woven sock lay-ups.

Compression, Pressure Injection, and Transfer Molding. The details of the compression, the pressure injection, and the transfer molding processes are too well known throughout the plastics industry to require description here.[81] It is sufficient to say that matched-die compression molding has been successfully employed in the manufacture of small missile radomes, while transfer molding and pressure injection molding have provided precision control, density, and low cost for the production of antenna fed pressurizing covers.

Production of radomes by matched tool processes is shown in Figures 8-13 and 8-14. Figure 8-13 shows polyurethane foam ingredients being mixed by an operator wearing a gas mask. In Figure 8-14, he is pouring it through a screen into a female die in which the outer skin rests, already cured. The male die, seen above it, is covered with the cured inner skin.

8-27. Lathe Turning

Some manufacturers deduced that lathe turning might be suited to missile radome manufacture. Just as ground lenses are more accurate than molded ones, it was expected that turned and ground radomes would provide more uniform microwave characteristics than molded ones.

After giving considerable attention to die alinement techniques, other manufacturers have used matched molds. However, the necessity of adjusting radome wall thickness to the small changes in dielectric properties that occur from batch to batch, is a problem, and the placing of a pressure duct in the wall is not as easy as in the bag molding process, used as an adjunct to lathe turning. Of course, a matched-die molding could be lathe finished.

In the usual process a male mandrel is wrapped with resin-mix impregnated, woven-glass fabric socks or pattern-cut flat pieces.



Figure 8-13. Mixing Polyurethane Foam (By permission of Brunswick-Balke-Collender)

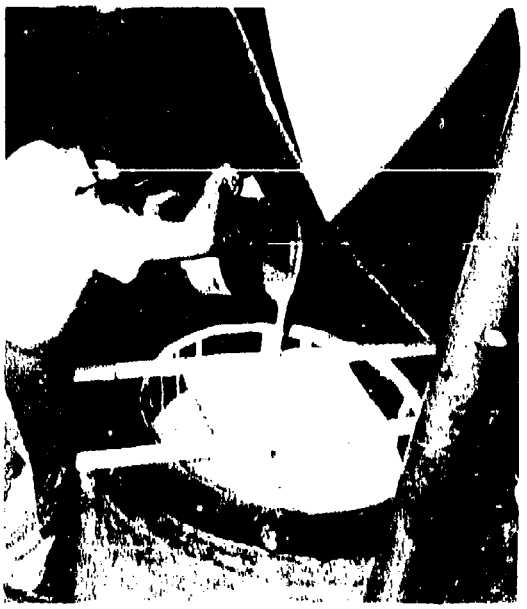


Figure 8-14. Pouring Foam Into Matched-Die Mold (By permission of Brunswick-Balke-Collender)

Naugatuck Chemical triallyl cyanurate resin, Vibrin 135, has been selected for high temperature strength and electrical characteristics. The total wall thickness is built up in a number of curings, and a transparent polyvinyl alcohol bag is used to facilitate wiping until the resin gels to attain freedom from voids. As each new series of layers is added, the outermost cured layer of the previous series is peeled off to provide a bonding surface.

The total number of layers is planned so that the final lathe grinding operation will not cut through any layer. To make this easy, the last group of layers is molded on a lathe cut base which will allow them to lie parallel to the final surface.

When the final outer surface has been ground, the radome is transferred to the surface finishing station, where it is rotated horizontally under heat lamps while a very thin coating of resin mix is applied. A boresight check may be performed just prior to finishing to determine whether any external thickness correction is needed.

Larger missile noses have been corrected with internal patches. Two contractors are known to employ insert phase measurements to locate areas in need of correction.

Progress in electrical design techniques has enabled these radomes to assume fineness ratios from 2.5 to over 4.0, and to possess pointed tips with apex angles less than 30°.

Fabrication of the half-wave and of the type B walls is very nearly the same, from the molder's viewpoint, except that type B walls comprise two solid quarter-wave thick shells that are slipped into each other and bonded together, with a few thin bands of loaded dielectric sandwiched in shallow grooves in the inner shell. (See References 48, 49, 50, 58, 83.)

In Figure 8-15 the lay-up of the fabric is shown. In Figure 8-16 it is shown being encased in a polyvinyl alcohol vacuum bag. Entrapped air is continually wiped out until gelling occurs, as shown in Figure 8-17. The automatic grinding of the cured build-up in a duplicating lathe shortly before the addition of the final outer layers is illustrated in Figure 8-18. A final polish grind will be given to the outermost surface. Tolerances of ± 0.001 inch may be attained. The last step in the process will be the post cure.

8-28. Tooling

Reference 81 is suggested to the reader for information on factors usually governing the type of mold, mold materials, and the design of molds for various processes. In radome fabrication the following factors, in order of importance, generally dominate in mold design: (1) part tolerances; (2) type of radome wall construction; (3) time available to tool-up; (4) quantity to be produced. Plaster, wood, plastic,



Figure 8-15. Lay-Up of Fabric, Missile Radome (By permission of McMillan Industrial Corp.)



Figure 8–16. Bagging Lay-Up, Missile Radome (By permission of McMillan Industrial Corp.)

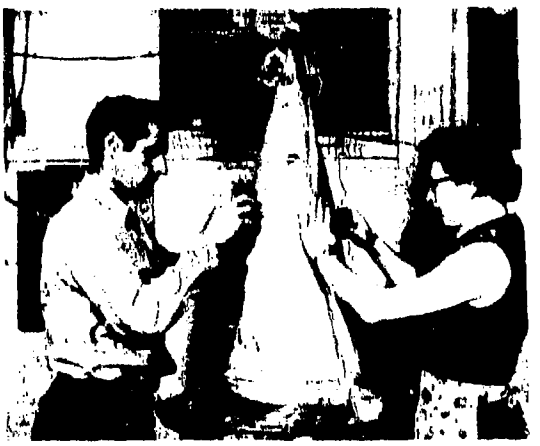


Figure 8–17. Wiping, Missile Radome (By permission of McMillan Industrial Corp.)

light sheet metal, and low density spray metal molds may be used to tool-up quickly if the first and second factors permit. However, if the quantity to be produced is so substantial that permanent cast or spun metal molds will be required, interim tooling must be regarded as an extra expense. Since part quality is the primary consideration in the radome market, product users generally prefer to invest in accurate permanent tooling.

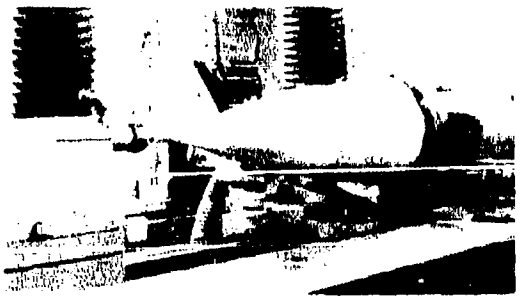


Figure 8–18. Lathe Grinding, Missile Radome (By permission of McMillan Industrial Corp.)

Methods of mass production are treated in Reference 82. Much material, published for the plastics industry, is available, and the prospective radome molder should evaluate it, bearing in mind the special requirement that large parts are to be molded with the accuracies usually specified only for small fittings.

For some time the expense and the long tool-up time associated with matched dies confined their use to foamed-in-place molding. The evolution of supersonic aircraft and missiles has, however, brought with it the need for radome strength plus transmission quality suited to high accuracy radar. This is leading to increased use of solid walls and matched dies or lathe turning methods.

A problem in fabrication with matched dies is that of maintaining the required tolerances in wall thickness in the scanned area of the radome. This problem is difficult to solve, since it requires extreme accuracy in the preparation and machining of the metal molds used in fabrication. Assume that steel has been machined at room temperature so as to give a cavity with a constant wall thickness of ± 0.005 inch, which is no mean feat for large molds. If the molds are heated unevenly to 250° F, the difference in wall thickness can theoretically vary another 0.010 inch, due to the difference in thermal expansion of certain areas. After molding-in this error, the molded radome will shrink another few thousandths of an inch. If these errors are accumulative, it is conceivable that a 0.250-inch, solid-wall radome could vary as much as ± 0.015 inch. One method of overcoming this difficulty has been to make the wall thickness oversize and to machine the glass-reinforced laminate wall to the desired tolerances. This is difficult to carry out unless the radome is a body of revolution.

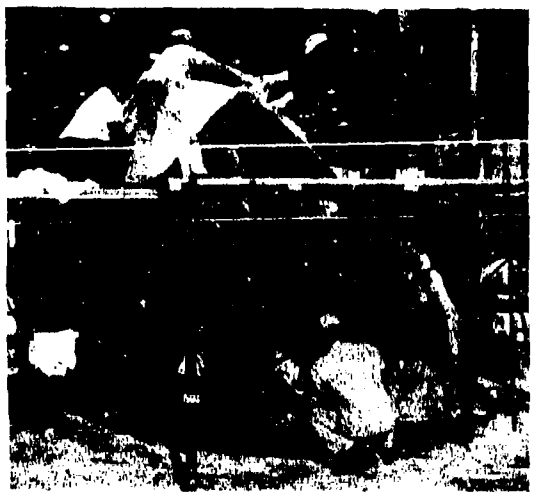


Figure 8–19. Lay-Up of Radome with Glass Fabric and Epoxy Resin (By permission of Goodyear Aircraft Corp.)

The low density core sandwich constructions will remain important in the ground radar field indefinitely, and will continue to have a place in the aircraft field with subsonic aircraft or in low load areas in supersonic use. For this reason tooling for bag molding remains in the picture.

Cast or spun metal molds are readily steam- or water-heated with jacketing or electrically heated with coils. Oven heating is less satisfactory but may be employed. Where pressure must be added to the effect of the vacuum bag a steam autoclave is convenient for large parts, while smaller parts may be pressurized by capping and pumping air into the mold cavity, the laminate being protected by the molding bag.

Ovens should be of a convection type capable of operating at up to 300° F. They should be equipped with vacuum outlets and reasonably accurate temperature and vacuum gages. Autoclaves should be capable of applying 60 pounds or more of pressure.

Metal molding cavities may be of spun or cast aluminum; chrome-plated steel; electro-formed nickel or other metal which gives suitable finish to, and parting from, the molded part. The surface of the cavity must be free of pits or scratches which would break the surface film of resin on the radome. It must be checked periodically for contour with templates and jigs, and the mold itself must be adequately supported to avoid distortion.

Cast resin and other types of molds must at least temporarily give substantially the same end result as metal molds. Glass fabric cavities are generally laminated with heat-resistant phenolic or polyester resins to a thickness of about 1/2 inch. The lay-up of a section of a large radome mold, using glass fabrics and epoxy resin, is shown in Figure 8-19.

Distensible rubber bags are generally between 1/16 and 1/8 inch thick. A compound commonly used has been Tyer Rubber Company No. 258. Non-distensible bags may be of Reynolds polyvinyl alcohol film or of neoprene-coated fabric such as DuPont Fairprene No. 5013.

Spray metal process construction of a female die for bag molding is illustrated in Figure 8-20. The metal is being applied directly to a mock-up of the part.

In Figure 8-21 a pressure-cast aluminum female die is being checked with an assembly of metal templates. Feeler gages are fitted between the template edges and the die surface.

The mounting edge of a radome which has been clamped into a trim fixture is being diamond-wheel ground in Figure 8-22.

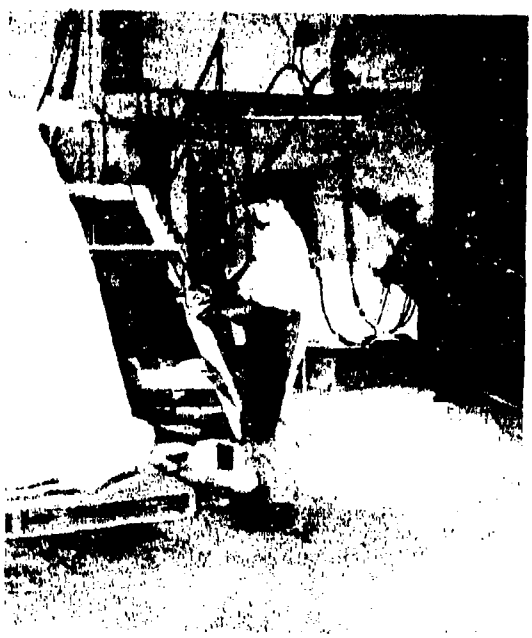


Figure 8–20. Spraying Metal on Mold Pattern (By permission of Brunswick–Balke–Collender)



Figure 8-21. Templating Pressure-Cast Aluminum Die (By permission of McMillan Industrial Corp.)

8-29. Methods of Obtaining Tolerances

The dependence of electrical performance upon the tolerances held in the manufacture of each radome leads the typical molder to be keenly interested in methods of achieving them. Quality must be sought, beginning with the obtaining of affidavits from the suppliers of the starting materials. On receipt, and again just before use, resins should be checked for viscosity and freshness. Cleanliness must be maintained in mixing them with catalysts and fillers. Control samples of proposed laminates must be prepared and tested for dielectric constant, loss tangent, and mechanical properties. Often the molder must certify that he has conducted such tests and achieved specification quality. Figure 8-23 shows an interferometer for use from -100 to 2,000° F for dielectric constant measurements.

The relative resin-fabric-air content of the laminate directly and profoundly affects strength and dielectric values. Pregelled, impregnated glass fabric with carefully controlled resin content may be prepared, but usually is purchased. The gelling guards against resin drainage in the laminate, and the laminate tends to be void free. Overlaps in lay-up lead to thickness buildups, sometimes beyond tolerance limits.

Honeycomb core material must be skillfully cut with specialized equipment to secure thickness accuracy. Unless the molder is adequately prepared, it may be better to buy honeycomb precut by the supplier to the desired tolerance. In Figure 8-24 honeycomb is being checked to a ±0.005-inch tolerance. Gravity, and curing viscosity effects, work against the uniform expansion of foamed-in-place core materials. The electrical harm will be most critical when the foam has a high electrical refractive index because of metallic loading. The loaded core material described in Reference 87 was designed for such a contingency.

In matched-die molding, accuracy of die dimensions is most important, but it is expensive. The total number of layers of fabric must be carefully planned in bag molding, single-die techniques. In prototypes a skin is sometimes built-up and cured to nearly the desired thickness, and a layer peeled off; then a carefully calculated addition of final layers is made. Careful wiping of the laid-up pieces of fabric insures not only freedom from voids, but, by removing excess resin, makes the total thickness more nearly a constant multiple of the total number of layers.

Laminating pressure and the relative humidity of the molding room have a very marked effect on thickness and strength. When the whole radome problem has been placed in the molder's hands, as it often is, his electrical engineering staff should avoid narrow banded designs wherever feasible.

Internal factors also control the effective electrical thickness. At the shorter wavelengths the sandwich constructions with low dielectric constant cores become so narrow banded that external and internal thickness tolerance become very tight unless exacting process control is used. The layer of resin which collects on the inner surface of each skin tends to vary. If this variation is excessive,

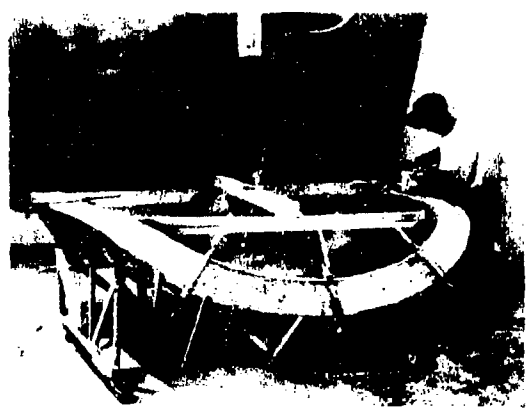


Figure 8-22. Diamond Wheel Grinding (By permission of Brunswick-Balke-Collender)

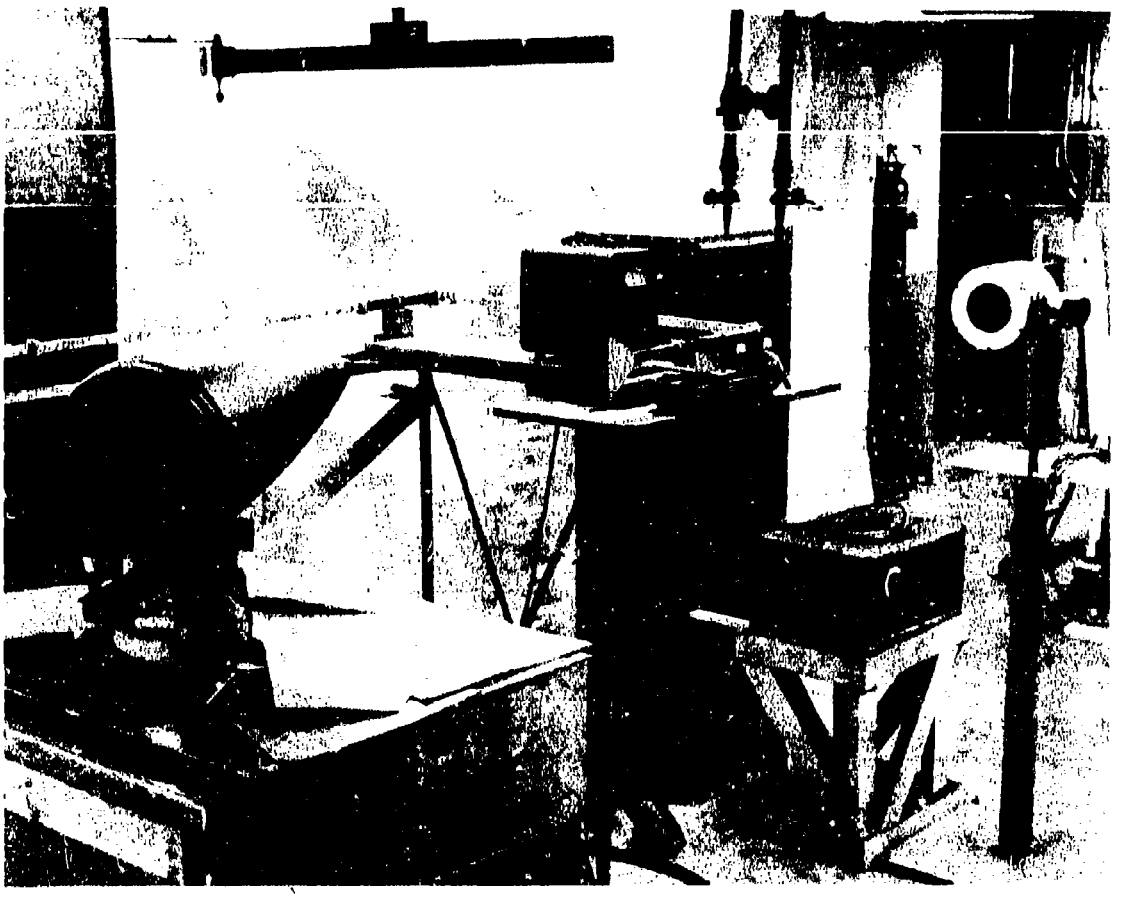


Figure 8–23. Wide Temperature Range Dielectric Constant Interferometer (By permission of McMillan Laboratory, Inc.)

electrical performance deteriorates noticeably. Variations in core density have a similar effect.

Grinding apparatus plays an important part in radome manufacture. Bearing surfaces for attachment to fuselage, or other, mounting rings must often meet exacting dimensional accuracy. Accurate grinding may (where specifications allow) be a vital factor in the control of the electrical performance of areas through which the radar beam passes. The rigidity and precision of grinder holders, guides, and reference points must be carefully planned. Mechanical and optical gages capable of spanning large distances with accuracy are available in adequate quantities in established radome molding plants. A multiple thickness gage fixture can be seen in use in Figure 8-25.

Thickness gages based upon various physical principles have been employed. General Electric, McMillan, and others have built magnetic gages. Radiation counters have been adapted to the purpose. Microwave thickness gages indicate the thickness from area to area as the radar would see it. For this reason these gages have become the principal control factor in several radome molding organizations. One such gage is shown in Figure 8-26. Their initial success has led the Wright Air Development Center to sponsor advances in their design. Among various methods of correcting wall thickness variations so detected, the Boeing Aircraft Company mechanized application of internal compensating patches has been notable. MIL-R-7705A(ASG) of 12 January 1955 requires test range electrical inspection. Figure 8-27

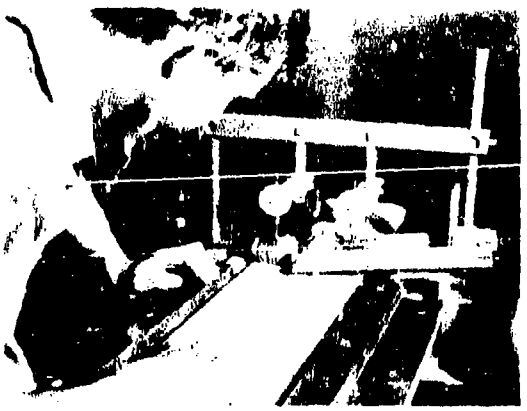


Figure 8–24. Controlling Honeycomb Core Thickness (By permission of Brunswick–Balke–Collender)

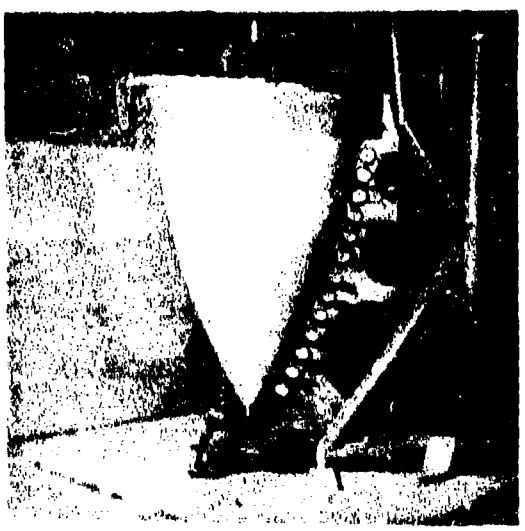


Figure 8–25. Multiple Thickness Gage Check (By permission of Brunswick–Balke–Collender)

shows a radome mounted over an AN/APS-20E on a CL-28 aircraft mock-up being placed upon a test tower of the Air Research and Development Command Ipswich Antenna Field Station.

8-30. Inspection Methods*

Except as a contractor may wish to conform to and exceed military specification standards,

*Radome test equipment and procedures are treated in Chapter 12.



Figure 8–26. Microwave Thickness Gage (By permission of McMillan Laboratory, Inc.)

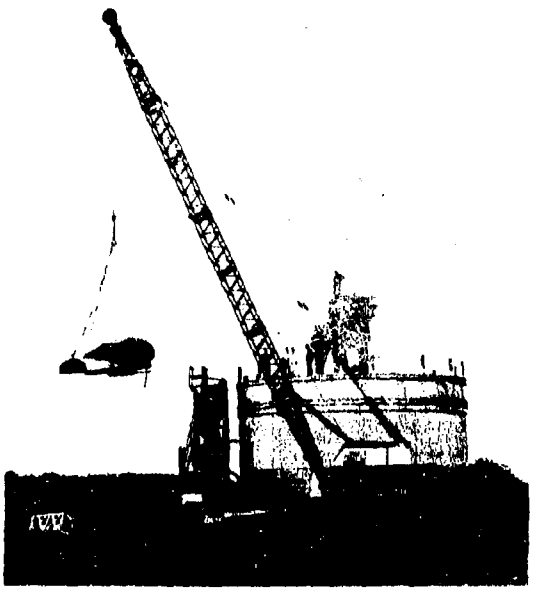


Figure 8–27. AN/APS-20E On CL-28 Mock-Up at Cambridge Research Center Test Range (By permission of McMillan Industrial Corp.)

MIL-R-7705A (ASG) of 12 January 1955 proves adequate for establishing inspection methods. For the present, microwave thickness gages, dielectric measuring equipment, and numerous other special electrical, mechanical, and chemical instruments find their principal roles in process control as means of obtaining tolerances in preparation for final inspection.

Adequate inspection departments, procedures, and records are essential factors in the production of radomes having optimum structural and electrical performance. These should cover tooling, incoming materials, materials in process, curing cycles, and the complete radome. All are highly important to the quality of the finished product.

Incoming material quality can be assured to a considerable extent by purchasing materials from reputable manufacturers under affidavit that they comply with the appropriate military specification. Routine tests should be performed on panels made up with incoming lots of fabric, resin, and core materials. Panel tests should also be performed on any materials which appear questionable during subsequent processing.

In-process control should include dimensional checks on core materials, premolded inserts, and other components as well as inspection of manufacturing procedures. These factors, perhaps, contribute the most to the performance of the finished part.

Inspection of the finished part should cover not only physical dimensions but such possible defects as blisters, wrinkles, lack of complete resin cure, and non-uniformity. Electrical and environmental performance provides the final criteria.

SECTION G. METHODS OF ATTACHMENT

In attaching solid or sandwich type radomes to the exterior of various aircraft, the designer usually has to take into account the fact that the radome must be removable for easy access to the scanner. This necessitates the use of mechanical fasteners such as nuts and bolts or Dzus fasteners.

Most radome housings are circular or elliptical in cross section at the point of attachment, so the use of a large number of nuts and bolts around the periphery of the base results in an attachment that is sufficiently strong to withstand the stress and moment systems imposed by even the largest radome housing.

In general, there are few published data relating the relative merit strength of various types of fastening. Figure 8-28 shows sketches of various types of attachment fittings used on the base of sandwich radomes. The reason for using an aluminum insert at the root of the radome is twofold: to transfer the loads from the aircraft to the skins of the sandwich radome, and to overcome the general low bearing strength of the glass-reinforced laminate. The extremely high compression and bearing loads caused by drawing up on nuts and bolts are taken by the various types of metal inserts shown in Figure 8-28.

Generally these aluminum inserts are bonded between the glass-reinforced skins with the same type of resin used in the fabrication of the radome skins. The surfaces of these metal inserts are prepared for bonding, usually by alkali cleaning and then by anodizing, as discussed in paragraph 8-15.

In some cases the metal inserts are primed with an adhesive primer that is baked on. The particular adhesive desired or the resin used in the fabrication of the radome is brushed on the faying surfaces of the radome skins and the metal insert and the assembly are cured under heat and pressure as a secondary operation.

The mounting holes are then jig-drilled in the metal insert, so that the radome can be precisely positioned on the aircraft.

Basic to the more effective use and application of solid and sandwich radome construction is the need of design criteria covering methods of attachment, under various conditions of support and loading. The accumulation of design data, however, is complicated by an almost unlimited number of possibilities and by the variety of conditions of each specific application with respect to stress and loading.

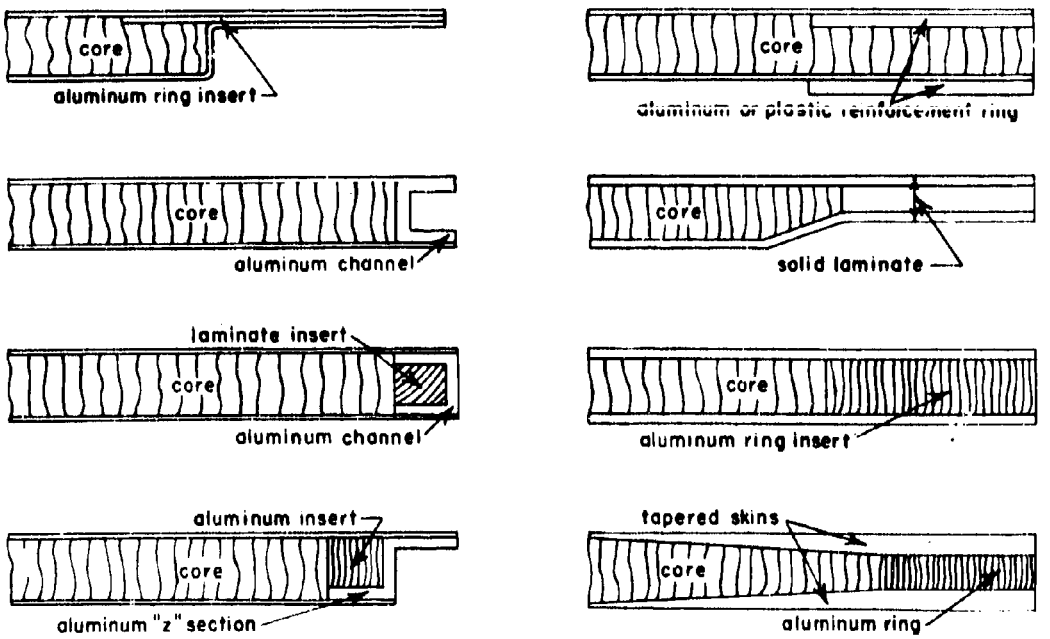


Figure 8–28. Sketches of Typical Glass–Reinforced Laminate Sandwich Radome Constructions, Showing Various Methods of Attachment

SECTION H. FINISHES FOR RADOMES

One of the major advantages usually given for reinforced plastics is the fact that they do not have to be painted, since any desired finish or color can be added to the resin in the form of a pigment.

However, for radomes used at the higher frequencies, the addition of even small amounts of pigment tends to increase the transmission loss; therefore, this practice is little used in reinforced plastic radome materials.

Finishes for radomes are usually functional, in that they are used to protect the reinforced plastic from such aircraft chemicals as deicer fluids, hydraulic fluids, or fuels; or to provide thermal resistance or rain erosion resistance (Chapter 7). In other instances paints are used on reinforced plastic parts to blend in with the color scheme of the rest of the aircraft.

In addition to the fact that any great thickness of protective coating affects the transmission properties of radomes, there is general opposition to the use of paints or other coatings on reinforced plastic parts, since they tend to hide blemishes or other unsatisfactory workmanship.

On visual examination most plastic reinforced laminates in the "as-molded" state appear to have a smooth continuous resin surface, since the clear resin does not tend to show any discontinuity. However, if low-pressure molded, reinforced-plastic parts are sprayed with a pigmented lacquer or enamel, small voids or discontinuities in the surface of the laminate can be seen immediately. These discontinuities or small voids of microscopic size are located at the junction of the crossing yarns in the woven fabric. In general, the larger the weave the larger are the small discontinuities in the resin on the surface of the laminate. In most instances this condition is eliminated by the use of one or two layers of fine weave fabrics (such as 112, 116, or 120) on the surface. Another approach to this problem is to use a pre-gelled resin coating on the surface of the mold or to use a paper or mat overlay, which tends to hold more resin on the surface. These two procedures, however, tend to produce a resin-rich surface which in extreme cases results in the formation of small cracks on the surface of the laminated part after it has been exposed to weather or extremes of

temperature. These small cracks tend to pick up moisture and destroy the electrical properties of the radome, and, therefore, this practice has not gained great favor.

In most cases when the radomes are to be painted or coated with a rain-erosion resistant material, the surface of the radome is sanded, and these small surface voids are filled with a lacquer or enamel filler, or with putty applied with a rubber squeegee. After the filler has dried, the surface of the radome is again sanded, and a primer is sprayed on.

Two fillers or putties that have been tested and are currently used almost universally are Duratite filler from Webb Products Company, and Filaplast P-24 from Brooklyn Varnish Manufacturing Company. The primer or surfacer that is used to a great extent in the industry, since it was developed primarily for polyester laminates, is Primer Surfacer P-40 from Brooklyn Varnish Manufacturing Company. There is no specification covering these materials. Generally the primer is never over one mil thick. The function of the primer is to make the plastic part very smooth and to improve the adhesion of the lacquer or enamel to the surface.

A lacquer is essentially a solvent solution of a thermoplastic resin, with or without pigment. It dries solely by solvent evaporation. Many lacquers air-dry rapidly. The dry film consists simply of the original thermoplastic resin. Common film-formers are the polymers of cellulose nitrate, cellulose acetate, ethyl cellulose, methyl methacrylate, vinyl chloride, and vinyl acetate.

An enamel is essentially a solvent solution of a thermosetting material, usually with pigment to give the required color.

Evaporation of solvent leaves a relatively soft film which must then be oxidized to form a hard, durable film. Enamel films generally have higher gloss and higher hardness, and have greater outdoor durability and solvent resistance than lacquer films.

An important factor in proper paint selection is the type of service required of the applied film. For outdoor exposure, pigmented nitrocellulose lacquers or alkyd enamel paints are generally required for adequate resistance to weathering.

The lacquers used on plastic and metal aircraft parts meet MIL-L-7178.[89] The enamels used meet MIL-E-5556.[90]

Probably the most widely used coating on radomes, however, is a neoprene rubber coating, meeting MIL-C-7439B, used to prevent rain erosion of the plastic laminate.[91]

At subsonic speeds, plastic laminates are rapidly eroded by even light rainfall. An uncoated radome may be completely eroded in a few minutes. To reduce the erosion of radomes, both Goodyear Tire and Rubber Company and Gates Engineering Company have developed neoprene rubber coatings that may be applied to exterior surfaces of plastic parts; these coatings give a decided increase in life expectancy, as discussed in Chapter 7.

On aircraft flying at high speeds through humid atmospheres, very high electrostatic charges are built up on the surface of the radomes. From time to time the potentials become high enough to cause discharge by arcing. In these cases, electromagnetic radiation is sufficient to reduce the efficiency of communication systems of the aircraft, as well as of the direction finders and other vital equipment, to almost zero. A conductive coating is used to prevent this static charge buildup. This coating is usually of the same base as the rain-erosion resistant coatings and meets the same specification.[91]

GLOSSARY

Accelerator. A chemical compound or substance which, when added to a catalyzed synthetic resin in minute amounts, hastens the polymerization or hardening of the resin.

Alkyd. A synthetic resin, consisting principally of esters formed from alcohol and acids, such as ethylene glycol and maleic acid.

Alkyd triallylcyanurate copolymer. The product formed from the polymerization of an alkyd resin and triallylcyanurate monomer.

Anodize. The formation of an aluminum oxide film on aluminum alloy by chemical and/or electrical methods.

Autoclave. A cylindrical steel vessel which is built so that it can withstand high pressures. In laminating, the resin-impregnated glass cloth is laid up on a mold and this assembly is put into the cylinder. Heat and pressure, usually in the form of steam, are then introduced into the cylinder, which forces the laminate to conform to the mold contour and simultaneously hardens the laminate.

Bag. A flexible cover through which molding pressure is exerted through the application of air pressure on one side and/or the drawing of a vacuum on the other.

Catalyst. A chemical that initiates or aids in a chemical reaction without taking part in the reaction or undergoing change itself.

Caul. A metal plate used in a press, usually with a very smooth surface that gives a plastic laminate a very high sheen.

Copolymer. A substance formed by the simultaneous polymerization of two or more monomers and/or polymers.

Cure. The terms cure, polymerize, or harden, as applied to resins, are used to describe a process in which a monomer or polymer is converted from a liquid or semisolid into a substance of higher molecular weight and different physical properties, usually by the addition of heat or chemicals.

Dielectric constant. Electromagnetic wave permittivity. When an electrical charge is placed in a homogeneous electric field, the force which acts upon it is proportional to the charge and to the magnitude of the field, the inverse of the proportionality being the dielectric constant times another constant factor which depends upon the system of units used.

Dielectric material. A material which can react by molecular mechanism to an electric field because it contains electric charge carriers that can be displaced; in radome construction, commonly thought of as a material, usually nonmetallic, through which a wave may be propagated.

Dzus fastener. A quick acting, aircraft type fastener produced by Dzus Fastener Company.

Electrical thickness. The number of wavelengths in a layer of material.

Epoxy. A group of synthetic resins based usually upon epichlorohydrin and a polyhydroxy compound.

Elastomer. A rubber like product formed by the polymerization or vulcanization of chemical substances.

Faying surfaces. In aircraft any two metal surfaces that overlap.

Flash. Excess plastic material which forms at the parting line of a mold during molding, and which usually must be removed from the finished article.

Gel. A somewhat gel-like, generally transparent, liquid-solid resin system, in which the resin has partially polymerized but has not become hard or rigid.

Gelation time. The time required for a given quantity of catalyzed resin to form a gel.

Laminate. To unite sheets of material by resin under heat and pressure. For example, sheets of glass cloth impregnated with a resinous composition.

Lay-up. The process of placing the reinforced resin-impregnated glass cloth or mat in position in the mold.

Loss tangent. An absorption coefficient, the dielectric loss tangent or dissipation factor; when the losses are low, power factor.

Polyester. Generic term referring to a resin composed of an organic acid and alcohol esterified and then polymerized to form a solid called a polyester. Usually used to refer to a resin comprising unsaturated polyesters capable of cross-linking to convert into a substantially infusible and insoluble product.

Polymerization. A chemical process usually resulting in the formation of a rigid plastic material whose molecular weight is a multiple of that of the original substance.

Polyurethane. A polymerized urethane generally formed by reaction of an isocyanate with a resin containing active hydrogen.

Post-cure. Some glass-reinforced laminate parts are given a preliminary cure in the press or oven usually at a relatively low temperature. The laminates are then re-

moved from the mold and are placed in an oven usually at a higher temperature to complete the cure or polymerization of the resin. This additional baking improves the physical properties of the laminate, especially for a high temperature environment.

Pot life. The period of time during which a resin will remain fluid and usable, after the addition of a hardener, catalyst, or catalyst-promoter combination.

Preform. A premolding or agglomeration of the reinforcing material, usually by precipitation or light pressure, prepared for efficient handling or loading of a mold.

Resol. Thermosetting resins, usually phenol-formaldehyde, at intermediate stage of reaction where they soften when heated and swell in contact with liquids.

Set-up. To harden or to become rigid, as in polymerizing or curing.

Thermoplastic. The property of softening under heat. A plastic that will become soft under heat.

Thermosetting. The property of undergoing a chemical change when heated, whereby a hardened product is obtained. Once the resin becomes hard, it will not soften appreciably under heat.

Triallylcyanurate. The allyl ester of cyanuric acid capable of cross-linking to form a solid resin.

Viscosity. Internal friction or resistance to flow of a liquid. The constant ratio of shearing stress to rate of shear usually is measured in poises.

REFERENCES

1. Goggin, W. C., and Bradshaw, R. R. Polyfiber, A New Approach to Molding Modern Plastics. 21, 101, July 1944.

2. Hopper, F. C. High Strength Epon Laminates. Wright Air Development Center Technical Report 52-5. January 1952. Supplement 1, September 1952. Supplement 2, October 1953. Supplement 3, October 1954.

3. Plastic Materials, Glass Fabric Base, Low Pressure Laminated. Military Specification MIL-P-8013A, January 1954.

4. Werren, F. Effects of Fabric Finish and West Exposure on Strength Properties of Glass Cloth Polyester Laminates. Wright Air Development Center Technical Report No. 53-483, 1953.

5. Biefeld, L. P., and Philippes, T. E. Finishes for Glass Fabrics for Reinforcing Polyester Plastics. Industrial Engineering & Chemistry 1953. 45.

6. Bjorksten, J., Yeager, L. I. Vinyl Silane Sizes for Glass Fabric. Modern Plastics 1952. 29. July 1952.

7. Steinman, R. Improvement of Wet Strength of Reinforced Plastics by Garan Finish. Modern Plastics 1951. 3-29

8. Erikson, P., Silver, I., and Perry, H. A. Universal Type Chemical Finishes for Glass Fibers Used in Reinforced Plastics. American Chemical Society 125th Annual Meeting.

9. Finish, Glass Fabric, for Reinforced Plastic Laminates. Military Specification MIL-F-9118, December 1953.

10. Eickner, H. W. Adhesive Bonding Properties of Various Metals as Affected by Chemical and Anodizing Treatments of the Surface. Forest Products Laboratory Report 1842, April 1954.

11. Adhesive, Aircraft Structural, Metal to Metal. Military Specification MIL-A-8331, June 1953.

12. Black, J. M., and Blomquist, R. F. Development of Metal Bonding Adhesive FPL-710 With Improved Heat Resistant Properties. N.A.C.A. RM 52F19, 1952.

13. Black, J. M., and Blomquist, R. F. Development of Metal Bonding Adhesives With Improved Heat Resistant Properties. N.A.C.A. RM 54 D01, 1954. Modern Plastics 32, 139, December 1954.

14. Investigation of Methods of Inspecting Bonds Between Cores and Faces of Sandwich Panels of the Aircraft Type. Forest Products Laboratory Report 1569, September 1947.

REFERENCES (Cont)

15. Fabrics, Woven Glass, Finished, for Plastic Laminates. Military Specification MIL-F-9084.

16. Hoffman, K. R. Development of Low-Pressure Laminates of Glass Fabric and Silicone Resins. USAF Technical Report No. 6223 and Supplement 1, May 1953.

17. Resin, Silicone, Low-Pressure Laminating. Military Specification MIL-R-25506, June 1956.

18. Plastic Materials, Low Pressure Laminated, Glass Fiber Base, Silicone Resin. Military Specification MIL-P-25518.

19. Korelitz, M. N. Development of High Strength-Heat Resistant Phenolic Laminating Resin. Wright Air Development Center Technical Report 52-161, July 1952.

20. Plastic Materials, Glass Fiber Base — Phenolic Resin, Low Pressure Laminated. Military Specification MIL-P-25515.

21. Wahl, N. E., and Preston, Harold M. Investigation of Heat Resistant Polyester Laminates. Wright Air Development Center Technical Report 55-342, August 1955.

22. Resin, Polyester, High Temperature Resistant, Low Pressure Laminating. Military Specification MIL-R-25042, May 1955.

23. Nelb, R. G.; Alexander, C. H., and Elliot, P. M. Heat Resistant Laminating Resins. USAF Technical Report No. 6602, 1952.

24. Botwick, M., Cummings, W., and Elliot, P. Polyester Heat Resistant Laminating Resins. Wright Air Development Center Technical Report 53-371 and Supplement 1, 1953.

25. Wier, J. E., and Pons, D. C. Flexural Tests of Structural Plastics at Elevated Temperatures. Wright Air Development Center Technical Report 53-307, 1953.

26. Plastic Materials, Heat Resistant, Glass Fiber Base, Polyester Resin, Low Pressure Laminated. Military Specification MIL-P-25395, June 1956.

27. Structural Honeycomb for Sandwich Construction. Hexcel Products Company, Brochure C., December 1952.

28. Norris, C. B. An Analysis of the Compressive Strength of Honeycomb Cores for Sandwich Construction. N. A. C. A. Technical Note 1251, 1947.

29. Ringelstetter, L. S., Voss, A. W., and Norris, C. B. Effect of Cell Shape on Compressive Strength of Hexagonal Honeycomb Structures. N.A.C.A. Technical Note 2243, 1950.

30. Voss, A. W., and Norris, C. B. Creep Tests of Sandwich Constructions Subjected to Shear at Normal Temperatures. Forest Products Laboratory Report 1806, 1949.

31. Werren, F. Shear-Fatigue Properties of Various Sandwich Constructions. Forest Products Laboratory Report No. 1837, 1952.

32. Werren, F., and Norris, C. B. Analysis of Shear Strength of Honeycomb Cores for Sandwich Constructions. N.A.C.A. Technical Note 2208, 1950.

33. Ericksen, W. S., and March, H. W. Compressive Buckling of Sandwich Panels Having Facings of Unequal Thickness. Forest Products Laboratory Report No. 1583-B, 1950.

34. Kuenzi, E. W., and Ericksen, W. S. Shear Stability of Flat Panels of Sandwich Construction. Forest Products Laboratory Report No. 1560, 1951.

35. Norris, C. B., and Boller, K. H. Wrinkling of the Facings of Sandwich Construction Subjected to Edgewise Compression. Forest Products Laboratory, No. 1810, November 1949.

36. Kuenzi, E. W., Flexure of Structural Sandwich Construction. Forest Products Laboratory, No. 1829, December 1951.

37. Kuenzi, E. W. Edgewise Compressive Strength of Panels and Flatwise Flexural Strength of Strips of Sandwich Constructions. Forest Products Laboratory, No. 1827, November 1951.

38. Methods of Test for Determining Strength Properties of Core Material for Sandwich Construction at Normal Temperatures. Forest Products Laboratory Report 1555, September 1950.

39. Methods for Conducting Mechanical Tests of Sandwich Construction at Normal Temperatures. Forest Products Laboratory Report 1556, February 1950.

40. Heebink, B., Werren, F., and Mohaupt, A. Effects of Certain Fabricating Variables on Plastic Laminates and Plastic Honeycomb Sandwich Construction. Forest Products Laboratory, No. 1843.

41. Supplement to Repair of Aircraft Sandwich Construction. Forest Products Laboratory Report 1584-A.

42. Core Material; Laminated Glass Fabric Base Plastic Honeycomb. Military Specification MIL-12050, 1949.

43. Foamed-in-Place, Alkyd-Isocyanate Type Core Material, for Aircraft and Missile Structural Applications. Military Specification MIL-C-8087.

44. Sandwich Construction, Plastic Resin, Glass Fabric Base, Laminated Facings and Alkyd-Isocyanate Foamed-in-Place Core, for Aircraft Structural Applications. Military Specification MIL-S-25392.

45. Wahl, N. E., Preston, H. M., and Campagna, P. J. Development of Heat-Resistant Foamed-in-Place Dielectric Core Materials for Sandwich Radomes. Wright Air Development Center Technical Report 54-249, March 1954.

46. Weyer, D. E., Ressell, J. R., and Hoffman, K. R. Development of a Heat Resistant Foamed-in-Place Low Density Silicone Resin Core Material. Wright Air Development Center Technical Report 53-146, Supplement 1, August 1954.

47. Laboratory for Insulation Research. Tables of Dielectric Materials, Vol. IV, Massachusetts Institute of Technology, O. N. R. Contracts N5ori — 07801 and 07858, January 1953.

48. Webber, A. H., Jr., editor. A Study of Broadbanding Techniques. McMillan Laboratory, Inc., Final Report, Air Material Command, Contract AF33(600)-28749, 31 January 1956.

49. Webber, A. H., Jr. A Study of Broadbanding Techniques. Proceedings of the Wright Air Development Center, Ohio State U. Radome Symposium, Wright Air Development Center Technical Report 56-393, August 1956.

50. McMillan, E. B., et al. Dielectric Wall for Transmission of Centimetric Radiation. U.S. Letters Patent No. 2,659,884, 3 August 1948.

51. Wheeler, H. A. High Frequency Electromagnetic Wave Translating Element. U.S. Letters Patent No. 2,511,610, 13 June 1950.

52. Von Hippel, A. R., Westphal, W. B., and Miles, P. A. Dielectric Analysis of Ferrites and Their Appraisal as Radome Materials. Laboratory for Insulation Research, Massachusetts Institute of Technology, Wright Air Development Center Contract AF33(616)-2191.

53. Slater, J. C. Introduction to Chemical Physics. McGraw-Hill Book Company, Inc., 1939.

54. Von Hippel, A. R. Dielectrics and Waves. John Wiley and Sons, Inc., New York, 1954.

55. Blair, G. R. High Temperature Dielectric and Loss Tangent Measurements. Proceedings of the Wright Air Development Center, Ohio State U. Radome Symposium, Wright Air Development Center Technical Report 56-393, August 1956.

56. McMillan, E. B. The Influence of Large In-Flight Temperature Changes on the Electrical Design of Missile Radomes. Proceedings of the Wright Air Development Center, Ohio State U. Radome Symposium, Wright Air Development Center Technical Report 56-393, August 1956.

57. Worthington, H. R., Jr. Improvement of Radome Performance by Means of Metal Grids. Pages 106-116, Vol. II, Proceedings of the Wright Air Development Center, Ohio State U. Radome Symposium, June 1955.

58. Jones, E. M. T., Cohn, S. B., and Robinson, L. A. Wide-Band Radomes Matched by Reactive Walls. Vol, I. Proceedings of the Wright Air Development Center, Ohio State U. Radome Symposium, pp. 52-67, June 1955.

59. Werren, F. Mechanical Properties of Plastic Laminates. Forest Products Lab. Report 1820, February 1951.

60. Werren, F., and Freas, A. D. Mechanical Properties of Cross-Laminated and Composite Glass-Fabric-Base Plastic Laminates. Forest Products Lab. Report 1821, February 1951.

61. Werren, F. Mechanical Properties of Plastic Laminates. U.S. Forest Products Lab. Report No. 1820 and Supplement A, 1953.

62. Jones, C. D. Properties of Glass-Fabric Reinforced Low-Pressure Laminates. U.S. Air Force Technical Report No. 5748, 1949.

63. Long, J. K. The Effect of Outdoor Exposure on Flexural and Other Properties of Some Plastic Materials. U.S. Air Force Technical Report No. 5698, 1948.

64. O'Brien, F. R. Investigation of Thermal Properties of Plastic Laminates. Wright Air Development Center Technical Report 54-306, Part I, 1954.

65. Axilrod, B. M., and Sherman, M. A. Flexural Properties of Some Glass-Fabric-Base Plastic Laminates at Elevated Temperatures. U.S. Air Force Technical Report 5940, 1950.

66. Simmons, W. F., and Cross, H. C. Elevated Temperature Properties of Glass-Fabric-Base Plastic Laminates. U.S. Air Force Technical Report No. 6172, 1951.

67. Vanecho, J., Remely, G. R., and Simmons, W. F. High-Temperature Creep-Rupture Properties of Glass-Fabric Plastic Laminates. Wright Air Development Center Technical Report 53-491, 1953.

68. O'Brien, F. R. Investigation of Thermal Properties of Plastic Laminates. Wright Air Development Center Technical Report 54-306, Part I, 1954.

69. Erickson, E. C., and Norris, C. B. Tensile Properties of Glass-Fabric Laminates with Laminations Oriented in Any Way. Forest Products Lab. Report No. 1853, November 1955.

70. Plastics for Aircraft. ANC -17 Bulletin, June 1955. Issued by Department of the Air Force, Department of the Navy, and Department of Commerce.

71. Silver, I., and Erickson, P. W. Improved Reinforced Plastics with the Universal Type Chemical Finish, NOL-24. NOL Report, February 1955.

72. Fontana, M. G., Bishop, S. M., and Spretnak, J. W. Mechanical Properties of Metals and Plastic Laminates at Low Temperatures. Wright Air Development Center Technical Report 5662, Part V, 1953.

73. George, D. A., Baker, H. A., and Sieffert, L. E. Impact Strength of Some Thermosetting Plastics at Low Temperatures. ASTM Bulletin No. 181, April, 1952.

74. O'Brien, F. R. Investigation of Thermal Properties of Plastic Laminates. Wright Air Development Center Technical Report 54-306, Part I, 1954.

75. Resin, Low Pressure Laminating. Military Specification MIL-R-7575A, 27 April 1953.

76. Sandwich Constructions and Core Materials; General Test Methods. Military Specification MIL-STD-401, 3 July 1952.

77. Mechanical Test Procedures for Radomes and Radome Materials. Aircraft Industries Association, ATC Report No. ARTC-3, July 1951.

78. Test Methods for Structural Plastic Laminates at Low Temperatures and at Elevated Temperatures. Aircraft Industries Association, ATC Report W-64, June 1954.

79. Werren, F. and Heebink, B. G. Effect of Defects on the Tensile and Compressive Properties of a Glass-Fabric-Base Plastic Laminate. Forest Products Lab. Report No. 1814, June 1950.

80. Leaderman, H. Radome Materials and Methods of Fabrication. Chapter 13, Radar Scanners and Radomes, Vol. 26, Radiation Laboratory Series, McGraw-Hill Book Company, Inc., 1948.

81. Sonneborn, R. H., Dietz, A. G. H., and Heyser, A. S. Fiberglass Reinforced Plastics. Reinhold Publishing Corporation, N. Y. C., 1954.

82. Morgan, P., editor. Glass Reinforced Plastics. Philosophical Library, Inc., N.Y.C., 1954.

83. The Society of the Plastics Industry, Inc. Plastics Engineering Handbook. Reinhold Publishing Corporation, N. Y., 1954.

84. Duplaga, E., and Pace, H. A. Foaming-in-Place of Alkyd Resins for Sandwich Radomes. Report GER 4097, Goodyear Aircraft Corporation, Air Materiel Command Contract W33-038 ac 15228, 22 December 1949.

85. Duplaga, E., and Pace, H. A. Foaming-in-Place of Alkyd Resins for Sandwich Radomes. Report GER 2423 Supplement I, Goodyear Aircraft Corporation Air Materiel Command Contract W33-038 ac 15228, 15 October 1952.

86. Duplaga, E., and Pace, H. A. Foaming-in-Place of Alkyd Resins For Sandwich Radomes. Report GER 4097 Supplement II, Goodyear Aircraft Corporation, Air Materiel Command Contract W33-038 ac 15228, 29 February 1952.

87. Editorial Staff, Electronic Design. Loaded-Core Sandwich for Radomes. January 15, 1956.

88. Toner, S. D., Wolock, I, and Reinhart, F. W. Effects of Molding Pressure on the Strength Properties of Several Types of Glass Fiber Reinforced Plastics. Wright Air Development Center Technical Report 55-256, December 1955.

89. Lacquer; Cellulose Nitrate, Gloss, for Aircraft Use. Military Specification MIL-L-7178.

90. Enamel, Camouflage, Quick Drying. Military Specification MIL-E-6556.

91. Coating, Rain Erosion Resistant with Anti-Static Surface Treatment, for Plastic Laminates. Military Specification MIL-C-7439 B.

92. Analysis of Compressive Strength of Honeycomb Cores for Sandwich Constructions. N.A.C.A. Technical Note 1251, April 1947.

93. Warren and Norris. Analysis of Shear Strength of Honeycomb Cores for Sandwich Constructions. N.A.C.A. Technical Note 2208, October 1950.

Chapter 9

INORGANIC MATERIALS AND RADOME CONSTRUCTION

by

Harold T. Smyth

School of Ceramics
Rutgers University
New Brunswick, New Jersey

Chapter 9

INORGANIC MATERIALS AND RADOME CONSTRUCTION

SECTION A. INTRODUCTION

9-1. Scope

At the time of writing (1956) ceramic materials by themselves have not been extensively used for radomes, largely because the commercial organizations engaged in ceramic fabrication have not been in a position to supply the required shapes finished to the specified dimensional tolerances.

Because of technical advances by industry and by various ceramic schools, it seems probable that this situation can be corrected. This section on inorganic materials will acquaint radome designers with the properties of the ceramic materials available, together with information on methods of fabrication, which may be expected to allow the close dimensional tolerances to be met.

Since lack of proper fabricating technique has slowed up the utilization of ceramic radomes, consideration of methods of manufacture is of equal importance with a study of the physical properties. The method used in the presentation of the information will therefore be as follows. Ceramic materials will be grouped according to some generally accepted classifications. The materials within each of the classifications will be considered one by one. Where extensive work has been carried out on the development of methods of manufacture of any of these materials this work will be described in detail, along with the description of the material. The sections on the separate materials will be followed by discussions of the mechanical, thermal, and electrical properties of ceramic materials in general.

9-2. Classification

Ceramic materials will be divided into the following classifications:

1. Dense fired bodies
2. Porous bodies
3. Glasses and materials derived therefrom
4. Glass bonded mica
5. Fusion cast materials.

SECTION B. DENSE FIRED BODIES

9-3. Definition and Characteristics

This classification is taken to include ceramic materials which have been formed to shape in the unfired state and then fired at a high temperature to a state approaching zero porosity. Properly chosen bodies so formed can have some or all of the following desirable properties:

1. High strength over a wide temperature range

2. Hardness

3. Homogeneity

4. Dielectric constant anywhere from four up to several thousand

5. Constancy of dielectric constant over a wide temperature range at high frequencies

6. Low dielectric loss.

9-4. Steatite

Steatite bodies include those which, in the fired state, consist largely of magnesia and silica approximately in a ratio to form the compound MgO·SiO2. Other ingredients are usually added to improve the forming properties, depending on the forming operation used, or to improve the dielectric properties. Barium oxide is frequently used to give lower dielectric losses.

Since the term steatite covers a number of similar materials, the physical properties listed later are only roughly representative of the class and are subject to variation depending on how each body is made up.

The Rutgers Program. The program at Rutgers University on the development of dense fired ceramic radomes started with steatite.[1, 2, 3] A number of radomes made from this material came close to satisfying the electrical performance requirements of one of the missile manufactures.

Steatite was chosen for the following reasons. Even before starting the work, it was realized that the dimensional tolerances were such that none of the usual ceramic fabricating methods would give the necessary thickness control, and that some machining would be necessary. Since steatite is considerably softer than alumina, which is probably a more desirable ultimate material, this machining development could be more easily accomplished with the softer material. Steatite radomes actually were produced for electromagnetic testing considerably sooner than would have been possible with alumina shapes. Their encouraging performance has done much to arouse interest in ceramic radomes in general.

Slip Casting. Of all the possible ways of forming the shape before firing, slip casting was chosen as most likely to give results with a minimum of development work. It is very possible that other methods may ultimately replace this, particularly if they can give such control of thickness and taper that machining in the fired state is unnecessary; however, radomes are now being produced by the slip casting method. Since the method works in spite of its inconveniences, a full description is in order.

Slip casting consists of making a fine, more or less stable, water suspension of the material. This suspension, or slip, is poured into a plaster of paris mold. The inside of the mold is of the same shape as, but slightly larger than, the outside of the shape to be formed. This is to allow for shrinkage in drying and firing.

The porous mold absorbs water from the slip and forms a wall whose thickness increases as the mold draws out more and more water. After the desired thickness is obtained the remaining slip is poured out, leaving the formed object.

Slip Control. Slip casting is an old art, and the control of clay slips is described in many text books on ceramics. Low dielectric loss, however, is necessary in a radome, and something better than the older electrical porcelains seemed indicated. This meant that clay could not be considered as a major ingredient or, in fact, in some cases, as an ingredient at all.

Workers experienced in dielectric work advised, and it was quickly borne out in practice, that where clay is not a major ingredient of the slip it is advantageous to work with prefired materials which are then reground, sized if necessary, and made into a slip with only such additions as are necessary to control deflocculation and give correct slip viscosity for casting and sufficient strength for handling after the piece is dry. Both from the standpoint of casting control and ultimate body homogeneity this approach is recommended to anyone attempting to produce ceramic radomes.

For this method, steatite turned out to be a very convenient material. There was a ready supply of scrap steatite available. This was material which had been rejected for dimensional defects but which was of satisfactory composition. The use of this material eliminated the necessity of extruding and prefiring the raw material.

Batch Preparation. The steatite scrap, in the form of thin spaghetti, was wet ground in a ball mill. If it is intended to form shapes which may be fired to exact dimensions without any further machining, it is extremely important to control the distribution of particle sizes going into the slip.

Contardi and Hund have described some experiments on the effect of different combinations of particle size on the properties of steatite slips.[4] The ground raw materials were divided into two fractions. Fraction A contained particles running in size from about 20 microns to 50 microns. Fraction B was nearly all below 4 microns. A slip using all B gave a body with a very smooth texture but with a firing shrinkage of almost 25 percent. Fraction A by itself could not be cast, since it settled out of suspension too rapidly. A blend of 70 percent A and 30 percent B gave a firing shrinkage of only 13 percent which was the lowest shrinkage of any combination of the two fractions. The texture of this optimum mix was just as good as that of the body using all fine material. This is in agreement with general ceramic experience that a properly chosen mixture of two different size fractions gives less void space in the dry state and consequently less firing shrinkage than either fraction by itself.

If the machining process is able to take care of any size variation caused by shrinkage which differs from batch to batch, then in many cases it is sufficient to decant off the supernatant slip after grinding and to use the resulting run-of-the-mill particle size distribution without any further effort to compound an exact size distribution without any further effort to compound an exact size mixture.

In the Rutgers project the ground slip was then dried. This dried ground material was mixed with a suitable addition of deflocculants and water to give a slip of the proper density and casting consistency. Table 9-I shows a formulation which was successfully used in the casting of steatite radomes.

Table 9-I. Formulations Successfully Used in Casting Steatite Radomes

Ball Milled Steatite Scrap	77,725 gm
Bentonite	777 gm
Superloid Gel (10 gm per 200 cc water)	785 gm
Sodium Silicate "N" brand (1 cc per 10 cc water)	100 cc
Ammonium Hydroxide, 28% (1 cc per 10 cc water)	500 cc
Sodium Hexametaphosphate (24.55 gm per 500 cc water)	2,600 cc
Distilled Water	31,500 cc

Any free iron was removed by a magnetic filter. The slip was then de-aired and stored ready for casting. Before each cast the specific gravity and viscosity were checked and adjusted if necessary.

Casting. A section drawing of the mold is shown in Figure 9-1. The removable top is used to form a flange that gives mechanical support and helps to prevent warping during the firing operations. This flange is not removed until after the final firing. Pieces up to 10 inches in diameter and 30 inches in length have been cast from such a mold.

The slip using the formulation of Table 9-I required about 45 minutes to build up a wall thickness of about 3/8 inch, which leaves sufficient stock to allow for machining if a wall thickness in the neighborhood of 1/4 inch is desired. The mold was then inverted and the remaining slip drained out. The wall thickness tended to be greater nearer the point, probably because of the greater hydrostatic pressure during the casting operation. It would be extremely difficult to achieve accurately a predetermined pattern of wall taper by control of the slip and draining conditions alone. After draining the mold was returned to the point-down position and allowed to remain like this for about 24 hours before the piece was removed. Removal

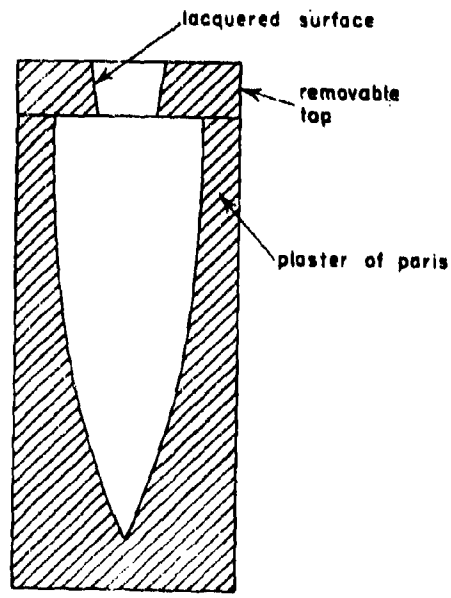


Figure 9-1. Section Drawing of Mold

was performed by allowing the piece to drop very gently onto a rubber ring on a steatite plate. Before firing the rubber ring was very carefully removed and pure sand substituted for it to support the radome during firing. At this time the radome was extremely fragile and machining operations could not be attempted.

Bisque Firing. Steatite in the final fired form is quite hard and could probably be machined only with the use of diamond tools. To avoid this necessity, in the early part of the program the radomes were first bisque-fired to 1,700° F. This gave them sufficient strength to be held in the lathe chuck, but achieved only a small part of the complete firing shrinkage. In this state, however, they can be readily machined with Carboloy tools.

It was the usual practice to machine the outside first to the desired contour on one lathe. The radome was then removed to another lathe equipped with a special holder to allow the inside to be machined. While the piece was still being held in the lathe the thickness could be constantly checked by the use of a specially made dial micrometer supplied by the Tubular Micrometer Co. In all of this operation allowance had to be made for the shrinkage to take place in the final firing.

Final Firing. After the proper thickness distribution had been achieved the piece was ready for final firing. All of the firing was done in a gas-fired kiln built specifically for the purpose. The kiln was of approximately square cross section with four gas burners in each of two opposite walls. Independent control of the upper and lower burners allowed a very good degree of temperature uniformity. During firing, the radome was enclosed in a stack of silicon carbide rings to prevent direct flame impingement and to improve the equality of the temperature distribution.

The final firing was carried out on a schedule requiring about 8 hours to reach a temperature of 2,200° F. The pieces were soaked for 1 hour at this temperature, after which time the kiln was shut down and allowed to cool.

After removal of the radome from the kiln, the flange was cut off with a diamond saw and the radome was ready for testing. There was about 13 percent linear shrinkage in the final firing operation. In spite of this, thickness tolerances of several thousandths of an inch could be held in the final piece. The shape itself might vary by considerably more than this, warpage of 1/8 to 1/4 inch being sometimes present.

Electrical testing of the steatite radomes made at Rutgers University was carried out by the Raytheon Manufacturing Co. The results were good enough to encourage extension of this work to other ceramic materials that held promise of being more suitable for radome construction in the long run. Perhaps the most obvious such material is alumina.

9-5. Alumina

While alumina is strictly a synonym for aluminum oxide, it is used loosely to describe any ceramic body high in alumina. It will be used here to include any ceramic body containing 90 percent or more of aluminum oxide.

Very pure alumina can be fired to very high strength and very good dielectric properties. It requires, however, firing temperatures well beyond 3,000° F. While such temperatures are not impossible they call for expensive kiln construction and high kiln maintenance costs. Hence the investigation was begun with compositions that could be fired around 2,800° F, which is attainable on fairly standard equipment.

With a little experimenting it was determined that a composition using 90 percent alumina, 6 percent talc and 4 percent ball clay could be fired to maturity at around 2,800° F to give a body with dielectric constant about 8 and a loss tangent of around 0.002. Somewhat similar bodies are in the catalogs of a number of manufacturers of ceramic dielectrics.

Machining. The obvious method of procedure seemed to be to follow as possible the techniques which had been successful with steatite. It was soon found, however, that machining of the bisque ware presented much greater difficulties than steatite. The wear on the tungsten carbide tools was so great that they would have to be ground several times during a single cut on the lathe. Therefore, the decision was made that, in spite of the hardness of the matured material, all machining would be done on the final fired shape. This eliminated the necessity of two firings but brought up some new problems in the machining operation.

The use of anything but diamond tools was out of the question for the very hard alumina surface. All of the machining was therefore done with metal-bonded diamond wheels. For the outside machining this presented no great problem. The greater part of the inside was done with a flat-faced diamond wheel mounted on a long quill. The interior of the point of the radome was shaped with a conical diamond reamer. A grit size of 100 was satisfactory for

final finishing, while a grit size of 30 was used for some of the roughing cuts.

At the time of writing (1956), no tests have been carried out on any of these alumina radomes.

9-6. Other Forming Methods

The methods described above allow considerable precision in the final piece but are certainly not ideal for large scale production. Further development can foreseeably follow several paths in achieving a more practical procedure. First, there may be developed more rapid machining techniques. These would reduce the necessity for precision control of shape and thickness in the ceramic forming and firing. While it is difficult to see how diamond tools could be dispensed with on anything as hard as vitrified alumina, it is very conceivable that a multiplicity of cutting tools all cutting at the same time could reduce the machining time to a small fraction of that presently necessary. Also, automatic measuring of the physical or electrical thickness while the piece is turning in the lathe would allow machining with a minimum of personal attention.

The second possible path is the development of the precision ceramic control required to render any machining in the fired state unnecessary. This may be achieved by such a technique as injection molding, used today in the production of spark plugs. In this the ceramic powder would be mixed with an appropriate amount of thermoplastic resin which, when hot, would allow the raw material to flow under pressure between a male and female mold.

Hydrostatic pressing has also been suggested. In this method the ceramic material with a suitable binder would be formed on a mandrel. This would be surrounded with a rubber or plastic envelope and subjected to a high hydrostatic pressure forcing the grains into as dense a packing as the particle size distribution would allow. With radomes even as large as those being considered for the smaller missiles, this calls for extremely heavy pressure vessels.

It might, however, allow machining in the unfired state while the piece was still on the mandrel. This would eliminate inside machining, always an awkward operation. With good particle size control it might very well allow thickness and taper tolerances to be met without any further machining.

With the present slip casting procedures there is much greater hydrostatic head at the point of the mold than there is at the other end. It has been suggested that centrifugal casting in which the mold would be rotating on its axis at some appropriate speed while the casting operation is being carried out could help to improve this situation. This works very well with cylindrical shapes and might be adapted to cones or ogives.

9-7. Other Materials

At the moment alumina, because of its strength, refractoriness, hardness, and good dielectric properties, is probably the most promising ceramic material for radome construction, at least among the dense nonporous bodies. There are, however, many other possible compositions out of which radomes might be made and one or another of these may look very desirable at some future time. While it would obviously be impossible to cover every possible combination of the many oxides available, some of the more simple types will be mentioned.

9-8. Beryllia[5]

Of all the materials which might come close to doing what alumina can do, and even perhaps a little more, beryllia probably looks the most promising. It has almost as good strength, almost the same thermal expansion, but it has one property that puts it in a class by itself among ceramic materials. The thermal conductivity is fabulously high, higher in fact than that of a number of metals. This gives it a great advantage in resistance to thermal shock, since thermal gradients are greatly reduced.

Its most serious drawback is its toxic properties. Many ceramic manufacturers are afraid of it. Although it can be handled safely if proper precautions are taken, the health hazard has slowed up the general use of this potentially useful material.

9-9. Magnesia[6]

Pure magnesia has a very high melting point, close to 5,072° F. In the pure state it is difficult to mature at reasonable temperatures. With small amounts of talc or ball clay as a flux, magnesia bodies have been matured at 2,800° F. The thermal conductivity is high. As a class these magnesia bodies are second only to beryllia bodies in this respect. The dielectric constant is close to 8 and with 2.5 percent talc the loss tangent is 0.0003. With 10 percent talc it is 0.001. The thermal expansion is about 50 percent greater than alumina or beryllia. The strength does not compare well with either alumina or beryllia.

9-10. Spinel[7]

Magnesia-alumina spinel is another material which might be useful because of its high melting temperature (3,875° F). The compound has the formula $MgO \cdot Al_2O_3$. Again some flux is necessary to obtain a body maturing at a reasonable temperature. Using various amounts of clay for this purpose, E.J. Smoke has made up several spinel bodies maturing from 2,600 to 2,800° F. The strengths are not high. The dielectric constants run from 6 to 7 with loss tangents of about 0.0004.

9-11. Forsterite[7]

Bodies consisting largely of forsterite, $2MgO \cdot SiO_2$, are very comparable in physical properties with steatite bodies. The loss tangents of the forsterite bodies are usually lower than those of steatites.

9-12. Zircon[8,9]

The pure compound zircon, $ZrO_2 \cdot SiO_2$, has a thermal expansion lower than most of the materials already mentioned. It can be used as an ingredient in ceramic dielectrics where low expansion is desired to improve thermal shock resistance. Some bodies of this type are described in the ceramic literature. The dielectric constants are in the 7 to 8 region. Loss tangents are around 0.001. Expansions are very much lower than either alumina or beryllia.

9-13. Cordierite[10]

The ternary compound cordierite, $2MgO \cdot 2Al_2O_3 \cdot 5SiO_2$, is another very low expansion material. Bodies have been developed with this compound as a major phase. Expansions are very low. Dielectric constants are in the neighborhood of 5 and loss tangents tend to run high.

9-14. Lithium Aluminum Silicates[11,12]

The lithia-alumina-silica diagram is rather remarkable in that it contains several regions which show negative expansions. When the fired body is found to contain either the compound beta-eucryptite or beta-spodumene, quite large negative expansions can occur. These can be just as bad from the standpoint of thermal shock resistance as high positive expansions. However, by proper control of the composition, bodies may be produced which have very close to zero expansion over a wide temperature range. Such bodies show extremely good thermal shock resistance. As might be expected of any silicate composition containing such a small alkali ion as lithium, losses tend to run high with loss tangents around 0.005.

SECTION C. POROUS BODIES

9-15. Approaches to Fabrication

For high temperature insulation and other applications porous ceramic materials have been manufactured for a long time. One of the commonest methods of producing the desired porosity is to incorporate in the body a certain amount of some material which will burn out in the firing process, leaving in its place pores of approximately the same size as the combustible particles. While this is satisfactory for applications where homogeneity of structure is not of prime importance, as in thermal insulation, it has not been considered a desirable procedure for making thin-walled radomes where the pores should be small compared with the wall thickness and where electrical requirements call for a high degree of homogeneity.

One of the most promising methods of attack has been the use of foaming agents in preparation of the ceramic material. A large amount of work along these lines has been carried out at Virginia Polytechnic Institute and at Ohio State University.

9-16. Foaming

The general method is to prepare the ceramic material in the form of a slip or water suspension which can be foamed by the addition of a foaming agent and a properly selected whipping action. The foam when formed must be stabilized by some ingredient in the batch which will set up as soon as or shortly after the foam has been formed. This ingredient has usually been plaster of paris.

A description, from the reports of A. J. Metzger at V.P.I., of the preparation of a representative body of this type follows.[13,14] As in any work of this kind there is an infinite number of combinations of raw materials out of which must be chosen the one to give the best combination of physical properties for the particular application. These properties include density and strength, as well as dielectric and thermal properties. In each case the radome designer and the ceramic manufacturer must work very closely together and each must be conscious of the other's desires and limitations.

The solids in Metzger's batch B77 are shown below.

Material	Percentage
Plaster of Paris	21.02
Pioneer Kaolin	34.14
A-2 Alumina	44.84

The liquid part of the batch consisted of water with 0.6 percent of Aresket 240. An anionic type foaming agent, this is a 40 percent solution of monobutyl biphenyl sodium monosulfonate supplied by the Monsanto Chemical Company.

The liquid-to-solid ratio was 48.72 to 51.28, arrived at after a large number of experiments looking toward a minimum fired density in the finished pieces.

The mixing cycle is quite critical and must be very closely controlled to give reproducible results. In Metzger's work the solid and liquid were blended for one minute, mixed at high speed with a Hobart mixer for 2 1/2 minutes and then at a slower speed for 1 minute. This indicates the care that is necessary to get reproducible results. The original reports should be consulted for the exact details on the relations between method of preparation and the properties of the final body.

Forming. The mold into which the foamed slip is poured consists of inner and outer metal forms. When conical shapes are being formed, waxed paper is used as a separating layer. After the material has set, the inner cone is removed, and after several hours the outer cone is taken off and the piece allowed to dry. Drying is carried out at 70° F at a relative humidity of 50 percent.

Firing. Firing involves not only the development of a ceramic bond but also the dissociation of the plaster of paris, with the liberation of sulfur trioxide. To allow this reaction to go to completion the piece is held at 2,200° F in a well-ventilated kiln for 12 hours. The kiln is then brought rapidly up to 2,552° F, where it is held for 3 hours, after which it is allowed to cool.

Bodies prepared in this way have a bulk density of about 30 pounds per cubic foot and a modulus of rupture approaching 400 pounds per square inch.

By their very nature, such bodies are porous and will readily absorb moisture. In this state they would not make good radomes, since the absorption of such moisture would seriously affect their dielectric properties. Something has to be done to make the surface impervious. Because of their great porosity they are rather difficult to glaze, since the melting glaze has a strong tendency to be absorbed by the body. It is necessary first to treat the surface so that a subsequently applied glaze can mature without soaking in.

Glazing. This has been done by the application to the surface of a finely ground mix of the same composition as the body itself. When fired on, this leaves a hard skin to which a glaze can be applied in the usual way. This skin also increases the modulus of rupture by about 25 percent.

The application of a glaze to this body increases the modulus of rupture to around 1,200 pounds per square inch and gives a surface which is truly impervious to moisture.

By a somewhat similar technique Giles and Hessinger[15,16] at Ohio State University have produced foamed wollastonite, $CaO \cdot SiO_2$, bodies with densities of around 25 pounds per cubic foot and modulus of rupture up to 250 pounds per square inch. The batch contained 70 parts wollastonite, 20 parts ball clay, and 10 parts barium carbonate, together with 20 parts of plaster of paris to stabilize the foam, plus some fluxes to lower the firing temperature and extend the firing range. Saponin was used as the foaming agent.

The same workers have also used mixtures of wollastonite, ball clay and zircon. A strength of 500 pounds per square inch was obtained at a density of 40 pounds per cubic foot and a strength of 100 to 200 pounds per square inch at a density of 20 pounds per cubic foot.

After the first firing, a fine coating of essentially the same composition as the body was fired on, after which a lead borosilicate glaze was applied and fired.

9-17. Wollastonite Bodies From Xonotlite

Kalousek and Dence of Owens Illinois Glass have developed a different approach to the problem of producing lightweight ceramic bodies.[17] They reacted freshly slaked calcium oxide and finely pulverized quartz in an autoclave at 250 pounds per square inch steam pressure. The raw materials were prepared as a slurry and poured into a mold of the desired shape. The material in the mold was autoclaved for 10 hours. The resulting solid piece would have a density from 15 to 35 pounds per cubic foot and was essentially of the composi-

tion xonotlite, $5CaO \cdot 5SiO_2 \cdot H_2O$. Hollow cones with base diameter of 8 inches and length of 24 inches could be made in this way.

It was found that these cones could be converted to wollastonite by slow heat treatment requiring 14 to 16 hours to reach 1,350° F. In spite of the relatively large shrinkage which accompanies the conversion of xonotlite into wollastonite, structurally sound wollastonite pieces could be obtained in this way. The porosity which had contributed to the low density in the xonotlite state remained, and wollastonite shapes having a density of 18 pounds per cubic foot could be obtained. The modulus of rupture of such pieces was 150 pounds per square inch.

The texture of the wollastonite bodies formed in this way is such that a glaze may be applied and fired without the necessity of first sealing the pores in a separate operation. It was found that glaze No. 3496 made by the Ferro Corporation gave satisfactory mechanical properties with reasonably low dielectric loss.

9-18. Dielectric Properties of Porous Ceramics

Metzger found that the dielectric constant of porous bodies made from alumina, kaolin, and plaster of paris could be expressed by the simple formula

$$\epsilon_r = 1 + 0.02\rho \qquad (9\text{-}1)$$

where ϵ_r is the relative dielectric constant and ρ is the density in lbs per cu ft. Giles and Hessinger have plotted the dielectric constant of porous wollastonite bodies and the curve can be expressed very closely by the expression

$$\epsilon_r = 0.92 + 0.022\rho \qquad (9\text{-}2)$$

Loss tangent at 9.4 kmc is about 0.002.

The wollastonite bodies made from xonotlite have a dielectric constant of about 1.4 and a loss tangent of about 0.001.

SECTION D. GLASSES

9-19. Possible Advantages of Glasses

While glasses do not have the refractoriness of such materials as alumina or beryllia, they are capable of withstanding temperatures considerably higher than most organic plastic materials. In addition, they lend themselves to a number of forming techniques which allow mass production methods with quite precise control of shape and thickness. Glass shapes have been blown or pressed for many years. Recently the development of centrifugal casting of such large shapes as television picture tubes has permitted thickness control of the order of ±0.010 inch or better. Also, work sponsored by Wright Air Development Center has resulted in centrifugal casting of radomes within tolerances of ±0.005 inch. While such control is probably not in itself satisfactory in the manufacture of half-wave radomes, it would greatly reduce the time required for final machining, and some machining still seems necessary for most ceramic radomes with the possible exception of glass-bonded mica.

9-20. Glass Properties

It is not possible in anything short of a full textbook to cover the variations in physical properties which can be obtained with glasses of different compositions. Dielectric constants may run from about 3.8 for vitreous silica, to 6 or 7 for the more common silicate glasses, to 8 to 10 for high-lead glasses, and up to 15 or greater for special glasses.

With the exception of vitreous silica and the few very high silica glasses (such as Corning Vycor), glasses in general do not have outstandingly good resistance to thermal shock, mostly because of their moderate strength, low thermal conductivity, and high elastic constants. Because of its extremely low expansion, vitreous silica has exceptionally good resistance to thermal shock; but, because of its very high viscosity at the usual glass working temperatures, it is difficult and expensive to form.

Other physical properties of the glasses will be discussed in the general discussion of physical properties of all ceramic materials.

9-21. New Glasses

Recently there have been developed some new materials such as Corning Ceram 607 BUZ (#8606) and 607 AVE (#8605), which possess some of the useful forming properties of glasses, and can, by heat treatment, be converted into bodies with much higher strength than the usual glasses. The shapes are formed in the usual way from glasses of special composition; if necessary, they may be machined while still in

the glassy state, when the machining can be carried out much more easily than on the usually harder ceramic materials.

The shapes are then heated to a carefully controlled predetermined temperature. Here they devitrify or crystallize. The change in volume is not very large in this process, and it appears probable that close dimensional tolerances can be maintained. The strength is greatly enhanced in the crystallization process. The dielectric properties compare favorably with those of other ceramic dielectric materials, and are listed in Tables 9-II and 9-III.

These materials were developed by Corning Glass and bear the trade names Fotoceram and Pyroceram.

SECTION E. GLASS-BONDED MICA AND FUSION-CAST CERAMIC MATERIALS

9-22. Glass-Bonded Mica and Ceramoplastics

Of all the ceramic materials which, up to the present time, have been worked on in the radome field, only two have shown that they can be formed, without machining, to radome shapes with dimensional tolerances satisfactory to the designers. These are glass-bonded mica and ceramoplastics, which are manufactured under the trade names of Mycalex and Supramica, respectively. These bodies consist of an intimate mixture of finely ground mica (natural or artificial) bonded with a specially selected low-temperature softening glass.

These materials, preheated to soften the glass, can be formed by injection molding in heated metal molds; since there is no further change in volume after forming other than the thermal contraction on cooling from the forming temperature, the only real limit to the dimensional tolerances that can be met on the finished piece are the precision with which the forming dies can be made. Small, full-scale, missile radomes have been made.

In addition, the nature of these materials is such that machining in the finished state is quite practical without diamond tools. This means that, for experimental and development work, different tapers may be cut on pieces from the same mold, thereby expediting the work and reducing the costs.

Both Mycalex 400 and Supramica 500 have a dielectric constant of about 7 with a loss tangent of 0.003 at 10 kmc.

At the present time probably the greatest weakness of materials of this kind is the low softening point of the glass, which must be such that the material is workable at temperatures compatible with reasonable life of the metal molds used. The materials are, however, capable of operating at temperatures several hundred degrees in excess of those recommended for most organic plastic materials. For example, Supramica 500 is capable of operating at a continuous temperature of 500° C and might very well be applicable to radomes for moderate speed missiles.

9-23. Fusion-Cast Ceramic Materials

One class of materials which is not usually considered for dielectric applications is that group of materials made by melting the ceramic raw materials in an electric furnace and pouring them into graphite, sand, or other molds. Many refractory shapes for glass and steel furnaces are made in this way. Since dielectric pieces are usually small it has not been practical for this process to compete with the usual ceramic forming methods. However, when the pieces required get to be as large as some radomes are now, some method like this may prove practical. Shapes such as fairly thin walled crucibles and some of the more complicated shapes used in feeder parts for glass tanks are now standard items. The possibilities of the method are such that radomes of these materials are not out of the question.

SECTION G. PHYSICAL PROPERTIES OF CERAMIC MATERIALS

9-24. Introduction

The following sections give a short discussion of the physical properties of ceramic materials in general.[19] Some more or less obvious generalities which may be helpful in promoting a greater appreciation of the possibilities and limitations of these materials are included as well as tables of the more important properties. In these tables the materials will be represented by one from each general category like alumina or beryllia. This means that the values are at best only a rough guide as to what may be done with a given kind of material. Individual

suppliers should be consulted before the designer goes too far. Where available sources do not list a particular property of one kind of material the writer has made an intelligent guess. Since much of the numerical data is taken from manufacturers' catalogs, no attempt is made to identify the source of each value, since this could not very well be done without making distinctions among the suppliers.

9-25. Mechanical Properties

From the mechanical standpoint certain properties are desirable for successful radome application. These are:

1. Strength at ordinary temperatures and at high temperatures
2. Resistance to impact
3. Resistance to thermal shock
4. Resistance to rain erosion
5. Resistance to moisture absorption
6. Lightness.

Some of these, such as lightness and strength, are to some extent incompatible. Knowing all the materials he has to choose from, the designer has to make the best possible compromise.

Strength. The strength of ceramic materials may be expressed in a number of ways. It may be listed as crushing (compressive) strength, tensile strength, or flexural strength (also called modulus of rupture). Details of the recommended methods of evaluating these may be found under test D116-44 in the ASTM Standards 1955, Part 6. In very rough numbers, the flexural strength is usually about twice the tensile strength and the compressive strength is seven to ten times the tensile strength.

The impact strength is measured as the kinetic energy expended in breaking a bar of specified cross section when the bar is struck by a pendulum which has been allowed to fall from a controlled and specified height. The details are listed under test D256-54T in the ASTM volume. There is some doubt as to the meaning of such a test. A true brittleness test should probably measure the energy just required to break the sample rather than the energy expended in breaking it, since a comparatively weak but very resilient sample might have good impact resistance.

Table 9-II shows representative strength values for a number of ceramic materials.

Table 9-II. Ceramic Mechanical Strength Values

Material	Tensile Strength (psi)	Compressive Strength (psi)	Flexural Strength (psi)
Alumina	27,000	280,000	50,000
Beryllia	22,000	225,000	34,000
Steatite	10,000	90,000	20,000
Forsterite	10,000	85,000	20,000
Zircon	13,000	75,000	24,000
Porcelain	6,000	50,000	11,000
Cordierite	5,000	35,000	16,000
Glass-bonded mica	7,000	35,000	15,000
Pressed glassware			5,000 - 10,000
Drawn glass tubing			10,000 - 20,000

Table 9-II. Ceramic Mechanical Strength Values (cont)

Material	Tensile Strength (psi)	Compressive Strength (psi)	Flexural Strength (psi)
Window glass			12,000 - 25,000
607 BUZ Ceram (#8606)			30,000
Porous Ceramics (15-40 lb/cu ft)			100 - 400

The strength of glasses is strongly affected by surface defects. On the other hand, the strength of glasses may be very materially increased by tempering. In this process the glass is chilled rapidly from a partially soft condition so that the exterior is in compression when the glass reaches room temperature. Since failure of a glass sample usually starts at a surface in tension, greater loads may be applied before the surface reaches the critical breaking tension. In this way the strength of simple shapes may be increased by a factor of 2.5 to 3.5.

Tempering has also been tried on other types of ceramic bodies with considerable success. Strengths of alumina and steatite samples have been increased up to 40 percent. Here the samples have to be heated to a temperature where strain can be relieved before quenching. With alumina, this means temperatures in excess of 2,500° F and with steatite 1,800° F.

9-26. Resistance to Impact

Ceramic materials, as contrasted with metals, are usually considered as brittle. This is probably associated with the fact that they do not show any plastic or viscous flow at room temperatures right up to the breaking point. Also, the elastic constants of most glasses and dense materials are high. The result is that when a ceramic piece is struck, its inability to flow, along with its high elastic constants, causes high instantaneous stresses that may result in fracture. Catalogs usually list impact strengths, but their interpretation is of doubtful value and no figures will be given here.

9-27. Resistance to Thermal Shock

Many radomes in service will undoubtedly be subjected to severe thermal shock. While the calculation of the stresses in any particular piece under these conditions is extremely complicated, certain properties will minimize the tendency to fail under sudden heating. These are:

1. Low coefficient of thermal expansion
2. High thermal conductivity
3. High strength
4. Low elastic constants.

Typical values of coefficients of thermal expansion are listed in Table 9-III. Thermal conductivity values are listed in Table 9-IV.

Thermal Conductivity. This property seems to be related to the simplicity and regularity of the ionic arrangement. Close packing of the oxygen ions with very small cations in the interstices to interfere with the passage of elastic waves through the lattice seems to favor high conductivity. Beryllia is the outstandingly conspicuous example. Magnesia is another example and alumina another. Spinel, having closely packed oxygen ions but having two kinds of cations in the interstices, has fairly high conductivity. As the complexity of the structure increases, the conductivity decreases correspondingly. Glasses, with their lack of regularity, in general have much lower conductivities than the crystalline bodies. Bodies with a considerable amount of glass phase, such as porcelain, have lower conductivity than those where the glass phase represents only a very small fraction of the total volume, such as the relatively pure oxide ceramics. Where porosity is present, the conductivity will be further decreased. Porous ceramic insulating bodies may have conductivities in the neighborhood of 0.03.

The values given in Table 9-IV are only intended as a rough guide, since the method of manufacture strongly influences the conductivity. In particular, to obtain a body which can be

Table 9-III. Ceramic Coefficients of Thermal Expansion

Material	Coefficient (in./in./°F) x 10^6
Alumina	4.5
Beryllia	4.7
Steatite	4.3
Forsterite	5.9
Zircon	2.6
Porcelain	3.3
Cordierite	1.3
Glass-bonded mica	5.6
Window glass	4.7
Borosilicate glass	1.3
96% silica glass	0.45
Vitreous silica	0.31
607 BUZ Ceram (#8606)	3.1

Table 9-IV. Ceramic Thermal Conductivities

Material	Thermal Conductivity (Btu/sq ft/hr/°F/ft)
Alumina	10
Beryllia	125
Steatite	1.4
Forsterite	1.9
Magnesia	20
Zircon	2.9
Porcelain	1.1
Cordierite	1.1
Glass-bonded mica	1.3
Soda lime glass	0.5
Vitreous silica	0.8

formed and fired with regular commercial processes and kilns, the main constituent of the high alumina or high beryllia bodies may only be 90 percent or less of the total body, the remaining part being fluxes to lower the firing temperature or may be ingredients added to give desirable working properties in the forming operation. Bodies made with beryllia ranging from 70 to 95 percent may have conductivities from 30 to 90, which are still high by ceramic standards.

High thermal conductivity is desirable in improving thermal shock resistance because it helps to reduce steep thermal gradients within the piece.

9-28. Elastic Constants

The values of the elastic constants are important both in impact resistance and in thermal shock resistance. In both cases low values of Young's modulus and modulus of rigidity are helpful. It is usually not possible to do much toward independently controlling these elastic constants. Usually whatever lowers the elastic constants also lowers the strength and possibly the thermal conductivity. For this reason it is hard to find any really successful attempts to show experimentally the effect of high or low elastic constants on either impact or thermal shock resistance. However, porous ceramic bodies are usually better in thermal shock than very dense bodies of comparable expansion and, since the strength and conductivity of these will be lower than the corresponding properties in a dense body of the same composition, the lower elastic constants must take the credit.

Values of Young's modulus for some materials are shown in Table 9-V. Rigidity modulus μ follows closely the same pattern as Young's modulus E. Since they are related by the formula

$$\mu = \frac{E}{2(1+\sigma)} \qquad (9\text{-}3)$$

and since Poisson's ratio σ is usually just a little below 0.25 for ceramic bodies, this is to be expected.

9-29 Hardness

It is out of place here to try to evaluate the data which have been compiled from time to time on resistance of different compositions to rain erosion. It does seem reasonable to expect that hardness will play an important part. With this in mind, the Knoop hardness values of a few ceramic materials are shown in Table 9-VI.

Table 9–V. Young's Modulus for Ceramics

Material	Modulus (psi x 10^{-6})
Alumina	43
Steatite	16
Zircon	22
Wollastonite (dense)	13
Silicate glasses	10
Wollastonite (18 lb/cu ft)	0.076
Glass-bonded mica	11
607 BUZ Ceram (#8606)	17.5
607 AVE Ceram (#8605)	19.5

Table 9–VI. Ceramic Knoop Hardness Values

Material	Hardness
Alumina	2,000
Beryllia	1,220
Glasses	300 - 500

The only materials usually listed as having hardness greater than that of alumina are carbides, borides, and diamond.

9-30. Refractoriness

From a mechanical standpoint the radome designer is interested in materials which will keep a reasonable amount of their strength at somewhat elevated temperatures. Table 9-VII lists, as a very rough guide, what are called safe operating temperatures for a few ceramic bodies. The term is purposely vague but might be taken as a temperature above which one could not depend upon dimensional stability. It is highly probable that the electrical requirements rather than the mechanical will determine the upper temperature limit.

Table 9–VII. Ceramic Safe Operating Temperatures

Material	Degrees (F)
Alumina (100%)	3,540
Alumina (96%)	3,100
Zircon	2,650
Alumina (84%)	2,550
Porcelain	2,185
Steatite	1,830
Forsterite	1,830
Glasses	700 - 900
Mycalex 400	700
Mycalex K-10	750

Approximate densities of some representative ceramic bodies are given in Table 9-VIII.

Table 9–VIII. Densities of Ceramics

Material	Density (lb/cu ft)
Alumina	220
Beryllia	185
Steatite	170
Forsterite	170
Zircon	230
Porcelain	145
Cordierite	125
Glass-bonded mica	190
Window glass	150
Borosilicate glass	140
96% silica glass	135
Vitreous silica	140
Porous wollastonite (strength 500 psi)	40
Porous wollastonite (strength 100-200 psi)	20
607 BUZ Ceram (#8606)	160
607 AVE Ceram (#8605)	160

SECTION H. ELECTRICAL PROPERTIES OF CERAMICS

9-31. Effect of Composition

Most conventional electrical ceramic materials consist of one or more crystalline phases held together with a glass phase. The composition of the glass phase, if present, is usually difficult to specify with any degree of precision, since it depends on the temperature and rate at which the final state of the material has been reached. Where silica is present in the body composition, as very often it is to some degree, a certain amount will help to form the glass phase and the rest may go into forming crystalline phases with the other oxides present. Usually only in the case of the very pure oxides, of necessity fired at very high temperatures, can one consider the glass phase as being negligible.

9-32. Dielectric Losses

Ceramic dielectrics made of very pure refractory oxides are usually very low in dielectric losses. Aluminum oxide and magnesium

oxide are examples. On the other hand, glasses can be made to give extremely high losses over the whole practical frequency range. Pure vitreous silica has an extremely low loss tangent, but as the impurities are increased, particularly the smaller alkali ions, the losses mount rapidly. One may consider that in a ceramic dielectric the crystalline phase governs the dielectric constant while the glass phase is mainly responsible for the losses. The art or science of making good dielectric materials therefore consists mainly in so controlling the glass phase that the losses are kept small.

At the frequencies at which radomes are designed to be used, any losses caused by d-c electrical conductivity in the glass or glass phase may usually be neglected. The losses probably arise mainly from the ability of some of the ions present to jump back and forth between two adjacent positions of equilibrium separated by a potential barrier. The relaxation time associated with such a process will be proportional to $e^{\phi/kT}$ where ϕ is the work required to lift the particular ion over the barrier, k is Boltzmann's constant and T is the absolute temperature. If there is a range of values of the potential barriers involved, there may be an extremely wide range of relaxation times, because of the exponential form of the relation between them.

Under the action of an alternating current field only those processes which have a relaxation time in the neighborhood of $1/2\pi f$ will contribute to the losses. All of those processes which have relaxation times lower than this value will contribute to the dielectric constant. The result is that the dielectric constant always decreases with increasing frequency while the loss tangent may increase or decrease. It so happens that in most ceramic materials the loss tangent decreases with increasing frequency up to about 10^7 cycles per second and then increases somewhat up to 10^{10} cycles per second.

If the composition of the material is such that there are very few processes present with relaxation times over the range from 10^2 up to 10^{10}, this means that the losses will be very low over this whole frequency range. It also means that the dielectric constant will vary very little over the same range. In general it may be noticed that in any good table of dielectric properties those materials that show the lowest losses also show the least variation of dielectric constant with frequency.

Table 9-IX lists typical values of dielectric constants and loss tangents for representative ceramic materials.

Table 9-IX. Dielectric Properties of Ceramic Materials

Material	Dielectric Constant	Loss Tangent (at 10^{10} cps)
Alumina	8.8	0.0018
Beryllia	4.2	0.0005
Magnesia	9.6	<0.0003
Steatite	5.8	0.004
Zircon bodies	11.4	0.001
	8.0	0.002
Forsterite	6.1	0.0003
Porcelain	5.4	0.008
Cordierite	5.0	0.003
Vitreous silica	3.78	0.00017
96% silica glass	3.82	0.00094
Soda lime glass	6.7	0.017
Borosilicate glass	4.5	0.0085
Soda potash lead glass	6.6	0.0063
Glass-bonded mica	7.1	0.0033
Foamed wollastonite (20 lb/cu ft)	1.38	0.003
Foamed wollastonite (30 lb/cu ft)	1.59	0.003
607 Buz Ceram (#8606)	5.45	0.0029

9-33. Temperature Effects

Of more importance in radome work than stability of dielectric constant with frequency is the stability with temperature at the design frequency. Any serious variation of the dielectric constant with temperature can very seriously affect radome performance.

The effect of a temperature rise is to decrease the relaxation time associated with any process. This means that at a fixed frequency the processes that contribute to the losses at an elevated temperature are the processes which at room temperature would have contributed to the losses at a lower frequency. Therefore, if a material has very low losses down from 10^{10} to 10^2 cycles per second, it will have a dielec-

tric constant which remains stable over a wide temperature range. At lower frequencies the temperature range over which the dielectric constant remains constant may be much less. The very high frequencies for which the radome must work, therefore, are an advantage from the standpoint of the temperature stability of the materials out of which the radome is made. For the best temperature stability, materials should be chosen which have low losses over the widest possible range down from the operating frequency. The pure oxides come closest to fulfilling these conditions. Measurements listed by Von Hippel show that the variations of dielectric constant with temperature follow the general pattern which would be expected from the considerations just discussed.[20]

9-34. Losses Versus Structure

As mentioned before, the dielectric losses are usually associated with the glass phase in the ceramic material. If the glass phase occupies only about 10 percent of the volume of the material and if, as is often the case, most of the impurities are concentrated in the glass phase, then comparatively small amounts of impurities can constitute a goodly percentage of the glass phase, with resultant high losses.

Studies of glass structure indicate that a large part of the losses are related to the way in which such ions as the alkali ions fit into the interstices of the glass. If there are many ions in interstices which are too large for them, then the losses will be high. Very small amounts of sodium or lithium do not have a great effect in increasing the losses, but larger amounts can cause very great losses because the excess ions have to fit themselves into interstices which are too large for them. Similarly, mixtures of ions can cause very much lower losses than the same mole percent of a single ion. Small ions are usually associated with greater losses than large ions. In steatite bodies the addition of barium has frequently been used to lower the losses because of the large size of the barium ion.

The relations between the ions present in a ceramic body and the losses can never be simple. Addition of alkalis or alkaline earths can affect many things besides modifying the composition of the glass phase. They can change the viscosity of the glass phase and change the rate of crystal formation or the species of crystal which is forming. All of these things have a very complicated effect on the composition and amount of the glass phase present.

Since it is possible to examine the structure of ceramic bodies either by observing thin sections in transmitted light or polished sections in reflected light, it might be expected that the connections between the amounts of the different phases present and the shapes in which they exist, on the one hand, and the dielectric properties, on the other, might be rather well worked out. Actually very little in the way of such an approach is available in the literature, and the development of dielectric ceramics has been largely a matter of trial and error.

Several authors have attempted to derive expressions for the dielectric properties of mixtures of phases. Probably the most convincing and satisfactory of these is the treatment of Niesel, who derives expressions both for the dielectric constant and also for the loss tangent.[21,22]

The cases covered in his papers include different shapes of crystals embedded in a continuous glass phase. He also treats the case of a polycrystalline material with randomly oriented crystals completely filling the space. Eichbaum has shown that Niesel's formulas may be used with considerable success to predict the dielectric properties of certain wollastonite bodies in which the volume fractions of the separate phases are determined by a counting method with a polished section under the microscope.[23] Much more work along these lines is called for.

Niesel's treatment does not cover the case of a dielectric with much interconnected porosity. Metzger has shown that certain empirical relationships may be used with considerable reliance in such cases.

In a manner analogous to the use of the so-called Gladstone-Dale index in the prediction of the refractive indices of glasses, it was assumed that in a porous ceramic body of given composition the quantity

$$\frac{\sqrt{\epsilon_r} - 1}{\rho} = k_1 = \text{a constant} \qquad (9\text{-}4)$$

for different porosities. ϵ_r is the relative dielectric constant and ρ is the density. If $k_1 p$ is much less than unity,

$$\epsilon_r = 1 + 2k\rho \qquad (9\text{-}5)$$

When the density is measured in pounds per cubic feet, the constant k, in this relation is 0.01.

The electrical properties of a glaze are determined by the material employed. From an electrical point of view, the glaze may be considered as a thin skin of dielectric constant higher than the porous ceramic core which it protects.

GLOSSARY

Autoclave. At apparatus for the treatment of ceramic and other materials at elevated temperatures and high pressures of water vapor.

Bisque fired. A ceramic body is said to be bisque fired when fired to a temperature sufficient to give it considerable handling strength but not sufficient to allow it to reach maturity or that state where the porosity reaches a very low value.

Compressive strength or crushing strength. This is the maximum compressive stress, in pounds per square inch, which a ceramic sample of a certain shape will withstand before fracture. For most ceramic bodies this is very much greater than either the tensile strength or modulus of rupture.

Decant. To pour off from a mixture of water and a solid material that fraction staying easily in suspension, leaving behind the solid material that has settled out or never gone into suspension.

Deflocculation. That state of a suspension in which each particle is separated from its neighbors, resulting in greater fluidity than when the particles tend to adhere to each other.

Diagram. Contraction for phase rule diagram which is a two- or three-dimensional plot showing the stable existence and coexistence of possible compounds, liquids, and solid solutions in a mix of known proportions of two or more oxides at different temperatures.

Modulus of rupture. The breaking strength of a bar of ceramic material when supported between knife edges and loaded in the middle. The strength is expressed as the stress in pounds per square inch in that layer of the bar in which the stress is greatest, assuming perfect elasticity up to the breaking point. This is computed according to the formula (for a bar of rectangular cross section).

$$M = \frac{3W\ell}{2ab^2}$$

where M is the modulus of rupture, W is the load in pounds required to break the bar, ℓ is the distance between the knife edges, a is the width, and b is the thickness, all measured in inches.

Phase. Any physically and chemically homogeneous fraction of a ceramic mix. Possible phases might be crystals of any of the oxides present or crystals of any compounds of solid solutions containing several oxides. Usually in a ceramic body containing any silica or other glass-forming oxide, there will also be a noncrystalline phase which will be a glass whose composition will depend on the composition of the original mix and the thermal history to which it has been exposed.

Relaxation time. Under the action of an applied electric field E there will be some molecular processes whose contribution to the electrical displacement D will not be instantaneous but will have the general form

$$D = D_0 \left\{1 - e^{-\frac{t}{\tau}}\right\}$$

where D_0 is a constant which gives their contribution to the displacement after a very long time and τ is a quantity with the dimensions of a time which is a characteristic of the process. When τ is large the process responds slowly but when τ is small the process responds rapidly. τ is called the relaxation time.

Slurry. A thick suspension of a finely ground solid in water or other liquid.

Steatite. A fired ceramic material with a chemical composition in the neighborhood of that of the compound enstatite $MgO \cdot SiO_2$.

Supernatant. Applies to that fraction of a mixture of solid and water in which the solid exists in a well dispersed suspension.

Tensile strength. The tensile stress in pounds per square inch required to cause fracture in a ceramic sample. Since most ceramic materials at room temperature exhibit no plastic flow up to the breaking point, it is necessary to use great care in preparing almost perfectly straight samples to avoid any bending effects.

REFERENCES

1. Technical Report No. 1, Project NONR 40403, Rutgers University, 15 June 1953.

2. Technical Report No. 2, Project NONR 40403, Rutgers University, 15 June 1954.

3. Technical Report No. 3, Project NONR 40403, Rutgers University, 15 June 1955.

4. Contardi, W. A. and Hund, G. J. Correlation of Particle Size Distribution with Firing Shrinkage in a Ceramic Whiteware Composition. Ceramic Age, 62, November 1953, p. 13.

5. Scholes, W. A. Thermal Conductivity of Bodies of High BeO Content. Jour. Am. Cer. Soc., 33, 1950, p. 111.

6. Snyder, N. H. and Ruh, E. Properties of High Magnesia Whitewares. Ceramic Age, 61, February 1953, p. 15.

7. Smoke, E. J. Spinel as Dielectric Insulator. Ceramic Age, 63, May 1954, p. 13.

8. Smoke, E. J. Low Loss Zircon Dielectrics. Ceramic Age, 61, February 1953, p. 15.

9. Hall, F. P. Low Loss Zircon Dielectrics. Ceramic Age, 61, March 1953, p. 12.

10. Gebler, K. and Wisely, Harriet R. Dense Cordierite Bodies. Jour. Am. Cer. Soc., 32, 1949, p. 163.

11. Smoke, E. J. Thermally Resistant Whitewares. Jour. Am. Cer. Soc., 33, 1950, p. 174.

12. Smoke, E. J. Ceramic Compositions Having Negative Linear Thermal Expansion. Ceramic Age, 62, July 1953, p. 13.

13. Metzger, A. J. Report VPI-128-24, V. P. I. Research Foundation, Inc., Blacksburg, Va., September 1952.

14. Metzger, A. J. Final Report, Navy Contract N383s-95917, Virginia Eng. Exp. Station, V. P. I., Blacksburg, Va., February 1955.

15. Proceedings of the Radome Symposium, Vol. I, The Ohio State University, Columbus, Ohio, June 1955.

16. Hessinger, P. S. Development and Evaluation of Ceramic Sandwich Construction for Radomes. Thesis. The Ohio State University, Columbus, Ohio, December 1955.

17. Kalousek, G. L. and Dence, R. B. Development and Fabrication of Inorganic Sandwich Radomes. W.A.D.C. Technical Report 54-197, April 1954.

18. Shand, E. B. Glass Engineering Handbook. Corning Glass Works, Corning, N.Y. 1955.

19. Smoke, E. J. and Koenig, J. H. Ceramics as Basic Engineering Materials. Mechanical Engineering, 78, 1956, p. 315.

20. Von Hippel, A. Dielectric Materials and Applications. The Technology Press of the Massachusetts Institute of Technology, 1954.

21. Niesel, W. Ann. der Phys., 10, 1952, p. 336.

22. Ann. der Phys., 12, 1953, p. 410.

23. Eichbaum, B. R. The Relationship Between Structure and Dielectric Properties in Some Ceramic Materials. Thesis. Rutgers University, New Brunswick, N. J., June 1956.

Chapter 10

AIRBORNE RADAR INSTALLATION TOPICS

by

Allen S. Dunbar

Dalmo-Victor Company
Belmont, California

INDEX OF SYMBOLS

A	Constant determined by atomic or molecular polarizability and temperature
a	Constant $\cong 8 \times 10^{-5}$ per ft
a^*	Velocity of sound
D	Distance
$F(\phi)$	Fresnel straight-edge diffraction pattern
$G(\phi)$	Composite far-field pattern
$G(0)$	Absolute gain of antenna
g_0	Gain factor
h	Altitude in ft
i	Angle of incidence with respect to normal and shock fronts
K	Constant for a given pattern
L	Diameter of spherical eddies
M	Mach number
P	Constant for a given pattern; parameter P determined by half-power beamwidth of antenna pattern
P_f	Free-space pattern
P_i	Relative strength of Image Antenna
$P(\theta,\phi)$	Beam shape
$P(\phi)$	Unperturbed far-field antenna pattern
p_1	Pressure in supersonic flow
p_2	Final pressure
r	Angle of refraction
S_0	Distance from nacelle to antenna
u_1	Velocity of object
u_2	Velocity of air in air prism
β	Angle which shock wave makes with axis of aircraft
$\overline{\Delta}\text{rms}$	Path error
$\Delta\epsilon$	Root-mean-square difference in dielectric constant in turbulent medium
$(\overline{\Delta\epsilon})^2$	Mean-square fluctuations of dielectric constant
ϵ_r	Dielectric constant of a gaseous medium
θ	Azimuth angle
θ_0	Angle intercepted at edge of reflecting surface in horizontal plane
κ	Square root of ratio of velocities in supersonic shock front
ρ_1	Density in air prism
ρ_2	Density in free air
ϕ	Elevation or depression angle
ϕ_0	Direction of beam maximum with respect to horizontal or angle intercepted at edge of reflecting surface in vertical plane
ϕ_1	Arbitrary elevation angle
ϕ_2	Maximum angle of shaped-beam portion of pattern
ϕ^*	Angle at which functions $e^{-p^2\phi^2}$ and $K \csc^2 \phi \cos \phi$ meet in common tangent

Chapter 10

AIRBORNE RADAR INSTALLATION TOPICS

SECTION A. INTRODUCTION

In the preceding chapters, methods of radome analysis, problems and techniques of design, and criteria of performance have been discussed. Until now, little has been said about the placement of the antenna and radome on the aircraft or missile airframe, the needs for stabilization of the scanner for certain types of radar systems, the swept volume of scanning antennas, nor about the effect that the location of the antenna with respect to the airframe may have upon the performance of the radar system as a whole.

In this chapter we shall consider the various factors which govern the size and location of the radome. We shall consider interference and diffraction effects which may result from the presence of the aircraft's wings or fuselage in close proximity to the radar antenna. The performance of the radar, despite the angular motions of the aircraft in flight, also requires consideration. In these matters we do not deal with the properties of the radome or its construction, but it will be obvious that the matters to be discussed become of considerable importance in the design of the radome.

SECTION B. STABILIZATION AND MOUNTING PROBLEMS

10-1. Pressurization

At an altitude of 50,000 ft or greater corona discharge will frequently occur on the antenna feed when the peak power is upward of 150 kilowatts. The pressurizing cover, or feedome, for the antenna feed must be large in order for corona not to occur at very high power and high altitude. The effect of the corona discharge is to heat the feedome, soften the plastic or resin, and cause a pressure bubble to form and burst with a consequent loss of pressure in the system and voltage breakdown in the transmission line. It is therefore advisable in some instances to pressurize the entire radome to avoid corona discharge on the feedome.

To pressurize the radome, the dome must itself be pressure tight and structurally strong enough to maintain the pressure at the extreme operating altitude. A seal must be provided at the seat of the radome mounting rim and the nacelle. Since aerodynamic heating may cause a considerable rise in temperature of the skin and radome, the seal must be of a suitable material to provide an adequate pressure seal at the extremes of temperature and pressure.

Thus far only experimental studies of radome pressurization have been performed. No design data is as yet available.

10-2. Stabilization[1]

Because aircraft in flight are unsteady vehicles, subject to roll, pitch, and yaw, stabilization of the radar antennas is often required to maintain the position of the radar beam in space despite the involuntary maneuvers of the craft. Stabilization is also required for maintaining

the position of the radar beam in space automatically despite the roll and pitch of an aircraft caused by flight maneuvers. Stabilization is usually essential to obtain the required accuracy in target location, fire control, and weapons guidance.

In antenna stabilization, one or more gyroscopes and a servomechanism automatically tilt the radar beam an equal amount in a direction opposite the pitching or rolling of the vehicle in which it is mounted, with the result that the radiated beam is unaffected by the changing attitude.

Stabilization may be accomplished by two methods: mechanical stabilization and data stabilization. Only mechanical stabilization need concern the radome and antenna nacelle designer; data stabilization is accomplished electronically within the radar system itself. Data stabilization is only a partial substitute for mechanical stabilization, since if the vehicle rolls or pitches to such an extent that the radar beam no longer scans the desired part of the field, data stabilization cannot compensate.

Platform Stabilization. Kinematically, the most nearly perfect airborne stabilization scheme is the one in which the antenna scanner is mounted on a gimbal system that maintains the axis of the scan truly vertical. The gyroscope provides a stable vertical reference. Separate servomechanisms, connected to the roll and pitch axes respectively, keep the scanner axis parallel to the axis of the gyroscope. Two arrangements of axes and antenna mounting are shown in Figure 10-1.

Line-of-Sight Stabilization. For this method of stabilization, no effort is made to maintain a level platform. Instead, referring to Figure 10-2, as the antenna rotates in its scanning function about the azimuth axis, a servomechanism maintains the angle $\emptyset$ at the proper value to compensate for both pitch and roll. Thus the beam scans in the horizontal plane or in a plane at a prescribed angle above or below the horizontal.

For a pencil-beam antenna, the results obtained with line-of-sight stabilization are essentially the same as with platform stabilization. For a shaped-beam antenna such as cosecant-squared, however, the results are different. Line-of-sight permits beam tilting with respect to the ground, as illustrated in Figure 10-6, whereas platform stabilization prevents this beam tilt.

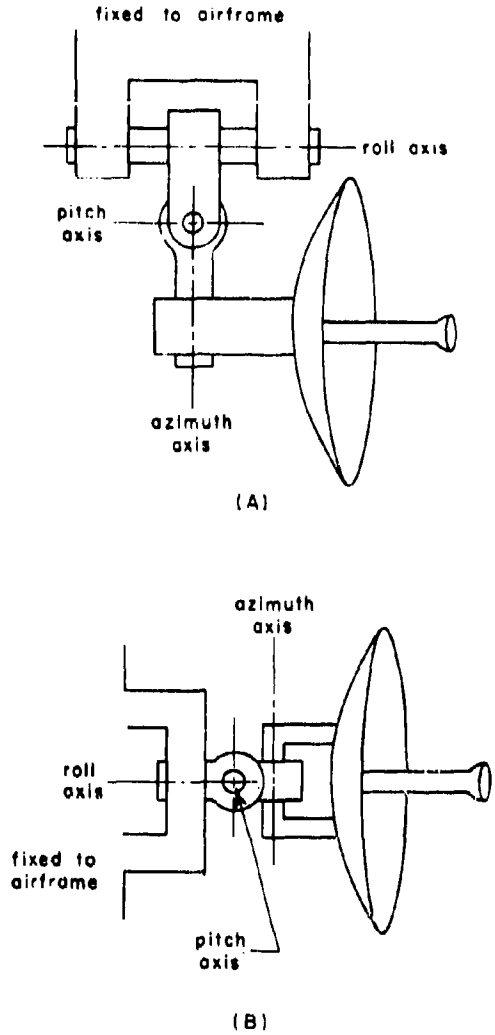


Figure 10-1. Two Arrangements For Platform Stabilization

By way of contrast, with pitch stabilization (no compensation for roll) the antenna scans in a plane tilted with respect to the horizontal plane.

Two different forms of line-of-sight stabilization are possible. In one, the gyro is a stable vertical mounted on the scanner; in the other, the gyro is a stable vertical mounted remotely from the scanner.

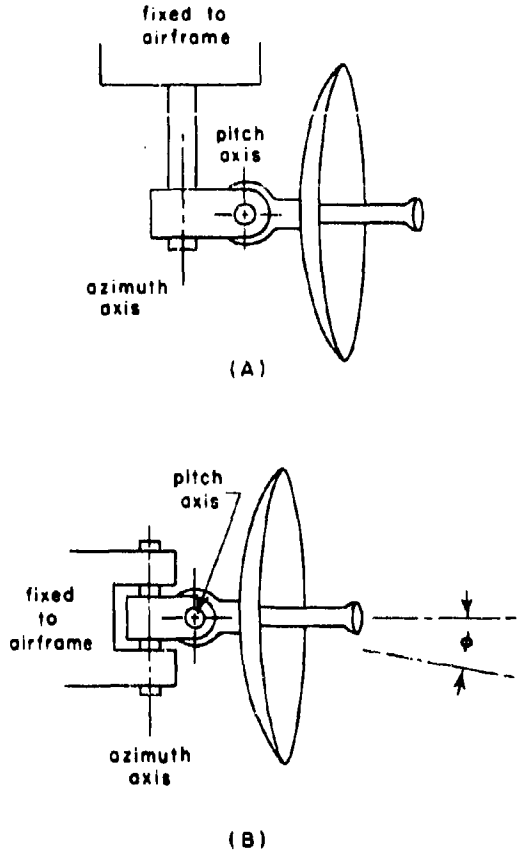


Figure 10-2. Two Mounting Arrangements For Line-Of-Sight Stabilization; Angle of Depression ϕ to Keep Beam Horizontal Given by $\sin \phi = \sin \alpha \sin R - \cos \alpha \sin P \cos R$ Where α = Azimuth Angle From Dead Ahead, R = Roll Angle, and P = Pitch Angle

Roll Stabilization. For some applications, pitch stabilization is not essential to the performance of the radar system, and only roll stabilization is required. Automatic stabilization about the roll axis is obtained by utilizing only the roll-gimbal axis of the platform stabilization.

Pitch Stabilization. Pitch stabilization is designed to compensate for changes of attitude of the aircraft in glide, climb, or angle of attack. Like roll stabilization, it is patterned after the platform stabilization method.

Yaw Stabilization. Compensation for yaw in an aircraft is necessary in only very limited cases. One of these is side-wise search radar, in which the antenna is oriented in such a manner as to constantly look perpendicular to the line of flight of the aircraft. This is most frequently accomplished by data stabilization, i.e., by altering the radar presentation to suit the circumstances. Sector scanners may be yaw-stabilized about the vertical axis by means of a horizontal gyroscope. It is unlikely, however, that yaw stabilization will materially affect the swept volume of the scanner, and consequently it is not likely that the radome will need to be larger in volume to accommodate the scanner.

10-3. Swept Volume

Platform and roll-stabilized scanners require an increase in the volume of the radome needed to house the scanner and the stabilization equipment. This results from the relative displacement of the scanner, as illustrated in Figure 10-3. The swept volume is determined by the moment arm of the stabilization system. Even the most compact platform or roll-stabilized scanner requires a larger radome than a line-of-sight stabilized scanner with an antenna of the same dimensions.

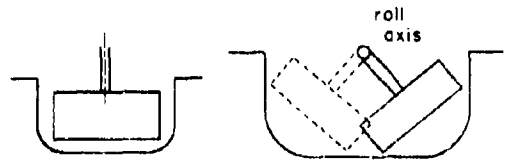


Figure 10-3. Increase in Radome Size for Roll-Stabilized Antenna

It should be noted, however, that roll-stabilized sector scanners do not increase the swept volume, because they can always be designed in such a manner that the roll axis is coincident with the geometric center of the scanner, and therefore may fit into a circularly symmetric radome. In other words, the scanner may be designed to fit into a radome that is symmetric about the roll axis. This is illustrated in Figure 10-4.

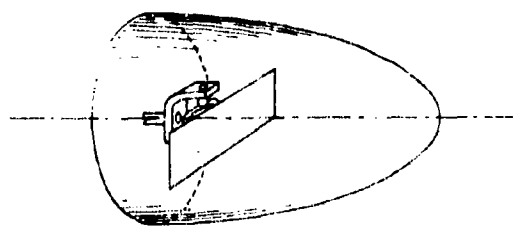


Figure 10-4. Axially-Symmetric Roll-Stabilized Sector Scanner Requiring no Increase in Radome Size

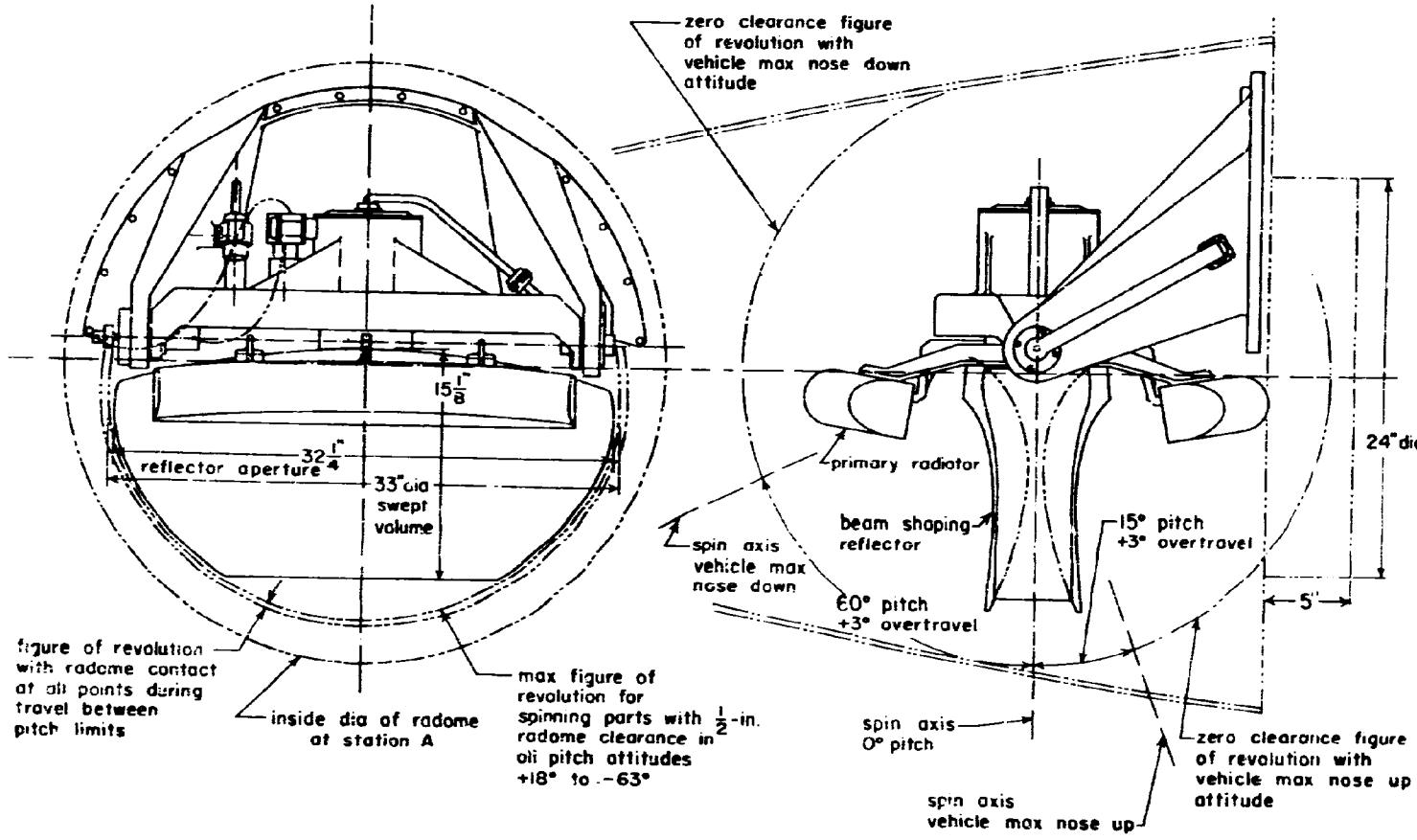


Figure 10–5. Clearance of Antenna in Radome

The swept volume of a scanner system is determined by the surface which is generated by the antenna structure in its extreme condition of stabilized motion. This surface then defines the smallest radome which can house the scanner system.

As an illustration let us consider a typical design problem. An antenna is to be designed for use in a missile. The antenna must have a shaped beam for ground mapping, and must scan $\pm 90^{\circ}$ in azimuth. The characteristics of the missile require that the antenna scanner be roll-stabilized, and the tactical application requires that the scanner be pitch-stabilized from $+18^{\circ}$ to -63°. The antenna system chosen consists of two identical shaped-beam antennas, back-to-back, continually rotating in azimuth, and alternately excited by means of a rotary switch. The roll axis is the centerline of the radome, which is symmetric about the longitudinal axis of the missile. Clearance between the radome inner surface and the antenna reflector is chosen to be no less than one-half inch for all conditions of pitch. The resulting antenna outline drawing and the clearance curves are shown in Figure 10-5. The clearance figure is generated by the circle of smallest radius within which the spinning antenna system can fit under all conditions of pitch. The radius of this sphere must, of course, be one-half inch less than the radius of the radome cross section, to maintain the one-half inch clearance.

Clearance. There is no rigid formula for specifying the clearance criteria for any given radome and antenna combination. The minimum clearance figure for a particular antenna will be determined by the size of the antenna, the type of radome and its construction, the conditions of shock and vibration which the system must experience, and the rate and angular limits of antenna scan. In general, small antennas will be housed in radomes which are relatively rigid, and consequently clearances can be small also. In certain guided missiles, which contain small conical scanner antennas for precision tracking, clearances of only a few thousandths of an inch can be maintained. On the other hand, very large antennas, which, because of their size cannot remain truly rigid under conditions of shock and vibration, require much greater clearance space between the antenna and the radome inner wall. A clearance of at least an inch will be required for large antennas (i.e., airborne-early-warning antennas and similar types). Clearance, therefore, will range from a small fraction of an inch for small antennas to an inch or more for large antennas.

10-4. Stabilization for Various Types of Antennas

Scanners designed for search about the azimuth axis require either platform or line-of-sight stabilization. Examples of such equipments are long range search (airborne-early-warning) and navigation and bombing radars. A cosecant-squared type of beam is commonly used to obtain uniform ground illumination and maximum radar mapping range. Poor stabilization results in non-uniform ground illumination, and this in turn adversely affects the radar mapping presentation and causes the maximum range of the target presentation to suffer.

A disadvantage of line-of-sight stabilization is the distortion that appears on the PPI (Plan Position Indicator). When the axis of rotation is not vertical, the plane of a cosecant-squared beam will be tilted away from the vertical by an amount equal to the cross-traverse angle, and is dependent on the heading of the scanner and the attitude of the aircraft. Consequently the beam will intersect the ground in a line different from the desired one. Ground targets will therefore appear displaced from their true positions as indicated in (A) of Figure 10-6. This condition can, of course, be corrected by the use of platform or roll stabilization with consequent increase in swept volume.

Navigation/bombing radars usually require platform, roll, or line-of-sight stabilization, depending upon the degree of azimuth scan, mission profile of the weapons system, and relative stability of the vehicle in which the radar is mounted. In general, navigation/bombing radars require the greatest degree of stabilization. Modern weapons systems may require stabilization for bombing radars up to $\pm 50^{\circ}$ in roll and between the limits of $+20^{\circ}$ to -60° in pitch. Navigational radars, of course, do not demand such a degree of stabilization. Typical requirements for navigational radars are $\pm 15^{\circ}$ in roll and pitch.

Fire control or gun aim radar for interceptor aircraft, tail warning and tail defense for bombers, and seeker antennas for active and semi-active guided missiles generally do not require platform or line-of-sight stabilization of the antenna scanner. This is primarily due to the fact that the scanner performs a search/track function which is symmetric with respect to the axis of the vehicle. Roll stabilization is sometimes required, particularly if the vehicle, such as a missile, is not itself roll-stabilized to some degree. Roll stabilization is also required for scanners whose search function is not axially symmetric with respect to the line

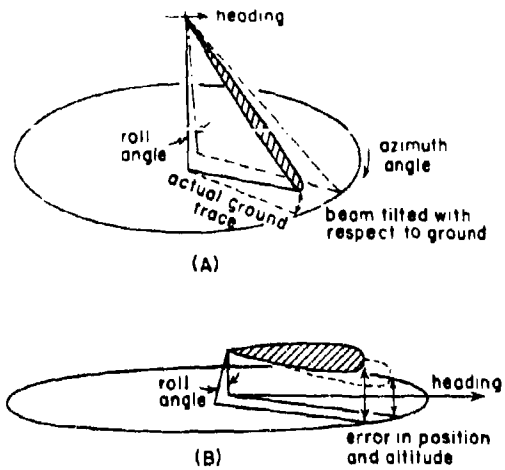


Figure 10–6. Beam Tilt Caused By Roll

of flight. For example, a wig-wag or palmer search scan for a search/track radar should be roll-stabilized so that the vertical and horizontal reference may be retained during roll of the aircraft in maneuvers. The degree of roll stabilization for use in modern high-speed aircraft may be as great as ±90°.

Long range search or airborne-early-warning radar require line-of-sight stabilization, but the complexity and large swept volume of platform stabilization is not justified. If the vertical beamwidth of the search radar antenna pattern is sufficiently broad, mechanical stabilization will not be needed, since all targets of interest will be within the scanned volume of space. The limits of stabilization for early warning radar need not be greater than ±20° in roll.

Sidewise search radar for aerial reconnaissance requires roll stabilization so that the range and presentation are not adversely affected by the roll of the aircraft. The stabilization may be as great as ±30°.

The tolerance permitted in the stabilization accuracy will vary with the application. In general, the tolerance may be stated in terms of a fraction of the beamwidth, typically about one-fourth the beamwidth. Navigation/bombing and reconnaissance radars require greater precision in roll stabilization for reasons which have already been discussed. Typical specifications for roll stabilization accuracy are ±1/4 degree.

Considerable importance must be attached to the proper location, vision, and axial orientation of the radar antenna in its installation.

The axial orientation of the antenna must be accurately adjusted to the angle of attack of the aircraft in normal flight, in order that the stabilization reference is also the inertial reference, with the vertical axis on the true vertical. This is important because the stabilization system is relieved of excessive effort and results in more accurate stabilization as well as less wear of the moving parts. Particularly in the case of unstabilized navigational and bombing antennas, improper axial orientation causes an uneven illumination of the ground, and results in the loss of uniform mapping. In the case of unstabilized search antennas, such as AEW radar, improper axial orientation causes the

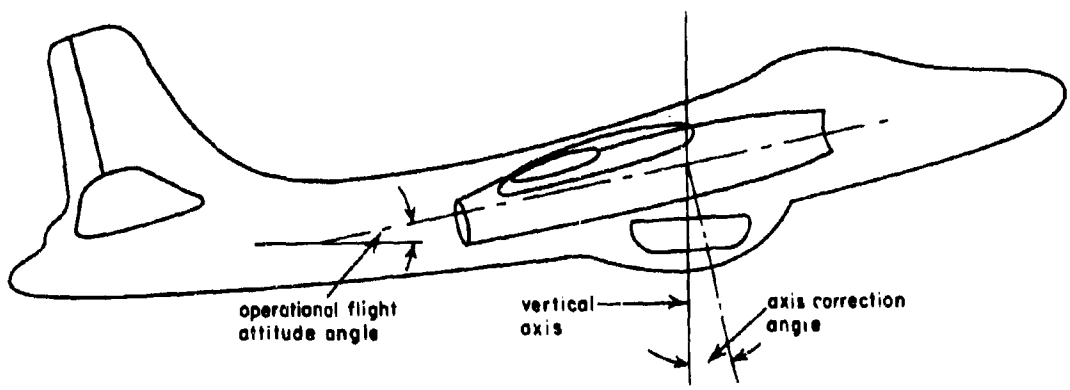


Figure 10–7. Axis Correction for Aircraft Attitude

possible loss of low altitude targets at long range and may contribute to excessive ground or seal clutter. The effect of roll on an unstabilized antenna is shown in Figure 10-6.

The vertical axis of the antenna rotation must be alined to the vertical at the best average attitude at which the aircraft is expected to fly operationally. This frequently implies tilting the axis slightly backward from the perpendicular to the fuselage centerline, as shown in Figure 10-7.

SECTION C. PATTERN DISTORTION BY AIRCRAFT STRUCTURE

10-5. Vision Requirements

The vision requirements of a radar installation will, of course, be determined by the purpose and function of the radar system. Among the several different types of radar systems used in aircraft and missiles are the following: (1) Airborne-Early-Warning Search Radar, (2) Height Finder, (3) Navigational Radar, (4) Radar Bomb Sight, (5) Aerial Reconnaissance, (6) Guidance and Fire Control Radar, (7) Active and Semi-Active Homing Systems, (8) Tail Warning and Tail Defense Radar, and (9) Direction Finders.

The radar must have the unobstructed vision required for its operation if it is to fulfill the purpose for which it was intended. The antenna must be housed in an aerodynamically acceptable radome which permits the field of vision required. Where a protrusion from the aircraft is permissible, vision and stabilization requirements can be satisfied more readily, but it must be recognized that in many high performance aircraft protrusion of the antenna and radome is not welcome.

A very common requirement is circular vision of the ground well out toward the horizon. The only good location for mounting the scanner is then below the fuselage. The problems of such a location include aerodynamic drag and requirements for stabilization. If rearward vision is not required, an antenna with circular scan may be mounted just below the nose, where the radome can be completely faired in. Scanners for fighter-interceptor aircraft are installed in locations that allow vision in the forward hemisphere. Installation in the nose of the aircraft is the obvious choice. It sometimes happens, however, that the nose is not available for radar installation, and in such circumstances an external housing becomes necessary. Possible types of installation might include a wing-tip pod, a nacelle faired into the leading edge of the wing, or a separate pod suspended beneath the wing. Scanners for protective fire control in bombers are located in a tail nacelle or other such locations where they can search for and track enemy fighters or missiles approaching from the rear or other anticipated directions.

10-6. Placement of Radome and Nacelle

In attempting to meet the vision requirements of the radar systems, provision for installation may be made in a great variety of ways. A number of radome placements are indicated in the diagrams of Figure 10-8.

In (A) of Figure 10-8 several radome installations are shown as part of a large aircraft. Radome (1) permits approximately 180° scan in the azimuth plane, with vision unlimited in the downward direction. Radomes (2) and (3) permit 360° scan in azimuth. Radome (4) represents an installation for an aerial reconnaissance antenna in the fuselage. Radome (5) is the same installation in a pod suspended beneath the wing.

In (B) of Figure 10-8 are shown (1) a radome which forms a part of the nose of the aircraft, permitting 180° scan, and (2) a tail installation permitting limited scan in the rear hemisphere.

In (C) of Figure 10-8 possible radome placements for vision in the forward hemisphere are illustrated: (1) a nose radome, (2) a wing nacelle, and (3) a wing tip pod.

In (D) of Figure 10-8 AEW (airborne-early-warning) radomes on a large aircraft are indicated: (1) a belly radome, and (2) a top radome.

In (E) of Figure 10-8 a nose radome on a large aircraft is shown; in (F) a chin radome and in (G) a nose radome with an instrumentation boom extending from the apex of the nose cone.

10-7. Interference Effects

In addition to the refraction and reflection which occur at the radome interfaces, and which contribute to boresight shift and radiation pattern distortion, discussed in Chapters 2, 3 and 4, there are two types of interference effects which should be considered. These effects are edge diffraction and skin reflection.

Of course, other obstacles, such as pitot tubes, refueling probes, guns, propellers, projectiles and missiles, may present serious

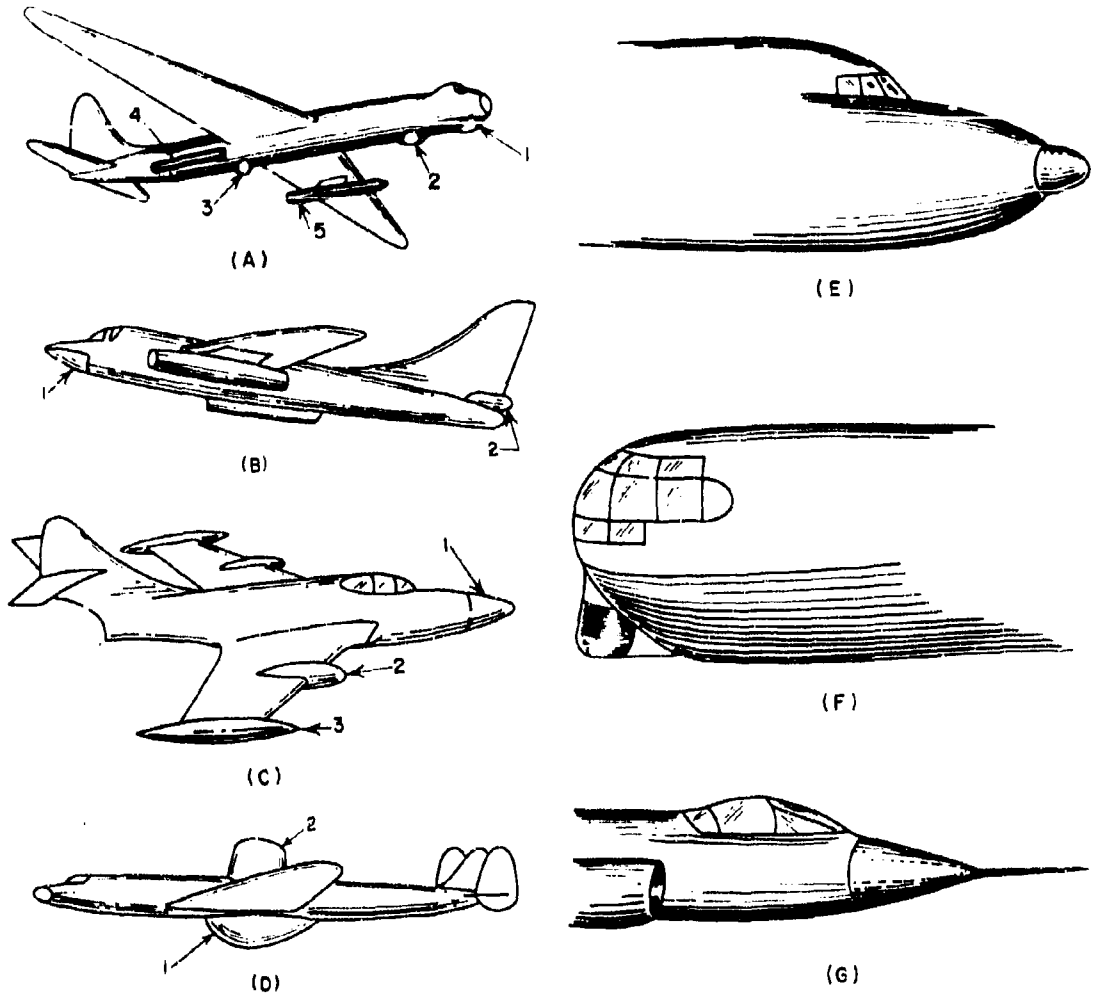


Figure 10-8. Placement of Radome in Aircraft

problems to the radar designer. The undesirable results of placing an obstruction in the field of an antenna include attenuation, boresight shift, beam distortion, and reflection. Very little quantitative data is available, however, on the effect of such obstacles. The reader wishing further information is referred to the bibliography.

Edge diffraction is distortion of the antenna radiation pattern as a result of an edge discontinuity protruding into the envelope of rays emanating from the antenna, or at least extending sufficiently close so that the edge is illuminated. This causes reradiation of that energy as if the edge were another antenna, as indicated in (A) of Figure 10-9. The original field pattern now has superimposed upon it another field pattern from the radiating edge. Constructive and destructive interference occurs, producing fringes in the otherwise unperturbed antenna pattern.

The other type of interference which adversely affects the radiation pattern is skin reflection. This is illustrated in (B) of Figure 10-9. If the rays from the antenna graze the outer reflecting surfaces of the airplane, it is possible that reflected energy will interfere with the direct rays and produce opposition and reinforcement in the antenna pattern. This results in the appearance of maxima and minima in the otherwise unperturbed pattern.

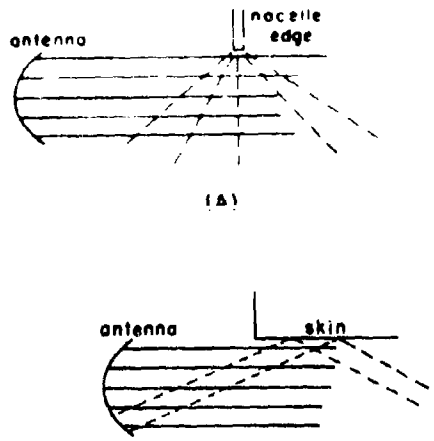


Figure 10–9. Interference Effects Due to (A) Diffraction and (B) Reflection

These two effects may cause one or more detrimental effects to the radar performance: (1) they may cause attentuation of the beam power, (2) they may produce a deflection of the beam to a new and unsuspected direction, and (3) they may distort the antenna pattern and render it less effective in performance of its function.

Synthesis of Edge Diffraction Patterns -- Analysis Based on Physical Optics. The exact analysis of the effect of a radiated electric field from a directive antenna streaming past an opaque edge presents some obvious difficulties. The edge is in the near field of the antenna, where the phase and amplitude of the wave may be rapidly varying. The nacelle edge is clearly not a knife edge, since it is a cylindrical section of some sort, and its physical position with respect to the antenna is very likely not constant as the antenna scans in azimuth.

The following discussion of edge diffraction is presented for the purpose of developing a physical picture of the edge diffraction phenomenon. The method to be used is based upon a number of assumptions which are somewhat dubious. It is hoped, however, that the discussion will assist the reader to gain an appreciation of the problems involved.

We assume, first, that the far-field power pattern in the elevation plane produced by a beam streaming past an opaque knife edge can be described by the product of the beam pattern and the Fresnel diffraction pattern of the knife edge:

$$G(\phi) = P(\phi)\, F(\phi) \qquad (10\text{-}1)$$

in which $G(\phi)$ is the composite far-field pattern, $P(\phi)$ the unperturbed far-field antenna pattern and $F(\phi)$ the Fresnel straight-edge diffraction pattern. The unperturbed antenna pattern is known, and for purposes of illustration will be described by a shaped beam for ground mapping. In a typical case, this pattern is well-fitted by the expression

$$\begin{aligned} P(\phi) &= g_0\, e^{-p^2\phi^2} \text{ for } \phi_1 \le \phi \le \phi^* \\ &= g_0\, K \csc^2\phi \cos\phi \text{ for } \phi^* \le \phi \le \phi_2 \end{aligned} \qquad (10\text{-}2)$$

in which ϕ is the angle of depression with the horizon as reference; g_0 is a gain factor; ϕ_1 is an arbitrary elevation angle determined by the geometry; ϕ^* is the angle at which the functions $e^{-p^2\phi^2}$ and $K \csc^2\phi \cos\phi$ meet in a common tangent, and ϕ_2 is the maximum angle of the shaped-beam portion of the pattern and P and K are constants for a given pattern. The parameter P is determined by the half-power beamwidth of the antenna pattern.

The statement of Equation (10-1) is open to criticism because we have assumed that the far-field pattern of the antenna is operated on by the edge diffraction pattern, when the edge is actually in the near field of the antenna.

Our method, however, is equivalent to a zero-wavelength approximation for the antenna, by means of which we draw the rays from the antenna, and then calculate the phase front at the plane of the edge by geometric optics. This analysis is obviously not exact, but the results of similar analyses are found to be surprisingly accurate.[2, 3]

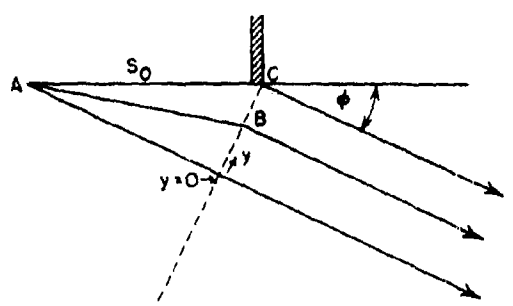


Figure 10–10. Edge Diffraction

The Fresnel straight-edge pattern due to a line source located at Point A at a distance S_0 behind an opaque edge is obtained in the following manner. Determine the field distribution in the plane containing the edge and lying along the y-axis of Figure 10-10. The far field is computed by integrating the equivalent Huygen's sources in this y-plane. The phase difference between the field at some point y = B and the field at the origin (y = 0) is expressed by $2\pi\delta/\lambda$, where

$$\delta = \sqrt{S_0^2 \cos^2 \phi + y^2} - S_0 \cos \phi \qquad (10\text{-}3)$$

By expanding the expression under the radical by means of the binomial expansion, and retaining only the first and second terms, we obtain

$$\delta \cong \frac{y^2}{2 S_0 \cos \phi} \qquad (10\text{-}4)$$

the usual Fresnel diffraction approximation. The integration is carried over the entire y-plane from $-\infty$ to the edge at $y = S_0 \sin \phi$, hence

$$F(\phi) = \left[\int_{-\infty}^{S_0 \sin \phi} e^{-i \frac{2\pi}{\lambda} \frac{y^2}{2 S_0 \cos \phi}} dy \right]^2 \qquad (10\text{-}5)$$

Substituting

$$t = y \sqrt{\frac{2}{\lambda S_0 \cos \phi}}$$

$$\text{and } v = S_0 \sin \phi \sqrt{\frac{2}{\lambda S_0 \cos \phi}} \qquad (10\text{-}6)$$

this becomes

$$F(\phi) = \left[\sqrt{\frac{\lambda S_0 \cos \phi}{2}} \int_{-\infty}^{v} e^{-\frac{i\pi t^2}{2}} dt \right]^2 \qquad (10\text{-}7)$$

The integral may now be recognized as the Fresnel integral, and may be found in the tables in the form

$$\xi = \int_0^v \cos \frac{\pi t^2}{2} dt$$

$$\eta = \int_0^v \sin \frac{\pi t^2}{2} dt \qquad (10\text{-}8)$$

The complex plot of these two integrals is a spiral*, known as the Cornu spiral, shown in Figure 10-11. Except for the cos ϕ term in Equation (10-7), the intensity of the straight-edge diffraction power pattern for each value of v is given by the square of the chord from the point $v = -\infty$ to v on the spiral. The relation between v and ϕ is given by Equation (10-6). Inside the shadow of the edge, the intensity diminishes smoothly to zero from its value corresponding to the chord from $v = -\infty$ to the origin of the coordinates η, ξ at v = 0. Outside the shadow, the intensity increases to a maximum and then oscillates in decreasing amplitude about a mean value.** This is illustrated in Figure 10-12, which shows the intensity distribution in the Fresnel straight-edge diffraction pattern.

As an illustration, consider the ground-mapping antenna mounted in an aircraft with its beam maximum in the direction ϕ_0 with respect to the horizon. This angle of depression is called the normalization angle. As the rays from the antenna pass the edge of the nacelle, edge diffraction may occur, and we shall assume that the rectilinearly projected shadow of the edge occurs also at the angle ϕ_0. The distance S_0 is

*See, for example, J. C. Slater and N. H. Frank, Introduction to Theoretical Physics, McGraw-Hill Book Co., 1933, pp. 315-323.

**See pp. 172-180 of Reference 3.

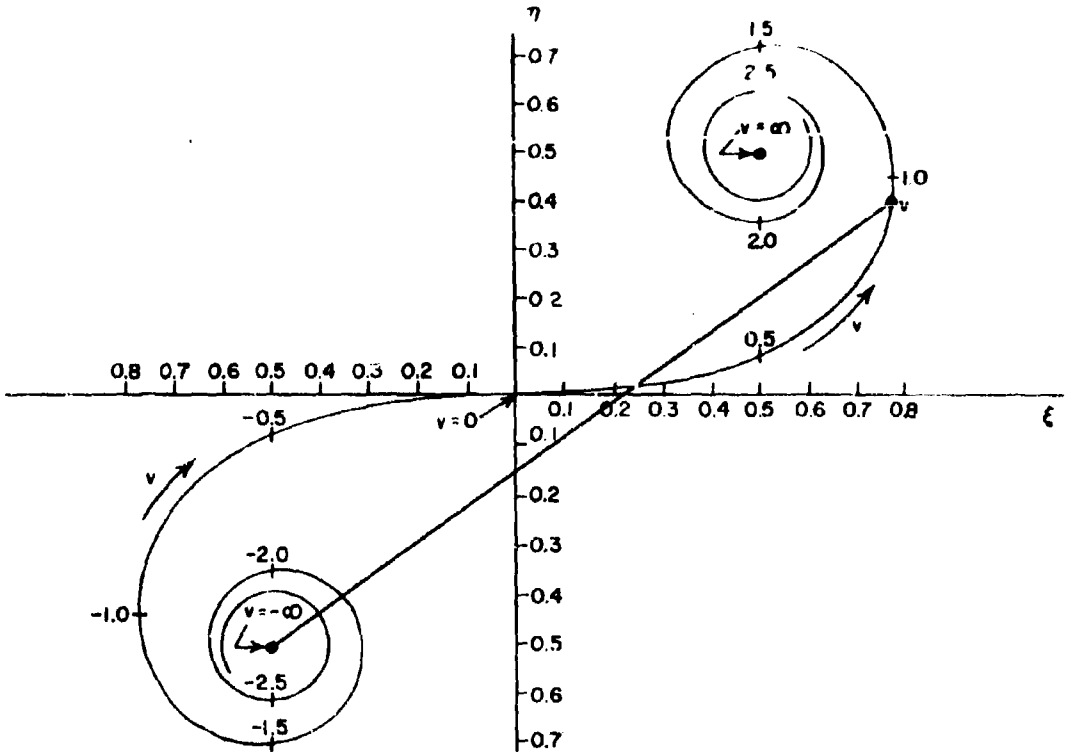


Figure 10–11. Cornu Spiral

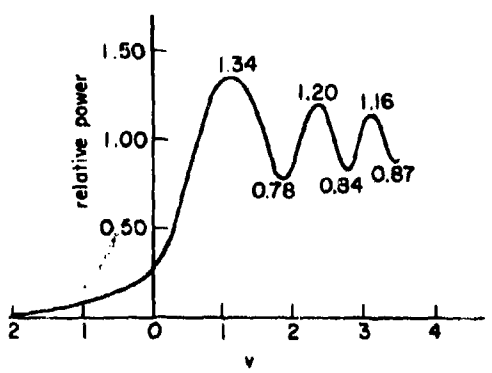


Figure 10–12. Intensity Distribution in Straight-Edge Diffraction Pattern

the distance from the edge to the antenna which, as shown in Figure 10-13, is 30 inches. The antenna vertical aperture is 10 inches, and the antenna projects from the fuselage 2 inches. The wavelength is 1.86 cm ≅ 0.715 inches. The beamwidth in the elevation plane is 5 1/2°; the angle of depression $\phi_0 = 8°$. The resulting composite pattern illuminating the ground is the product of the $\csc^2 \phi \cos \phi$ shaped-beam pattern by the straight-edge diffraction pattern. The result is shown in Figure 10-14.

This illustration, of course, represents an extreme condition not likely to occur in a typical installation. However, it will be seen that edge diffraction produces a deflection of the beam and introduces a series of maxima and minima into the shaped-beam pattern which might cause poor illumination of the ground.

Synthesis of Surface-Reflection Interference Patterns. A thorough synthesis of the antenna secondary radiation patterns in the presence of the aircraft fuselage and wings would be immensely difficult due to the complexity of the aircraft shape and task of mathematically describing the interference phenomena. However, one can employ approximate synthesis methods to get a physical picture of the pattern deterioration that may be expected due to the proximity of the reflecting surfaces of fuselage and wings.

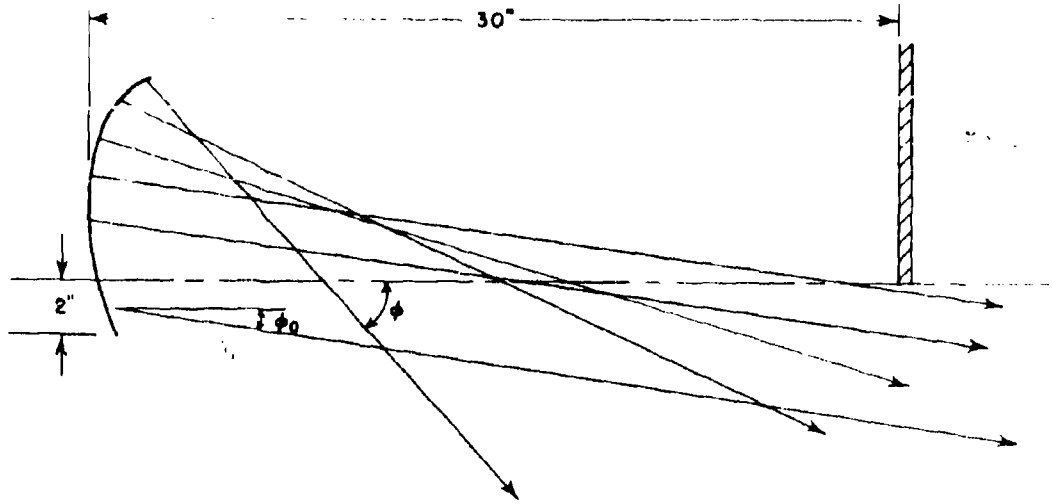


Figure 10-13. Diffraction of Shaped-Beam Antenna in Nacelle

The obviously complex shape of the airplane makes it unsuitable in the evaluation of far-field integrals wherein one must mathematically describe the shape of the plane's reflecting surfaces. A simplified planar model can be constructed from the specific aircraft configuration and dimensions. Consider, for example, a large four-engine aircraft whose wing is perpendicular to the fuselage and the wing root is slightly above the midpoint of the fuselage. A simplified diagram of the airplane can be constructed as shown in Figure 10-15. Similarly, simplified diagrams can be constructed for other aircraft to meet the requirements for an approximate synthesis of the radiation pattern.

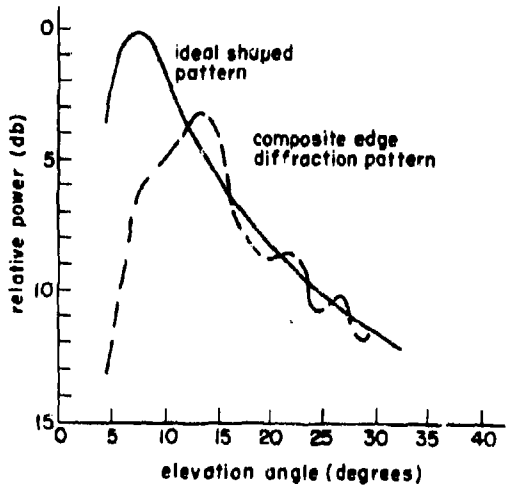


Figure 10-14. Effect of Diffraction on Shaped Beam

The method of analysis to be used neglects the divergence of scattered energy due to surface curvature. We might, for example, calculate the currents set up on the reflecting surfaces, assuming them to be proportional to the incident field at each point of the aircraft surface. A divergence factor to account for curvature of the surfaces could be introduced, and the resulting scattered field obtained as an integral over the reflecting surfaces. A number of difficulties present themselves, however, for, as in the case of edge diffraction, the reflecting surfaces are in general in the near field of the antenna. Therefore, the method to be presented is intended to develop a physical picture of the interference phenomena, but it is not presented as an accurate analysis.

With the example sketched in Figure 10-15, let us assume that an antenna for 360° search is mounted on the underside of the airplane at the position of intersection of wings and fuselage. The antenna is approximately 17 by 4 feet in major dimensions, operating at about 3000 megacycles. The elevation pattern of the antenna may be affected by reflections from the wing and fuselage. The antenna pattern is a pencil beam, approximately 6° at half power in the vertical plane and 1-1/2° at half power in the horizontal plane. The pattern shape can be described to good approximation by the familiar exponential form

$$P(\phi) = e^{-p^2 \phi^2} \qquad (10\text{-}9)$$

If we define ϕ and θ as the azimuth and elevation angles respectively, and if we make the usual assumption that the power pattern is separable, then the free space far field pattern may be approximated by

$$P(\theta, \phi) = G(0)\, e^{-p_1^2 \theta^2}\, e^{-p_2^2 \phi^2} \qquad (10\text{-}10)$$

where G(0) is the absolute gain of the antenna and $P(\theta, \phi)$ is the beam shape.

If we now evalute p_1 and p_2 by matching the approximate pattern to the half-power beamwidths, Equation (10-10) may be expressed as

$$P(\theta, \phi) \cong G(0)\, e^{-1000 \theta^2}\, e^{-300 \phi^2} \qquad (10\text{-}11)$$

for the antenna in our present example.

As the antenna changes its attitude in azimuth and elevation, and as the airplane changes its attitude in roll or pitch, portions of the main beam may be intercepted by the fuselage or the wing or by both. The intercepted energy generates currents on the conducting surface which in turn reradiate a reflected pattern, which will combine with regard to phase with the free-space pattern, to form the composite interference pattern.

The reflected radiation pattern may be considered to emanate from an image antenna and,

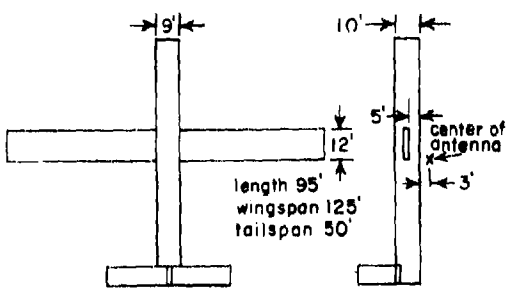


Figure 10-15. Simplified Diagram of Airplane

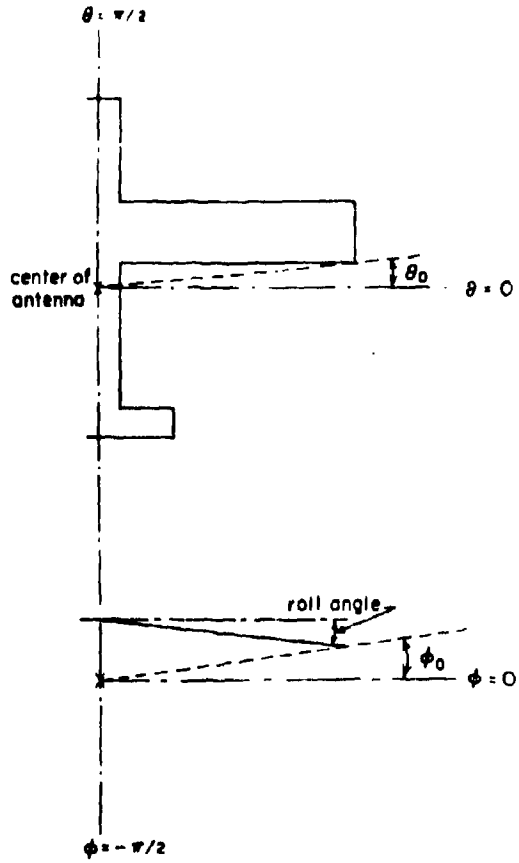


Figure 10-16. Geometry for Calculation of Interference Patterns with Antenna Pointing Broadside

although the Principle of Images may be rigorously applied only to plane reflectors of infinite extent, one can, to a first order approximation, apply the principle to the case in which the reflector is finite but large compared to the wavelength by adjusting the strength of the reradiated power in proportion to the fraction of the total energy intercepted by the imaging surfaces.*

If θ_0 and φ_0 are defined as the angles intercepted at the edges of the reflecting surfaces in the horizontal and vertical planes respectively, as indicated in Figure 10-16, then P_i, the relative strength of the image antenna, is given by

*G. M. Hahn, unpublished.

$$P_i \cong \frac{\int_{\theta_0}^{\pi/2}\int_{\phi_0}^{\pi/2} e^{-p_1^2\theta^2} e^{-p_2^2\phi^2}\,\theta d\theta d\phi}{2\int_0^{\pi/2}\int_0^{\pi/2} e^{-p_1^2\theta^2} e^{-p_2^2\phi^2}\,\theta d\theta d\phi} \qquad (10\text{-}12)$$

or

$$P_i \cong \frac{1}{} \int_{P_1\theta_0}^{\infty}\int_{P_2\phi_0}^{\infty} e^{-\theta^2} e^{-\phi^2}\,\theta d\theta d\phi \qquad (10\text{-}13)$$

It is convenient to employ the error integral $E_n(x)$ defined[4] as

$$\left(\frac{1}{n}\right)! \, E_n(x) = \int_0^x e^{-t^n}\,dt \qquad (10\text{-}14)$$

then

$$P_i \cong \left[1-E_1(p_1\theta_0)\right]\left[1-E_2(p_2\phi_0)\right] \qquad (10\text{-}15)$$

which is a simplified form for computation.

The interference pattern is now calculated by the phase addition of two sources spaced a distance D apart, as shown in Figure 10-17. If we

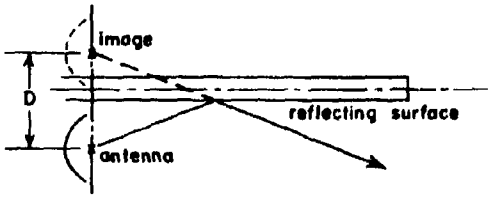


Figure 10-17. Antenna Imaged in Reflecting Surface

let P_f be the free-space pattern and P_i the relative strength of the image, the composite pattern $P'(\phi)$ in the elevation plane is given by

$$P'(\phi) = P_f \left| e^{-i\frac{\pi D}{\lambda}\sin\phi} \pm P_i^{1/2} e^{+i\frac{\pi D}{\lambda}\sin\phi}\right|^2 \qquad (10\text{-}16)$$

where the plus or minus term is chosen according to the polarization of the incident radiation. If the polarization is parallel to the plane of the reflecting surface, the minus term is taken.

From the geometry of the problem it is obvious that the maximum effect of reflection interference will be experienced when the beam is directed forward or aft along the fuselage, or directly sideways along the wing. A plot of the beam shift due to the reflection interference shows that, for the conditions of our example, one may expect downward beam shifts as the antenna rotates. For a 4 1/2° pitch, nose-up, the forward beam shift is negligible, but when the beam is directed aft, the depression of the beam as a function of azimuth angle is shown in Figure 10-18. The aircraft's normal flight attitude is 4 1/2° nose-up. Obviously this depression angle will also be a function of the roll of the aircraft. This effect is illustrated by Figure 10-19, in which the beam depression is plotted as a function of roll angle. Note that in all cases the antenna is stabilized with its main beam horizontal. Wing-up roll has a diminishing effect; wing-down roll gradually increases the beam depression from approximately 1/2° to 6° at 6° roll. It is immediately apparent that roll can cause severe interference as the angle increases.

The beam depression caused by reflection is also accompanied by the appearance of interference maxima and minima in the antenna pattern. Obviously the beam is least affected in wing-up roll or nose-up pitch, when the beam is looking forward or sideways. With the beam looking aft, and the plane in a 4° nose-up attitude, the beam shape becomes a series of sharp lobes. This pattern is compared to the unperturbed elevation pattern in Figure 10-20. The lobes are approximately 1° between half-power points, 3 1/2° separation. Similarly, the pattern is distorted by reflection from the wing in roll. For a 3° wing-up roll the pattern is essentially the free-space pattern. As the wing rolls down, the pattern deteriorates until it consists of a series of sharp lobes, approximately 1° between half-power points and 3 1/2° separation. This is illustrated by the computed patterns in Figure 10-21 for 3° wing-up roll, 0° roll, 3° wing-down roll, and 6° wing-down roll. The pattern dis-

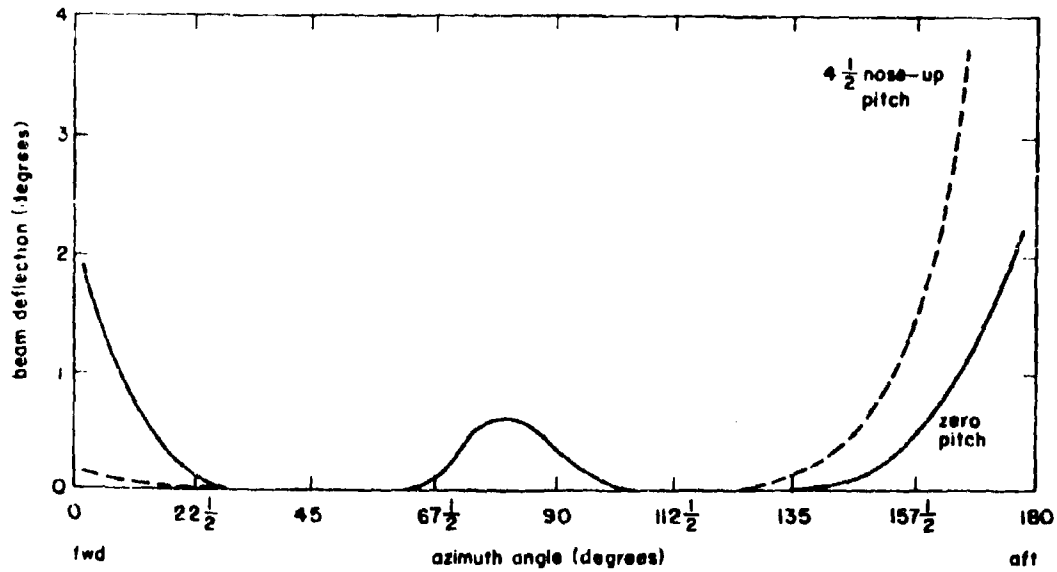


Figure 10–18. Depression of the Beam Versus Azimuth Angle

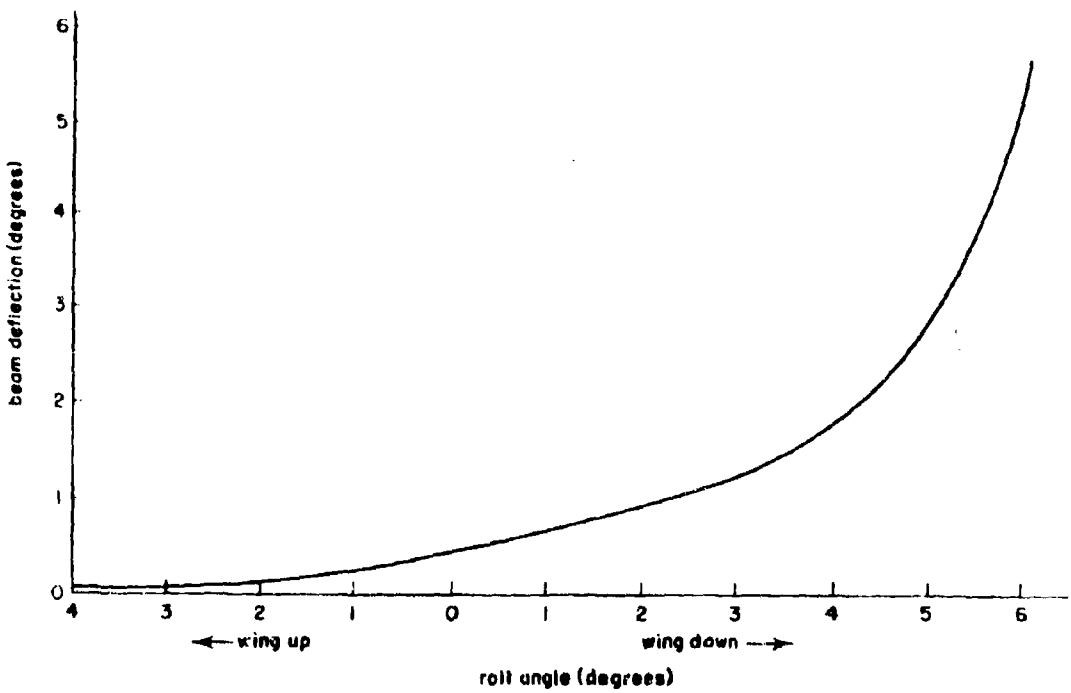


Figure 10–19. Depression of the Beam Versus Roll Angle

tortions predicted by these computations indicate the type of distortions to be expected, but are probably worse than one will encounter in practice because the divergence caused by curvature of the aircraft surfaces would reduce the effect of the image.

Similar wing- or fuselage-reflection interference may appear in the elevation pattern of a ground-mapping radar. The method of computation of the expected effects is similiar to that given above, with the exception, of course, that P_f, the free-space pattern, is shaped in elevation for uniform illumination of the ground. Thus, a typical expression for P_f would be

$$P_f \phi = G_0 \, e^{-p^2 \phi^2} \text{ for } \phi_1 \leq \phi \leq \phi^* \qquad (10\text{-}17)$$

$$= G_0 \, K \csc^2 \phi \cos \phi \text{ for } \phi^* \leq \phi \leq \phi_2$$

The image pattern P_i is computed as before, and the interference pattern is the vector sum of the two:

$$P^1(\phi) = P_f \left| e^{-i \frac{\pi D}{\lambda} \sin \phi} \right. \qquad (10\text{-}18)$$

$$\left. + P_i^{1/2} e^{+i \frac{\pi D}{\lambda} \sin \phi} \right|^2$$

The effect upon the shaped-beam pattern is similar to that observed for the pencil beam. Maxima and minima in the pattern are produced by the interfering reflected radiation, and since good ground mapping requires very nearly uniform illumination of the ground along the beam track, these maxima and minima produce light and dark fringes on the radar presentation.*

The most pronounced effects will occur under conditions of roll, at which time the fringes will appear in the direction of wing-down roll, and up or down pitch, at which time the fringes will appear either forward or aft and along the axis of the aircraft.

The measurements of the radiation pattern of an actual installation are shown in Vol. 26 of the Radiation Laboratory Series, "Radar Scanners and Radomes."**

*See pp. 251-3 of Reference 1.

**See pp. 452-54 of Reference 1.

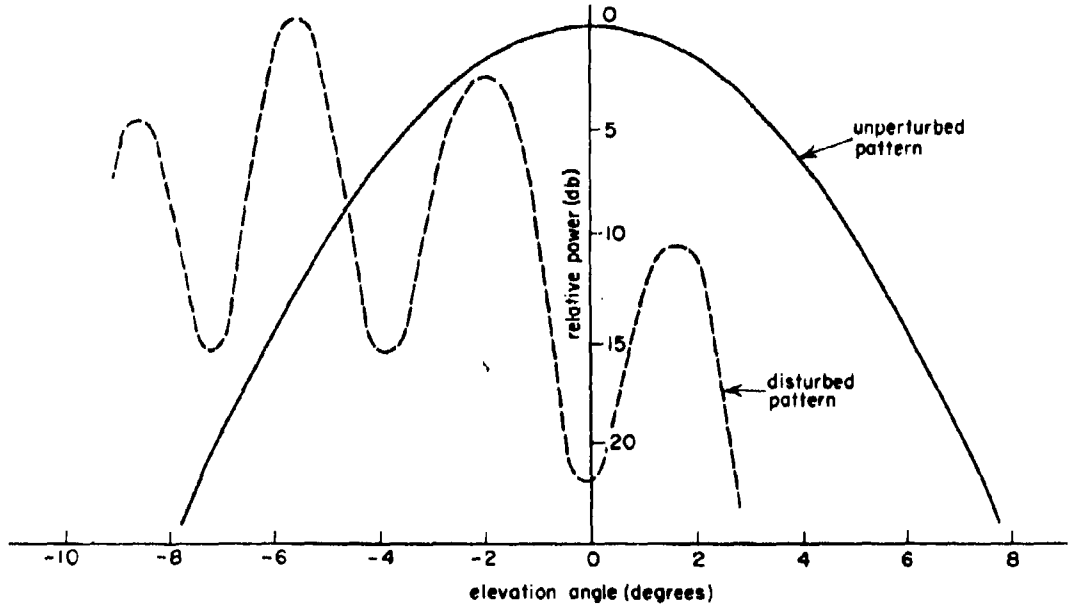


Figure 10-20. Distortion of Pattern by Reflection from Fuselage

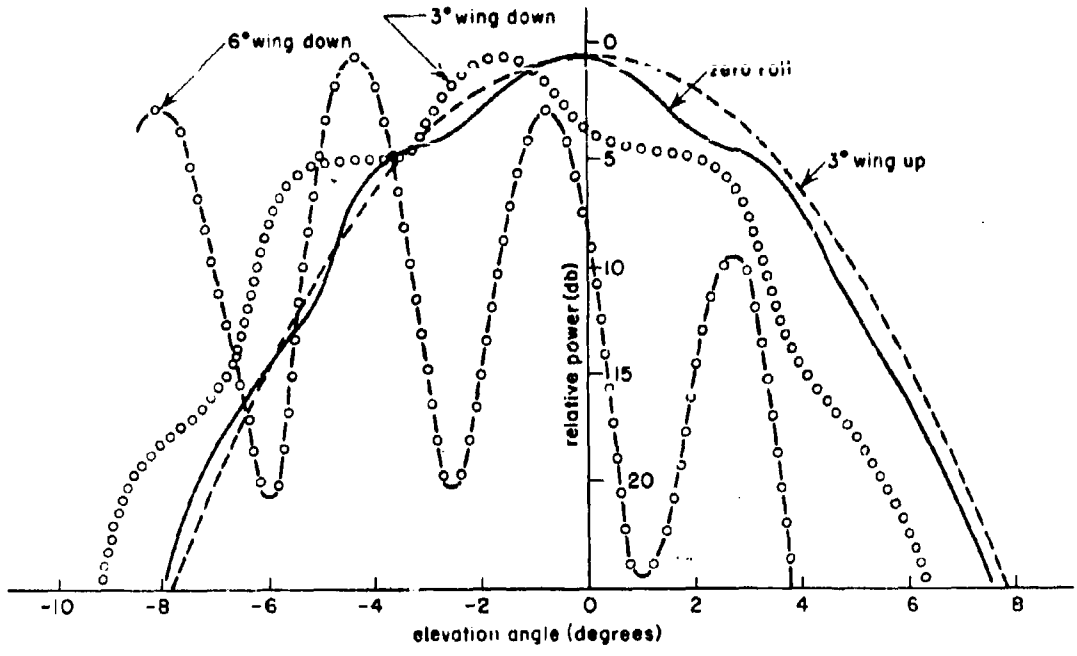


Figure 10-21. Distortion of Pattern by Reflection from Wing

The antenna was installed in the belly of the aircraft. The antenna, which was a shaped cylindrical reflector with line source, projected 4 in. from the skin line of the aircraft, thus permitting a generally forward view along the fuselage. The patterns show the ideal elevation pattern, free from interfering reflected radiation, and the pattern resulting from reflection from the fuselage. The antenna was looking directly along the fuselage in the forward direction. It is obvious that the resulting interference pattern would affect the ground mapping presentation.

10-8. Nacelle Clearance

To prevent or at least minimize the effects of edge diffraction and interference due to surface reflection, the antenna position in the nacelle must permit unimpaired vision in all directions of concern to the system operation. Certain "rules of thumb" have become accepted for determining the minimum angles for clearance between obstructions and rays drawn from the antenna. Thus, all rays should clear any obstruction by 1 1/2 inches, and further, an angular clearance of 5° above the centerline of the principal beam should be provided to allow for beam divergence.

Microwave absorber may be used to reduce some of the adverse effects of reflections from the nacelle walls.

10-9. Allowable Pattern Distortion

The allowable distortion of the radiation pattern of the antenna by edge diffraction or interference can be determined only from a knowledge of the application of the radar system. However, it can be assumed that minima in the pattern caused by diffraction or interference in excess of 1 1/2 db are cause for alarm, as is deflection of the beam in excess of 1/4 beamwidth. These distortion criteria are not definitive, since conditions will vary with the requirements.

SECTION D. PATTERN DISTORTION BY AIRCRAFT ENVIRONMENT; EFFECTS OF SHOCK FRONT AND TURBULENCE

10-10. Introduction

By a simple extension of conception, the term "radome" may be thought of as including the air itself in the vicinity of the aircraft, at least as it may be responsible for departure from performance of the antenna in free-space conditions. In subsonic aircraft, these deviations

are insignificant, but at supersonic speeds both the shock front and the turbulence in the region between the shock front and the aircraft can influence antenna performance.[5]

The air surrounding a supersonic aircraft may be divided into four principal regions. Thus, in Figure 10-22, we have:

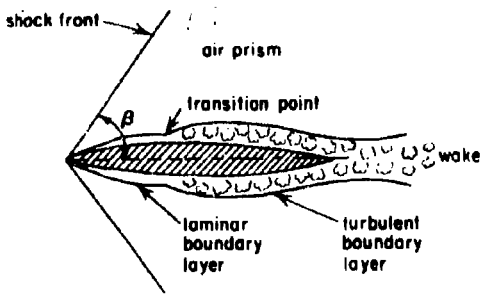


Figure 10-22. Section of Airfoil in Supersonic Flight

The Shock Front. An object moving at a speed greater than the velocity of sound produces a head wave in the atmosphere which travels with the object. If u_1 is the velocity of the object, and a^* the velocity of sound corresponding to the conditions of temperature and pressure, the Mach number

$$M = \frac{u_1}{a^*} \qquad (10\text{-}19)$$

When M is greater than one, i.e., the speed is supersonic, the pressure of the air undergoes a rapid change along the line which defines the shock front or head wave. If the object enters a medium whose pressure is p_1, the pressure increases at the shock front, and the velocity of the air enclosed by the shock front decreases with respect to the object. Similarly the density increases for this wave. Since the speed has decreased, it is also inferred that the temperature has increased.

The Boundary Layer. Surrounding the skin of a supersonic aircraft is a thin layer of air characterized by large velocity and temperature gradients. The velocity of the air relative to the moving aircraft is retarded by friction. The boundary layer is laminar near the leading edges of the aircraft surfaces, but becomes turbulent at the transition point, which occurs some distance behind the leading edge.

The Air Prism. This may be thought of as the region between the boundary layer and the shock front. Although the mean square fluctuation of the dielectric constant has not been measured, it is believed to be somewhat higher than the level in the undisturbed atmosphere.

$$\left[\overline{\left(\frac{\Delta\epsilon}{\epsilon}\right)^2} \approx 2 \times 10^{-12}\right] \qquad (10\text{-}20)$$

The Wake. For a region extending behind the aircraft the turbulence persists, and the flow in the wake immediately behind the aircraft is at first subsonic and then accelerates again to supersonic speed at some distance behind the aircraft. In addition to the naturally occurring wake, there is, of course, the jet exhaust, which is characterized by high temperature and extensive ionization of the exhaust gases.

10-11. Transmission Through the Shock Front

The following analysis, based on weak shock wave theory, will denote the effects on microwave transmission through the shock front.[6] Certain facts must be noted, however, to determine the dielectric character of the shock front.

It is found that, given the aircraft velocity u_1 and the velocity of sound a^*, the velocity of the air in the air prism adjacent to the shock front is

$$u_1 = \kappa^2 u_2 \qquad (10\text{-}21)$$

and that the ratio of densities in the free air and in the air prism is

$$\frac{\rho_2}{\rho_1} = \kappa^2 = \frac{2.4\,M^2}{2 + 0.4\,M^2} \qquad (10\text{-}22)$$

Thus, a flow at supersonic speed after passing through the shock wave must be reduced to a subsonic flow. The final pressure, p_2, is greater than p_1, the pressure in the supersonic flow (or in this case, the free air), and consequently the shock wave is a compression wave. The density must also increase as the flow passes through the shock wave.

Now the dielectric constant ϵ_r of a gaseous medium, as given by the Clausius-Mossotti law, is a function of the density, and in fact, may be written in the form

$$\frac{\epsilon_r - 1}{\epsilon_r - 2} = A\rho \qquad (10\text{-}23)$$

where A is a constant determined by the atomic or molecular polarizability and the temperature. Consequently, to a first approximation, the dielectric constant ϵ_{r_2} of the air in the air prism is related to the dielectric constant ϵ_{r_1} of the free air by the expression.

$$\frac{\epsilon_{r_2} - 1}{\epsilon_{r_2} + 2} = \frac{\epsilon_{r_1} - 1}{\epsilon_{r_1} + 2}\left(\frac{\rho_2}{\rho_1}\right) \qquad (10\text{-}24)$$

This may be reduced to

$$\epsilon_{r_2} = \frac{\epsilon_{r_1}(2\kappa^2 + 1) - 2(\kappa^2 - 1)}{\kappa^2 + 2 - \epsilon_{r_1}(\kappa^2 - 1)} \qquad (10\text{-}25)$$

Therefore a ray passing through the interface between the denser air of the air prism and the less dense free air ahead of the shock front will experience refraction through an angle r with respect to the normal to the shock front given by Snell's law,

$$r = \sin^{-1}\left(\sqrt{\frac{\epsilon_2}{\epsilon_1}}\sin i\right) \qquad (10\text{-}26)$$

where i is the angle of incidence with respect to the normal to the shock front. When $\sqrt{\epsilon_2/\epsilon_1}$ sin i becomes equal to or greater than unity, total reflection will occur, and no transmission through the shock front can exist.

The dielectric constant of air at standard atmospheric conditions of pressure and temperature is very closely

$$\epsilon_{r_1} = 1.000590 \qquad (10\text{-}27)$$

Thus, the critical angle at which total reflection will occur at various Mach numbers and standard atmospheric conditions is shown in Table 10-I.

Table 10-I

Critical Angle for Total Reflection From Shock Front for Various Mach Numbers

M	ϵ_{r_2}	$\epsilon_{r_2}/\epsilon_{r_1}$	Critical Angle (degrees)
1.4	1.00101	1.00042	88.8
1.7	1.00133	1.00074	88.4
3.2	1.00236	1.00177	87.6
5.0	1.00295	1.00236	87.2

The deflection suffered by a ray incident at angle i on the shock front is tabulated in Table 10-II for Mach 3.2. It is evident that refraction by the shock wave is small, but that a boresight shift of the radar beam might occur. This boresight shift would not be serious except at high incidence angles.

The angle which the shock wave makes with the axis of the aircraft is given approximately by

$$\sin\beta = \frac{a^*}{u_1} = \frac{1}{M} \qquad (10\text{-}28)$$

Thus at Mach 3, the angle β (indicated on Figure 10-22) is 20°. When the radar antenna is pointing along the axis of the aircraft, the angle of incidence will be 70°. It would appear possible, therefore, for the refraction at the shock front to introduce a boresight error of a few milliradians at large Mach numbers. Thus far, however, this subject has received little attention.*

The data given here is only an approximation, based upon the assumption that the air prism is of uniform density and the shock front is a sharp interface between two homogeneous dielectrics.

*C. L. Kober has made a preliminary investigation of refraction and reflection by the shock wave, but his paper has not been published (1956) and the results were not available to the author of this chapter.

Table 10-II

Refraction at the Shock Wave for Mach 3.2

Angle of Incidence (degrees)	Deflection of Ray (minutes) Mach 3.2
20	1.0
30	1.6
40	2.5
50	3.5
60	5.1
70	8.3

The shock front obviously cannot be a mathematical discontinuity. There must be a transition layer of some sort, representing a shock wave of finite thickness. It has been shown[7] that the thickness of the shock wave is of the form

$$T = \frac{1}{u_1 - u_2} \text{ cm} \qquad (10\text{-}29)$$

where u_1 and u_2 are expressed in cm/sec. Thus at Mach 2, the thickness would be approximately 0.25×10^{-4} centimeter. However, as noted above, the density of the air prism is certainly not uniform, which will further modify the behavior of the refraction by the air prism.

10-12. Turbulence in the Boundary Layer

It has been estimated[8] that in the typical supersonic turbulent boundary layer, associated with flow over a flat plate,

$$\left(\frac{\overline{\Delta\epsilon}}{\epsilon}\right)^2 \cong 2.5 \times 10^{-11} M^4 \qquad (10\text{-}30)$$

in which $(\overline{\Delta\epsilon})^2$ is the mean-square fluctuation of the dielectric constant and M is the Mach number as defined earlier. At high altitudes it may be assumed, in the absence of direct evidence, that $\overline{\Delta\epsilon}$ is proportional to the density, which for a standard atmosphere gives

$$\left(\frac{\overline{\Delta\epsilon}}{\epsilon}\right)^2_h = \left(\frac{\overline{\Delta\epsilon}}{\epsilon}\right)^2 e^{-ah} \qquad (10\text{-}31)$$

where $a \cong 8 \times 10^{-5}$ per foot and h is the altitude in feet. Consequently, the mean-square fluctuation of the dielectric constant is found to be very small, even for very large Mach numbers.

The effects of the fluctuations in dielectric constant will be to scatter radiation incident upon and passing through the turbulent boundary layer. In pulse radars the scattered noise power from the outgoing pulse is at too short range from the antenna to interfere with a received signal, and the scattered power from the reflected pulse is insignificant compared to the reflected pulse itself. On the other hand, the effects of turbulence cannot be dismissed altogether, for it appears that the boundary layer can have serious effects on the performance of optical instruments and on the signal-to-noise ratio of some c-w radars.[9,10]

10-13. Turbulence in the Air Prism[11, 12]

Because of the lack of reliable information on the nature of the turbulence in the air prism, the possible effect of scattering from turbulent air in this region will not be discussed further here. In contrast with the thin boundary layer having intense turbulence, it is probably an extended region containing relatively weak turbulence.

10-14. The Wake

The flow of air in the wake of a body traveling at supersonic velocity is highly turbulent. As in the case of the turbulent boundary layer, velocity of the flow, at any given coordinate point in the medium behind the supersonic vehicle, is varying with time in an unpredictable manner. Likewise there are fluctuations of temperature and density, and consequently there will also be fluctuations in dielectric constant. The mean-square fluctuation of dielectric constant $(\overline{\Delta\epsilon})^2$ can be expected to be of the same order of magnitude as that in the turbulent boundary layer. The turbulent medium of the wake, however, is much more extensive than the thickness of the boundary layer, and it is reasonable to suppose that the wake may have an influence on the performance of antennas which transmit and receive through it, such as tail-defense radar.

To earn some appreciation of the effect of transmission through the turbulent wake, let us examine the reduction in antenna gain produced by the deviation of the phase of the incident wave from that of a plane wave. It may be shown[13] that for a small deviation the relative decrease in gain caused by the rms (root-mean-square) path error $\overline{\Delta}$ is

$$\frac{\Delta G}{G} = \frac{4\pi^2}{\lambda^2} \bar{\Delta}^2 \qquad (10\text{-}32)$$

We assume that the wake is composed of a random distribution of spherical eddies whose diameter is L. Then the rms path error will be approximately

$$\bar{\Delta} \cong \frac{1}{4} L \, (\Delta\epsilon) \qquad (10\text{-}33)$$

where $\Delta\epsilon$ is the rms difference in dielectric constant in the turbulent medium. This has been found earlier to be in the order of 10^{-5}, hence the relative reduction in gain will be

$$\frac{\Delta G}{G} \cong 2.5 \times 10^{-5} \left(\frac{L}{\lambda}\right)^2 \qquad (10\text{-}34)$$

It is immediately obvious that unless L is large compared to the wavelength, little change will be experienced by the antenna. Similarly, it is apparent that a considerable effect on the image quality of an optical system will be felt as a result of transmission of light through the turbulent region.

There exist in the wake of the aircraft traveling at supersonic velocity, in addition to the turbulent air, the hot exhaust gases of the jet or rocket propulsion motor. When electromagnetic signals pass through an ionized medium such as hot exhaust gases from a jet engine or rocket, refraction, reflection, absorption, and random amplitude modulation of the transmitted signal may occur. Beam deviation of as much as 15° and attenuation up to 50 db per meter as well as considerable incidental modulation have been measured with jet flames at X-Band.[14,15]

The absorption loss and reflection coefficient due to a gaseous medium with a free charge is determined by the conductivity of the charged gaseous medium, which in turn is a function of the number of free electrons per unit volume and the mean free time between electron collisions. In the neighborhood of the motor throat, the electron density is known to be in the range of 10^{13} electrons per cubic centimeter. The resulting transmission loss at microwave frequencies in the exhaust flame is in excess of 10 decibels per meter. However, the absorption path length varies over a very wide range, depending upon the flame dimensions, dispersion of the ionized gases, and direction of propagation. The electron densities in the wake will obviously differ from that in the flame by several orders of magnitude, and consequently the net absorption due to transmission through the wake can be expected to be appreciably less than that due to the flame in the immediate neighborhood of the motor throat. Very little data is yet available, however, on the effect of transmission loss and reflection due to the ionized exhaust gases in the wake.

Up to now, neither agreement nor disagreement has been firmly established between theory and experiment with jet flames. Theory is difficult to apply to the problem because of the unpredictable nature of the flame boundary conditions, the difficulty of obtaining accurate temperature measurements, and the difficulty of controlling fuel impurities and conditions of combustion. Further experiments and analysis must be made in order to explain quantitatively the attenuation, beam deviation, and incidental modulation produced by jet exhaust gases.

GLOSSARY

Azimuth Axis. A line, usually vertical, about which rotation in azimuth takes place. The line will be truly vertical only in a platform stabilized system.

Pitch Axis. A line perpendicular to the azimuth and to the longitudinal axis of the aircraft about which rotation in elevation takes place.

Roll Axis. A line perpendicular to the azimuth and pitch axes about which rotation takes place.

Roll. Rotation of an aircraft about its own longitudinal axis.

Cross-traverse Angle. The angle, measured about horizontal line-of-sight, between the vertical plane through the line of sight and the plane containing the line of sight and the azimuth axis. (See Figure 10-6.)

REFERENCES

1. Cady, W. M., Karelitz, M. B., and Turner, L. A. Radar Scanners and Radomes. Vol. 26, MIT Radiation Laboratory Series, McGraw-Hill Book Co., Inc., New York, 1948, pp. 104-116 and 194-206.

2. Bachynski, M. P., and Bekefi, G. Transactions, IRE, AP-4. 1956, pp. 412-21.

3. Valasek, J. Theoretical and Experimental Optics. John Wiley and Sons, New York, 1949, pp. 185-6.

4. Jahnke and Emde. Tables of Functions. Dover Publications, 1943, p. 23.

5. Peake, W. H. Turbulence in the Environment of a Supersonic Aircraft as a Radome Problem. Proceedings of the Radome Symposium, Vol. II, The Ohio State University, June 1955, pp. 75-85.

6. Leipmann, H. W. and Puckett, A. E. Introduction to Aerodynamics of a Compressible Fluid. John Wiley and Sons, New York, 1950, pp. 38-56.

7. Durand, W. F. Aerodynamic Theory. Vol. III, Durand Reprinting Committee, Pasadena, Calif., 1943, p. 218.

8. Chu, S. T. Review of Turbulence Theories with Applications to Fluctuation Fields Inside a Supersonic Boundary Layer. Project Report 486-31, The Ohio State University Research Foundation, December 1954.

9. Peake, W. H. Transmission of Light Waves Through a Supersonic Turbulent Boundary Layer. Project Report 486-30, The Ohio State University Research Foundation, April 1955.

10. Peake, W. H. Turbulence in the Environment of a Supersonic Aircraft as a Radome Problem. Proceedings of the OSU-WADC Radome Sumposium, Vol. II, The Ohio State University June 1955, pp. 75-85.

11. Kovasznay, L. S. G. B-58 Doppler Radar. A Study of Radar Scattering in Supersonic Turbulent Flows. Report MIR 16-838, Prime Contract USAF 33(038)-21250, Raytheon Manufacturing Company, Bedford, Massachusetts, June 1956. (Unclassified)

12. Peake, W. H. Some Possible Effects of Turbulence on the Performance of Antennas Mounted on Supersonic Aircraft. Report 667-3, Contract AF33(616)-3353, Antenna Laboratory, The Ohio State University Research Foundation, October 1, 1956. (Confidential)

13. Spencer, R. C. A Least Square Analysis of the Effect of Phase Errors on Antenna Gain, Report E 5025, Air Force Cambridge Research Center, January 1944.

14. Robertson and Stevens. The Effects of Jet Flames on Electromagnetic Wave Propagation. Memo 4-55, Jet Propulsion Laboratory, California Institute of Technology, Pasadena, Calif., March 1950.

15. Becker, Bourdeau, and Burnight. Upper Atmosphere Research, Report II, Part II. Report R-3031, Naval Research Laboratory, December 1946.

Chapter 11

RADOME WALL MEASUREMENTS AND EVALUATIONS

by

Melvin J. Kofoid

Boeing Airplane Company
Seattle, Washington

INDEX OF SYMBOLS

I.P.D.	Insertion phase difference
Δ	Insertion phase delay
ϵ_r	Relative dielectric constant of a dielectric
tan δ	Dissipation factor of a dielectric
d	Physical thickness of a radome wall
λ_0	Free-space wavelength
θ	Angle of incidence
d'	Free-space change in interferometer spacing to produce balance when dielectric wall is inserted between the horns
T^2	Power transmission coefficient

Chapter 11

RADOME WALL MEASUREMENTS AND EVALUATIONS

SECTION A. INTRODUCTION

11-1. Need for Measurements

In developing and producing radomes to meet exacting electrical performance requirements, it is generally desirable and often mandatory to evaluate the electrical properties of the radome wall. Range tests to determine the transmission and beam-bending characteristics of the radome may be, by themselves, inadequate. These remarks are particularly pertinent to the development of radomes with half-wave walls or quarter-wave-face sandwich walls because of the high importance of obtaining the design values of the dielectric constants and the wall thicknesses in these constructions.

The first experimental step in any careful radome development should be to make a sufficiently near perfect radome for precise engineering analysis. Unless the model is an exact representation of the engineering design, the measured performance data may be of little value. Bitter experience attests to the fact that a single excellent test specimen may permit a complete performance analysis, whereas tests on a hundred imperfect units may leave essential questions unanswered.

Theoretically, once a satisfactory design has been established, as confirmed by measuring the effects on a radar beam of a radome known to be constructed as designed, no further engineering evaluation tests are needed. It is only necessary that means be provided for inspecting e production radomes to assure their bein, sufficiently close to the original model. In practice, engineering evaluations must be made at the start on enough radomes, perhaps twenty, to establish the maximum manufacturing tolerances that can be allowed while assuring that the desired performance characteristics will be obtained.

In general, range tests as a means for inspection of production radomes constitute an unduly costly and time-consuming approach to the quality-control problem. An inherent shortcoming of range tests is that the overall performance of the radome is determined but the specific deficiencies of the radome fabrication are not disclosed. What is needed are facilities that will permit analysis of the radome wall at every point. Equipment enabling such analysis is not only useful but is often essential in (1) research and development studies, (2) ensuring that a test specimen is constructed as designed, (3) quality control, (4) economical production inspection, and (5) field inspection.

Another particularly important need for radome wall analysis facilities arises from the fact that the electrical performance requirements of some radomes for precision direction-indicating radars are so exacting that the radome must be made to the design values within extremely small tolerances. With these radomes the allowable electrical and physical wall thickness tolerances appear to be less than can be obtained with certainty by any present production fabrication technique. With analysis techniques available, it is possible and practical to avoid going to extremes in attempts to obtain almost impossible tolerances in the original fabrication. Instead, radomes can be made to reasonable but insufficiently small tolerances, analyzed, and then corrected to be within the

desired tolerances. The amount of correction required can be made very small; it is just the wall thickness difference between reasonably obtained tolerances and the extremely small desired tolerances. The practical feasibility and practicality of this sort of a procedure has been firmly established.[1] It is important to realize that a corrected radome needs no later inspection — the radome has been made to specification. Further, the correction procedure allows the number of rejects of physically sound radomes to be reduced to essentially zero.

The wall evaluation measurements on radomes with exacting performance requirements and high incidence angles should be made with higher accuracy than is generally realized. What is often not appreciated is that if the insertion phase difference (I.P.D.) of a wall differs from the design value by only 1.0° at a low angle, the I.P.D. may differ from the design value by a much larger amount at a high angle such as 80°

This important quantity, insertion phase difference, was defined by Equation (2-47), Chapter 2, and was designated by T' or $\Delta = -T'$, depending on whether one speaks of insertion phase advance or delay, respectively. It is the difference in the phase of the field at a point along the axis of propagation in the region beyond the radome, with and without the radome inserted.

11-2. Quantities to be Measured

The measurable quantities that are significant in the evaluation of radome walls depend on the type of wall construction. It is convenient for a discussion of these quantities to consider the various constructions in three groups.

Measurements on Sandwich Walls with Lightweight Cores. With lightweight-core sandwich wall constructions the only practical physical thickness measurement on a finished radome is that of the overall thickness. The skins can be fabricated to have thicknesses very close to known repeatable values by using a specified number of layers of a particular glass cloth laid up in a definite manner with respect to its weave. The overall physical thickness variations are then, in the main, due to core thickness variations.

As long as the skins are reasonably thin, small variations in their values of dielectric constant and dissipation factor are reduced to secondary importance; it is sufficient to evaluate these quantities by tests on small specimens of dielectric made as similar as possible to the skin material.

Although the magnitude of the I.P.D. of a lightweight sandwich wall is sensitive to any variations in thickness or dielectric constant, measurements of the I.P.D. alone appear to be in general of little value for analysis in applications where transmission is the most important requirement; a wall can differ from the correct design in more than one quantity and yet have the correct value of I.P.D. But the measurement of the wall I.P.D. does become important if a wall is used in a direction-indicating radar radome where the phase shifts, as such, are of high importance.

Simple local power-reflection-coefficient magnitude measurements of all areas are preferable for quality control and electrical inspection of lightweight-core sandwich wall radomes in general. The reflection measurements are sufficient to prove a properly made radome to be satisfactory or to reveal any existing areas of improper construction.

Measurements on Combinations of Solid Sheets. An important example of a wall composed of a combination of solid (nominally homogeneous) sheets is found in the inverted-sandwich construction. It is necessary to evaluate the I.P.D. and the dielectric constant of the quarter-wave face layers of this wall in the same manner and to the same order of precision as is required with a single-layer half-wave wall. The core dielectric constant must be evaluated with comparable exactness. When the phase shifts through the total wall are important, the electric thickness of the core must also be accurately maintained. The basic measurement problems are the same, but the actual problem of producing a wall to the design specification is very much more difficult in the case of the inverted sandwich than in that of the half-wave wall; this is because each layer of the sandwich must be individually and fully evaluated as the radome is built.

The considerations are similar for other precision walls of multiple solid-layer construction. Also pertinent in the evaluation of such constructions are essentially all of the matters discussed for single-layer walls in the following paragraph.

Measurements on Single-Layer Walls. Because of the particular importance of the half-wave wall, it will be assumed as the basis for the following discussion of single-layer walls.

In a homogeneous single-layer radome wall, the quantities of importance are the electric and physical thicknesses of the wall and the relative dielectric constant ϵ_r and the dissipation factor $\tan \delta$ of the dielectric. All but the

last can be determined with good accuracy by non-destructive testing.

Primarily to offer some meaning to people unacquainted with electromagnetic theory, the electrical thickness of a radome wall, as opposed to the physical thickness, is commonly spoken of, but it is always the insertion phase difference that is measured. In a precision direction-pointing radome the perfection required in the radome wall could be met with small physical wall tolerances only if the wall material were highly homogeneous — which, generally, it certainly is not. The need for homogeneity in the material arises because the cardinal quantity in this type of radome is not how thick the wall is physically, but how thick it is electrically. The electrical thickness is a complex function of the physical thickness and of the dielectric constant. Errors in either of these quantities can be equally damaging; further, if there are errors in both, the detrimental effects of the two can be additive.

It must be realized that an evaluation of the I.P.D. alone is not sufficient to assure that the wall is proper; the physical wall thickness must also be measured. Two walls can have identical values of I.P.D. yet have different values of physical wall thickness and dielectric constant; clearly, if one is the proper design for a specific performance, the other is not. In practice, it is expedient to evaluate a wall by first measuring the physical thickness to insure that it is within a few percent of the design value. Then, as a final criterion, the I.P.D. is measured. When the I.P.D. is within design tolerances, which can be made less that 1 percent if a correction technique is employed, the radome wall is assuredly very close to the design requirements. The error in dielectric constant will be no greater than is accounted for in the two thickness tolerances.

The dielectric constant of a wall may be determined from measurements of the physical thickness and of the I.P.D. of the radome wall, as is discussed later in this chapter. If these latter quantities are found to be correct, the dielectric constant is correct.

The dissipation factor of a completed radome, even when it has a value greater than 0.01, can be evaluated by a non-destructive method with only fair accuracy. Fortunately, the obtainable accuracy is usually compatible with the need; its value is not a critical quantity and may not even be an important quantity as long as it remains small. Normally tan δ is evaluated only by auxiliary measurements on small specimens for standard dielectric tests. In the remote event that evaluations of tan δ are needed on finished radomes, they can be obtained by the free-space method described later for measuring the value of tan δ of test panels.

SECTION B. FACILITIES FOR MEASUREMENT

11-3. Insertion Phase Difference Measurements

Choice of Method. The I.P.D. of radome walls has been evaluated by three basically different methods. A direct evaluation of the I.P.D. can be obtained with the traditional microwave interferometer. An indirect evaluation of the I.P.D. can be made by (1) measuring the complex reflection of a wall and calculating the I.P.D. from the results or (2) determining the frequency at which the wall is a half-wavelength thick as revealed by a minimum in the reflection magnitude. In either case the measurement is accomplished with a single-horn method.

The interferometer method has the basic advantages of direct measurement, higher accuracy capabilities, and absolute calibration; the interferometer is essentially an absolute measurement instrument in that it is self-calibrating once the frequency is established. The complex-reflection measurement and the minimum-reflection measurement methods possess the feature of using a single-horn test head unit small enough to be manually moved over the exterior surface of a radome for cursory evaluations.

With some radome shapes it may be mechanically inconvenient to hold one horn of an interferometer inside the radome, and for this reason a gage with a single exterior horn may appear to be the preferable means. However, in general it will also be necessary to measure the physical thickness of the wall. If, as with all methods in use that are suitable for quantity work, the physical thickness gage is one requiring support of a gage element inside the radome, the interferometer horn may be supported by the same mount and offers little added complication. Further, if the I.P.D., and probably the physical thickness as well, are to be recorded in such a manner that the position of any measurement on the radome can be found again later so that a thickness correction can be made, the complication of supporting a second horn is a very minor part of the total facilities needed.

It appears that the single-horn methods will find their principal use in two sorts of applications. First, they are convenient for cursory inspection in the factory or in the field, especially where only a limited number of radomes of a kind are to be checked and moderate accu-

racy is sufficient. Secondly, they can be very useful in quality control work where the task is primarily not to determine the I.P.D. with high precision but rather to assure that the I.P.D. of the walls of the items produced are the same as that of a master model.

Interferometer Methods — Basic Manually Balanced Instrument. Interferometers of the basic type with manual balancing have been utilized in both experimental and production checking of radome walls.

In its simplest form the microwave interferometer is as shown in Figure 11-1. Since this instrument, its use, and its accuracy have been carefully discussed by Redheffer and others,[2,3] only a few general comments on it are given here. However, many remarks in the following section on the automatic-nulling interferometer are also clearly applicable to the simpler basic instrument and its use.

The test sheet of dielectric, or radome wall, is placed in the path of the beam traveling in free space between two horns in the test branch of the circuit. The instrument is balanced by matching at the second tee, in amplitude and phase, the signal that passes through the test branch with the signal traveling through the reference branch. The signal amplitudes are matched by adjusting the attenuator in the reference branch. The signals are matched in phase by moving the receiving horn in its axial direction to alter the horn separation and hence the electric circuit length. The circuit is balanced both with and without the dielectric present; the difference in position of the receiving horn for the two conditions, expressed in terms of free-space phase, is the I.P.D.; i.e., it is identically the phase difference introduced by the presence of the sheet. The situation is as simple as stated only if there is no interaction between the faces of the wall and between the wall and the transmitting horn. The error introduced by interaction between the panel and the transmitting antenna can be partly eliminated by moving the panel one-quarter wavelength along the axis of propagation and averaging the readings so obtained.[3] A sheet with an I.P.D. of less than 360° has been assumed; if the I.P.D. is greater than this, the fact must be ascertained by prior or subsequent knowledge.

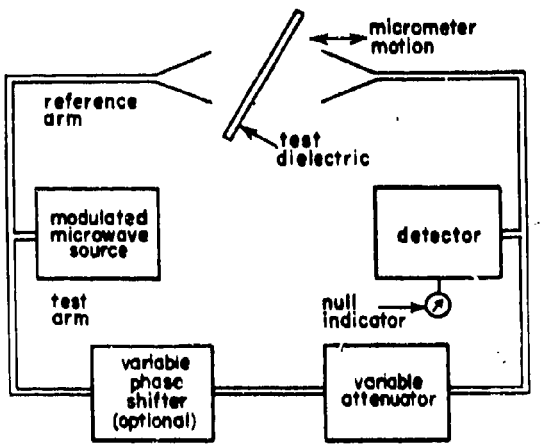


Figure 11-1. Basic Microwave Interferometer Arrangement

Interferometer Methods — Automatically Balanced Instrument. Precision interferometers for rapid continuous measurement of the insertion phase of every area of a radome wall have been developed to facilitate the production of radomes with solid half-wave and similar walls.[4] In addition to the interferometer proper, the principal electrical apparatus associated with it and necessary for the accomplishment of the complete task of measurement, recording, and playback to control wall thickness correction apparatus, are also indicated in the discussion that follows. The specific construction and performance information given all pertain to a particular X-band research model.

To simplify the equipment required for automatic nulling, the interferometer arrangement used is one in which the phase balance is independent of the magnitudes of the test and reference signals. The basic circuit shown in Figure 11-2 utilizes a phase-sensitive detector in an automatic phase plotter circuit similar to those described by Hines[5] and Bacon.[6]

A 1,000-cycle sinusoidally modulated fixed-frequency microwave signal is divided between a test and a reference arm. The test arm signal is passed through the test dielectric placed between the two microwave horns and is then brought to the H arm of a magic T. The reference arm signal is brought through a calibrated phase shifter to the E arm of the magic T. The colinear arms of the magic T are identically terminated in matched bolometers. The two bolometer outputs are compared in a bridge; the output of the bolometer bridge is zero when the difference in the magnitudes of the modulation frequency voltages on the bolometers is zero. As can be understood from a study of the vector diagram of Figure 11-3, the interferometer is balanced and the bolometer bridge output is zero when the test and reference micro-

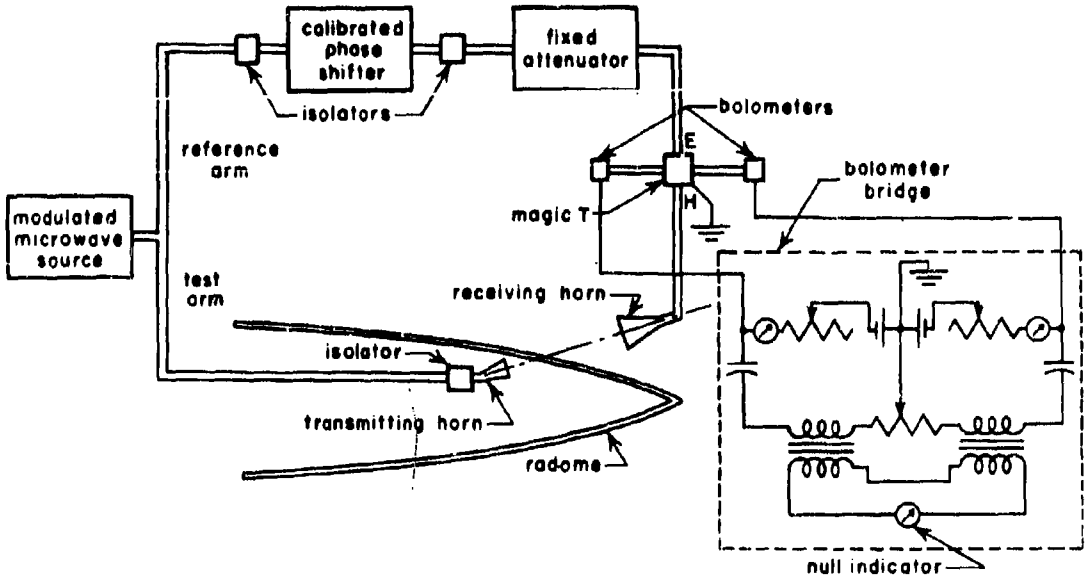


Figure 11-2. Interferometer Arrangement in which Phase is Measured Independently of Amplitude

wave signals imposed upon the H and E arms, respectively, of the magic T are 90° out of phase.

Since the interferometer balance is obtained by adjustment of only a phase-shifter, the balancing is readily made automatic by feeding the bridge unbalance signal to a servo system, which positions the phase shifter. As indicated in Figure 11-4, the phase shifter mechanical motions are translated into electric signals, which are sent to a paper strip recorder for information storage.

The size of the area measured at any time can by made small by using a 1- by 1-inch transmitting horn located within an inch, or less, of the interior radome surface.

In making precision phase shift measurements, the principal problem is to minimize reflections of microwave energy in the entire interferometer arrangement. The goal is to have the original wave supplied by the microwave source at the first tee to be the only wave passing through the test dielectric or through the calibrated phase shifter, respectively.

Phase shifts through reflective elements in series are not linearly additive; a change in the phase shift through one of the elements will not cause an identical change in the total phase shift through the series of elements.[7] Hence, if there

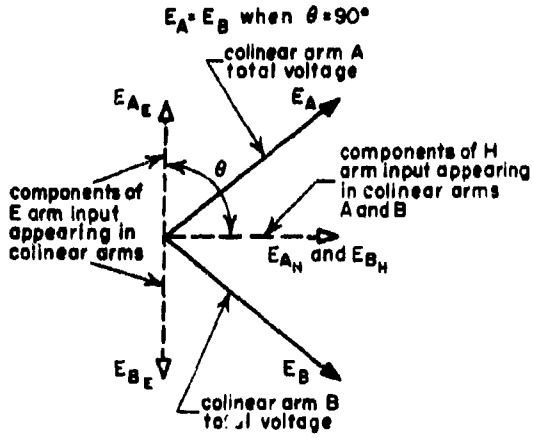


Figure 11-3. Voltage Vector Relationships in Magic T of Interferometer which Measures Phase Independently of Amplitude

is appreciable reflection from the phase shifter and from one or more other elements in the branch containing the phase shifter, the calibration of the phase shifter will be different whenever the reflection from any element in the branch is changed. This is assuming a reflective element is causing an unwanted wave to pass through the phase shifter in the forward direction. Obviously, the phase shifter must be calibrated in place. The same sort of considerations apply in the test arm. If any appreciable

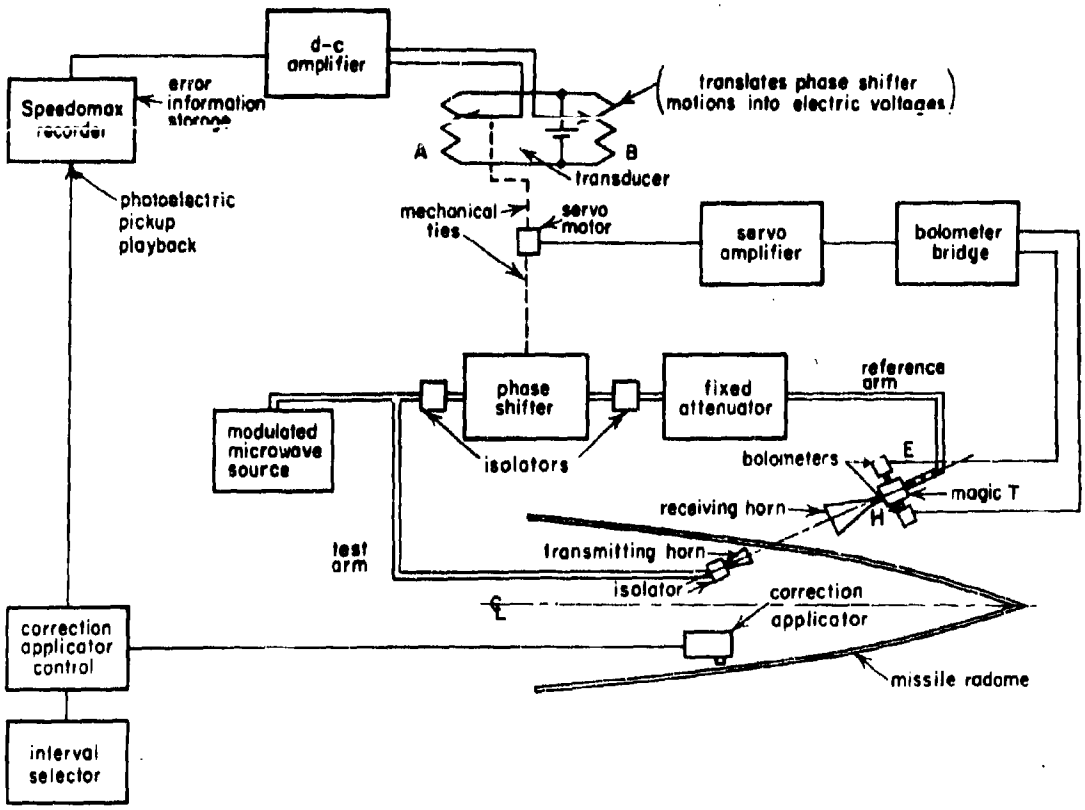


Figure 11-4. Elements of Semiautomatic Apparatus for Measuring and Correcting the Electrical Thickness of Radome Walls

energy is reflected from the test dielectric and re-reflected to pass through the test dielectric, accurate phase shift measurement is impossible. This is because the resultant wave arriving at the magic T is not in the same phase position the original wave alone would have been.[8]

The microwave circuits should be carefully arranged with the above facts in mind. The transmitting horn is preferably oriented to make an incidence angle with the dielectric surface close to Brewster's angle, which is approximately 60° for the dielectrics expected to be tested; the incident energy is parallel polarized. Thus, the energy reflected from the dielectric is minimized. A unidirectional element is located just preceding the transmitting horn and dissipates most of the energy reflected into this horn from the dielectric. The energy reflected into the transmitting horn from the receiving horn is kept small by isolation effected by horn separation. Unidirectional elements are placed on either sides of the phase shifter to reduce errors from reflections in the reference arm elements.

It is impractical to maintain exactly the distance from the transmitting horn to the radome as the radome is moved to permit examination of different areas. Further, it is impossible to obtain zero reflection from the radome. Therefore, if a radome of uniform electric thickness is being tested, the indicated phase measurement will vary slightly as the radome is moved. This effect cannot be reduced to an undetectable quantity, but to a value sufficiently small to permit measurements with the desired accuracy.

In one instrument the master phase shifter consisted of a long thin quartz slab placed in the E-vector plane inside a rectangular waveguide with provision for precise transverse positioning. It produced a voltage standing wave ratio of 1.03 to 1.10, depending on the slab location. A maximum phase shift of 300° could be introduced. A second identical phase shifter was

inserted in the interferometer to allow initial balancing with the master phase shifter at a preferred scale position.

The microwave source must be a highly stabilized frequency source. Then the two microwave branches of the interferometer need be only roughly the same electric length; if the generator is a klystron in a stabilized local oscillator circuit, the long-time frequency stability of the generator can be made about 0.01 megacycle and it will not be necessary to make the interferometer frequency-insensitive by meeting the criterion for length of lines and horn separation for minimizing the effect of drift.[9] Preferably, however, the criterion should still be roughly met.

The bolometers must be very well matched both in sensitivity and in transient heating and cooling characteristics. Because of thermal lag, the output of a bolometer receiving energy from a sine-wave modulated signal will not be a sine wave. Further, if the transient heating and cooling characteristics of the bolometers are not the same, the two bolometer output signals may have a phase difference in their fundamental components that will make the necessary high-sensitivity null impossible.

The output of the bolometer bridge must be amplified through a narrow-band amplifier[4] to insure nulling of the fundamental components only. A mechanical tuning fork may be used to obtain frequency stability in the modulation signal generator. The output of the narrow-band amplifier is fed to the amplifier of the servo system, which positions the phase shifter.

Considerable difficulty may be encountered in avoiding modulation-frequency magnetic pickup and extraneous voltages in the low-signal-level circuitry up to the input of the narrow-band amplifier.

Extensive use of microwave absorbing material is generally required to minimize back reflection from structures and apparatus in the general vicinity of the horns.

As a transducer for translating phase shifter motions into electric voltages the d-c Wheatstone bridge arrangement, as shown in Figure 11-4, may be used. Identical multiturn Helipot potentiometers each form two arms of the bridge. The sliders of the potentiometers are connected to the detector (a Weston D-C Inductronic Amplifier), which draws no current but supplies a large output signal. The motion of the slider of potentiometer "A" is mechanically linked to the motion of the phase shifter. This slider moves a large fraction of the potentiometer length when a radome wall is inserted between the microwave horns. But it moves over only small excursions, prompted by variations in electrical wall thickness, as the radome is moved and different parts of the wall are examined. The slider of potentiometer "B" is positioned so that the bridge is balanced when the radome wall thickness is the design value. Then as slider "A" is automatically moved with the phase shifter, the bridge output is indicative of the deviation, or error, in I.P.D. from the given design value. Over the small range used in indicating the errors, the output is essentially linear with phase shift. The errors in thickness for missile radome walls with a taper design, or with any particular wall thickness variation design whatsoever, are readily indicated by simply driving the slider of potentiometer "B" to the position corresponding to the design thickness required at the spot being inspected.

The master phase shifter is calibrated against changes in the free-space separation of the transmitting and receiving horns with no dielectric between the horns. The receiving horn is mounted on an axially movable mount; its position is read on a precision dial gage with 0.0001 inch divisions. As one performance check, after precise nulling the receiving-to-transmitting-horn separation should be increased exactly one half free-space wavelength. However, because of nonuniformity of the field, an exact null will not exist at this second position. The phase shifter will have to be moved slightly to obtain an exact null. The allowable discrepancy depends on the overall instrument accuracy being sought; when necessary a correction can be made.

An important feature of the design of the interferometer arrangement described is that the entire instrument can be readily checked for error by a rapid three-step procedure:

1. Perfection of the bolometer bridge balance is assured by simultaneous application of the identical test signal to both inputs of the bridge and obtaining a zero output signal.

2. If identical microwave signals are sent into the colinear arms of the magic T, assurance of a null is obtained by removing the transmitting horn and replacing it with a short. Only the reference signal now arrives at the magic T. By virtue of previously checked perfection of the tee, the reference signal should divide equally into the side arms and their bolometers. Only lack of perfection in bolometer impedance match and characteristics can then prevent a null.

3. The master phase shifter calibration is checked in the following manner. The shift incurred due to the insertion of the test dielectric is noted. Next, without the dielectric present, the receiving horn is moved to cause the identical change in phase shifter positions. The shift of the horn in terms of degrees of electric phase is the I.P.D.

An instrument has been built in which the accuracy of the I.P.D. measurements has been ascertained to be about 0.5°. Under automatic operation the instrument always responds to changes of 0.15°.

Single-Horn Complex-Reflection Measurement Method. A gage for electrical thickness has been developed which is basically a single-horn reflectometer for measuring the phase and amplitude of the wave reflected from a radome compared to a suitable reference.

The basic operation of the instrument can be explained by referring to the simplified functional diagram of Figure 11-5. A microwave signal passes through a bidirectional coupler and then through a small probing horn to impinge on the radome wall. Energy reflected from the wall back through the horn also passes through the bidirectional coupler. A comparison of the phase and magnitude of the forward and reflected wave outputs of the directional coupler leads to an evaluation of the I.P.D. of the dielectric wall. More specifically, reference settings for the phase shifter and attenuator may be obtained with the horn shorted by a plate of metal to get complete reflection. The device then measures the reflection coefficient of the radome wall with respect to this reference termination. The instrument is known to be balanced when the signal level in the difference arm of the magic T comparator is zero.

Both the reflection-coefficient magnitude and the I.P.D. are obtained by calculations based upon the measured phase shift and attenuation. In practice the interpretation of the readings of the phase shifter and attenuator dials is accomplished through the use of a special slide rule computer, graphic computers, or by actual computation, depending on the quantity and exactness of the information needed.

A model of this instrument operating at X-band frequencies has been carefully developed in which only the probe horn, the directional

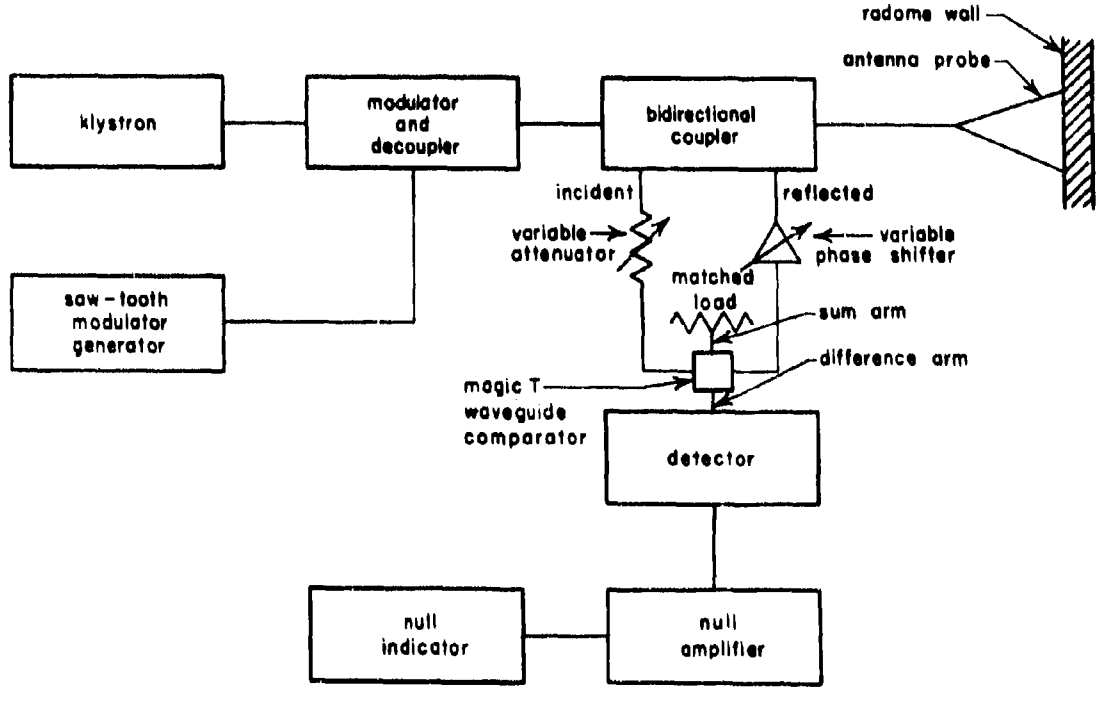


Figure 11-5. Apparatus for Measurement of Complex-Reflection Coefficient

couplers, and the microwave bridge are incorporated into a lightweight test head which can be easily moved over a radome surface. The complete equipment including a stabilized frequency source is portable. The apparatus is discussed in detail in development reports.[11] Automatic balancing is planned in a succeeding model.

A disadvantage of the present instrument is that the entire periphery of the horn mouth must be in contact with the dielectric surface or the readings will be changed. In practice this means there must be a different empirical correction factor for every different degree of simple or compound wall curvature. This disadvantage exists even in quality control applications where simply the phase shifter readings, rather than a knowledge of the electric thickness or reflection coefficient, would suffice. Also because any dielectric wall placed over the mouth of the probe horn perturbs the field, the field distribution at the mouth will be different with every different wall construction or dielectric constant. In careful work it appears that these phenomena will have to be recognized and evaluated. For example, with a sandwich-type wall with nonsymmetrical skins the field at the mouth of the horn will be different depending on which side of the wall the horn is placed — but the wall actually has only one value of I.P.D. At the present time evaluation tests of a conclusive nature have not been performed. It is anticipated that with proper antenna design these undesirable effects may be reduced.

The instrument does not permit accurate measurements at the frequency at which the wall is a half-wavelength thick at normal incidence if the dielectric has low loss; this is because the reflected signal will be negligible. Shifting the frequency to obtain sufficient reflection is only a slight inconvenience in work with ordinary dielectrics; however, with frequency-sensitive artificial dielectrics shifting from the design frequency probably would not be allowable and hence measurements could not be made.

The absolute accuracy sought in the development of the instrument is 1.0 percent with a sensitivity of 0.1 percent at a center X-band frequency; the accuracy decreases at lower and higher frequencies.

Single-Horn Minimum-Reflection Method. The I.P.D. of a single-layer wall can be evaluated through a measurement of the frequency at which the reflection is a minimum. The method to be described is based on the fact that the reflection at normal incidence from a solid dielectric wall is a minimum when the electrical thickness of the wall is a whole number of half-wavelengths. The method has been carefully evaluated and is now being put into practical use.[12]

The basic elements of this single-horn system are as indicated in Figure 11-6. The oscillator is continually swept through the frequency range of interest at a fairly constant rate by mechanical or electronic means. The microwave oscillator is isolated from the rest of the system by the presence of a ferrite modulator. The small E-plane flared horn is experimentally matched (by insertion of a small dielectric slab) to have a standing wave ratio of less than 1.05 over a frequency range of 8,200 to 10,000 mc. The front of the horn is preferably located about three-quarters inch from the dielectric wall for a 1.5 inch aperture horn. The power reflected from the panel (plus, unavoidably, that reflected from the horn) is indicated by a power-ratio meter, which compares the outputs of a forward and reverse direction sampling directional coupler. The power-ratio meter output is portrayed as a function of frequency on an oscilloscope. The frequency at which the minimum occurs is noted.

Several fundamental difficulties must be recognized in making measurements of the part of the emitted power that is reflected back into the horn by the dielectric. The reflection from the horn itself must be reduced to a negligible value over the operating frequency range to permit sensitive operation in determining the minimum reflection from the dielectric wall. Also, for sensitive operation the general level of the reflected power, with respect to the power leaving the horn, must be as high as possible. However, because of the nature of the near field,

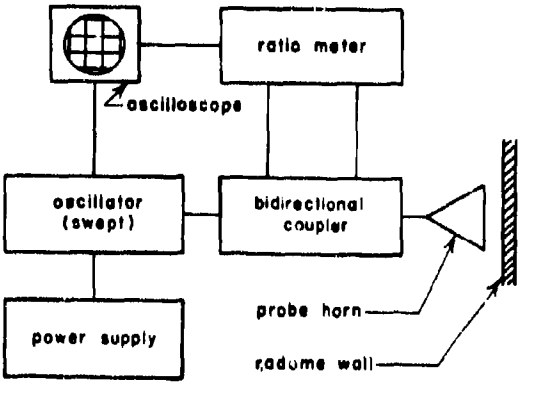


Figure 11-6. Circuit Arrangement for the Measurement of Reflection Amplitude

a placement of the dielectric too close to the horn mouth will produce errors. These arise from the fact that the reflection from the front interface of the wall becomes large with respect to that from the rear interface.

In practice, this method has been found capable of yielding medium-precision results if suitable care is taken in designing the apparatus. Two very important inherent features make this a singularly attractive one-horn measurement method. First, the results are changed but little if the variations in the wall-to-horn spacing are kept less than ±5 percent; useful results can be obtained even if the variations approach ±10 percent. Secondly, curvature of the radome wall in itself is reported to have but a very small effect on the results.

Ignoring the very small effect of loss, the I.P.D. of the dielectric wall in degrees is found from the following simple equation.

$$\text{I.P.D.} = 360\left(\frac{1}{2} - \frac{d}{\lambda_0}\right)\text{degrees} \qquad (11\text{-}1)$$

where λ_0 = the free-space wavelength corresponding to minimum reflection. It is anticipated that a repeatability as close as 1^0 may be obtained with this method. The absolute accuracy may be much poorer than this.

11-4. Reflection Measurements

The very equipment used in the above system for determining the I.P.D. by the minimum-reflection method can be used to measure the magnitude of reflections at any one frequency. The power-ratio meter indicates percent reflection directly.

In general, the indicated reflection will not be the true plane-wave reflection. The discrepancy is due to the "near-field nature" of the waves in the dielectric wall being tested. Different readings will be obtained with different horn sizes and horn-to-wall separations. With lightweight sandwich-type walls the error in indicated power reflection coefficient may be as little as 1 or 2 percent with the horn in contact with the surface. With a solid wall it may be found that a small horn will have to be separated from the wall a large fraction of a wavelength to obtain good correspondence between the indicated and the true values.

Nevertheless, the method can be highly useful. The apparatus is sensitive and the repeatability of readings can be made excellent. Empirically, by taking readings on a wall of similar construction whose performance is known or can be calculated, the apparatus can be calibrated for testing any particular design of radome. Often test conditions can be arranged so that the indicated value may be sufficiently accurate.

11-5. Physical Thickness Measurements

Because of a highly reentrant shape or simply because of large size, with many radomes rather special facilities are required to obtain accurate measurement of the physical wall thickness. Even with small nearly flat radomes, the measurements usually cannot be made without facilities that, although perhaps simple, must be specially constructed. Several distinctly different types of gages have been developed for radome wall measurements; each has unique advantages in certain situations.

Mechanical Gages. When possible in the simpler situations, various versions of large-throat mechanical micrometers are used. Usually it is most convenient to build a device with a dial gage as the indicator in a general arrangement as shown in Figure 11-7. It is essential that the axis of the dial gage plunger and of the anvil be well aligned and normal to the radome surface. If a wall has small irregularities in its surfaces, the readings will change slightly with radius of curvature of the end of the plunger and of the anvil.

Severe limitations are found in the above type of gaging when the problem of evaluating a large highly pointed radome is considered. The anvil must be supported inside on the end of a boom. The weight of the radome resting on the anvil will cause the boom to deflect and thereby produce a direct error in the measurement. With heavy radomes the anvil may indent the surface and thereby cause additional error. When insufficient care is exercised, lightweight-core

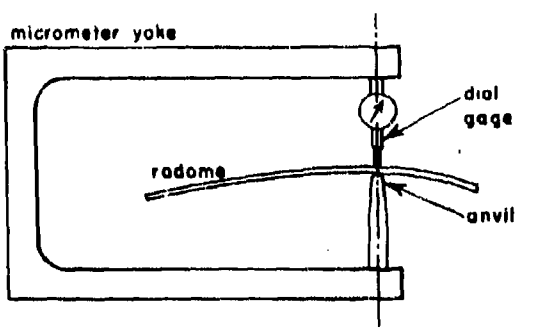


Figure 11-7. Mechanical Micrometer for Measuring the Physical Thickness of Radome Walls

radomes with thin skins may suffer physical damage due to penetration of the end of the anvil through the inner skin.

An Electromechanical Gage. The arrangement with the anvil supported by a boom would be greatly improved if the anvil were replaced by a second dial gage, as shown in Figure 11-8. Then the greatest loading that could be exerted on the boom would be the insignificant thrust produced by the plunger of the lower dial gage. Clearly, the algebraic sum of the changes in the dial gage readings, with and without the radome present, is the wall thickness. Further, movement of the radome wall in the direction of the axis of the plungers cannot alter the reading.

A highly useful practical gage has been built using the above basic ideas.* Refer to Figure 11-9. The two dial gages have been replaced by electrical displacement detection units. These units operate on the principle that the mutual inductance of two stationary coils in a unit is altered when a small slug of commonly shared magnetic core material is displaced axially; this core element is mounted on a nonmagnetic probe which becomes the equivalent of a dial gage plunger. By bucking the output signals of the two detection units and feeding the difference signal to a servo-operated balance unit, and indication of the algebraic sum of the motions of the probe of the upper and lower detection units is obtained.

The radome wall can be moved in the direction of the probe axis without introducing appreciable error as long as the pickup units are operating in their range of linearity -- which can be as great as 0.5 inch.

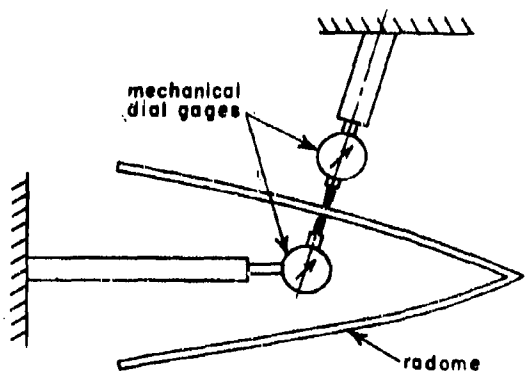


Figure 11-8. Arrangement of Improved Mechanical Micrometer for Radome Walls

* Developed by C. W. Bowlby, Boeing Airplane Company.

The upper sensing element is preferably attached to a micrometer-feed movable mount which, after the indicator is set to zero without the radome present, is raised precisely the amount of the design thickness of the radome wall. The indicator then reads the error from the design thickness. This arrangement allows basic calibration of the indicator against the precision micrometer. Measurement accuracies of 0.0005 inch are readily obtained. The displacement detection units and a servo-operated indicating unit are commercially available equipment.

An Electrical Gage. A gage that is completely electrical in its operation has been developed for measuring the physical thickness of dielectric walls independent, for all practical purposes, of tan δ and ϵ_r of the dielectric.[13] The operation of the instrument is based on the variation of the mutual inductance of two coils, fixed in relationship to each other, when they are brought near a metal surface. Mutual inductance is used because a greater and more linear indication can be obtained than from self-inductance.

The two coils are contained in a sensing head about 2.0 inches in diameter and 5.0 inches long which is connected by a convenient length of cable to an indicator and power supply unit. The coils are located in one end of the sensing head. After this end of the head is placed in contact with one surface of a dielectric sheet, the mutual inductance of the coils is changed when a thin sheet of metal is placed on the opposite surface; the magnitude of the effect will increase as the thickness of the sheet is decreased.

The operating frequency is made sufficiently high that the metal may be aluminum foil as thin as 0.003 inch. The foil must be in intimate contact with the dielectric surface, as any air gap between the metal and the wall will make the indicated thickness too large. In practice the sensing head is rocked to obtain a minimum reading; the head is then normal to the surface. If the gage is calibrated by measuring flat sheets of dielectric, a correction factor must be applied when measurements are made on a curved surface. The correction must be made because of the air gap that then exists between the bottom of the sensing head and the surface upon which it is placed; the mutual-inductance curve is unchanged but the zero point is shifted. When a compound-curvature surface has one

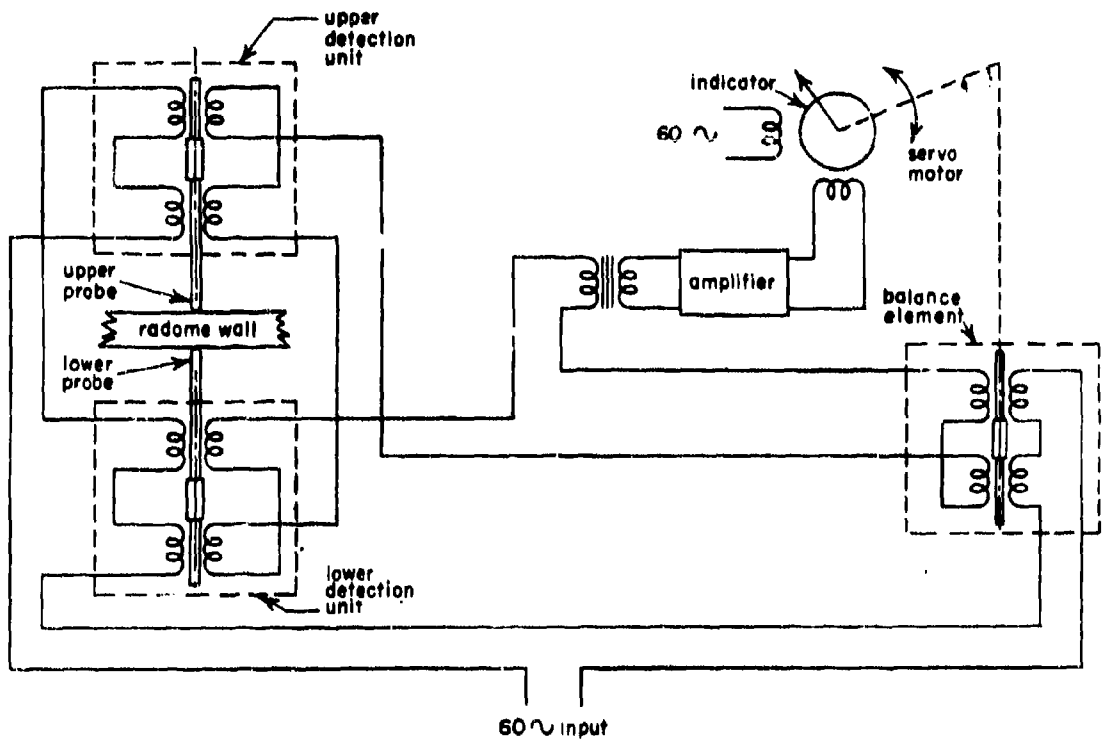


Figure 11-9. Circuit of Electrical Gage for Measuring the Physical Thickness of Radome Walls

radius much larger than the other, as in an ogive, using the calibration for the smaller radius of curvature will permit measurements with good accuracy. Gages can be made to have an accuracy of 0.001 inch and a repeatability of less than 1 percent.

An advantage of the mutual-inductance gage is that the wall of a finished radome can be checked without any mechanical setup. Also, the gage has special merit in that it can be used to measure the physical thickness of a radome laid up on a metal mandrel before the radome is removed. Backing the dielectric wall with a magnetic material such as the cast iron of a mandrel causes a slight shift of the instrument zero but does not alter the slope of the output curve.

This instrument is, of course, not applicable to metal-loaded wall structures.

11-6. Dielectric Constant Evaluation

The interferometer finds use in the important auxiliary task of accurate nondestructive determination of the dielectric constant of solid radome walls and test panels. Since the I.P.D. is measured directly and means can be provided to measure the physical wall thickness with a high degree of exactness, the free-space measurement method allows not only rapid but also very accurate evaluations of the dielectric constant. Its accuracy is basically due to the absence of the necessity for excellent fits or contacts with the metal surfaces in a waveguide or a cavity.

For normal incidence, the relative dielectric constant ϵ_r in terms of the wall thickness, d, and the "free-space insertion phase distance," d', is (neglecting loss and interaction between the faces of the wall)

$$\epsilon_r \cong \left(1 + \frac{d'}{d}\right)^2 \qquad (11\text{-}2)$$

For arbitrary incidence at angle θ with either polarization, the corresponding equation is[14]

$$\epsilon_r \cong 1 + \frac{2d'}{d}\cos\theta + \left(\frac{d'}{d}\right)^2 \qquad (11\text{-}3)$$

which becomes

$$\epsilon_r \cong 1 + \frac{d'}{d} + \left(\frac{d'}{d}\right)^2 \qquad (11\text{-}4)$$

when $\theta = 60^\circ$. This angle, being high enough to minimize interaction between horn and wall and also being near the Brewster angle for most commonly used dielectrics, is conveniently suitable for radome work. Good accuracies will be obtained from these equations when the polarization is parallel and the incidence angle is at or near the Brewster angle. Plots of ϵ_r versus d'/d for these conditions are given in Reference 14. The quantity d' is identically the distance in free-space having a phase shift equal to the I.P.D.

Aside from providing high accuracy in evaluating homogeneous dielectrics, the interferometer is uniquely useful in evaluating slightly nonhomogeneous dielectrics. For example loaded dielectrics may be so nonhomogeneous throughout a volume only as large as a waveguide specimen as to make dielectric constant measurements almost meaningless. But in use in radomes and lenses it is the average value over a reasonable intercepted area which must be maintained. The interferometer does inherently measure the dielectric constant as an average value over an area of suitable size.

A less accurate, but often sufficiently accurate, evaluation of dielectric constant can be quickly obtained by measuring the I.P.D. with the single-horn minimum-reflection method.

11-7. Dissipation Factor Evaluation

The dissipation factor of a solid flat panel can be determined with a degree of accuracy useful in radome work by a free-space measurement. Under certain environmental conditions, in particular that of rapid heating, this is the only approach developed that can yield useful results. The measurements can be made with the same general type of microwave equipment as is used in the conventional transmission and I.P.D. tests on panels.

The method is based on the measurement of the power transmission efficiency under a condition of minimum power reflection; this experimental result is used in conjunction with an I.P.D. measurement and calculations to evaluate the dissipation factor tan δ.

At the specified frequency, the power transmission efficiency is measured with parallel polarization at sufficiently close to Brewster's angle to make the reflection very low. The reflection cannot be made zero because there is loss and because the field is divergent to some degree and only the central ray can be caused to strike at Brewster's angle. If the reflection could be made zero, the power transmission coefficient, T^2, would be unity except for the attenuation due to ohmic loss. Then tan δ could be evaluated accurately. The unavoidable reflection may give rise to a small, but tolerable, error, since in this method the reflection must be assumed to be zero.

In addition to T^2 the physical thickness d and the I.P.D. must be measured to allow the evaluation of tan δ. Because the dielectric constant and hence the I.P.D. varies slowly with frequency in the microwave region, it is not necessary to measure the I.P.D. at the transmission measurement frequency, but merely at a convenient frequency not too far removed.

The quantities T^2, d, ϵ_r, and tan δ are related by Equation (2-47), Chapter 2. It is not convenient to solve for tan δ directly. Instead, tan δ is found by interpolation between curves relating it to one of the other parameters, the remaining parameters being fixed.

The quantity ϵ_r of the sheet is calculated from the measured values of d and I.P.D. For a particular value of ϵ_r and of d, a single curve of tan δ vs. T^2 could be calculated; it would be for incidence at the value of Brewster's angle determined for the given value of ϵ_r. But, since the curve would be of no value for other values of ϵ_r and d, maximum benefits from the calculations will be obtained if, for each of a number of values of ϵ_r, separate families of curves are prepared, each family with a number of curves for the same selected values of the parameter d. The values of d and of ϵ_r are chosen systematically with values straddling those expected to be encountered in the test panels. A collection of such curves will allow evaluation of tan δ throughout their range of values of ϵ_r, d, and tan δ by interpolation. Admittedly, tan δ will usually be determined with only fair to poor accuracy if tan δ is large, i.e., roughly, if tan $\delta > 0.02$. But this is not as unfortunate as it may seem, because there appears little need to know tan δ accurately in radome work if tan $\delta > 0.02$. Generally, it is necessary to know it only with an accuracy of perhaps 10 percent; if it is much larger, it is only necessary to know that it is so large and hence generally an entirely unsatisfactory value. If tan δ is so small that it reduces T^2 very little below unity, although the accuracy of determination again deteriorates, the situation is again alleviated by the fact that knowing roughly that tan δ is so small is sufficient for radome work.

11-8. Measurements Under Special Environment

Relatively exact measurements of ϵ_r and tan δ on small waveguide or cavity specimens can

be obtained at room temperature and perhaps even at high elevated temperatures if sufficient time is allowed for stabilization of the temperatures to some particular condition in the pertinent parts of the equipment. However, if what is needed are the electrical properties of a dielectric upon being heated to a prescribed high temperature in a particular short time of less than the equipment stabilization time, none of the laboratory methods in which a specimen is placed in a test chamber and then heated can be used. These methods certainly cannot be used if the material changes its characteristics at elevated temperature in the time concerned. With most plastics used in radomes the degree of polymerization does change appreciably with time at temperature. Of even greater importance may be the change in electrical properties of specimens of material from which moisture can be driven out due to the decrease in moisture content with time at elevated temperature. Also, in general, the laboratory methods that involve placing a specimen in a chamber cannot be used to obtain a direct answer if the condition to be simulated in one in which a temperature gradient exists through the wall. However, by free-space measuring methods good measurements of ϵ_r and useful measurements of tan δ can be obtained under a great variety of conditions simulating those existing in practice.[15]

In the free-space test for either ϵ_r or tan δ, two sorts of equipment are needed. One part is the microwave equipment. The second part is an environmental chamber and the associated apparatus for sliding a panel out of the chamber and into the space between the microwave test horns. In the environmental chamber arrangements can be made to cause a panel to be initially in equilibrium with room temperature air at a particular humidity. The panel can then be heated at any rate compatible with the limitations of present heat sources; if desired, the panel can be heated from one side only. Thus, the moisture and temperature conditions existing in the radome at a particular time in flight often may be fairly well established in a test panel at the time of measurement. Then, for measurement the panel may be rapidly shot out of the environmental chamber into a proper position and orientation between the microwave test horns. The measurement must be made rapidly; i.e., in a few seconds in extreme cases, to assure an evaluation before the dielectric has cooled significantly. This requires adequate, though not necessarily special, physical thickness gages and microwave equipment.

An automatic-nulling interferometer is very convenient for rapidly measuring the I.P.D. If the instrument is preset roughly to the correct value, a reading can be obtained within several seconds after the panel is shot into position by, at that time, energizing the automatic nulling servo system and then deenergizing the servo system as soon as the interferometer balance is obtained. A rapid reading of transmission efficiency can also be readily made.

If a reading is obtained rapidly and if the panel is returned to the environmental chamber immediately after the measurement is made, cooling of the measuring apparatus may be unnecessary.

SECTION C. MEASURED DATA AND ITS UTILIZATION

11-9. Choice of Test Frequency

The phase shift incurred in passing through a solid wall is a function of the dielectric constant. With most natural dielectrics ϵ_r changes so slowly through the X-band and lower microwave frequency band ranges that, for radome work, ϵ_r usually can be assumed constant through each band. In the K-band ϵ_r can be assumed nonvarying over limited frequency ranges. Where ϵ_r can be considered constant, I.P.D. measurements can be made (for the purpose of calculating ϵ_r) at any convenient frequency, i.e., the operating frequency of an available interferometer, and do not necessarily have to be made at the design frequency. The I.P.D. at the design frequency for low-loss walls can be calculated from the results of measurements at another frequency through use of the equation for the insertion phase delay

$$\Delta = \frac{\lambda_0}{2\pi}\left[\tan^{-1}(A \tan D) - \frac{2\pi d}{\lambda_0}\cos\theta\right] \quad (11\text{-}5)$$

where $D = \frac{2\pi d}{\lambda_0}\sqrt{\epsilon_r - p}$ with $p = \sin^2\theta$

$$A_{\parallel} = \frac{(\epsilon_r)^2(1-p) + \epsilon_r - p}{2\epsilon_r\sqrt{1-p}\sqrt{\epsilon_r - p}}$$

$$A_{\perp} = \frac{\epsilon_r + 1 - 2p}{2\sqrt{1-p}\sqrt{\epsilon_r - p}}$$

for parallel and perpendicular polarizations, respectively.

11-10. Selection of Test Stations

Because of diffraction phenomena, the far field of an electromagnetic beam is only slightly

distorted by variations in radome wall thickness over areas with a maximum dimension small compared to the antenna dimensions, as long as the thickness averaged over areas appreciable with respect to that of the radiator is the proper value.

The above fact is pertinent to the matter of the selection of test stations in measuring radome wall thicknesses. It is sufficient, and not merely an undesirable practical compromise, to measure radome wall thickness errors at stations located at intelligently selected intervals rather than to attempt to measure the wall essentially everywhere. The test stations should be located closer together in the more important areas, for example, near the nose of an ogival radome where the power intensities are relatively large at high angles of incidence.

11-11. Value of Parallel Recording of Electrical and Physical Thicknesses

With radomes requiring the highest precision in wall thickness, facilities for continuous recording as the thickness gages scan the wall area is highly desirable. Of particular value, if the dielectric is not homogeneous, is the side-by-side recording on a paper chart of the electrical and physical thickness errors. Where the dielectric constant is uniform, the records of two thickness errors will increase and decrease together. In contrast, if over an area there is no physical thickness error but there is an electrical thickness error, it is clear that the dielectric constant is improper. This type of information portrayal is invaluable in developing tooling and materials for producing half-wave wall radomes.

11-12. Establishment of Wall Thickness Tolerances

Final judging of the adequacy of the performance of any actual radome rests on the results of operational pointing-error or transmission tests.

The allowable wall thickness tolerances can be established only by pointing-error or transmission tests on a sufficient number of radomes of the particular design, all of which have thickness variations such that the largest are close to, but are not in excess of, a particular tolerance. The tolerance of the radomes in the test groups should be increased until the maximum value with which a sizeable group of radomes will meet the specified electrical performance tests has been established.

With the tolerance established, the error tests can be eliminated in favor of thickness gage measurements for production inspection of half-wave wall radomes and reflection gage measurements for sandwich-type wall radomes.

11-13. Evaluation of Radomes for High-Temperature Operation

Attempts to evaluate the performance of a radome and its antenna at high temperatures have been discouraging. Therefore, considerable thought has been given to the matter of establishing, from room-temperature tests combined with calculation, the performance that will be obtained when the dielectric is at elevated temperature. A warning is sounded that this procedure may not be quick and simple.

In the case of a half-wave-wall nose radome with small allowable boresight errors, the magnitude of the task can be seen by a brief statement of the steps of what appears to be a reasonable method.

Initially, a test radome is built to operate at about the design frequency at room temperature. By room-temperature range tests the boresight-error performance at the optimum frequency for the radome, as built, is established and found to be within the allowable limits for the final radome at high temperature. It is then assumed that what is required is a radome with a wall that at the elevated temperature will have I.P.D. characteristics with as low slopes and as little difference between polarizations, in the range of incidence angles of importance, as the wall of the test model had at room temperature.

This wall thickness can be established by successive calculations, at the design frequency, of the I.P.D. characteristics for thicknesses selected by a cut-and-try procedure and using the high-temperature values of ϵ_r. With the high-temperature wall thickness established, the change in thickness in cooling to room temperature and thus the thickness at room temperature is found. The final radome, built to this thickness, should give very closely the same boresight error performance as the first-evaluated test model did at its optimum frequency, if the final radome is tested at room temperature at the frequency

$$f = f_t \times \frac{d_t}{d} \qquad (11\text{-}6)$$

where f_t = optimum frequency of test radome,

d_t = physical thickness of test radome,

d = physical thickness of final design.

11-14. Effect of Loss on Phase Shift

The presence of loss in the dielectric changes the I.P.D. of a wall from the lossless-dielectric value so little as to be of no practical consequence in most work.

Even in high-precision half-wave walls at X-band, the effect is so small as to be of no interest if the design angle is in excess of 60°, ϵ_r is in excess of 4, and tan δ is less than 0.02. At lower angles and smaller values of ϵ_r, the magnitude of the effect should be examined in precise work.

11-15. Dielectric Constant of Laminate Walls

In general, with a laminate, ϵ_r varies with both polarization and angle of incidence. This is because ϵ_r has one value for the component of electric field lying in the plane of the laminations and another value for the component that is normal to it.

The laminate may be thought of as a stack of sheets in which alternate sheets of glass and resin themselves have, respectively, high and low values of ϵ_r. The effective ϵ_r for the stack is lower when the electric field vector is normal to the stack than when it is parallel to the sheets. For example, with a common polyester-resin impregnated glass-cloth laminate the values for the two orientations were found to be $\epsilon_r = 4.2$ and $\epsilon_r = 4.4$, respectively. This difference in ϵ_r is large enough to necessitate its being taken into account in precision high-incidence-angle radome design.

11-16. Importance of the Effect of Moisture on Electrical Wall Thickness

With most materials used, other than solid glass or ceramic, the moisture absorption in a half-wavelength wall can be of practical consequence even under moderate humidity conditions.

A case of particular interest is found in radomes for high-temperature operation. In manufacture they are generally cured for many hours at a temperature as high, or higher than, the operating temperature. At the end of the curing process the finished radomes have a very low moisture content. A period of at least a number of days is required for the moisture content to increase to become stabilized with the normal room conditions. If careful I.P.D. measurements are made, it will be found that the electrical wall thickness increases during the moisture-stabilization period. The increase can be large enough to be important in evaluating the most precise radomes. Therefore, all testing of such radomes should be made after the same degree of moisture stabilization.

11-17. Simplification in Inspection Tests

Both procedure and equipment for inspection tests can generally be much simpler than those for engineering evaluation tests.

A regrettably vast amount of work has been expended in the past on boresight-error and transmission-efficiency tests merely for inspection purposes. To avoid continuance of the situation, suitable and simpler inspection facilities must be made available and a very considerable amount of correlation data must be obtained.

As exemplified by the apparatus described for physical and electrical wall thickness and reflection measurements, sufficient means are available to implement rapid, relatively low-cost, production-line quality-analysis testing.

The principal deterring factor in putting these tools into use is the lack of data establishing what tolerances can be allowed if a particular kind of radome is to have at least certain specified minimum-performance characteristics. To obtain such data may be an extensive or a simple task, depending on the radome shape, the range of look angles, the antenna power pattern, the quality required, and whether assurance is needed that every radome passed will be satisfactory or if a statistical sampling will suffice.

It does not necessarily follow that, for instance, a radome with very exacting boresight-error requirements is costly to inspect. A nearly flat honeycomb-core radome struck at modestly low incidence angles will produce only extremely low boresight errors if it is made uniformly without any skin laps or construction defects such as core-cell filling. A simple check for low uniform reflection with a single-horn gage passed over all of one surface will give a 100 percent check for construction defects. If the requirements are stringent enough and the radome is small enough so that any with a defect can be discarded, the simple inspection suffices and the cost of boresight testing every unit is avoided. However, a complicated situation will exist if the requirements are less exacting and modest defects become permissible; then a large group of radomes must be tested on the boresight-error range and examined with the reflection gage to establish the limits in the readings of the latter which occurred with radomes having acceptable range performance.

11-16. Interpretation of Requirements

Those responsible for the effort of designing radomes and proving them adequate often may do well to accept statements of performance requirements with a little skepticism and an inquiring mind.

When a single minimum-transmission or maximum-boresight-error limit is stated, it may be that, although the excellence in performance requested is necessary at some look angles, possibly it is not needed at the very look angles where it is hardest to obtain.

Requirements are often established by statistical studies. In that instance it may be important to ask whether, on a statistical basis, the beam passes through the most troublesome areas a sufficient fraction of the total time to make it necessary to require the general requested performance in that area. Occasionally, it will be found that the requirements can be relaxed with very little degradation in the radar capability.

With respect to temperature requirements, the most often quoted figure is that of the gas just outside of the exterior radome surface; the temperatures in the radome wall may be much lower than this, expecially in the case of missiles with a short time of flight. The radome problems may be much less difficult than would be inferred from the statement of a single unqualified temperature.

Too often radome requirements are accepted without any inquiry as to how they were established. A part of the work of any radome group should be to study the necessity of the requirements and to emphasize that any relaxations in stringent requirements will almost always be reflected in lower costs and higher production rates.

REFERENCES

1. Kofoid, M. J. A Procedure for Making Precision Half-Wave Solid Wall Radomes. Proceedings of 1955 W.A.D.C. -Ohio State University Radome Symposium, Vol. II, pp. 232-237.
2. Redheffer, R. M. The Measurement of Dielectric Constants. Chapter 10 of Techniques of Microwave Measurements. M.I.T. Radiation Laboratory Series, Vol. 11, pp. 591-606, McGraw-Hill Book Co., Inc., 1947.
3. Redheffer, R. M., and Winkler, E. D. The Measurement of Dielectric Constants in the One Centimeter Band. Report 483-15, M.I.T. Radiation Laboratory, May 1945, pp. 8-21.
4. Kofoid, M. J. Automatic Measurement of Phase Retardation for Radome Analysis. Review of Scientific Instruments, Vol. 27, July 1956, pp. 450-452.
5. Hines, J. N. An Automatic Phase Plotter. Technical Report 301-31, 30 April 1951, Antenna Laboratory, The Ohio State University Research Foundation. Prepared under Contract W33-038 ac 16520.
6. Bacon, J. An Automatic X-Band Phase Plotter. Technical Report 531-7, 1 September 1954, Antenna Laboratory, The Ohio State University Research Foundation. Prepared under Contract AF 33(616)-277.
7. Redheffer, R. M. Electrical Properties of Double Wall and Sandwich Radomes. Report 483-11, M.I.T. Radiation Laboratory, February 1945, p. 2.
8. Redheffer, R. M., and Winkler, E. D. The Measurements of Dielectric Constants in the One Centimeter Band. Report 483-15, M.I.T. Radiation Laboratory, May 1945, pp. 6-7.
9. Redheffer, R. M., and Winkler, E. D. The Measurement of Dielectric Constants in the One Centimeter Band. Report 483-15, M.I.T. Radiation Laboratory, May 1945, pp. 9-10.
10. Bacon, J. Selective Bolometer Amplifier. Technical Report 301-24, 15 September 1950, Antenna Laboratory, The Ohio State University Research Foundation. Prepared under Contract W33-038 ac 16520.
11. Electric Thickness Gage. Dalmo Victor Company Scientific Reports for W.A.D.C., Contract AF 33(616)-3092.

REFERENCES (Cont)

12. Hope H. R. Electrical Thickness Measurement by a Single Horn Method. Proceedings of the OSU-WADC Radome Symposium, Technical Report 56-393, August 1956, Vol. 1, pp. 190-196.

13. Woods, W. W. Thickness Gage for Dielectric Materials. A.I.E.E., Trans., Vol. 73, Part I, 1954, pp. 320-324.

14. Technique of Microwave Measurements. M.I.T. Radiation Laboratory Series, Vol. 11, p. 600, McGraw-Hill Book Co., Inc., 1947.

15. Blair, G. R. High Temperature Dielectric and Loss Tangent Measurements. Proceedings of the OSU-WADC Radome Symposium, Technical Report 56-393, August 1956, Vol. II, pp. 196-204.

Chapter 12

MEASUREMENT OF THE ELECTRICAL CHARACTERISTICS OF DIELECTRIC MATERIALS AND RADOMES

by

E. O. Hartig

Aerophysics Laboratories
Goodyear Aircraft Corporation
Litchfield Park, Arizona

and

W. E. L. Boyce

Convair Division
General Dynamics Corporation
San Diego, California

(Formerly Aerophysics Laboratories
Goodyear Aircraft Corporation
Litchfield Park, Arizona)

INDEX OF SYMBOLS

A	amplitude of the r-f signals
AFC	automatic frequency control
AGC	automatic gain control
B	amplitude of the r-f signals
D	major antenna aperture dimension
d	sample thickness
$e^{j\omega t}$	harmonic time dependance
$e^{j\omega t-\gamma z}$	propagation behavior in z-direction for all components of vectors $\underline{E}$ and $\underline{H}$
k_c	characteristic or eigenvalues of the differential equations
m(t)	a function that describes amplitude modulation of the test signal
r	ratio of the voltage at two points on either side of the minimum to the voltage at the minimum
S	Voltage-standing-wave ratio (in equations)
SWR	voltage-standing-wave ratio (in text)
$s = s_0$	line length
$\tan \delta_e$	electric loss tangent
$\tan \delta_m$	magnetic loss tangent
$\tan \delta_w$	attenuation in the guide
TE	waves transverse electric waves
TEM waves	transverse electromagnetic waves
TM waves	transverse magnetic waves
Z_G	generator impedance
$Z_{max.}$	impedance at a point of maximum voltage
$Z_{min.}$	impedance at a point of minimum voltage
Z_0	characteristic wave impedance
Z_{oc}	input impedance at Z = 0 when the dielectric is terminated in an open circuit
Z_R	load impedance
Z_{sc}	input impedance at z = 0 when the dielectric is terminated in a shorting plate
Z_{02}	characteristic wave impedance of the dielectric-filled section
z-direction	direction of propagation
z_m	voltage minimum position
γ	characteristic propagation constant
γ_2	characteristic propagation constant of the dielectric-filled guide
Δ	known distance from short-circuited end of waveguide
Δ	total boresight error
Δ_1	in-plane component
Δ_c	crosstalk component
Δs	half maximum power width
Δz	distance between two points on either side of a minimum voltage
Δz_1	minimum width on the shorted line measured a distance z_1 from the short circuit
$\Delta\phi$	relative phase shift
ϵ_0	dielectric constant of free space
ϵ_r	relative real permittivity or relative dielectric constant
ϵ^*	complex permittivity
λ_g	guide wavelength
λ_0	free space wavelength
μ^*	complex permeability
μ_0	permeability of free space
μ_r	relative real permeability
ϕ	phase difference between the amplitudes of the r-f signals
∇_t^2	two dimensional Laplacian operator taken in the transverse plane

Chapter 12

MEASUREMENT OF THE ELECTRICAL CHARACTERISTICS OF DIELECTRIC MATERIALS AND RADOMES

SECTION A. REVIEW OF WAVEGUIDE PRINCIPLES

12-1. Complex Permittivity and Permeability

The fundamental quantities that one must consider in the choice of materials for the electrical design of a radome are the complex permittivity (dielectric constant) and the complex permeability. For simple mediums the electromagnetic field equations are linear, and these two quantities completely specify the material. The complex permittivity is usually separated into a real and imaginary part as follows:

$$\epsilon^* = \epsilon - j\epsilon'' = \epsilon_0 \epsilon_r (1 - j \tan \delta_e) \qquad (12\text{-}1)$$

$$\tan \delta_e = \frac{\epsilon''}{\epsilon} = \frac{\sigma}{\omega \epsilon} \text{ and } \epsilon_r = \frac{\epsilon}{\epsilon_0} \qquad (12\text{-}2)$$

Here ϵ_0 is the dielectric constant of free space. The dimensionless quantity $\tan \delta_e$ is called the electric loss tangent and is a measure of the energy loss by heating due to ohmic losses in the material. The quantity ϵ_r is called the relative real permittivity or more simply the relative dielectric constant.

Analogous to the complex permittivity, it is convenient with certain types of materials to define a complex permeability to account for the magnetic losses in the material. Thus,

$$\mu^* = \mu - j\mu'' = \mu_0 \mu_r (1 - j \tan \delta_m) \qquad (12\text{-}3)$$

$$\tan \delta_m = \frac{\mu''}{\mu} \text{ and } \mu_r = \frac{\mu}{\mu_0} \qquad (12\text{-}4)$$

Here μ_0 is the permeability of free space. The quantity $\tan \delta_m$ is called the magnetic loss tangent, and the term μ_r is called the relative real permeability. Since the quantities ϵ_r, μ_r, $\tan \delta_e$, and $\tan \delta_m$ are all dimensionless quantities that completely describe the dielectric material, the radome engineer has, in general, chosen to work with these quantities rather than the complex permittivity and permeability.

In the lower frequency ranges the characteristics of dielectric materials are of interest in the design of capacitors, insulators, etc., and over the years a large number of measuring techniques have been devised to determine these properties.[1,2] These methods generally make use of the fact that the dielectric sample is very small compared to the measuring wavelength. For these cases, the sample may be considered as a lumped constant element. However, for frequencies above several hundred megacycles it is generally not feasible to make use of the lumped constant concept and measurements are most easily made on the basis of the distributed circuit concept of transmission lines. Waveguides and coaxial lines are particularly well suited for the measurement of the characteristics of dielectric materials, since the electromagnetic fields are completely enclosed in the metal conductors and interference effects are automatically eliminated. In general, the properties of interest in these measurements are Z_0, the characteristic wave impedance, and γ, the characteristic propagation constant. Once these two factors are known, they may be converted easily to ϵ^* and μ^*.

12-2. General Analysis of Guided Waves

Before proceeding to a discussion of the measurement of the dielectric parameters, it is well to review some of the fundamental properties of guided waves.[3,4] First, consider Maxwell's electromagnetic equations for simple mediums with harmonic time dependence $e^{j\omega t}$.

$$\nabla \times \underline{E} + j\omega \mu^* \underline{H} = 0 \qquad (12\text{-}5)$$

$$\nabla \times \underline{H} - j\omega \epsilon^* \underline{E} = 0 \qquad (12\text{-}6)$$

$$\nabla \cdot \underline{E} = 0 \qquad (12\text{-}7)$$

$$\nabla \cdot \underline{H} = 0 \qquad (12\text{-}8)$$

Taking the curl of Equations (12-5) and (12-6) and solving the first for $\underline{E}$ and the second for H gives,

$$\nabla^2 \underline{E} + \omega^2 \mu^* \epsilon^* \underline{E} = 0 \qquad (12\text{-}9)$$

$$\nabla^2 \underline{H} + \omega^2 \mu^* \epsilon^* \underline{H} = 0 \qquad (12\text{-}10)$$

In the discussion that follows, the direction of propagation will be taken as the z-direction, and it will be assumed that the propagation behavior in this direction may be taken as $e^{j\omega t - \gamma z}$ for all components of $\underline{E}$ and $\underline{H}$. Any suitable system of coordinates may be used to describe the transverse fields that lie in a plane normal to the direction of propagation.

With this assumption we obtain the differential equations that describe the behavior of the z-components of the electric and magnetic fields in the dielectric region bounded by the metal conducting walls of the guide.

$$\nabla_t^2 E_z + (\omega^2 \mu^* \epsilon^* + \gamma^2) E_z = 0 \qquad (12\text{-}11)$$

$$\nabla_t^2 H_z + (\omega^2 \mu^* \epsilon^* + \gamma^2) H_z = 0 \qquad (12\text{-}12)$$

The ∇_t^2 operator is the two-dimensional Laplacian operator taken in the transverse plane. In rectangular coordinates it is

$$\nabla_t^2 F = \frac{\partial^2 F}{\partial x^2} + \frac{\partial^2 F}{\partial y^2} \qquad (12\text{-}13)$$

and in cylindrical coordinates it becomes

$$\nabla_t^2 F = \frac{\partial^2 F}{\partial r^2} + \frac{1}{r}\frac{\partial F}{\partial r} + \frac{1}{r^2}\frac{\partial^2 F}{\partial \phi^2} \qquad (12\text{-}14)$$

Thus the solution to Equations (12-11) and (12-12) give the z-components of the electric and magnetic fields. The boundary conditions imposed on these differential equations are determined by the cross section and the electrical properties of the conducting guide. If we assume perfectly conducting walls, the tangential component of the electric field must vanish over the surface of the guide. These boundary conditions give rise to a relation that connects the characteristic propagation constant, γ, with the frequency and the dimensions of the waveguide.

If a quantity k_c is introduced, defined by

$$k_c^2 = \gamma^2 + \omega^2 \epsilon^* \mu^* \qquad (12\text{-}15)$$

then the numbers k_c are called the characteristic or eigenvalues of the differential equations. For each eigenvalue k_c of the Equations (12-11) or (12-12) there corresponds a function that describes the z-component of the field. Once the z-components of the field are known the transverse components may be easily derived from the Maxwell curl Equations (12-5) and (12-6).

In the general study of guided waves, it is convenient to divide the solutions into three general types of waves TEM, TE, and TM, each of which can coexist independent of each other.

1. Transverse electromagnetic waves (TEM) contain no electric or magnetic field components in the direction of propagation. They derive their name from the fact that the electric and magnetic field components are all in the transverse plane.

2. Transverse electric waves (TE) contain magnetic, but no electric, fields in the direction of propagation.

3. Transverse magnetic waves (TM) contain electric, but no magnetic, field components in the direction of propagation.

Detailed analyses of waveguides operating in these modes may be found in a number of texts that treat the transmission of waves. For convenient reference the following important results for coaxial, rectangular, and circular guides are summarized in paragraph 12-3. The guide geometries are sketched in Figures 12-1, 12-2, and 12-3.

12-3. Summary on Guided Waves

a. Characteristic wave impedance for TEM and TE waves

$$Z_0 = \frac{j\omega\mu^*}{\gamma} \qquad (12\text{-}16)$$

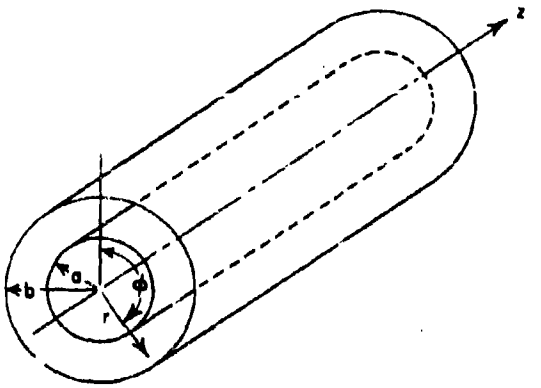


Figure 12-1. Coaxial Waveguide Notation

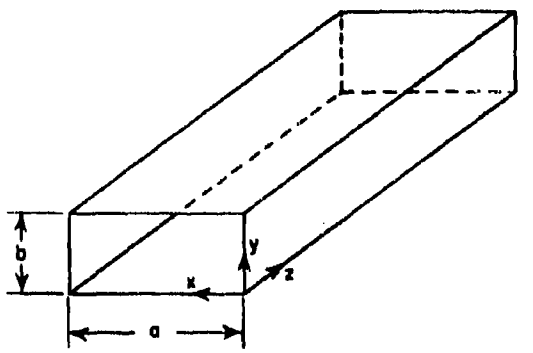


Figure 12-2. Rectangular Waveguide Notation

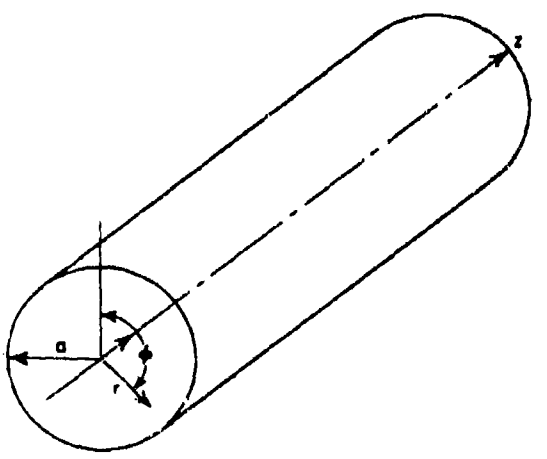


Figure 12-3. Circular Waveguide Notation

Characteristic wave impedance for TM waves

$$Z_0 = \frac{\gamma}{j\omega\epsilon^*} \qquad (12\text{-}17)$$

b. Characteristic propagation constant

$$\gamma = \alpha + j\beta = \sqrt{(k_c)^2 - \omega^2\ \epsilon^*\ \mu^*} \qquad (12\text{-}18)$$

where $k_c = 0$ for TEM coaxial mode

$$k_c^2 = \left(\frac{m\pi}{a}\right)^2 + \left(\frac{n\pi}{b}\right)^2 \quad \begin{matrix}\text{for TE and TM}\\ \text{rectangular}\\ \text{guide modes}\end{matrix} \qquad (12\text{-}19)$$

k_c is given by the equations

$$J_n (k_c\, a) = 0 \quad \text{for TM circular mode} \qquad (12\text{-}20)$$

$$J'_n (k_c\, a) = 0 \quad \text{for TE circular mode} \qquad (12\text{-}21)$$

where J_n is a Bessel function of the first kind of order n and

$$J'_n (x) = \frac{\partial J_n(x)}{\partial x} \qquad (12\text{-}22)$$

c. Cutoff frequency

$$f_c = \frac{k_c}{2\pi\sqrt{\epsilon\mu}} \qquad (12\text{-}23)$$

d. Cutoff wavelength

$$\lambda_c = \frac{2\pi}{k_c} \qquad (12\text{-}24)$$

e. Guide wavelength (lossless case)

$$\lambda_g = \frac{\lambda}{\sqrt{1 - \left(\frac{\lambda}{\lambda_c}\right)^2}} \qquad (12\text{-}25)$$

where $\lambda = 1/\sqrt{\mu\epsilon}\ f$ = wavelength in unbounded dielectric.

SECTION B. IMPEDANCE MEASUREMENTS USING A TRANSMISSION LINE

12-4. Fundamental Relations

Since the majority of the methods for determining the electrical characteristics of dielectrics call for an input impedance measurement, it is well to review some of the fundamentals of transmission line theory.[5,6,7] In terms of the parameters γ and Z_0, the treatment of two-conductor transmission lines and hollow waveguides is identical. Accordingly, in this discussion no distinction will be made between the types of transmission. In addition the terms transverse electric and magnetic fields are used interchangeably with voltage and current.

Consider the line in Figure 12-4 of length s having a characteristic propagation constant γ, a characteristic impedance Z_0, a load impedance Z_R, and a generator impedance Z_G. From simple transmission line theory the input impedance at any point z is given in terms of the terminating impedance Z_R and the properties of the line by

$$Z(z) = Z_0 \frac{Z_R + Z_0 \tanh \gamma z}{Z_0 + Z_R \tanh \gamma z} \qquad (12\text{-}26)$$

The desired impedance Z_R may then be obtained from a measurement of $Z(z)$ by solving this equation. The same operation is commonly performed graphically, in cases where such methods are sufficiently accurate, by using an impedance diagram such as the Smith Chart.[8]

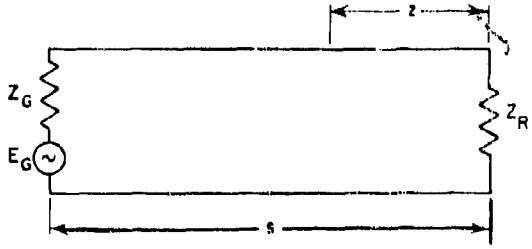


Figure 12-4. Transmission Line Notation

In most air-filled microwave coaxial and waveguide transmission lines it is permissible to neglect the attenuation in the transmission line itself and to assume $\gamma \cong j\beta$. With this assumption it can be shown that the input impedance at a point of minimum voltage (and maximum current) on the line is given simply by

$$Z_{min}(z) = \frac{Z_0}{S} \qquad (12\text{-}27)$$

where S is the voltage standing wave ratio (SWR). Similarly, the input impedance at a maximum voltage point is

$$Z_{max}(z) = SZ_0 \qquad (12\text{-}28)$$

Measurements of the distance z to a minimum or maximum voltage point and of the SWR are thus sufficient to specify the impedance Z_R.

The direct measurement of high SWR's presents several experimental problems. First, the range over which the detector must respond according to an accurate mathematical law may be too great. Secondly, it is difficult to measure the voltage at a maximum without disturbing the field. It is desirable, therefore, to determine the SWR from measurements made near a voltage minimum. A common procedure for dealing with relatively high SWR (≥ 10) is to measure the distance Δz between two points on either side of a minimum (see Figure 12-5) and the ratio, r, of the voltage at these points to the voltage at the minimum.[9] The SWR is then given by

$$S \cong \frac{(r^2 - 1)\lambda_g}{\pi \Delta z} \qquad (12\text{-}29)$$

Or, if the points are chosen so that their fields are 3 db in magnitude above those of the minimum, Equation (12-29) becomes simply

$$S \cong \frac{\lambda_g}{\pi \Delta z} \qquad (12\text{-}30)$$

The ratio r may be selected for convenience so that a compromise between the accuracy of its measurement and accuracy of the Δz measurement is reached. The farther away from the minimum the measurement is made, however, the greater will be the probe disturbance on the guide fields.

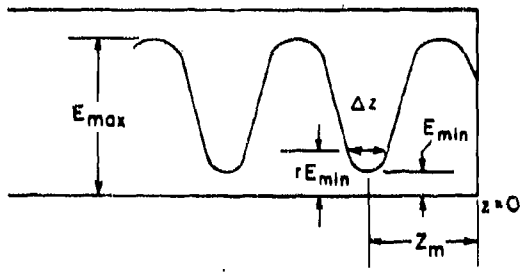


Figure 12-5. Notation for Impedance Measurements

12-5. Impedance Measurement Using Slotted Line

The most common method for measuring impedance at microwave frequencies[10] is by connecting the impedance to a slotted low-loss transmission line or waveguide and measuring the SWR and the distance from the terminating impedance to a voltage minimum position. The impedance at the minimum, Z_{min}, is then given by Equation (12-27), and the desired impedance, Z_R, is obtained by transforming Z_{min} by Equation (12-26) or by its graphical equivalent.

If a low-loss line (with $\gamma \cong j\beta$) is used and the impedance Z_R is such that the SWR is not too high (line attenuation much smaller than load attenuation), Equation (12-26) may be simplified to

$$Z(z) \cong Z_0 \frac{(Z_R + j\, Z_0 \tan \beta z)}{(Z_0 + j\, Z_R \tan \beta z)} \qquad (12\text{-}31)$$

The line attenuation is thus neglected, and therefore it is desirable to make the measurement of Z_{min} at the voltage minimum nearest the load.

If the line loss is low ($\gamma \cong j\beta$) but the load Z_R is such that line attenuation cannot be neglected, Equation (12-31) may still be used by first correcting the value of the measured Z_{min} as follows. The lines losses may be determined by measuring two minimum widths, one with the load Z_R in place and the other with the load replaced by a shorting plate. If the loss in the shorting plate is negligible, all of the attenuation can be attributed to the line and a simple correction applies to the measured value Δz. Thus

$$(\Delta z)_{corrected} = (\Delta z)_{measured} - \frac{z_m}{z_1}(\Delta z_1) \qquad (12\text{-}32)$$

Here Δz_1 is the minimum width on the shorted line measured a distance z_1 from the short circuit, and z_m is the distance from the load Z_R to the voltage minimum where Δz is measured.

If the loss in the short is not negligible it is necessary to measure the width Δz_1 at successive voltage minimums along the line. If these values are then plotted with Δz_1 as ordinates against the distances from the short as abscissas, a straight line is obtained. The intersection of this straight line with the ordinate gives the contribution to Δz_1 due to the loss in the short, while the scope of the line is a measure of the widening of Δz_1 per unit length due to attenuation in the guide wall. Therefore, the product of this measured slope times the distance to the voltage minimum z_m gives the correction term that must be subtracted from the measured value of Δz.

12-6. Resonance Method of Impedance Measurement

An alternate method to using a traveling detector and a slotted line is that of using a fixed detector and a method for varying the line length. Usually the line is fed by a small loosely coupled loop, which is fixed to the face of a movable shorting plunger (Figure 12-6). An important requirement is that the loop present a voltage at the face of the plunger that is independent of the line length. The fixed detector may be placed at any point in the line, since it is merely a pickup to indicate resonance; however, care should be taken to see that it is loosely coupled.

The line will be resonant when the line length $s = s_0$ is equal to the distance from the load to the voltage minimum z_m for the standing-wave-ratio method. Similarly, the half maximum power width, Δs, of the resonance curve is equal to the double minimum power width of the minimum-probing method. It is therefore evident from Equations (12-27) and (12-31) that the terminating impedance is given by

$$Z_R = Z_0 \frac{1 - jS \tan \beta s_0}{S - j \tan \beta s_0} \qquad (12\text{-}33)$$

and the SWR by analogy with Equation (12-30) is given by

$$S \cong \frac{\lambda_g}{\pi \Delta s} \qquad (12\text{-}34)$$

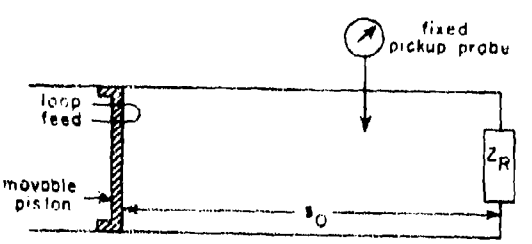


Figure 12-6. Resonance Method

The loss in the guide walls and shorting piston may be determined by measuring the half-power width of the resonance curve with the load replaced by a shorting plate. The corrected value of Δs is then obtained by subtracting this resonance width of the shorted guide from the resonance width of the guide terminated in the load Z_R.

SECTION C. SHORTED-LINE METHOD FOR OBTAINING DIELECTRIC PROPERTIES

The shorted-line method, developed by von Hippel and others,[11-17] remains probably the most useful and satisfactory method of measuring the electrical characteristics of dielectrics. For this reason, the discussion is limited to this method rather than trying to cover all of the methods that have been reported.[18]

In the shorted-line method for measuring dielectric properties, one places the sample at a known distance, Δ, from the short-circuited end of a waveguide (Figure 12-7). The input impedance ($z = 0$) is measured for two different values of Δ. The values of the relative dielectric constant, ϵ_r, the relative permeability, μ_r, the electric loss tangent, tan δ_e, and the magnetic loss tangent, tan δ_m, can then be calculated from the two measured values of input impedance. In theory, any two different values* of Δ can be used to determine completely the properties of the dielectric. In practice, however, the calculations are much simplified if values of $\Delta = 0$ and $\Delta = \lambda_g/4$ are used. These two conditions correspond, respectively, to the two cases where the dielectric is terminated in a short circuit and in an open circuit.

12-7. Simplified Procedure for Unity Permeability

By far the greatest majority of the materials encountered by the radome engineer have a relative complex permeability of unit,** and in these cases a single impedance measurement is sufficient to determine the relative dielectric constant and the electric loss tangent. Again, any value of Δ may be used for the measurement, but the calculations are much simplified if the dielectric is terminated in either a short circuit or an open circuit. These two cases will be treated below.

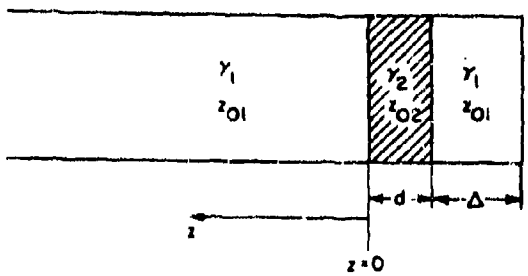


Figure 12-7. Shorted-Line Method

Short-Circuit Method. When the dielectric (medium 2) is terminated in a shorting plate ($\Delta = 0$) the input impedance at $z = 0$ will be denoted by Z_{sc}. From Equation (12-26) with $Z_R = 0$, the well known expression for the input impedance of a shorted line is obtained. Thus

$$Z_{sc} = Z_{02} \tanh \gamma_2 d \qquad (12\text{-}35)$$

where the notation used is given in Figure 12-8.

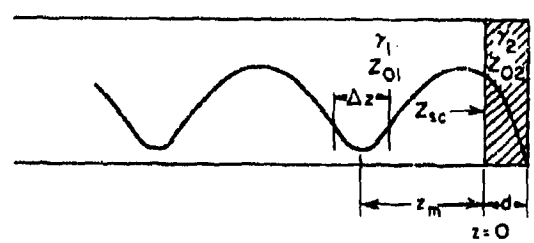


Figure 12-8. Notation for Short-Circuit Method

The normalized input impedance Z_{sc}/Z_{01} is a directly measurable quantity that can be determined experimentally by either the traveling SWR probe or the resonance method described previously.

The Summary on Guided Waves, paragraph 12-3, shows that for TEM and TE modes the characteristic wave impedance can be expressed very

*Except where the two values of Δ are separated by an integral number of half wave lengths in the guide.

**Exceptions to this are artificial dielectrics, metal loaded dielectrics and ferromagnetic materials.

simply in terms of the characteristic propagation factor. Thus for $\mu^* = \mu_0$

$$Z_{02} = \frac{j\omega\mu_0}{\gamma_2} \text{ and } Z_{01} = \frac{j\omega\mu_0}{\gamma_1} \qquad (12\text{-}36)$$

Dividing both sides of Equation (12-35) by Z_{01} and using Equation (12-36),

$$\frac{Z_{sc}}{Z_{01}} = \frac{\gamma_1}{\gamma_2} \tanh \gamma_2 d \qquad (12\text{-}37)$$

If we neglect the attenuation in the air-filled guide, $\gamma_1 \cong j\,(2\pi/\lambda_g)$ and Equation (12-37) may then be written

$$\frac{\tanh \gamma_2 d}{\gamma_2 d} = \frac{-j\lambda_g}{2\pi d} \frac{Z_{sc}}{Z_{01}} \qquad (12\text{-}38)$$

Thus Equation (12-38) is a transcendental equation relating the unknown complex propagation constant $\gamma 2$ with the measurable quantities Z_{sc}/Z_{01}, λ_g and d. Now, if the right-hand side of Equation (12-38) is written in polar form,

$$\frac{-j\lambda_g}{2\pi d} \frac{Z_{sc}}{Z_{01}} = C \angle \xi \qquad (12\text{-}39)$$

Equation (12-38) becomes

$$\frac{\tanh \gamma_2 d}{\gamma_2 d} = C \angle \xi \qquad (12\text{-}40)$$

In spite of its simple form, the solution for this equation cannot be obtained directly. Roberts and von Hippel have obtained a convergent series solution for the case when $\beta_2 z_m$ is an odd multiple of a quarter wavelength and the SWR is large. They have also plotted complete charts of the function [11, 19]

$$\frac{\tanh T \angle \tau}{T \angle \tau} = C \angle \xi \qquad (12\text{-}41)$$

In these charts, contours of constant C and ξ are plotted on a graph having the argument τ as the ordinate and the magnitude T as the abscissa. It is evident that Equation (12-40) is identical to Equation (12-41) if

$$\gamma_2 d = T \angle \tau \qquad (12\text{-}42)$$

Therefore, the procedure is to determine $C \angle \xi$ first from the measured quantities in Equation (12-39); the charts defined by Equation (12-41) are then used to determine $T \angle \tau = \gamma_2 d$. Unfortunately, the value of $\gamma_2 d$ determined by this method will be multivalued. This ambiguity can be removed if the measurements are made on two samples or if the approximate value of the dielectric constant is known.

Once the characteristic propagation constant γ_2 has been determined, the dielectric properties of the material can be obtained rather simply. The equation relating these two quantities is given in paragraph 12-3

$$\gamma_2^2 = k_c^2 - \omega^2 \epsilon^* \mu_0 \text{ where } \mu^* = \mu_0 \qquad (12\text{-}43)$$

From Equations (12-43) and (12-1) and from the k_c vs. λ_c relation in paragraph 12-3,

$$\gamma_2^2 = \left(\frac{2\pi}{\lambda_c}\right)^2 - \omega^2 \mu_0 \epsilon_0 \epsilon_r (1 - j \tan \delta_e) \qquad (12\text{-}44)$$

Introducing into Equation (12-44) the relation

$$\omega^2 \mu_0 \epsilon_0 = \left(\frac{2\pi}{\lambda_0}\right)^2 \qquad (12\text{-}45)$$

and rearranging the expression for the dielectric properties we obtain

$$\epsilon_r (1 - j \tan \delta_e) = \left(\frac{\lambda_0}{\lambda_c}\right)^2 - \left(\frac{\gamma_2 \lambda_0}{2\pi}\right)^2 \qquad (12\text{-}46)$$

Thus the real part of Equation (12-46) relates the dielectric constant ϵ_r, while the imaginary part relates the electric loss tangent $\tan \delta_e$ with the known quantities on the right side of the equation. The values of the cutoff frequencies are given in paragraph 12-3. For the dominant modes they are

$\lambda_c = \infty$ for coaxial TEM mode
$\lambda_c = 2\pi/1.84 \times$ radius for TE_{11} mode in circular guide
$\lambda_c = 2 \times$ width for TE_{10} mode in rectangular guide.

While the above method applies for any sample length, more accurate results will be obtained if the electrical length of the sample in the guide

is equal to an odd multiple of a quarter-wave. The power losses at the face of the dielectric will be at a maximum, and so the standing-wave-ratio will be a minimum for this length. Thus the losses in the dielectric are increased with respect to the losses in the guide wall and the overall accuracy in determining tan δ_e is increased.

Open-Circuit Method. Analogous to the short-circuit method described above, an open-circuit measurement can be used to obtain the dielectric properties of a nonmagnetic material. The open-circuit measurement is obtained by placing the shorting plate a quarter wavelength ($\Delta = \lambda_g/4$) behind the dielectric in the arrangement of Figure 12-9. This reflects an open circuit at the back face of the dielectric and so from Equation (12-26) the input impedance of the open-circuited dielectric is

$$Z_{oc} = Z_{02} \coth \gamma_2 d \qquad (12\text{-}47)$$

By analogy with the short-circuit case, this leads to an equation of the form

$$\frac{\coth T\angle\tau}{T\angle\tau} = C\angle\xi \qquad (12\text{-}48)$$

where $T\angle\tau$ is defined by Equation (12-42) and $C\angle\xi$ by analogy with Equation (12-39) is

$$C\angle\xi = \frac{-j\lambda_g}{2\pi d}\frac{Z_{oc}}{Z_{01}} \qquad (12\text{-}49)$$

Curves are again available[20] for determining $T\angle\tau$. Once this has been established, the characteristic propagation factor γ_2 is determined from Equation (12-42). The relative dielectric constant and electric loss tangent are then determined from Equation (12-46). The optimum electrical length for the samples in this case is any integral multiple of a half-wave. For this length the SWR is a minimum and thus tan δ_e can be most accurately determined.

Combined Open- and Short-Circuit Method. The transcendental equation and the ambiguity in $\gamma_2 d$ are avoided provided both a short-circuit and an open-circuit measurement are taken.[16] To arrive at this result, multiply Equation (12-35) and Equation (12-47) and we obtain

$$Z_{sc}\, Z_{oc} = (Z_{02})^2 \qquad (12\text{-}50)$$

Referring to paragraph 12-3 we see that for TEM and TE modes

$$\left.\begin{aligned} Z_{01} &= \frac{j\omega\mu_0}{\gamma_1} \\ Z_{02} &= \frac{j\omega\mu_0}{\gamma_2} \end{aligned}\right\} \mu^* = \mu_0 \qquad (12\text{-}51)$$

Now, dividing both sides of Equation (12-50) by Z_{01}^2 and substituting Equation (12-51), in the right side of the equation we obtain

$$\frac{Z_{sc}\, Z_{oc}}{(Z_{01})^2} = \left(\frac{\gamma_1}{\gamma_2}\right)^2 \qquad (12\text{-}52)$$

In the air-filled guide $\gamma_1 \cong j(2\pi/\lambda_g)$ and so Equation (12-52) reduces to

$$\gamma_2 = \frac{j2\pi}{\lambda_g\left(\frac{Z_{sc}}{Z_{01}} \cdot \frac{Z_{oc}}{Z_{01}}\right)^{1/2}} \qquad (12\text{-}53)$$

Thus, the above equation gives an expression for γ_2 in terms of the normalized short-circuit and open-circuit impedances and the characteristic wavelength in the air-filled guide. Once γ_2 has been established, the relative dielectric constant and the electric loss tangent can be obtained by equating the real and imaginary parts of Equation (12-46).

The principal disadvantage to this method is that it is difficult to account for wall losses in the sample holder.

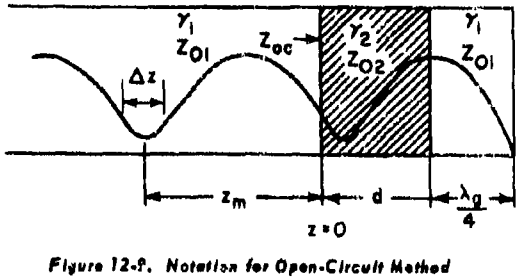


Figure 12-9. Notation for Open-Circuit Method

12-8. Simplification for Medium-Loss Materials Having Unity Permeability

Dakins and Works[14] have shown that for low- and medium-loss materials certain simplifying approximations can be made in Equation (12-38) that make it possible to solve for ϵ_r and tan δ_e directly, thus eliminating the complex transcendental involving $\tanh \gamma_2 d/\gamma_2 d$. This simplified solution is obtained by starting with Equation (12-38) with Equation (12-31) written for Z_{sc}/Z_{01}. Thus,

$$\frac{\tanh \gamma_2 d}{\gamma_2 d} = \frac{-j\lambda_g}{2\pi d}\left(\frac{1 - j\, S \tan \beta_1 z_m}{S - j \tan \beta_1 z_m}\right) \qquad (12\text{-}54)$$

By equating the real parts of Equation (12-54) and assuming that $\gamma_2 d$ and $1/S$ are small, an expression is secured for $\beta_2 d$ involving only the position of the voltage minimum z_m, the sample thickness d and the guide wavelength λ_g. Thus,

$$\frac{\tan \beta_2 d}{\beta_2 d} \quad \frac{\lambda_g \tan \frac{2\pi}{\lambda_g} z_m}{2\pi d} \tag{12-55}$$

The right-hand side of Equation (12-55) is determined from the measured quantities. Once this is known, $\beta_2 d$ is determined from a table[21] of tan x/x. Unfortunately, $\beta_2 d$ is multivalued. If the correct value cannot be selected by previous knowledge of the material, a second measurement is necessary using a different length. Once $\beta_2 d$ has been determined ϵ_r is easily determined by equating the real part of Equation (12-46) and neglecting γ^2. Thus,

$$\epsilon_r = \lambda_0^2 \left\{ \frac{1}{\lambda_c^2} + \left(\frac{\beta_2 d}{2\pi d} \right)^2 \right\} \tag{12-56}$$

Similarly, equating the imaginary parts of Equation (12-54) leads to an equation for tan δ_e.

$$\tan \delta_e = \frac{\Delta z}{d} \left[\frac{\beta_2 d \left(1 + \tan^2 \frac{2\pi}{\lambda_g} z_m \right)}{\beta_2 d \left(1 + \tan^2 \beta_2 d \right) - \tan \beta_2 d} \right] \tag{12-57}$$

$$\left[1 - \left(\frac{\lambda_0}{\lambda_c} \right) \frac{1}{\epsilon_r} \right]$$

The Equations (12-55) to (12-57) are accurate to ±1 percent for values of tan $\delta_e \leq 0.1$ and for $\alpha_2 d \leq 0.25$. This includes the greatest majority of all low- and medium-loss materials such as are used in radome constructions. Generally speaking, if the SWR ≥ 10, these equations are applicable.

If the dielectric is terminated in an open circuit instead of a short circuit, Equations (12-54) to (12-57) remain applicable, provided tanh $\beta_2 d$ is replaced by coth $\beta_2 d$.

12-9. Corrections for Loss in the Waveguide Wall

When making high SWR measurements it is not permissible to neglect the line loss between the probe and the load.

These losses are determined by measuring the twice minimum power points around the voltage node with the empty guide terminated in a short circuit. The correction is then applied according to Equation (12-32). This accounts for the line losses between the probe and the front face of the dielectric. However, in making measurements on very low-loss materials, it may also be necessary to correct for the loss in the wall of the dielectric-filled section. Unfortunately, the loss in the guide wall cannot be separated easily from the dielectric loss. Theoretical values for the damping due to imperfectly conducting walls are given in a number of textbooks. However, since the attenuation in the guide walls is dependent largely upon surface finish, the theoretical value may be in considerable error. Actual measurements of the wall losses are therefore preferred.

It is convenient to express the attenuation in the guide as a loss tangent, tan δ_w. From Equation (12-57) this may be expressed in terms of measured quantities in the empty guide as follows:*

$$\tan \delta_w = \frac{\Delta z_1}{z_1} \left[1 - \left(\frac{\lambda_0}{\lambda_c} \right)^2 \right] \tag{12-58}$$

This value for tan δ_w is not independent of the dielectric filling the guide, but, in general, is a function of the dielectric constant and permeability of the sample. Westphal and von Hippel[22] have derived theoretical ratios of wall loss with the sample present (tan δ_{ws}) to wall loss of the empty guide (tan δ_w). These ratios enable one to correct the value of tan δ_w to take into account the dielectric. However, for nonmagnetic material this ratio becomes unity for the TEM mode, and it does not differ greatly from unity for TE modes. Thus, as a first approximation Equation (12-58) may be used directly as a correction factor for the guide loss in a dielectric-filled sample holder. The procedure, therefore, for low-loss materials, is to determine tan δ_e from Equation (12-57). The correction for wall loss is then made by subtracting tan δ_w given by Equation (12-58) from tan δ_e.

*Negligible losses in the shorting plate are assumed.

12-10. Measurements on Magnetic Materials[23]

For materials having a relative permeability equal to a value other than unity, it is necessary to make two independent measurements on the sample to determine the four quantities ϵ_r, μ_r, $\tan \delta_e$ and $\tan \delta_m$, which describe the dielectric. One of the simplest procedures is to measure the input impedance of a short-circuited and open-circuited section of dielectric-filled guide. The characteristic wave impedance of the dielectric-filled section, Z_{02}, is then the geometrical mean of its short-circuited and open-circuited impedances. In addition, the characteristic propagation constant of the dielectric-filled guide γ_2 is simply related to the ratio of the square root of its short-circuited and open-circuited impedances. Knowing Z_{02} and γ_2, the values of the complex permittivity and permeability can be calculated.

To arrive at these results we start with the familiar expressions for Z_{sc} and Z_{oc}

$$Z_{sc} = Z_{02} \tanh \gamma_2 d \tag{12-59}$$

$$Z_{oc} = Z_{02} \coth \gamma_2 d \tag{12-60}$$

From these

$$\sqrt{\frac{Z_{sc}}{Z_{oc}}} = \tanh \gamma_2 d \tag{12-61}$$

and

$$\sqrt{\left(\frac{Z_{sc}}{Z_{01}}\right)\left(\frac{Z_{oc}}{Z_{01}}\right)} = \frac{Z_{02}}{Z_{01}} \tag{12-62}$$

Equations (12-61) and (12-62) above are the basic equations that will be used in calculating ϵ_r, μ_r, $\tan \delta_e$, and $\tan \delta_m$. Note that the quantities on the left in these two equations are the measured quantities that are determined by the standard impedance-measuring techniques discussed earlier.

To determine the characteristic propagation constant in the dielectric γ_2, it is convenient to change $\tanh \gamma_2 d$ to the exponential form. Thus,

$$\sqrt{\frac{Z_{sc}}{Z_{oc}}} = \tanh \gamma_2 d = \frac{e^{2\gamma_2 d} - 1}{e^{2\gamma_2 d} + 1} \tag{12-63}$$

From this

$$e^{2\gamma_2 d} = \frac{1 + \sqrt{\frac{Z_{sc}}{Z_{oc}}}}{1 - \sqrt{\frac{Z_{sc}}{Z_{oc}}}} \tag{12-64}$$

Now introduce $R \angle \theta$ defined by

$$\frac{1 + \sqrt{\frac{Z_{sc}}{Z_{oc}}}}{1 - \sqrt{\frac{Z_{sc}}{Z_{oc}}}} = R \angle \theta \tag{12-65}$$

into Equation (12-64)

$$e^{2(\alpha_2 d + j\beta_2 d)} = R \angle \theta \tag{12-66}$$

From this it follows immediately that

$$\alpha_2 = \frac{\ln R}{2d} \tag{12-67}$$

and

$$\beta_2 = \frac{\theta + 2m\pi}{2d} \quad m = 1, 2, 3, \ldots \tag{12-68}$$

Unfortunately, β_2 is not uniquely determined by Equation (12-68). The proper value of β_2 can be selected from the possible values if the approximate value of β_2 is known.

Now, returning to our other basic Equation (12-62) and using the fact that $Z_0 = j\omega\mu^*/\gamma$ for all TEM and TE modes

$$\sqrt{\left(\frac{Z_{sc}}{Z_{01}}\right)\left(\frac{Z_{oc}}{Z_{01}}\right)} = \frac{Z_{02}}{Z_{01}} = \frac{\gamma_1 \mu_2^*}{\gamma_2 \mu_1^*} \tag{12-69}$$

In the air-filled guide $\mu_1^* = \mu_0$ and $\delta_1 \cong j(2\pi/\lambda_g)$ Thus, (12-69) becomes

$$\sqrt{\left(\frac{Z_{sc}}{Z_{01}}\right)\left(\frac{Z_{sc}}{Z_{01}}\right)} = j\,\frac{2\pi\mu_r(1 - j\tan\delta_m)}{\lambda_g(\alpha_2 + j\beta_2)} \tag{12-70}$$

Now let

$$P + jQ = \sqrt{\frac{Z_{sc}}{Z_{01}}\,\frac{Z_{oc}}{Z_{01}}} \tag{12-71}$$

and hence from (12-70)

$$P = \frac{2\pi\mu_r}{\lambda_g}\left(\frac{\beta_2 + \alpha_2 \tan\delta_m}{\alpha_2^2 + \beta_2^2}\right) \qquad (12\text{-}72)$$

$$Q = \frac{2\pi\mu_r}{\lambda_g}\left(\frac{\alpha_2 - \beta_2 \tan\delta_m}{\alpha_2^2 + \beta_2^2}\right) \qquad (12\text{-}73)$$

Now, (12-72) and (12-73) can be solved for μ_r and $\tan\delta_m$. Thus,

$$\mu_r = \frac{\lambda_g}{2\pi}(\beta_2 P + \alpha_2 Q) \qquad (12\text{-}74)$$

$$\tan\delta_m = \frac{\alpha_2 P - \beta_2 Q}{\beta_2 P + \alpha_2 Q} \qquad (12\text{-}75)$$

The two properties remaining to be determined now are ϵ_r and $\tan\delta_e$. To obtain these quantities use the expression from paragraph 12-3 for the characteristic propagation constant in medium (2). Thus

$$\gamma_2^2 \equiv (\alpha_2 + j\beta_2)^2 = k_c^2 - \omega^2 \epsilon_2^* \mu_2^* \qquad (12\text{-}76)$$

Using $k_c = (2\pi/\lambda_c)$ and $\omega^2\epsilon_0\mu_0 = (2\pi/a\lambda_0)^2$ and writing ϵ_2^* and μ_2^* in the complex form

$$(\alpha_2 + j\beta_2)^2 = \left(\frac{2\pi}{\lambda_c}\right)^2 - \left(\frac{2\pi}{\lambda_0}\right)^2 \epsilon_r \mu_r (1 - j\tan\delta_e)(1 - j\tan\delta_m) \qquad (12\text{-}77)$$

Separating the real and imaginary parts

$$\alpha_2^2 - \beta_2^2 + 2j\alpha_2\beta_2 = \left(\frac{2\pi}{\lambda_0}\right)^2 \left\{\left(\frac{\lambda_0}{\lambda_c}\right)^2 - \epsilon_r\mu_r\left[(1 - \tan\delta_e \tan\delta_m)\right] - \left[j(\tan\delta_e + \tan\delta_m)\right]\right\} \qquad (12\text{-}78)$$

Equating the real part

$$\alpha_2^2 - \beta_2^2 = \left(\frac{2\pi}{\lambda_0}\right)^2 \left[\left(\frac{\lambda_0}{\lambda_c}\right)^2 - \epsilon_r\mu_r(1 - \tan\delta_e \tan\delta_m)\right] \qquad (12\text{-}79)$$

Equating the imaginary part

$$2\alpha_2\beta_2 = \left(\frac{2\pi}{\lambda_0}\right)^2 \left[\epsilon_r \mu_r (\tan\delta_e + \tan\delta_m)\right] \qquad (12\text{-}80)$$

Equations (12-79) and (12-80) may be solved for ϵ_r and $\tan\delta_e$ to obtain

$$\epsilon_r = \frac{\left(\frac{\lambda_0}{\lambda_c}\right)^2 - \left(\frac{\lambda_0}{2\pi}\right)^2 (\alpha_2^2 - \beta_2^2 + 2\alpha_2\beta_2 \tan\delta_m)}{\mu_r(1 + \tan^2\delta_m)} \qquad (12\text{-}81)$$

and

$$\tan\delta_e = \frac{2\alpha_2\beta_2}{\epsilon_r\mu_r}\left(\frac{\lambda_0}{2\pi}\right) - \tan\delta_m \qquad (12\text{-}82)$$

Summarizing, the procedure for determining ϵ_r, μ_r, $\tan\delta_e$ and $\tan\delta_m$ starts first with a measurement of Z_{sc}/Z_{01} and Z_{oc}/Z_{01}. From these measurements we determine $R\angle\theta$ from Equation (12-65). Once this has been determined we obtain the values of α_2 and β_2 from Equations (12-67) and (12-68). Now, obtain expressions for P and Q defined by Equation (12-71). From the values of P, Q, α_2 and β_2, two of the desired quantities μ_r and $\tan\delta_m$ are obtained from Equations (12-74) and (12-75). Finally, the values of ϵ_r and $\tan\delta_e$ are obtained from Equations (12-81) and (12-82).

12-11. Typical Equipment for Dielectric Measurements

Shorted-Line Method. The equipment required for making dielectric measurements using the shorted-line method is of the same general type that is used for impedance measurements on a transmission line. Figure 12-10 shows a typical slotted-line arrangement for making dielectric-constant measurements in a coaxial or hollow guide. The equipment consists of a slotted waveguide; a traveling tunable pickup probe; a tuned audio amplifier; a square-wave modulated signal generator, a ferrite isolator, and a dielectric sample holder closed by a short-circuiting

plate. Radio frequency energy from the square-wave modulated signal generator is fed through the isolator into the line. By means of the pick-up probe in the slotted line one determines the twice minimum power width and the position of the voltage minimum of the standing-wave pattern set up in the guide. These two measurements can then be used to determine the input impedance at the front face of the dielectric sample. By measuring this impedance first with the dielectric terminated in a short circuit and then in an open circuit, one can determine the complete characteristics of the dielectric material. For nonmagnetic materials, one such impedance measurement is sufficient to determine the properties of the material.

Resonant Cavity Method. A typical arrangement using the resonant cavity method is shown in Figure 12-11. Operation is quite similar to the SWR method except that the pickup probe remains stationary and the shorting piston is varied in position. By determining the half-power width and the plunger position at resonance one can determine the input impedance at the face of the dielectric (paragraph 12-7). From this point the procedure is identical to the traveling probe method.

Figure 12-12 shows a commercial version of a microwave dielectrometer capable of making dielectric measurements at 1000, 3000, and 8500 megacycles. For the two lower frequency ranges a coaxial guide is used for the measure-

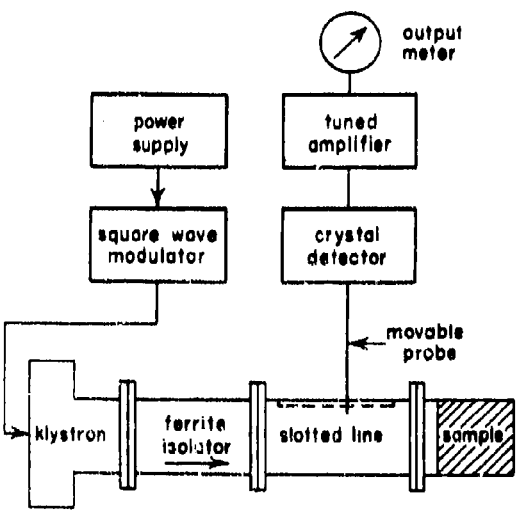


Figure 12-10. Typical Equipment for Dielectric Measurements Using Slotted-Line Method

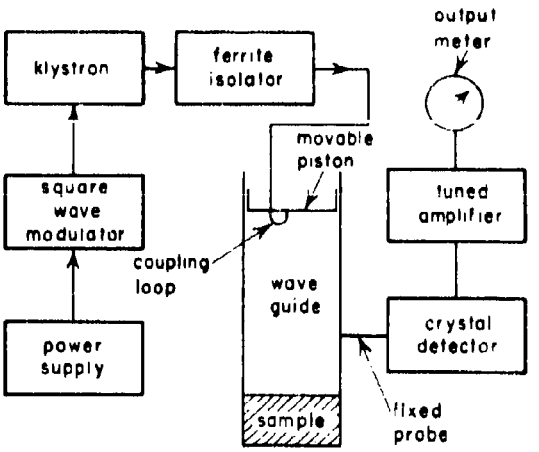


Figure 12-11. Typical Equipment for Dielectric Measurements Using Resonance Method



Figure 12-12. Microwave Dielectrometer (By permission of Central Research Laboratories, Inc.)

ment, whereas at 8500 megacycles the center conductor is removed and the circular pipe is operated in the TE_{11} mode. The equipment is adaptable to either the standing-wave-ratio or the resonance-curve method.

Surface-Wave Dielectrometer. Recently a dielectrometer employing a surface-wave tech-

nique has been developed.[24] The objectives of the program were to design and construct a laboratory instrument for measuring the ϵ_r and tan δ of solid materials at frequencies from 10,000 megacycles up and over a temperature range of -65 to +600° C.

The device utilizes a surface-wave transmission line. The dielectric sample, in the form of a flat sheet, is placed on a flat metal surface so as to form the surface-wave line. This transmission line is terminated in a short circuit. The dielectric constant and loss tangent are determined from measurements of guide wavelength, standing wave ratio, and minimum position and width on the surface-wave line.

A strip of the base plate upon which the sample rests is free to move in a translatory manner along the direction of propagation of the surface wave. The strip contains a section of rectangular waveguide which has a slot cut in its end. The slot presses against the bottom of the sample where the sample rests on the base plate. The slot output is proportional to the field in the surface-wave transmission line.

12-12. Sources of Error

Although the major sources of error in the several methods described can be enumerated, it is difficult to estimate the overall measurement error unless a specific design is considered in detail. In general, accuracies of the order of 1 percent for the dielectric constant and 2 percent for the loss tangent have been obtained with carefully designed equipment. A few of the more important sources of error are:

Impure Signal Source. If the signal source for making the dielectric measurements is not monochromatic, it can introduce errors, particularly in the measurement of the SWR. The reason is, of course, that each of the frequency components has a different voltage minimum position. This has the effect of increasing the width of the twice-minimum power points of the standing-wave pattern and thus limits the measurement accuracy.

To reduce this effect, the oscillator power supply should be well regulated and the oscillator itself should be isolated from all mechanical vibrations. The use of a spectrum analyzer as a signal monitor provides an excellent check on signal behavior during measurement, warning the operator when signal purity deteriorates.

Improper Isolation of the R-F Generator. The shorted-line method of dielectric measurement leads to high mismatches that are variable in phase. For this reason it is necessary to isolate the generator carefully so that, in spite of the high and variable mismatch, the frequency will remain the same when the two measurements are taken with and without the sample. This can be accomplished with an attenuator pad or by means of a ferrite isolator. The latter is to be preferred since it attenuates the reflected wave but not the forward wave. This reduces the power requirements of the generator.

Probe Loading. Another source of error is introduced if the pickup probe is extended too far into the slotted line. Since its primary effect is to decrease the standing wave ratio, it is a relatively simple matter to check for probe loading by measuring the width of the twice-minimum power points for two probe depths. If these two width measurements give the same results, probe loading is negligible; if they do not, the probe should be further withdrawn from the guide.

Sample Fit and Homogeneity. In order to obtain accurate measurements on the dielectric, the sample must be homogeneous and in close contact with walls and with plane parallel ends perpendicular to the longitudinal axis. In addition, the ends of the sample should be slightly chamfered to allow proper seating of the sample against the shorting plate. In practice, faulty geometry or nonhomogeneity accounts for the majority of the error in measuring dielectric constants of low-loss materials.

Higher Order Modes. Even though the air-filled measuring line is designed to propagate only the dominant mode, it may be possible for higher order modes to exist in the dielectric-filled section. When this occurs, the loss-tangent measurements are likely to be in error, since a portion of the energy is converted to higher order modes. Thus the measured loss factor appears higher than its actual value. Excitation of the higher order modes can, however, be largely eliminated by making sure that the ends of the sample are perpendicular to the longitudinal axis of the guide.

Wall Losses. While in principle it is possible to take into account all of the losses in the guide wall, it is nevertheless important to minimize these losses, as it is easily seen that they destroy the inherent accuracy of the measurements. This is immediately apparent by considering the fact that the loss tangent depends essentially on the difference of the widths of the two minima when the sample is present or removed. For low-loss materials this difference will be small. Therefore, the width for the empty guide must

be kept small in order to obtain good accuracy. To obtain a low-loss measuring line, careful attention should be given to the surface condition of the guide and to the design of the shorting plate. In the standing-wave-ratio method care must be taken to assure that the guide does not radiate. This effect is reduced by the use of a narrow slot and by arranging the probe carriage in such a way as to cover the slot completely for all probe positions. The resonant cavity method requires a movable piston with low loss independent of position in the guide. This is generally accomplished with a choke-plunger type of short circuit.

SECTION D. THE MEASUREMENT OF RADOME TRANSMISSION, REFLECTION, AND PATTERN DISTORTION

12-13. Radome Design Objectives

A primary radome design objective is that the radome transmit a high percentage of the energy radiated by the antenna. Reflection and absorption of the radiated energy can cause a transmission loss and result in an appreciable reduction in radar range, especially since the transmission loss is experienced on both transmission and reception. Since radar range is proportional to the fourth root of the transmitted power the reduced radar range is given by Range (percent of that obtainable without radome) =

$$\sqrt{\text{percent one-way transmission efficiency}}$$

As an extreme example, for very streamlined radomes, transmission in certain areas may drop as low as 50 percent. Thus, the radar range on a given target would be reduced to 71 percent of that obtainable without a radome.

A second design objective is that the radome reflect very little energy back into the transmitting antenna. This requirement is especially severe in c-w radar systems where the reflected signal may obscure the radar return from distant targets. In pulse radar systems the reflection requirements are not as stringent; however, reflection of energy back into the transmission line causes a standing wave in the line and changes the input impedance, as seen by the magnetron. This impedance change, if significant, can result in frequency pulling of the magnetron with a resultant deterioration of the system performance. Even with automatic frequency control (AFC), magnetron pulling can be a serious problem, since the AFC may not be able to follow rapidly enough to correct for abrupt changes in radome reflections.

A third design objective is that the radome shall not seriously modify the antenna radiation pattern. For example, if the radome causes a substantial increase in side lobe level it may allow targets to be picked up by the side lobes with resultant confusion as to their direction. In addition, ground and sea clutter is increased by larger side lobes thus obscuring airborne targets. Another type of pattern distortion is beam bending. This can lead to serious system errors, particularly in tracking-, bombing-, and navigational-type radars.

Since the electrical performance of a radome cannot, in general, be accurately predicted on a theoretical basis, it is necessary to make laboratory tests to determine the transmission, reflection, and pattern distortion caused by the radome. The effect of the radome on overall system performance can then be inferred from the results of these measurements.

12-14. The Measurement of Radome Transmission

Radome transmission efficiency, as it is generally defined, is the ratio of power transmitted by an antenna in the presence of a radome to the power that would be transmitted if the radome were removed. By virtue of the reciprocity theorem, this transmission is the same whether the antenna be used as a receiver or transmitter. Therefore, the radome transmission efficiency is identical for transmission or reception. For pencil-beamed antennas, transmission measurements are usually confined to the maximum of the radiated pattern. However, for cosecant-squared or other shaped-beam antennas, it is frequently desirable to make measurements at a number of points in the elevation pattern.

Radome transmission measurements are made by electrically aligning a transmitter and a receiving antenna and noting the difference in power putput when the radome is placed over the receiving antenna. The relative motion between the radome and antenna during scanning is simulated by rotating the radome about the gimbal axis of the fixed antenna. Figure 12-13 shows a typical arrangement of equipment for making automatic transmission measurements. The transmitter, fed by a square-wave modulated klystron, sends an essentially plane wave toward the radome housing the receiving antenna. This wave passes through the radome

and is picked up by the receiving antenna. The output of the antenna is detected by an accurate square-law device, such as a bolometer, and is then fed to an amplifier tuned to the modulation frequency. The amplifier output actuates a linear recorder whose paper drive is linked electrically or mechanically to the rotation of the radome about the antenna gimbal axis. The recorded output is then directly proportional to the power at the receiver. The test procedure is to establish first a reference by taking a measurement with the antenna uncovered. The radome is then put in place and rotated through the desired gimbal angle and the output is recorded. Finally, a measurement is made again with the antenna uncovered to assure that nothing has changed during the measurements.

The laboratory measurements should simulate as closely as possible the actual installation in the aircraft. The radar system antenna should be used where possible, and its location should correspond to that in the aircraft installation. Gimbaling and polarization should be accurately simulated. The transmission should also be examined with the antenna slightly displaced from the gimbal axis to be sure that the transmission does not fluctuate seriously within the placement tolerances of the antenna. The measurements should always be carried out in a reflection-free area. A room lined with microwave absorber is quite convenient for measurements on small aperture antennas, whereas an outdoor site is generally used for larger antennas.

The spacing between the transmitting and receiving antenna is dictated by the size of the antenna and the wavelength. According to theory, the wavefront falling on the receiving antenna aperture must be a plane wave. Since the wavefront is usually approximately spherical, this condition will be satisfied exactly only in the limiting case of infinite spacing. However,[25] the phase errors across the aperture will not exceed $\pi/8$ radians provided a spacing of $d \geq 2D^2/\lambda_0$ is chosen. Here D is the major antenna aperture dimension, and λ_0 is the free space wavelength. For such small phase variations from a plane wave the changes in antenna radiation patterns are very slight. The general effect of quadratic phase errors of this type is to produce an apparent decrease in antenna gain and an increase in the minimum, but very little change of the maximum or of the side lobe structure.[26] The separation $2D^2/\lambda_0$ also assures an essentially uniform intensity distribution over the aperture and negligible interaction between the two antennas.

If the radar system antenna is not available, an antenna of approximately the same dimensions can be used for the transmission measurements. This antenna should be positioned within the radome in such a way as to simulate the ray

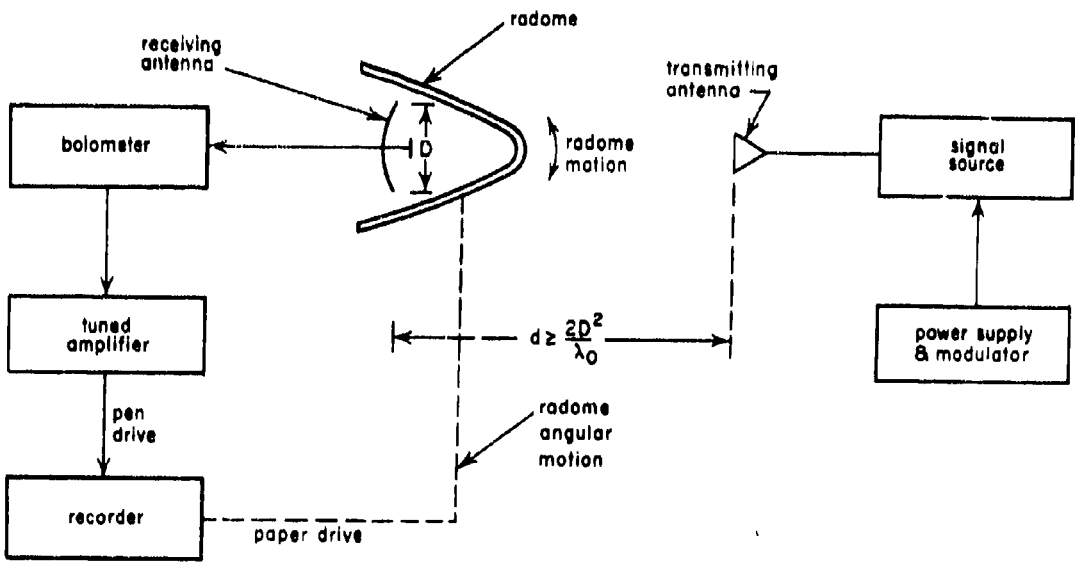


Figure 12-13. Apparatus for Radome Transmission Tests

geometry of the radar antenna for various scan positions. The substitute antenna should be chosen to produce minimum interaction with the radome. While these measurements are useful for a qualitative evaluation of the radome, it should be recognized that accurate quantitative measurements related to system performance can be made only with the radar system antenna.

12-15. The Measurement of Radome Reflection

Radome reflection is defined as the percentage of transmitted energy that is reflected back from the radome into the antenna feed line. The effect of this reflected wave is to set up a standing wave on the transmission line, thus changing the antenna input impedance as seen by the transmitter. To measure radome reflection, the uncovered antenna is first carefully matched to free space with a tuning screw or other matching device. The radome is then placed over the antenna and the reflection coefficient of the antenna feed is determined by using a slotted section of transmission line and measuring the SWR. From this measurement the radome reflection is given by

$$|\rho|^2 = \left|\frac{S-1}{S+1}\right|^2 \qquad (12\text{-}83)$$

where ρ is the amplitude ratio of the reflected voltage wave to the transmitted wave and S is the standing wave ratio. The phase of the reflected wave can also be determined by noting the position of the voltage null in the standing wave pattern. An alternate method for measuring radome reflection is by directly sampling the incident and reflected waves and obtaining their ratio. This method provides information on the magnitude of the reflection but does not readily provide phase information as does the slotted line, unless the complexity of the equipment is increased by including a system to compare the phase of the sampled incident and reflected waves.

In actual practice the antenna is rarely perfectly matched to free space, so that the reflected wave in the antenna feed line is made up of (1) the antenna reflection and (2) the radome reflection. The manner in which the two signals add is, of course, dependent upon the phase relations between them. The worst case occurs when the two reflections are in phase so that their intensities add. The most favorable situation occurs when the two reflected signals are 180° out of phase and the intensities subtract. Therefore, to evaluate system performance, reflection measurements should also be made with the radome in place, but with all auxiliary matching devices removed from the antenna; i.e., with the antenna as it would be under normal operating conditions. Once the antenna feed line reflections have been established, an estimate of magnetron pulling can be made by a study of its Rieke diagram.[27]

Radome reflections are most serious when the incident transmitted wave is nearly normal to the radome, such as in a hemisphere. In this case a large percentage of the energy reflected from the radome wall is focused back into the transmitting antenna. However, for more streamlined shapes, the energy is randomly reflected and only a very small portion is directed back so as to cause a mismatch in the radiating system.

Figure 12-14 shows a block diagram of typical equipment for measuring radome reflection using the slotted-line technique. The radome is placed over the radar system antenna in such a way as to simulate various positions of the antenna during a scanning operation. Precautions should be taken to assure that the reflections from walls and other nearby objects do not affect the SWR or the voltage minimum position. This problem is generally avoided by making the measurements in a microwave absorbing room or by directing the antenna toward an open space. To check the adequacy of the site, the radome antenna should be moved to several positions and the SWR and minimum position noted. If no change occurs, the site may be considered satisfactory. Other possible sources of measurement errors[28] arise from (1) probe loading, (2) improper calibration of the detector, (3) insufficient isolation of the signal generator, and (4) impure signal source. However, proper operating techniques will eliminate or minimize all of these sources of errors.

Figure 12-15 gives the reflectometer method for measuring radome reflections. Here directional couplers are used to sample the magnitude of the incident and the reflected wave. The detected outputs from the couplers feed separate amplifiers and output meters. The system is calibrated by employing a short circuit in place of the antenna to establish unity reflection. The amplifier gains are then adjusted to read equal outputs. The short is next replaced by the antenna, and the radome is placed in position. The two output meter indications are then directly proportional to the incident and reflected waves, and the reflection coefficient is obtained by taking their ratio. The entire operation can be performed with a new commercial instrument[29] called a ratio meter, which automatically combines forward and reverse signals and displays their ratio directly.

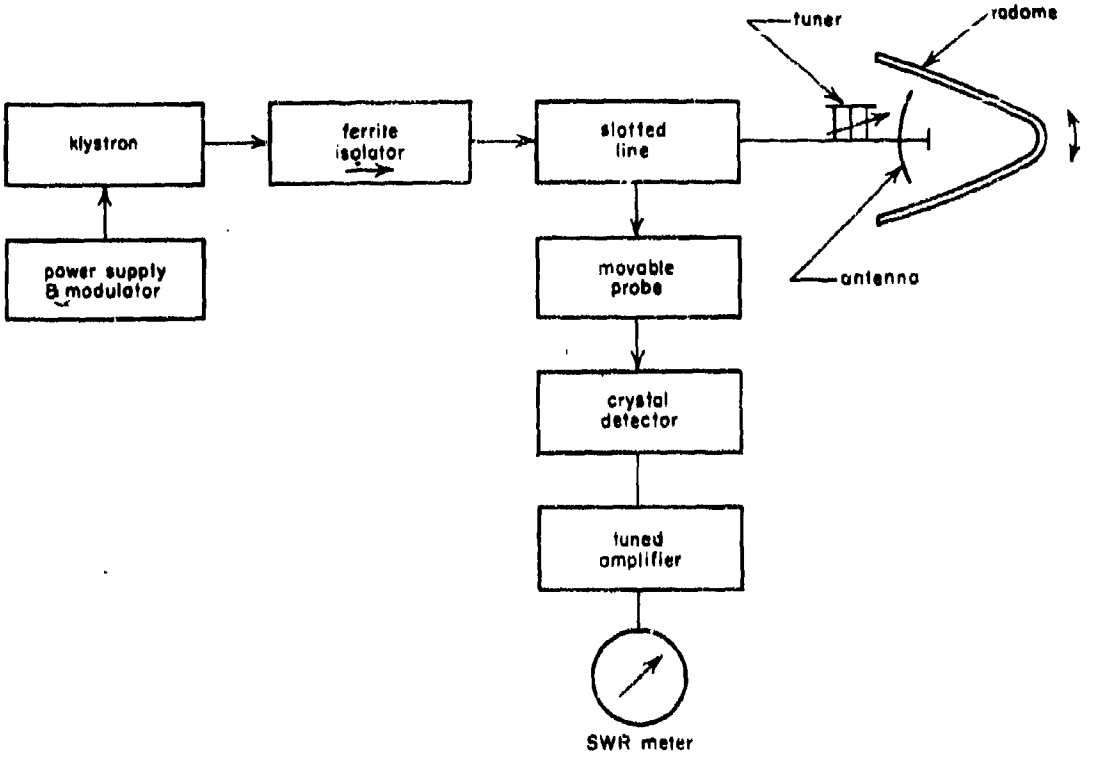


Figure 12-14. Reflection Measurements by the Slotted-Line Method

In principle the reflectometer is superior to the slotted line for measuring small reflections, because it measures the ratio of two quantities of dissimilar magnitude (i.e., reflected voltage/incident voltage). The slotted line, on the other hand, for small reflections measures the ratio of two quantities of similar magnitude (i.e., [incident voltage + reflected voltage] / [incident voltage - reflected voltage]). Possible errors in the reflectometer system, however (e.g., limited directivities of the couplers and inaccuracies in the response laws of the detectors), require a calibration procedure to achieve an overall accuracy comparable to that of precision slotted lines. Typical figures of error in reflection coefficients obtained with a reflectometer using a ratio meter are ±0.02 for $|\rho| = 0.1$ and ±0.04 for $|\rho| = 0.4$. Greater accuracies may be obtained at lower reflection coefficients and/or with single-frequency operation.

12-16. The Measurement of Radome Pattern Distortion

In evaluating radar system performance, antenna patterns provide probably more useful data than any other type of measurement on the radiating system. If taken with the aid of a mockup of the actual aircraft installation, the effects of the surrounding structure as well as the radome can be evaluated. By careful examination of the radiation patterns it is frequently possible to correlate the beam distortion with certain radome areas or structural members. Once the interfering surface has been identified, it can usually be corrected.

A block diagram of the basic equipment for making antenna pattern measurements[30,31] is given in Figure 12-16. The radar system antenna, which is used for receiving, is placed in the radome at the correct gimbal position. The transmitting antenna, located a distance $d \geq 2D^2/\gamma_0$, illuminates the receiving antenna with a wave that is essentially plane. The radiation pattern is obtained by recording the power at the receiving antenna as a function of its angular rotation with respect to a line of sight between the transmitter and receiver. Radome distortion is determined by making separate radiation patterns with and without the radome for a number of representative positions of the radome with respect to the antenna.

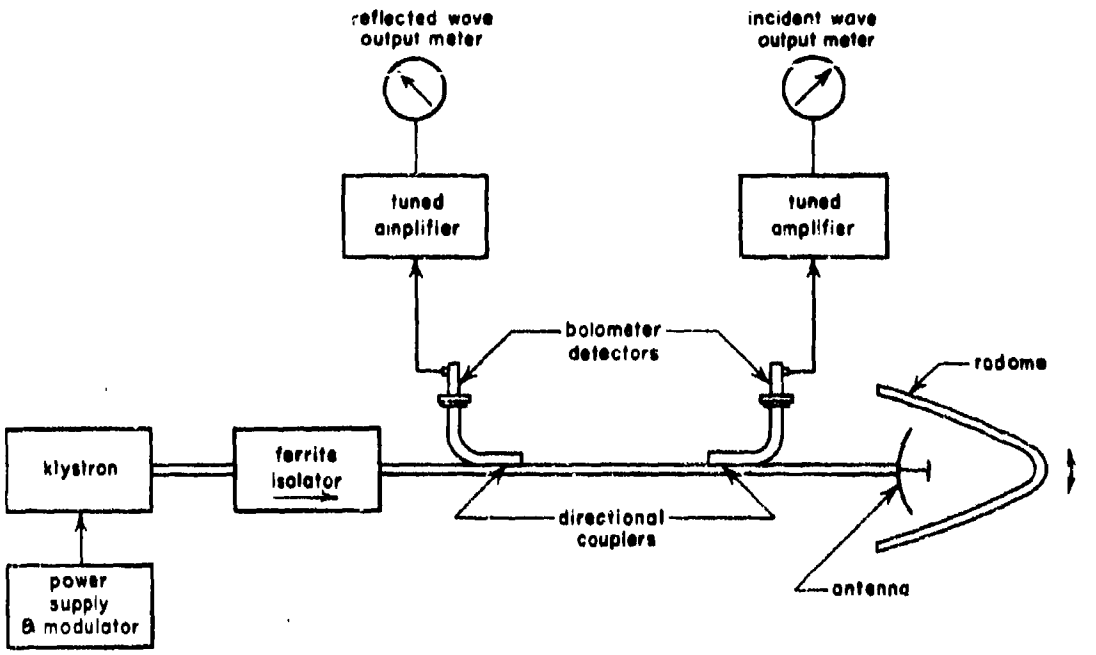


Figure 12-15. Reflectometer Method for Radome Reflection Tests

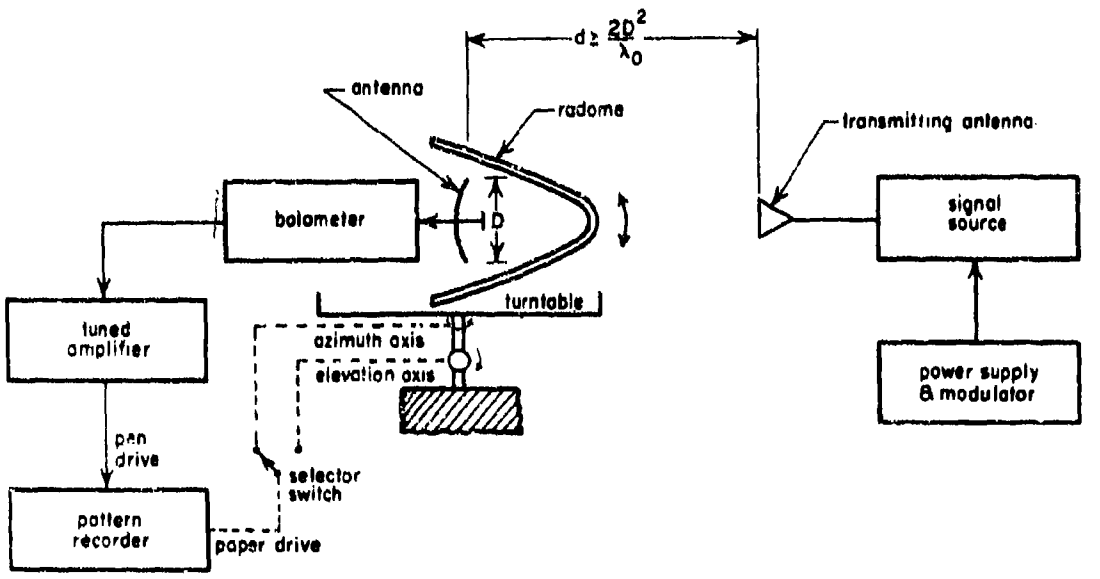


Figure 12-16. Typical Pattern Measurement Equipment

For convenience of measurements, the mount on which the antenna and radome is placed should provide both azimuth and elevation motion. These motions in turn are servolinked to the recorder so that the paper passes beneath the pen in synchronism with the antenna rotation. Figure 12-17 shows a photograph of an antenna mount of this general type, which is currently in use at the Naval Air Development Center, Johnsville, Pa.

The simplest recorder for pattern measurements is merely a recording voltmeter attached to the output of the tuned amplifier. Since the bolometer detector is square law the output of the recorder is directly proportional to the antenna power pattern. While a linear power plot is quite satisfactory for recording the patterns of low gain antennas, it is unsatisfactory for determining the side lobe structure of high gain antennas, since it will, in general, be 20-40 db below the level of the main beam. Therefore, when maximum dynamic range is required, a logarithmic recorder should be used. Among the types of recorders that have been used for logarithmic plotting[32] are (1) a recording voltmeter driven by a logarithmic amplifier; (2) a motor-driven logarithmic potentiometer actuated by a servoamplifier so as to balance out the input from a square-law detector; and (3) a servomotor, which adjusts a beyond-cutoff attenuator so as to maintain a constant r-f output. Of the three, the logarithmic amplifier is the least reliable, since its characteristics are difficult to maintain with tube aging. With any of the above systems the antenna and the paper drives should be synchronized electrically either by selsyns or synchronous motors. The former method is usually preferred because the antenna rotation and paper location are permanently tied together. Good tracking accuracy is maintained by reduction gearing of the selsyns.

The measurement accuracy of antenna radiation patterns, especially in the side lobe structure, is determined primarily by the measuring site. In theory the requirements of the site are quite simple: (1) The distant transmitter must produce an incident wave at the receiving antenna, which is essentially plane (constant phase and amplitude) across its aperture, and (2) the field strength of the transmitted wave must be of sufficient amplitude to allow accurate pattern measurement. In practice the former condition is met only within certain tolerances, since finite spacing and reflections cause deviations from an ideal plane-wave front. Phase and amplitude variations across the aperture due to finite spacing can be largely eliminated by choos-

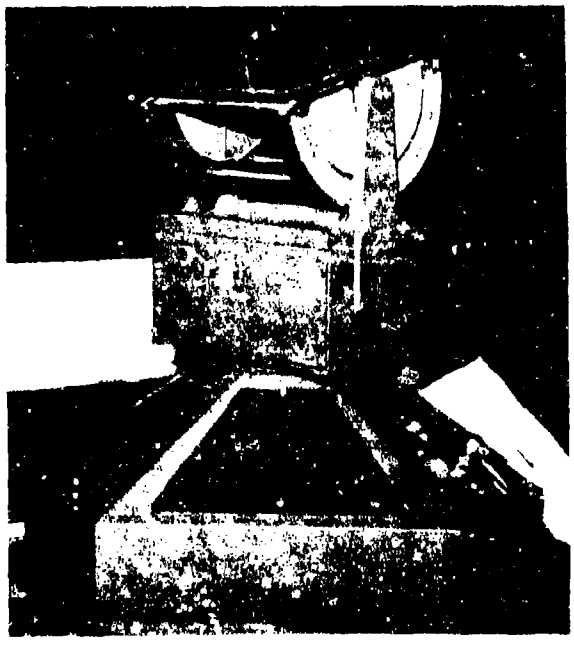


Figure 12-17. Antenna Test Mount (By permission of the U. S. Navy)

ing an antenna separation equal or greater than $2D^2/\lambda_0$. However, spurious reflections, especially from the ground, can interfere with the direct signal to produce significant variations of the incident field of the receiver. Several methods are available for controlling ground reflections. The most obvious is to place the antennas on towers or at the edge of buildings high above the ground. Another method is to absorb or break up the reflection from the ground with a screen of microwave absorber or a wire fence perpendicular to the direction of propagation. As an added precaution, whenever possible, patterns should be taken in azimuth to minimize ground reflections. In addition to ground reflections, care should be taken to eliminate other reflections, especially from large objects such as buildings.

The adequacy of the site must usually be established by experimental testing. The measurements can be in the form of an experimental study on and antenna having a standard pattern, or phase and amplitude measurements can be taken to establish the adequacy of the plane-wave front. Amplitude measurements are made by moving a pickup probe over the region of interest and noting the uniformity of the field. Phase measurements are made by comparing the output from the movable pickup probe with a reference signal obtained from a stationary probe.

The required level of transmitter power depends on the gains of the two antennas, the antenna spacing, the receiver sensitivity, and the wavelength. If the side lobe structure is to be studied, sufficient transmitter power must be provided so that, in general, the maximum of the beam will be 30-40 db out of the noise. The most common types of power sources are (1) reflex klystrons, (2) two-cavity klystrons, and (3) magnetrons. In general, the reflex klystron is most convenient to use; however, its power output is somewhat limited. Therefore, in certain secondary pattern measurements, involving large antennas and long transmission paths, a two-cavity klystron or magnetron is to be preferred.

In considering the sensitivity of microwave measurement setups one should not overlook the fact that it is often possible to improve the signal-to-noise ratio 30 db or more by a suitable choice of detector, whereas an equivalent improvement by a generator-power increase would be impractical. The nonlinear element followed by a narrowband amplifier is one of the least sensitive detector systems. Above it in sensitivity stand well-designed ordinary superheterodyne receivers, and still further improvements are obtained with a superheterodyne system using (1) a rotating-guide phase shifter[33] (-135 dbw) or (2) synchronous detection (-140 dbw). These sensitivities are nominal values obtainable at K band and compare with -130 dbw for ordinary superheterodynes, -100 dbw for 1N26 crystal with 4 cycles per second bandwidth audio amplifier, and -90 dbw for a type 614 bolometer with a similar audio amplifier.

SECTION E. THE MEASUREMENT OF BORESIGHT ERRORS

12-17. Errors Caused by Radomes

As discussed in Chapter 2, the purpose of a tracking radar is to provide angular and angular rate information for gun laying, missile guidance, and other applications where precision directional information is required. In general, these systems derive error signals by comparing the radar return with some type of reference signal. This error signal is then used to actuate a servosystem that repositions the antenna to reduce the error signal to zero. Among the radars now being used for such precision tracking are (1) conical scanning and (2) monopulse systems.

In general, the presence of the radome causes an angular displacement of the antenna pattern, thus producing a boresight error in the angular-position measurement. Similarly, a changing boresight error with changing antenna heading results in erroneous information on change in target heading. This false information, fed to a computer of a gun-laying system, can result in appreciable system error and can lead to possible system instability.

In missile-guidance systems designed for proportional navigation, an error in angular-bearing rate can have serious effects on missile performance. Large values of error rates lead to intolerable miss distances and, if very large, can result in missile instability. This introduces a requirement that the radome produce minimum distortion on the radome pattern.

Since system performance is critically dependent on boresight error and error rate, it is important that precise measurements be made on the radome to determine angular errors prior to its actual use in a system. Boresight measurements are made by electrically aligning

a transmitting conical-scan or monopulse antenna with a receiver and noting the variation in the position of the null when the radome is placed over the antenna and rotated in azimuth to simulate the relative motion between the antenna and radome. Since pointing accuracies of a few hundredths of a degree are generally required, it is very difficult in practice to make these measurements by a direct angular displacement of the antenna. However, the problem is easily overcome by fixing the angular position of the transmitting antenna and using the receiver to search for a null in a plane transverse to the direction of propagation. The boresight error can be determined easily from a knowledge of the antenna separation and a measurement of the linear displacement of the null from its no-radome position. Ideally, of course, the receiving antenna should be moved on the surface of a sphere having its center at the phase center of the transmitting antenna. However, the error encountered in moving the receiving antenna along a plane surface is entirely negligible for the distances and errors normally involved. For the sake of convenience, at times it may be desirable to interchange the receiver and transmitter. This is quite permissible since the measurements obey the laws of reciprocity.

The boresight error is usually measured in terms of two components, one parallel to the antenna offset plane and the other perpendicular to it. This offset plane is defined by the plane of relative motion between the antenna and radome. The total boresight error Δ is, therefore, the vector sum of the in-plane component Δ_i and the crosstalk component Δ_c. Thus,

$$\Delta = \sqrt{\Delta_i^2 + \Delta_c^2} \qquad (12\text{-}84)$$

Generally the boresight error rate is not measured directly but is obtained from plots of in-plane and crosstalk errors versus antenna offset. The rate of change of error is determined from the slope of the curves.

12.18. Boresight Measurement Equipment for Conical Scan Antennas

A conical scanning radar system usually incorporates a mechanically scanning parabolic antenna radiating a pencil beam. The antenna rotates continuously about its mechanical axis and is slightly tilted with respect to this axis, so that the center of the rotating beam describes a cone in space. A target falling within the beam will produce an echo, which is amplitude modulated at the scan rate due to the rotation of the antenna. If the target falls on the spin axis the modulation will disappear. In the radar system this amplitude-modulated signal is compared against sine and cosine reference voltages from the scan motor to derive azimuth and elevation error signals for actuating a servosystem that repositions the antenna to reduce the error signal to zero.

Figure 12-18 shows a typical arrangement of equipment[34] for making radome boresight error measurements on a conical scan antenna. Here the scanning antenna housed in the radome is used as a receiver, and its output is detected with a crystal. The scanning antenna is fixed in position, and a gimbal arrangement is provided to orient the radome about the gimbal axis of the antenna. A transmitting antenna that can be manually positioned in a plane normal to the scan axis is used to determine the null position. For a conical scan system this corresponds to the position in the transverse plane where the fundamental frequency of the scanning modulation disappears. This signal is detected by observing the output of the error amplifier which is tuned to the scanning frequency.

In-plane and crosstalk-plane components of the boresight error are obtained by comparing the location of the null with the radome present to its position without the radome. Boresight measurements for other gimbal positions and polarizations are continued on a point-by-point basis until the entire area of interest in the radome has been explored. Rate of change of the boresight error may be computed from the plotted test data if required.

One of the principal considerations in testing the radome is to simulate correctly the polarization and gimbal positions of the antenna. While it is certainly desirable to have both azimuth and elevation gimbals for positioning the radome about the antenna, a single azimuthal gimbal is generally sufficient provided a means is available for changing the polarization. Thus, by measuring a series of horizontal cuts through the radome for various orientations of polarization, it is possible, at least in theory, to reconstruct any desired gimbal cut through the radome. Generally measurements of greatest interest are horizontal radome cuts with the polarization (1) perpendicular, (2) parallel, and (3) 15° to the plane of offset. By the previous definition, errors in the horizontal plane are then designated as in-plane components, whereas errors in the vertical plane as the crosstalk components.

Special attention should be given to the elimination of spurious reflections that may destroy the basic accuracy of the measurements. Boresight measurements on small radomes are best

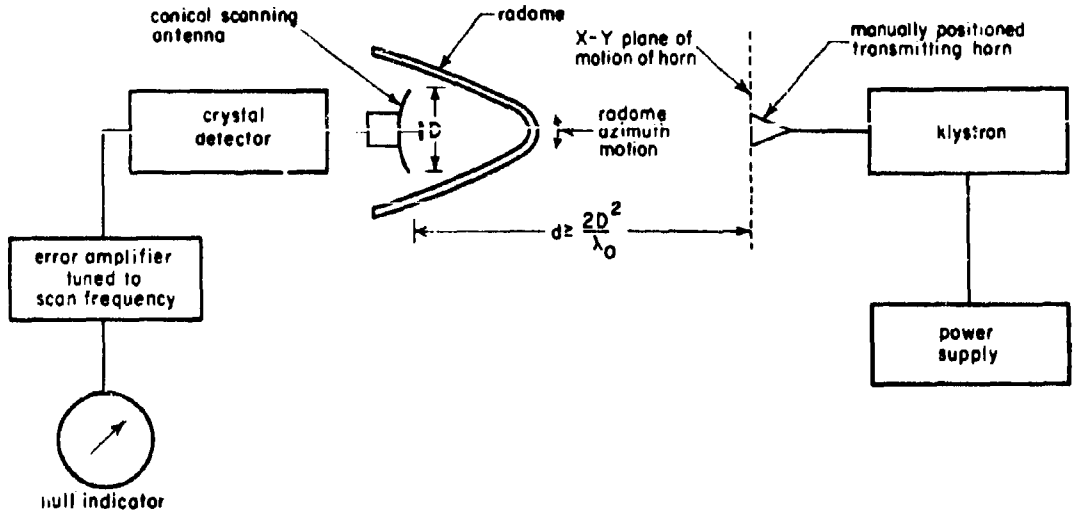


Figure 12-18. Typical Boresight Measurement Equipment for a Conical Scanning Antenna

carried out in a microwave absorbing room to eliminate reflections from nearby objects. However, for large antennas size and cost may make such a room impractical, and in these cases the measurements can best be carried out in an outdoor site. Particular consideration should be given to the design of the radome mount to assure that it simulates the actual antenna-radome installation correctly. A useful precaution against reflections is to cover all surfaces of the mount with a microwave absorbing material. Obviously the beam shift due to motion of the gimbals alone (no radome present) must be made small in comparison to the beam shift introduced by the radome being tested.

12-19. Automatic Boresight Measurement Equipment

Measurement of boresight error on a point-by-point basis is obviously very laborious and time consuming. For this reason automatic equipment for carrying out these measurements is considered essential in research and development programs and for production testing. Apparatus for making automatic measurements is similar to that described above, except that a servosystem is used to position the horn into the null of the conically scanning antenna automatically. This null position is then recorded as the radome moves about the gimbal axis of the antenna.

Figure 12-19 shows a typical arrangement of equipment[35,36] for making automatic boresight measurements. Electromagnetic energy is received by a conically scanning antenna through a radome that is swept in a horizontal plane about the antenna gimbal axis. This impinging energy is transmitted by a horn antenna that is servopositioned in a plane normal to the antenna scan axis. If the horn is not in the null position, a modulation at the fundamental of the scanning frequency will appear in the detected antenna signal. Phase comparison of the error signal with sine and cosine reference voltages from the conically scanning antenna yields horizontal and vertical signals, which actuate the servosystem to reposition the receiving horn into the null. As the radome is moved about the dish, the receiving horn is continually nulled and its horizontal and vertical position is automatically recorded in synchronism with the radome motion. For small angles linear motion of the horn is directly proportional to angular displacement, so the recorder may be calibrated directly in terms of angular in-plane and cross-talk error.

Since it is desirable to be able to change polarization, provisions must be made to rotate the entire antenna assembly about its axis. Usually this can be accomplished rather simply; however, it should be recognized that rotating the antenna also rotates the phase of the reference signal with respect to the horizontal and vertical motion to which the horn is restricted. Therefore, it is necessary to add a variable phase shifter in the reference channel so that the reference signal can always be returned to the horizontal and vertical planes. A convenient way of doing this is to feed the sine and cosine

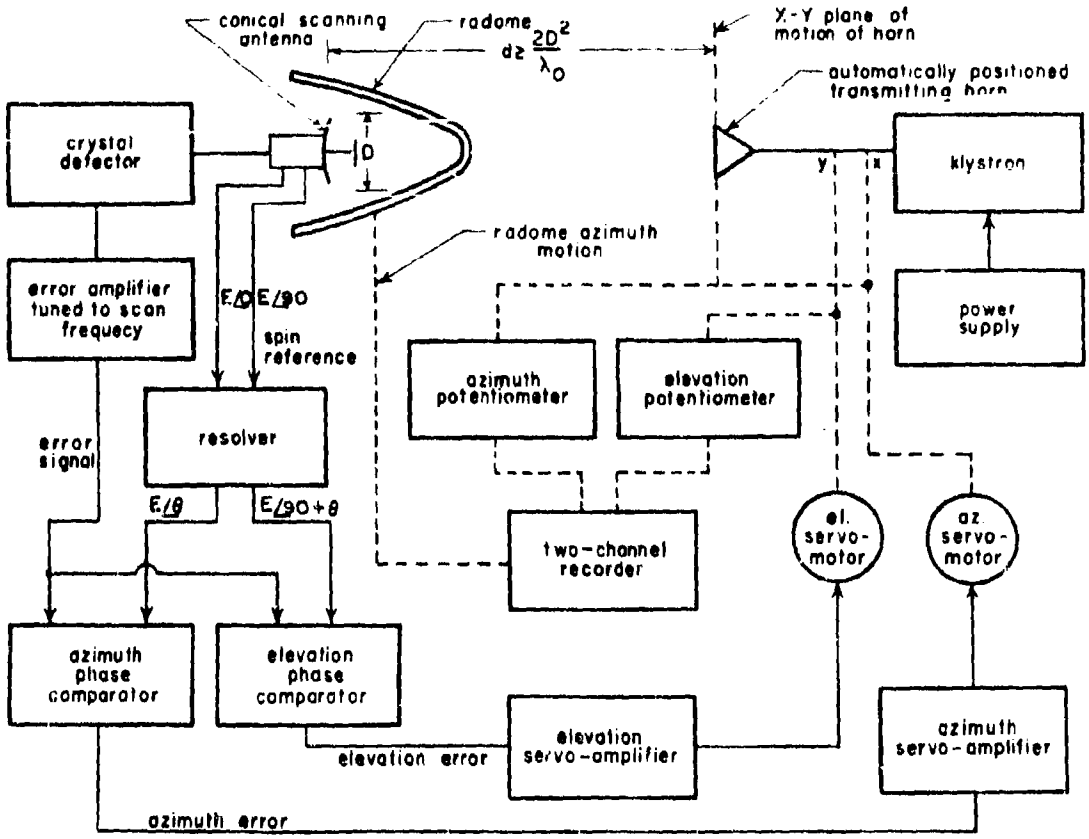


Figure 12-19. Automatic Boresight Measurement Equipment

reference signals to the two stator windings of a resolver. The outputs from the two rotor windings then are quadrature signals displaced in phase from the input signals by an angle equal to the angular displacement of the rotor. This, then, provides a simple method for adjusting the reference phase to correspond to the horizontal and vertical motion of the horn.

The performance of the servosystem obviously depends to a large extent on the signal-to-noise ratio of the error signal. Since all of the useful error information is contained at the scan frequency, it is desirable to employ a band-pass filter at this frequency, thus eliminating all other unwanted frequencies. However, if narrow-band filtering is used, it is essential to maintain a constant scan frequency to avoid phase and amplitude changes at the output of the filter. For this reason, sometimes it is desirable to add an auxiliary servosystem to control the motor speed. Such a device is quite simple, usually consisting of a frequency discriminator with magnetic-amplifier feedback to control the motor-driving voltage.

12-20. Boresight Measurements on Monopulse Systems

Monopulse is a name given to a general class of tracking radar systems that do not use mechanical scanning antennas.[37] Included in this category are (1) phase-comparison systems, (2) amplitude-comparison systems, and (3) phase-amplitude systems.

The phase-comparison system determines the direction of the target by comparing the phase of the radar return picked up by four antennas spaced several wavelengths apart. Figure 12-20 gives a functional block diagram of such a system. The four horns are interconnected with four hybrid junctions which allow separate transmission and reception channels. The sum channel, used for transmission, feeds all four horns in phase, thus producing a pencil-beam

pattern along the axis of the four-horn array. The elevation channel, on reception, combines the signal from the two top horns 180° out of phase with the signal from the two bottom horns. Thus a sharp null exists along the antenna horizontal axis in the elevation reception pattern. Similarly, azimuth error is obtained from an output that combines out-of-phase signals from the right and left horns to produce a null along the antenna vertical axis. The voltage received in the sum channel is used as a reference against which the azimuth and elevation signals are compared in phase to derive an error signal for actuating the antenna servos.

The amplitude-comparison system determines target direction by comparing the amplitude of the radar return picked up by four antennas located essentially at a point and pointed so that their beams diverge. The microwave plumbing is essentially the same as that of the phase-comparison system. Elevation information is obtained by comparing the difference in amplitude between the top and bottom antennas, while azimuth information is obtained from a left-right comparison. Again the sum signal is used as a reference for establishing error signals for servo actuation.

The phase-amplitude system determines target direction by using amplitude information in one plane and phase information in the other. The system uses two antennas with the beams oriented so that they converge in azimuth and diverge in elevation. Azimuth information is obtained by comparing the phase of the two antennas, whereas elevation information is obtained from an amplitude comparison.

The arrangement of equipment for making point-by-point radome-boresight-error measurements with a monopulse antenna is given in Figure 12-21. As in the case of the conical-scan antenna, boresight error is measured by a displacement of the null position in a plane normal to the line of sight between the two antennas. Separate error signal channels are required when using a phase-comparison or an amplitude-comparison monopulse antenna. To obtain the correct null both channels must be nulled simultaneously. For the phase-amplitude system, only one such error channel is required. Note that the error signals obtained by this method are unsatisfactory for servo operation since they provide no directional sense information.

Automatic radome-boresight measurements are made most conveniently on a monopulse

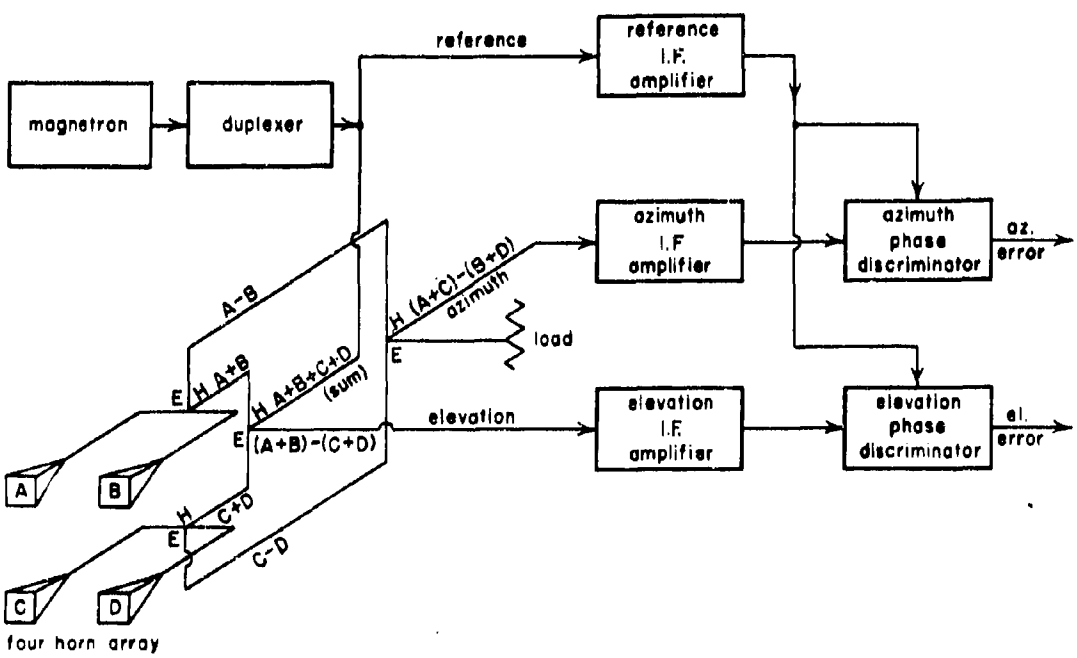


Figure 12-20. Functional Diagram of a Four-Horn Phase-Comparison System

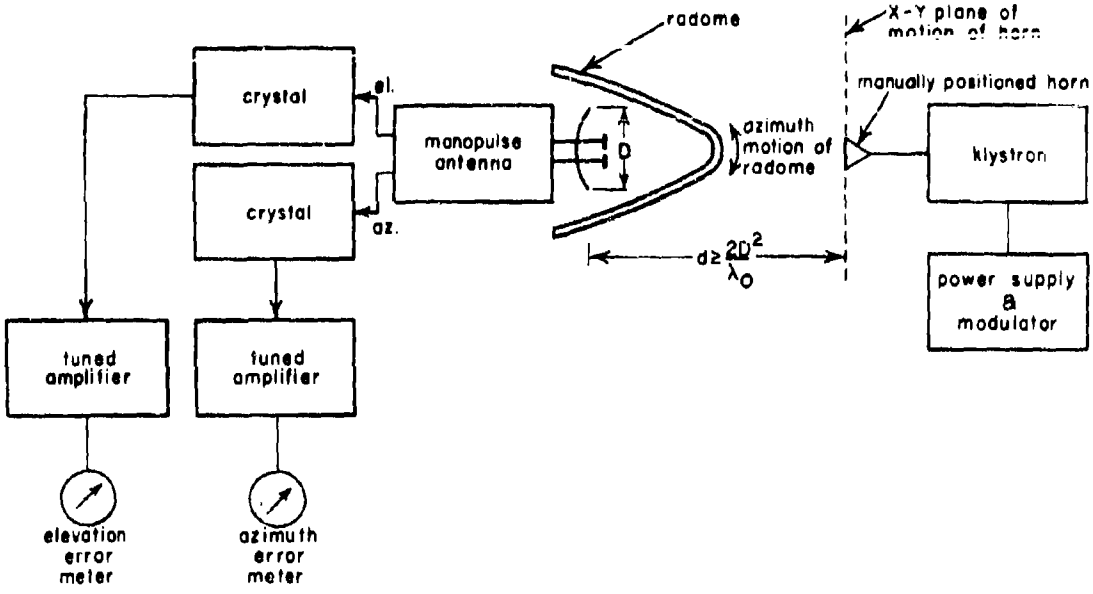


Figure 12-21. Boresight Test Equipment for use with a Monopulse Antenna

system by utilizing the actual radar system operating as a receiver. Azimuth and elevation error signals from the phase discriminators are then directly available for actuating a servo-system, which positions the transmitting horn into the null of the monopulse antenna. In principle, of course, these same error signals can be obtained from microwave phase discriminators, the need for the radar thus being eliminated. However, to accomplish this it is necessary, in general, to make rather extensive modifications to the microwave plumbing. These modifications may therefore cast some doubt on the validity of the final measurements. For this reason the preferred method is to use the actual radar receiving channels.

SECTION F. PHASE AND AMPLITUDE MEASUREMENTS IN THE NEAR FIELD

The measurement of the intensity and phase distribution in the immediate vicinity of a radome that contains a radiating antenna is of interest in studying the causes of boresight error and for checking certain design criteria. By comparing the measurements with those made on the antenna alone, the effects of the radome may be detected and correlated with the far-zone pattern and the boresight error. It is generally most convenient to take these amplitude and phase measurements along a plane perpendicular to the axis of the antenna, although certain investigators[38] have made these measurements along the outer surface of the radome. However, correlation of the radiation pattern with the near-zone field can be most easily accomplished when the measurements are in a plane. In this case, a first order approximation to the boresight error is given simply by the linear term of phase variation caused by the radome.

12-21. Equipment for Near-Zone Measurements

A block diagram of equipment suitable for making near-zone phase and amplitude measurements[39,40] is given in Figure 12-22. The klystron output, after suitable isolation, is fed to the antenna radome under test. In addition, a power-divider provides a reference signal, which branches off to a calibrated phase shifter and thence to the H-plane arm of a magic T. The near-field energy radiated from the antenna is received by a small pickup probe and fed to the E-plane arm of the magic T. These signals are then detected with a matched crystal or bolometer in the third arm of the magic T. The output of the detector is then indicated on a voltmeter connected to an amplifier tuned to the modulating frequency of the klystron. The measurement procedure is to place the pickup probe at the desired near-field position, and the calibrated phase shifter is adjusted until

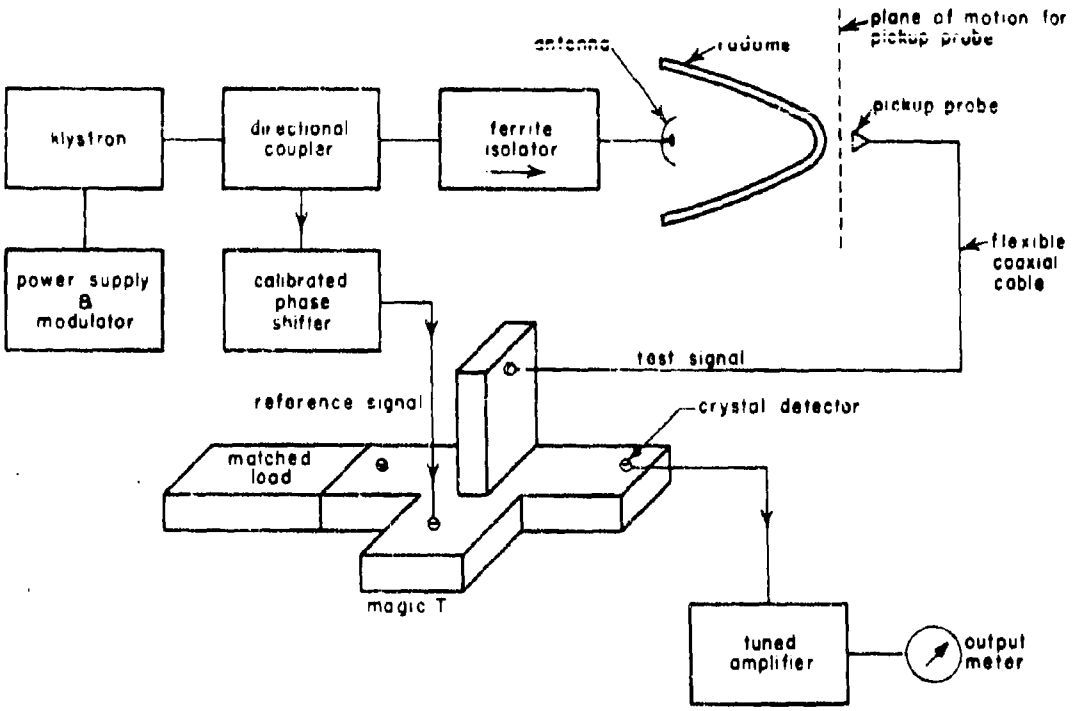


Figure 12-22. Equipment for Near-Field Phase and Amplitude Measurements

the voltmeter indicates a minimum value. At this point the two signals are 180° out of phase. Since only relative phase across the aperture is of interest, this first measurement may be taken as a reference, and the relative phase for the subsequent positions of the probe is given by the difference in phase shifter positions referred to the first reading.

To obtain a well-defined null at the detector, it is important that the measured signal and reference be approximately equal in amplitude. However, since the power from the probe varies with aperture position, it is not always possible to keep the levels the same. Although, in principle, the power level of the probe or reference may be changed during the phase measurements by means of a variable attenuator, it is generally unadvisable to do so because of the probability of a phase change in the attenuator. The recommended procedure is to set the power level of the reference signal to the average power level obtained from the pickup probe as it moves across the aperture. Such a procedure will, of course, result in a broad null at points where the probe signal differs from this average. This difficulty may be overcome by using a balanced detector system, as discussed in Chapter 11, or as discussed below in a slightly different form for automatic near-field measurements.

Reflections from nearby objects, can, of course, cause errors in measurements, and, for this reason, it is desirable to make all measurements in a room covered with microwave absorber. To obtain the near-zone amplitude distribution the reference signal to the magic T is removed and the output of the tuned amplifier is then directly proportional to the square of the field intensity.

There are several requirements that the pickup probe must satisfy to obtain accurate near-field phase and amplitude measurements:

1. The probe must be small enough to measure the field essentially at a point. If this condition is not met, the probe will have an integrating effect and all rapid field variations will be averaged out in the measurements.

2. The probe, its supporting structure, and any associated cables or waveguide must not disturb the field to a degree that the accuracy of the measurements will be destroyed.

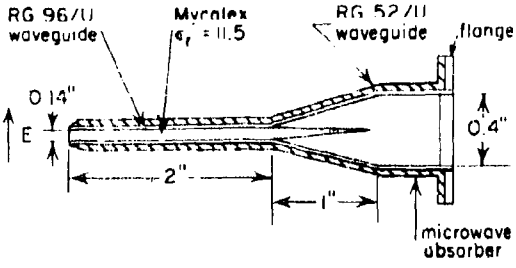


Figure 12-23. X-Band Pickup Probe

3. The polarization must be correct.

4. The probe must have sufficient gain to provide a signal large enough for accurate measurements.

Richmond and Tice[41] have investigated the design of near-field pickup probes and have come up with the rather simple dielectric-loaded probe shown in Figure 12-23. This probe has been rather extensively tested and proved satisfactory for measurements in the X-band region.

Many of the instrumentation problems of these near-field measurements are identical to those encountered in the electrical thickness gages discussed in Chapter 11. The interferometer type thickness gage is essentially the same device as the probing system of Figure 12-22.

12-22. Discussion of Calibrated Phase Shifters

In the measurement procedure described above, the calibrated phase shifter is used as a standard against which the unknown phase is compared. Naturally, the accuracy of the measurements is directly related to the calibration of the phase shift. It is, therefore, extremely important that this calibration be accurately known. For this reason it is desirable to choose a phase shifter in which the phase change is linearly related to displacement or rotation. Several such devices are discussed below:

Slotted-Line Phase Shifter. One of the simplest and best known phase shifters is obtained by feeding the r-f reference into a tunable sliding probe of a slotted-waveguide section terminated at one end in a matched load (Figure 12-24). The phase shifted signal is then obtained from the other end of the guide, the phase shift being directly proportional to the position of the probe along the line. The shift of position of this slotted section probe through one guide wave length corresponds to a phase shift of 360°. Thus,

$$\Delta\varphi = 360^{\circ}\frac{d}{\lambda_g} \qquad (12\text{-}85)$$

where $\Delta\varphi$ is the relative phase shift, λ_g is the wave-length in the guide, and d is the displacement of the slotted-line probe with respect to an arbitrary reference.

To assure good linearity, the probe must be loosely coupled to the slotted line and the load terminating the line must be a good match. For ±1° phase linearity in the slotted section, the voltage-standing-wave ratio of the termination should not exceed 1.03.

Phase Shifter Employing a Movable Piston. A very simple and accurate phase shifter can be constructed from a directional coupler and a movable shorting piston in an arrangement like that shown in Figure 12-25. The reference signal is fed into the branch arm 3 of the directional coupler. The majority of this energy is absorbed in the matched load terminating the branch arm; however, a fraction of the energy (determined by the coupling factor) couples into the main guide in a backward direction. A shorting piston in arm 1 intercepts this backward-traveling wave and reflects it forward* into arm 2. It is evident that the relative phase at the output of arm 2 is directly proportional to the position of the movable shorting piston. Since the energy travels from the coupling slot to the piston and back to arm 2 it is evident that

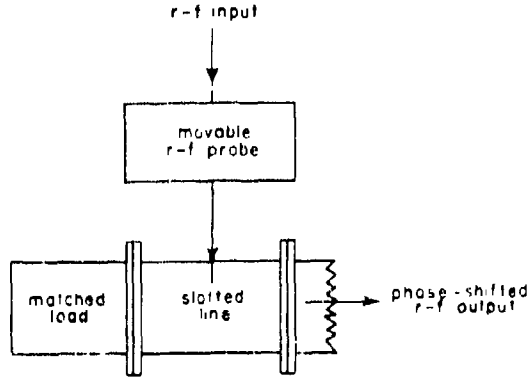


Figure 12-24. Slotted-Line Phase Shifter

* It is apparent that a small fraction of this energy is reflected back to arm 3. However, this signal is down by the square of the coupling factor and is therefore negligible for coupling coefficients of approximately -20 db.

moving the piston through half a guide wavelength shifts the phase by 360°. Thus,

$$\Delta\phi = 360^{\circ}\,\frac{2d}{\lambda_g} \qquad (12\text{-}86)$$

where $\Delta\phi$ is the relative phase and d is the displacement of the shorting piston with respect to an arbitrary reference.

The accuracy of this type of phase shifter is directly related to the directivity of the coupler. For ±1° phase linearity the directivity should be 30 db or greater. In addition, coupling coefficients of -20 db or smaller should be chosen in order to reduce the reflections into arm 3. However, larger coupling coefficients may be used provided a ferrite isolator is used in the reference arm. These requirements on the directional coupler are not unusually severe and are met by several commercially available units.

Rotary Phase Shifter. A 180° differential phase shifter (half-wave plate) has the useful property that if it is placed in an incident field of fixed linear polarization and rotated through an angle θ it will cause a rotation of the emergent polarization equal to twice θ. When this fact is applied to both components of a circularly polarized wave, it becomes apparent that the emergent wave will be circularly polarized in the opposite sense with the instantaneous orientation of the polarization rotated through twice the rotational angle of the half-wave plate. Since with circular polarization a change in instantaneous polarization corresponds to a phase shift, rotation of the half-wave plate provides a convenient technique for shifting the phase.

A phase changer, based on the above principle, [42] and having a phase shift equal to twice the angular rotation can be constructed from two quarter-wave plates and one half-wave plate assembled in tandem in the arrangement shown in Figure 12-26. The input section consists of a rectangular-to-circular waveguide (TE_{11} mode) transition.

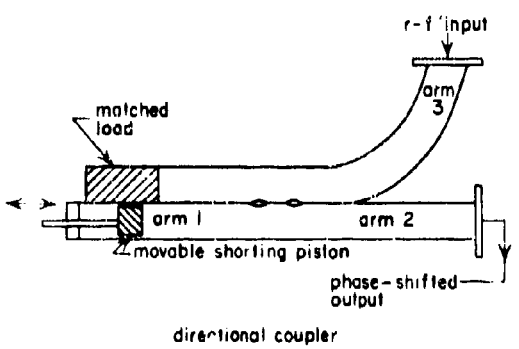


Figure 12-25. Movable Piston Phase Shifter

The first quarter-wave plate converts the incident linearly polarized wave into a circularly polarized wave. Next, the wave passes through a half-wave plate mounted in a bearing so it is free to rotate about its axis. A rotation of the 180° differential section through an angle θ rotates the instantaneous orientation of the polarization through twice θ thereby shifting the phase of the emergent circularly polarized wave by twice θ. The second quarter-wave plate reconverts the circular polarization back to a linearly polarized wave.

An X-band phase shifter based on this principle is now commercially available through the Hewlitt-Packard Company [43] and is convenient for phase measurements. Accuracies of ±2° are quoted by the manufacturer.

12-23. Automatic Near-Field Measurement Equipment

In practice, point-by-point near-field radome investigations become quite laborious, since it is necessary to make numerous phase and amplitude measurements over the radome-antenna aperture. For this reason it is quite desirable to be able to make these measurements automatically. Apparatus for accomplishing this task [44,45,46] is basically the same as that discussed above, except for the fact that a servo-system is used to drive the phase shifter into the null position. The probe is programmed to explore the field, and, as it does so, the phase-shifter position and the field intensity are recorded.

The magic T, phase-comparison circuit of the type described above is unsatisfactory for servo control since it provides no directional sense information. That is, phase errors on either side of the null provide an error signal of the same polarity. For servo application a dynamic phase comparator, or phase discriminator, is required. With a phase discriminator the error signal changes polarity as the phase goes through the null position. This then provides the desired control voltage for servo operation. Figure 12-27 shows a coherent phase discriminator that uses a matched pair of crystals in the two colinear arms of a magic T. The test signal that is fed to the E-plane arm is assumed to be square-wave modulated. The reference signal is unmodulated and is fed to the H-plane arm. It is evident that the H-plane arm will feed the two

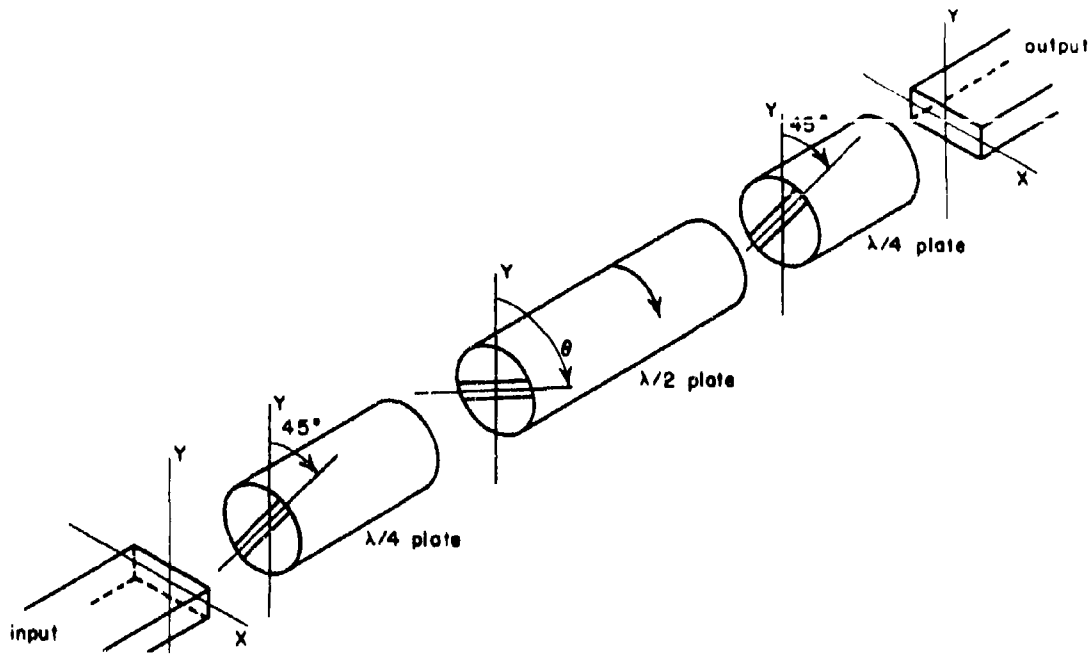


Figure 12-26. Rotary Phase Shifter

crystals in phase, while the E-plane arm will feed them 180° out of phase. Therefore the difference in amplitude between the two square-law detectors is

$$\frac{1}{2}\left|Am(t) + Be^{j\phi}\right|^2 - \frac{1}{2}\left|Am(t) - Be^{j\phi}\right|^2 = ABm(t)\cos\phi \qquad (12\text{-}87)$$

where A and B are the amplitudes of the r-f signals, ϕ is the phase difference between them, and $m(t)$ is a function that describes amplitude modulation of the test signal. Thus, when ϕ equals 90°, no potential difference exists between the two detectors and the transformer current is zero. However, if the two signals are not in phase quadrature a current will flow through the transformer and its instantaneous direction of flow will be determined by whether ϕ is smaller or larger than 90°. The current reversal as ϕ passes through 90° corresponds to a 180° phase shift in the output signal from the transformer. This phase shift is detected by synchronously rectifying the transformer output against the modulation signal as a reference. The final filtered output of the synchronous rectifier is therefore a d-c voltage, which instantaneously changes polarity as the phase goes through the null position. Note that in this system there is no need for the amplitudes of the test signal and reference to be approximately equal as long as the crystals have identical dynamic characteristics. In addition the coherent phase discriminator has unusual sensitivity,[47] with sensitivities of -125 dbw being easily obtainable at X band.

Figure 12-28 shows a typical arrangement of equipment for making automatic amplitude and phase measurements in the near field of the antenna-radome combination. Radio frequency energy from an unmodulated klystron oscillator is fed to the antenna radome under test. The near-field energy radiated from the antenna is received by a small pickup horn which explores the aperture field. The received signal is then amplitude modulated with the ferrite modulator (Gyraline) at an audio rate. A portion of this signal is fed to a coherent phase discriminator of the type described above. The unmodulated reference to the phase discriminator is obtained from the klystron after passing through the calibrated phase shift. The error signal from the phase discriminator serves to actuate a servomotor that is geared to the calibrated phase shifter. This, in turn, positions the phase shifter to as to maintain a constant phase difference of 90° between the test signal and the reference. A recording system continually plots the posi-

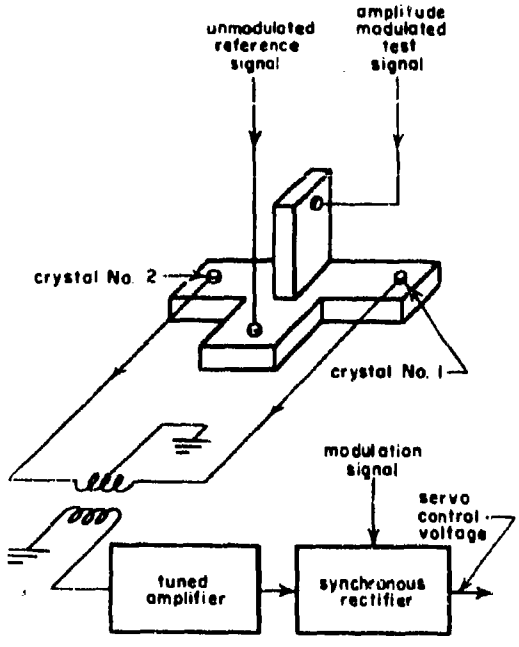


Figure 12-27. Coherent Phase Discriminator

tion of the calibrated phase shifter as the field is explored with the receiving probe.

Near-field amplitude measurements are made by feeding a portion of the modulated r-f signal from the pickup probe to a square-law detector and thence to a tuned amplifier and recorder. Thus, measurements of the phase and amplitude are made automatically and simultaneously as the pickup probe explores the aperture field.

To prevent the possibility of any signal coupled back from the phase discriminator from becoming modulated, a ferrite isolator is placed between the modulator and the phase discriminator. Thus the test signal passes through the isolator essentially unattenuated, but any signal entering the isolator from the reverse direction is highly attenuated. This isolator virtually eliminates interaction effects in the system.

Since the output of the phase discriminator is directly proportional to the field intensity, it is evident that the servoloop gain will vary considerably as the probe moves across the aperture field of the antenna. To overcome this difficulty, an automatic gain control (AGC) capable of varying the error signal amplifier gain inversely with the field intensity is used. Thus, within the operating range of the AGC, the error signal amplifier output is independent of field intensity variations. In practice an AGC circuit that operates over a 30 to 40 db range is satisfactory for most near-zone measurements, since intensity variations of interest across the aperture do not, in general, exceed this value.

Care must be taken to insure that the AGC detector is sensitive enough to operate effectively at the signal levels available from the probe. In the system of Figure 12-28, for example, since the balanced r-f phase detector is more sensitive than the crystal AGC detector, the overall system sensitivity is limited below the optimum value by the AGC detector.

The accuracy of servotracking depends in part on the noise level in the null. To reduce this noise level, special attention should be given to the design of the klystron power supply to achieve minimum voltage ripple. In addition, some investigators[47,48,49] have taken the added precaution of submerging the klystron in a tank of oil to reduce the noise and drift further.

The flexing of the coaxial cable as the pickup probe moves across the aperture may cause an apparent phase shift in the field. For this reason, precautions should be taken to assure minimum cable bending. Measurements[47] taken on a 4-foot section of RG-9U cable suspended vertically with the lower end moved ±9 inches of vertical indicate an attendant phase error of ±1°. This is, therefore, within tolerable limits of most measurements.

12-24. Near-Field Measurements Using the Scattering Method

Linear Conducting Scatterer. An alternate method[50,51] for near-field radome measurements makes use of the scattering from a thin linear conductor supported on a nylon thread. The wave scattered by the conductor, as it is moved across the aperture, is separated from the transmitted wave by a carefully tuned hybrid junction. The signal appearing at the receiver arm of the hybrid is proportional to the square of the tangential electric field component at the scatterer. Therefore, the amplitude and phase at any point in the field can be determined by the phase and amplitude of the signal at the receiver arm. The principle advantage of the scattering technique is that it produces minimum distortion of the field, since there are no cables or waveguides to connect to the scatterer. For example, accurate measurements have been made inside a waveguide and in the region between the antenna and the radome.

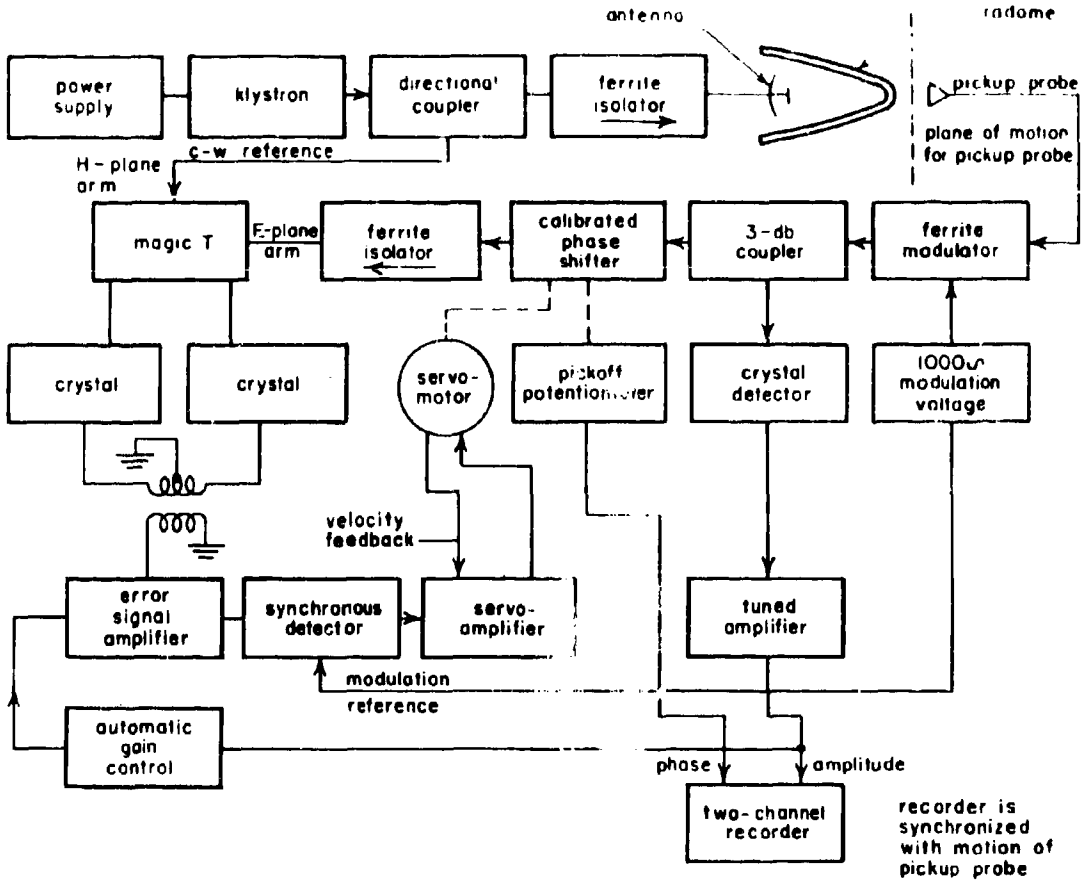


Figure 12-28. Automatic Equipment for Near-Field Measurements

Figure 12-29 gives an abbreviated block diagram of the measuring system. The klystron is connected to the H-plane arm of the magic T and the E-plane arm is the receiver channel. The two remaining arms are terminated in the antenna and a resistive load. If the input impedance of the antenna is perfectly matched to the load, no power is coupled from the klystron to the receiver. In practice the antenna must be tuned until the T isolation is approximately 100 db. Energy scattered from the thin conductor produces a reflected wave at the antenna terminal, which is separated by the hybrid junction and produces the desired signal in the receiving arm.

The principle disadvantage of this method stems from the fact that the scatterer must be short to indicate the field at a point and it must be thin to discriminate against orthogonal polarization. Hence, the scattered signal is small, and so the isolation between transmitter and receiver must be very large (about 100 db). To achieve such large isolation, the antenna and load must be tuned to a very high degree of balance. Since the tuning is frequency sensitive, a monochromatic drift-free signal source is required. In addition the antenna must be retuned for each position of the radome.

Modulated Scatterer. The isolation requirement can be considerably relaxed provided a modulation is added to the scattered wave. Since the transmitted wave is unmodulated, a coherent phase discriminator can be used to distinguish between scattered energy and transmitter leakage. Horton[52] has suggested a method for phase modulating the scattered wave by vibrating the scatterer in a plane parallel to the direction of propagation. This vibration is accomplished by applying a forcing function to the thread supporting the scatterer. Richmond[53],

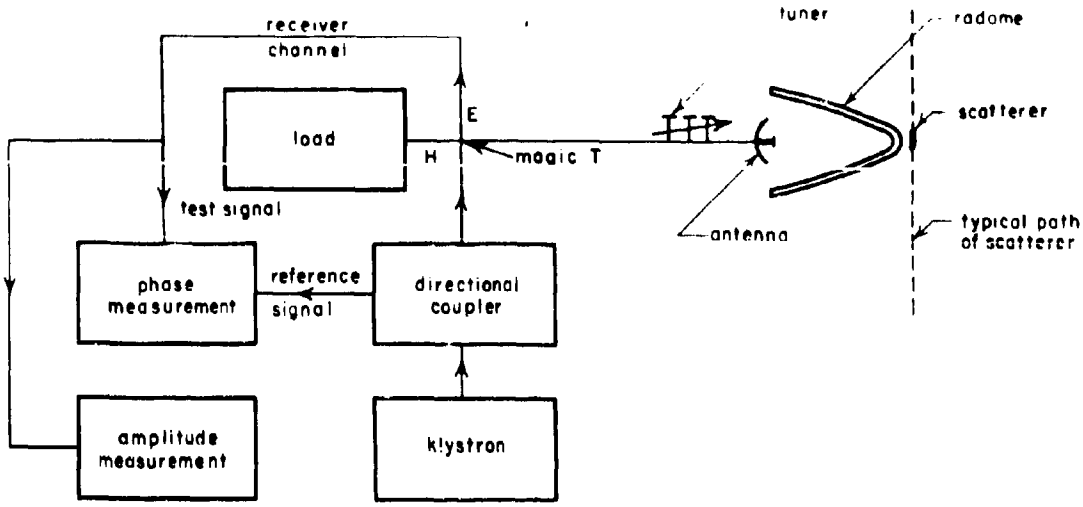


Figure 12-29. Abbreviated Block Diagram of Scattering Method

on the other hand, has amplitude-modulated the scattered wave by placing a nonlinear impedance at the center of the dipole and applying an audio voltage through slightly conducting threads. The required isolation of the magic T is reduced approximately 55 db by the use of this modulation technique.

Comparison of Methods.[54] The direct probing method is relatively straightforward and simple and can probably be used for the greatest majority of radome near-field measurements, especially along a reference plane such as indicated in Figures 12-22 and 12-26. Care should be taken to minimize the distortion produced by the probe support and feed cable or waveguide. On the other hand, in contrast with the scattering method, it is doubtful whether the direct probing method could be used satisfactorily to measure the detailed field structure inside a waveguide or in the region between the antenna and radome.

As discussed above, the use of the linear conducting scatterer normally requires a very stable signal source and critical tuning of the magic T to obtain the required isolation. These requirements are greatly relaxed if the measurements are to be made in a region where the field is relatively strong, such as that between the antenna and the radome. This method eliminates the problems of field distortion by the support and feed line. The necessary readjustment of the T if the radome is moved might be objectionable for some purposes.

Modulating the scatterer essentially eliminates the problems of frequency stability and T balance; also the sensitivity is greatly improved. The method is limited by the minimum physical size of the available nonlinear impedance.

In summary, direct probing is probably preferable in regions of fairly weak signals and where the distortion due to the supporting structure and feed line is not too serious. A scattering method is probably preferable in regions of strong signal and where great care must be taken to avoid distorting the field by inserting the probe.

REFERENCES

1. Von Hippel, A. R., Editor. Dielectric Materials and Applications. The Technology Press of MIT and John Wiley and Sons, New York, 1954, pp. 47-62.

2. Wind, M., and Rapaport, H., Editors. Handbook of Microwave Measurements. Polytechnic Institute of Brooklyn, 1954.

3. Ramo, S., and Whinnery, J. R. Fields and Waves in Modern Radio. John Wiley and Sons, New York, 1953, Chapters 8 and 9.

4. Slater, J. C. Microwave Transmission. McGraw-Hill Book Company, New York, 1942, Chapters III and IV.

5. See Chapter 1 of Reference 3.

6. Everitt, W. L. Communication Engineering. McGraw-Hill Book Company, New York, 1937, Chapter I.

7. Sarbacher, R. I., and Edson, W. A. Hyper and Ultrahigh Frequency Engineering. John Wiley and Sons, New York, 1943, Chapter 9.

8. Smith, P. H. Transmission-Line Calculator. Electronics, Vol. 12, pp. 29-31, January 1939.

9. See p. 67 of Reference 1.

10. King, R. W. P., Mimno, H. R., and Wing, A. H. Transmission Lines Antennas and Wave Guides. McGraw-Hill Book Company, New York, 1945, Chapter I.

11. Roberts, S., and von Hippel, A. R. A New Method for Measuring Dielectric Constant and Loss in the Range of Centimeter Waves. Journal of Applied Physics, Vol. 17, 1946, p. 610.

12. Von Hippel, A. R. Dielectrics and Waves. John Wiley and Sons, New York, 1954, pp. 73-82.

13. See pp. 63-122, of Reference 1.

14. Dakins, T. W., and Works, C. W. Microwave Dielectric Measurements. Journal of Applied Physics, Vol. 18, 1947, p. 789.

15. Redheffer, R. M., Wildman, R. C., and O'Gorman, V. The Computation of Dielectric Constants. Journal of Applied Physics, Vol. 23, 1952, p. 505.

16. Surber, W. H., Jr., and Crouch, G. E., Jr. Dielectric Measurement Methods for Solids at Microwave Frequencies. Journal of Applied Physics, Vol. 19, 1948, p. 1130.

17. Gevers, M. Measurement of Dielectrics and Magnetic Properties of Solids at Microwave Frequencies. Precision Electrical Measurements, Philosophical Library, New York, Vol. 3, 1956, pp. 1-15.

18. An excellent survey of the various methods is given in: Montgomery, C. G. Techniques of Microwave Measurements. Radiation Laboratory Series, Vol. 11, McGraw-Hill Book Company, New York, 1947, Chapter 10.

19. See pp. 88-101 of Reference 1.

20. See pp. 102-103 of Reference 1.

21. For tables of tan x/x see pp. 104-115 of Reference 1.

22. See p. 86 of Reference 1.

23. The writer acknowledges with pleasure the helpful suggestions of H. F. Mathis (Goodyear Aircraft Corporation, Akron, Ohio) regarding measurements on magnetic materials.

24. Ehrlich, M. J., and Williams, I. K. A Dielectrometer for Millimeter Wavelengths and Elevated Temperatures. Presented at O. S.U.-W.A.D.C. Radome Symposium, June 4-6, 1956. Published in Proceedings of the National Conference on Aeronautical Electronics, May 14-16, 1956, Dayton, Ohio.

25. Silver, S. Microwave Antenna Theory and Design. Radiation Laboratory Series, Vol. 12, McGraw-Hill Book Company, New York, 1949, pp. 574-575.

26. See pp. 188-190 of Reference 25.

27. Boulding, R. S. H. The Resonant Cavity Magnetron. Van Nostrand, New York, 1952, pp. 86-91.

28. Montgomery, C. G. Technique of Microwave Measurements. Radiation Laboratory Series, Vol. 11, McGraw-Hill Book Company, New York, 1947, pp. 473-514.

29. Ratio Meter, Model 416A, Hewlett-Packard Co., Palo Alto, Calif.

30. King, D. D. Measurements at Centimeter Wavelength. Van Nostrand, New York, 1952, pp. 258-272.

31. See pp. 574-580 of Reference 25.

32. See pp. 263-265 of Reference 25.

33. Yaw, D. F. A K-Band Superheterodyne System Using A Rotating-Guide Phase Shifter. Technical Report 444-19, 15 February 1955, Antenna Laboratory, The Ohio State University Research Foundation, prepared under contract DA36-039 sc 5506.

34. Paiss, M. H., and Schlieben, E. W. Development of a Measurement System for Beam Deflection Tests on Radomes. U.S. Naval Air Development Center, Johnsville, Pa., Report No. NADC-EL-5101, 3 August 1951.

35. Instructions for Precision Radome Boresight Test Equipment. Goodyear Aircraft Corporation, Akron, Ohio, GER-6208, 27 July 1954.

36. Horton, M. C. Automatic Equipment for Measurement of Radome Angular Error. Symposium on Guided Missile Radomes, Washington, D.C., June 18-19 1952.

37. Page, R. M. Monopulse Radar. IRE 1955 National Convention Record, Part 8, pp. 132-134.

38. Rickmond, J. H., and Tice, T. E. Fields Measured Near a Typical Radome. Antenna Laboratory, The Ohio State University Research Foundation, Report 531-4, 31 July 1953.

39. See pp. 570-573 of Reference 25.

40. Hata, F. T., and Sledge, O. D. Investigation of Electromagnetic Field Distortions Caused by Dielectric Sheets, Wedges and Radomes Placed Near an Antenna. National Bureau of Standards, Corona, Calif., Report 10E-251, 31 August 1953.

41. Richmond, J. H., and Tice, T. E. Probes for Near-Field Measurements. IRE Transactions on Microwave Theory and Techniques, Vol. MTT-3 No. 3, April 1955, pp 32-34.

42. Fox, G. A. An Automatic Waveguide Phase Changer. Proc. IRE, Vol. 35, 1947, p. 1489.

43. Waveguide Phase Shifter, Model X855A Hewlett-Packard Co., Palo Alto, Calif.

44. Automatic Equipment for Making X-Band Amplitude and Phase Measurements. Goodyear Aircraft Corporation, Akron, Ohio, GER 6657, 21 March 1955.

45. Bacon, J. An Automatic X-Band Phase Plotter. Antenna Laboratory, The Ohio State Research Foundation, Report 531-7, 1 September 1954.

46. Hines, J. N. An Automatic Phase Plotter. Antenna Laboratory, The Ohio State University Research Foundation, Report 301-31, 30 April 1951.

47. Richmond, J. H. Measurement of Time-Quadrature Components of Microwave Signals. IRE Transactions on Microwave Theory and Techniques, Vol. MTT-3, No. 3, April 1955, pp. 13-15.

48. Hines, J. N., and Tice, T. E. An Investigation of Reflection Measuring Equipment. Antenna Laboratory, The Ohio State University Research Foundation, Report 478-13, 1 June 1953.

49. Upson, J. and Hines, J. N. An Indoor Echo-Area Measuring System. Antenna Laboratory, The Ohio State University Research Foundation, Report 612-11, 1 November 1956.

50. Tice, T. E., and Richmond, J. H. Equipment for Measuring the Field Near a Radome. Antenna Laboratory, The Ohio State University Research Foundation, Report 531-5, 16 October 1953.

51. Justice, R., and Runsey, V. H. Measurement of Electric Field Distributions. IRE Transactions on Antennas and Propagation, Vol. AP-3, No. 4, October 1955.

52. Horton, M. C. Automatic Radome Test Equipment. Presented at the Symposium on Antennas and Propagation. Sponsored by the Research and Development Board, Berkeley, Calif., August 1953.

53. Richmond, J. H. A Modulated Scattering Technique for Measurement of Field Distributions. IRE Transactions on Microwave Theory and Techniques, Vol. MTT-3, No. 4, July 1955, pp. 13-15.

54. Richmond, J. H., and Tice, T. E. A Survey of Microwave Near Field Measuring Techniques. Presented at URSI-IRE Meeting, Washington, D. C., May 3, 1956.

Chapter 13

PRACTICAL COMPUTATIONAL DESIGN PROCEDURES

by

Samuel Wolin

U.S. Naval Air Development Center
Johnsville, Pennsylvania

INDEX OF SYMBOLS

A_i	Center of the respective area elements of the dish aperture
a_i	"Effective" radiator amplitudes
d	Thickness of one layer of a panel
d/λ_0	Thickness-to-wavelength ratio
d_c	Core thickness
d_c/λ_0	Thickness-to-wavelength ratio
d_s	Skin thickness
d_s/λ_0	Thickness-to-wavelength ratio
d_t	Total wall thickness
$\dot{E}_{ra}(\rho, 0)$	Relative electric field intensity at point $P(\rho, 0)$
$e^{j\omega t}$	Time factor
LCP	Left-circularly polarized
$\dot{R}$	With T, functions of d/λ_0 with various fixed θ or as functions of θ for various fixed d/λ_0
RCP	Right-circularly polarized
$R'_{\parallel}$, $R'_{\perp}$	Reflection phase shifts, parallel and perpendicular polarizations, respectively (radians)
S_i	Antenna aperture power density appropriate to the area A_i
T^2	Power transmission coefficient
$T^2_{\parallel}$, $T^2_{\perp}$	Power transmission coefficients, parallel and perpendicular polarization, respectively
T^2_{RCP}	Constant power transmission
$\dot{T}$	With $\dot{R}$, functions of d/λ_0 with various fixed θ or as functions of θ for various fixed d/λ_0
$\hat{T}'_{\parallel}$, $\hat{T}'_{\perp}$	Lead angles corresponding to the time factor $e^{j\omega t}$, parallel and perpendicular polarization, respectively
$\hat{T}_{\parallel}$, $\hat{T}_{\perp}$	Transmission coefficients for parallel and perpendicular polarization, respectively
$\tan \delta_c$	Loss tangent of core
$\tan \delta_s$	Loss tangent of skin
X'_i	X' -coordinate of the center of A_i
Δ	Insertion phase delay
$\Delta_{\parallel}$, $\Delta_{\perp}$	Insertion phase delays, parallel and perpendicular polarization, respectively (radians)
Δ_i	Phase delay of the radiators
$\frac{\Delta T^2}{\Delta d_c}$	Transmission loss (percent per hundredth inch deviation in core thickness at optimum core thickness)
$\frac{\Delta T^2}{\Delta d_s}$	Transmission change (percent per hundredth inch change in skin thickness at optimum core thickness)
$\frac{\Delta T^2}{\Delta \epsilon_c}$	Transmission loss (percent per unit change in ϵ_c at optimum core thickness)
$\frac{\Delta T^2}{\Delta \epsilon_s}$	Transmission loss (percent per unit deviation in ϵ_s at optimum skin thickness)
δ	Relative phase shift
ϵ_c	Core dielectric constant
ϵ_r	Dielectric constant
ϵ_s	Skin dielectric constant
θ	Angle of incidence
λ_0	Free space wavelength
ξ	Polarization angle
θ_{RCP}	Insertion phase delay
θ_{LCP}	Phase delay

Chapter 13

PRACTICAL COMPUTATIONAL DESIGN PROCEDURES

SECTION A. REFLECTION AND TRANSMISSION OF ELECTROMAGNETIC WAVES AT ARBITRARY INCIDENCE ANGLES BY LOSSY PLANE DIELECTRIC PANELS

13-1. Available Data

Equations for computing complex transmission and reflection coefficients for flat panels composed of any number of homogeneous dielectric layers in tandem were given in Chapter 2. Many tables and curves have been prepared from these (or from other essentially identical) equations for the important cases of perpendicular and parallel polarizations. Perhaps the most extensive efforts have been exerted by U. S. Naval air development groups and U. S. Air Force development groups to expand the available data toward some semblance of completeness. The single-layer wall has received most attention, and transmission data for it are now relatively complete (in the lossless case) for first and second order thicknesses with relative dielectric constants up to 10. The problem of the symmetrical "A" sandwich has also been attacked vigorously. While the parameters of this structure are so numerous that degrees of data completeness are difficult to define, it now appears that sufficient data are available to indicate the transmission possibilities of this configuration, at least for dielectric constants up to 6.0 and 1.4 (for the skins and core respectively). "B" and "C" sandwiches have also received considerable attention, and limited discussions of multilayer structures have appeared. A large part of the currently available data may be found in References 1 through 49.

13-2. Data Calculation and Presentation

Most calculations of plane-wave coefficients are now carried out on high-speed digital computers. The economy of such calculations thus depends on setting up the equations of Chapter 2 in a manner for the most efficient machine evaluation. A matrix formulation is ideal from the standpoint of rapid programming and checking. The exact form of reiteration to be used, however, depends on which coefficients are desired and on the nature of the multilayer panel. Processing the data received from computers can constitute an expensive portion of a computation program. Complete machine handling (calculation, plotting, and crossplotting) is extremely desirable to minimize human errors.

The complex reflection and transmission coefficients are functions of incidence angle, polarization, and panel design (layer thickness and electrical characteristics). In a two-dimensional plot to describe some property, such as $T_\perp^2$ (the power transmission coefficient), or $\Delta_\perp$, (the insertion phase delay), we must therefore fix all but two parameters and relate the desired quantity to these parameters by a family of curves (for example, $T_\perp^2$ versus d/λ_0 for various fixed θ). A majority of the calculations to date have presented $\dot{T}$ and $\dot{R}$ as functions of d/λ_0 with various fixed θ or as functions of θ for various fixed d/λ_0, where d is the thickness of one layer of a panel (for example, the core thickness for an "A" sandwich).

As discussed in Chapter 3, however, in connection with wall design problems, graphs of $\dot{T}$ and $\dot{R}$ are not always the most convenient form. Since for all practical radome materials developed thus far, $\dot{T}_\perp \neq \dot{T}_\parallel$ and, furthermore,

$[\]_{\theta_1}$ / $\dot{T}_{\perp}]_{\theta_2}$ and $\dot{T}_{\parallel}]_{\theta_1}$ / $\dot{T}_{\parallel}]_{\theta_2}$, radome designers often desire to taper wall thickness so that $\dot{T}_{\perp}$ or $\dot{T}_{\parallel}$ (or at least $\Delta_{\perp}$ or $\Delta_{\parallel}$) remain constant over a desired range of θ. The required data then take the form of plots of d/λ_0 versus θ for fixed values of T^2 or Δ. While this may be the most convenient form, it is not the easiest to obtain, because of the nature of the equations relating d/λ_0 to θ. A limited amount of data obtained by direct solutions of this form have been obtained for simple wall structures.[14,20] It is felt, however, that the use of solutions for $\dot{T}$ and $\dot{R}$ as functions of d/λ_0 or θ followed by appropriated crossplots to obtain families of constant T^2, constant Δ, or other curves relating d/λ_0 and θ is the most practical procedure for multilayer walls.

Other forms of data curves considered useful in wall design problems are plots of panel electrical thickness and of the relative phase shift, δ, between $\dot{T}_{\parallel}$ and $\dot{T}_{\perp}$.

13-3. Accuracy

Most plots given for T^2 can be read to within 2 or 3 figures in the third decimal place. Plots of Δ will usually yield a value within 2^0 or 3^0 of the presumed correct one. Whether such accuracies are adequate for a wall design problem depends on the nature of the complete antenna-radome-radar system. If they are not, it is a simple matter to specify additional accuracy in the machine evaluation. It should be noted that the usable computational accuracy is limited by the attainable manufacturing tolerances.

In regard to the neglect of losses and the use of approximate equations for low-loss materials, the present trend is toward the exact calculation. If a decision is made to use simpler, approximate equations because of low loss, the increased programming time in determining which terms can be neglected is often not compensated by the resulting reduction of machine running time. This is a matter, however, that must be decided for the particular panel of interest.

13-4. Graphical Calculation

Since the propagation of plane waves through a series of dielectric layers is the same kind of problem as that of transmission of TEM waves along two-conductor lines, techniques suitable for the latter case are applicable to the former. In particular, transmission line charts, such as the Smith chart,[50] are convenient in obtaining rapid graphical solutions in both cases. The accuracy of such calculations cannot compare with that of an analytical evaluation, but the graphical solution has the advantage of speed and a pictorial display of effects produced by parameters of the various layers. Detailed procedures for determining $\dot{T}$ and $\dot{R}$ using transmission line charts have been described by Mathis[37,51] and Snow.[26]

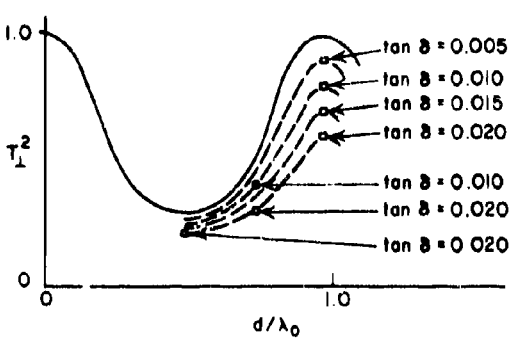
13-5. Graphs of Transmission and Reflection Coefficients

Representative curves of transmission, reflection, and phase delay for perpendicular and parallel polarizations incident on solid homogeneous panels with dielectric constant $\epsilon_r = 1.2$, 2, and 4 are shown in Figures 13-1 through 13-18. Curves of power transmission coefficients and relative phase delays for typical "A" sandwiches with skin dielectric constant $\epsilon_s = 3.7$ and core dielectric constant $\epsilon_c = 1.4$ are shown in Figures 13-19 through 13-33. Curves of insertion phase delay versus normalized skin and core thicknesses are given in Figures 13-34 through 13-37. Graphs of T^2 and Δ for symmetrical "C" sandwiches appear in Figures 13-38 through 13-41.

For the case of Figures 13-1 through 13-18, inclusive, the curves are plotted only for the lossless case and points are used to show lossy cases. Lossy information for $\tan\delta = 0.005$, 0.010, 0.015, and 0.020 is indicated by the following markings for various angles of incidence:

o for 0^0	\ for 70^0
- for 30^0	Δ for 75^0
• for 50^0	/ for 80^0
x for 60^0	□ for 85^0

When four markings are included, the one closest to the lossless case indicates a tan $\delta = 0.005$ and the second, third, and fourth give data for $\tan\delta = 0.010$, 0.015, and 0.020, respectively. With two markings, the information is given for $\tan\delta = 0.010$ and 0.020. One mark only indicates $\tan\delta = 0.020$. This is illustrated below.



A limited number of coefficients for circular and elliptical polarizations have been computed (References 8, 39, 52). If a right-circularly polarized wave (RCP) is incident on a panel for which $\hat{T}_{\parallel}$ is not equal to $\hat{T}_{\perp}$, the emerging wave on the opposite side of the panel will contain both RCP and left-circularly polarized wave (LCP) components. The equations applicable to such a situation were given in Chapter 2. Typical crossplots showing wall thickness contours for constant T^2 and constant Λ for the RCP and LCP components emerging from homogeneous-wall "A" sandwiches, and "C" sandwich panels are shown in Figures 13-42 through 13-47.

13-6. Wall Dimension Tolerances

For design and fabrication purposes it is important to know the effects of small variations in thickness and dielectric constants on radome transmission. Typical tolerance curves for such variations are shown in Figures 13-48 through 13-52. The tolerances shown for skin thicknesses, dielectric constants, and loss tangents are representative of radomes now in use. The accuracy holds precisely only near the optimum thickness for one angle of incidence. For streamlined radomes of constant thickness, angles of incidence vary widely, and the optimum thickness exists at any time over only a small portion of the surface. It is clear, therefore, that in such a case the tolerance curves must be used with reservation. Thicknesses are usually at their optimum for angles of incidence somewhat higher than the average angle of incidence. Because of this and because tolerances become more critical at higher angles, a safe procedure to follow is to read values from the curves at an angle equal to, or slightly higher than, the angle at which optimum thickness exists.

SECTION B. CALCULATION OF THE FAR-FIELD RADIATION PATTERN FOR AN ANTENNA-RADOME SYSTEM*

13-7. A Ray-Tracing Method

Let us now consider a detailed calculation of the far-field pattern of an antenna-radome combination using a ray-tracing technique. A linearly polarized paraboloidal antenna and its radome may be considered to produce effects similar to an antenna array of "effective" radiators, each located at the center of the respective area elements, A_i, of the dish aperture (Figure 13-53). To determine the amplitude and phase distribution of these "effective" radiator elements, rays perpendicular to the antenna aperture are drawn from each A_i to the radome wall. At the point of intersection of each ray with the radome, the angle of incidence θ, and the polarization angle ξ are noted. The "effective" radiator amplitudes a_i are then computed by the formula.

$$a_i = T_{e_i} \sqrt{S_i} \tag{13-1}$$

and the phase delays Λ_i of the radiators are given by

$$\Delta_i = -\left[\hat{T}'_{e_i} + \frac{2\pi d_t}{\lambda_0} \cos\theta\right] \tag{13-2}$$

where the original antenna aperture phase distribution is assumed to be uniform, where S_i is the antenna aperture power density appropriate to the area A_i,

$$T_{e_i} = \left[(T_{\perp} \sin^2\xi)^2 + (T_{\parallel} \cos^2\xi)^2 + 2T_{\perp} T_{\parallel} \sin^2\xi \cos^2\xi \cos\delta\right]^{1/2} \tag{13-3}$$

$$\hat{T}'_{e_i} = \arcsin\left[\frac{T_{\parallel} \cos^2\xi \sin\delta}{T_{e_i}}\right] - \hat{T}'_{\perp} \tag{13-4}$$

and where d_t = total wall thickness.

$$\delta = \hat{T}'_{\parallel} - \hat{T}'_{\perp} \tag{13-5}$$

and, of course $\hat{T}_{\parallel} = T_{\parallel} e^{j\hat{T}'_{\parallel}}$ and $\hat{T}_{\perp} = T_{\perp} e^{j\hat{T}'_{\perp}}$ are the transmission coefficients for parallel and perpendicular polarizations (defined according to "normal phase convention"). Note: $\hat{T}'_{\parallel}$ and $\hat{T}'_{\perp}$ are lead angles corresponding to the time factor $e^{j\omega t}$. Equations (13-3) and (13-4)

*A number of practical analyses and computational procedures which could properly be discussed here have already been treated in previous chapters. Sections in which this material may be found include Chapter 2 (Section G), "The Radome Shape"; Chapter 2 (Section H), "The Focusing Effect of Streamlined Radomes"; Chapter 2 (Section I), "Diffraction by Radomes"; Chapter 3 (Section C), "Radome Shape"; Chapter 3 (Section E), "Wall Thickness"; Chapter 4 (Section F), "Prediction of Boresight Errors."

are derived in Reference 25. For a linear polarization incident on the radome wall, they give the corresponding linear component of the emerging elliptically polarized wave (a special case of Equation (2-96) of Chapter 2).

We may now compute the field at a far-field point P $(\rho, 0)$ in the horizontal XZ-plane (Figure 13-54). An array of equispaced radiators corresponding to strip 4 of Figure 13-54 is shown in Figure 13-55. Plane x'Ez' shown in Figure 13-55 represents a plane passing through the center line of one of the strips shown in Figure 13-54 (such as strip 4) and is perpendicular to the y-axis. From standard antenna theory, the relative electric field intensity at point P $(\rho, 0)$, due to all the equispaced radiators shown in Figure 13-54, is equal to the vector sum of their respective field intensities, and is given by

$$\dot{\bar{E}}_{ra}(\rho, 0) = a_1 A_1 e^{j\phi_1} + a_2 A_2 e^{j\phi_2} + \ldots + a_i A_i e^{j\phi_i} + \ldots + a_n A_n e^{j\phi_n} \tag{13-6}$$

$$\phi_i = -\left[\frac{2\pi X_i'}{\lambda_0}\right] \cdot \sin\rho + \Delta_i \tag{13-7}$$

X_i' being the X' coordinate of the center of A_i. Application of Euler's formula to Equation (13-6) gives

$$\dot{\bar{E}}_{ra}(\rho, 0) = \sum_{i=1}^{n} a_i A_i \cos\phi_i + j\sum_{i=1}^{n} a_i A_i \sin\phi_i \tag{13-8}$$

hence

$$\left|\dot{\bar{E}}_{ra}(\rho, 0)\right|^2 = \left[\sum_{i=1}^{n} a_i A_i \cos\phi_i\right]^2 + \left[\sum_{i=1}^{n} a_i A_i \sin\phi_i\right]^2 \tag{13-9}$$

We may normalize this expression, with respect to the field produced by the antenna alone along its axis, by noting that the relative far field in that case, $\left|\dot{\bar{E}}_a(0, 0)\right|^2$, is given by

$$\left|\dot{\bar{E}}_a(0, 0)\right|^2 = \left[\sum_{i=1}^{n} A_i \sqrt{S_i}\right]^2 \tag{13-10}$$

Then

$$\frac{\left|\dot{\bar{E}}_{ra}(\rho, 0)\right|^2}{\left|\dot{\bar{E}}_a(0, 0)\right|^2} = \frac{\left[\sum_{i=1}^{n} a_i A_i \cos\phi_i\right]^2}{\left[\sum_{i=1}^{n} A_i \sqrt{S_i}\right]^2} + \frac{\left[\sum_{i=1}^{n} a_i A_i \sin\phi_i\right]^2}{\left[\sum_{i=1}^{n} A_i \sqrt{S_i}\right]^2} \tag{13-11}$$

Equation (13-9) or (13-11) will yield the XZ-plane power pattern of the antenna-radome combination. Notice that a different set of a_i and Δ_i will be required for each orientation of the antenna with respect to the radome. Generally a number of calculations for different scan positions will be desired.

Similarly by computing $\left|\dot{\bar{E}}_{ra}(0, \sigma)\right|^2$ for various values of σ, the radiation pattern in the XY-plane of the antenna-radome system can be obtained.

13-8. Other Ray-Tracing Techniques

Several commonly used ray-tracing methods were discussed in Chapters 2 and 4. Compared with other ray-tracing procedures the one considered here is more complex than some and less complex than others. The implicit assumption here is that energy travels through the radome as if the antenna produced a well-collimated plane-wave beam inside the radome. Reflections in the region between antenna and radome are neglected. More elaborate methods for tracing rays from the antenna to a plane outside the radome (followed by the usual numerical integration to obtain the far field pattern) may yield more accurate results. But the best of ray-tracing techniques will give only crude approximations for some radome configurations (those in the "small radome" category). On the other hand, investigators have found simplified calculations using only two to five rays to be useful[53] in some cases.

REFERENCES

1. Wolin, S. Tables of Fresnel's Coefficients, Snell's Law and Other Radome Design Quantities. Report NADC-EL-5104. U. S. Naval Air Development Center, Johnsville, Pennsylvania, 22 January 1952.

2. Wolin, S. Supplementary Tables of Fresnel's Coefficients, Snell's Law, and Other Radome Design Quantities. Report NADC-EL-53183. U. S. Naval Air Development Center, Johnsville, Pennsylvania, 9 July 1954. (AD-37 153)

3. Wolin, S. Tables of Amplitude and Phase of the Function $1+ae^{j\phi}$. Report NADC-EL-5114, U. S. Naval Air Development Center, Johnsville, Pennsylvania, 28 August 1952. (ATI-171767)

4. DiToro, J. A. Graphs of Transmission and Phase Data of Plane Dielectric Sheets for Radome Design. Report NADC-EL-5315, U. S. Naval Air Development Center, Johnsville, Pennsylvania, 1 July 1953. (AD-45 316)

5. DiToro, J. A. Supplementary Graphs of Transmission and Phase Delay of Plane Dielectric Sheets and Sandwich Constructions for Radome Design. Report NADC-EL-5313, U. S. Naval Air Development Center, Johnsville, Pennsylvania, 16 June 1954. (AD-45 543)

6. Wolin, S. Tables of Transmission and Reflection Coefficients of Lossy, Homogeneous Dielectric Sheets. Report NADC-EL-52195, Vol. 1, U. S. Naval Air Development Center, Johnsville, Pennsylvania, 11 February 1954. (AD-36 518)

7. Wolin, S. Tables of Transmission and Reflection Coefficients of Lossy, Homogeneous Dielectric Sheets. Report NADC-EL-52195, Vol. 2, U. S. Naval Air Development Center, Johnsville, Pennsylvania, 7 October 1954.

8. Webster, R. E., and Moore, D. P. Transmission Coefficients of Elliptically Polarized Waves Incident on Homogeneous Isotropic Panels. Report 663-5, Contract AF 33(616)-3277, Antenna Laboratory, The Ohio State University Research Foundation, 31 December 1956.

9. Kofoid, M. J. Calculated Electrical Transmission Characteristics of Half-Wavelength Thick Solid Plane Sheets. Document No. D-13622, Boeing Airplane Co., Seattle, Washington, 24 October 1952 (revised 12 March 1954). (AD-42 401)

10. Lengyel, B. A., Langenberg, D. N., and Henschke, R. A. Transmission Through Half-Wave Sheets. Technical Memorandum No. 327, Hughes Aircraft Co., Culver City, California, 1 November 1953. (AD-22 010)

11. Everhart, E. M. Radome Wall Reflections at Variable Angles of Incidence. Report 483-20, Radiation Laboratory, Massachusetts Institute of Technology, 4 January 1946.

12. Radome Engineering Manual. Published by direction of the Chief of the Bureau of Aeronautics and the Commanding General of the Air Materiel Command. AMC Manual No. 80-4, NAVAER 16-45-502, 1 October 1948.

13. Weedon, M. G. B., and Stott, A. L. Calculations on the Transmission of Electromagnetic Waves Through Plane Dielectric Sheets. Technical Note No. G. W. 282, Royal Aircraft Establishment, Great Britain, November 1953. (Confidential) (AD-25 2779)

14. Luoma, E. J. Phase Retardation Design Curves for Solid Lossless Dielectric Panels. Technical Report 56-116, Wright Air Development Center, Wright-Patterson Air Force Base, Ohio, February 1956. (AD 110514)

15. Cady, W. M., Karelitz, M. B., and Turner, L. A. Radar Scanners and Radomes. McGraw-Hill Book Co., New York, 1948, p. 26. (Vol. 26, Massachusetts Institute of Technology Radiation Laboratory Series.)

16. Wiederhorn, N. M., and Kay, A. F. Radome Design Criteria for Precision Guidance Radar. Final Report, Contract AF 33(038)-12283, McMillan Laboratory, Ipswich, Massachusetts, 1 June 1954. (Confidential) (AD-49 428)

17. Kotik, J. Some Remarks on Thin Dielectric Walls. Report No. 12283-8M, Contract AF 33(038)-12283, McMillan Laboratory, Ipswich, Massachusetts, 15 March 1953. (Confidential)

18. Transmission Through a Lossy Dielectric Sheet. Document No. D-13645, Boeing

Airplane Co., Seattle, Washington, 27 October 1952.

19. Undesser, K. Reflection Transmission Phase Delay Calculation in Radome Design. The Glenn L. Martin Company. (Confidential)

20. Horton, M. C., Boyce, W. E. L., and Hartig, E. O. Optical Theory for Microwave Transmission Through Dielectric Wall Structures. Report No. GER-5530, Goodyear Aircraft Corp., Akron, Ohio, 4 August 1953. (AD-42 719)

21. Lengyel, B. A. Half-Wave Radomes. (Hughes Aircraft Co., Culver City, California) Office of Naval Research, Washington, D. C., Symposium on Guided Missile Radomes, June 1953, pp. 135-138. (Confidential) (AD-36 188)

22. Kay, A. F. Geometry of Reflection and Transmission Coefficients. Report 12283-7E, Contract AF 33(038)-12283, McMillan Laboratory, Ipswich, Massachusetts, 14 March 1952. (Secret)

23. Gonshor, H. Optimizing Reflection from a Plane Sheet of Large Dielectric Constant over a Range of Incidence Angles. Report 12283-8J, Contract AF 33(028)-12283, McMillan Laboratory, Ipswich, Massachusetts, 15 August 1952. (Confidential)

24. Kay, A. F. The Electrical Design of the Homogeneous Radome Wall. Report 12283-8K, Contract AF 33(038)-12283, McMillan Laboratory, Ipswich, Massachusetts, 15 February 1953. (Confidential)

25. Wolin, S. Theory of Lossy High-Incidence Radomes. Report NADC-EL-5116, U. S. Naval Air Development Center, Johnsville, Pennsylvania, 15 January 1952.

26. Snow, O. J. Report on Applications of the Impedance Concept to Radome Wall Design. Report NADC-EL-52196, U. S. Naval Air Development Center, Johnsville, Pennsylvania, 6 April 1953.

27. Kofoid, M. J. Bomarc Radome Design. (Boeing Airplane Co., Seattle, Washington) Symposium on Guided Missile Radomes (Supplement), Office of Naval Research, Washington, D. C., June 1953. (Secret) (AD-38 581)

28. Redheffer, R. M. Transmission and Reflection of Single Plane Sheets. Report 483-4, Radiation Laboratory, Massachusetts Institute of Technology, 12 July 1944.

29. Wolin, S. Tables of Transmission and Reflection Coefficients of Lossy, Symmetrical Dielectric Radome Sandwiches. Report NADC-EL-52188, U. S. Naval Air Development Center, Johnsville, Pennsylvania, 22 October 1953.

30. Bowlby, C. W. Calculated Electrical Transmission Characteristics of Symmetrical Sandwich Flat Sheets. Document D-13643, Boeing Airplane Co., Seattle, Washington, 30 October 1952.

31. Wolin, S. Electrical Design of Lossy High-Incidence Radomes. Report ADC EL-123-50, U. S. Naval Air Development Center, Johnsville, Pennsylvania, 11 July 1950.

32. Everhart, E. M. X-Band Sandwiches at Variable Angles of Incidence. Report 483-8, Radiation Laboratory, Massachusetts Institute of Technology, 19 December 1944.

33. Redheffer, R. M. Transmission and Reflection of Parallel Plane Sheets. Report 483-12, Radiation Laboratory, Massachusetts Institute of Technology, 26 January 1945.

34. Dowker, Y. Transmission of Lossy Sandwiches. Report 483-22, Radiation Laboratory, Massachusetts Institute of Technology, 23 January 1946.

35. Croswell, W. F. Constant Phase Retardation Characteristics of an "A" Sandwich Radome. Report TR-56-32, Wright Air Development Center, Ohio, December 1955. (Confidential) (AD-95 556)

36. Hartig, E. O., and Horton, M. C. The Theory of the Lossless Double Symmetrical Sandwich Radome. Report GER-2731, Contract W33-038ac-14153, Goodyear Aircraft Corp., Akron, Ohio, 2 July 1951.

37. Mathis, H. F. Methods of Determining Sandwich Transmission Characteristics. Report GER-7182, Contract AF 33(616-2213, Goodyear Aircraft Corp., Akron, Ohio, 12 December 1955. (AD-91 145)

38. Wolin, S. Formulas for Calculating Transmission Coefficients for Low Loss Radome Sandwiches by the Vector Method. U.S. Naval Air Development Center, Johnsville, Pennsylvania, 6 December 1948.

39. Webster, R. E., and Moore, D. P. Transmission Coefficients of Circularly Polarized Waves Incident on "A" and "C" Sandwich Panels. Report 663-6, Contract AF 33(616)-3277, Antenna Laboratory, The Ohio State University Research Foundation, 31 December 1956.

40. Lippmann, B. A. and Oppenheim, A. Analysis of Plane Slabs. Contract Nonr-123000, Technical Research Group, New York, 30 April 1954. (AD-39 181)

41. Speer, W. Matrix Method of Radome Transmission Computation. Memorandum Report No. EG-MR-3, Douglas Aircraft Co., El Segundo, California, 4 January 1951. (ATI 178476)

42. Henschke, R. A. Application of Matrices to the Problem of Transmission Through a Multi-Layered Dielectric Wall. Hughes Aircraft Co., Culver City, California.

43. Wolin, S. Reflection and Transmission of Electromagenetic Waves by Multilayer Plane Dielectric Sheets at Arbitrary Incidence. Report NADC-EL-5293, U. S. Naval Air Development Center, Johnsville, Pennsylvania, 6 August 1952.

44. Barrar, R. B. Methods of Design of Experimental Radomes of Report 8Q. Report 8U, Contract AF 33(038)-12283, McMillan Laboratory, Ipswich, Massachusetts, (Confidential) (AD-40 640)

45. Redheffer, R. M., Sampson, H., Janus, N. N., and Webber, A. H. A Study of Broadbanding Techniques. Final Report, Contract AF 33(600)-28749, McMillan Laboratory, Ipswich, Massachusetts, 31 January 1956. (Confidential) (AD-90 649)

46. Redheffer, R. M. Theoretical Sandwich Design for Phase. Section C, McMillan Laboratory, Ipswich, Massachusetts, 14 March 1952.

47. Wiederhorn, N. M. Design and Fabrication of a B Sandwich Streamlined Radome. Final Report, Contract AF 33(038)-16606, McMillan Laboratory, Ipswich, Massachusetts, 17 February 1954. (AD-29 262)

48. McMillan, E. B. The B Sandwich in Missile Radomes, Lenses and Broadband Radomes. (McMillan Laboratory) Proceedings of the O.S.U.-W.A.D.C. Radome Symposium, Vol. 2, June 1955, pp. 231-237. (Confidential) (AD-86 660)

49. Wolin, S. Ray Deflection Through a Medium Having a Continuously Varying Refractive Index. Report NADC-EL-5294, U. S. Naval Air Development Center, Johnsville, Pennsylvania, 28 August 1952.

50. Smith, P. H. Transmission-Line-Calculator. Electronics, Vol. 12, pp. 29-31, January 1939.

51. Mathis, H. F. Transmission Characteristics of Sandwiches. I.R.E. Transactions, Vol. MTT-3, pp. 57-58, October 1955.

52. Boyce, W. E. L. The Angular Error Characteristics of a Radome as a Function of the Polarization of the Field Incident on the Radome. (Goodyear Aircraft Corp., Akron, Ohio) Proceedings of the O.S.U.-W.A.D.C. Radome Symposium, Vol. 2, June 1955, pp. 205-230. (Confidential) AD-86 660)

53. Pressel, P. I. Boresight Prediction Technique. Proceedings of the O.S.U.-W.A.D.C. Radome Symposium, W. A. D. C. Technical Report 56-393, Vol. I, August 1956. (AD 97150)

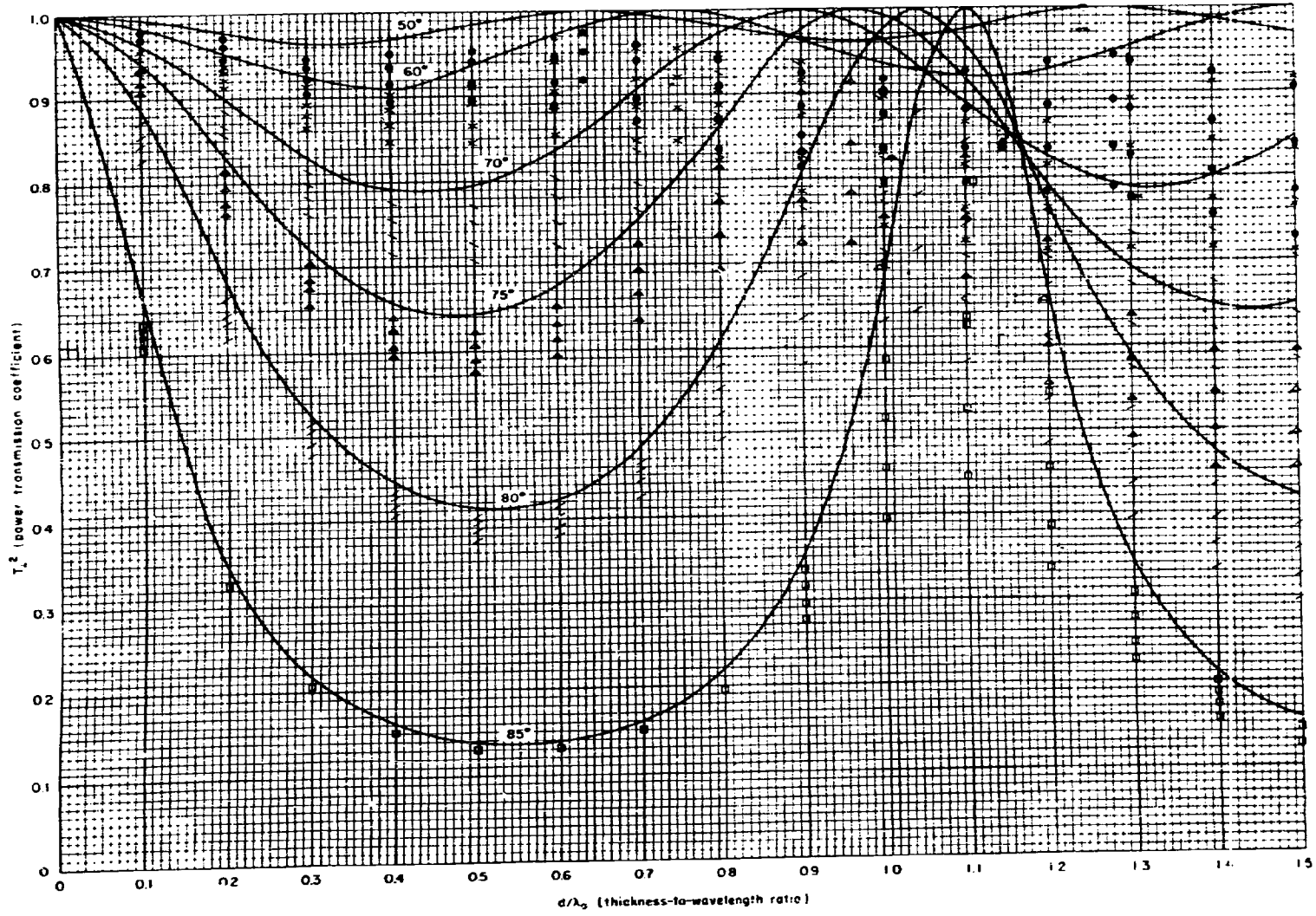


Figure 13–1. Power Transmission Coefficient of a Plane Sheet of Dielectric Constant 1.2, Perpendicular Polarization, θ = 50° To 85°

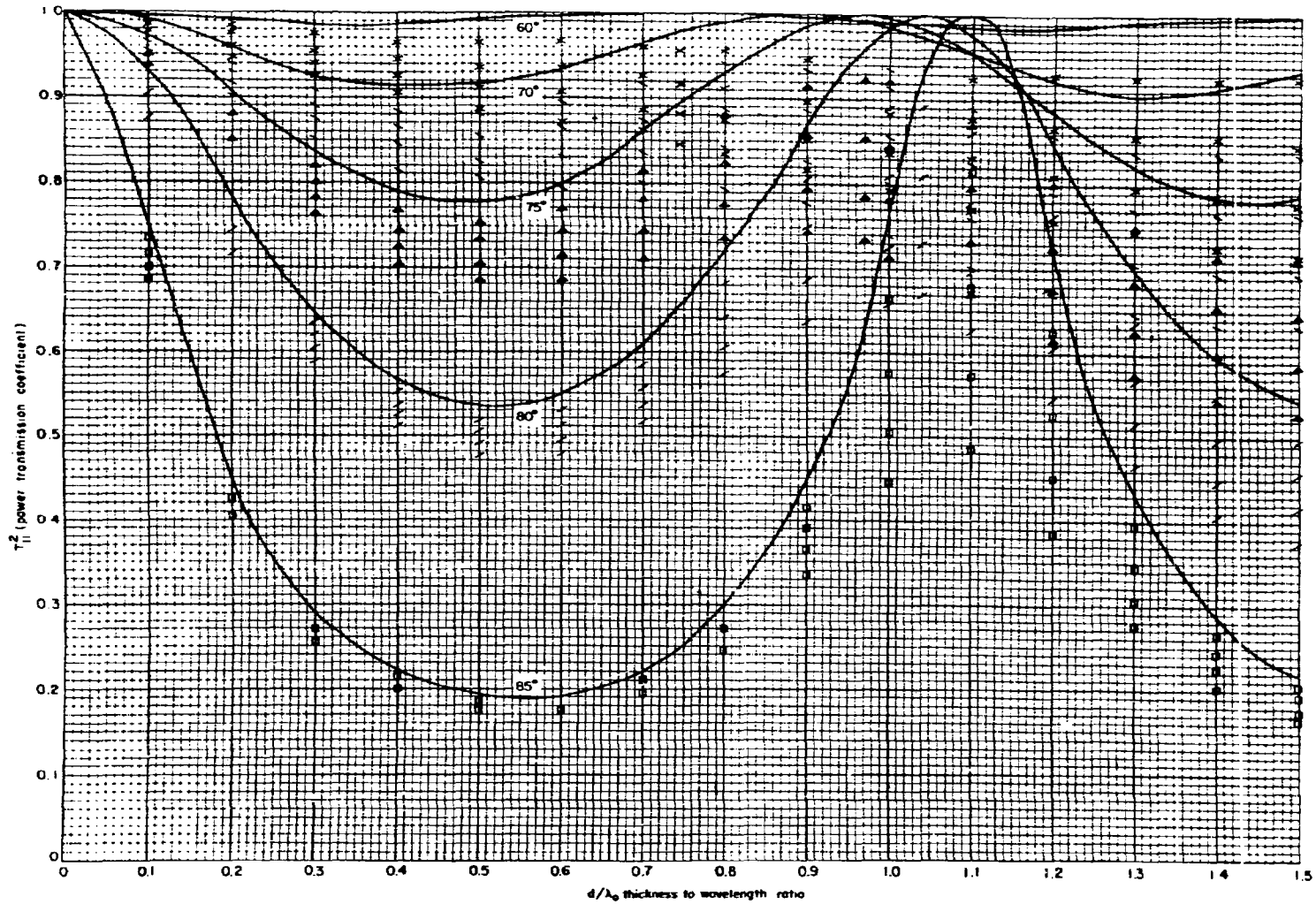


Figure 13–2. Power Transmission Coefficient of a Plane Sheet of Dielectric Constant 1.2, Parallel Polarization, θ = 60° To 85°

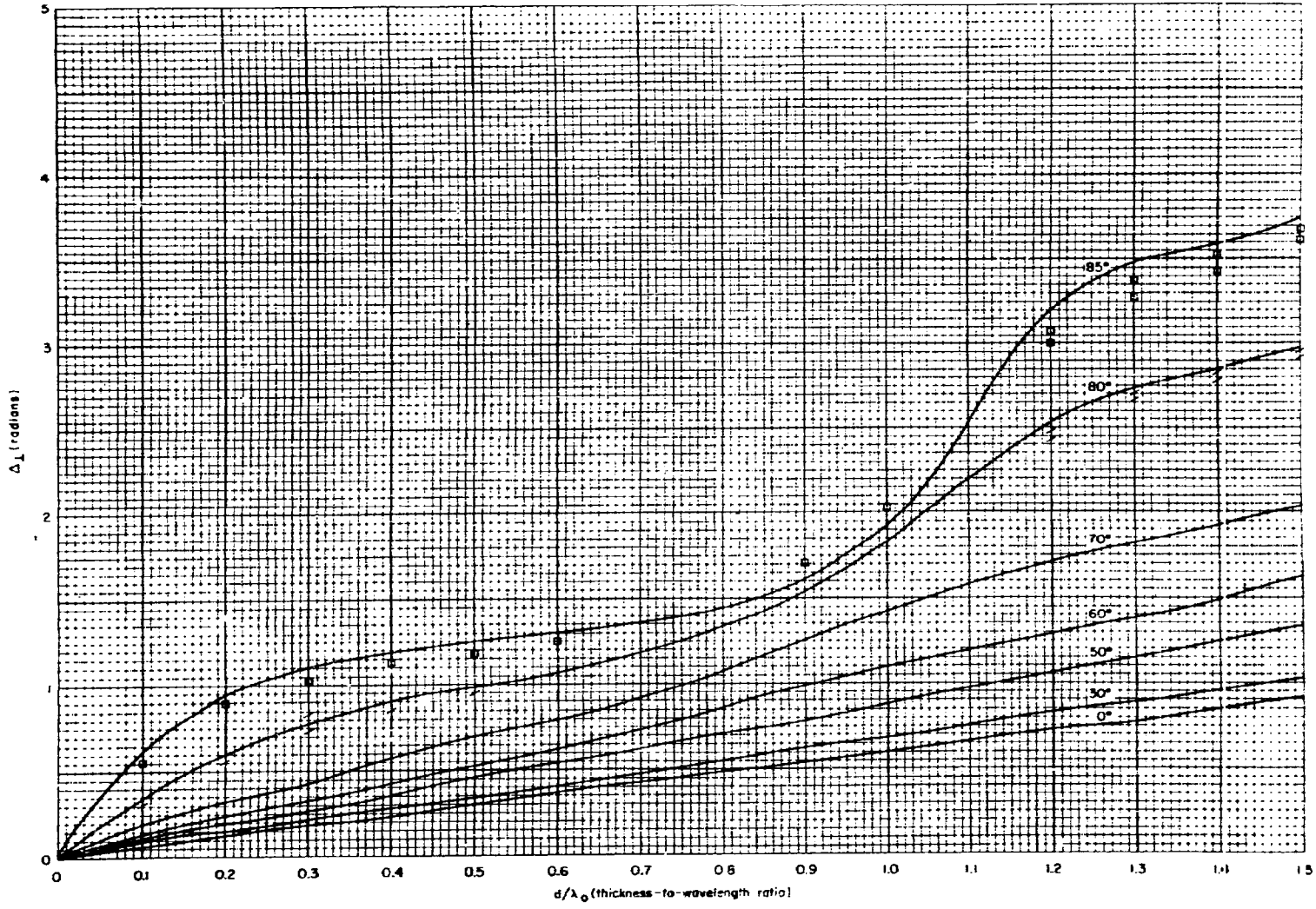


Figure 13–3. Insertion Phase Delay of a Plane Sheet of Dielectric Constant 1.2, Perpendicular Polarization, $\theta = 0°$ To 85°

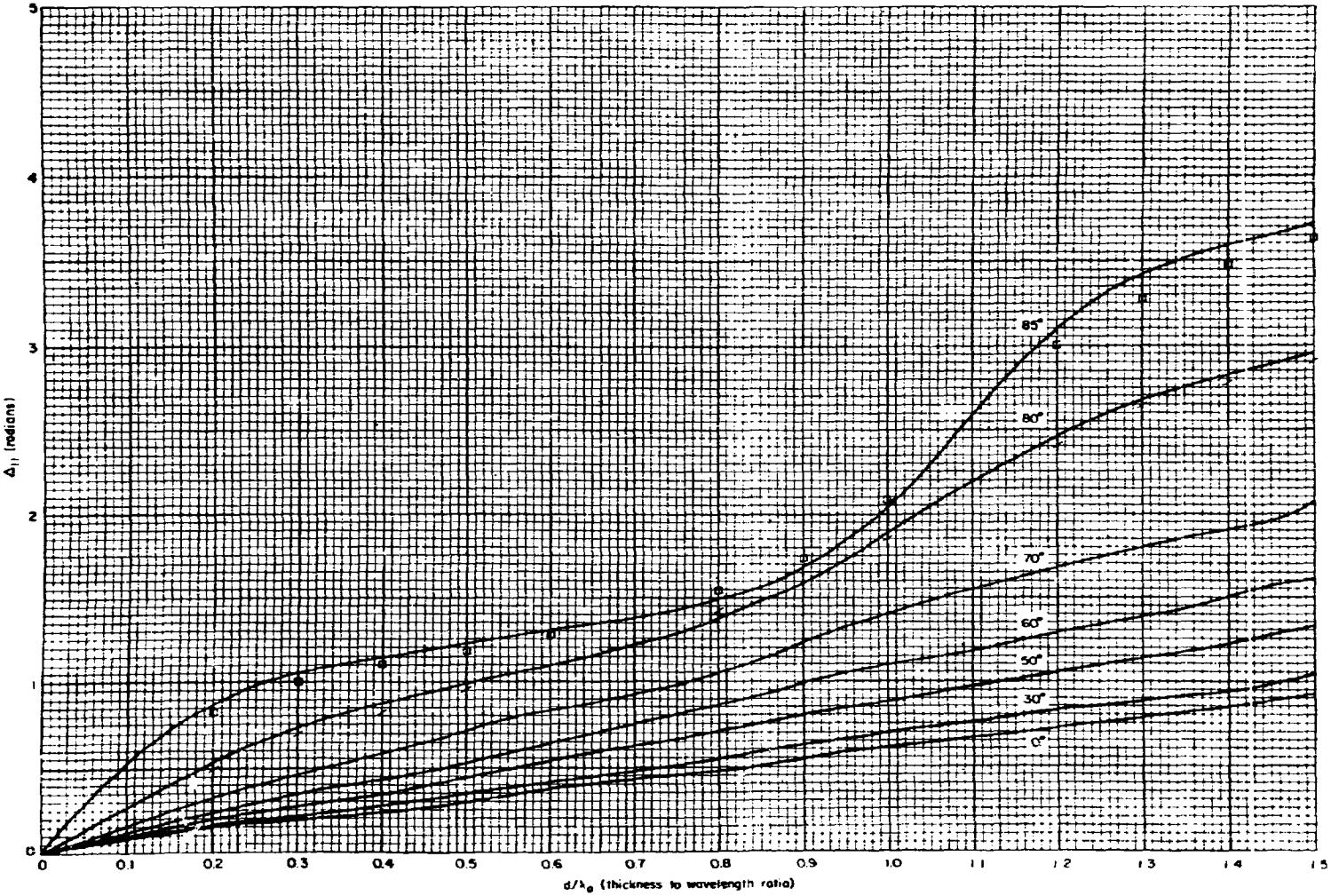


Figure 13–4. Insertion Phase Delay of a Plane Sheet of Dielectric Constant 1.2, Parallel Polarization, ϵ = 0° To 85°

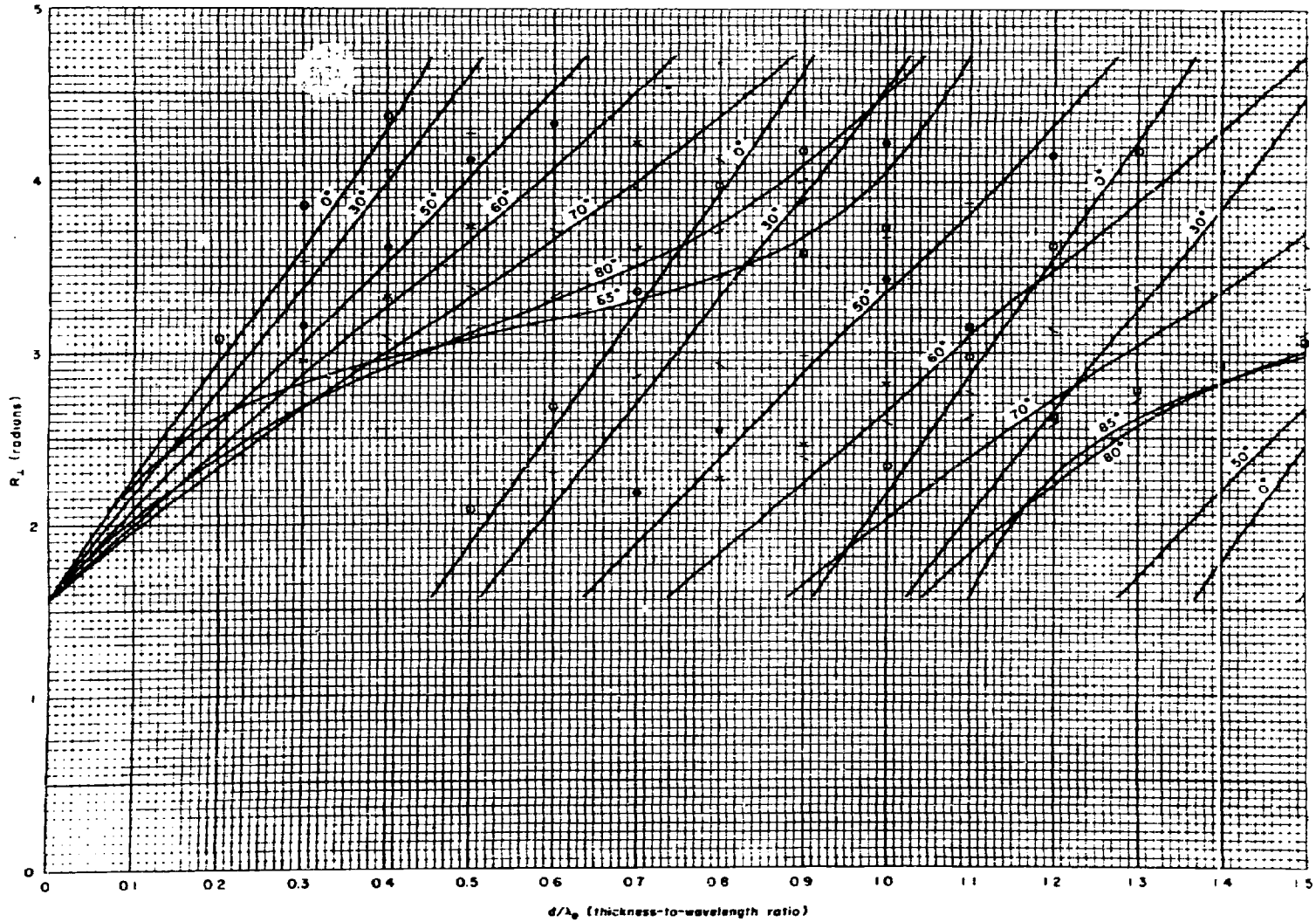


Figure 13–5. Reflection Phase Shift of Plane Sheet of Dielectric Constant 1.2, Perpendicular Polarization, $\theta = 0°$ To 85°

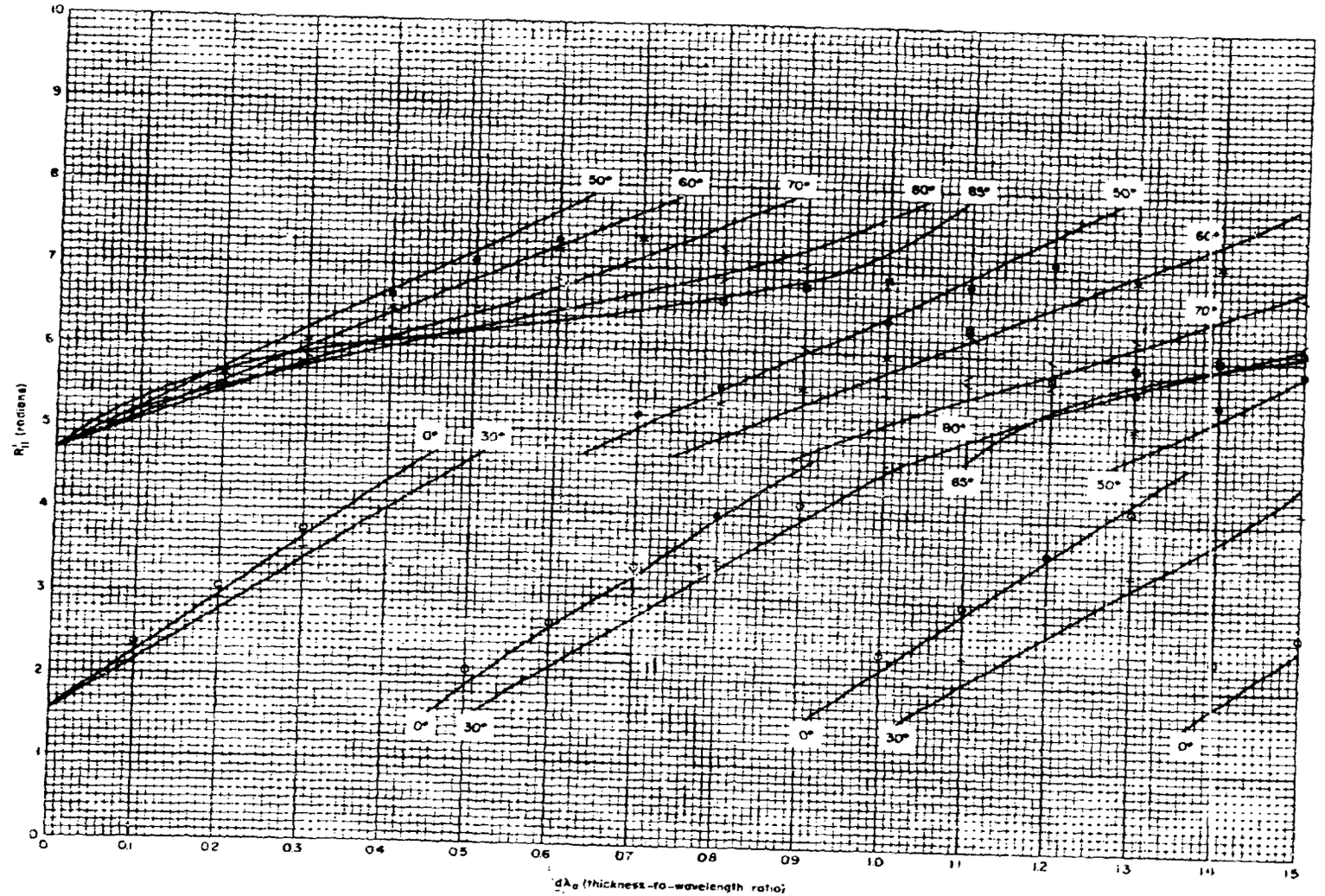


Figure 13–6. Reflection Phase Shift of Plane Sheet of Dielectric Constant 1.2, Parallel Polarization, $\theta = 0°$ To 85°

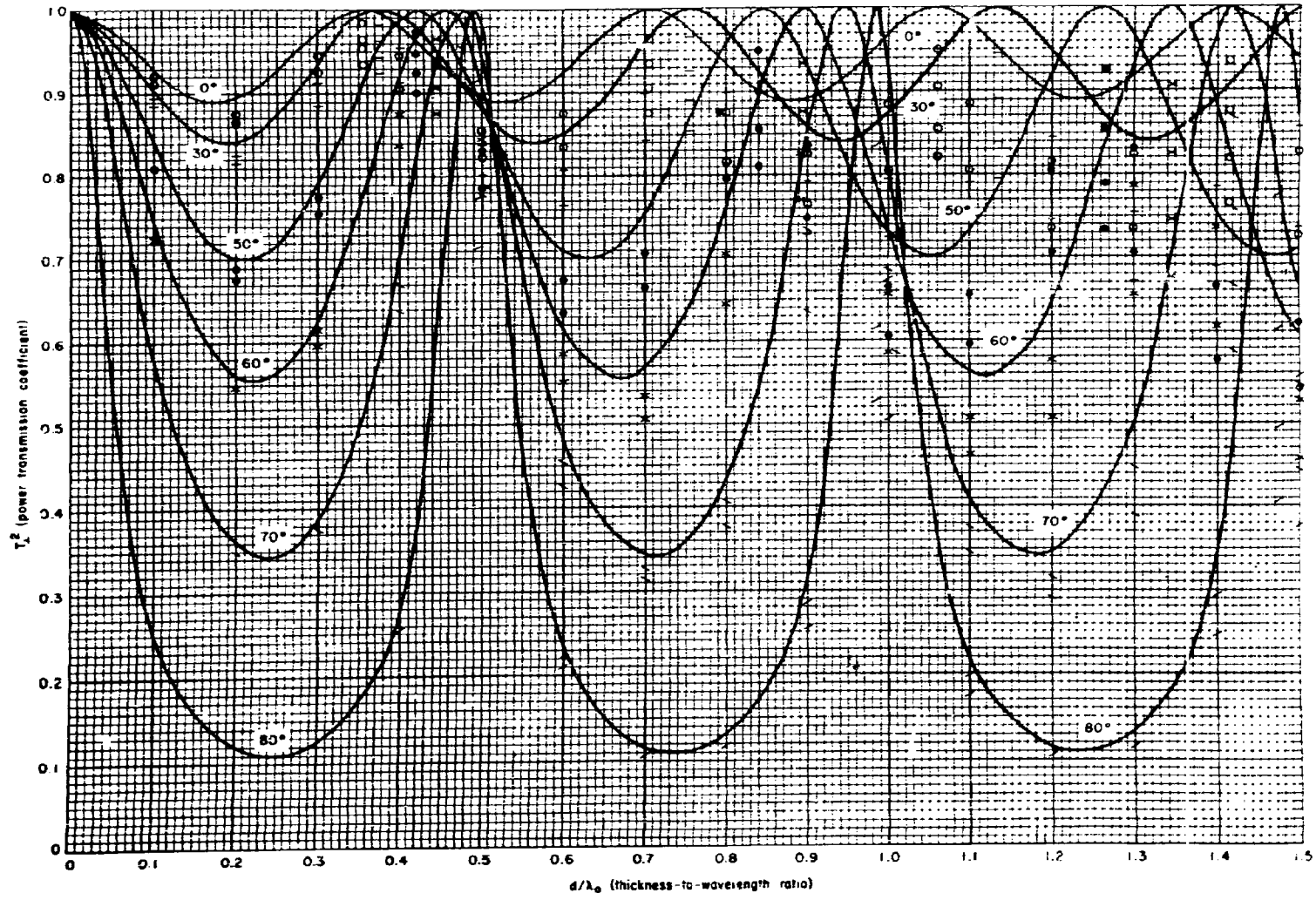


Figure 13–7. Power Transmission Coefficient of a Plane Sheet of Dielectric Constant 2, Perpendicular Polarization, $\theta = 0°$ To 80°

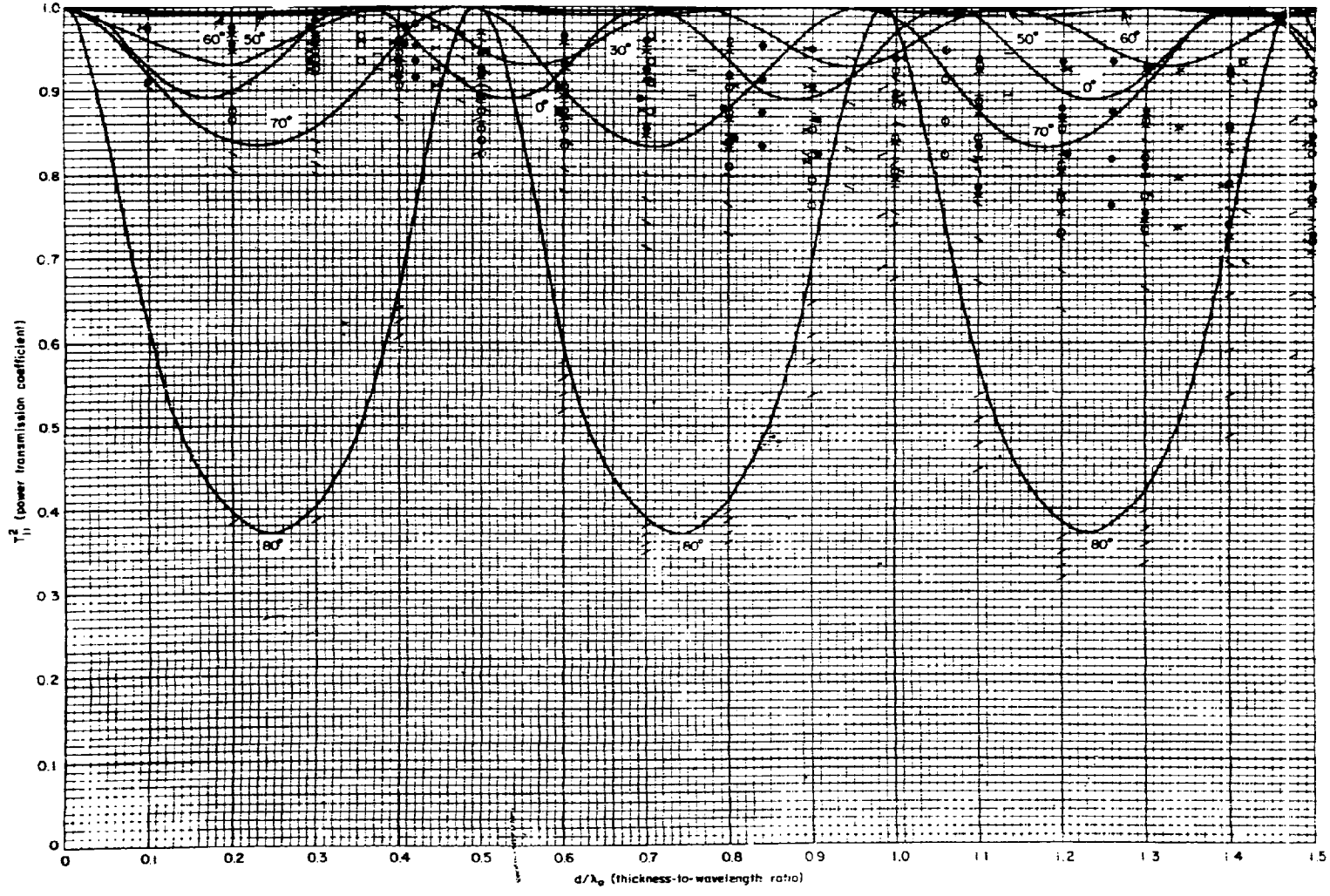


Figure 13–8. Power Transmission Coefficient of a Plane Sheet of Dielectric Constant 2, Parallel Polarization, $\theta = 0°$ To 80°

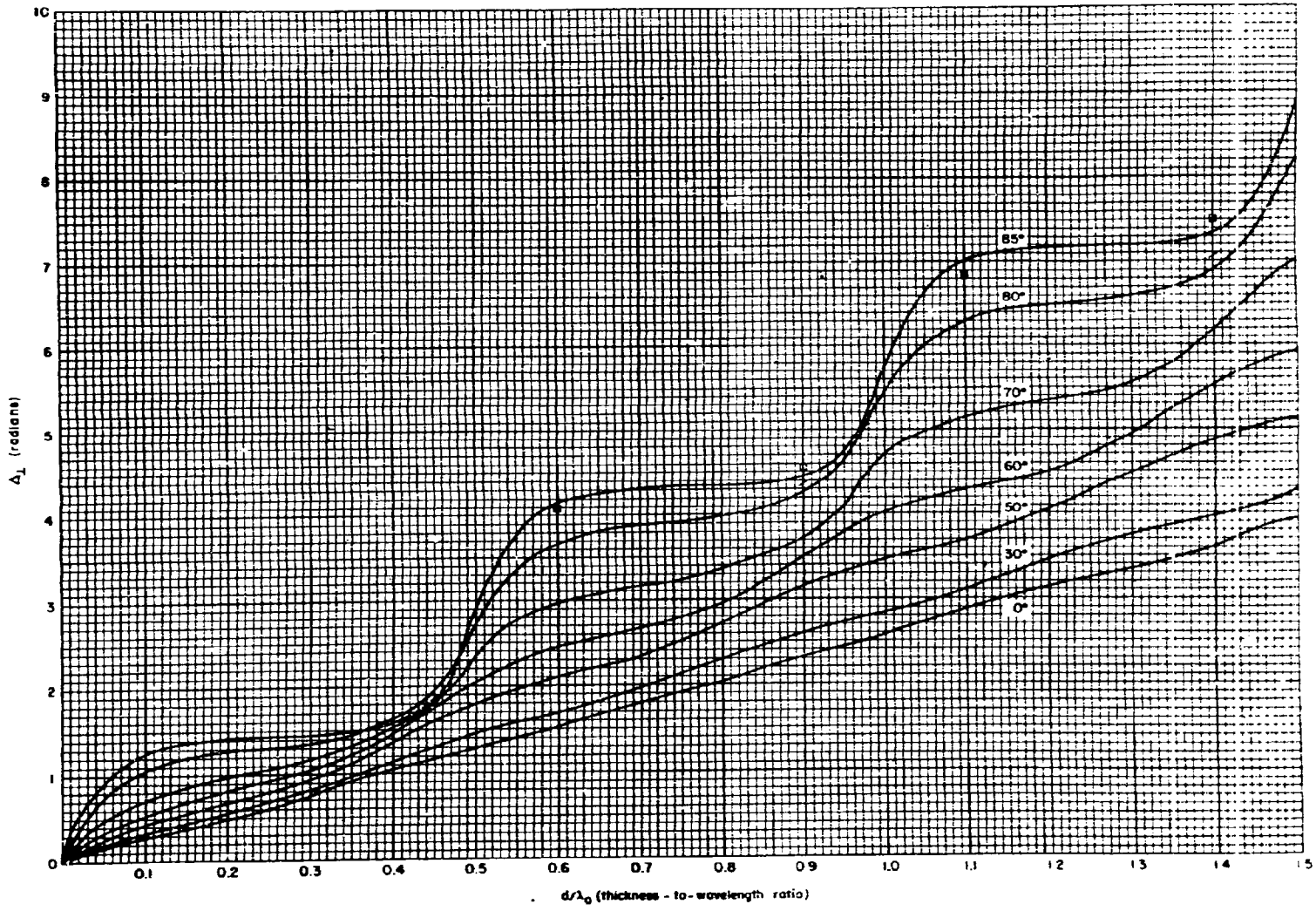


Figure 13–9. Insertion Phase Delay of a Plane Sheet of Dielectric Constant 2, Perpendicular Polarization, $\theta = 0°$ To 85°

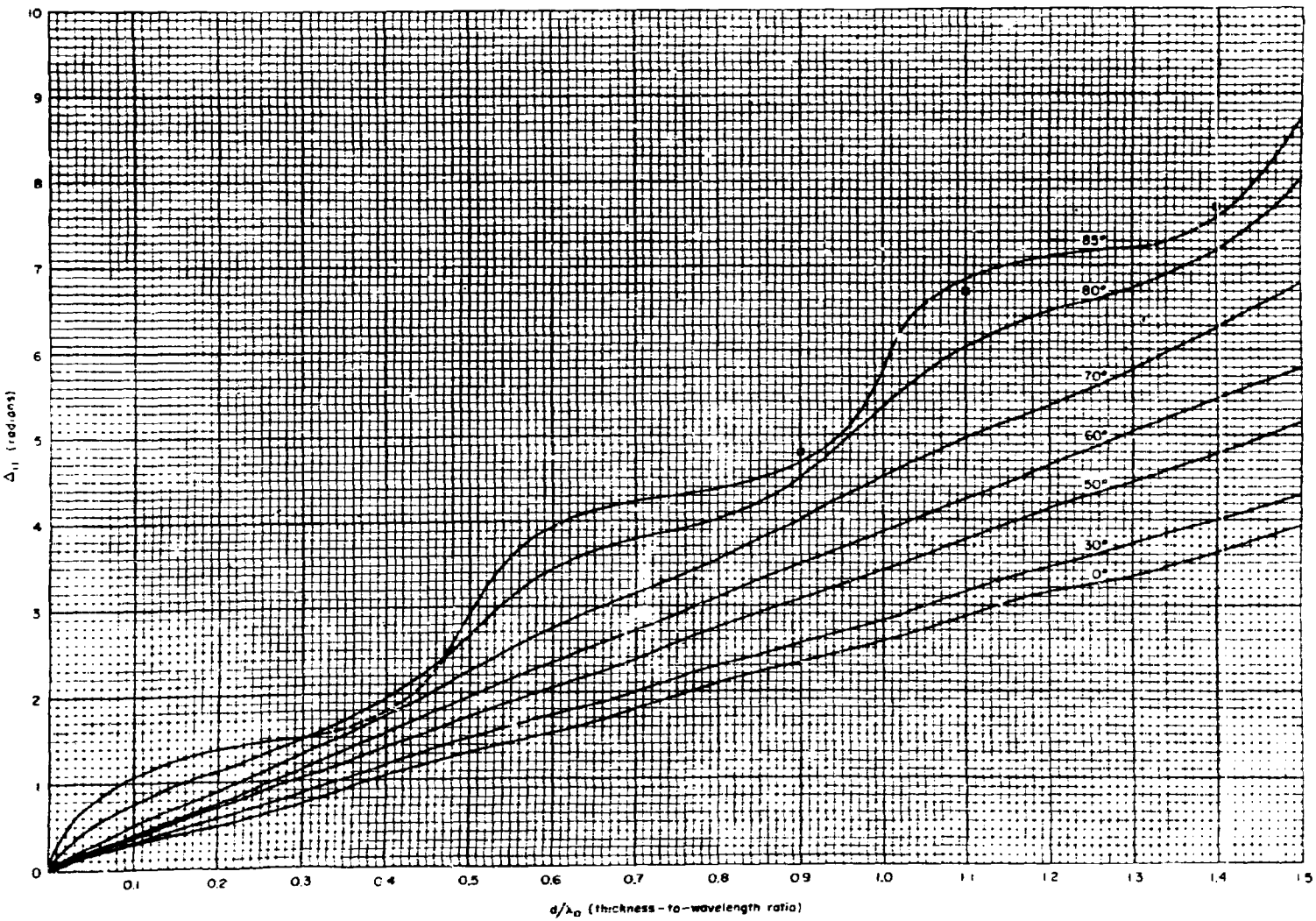


Figure 13–10. Insertion Phase Delay of a Plane Sheet of Dielectric Constant 2, Parallel Polarization, $\theta = 0°$ To 85°

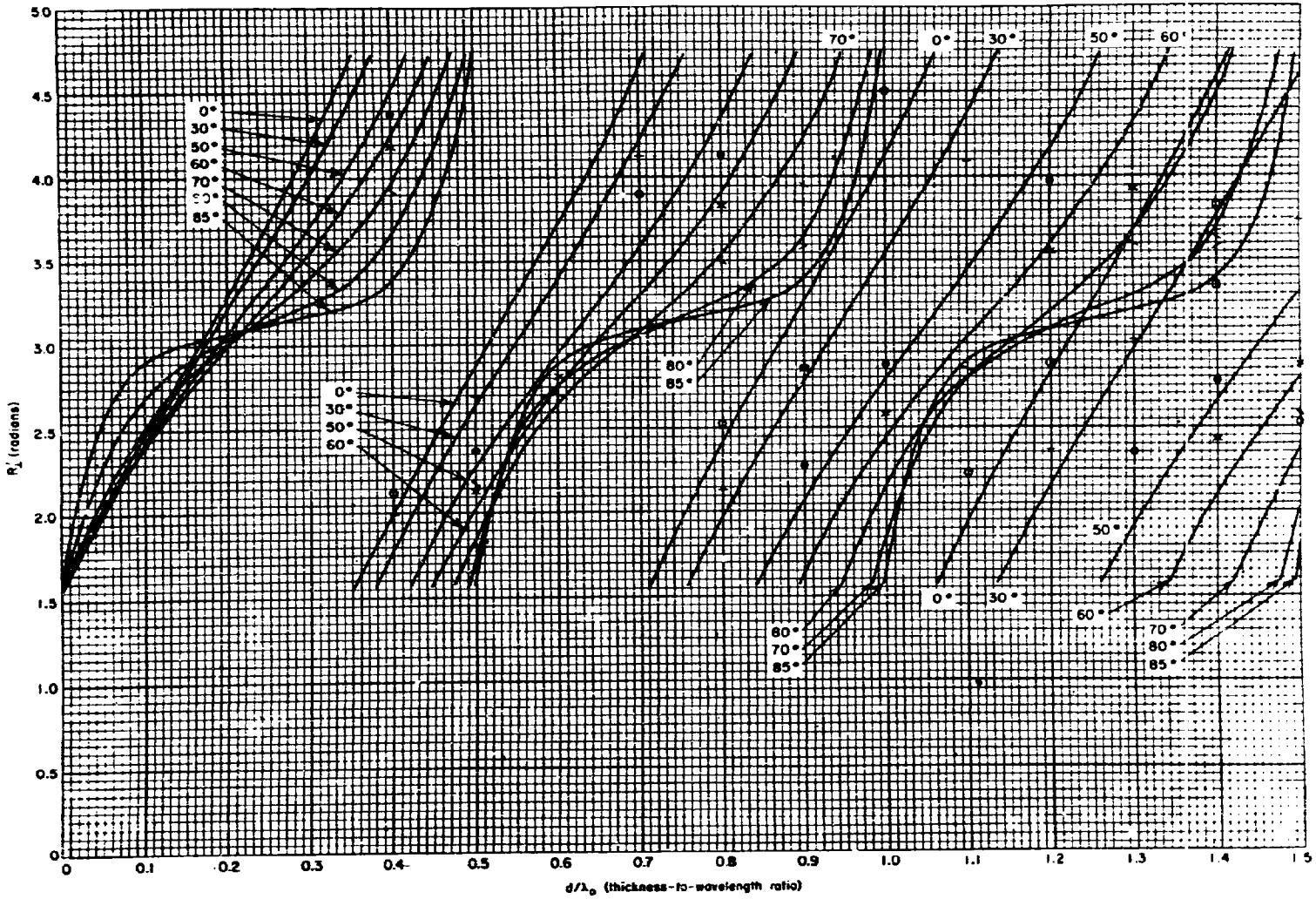


Figure 13–11. Reflection Phase Shift of Plane Sheet of Dielectric Constant 2, Perpendicular Polarization, $\theta = 0°$ To 85°

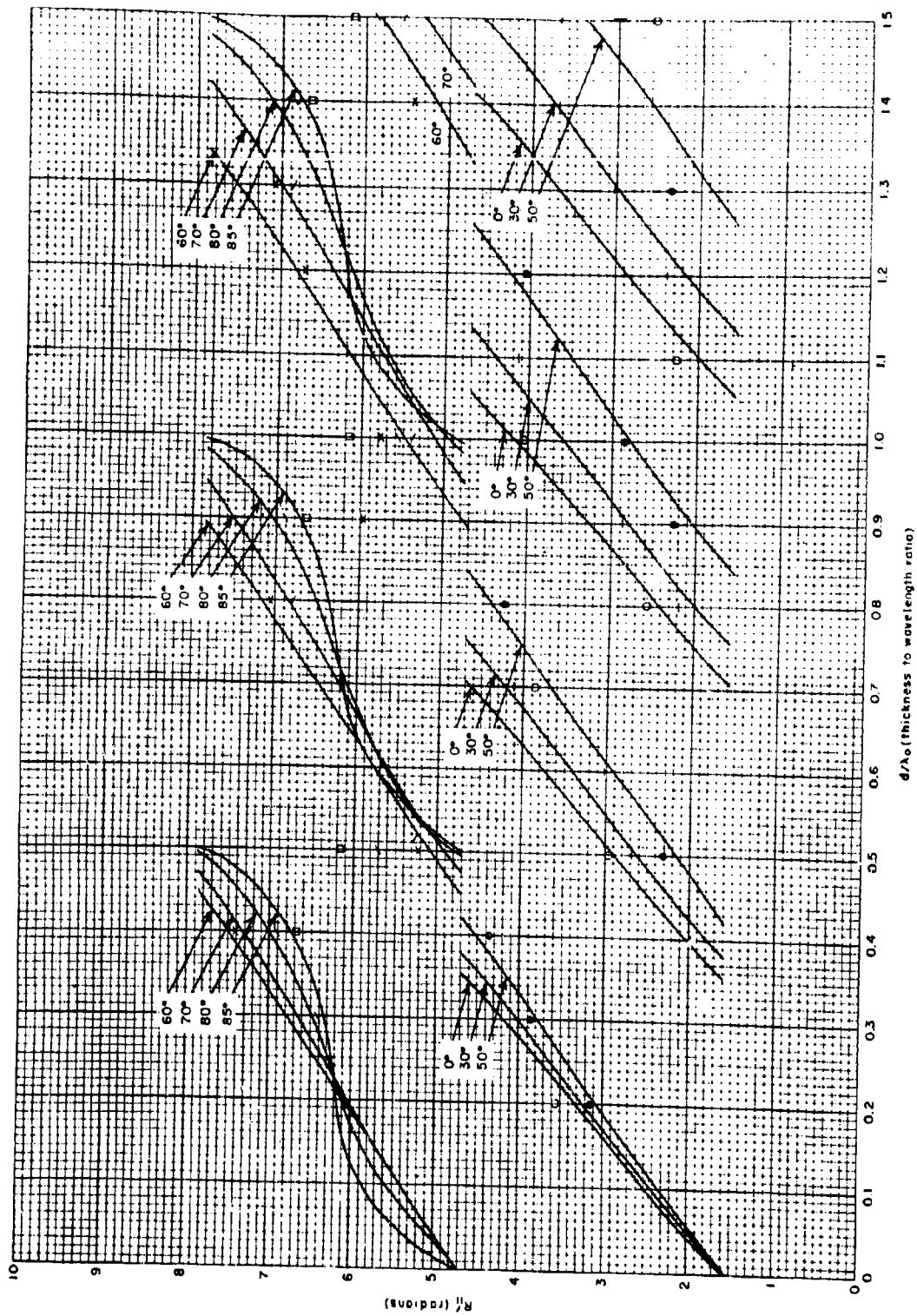


Figure 13–12. Reflection Phase Shift of Plane Sheet of Dielectric Constant 2, Parallel Polarization, $\phi = 0°$ To 85°

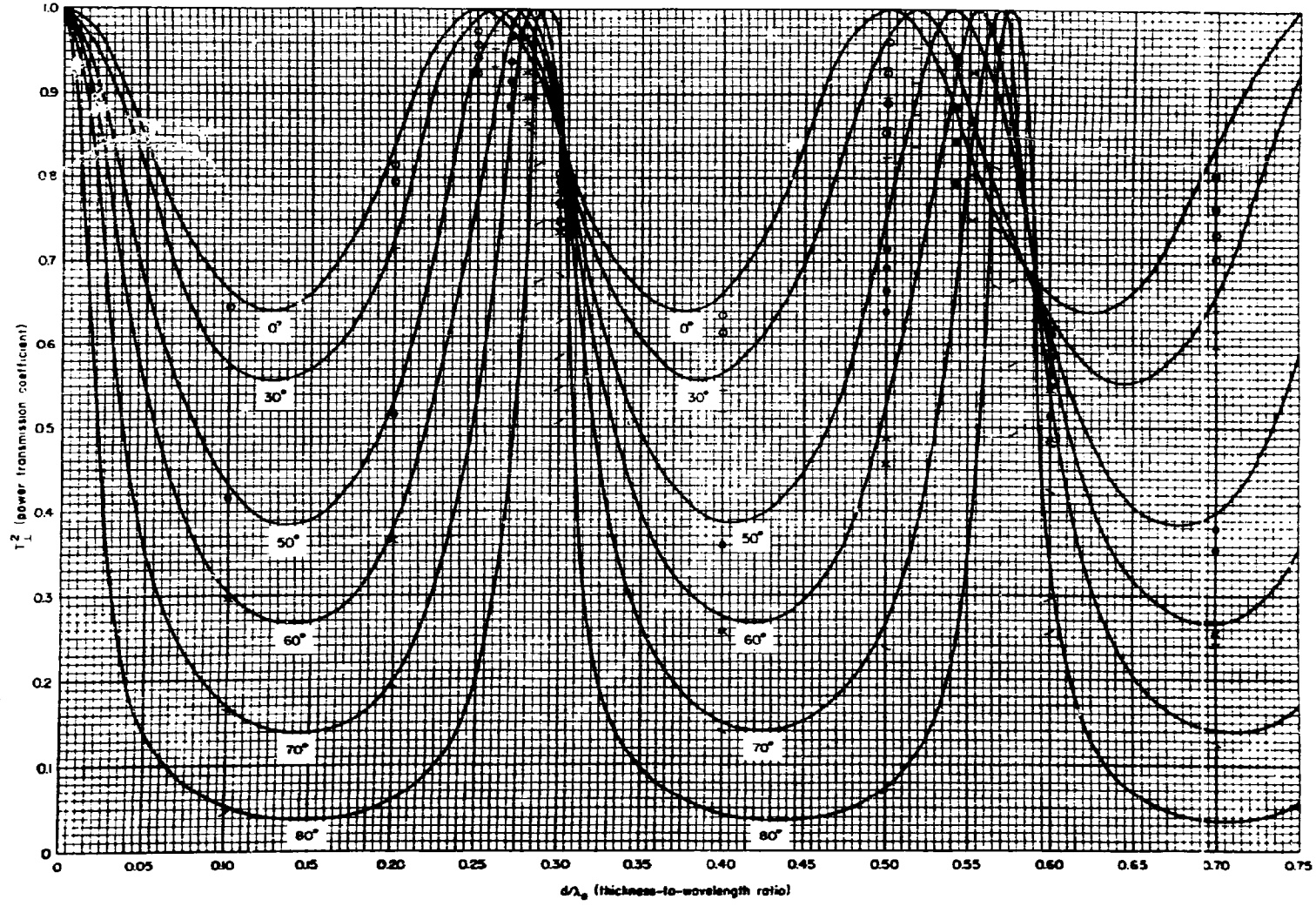


Figure 13–13. Power Transmission Coefficient of a Plane Sheet of Dielectric Constant 4, Perpendicular Polarization, θ = 0° To 80°

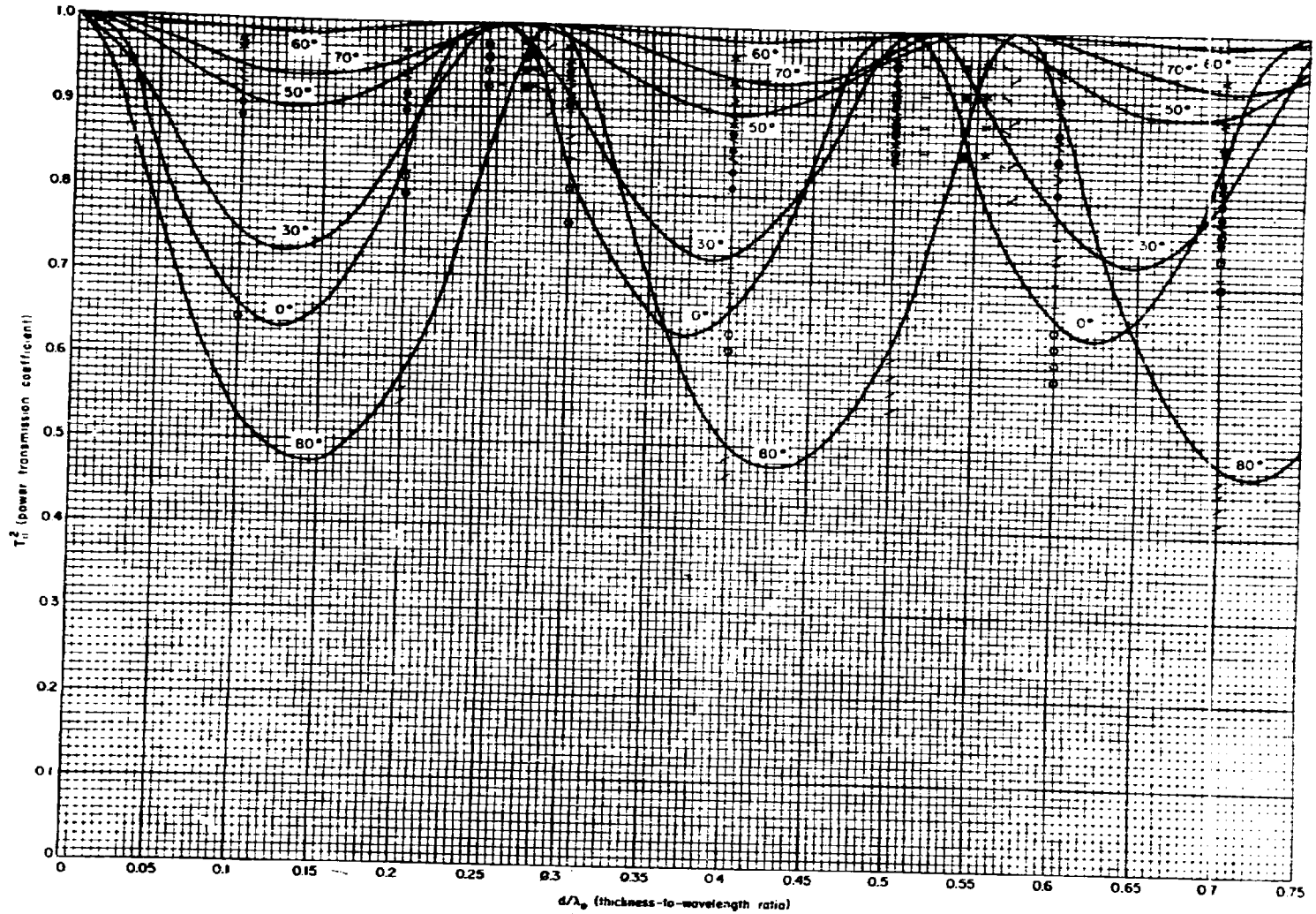


Figure 13–14. Power Transmission Coefficient of a Plane Sheet of Dielectric Constant 4, Parallel Polarization, $\theta = 0°$ To $80°$

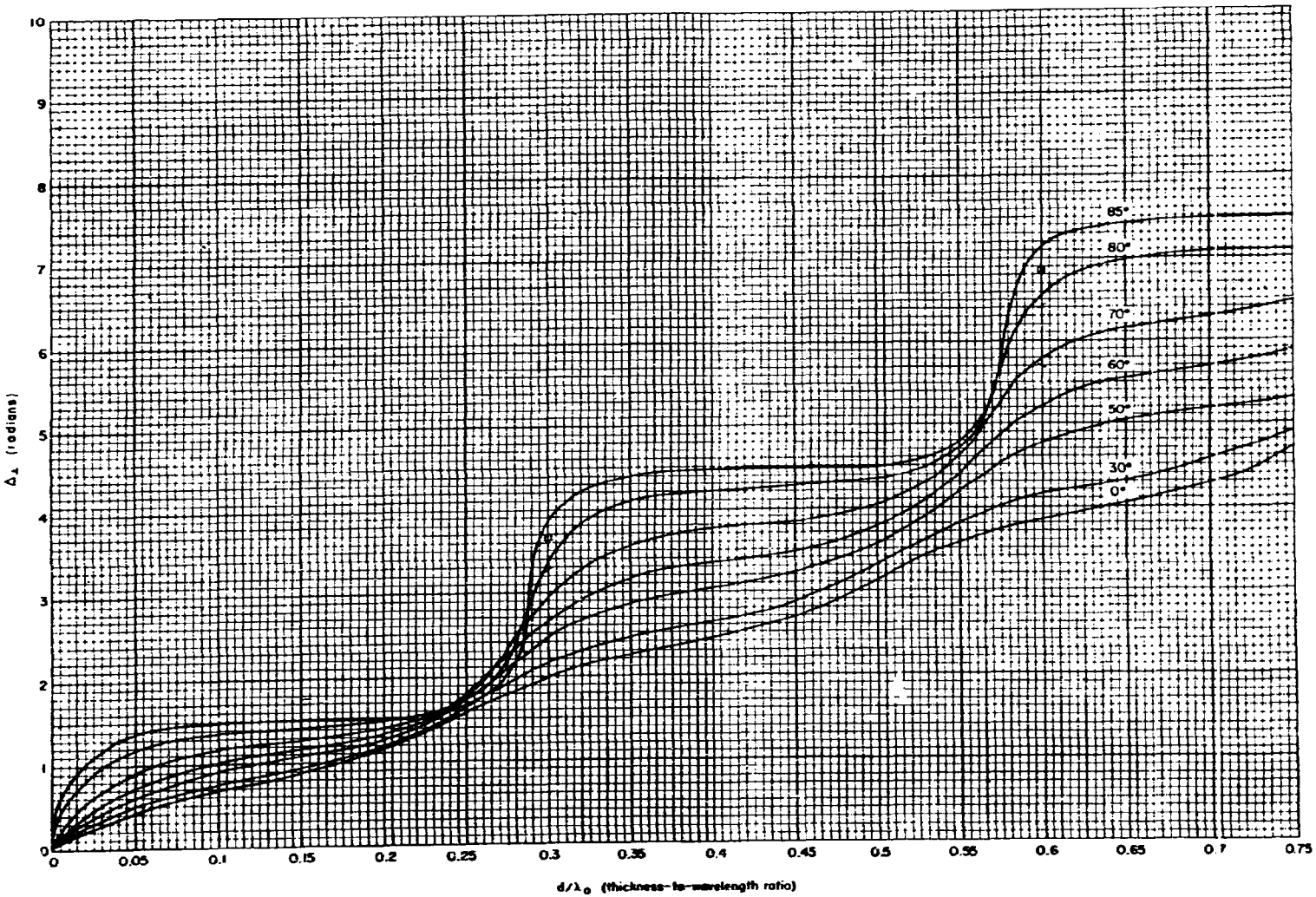


Figure 13–15. Insertion Phase Delay of a Plane Sheet of Dielectric Constant 4, Perpendicular Polarization, $\phi = 0°$ To 85°

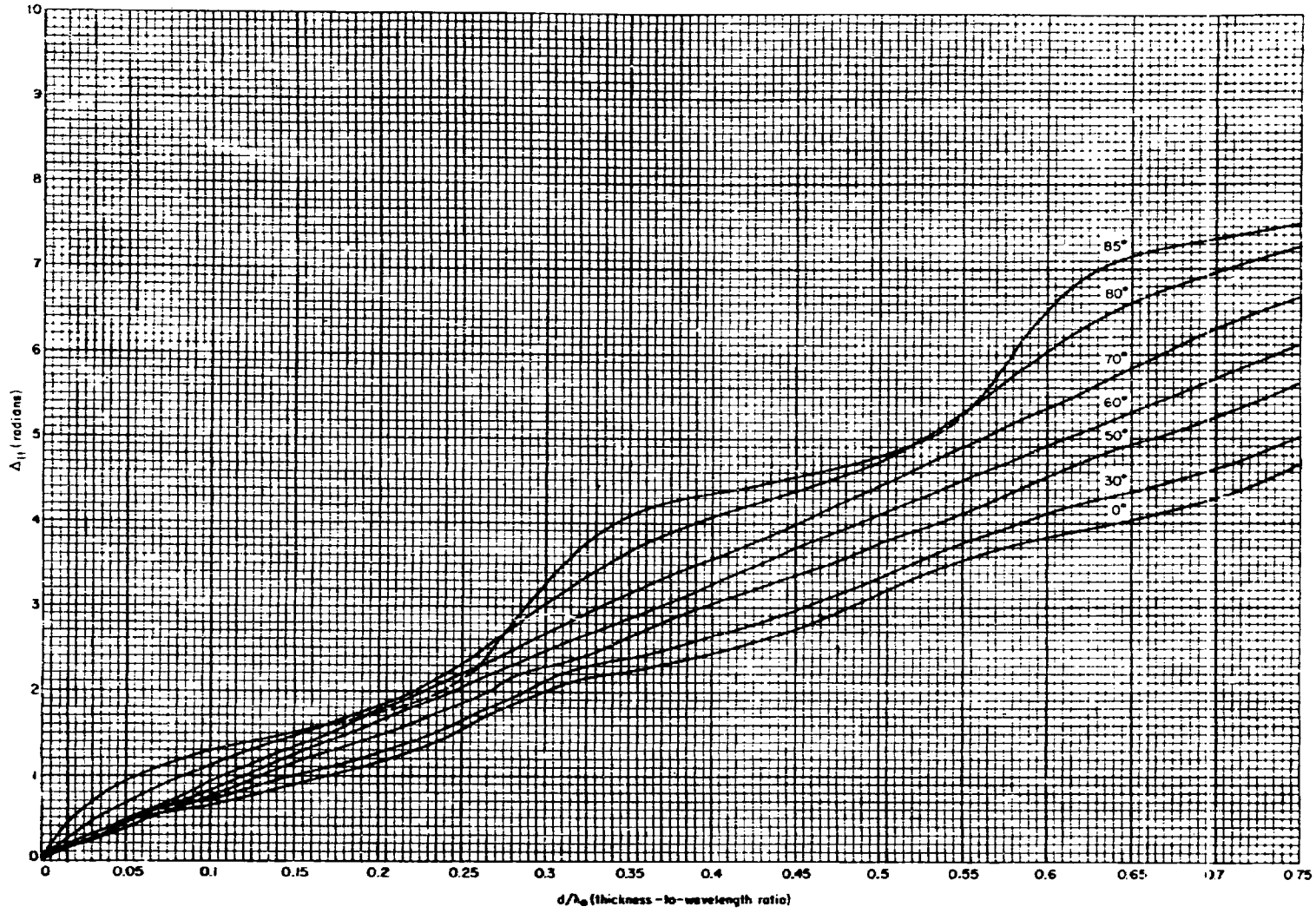


Figure 13–16. Insertion Phase Delay of a Plane Sheet of Dielectric Constant 4, Parallel Polarization, $\theta = 0°$ To 85°

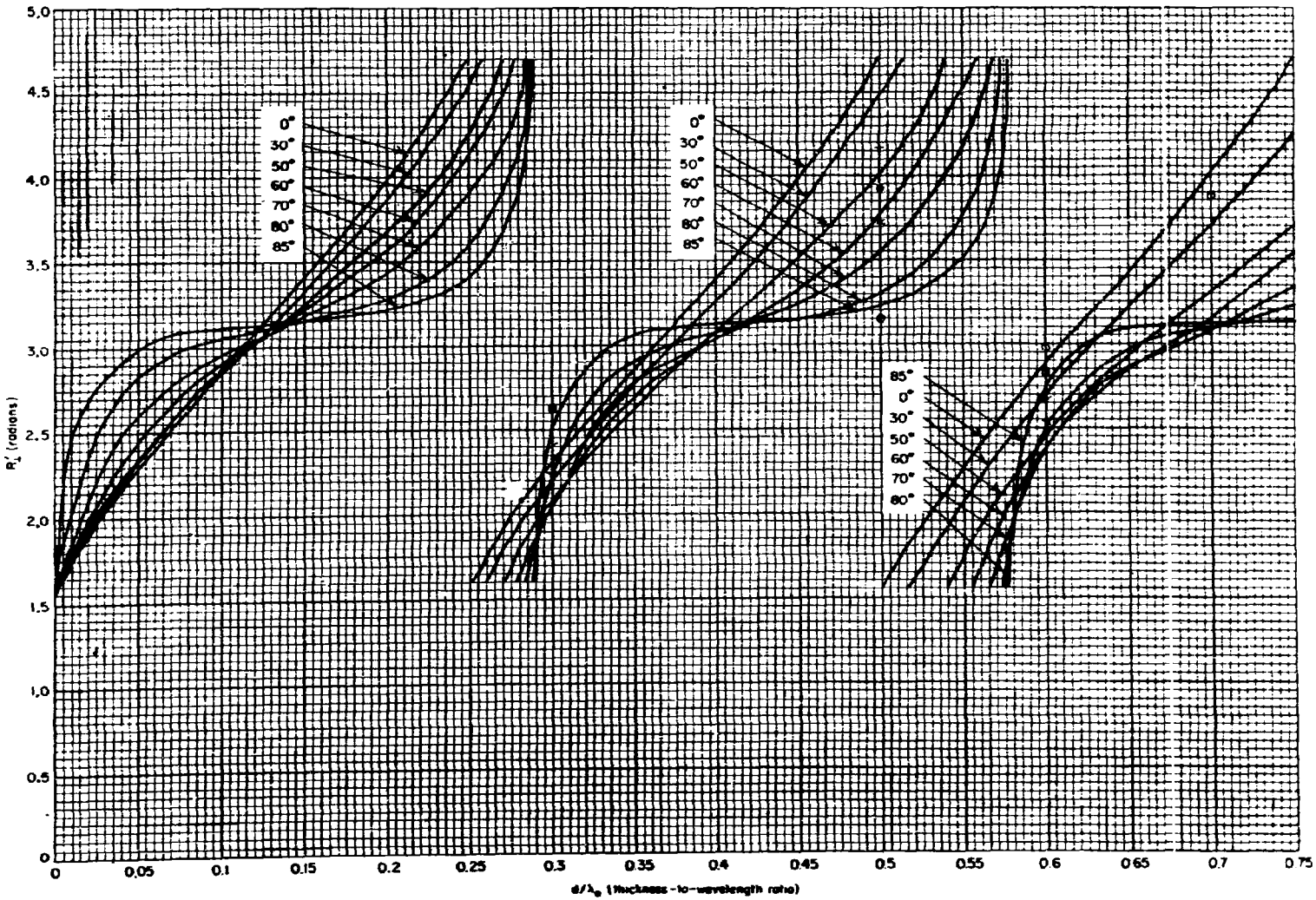


Figure 13–17. Reflection Phase Shift of a Plane Sheet of Dielectric Constant 4, Perpendicular Polarization, $\theta = 0°$ To $85°$

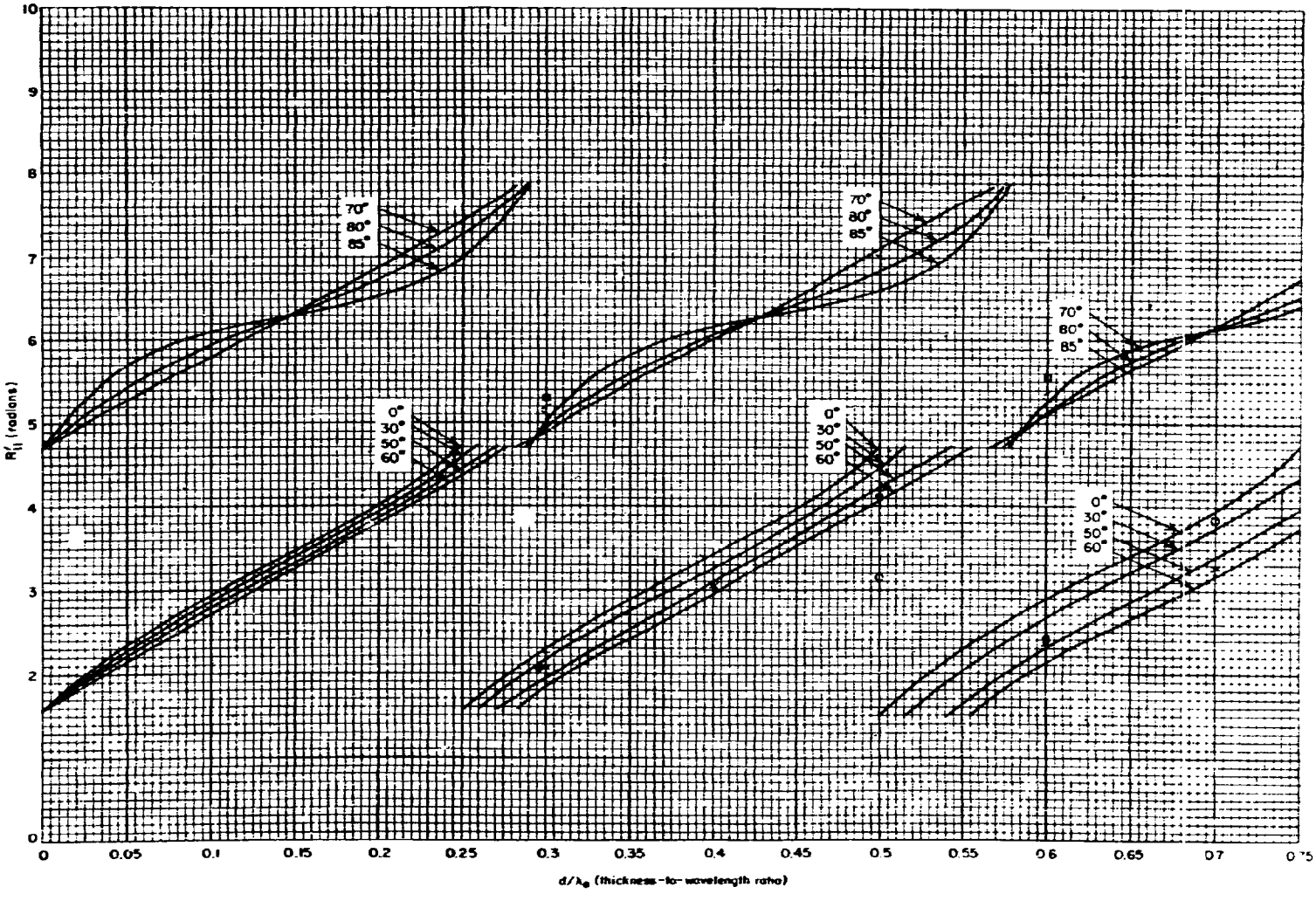


Figure 13–18. Reflection Phase Shift of a Plane Sheet of Dielectric Constant 4, Parallel Polarization, $\theta = 0°$ To 85°

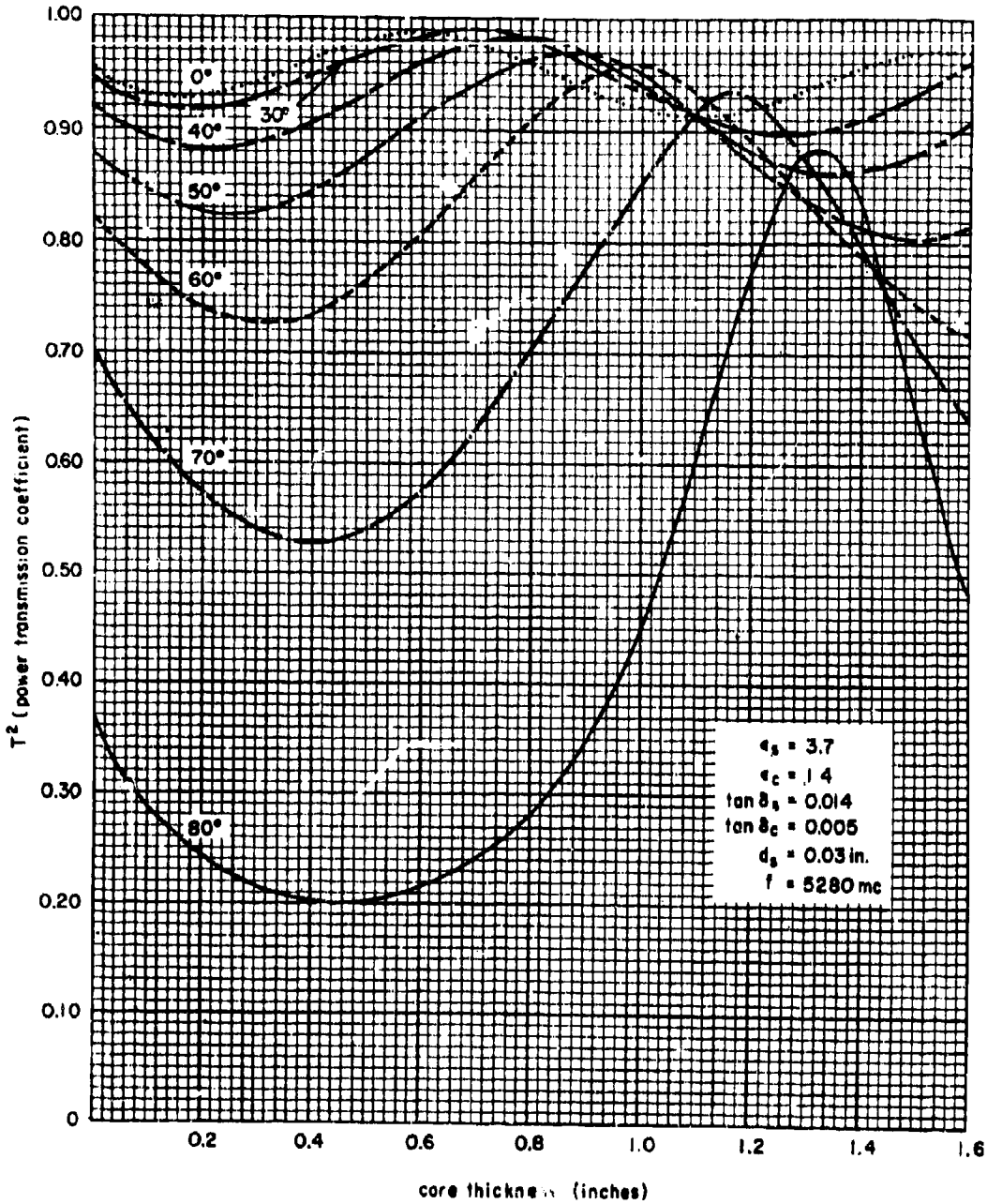


Figure 13-19. Power Transmission Versus Core Thickness for an "A" Sandwich for Various Angles of Incidence at 5280 mc With Perpendicular Polarization

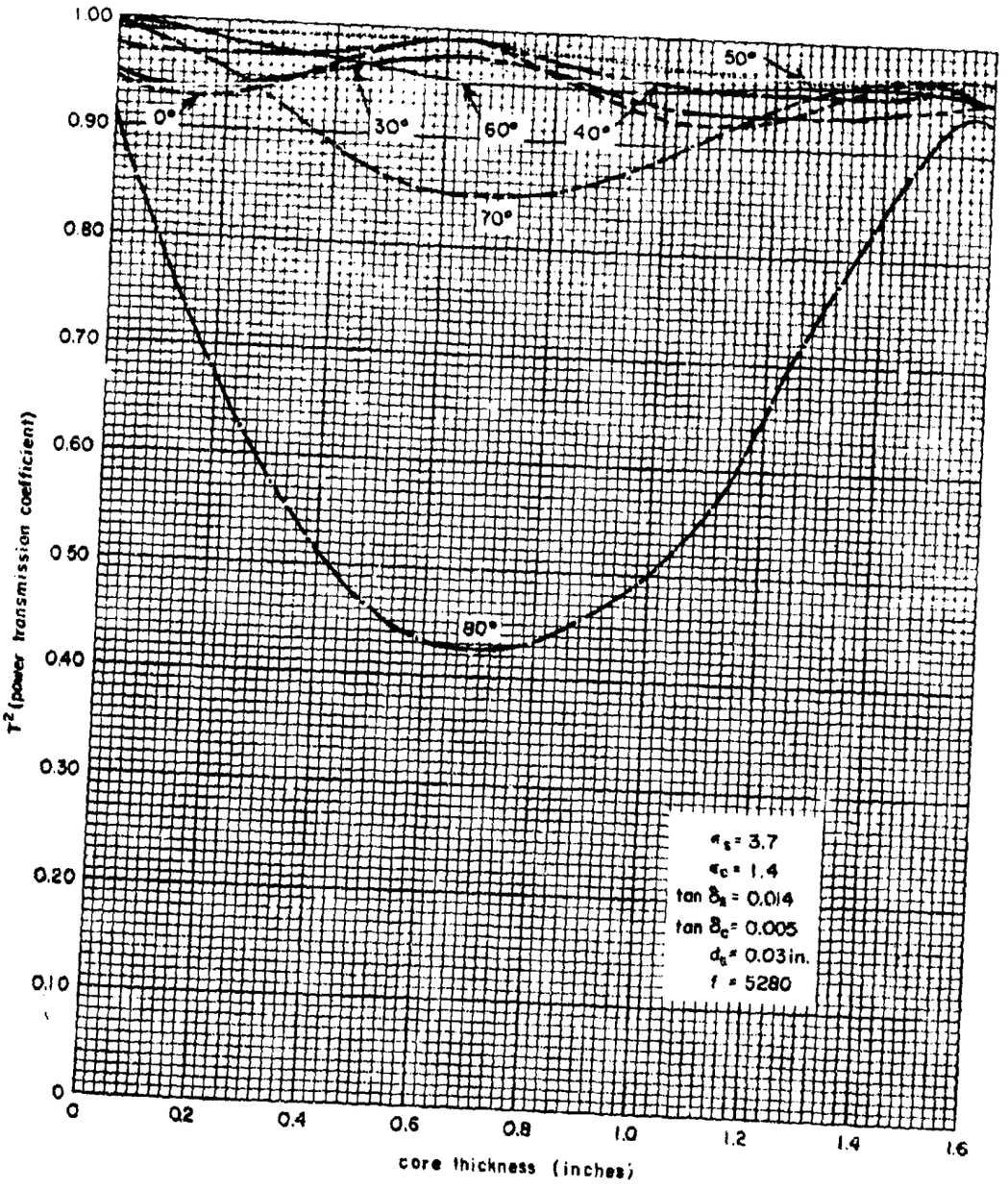


Figure 13–20. Power Transmission Versus Core Thickness for an "A" Sandwich for Various Angles of Incidence At 5280 mc With Parallel Polarization

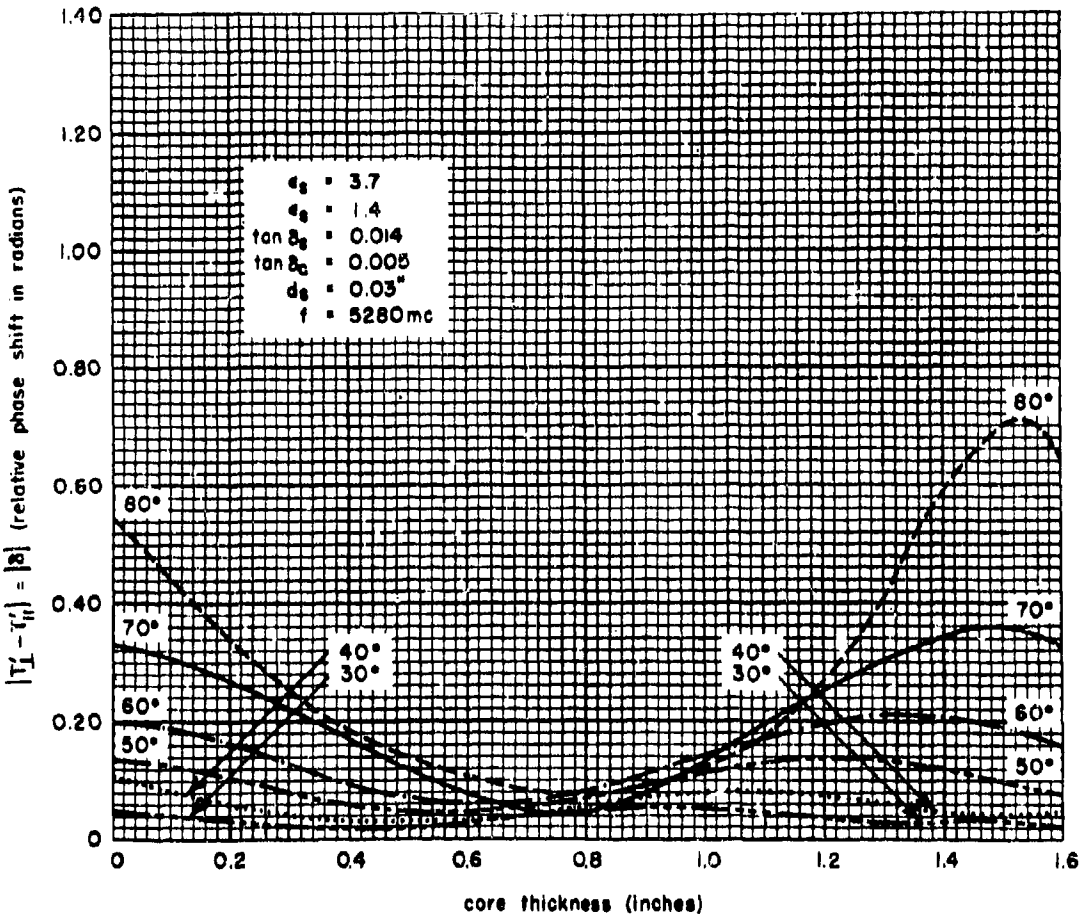


Figure 13–21. Relative Phase Shift Versus Core Thickness for an "A" Sandwich for Various Angles of Incidence at 5280 mc

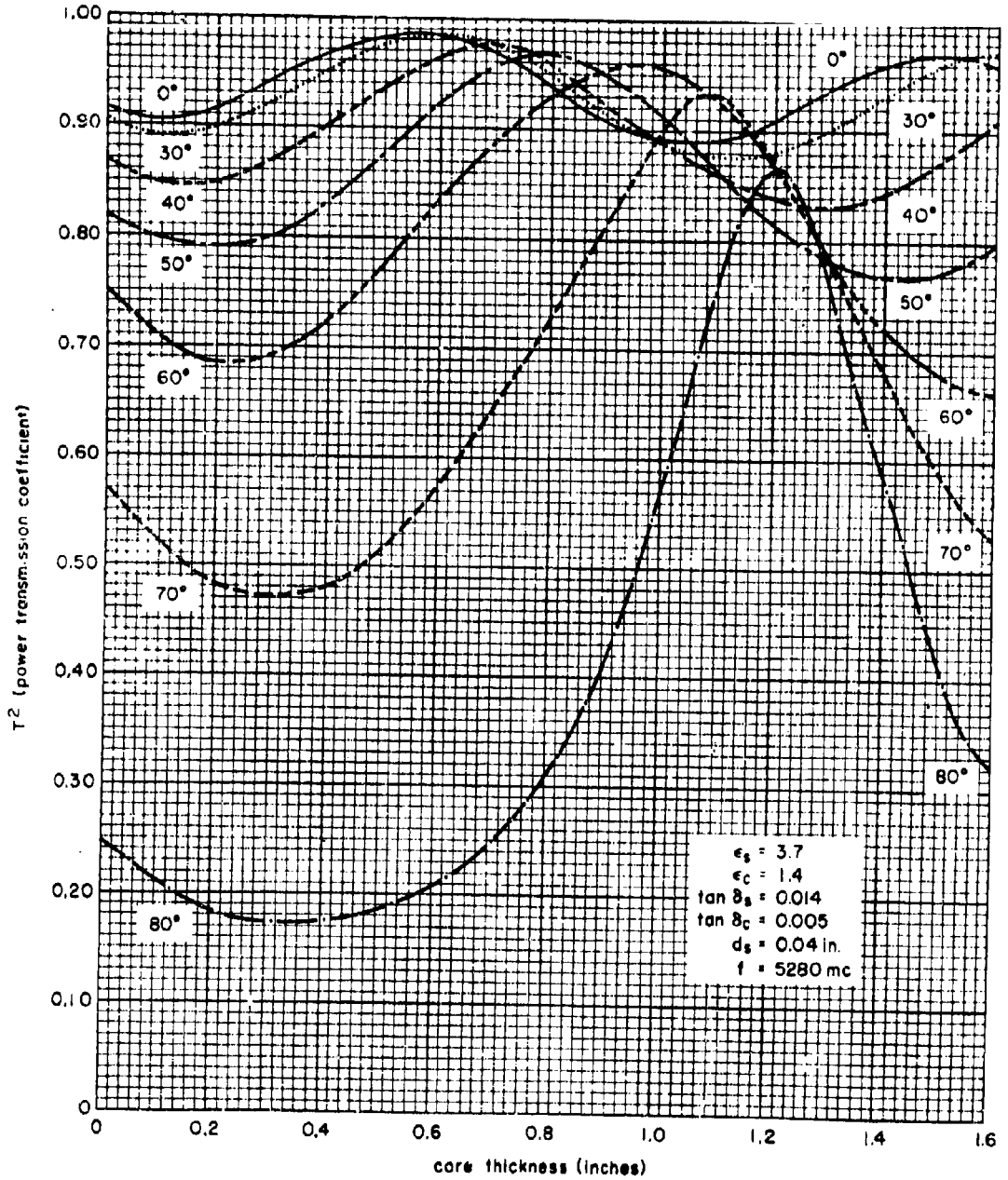


Figure 13–22. Power Transmission Versus Core Thickness for an "A" Sandwich for Various Angles of Incidence At 5280 mc With Perpendicular Polarization

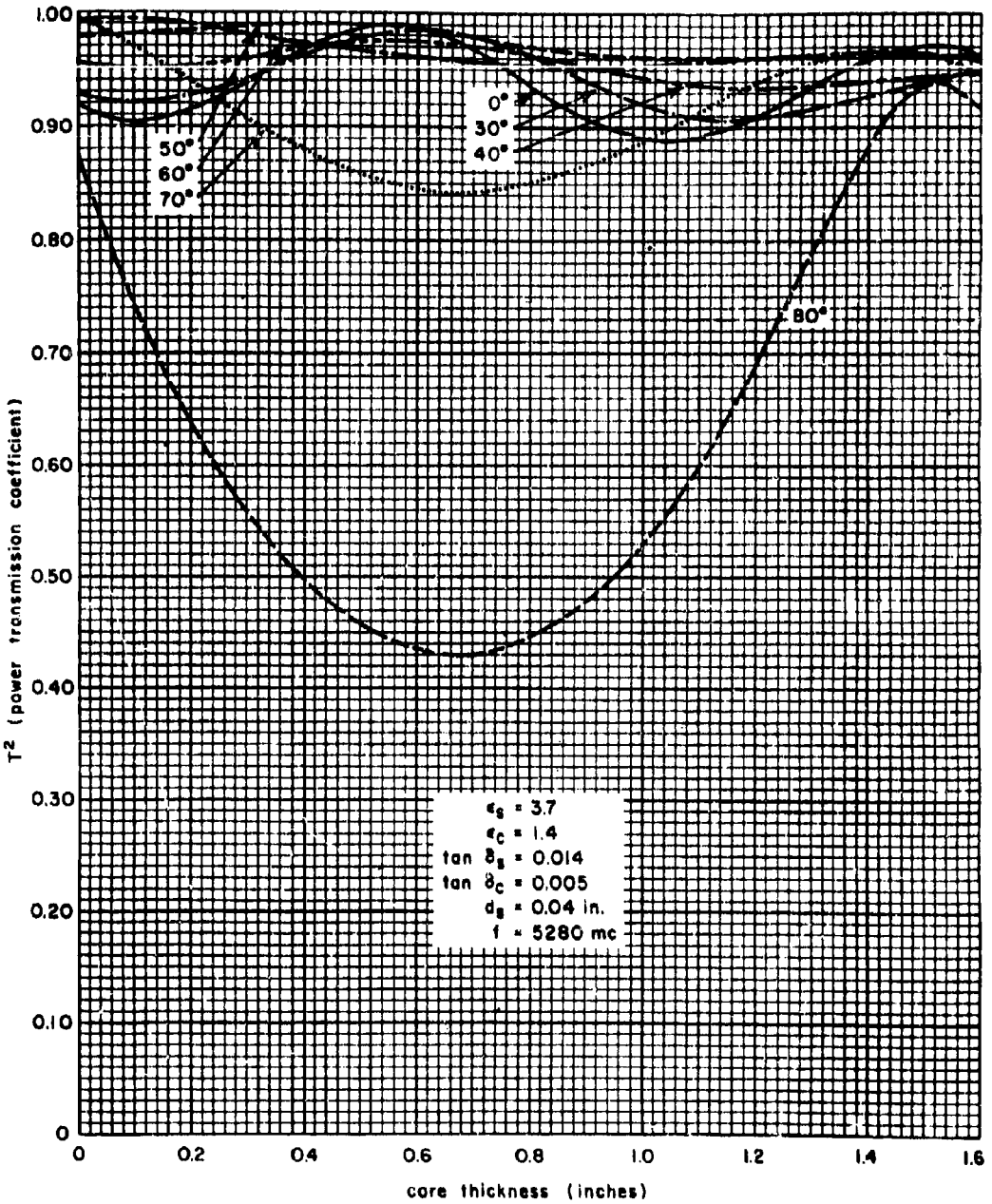


Figure 13–22. Power Transmission Versus Core Thickness for an "A" Sandwich for Various Angles of Incidence at 5280 mc With Parallel Polarization

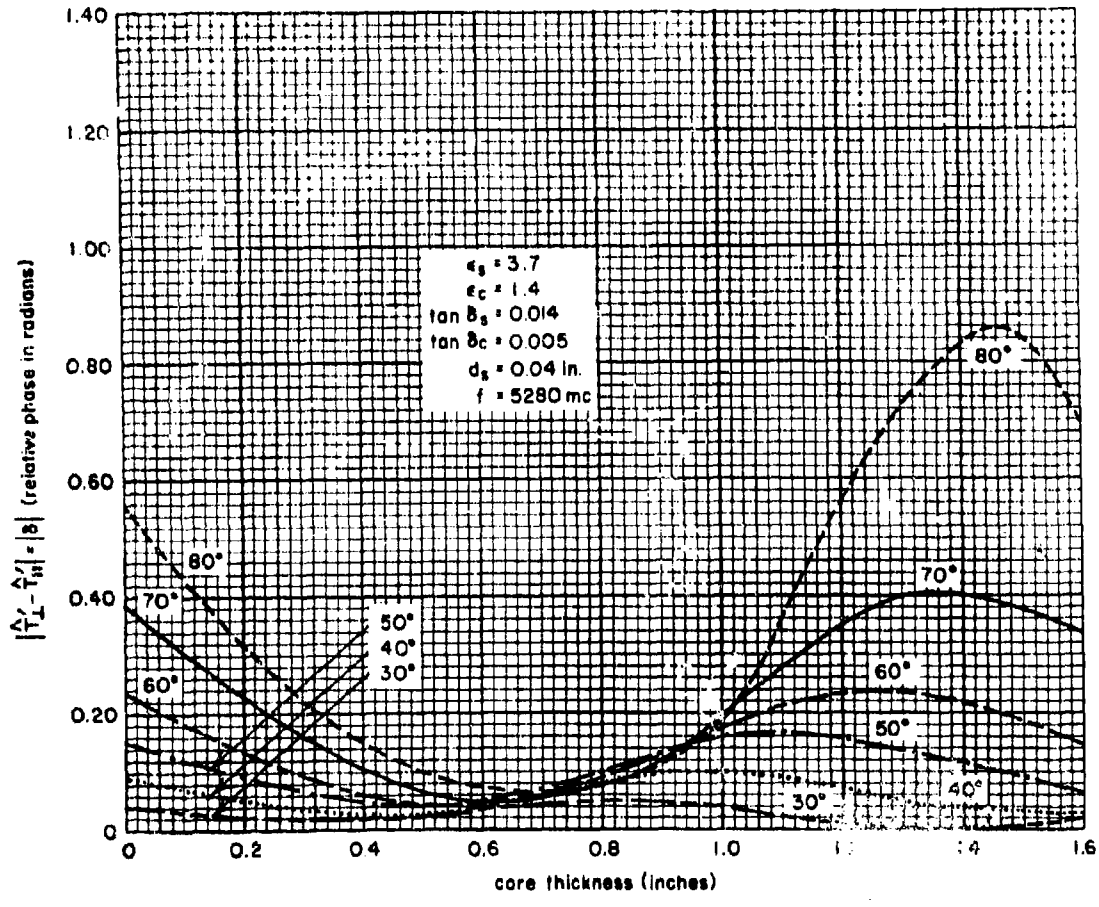


Figure 13–24. Relative Phase Shift Versus Core Thickness for an "A" Sandwich for Various Angles of Incidence at 5280 mc

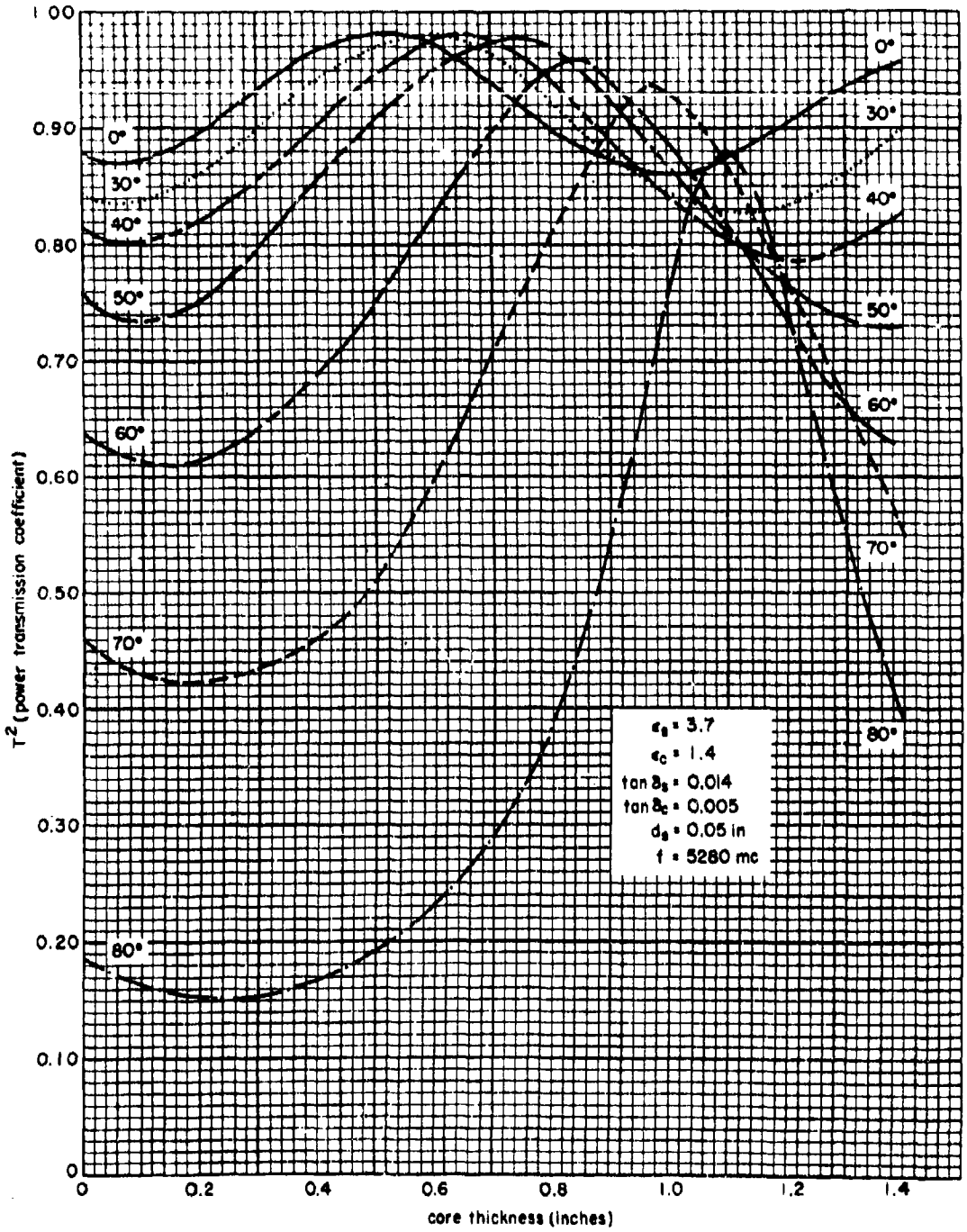


Figure 13–25. Power Transmission Versus Core Thickness for an "A" Sandwich for Various Angles of Incidence at 5260 mc With Perpendicular Polarization

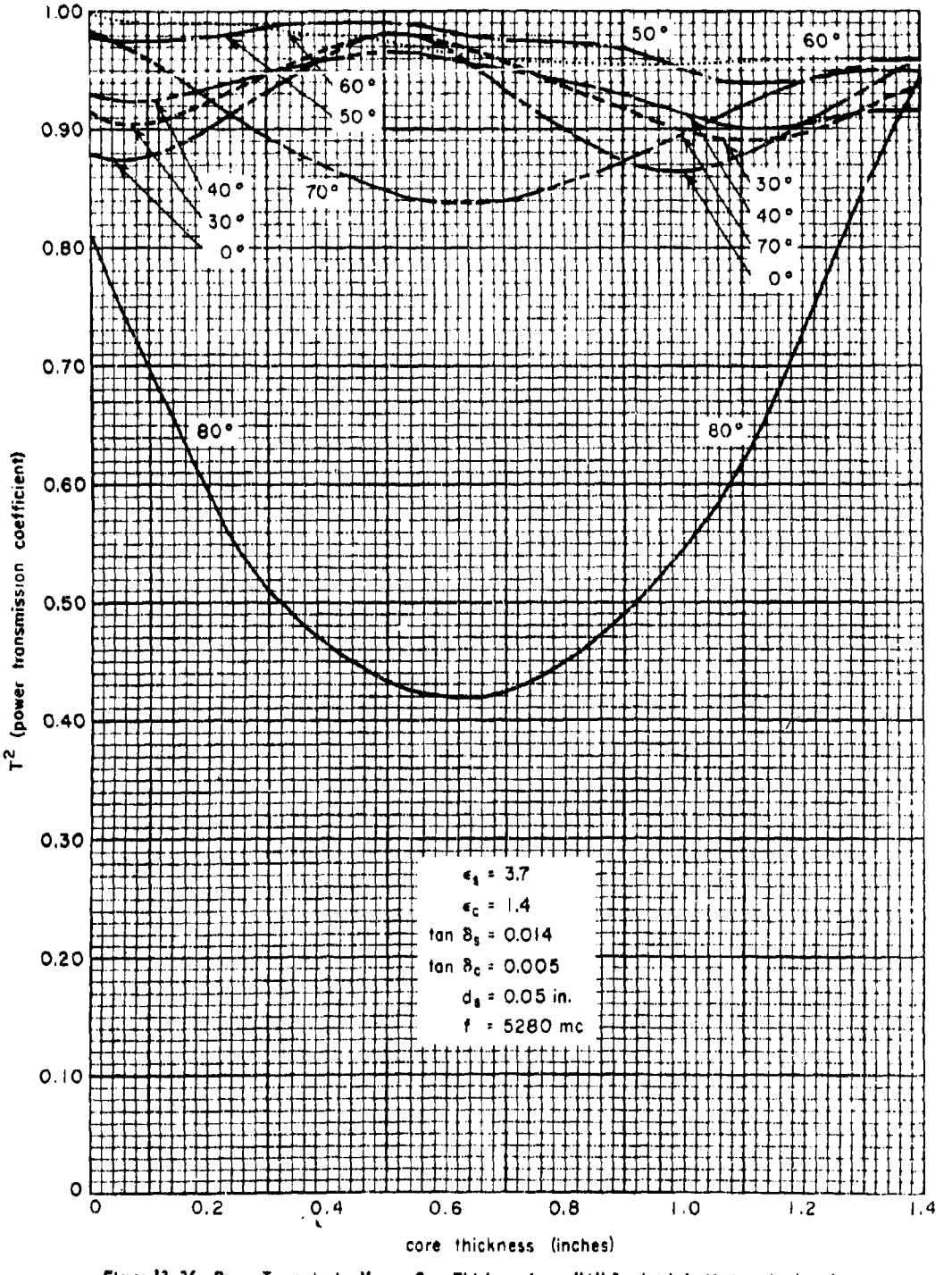


Figure 13-26. Power Transmission Versus Core Thickness for an "A" Sandwich for Various Angles of Incidence at 5280 mc With Parallel Polarization

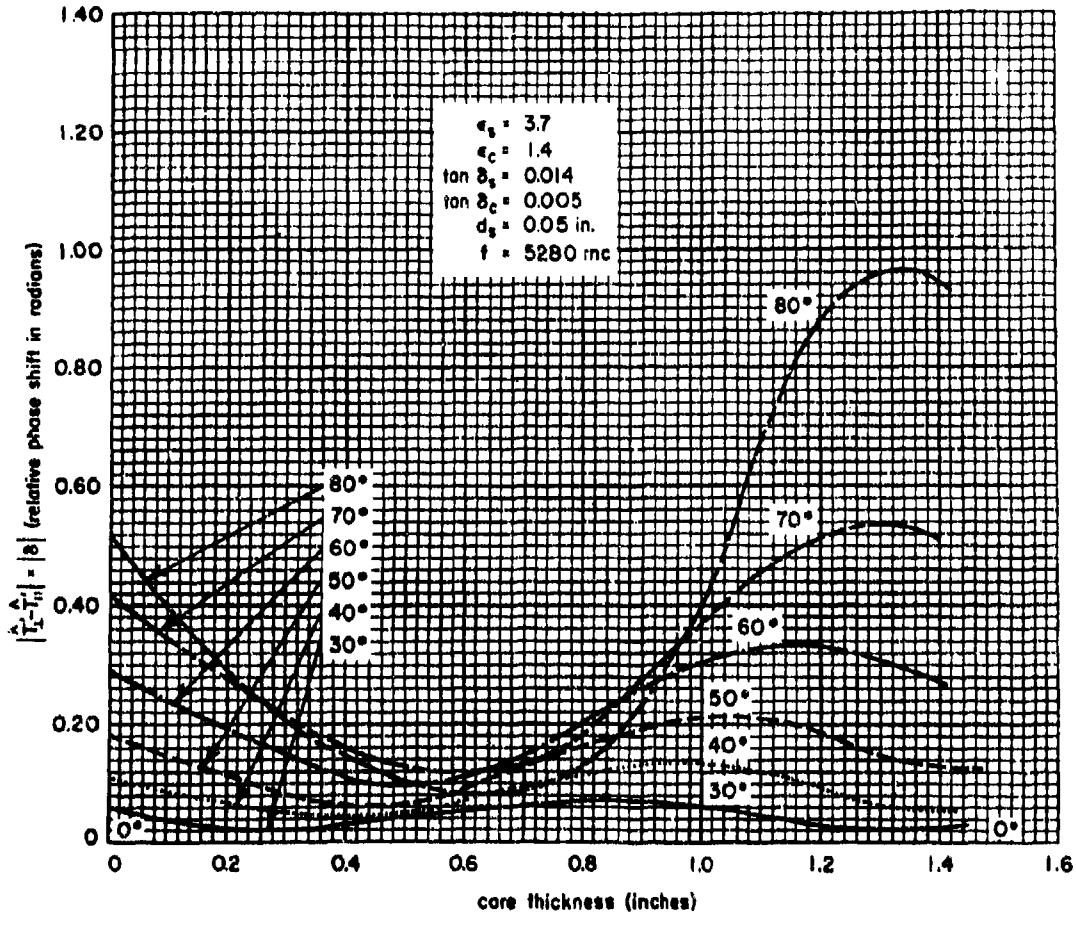


Figure 13–27. Relative Phase Shift Versus Core Thickness for an "A" Sandwich for Various Angles of Incidence at 5280 mc

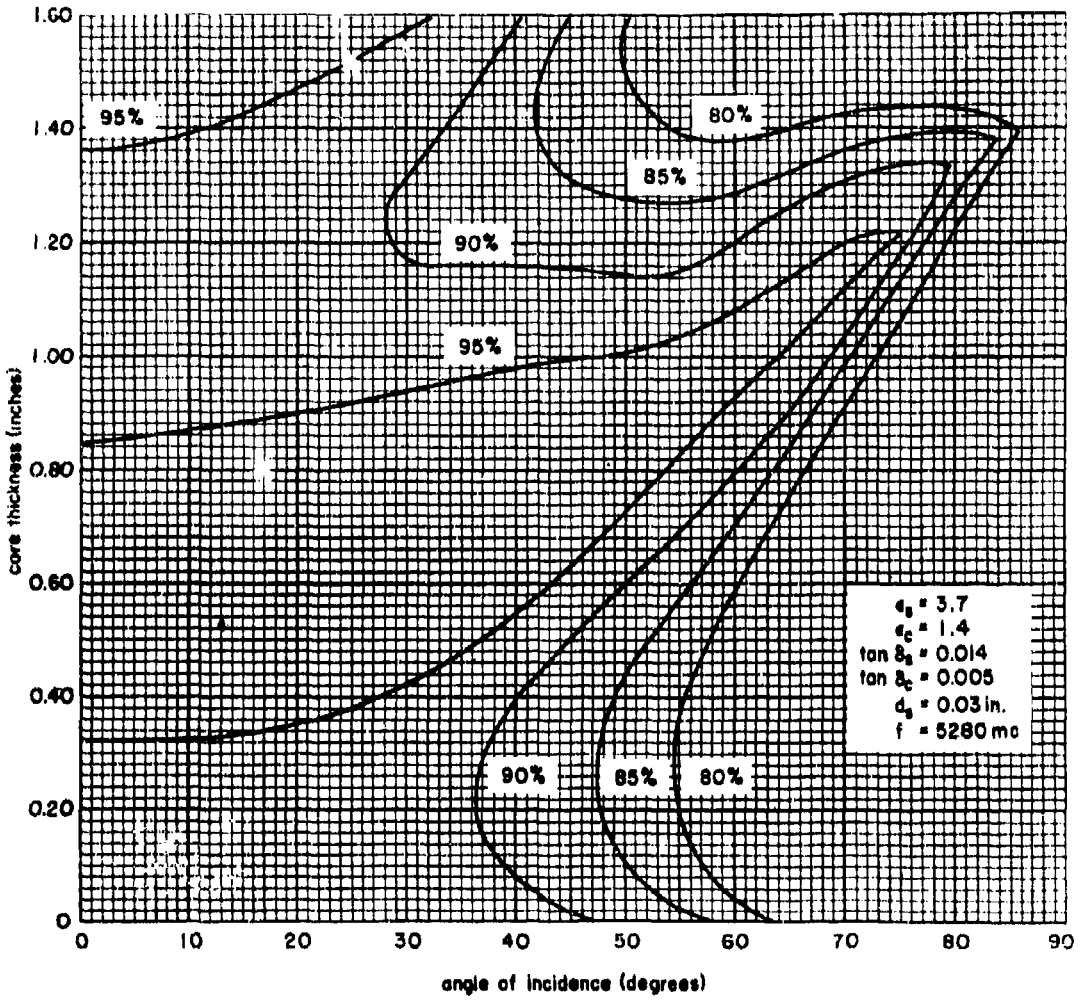


Figure 13–28. Constant Power Transmission Contours for an "A" Sandwich for Various Angles of Incidence and Core Thicknesses at 5280 mc With Perpendicular Polarization

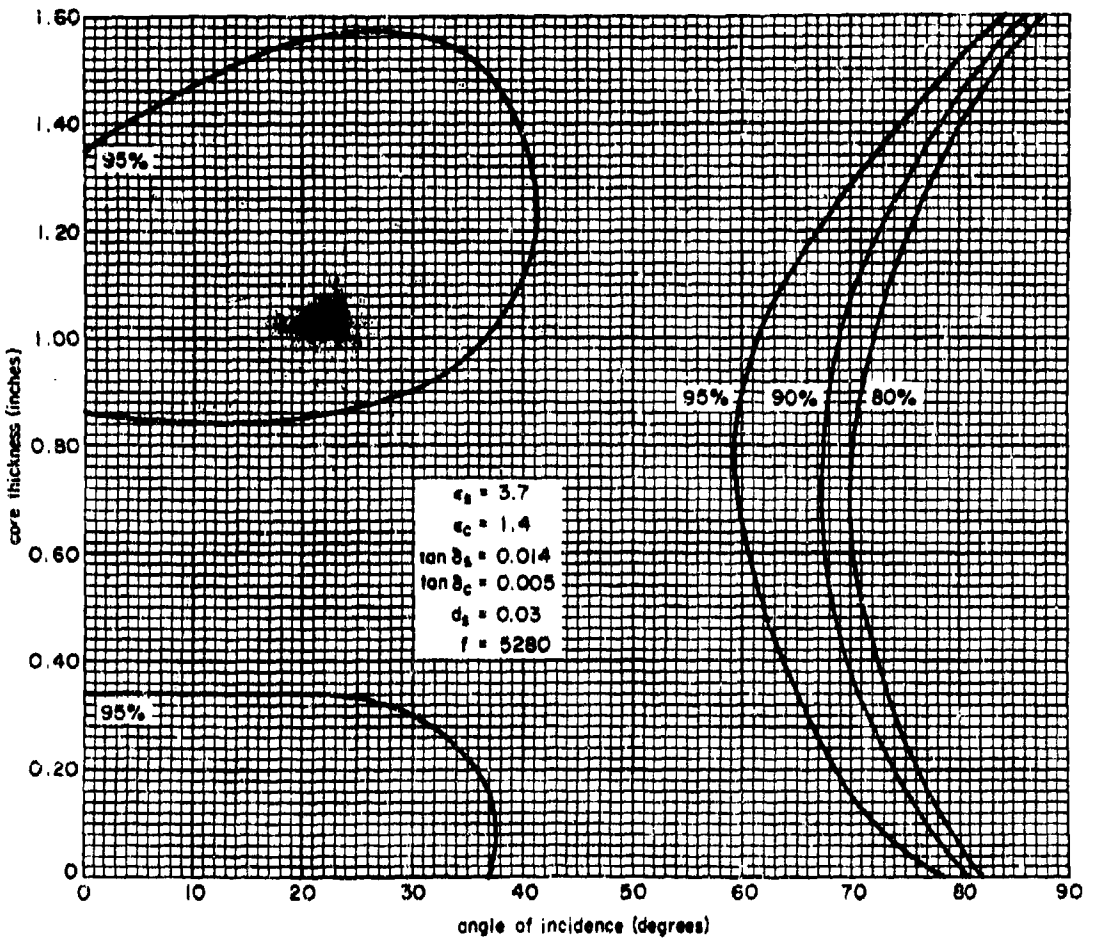


Figure 13-29. Constant Power Transmission Contours for an "A" Sandwich for Various Angles of Incidence and Core Thicknesses at 5280 mc With Parallel Polarization

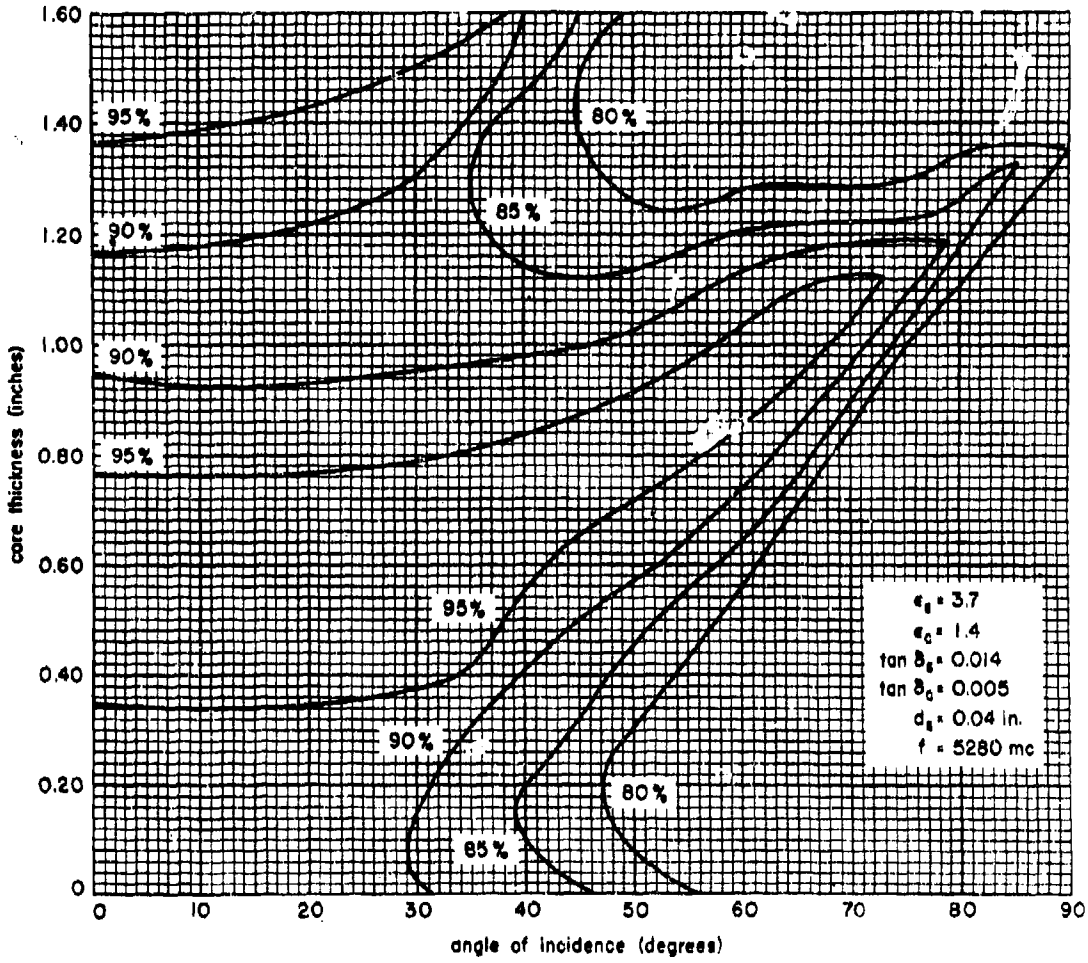


Figure 13–30. Constant Power Transmission Contours for an "A" Sandwich for Various Angles of Incidence and Core Thicknesses at 5280 mc With Perpendicular Polarization

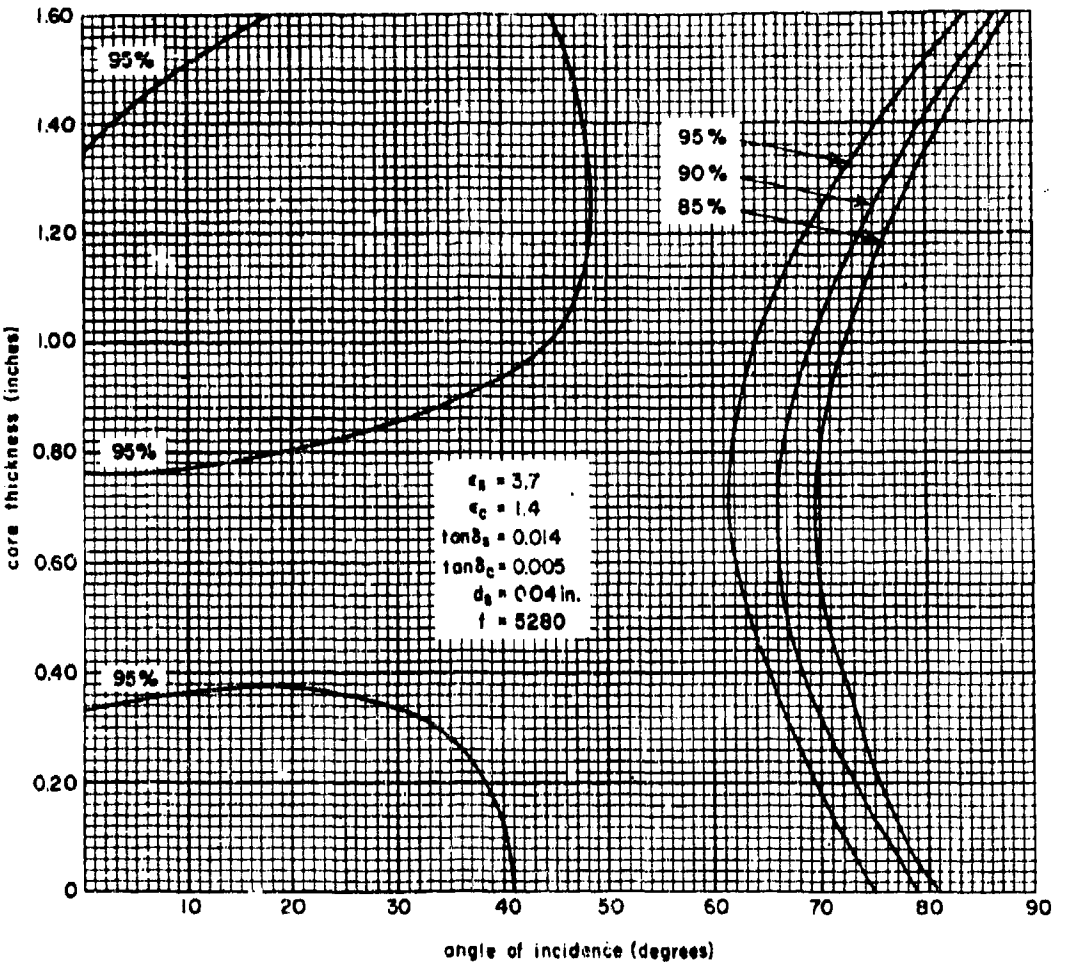


Figure 13-31. Constant Power Transmission Contours for an "A" Sandwich for Various Angles of Incidence and Core Thicknesses at 5280 mc With Parallel Polarization

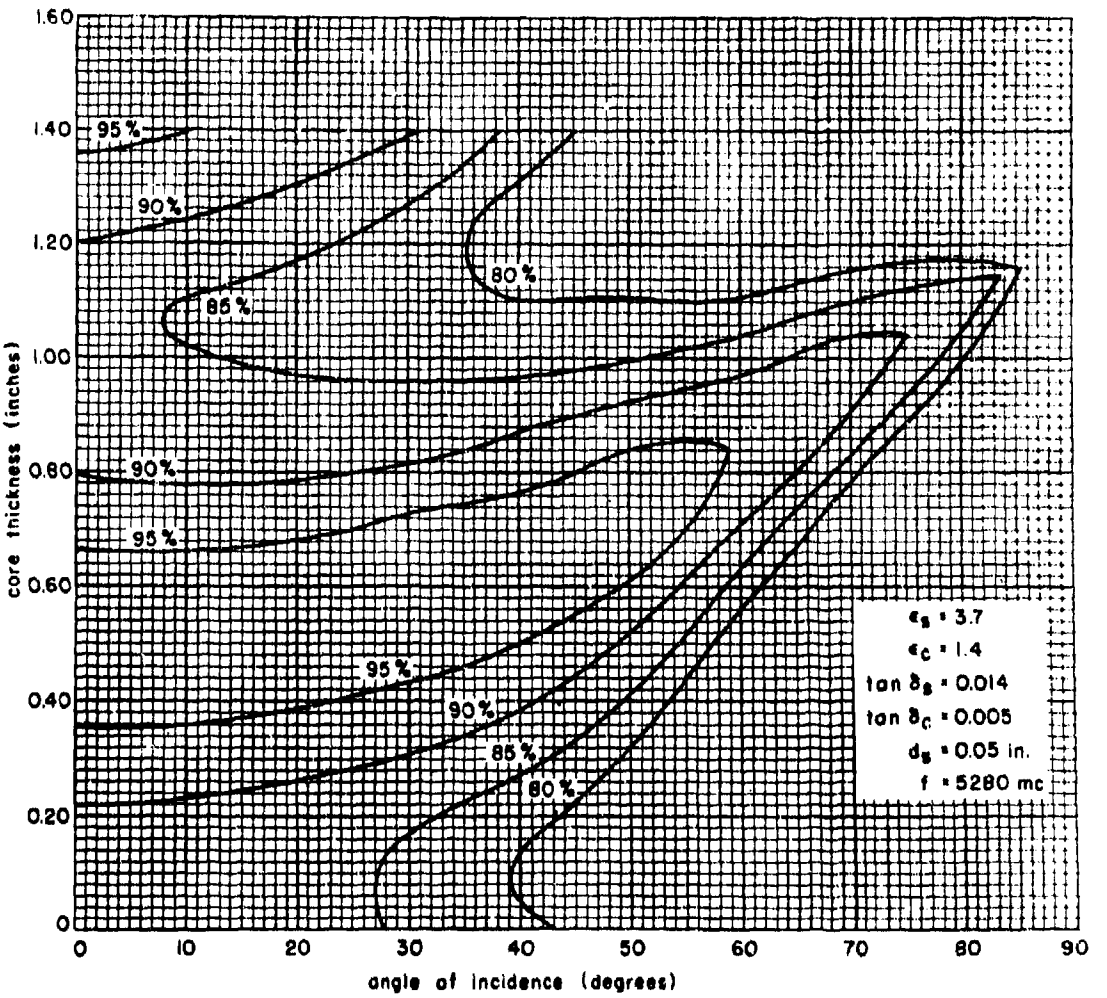


Figure 13-32. Constant Power Transmission Contours for an "A" Sandwich for Various Angles of Incidence and Core Thicknesses at 5280 mc With Perpendicular Polarization

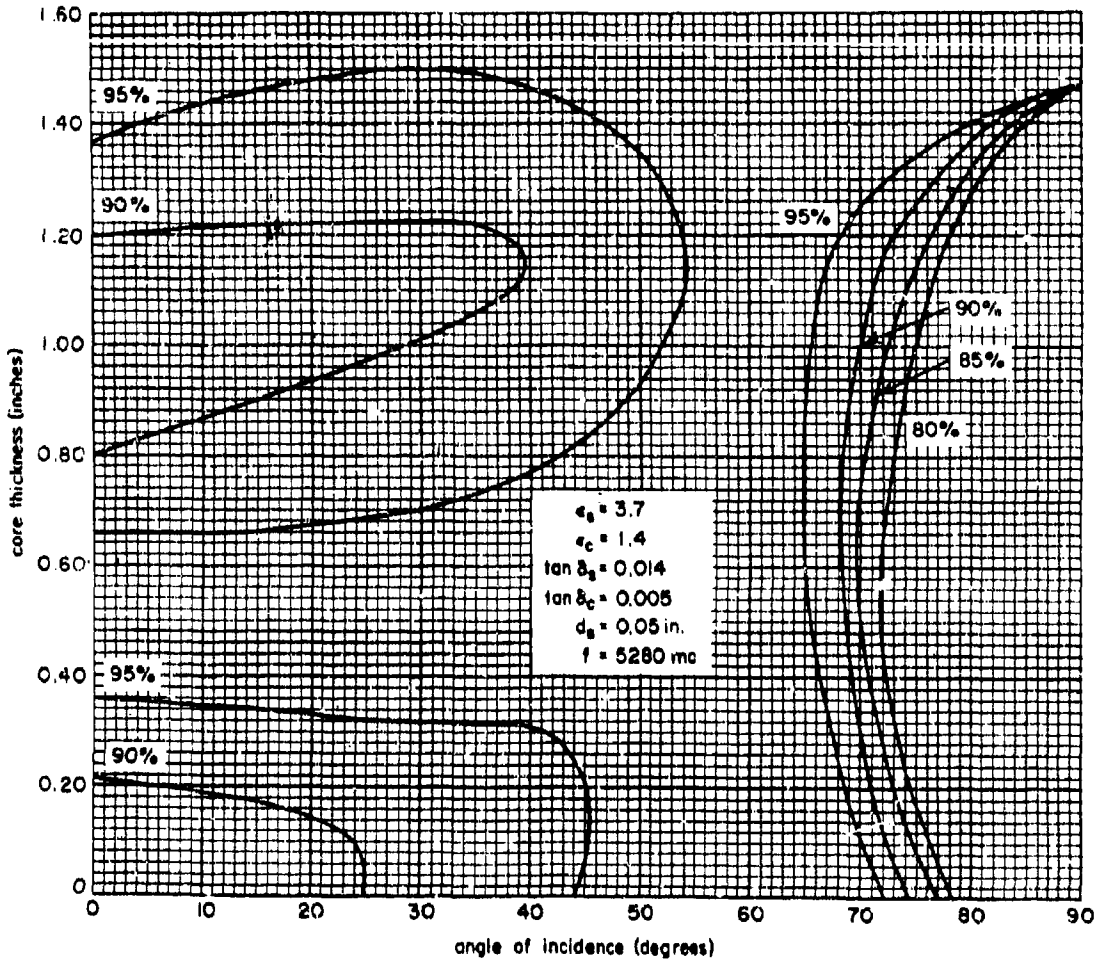


Figure 13-33. Constant Power Transmission Contours for an "A" Sandwich for Various Angles of Incidence and Core Thicknesses at 5280 mc with Parallel Polarization

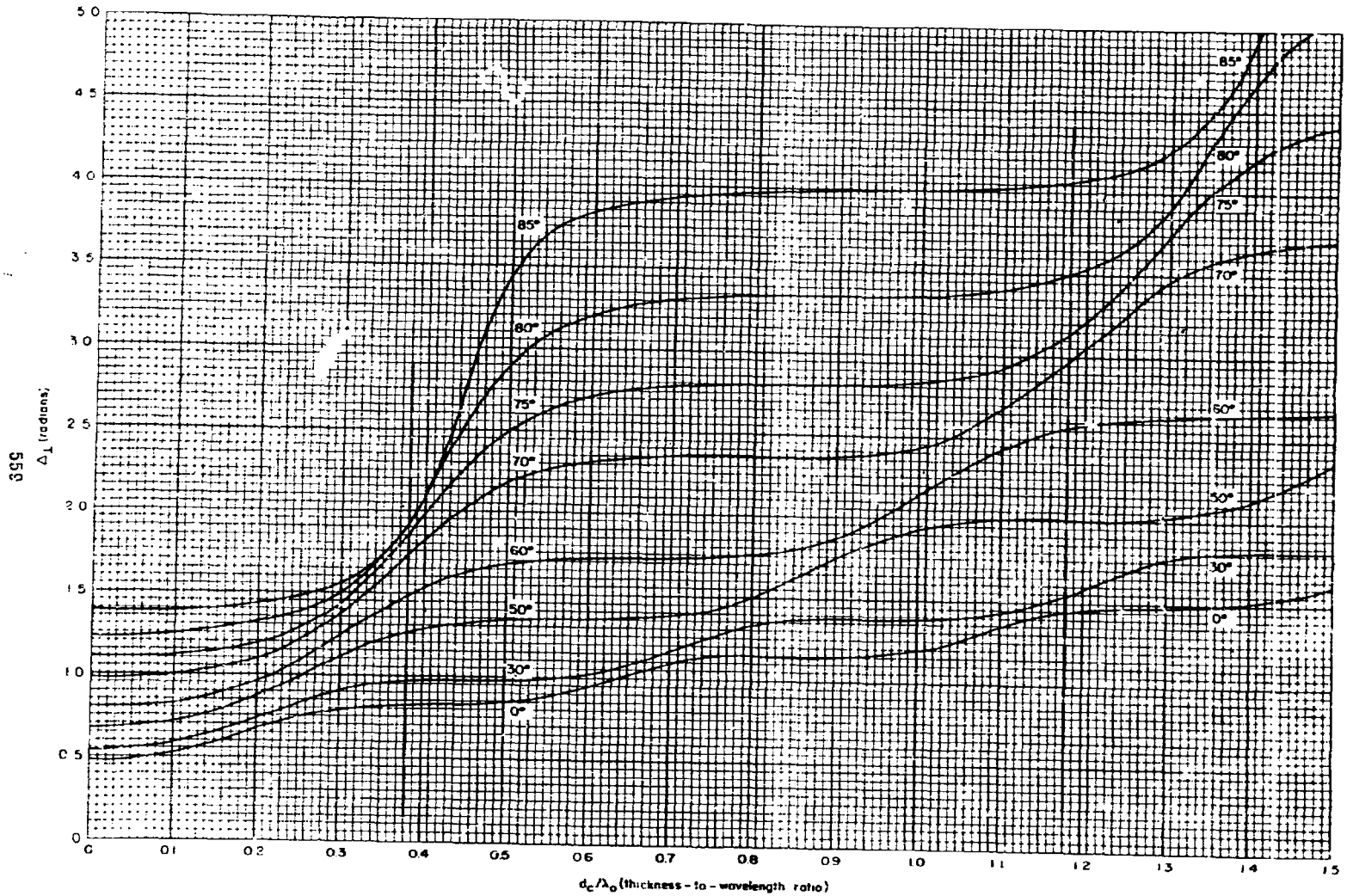


Figure 13–34. Insertion Phase Delay Through an "A" Sandwich, Perpendicular Polarization ($d_s/\lambda_0 = 0.030$, $\theta = 0°$ To $85°$. $\epsilon_s = 4.0$, $\epsilon_c = 1.25$, tan $\delta_s = 0.014$, tan $\delta_c = 0.005$)

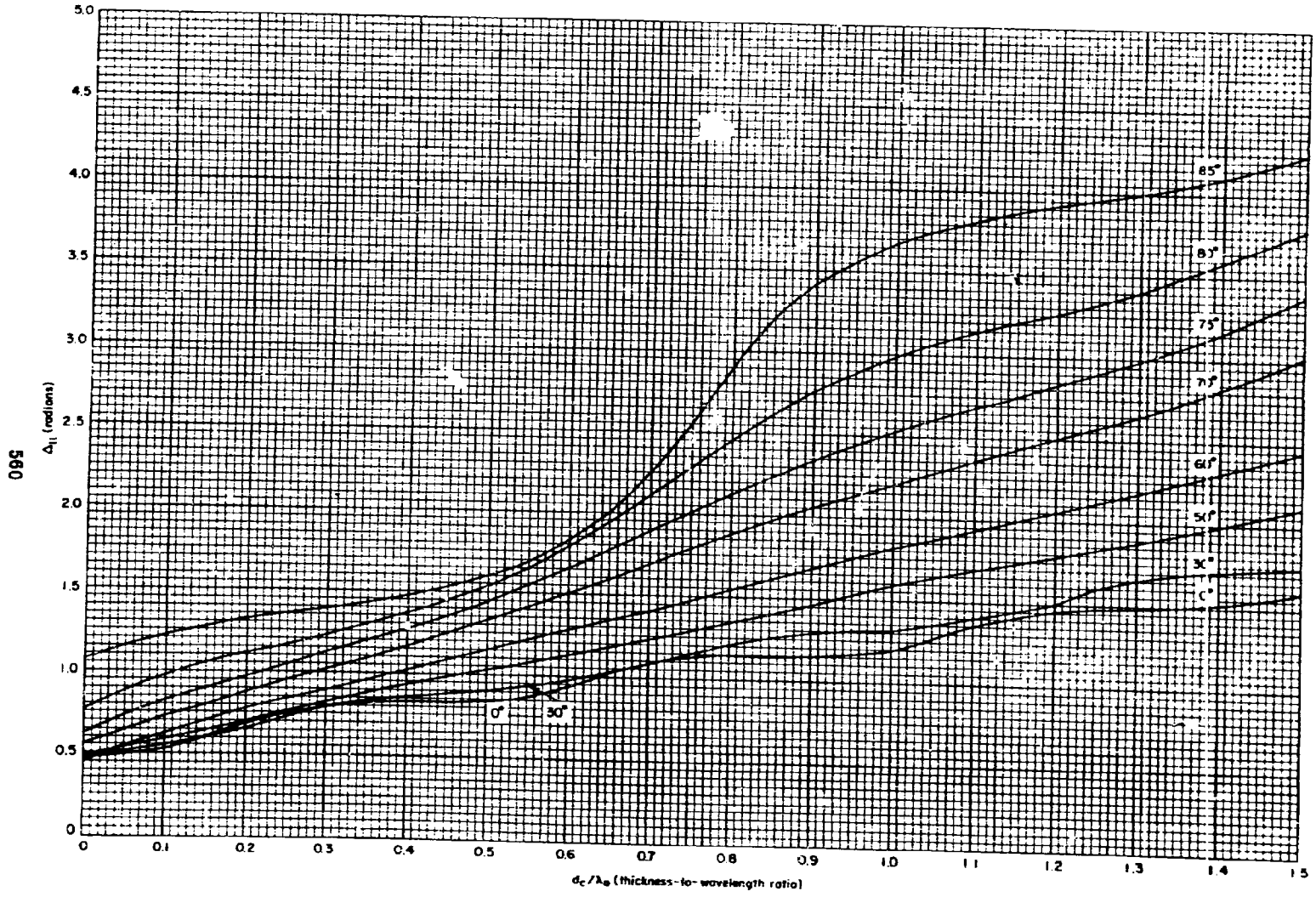


Figure 13–35. Insertion Phase Delay Through an "A" Sandwich, Parallel Polarization ($d_s/\lambda_0 = 0.030$, $\theta = 0°$ To 85°, $\epsilon_s = 4.0$, $\epsilon_c = 1.25$, ten $\delta_s = 0.014$, ten $\delta_c = 0.505$)

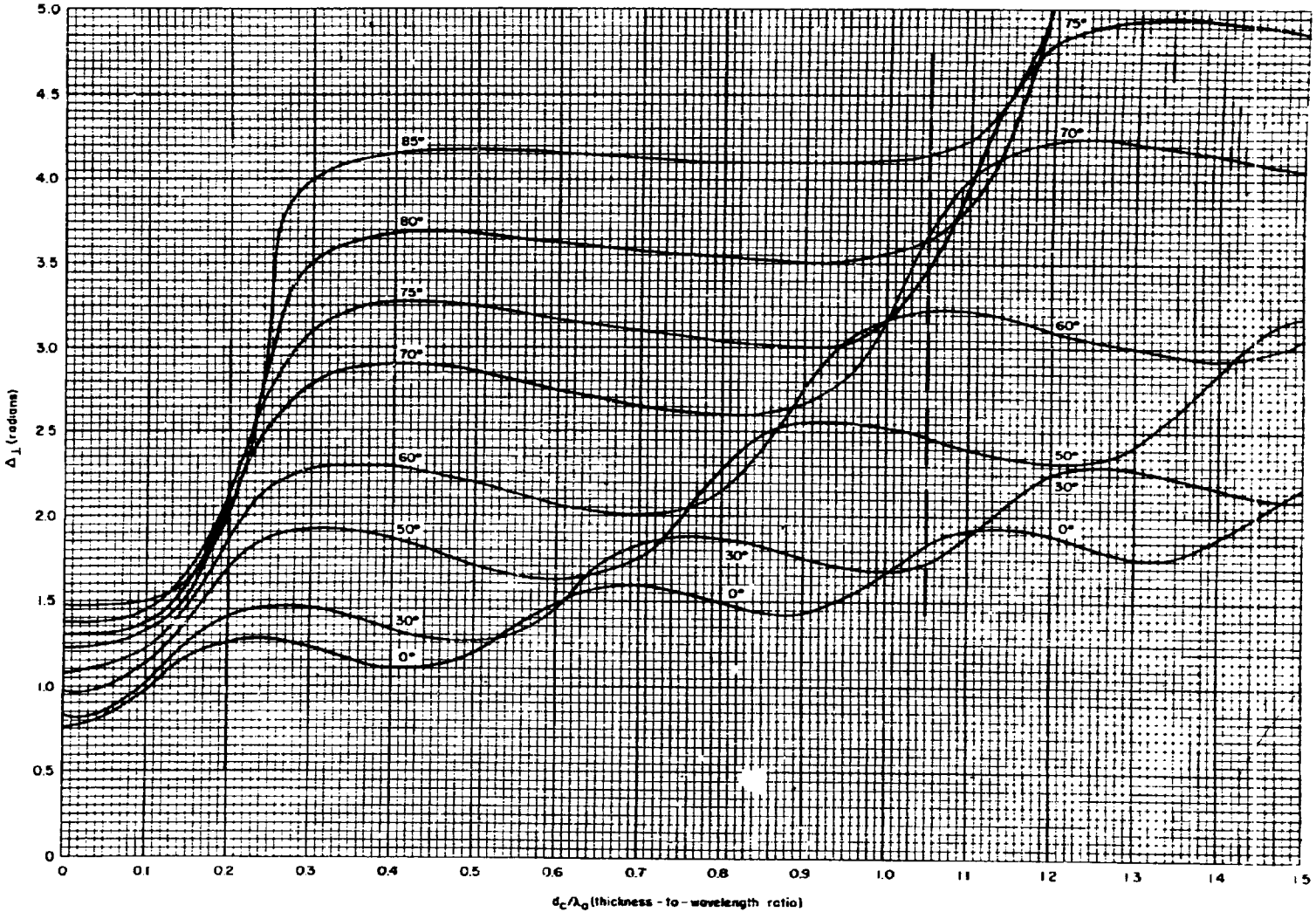


Figure 13–36. Insertion Phase Delay Through an "A" Sandwich, Perpendicular Polarization ($d_s/\lambda_0 = 0.060$, θ=0° To 85°, $\epsilon_s = 4.0$, $\epsilon_c = 1.25$, tan $\delta_s = 0.014$, tan $\delta_c = 0.005$)

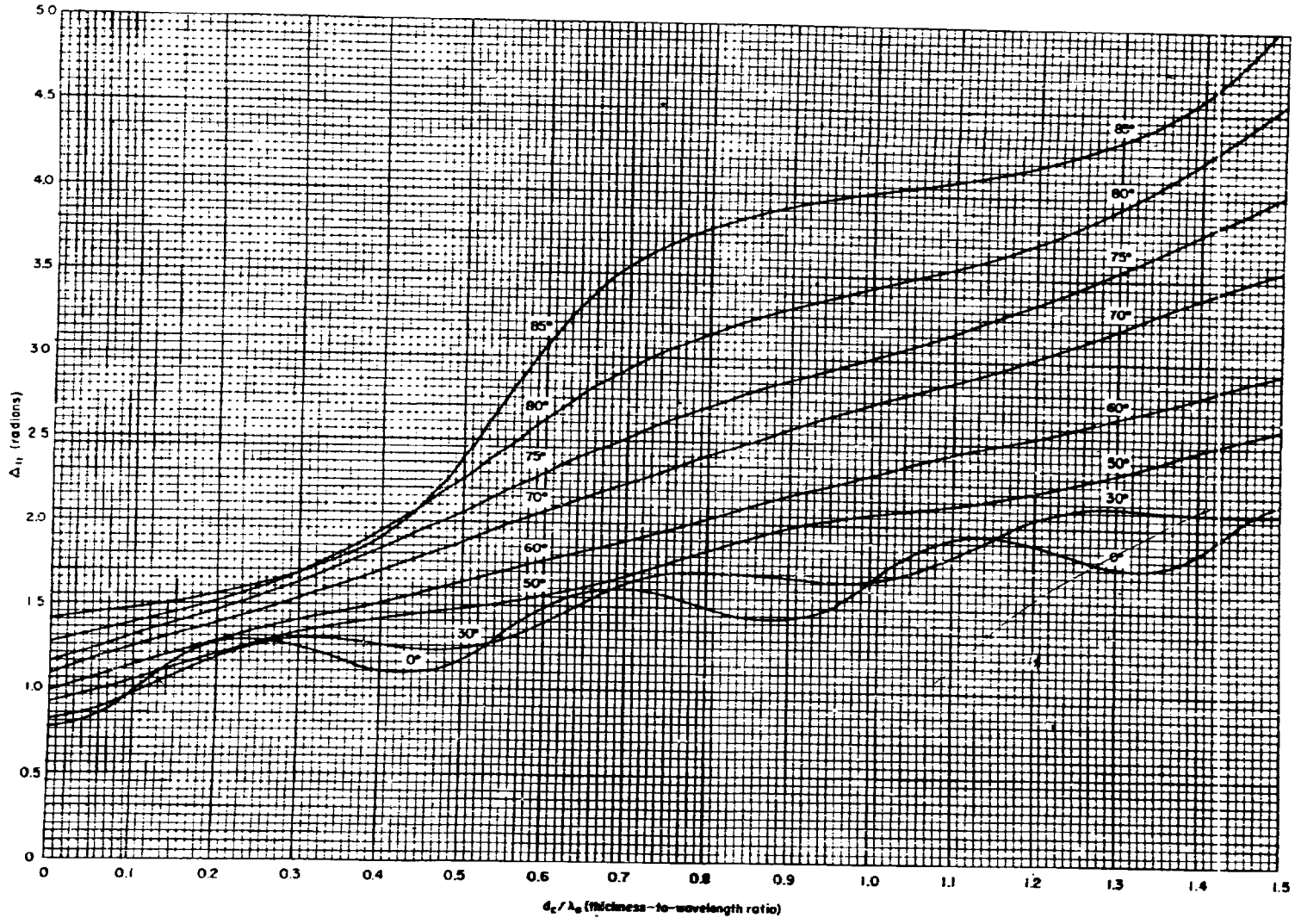


Figure 13–37. Insertion Phase Delay Through an "A" Sandwich, Parallel Polarization ($d_s/\lambda_0 = 0.060$, $\theta = 0°$ To 85°, $\epsilon_s = 4.0$, $\epsilon_c = 1.25$, tan $\delta_s = 0.014$, tan $\delta_c = 0.005$)

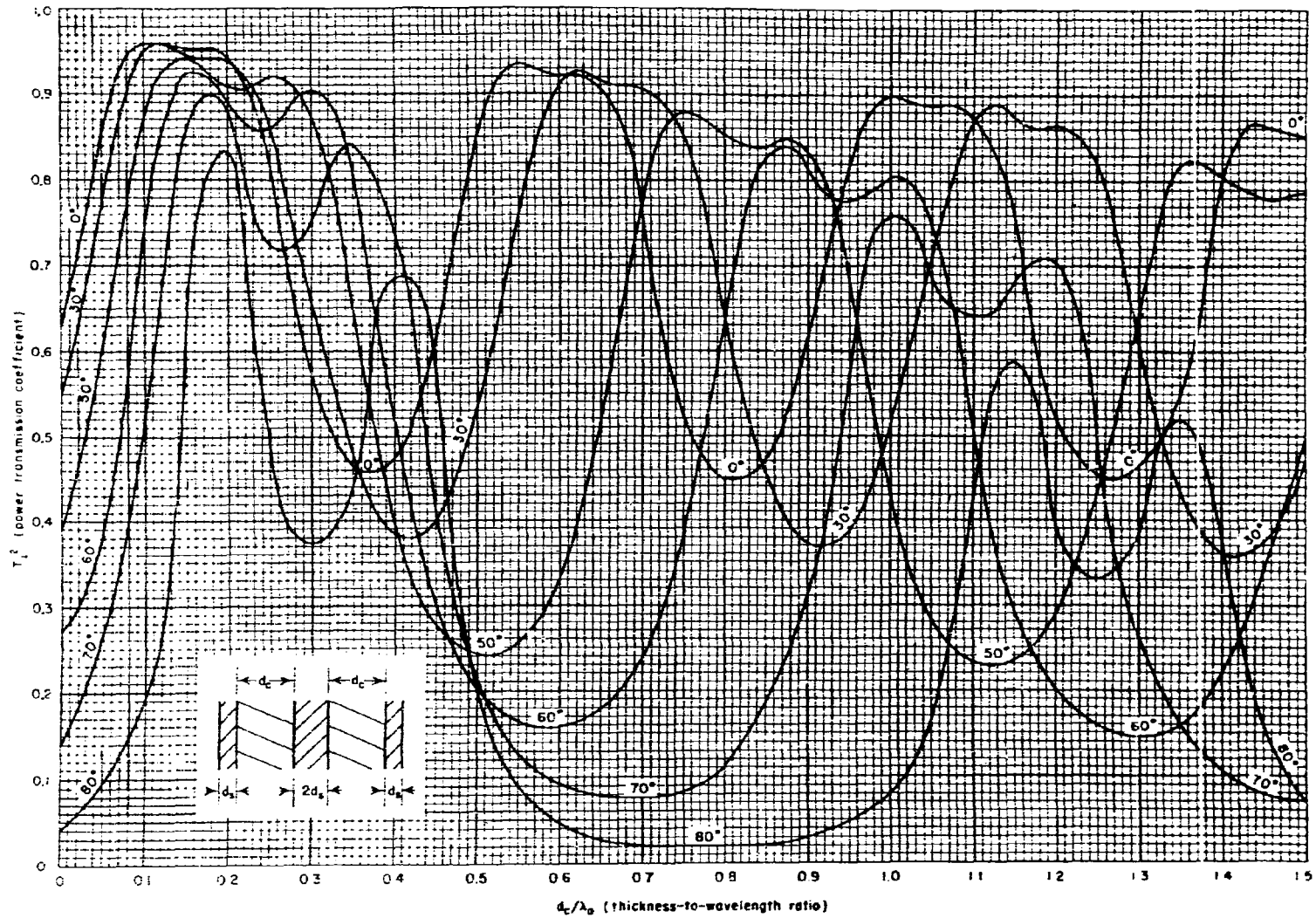


Figure 13–38. Power Transmission Coefficient of a Double Sandwich, Perpendicular Polarization ($d_s/\lambda_0 = 0.030$, $\theta = 0°$ To $80°$, $\epsilon_s = 4.0$, $\epsilon_c = 1.25$, $\tan \delta_s = 0.014$, $\tan \delta_c = 0.005$)

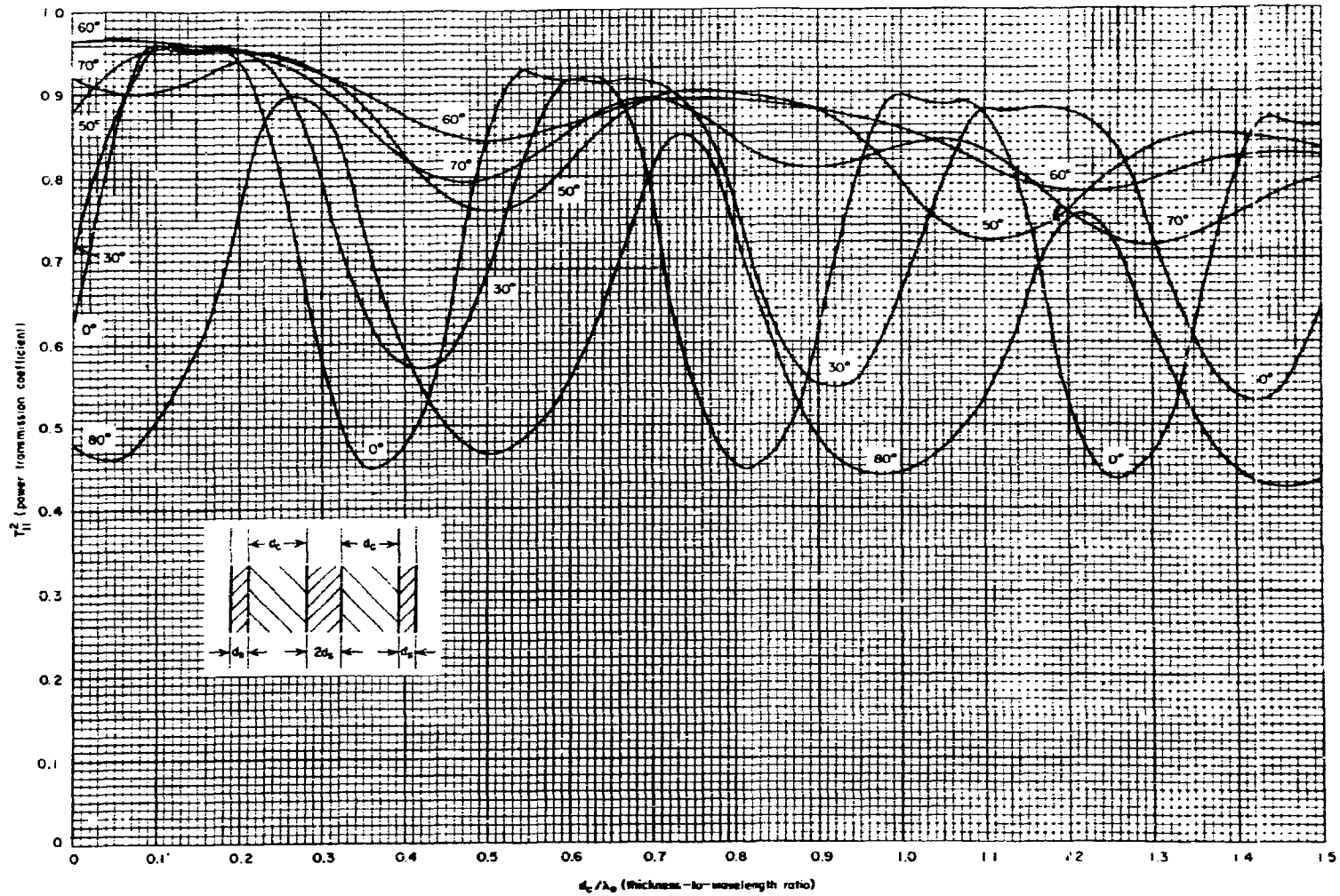


Figure 13–39. Power Transmission Coefficient of a Double Sandwich, Parallel Polarization ($d_s/\lambda_0 = 0.030$, $\theta = 0°$ To $80°$, $\epsilon_s = 4.0$, $\epsilon_c = 1.25$, $\tan \delta_s = 0.014$, $\tan \delta_c = 0.005$)

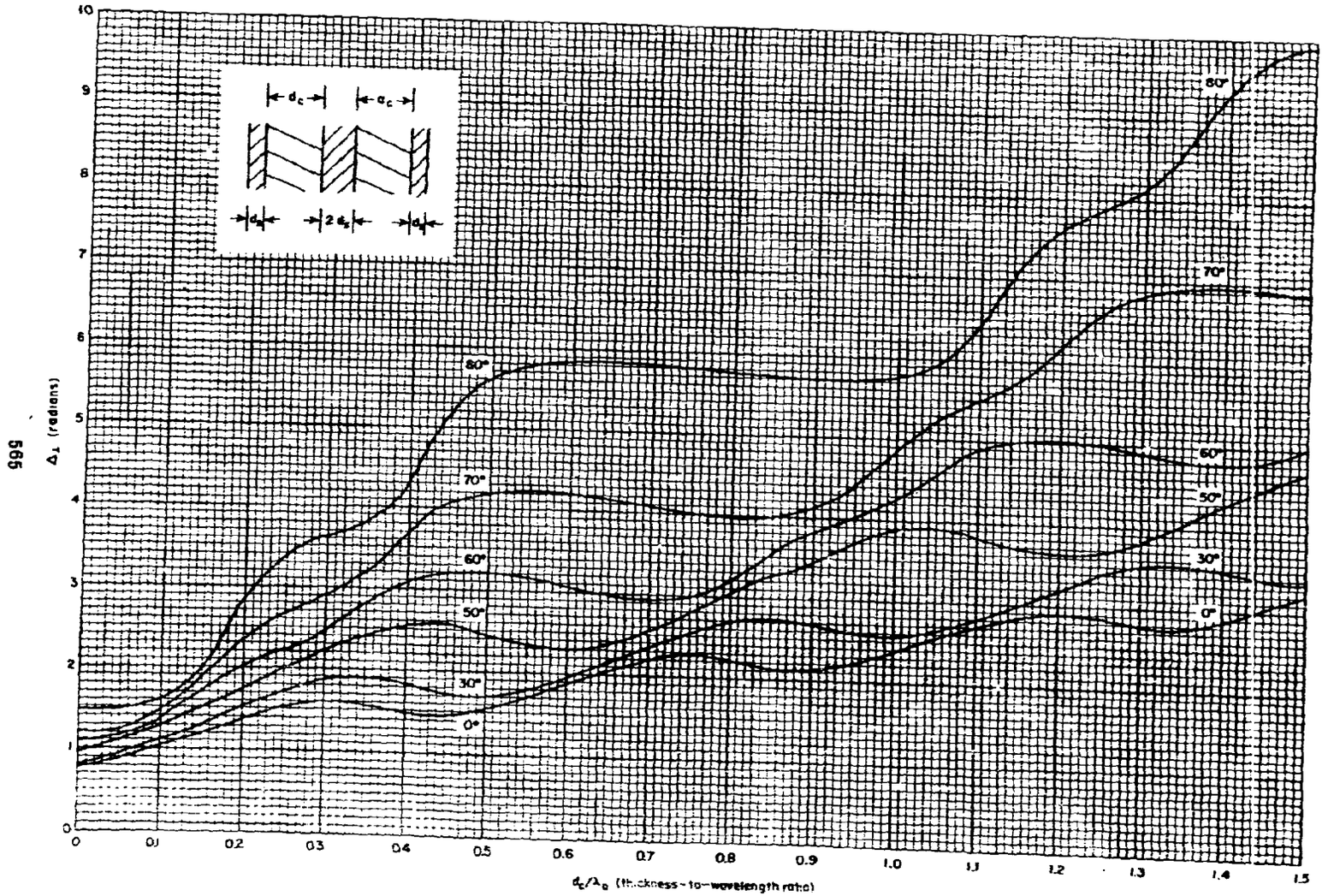


Figure 13–40. Insertion Phase Delay of a Double Sandwich, Perpendicular Polarization (d_s/λ_0 0.030, θ = 0° To 80°, ϵ_s = 4.0, ϵ_c = 1.25, tan δ_s = 0.014, tan δ_c = 0.005)

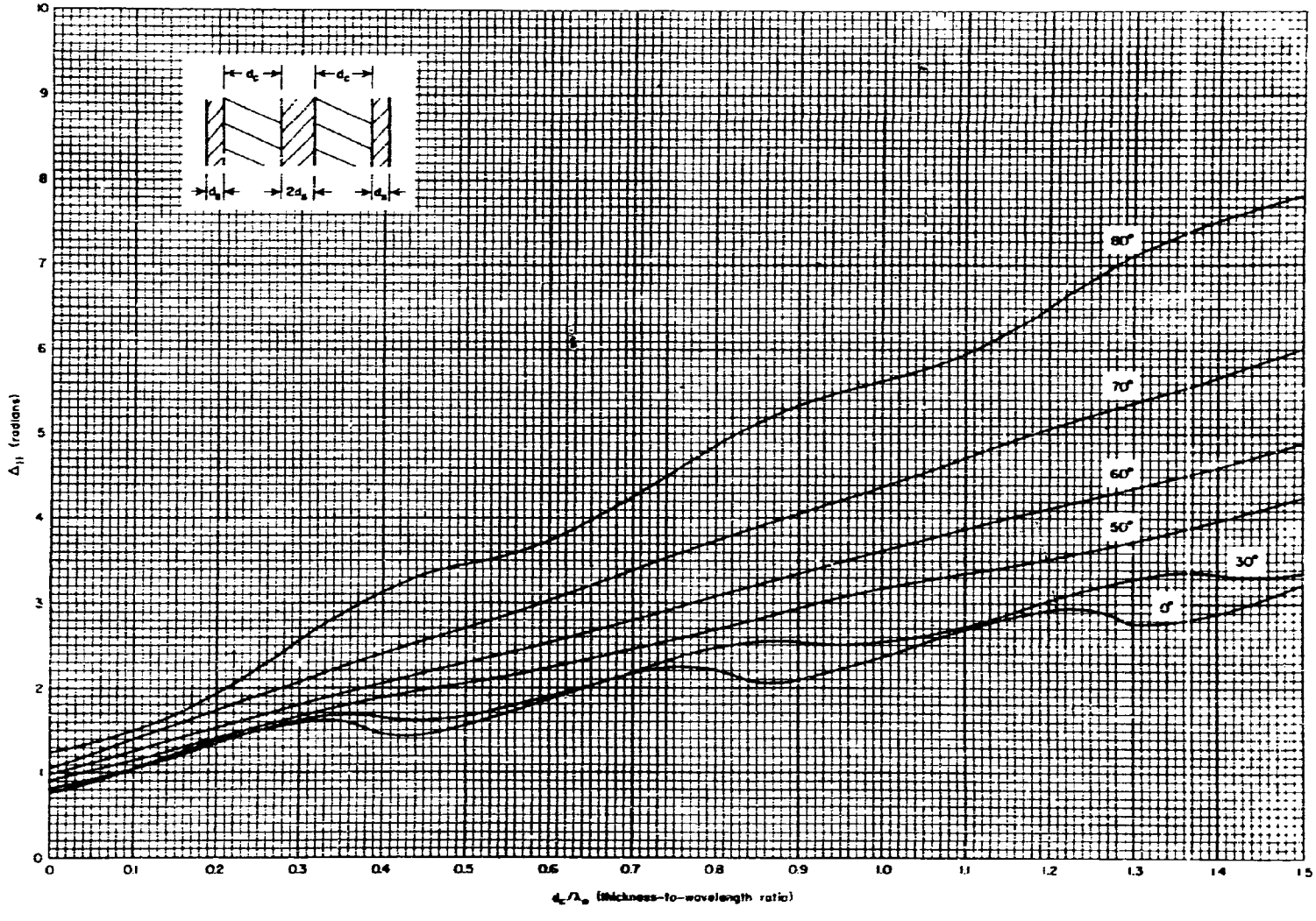


Figure 13–41. Insertion Phase Delay of a Double Sandwich, Parallel Polarization ($d_s/\lambda_0 = 0.030$, $\theta = 0°$ To 80°, $\epsilon_s = 4.0$, $\epsilon_c = 1.25$, tan $\delta_s = 0.014$, tan $\delta_c = 0.005$)

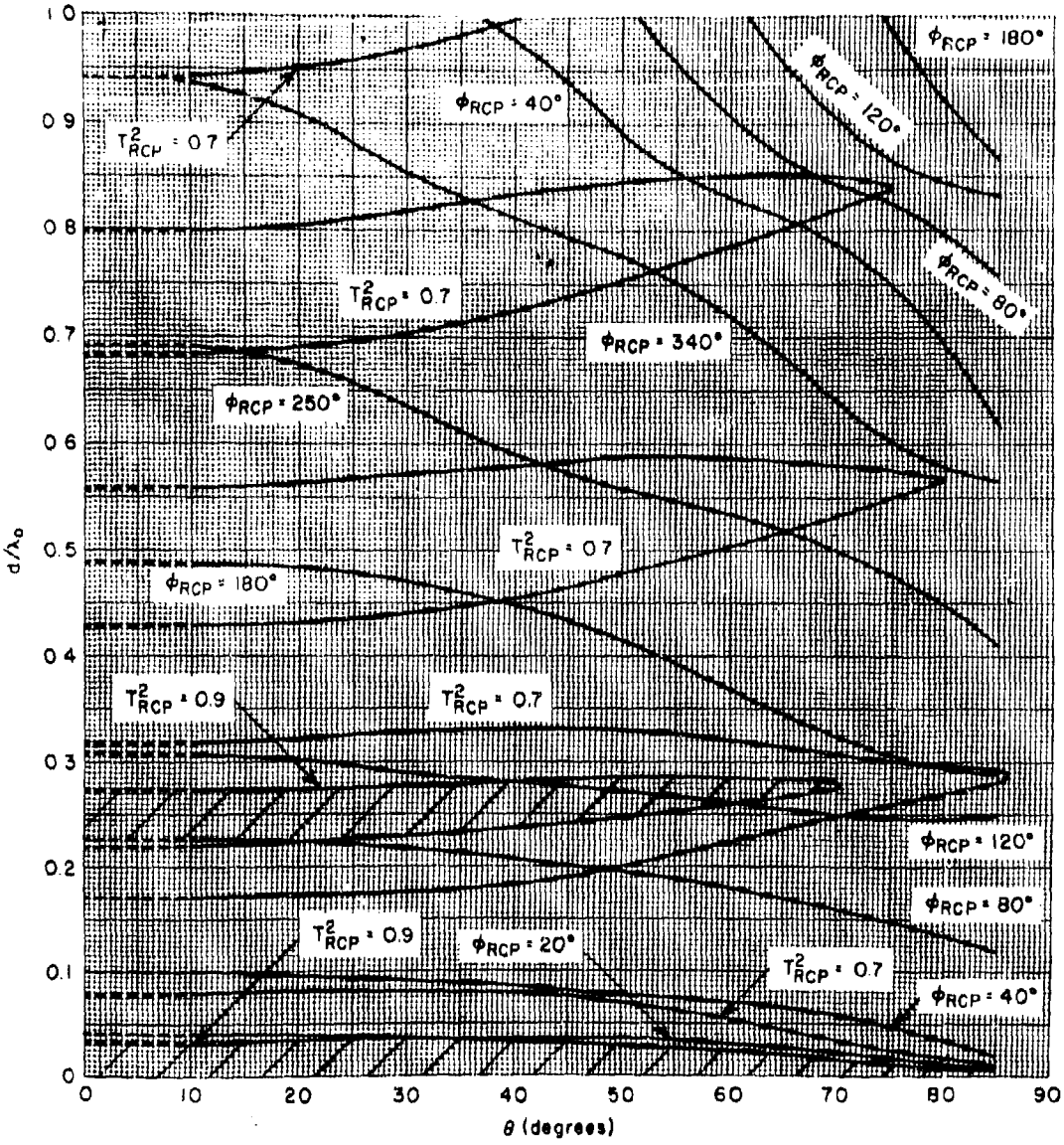


Figure 13–42. Contours of Constant Power Transmission (T^2_{RCP}) and Insertion Phase Delays (ϕ_{RCP}), Homogeneous Panels; Transmitted Preserved Incident Component for Right-Circularly Polarized Incident Waves (ϵ_r = 4.1, tan δ = 0.014)

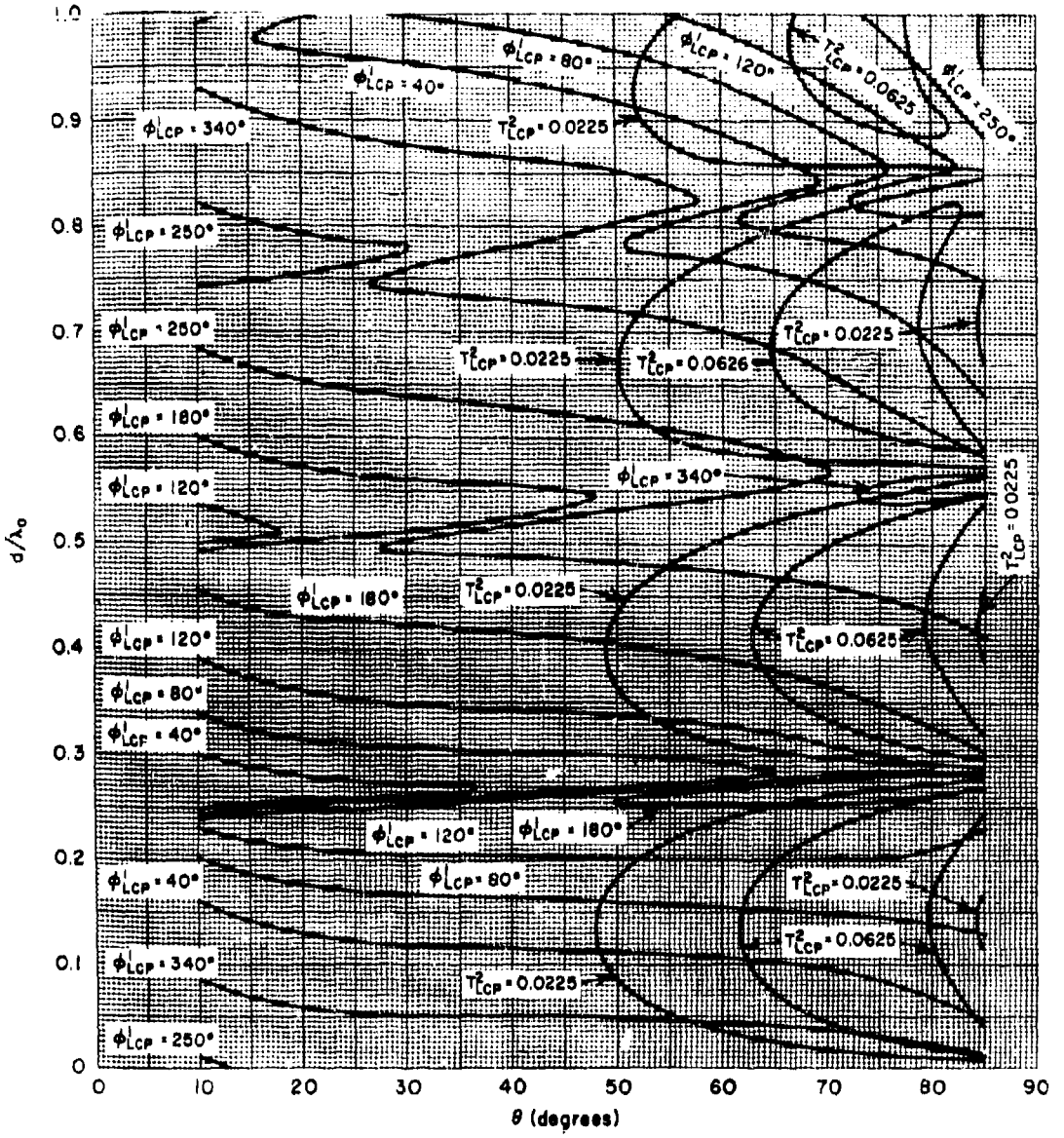


Figure 13–43. Contours of Constant Power Transmission (T^2_{LCP}) and Phase Delay (ϕ^1_{LCP}) for Homogeneous Panels; Transmitted Depolarized Component for Right-Circularly Polarized Incident Waves (ϵ_r 4.1, tan δ = 0.014)

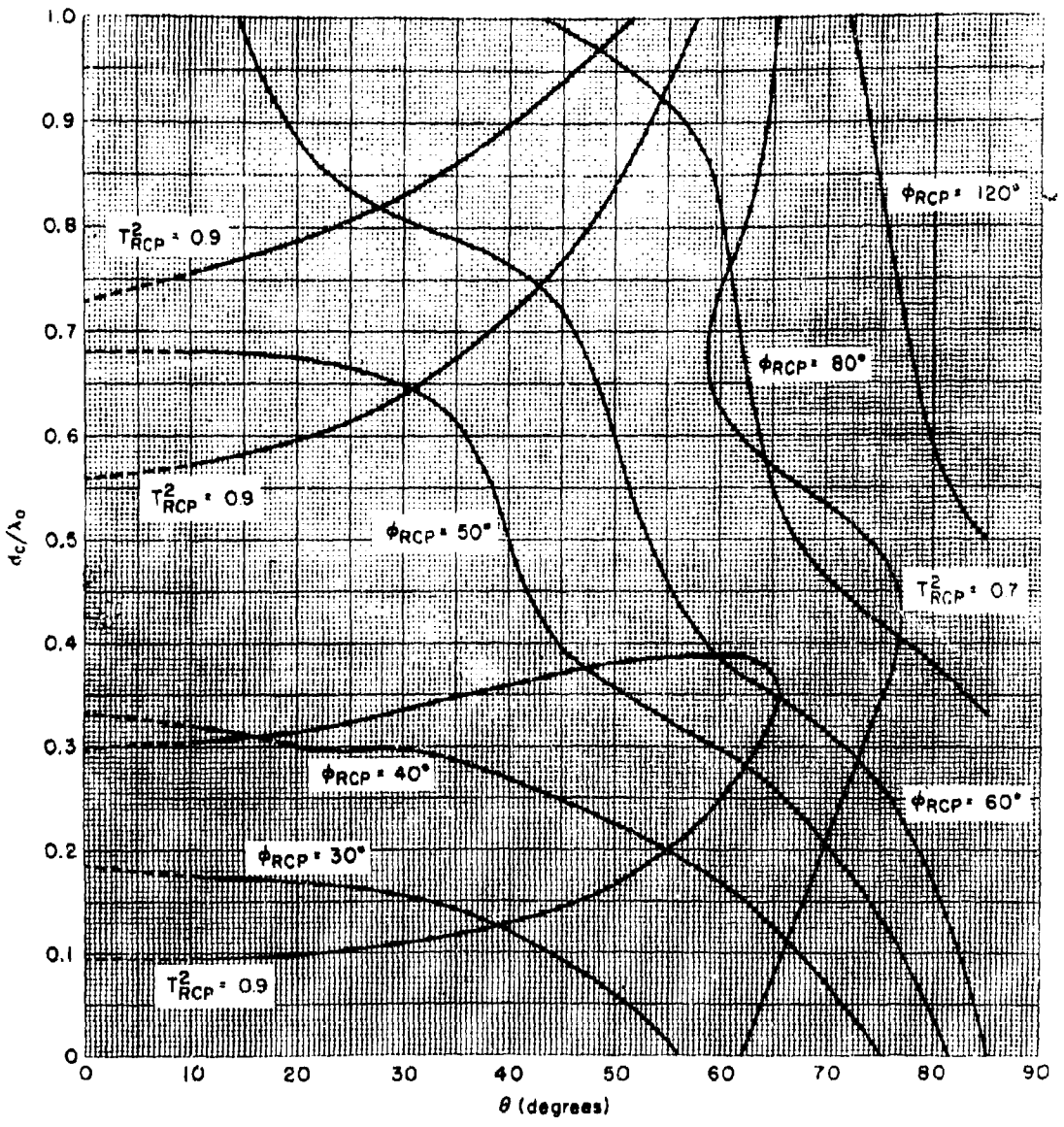


Figure 13–44. Contours of Constant Power Transmission (T^2_{RCP}) and Insertion Phase Delays (Φ_{RCP} = Δ) for "A" Sandwich Panels; Transmitted Preserved Incident Component for Right–Circularly Polarized Incident Waves (ϵ_s = 4.2, tan δ_s = 0.015, ϵ_c = 1.2, tan δ_c = 0.005, d_s/λ_o = 0.0238)

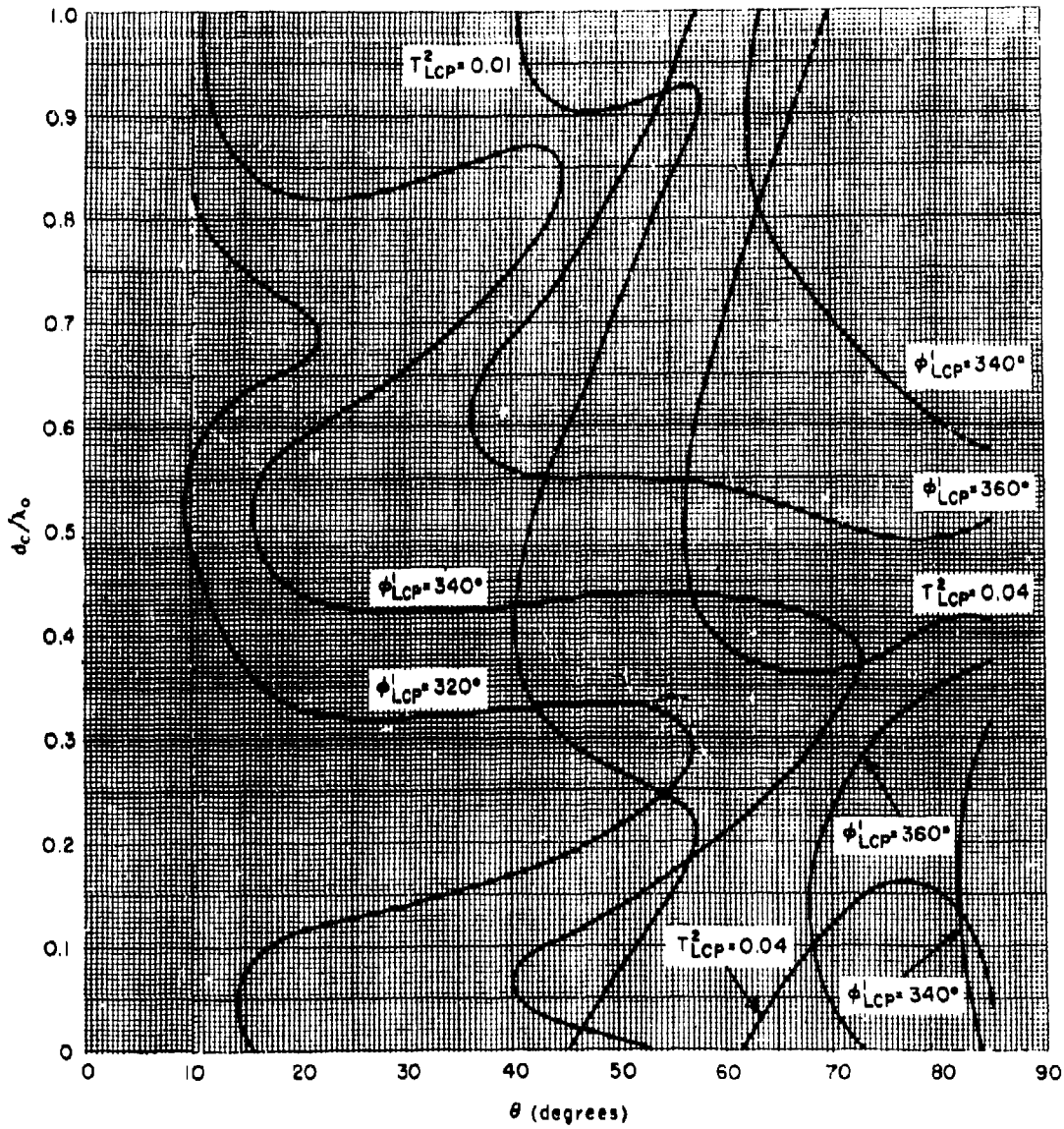


Figure 13-45. Contours of Constant Power Transmission (T^2_{LCP}) and Phase Delays (ϕ^1_{LCP}) For "A" Sandwich Panels; Transmitted Depolarized Component for Right-Circularly Polarized Incident Waves (ϵ_s =4.2, tan δ_s =0.015, ϵ_c =1.2, tan δ_c =0.005, d_s/λ_o =0.0238)

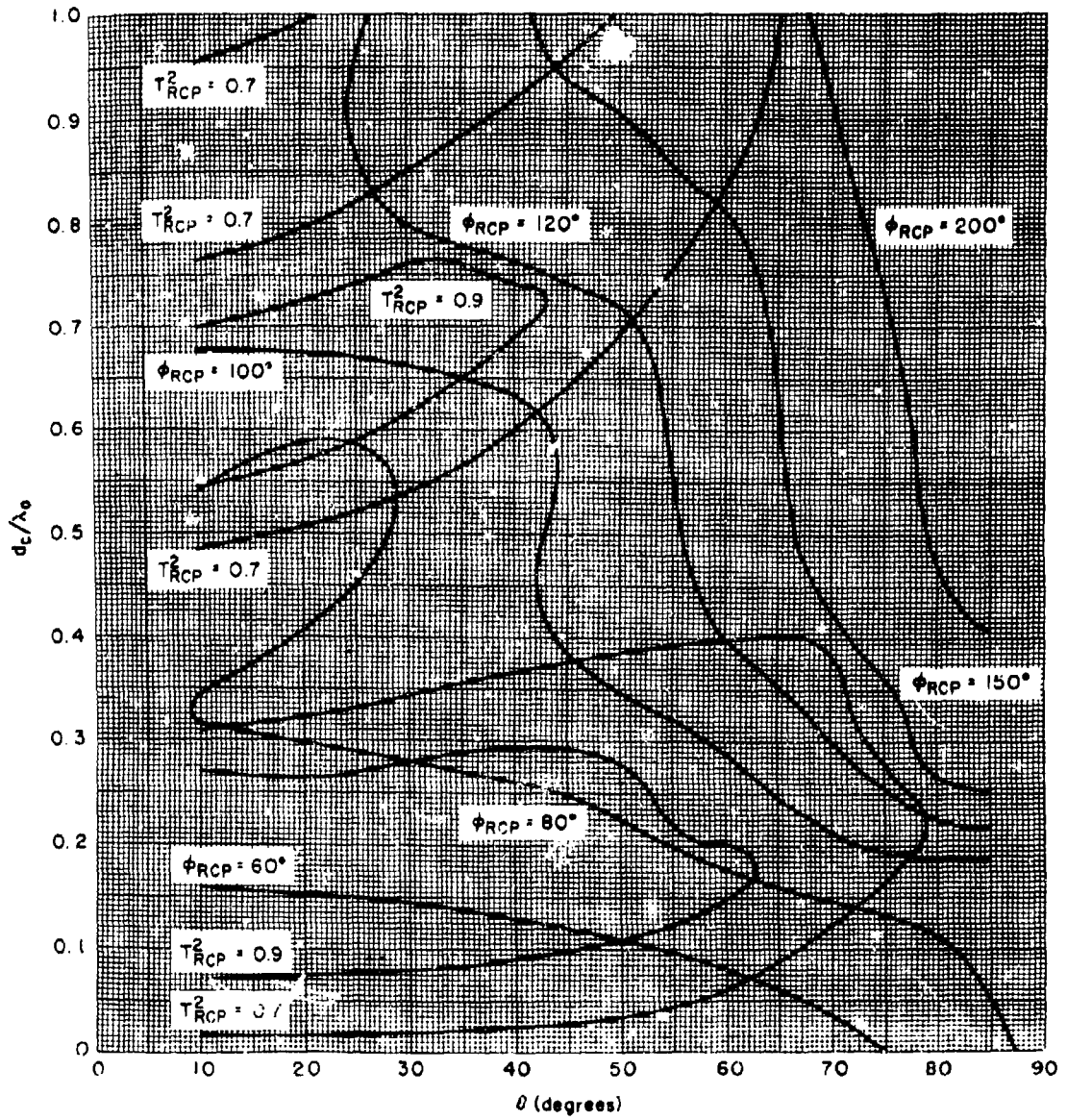


Figure 13-46. Contours of Constant Power Transmission (T^2_{RCP}) and Insertion Phase Delays (ϕ_{RCP}) for "C" Sandwich Panels Composed of Two "A" Sandwiches in Tandem with ϵ_s = 4.2, tan δ_s = 0.015, ϵ_c = 1.2, tan δ_c = 0.005, d_s/λ_o = 0.0238); Transmitted Preserved Incident Component for Right-Circularly Polarized Incident Waves

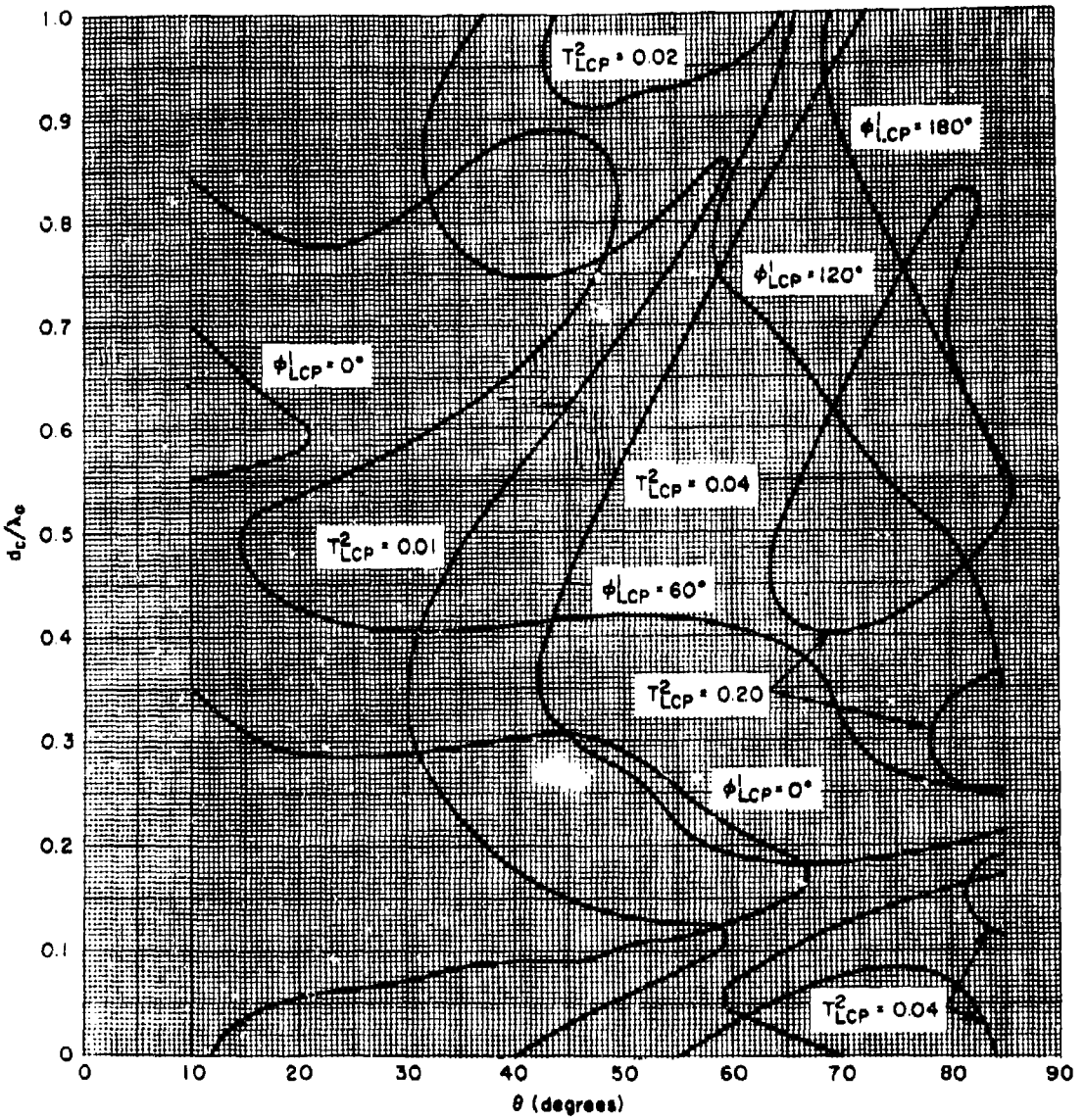


Figure 13-47. Contours of Constant Power Transmission (T^2_{LCP}) and Phase Delays (ϕ^1_{LCP}) for "C" Sandwich Panels Composed of Two "A" Sandwiches in Tandem with ϵ_s =0.015, ϵ_c =1.2, tan δ_c =0.005, d_s/λ_o =0.0238; Transmitted Depolarized Component for Right-Circularly Polarized Incident Waves

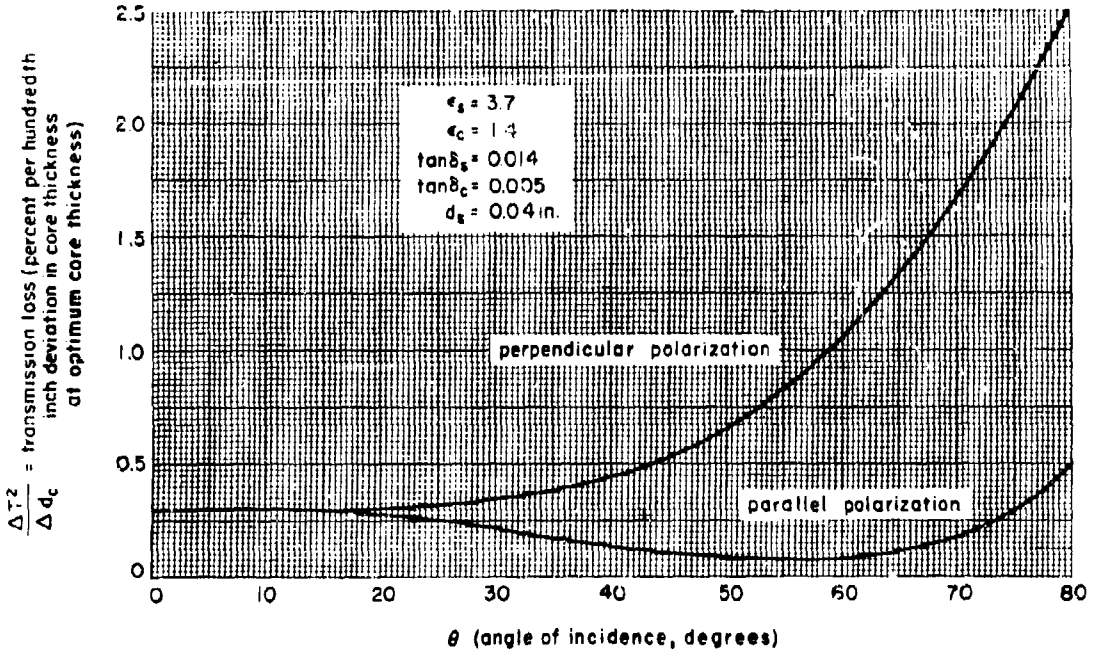


Figure 13–48. Core Tolerance Curves for an "A" Sandwich, 9375 mc, Perpendicular and Parallel Polarizations

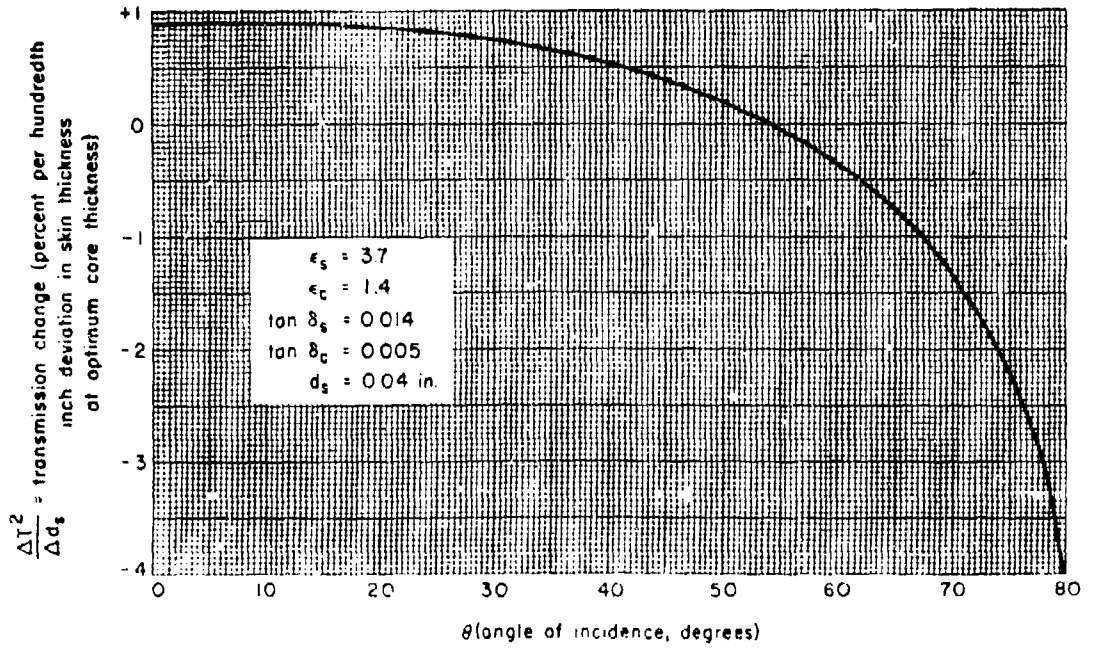


Figure 13–49. Skin Tolerance Curve for an "A" Sandwich, 9375 mc, Parallel Polarization

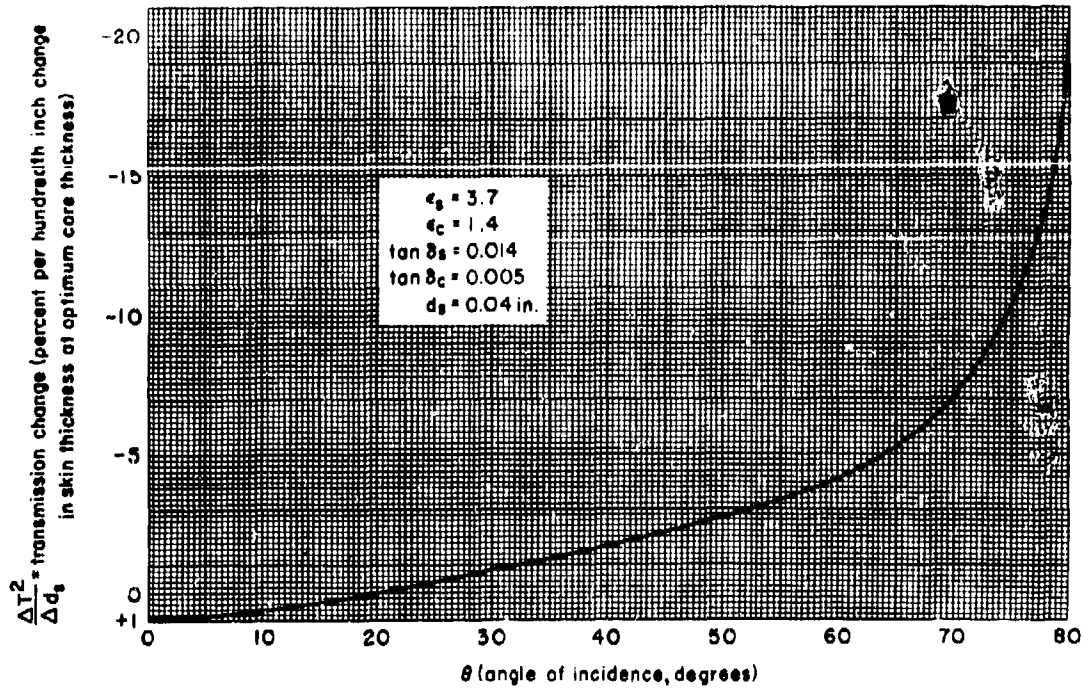


Figure 13–50. Skin Tolerance Curve for an "A" Sandwich, 9375 mc, Perpendicular Polarization

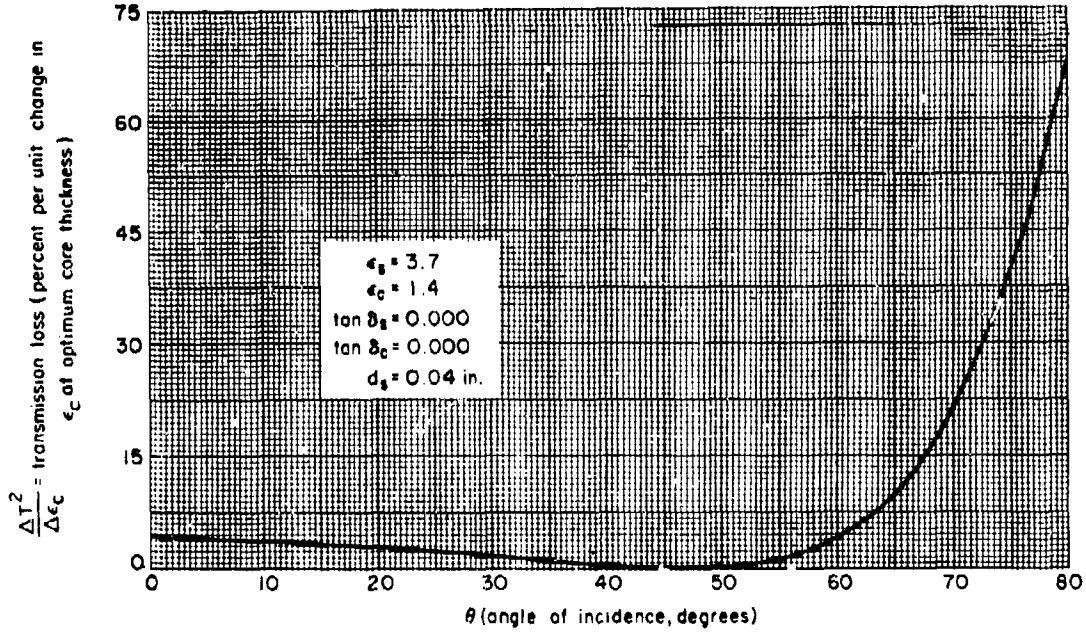


Figure 13–51. Core Dielectric Tolerance Curve for an "A" Sandwich, 9375 mc, Perpendicular Polarization

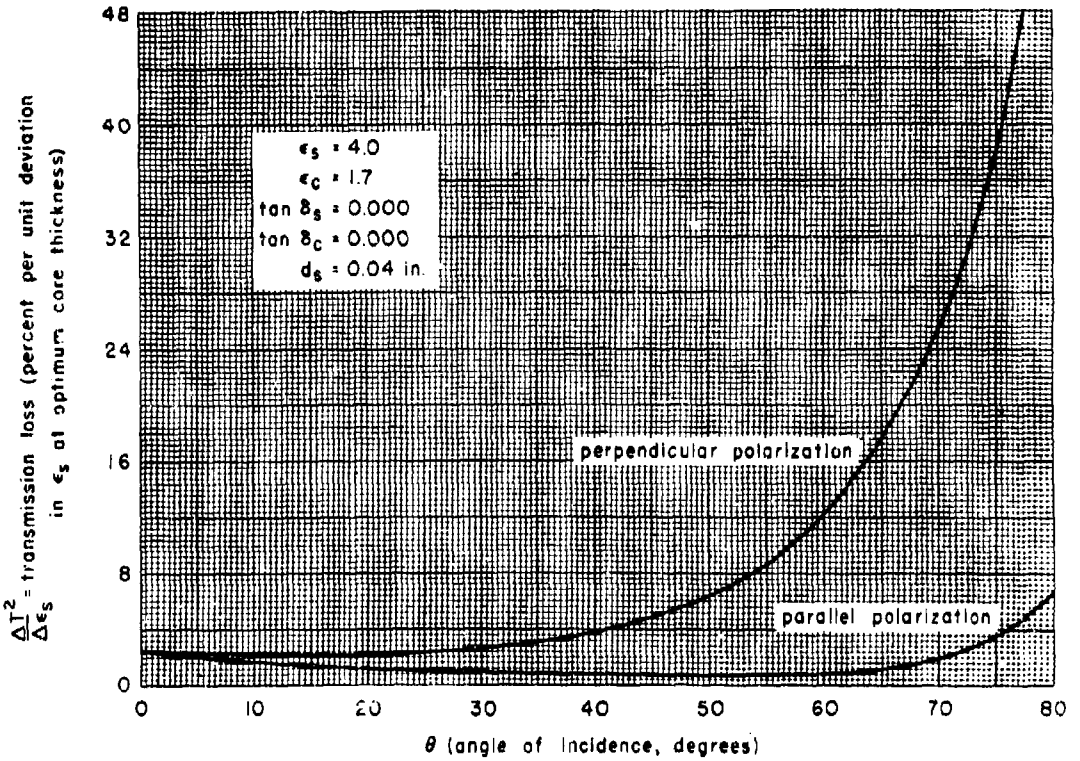


Figure 13–52. Skin Dielectric Tolerance Curves for an "A" Sandwich, 9375 mc, Perpendicular and Parallel Polarizations

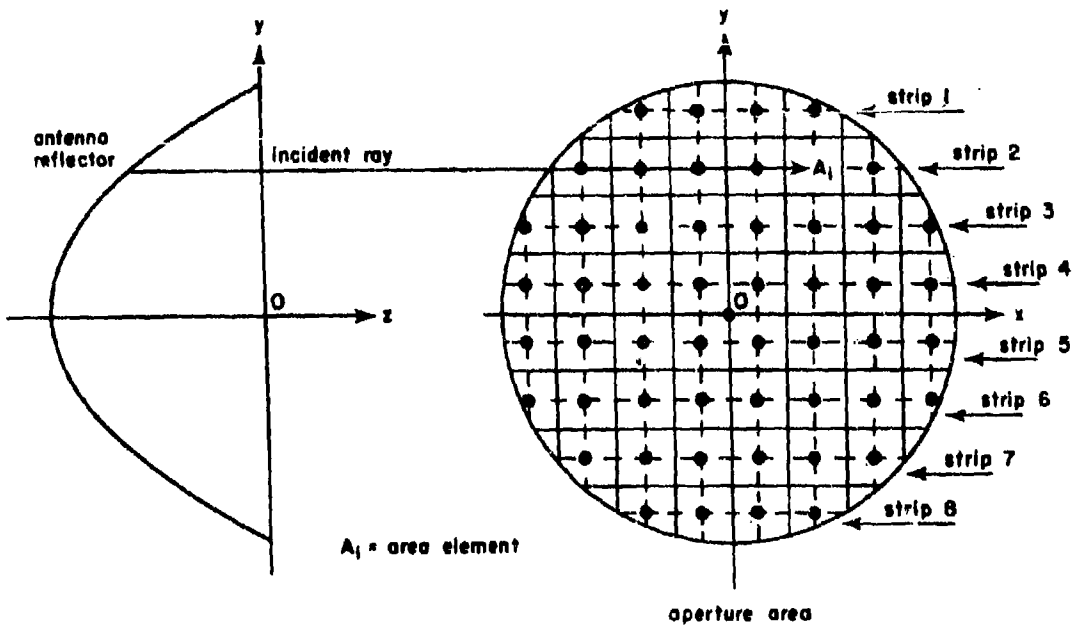


Figure 13–53. Equivalent Antenna System of a Paraboloidal Antenna and Its Radome

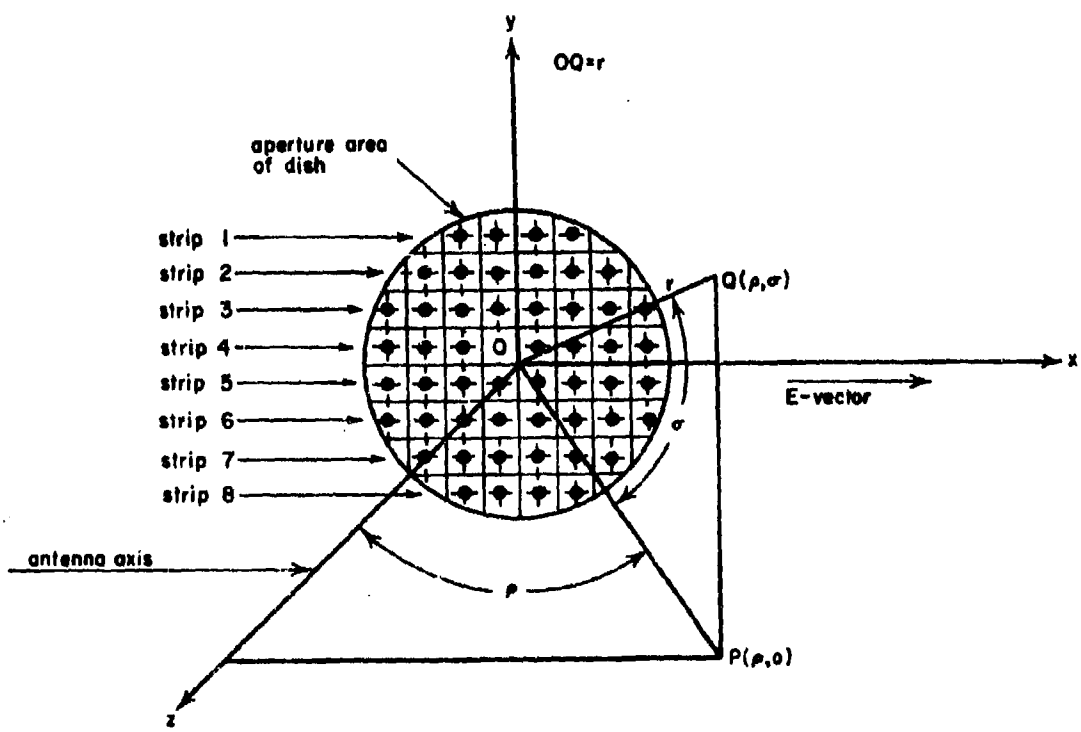


Figure 13–54. Antenna–Radome Radiating System

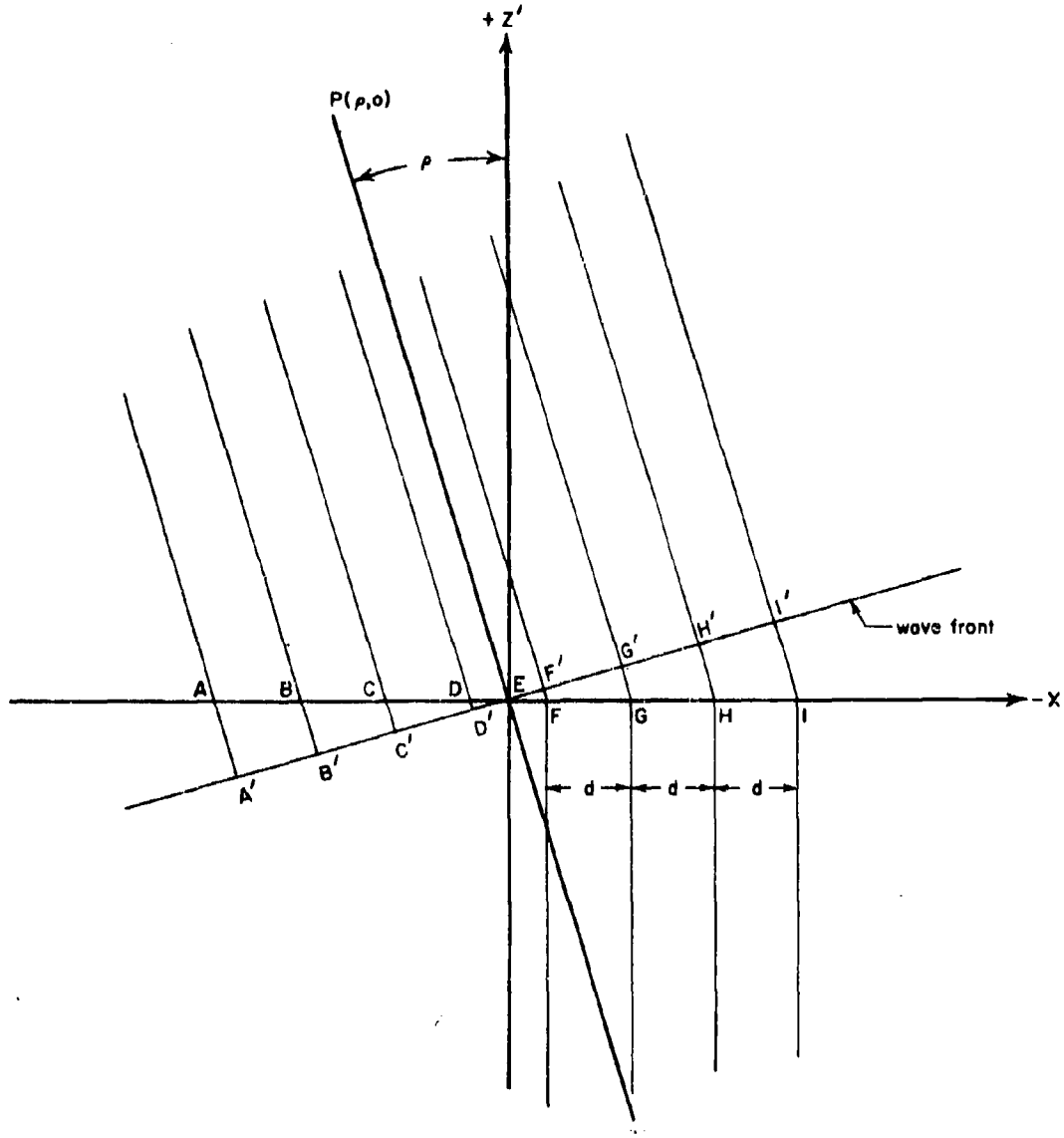


Figure 13–55. Array of Equispaced Radiators

BIBLIOGRAPHY

KEY TO ABBREVIATIONS

ADC	Air Development Center
AFB	Air Force Base
AIEE	American Institute of Electrical Engineers
AMC	Air Materiel Command
ARDC	Air Research and Development Command
ASTIA	Armed Services Technical Information Agency
ASTM	American Society for Testing Materials
IRE	Institute of Radio Engineers
MIT	Massachusetts Institute of Technology
NACA	National Advisory Committee for Aeronautics
NADC	Naval Air Development Center
NAMC	Naval Air Materiel Center
NAVAER	Navy Bureau of Aeronautics (formerly BUAER)
ONR	Office of Naval Research
RDB	Research and Development Board
SAE	Society of Automotive Engineers
URSI	International Scientific Radio Union
US	United States
WADC	Wright Air Development Center

SECTION A. ELECTRICAL THEORY, DESIGN, AND MEASUREMENTS

1. The Homogeneous Flat Sheet

1. DiToro, J. A. Graphs of Transmission and Phase Data of Plane Dielectric Sheets for Radome Design. Report NADC-EL-5313. Aeronautical Electronic and Electrical Lab., NADC, Johnsville, Pa., 1 July 1953 (ASTIA catalog no. AD-45316). Supplementary Graphs of Transmission and Phase Delay of Plane Dielectric Sheets and Sandwich Constructions for Radome Design. Supplement to report NADC-EL-5313, 16 June 1954 (AD-45543).

2. Everhart, E. M. Radome Wall Reflections at Variable Angles of Incidence. Report 483-20, Radiation Lab., MIT, 4 Jan 1946.

3. Kofoid, M. J. Calculated Electrical Transmission Characteristics of Half-Wavelength Thick Solid Plane Sheets. Document D-13622, Boeing Airplane Co., Seattle, Wash., 24 Oct 1952 (rev. 12 Mar 1954) (AD-42401).

4. Lengyel, B. A., Langenberg, D. N., and Henschke, R. A. Transmission Through Half-Wave Sheets. Technical memorandum 327, Hughes Aircraft Co., Culver City, Calif., 1 Nov 1953 (AD-22010).

5. Luoma, E. J. Phase Retardation Design Curves for Solid Lossless Dielectric Panels. Technical report 56-116, WADC, Wright-Patterson AFB, Ohio, Feb 1956 (AD-110514).

6. Miller, D. L. Radar Transmission Test of Radome Panel — P-58 — Applicable to F-86D Airplanes — NAA Model NA-165 — Class — Fighter. Report NA-50-137, North American Aviation, Engineering Research Lab., Los Angeles, Calif., 27 Jan 1950.

7. Pinney, E. J., and Colvin, D. H. Boresight Errors for the Solid Wall Radome. Document D-13695, Boeing Airplane Co., 24 Nov 1952 (Confidential).

8. Radome Engineering Manual. Published by direction of the Chief of the Bureau of Aeronautics and the Commanding General of the Air Materiel Command. AMC Manual 80-4, NAVAER 16-45-502, 1 Oct 1948.

9. Richmond, J. H. Antenna Pattern Distortion by Dielectric Sheets. Proceedings of the Ohio State U. –WADC Radome Symposium. Vol. I, June 1955.

10. Richmond, J. H. Electromagnetic Transmission Through Dielectric Sheets. Technical report 531-12, Antenna Lab., Ohio State U. Research Foundation, Columbus, 1 Sept 1955.

11. Transmission Through a Lossy Dielectric Sheet. Document D-13645, Boeing Airplane Co., Seattle, Wash., 27 Oct 1952.

12. Webster, R. E., and Moore, D. P. Transmission Coefficients of Elliptically Polarized Waves Incident on Homogeneous Isotropic Panels. Report 663-5, Antenna Lab., Ohio State U. Research Foundation, Columbus, 31 Dec 1956.

13. Weedon, M. G. B., and Stott, A. L. Calculations on the Transmission of Electromagnetic Waves Through Plane Dielectric Sheets. Technical note GW 282, Royal Aircraft Establishment, Great Britain, Nov 1953 (Confidential) (AD-25779).

14. Wolin, S. Tables of Amplitude and Phase of the Function $1 + ae^{jb}$. Report NADC-EL-5114, NADC, Johnsville, Pa., 28 Aug 1952 (ATI-171767).

15. Wolin, S. Tables of Fresnel's Coefficients, Snell's Law and Other Radome Design Quantities. NADC, Johnsville, Pa., report NADC-EL-5104, 22 Jan 1952. Supplementary Tables of Fresnel's Coefficients, Snell's Law, and Other Radome Design Quantities. Report NADC-EL-53189, 9 July 1954 (AD-37153).

16. Wolin, S. Tables of Transmission and Reflection Coefficients of Lossy, Homogeneous Dielectric Sheets. Report NADC-EL-52195, NADC, Johnsville, Pa., 2 vols.: vol. 1, 11 Feb 1954 (AD-36518); vol. 2, 7 Oct 1954.

2. The Thin Sheet

17. DiToro, J. A. Graphs of Transmission and Phase Data of Plane Dielectric Sheets for Radome Design. Report NADC-EL-5313, Aeronautical Electronic and Electrical Lab., NADC, Johnsville, Pa., 1 July 1953 (AD-45316). Supplementary Graphs of Transmission and Phase Delay of Plane Dielectric Sheets and Sandwich Constructions for Radome Design. Supplement to report NADC-EL-5313, 16 June 1954 (AD-45543).

18. Kofoid, M. J. A Procedure For Making Precision Half-Wave Solid Wall Radomes. Proceedings of the Ohio State U. –WADC Radome Symposium, vol. II, June 1955, pp. 232-237.

19. Kotik, J. Some Remarks on Thin Dielectric Walls. Report 12283-8M, McMillan Lab., Ipswich, Mass., 15 Mar 1953 (Confidential).

20 Radome Engineering Manual. Published by direction of the Chief of the Bureau of Aeronautics and the Commanding General of the Air Materiel Command. AMC Manual 80-4, NAVAER 16-45-502, 1 Oct 1948.

21. Redheffer, R. M. The Interaction of Microwave Antennas with Dielectric Sheets. Report 438-18, Radiation Lab., MIT, 1 Mar 1946.

22. Wiederhorn, N. M., and Kay, A. F. Radome Design Criteria for Precision Guidance Radar. Final report, document 1276, McMillan Lab., Ipswich, Mass., 1 June 1954 (Confidential) (AD-49428).

23. Wolin, S. Tables of Transmission and Reflection Coefficients of Lossy, Homogeneous Dielectric Sheets. Report NADC-EL-52195, Aeronautical Electronic and Electrical Lab., NADC, Johnsville, Pa., 2 vols.: vol. 1, 11 Feb 1954 (AD-36518); vol. 2, 7 Oct 1954 (AD-45318).

3. The Half-Wave Sheet

24. Cady, W. M., Karelitz, M. B., and Turner, L. A. (ed.). Radar Scanners and Radomes. McGraw-Hill Book Co., New York, 1948. (Vol. 26, MIT Radiation Lab. Series.)

25. DiToro, J. A. Graphs of Transmission and Phase Date of Plane Dielectric Sheets for Radome Design. Report NADC-EL-5313, Aeronautical Electronic and Electrical Lab., NADC, Johnsville, Pa., 1 July 1953 (AD-45316). Supplementary Graphs of Transmission and Phase Delay of Plane Dielectric Sheets and Sandwich Constructions for Radome Design. Supplement to

report NADC-EL-5313, 16 June 1954 (AD-45543).

26. Everhart, E. M. Radome Wall Reflections at Variable Angles of Incidence. Report 463-20, Radiation Lab., MIT, 4 Jan 1946.

27. Gonshor, H. Optimizing Reflection from a Plane Sheet of Large Dielectric Constant over a Range of Incidence Angles. Report 12283-8J, McMillan Lab., Ipswich, Mass., 15 Aug 1952 (Confidential).

28. Horton, M. C., Boyce, W. E. L., and Hartig, E. O. Optical Theory for Microwave Transmission Through Dielectric Wall Structures. Report GER-5530, Goodyear Aircraft Corp., Akron, Ohio, 4 Aug 1953 (AD-42719).

29. Kay, A. F. The Electrical Design of the Homogeneous Radome Wall. Report 12283-8K, McMillan Lab., Ipswich, Mass., 15 Feb 1953 (Confidential).

30. Kay, A. F. Geometry of Reflection and Transmission Coefficients. Report 12283-7E, McMillan Lab., Ipswich, Mass., 14 Mar 1952 (Secret).

31. Kofoid, M. J. Bomarc Radome Design. Boeing Airplane Co., Seattle, Wash. In Symposium on Guided Missile Radomes (Supplement), ONR, Washington, D. C., June 1953 (Secret) (AD-38581).

32. Kofoid, M. J. Calculated Electrical Transmission Characteristics of Half-Wavelength Thick Solid Plane Sheets. Document D-13622, Boeing Airplane Co., Seattle, Wash., 24 Oct 1952 (rev. 12 Mar 1954) (AD-42401).

33. Lengyel, B. A. Half-Wave Radomes. Hughes Aircraft Co., Culver City, Calif. In Symposium on Guided Missile Radomes, ONR, Washington, D. C., June 1953 (Confidential) (AD-36188).

34. Lengyel, B. A., Langenberg, D. N., and Henschke, R. A. Transmission Through Half-Wave Sheets. Technical memorandum 327, Hughes Aircraft Co., Culver City, Calif., 1 Nov 1953 (AD-22010).

35. Luoma, E. J. Phase Retardation Design Curves for Solid Lossless Dielectric Panels. Technical report 56-116, WADC, Wright-Patterson AFB, Ohio, Feb 1956 (AD-110514).

36. Radome Engineering Manual. Published by direction of the Chief of the Bureau of Aeronautics and the Commanding General of the Air Materiel Command. AMC Manual 80-4, NAVAER 16-45-502, 1 Oct 1946.

37. Redheffer, R. M. Transmission and Reflection of Single Plane Sheets. Report 483-4, Radiation Lab., MIT, 12 July 1944.

38. Snow, O. J. Report on Applications of the Impedance Concept to Radome Wall Design. Report NADC-EL-52196, NADC, Johnsville, Pa., 6 Apr 1953.

39. Transmission Through a Lossy Dielectric Sheet. Document D-13645, Boeing Airplane Co., Seattle, Wash., 27 Oct 1952.

40. Undesser, K. Reflection Transmission Phase Delay Calculation in Radome Design. The Glenn L. Martin Co., Baltimore, Md. (Confidential).

41. Webster, R. E., and Moore, D. P. Transmission Coefficients of Elliptically Polarized Waves Incident on Homogeneous Isotropic Panels. Report 663-5, Antenna Lab., Ohio State U. Research Foundation, Columbus, 31 Dec 1956.

42. Weedon, M. G. B., and Stott, A. L. Calculations on the Transmission of Electromagnetic Waves Through Plane Dielectric Sheets. Technical note GW282, Royal Aircraft Establishment, Great Britain, Nov 1953 (Confidential) (AD-25779).

43. Wolin, S. Tables of Amplitude and Phase of the Function $1 + ae^{jb}$. Report NADC-EL-5114, NADC, Johnsville, Pa., 28 Aug 1952 (ATI-171767).

44. Wolin, S. Tables of Fresnel's Coefficients, Snell's Law and Other Radome Design Quantities. Report NADC-EL-5104, NADC, Johnsville, Pa., 22 Jan 1952. Supplementary Tables of Fresnel's Coefficients, Snell's Law, and Other Radome Design Quantities. Report NADC-EL-53189, 9 July 1954 (AD-37153).

45. Wolin, S. Tables of Transmission and Reflection Coefficients of Lossy, Homogeneous Dielectric Sheets. Report NADC-EL-52195, NADC, Johnsville, Pa., 2 vols.: vol. 1, 11 Feb 1954 (AD-36518); vol. 2, 7 Oct 1954.

46. Wolin, S. Theory of Lossy High-Incidence Radomes. Report NADC-EL-5116, NADC, Johnsville, Pa., 15 Jan 1952.

47. Wiederhorn, N. M., and Kay, A. F. Radome Design Criteria for Precision Guidance Radar. Final report, document 1276, McMillan Lab., Ipswich, Mass., 1 June 1954 (Confidential) (AD-49428).

4. The "A" Sandwich

48. Bowlby, C. W. Calculated Electrical Transmission Characteristics of Symmetrical Sandwich Flat Sheets. Document D-13643, Boeing Airplane Co., Seattle, Wash., 30 Oct 1952.

49. Cady, W. M., Karelitz, M. B., and Turner, L. A. (ed.). Radar Scanners and Radomes. McGraw-Hill Book Co., New York, 1948. (Vol. 26, MIT Radiation Lab. Series.)

50. Croswell, W. F. Constant Phase Retardation Characteristics of an "A" Sandwich Radome. Report TR-56-32, WADC, Wright-Patterson AFB, Ohio, Dec 1955 (Confidential) (AD-95556).

51. DiToro, J. A. Supplementary Graphs of Transmission and Phase Delay of Plane Dielectric Sheets and Sandwich Constructions for Radome Design. Supplement to report NADC-EL-5313, Aeronautical Electronic and Electrical Lab., NADC, Johnsville, Pa., 16 June 1954 (AD-45543).

52. Dowker, Y. Transmission of Lossy Sandwiches. Report 483-22, Radiation Lab., MIT, 23 Jan 1946.

53. Everhart, E. M. Radome Wall Reflections at Variable Angles of Incidence. Report 483-20, Radiation Lab., MIT, 4 Jan 1946.

54. Everhart, E. M. X-Band Sandwiches at Variable Angles of Incidence. Report 483-8, Radiation Lab., MIT, 19 Dec 1944.

55. Hartig, E. O., and Horton, M. C. The Theory of the Lossless Double Symmetrical Sandwich Radome. Report GER-2731, Goodyear Aircraft Corp., Akron, Ohio, 2 July 1951.

56. Henschke, R. A. Application of Matrices to the Problem of Transmission Through a Multi-Layered Dielectric Wall. Research and Development Lab., Hughes Aircraft Co., Culver City, Calif.

57. Lippmann, B. A. and Oppenheim, A. Analysis of Plane Slabs. Technical Research Group, New York, 30 Apr 1954 (AD-39181).

58. McMillan, E. B. The Half-Wave (Loaded Core) Sandwich. Proceedings of the Ohio State U. —WADC Radome Symposium, vol. I, 1955, pp. 132-136.

59. McMillan, E. B., Parker, R. S., and Redheffer, R. M. Radome Wall with High Dielectric Constant Core — The Two Outer Layers at Optimum Thickness. McMillan Lab., Ipswich, Mass., 12 Jan 1950.

60. Mathis, H. F. Methods of Determining Sandwich Transmission Characteristics. Report GER-7182, Goodyear Aircraft Corp., Akron, Ohio, 12 Dec 1955 (AD-91145).

61. Radome Engineering Manual. Published by direction of the Chief of the Bureau of Aeronautics and the Commanding General of the Air Materiel Command. AMC Manual 80-4, NAVAER 16-45-502, 1 Oct 1948.

62. Redheffer, R. M. Electrical Properties of Double Wall and Sandwich Radomes. Radome Bulletin No. 11, report 483-11, Radiation Lab., MIT, 1 Feb 1945 (Confidential).

63. Redheffer, R. M. Transmission and Reflection of Parallel Plane Sheets. Report 483-12, Radiation Lab., MIT, 26 Jan 1945.

64. Snow, O. J. Report on Applications of the Impedance Concept to Radome Wall Design. Report NADC-EL-52196, NADC, Johnsville, Pa., 6 Apr 1953.

65. Speer, W. Matrix Method of Radome Transmission Computation. Memorandum report EG-MR-3, Douglas Aircraft Co., El Segundo, Calif., 4 Jan 1951 (ATI-178476).

66. Webster, R. E., and Moore, D. P. Transmission Coefficients of Circularly Polarized Waves Incident on "A" and "C" Sandwich Panels. Report 663-6, Antenna Lab., Ohio State U. Research Foundation, Columbus, 31 Dec 1956.

67. Wolin, S. Electrical Design of Lossy High-Incidence Radomes. Report ADC EL-123-50, NADC, Johnsville, Pa., 11 1950.

68. Wolin, S. Formulas for Calculating Transmission Coefficients for Low Loss Radome Sandwiches by the Vector Method. NADC, Johnsville, Pa., 6 Dec 1948.

69. Wolin, S. Reflection and Transmission of Electromagnetic Waves by Multilayer Plane Dielectric Sheets at Arbitrary Incidence. Report NADC-EL-5293, NADC, Johnsville, Pa., 6 Aug 1952.

70. Wolin, S. Tables of Transmission and Reflection Coefficients of Lossy, Symmetrical Dielectric Radome Sandwiches. Report NADC-EL-52188 (Supplement to report ADC EL-123-50, 11 July 1950), Aeronautical Electronic and Electrical Lab., NADC, Johnsville, Pa., 22 Oct 1953.

71. Wolin, S. Theory of Lossy High-Incidence Radomes. Report NADC-EL-5116, NADC, Johnsville, Pa., 15 Jan 1952.

5. The "B" Sandwich

72. Barrar, R. B. Methods of Design of Experimental Radomes of Report 8Q. Report 12283-8U, McMillan Lab., Ipswich, Mass. (Confidential) (AD-40640).

73. Cady, W. M., Karelitz, M. B., and Turner, L. A. (ed.). Radar Scanners and Radomes. McGraw-Hill Book Co., New York, 1948. (Vol. 26, MIT Radiation Lab. Series.)

74. Hartig, E. O., and Horton, M. C. The Theory of the Lossless Double Symmetrical Sandwich Radome. Goodyear Aircraft Corp., Akron, Ohio, 2 July 1951.

75. Henschke, R. A. Application of Matrices to the Problem of Transmission Through a Multi-Layered Dielectric Wall. Research and Development Lab., Hughes Aircraft Co., Culver City, Calif.

76. McMillan, E. B. The B Sandwich in Missile Radomes, Lenses and Broadband Radomes. Proceedings of the Ohio State U. — WADC Radome Symposium, vol. II, June 1955, pp. 231-237 (Confidential) (AD-86660).

77. Mathis, H. F. Methods of Determining Sandwich Transmission Characteristics. Report GER-7182, Goodyear Aircraft Corp., Akron, Ohio, 12 Dec 1955 (AD-91145).

78. Lippmann, B. A., and Oppenheim, A. Analysis of Plane Slabs. Technical Research Group, New York, 30 Apr 1954 (AD-39181).

79. Luoma, E. J. Phase Retardation Design Curves for Solid Lossless Dielectric Panels. Technical report 56-116, WADC, Wright-Patterson AFB, Ohio, Feb 1956 (AD-110514).

80. Redheffer, R. M. Electrical Properties of Double Wall and Sandwich Radomes. Report 483-11, Radiation Lab., MIT, Feb 1945.

81. Redheffer, R. M. Beam Alignment in Radomes. Part II. Section C, Theoretical Sandwich Design for Phase. Technical report 7, McMillan Lab., Ipswich, Mass., 14 Mar 1952.

82. Redheffer, R. M., Sampson, H., Janus, N. N., and Webber, A. H. A Study of Broadbanding Techniques. Final report, McMillan Lab., Ipswich, Mass., 31 Jan 1956 (Confidential) (AD-90649).

83. Snow, O. J. Report on Applications of the Impedance Concept to Radome Wall Design. Report NADC-EL-52196, NADC, Johnsville, Pa., 6 Apr 1953.

84. Speer, W. Matrix Method of Radome Transmission Computation. Memorandum report EG-MR-3, Douglas Aircraft Co., El Segundo, Calif., 4 Jan 1951 (ATI-178476).

85. Webster, R. E., and Moore, D. P. Transmission Coefficients of Circularly Polarized Waves Incident on "A" and "C" Sandwich Panels. Report 663-6, Antenna Lab., Ohio State U. Research Foundation, Columbus, 31 Dec 1956.

86. Wiederhorn, N. M. Design and Fabrication of a B Sandwich Streamlined Radome. Final report, contract AF 33(038)-16606, McMillan Lab., Ipswich, Mass., 17 Feb 1954 (AD-29262).

87. Wolin, S. Formulas for Calculating Transmission Coefficients for Low Loss Radome Sandwiches by the Vector Method. NADC, Johnsville, Pa., 6 Dec 1948.

88. Wolin, S. Reflection and Transmission of Electromagnetic Waves by Multilayer Plane Dielectric Sheets at Arbitrary Incidence. Report NADC-EL-5293, NADC, Johnsville, Pa., 6 Aug 1952.

6. The "C" Sandwich

89. Hartig, E. O., and Horton, M. C. The Theory of the Lossless Double Symmetrical Sandwich Radome. Report GER-

2731, Goodyear Aircraft Corp., Akron, Ohio, 2 July 1951.

90. Henschke, R. A. Application of Matrices to the Problem of Transmission Through a Multi-Layered Dielectric Wall. Research and Development Lab., Hughes Aircraft Co., Culver City, Calif.

91. Kay, A. F. Reflection of a Plane Wave by a Stratified Medium. Document 1294, McMillan Lab., Ipswich, Mass., 22 Nov 1954.

92. Lippmann, B. A., and Oppenheim, A. Analysis of Plane Slabs. Technical Research Group, New York, 30 Apr 1954 (AD-39181).

93. Mathis, H. F. Methods of Determining Sandwich Transmission Characteristics. Report GER-7182, Goodyear Aircraft Corp., Akron, Ohio, 12 Dec 1955 (AD-91145).

94. Redheffer, R. M. Transmission and Reflection of Parallel Plane Sheets. Report 483-12, Radiation Lab., MIT, 26 Jan 1945.

95. Redheffer, R. M., Sampson, H., Janus, N. N., and Webber, A. H. A Study of Broadbanding Techniques. Final report, McMillan Lab., Ipswich, Mass., 31 Jan 1956 (Confidential) (AD-90649).

96. Speer, W. Matrix Method of Radome Transmission Computation. Memorandum report EG-MR-3, Douglas Aircraft Co., El Segundo, Calif., 4 Jan 1951 (ATI-178476).

97. Wolin, S. Reflection and Transmission of Electromagnetic Waves by Multilayer Plane Dielectric Sheets at Arbitrary Incidence. Report NADC-EL-5293, Aeronautical Electronic and Electrical Lab., NADC, Johnsville, Pa., 6 Aug 1952.

98. Wolin, S. Tables of Transmission and Reflection Coefficients of Lossy, Symmetrical Dielectric Radome Sandwiches. Report NADC-EL-52188 (supplement to report ADC EL-123-50, 11 July 1950), Aeronautical Electronic and Electrical Lab., NADC, Johnsville, Pa., 22 Oct 1953.

99. Snow, O. J. Report on Applications of the Impedance Concept to Radome Wall Design. Report NADC-EL-52196, NADC, Johnsville, Pa., 6 Apr 1953.

7. Tolerances in Thickness and Dielectric Constant

100. Boyce, W. E. L. The Angular Error Characteristics of a Radome as a Function of the Polarization of the Field Incident on the Radome. Proceedings of the Ohio State U. –WADC Radome Symposium, vol. II, June 1955, pp. 205-230 (Confidential) (AD-86660).

101. Cady, W. M., Karelitz, M. B., and Turner, L. A. Radar Scanners and Radomes. McGraw-Hill Book Co., New York, 1948. (Vol. 26, MIT Radiation Lab. Series.)

102. Conant, G. H., Jr., Wachendorf, F., and others. Investigations on the Properties of Radomes. A Study of the Geometrical and Physical Problems of Microwave Transmission Through Radome Walls. Engineering report 296, Perkin-Elmer Corp., Norwalk, Conn., 31 May 1954 (Secret).

103. Everhart, E. M. Radome Wall Reflections at Variable Angles of Incidence. Report 483-20, Radiation Lab., MIT, 4 Jan 1946.

104. Gonshor, H. Optimizing Reflection from a Plane Sheet of Large Dielectric Constant over a Range of Incidence Angles. Report 12283-8J, McMillan Lab., Ipswich, Mass. 15 Aug 1952 (Confidential).

105. Kay, A. F. The Electrical Design of the Homogeneous Radome Wall. Report 12283-8K, McMillan Lab., Ipswich, Mass., 15 Feb 1953 (Confidential).

106. Kotik, J. Some Remarks on Thin Dielectric Walls. Report 12283-8M, McMillan Lab., Ipswich, Mass., 15 Mar 1953 (Confidential).

107. Luoma, E. J. Phase Retardation Design Curves for Solid Lossless Dielectric Panels. Technical report 56-116, WADC, Wright-Patterson AFB, Ohio, Feb 1956 (AD-110514).

108. Mathis, H. F. Transmission Characteristics of Sandwiches. IRE Transactions, vol. MTT-3, Oct 1955, pp. 57-58.

109. Pinney, E. J. The Transmission Efficiency of an Imperfectly Flat Sheet. Document D-14101, Boeing Airplane Co., Seattle, Wash., 10 Apr 1953.

110. Pressel, P. I. Boresight Prediction Technique. WADC technical report 56-393, Proceedings of the Ohio State U.—WADC Radome Symposium, vol. I, Aug 1956 (AD-97150).

111. Redheffer, R. M. Transmission and Reflection of Single Plane Sheets. Report 483-4, Radiation Lab., MIT, 12 July 1944.

112. Smith, P. H. Transmission-Line Calculator. Electronics, vol. 12, Jan 1939, pp. 29-31.

113. Some Tests to Determine the Effects of Dielectric Constant, Shape, and Wall Thickness Taper on Radome Aberration. Report LEL.t.053, English Electric Co., Great Britain, 28 Jan 1955 (Secret).

114. Wolin, S. Electrical Design of Lossy High-Incidence Radomes. Report ADC EL-123-50, NADC, Johnsville, Pa., 11 July 1950.

115. Wolin, S. Ray Deflection Through a Medium Having a Continuously Varying Refractive Index. Report NADC-EL-5294, NADC, Johnsville, Pa., 28 Aug 1952.

8. Polarization

116. Bailin, L. L., Golvin, B., and McEuen, A. H. Some Considerations of Radome Errors. Presented at the RDB Symposium on Antennas and Radomes, San Francisco, 1 Aug 1951.

117. Barrar, R. B. and Webber, A. H. Elliptic Polarization Experiments. Report 8T, contract AF 33(038)-12283, McMillan Lab., 1954.

118. Boyce, W. E. L. The Angular Error Characteristics of a Radome as a Function of the Polarization of the Field Incident on the Radome. Proceedings of the Ohio State U. —WADC. Radome Symposium, vol. II, June 1955.

119. Cady, W. M., Karelitz, M. B., and Turner, L. A. Radar Scanners and Radomes. McGraw-Hill Book Co., New York, 1948. (Vol. 26, MIT Radiation Lab. Series.)

120. Hata, F. T. Depolarization Effects on Radome Errors. Proceedings of the Ohio State U. —WADC Radome Symposium, vol. II, June 1955, pp. 117-131 (Confidential) (AD-86660).

121. Kales, M. L. Elliptically Polarized Waves and Antennas. IRE Proceedings, vol. 39, part III, May 1951, pp. 544-549.

122. Kennaugh, E. M. Effects of Type of Polarization on Echo Characteristics. Report 389-1, Antenna Lab., Ohio State U., Columbus, 16 Sept 1949. Report 389-2, 16 Dec 1949. Report 389-9, 16 June 1951.

123. Kotik, J. The Variation of Tracking Error with Dish Illumination Polarization in 1-way and 2-way Conical Scanning Systems. Contract Nonr-123700, McMillan Lab., Ipswich, Mass., 15 Nov 1954 (Confidential) (AD-50472).

124. Luoma, E. J. Phase Retardation Design Curves for Solid Lossless Dielectric Panels. Technical report 56-116, WADC, Wright-Patterson AFB, Ohio, Feb 1956 (AD-110514).

125. Redheffer, R. M. Elliptical Polarization Produced by Streamlined Radomes. Report 483-13, Radiation Lab., MIT, 12 Feb 1945 (ATI-13762).

126. Rumsey, V. H., Deschamps, G. A., Kales, M. L., and Bohnert, J. I. Techniques for Handling Elliptically Polarized Waves with Special Reference to Antennas. IRE Proceedings, May 1951, pp. 533-552.

127. Sinclair, G. The Transmission and Reception of Elliptically Polarized Waves. IRE Proceedings, vol. 37, Feb 1948, pp. 155-158.

128. Snow, O. J. Discussion of the Ellipticity Produced by Radomes and Its Effect on Crossover-Point Position for Conically Scanning Antennas. Report NADC-EL-5108, NADC, Johnsville, Pa., 13 Nov 1951 (Confidential).

129. Thormahlen, W., and Huynen, J. R. Interim Engineering Report No. 2 on Effect of Polarization on the Radar Return from Ground Targets and Rain. Report R-135-867, Dalmo-Victor Co., San Carlos, Calif., 3 June 1953 (Confidential).

130. Webster, R. E. Elliptical Polarizations and Radome Errors. Report 683-3, contract AF 33(616)-3277, Antenna Lab., Ohio State U., Columbus, 15 Nov 1956.

131. Webster, R. E., and Moore, D. P. Transmission Coefficients of Circularly Polarized Waves Incident on "A" and "C"

Sandwich Panels. Report 663-6, contract AF 33(616)-3277, Antenna Lab., Ohio State U., Columbus, 31 Dec 1956.

132. Webster, R. E., and Moore, D. P. Transmission Coefficients of Elliptically Polarized Waves Incident on Homogeneous Isotropic Panels. Report 663-5, contract AF 33(616)-3277, Antenna Lab., Ohio State U., Columbus, 31 Dec 1956.

133. Williams, D. D. A Theory of the Dependence of Radome Error on Signal Polarization. Proceedings of the Ohio State U. —WADC Radome Symposium, vol. I, June 1955, pp. 68-76.

134. Wolin, S. Electrical Design of Lossy High-Incidence Radomes. Report ADC EL-123-50, NADC, Johnsville, Pa., 11 July 1950.

135. Wolin, S. Theory of Lossy High-Incidence Radomes. Report NADC-EL-5116, NADC, Johnsville, Pa., 15 Jan 1952.

9. Magnetic Radome Materials

136. Dispersion and Absorption of Ferromagnetic Semiconductors. Semi-annual progress report 1, Lab. for Insulation Research, MIT, Cambridge, Mass., 31 Mar 1954.

137. Fox, A. G., Miller, S. E., and Weiss, M. T. Behavior and Application of Ferrites in the Microwave Region. The Bell System Technical Jour., vol. XXXIV, Jan 1955, p. 93.

138. Schramm, C. K., Jr. Propagation Constant and the Radome. WADC technical report 53-297, Wright Air Development Center, Aug. 1953 (AD-21967).

139. Von Hippel, A. R., Westphal, W. B., and Miles, P. A. Dielectric Analysis of Ferrites and Their Appraisal as Radome Materials. WADC technical report 55-149, MIT, Feb 1955 (AD-76793).

140. Wachendorf, F. Investigation on the Properties of Radomes. Report 423, Perkin-Elmer Corp., Norwalk, Conn., 31 Dec 1955 (Secret).

10. Anisotropic Materials and Construction

141. Cutler, S., and Kotik, J. The Propagation of Electromagnetic Waves Through Anistropic Multilayers. Contract AF 19 (604)-1307, Technical Research Group, New York, 30 Jan 1956 (AD-87092).

142. Friedman, B. Modes in Anisotropic Structures. Report 3, Contract AF 19(604)-1015, Technical Research Group, New York, Jan 1955.

143. Hurd, R. A. Diffraction by a Metal Plate Lens for Arbitrary Incidence and Polarization. Report ERB-359: NRC 3599, National Research Council, Canada, Mar 1955 (AD-70532).

144. Investigation of Variable Index of Refraction Lenses. Report 5224-1263, Sperry Gyroscope Co., Great Neck, N. Y., Sept 1952.

145. Jones, E. M. T., Cohn, S. B., and Robinson, L. A. Wide-Band Radomes Matched by Reactive Walls. Proceedings of the Ohio State U. —WADC Radome Symposium, vol. I, June 1955, pp. 52-67.

146. Jones, E. M. T., and Robinson, L. A. Research and Development on the Electrical Properties of Metal Inclusions for Radomes. Report 1, contract AF 33(616)-3495, Stanford Research Inst., Menlo Park, Calif., July 1956.

147. Kirschbaum, H. S. A Polarizing, Reinforced, Broad-Band Anisotropic Panel. Proceedings of the Ohio State U—WADC Radome Symposium, June 1956.

148. Klotzbaugh, G. A., Flarherty, J. M., and Hughes, R. H. A Study of Artificial Dielectrics with Unity Dielectric Constants. Report GR-177, Westinghouse Electric Corp., East Pittsburgh, Pa., 2 Apr 1954 (Confidential) (AD-41732).

149. Kotik, J. The Dielectric Tensor of Alternating-Layer Material with Application to Honeycomb and Broadband Radomes. Proceedings of the Ohio State U.—WADC Radome Symposium, June 1956.

150. Kotik, J. Propagation Through Dielectric Honeycomb Material. Contract AF 33 (616)-2973, Technical Research Group. New York, July 1955 (AD-67674).

151. Lippmann, B. A., and Oppenheim, A. Cascaded Arrays. Contract Nonr-123000, Technical Research Group, New York, 30 Apr 1954 (AD-39182).

152. Lippmann, B. A., and Oppenheim, A. Loaded Dielectrics. Contract Nonr-123000, Technical Research Group, New York, 30 Apr 1954.

153. Paiss, M. H. Investigation of Metal-Ribbed Radomes. Report NADC-EL-L5315, NADC, Johnsville, Pa., 27 Apr 1953.

154. Radome Problem In Guided Missiles, The. Final report, contract N6 ONR-27-23 (sponsored by ONR), Princeton U., Princeton, N. J., 1 Mar 1952 (Secret).

155. Smith, R. S. Dependence of Dielectric Constant on Density of Aggregates. Technical report 12, University of Pennsylvania, 1 Apr 1955.

156. Worthington, H. R., Jr. Improvement of Radome Preformance be Means of Metal Grids. Proceedings of the Ohio State U. —WADC Radome Symposium, vol. II, June 1955, pp. 106-116 (Confidential) (AD-56660).

157. Worthington, H. R., Jr. Investigation of Cabinet Principle for Possible Radome Application. Report NADC-EL-5372, NADC, Johnsville, Pa., 6 May 1953 (Confidential).

158. Worthington, H. R., Jr. Investigations of the Microwave Transmitting Properties of Metal Screens. Report NADC-EL-53188, NADC, Johnsville, Pa., 26 Jan 1954 (Confidential).

159. Worthington, H. R. Metal Screens for Radome Materials. ONR Symposium on Guided Missile Radomes, Washington, D. C., June 1953, pp. 117-132 (Confidential).

11. The Radome Shape

160. Barrar, R. B. Methods of Design of Experimental Radomes of Report 8Q. Report 12283-8U, contract AF 33(038)-12283, McMillan Lab., Ipswich, Mass. (Confidential) (AD-40640).

161. Bird, J. L., and Fry, J. A. Some Tests to Determine the Effects of Dielectric Constant, Shape, and Wall Thickness Taper on Radome Aberration. Report LEL.t. 053, English Electric Co., Great Britain, 28 Jan 1955 (Secret) (AD-75842).

162. King-Hele, D. G., Bowcock, K. J., and Peattie, I. W. Effects of Radome Shape on the Weights of Surface-to-Air Guided Missiles, Including "Optimum" Designs for Ramjets and Rockets of Various Ranges. Technical note GW 220, Royal Aircraft Establishment, Great Britain, Nov 1952 (Secrete).

163. Luoma, E. J. Phase Retardation Design Curves for Solid Lossless Dielectric Panels. Technical report 56-116, Wright-Patterson AFB, Ohio, Feb 1956 (AD-110514).

164. Radome Problem In Guided Missiles, The. Final report, contract N6 ONR-27-23 (sponsored by ONR), Princeton U., Princeton, N. J., 1 Mar 1952 (Secret).

165. Wiederhorn, N. M., and Kay, A. F. Radome Design Criteria for Precision Guidance Radar. Final report, contract AF 33(038) -12283, McMillan Lab., Ipswich, Mass., 1 June 1954 (Confidential) (AD-49428).

166. Wiederhorn, N. M., Kay, A. F. and Kotik, J. The Dependence of Radome Error on Shape, Wall Structure, and Taper. Report 12283-8Q, McMillan Lab., Ipwich, Mass., 31 Mar 1954 (Confidential) (AD-32198).

12. The Focusing Effect of Streamlined Radomes

167. Baechle, J. R., Richmond, J. H., and Stickler, D. C. Antenna Pattern Distortion by a Wedge-Shaped Radome. Report 655-2, contract AF 33(616)-3212, Antenna Lab., Ohio State U., Columbus, 1 Mar 1956 (Confidential).

168. Hata, F. T. Investigation of Electromagnetic Field Distortion Caused by Dielectric Sheets, Wedges, and Radomes Placed Near an Antenna. ONR Symposium on Guided Missile Radomes, Washington, D. C., June 1953 (Confidential).

169. Kay, A. F. Simple Mathematical Models of Radomes. Report 12283-8-O, McMillan Lab., Ipswich, Mass., 23 Spet 1953 (Confidential) (AD-31771).

170. Paiss, M. H. Interim Report, Summary of Beam Deflection Investigations for the Period 1 October 1950 to 1 February 1953. Report NADC-EL-5399, 27 Oct 1953 (Confidential).

171. Paiss, M. H. Results of Beam-Deflection Tests on One-Piece Radomes, Serial

Numbers A19-9, A19-10, and A19-7 for Navy Models F3D-1 and F3D-2 Aircraft. Report NADC-EL-L5201, 3 Apr 1953 (Confidential).

172. Richmond, J. H. The Focusing Effect of Radomes. Report 655-3, contract AF 33 (616)-3212, Antenna Lab., Ohio State U., Columbus, 1 June 1956 (AD-103460).

173. Sledge, O. D., and Hata, F. T. Investigation of Electromagnetic Field Distortions Caused by Dielectric Sheets, Wedges, and Radomes Placed Near an Antenna. Report 10-E-251, National Bureau of Standards, Corona, Calif., 31 Aug 1953 (Confidential).

174. Tice, T. E., and Richmond, J. H. Fields Measured Near a Typical Radome. Report 531-4, contract AF(616)-277, Antenna Lab., Ohio State U., Columbus, 31 July 1953.

175. Wiederhorn, N. M., Kay, A. F., and Kotik, J. The Dependence of Radome Error on Shape, Wall Structure, and Taper. Report 12283-8Q, McMillan Lab., Ipswich, Mass., 31 Mar 1954 (Confidential) (AD-32198).

176. Wolin, S. Theory of Lossy High-Incidence Radomes. Report NADC-EL-5116, NADC, Johnsville, Pa., 15 Jan 1952.

13. Diffraction by Radomes

177. Angulo, C. M. Diffraction of Surface Waves by a Semi-Infinite Dielectric Slab. Report AF 1291/1, contract AF 19(604)-1391, Brown U., Providence, R. I., Aug 1955 (AD-78552).

178. Barrar, R. B. The Diffraction of an Electromagnetic Plane Wave by a Curved Wall. Report 12283-8L, contract AF 33(038)-12283, McMillan Lab., Ipswich, Mass., 16 Mar 1953 (Confidential).

179. Bronwell, A. B., and Beam, R. E. Theory and Application of Microwaves. McGraw-Hill Book Co., New York, 1947.

180. Cohen, M. H. Application of the Reaction Concept to Scattering Problems. IRE Transactions, vol. AP-3, Oct 1955.

181. Damonte, J. B., Gaetano, A., and Gunter, R. C., Jr. Radome Error Prediction Study. Third quarterly scientific report, report R-510-1187, Dalmo-Victor Co., San Carlos, Calif., 8 Apr 1955 (Secret). Hahn, [illegible], Gunter, R. C., Jr., and Pinney, E. [illegible] Radome Error Prediction Study. [illegible] quarterly scientific report, report R-510-1217, 15 July 1955 (Secret).

182. Gonshor, H. Beam Alignment in Radomes – Part III. Section J, Optimizing Reflection from a Plane Sheet of Large Dielectric Constant over a Range of Incidence Angles. Interim engineering report 8J, McMillan Lab., Ipswich, Mass. (Confidential).

183. Goubau, G. On the Excitation of Surface Waves. IRE Proceedings, July 1952, pp. 865-868.

184. Hata, F. T. Investigation of Electromagnetic Field Distortion Caused by Dielectric Sheets, Wedges, and Radomes Placed Near an Antenna. ONR Symposium on Guided Missile Radomes, Washington, D. C., June 1953 (Confidential).

185. Hatkin, L. Analysis of Propagation Modes in Dielectric Sheets. IRE Proceedings, vol. 42, Oct 1954, pp. 1565-1568 (AD-58261).

186. Kay, F. Beam Alignment in Radomes. Part II. Section E, Geometry of Reflection and Transmission Coefficients. Technical Report 7, McMillan Lab., Ipswich, Mass. (Secret).

187. Januskevich, N. N. Beam Alignment in Radomes. Part II. Section H, The Radome as a Functional Part of the Antenna System. Technical report 7, McMillan Lab., Ipswich, Mass.

188. Kay, A. F. Beam Alignment in Radomes. Part III. Section O, Simple Mathematical Models of Radomes. Report 12283-8-O, McMillan Lab., Ipswich, Mass., 23 Sept 1953 (Confidential) (AD-31771).

189. Kay, A. F. The Exitation of Surface Waves in Multilayered Media. Contract AF 19(604)-1126, Technical Research Group, New York, Oct 1954 (AD-55911).

190. Kay, A. F. The Two-Step Antenna Model of Radome Boresight Errors. Contract Nonr-124700, McMillan Lab., Ipswich, Mass., 10 Mar 1954 (Confidential) (AD-27077).

191. Kay, A. F. and Barrar, R. B. Lloyd's Mirror Effect in Radome Error. Contract Nonr-124700, McMillan Lab.,

Ipswich, Mass., 18 Mar 1954 (Confidential) (AD-50473).

192. Kay, A. F. and Kotik, J. The Propagation of Plane and Surface TE Waves in Semi-Infinite, Thin Dielectric Panels. Symposium on Microwave Optics, McGill U., Montreal, Canada, vol. 1, June 1953.

193. Kay, A. F., and Zucker, F. J. Efficiency of Surface Wave Excitation. 1955 IRE Convention Record, part 1, pp. 1-5.

194. Mason, S. J. Beam Alignment in Radomes. Part II, Section F, Trapped Waves. Report 12283-7-F, McMillan Lab., Ipswich, Mass., 29 Aug 1952 (Secret).

195. Mason, S. J., and Redheffer, R. M. Diffraction. Report 12283-4, contract AF 33(038)-12283, McMillan Lab., Ipswich, Mass., 17 Feb 1951.

196. Philipson, L. L., and Adler, D. E. On Scattering by a Thin Dielectric Ring. Proceedings of the Ohio State U.-WADC Radome Symposium, vol. II, 1956, pp. 47-56 (Confidential) (AD-97151).

197. Radome Problem in Guided Missiles, The. Final report, contract N6 ONR-27-23 (sponsored by ONR), Princeton U., Princeton, N. J., 1 Mar 1952 (Secret).

198. Ramo, S., and Whinnery, J. R. Fields and Waves in Modern Radio. John Wiley and Sons, New York, 1944.

199. Rhodes, D. R. On the Theory of Scattering by Dielectric Bodies. Report 475-1, contract AF 18(600)-19, Antenna Lab., Ohio State U., Columbus, 1 July 1953.

200. Richmond, J. H. Antenna Pattern Distortion by Dielectric Sheets. IRE Transactions, vol. AP-4, Apr 1956, pp. 139-142.

201. Richmond, J. H. Antenna Pattern Distortion by Dielectric Sheets. Proceedings of the Ohio State U.—WADC Radome Symposium, vol. I, June 1955, pp. 94-105.

202. Richmond, J. H. Report on contract AF 33(616)-3212, Antenna Lab., Ohio State U., Columbus, 1956.

203. Rix, N. D. The Ripple Tank as a Device for Studying Wave Propagation. Jour. Acous. Soc. America, vol. 21, 1949.

204. Sledge, O. D., and Hata, F. T. Investigation of Electromagnetic Field Distortions Caused by Dielectric Sheets, Wedges, and Radomes Placed Near an Antenna. Report 10-E-251, National Bureau of Standards, Corona, Calif., 31 Aug 1953 (Confidential).

205. Squires, M. An Introductory Study of Radome Aberration as a Factor in Proportional Navigation. Technical note GW 281, Royal Aircraft Establishment, Great Britain, Dec 1953 (Secret).

206. Stratton, J. A. Electromagnetic Theory. McGraw-Hill Book Co., New York, 1941.

207. Walbridge, N. L., Smith, H. M., and Woodward, L. A. Water Ripple Analogue of Electromagnetic Wave Propagation. Report 2, contract Nonr-597-(01), University of Vermont, Jan 1955 (AD-57875).

208. Walbridge, N. L., Woodward, L. A., and Smith, H. M., Jr. The Ripple Tank Analogue as an Aid in Radome Design. Proceedings of the Ohio State U.-WADC Radome Symposium, vol. I, June 1955, pp. 106-116.

209. Wass, C. A. A. Note on Radome Aberration. Technical note GW 130, Royal Aircraft Establishment, Great Britain, Aug 1951 (Secret).

210. Wiederhorn, N. M., and Kay, A. F. The Displacement of Radar Beams by Dielectric Sheets and Wedges. Report 12283-8P, contract AF 33(038)-12283, McMillan Lab., Ipswich, Mass., 5 Apr 1954 (Confidential).

211. Woonton, G. A. The Effect of an Obstacle in the Fresnel Field on the Distant Field of a Linear Radiator. Jour. of Applied Physics, vol. 21, June 1950, pp. 577-580.

212. Tai, C. T., and Barnett, R. I. Characteristics of Large Spherical Radomes. Proceedings of the Ohio State U.—WADC Radome Symposium, vol. I, June 1955, pp. 77-93.

213. Tice, T., and Adney, J. Transmission Through a Dielectric Spherical Shell. Report 531-3, contract AF 33(616)-277, Antenna Lab., Ohio State U., Columbus, 1 Aug 1953.

14. Luneberg Lens and Streamlined Lens Radomes

214. Braun, E. H. Radiation Characteristics of the Spherical Luneberg Lens. IRE Transactions, vol. AP-4, Apr 1956, pp. 132-138.

215. Chait, H. N. A Microwave Schmidt System. Report 3989, Naval Research Lab., Washington, D. C., 14 May 1952.

216. Cohen, M. H. Electromagnetic Scattering by Dielectric Bodies. Report 475-14, Antenna Lab., Ohio State U., 30 June 1954. Also presented at URSI-IRE Meeting, Washington, D. C., May 1954.

217. Einbinder, H. Variable Dielectric Lenses Whose Refractive Index Varies Along and Normal to Their Axis of Symmetry. Third quarterly scientific report, contract AF 33(616)-2646, Technical Research Group, New York, Apr 1955 (AD-68118).

218. Hart, R. W. and Montroll, E. W. On the Scattering of Plane Waves by Soft Obstacles. I. Spherical Obstacles. Jour. Appl. Phys., vol. 22, Apr 1951, pp. 376-386.

219. Investigation of Variable Index of Refraction Lenses. Report 5224-1263, Sperry Gyroscope Co., Great Neck, N. Y., Sept 1952.

220. Jasik, H. The Electromagnetic Theory of the Luneberg Lens. Report TR-54-121, AF Cambridge Research Center, Nov 1954 (AD-61510).

221. Kay, A. F. Lens Radomes. Second quarterly scientific report, contract AF 33(616)-2646, Technical Research Group, New York, Feb 1955 (AD-59379). Fourth . . . report, Aug 1955 (AD-68869). Summary report, Aug 1955 (AD-72607). Fifth. . .report, 3 Nov 1955 (AD-77071). Sixth. . .report, Feb 1956.

222. Kay, A. F. Streamlined Lens Radome. Proceedings of the Ohio State U.-WADC Radome Symposium, June 1956.

223. Kay, A. F., and Einbinder, H. Lens Radomes. First quarterly scientific report, contract AF 33(616)-2646, Technical Research Group, New York, Nov 1954 (AD-46405).

224. Keller, J. B. Reflection and Transmission of Electromagnetic Waves by Thin Curved Shells. Research report 172-5, Mathematical Research Group, Auxiliary to Square College, New York U., New York.

225. Lippman, B. A. An Elementary Discussion of the Luneberg Lens. Report AFCRC-TN-54-371, technical report 1, contract AF 19(604)-1015. Technical Research Group, New York, 30 June 1954.

226. Montroll, E. W., and Hart, R. W. Scattering of Plane Waves by Soft Obstacles. II. Scattering by Cylinders, Spheroids, and Disks. Jour. Appl. Phys., vol. 22, Oct 1951, pp. 1278-1289.

227. Montroll, E. W., and Greenberg, J. M. Scattering of Plane Waves by Soft Obstacles. III. Scattering by Obstacles With Spherical and Circular Cylindrical Symmetry. Phys. Rev., vol. 86, 15 June 1952, pp. 889-897.

228. Philipson, L. L. and Adler, D. E. On Scattering by a Thin Dielectric Ring. Proceedings of the Ohio State U.-WADC Radome Symposium, Aug 1956 (Confidential).

229. Rhodes, D. R. On the Theory of Scattering by Dielectric Bodies. Report 475-1, Antenna Lab., Ohio State U., 1 July 1953.

230. Schetne, H. A. The Use of Dielectric Rings in Reducing Radome Error. Technical memorandum 403, Hughes Aircraft Co., 15 June 1955.

231. Silver, S. (ed.). Microwave Antenna Theory and Design. McGraw-Hill Book Co., New York, 1949. (Vol. 12, MIT Radiation Lab. Series.)

232. Sledge, O. D., and Hata, F. T. Investigation of Electromagnetic Field Distortions Caused by Dielectric Sheets, Wedges, and Radomes Placed Near an Antenna. Report 10-E-251, National Bureau of Standards, Corona, Calif., 31 Aug 1953 (Confidential).

233. Sternberg, R. L. Successive Approximation and Expansion Methods in the Numerical Design of Microwave Dielectric Lenses. Jour. of Mathematics and Physics, vol. 34, Jan 1956.

234. Tai, C. T. The Electromagnetic Theory of the Spherical Luneberg Lens. Report 667-17, contract AF 33(616)-3353, Antenna Lab., Ohio State U., Columbus, 31 Aug 1956

235. Wiederhorn, N. M., and Kay, A. F. The Displacement of Radar Beams by Dielectric sheets and Wedges. Document 1270, McMillan Lab., Ipswich, Mass., 5 Apr 1954 (Confidential).

236. Wright, W. W. A Three-Dimensional Luneberg Lens. First quarterly progress report, Scientific Associates, Atlanta, Ga., 15 May 1954. Second. . .report, 15 Aug 1954.

237. Wright, W. W., Rhodes, J. E., and Robinson, G. P. A Three-Dimensional Luneberg Lens. Final report, Scientific Associates, Atlanta, Ga., 15 Dec 1954.

15. Radomes for Millimeter Wavelengths

238. Jenness, J. R., Jr. The Development of Irdomes. Report NADC-EL-5453, NADC, Johnsville, Pa., 23 June 1954 (Confidential).

239. Richmond, J. H. and Stickler, D. C. Radomes for Millimeter Wavelengths. Report 655-4, contract AF 33(616)-3212, Antenna Lab., Ohio State U., Columbus, 1 Sept 1956.

240. Snow, O. J. The Development of Irdomes. Report ADC EL-19-51, NADC, Johnsville, Pa., 24 Jan 1951 (Confidential).

241. Snow, O. J. The Development of Irdomes. Report NADC-EL-5107, NADC, Johnsville, Pa., 11 Oct 1951 (Confidential).

16. Broadband Radome Design

242. Notes on Electrical Design of Radomes. Radome Division, US NAMC Philadelphia, Pa., May 1946. (Based in part on RadLab 483 Series of reports.)

243. Study of Broadbanding Techniques, A. Report on WADC contract AF33(600)-28749, McMillan Lab.

244. Webber, A. H., Jr. (ed.). A Study of Broadbanding Techniques. Final report, AMC, contract AF33(600)-28749, McMillan Lab., 21 Jan 1956.

245. Webber, A. H., Jr. A Study of Broadbanding Techniques. WADC technical report 56-393, Proceedings of the Ohio State U. — WADC Radome Symposium, Aug 1956.

246. Wolin, S. Electrical Design of Lossy Radomes. US NADC report ADC-EL-123-50, 11 July 1950.

17. Guidance and Fire Control Radome Design

247. Ament, W. S., MacDonald, F. C., and Passerini, H. J. Quantitative Measurements of Radar Echoes from Aircraft; VI, Corrected F-86 Amplitude Distribution and Aspect Dependence. Letter C-3640-143A/52, Naval Research Lab., 15 Dec 1952; VIII, B-45, memorandum report 116, 28 Jan 1953; XI, B-29, memorandum report 164, 25 May 1953 (Confidential).

248. Ayer, D. R., and Clarke, R. L. Investigation of the High Incident Angle Radome Problem — Model MX-776B — Project Rascal. Report 56-984-001, Bell Aircraft Corp., Buffalo, N. Y., 1 May 1950 (Confidential).

249. Barker, C. B., and Lengyel, B. A. The Effect of Beam Distortion in Conical Scanning. Technical Memorandum 404, Research Lab., Hughes Aircraft Co., Apr 1955.

250. Berman, B. The Attack of a Rocket Bearing Interceptor on a Passive B-29 Type Bomber. Technical memorandum 243, Fire Control System Lab., Hughes Aircraft Co., 10 Nov 1950.

251. Bomarc Radome Development. Report GER-5927, Goodyear Aircraft Corp., Akron, Ohio, 8 Mar 1954 (Secret) (AD-31850).

252. Briggs, E. Static Tests of F-80 Metal Radome Installation — Model 56 — Technical Data. Report 56-929-434, Bell Aircraft Corp., Buffalo, N. Y., 24 May 1950 (Confidential).

253. Carroll, P. J. Angular Error and Miss Distance Due to Radome Error in Airborne Radar Turret Fire Control. Report NADC-EL-5461, Aeronautical Electronic and Electrical Lab., NADC, Johnsville, Pa., 26 July 1954 (AD-38497).

254. Cope, D. and Donhaiser, J. A Radome and Its Correction to a Boresight Dome on a Production Basis. Proceedings of the Ohio State U.—WADC Radome Symposium, June 1956.

255. Cox, W. G. A Design Procedure for Boresight Radomes for Monopulse Systems. Proceedings of the Ohio State U.—WADC Radome Symposium, vol. II, June 1955, pp. 160-170.

256 Davis, K. S., Cully, R. A., and Begley, W. W. Development of Doppler Radome for SM-62 Snark Missile. Interim report NAI-55-38, Northrup Aircraft, Hawthorne, Calif., 1 Mar 1955 (Confidential).

257. Dunbar, A. S., Gunter, R. C., and Hahn, G. M. Radome Error Prediction Study. (Secret) First quarterly scientific report, report R-510-1074, 8 Oct 1954. Dunbar and Gunter. Second. . .report, R-510-1125, 13 Jan 1955. Damonte, J. B., Gaetano, A., and Gunter. Third. . .report, R-510-1187, 8 Apr 1955. Hahn, Gunter, and Pinney, E. J. Fourth. . .report, R-510-1217, 15 July 1955.

258. Echo Measurements of the F-80 Aircraft at 2600 Mc. Data Set 10, Antenna Lab., Ohio State U. Research Foundation, 15 Aug 1952.

259. Echo Measurements of the F-86 Aircraft at 2600 Mc. Data Set 7, Antenna Lab., Ohio State U. Research Foundation, 10 May 1952.

260. Effect of Beam Distortion in Conical Scanning, The. Technical memorandum 404, Research Lab., Hughes Aircraft Co., Culver City, Calif, May 1955.

261. Falcon Radome Development (Secret). Report GER-5893, Goodyear Aircraft Corp., Akron, Ohio, 18 Feb 1954. Report GER-6078, 14 May 1954 (AD-33998).

262. Fire Control Errors Caused by Radome Errors. The Integrated Electronic and Control System - Project MX-1179. Study report, part IV-1, Research and Development Lab., Hughes Aircraft Co., Culver City, Calif., 1 Mar 1952.

263. Galindo, V. and Adler, D. F. Experimental Studies on Dependence of Boresight Error on Various Obstacle Parameters. Technical memorandum 431, Research Lab., Hughes Aircraft Co., 17 Jan 1956.

264. Galindo, V. and Hata, F. T. A Study of the Radiation Field of the GAR-3 Falcon Missile System. Technical memorandum 436, Research Lab., Hughes Aircraft Co., Mar 1956.

265. Gerwin, H. L. and Hastings, A. E. Further Design and Development of Components for Simultaneous Lobing Radar Tab. Report R-3221, Naval Radiation Lab., Jan 1948.

266 Hahn, G. M., Gunter, R. C., Jr., and Pinney, E. J. Radome Error Prediction Study. Report R-510-1217, Dalmo-Victor Co., San Carlose Calif., 15 July 1955 (Secret).

267. Haight, E. C. Proposed Test Program F-80 (Fighter) Radome Installation. Report 56-929-432, Bell Aircraft Corp., Buffalo, N. Y., Feb 1950 (Confidential).

268. Hay, D. R. Radar Cross Sections of Aircraft. Eaton Electronics Research Lab., McGill U., 1 June 1952.

269. Kay, A. F. Summary of Sections A Through Q, Section R in A Study of Radome and Radar Antenna Installation and Design Criteria; Beam Alignment in Radomes. Part III, Missile Radome Design Principles. Report 12283-8R, McMillan Lab., Ipswich, Mass., 24 Aug 1953 (Confidential).

270. Kay, A. F. The Two-Step Antenna Model of Radome Boresight Errors. McMillan Lab., Ipswich, Mass., 10 Mar 1954 (Confidential) (AD-27077).

271. Kotik, J. The Variation of Tracking Error with Dish Illumination Polarization in 1-way and 2-way Conical Scanning Systems. Report 1293, contract NONR-1247(00), McMillan Lab., Nov 1954.

272. Januskevich, N. N. Beam Alignment in Radomes for Conical Scanning — I. Technical report 5, McMillan Lab.

273. McMillan, E. B. Outline of Work on Sparrow II Radome. McMillan Lab., Ipswich, Mass., 8 Jan 1953 (Confidential).

274. McMillan, E. B., and Kay, A. F. The Design of McMillan Sparrow II Radomes. McMillan Lab., Ipswich, Mass., 8 Jan 1953 (Confidential).

275. Moreno, T., Mathews, W. E., and Greenbaum, M. The Effect of Radome Error on Falcon Navigation. Technical memorandum 258, Hughes Aircraft Co., 15 Oct 1951 (Secret).

276. Muchmore, R. R., and Weiss, L. Radar Echo Scintillation from P-80 and A-20 Airplanes. Technical Memorandum 212, Guided Missile Lab., Hughes Aircraft Co., 30 Nov 1948.

277. Navigation, Bombing, and Missile Guidance System for U S A F Project MX 1964 Phase I -- Ray Tracing and Transmission Calculations. Search Radar Program technical subject report 4, Sperry report 5223-1342-4, Sperry Gyroscope Co., Great Neck, N. Y., May 1954 (Confidential).

278. Oleesky, S. S. Bureau of Aeronautics Specification, Radome -- Model XSSM-N-6 Missile. Report ADC EL-13, 31 Jan 1950 (Confidential).

279. Oleesky, S. S. Development of Radome for CTV-2 Pilotless Aircraft. Report ADS EL-84-49, 25 Apr 1949 (Confidential).

280. Paiss, M. H., and Oleesky, S. S. Design of Radome for P/A-VII Pilotless Aircraft. Report ADS EL-126-49, Aeronautical Electronic and Electrical Lab., NADC, Johnsville, Pa., 1 July 1949 (Confidential).

281. Philips, E. T. The Effect of Radomes on Missile Guidance. Preprint 809, SAE National Aeronautic Meeting, Los Angeles, Calif., 1-4 Oct 1952.

282. Radome Design Criteria for Precision Guidance Radar -- A Study of Radome and Radar Antenna Installation Design Criteria. Final report, document 1276, McMillan Lab., Ipswich, Mass. 1 June 1954 (Confidential).

283. Radome Problem in Guided Missiles, The. Final report, contract N6 ONR-27-23 (sponsored by ONR), Princeton U., Princeton, N. J., 1 Mar 1952 (Secret).

284. Shank, H. C. Development of the 083 Needle-Nosed Radome and Evaluation of its Electrical Characteristics. Report 9678, Lockheed Aircraft Corp., Burbank, Calif., 3 Feb 1954 (Confidential).

285. Siegel, W. Radome Boresight Errors in Monopulse and Conical Scan Systems. Proceedings of the Ohio State U.-WADC Radome Symposium, vol. II, June 1955, pp. 151-159.

286. Silver, S. Polarization Errors in Semi-Active Systems. Appendix H in The Radome Problem in Guided Missiles, final report, contract N6 ONR-27-23 (sponsored by ONR), Princeton U., Princeton, N. J., 1 Mar 1952 (Secret).

287. Silvertt, G. Modification of the Radar Range Equation For Arbitrary Targets and Arbitrary Polarization. Report 302-19, contract W36-039sc33634, Antenna Lab., Ohio State U., Sept 1948.

288. Snow, O. J. Discussion of the Ellipticity Produced by Radomes and its Effect on Crossover-Point Position for Conically Scanning Antennas. Report NADC-EL-5108, Aeronautical Electronic and Electrical Lab., NADC, Johnsville, Pa., 13 Nov 1951 (Confidential).

289. Snow, O. J. Theoretical Prediction of Boresight Shift for a 35-Degree Conical Radome. In Symposium on Guided Missile Radomes, Washington, D. C., June 18-19, 1953, ONR, Washington, D. C., 1953, pp. 149-59 (Confidential).

290. Some Effects of Radomes on Gun-Laying Radar Accuracy -- And Appendixes A thru E. General Electric Co., Commercial Equipment Div., Syracuse, N. Y., 28 Feb 1951 (Confidential).

291. Sparrow III Radome. Report M/R 16-425, Raytheon Mfg. Co., Missile and Radar Div., Bedford, Mass., 19 May 1954 (Confidential).

292. Squires, M. An Introductory Study of Radome Aberration as a Factor in Proportional Navigation. Technical note GW 281, Royal Aircraft Establishment, Great Britain, Dec 1953 (Secret).

293. Stress Analysis for a P/A VII Conical Nose Radome (Analytical Branch Memo). Naval Air Test Center, Pilotless Aircraft Development Lab., Johnsville, Pa., Sept 1948.

294. Symposium on Guided Missile Radomes, Washington, D. C., June 18-19, 1953 (Supplement). ONR, Washington, D. C. (Confidential) (AD-38581).

295. Tsuda, G., and Jenkins, V. Pointing Error Correction on Interceptor-Type Radomes as Performed on the Hughes Automatic Pointing Error Measuring Facility. Technical memorandum 428, Hughes Aircraft Co., 1 Mar 1956.

296. Wanlass, S. D., Tanielian, G., and Jacob, D. M. X-Band Radar Cross-Section Measurements. Technical memorandum 371, Guided Missile Lab., Hughes Aircraft Co., 1 Aug 1954.

297. Wolin, S. Theoretical Prediction of Boresight Shifts Due to Radomes. Report NADC-EL-5497, Aeronautical Electronic and Electrical Lab., NADC, Johnsville, Pa., 21 Sept 1954 (Confidential) (AD-45257).

18. Search Radome Design

298. Antenna and Radome Design – Doppler Radar Program – Navigation, Bombing, and Pod Guidance System for United States Air Force Project MX-1964 (Phase I). Technical subject report 8, Sperry report 5223-1366-8, Sperry Gyroscope Co., Great Neck, N. Y., Jan 1955 (Confidential).

299. Cady, W. M., Karelitz, M. B., and Turner, L. A. Radar Scanners and Radomes, McGraw-Hill Book Co., New York, 1952 (3rd ed.). (Vol. 26, MIT Radiation Lab. Series.)

300. Radome for Electromagnetic Reconnaissance System – RB-58 Ferret (Electromagnetic) Reconnaissance System – Vol. III – Phase I. Final engineering report, Melpar, Inc., Alexandria, Va. (Secret).

301. Radome Engineering Manual Published by direction of the Chief of the Bureau of Aeronautics and the Commanding General of the Air Materiel Command. AMC Manual 80-4, NAVAER 16-45-502, 1 Oct 1950

302. Reintjes, F. J., and Coate, G. T. Principles of Radar, McGraw-Hill Book Co., New York, 1952 (3rd ed.).

303. Siegel, W. Theoretical Analysis and Experimental Verification of Radomes on Monopulse Scan. Glenn L. Martin Co., Baltimore, Md. (Confidential). Scientific report 1, phase 1, Martin report ER 7146, 15 Feb 1955 (AD-59198). Scientific report 2, phase 1, Martin report ER 7282, 15 May 1955 (AD-66105). Scientific report 3, phase 2, Martin report ER 7283 (AD-68762).

19. Measurements

304. Adney, J. E., Jr., Tice, T. E., and others. Analysis and Measurement of Transmission Through Radomes. Report 531-1, Antenna Lab., Ohio State U. Research Foundation, Columbus, 23 Jan 1953.

305. Analysis of the Sources of Radome Error, An. Appendix B in The Radome Problem in Guided Missiles, final report of the Princeton University Radome Study, contract N6 ONR-27-23 (sponsored by ONR), Princeton U., Princeton, N. J., 1 Mar 1952 (Secret).

306. Arcidiacono, T. AN/APS-42 Radome Pressure Distribution (Model C-119G). Engineering report R110-041, Fairchild Aircraft Div., Fairchild Engine and Airplane Corp., Hagerstown, Md., 18 Feb 1953.

307. Automatic Equipment for Making X-Band Amplitude and Phase Measurements. Report GER-6657, Goodyear Aircraft Corp., Akron, Ohio, 21 Mar 1954.

308. Bacon, J. An Automatic X-Band Phase Plotter. Technical report 531-7, Antenna Lab., Ohio State U. Research Foundation, Columbus, 1 Sept 1954.

309. Bacon, J. Selective Bolometer Amplifier. Technical report 301-24, Antenna Lab., Ohio State U. Research Foundation, 15 Sept 1950.

310. Blair, G. R. High Temperature Dielectric and Loss Tangent Measurements. WADC technical report 56-393, Proceedings of the Ohio State U.–WADC Radome Symposium, Aug 1956.

311. Branson, E. C. Boresight Shift Measurements on Hemispherical Radomes of Various Core Thicknesses. No. 142, Emerson Electric Mfg. Co., Armament Dept., St. Louis, Mo., Apr 1949.

312. Branson, E. C. Radome Signal Shift Measurements. Report 130, Emerson Electric Mfg. Co., St. Louis, Mo., Dec 10 1948 (Confidential).

313. Dakins, T. W., and Works, C. W. Microwave Dielectric Measurements. Jour. of Applied Physics, vol. 18, 1947.

314. Damonte, J. B., Hahn, G. M., and Gunter, R. C., Jr. Error Prediction Methods. Proceedings of the Ohio State U.–WADC Radome Symposium, vol. III, June 1955, pp. 9-19.

315. DeWoskin, N. Set-up and Procedure for Boresight Shift Measurements on Radomes. Engineering report 120, Emerson Electric Mfg. Co., Armament Dept., St. Louis, Mo., 27 July 1948.

316. Dielectrometer for Millimeter Wavelengths. First and second quarterly reports, Microwave Radiation Co., Gardena, Calif., 1955.

317. Dunbar, A. S., Gunter, R. C., and Hahn, G. M. Radome Error Prediction Study. Report 5-510-1074, Dalmo-Victor Co., San Carlos, Calif., 8 Oct 1954 (Secret).

318. Ehrlich, M. J., and Williams, I. K. A Dielectrometer for Millimeter Wavelengths and Elevated Temperatures. Presented at Ohio State U.–WADC Radome Symposium, 4-6 June 1956. Published in Proceedings of the National Conference on Aeronautical Electronics, 14-16 May 1956, Dayton, Ohio.

319. Electric Thickness Gage. Scientific reports for WADC under contract AF 33 (616)-3092. Dalmo-Victor Co., San Carlos, Calif.

320. Electrical Test Procedures for Radomes and Radome Materials. Aircraft Industries Association. ATC report ARTC -4, 1 Dec 1951, and ARTC-WR-54-29, 1 June 1954, proposing certain additions.

321. Emerson, F. M., Dill, D. G., Doolin, W. A., and Grant, E. G. Radome Transmission Computers. Report ES 15290, Engineering Dept., Douglas Aircraft Co., El Segundo, Calif., 17 Aug 1949.

322. Gevers, M. Measurement of Dielectrics and Magnetic Properties of Solids at Microwave Frequencies. Precision Electrical Measurements, Philosophical Library, New York, vol. 3, 1956, pp. 1-15.

323. Hahn, G. M. and Pinney, E. J. Three-Dimensional Error Prediction. Proceedings of the Ohio State U.–WADC Radome Symposium, June 1956.

324. Hata, F. T., and Sledge, O. D. Investigation of Electromagnetic Field Distortions Caused by Dielectric Sheets, Wedges and Radomes Placed Near an Antenna. Report 10E-251, National Bureau of Standards, Corona, Calif., 31 Aug 1953.

325. Haupt, L. O., Jr. An Improved Radome Test Method. NAMC, Naval Aircraft Factory, Philadelphia, Pa., 30 Dec 1944 (Confidential).

326. Hines, J. N. An Automatic Phase Plotter. Technical report 301-31, Antenna Lab., Ohio State U. Research Foundation, 30 Apr 1951.

327. Hines, J. N., and Tice, T. E. An Investigation of Reflection Measuring Equipment. Report 478-13, Antenna Lab., Ohio State U. Research Foundation, 1 June 1953.

328. Hope, H. R. Electrical Thickness Measurement by a Single Horn Method. Technical report 56-393, Proceedings of the Ohio State U.–WADC Radome Symposium, vol. I, Aug 1956, pp. 190-196.

329. Horton, M. C. Automatic Equipment for Measurement of Radome Angular Error. Symposium on Guided Missile Radomes, Washington, D. C., 18-19 June 1952.

330. Horton, M. C. Automatic Radome Test Equipment. Presented at the Symposium on Antennas and Propagation, sponsored by RDB, Berkeley, Calif., Aug 1953.

331. Instructions for Precision Radome Boresight Test Equipment. Report GER-6208, Goodyear Aircraft Corp., Akron, Ohio, 27 July 1954 (AD-56450).

332. Justice, R., and Rumsey, V. H. Measurement of Electric Field Distributions. IRE Transactions on Antennas and Propagation, vol. AP-3, Oct 1955.

333. Kay, A. F. The Two-Step Antenna Model of Radome Boresight Errors. Contract NONR-1247(00), McMillan Lab., 10 Mar 1954.

334. King, D. D. Measurements at Centimeter Wavelength. Van Nostrand Co., New York, 1952.

335. Kofoid, M. J. Automatic Measurement of Phase Retardation for Radome Analysis. Rev. of Scientific Instruments, vol. 27, July 1956, pp. 450-452.

336. Kofoid, M. J. A Procedure for Making Precision Half-Wave Solid Wall Radomes. Proceedings of Ohio State U.–WADC Radome Symposium, vol. II, 1955, pp. 232-237.

337. Lengyel, B. A., and Simmons, A. J. An Interferometer for Microwaves. Report 3562, Naval Research Lab., Washington, D. C., 3 Nov 1949.

338. McMillan, E. B., and McKringer, F. H. Installation and Testing of Radomes. Chapter 14 of Radar Scanners and Radomes, McGraw-Hill Book Co., New York, 1948. (Vol. 26, MIT Radiation Lab. Series.)

339. Montgomery, C. G. Technique of Microwave Measurements. McGraw-Hill Book Co., New York, 1947, (Vol. II, MIT Radiation Lab. Series.)

340. Olson, A. R. Beam Alignment in Radomes. Part II. Section I, Experimental Data. Technical report 7, McMillan Lab. (Secret).

341. Paiss, M. H. Electronic Correction of Boresight Shift in Symmetrical Antenna-Radome Systems. Report NADC-EL-52122, Aeronautical Electronic and Electrical Lab., NADC, Johnsville, Pa., 21 Jan 1953 (Confidential).

342. Paiss, M. H. Development of a Measurement System for Beam-Deflection Tests on Radomes. Report NADC-EL-5101. BUAER TED Project ADC EL-800, 3 Aug 1951 (Confidential).

343. Paiss, M. H., and Schlieben, E. W. Development of a Measurement System for Beam Deflection Tests on Radomes. Report NADC-EL-5101, NADC, Johnsville, Pa., 3 Aug 1951.

344. Perry, H. A. Electrical Test Methods for Radomes. No. R-483-26, Radiation Lab., MIT, Cambridge, Mass., JAN 1946.

345. Redheffer, R. M. The Measurement of Dielectric Constants. Chapter 10 of Technique of Microwave Measurements, McGraw-Hill Book Co., New York, 1947. (Vol. II, MIT, Radiation Lab. Series.)

346. Redheffer, R. M. and Winkler, E. D. The Measurement of Dielectric Constants in the One Centimeter Band. Report 483-15, Radiation Lab., MIT, May 1945.

347. Rhodes, D. R. An Investigation of Pulsed Radar Systems for Model Measurements. Report 475-6, Antenna Lab., Ohio State U., 1 Dec 1953.

348. Richmond, J. H. Measurement of Time-Quadrature Components of Microwave Signals. IRE Transactions on Microwave Theory and Techniques, vol. MTT-3, Apr 1955, pp. 13-15.

349. Richmond, J. H. A Modulated Scattering Technique for Measurement of Field Distributions. Technical report 531-11, Antenna Lab., Ohio State U. Research Foundation, Columbus, 31 Mar 1955.

350. Richmond, J. H. A Modulated Scattering Technique for Measurement of Field Distributions. IRE Transactions on Microwave Theory and Techniques, vol. MTT-3, July 1955, pp. 13-15.

351. Richmond, J. H. Simplified Calculation of Antenna Patterns, with Application to Radome Problems. IRE Transactions, vol. MTT-3, July 1955.

352. Richmond, J. H., and Tice, T. E. Probes for Microwave Near-Field Measurements. Report 531-6, Antenna Lab., Ohio State U. Research Foundation, Columbus, 30 June 1954 (AD-48219).

353. Richmond, J. H., and Tice, T. E. Probes for Near-Field Measurements. IRE Transactions on Microwave Theory and Techniques, vol. MTT-3, Apr 1955, pp. 32-34.

354. Richmond, J. H., and Tice, T. E. A Survey of Microwave Near-Field Measuring Techniques. Presented at URSI-IRE Meeting, Washington, D. C., 3 May 1956.

355. Roberts, S., and Von Hippel, A. R. A New Method for Measuring Dielectric Constant and Loss in the Range of Centimeter Waves. Jour. of Applied Physics, vol. 17, 1946, p. 610.

356. Siegel, W. Theoretical Analysis and Experimental Verification of Radomes on Monopulse Scan. (Confidential). Glenn L. Martin Co., Baltimore, Md. Scientific report 1, phase 1, Martin report ER 7146, 15 Feb 1955 (AD-59198); scientific report 2, phase 1, Martin report ER 7282, 15 May 1955 (AD-66105); scientific report 3, phase 2, Martin report ER 7283, (AD-68762).

357. Snow, O. J. Some Theoretical Aids for Studies on Crossover-Point Shifts Due to Radomes. Report NADC-EL-5276, BUAER TED Project ADC-EL-800, 28 Aug 1952 (Confidential).

358. Surber, W. H., Jr., and Crouch, G. E., Jr. Dielectric Measurement Methods for Solids at Microwave Frequencies. Jour. of Applied Physics, vol. 19, 1948, p. 1130.

359. Tice, T. E., Adney, J. E., and Richmond, J. H. Analysis and Measurements of Transmission Through Radomes. Report 531-2, Antenna Lab., Ohio State U. Research Foundation, Columbus, 27 Feb 1953.

360. Tice, T. E., and Richmond, J. H. Equipment for Measuring the Fields Near a Radome. Report 531-5, Antenna Lab., Ohio State U. Research Foundation, Columbus, 16 Oct 1953 (Confidential) (AD-21144).

361. Tice, T. E., and Richmond, J. H. Fields Measured near a Typical Radome. Report 531-4, Antenna Lab., Ohio State U. Research Foundation, Columbus, 31 July 1953 (Confidential).

362. Upson, J. and Hines, J. N. An Indoor Echo-Area Measuring System. Report 612-11, Antenna Lab., Ohio State U. Research Foundation, 1 Nov 1956.

363. Walcutt, R. P. Test Equipment for Transmission and Reflection Coefficient Measurement for Microwave Radomes. Final engineering report, contract AF 33 (038)-23594, 1 June 1954 (AD-37813).

364. Wind, M., and Rapaport, H. (ed.). Handbook of Microwave Measurements. Polytechnic Inst. of Brooklyn, 1954.

365. Winzemer, A. M. Graphical Analysis of the Radiation Patterns of Constant-Echo Radar Antennas. Report ADS EL-117-49, Aeronautical Electronic and Electrical Lab., NADC, Johnsville, Pa., 16 June 1949 (Confidential).

366. Winzemer, A. M. Methods for the Continuous Measurement of Radome Reflections During Antenna Scan with Antenna Reflections Present. Report ADS EL-138-49, Aeronautical Electronic and Electrical Lab., NADC, Johnsville, Pa., 26 July 1949 (Confidential).

367. Woods, W. W. Thickness Gage for Dielectric Materials. AIEE Transactions, vol. 73, part I. 1954, pp. 320-324.

368. Yaw, D. F. A K-Band Superheterodyne System Using A Rotating-Guide Phase Shifter. Technical report 444-19, 15 Feb 1955, Antenna Lab., Ohio State U. Research Foundation.

20. Diffraction by Aircraft Structure and Environment

369. Barnett, R. I., Jr., and Tai, C. T. Effect of a Half-Plane Sheet Upon the Radiation Pattern of a Dolph-Tchebyscheff Array. Report 678-4, Antenna Lab., Ohio State U., 15 Nov 1956.

370. Chu, S. T. Review of Turbulence Theories with Applications to Fluctuation Fields Inside a Supersonic Boundary Layer. Project report 486-31, Ohio State U. Research Foundation, Dec 1954.

371. Kober, C. Environmental Conditions of Bombing Radar Antennas for Supersonic Aircraft. Laboratory memorandum, Armament Lab., WADC, 15 Oct 1953.

372. Kovasznay, L. S. G. B-58 Doppler Radar, A Study of Radar Scattering in Supersonic Turbulent Flows. Report MIR 16-838, Raytheon Mfg. Co., Bedford, Mass., June 1956.

373. Liepmann, H. W. and Puckett, A. E. Introduction Aerodynamics of a Compressible Fluid. John Wiley and Sons, New York, 1950.

374. Peake, W. H. Some Possible Effects of Turbulence on the Performance of Antennas Mounted on Supersonic Aircraft. Report 687-3, contract AF 33(616)-3353, Antenna Lab., Ohio State U. Research Foundation, 1 Oct 1956 (Confidential).

375. Peake, W. H. Transmission of Light Waves Through a Supersonic Turbulent Boundary Layer. Project report 486-34, Antenna Lab., Ohio State U., 30 Apr 1955.

376. Peake, W. H. Turbulence in the Environment of a Supersonic Aircraft as a Radome Problem. Proceedings of the Ohio State U.–WADC Radome Symposium, vol. II, June 1955, pp. 75-85.

377. Robertson and Stevens. The Effects of Jet Flames on Electromagnetic Wave Propagation. Memo 4-55, Jet Propulsion Lab., California Inst. of Technology, Pasadena, Calif., Mar 1950.

378. Sprague, R. S. Electromagnetic Radiation Bending in the Vicinity of the B-58 and Its Effect on Sensing Elements During Supersonic Flight. Report to contract AF 33 (038)-21250, Physics Section, Convair, Forth Worth, Texas, 1 Jan 1954 (Secret).

379. Ambrogi, J. N., Jr. Electrical, Physical, and Dielectric Properties of Radomes and Radome Materials. Report ADC EL-41-50, Aeronautical Electronic and Electrical Lab., NADC, Johnsville, Pa., Aug 1949 (Confidential).

380. Biefeld, L. P., and Philippes, T. E. Finishes for Glass Fabrics for Reinforcing Polyester Plastics. Industrial Engineering & Chemistry, 1953.

381. Bjorksten, J., and Yeager, L. I. Vinyl Silane Sizes for Glass Fabric. Modern Plastics, July 1952.

382. Black, J. M., and Blomquist, R. F. Development of Metal Bonding Adhesive FPL -710 With Improved Heat Resistant Properties. NACA no. RM 52 F19, 1952.

383. Black, J. M., and Blomquist, R. F. Development of Metal Bonding Adhesives With Improved Heat Resistant Properties. NACA no. RM 54 D01, 1954. Modern Plastics, vol. 32, Dec 1954, p. 139.

384. Botwick, M., Cummings, W., and Elliot, P. Polyester Heat Resistant Laminating Resins. WADC Technical report 53-371 and supplement 1, 1953.

385. Burkley, J. K., and others. Radome Materials Research and Fabrication Development Service. Report GER-1656, Goodyear Aircraft Corp.

386. Campagna, P. J., Preston, H. M., and Wahl, N. E. Development of Heat-Resistant Foamed-in-Place Dielectric Core Materials for Sandwich Radomes. Technical report 54-249, Cornell Aeronautical Lab., Buffalo, N. Y., Mar 1954 (AD-48277).

387. Close, G. C. Douglas Mass-Produces Plastic Airframe Parts. Machinery (New York), vol. 59, Apr 1953, pp. 196-98.

388. Copeland, C. R. Fabrication of Glass Radomes. Scientific report no. 1, contract AF 33(600)-29310, Corning Glass Works, Corning, N. Y. (AD-66130).

389. Dunn, W. A. Development of Low Dielectric Constant Glasses. Final engineering report, contract AF 33(038)-8063, Glass Fibers, Inc., Waterville, Ohio, Dec 1950.

390. Duplaga, E., Milone, C. R., and others. Radome Materials Research and Fabrication Development Service. Final engineering report supplement 1, report GER 4618, Goodyear Aircraft Corp., 29 Feb 1952.

391. Duplaga, E., and Pace, H. A. Foaming-in-Place of Alkyd Resins for Sandwich Radomes. Report GER-4097, Goodyear Aircraft Corp., Akron, Ohio, 22 Dec 1949. Report GER-4097 supplement II, 29 Feb 1952. Report GER-2423 supplement I, 15 Oct 1952.

392. Eickner, H. W. Adhesive Bonding Properties of Various Metals as Affected by Chemical and Anodizing Treatments of the Surface. US Forest Products Lab. report 1842, Apr 1954.

393. Erikson, P., Silver, I., and Perry, H. A. Universal Type Chemical Finishes for Glass Fibers Used in Reinforced Plastics. American Chemical Society 125th Annual Meeting.

394. Falcon Radome Development (Secret). Report GER-5893, Goodyear Aircraft Corp., Akron, Ohio, 18 Feb 1954. Report GER-6078, 14 May 1954 (AD-33998).

395. Foam Plastics as Engineering Materials. Product Engineering, vol. 23, Apr 1952, pp. 192-98.

396. Fyall, A. A. Dielectric Measurements on Various Radome Materials and the Effect of Moisture Absorption and Temperature. Royal Aircraft Establishment, Great Britain, Oct 1953 (technical note no. Chem 1209; encl. 1 to Air Attache, London report TR-434-54) (Confidential) (AD-27247).

397. Fyall, A. A., and Sewell, J. H. Dielectric Measurements on Some Laminating Resins and the Effect of Moisture Absorption and Temperatures. Technical note no. Chem 1233, Royal Aircraft Establishment, Great Britain, June 1954 (AD-40918).

398. Fyall, A. A., and Sewell, J. H. The Dielectric Properties of Some Rubber-Based Core Materials for Sandwich Radomes and the Effects of Moisture, Temperature and Frequency. Technical note no. Chem 1209, Royal Aircraft

Establishment, Great Britain, Jan 1954 (AD-29867).

399. Glasscloth Laminating. Aircraft Production, vol. 15, June 1953, pp. 203-208.

400. Goggin, W. C., and Bradshaw, R. R. Polyfiber, A New Approach to Molding. Modern Plastics, vol. 21, July 1944, pp. 101-107.

401. Heebink, B., Werren, F., and Mohaupt, A. Effects of Certain Fabricating Variables on Plastic Laminates and Plastic Honeycomb Sandwich Construction. US Forest Products Lab. report 1843.

402. Hoffman, K. R. Development of Low-Pressure Laminates of Glass Fabric and Silicone Resins. USAF technical report 6223 and supplement 1, June 1956.

403. Hopper, F. C. High Strength Epon Laminates. WADC technical report 52-5, Jan 1952. Supplement 1, Sept 1952. Supplement 2, Oct 1953. Supplement 3, Oct 1954.

404. How Mammoth Plastic Radome Is Made. Aviation Week, vol. 59, 7 Dec 1953, p. 58.

405. Investigation of Methods of Inspecting Bonds Between Cores and Faces of Sandwich Panels of the Aircraft Type. US Forest Products Lab. report 1569, Sept 1947.

406. Jones, E. M. T., Cohn, S. B., and Robinson, L. A. Wide-Band Radomes Matched by Reactive Walls. Proceedings of the Ohio State U.—WADC Radome Symposium, vol. I, June 1955, pp. 52-67.

407. Korelitz, M. N. Development of High Strength-Heat Resistant Phenolic Laminating Resin. WADC technical report 52-161, July 1952.

408. Kuenzi, E. W. Flexure of Structural Sandwich Construction. US Forest Products Lab. report 1829, Dec 1951.

409. Leaderman, H. Radome Materials and Methods of Fabrication. Chapter 13 in Radar Scanners and Radomes. McGraw-Hill Book Co., New York, 1948. (Vol. 26, MIT Radiation Lab. Series.)

410. Loaded-Core Sandwich for Radomes. Electronic Design, 15 Jan 1956.

411. Loaded Foam Sandwich Radome. WADC technical report 56-261, contract AF33 (616)-2966, Emerson & Cuming, Canton, Mass. (AD-110686).

412. Loaded Foam Sandwich Radome. First and second quarterly reports, contract AF33(616)-3486, Emerson & Cuming, Canton, Mass.

413. McMillan, E. B., and others. Antenna Housing. US Letters Patent no. 2,617,934; 2 May 1945.

414. McMillan, E. B., and Others. Dielectric Wall for Transmission of Centimetric Radiation. US Letters Patent no. 2,659, 884; 3 Aug 1949.

Military specifications. See the following.

Adhesive, Aircraft Structural, Metal to Metal. Military Specification MIL-A-8331, June 1953.

Core Material; Laminated Glass Fabric Base Plastic Honeycomb. Military Specification MIL-12050, 1949.

Enamel, Camouflage, Quick Drying. Military Specification MIL-E-5556.

Fabrics, Woven Glass, Finished, for Plastic Laminates. Military Specification MIL-F-9084.

Finish, Glass Fabric, for Reinforced Plastic Laminates. Military Specification MIL-F-9118, Dec 1953.

Foamed-in-Place, Alkyd-Isocyanate Type Core Material, for Aircraft and Missile Structural Applications. Military Specification MIL-C-8087.

Lacquer; Cellulose Nitrate, Gloss, for Aircraft Use. Military Specification MIL-L-7178.

Plastic Materials, Glass Fabric Base, Low Pressure Laminated. Military Specification MIL-P-8013A, Jan 1954.

Plastic Materials, Glass Fiber Base, Low Pressure Laminated, Aircraft Structure; Process and Inspection Requirements. Military Specification MIL-P-9400.

Plastic Materials, Glass Fiber Base—Phenolic Resin, Low Pressure Laminated. Military Specification MIL-P-25515.

Plastic Materials, Heat Resistant, Glass Fiber Base, Polyester Resin, Low Pressure Laminated. Military Specification MIL-P-25395, June 1956.

Plastic Materials, Low Pressure Laminated, Glass Fiber Base, Silicone Resin. Military Specification MIL-P-25518.

Resin, Low Pressure Laminating. Military Specification MIL-R-7575A, 27 Apr 1953.

Resin, Polyester, High Temperature Resistant, Low Pressure Laminating. Military Specification Mil-R-25042, May 1955.

Resin, Silicone, Low-Pressure Laminating. Military Specification MIL-R-25506, June 1956.

Sandwich Construction, Plastic Resin, Glass Fabric Base, Laminated Facings and Alkyd-Isocyanate Foamed-in-Place Core, for Aircraft Structural Applications. Military Specification MIL-S-25392.

Sandwich Constructions and Core Materials; General Test Methods. Military Specification MIL-STD-401, July 1952.

415. Moore, H. R. Applications of Expanded Plastics. Proceedings of the Fourth Annual Technical and Management Conference, Reinforced Plastics Div., Society of the Plastics Industry, Nov 1949. Also published in Plastics (England), Apr 1950, pp. 93-95.

416. Moore, H. R. Low Temperature Processing of Alkyd Diisocyanate Foams. Proceedings of the Ninth Annual Technical and Management Conference, Reinforced Plastics Div., Society of the Plastics Industry, Feb 1954.

417. Morgan, P. (ed.). Glass Reinforced Plastics. Philosophical Library, New York, 1954.

418. Nelb, R. G., Alexander, C. H., and Elliot, P. M. Heat Resistant Laminating Resins. USAF technical report 6602, 1952.

419. Nilo, S. C. Materials Developments and Fabrication Processes in Radomes for USAF Ground Electronic Equipment. Technical note RADC-TN-56-18, Rome Air Development Center, Feb 1956.

420. Pace, H. A. Foaming-in-Place of Alkyd Resins for Sandwich Radomes. Report GER-4097, Goodyear Aircraft Corp., 22 Dec 1949. (There is an Addendum II to this report.)

421. Plastics for Aircraft. ANC-17 Bulletin, June 1955. Issued by Dept. of the Air Force, Dept. of the Navy, and Dept. of Commerce.

422. Plastics in Aircraft. Modern Plastics, vol. 28, Apr 1951, pp. 73-78, 177.

423. Quint, R. W., and Kimmel, B. G. Development of a High-Temperature Resistant, Low-Density Foam Material for Sandwich-Type Radomes. Technical memorandum 286, Hughes Aircraft Co., Culver City, Calif., 1 Aug 1952 (Secret).

424. Radome Fabrication Techniques. Electronics, vol. 25, Sept 1952, pp. 166 ff.

425. Raffel, B. D. Interim Engineering Report on Radome Materials Research and Fabrication Development Service — Appendix 36, Report GER-451, part XXXVIII, Goodyear Aircraft Corp., Akron, Ohio, May 1950.

426. Russell, E. W. Materials for Optical and Radar Transparencies. A Review. Technical note no. Chem 1201, Royal Aircraft Establishment, Great Britain, Aug 1953 (Confidential) (AD-27677).

427. Sandwich Construction for Aircraft. Part I, Fabrication, Inspection, Durability and Repair, Feb 1951. Part II, Materials Properties and Design Criteria, 1955 (2nd ed.). Bulletin ANC-23, issued by Dept. of the Air Force, Dept. of the Navy, and Dept. of Commerce.

428. Schwartz, R. T. Plastic Sandwich Construction Material for Radomes. Report TSEAM-M5034/ADD III, Engineering Div., AMC, Wright-Patterson AFB, Dayton, Ohio, Feb 1946.

429. Silver, I., and Erickson, P. W. Improved Reinforced Plastics with the Universal Type Chemical Finish, NOL-24. NOL report, Feb 1955.

430. Society of the Plastics Industry, The. Plastics Engineering Handbook. Reinhold Publishing Corp., New York, 1954.

431. Sonneborn, R. H., Dietz, A. G. H., and Heyser, A. S. Fiberglas Reinforced Plastics. Reinhold Publishing Corp., New York, 1954.

432. Sporcic, J. A., and Whann, R. L. Problems Associated with the Manufacturing of Radomes. Preprint 807, SAE National Aeronautic Meeting, Los Angeles, 1-4 Oct 1952.

433. Steinman, R. Improvement of Wet Strength of Reinforced Plastics by Garan Finish. Modern Plastics, 1951.

434. Structural Honeycomb for Sandwich Construction. Hexcel Products Co., brochure C, Dec 1952.

435. Supplement to Repair of Aircraft Sandwich Construction. US Forest Products Lab. report 1584-A.

436. Tables of Dielectric Materials, vol IV. Lab. for Insulation Research, MIT, Jan 1953.

437. Teel, L. L. Final Engineering Report on Development of Missile Radome Materials — and Appendixes I-IV. PRL-122-17, Polamold Research Lab., Springfield, Ohio, Aug 1949.

438. Teel, L. L. Interim Engineering Report on Development of Missile Radome Materials — and Appendixes I-XIX — 1 May to 30 July 1949. PRL-122-16, Polamold Research Lab., Springfield, Ohio (published by AMC, Wright-Patterson AFB, Dayton, Ohio), July 1949.

439. Wahl, N. E., Campagna, P. J., and Preston, H. M. Development of Foamed Core Material for Radomes. Report UB-691-M-13, Cornell Aeronautical Lab., Buffalo, N. Y., 10 Mar 1953. Report UB-691-M-15, 20 Aug 1953 (AD-20741). Report UB-691-M-16, 27 Nov 1953. Report UB-691-M-17, 28 Dec 1953 (AD-34822).

440. Wahl, N. E., and Preston, H. M. Investigation of Heat Resistant Polyester Laminates. WADC technical report 55-342, Aug 1955.

441. Wahl, N. E., Preston, H. M., and Campagna, P. J. Development of Heat-Resistant Foamed-in-Place Dielectric Core Materials for Sandwich Radomes. WADC technical report 54-249, Mar 1954.

442. Werren, F. Effects of Fabric Finish and West Exposure on Strength Properties of Glass Cloth Polyester Laminates. WADC technical report 53-483, 1953.

443. Weyer, D. E., Russell, J. R., and Hoffman, K. R. Development of a Heat-Resistant Foamed-in-Place Low Density Silicone Resin Core Material. WADC technical report 53-146, supplement 1, Aug 1954.

SECTION C. INORGANIC MATERIALS FABRICATION

444. [Ceramic Radome Production.] Technical Report No. 1, April 15, 1952 — June 15, 1953. New Jersey Ceramic Research Station, Rutgers U., New Brunswick, N. J. Technical Report No. 3, June 15, 1954 — June 15, 1955 (AD-71992).

445. Contardi, W. A., and Hund, G. J. Correlation of Particle Size Distribution with Firing Shrinkage in a Ceramic Whiteware Composition. Ceramic Age, vol. 62, Nov 1953, p. 13

446. Dunn, W. A. Development of Low Dielectric Constant Glasses — Final Engineering Report. Glass Fibers, Inc., Waterville, Ohio, Dec 1950.

447. Eichbaum, B. R. The Relationship Between Structure and Dielectric Properties in Some Ceramic Materials. Thesis. Rutgers U., New Brunswick, N. J., June 1956.

448. Everhart, J. O., Giles, T. M., and Bole, G. A. Investigation of Foamed Ceramic Radome Dielectrics. Quarterly report 1, Ohio State U. Research Foundation, Columbus, 2 Nov 1954 (AD-51295).

449. Fabrication of Radomes, Sandwich Inorganic Dielectrics and Processes. Interim engineering report 2, Owens-Illinois Glass Co., Toledo, Ohio.

450. Gebler, K., and Wisely, H. R. Dense Cordierite Bodies. Jour. Am. Cer. Soc., vol. 32, 1949, p. 163.

451. Hall, F. P. Low Loss Zircon Dielectrics. Ceramic Age, vol. 61, Mar 1953, p. 12.

452. Harrison, E. W. Glass Radome for Missile Applications. Aer-EL-825, serial no. 05205, Bureau of Aeronautics, Dept. of the Navy, 26 Apr 1951 (Confidential).

453. Hessinger, P. S. Ceramic Radomes for Aircraft. Bull. of the Am. Ceramic Soc., vol. 34, 15 May 1955, pp. 145-150.

454. Hessinger, P. S. Development and Evaluation of Ceramic Sandwich Construction for Radomes. Thesis. Ohio State U., Columbus, Dec 1955.

455. Kalousek, G. L., and Dence, R. B. Development and Fabrication of Inorganic

Sandwich Radomes. WADC technical report 54-197, Owens-Illinois Glass Co., Toledo, Ohio, Apr 1954 (AD-39670).

456. Olcesky, S. S. Development of Lightweight Ceramic Materials for Use in the Construction of Radomes for High-Temperature Applications. Report ADS EL-139-49, Aeronautical Electronic and Electrical Lab., NADC, Johnsville, Pa., 22 July 1949.

457. Schofield, H. Z., Lynch, J. F., and Duckworth, W. H. Final Summary Report on Fundamental Studies of Ceramic Materials. Battelle Memorial Inst., Columbus, Ohio, Mar 1949.

458. Scholes, W. A. Thermal Conductivity of Bodies of High BeO Content. Jour. Am. Cer. Soc., vol. 33, 1950, p. 111.

459. Shand, E. B. Glass Engineering Handbook. Corning Glass Works, Corning, N. Y., 1955.

460. Shanley, F. R., Knapp, W. J., and Needham, R. A. Prestressed Ceramic Structures. WADC technical report 54-75, part II, Aeronautical Research Lab., University of California, Los Angeles, Jan 1955.

461. Smoke, E. J. Ceramic Compositions Having Negative Linear Thermal Expansion. Ceramic Age, vol. 62, July 1953, p. 13.

462. Smoke, E. J. Low Loss Zircon Dielectrics. Ceramic Age, vol. 61, Feb 1953, p. 15.

463. Smoke, E. J. Spinel as Dielectric Insulator. Ceramic Age, vol. 63, May 1954, p. 13.

464. Smoke, E. J. Thermally Resistant Whitewares. Jour. Am. Cer. Soc., vol. 33, 1950, p. 174.

465. Smoke, E. J., and Koenig, J. H. Ceramics as Basic Engineering Materials. Mechanical Engineering, vol. 78, 1956, p. 315.

466. Snyder, N. H., and Ruh, E. Properties of High Magnesia Whitewares. Ceramic Age, vol. 61, Feb 1953, p. 15.

467. Von Hippel, A. Dielectric Materials and Applications. Technology Press, MIT, 1954.

SECTION D. RAIN EROSION

468. Armi, E. L., and Smith, E. F. Supersonic Rain-Erosion Tests of Falcon Radomes. Hughes Aircraft Co. report 4W 11-377, Apr 1955.

469. Behrens, F. H. The Use of a Neoprene Cement Coating for the Protection of Laminated Aircraft Parts from Damage due to Rain Erosion. Memorandum report MCREE 49-12, WADC, 1 Mar 1949.

470. Coating, Rain Erosion Resistant with Anti-Static Surface Treatment, for Plastic Laminates. Military Specification MIL-C-7439B.

471. Development of a Heat-Resistant, Rain Erosion-Resistant Coating. WADC technical report 53-511. In two parts, part 1 dated Nov 1954.

472. Dittmann, W. L., Feldman, A. L., and Holmes, R. F. A Study of Rain Erosion Testing Methods for Supersonic Speeds. WADC technical report 53-173, Convair, San Diego, Calif., Nov 1953 (Confidential). See also the following (Confidential) progress reports for this study.
Whitley, W. H., and Steeger, E. J. Phase II Progress Report No. 6, for Sept-Oct 1954. Progress Report No. 7, for Nov-Dec 1954.
Dittmann and others. Progress Reports Nos. 8-10, for Jan-Mar 1955. Progress Reports Nos. 11-15, for Apr-Aug 1955.

473. Engel, O. G. Mechanism of Rain Erosion. National Bureau of Standards.
Part 2: A Critical Review of Erosion by Water Drop Impact. WADC technical report 53-192 part 2, Aug 1953 (AD-18703).
Part 3: Mechanism Studies on Plastics and Metals. WADC technical report 53-192 part 3, Dec 1953 (AD-27597).
Part 4: Cavitation as a Result of Waterdrop Collisions With Solid Surfaces. WADC technical report 53-192 part 4, Jan 1954.

474. Hunter, I. M. Basic Principles of Radome Designs with Special Reference to Rain Erosion. TRE technical note 185, Telecommunications Research Establishment, Great Britain, Mar 1953.

475. Lapp, R. R., Stutzman, R. H., and Wahl, N. E. A Study of the Rain Erosion of Plastics and Metals. WADC technical report 53-185, Cornell Aeronautical Lab., Buffalo, N. Y., Feb 1954. Part II, technical report 53-185 part 2, May 1955.

476. Morley, C. Rain Erosion of a Conventional Plastic Laminated Radome. Technical note 156, Telecommunications Research Establishment, Gt. Malvern, England, Apr 1952 (Confidential).

477. Rain Erosion Testing Meeting Sponsored by W-25 Radome Mechnical Testing Subcommittee Held on March 28, 1950 and March 30, 1950 at Lockheed Aircraft and North American Aviation. Report ARTC-WR-50-44, Aircraft Research and Testing Committee, 19 Apr 1950.

478. Robinson, R. O., Jr., and Robertson, A. L. Interim Report on APL/JHU Terrier Radome Materials Test Program. 24 Oct 1955.

479. Serafini, J. S. Impingement of Water Droplets on Wedges and Diamond Airfoils at Supersonic Speeds. Technical note 2971, NACA, Washington, D. C., July 1953. Prepared by Lewis Flight Propulsion Lab., Clevelend, Ohio (AD-14597).

480. Study of Rain Erosion of Aircraft Materials at Supersonic Velocities, A. WADC technical report 55-195, Aug 1956.

481. Study of the Rain Erosion of Plastics and Metals, A. WADC technical report 52-20, Sept 1952.

482. Study of the Rain Erosion of Plastics and Metals, A. WADC technical report 53-185, Feb 1954. Part II, May 1955. Part III, n. d.

483. Study of Rain Erosion Testing Methods for Supersonic Speeds, A. Phase II. Progress reports 1 through 5, Consolidated Vultee Aircraft Corp., San Diego, Calif., 1953-1954. Reports 4 and 5 by R. J. Reich.

484. Stutzman, R. H., Lapp, R. E., and Wahl, N. E. A Study of Erosion of Aircraft Materials at High Speeds in Rain. Reports PC-962-M-3 through PC-962-M-9, Cornell Aeronautical Lab., Buffalo, N. Y., Mar-Sept 1955.

485. Wahl, N. E. Final Report on the Comparative Evaluation of Rain Erosion Properties of Plastics and Other Materials, Vol. I, report PC-467-M-17, Cornell Aeronautical Lab., Buffalo, N. Y., 25 Jan 1949.

486. Whitley, W. H. Radome Rain Erosion, Report RT-136, Consolidated Vultee, San Diego, Calif., 31 Mar 1953 (Confidential).

487. Whitley, W. H. Rain Erosion Test Facility. Report RT-137, Consolidated Vultee, San Diego, Calif., 5 June 1953 (Confidential).

488. WADC technical report 53-192. Includes the following parts.
Part I, Impact Pressure in Solid-Liquid Sphere Collisions, July 1953.
Part II, A Critical Review of Erosion by Water Drop Impact, Aug 1953.
Part III, Mechanism Studies on Plastics and Metals, Dec 1953.
Part IV, Cavitation as a Result of Waterdrop Collision with Solid Surfaces, Jan 1954.
Part V, Further Studies of Cavitation in Liquid Drops on Impact, Mar 1955.
Part VI, Dimensional Analysis of Rain Erosion Damage, July 1955.
Part VII, Mechanism Studies on 2S and 3S Aluminum.
Part VIII, On the Breakup of a Waterdrop in the Zone Behind a Detached Shock Wave, Aug 1955.

SECTION E. EFFECT OF TEMPERATURE, STRESS, AND AERODYNAMIC FACTORS

489. Abramson, A. E., and Torgeson, W. L. Report of Progress on a Study of Heating Requirement for Radomes — and Appendixes A thru C — 1 July thru 31 Aug 1952. Washington Machine and Tool Works, Research Div., Minneapolis, Minn., 1 Sept 1952.

490. Acker, C. H. Aerodynamic Heating Applied to Radome Design. Report NADC-

EL-5503, for Navy Bureau of Aeronautics, 7 Mar 1955 (Confidential).

491. Ambrogi, J. N., Jr. Bureau of Aeronautics Specification Gun-Blast Radome Type CW-22A/A. Report ADC EL-29, Aeronautical Electronic and Electrical Lab., NADC, Johnsville, Pa., 15 Aug 1950.

492. Ambrogi, J. N., Jr. Environmental Testing by the Navy, in Symposium on Guided Missile Radomes, ONR, Washington, D. C., June 18-19, 1953. ONR, Washington, D. C., pp. 7-27 (Confidential).

493. Ambrogi, J. N., Jr. The Gun Blast Problem in Radome Design. Report ADS EL-73-49, Aeronautical Electronic and Electrical Lab., NADC, Johnsville, Pa., 26 Apr 1949 (Confidential).

494. Amerman, A. E. Test Installation and Icing-Flight Tests of a Heated-Model Radome. WADC technical report 55-60, Aeronautical Icing Research Lab., Smith, Hinchman & Grylls, Apr 1955.

495. Analysis of Compressive Strength of Honeycomb Cores for Sandwich Constructions. NACA technical note 1251, Washington, D. C., Apr 1947.

496. Axilrod, B. M., and Sherman, M. A. Flexural Properties of Some Glass Fabric Base Plastic Laminates at Elevated Temperatures. USAF technical report 5940, AMC, Wright-Patterson AFB, Ohio, Feb 1950.

497. Banet, L., and Bracciaventi, J. Critical Thermal Energies of Plastic Radome Materials Submitted by the Wright Air Development Center, Department of the Air Force. Report 5046-3, part 56, Material Lab., New York Naval Shipyard, Brooklyn, N. Y., 9 July 1954.

498. Boller, K. H. Fatigue Tests of Glass-Fabric Laminates Subject to Axial Loading. US Forest Products Lab. reports 1823 and 1823-A, Madison, Wisc., Apr 1954.

499. Boller, K. H. Stress-Rupture Tests of a Glass-Fabric Base Plastic Laminate. US Forest Products Lab. report 1839, Madison, Wisc., June 195

500. Brown, B. J. Icing-Intensity Data for the 1953-54 Season. WADC technical report 54-277, Aeronautical Icing Research Lab., Smith, Hinchman & Grylls, June 1954 (Unclassified). See also monthly project status reports (Confidential) for Oct-Dec 1954 and quarterly project status report (Confidential) for first quarter 1955, on contract AF 33(600)-8114.

501. Brown, B. J. An Investigation of Instruments for the Measurement of Icing Intensity. WADC technical report 55-9, Aeronautical Icing Research Lab., Smith, Hinchman & Grylls, Mar 1955.

502. Cartolano, D. H. Evaluation of the Mechanical Properties of APS-23 Radome Material. Materials Lab. technical note WCRT 54-212, ARDC, Wright-Patterson AFB, Ohio, Nov 1954 (Confidential).

503. Cole, F. B. Radome Icing Tests — Model F-94. Report 7277, Lockheed Aircraft Corp., Burbank, Calif., 6 Feb 1950.

504. Crandell, R. M. Radome Anti-Icing System Development — Model F-94. Report 8246, Lockheed Aircraft Corp., Burbank, Calif., 9 Oct 1951.

505. Dixon, L. A., Jr. Physical Properties of Lockfoam Specimens Taken from an F-94C Elliptical Radome. Report 8730, Lockheed Aircraft Corp., Burbank, Calif., 8 Aug 1952.

506. Drucker, D. C. Stress-Strain Relations in the Plastic Range: A Survey of Theory and Experiment. No. A11 S1, Brown U., Providence, R. I., for ONR, Dec 1950.

507. Effect of Prestressing in Tension or Compression on the Mechanical Properties of Two Glass-Fabric-Base Plastic Laminates. US Forest Products Lab. report 1811, Madison, Wisc., Sept 1950.

508. Effect of Thickness on Strength of Glass-Fabric-Base Plastic Laminates. US Forest Products Lab. report 1831, Madison, Wisc., May 1954.

509. Enterline, R. R. Test on Nose Radome and Radar Support Structure, Model C-119. Engineering report R110-225, Fairchild Aircraft Div., Fairchild Engine and Airplane Corp., Hagerstown, Md., 19 Nov 1953 (AD-32500).

510. Ericksen, W. S., and March, H. W. Compressive Buckling of Sandwich Panels Having Facings of Unequal Thickness. US Forest Products Lab. report 1583-B, Madison, Wisc., 1950.

511. Erickson, E. C., and Norris, C. B. Tensile Properties of Glass-Fabric Laminates with Laminations Oriented in Any Way. US Forest Products Lab. report 1853, Madison, Wisc., Nov 1955.

512. Fabris, R. MCR618 Stress Analysis, Nose Radome Structure (Model C-119G). Engineering report R110-309, Fairchild Aircraft Div., Fairchild Engine and Airplane Corp., Hagerstown, Md., 2 Mar 1953.

513. Fontana, M. G., Bishop, S. M., and Spretnak, J. W. Mechanical Properties of Metals and Plastic Laminates at Low Temperatures. WADC technical report 5662 part V, 1953.

514. Forster, C. A. Finite Difference Methods Applied to the Heat Conduction Equation. Report LAt 045, English Electric Co., Great Britain, 17 Feb 1953.

515. George, D. A., Baker, H. A., and Sieffert, L. E. Impact Strength of Some Thermosetting Plastics at Low Temperatures. ASTM bulletin 181, Apr 1952.

516. Gibbons, C. A. Radome Anti-Icing Tests-Instrumentation Problems Encountered. Preprint 811A, SAE National Aeronautic Meeting, Los Angeles, 1-4 Oct 1952.

517. Gullotti, D. V., Carlson, R. L., and Simmons, W. F. First Progress Report on the Strength of Plastic — Glass Fiber Laminates at Elevated Temperatures: Dynamic-Modulus and Compression-Test Programs. Report for WADC Battelle Memorial Institute, Columbus, Ohio, 15 July 1954.

518. Hall, J. Experimental Model Large Size Radome To Be Standard Radome for Radar Equipment. Report 169-17, Lincoln Industries, Damascus, Va., 10 June 1953 (rev. 1 Sept 1953) (AD-33089). Report 169-19, 10 Oct 1953 (AD-33089).

519. Hummel, H. A. Design of Radomes Resistant to Gun Blast. Preprint 808, SAE, National Aeronautic Meeting, Los Angeles, 1-4 Oct 1952.

520. Investigation of Sandwich Constructions Under Lateral and Axial Loads. NACA technical note 3090, Washington, D. C.

521. Investigation of the Thermal Properties of Heat-Resistant Plastic Laminates. Southern Research Inst., Birmingham, Ala. Progress reports to WADC: First, 7 Aug 1953; Second, 26 Aug 1953; Third, 4 Nov 1953; Fourth, 18 Jan 1954. Supplement S2, progress reports: First, 23 June 1954; Second, 19 Aug 1954; Third, 12 Oct 1954; Fourth, 15 Dec 1954.

522. Jailer, R. W. Evaluation of Northern Hemisphere Icing Probabilities. WADC technical note 55-225, The American Power Jet Co., June 1955.

523. Jones, C. D Properties of Glass-Fabric Reinforced Low-Pressure Laminates. USAF technical report 5748, 1949.

524. Kaspin, S., and Bean, R. C. Electrical Characteristics of a Multi-Band, Anti-Iced Radome for the Model RB-66C Airplane. Engineering report LB-16982, Douglas Aircraft Co., Long Beach, Calif., 8 Oct 1953 (Confidential).

525. King-Hele, D. G., Bowcock, K. J., and Peattie, I. W. Effects of Radome Shape on the Weights of Surface-to-Air Guided Missiles, Including "Optimum" Designs for Ramjets and Rockets of Various Ranges. Technical note GW 220, Royal Aircraft Establishment, Great Britain, Nov 1952 (Secret).

526. Kotik, J. An Estimate of Radome Deflection and Boresight Error Resulting from Aerodynamic Forces Acting on a Conical Radome. Document 1267, McMillan Lab., Ipswich, Mass., 15 Mar 1954 (Confidential).

527. Kuenzi, E. W. Edgewise Compressive Strength of Panels and Flatwise Flexural Strength of Strips of Sandwich Constructions. US Forest Products Lab. report 1827, Madison, Wisc., Nov 1951.

528. Kuenzi, E. W., and Ericksen, W. S. Shear Stability of Flat Panels of Sandwich Construction. US Forest Products Lab. report 1560, Madison, Wisc., 1951.

529. Kuhn, A. H. Static Test of B-47B (Bomber) Fiberglas Radome 12-2225. No. 25318, Boeing Airplane Co., Seattle, Wash., Nov 1949.

530. Kuldell, P. D. Wind-Tunnel Tests of a 1/13 Scale Model P2V-3W Airplane to Determine the Effect of Changing the Radome Shape. Aero report 822, David W. Taylor Model Basin, Aerodynamics Lab., Washington, D. C., July 1952 (Confidential).

531. Lake, H. G. An Investigation of the Problem of Ice Removal from B-29 Radomes, WADC technical report 52-46, Weapons Components Div., Wright-Patterson AFB, Ohio, Jan 1952.

532. Lenherr, F. E. Survey of Radome Anti-Icing Methods—Model F-89, Report TDM-42, Northrup Aircraft, Hawthorne, Calif., 25 Apr 1951.

533. Lenherr, F. E., and Young, R. W. Development of Spray System for Radome Anti-Icing—and Appendixes I thru VIII—Model F-89C and D—Progress Report I. Report TDM-68, Northrup Aircraft, Hawthorne, Calif., 10 June 1952.

534. Lesley, R. F. Heat-Transfer Test of a Three-Inch-Thick Dual-Wall Radome Panel, Report GER-4946, Goodyear Aircraft Corp., Akron, Ohio, 22 Sept 1952.

535. Long, J. K. The Effect of Outdoor Exposure on Flexural and Other Properties of Some Plastic Materials. USAF technical report 5698, 1948.

536. McMillan, E. B. The Influence of Large In-Flight Temperature Changes on the Electrical Design of Missile Radomes, WADC technical report 56-393, Proceedings of the Ohio State U.—WADC Radome Symposium, Aug 1956.

537. Manson, S. S. Behavior of Materials Under Conditions of Thermal Stress. NACA report 1170, Washington, D. C.

538. March, H. W., and Kuenzi, E. W. Buckling of Cylinders of Sandwich Construction in Axial Compression, US Forest Products Lab. report 1830, Madison, Wisc., June 1952,

539. March, H. W., and Kuenzi, E. W. Buckling of Sandwich Cylinders in Torsion. US Forest Products Lab. report 1840, Madison, Wisc., June 1953.

540. Mark, M. Moments of Inertia and Deflection of Plastic Sandwich Beams. Modern Plastics, vol. 32, Mar 1955, p. 146.

541. Matheny, C. E., and Smith, V. A. Determination of the Aerodynamic Loads on the A.E.W. Radome — TED No. NACA 2416. No. MR-L4J31, NACA, Washington, D. C., Oct 1944.

542. Measurement of Fiberglass-Radome Temperatures with Thermocouples, Test no. T-29564, Boeing Aircraft Co., Seattle, Wash., 28 Oct 1955.

543. Mechanical Test Procedures for Radomes and Radome Materials, ATC report ARTC-3, Aircraft Industries Association, July 1951.

544. Methods for Conducting Mechanical Tests of Sandwich Construction at Normal Temperatures, US Forest Products Lab. report 1556, Madison, Wisc., Feb 1950.

545. Methods of Test for Determining Strength Properties of Core Material for Sandwich Construction at Normal Temperatures, US Forest Products Lab. report 1555, Madison, Wisc., Sept 1950.

546. Miller, D. L. Transmission Efficiency of a Fluted Core Radome (165-31010) Subjected to Icing Conditions — Applicable to F-86D Airplanes — NAA Model NA-165 — Class — Fighter. Report NA-50-894, North American Aviation, Engineering Research Lab., Los Angeles, Calif., 17 Aug 1950.

547. Miller, F. H. An Analysis of the Radome Anti-Icing System for the F-86D Interceptor Airplane — and Appendix — NAA Model NA-165. Report NA-51-1283, North American Aviation, Los Angeles, Calif., 7 Feb 1952.

548. Nichols, F. L. Temperature Distribution Characteristics of a Proposed Radome Construction for the F-86D Airplane — NAA Model NA-165 — Class — Fighter. Report NA-50-252, North American Aviation, Los Angeles, Calif., 24 Feb 1950.

549. Norris, C. B. An Analysis of the Compressive Strength of Honeycomb Cores for Sandwich Construction. NACA technical note 1251, Washington, D. C., 1947.

550. Norris, C. B., and Boller, K. H. Wrinkling of the Facings of Sandwich Construction Subjected to Edgewise Compression, US Forest Products Lab. report 1810, Madison, Wisc., Nov 1949. Supplementary report 1810-A, Wrinkling...Compression — Sandwich Constructions Having Honeycombed Cores, June 1953.

551. O'Brien, F. R. Investigation of Thermal Properties of Plastic Laminates, WADC technical report 54-306 part I, 1954.

511. Erickson, E. C., and Norris, C. B. Tensile Properties of Glass-Fabric Laminates with Laminations Oriented in Any Way. US Forest Products Lab. report 1853, Madison, Wisc., Nov 1955.

512. Fabris, R. MCR618 Stress Analysis, Nose Radome Structure (Model C-119G). Engineering report R110-309, Fairchild Aircraft Div., Fairchild Engine and Airplane Corp., Hagerstown, Md., 2 Mar 1955.

513. Fontana, M. G., Bishop, S. M., and Spretnak, J. W. Mechanical Properties of Metals and Plastic Laminates at Low Temperatures. WADC technical report 5662 part V, 1953.

514. Forster, C. A. Finite Difference Methods Applied to the Heat Conduction Equation. Report LAt 045, English Electric Co., Great Britain, 17 Feb 1953.

515. George, D. A., Baker, H. A., and Sieffert, L. E. Impact Strength of Some Thermosetting Plastics at Low Temperatures. ASTM bulletin 181, Apr 1952.

516. Gibbons, C. A. Radome Anti-Icing Tests-Instrumentation Problems Encountered. Preprint 811A, SAE National Aeronautic Meeting, Los Angeles, 1-4 Oct 1952.

517. Gullotti, D. V., Carlson, R. L., and Simmons, W. F. First Progress Report on the Strength of Plastic — Glass Fiber Laminates at Elevated Temperatures: Dynamic-Modulus and Compression-Test Programs. Report for WADC Battelle Memorial Institute, Columbus, Ohio, 15 July 1954.

518. Hall, J. Experimental Model Large Size Radome To Be Standard Radome for Radar Equipment. Report 169-17, Lincoln Industries, Damascus, Va., 10 June 1953 (rev. 1 Sept 1953) (AD-33089). Report 169-19, 10 Oct 1953 (AD-33089).

519. Hummel, H. A. Design of Radomes Resistant to Gun Blast. Preprint 808, SAE, National Aeronautic Meeting, Los Angeles, 1-4 Oct 1952.

520. Investigation of Sandwich Constructions Under Lateral and Axial Loads. NACA technical note 3090, Washington, D. C.

521. Investigation of the Thermal Properties of Heat-Resistant Plastic Laminates. Southern Research Inst., Birmingham, Ala. Progress reports to WADC: First, 7 Aug 1953; Second, 26 Aug 1953; Third, 4 Nov 1953; Fourth, 18 Jan 1954. Supplement S2, progress reports: First, 23 June 1954; Second, 19 Aug 1954; Third, 12 Oct 1954; Fourth, 15 Dec 1954.

522. Jailer, R. W. Evaluation of Northern Hemisphere Icing Probabilities. WADC technical note 55-225, The American Power Jet Co., June 1955.

523. Jones, C. D. Properties of Glass-Fabric Reinforced Low-Pressure Laminates. USAF technical report 5748, 1949.

524. Kaspin, S., and Bean, R. C. Electrical Characteristics of a Multi-Band, Anti-Iced Radome for the Model RB-66C Airplane. Engineering report LB-16982, Douglas Aircraft Co., Long Beach, Calif., 8 Oct 1953 (Confidential).

525. King-Hele, D. G., Bowcock, K. J., and Peattie, I. W. Effects of Radome Shape on the Weights of Surface-to-Air Guided Missiles, Including "Optimum" Designs for Ramjets and Rockets of Various Ranges. Technical note GW 220, Royal Aircraft Establishment, Great Britain, Nov 1952 (Secret).

526. Kotik, J. An Estimate of Radome Deflection and Boresight Error Resulting from Aerodynamic Forces Acting on a Conical Radome. Document 1267, McMillan Lab., Ipswich, Mass., 15 Mar 1954 (Confidential).

527. Kuenzi, E. W. Edgewise Compressive Strength of Panels and Flatwise Flexural Strength of Strips of Sandwich Constructions. US Forest Products Lab. report 1827, Madison, Wisc., Nov 1951.

528. Kuenzi, E. W., and Ericksen, W. S. Shear Stability of Flat Panels of Sandwich Construction. US Forest Products Lab. report 1560, Madison, Wisc., 1951.

529. Kuhn, A. H. Static Test of B-47B (Bomber) Fiberglas Radome 12-2225. No. 25316, Boeing Airplane Co., Seattle, Wash., Nov 1949.

530. Kuldell, P. D. Wind-Tunnel Tests of a 1/13 Scale Model P2V-3W Airplane to Determine the Effect of Changing the Radome Shape. Aero report 822, David W. Taylor Model Basin, Aerodynamics Lab., Washington, D. C., July 1952 (Confidential).

552. Oleesky, S. S. Development of a High-Temperature Missile Radome, Report ADC EL-10-51 Aeronautical Electronic and Electrical Lab., NADC, Johnsville, Pa., 20 Oct 1950.

553. Oleesky, S. S. The Effect of Elevated Temperature on Transmission of Microwave Energy Through Dielectric Sheets, Report ADS EL-148-49, Aeronautical Electronic and Electrical Lab., Naval Air Development Station, Johnsville, Pa., 22 July 1949.

554. Oleesky, S. S. Heat Requirements for a Nose Radome to Prevent Icing Under Conditions of Laminar Flow, 21 Dec 1948 to 30 April 1949, (Interim Report), Report ADS EL-118-48, Aeronautical Electronic and Electrical Lab., Naval Air Development Station, Johnsville, Pa., May 1949.

555. Oleesky, S. S. A Study of the Problem of Anti-Icing for Radomes and Its Possible Solutions, Report ADC EL-86-50, Aeronautical Electronic and Electrical Lab., NADC, Johnsville, Pa., 13 Jan 1950.

556. Raville, M. E. Analysis of Long Cylinders of Sandwich Construction Under Uniform External Lateral Pressure, US Forest Products Lab. report 1844, A and B, Madison, Wisc., 1954.

557. Ringelstetter, L. S., Voss, A. W., and Norris, C. B. Effect of Cell Shape on Compressive Strength of Hexagonal Honeycomb Structures, NACA technical note 2243, Washington, D. C., 1950.

558. Ritchie, V. S., and Greenberg, M. J. Determination of Pressure Distributions over a Radome Model at High Speeds – TED No. NACA 2409, No. CMR-L4J14, Langley Memorial Aeronautical Lab., Langley Field, Va. (published by NACA, Washington, D. C.), Oct 1944 (Confidential).

559. Roark, R. J. Formulas for Stress and Strain, McGraw-Hill Book Co., New York, 1954.

560. Roberts, M. L. Static Test of AN/APS-4 Airborne Radar Nacelle, No. NAM-31168, Aeronautical Materials Lab., NAMC, Philadelphia, Pa. (published by Bureau of Aeronautics, Washington, D. C.), Feb 1945 (Confidential).

561. Sandwich Construction for Aircraft, Bulletin ANC-23, part II, 1955.

562. Schleicher, R. L. (approver). Static Test of Radome Assembly for the Model F-86D Airplane – NAA Model No. NA-165, Report NA-51-355, North American Aviation, Engineering Dept., Los Angeles, Calif., 12 Apr 1951.

563. Schramm, C. K., Jr. The Effect of Water and Ice on Microwave Transmission Through Radomes, Technical note WCLC-53-2, Components and Systems Lab., WADC Wright-Patterson AFB, Ohio, Feb 1953.

564. Simmons, W. F., and Cross, H. C. Elevated Temperature Properties of Glass-Fabric-Base Plastic Laminates, USAF technical report 6172, 1951.

565. Strength of Metal Aircraft Elements, ANC document 5a, Aircraft Committee of the Munitions Board, 1949.

566. Survey of the Status of High-Temperature Radome Materials, A, Project Rand research memorandum RM-1516, Battelle Memorial Inst., Columbus, Ohio, 29 Apr 1955 (Secret).

567. Test Methods for Structural Plastic Laminates at Low Temperatures and at Elevated Temperatures, ATC report W-64, Aircraft Industries Association, June 1954.

568. Thermal Barriers, American Society of Mechanical Engineers, Dec 1944.

569. Thermal Data Handbook, The, Report AFSWP-700, 1954 (Secret).

570. Timoshenko, S. P., and Goodier, J. N. Theory of Elasticity, McGraw-Hill Book Co., New York, 1951 (2nd ed.).

571. Tomashot, R. C. Thermal Radiation Effects on Glass-Fabric Reinforced Plastics, Technical note WCRT CWRT 55-44, WADC, Wright-Patterson AFB, Ohio, Mar 1955.

572. Toner, S. D., Wolock, I., and Reinhart, F. W. Effects of Molding Pressure on the Strength Properties of Several Types of Glass Fiber Reinforced Plastics, WADC technical report 55-256, Dec 1955.

573. Torgeson, W. L., and Abramson, A. E. A Study of Heat Requirements for Anti-Icing Radome Shapes with Dry and Wet Surfaces. WADC technical report 53-284, Research, Inc., Minneapolis, Minn., Sept 1953.

574. Vanecho, J., Remely, G. R., and Simmons, W. F. High-Temperature Creep-Rupture Properties of Glass-Fabric Plastic Laminates. WADC technical report 53-491, 1953.

575. Von Karman, T., and Tsien, H. S. The Buckling of Spherical Shells by External Pressure. Jour. of the Aero. Sciences, Dec 1939.

576. Voss, A. W., and Norris, C. B. Creep Tests of Sandwich Constructions Subjected to Shear at Normal Temperatures. US Forest Products Lab. report 1806, Madison, Wisc., 1949.

577. Warren and Norris. Analysis of Shear Strength of Honeycomb Cores for Sandwich Constructions. NACA technical note 2208, Washington, D. C., Oct 1950.

578. Werren, F. Mechanical Properties of Plastic Laminates. US Forest Products Lab. report 1820, Madison, Wisc., Feb 1951. Supplementary report 1820-A, Feb 1953.

579. Werren, F. Shear-Fatigue Properties of Various Sandwich Constructions. US Forest Products Lab. report 1837, Madison, Wisc., 1952.

580. Werren, F., and Freas, A. D. Mechanical Properties of Cross-Laminated and Composite Glass-Fabric-Base Plastic Laminates. US Forest Products Lab. report 1821, Madison, Wisc., Feb 1951.

581. Werren, F., and Heebink, B. G. Effect of Defects on the Tensile and Compressive Properties of a Glass-Fabric-Base Plastic Laminate. US Forest Products Lab. report 1814, Madison, Wisc., June 1950.

582. Werren, F. and Norris, C. B. Analysis of Shear Strength of Honeycomb Cores for Sandwich Constructions. NACA technical note 2208, Washington, D. C., 1950.

583. White, J. S. Gun Blast Tests on Radomes for X Band Transmission. Radiation Lab., MIT, Cambridge, Mass., July 1943 (Confidential).

584. Wier, J. E., and Pons, D. C. Flexural Tests of Structural Plastics at Elevated Temperatures. WADC technical report 53-307, National Bureau of Standards, Jan 1954.

585. Zophres, W. Buckling Criteria for Sandwich Shells. Proceedings of the Ohio State U.—WADC Radome Symposium, June 1956.

SECTION F. MISCELLANEOUS

586. Adney, J. E., and Tice, T. Transmission Through a Dielectric Spherical Shell. Report 531-3, Antenna Lab., Ohio State U. Research Foundation, Columbus, 1 Aug 1953.

587. Amason, M. P., and McCloud, W. W. Radome Performance Studies (Confidential). Douglas Aircraft Co., Santa Monica, Calif. Interim report 4 (report SM-18232), 25 Jan 1954 (AD-49800). Final report (report SM-14950), 6 vols., 11 May 1954: vol. 1 (AD-46432); vol. 2 (AD-35193); vol. 3 (AD-35194); vol. 4 (AD-33195); vol. 5 (AD-33196); vol. 6 (AD-33197).

588. Ambrogi, J. N., Jr. Bureau of Aeronautics Specification CW-22A/A Radome. Report ADC EL-27, Aeronautical Electronic and Electrical Lab., NADC, Johnsville, Pa., 15 Aug 1950.

589. Ambrogi, J. N., Jr. Bureau of Aeronautics Specification CW-149/AP Radome for AN/APS-20 Equipment. Report ADC EL-28, Aeronautical Electronic and Electrical Lab., NADC, Johnsville, Pa., 15 Aug 1950.

590. Ambrogi, J. N., Jr. Electric, Physical, and Dielectric Properties of Radomes and Radome Materials. Report ADC EL-41-50, 23 Aug 1949 (Confidential).

591. Analytical Method of Determining Absolute Values of Antenna Characteristics for Experimentally Obtained Conical Field Patterns. Technical memorandum report 94, Naval Air Missile Test Center, Point Mugu, Calif., Nov 1954.

592. Barker, C. B., and Lengyel, B. A. The Effect of Beam Distortion in Conical Scanning. Technical memorandum 404, Research Lab., Hughes Aircraft Co., Apr 1955.

593. Bailin, L. L. and Silver, S. Exterior Electromagnetic Boundary Value Problems for Spheres and Cones. IRE Transactions on Antennas and Propagation, vol. AP-4, Jan 1956, pp. 5-16.

594. Barrar, R. B. The Diffraction of an Electro-Magnetic Plane Wave by a Curved Panel, Section L in A Study of Radome and Radar Antenna Installation and Design Criteria: Beam Alignment in Radomes—Part III. Engineering report 12283-8L, McMillan Lab., Ipswich, Mass., 16 Mar 1953 (Confidential).

595. Barrar, R. B. Methods of Design of Experimental Radomes of Report 8Q. Document 1277, supplement to report 8Q (AD-32198), McMillan Lab., Ipswich, Mass., 1954 (Confidential) (AD-40640). (Part of A Study of Radome and Radar Antenna Installation and Design Criteria.)

596. Barrar, R. B. and Dolph, C. L. On a Three-Dimensional Transmission Problem of Electromagnetic Theory. Jour. of Rational Mechanics and Analysis, vol. 3, Nov 1954.

597. Barrar, R. B., Kay, A. F., and Redheffer, R. M. A Graphical Procedure for Accurate Determination of the Dielectric Constant of a Panel from the Measurement of Its Transmission Phase, Section N in A Study of Radome and Radar Antenna Installation and Design Criteria: Beam Alignment in Radomes—Part III. Engineering report 12283-8N, McMillan Lab., Ipswich, Mass., 23 June 1953.

598. Baxter, J. P., 3rd. Scientists Against Time. Little, Brown and Co., Boston, Mass., 1952.

599. Beam Alignment in Radomes, Part I. Technical report 6, McMillan Lab.

600. Beaudry, Jr., and Garcia, W. Specification for Radome for the Model 8 Airplane. Consolidated Vultee Aircraft Corp., San Diego, Calif., 14 May 1953 (Confidential) (AD-38952).

601. Becker, Bourdeau, and Burnight. Upper Atmosphere Research, Report II, Part II. Report R-3031, Naval Research Lab., Dec 1946.

602. Bird, W. W. Design and Fabrication of Experimental Radome and Associated Equipment for Volir Antenna. Report UB-747-D-19, Cornell Aeronautical Lab., Buffalo, N. Y., 2 vols., 30 Jan 1953.

603. Birks, J. B. Dielectric Transmission and Scanner-Nacelle Design. Report T.1677 G10/R146/JBB. Telecommunications Research Establishment, Gt. Malvern, England.

604. Blalock, J. E., and Putnam, R. H. Wind-Tunnel Tests of a 1/13-Scale Model PB-1W (Patrol) Airplane with Alternative Radome Installations. No. C-317 Aero 789, David W. Taylor Model Basin, Washington, D. C., June 1950.

605. Bomarc Radome Development. Report GER-5927, Goodyear Aircraft Corp., Akron, Ohio, 8 Mar 1954 (Secret) (AD-31850). Second quarterly progress report, report GER-6080, 8 June 1954 (Secret) (AD-42758).

606. Boulding, R. S. H. The Resonant Cavity Magnetron. Van Nostrand, New York, 1952.

607. Cady, W. M., Karelitz, M. B., and Turner, L. A. Radar Scanners and Radomes. McGraw-Hill Book Co., New York, 1948. (Vol. 26, MIT Radiation Lab. Series.)

608. Carlson, J. F. Proof Test of Plastic Radome Model XB-48-2. No. ETR-937, Glenn L. Martin Co., Baltimore, Md., Sept 1948.

609. Cogar, B. R., and Seaman, J. P. Electrical Properties of Radome Materials, Measured from 30 December 1944 to 4 June 1944. No. PE-1.15-MAH F42(R), NAMC, Naval Aircraft Factory, Philadelphia, Pa., 4 June 1945 (Confidential).

610. Cohen, M. H. Electromagnetic Scattering by Dielectric Bodies. Report 475-14, Antenna Lab., Ohio State U. Research Foundation, Columbus, 30 June 1954.

611. Conant, G. H., Jr., Wachendorf, F., and others. Investigations on the Properties of Radomes. A Study of the Geometrical and Physical Problems of Microwave Transmission Through Radome Walls. Engineering report 298, Perkin-Elmer

Corp., Norwalk, Conn., 31 May 1954 (Secret) (AD-34081). Also, Wachendorf, engineering report 337, 31 Oct 1954 (Secret); and (final) engineering report 381, 31 Mar 1955 (Secret).

612 Daugherty, D. J., and Palmer, J. Interim Report on Electrical Characteristics of an Anti-Iced Radome, Engineering report LB-16398, Douglas Aircraft Co., Long Beach, Calif., 16 May 1951.

613. Design and Construction of Experimental Model Large Size Radome to Be Standard Radome For Radar Equipment, Lincoln Industries, Damascus, Va., for Rome ADC Griffis AFB, Rome, N. Y. Engineering reports nos. 10, 10 Nov 1952; 12, 10 Jan 1953; 14, 10 Mar 1953; 16, 10 May 1953; 17, 10 June 1953 (revised 1 Sept 1953); 18, 10 Sept 1953.

614. Development of an Artificial Dielectric for Use in Radome Design, Document D-13977, Boeing Airplane Co., Seattle, Wash., 2 Mar 1953.

615. Development of Microwave Absorbing Materials, Third quarterly report, Bjorksten Research Lab., Madison, Wisc., 31 Mar 1955 (Confidential) (AD-68286).

616. Dickinson, J. C., Jr. Problems Concerned with the Use of Artificial Dielectrics in Radomes, Thesis. Report GE-55-2, Inst. of Technology, Wright-Patterson AFB, Ohio, Aug 1955 (AD-72803).

617. Discussion of the Effect of Nose Radomes on the H-Plane APS-10 Radiation Patterns and on the Usability of the "Safety Circle," A, Technical note 1, American Airlines System, 24 Sept 1947.

618. DiToro, J. A. Graphs of Transmission and Phase Data of Plane Dielectric Sheets for Radome Design, Report NADC-EL-5313, Aeronautical Electronic and Electrical Lab., NADC, Johnsville, Pa., 1 July 1953.

619. Dunbar, A. S., and Gunter, R. C. Second quarterly scientific report, report R-510-1125, 13 Jan 1955, to Radome Error Prediction Study, Dalmo-Victor Co., San Carlos, Calif.

620. Durand, W. F. Aerodynamic Theory, Vol. III, Durand Reprinting Committee, Pasadena, Calif., 1943.

621. Eggleston, W. Scientists at War, Hunter Rose Co., Canada, 1950.

622. Electrical Characteristics of Radomes, Section 7, report GET 1948-1, General Electric Co., Schenectady, N. Y. (Confidential).

623. Evaluation of Model PBM-5 Airplane Equipped with AN/APS-31B Radar Housing, Naval Air Test Center, Patuxent River, Md., 19 Jan 1952.

624. Everitt, W. L. Communication Engineering, McGraw-Hill Book Co., New York, 1937.

625. Falcon Radome Development, Third quarterly progress report, report GER-6220, Goodyear Aircraft Corp., Akron, Ohio, 30 July 1954 (Secret) (AD-41841).

626. Fluke, C., Kraft, J., and Singer, T. Radome Problem (AF Problem 93), Problem report 57 (progress report 28), Computation Lab., Harvard U., Cambridge, Mass., 1 July 1953.

627. Forbes, R. H., and Noe, B. Microwave Electrical Characterisitcs of Radome Materials at 8.5 Kilomegacycles per Second, WADC technical report 54-273, Apr 1954.

628. Fourth Symposium on the U.S.A.F. Antenna Research and Development Program, The, Report on symposium sponsored by WADC, Wright-Patterson AFB, Ohio, on 17-21 Oct 1954 (Confidential).

629. Fox, G. A. An Automatic Waveguide Phase Changer, IRE Proceedings, vol. 35, 1947, p. 1489.

630. Fyall, A. A. Dielectric Measurements on Various Radome Materials and the Effect of Moisture Absorption and Temperature, Royal Aircraft Establishment, Great Britain, Oct 1953. (Technical note no. Chem 1209; encl. 1 to Air Attache, London report TR-434-54.) (Confidential) (AD-27247).

631. Gade. Radome — AS-316()/AFS-23 Radar, Document D10-957, Boeing Airplane Co., Seattle, Wash., 17 Dec 1951 (rev. B, 28 Dec 1951).

632. Garcia, W. Radome Design for Highspeed Aircraft, Aero Digest, vol. 67, Dec 1953, p. 74.

633. Garcia, W. Radome Optical System Problems on Supersonic Aircraft. Preprint 810. SAE National Aeronautic Meeting, Los Angeles, 1-4 Oct 1952.

634. General Specification for Radomes. Military Specification MIL-R-7705A, Jan 1955.

635. Hahn, G. M., Gunter, R. C., Jr., and Pinney, E. J. Radome Error Prediction Study. Quarterly scientific report 4, report R-510-1217, Dalmo-Victor Co., San Carlos, Calif., 15 July 1955 (Secret) (AD-67185).

636. Hoel, P. G. Introduction to Mathematical Statistics. John Wiley and Sons, New York, 1954.

637. Horton, M. C., Boyce, W. E. L., and Hartig, E. O. Optical Theory for Microwave Transmission Through Dielectric Wall Structures. Report GER-5530, Goodyear Aircraft Corp., Akron, Ohio, 4 Aug 1953.

638. Investigation of Babinet Principle for Possible Radome Application. First progress report, report NADC-EL-5372, Bjorksten Research Lab., Madison, Wisc., 6 May 1953 (Confidential).

639. Investigation and Design of Rigid Radome for Radar Sets AN/FPS-4 and AN/TPS-1D. Phase 1 final engineering report, report Z-PR-70026, Zenith Plastics Co., Gardena, Calif., 21 Jan 1955 (AD-67677). Phase 2 final engineering report, report Z-PR-70026-2, 3 Mar 1955 (AD-67991).

640. Jahnke and Emde. Tables of Functions, Dover Publications, 1943.

641. Januskevich, N. N. Graphical Device, Section G in A Study of Radome and Radar Antenna Installation and Design Criteria: Beam Alignment in Radomes—Part II. Technical report 12283-7G, McMillan Lab., Ipswich, Mass., 14 Mar 1952 (ATI-155959).

642. Jenkins, F. A., and White, H. E. Fundamentals of Physical Optics, McGraw-Hill Book Co., New York, 1937.

643. Kaliszewski, T. Experimental Study of Collinear Slot Antenna (An Application of Babinet's Principle). Technical report 202, Cruft Lab., Harvard U., Cambridge, Mass., 6 Sept 1954.

644. Kay, A. F. Design of a Broadband Absorber or Reflectionless Panel. Document 1140, McMillan Lab., Ipswich, Mass. (Confidential).

645. Kay, A. F. The Electrical Design of the Homogeneous Radome Wall, Section K in A Study of Radome and Radar Antenna Installation and Design Criteria: Beam Alignment in Radomes—Part III. Engineering report 12283-8K, McMillan Lab., Ipswich, Mass., 15 Feb 1953 (Confidential).

646. Kay, A. F. Simple Mathematical Models of Radomes, Section O in A Study of Radome and Radar Antenna Installation and Design Criteria: Beam Alignment in Radomes—Part III. Report 12283-8-O, McMillan Lab., Ipswich, Mass., 23 Sept 1953 (Confidential) (AD-31771).

647. Kay, A. F. A Survey of Radome Problems. Scientific report 1, Technical Research Group, New York, Mar 1955 (Secret) (AD-63142).

648. Kay, A. F. Tapered Radomes, Section D in A Study of Radome and Radar Antenna Installation and Design Criteria: Beam Alignment in Radomes—Part II. Technical report 12283-7, McMillan Lab., Ipswich, Mass., 14 Mar 1952.

649. Kay, A. F. The Two-Step Antenna Model of Radome Boresight Errors. McMillan Lab., Ipswich, Mass., 10 Mar 1954 (Confidential).

650. Kay, A. F., and Barrar, R. Lloyd's Mirror Effect in Radome Error. Document 1268, McMillan Lab., Ipswich, Mass., 18 Mar 1954 (Confidential).

651. Kay, A. F., and McMillan, E. B. Radome Design Theory for Phase and Reflection. McMillan Lab., Ipswich, Mass., 1 Jan 1953 (Confidential).

652. Kay, A. F., Redheffer, R. M., and McMillan, E. B. Conclusions and Program Summarized, Section B in A Study of Radome and Radar Antenna Installation and Design Criteria: Beam Alignment in Radomes—Part II. Final engineering report for period covered. McMillan Lab., Ipswich, Mass., 29 Feb 1952.

653. Keller, J. B. Reflection and Transmission of Electromagnetic Waves by Thin Curved

Shells, Research report 172-5, Mathematics Research Group, Washington Square College, New York U., New York, Feb 1948.

654. Kelly, J. M., Stenoien, J., and Isbell, D. Development of an Artificial Dielectric for Use in Radome Design. Report D-13977, Boeing Airplane Co., Seattle, Wash., 2 Mar 1953 (AD-49559).

655. King, R. W. P., Mimno, H. R., and Wing, A. H. Transmission Lines Antennas and Wave Guides. McGraw-Hill Book Co., New York, 1945.

656. King-Hele, D. G., Bowcock, K. J., and Peattie, L. W. Effects of Radome Shape on the Weights of Surface-to-Air Guided Missiles, Including "Optimum" Designs for Ramjets and Rockets of Various Ranges. Technical note GW 220, Royal Aircraft Establishment, Great Britain, Nov 1952 (Secret).

657. Klotzbaugh, G. A., Flarherty, J. M., and Hughes, R. H. A Study of Artificial Dielectrics with Unity Dielectric Constant. Final report, report GR-177, Westinghouse Research Lab., East Pittsburgh, Pa., 2 Apr 1954 (Confidential).

658. Kotik, J. Some Remarks on Thin Dielectric Walls, Section M in A Study of Radome and Radar Antenna Installation and Design Criteria: Beam Alignment in Radomes—Part III. Engineering report 12283-8M, McMillan Lab., Ipswich, Mass., 15 Mar 1953 (Confidential).

659. Kotik, J. Summable Divergent Integrals and a Far Field Paradox. Scientific report 2, Technical Research Group, New York, 1 May 1955.

660. Lenherr, F. E., and Young, R. W. Development of a Spray System for Radome Anti-Icing (Models F-89C and F-89D). Progress report 2, report TDM-68-II, Northrup Aircraft, Hawthorne, Calif., 24 Oct 1952 (AD-9174). Final report, report TDM-68-III, 15 Jan 1953 (AD-11981).

661. Lippmann, B. A., and Oppenheim, A. Equivalent Circuit Approach to the Radome Problem. Technical Research Group, New York, 30 Apr 1954, 3 vols. (vol. 1, Loaded Dielectrics; vol. 2, Analysis of Plane Slabs; vol. 3, Cascaded Arrays).

662. List, B. H. Research on Methods of Reducing Radar Cross Section of Aircraft. Scientific report 1, Battelle Memorial Inst., Columbus, Ohio, 31 Aug 1955 (Secret).

663. McCloud, W. W. Radome Performance Studies. Report SM-14833, Douglas Aircraft Co., Santa Monica, Calif., 5 June 1953 (Confidential).

664. McDonough, J. A. Study of Radome and Reflector for ASDE. Final engineering report 2390-4, report RADC-TR-55-76, Airborne Instruments Lab., Mineola, N. Y., Oct 1954 (AD-72032).

665. McMillan, E. B. Introduction, Section A in A Study of Radome and Radar Antenna Installation and Design Criteria: Beam Alignment in Radomes—Part II. Technical report 7, McMillan Lab., Ipswich, Mass., 1952 (Secret).

666. McMillan, E. B., and Redheffer, R. M. A Study of Radome and Radar Antenna Installation and Design Criteria. Technical report 12283-6, McMillan Lab., Ipswich, Mass., 21 Aug 1951.

667. Manushian, J. Electromagnetic Propagation Characteristics of Space Arrays of Aperture-in-Metal Discontinuities and Complementary Structures. Report 36, Div. of Elec. Engineering, University of California, Berkeley, Calif. Inst. of Engineering Research Studies, no. 60, issue no. 126, 26 Sept 1954.

668. Matthaei, G. L. Synthesis of Chebyshev Impedance Matching Networks, Filters, and Interstages. Report 43, Div. of Elec. Engineering, University of California, Berkeley, Calif. Inst. of Engineering Research Studies, no. 60, issue no. 139, 20 June 1955.

669. Oleesky, S. S. Bureau of Aeronautics Specification, Radome for Radar Set AN/APS-4, Detail Specification. Report ADC EL-25, Aeronautical Electronic and Electrical Lab., NADC, Johnsville, Pa., 2 Aug 1950.

670. Oleesky, S. S. Designing Radomes for Supersonic Speeds. Electronics, Jan 1954.

671. Oleesky, S. S. Electrical Design of Bow Radome for AN/APS-41 Antenna Assembly on Navy Model XP5Y-1 Aircraft. Report

ADS EL-94-49, 13 May 1949 (Confidential).

672. Oleesky, S. S. Redesign of Radome for Radar Set AN/APS-4—and Appendix I and II. Report ADC-EL-171-50, Aeronautical Electronic and Electrical Lab., NADC, Johnsville, Pa., Aug 1950.

673. Oleesky, S. S. Repairing Reinforced Plastics; with Special Emphasis on Preservation of Electrical Characteristics of Radomes. Modern Plastics, vol. 29, Feb 1952, pp. 99-100.

674. Page, R. M. Monopulse Radar. IRE 1955 National Convention Record, part 8, pp. 132-134.

675. Paiss, M. H. Electronic Correction of Boresight Shift in Symmetrical Antenna-Radome Systems. Report NADC-EL-52122, Aeronautical Electronic and Electrical Lab., NADC, Johnsville, Pa., 21 Jan 1953 (Confidential).

676. Paiss, M. H. Practical Notes on the Effect of Radomes on Airborne Microwave Antennas with Emphasis on the Boresight Shift Problem. Paper given at the National Conference in Airborne Electronics, Dayton, Ohio, May 1952. Published in IRE Airborne Electronics.

677. Proceedings of the Radome Symposium. The Ohio State U.—WADC Radome Symposium, presented at The Ohio State University, Columbus, Ohio, June 1955, 3 vols. (Confidential).

678. Progress of Study of Radome Transmission Computers. No. NS63s-13967, Douglas Aircraft Co., 3 June 1949. Bound with report ADS EL-2-50, Aeronautical Electronic and Electrical Lab., NADC, Johnsville, Pa. (Confidential).

679. Radome for Electromagnetic Reconnaissance System — RB-58 Ferret (Electromagnetic) Reconnaissance System — Vol. III — Phase I. Final engineering report, 29 July 1953-24 May 1954, Melpar, Inc., Alexandria, Va. (Secret) (AD-42058(a)).

680. Radome Performance Studies. Final report, report SM-14960, Engineering Dept., Douglas Aircraft Co., Santa Monica, Calif., 11 May 1954, 6 vols. (Confidential).

681. Radome Problem in Guided Missiles, The. Final report, contract N6 ONR-27-23 (sponsored by ONR), Princeton U., Princeton, N. J., 1 Mar 1952 (Secret).

682. Radomes—A Report Bibliography. ASTIA Reference Center. ARC 2050, Technical Information Div., Library of Congress, Washington, D. C., Mar 1955 (Secret).

683. Ramo, S., and Whinnery, J. R. Fields and Waves in Modern Radio. John Wiley and Sons, New York, 1953.

684. Redheffer, R. M. Beam Alignment in Radomes — Part I. Technical report 12283-6, McMillan Lab., Ipswich, Mass., 21 Aug 1951.

685. Redheffer, R. M. Beam Alignment in Radomes. Part II, Section C. Theoretical Sandwich Design for Phase. Technical report 7, McMillan Lab., Ipswich, Mass., 14 Mar 1952.

686. Redheffer, R. M. Electrical Properties of Double Wall and Sandwich Radomes, No. R-483-11, Radiation Lab., MIT, Cambridge, Mass., Jan 1945.

687. Redheffer, R. M. An Outline of the Electrical Properties of Radomes. No. R-483-2, Radiation Lab., MIT, Cambridge, Mass., Dec 1943.

688. Redheffer, R. M., Mason, S. J., and McMillan, E. B. Preliminary Study of Antennas and Obstacles, in A Study of Radome and Radar Antenna Installation and Design Criteria. Interim engineering report, technical report 12283-1, McMillan Lab., Marblehead, Mass., 17 July 1950.

689. Redheffer, R. M., Wildman, R. C., and O'Gorman, V. The Computation of Dielectric Constants. Jour. of Applied Physics, vol. 23, 1952, p. 505.

690. Reintjes, J. F., and Coate, G. T. Principles of Radar. McGraw-Hill Book Co., New York, 1952 (3rd ed.).

691. Research and Development Five Radomes and Data. Report U-12224-28, Stupakoff Ceramic and Mfg. Co., 10 Dec 1951.

692. Richmond, J. H. Measurement of Time-Quadrature Components of Microwave Signals. Technical report 531-9, Antenna Lab., Ohio State U. Research Foundation, Columbus, 15 Oct 1954.

693. Richmond, J. H. Simplified Calculation of Antenna Patterns, with Application to Radome Problems — A Study of Radome and Radar Antenna Installation Design Criteria. Engineering report 531-10, Antenna Lab, Ohio State U. Research Foundation, Columbus, 15 Nov 1954 (AD-51292).

694. Richmond, J. H. A Study of Radome and Radar Antenna Installation Design Criteria. Final engineering report 531-8, Antenna Lab., Ohio State U. Research Foundation, Columbus, 1 Sept 1955 (AD-50183).

695. Russell, E. W. Materials for Optical and Radar Transparencies. A Review. Technical note no. Chem 1201, Royal Aircraft Establishment, Great Britain, Aug 1953 (Confidential).

696. Sampson, J. H. A Modified Treatment of Some Reflection Problems. Document 1302, McMillan Lab., Ipswich, Mass., 31 Dec 1954.

697. Sampson, J. H. On the Reflection Coefficient of Non-homogeneous Media. Document 1303, McMillan Lab., Ipswich, Mass., 31 Dec 1954.

698. Sampson, J. H. Summary Report for Contract No. AF 18(600)-1044. Document 1301, McMillan Lab., Ipswich, Mass., 20 Dec 1954 (Confidential).

699. Sarbacher, R. L, and Edson, W. A. Hyper and Ultrahigh Frequency Engineering. John Wiley and Sons, New York, 1943.

700. Schlieben, E. W. Electrical Design of Radome for Airborne Radar Height Finder Antenna Assembly on Model PO-1W Aircraft. Report ADS EL-25-49, 24 Nov 1948 (Confidential).

701. Schlieben, E. W. Radomes and Aircraft Design. Aeronautical Engineering Rev., vol. 11, May 1952, pp. 69-81.

702. Schoeffel, M. F. Brief Qualitative Evaluation of Critical Flying Qualities with the Modified APS-31 Radome Carried as an External Store — Model AD-4 Airplane. US Naval Air Test Center, Flight Test Div., Patuxent River, Md., June 1950 (Confidential).

703. Schramm, C. K., Jr. Propagation Constant and the Radome. WADC technical report 53-297, Electronic Components Lab., WADC, Wright-Patterson AFB, Ohio, Aug 1953 (AD-21967).

704. Schultz, R. Radomes for AN/APG-30 Radar. Report 395, Emerson Electric Mfg. Co., St. Louis, Mo., 23 June 1952 (Confidential).

705. Shipley, G. E., and Setter, D. E. Development of Reinforced Plastic Conical Radome (VHF) and Its Associated Structural Parts for Coaxial Location of TACAN/VOR Antennae. Technical note RADC-TN-55-8, Rome Air Development Center, Griffiss AFB, Rome, N. Y., Aug 1955 (AD-73240).

706. Silver, S. (ed.). Microwave Antenna Theory and Design. McGraw-Hill Book Co., New York, 1949. (Vol. 12, MIT Radiation Lab. Series.)

707. Slater, J. C. Introduction to Chemical Physics. McGraw-Hill Book Co., New York, 1939.

708. Slater, J. C. Microwave Transmission. McGraw-Hill Book Co., New York, 1942.

709. Smith, P. H. Transmission-Line Calculator. Electronics, vol. 12, Jan 1939, pp. 29-31.

710. Snow, O. J. Applications of the Impedance Concept to Radome Wall Design. Report NADC-EL-52196, Aeronautical Electronic and Electrical Lab., NADC, Johnsville, Pa., 6 Apr 1953.

711. Snow, O. J. Some Theoretical Aids for Studies on Crossover Point Shifts Due to Radomes. Report NADC-EL-5276, Aeronautical Electronic and Electrical Lab., NADC, Johnsville, Pa., 28 Aug 1952 (Confidential).

712. Snow, O. J. Studies of Computers for Solving Problems of Radome Transmission. Report ADS EL-2-50, Aeronautical Electronic and Electrical Lab., Naval Air Development Station, Johnsville, Pa., 1 Aug 1950 (Confidential).

713. Soller, T., Starr, M. A., and Valley, G. E., Jr. Cathode Ray Tube Displays. McGraw-Hill Book Co., New York, 1948. (Vol. 22, MIT Radiation Lab. Series.)

714. Some Tests to Determine the Effects of Dielectric Constant, Shape, and Wall

Thickness Taper on Radome Aberration. Report LEL.t.053. English Electric Co., Great Britain, 28 Jan 1955 (Secret) (AD-75842).

715. Speer, William. Matrix Method of Radome Transmission Computation — and Appendixes 1 thru 3. Memorandum report EG-MR-3, Douglas Aircraft Co., El Segundo, Calif., 4 Jan 1951 (revision A, 23 Feb 1951).

716. Spencer, R. C. Back Scattering from Various Shaped Objects. No. WLCEC-1-6/10/46, preliminary report, Watson Lab., Cambridge Field Station, Cambridge, Mass.

717. Spencer, R. C. A Least Square Analysis of the Effect of Phase Errors on Antenna Gain. Report E 5025, USAF Cambridge Research Center, Jan 1944.

718. Sporcic, J. A., and Whann, R. L. Radomes. Aircraft Production, vol. 14, Dec 1952, pp. 424-430.

719. Stakgold, I. Stationary Forms for the Scattering Cross Section of an Obstacle. Technical report 231, Cruft Lab., Harvard U., Cambridge, Mass., 10 Oct 1955.

720. Stratton, J. A. Electromagnetic Theory. McGraw-Hill Book Co., New York, 1941.

721. Study of Radome and Radar Antenna Installation Design Criteria. Final engineering report 531-13, Antenna Lab., Ohio State U. Research Foundation, 1 Sept 1955 (Confidential) (AD-76042).

722. Suesskind, C. Investigation of Obstacle-Type Artificial Dielectrics. No. Yale/U-Fit-(af122), final report, Dunham Lab. of Electrical Engineering, Yale U., New Haven, Conn., June 1951.

723. Symposium on Guided Missile Radomes, Washington, D. C., June 18-19, 1953 (Supplement). ONR, Washington, D. C. (Confidential) (AD-38581).

724. Tai, C. T., and Barnett, R. I. Characteristics of Large Spherical Radomes, in Proceedings of the Radome Symposium Presented at The Ohio State University, Columbus, Ohio, June, 1955. Ohio State U., Columbus, 1955, 3 vols. (Confidential).

725. Thompson, R. L. Clearview Windows in Presence of Radome, Model YC-124A Serial 42-65406. Report DEV-888, Douglas Aircraft Co., Santa Monica, Calif., 16 Nov 1951.

726. Tice, T. E., and Adney, J. E. Transmission Through a Dielectric Spherical Shell. Technical report 531-3, Antenna Lab., Ohio State U. Research Foundation, Columbus, 1 Aug 1953 (Confidential).

727. Undesser, K. Reflection Transmission Phase Delay Calculation in Radome Design. Electronics Dept., Engineering Div., The Glenn L. Martin Co., Baltimore, Md. (Confidential).

728. Valasek, J. Theoretical and Experimental Optics. John Wiley and Sons, New York, 1949.

729. Von Hippel, A. R. (ed.). Dielectric Materials and Applications. Technology Press of MIT, and John Wiley and Sons, New York, 1954.

730. Von Hippel, A. R. Dielectrics and Waves. John Wiley and Sons, New York, 1954.

731. Wallis, F. E. Radome Configuration, Incident Angles, Materials, Electrical Transmission, Beam Deflection, and De-Icing Methods. Progress report, Zenith Plastics Co., Gardena, Calif., 27 July 1954 (AD-44482).

732. Water Ripple Analogue of Electro-Magnetic Wave Propagation. Technical report 1, University of Vermont and State Agricultural College, Sept 1952. Technical report 2, Jan 1955.

733. Wheeler, H. A. High Frequency Electromagnetic Wave Translating Element. US Letters Patent no. 2,511,610, 13 June 1950.

734. Wiederhorn, N. M., Kay, A. F., and Kotik, J. The Dependence of Radome Error on Shape, Wall Structure, and Taper. Report 12283-8Q, McMillan Lab., Ipswich, Mass., 31 Mar 1954 (Confidential).

735. Wolin, S. Bibliography of U.S. Navy Publications on the Development and Test of Radomes and Irdomes. Report NADC-EL-5466, Aeronautical Electronic and Electrical Lab., NADC, Johnsville, Pa., 1 July 1954 (Confidential).

736. Wolin, S. Electrical Design of Lossy High-Incidence Radomes. Report ADC EL-123-50, Aeronautical Electronic and Electrical Lab., NADC, Johnsville, Pa., 11 July 1950.

737. Wolin, S. Equations for Transmission Coefficients of Lossy Radome Sandwiches. Aeronautical Electronic and Electrical Lab., NADC, Johnsville, Pa., 10 Jan 1950.

738. Wolin, S. Ray Deflection Through a Homogeneous Dielectric Radome. Report NADC-EL-5272, Aeronautical Electronic and Electrical Lab., NADC, Johnsville, Pa., 6 Aug 1952.

739. Wolin, S. Ray Deflection Through A Medium Having a Continuously Varying Refractive Index. Jour. of the Optical Soc. of Am., vol. 43, May 1953, pp. 373-75.

740. Wolin, S. Supplementary Tables of Fresnel's Coefficients, Snell's Law, and Other Radome Design Quantities. Report NADC-EL-53189, Aeronautical Electronic and Electrical Lab., NADC, Johnsville, Pa., 9 July 1954 (AD-37153).

741. Wolin, S. Tables of Amplitude and Phase of the Function $1+ae^{jb}$. Report NADC-EL-5114, Aeronautical Electronic and Electrical Lab., NADC, Johnsville, Pa., 28 Aug 1952.

742. Wolin, S. Tables of Fresnel's Coefficients, Snell's Law and Other Radome Design Quantities. Report ADC EL-5104, Aeronautical Electronic and Electrical Lab., NADC, Johnsville, Pa., 22 Jan 1952.

743. Wolin, S. Tables of Transmission and Reflection Coefficients of Lossy, Symmetrical Dielectric Radome Sandwiches. Report NADC-EL-52188, Aeronautical Electronic and Electrical Lab., NADC, Johnsville, Pa., 22 Oct 1953.

744. Wolin, S. Theory of Lossy High-Incidence Radomes. Report NADC-EL-5116, Aeronautical Electronic and Electrical Lab., NADC, Johnsville, Pa., 15 Jan 1952.

745. Woodburn, J. W. Radome Incident Ray Survey, Model RB-50. Document WD-12591, Boeing Airplane Co., Wichita, Kans., 2 Apr 1952.

746. Young, C. A. AI Mark 10 in the Brigand Night Fighter Trainer – Zinc Spray Screening of the Radome. Technical note 148, Telecommunications Research Establishment, Gt. Malvern, England, 17 Mar 1952 (Secret).

747. Youngren, F. R. The Design of a High Incidence Angle Radome for a Plane Polarized Antenna. No. M/R 16-506, Raytheon Mfg. Co., Missile and Radar Div., Bedford, Mass., 11 Nov 1954 (Confidential).

INDEX

For convenience in finding the subject topics in TR 57 67, a combined index is included in both volumes. The volume number, in boldface, precedes the page number of each index entry.

A

"A" sandwich, 1-238, 1-271, 1-544, 1-569, 2-92, 2-94
 alumina, 2-269, 2-270
 construction, 2-5
 foamed-in-place radomes, 1-13
 radome, 2-107
 attachment, 2-61
 power transmission, 2-103
 three-layer, 1-8
 transmission and phase delay, contours, 1-43
 transmission curves, 2-128
Ablative cover, 2-19, 2-49
Ablative materials, 2-446, 2-448
 dielectric constant, 2-455
 loss tangent properties, 2-454
Ablative window, 2-429
Absorption, dielectric, 2-362
 energy, 2-392
Acceleration boost, 2-418, 2-426
Acrylic resins, 2-319
Adiabatic calorimetry, 2-384
Aerodynamic, configuration, 2-6, 2-31
 design factors, 2-9
 forces, 2-51
 heat, 2-44, 2-417
 heat simulation, 2-242
 loads, 1-281
Air loading, unsymmetrical, 1-282
Air pressure, 1-322
Air prism, 1-456
Air, thermal conductivity, 1-289
Airborne radar, 1-439, 2-86
 dual-frequency, 2-90
 installation, 1-439
 pressurization, 1-439
Aircraft, attitude axis correction, 1-444
 early-warning radomes, 1-19
 environment, 1-455
 supersonic, 2-452
Alumina, 1-422, 2-36, 2-46, 2-50, 2-260, 2-440
 "A" sandwich, properties 2-270
 skins, 2-269
 bend strength, 2-263, 2-265
 dielectric constant vs. temperature, 2-237
 electrical properties, 2-80
 emittance, 2-268
 loss tangent vs. temperature, 2-267
 machining, 1-422
 modulus & elasticity, 2-266
 mosaic, 2-269
 properties, 2-265
 porous, 2-268
 radome, blanks, 2-284
 fabrication, 2-288
 flight simulation, 2-243
 sizes, 2-288
 skin temperature, 2-246, 2-250
 sandwich, core, 2-270
 materials, 2-268
 multilayer, 2-289
 skin, 2-270
 specific heat, 2-266
 thermal conductivity, 2-267
 thermal expansion, 2-266
 tiles, 2-271
 joints and adhesives, 2-271
Aluminum die, pressure-cast, 1-404
Aluminum phosphate, 2-445
 glass reinforced, 2-284, 2-446
Amplitudes, near-field, 1-68, 1-70, 1-507
 comparison, 1-136
 monopulse system, 1-203
Ambient loads, 1-283
AN/APS-20E radome, 1-397
Anechoic chamber, aperture-type, 2-394
 Eccosorb, 2-397
 funnel, 2-395
 microwave, 2-391
 shapes, 2-393
Angle, offset, 2-39

Angle of incidence, 1-55, 1-63, 2-38, 2-84, 2-92
Anisotropic capacitor, 1-58
Anisotropic constructions, 1-55
Anisotropic materials, 1-55
Anisotropy, 1-53
Antenna, clearance, 1-443
 conical scan, 1-209, 1-503
 conical transmission line, 2-147
 cosecant-squared, 1-98
 depolarization, 1-153
 deviation, 1-153
 elevation planes, 1-114
 half-wave dipole, 1-220
 horn, 1-69, 2-104
 lens, 2-147
 mount, 1-501
 oblique planes, 1-114
 obstacles, 2-154
 paraboloidal, 1-576
 pattern, 2-114, 2-397, 2-406
 cosecant-squared, 1-98
 E-plane, 2-42
 distortion, 1-101, 2-152, 2-155
 H-plane, 1-75, 2-43
 parameters, 2-41
 perturbation, 2-404
 performance degradation, 1-101
 planes, oblique, 1-114
 polarization, parallel, 1-153
 radome, 1-126
 -radome design, 1-10
 -radome interaction, 1-77, 1-221
 -radome radiating system, 1-576
 -radome systems, 1-188, 1-521
 search radar, 1-97
 stabilization, 1-443
 systems, monopulse, 2-138
Anti-icing, 1-317
Antistatic rain erosion coatings, 1-344
Aperture-type anechoic chamber, 2-394
Araldites, 2-318
Armstrong 2755 Cork, 2-449
AR-1075—HT polyester, 2-316
Artificial dielectrics, 1-19
Asymmetry, 1-215
Attachments, 1-407
 "A" sandwich radome, 2-61
 ceramic radomes, 2-49
 chemical, 2-51, 2-54, 2-56
 joints, 2-53
 mechanical, 2-51, 2-55, 2-58
 radome, 2-48
Altitude axis correction, aircraft, 1-444
Avcoat II, 2-453
Axial load, 1-302
Axial support, radome, 2-149
Axially symmetric sector scanner, 1-441
Azimuth run, 1-207

B

"B" sandwich, 1-238, 1-271
 construction, 2-5
 radomes, 1-11, 1-47
Baffle chamber, 2-396
Bag molding, 1-392
Bakelite, 2-318
Ballistic range, 2-209
Ballistic reentry, 2-418
 surface temperatures, 2-425
 vehicles, 2-451
Bandwidth, 1-237, 2-42, 2-117
Barium aluminum silicate, 2-443
Batch preparation, steatite radome, 1-420
BC1 No. 6601-F polyamide resin, 2-319
Beam depression, 1-452
Beam deviation, 1-190
Beam tilt, 1-444
Beamrider missiles, 1-145
 applications, 1-146
Bearing blocks, preparation, 1-392
Bend strength, alumina, 2-263, 2-265
Beryllia, 1-423, 2-261, 2-280, 2-441
 dielectric constant, 2-283
 emittance, 2-283
 loss tangent, 2-283
 modulus of elasticity, 2-281
 modulus of rupture, 2-280
 thermal conductivity, 2-282
 thermal expansion, 2-281
 radomes, production, 2-292
Bisque firing, steatite radome, 1-422
Bisque machining, 2-287
Blast pressure, 1-283
Blister radome, semistreamlined, 1-9
Bomarc radome, 1-16
Bond strength and flexibility, 1-298
Bonding adhesives, 1-376
Boresight error, 1-502, 2-42, 2-100
 monopulse system, 1-199
 prediction, 1-17
 integral equation technique, 2-103
 optical technique, 2-101
 scattering technique, 2-102
Boresight ranges, 2-397, 2-406

Boresight test setup, 2-238
Boron nitride, 2-443
Branson Vidigage, 2-348
Brewster angle, 2-172
Boundary layer, 1-456
 temperature, 1-291
Broadband radomes, 1-237, 2-116, 2-125
 multilayer, 2-120
 surface treatment, 2-125
Buckling, 1-316
 coefficients, 1-306
 sandwich wall, 1-301
 solid wall, 1-302
 thermal, 1-295

C

"C" sandwich, 1-238, 1-572
 construction, 2-5
 radomes, 1-47
Calorimeter, copper block, 2-387
 "dropping," 2-385
Calorimetry, adiabatic, 2-384
Capacitor, anisotropic, 1-58
 isotropic, 1-58
Casting, steatite radome, 1-421
Catalysts, 1-373
Cavitation effect, 1-346
Cavity effect, 1-149
Centrifuge, 2-206
Ceramic materials, 1-419, 2-29
 elastic constants, 1-430
 electrical properties, 1-431
 Knoop hardness, 1-431
 physical properties, 1-427
 refractoriness, 1-431
 temperature effects, 1-432
 thermal conductivity, 1-429
 thermal expansion coefficients, 1-430
Ceramic radomes, 1-18, 2-259
 attachment, 2-49
 fabrication, 2-284
 properties, 2-260
Ceramics, 2-440
 dense fired, 1-419
 density, 1-431
 nonoxide, 2-362
 oxide, 2-262, 2-361
 porous, 1-424
 radiation effects, 2-250
 subsonic rain erosion properties, 1-340
Ceramoplastics, 1-427
Chemical attachments, 2-51, 2-54, 2-56
Chemical-mechanical attachments, 2-59
Chin radome, 1-11, 2-151
 fluted core, 1-394
Chopped fiber preform, 1-400
Circ-gore filament winding, 2-308
Circ-longo drop-stitch filament winding, 2-306
Circ-longo grind process, 2-309
Circ-longo sock process, 2-309
Circo fibers, 2-307
Circularly polarized incident waves, 1-567
Coatings, erosion, 1-397
 neoprene, 1-12
 polyurethane, 1-339
 rain erosion, 1-344
 properties, 1-335
Coaxial line dielectric measurements, 2-365
Coaxial waveguide, 1-485
Coherent phase discriminator, 1-512
Command guidance, 1-145
Compressive strength, 1-400, 2-389
Computer design of radomes, 2-90
Conductive heat transfer, 2-236
Conductivity, thermal, 1-284, 2-380
Cone angles, 1-290
 effect, 1-354
Conical fairing, 1-61
 ogive radome, 1-63
Conical radome, 1-105, 1-282
Conical scan antenna, 1-503
 axis, 1-209
Conical scan radar system, 1-132
Conical transmission line antenna, 2-147
Construction, half sandwich, 2-6
 sandwich radomes, 1-378
 sandwich wall, 1-301
 solid-wall radomes, 1-378
Convective heat transfer, 2-231
Copper block calorimeter, 2-387
Cordierite, 1-434
Core, construction, 1-394
 fluted, 1-380
 foam, 1-380
 honeycomb, 1-378, 1-396
 joint gaps, 1-299
 materials, 1-378
 shear strength, 1-298
 thickness, 1-259, 1-275, 1-298
 tolerance, 1-573
Cork, Armstrong 2755, 2-449
Cornu spiral, 1-448
Cosecant-squared antenna, 1-98
Creep, 1-316

Cristobalite, 2-276
Cross-polarization suppression, 2-104
Crosstalk error, 2-86
Curing, filament-wound radomes, 2-309
Cut-bar thermal conductivity measurements, 2-331
Cutting planes, 2-85
Cylinders, isotropic, 1-307
Cylindrical radome, 1-189
Cylindrical ring stresses, 2-66
Cylindrical sandwich, 1-303

D

DC-2106 silicone resin, 2-319
Deflection, 1-325
Dense fired ceramics, 1-419
Density, ceramics, 1-431
Depolarization, 1-151
 antenna, 1-153
 target, 1-154
DER-DEN resins, 2-318
Deviation, antenna, 1-153
Diamond wheel grinding, 1-404
Dielectric constant, 1-48, 1-68, 1-474, 1-478, 1-526, 2-31, 2-38
 ablation materials, 2-455
 alumina sandwich skin and core, 2-270
 beryllia, 2-283
 calculations, 2-377
 interferometer, 1-405
 measurements, 2-354
 Pyroceram, 2-274
 slip-cast sintered fused silica, 2-278
 vs. resin content, E-Glass and Vibrin 135, 2-300
 vs. resin content, hollow glass and Vibrin 135, 2-301
 vs. resin content, S-994 Glass and Vibrin 135, 2-302
 vs. temperature, 2-363
 alumina, 2-267
Dielectric diffraction, 1-74
Dielectric dispersion and absorption, 2-362
Dielectric homogeneity, 1-495
Dielectric instrumentation, microwave, 2-335
Dielectric loadings, 1-59
Dielectric loss, 1-431, 1-478, 1-495
Dielectric materials, electrical characteristics, 1-483
 high temperature, 2-362
 thermal properties, 2-379
Dielectric measurements, 2-364
 coaxial line, 2-365
 free-space, 2-374
 interferometer, 2-374
 open-circuit method, 1-490
 resonant cavity, 1-494, 2-370
 slotted-line method, 1-494
 waveguide, 2-367
Dielectric patches, 1-209
Dielectric properties, porous ceramics, 1-426
 resins, glasses, and laminates, 2-321
Dielectric rings, 1-208, 1-214
 scattering, 1-218
Dielectric sheets, 2-106
Dielectric thickness, 2-354
Dielectrics, artificial, 1-19
 inhomogeneous, 1-58
 lossy, 1-519
 medium-loss, 1-490
 plane, 1-519
Dielectrometer, 2-325, 2-352, 2-366
 microwave, 1-494
 surface-wave, 1-494
Diffraction, dielectric, 1-74
 edge, 1-447
Diffusivity, thermal, 2-382
Dilatometer, sapphire rod, 2-392
Dipole antenna, half-wave, 1-220
Dipole feed through radomes, 2-113
Dispersion, dielectric, 2-362
Dissipation factor, solid wall, 1-475
Distortion, antenna pattern, 2-152, 2-155
Double sandwich, 1-563
Double-wall radomes, 1-7, 2-6
Drag coefficient, 2-11
Driving point resistance, 2-117
"Dropping" calorimetry, 2-385
Duroid 5650, 2-451
Dynamic modulus measurement, 2-390

E

ECCO interferometer, 2-357
Eccosorb anechoic chamber, longitudinal baffle, 2-397
Edge compression, 1-308
Edge diffraction, 1-447
E-Glass, 2-298, 2-300
Elastic constants, ceramic materials, 1-430
Elastic moduli, 2-389

Electrical design considerations, 2-79
flat window, 2-431
hypersonic, 2-430
window, 2-416
Electrical factors, 2-26
Electrical gage, 1-473
Electrical grinding control, 2-310
Electrical index, 2-21
Electrical non-uniformity, radome walls, 1-207
Electrical properties, alumina, 2-80
ceramic materials, 1-431
joints, 1-387
Electrical requirements, 1-105, 2-19
search radomes, 1-99
Electrical tests, 2-22, 2-63
Electrical thickness, radome wall, 1-468
effect of moisture, 1-478
Electromagnetic field theory, 1-27
Electromagnetic tensioner, 2-303
Electromagnetic windows, 2-448
shape, 2-97, 2-99
stresses, 2-426
Electromechanical gage, 1-473
Electronic guidance, current missiles, 1-140
Elevation planes, antenna, 1-114
Ellipsoidal shape, 2-7
Ellipsoidal missile radome, 1-170
Elliptical polarization, 1-50, 1-169
transmission coefficients, 1-51
Emissivity, 1-284
Emittance, beryllia, 2-283
Pyroceram, 2-274
slip-cast sintered fused silica, 2-279
Environment, aircraft, 1-455
rain, 2-201
thermal, 2-416
thermal shock, 2-28
Environmental considerations, precipitation static, 1-319
Environmental design, 1-316
radome, 1-281
Environmental factors, 2-26
Environmental requirements, 2-22
Environmental testing, 1-326, 2-61
E-plane antenna pattern, 2-42
E-plane transmission loss, 2-39
Epon 828 laminates, 2-318
Epoxy resins, 1-339, 1-372, 1-403
VC-8359, 2-315
Equiangular shape, 2-7
Erosion, coating, 1-397
rain, 2-203
simulator, Mithras, 2-208
Error, boresight, 1-502
crosstalk, 2-86
in-plane, 1-201, 1-217
Exhausts, rocket motor, 2-235
Expanded hardboard radomes, 1-7
Expansion, thermal, 2-390
Exposure time, thermal shock, 1-284
External pressure, 1-305

F

Fabric, lay-up, 1-393
glass, 1-403
preparation, 1-392
Fabrication, alumina radome, 2-288
ceramic radomes, 2-284
composite radome, 2-312
glass-ceramic radome, 2-289
glass fiber filament, 2-302
multilayer alumina sandwich radome, 2-289
plastic radomes, 1-391
Fabry-Perol interferometers, 2-375
Face thickness, 1-298
Fairing, ogive, 1-65
Far-field antenna patterns, 1-75, 1-521
horn antenna, 2-105
interference, 1-102
Far-field zones, 1-222
Fatigue, 1-315
Feed-through radomes, dipole, 2-113
Feeler gauge thickness measurement, 2-311
Fiber, polystyrene, 1-7
Fiber reinforced plastic radomes, 2-295
Fiberglass yarn filaments, 2-299
Fibers, glass, 1-367, 2-296
Field-probe evaluation, 2-405
Filament winding, 2-306
circ-gore, 2-308
circ-longo drop-stitch, 2-306
helical, 2-306
Filament-wound radomes, curing, 2-309
finishing process, 2-313
Filaments, fiberglass yarn, 2-299
Fineness ratio, 1-61, 2-11, 2-21
Finishing process, 1-395
filament-wound radome, 2-313
radome, 2-290
sintered radome, 2-291
Fire control radar systems, 1-131, 1-178
Fire control radomes, 1-14, 1-129

Firing ceramics, 1-425
Flat panel (see "Panel" and "Wall" entries)
Flat-plate heating, 2-423
Flat sandwich, 1-38, 1-301
Flat sheet, homogeneous, 1-27
 lossless, 1-34
Flat window, electrical design, 2-431
Flexural strength, 1-390, 2-389
Flight simulation, alumina radome, 2-243
Fluorocarbon resin, 2-319
Flush-faired radomes, 1-11
Flush-mounted radiating systems, 2-137, 2-142
Fluted core, 1-380
 chin radome, 1-394
 wall construction, 1-299
Foam, core, 1-380
Foam, polyurethane, 1-380, 1-400
Foaming, 1-424
Foamed-in-place core wall construction, 1-299
Foamed-in-place radomes, 1-13
Focusing effect, streamlined radomes, 1-66
Forming, 1-425
Forming and shaping radome blanks, 2-286
Forsterite, 1-424
Four-horn phase comparison system, 1-506
Free-space, dielectric measurements, 2-374
 vswr evaluation, 2-405
 wavelength, 2-38
Frequency, 1-241
 rain, 2-201
 vs. wavelength conversions, 2-198
Friction tensioner, 2-303
Funnel anechoic chambers, 2-395
Fused silica, 2-273
 nose cone, 2-247
 slip-casting process, 2-291
Fusion cast materials, 1-427

G

Gage, electrical, 1-473
 in-process, 2-346
 inside diameter, 2-346
Generator, r-f, 1-495
Geodesic lenses, 2-147
Geometrical optics, 1-189
Glass, 1-426
 -bonded mica, 1-427
 -ceramics, 2-260
 properties, 2-271
 radome fabrication, 2-289
Glass (cont)
 cloth, 1-390
 dielectric properties, 2-321
 fabric, 1-403
 filament fabrication, 2-302
 sizing, 1-375
 fibers, 1-367, 2-296
 composition and properties, 2-299
 laminates, 2-281
 tension, 2-303
 laminate, aluminum phosphate-5994, 2-445
 recrystallized, 2-362
 refractory, 2-362
 reinforced aluminum phosphate, 2-284, 2-446
 reinforced plastics, longitudinal, 1-388
 low-pressure, 1-388
 mechanical properties, 1-388
 parallel laminated, 1-388
 reinforced sandwich radome, 1-408
 subsonic rain erosion properties, 1-340
Glazing, 1-425
Glide reentry, 2-418
 vehicles, 2-450
Gore filament pattern, 2-309
Gratings, 2-104
Grinding, circ-longo process, 2-309
 electrical control, 2-310
 ultrasonic control, 2-310
 radome blanks, 2-287
Ground illumination, 1-97
Guarded hot-plate, 2-382
Guidance radomes, 1-16
Guidance systems, 1-140
 effect of radome errors, 1-178
 radomes, 1-129
 proportional navigation, 1-144
 remote, 1-145
 self-contained, 1-141
Guided missiles, 1-141
Gunfire control radomes, 1-16

H

Haack-Von Karman shape, 2-8
Half-sandwich construction, 2-6
Half-wave dipole antenna, 1-220
Half-wave homogeneous flat sheet, 1-35
 first-order, 1-36
Half-wave radome, 2-81
Half-wave wall, 1-121, 1-191, 2-117
 higher-order, 1-81
Handling precautions, 2-48

Hardboard, expanded, 1-7
Heat flow, planar, 2-381
Heat resistant rain erosion coatings, 1-344
Heat simulation, aerodynamic, 2-242
Heat transfer, coefficient, 1-284
 conductive, 2-236
 convective, 2-231
 radiative, 2-236
Heating, aerodynamic, 2-44, 2-417
 flat-plate, 2-432
 laminar, 2-420
 sonic point, 2-421, 2-424
 turbulent, 2-421, 2-424
 rates, 2-419, 2-424, 2-426
Helical filament winding, 2-306
Helium plasma effects, 2-436
Hemispherical radome, 1-60, 1-104, 1-217, 2-250
Hetron 92, 2-316
Hollow glass, 2-301
Homing missiles, 1-142
Homogeneity, dielectric, 1-495
Homogeneous flat sheet, 1-27
 half-wave, 1-35
 thin, 1-33
Homogeneous panels, 1-567
Homogeneous radomes, transmission coefficient, 2-130
Honeycombs, 2-312
 core, 1-378, 1-396
 lay-up, 1-396
 thickness, 1-406
 sandwich radomes, 1-10
 wall construction, 1-298
Horns, 2-89
 antenna, 1-69, 2-104
 far-field pattern, 2-105
 interferometer, 2-344
Hot-air deicing, 1-318
Hot flue, 2-231
Hot-gas wind tunnel, 2-232
Hot-plate, guarded, 2-382
Hot salt bath, 2-236
H-plane, 1-229
 antenna patterns, 1-75, 2-43
 near-field amplitudes, 1-70
 near-field, phase, 1-70
 transmission loss, 2-40
Hybrid impregnation resin bath, 2-305
Hydraulic jacks, 1-322
Hydrocarbon resin, 2-315
Hypersonic, electrical design, 2-430
 materials, 2-439
 radomes, 2-413
 structural design, 2-426
 vehicles, 2-453
 velocities, 2-417

I

Ice calorimeter, 2-386
Icing control, 1-316
 anti-icing fluid, 1-317
 hot-air system, 1-318
 internal heating, 1-318
 rubber boot, 1-317
Illumination, ground, 1-97
Impact, 1-314
 resistance, 1-296, 1-429
 testing, 1-327
Incidence angle, 1-55, 1-110, 1-114, 1-275, 1-519, 2-38, 2-84, 2-92
 components, 1-117
Incident polarization, 1-153
 elliptical, 1-169
 linear, 1-168
 parallel, 1-153
Incident waves, linearly polarized, 1-174
 polarized, 1-153
 right-circularly polarized, 1-567
Inertia loads, 1-282, 2-51
Infrared systems, 1-88, 2-237
Inhomogeneities, radome surface, 1-210
Inhomogeneous, dielectrics, 1-58
 plasmas, 2-435
 radome reflection, 2-132
 radomes, 2-128
 transmission coefficient, 2-130
Inorganic laminates, 2-443
Inorganic materials, 1-366, 1-419
Inorganic matrix materials, 2-296
In-plane error, 1-201, 1-217
In-process gage, 2-346
Insertion phase, 1-34, 1-528, 1-560, 2-88, 2-159
 contours, single sheet, 1-106
 delay, 1-124
 "A" sandwich radome, 2-108
 lossless plane dielectric sheet, 1-83
 difference, 1-465, 2-84, 2-92
 constant, 2-84
 effects, 1-122
 variation vs. angle of incidence, 1-55
 vs. incidence angle, 1-120

Inserts, 1-392
Inside diameter gage, 2-346
Inspection methods, 1-406
Instability buckling, 1-301
Installation, airborne radar, 1-439
Instrumentation, 1-325
Integral equation, 1-195, 2-103
Interceptor radome, 1-168, 1-218
Interface reflection coefficients, 1-27, 1-56, 2-169
 phase angle, 2-171
Interference, 1-101
 effects, 1-445
Interferometer, 2-337
 dielectric constant, 1-495
 dielectric measurements, 2-374
 ECCO, 2-357
 horn, 2-344
 magic T, 1-467
 Michelson, 2-375
 micrometer, 1-466
 reflection, 2-310
 two-horn, 1-465
 tables, 2-339
 Fabry-Perol, 2-375
Interlaminar shear values, 2-297
Internal heating, 1-318
Internal pressure, 1-283
Isotropic capacitor, 1-58
 cylinders, 1-307
 plasma, simulated, 2-437
 sandwich, 1-306

J

JC-1571 hydrocarbon resin, 2-315
Jet engine exhaust, 2-232
Jets, plasma, 2-235
Joint gaps, core, 1-299
Joint loading, 2-52
Joints, attachment, 2-53
 electrical properties, 1-387

K

K-band radomes, 1-9
KEL-F81 fluorocarbon resin, 2-319
Knitted-sock laminated radomes, 1-10
Knoop hardness, ceramic materials, 1-431

L

Laminac 4110, 2-316
Laminated radomes, 1-10
 knitted-sock, 1-10
Laminated wall construction, 2-5
Laminates, 1-367
 dielectric properties, 2-321
 Epon 828, 2-318
 glass fiber, 2-281
 inorganic, 2-443
 organic resin-fiberglass, 2-441
 polyamide resin-fiberglass, 2-444
 slotted, 1-338
 resins, 1-13
 void elimination, 1-393
 walls, 1-478
Lathe grinding, 1-402
Lathe turning, 1-400
Lens, 1-206
 antennas, 2-147
 feeding, 1-80
 geodesic, 2-147
 Luneberg, 1-78
 manufacture, 1-79
 radome transmission loss, 1-80
Lightning, 1-319
Line-of-sight stabilization, 1-440
Linear polarization, 1-51, 1-168
Lithium aluminum silicates, 1-424
Lloyd's mirror effect, 1-76
Load application, 1-322
Load, axial, 1-302
Loaded core sandwiches, 1-18
Loads, 1-297
 ambient, 1-283
 aerodynamic, 1-281
 dielectric, 1-59
 inertia, 1-282
 joint, 2-52
 operational, 2-51
 pickup probe, 1-495
Lobe comparison, sequential, 1-147
Lobing, sequential, 1-133
Log spiral, 1-64
Logarithmic shape, 2-7
Longitudinal-baffle Eccosorb anechoic chamber, 2-397
Longitudinal heat-flow measurements, 2-381
Longitudinal plastics, glass, reinforced, 1-388
Longo fibers, 2-307
Look angle, 2-86
Loss, correction, 1-490
 dielectric, 1-431, 1-478, 1-495
 reflection, 2-38

Loss tangent, alumina sandwich skin and core, 2-270
beryllia, 2-283
calculations, 2-378
measurements, 2-357
properties, ablation materials, 2-454
Pyroceram, 2-274
slip-cast sintered fused silica, 2-278
vs. temperature, 2-363
alumina, 2-267
Lossless dielectric, Snell's law, 2-173
Lossless homogeneous plane sheets, 1-49
Lossless plane dielectric sheet, 1-82
Lossless plane sheet, 1-85
Lossless thin flat sheets, 1-34
Lossy dielectrics, 1-519
Low density materials, 1-381
Low-frequency resonant cavities, 2-373
Lumped fields, 1-196
Luneberg lens, 1-78

M

Mach number factors, 2-11
Machining, alumina, 1-422
Magic T, interferometer, 1-467
Magnesia, 1-423, 2-442
Magnetic materials, 1-54
measurements, 1-492
Magnetic tensioner, 2-303
Magnetron, frequency pulling, 1-100
performance, 1-100
Marco vacuum injection, 1-399
Matched-die mold, 1-401
Matched-tool molding, 1-396
Materials, 2-32
ablative, 2-446, 2-448
alumina sandwich, 2-268
anisotropic, 1-55
ceramic, 1-419, 2-29
construction, 2-257
core, 1-378
dielectric, 1-483
full density, 1-383
fusion cast, 1-427
hypersonic, 2-439
inorganic, 1-366
low density, 1-381
magnetic, 1-492
organic, 1-365
plastic, 1-335
rain-resistant, 2-203
testing, high temperatures, 2-361
Matrix formulation, 1-40
Matrix materials, inorganic, 2-296
Measurements, dielectric, 2-364
near-field, 1-221, 1-230, 1-507
no-dome, 1-224
radar cross section, 1-154
radome wall, 1-463
specific heat, 2-384
tensile strength, 2-69
transmission impedance, 1-486
Mechanical, attachment, 2-51, 2-55, 2-58
-chemical attachments, 2-59
factors, 2-27
micrometer, 1-472
properties, glass reinforced plastic, 1-388
properties, testing, 2-64
physical properties, 2-385
strength, 2-71
Mechanism, rain erosion, 1-345
Medium-loss dielectrics, 1-490
Melamine resins, 1-368
Metal ribs, 2-151
Metal-loaded radomes, 2-104, 2-125
perforated, 2-106
Metal sheets, 1-59
Metal slats, 1-59
Mica, glass-bonded, 1-427
Michelson interferometers, 2-375
Micrometer, 1-472
Microwave, anechoic chambers, 2-391
dielectric instrumentation, 2-335
dielectrometer, 1-494
interferometer, 1-466
radar, 1-5
reflectometer, 2-353
thickness gage, 1-406, 2-351
nonmetals, 2-352
Millimeter-wavelength radomes, 1-80, 2-135
phase data, 2-137
wall construction, 1-84
Missiles, beamrider, 1-145, 1-146
guidance radomes, 1-16
homing, 1-142
radome, 1-401
ellipsoidal, 1-170
fabric lay-up, 1-401
supersonic, 2-452
Mithras erosion simulator, 2-208
Modulated scatterer, 1-514
Modulus of elasticity, 1-390, 2-389
alumina, 2-266
"A" sandwich, 2-271

Modulus of elasticity (cont)
beryllia, 2-281
Pyroceram, 2-272
Modulus of rupture, beryllia, 2-280
Pyroceram, 2-272
Moisture, 1-320
effects, 1-478
Mold, matched-die, 1-401
Molten metal bath, 2-236
Molding, matched tool, 1-396
Monopulse system, 1-505, 2-138
amplitude comparison, 1-203
boresight errors, 1-199
errors, 1-136
radiation pattern difference, 1-135
sum radiation pattern, 1-134
time sequential systems, 1-136
Mosaic alumina construction, 2-269
Movable piston phase shifters, 1-509
Multilayer sandwiches, 1-239, 2-121
"A" sandwich radome, 1-8
alumina radome, fabrication, 2-289
construction, 2-6
panels, 1-38
wall radome, 1-273
Multiple thickness gage, 1-406

N

Nacelle, clearance, 1-454
lining absorbers, 1-10
placement, 1-445
Navigation, proportional, 1-144
Near-field, amplitude, 1-68
measurements, 1-507
distribution, 1-230
H-plane amplitude, 1-70
H-plane phase, 1-70
measurements, 1-221
phase measurements, 1-507
reflection, 1-102
Neoprene protective coating, 1-12
91-LD Phenolic resin, 2-319
No-dome measurements, 1-224
Nondimensional time, 1-310
Nonoxide ceramics, 2-362
Nose blunting, ogival shape, 2-11
Nose cone, fused silica, 2-247
slotted arrays, 2-144
Nose laminar heating, 2-420
Nose mounted ogival shaped radomes, 2-433
Nose radomes, 1-14, 1-238
Nuclear radiation, 1-321
Null shift measurements, 2-352
Nypol 46-4001 and 46-4020 acrylic resins, 2-319

O

Oblique planes, antenna, 1-114
Obstacles, antenna, 2-154
Offset angle, 2-39
Offset run, 1-207
Ogive, 1-162
fairing, 1-65
plastic, 1-358
radome, 1-172, 2-433
conical fairing, 1-63
shape, 2-8
nose blunting, 2-11
181 glass cloth, 1-390
One-half wave wall, 2-117
One-half wavelength, multiple, 2-4
radome, 2-31
thickness, 2-31
Open-circuit method, 1-490
Operational loads, 2-51
Optics, 1-447
boresight error prediction, 2-101
geometrical, 1-189
theory, 1-27
Orbital decay reentry, 2-418, 2-426
Organic materials, 1-365
properties, 1-381
resin-fiberglass laminates, 2-441
Oxide ceramics, 2-262, 2-361
Oxyacetylene burners, 2-252
Oxyacetylene test facility, 2-246
Oxyhydrogen burners, 2-233
Oxyhydrogen rocket motor, 2-243
Oxypropane burners, 2-232

P

Panels, flat (see also "Walls" entries), 2-91
homogeneous, 1-567
multilayer, 1-38
Parabolic shape, 2-8, 2-10
antenna, 1-576
Parachute, 1-353
Parallel laminated glass reinforced plastics, 1-388
Parallel polarization, 1-32, 1-153, 1-527, 1-573, 2-34
antenna, 1-153
Parallel-ray theory, 1-75

Parallel-ray transmission, 1-75
Parameters, antenna pattern, 2-41
Paraplex P-43, 2-316
Pass bands, 2-118
Patches, dielectric, 1-209
Pattern, antenna, 1-97, 2-114, 2-397, 2-406
 gore filament, 2-309
 distortion, 1-101, 2-39
 plasma antenna, 2-436
 radar, 1-445, 1-455
 radome, 1-499
 scattering, 2-158
Perforated metal-loaded radome, 2-106
Permittivity, complex, 1-483
Perpendicular polarization, 1-28, 1-241, 1-526, 1-573, 2-35, 2-84
Phantom feed, 1-150
Phase-amplitude system, 1-136
Phase comparison, 1-136
 monopulse system, 1-200
 four-horn system, 1-506
Phase data, 2-81, 2-137
Phase delay, 1-11
Phase shift, 1-478, 1-509
 reflection, 1-530
Phase variation, 2-39
Phenolic-nylon, Tayloron, 2-449
Phenolic resin, 1-367, 2-319
 plyophens 23-017, 2-319
Phenylsilane resins, 2-320
Physical design considerations, 2-1
Physical properties, ceramic materials, 1-427
Pickup probe, 1-509
 loading, 1-495
Pitch stabilization, 1-441
Placement, radome, 1-445
Planar heat flow, 2-381
Plane dielectric sheet, 1-32, 1-526
Plane dielectric, 1-519
Plane sheet refraction, 1-66
Plane-wave, reflection, 1-28
 refraction, 1-31
 transmission, 1-28
Plasma, antenna pattern distortion, 2-436
 effects, 2-433
 helium, 2-436
 inhomogeneous, 2-435
 jets, 2-235
 resonance, 2-438
Plastic-alumina radomes, 2-269
Plastics, classification, 1-366
 fiber reinforced, 2-295
Plastics (cont)
 glass reinforced, 1-388
 low-pressure, 1-388
 reinforcements, 1-374
 materials, 1-335
 rain erosion properties, 1-335
 ogive, 1-358
 radiation effects, 2-249
 radomes, fabrication methods, 1-391
 reinforced, 1-366
Platform stabilization, 1-440
Plyophens 23-017 phenolic resin, 2-319
Plywood radomes, 1-5
Pointing errors, 1-147, 1-150
Poisson's ratio, Pyroceram, 2-273
 slip-cast sintered fused silica, 2-277
Polarization, 1-50
 efficiency, 1-177
 elliptical, 1-50
 linear, 1-51, 1-168
 gratings, 2-104
 incident, 1-153
 parallel, 1-32, 1-153, 1-527, 1-573, 2-34
 phenomena, 1-152
 relative, 1-117
Polarized incident wave, 1-153
Polyamide resin, BC1 No. 6601-F, 2-319
 fiberglass laminate, 2-444
Polyester, AR-1075-HT, 2-316
 resins, 1-370, 2-316
 Selectron, 2-251
 Vibrin, 2-251
Polyfiber radomes, 1-365
Polylite ED-386, 2-316
Polystyrene fiber, 1-7
 K-band radomes, 1-9
Polyurethane, 1-339
 foams, 1-380, 1-400
Porous alumina, 2-268
Porous ceramics, 1-424
 dielectric properties, 1-426
Post-curing, 1-395
Power reflection, 1-271
 coefficient, 2-354
Power shape, 2-8, 2-10
Power transmission, "A" sandwich radome, 2-108
 coefficient, 1-526, 1-532, 2-34, 2-122, 2-357
 solid-wall radome, 2-119
 lossless homogeneous plane sheets, 1-49
 lossless plane dielectric sheet, 1-82

Power transmission (cont)
constant, 1-124, 1-554
contours, 2-172
minimum, 2-120
coefficient, 2-119
solid wall radome, 2-120
vs. core thickness, 1-544
Precipitation static, 1-319
Prefabricated foam wall construction, 1-299
Preform molding, 1-399
Pre-impregnation resin bath, 2-305
Preserved incident component, 1-567
Pressure, 1-325
-cast aluminum die, 1-404
injection, 1-400
load, 2-51
slip-casting, 2-287
Pressurization, 1-439
Production, beryllia radomes, 2-292
Protective cover, 2-18
Pyroceram, 2-34, 2-46, 2-50, 2-260, 2-362, 2-441
dielectric constants, 2-274
emittance, 2-274
loss tangent, 2-274
modulus of elasticity, 2-272
Poisson's ratio, 2-273
sensitivity measurement, 2-355
specific heat, 2-274
thermal conductivity, 2-273
thermal expansion, 2-273

Q

Quadripod space frame, 2-150
Quality control, 2-346

R

Radar, airborne, 1-439
antenna configuration, 1-166
conical scan, 1-132
fire control, 1-131, 1-178
cross section measurement, 1-154
cross section vs. target scattering, 1-156
microwave, 1-5
pattern distortion, 1-445, 1-455
range reduction, 1-99
VHF, 1-3
Radial plane definition, 2-99
Radiated field, 1-221
Radiating system, antenna-radome, 1-576
flush-mounted, 2-137, 2-142
Radiation effects, 2-248
ceramics, 2-250
plastics, 2-249
Selectron polyesters, 2-251
Vibrin polyesters, 2-251
Radiation, nuclear, 1-321
Radiation pattern, far-field, 1-521
Radiation pattern difference, monopulse antenna, 1-135
Radiative heat transfer, 2-236
Radome, airborne, 2-86
antenna systems, 1-188
anti-icing, 1-15
applications, 1-6
blanks, alumina, 2-284
forming and shaping, 2-286
grinding, 2-287
blister, 1-9
bonding adhesives, 1-376
boresight errors, monopulse system, 1-199
prediction, 1-17
broadband, 2-120, 2-125
ceramic, 1-18, 2-259
chemical attachment, 2-51, 2-54, 2-56
composite, 2-312
conical, 1-95, 1-282
construction, 1-365, 1-419
cylindrical, 1-189
de-icing, 1-18
depolarization, 1-167
diffraction, 1-
dipole feed-through, 2-113
double-wall, 1-7, 2-6
electrical design problem, 1-6
errors, 1-148, 1-502
correction, 1-205
correction, vector method, 1-214
measurement, 1-207
monopulse, 1-136, 1-199
prediction, 1-187
fabrication, 1-391
finishes, 1-408
geometry, 1-111
guidance, 1-16
high-temperature, 2-327, 2-358
homogeneous, 2-130
inhomogeneous, 2-130
loft lines, 1-115
materials, 1-297, 2-24
anisotropic, 1-55
inorganic, 1-419
magnetic, 1-54

Radome (cont)
materials (cont)
organic, 1-381
metal-loaded, 2-104, 2-125
millimeter-wavelength, 1-80, 2-135
missile, 1-401
ogival shaped, 1-172, 2-433
one-half wavelength, 2-31
pattern distorted, 1-499
placement, 1-445
plastic, 1-391
plastic-alumina, 2-269
plywood, 1-5
polyfiber, 1-365
resonant-wall, 2-110
sandwich, 1-9, 1-396
design curves, 2-173
search, 1-97, 1-99
semistreamlined, 1-9
shape, 1-60, 1-104, 1-297, 2-91, 2-97
weight factor, 1-106
size, 1-441
limitations, 2-48
skin temperature, 1-292
slotted metal, 2-111
solid-wall, 2-117
spheroidal, 1-61, 1-63
strength factors, 1-297
supersonic, 1-16
surface inhomogeneities, 1-210
transmission efficiency, 1-496
reflection, 1-498
scattering technique, 1-194
structural support, 2-149
structural design, 1-281
subsonic, 1-282
testing, 2-60
thick-shell, 2-67
thin-shell, 2-31
toroidal, 2-250
tunable, 2-131, 2-133, 2-135
types, 2-3
wall, measurements, 1-468
wall thickness, electrical, 1-468
wedge, 2-104
wire grid loaded, 2-106
Rain, classifications, 2-292
environment, 2-201
erosion, 1-11, 2-203
coatings, 1-335, 1-344
mechanism, 1-345
plastic materials, 1-335
Rain (cont)
erosion (cont)
rain gun, 2-207
rocket sled, 2-210
simulation, 2-206
subsonic, 1-331
supersonic, 1-17, 1-331, 1-350
test, 1-332
test results, 2-228, 2-230
time vs. missile velocity, 2-231
frequency, 2-201
gun, 2-207
intensity, 1-355, 2-201
particle size distribution, 2-205
rate vs. altitude, 2-204
resistant materials, 2-203
Rainfall, accumulation, 2-202
intensity, 1-355
rate, 2-202
Range, ballistic, 2-209
boresight, 2-397, 2-406
Ray tracing, 1-189
techniques, 1-521
boresight error prediction, 2-101
Recrystallized glass, 2-362
Rectangular waveguide, 1-485
Reentry, ballistic, 2-418
glide, 2-418
vehicles, 2-450
orbital decay, 2-418, 2-426
Reflection, 1-447, 2-132
coefficient, 1-520
complex, 1-470
interferometer, 2-310
loss, 2-38
measurement, slotted line method, 1-499
near-field, 1-102
phase shift, 1-530
plane-wave, 1-28
radome, 1-498
test, 2-350
Reflectometer, 1-500, 2-337
high-temperature, 2-359
microwave, 2-353
Refraction, 1-148
magnitude, 1-148
plane sheet, 1-66
plane-wave, 1-31
theory, 1-76
Refractive shift, 1-54, 1-67
Refractoriness, 1-431

Refractory glass, 2-362
Reinforced plastic radomes, 1-366, 2-295
Reinforcements, plastics, 1-374
Resin bath, 2-304
 hybrid impregnation, 2-305
 pre-impregnation, 2-305
 wet-dip, 2-304
Resin-fiberglass laminate, polyamide, 2-444
 organic, 2-441
Resins, DER-DEN, 2-318
 dielectric properties, 2-321
 epoxy, 1-339, 1-372, 1-403
 laminating, 1-13
 melamine, 1-368
 phenolic, 2-319
 phenylsilane, 2-320
 polyester, 2-316
 preparation, 1-392
 properties, 2-315
 silicone, 2-319
 systems, interlaminar shear values, 2-297
Resistance, driving-point, 2-117
 impact, 1-296, 1-429
 thermal shock, 2-28
Resonance, 1-487
 plasma, 2-438
Resonant cavities, low frequency, 2-373
 dielectric measurements, 1-494, 2-370
Resonant-wall radomes, 2-110
R-F generator, 1-495
Ribs, metal, 2-151
Ring, geometry, 1-219
 dielectric, 1-208, 1-214
Rocket motor exhausts, 2-235
Rocket sled, 1-355
 rain erosion simulator, 2-211
 test facilities, 2-211
 test results, 2-213
 track, SNORT, 2-211
Roll run, 1-207
 fixed polarization, 1-209
Roll stabilization, 1-441
R-7145 silicone resin, 2-320
Rubber boot, 1-317

S

Sandwich, "A", 1-238, 1-271, 1-544, 1-569, 2-92, 2-94
 construction, 2-5
 alumina materials, 2-268
Sandwich (cont)
 "B", 1-238, 1-271
 construction, 2-5
 radomes, 1-11, 1-47
 "C", 1-238, 1-572
 radomes, 1-47
 cylindrical, 1-303
 design, 2-89
 design curves, 2-173
 double, 1-563
 flat, 1-38, 1-301
 honeycomb, 1-10
 isotropic, 1-306
 loaded core, 1-18
 multilayer, 1-239, 2-121
 radome, 1-9, 1-396
 alumina, 2-289
 construction, 1-378
 glass reinforced, 1-408
 multilayer, 1-8
 single, 2-129
 symmetrical, 1-41
 thick-skin, 2-129
 wall, 1-123, 1-301
 buckling, 1-301
 lightweight cores, 1-464
Sapphire rod dilatometer, 2-392
Scattering, 1-218
 patterns, 2-158
 radome error prediction, 1-194, 2-102
 target, 1-156
Screening tests, 2-240
Search radomes, 1-97
 electrical requirements, 1-99
Sector scanner, 1-441
Selectron 5016, 2-316
Selectron polyesters, 2-251
Sensitivity measurement, Pyroceram, 2-355
Sequential lobing, 1-133
 comparison, 1-147
Shaped-beam antenna, 1-450, 2-155
Shapes, anechoic chamber, 2-393
Shapes, electromagnetic window, 2-97
Shapes, radome, 1-60, 1-104, 1-297, 2-91, 2-97, 2-99
 ellipsoidal, 2-7
 ogival, 2-8
 parabolic, 2-8, 2-10
 power, 2-8
 requirements, 1-194
 strength factor, 2-70
 typical, 2-98

Shear loads, 1-303
Shear strength, core, 1-298
Shear stress coefficients, 1-303
Sheets, dielectric, 1-59
Sheffield thickness gage, 2-346
Shift, refractive, 1-54
Shock front, 1-455
Shock testing, 1-327
Shock wave, effect, 1-348
 refraction, 1-458
Silica, fused, 2-273
 vitreous, 2-273
Silicate, barium aluminum, 2-443
 lithium aluminum, 1-424
Silicone resin, DC-2106, 1-390, 2-319
 R-7145, 2-320
Silicones, 1-369
Simulated isotropic plasma, 2-437
Simulation, rain erosion, 2-206
Simultaneous lobe comparison, 1-133
 errors, 1-137, 1-147
Single-horn interferometer, 1-465
Single-horn reflectometer, 1-470
Single-layer walls, 1-464
Single sandwich radome, 1-259
Single sheet, 1-106
Sintered fused silica, 2-260, 2-275
 finishing process, 2-291
 radome fabrication, 2-290
 surface treatments, 2-291
Sintering, 2-287
Sintering process, fused silica, 2-291
Size, radome, 1-441, 2-48, 2-91
 alumina, 2-288
Sizing, glass fabric, 1-375
Skin layers, curing, 1-394
Skin temperature, alumina radome, 2-246, 2-250
 transient, 1-287
Skin thickness, 1-259
Skin tolerance, 1-573
Sled, rocket, 1-355
Slip-cast, forming, 2-286
 fused silica, 2-441
 sintered fused silica, 2-276, 2-278
 emittance, 2-279
 Poisson's ratio, 2-277
 specific heat, 2-278
 strength, 2-277
 thermal conductivity, 2-277
 thermal expansion, 2-278
Slip casting, 1-420
 fused silica process, 2-291
 pressure, 2-287
Slip control, 1-420
Slotted arrays, nose cone, 2-144
Slotted laminates, 1-338
Slotted line, 1-494
 phase shifters, 1-509
 radome reflection measurement, 1-499
Slotted metal radomes, 2-111
 transmission coefficient, 2-111
 transmission loss, 2-112
Slotted waveguide, 2-138
 arrays, TE mode, 2-138
 arrays, TM mode, 2-138
Snell's law, lossless dielectric, 2-173
S-994 glass, 2-302
SNORT rocket sled track, 2-211
Sock process, circ-longo, 2-309
Solid sheet, 1-464
 dielectric, 1-120
Solid wall, 1-301
 buckling, 1-302
 construction, 2-4
 dissipation factor, 1-475
 radome, 1-238, 1-241, 2-117
 bandwidth, 2-117
 construction, 1-8, 8
 design curves, 2-172
 one-half wave, 2-117
 transmission coefficient, 2-118
 transmission curves, 2-128
Sonic point heating, 2-421, 2-424
Space frames, 2-149
 quadripod, 2-150
Specific heat, air, 1-288
 alumina, 2-266
 measurements, 2-384
 Pyroceram, 2-274
 slip-cast sintered fused silica, 2-278
 vs. temperature, beryllia, 2-282
Spherical mode transformation, 1-197
Spheroid, 1-61
Spheroidal lens-radome, 1-79
Spheroidal radomes, 1-63
Spinel, magnesia-alumina, 1-424
Stabilization, 1-439
 antenna, 1-443
Stagnation point, electrical effects, 2-20
 heating, 2-420
Stagnation temperature, 1-285, 2-15, 2-17, 2-46

Static testing, 1-321
elevated temperatures, 1-323
instrumentation, pressure, 1-325
Steatite, 1-420
bisque firing, 1-422
final firing, 1-422
radome batch preparation, 1-420
radome casting, 1-421
Stop bands, 2-118
Streamlined lens-radomes, 1-77
Streamlined radomes, 1-66
focusing effect, 1-66
Strength, radome, 1-297, 2-70
shape, 2-70
slip-cast sintered fused silica, 2-277
tensile, 2-385
thermal environment, 2-70
vs. temperature, alumina, 2-264
Stress, cylindrical ring, 2-66
electromagnetic window, 2-426
methods, 1-300
rupture, 1-316
thermal, 2-44
shock, 1-309
thick-shell radomes, 2-67
thin-shell radome, 2-67
variation, 2-68
Structural design, hypersonic, 2-426
radome, 1-281
window, 2-416
Structural factors, 2-47
Structural requirements, 2-22
Structural support, 2-149
Structural testing, high-temperature, 2-239
Stypols, 2-316
Subsonic radome, 1-282
Subsonic rain erosion, 1-334
ceramics, 1-340
glass, 1-340
Supersonic aircraft, 2-452
Supersonic missiles, 2-452
Supersonic radomes, 1-16
Supersonic rain erosion, 1-17, 1-360
parachute testing, 1-353
test methods, 1-351
Supersonic wind tunnel, 2-232
Support, axial, 2-149
Support, effect on rain erosion, 1-338
Surface-reflection interference, 1-449
Surface temperature, 2-14, 2-29, 2-419, 2-424, 2-426
ballistic reentry, 2-425
Surface treatment, 2-125
Surface-wave dielectrometer, 1-494
Symmetrical sandwiches, 1-41

T

Taper, 1-206
Target depolarization, 1-154
Target scattering, 1-156
Tayloron phenolic-nylon, 2-449
TE mode slotted waveguide arrays, 2-138
Teflon, 2-319
Teflon TFE, 2-450
Temperature, 1-325
boundary layer, 1-291
distribution, 1-284
effects, 1-337, 1-432
equilibrium, 1-287
high, dielectric materials, 2-362
radomes, 1-378, 1-477
reflectometer, 2-359
structural test setup, 2-239
structural testing, 2-239
test facility, 2-237
testing, 2-358
transmission gage, 2-358
recovery factor, 1-290
skin, 2-287, 2-292
surface, 2-14, 2-29, 2-419, 2-424, 2-426
Tensile strength, 2-385
measurement, 2-69
Tensile thermal stress, 2-17, 2-30, 2-47
Tension, glass fiber, 2-303
Tensioner, electromagnetic, 2-303
friction, 2-303
magnetic, 2-303
Terminal guidance, 1-143
Tests, 2-60
electrical, 2-32, 2-63
elevated temperatures, 1-327
environmental, 1-326
low temperature, 1-327
rain erosion, 1-332
results, 2-213, 2-228, 2-230
reflection, 2-350
rocket sled, 2-211
screening, 2-240
supersonic rain erosion, 1-351
thermal, 2-62
thermal shock, 1-326, 2-229
through-transmission, 2-350
Thermal buckling, 1-295

Thermal conductivity, 1-284, 1-429, 2-380
air, 1-289
alumina, 2-267
beryllia, 2-282
cut-bar, 2-381
Pyroceram, 2-273
slip-cast sintered fused silica, 2-277
Thermal diffusivity, 2-382
Thermal environment, 2-70, 2-416
Thermal expansion, 2-390
alumina, 2-266
beryllia, 2-281
ceramic materials, 1-430
Pyroceram, 2-273
slip-cast sintered fused silica, 2-278
Thermal factors, 2-26
Thermal properties, 2-62
dielectric materials, 2-379
Thermal shock, 1-284, 2-429
environment, 2-28
resistance, 2-28
stress, 1-309
tests, 1-326, 2-229, 2-240
oxyacetylene burners, 2-252
oxyhydrogen burners, 2-233
oxypropane burners, 2-232
Thermal stress, 1-295, 1-313, 2-16, 2-44
tensile, 2-17, 2-30, 2-47
Thermally reflective rain erosion coatings, 1-344
Thermocouple, 1-326
Thermolag 500, 2-452
Theta patterns, 2-145
Thick-shell radomes, stresses, 2-67
Thick-skin single sandwich, 2-129
Thickness, 2-38
core, 1-275, 1-298
dielectric, 2-354
electrical, 1-478
face, 1-298
gage, 1-406
microwave, 1-406, 2-351
null shift measurements, 2-352
ultrasonic, 2-348
honeycomb core, 1-378, 1-396
measurement, 2-311
one-half wavelength radome, 2-31
sandwich wall, 1-123
solid-wall, 1-238
thin-wall radome, 2-31
tolerance, 1-48, 1-521
Thin flat sheets, 1-56
Thin homogeneous flat sheet, 1-33
Thin-shell radomes, stresses, 2-67
Thin wall, 1-120, 2-117
construction, 2-4, 2-30
radome, 2-31
Three-layer "A" sandwich radome, 1-3
Three-layer sandwiches, 2-120
Through-transmission test, 2-350
Tiles, alumina, 2-271
Time sequential antenna systems, 1-136
Time sequential lobe comparison systems, 1-132
Tip radii, 2-29, 2-48
TM mode slotted waveguide arrays, 2-138
Tolerances, 1-404
core, 1-573
thickness, 1-48
Tooling, 1-401
Toroidal radomes, 2-250
Transfer molding, 1-400
Transformation spherical mode, 1-197
Transmission, 1-113, 1-273
characteristics, 2-90
coefficients, 1-37, 1-520
axial ratios, 1-51
elliptical polarization, 1-51
homogeneous radomes, 2-130
inhomogeneous radomes, 2-130
lossless plane sheet, 1-85
slotted metal radomes, 2-111
solid dielectric sheet, 1-119
solid-wall radome, 2-118
variation, 1-149
constant, 2-84
contours, 1-106
"A" sandwich, 1-43, 2-128
solid-wall radome, 2-128
efficiency, 1-241
radome, 1-496
tunable radome, 2-133, 2-135
gage, high-temperature, 2-358
impedance measurement, 1-486
resonance method, 1-487
loss, 2-33
E-plane, 2-39
H-plane, 2-40
lens-radome, 1-80
slotted metal radome, 2-112
millimeter-wavelength radome, 2-136
parallel-ray, 1-75
plane-wave, 1-28
thin wall radome, 2-80

Trapped waves, 1-77, 1-151
Tunable radome, 2-131, 2-133, 2-135
Turbulence, 1-455, 1-458
Turbulent heating, 2-421, 2-424
Two-horn interferometer, 1-465

U

Ultrasonic grinding control, 2-310
Ultrasonic thickness gage, 2-348
Uniform ground illumination geometry, 1-98
Unsymmetrical air loading, 1-282

V

Vacuum injection, 1-399
VC-8359 epoxy resin, 2-315
Vehicles, ballistic reentry, 2-451
 hypersonic, 2-453
Velocities, hypersonic, 2-417
 effect, 1-354
VHF radar, 1-3
Vibration testing, 1-327, 2-251
Vibrational forces, 2-52
Vibrin, 2-298
Vibrin 135, 2-300
Vibrin 135-136A, 2-315
Vibrin polyesters, radiation effects, 2-251
Vidigage, Branson, 2-348
Viscosity, air, 1-290
Vitreous silica, 2-273
 properties, 2-275
VSWR evaluation, free-space, 2-405

W

Waffle core, 1-300
Walls (see also "Panels" entries)
 construction, 1-297, 2-3, 2-23
 fluted core, 1-299
 framed-in-place core, 1-299
 honeycomb, 1-298
 laminated, 2-5
 lost wax core, 1-300
 millimeter-wavelength radome, 1-84
 prefabricated foam, 1-299
 solid, 2-4
 waffle core, 1-300
Walls (cont)
 dimension tolerances, 1-521
 gage, electromechanical, 1-473
 half-wave, 1-121, 1-191, 2-117
 laminate, 1-478
 measurements, 1-463
 sandwich, 1-123, 1-301
 solid, 1-301
 thin, 1-120
 thickness, 1-118, 2-46
 gage, 2-346
 tolerances, 1-477, 2-44, 2-80
Waveguide, circular, 1-485
 coaxial, 1-485
 dielectric measurements, 2-367
 principles, 1-483
 rectangular, 1-485
 slotted, 2-138
 wall, loss correction, 1-490
Wavelength, free-space, 2-38
Wedge radome, 1-68, 2-104
Weight factor, 1-106
Wet-dip resin bath, 2-304
Wind tunnel, supersonic, 2-232
Window, ablative, 2-429
 electrical design, 2-416
 electromagnetic, 2-448
 flat, 2-431
 structural design, 2-416
Wire grids, 1-59, 2-106
Wollastonite, 1-425

X

X-band, 1-509
Xonotlite, conversion, 1-425

Y

Yaw, stabilization, 1-441

Z

Zircon, 1-424
Zirconia, 2-282
Zytol 101 polyamide resin, 2-319

UNCLASSIFIED

Security Classification

DOCUMENT CONTROL DATA · R&D

(Security classification of title, body of abstract and indexing annotation must be entered when the overall report is classified)

1. ORIGINATING ACTIVITY (Corporate author)
McGraw-Hill Book Co., Inc., Technical Writing Service
330 West 42nd Street,
New York, New York 10036

2a. REPORT SECURITY CLASSIFICATION
Unclassified

2b. GROUP

3. REPORT TITLE

TECHNIQUES FOR AIRBORNE RADOME DESIGN, VOLUME I

4. DESCRIPTIVE NOTES (Type of report and inclusive dates)

5. AUTHOR(S) (Last name, first name, initial)

Tice, Thomas E. Tice, Dr.,

6. REPORT DATE	7a. TOTAL NO. OF PAGES	7b. NO OF REFS
December 1966	690	

8a. CONTRACT OR GRANT NO.	9a. ORIGINATOR'S REPORT NUMBER(S)
AF33(616)-3279	
b. PROJECT NO. 4158	
c. Task No. 41536	9b. OTHER REPORT NO(S) (Any other numbers that may be assigned this report)
d.	AFAL-TR-66-391, Vol I

10. AVAILABILITY/LIMITATION NOTICES
This document is subject to special export controls and each transmittal to foreign governments or foreign nationals may be made only with prior approval of AFAL (AVPT), Wright-Patterson AFB, Ohio.

11. SUPPLEMENTARY NOTES	12. SPONSORING MILITARY ACTIVITY
	Air Force Avionics Laboratory Research and Technology Division Wright-Patterson AFB, Ohio

13. ABSTRACT

This report was written to provide a summary of the current status of the knowledge of radome design. It is intended to provide scientists and engineers working on radomes with a concise reference containing most of the information they will need. Topics covered include electrical theory, design, and measurements; organic and inorganic materials fabrication; rain erosion; and the effects of temperature, stress, and aerodynamic factors. A comprehensive bibliography is included.
(This abstract is subject to special export controls and each transmittal to foreign gobernments or foreign nationals may be made only with prior approval of AFAL (AVPT), Wright-Patterson AFB, Ohio.

DD FORM 1 JAN 64 1473

UNCLASSIFIED

Security Classification

UNCLASSIFIED

Security Classification

14 KEY WORDS	LINK A		LINK B		LINK C	
	ROLE	WT	ROLE	WT	ROLE	WT
Reentry Radome Design Techniques Ceramic Radome Techniques Hyperenvironmental Radome Design						

INSTRUCTIONS

1. ORIGINATING ACTIVITY: Enter the name and address of the contractor, subcontractor, grantee, Department of Defense activity or other organization *(corporate author)* issuing the report.

2a. REPORT SECURITY CLASSIFICATION: Enter the overall security classification of the report. Indicate whether "Restricted Data" is included. Marking is to be in accordance with appropriate security regulations.

2b. GROUP: Automatic downgrading is specified in DoD Directive 5200.10 and Armed Forces Industrial Manual. Enter the group number. Also, when applicable, show that optional markings have been used for Group 3 and Group 4 as authorized.

3. REPORT TITLE: Enter the complete report title in all capital letters. Titles in all cases should be unclassified. If a meaningful title cannot be selected without classification, show title classification in all capitals in parenthesis immediately following the title.

4. DESCRIPTIVE NOTES: If appropriate, enter the type of report, e.g., interim, progress, summary, annual, or final. Give the inclusive dates when a specific reporting period is covered.

5. AUTHOR(S): Enter the name(s) of author(s) as shown on or in the report. Enter last name, first name, middle initial. If military, show rank and branch of service. The name of the principal author is an absolute minimum requirement.

6. REPORT DATE: Enter the date of the report as day, month, year; or month, year. If more than one date appears on the report, use date of publication.

7a. TOTAL NUMBER OF PAGES: The total page count should follow normal pagination procedures, i.e., enter the number of pages containing information.

7b. NUMBER OF REFERENCES: Enter the total number of references cited in the report.

8a. CONTRACT OR GRANT NUMBER: If appropriate, enter the applicable number of the contract or grant under which the report was written.

8b, 8c, & 8d. PROJECT NUMBER: Enter the appropriate military department identification, such as project number, subproject number, system numbers, task number, etc.

9a. ORIGINATOR'S REPORT NUMBER(S): Enter the official report number by which the document will be identified and controlled by the originating activity. This number must be unique to this report.

9b. OTHER REPORT NUMBER(S): If the report has been assigned any other report numbers *(either by the originator or by the sponsor)*, also enter this number(s).

10. AVAILABILITY/LIMITATION NOTICES: Enter any limitations on further dissemination of the report, other than those imposed by security classification, using standard statements such as:

(1) "Qualified requesters may obtain copies of this report from DDC."

(2) "Foreign announcement and dissemination of this report by DDC is not authorized."

(3) "U. S. Government agencies may obtain copies of this report directly from DDC. Other qualified DDC users shall request through _____."

(4) "U. S. military agencies may obtain copies of this report directly from DDC. Other qualified users shall request through _____."

(5) "All distribution of this report is controlled. Qualified DDC users shall request through _____."

If the report has been furnished to the Office of Technical Services, Department of Commerce, for sale to the public, indicate this fact and enter the price, if known.

11. SUPPLEMENTARY NOTES: Use for additional explanatory notes.

12. SPONSORING MILITARY ACTIVITY: Enter the name of the departmental project office or laboratory sponsoring *(paying for)* the research and development. Include address.

13. ABSTRACT: Enter an abstract giving a brief and factual summary of the document indicative of the report, even though it may also appear elsewhere in the body of the technical report. If additional space is required, a continuation sheet shall be attached.

It is highly desirable that the abstract of classified reports be unclassified. Each paragraph of the abstract shall end with an indication of the military security classification of the information in the paragraph, represented as *(TS), (S), (C), or (U)*.

There is no limitation on the length of the abstract. However, the suggested length is from 150 to 225 words.

14. KEY WORDS: Key words are technically meaningful terms or short phrases that characterize a report and may be used as index entries for cataloging the report. Key words must be selected so that no security classification is required. Identifiers, such as equipment model designation, trade name, military project code name, geographic location, may be used as key words but will be followed by an indication of technical context. The assignment of links, rules, and weights is optional.

UNCLASSIFIED

Security Classification